マイクロフィルム用資料

ISSN 0386-5878
Technical Memorandum
of PWRI No.3843

PROCEEDINGS OF THE 17TH U.S. -JAPAN BRIDGE ENGINEERING WORKSHOP

NOVEMBER 12,13 AND 14, 2001

PUBLIC WORKS RESEARCH INSTITUTE
Independent Administrative Institutions

1-6, Minamihara, Tsukuba-shi, Ibaraki-ken, 305-8516 Japan

Copyright © (2002) by P.W.R.I.

All rights reserved. No part of this book may be reproduced by any means, nor transmitted, nor translated into a machine language without the written permission of the Chief Executive of P.W.R.I.

この報告書は、独立行政法人土木研究所理事長の承認を得て刊行したものである。したがって、本報告書の全部又は一部の転載、複製は、独立行政法人土木研究所理事長の文書による承認を得ずしてこれを行ってはならない。

Technical Memorandum
of PWRI No. 3843

PROCEEDINGS OF THE 17TH U.S. - JAPAN BRIDGE ENGINEERING WORKSHOP

by

Hiroshi Sato

Synopsis:

The proceedings document the results of the 17th U.S. - Japan Bridge Engineering Workshop which was held at Tsukuba, Japan, on November 12, 13 and 14, 2001, under the auspices of the Panel on Wind and Seismic Effects, UJNR. The Workshop was organized by Task Committee G "Transportation Systems" (U.S. side chairman: Mr. J. D. Cooper, FHWA, Japan side chairman: Dr. H. Sato, PWRI) of the Panel.

Key Words: Bridge Management, Health Monitoring, Seismic Design, Seismic Retrofitting , UJNR

FOREWORD

The 17th U.S.- Japan Bridge Engineering Workshop is a continuation of a series of technical interchanges between the United States and Japan on all topics related to bridge engineering. This series of Workshops have been conducted under the auspices of Task Committee G "Transportation Systems" of the U.S.-Japan panel on Wind and Seismic Effects, which is one of some panels making up the United States - Japan Cooperative Program in Natural Resources(UJNR). The previous workshops are indicated in the table.

WORKSHOP	DATE	PLACE
First	February 20-22,1984	Tsukuba, *Japan*
Second	August 19-20,1985	San Francisco, CA, *United States*
Third	May 8-9,1987	Tsukuba, *Japan*
Forth	May 11-12,1988	San Diego, CA, *United States*
Fifth	May 9-10,1989	Tsukuba, *Japan*
Sixth	May 7-8,1990	Lake Tahoe, NV, *United States*
Seventh	May 8-9,1991	Tsukuba, *Japan*
Eighth	May11-12,1992	Chicago, IL, *United States*
Ninth	May 10-11,1993	Tsukuba, *Japan*
Tenth	May 10-11,1994	Lake Tahoe, NV, *United States*
Eleventh	May 30-31,1995	Tsukuba *Japan*
Twelfth	October 29-30,1996	Buffalo, NY, *United States*
Thirteenth	October 2-3,1997	Tsukuba, *Japan*
Fourteenth	November 3-4,1998	Pittsburgh, PA, *United States*
Fifteenth	November 9-10,1999	Tsukuba, *Japan*
Sixteenth	October 2-4,2000	Lake Tahoe, NV, *United States*
Seventeenth	November 12-14,2001	Tsukuba, *Japan*

The 17th U.S. - Japan Bridge Engineering Workshop was organized by Hiroshi Sato, Phillip Yen, Jiro Fukui, Masahiro Nishitani, Manos Maragakis and David Sanders. The principal funding for the workshop was provided by PWRI.

The workshop was held in the NILIM, Tsukuba. The participants of the Workshop reached the total of 89 persons (73 persons from Japan side and 16 from the U.S. side). The main topics of this workshop were 1) seismic performance evaluation including experimental testing and post-earthquake damage evaluation technology, and 2) bridge management including bridge inspection, health monitoring, repair and retrofit technology. In the Workshop, there were 48 presentations (31 papers from Japan side and 17 from the U.S. side).

The study tour was held in three locations: Shizuoka, Mie and Hyogo. On the first day, the delegation visited some repairing and retrofitting sites in Tomei Expressway such as Sena Va., Koyaizu, Va. and Muramatsu Va., etc., in Shizuoka. On the second day, the delegation visited Kiso-gawa Bridge, Ibi-gawa Bridge and Nabeta Va. (the 2nd Tomei Expressway), in Mie. Details of the sites were explained by Japan Highway Public Corporation. On the third day, the delegation visited bridge construction sites in Hanshin Expressway such as corrugated steel web PC bridge and weathering steel bridge, in Hyogo. Details of the sites were explained by Hanshin Expressway Public Corporation.

Participants of the Workshop

TABLE OF CONTENTS

FOREWORD

WORKSHOP PROGRAM 1

PAPERS

SESSION 2: SEISMIC 1 13
(1) Numerical Analysis of the Effects of Liquefaction-induced Ground Flow on Bridge Foundation 15
(Keiichi Tamura and Takuo Azuma)
(2) Seismic Evaluation of the New East-Bay Replacement Spans of the San Francisco-Oakland Bay Bridge 27
(Charles Seim)
(3) Survey on Damaged Piles Adjacent to Quay Wall after a Large Earthquake 35
(Jiro Fukui and Masahiro Nishitani)
(4) Behaviour of Buildings, Bridges and Dams in Bhuj Earthquake of Jaunary 26, 2001 43
(S.K.Thakkar, R. N. Dubey and Pankaj Agarwal)

SESSION 3: MAINTENANCE 1 55
(1) Intelligent Road Surface Inspection System 57
(Shigeru Matsumoto and Koichi Sugioka)
(2) The Effect of Reinforcement of Carbon Fiber Sheets on PC Girders Damaged by Alkali-silica Reaction 67
(Hidetoshi Takagi, Kimitaka Uji, Katsuro Kokubu, Hirokazu Kitazawa, Takehiko Maruyama, Yoshio Sohda, Akira Kobayashi, Nobuhiro Hisabe and Hideaki Fukagawa)
(3) The Application of Water Jet Technology for Removal on Concrete Structure 75
(Syoji Nojima, Koichiro Shito, Yasushi Kamihigashi and Hiroyuki Takenouchi)

SESSION 4: GENERAL 89
(1) First GFRP Pedestrian Bridge in Japan 91
(Shoichi Saeki, Kazuo Yamashiro, Nobuhiko Kitayama, Iton Chou, Naoki Yamamoto and Seishi Meiarashi)
(2) Federally Assisted Bridge Programs in the United States: Past, Present and Future 103
(Raymond McCormick and Edgar P. Small)
(3) Structural Behavior of Steel Girder-RC Pier Composite Rigid Frame Bridge 115
(Noriyuki Suzuki, Yoshinori Igase, Koichi Nishikawa and Toru Sato)
(4) Aerodynamic Stability of a Suspension Bridge with Open Grating Deck 129
(Katsuya Ogihara, Naoki Wada and Shinji Takamori)
(5) Behavior of Prestressed Concrete Beam with New Type of Artificial Lightweight Aggregates made from Fly Ash 139
(Michihiro Sakurada, Hiroyoshi Watanabe, Takashi Ohura and Motoyuki Suzuki)
(6) Fatigue of Aluminum Deck Fabricated by Friction Stir Welding 153
(Ichiro Okura, Nobuyasu Hagisawa, Makoto Naruo and Hitoshi Toda)

SESSION 5: SEISMIC 2 167
(1) Performance of Flared Columns with Gaps 169
(Hisham M. Nada, David H. Sanders and M. "Saiid" Saiidi)
(2) Seismic Retrofitting for Bridges in Osaka City 181
(Kenji Shimoda, Shigeo Takei, Tadaaki Maruyama, Kozo Nishimori and Yukiko Mitsugi)
(3) Retrofit Design and Strategy of the San Francisco-Oakland Bay Bridge Continuous Truss Spans Support Towers Based on ADINA. 195
(R. B. Heninger and R. W. Wolfe)
(4) Preliminary Study on Seismic Retrofit of the Gerber Truss Bridge, the Minato Bridge 201
(Jota Toki, Hidesada Kanaji and Yukio Adachi)
(5) Study on Seismic Behavior of Concrete Columns Strengthened with PC Confined Method 215
(Kiyoshi Kirikawa)

(6) Bridge Condition Monitoring and Assessment 227
(Li-Hong Sheng)

SESSION 6: SEISMIC 3 235
(1) Recommended LRFD Guidelines for the Seismic Design of Highway Bridges 237
(M. Lee Marsh, Ronald L. Mayes and Ian M. Friedland)
(2) A Comparative Study on US-Japan Seismic Isolation Design of Highway Bridges 251
(Hidesada Kanaji, Hamid Ghasemi, Phillip Yen and Sunwoo Park)
(3) An Evaluation of Seismic Bridge Joint Design using Strut-and-Tie Concepts 265
(Sri Sritharan)
(4) Loading Tests on Cap Beams to Evaluate Shear Strength against Earthquakes 277
(Kenji Kosa, Jyunko Taguchi, Satoshi Yoshihara and Katsunori Tanaka)
(5) Seismic Testing of Retrofits in the Central and Southeastern United States 289
(Reginald DesRoches, Thomas Pfeifer and Roberto T. Leon)

SESSION 7: MAINTENANCE 2 301
(1) Structural Health Monitoring in Civil Infrastructures and R & D of SHM of Bridges at the University of Tokyo 303
(Yozo Fujino and Masato Abe)
(2) Evaluation of P-T Tendons Based on Magnetic Flux Leakage and Impact-Echo Techniques 319
(Al Ghorbanpoor)
(3) Experimental Study on the Measuring Method of Steel Girder Stress by Magnetostrictive Method 327
(Ichiro Masuda, Ryosuke Murai, Sinji Nakaya and Seiichi Abuku)
(4) A Concept toward Durable Bridge Design by Use of Weathering Steel 337
(Hiroshi Kihira)
(5) Long-Term Remote Monitoring System for Steel Bridges by Applying Fiber-optic Communication Network 351
(Yuusuke Kobayashi and Chitoshi Miki)

Breakout A1: BRIDGE MANAGEMENT 1 359
(1) A Summary of Current Bridge Management Research of the Federal Highway Administration 361
(Steven B. Chase)
(2) Pontis 4.0 - A Next Generation Bridge Management System 373
(William E. Robert and Allen R. Marshall)
(3) Current State and Revise Policy of the PWRI Bridge Management System 383
(Nobuyuki Hirahara and Akira Moriyama)
(4) Preservation, Improvement and Natural Hazard Considerations in Bridge Management Systems 393
(Edgar P. Small)
(5) Maintenance and Management of Bridges in the Metropolitan Expressway 407
(Tadashi Yoshikawa)

Breakout A2: EARTHQUAKE ENGINEERING 1 419
(1) Size Effect on Ductile Behavior of Reinforced Concrete Columns under Cyclic Loading 421
(Jun-ichi Hoshikuma, Shigeki Unjoh and Kazuhiro Nagaya)
(2) Impulsive Seismic Performance Testing of Reinforced Concrete Bridge Column-Cap Beam Joints 435
(Andre Filiatrault, Natalie Gibson and Scott A. Ashford)
(3) Development of Experimental Guidelines for Bridge Column Testing 449
(Jerry J. Shen and W. Phillip Yen)
(4) Evaluation of Seismic Performance of High-strength Reinforced Concrete Members 457
(Chihiro Kawatoh and Shigeki Unjoh)

Breakout B1: BRIDGE MANAGEMENT 2 467
(1) Study on Required Cover Depth of Concrete Highway Bridges in Coastal Environment 469
(Yoshiki Tanaka, Hirotaka Kawano, Hiroshi Watanabe and Tomoyoshi Nakajo)
(2) Sensitivity Study of a Chloride Penetration Model on Life-Cycle Cost of Post-tensioned Bridges 485
(Shoichi Ogawa and Tamio Yoshioka)
(3) Performance of Electrochemical Chloride Extraction Technology for Concrete Bridge Members Rehabilitation and Ongoing Laboratory Research 499
(Gerardo G. Clemeña, Stephen Sharp and Y. Paul Virmani)

(4) Repairing and Retrofitting the Prestressed Concrete Simple T-Girder Bridge Damaged by Salt-Induced Corrosion 513
(Katsunori Ishimura, Sadaaki Nakamura, Toshio Hosaki and Kazuyoshi Nishina)
(5) Upgrading Concrete Bridges with PBO Prestressing Upgrading Technique (P-PUT) 521
(Z. S. Wu, K. Iwashita, K. Hayashi, T. Higuchi, S. Murakami and Y. Koseki)

Breakout B2: EARTHQUAKE ENGINEERING 2 531
(1) Shake Table Test of Bridge Restrainers at Intermediate Hinges 533
(Fabio Sanchez-Camargo, E. Manos Maragakis, M. Saiid Saiidi and Allaoua Kartoum)
(2) Shaking Table Test of RC Column Subjected to Bilateral Excitation 545
(Hideaki Nishida, Shigeki Unjoh and Kazuhiro Nagaya)
(3) Cyclic Testing of Steel Bridge Truss Pier Brace Members 557
(Michel Bruneau, Kangmin Lee and John Mander)
(4) Structural Health Monitoring and Damage Detection with Dynamic Response 565
(Koichi Yokoyama, Zhishen WU and Bin XU)

OTHER PAPERS 577
Corrosion of Post-Tensioned Tendons in Florida Bridges 579
(Rodney G. Powers, Alberto A. Sagüés and Yash Paul Virmani)
Accelerated Corrosion Test Method for Post-Tensioned Grouts 595
(Niel G. Thompson, Yash P. Virmani and David R. Lankard)

RESOLUTIONS 607

APPENDICES
List of Participants 611
Photos of Study Tour 633

Workshop Program

PROGRAM SCHEDULE

17th U.S.-JAPAN

BRIDGE ENGINEERING WORKSHOP

November 12, 13 and 14, 2001
Tsukuba City, Japan

Public Works Research Institute

17th U.S.-JAPAN BRIDGE ENGINEERING WORKSHOP
PROGRAM SCHEDULE

November 12,13 and 14, 2001
Tsukuba City, Japan

Monday, November 12, 2001 Place: Conference Room (8F) NILIM

SESSION 1: OPENING SESSION 9:00 - 9:15

(Co-Chairmen: Hiroshi Sato, W. Phillip Yen)

Welcome Remarks: Tadahiko Sakamoto (Chief Executive, PWRI)
Remarks: W. Phillip Yen (Acting Chairman for the U.S. Side)
Remarks: Hiroshi Sato (Chairman for the Japan Side)

SESSION 2: SEISMIC 1 9:20 - 10:35

(Co-Chairmen: Ken-ichi Tokida, Michel Bruneau)

(1) Keiichi Tamura and Takuo Azuma (9:20 - 9:32)
"Numerical Analysis of the Effects of Liquefaction-induced Ground Flow on Bridge Foundation"

(2) Charles Seim (9:32 - 9:44)
"Seismic Evaluation of the New East-Bay Replacement Spans of the San Francisco-Oakland Bay Bridge"

(3) Jiro Fukui and Masahiro Nishitani (9:44 - 9:56)
"Survey on Damaged Piles Adjacent to Quay Wall after a Large Earthquake"

(4) S.K.Thakkar, R. N. Dubey and Pankaj Agarwal (9:56 - 10:11)
"Behaviour of Buildings, Bridges and Dams in Bhuj Earthquake of Jaunary 26, 2001"

DISCUSSION (10:11 - 10:35)

COFFEE BREAK 10:35 - 10:50

SESSION 3: MAINTENANCE 1 10:50 - 12:00

(Co-Chairmen: Jiro Fukui, Al Ghorbanpoor)

(1) Shigeru Matsumoto and Koichi Sugioka (10:50 - 11:02)
"Intelligent Road Surface Inspection System"

(2) Hidetoshi Takagi, Kimitaka Uji, Katsuro Kokubu, Hirokazu Kitazawa, Takehiko Maruyama, Yoshio Sohda, Akira Kobayashi, Nobuhiro Hisabe and Hideaki Fukagawa (11:02 - 11:14)
"The Effect of Reinforcement of Carbon Fiber Sheets on PC Girders Damaged by Alkali-silica Reaction"

(3) Syoji Nojima, Koichiro Shito, Yasushi Kamihigashi and Hiroyuki Takenouchi (11:14 - 11:26)
"The Application of Water Jet Technology for Removal on Concrete Structure"

DISCUSSION (11:26 - 12:00)

PHOTOGRAPH *(Entrance of NILIM Main Building)* 12:00 - 12:15

LUNCH *(Conference Room, 1F)* 12:15 - 13:25

SESSION 4: GENERAL 13:25 -15:05

(Co-Chairmen: Koichiro Fumoto, Manos Maragakis)

(1) Shoichi Saeki, Kazuo Yamashiro, Nobuhiko Kitayama, Iton Chou, Naoki Yamamoto and Seishi Meiarashi (13:25 - 13:37)
"First GFRP Pedestrian Bridge in Japan"

(2) Raymond McCormick and Edgar P. Small (Presented by Steven B. Chase) (13:37 - 13:49)
"Federally Assisted Bridge Programs in the United States: Past, Present and Future"

(3) Noriyuki Suzuki, Yoshinori Igase, Koichi Nishikawa and Toru Sato (13:49 - 14:01)
"Structural Behavior of Steel Girder-RC Pier Composite Rigid Frame Bridge"

(4) Katsuya Ogihara, Naoki Wada and Shinji Takamori (14:01 - 14:13)
"Aerodynamic Stability of a Suspension Bridge with Open Grating Deck"

(5) Michihiro Sakurada, Hiroyoshi Watanabe, Takashi Ohura and Motoyuki Suzuki (14:13 - 14:25)
"Behavior of Prestressed Concrete Beam with New Type of Artificial Lightweight Aggregates made from Fly Ash"

(6) Ichiro Okura, Nobuyasu Hagisawa, Makoto Naruo and Hitoshi Toda (14:25 - 14:37)
"Fatigue of Aluminum Deck Fabricated by Friction Stir Welding"

DISCUSSION (14:37 - 15:05)

COFFEE BREAK 15:05 - 15:20

SESSION 5: SEISMIC 2 15:20 - 17:00

(Co-Chairmen: Keiichi Tamura, David Howard Sanders)

(1) Hisham M. Nada, David H. Sanders and M. "Saiid" Saiidi (15:20 - 15:32)
"Performance of Flared Columns with Gaps"

(2) Kenji Shimoda, Shigeo Takei, Tadaaki Maruyama, Kozo Nishimori and Yukiko Mitsugi (15:32 - 15:44)
"Seismic Retrofitting for Bridges in Osaka City"

(3) R. B. Heninger and R. W. Wolfe (15:44 - 15:56)
"Retrofit Design and Strategy of the San Francisco-Oakland Bay Bridge Continuous Truss Spans Support Towers Based on ADINA."

(4) Jota Toki, Hidesada Kanaji and Yukio Adachi (15:56 - 16:08)
"Preliminary Study on Seismic Retrofit of the Gerber Truss Bridge, the Minato Bridge"

(5) Kiyoshi Kirikawa (16:08 - 16:20)
"Study on Seismic Behavior of Concrete Columns Strengthened with PC Confined Method"

(6) Li-Hong Sheng (16:20 - 16:32)
"Bridge Condition Monitoring and Assessment"

DISCUSSION (16:32 - 17:00)

RECEPTION AT OKURA FRONTIER HOTEL TSUKUBA 18:30 - 20:30
(HOSTED BY JAPAN SIDE)

Tuesday, November 13, 2001

Place: Conference Room (8F) NILIM

SESSION 6: SEISMIC 3

9:00 - 10:25

(Co-Chairmen: Tsutomu Nishioka, Charles Seim)

(1) M. Lee Marsh, Ronald L. Mayes and Ian M. Friedland (9:00 - 9:12)
"Recommended LRFD Guidelines for the Seismic Design of Highway Bridges"

(2) Hidesada Kanaji, Hamid Ghasemi, Phillip Yen and Sunwoo Park (9:12 - 9:24)
"A Comparative Study on US-Japan Seismic Isolation Design of Highway Bridges"

(3) Sri Sritharan (9:24 - 9:36)
"An Evaluation of Seismic Bridge Joint Design using Strut-and-Tie Concepts"

(4) Kenji Kosa, Jyunko Taguchi, Satoshi Yoshihara and Katsunori Tanaka (9:36 - 9:48)
"Loading Tests on Cap Beams to Evaluate Shear Strength against Earthquakes"

(5) Reginald DesRoches, Thomas Pfeifer and Roberto T. Leon (9:48 - 10:00)
"Seismic Testing of Retrofits in the Central and Southeastern United States"

DISCUSSION (10:00 - 10:25)

COFFEE BREAK 10:25 - 10:40

SESSION 7: MAINTENANCE 2

10:40 – 12:05

(Co-Chairmen: Hiroshi Watanabe, Li-Hong Sheng)

(1) Yozo Fujino and Masato Abe (10:40 - 10:52)
"Structural Health Monitoring in Civil Infrastructures and R & D of SHM of Bridges at the University of Tokyo"

(2) Al Ghorbanpoor (10:52 -11:04)
"Evaluation of P-T Tendons Based on Magnetic Flux Leakage and Impact-Echo Techniques"

(3) Ichiro Masuda, Ryosuke Murai, Sinji Nakaya and Seiichi Abuku (11:04 - 11:16)
"Experimental Study on the Measuring Method of Steel Girder Stress by Magnetostrictive Method"

(4) Hiroshi Kihira (11:16 - 11:28)
"A Concept toward Durable Bridge Design by Use of Weathering Steel"

(5) Yuusuke Kobayashi and Chitoshi Miki (11:28 - 11:40)
" Long-Term Remote Monitoring System for Steel Bridges by Applying Fiber-optic Communication Network "

DISCUSSION (11:40 - 12:05)

LUNCH *(Conference Room, 1F)* 12:05 - 13:20

Breakout A1: BRIDGE MANAGEMENT 1 13:20 - 17:00

Place: Conference Room 526 (5F) NILIM

(Co-Chairmen: Koichiro Fumoto, Steven B. Chase)

(1) Steven B. Chase (13:20 - 13:35)
"A Summary of Current Bridge Management Research of the Federal Highway Administration"

(2) William E. Robert and Allen R. Marshall (13:35 - 13:50)
"Pontis 4.0 - A Next Generation Bridge Management System"

(3) Nobuyuki Hirahara and Akira Moriyama (13:50 - 14:05)
"Current State and Revise Policy of the PWRI Bridge Management System"

(4) Edgar P. Small (14:05 - 14:20)
"Preservation, Improvement and Natural Hazard Considerations in Bridge Management Systems"

(5) Tadashi Yoshikawa (14:20 - 14:35)
"Maintenance and Management of Bridges in the Metropolitan Expressway"

DISCUSSION (14:35 - 15:10)

COFFEE BREAK (15:10 - 15:40)

DISCUSSION/PLANNING (15:40 - 17:00)

Breakout A2: EARTHQUAKE ENGINEERING 1 13:20 - 17:00

Place: Conference Room (8F) NILIM

(Co-Chairmen: Shigeki Unjoh, W. Phillip Yen)

(1) Jun-ichi Hoshikuma, Shigeki Unjoh and Kazuhiro Nagaya (13:20 - 13:35)
"Size Effect on Ductile Behavior of Reinforced Concrete Columns under Cyclic Loading"

(2) Andre Filiatrault, Natalie Gibson and Scott A. Ashford (13:35 - 13:50)
"Impulsive Seismic Performance Testing of Reinforced Concrete Bridge Column-Cap Beam Joints"

(3) Fumihiko Yazaki (13:50 - 14:05)
"ISO 22762 Elastometric Isolator, Progress Report"

(4) Jerry J. Shen and W. Phillip Yen (14:05 - 14:20)
"Development of Experimental Guidelines for Bridge Column Testing

(5) Chihiro Kawatoh and Shigeki Unjoh (14:20 - 14:35)
"Evaluation of Seismic Performance of High-strength Reinforced Concrete Members"

DISCUSSION (14:35 - 15:10)

COFFEE BREAK (15:10 - 15:40)

DISCUSSION/PLANNING (15:40 - 17:00)

RECEPTION AT LAMBROISIE DE KAGETSUROH 18:30 - 20:30
(HOSTED BY U.S. SIDE)

Wednesday, November 14, 2001

Breakout B1: BRIDGE MANAGEMENT 2 9:00 - 11:45

Place: Conference Room 526 (5F) NILIM

(Co-Chairmen: Hirotaka Kawano, Gerardo G. Clemeña)

(1) Yoshiki Tanaka, Hirotaka Kawano, Hiroshi Watanabe and Tomoyoshi Nakajo (9:00 - 9:15)
"Study on Required Cover Depth of Concrete Highway Bridges in Coastal Environment"

(2) Shoichi Ogawa and Tamio Yoshioka (9:15 - 9:30)
"Sensitivity Study of a Chloride Penetration Model on Life-Cycle Cost of Post-tensioned Bridges"

(3) Gerardo G. Clemeña, Stephen Sharp and Y. Paul Virmani (9:30 - 9:45)
"Performance of Electrochemical Chloride Extraction Technology for Concrete Bridge Members Rehabilitation and Ongoing Laboratory Research"

(4) Katsunori Ishimura, Sadaaki Nakamura, Toshio Hosaki and Kazuyoshi Nishina (9:45 - 10:00)
"Repairing and Retrofitting the Prestressed Concrete Simple T-Girder Bridge Damaged by Salt-Induced Corrosion"

(5) Z. S. Wu, K. Iwashita, K. Hayashi, T. Higuchi, S. Murakami and Y. Koseki (10:00 - 10:15)
"Upgrading Concrete Bridges with PBO Prestressing Upgrading Technique (P-PUT) "

DISCUSSION (10:15 - 10:45)

COFFEE BREAK (10:45 - 11:00)

DISCUSSION/PLANNING (11:00 - 11:45)

Breakout B2: EARTHQUAKE ENGINEERING 2 9:00 - 11:45

Place: Conference Room (8F) NILIM

(Co-Chairmen: Shigeki Unjoh , W. Phillip Yen)

(1) Fabio Sanchez-Camargo, E. Manos Maragakis, M. Saiid Saiidi and Allaoua Kartoum (9:00 - 9:15)
"Shake Table Test of Bridge Restrainers at Intermediate Hinges"

(2) Hideaki Nishida, Shigeki Unjoh and Kazuhiro Nagaya (9:15 - 9:30)
"Shaking Table Test of RC Column Subjected to Bilateral Excitation"

(3) Michel Bruneau, Kangmin Lee and John Mander (9:30 - 9:45)
"Cyclic Testing of Steel Bridge Truss Pier Brace Members"

(4) Koichi Yokoyama, Zhishen WU and Bin XU (9:45 - 10:00)
"Structural Health Monitoring and Damage Detection with Dynamic Response"

DISCUSSION (10:00 - 10:45)

COFFEE BREAK (10:45 - 11:00)

DISCUSSION/PLANNING (11:00 - 11:45)

CLOSING SESSION 11:45 - 12:00

(Co-Chairmen: Hiroshi Sato, W. Phillip Yen)

Settlement of Resolution
Remarks: W. Phillip Yen (Acting Chairman for the U.S. side)
Closing Remarks: Hiroshi Sato (Chairman for the Japan side)

SESSION 2: SEISMIC 1

(1) Numerical Analysis of the Effects of Liquefaction-induced Ground Flow on Bridge Foundation

(Keiichi Tamura and Takuo Azuma)

(2) Seismic Evaluation of the New East-Bay Replacement Spans of the San Francisco-Oakland Bay Bridge

(Charles Seim)

(3) Survey on Damaged Piles Adjacent to Quay Wall after a Large Earthquake

(Jiro Fukui and Masahiro Nishitani)

(4) Behaviour of Buildings, Bridges and Dams in Bhuj Earthquake of Jaunary 26, 2001

(S.K.Thakkar, R. N. Dubey and Pankaj Agarwal)

NUMERICAL ANALYSIS OF THE EFFECTS OF LIQUEFACTION-INDUCED GROUND FLOW ON BRIDGE FOUNDATION

Keiichi Tamura[1] and Takuo Azuma[2]

ABSTRACT

The liquefaction-induced ground flow inflicted serious damage to various engineering structures including highway bridges in the Hyogo-ken Nanbu (Kobe) Earthquake of 1995. Although highway bridges did not suffer destructive damage due to liquefaction, liquefaction-induced ground flow caused large deformation of bridge foundations. In this paper, we propose a new technique for examining the effects of liquefaction-induced ground flow on bridge foundation. This technique is comprised of the three steps of analysis, i.e., liquefaction potential estimation, ground deformation analysis and seismic deformation analysis. The first two steps aim to obtain ground deformation resulting from liquefaction-induced ground flow, and the third step is to compute the deformation of bridge foundation caused by ground deformation. Comparing the results of numerical analysis with those observed in the 1995 Kobe Earthquake, the validity of proposed technique is demonstrated.

INTRODUCTION

The Hyogo-ken Nanbu (Kobe) Earthquake of 1995 caused extensive soil liquefaction over a wide area of offshore reclaimed lands and natural deposits (Japanese Geotechnical Society, 1996; Japan Society of Civil Engineers, 1996). Besides that, near the water's edge, liquefaction induced ground flow with the movement of sea walls. Aerial photogrammetry revealed that the maximum residual displacement of ground flow reached 3 to 4m (Hamada *et al.*, 1995; Public Works Research Institute, 1997). The liquefaction-induced ground flow inflicted serious damage to various engineering structures including highway bridges in the 1995 Kobe Earthquake. Although highway bridges did not suffer destructive damage due to liquefaction, liquefaction-induced ground flow caused large deformation of bridge foundations. Tamura *et al.* (1996, 2000) studied the ground flow force acting on bridge foundation by back analysis of damaged foundations, and the results were incorporated into the Design Specifications for Highway Bridges (Japan Road Association, 1996a), which were revised after the Kobe Earthquake. Due to the complexities of liquefaction-induced ground flow, vigorous efforts have still been continuing to study its mechanism and influence upon structures (e.g., Hamada and Wakamatsu, 1998; Ogasawara *et al.*, 2000; Tamura and Azuma, 1997; Towhata *et al.*, 1999; Yasuda *et al.*, 1999).

This paper presents a newly proposed technique for examining the effects of liquefaction-induced ground flow on bridge foundation. In this technique, we first assess liquefaction potential and estimate the degree of liquefaction. Then, we obtain ground deformation resulting from liquefaction-induced ground flow by self-weight analysis of the ground, in which shear modulus of soil is reduced according to the degree of liquefaction. Finally, we

[1] Team Leader, Ground Vibration Research Team, Public Works Research Institute, Japan
[2] Research Administration and International Cooperation Division, National Institute for Land and Infrastructure Management, Japan

compute the deformation of bridge foundation by statically applying ground displacements to the foundation. We calibrate the proposed technique by comparing the analytical results with the field measurement data in the 1995 Kobe Earthquake. The bridge pier analyzed is located at the south edge of Uozakihama man-made island, and suffered 62cm residual displacement in the longitudinal direction due to liquefaction-induced ground flow (Public Works Research Institute, 2000).

METHOD

As illustrated in Figure 1, we first estimate liquefaction potential at several locations that possess different soil profiles. We employ a 1-D equivalent linear method for seismic response analysis of the ground, and the liquefaction resistance factor is computed using the cumulative damage theory, which was originally developed in the area of fatigue failure. Secondly, we compute ground deformation resulting from liquefaction-induced ground flow by self-weight analysis of the ground, in which shear modulus of soil is reduced according to the degree of liquefaction. Deformation caused by self-weight of the ground is computed by a 2-D finite element method, and the resultant deformation is regarded as that caused by ground flow. Thirdly, we obtain distribution of ground displacement along bridge foundation, and statically apply it to the foundation, in which the bridge foundation is so idealized that a rigid footing is supported by piles that are supported by soils, considering nonlinear properties of pile bodies and the ground.

ESTIMATION OF LIQUEFACTION POTENTIAL

Figure 2 gives a schematic view of the model for 2-D self-weight analysis. The bridge pier analyzed is located 31m apart from the water's edge. Locations where we estimate liquefaction potential are the front and back of the quay wall, and the horizontally layered site that is far behind the quay wall. These three locations, which are indicated in Figure 2, are chosen to represent the typical soil profiles in the analytical model.

We compute the dynamic shear stress ratio during an earthquake, in which the 1-D equivalent linear analysis code "SHAKE" (Schnabel et al., 1972) is employed. Figures 3 and 4 show soil profile models and dynamic properties of soils, respectively. Then, we obtain the liquefaction strength ratio R_L using the modified cumulative damage theory developed by Tatsuoka *et al.* (1986). In the modified cumulative damage theory, time history of shear stress ratio is decomposed into pulses that up- and down-cross the 0-line. Applying the amplitude of each pulse to the equivalent cyclic shear stress ratio by means of the liquefaction strength curve, the corresponding number of cycles can be obtained. Figure 5 shows the liquefaction strength curve used (Port and Harbour Research Institute, 1995). The sum of reciprocal of cyclic numbers is called the cumulative damage D, and soil is regarded to liquefy when D exceeds 1.0. We calculate D by changing the amplitude of shear stress ratio, and define the peak amplitude of it as R_L when D exceeds 1.0.

The maximum shear stress ratio L_{max} is obtained from the result of seismic response analysis, and finally the liquefaction resistance factor F_L is defined as $F_L=R_L/L_{max}$. Two horizontal components of strong motion record obtained at 83m below the ground surface in the diluvial gravel layer at Port Island are employed as input motions, and that yields smaller F_L is adopted for the following analysis. Figure 6 gives computation results of L_{max}, R_L and F_L.

GROUND DEFORMATION ANALYSIS

Prior to the ground deformation analysis in which the reduced shear modulus resulting from liquefaction is used, we estimate the initial shear modulus G_N from the blow count per foot by the standard penetration test as follows (Japan Road Association, 1996b):

$$E_0=28N \tag{1}$$
$$G_N= E_0/2(1+\nu) \tag{2}$$

where,

E_0: modulus of deformation (kgf/cm^2)
N: blow count per foot by the standard penetration test
G_N: shear modulus (kgf/cm^2)
ν: Poisson's ratio

In the ground deformation analysis, we reduce the shear modulus of liquefied layer according to the liquefaction resistance factor F_L. Yasuda *et al.* (1999) studied the change of shear modulus before and after liquefaction by laboratory tests in which sand samples were subjected to monotonic load after subjected to cyclic load causing liquefaction. Their results are expressed as the relationship between F_L and reduction ratio of shear modulus, which is indicated by open circles in Figure 7, and we derive the following equation by smoothly fitting the data:

$$G_l / G_N = \exp\left\{-5.6/\left(F_L^{0.35}+0.31F_L^{18}\right)\right\} \tag{3}$$

where G_l denotes the shear modulus of liquefied soil. Using eq.(3), the reduction ratios are obtained as 1/450 for fill sand, 1/370 for backfill sand, 1/130 for land-side replaced sand and 1/750 for sea-side replaced sand. In the following self-weight analysis, we assume the shear modulus of surface non-liquefied layer 150 times as large as that of liquefied fill sand, which yields surface ground displacement that is consistent with measurement after the 1995 Kobe Earthquake. Tables 1 and 2 summarize soil properties before and after liquefaction.

We employ a 2-D finite element method for self-weight analysis. The analytical model, which is shown in Figure 2, consists of 2,255 nodes and 2,142 elements. We restrict horizontal motion on the lateral boundaries and restrict both horizontal and vertical motions on the bottom boundary. Joint elements are placed at the back and bottom of quay wall to allow slip and exfoliation. Figure 8 shows the computed ground deformation. We see from this figure that the quay wall moves toward the sea, standing almost up straight. Ground behind the quay wall subsides, while sea bottom in front of the quay wall rises up. Shear strains are concentrated beneath the quay wall.

Horizontal displacement and settlement on the ground surface are plotted against distance from the water's edge in Figure 9. Those surveyed after the 1995 Kobe Earthquake are also shown in the same figure. The general trend of computed displacement agrees with that of field measurement. Large settlement is observed over the 30m range from the water's edge. Figure 10 gives the distribution of horizontal displacement at the location of bridge pier

analyzed, i.e., 31m apart from the water's edge. Displacement on the ground surface is estimated as 1.8m at this location. Ground displacement increases markedly from 18m below the surface. Note that this depth corresponds to the lower bound of liquefied layer and ground displacement is mainly amplified in this layer.

SEISMIC DEFORMATION ANALYSIS

A bridge foundation is so idealized that a rigid footing is supported by piles that are supported by soils, considering nonlinear properties of pile bodies and the ground, as illustrated in Figure 11. This model was developed after the 1995 Kobe Earthquake (Japan Road Association, 1995), and has been incorporated into the Design Specifications for Highway Bridges (Japan Road Association, 1996b). Figure 12 presents the foundation model for seismic deformation analysis. This model consists of 635 nodes and 266 elements (210 beam elements and 56 spring elements). We allow both horizontal and vertical motions and restrict rotational motion at the tip of pile.

Ground deformation along the pile foundation, which was obtained in the former section, is statically applied to the foundation model through springs. Dead load of superstructure is also applied to the footing. Figure 13 shows pile deformation and distribution of bending moment. Number of cracks and crack width that were monitored by borehole camera are also shown in the same figure. Horizontal displacement at the top of pile is computed as 60cm. The residual displacement after the 1995 Kobe Earthquake, which was measured at the bottom of pier column, is 62cm. The computed displacement coincides with the measured one. Bending moment at the top of pile and that between 20 and 23m exceed the yield moments. This is consistent with the fact that wide cracks were observed at those depths.

CONCLUSIONS

In order to estimate the effects of liquefaction-induced ground flow on bridge foundation, we propose a new technique that integrates liquefaction potential estimation, ground deformation analysis and seismic deformation analysis. We apply this technique to the bridge foundation that suffered residual displacement due to liquefaction-induced ground flow in the 1995 Kobe Earthquake, and compare the analytical results with field measurements. The following conclusions may be deduced from the present study.

1) Ground deformation analysis with appropriate assessment of soil properties yields a good approximation of the ground displacement caused by liquefaction-induced ground flow. Analytical result agrees well with the measured attenuation characteristics of ground displacement with the increase of distance from the water's edge.

2) The seismic deformation analysis well estimates the deformation of pile foundation. Pile deformation and bending moment by the proposed method are consistent with the residual displacement of bridge pier and measured crack distributions.

ACKNOWLEDGMENTS

The authors would like to express deep appreciation to the personnel of Kobe City for providing the valuable strong motion data obtained at Port Island.

REFERENCES

Hamada, M., Isoyama, R. and Wakamatsu, K. (1995). *The 1995 Hyogoken-Nanbu (Kobe) Earthquake, Liquefaction, Ground Displacement and Soil condition in Hanshin Area*, Association for Development of Earthquake Prediction.

Hamada, M. and Wakamatsu, K. (1998). "A Study on Ground Displacement Caused by Soil Liquefaction", *Journal of JSCE*, No.596 (in Japanese).

Japan Road Association (1995). *Reference for Applying the Guide Specifications for Reconstruction and Repair of Highway Bridges which Suffered Damage due to the Hyogo-ken Nanbu Earthquake of 1995* (in Japanese).

Japan Road Association (1996a). *Design Specifications for Highway Bridges, Part V Seismic Design* (in Japanese).

Japan Road Association (1996b). *Design Specifications for Highway Bridges, Part IV Foundations* (in Japanese).

Japan Society of Civil Engineers (1996). *The 1995 Hyogoken-Nanbu Earthquake - Investigation into Damage to Civil Engineering Structures -*.

Japanese Geotechnical Society (1996). *Special Issue on Geotechnical Aspects of the January 17 1995 Hyogoken-Nambu Earthquake*.

Ogasawara, M. *et al.* (2000). "A Study on Design Method of Bridge Foundation against Ground Flow", *Journal of JSCE*, No.645 (in Japanese).

Port and Harbour Research Institute (1995). "Mechanism of Damage to Port Facilities during 1995 Hyogo-ken Nanbu Earthquake", *Technical Note of PHRI*, No.813.

Public Works Research Institute (1997). "Report on the Disaster Caused by the 1995 Hyogoken Nanbu Earthquake", *Journal of Research*, Vol.33, Public Works Research Institute.

Public Works Research Institute (2000). "Back Analysis of Liquefaction-Induced Ground Flow Force Acted on Bridge Foundation", *Technical Memorandum of PWRI*, No.3770.

Schnabel, P. B., Lysmer, J. and Seed, H. B. (1972). "SHAKE - A Computer Program for Earthquake Response Analysis of Horizontally Layered Sites", *EERC Report*, No.72-12, University of California, Berkeley.

Tamura, K., Azuma, T. and Hamada, T. (1996). "Seismic Design Treatment of Liquefaction- Induced Ground Flow", *Proc. of Third U.S.-Japan Workshop on Seismic Retrofit of Bridges*, U.S.-Japan Panel on Wind and Seismic Effects, UJNR.

Tamura, K. and Azuma, T. (1997). "Experimental Study of the Effects of Liquefaction- Induced Ground Flow on Bridge Foundation", *Proc. of 13th U.S.-Japan Bridge Engineering Workshop*, U.S.-Japan Panel on Wind and Seismic Effects, UJNR.

Tamura, K., Azuma, T. and Hamada, T. (2000). "Seismic Design of Bridge Foundations against Liquefaction-Induced Ground Flow", *Proc. of 12th World Conference on Earthquake Engineering*.

Tatsuoka, F., Maeda, S., Ochi, K. and Fujii, S. (1986). "Prediction of Cyclic Undrained Strength of Sand Subjected to Irregular Loading", *Soils and Foundations*, Vol.26, No.2.

Towhata, I., Orense, R. P. and Toyota, H. (1999). "Mechanical Principles in Prediction of Lateral Ground Displacement Induced by Seismic Liquefaction", *Soils and Foundations*, Vol.39, No.2.

Yasuda, S. *et al.* (1999). "A Simplified Practical Method for Evaluating Liquefaction- Induced Flow", *Journal of JSCE*, No.638 (in Japanese).

Table 1 Soil properties before liquefaction

Location		Modulus of Deformation E_0 (tf/m^2)	Poisson's Ratio ν	Angle of Shear Resistance ϕ (deg)	Unit Weight γ(tf/m^3)
Fill Sand	Above Groundwater	2800	0.33	30	1.80
	Below Groundwater	2800	0.33	30	0.77
Replaced Sand	Land-side	2800	0.33	30	0.77
	Sea-side	2800	0.33	30	0.77
Alluvial Clay	Land-side	2400	0.45	0	0.57
	Sea-side	9300	0.45	0	0.57
Diluvial Sand 1	Land-side	19500	0.33	30	0.77
	Beneath Quay Wall	26000	0.33	30	0.77
	Sea-side	8000	0.33	30	0.77
Diluvial Sand 2	Land-side	44000	0.33	30	0.77
	Sea-side	25000	0.33	30	0.77
Foundation Rubble	Land-side	2800	0.33	30	0.77
	Beneath Quay Wall	2800	0.33	30	0.77
	Sea-side	484	0.33	30	0.77
Quay Wall	Above Groundwater	2.5×10^6	0.167	-	2.20
	Below Groundwater	2.5×10^6	0.167	-	1.17

Table 2 Soil properties after liquefaction

Location		Liquefaction Resistance Factor F_L	Shear Modulus Reduction G_I/G_N	Shear Modulus G_I (tf/m^2)	Modulus of Deformation E_0 (tf/m^2)	Poisson's Ratio ν
Fill Sand (Above Groundwater)		-	1/3	352.7	938.1	0.33
Fill Sand (Below Groundwater)		0.79	1/448	2.086	6.25	0.499
Backfill Sand		0.84	1/374	2.497	7.49	0.499
Replaced Sand	Land-side	0.97	1/133	7.016	21.03	0.499
	Sea-side	0.63	1/752	1.241	3.72	0.499

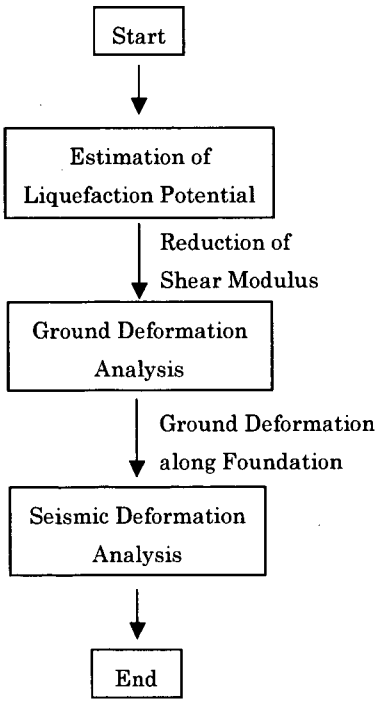

Figure 1 Analytical flow

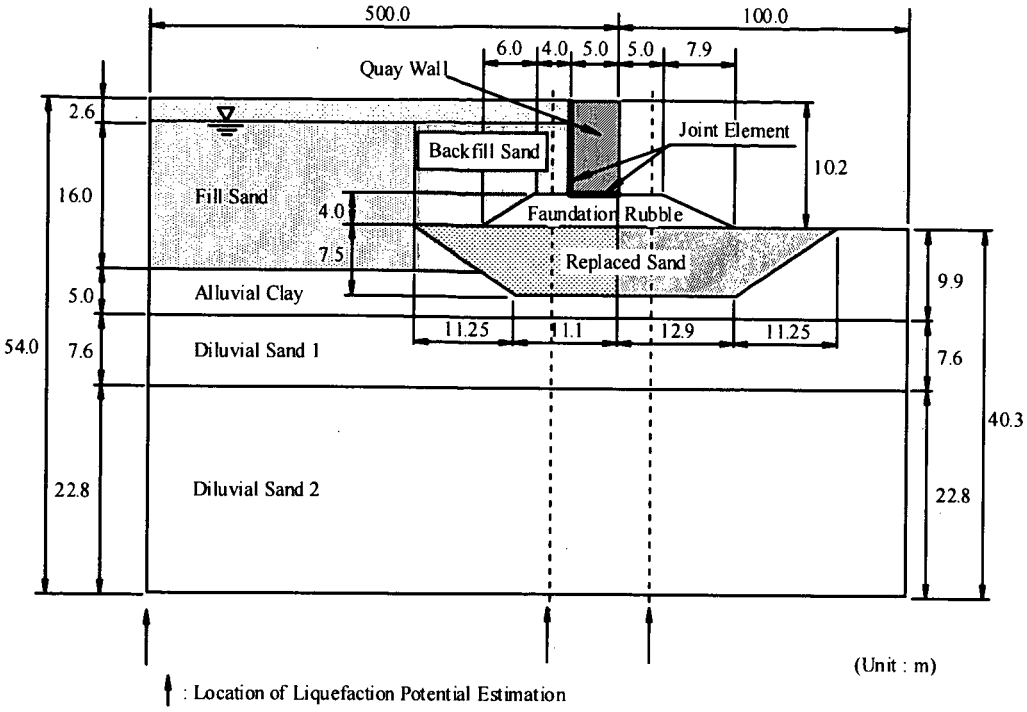

Figure 2 Analytical model

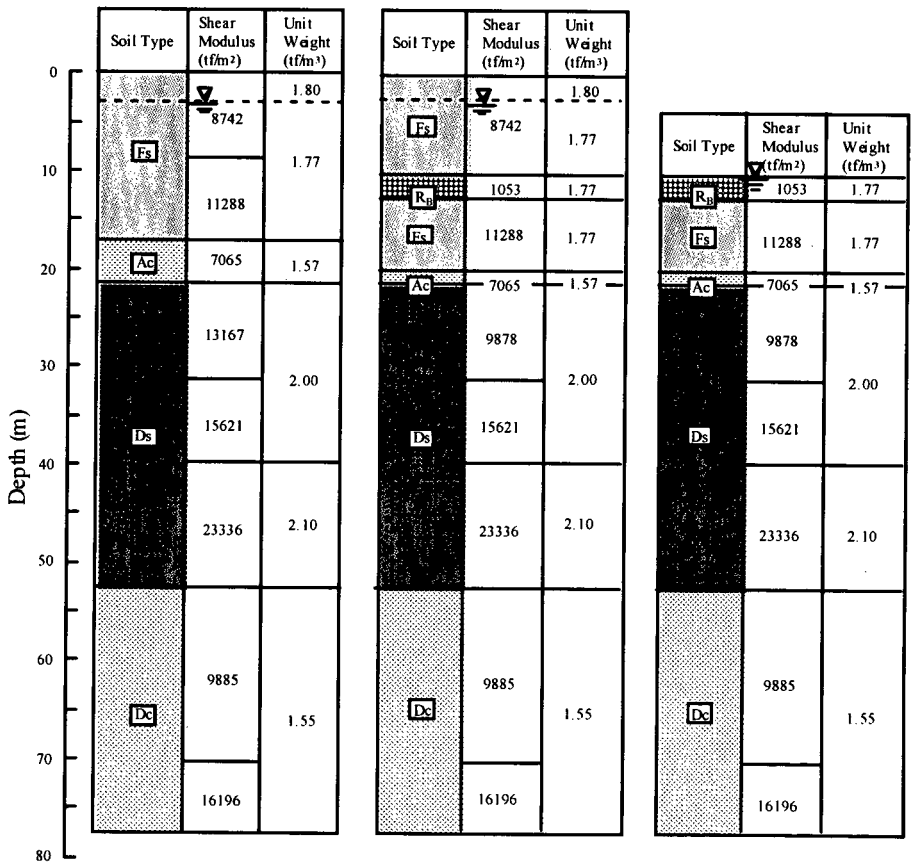

(a) Horizontally Layered Part (b) Back of Quay Wall (c) Front of Quay Wall

Figure 3 Soil profile

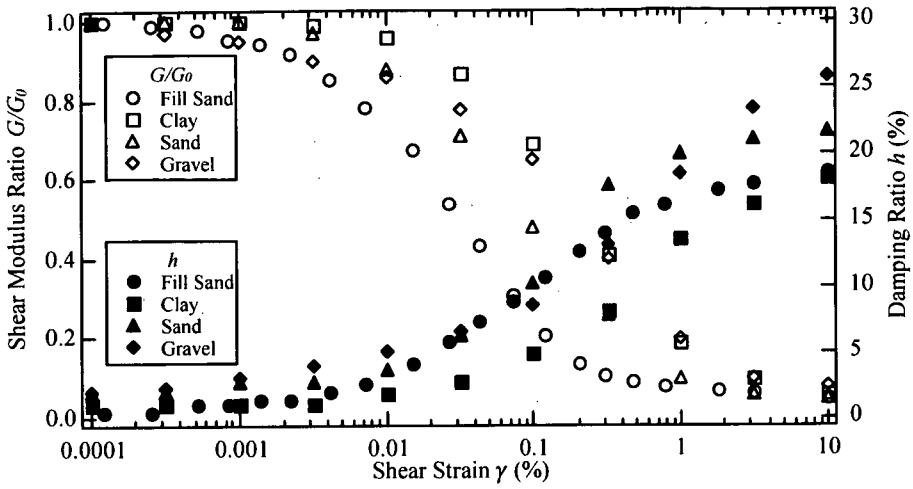

Figure 4 Dynamic property of soil

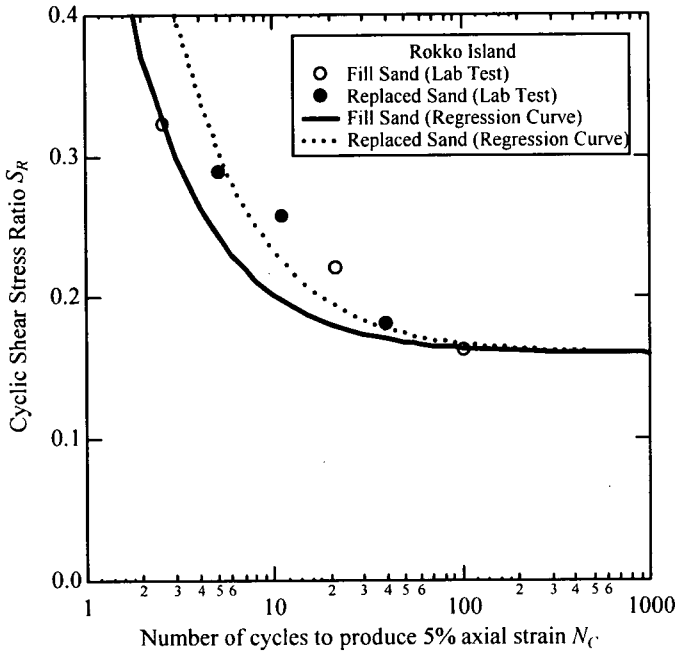

Figure 5 Liquefaction strength curve

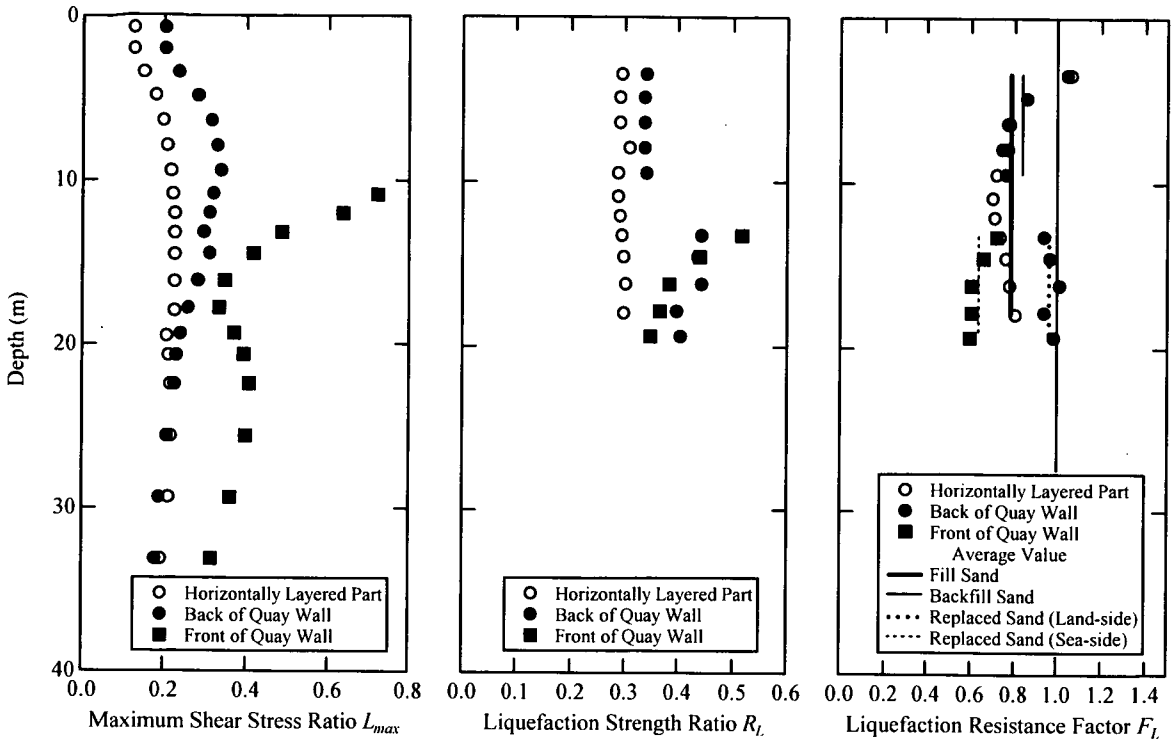

Figure 6 Results of liquefaction potential estimation

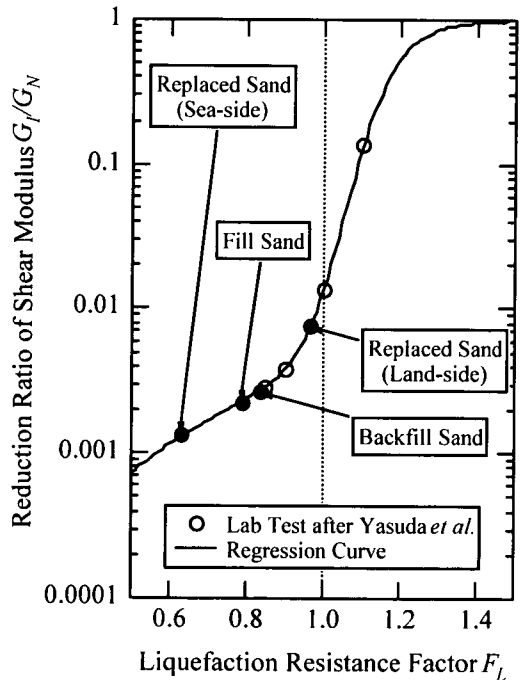

Figure 7 Reduction of shear modulus

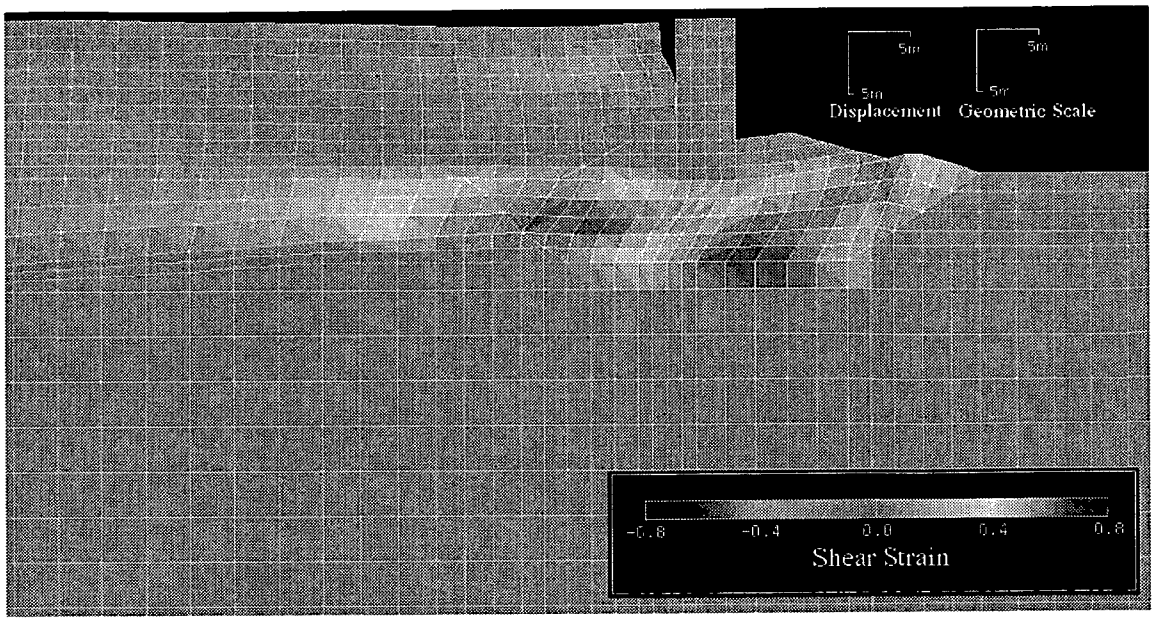

Figure 8 Ground deformation

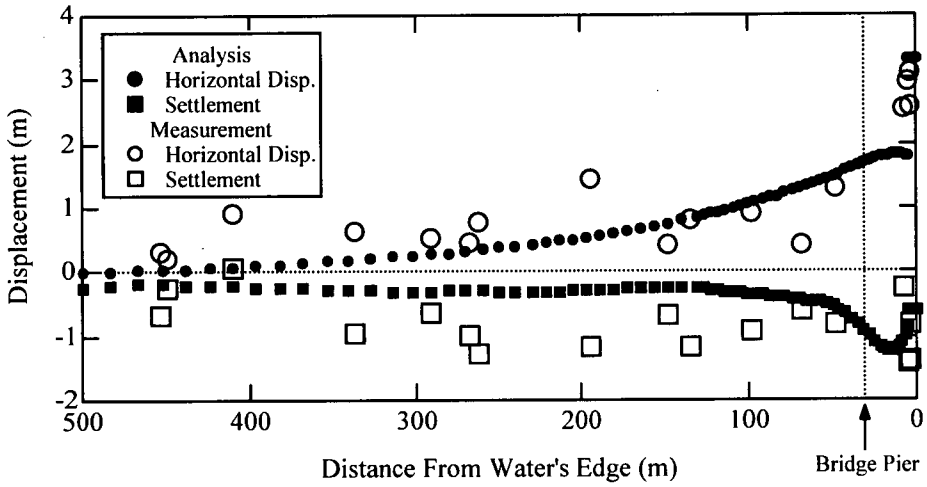

Figure 9 Ground surface displacement

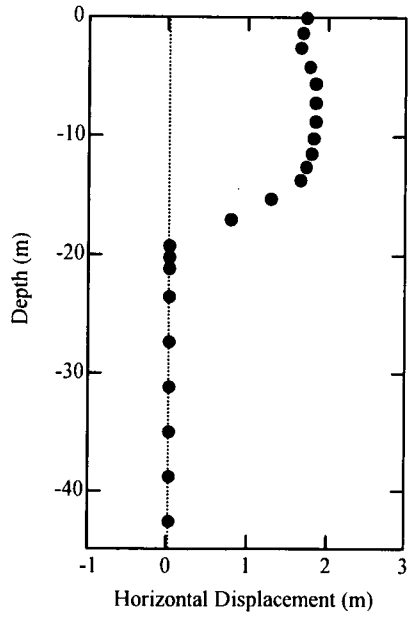

Figure 10 Distribution of ground displacement along the foundation

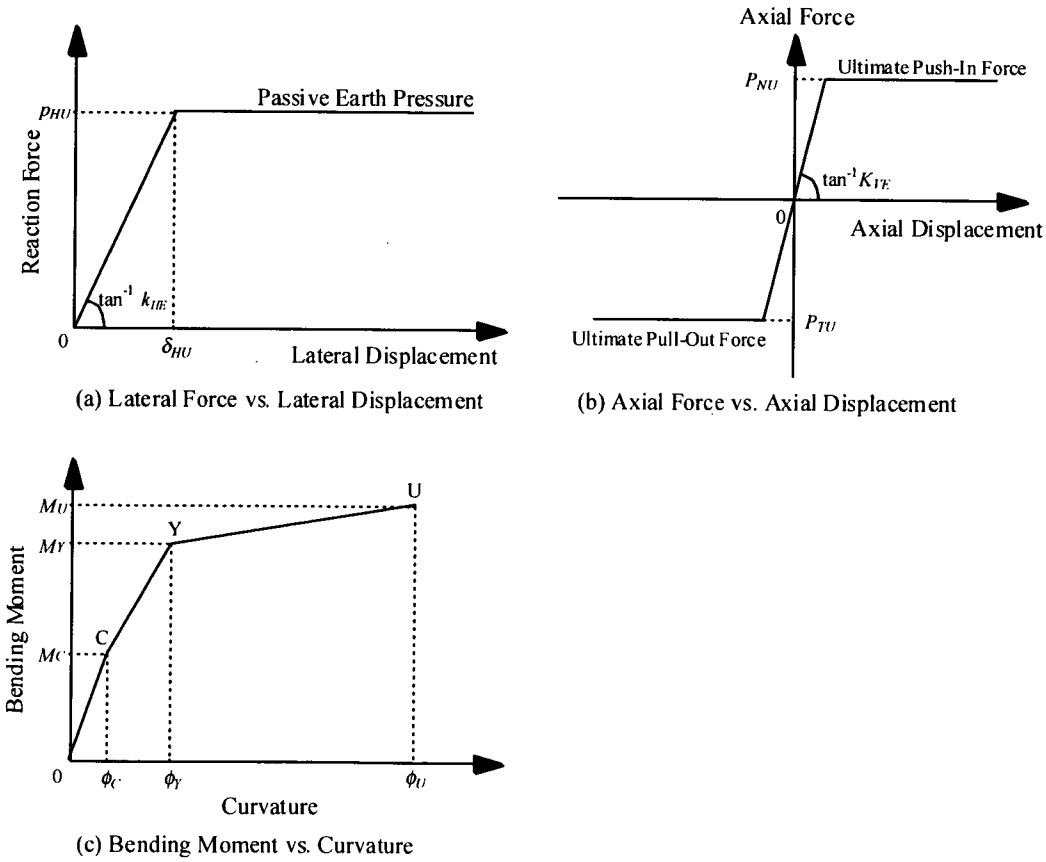

Figure 11 Idealization of pile foundation for nonlinear analysis

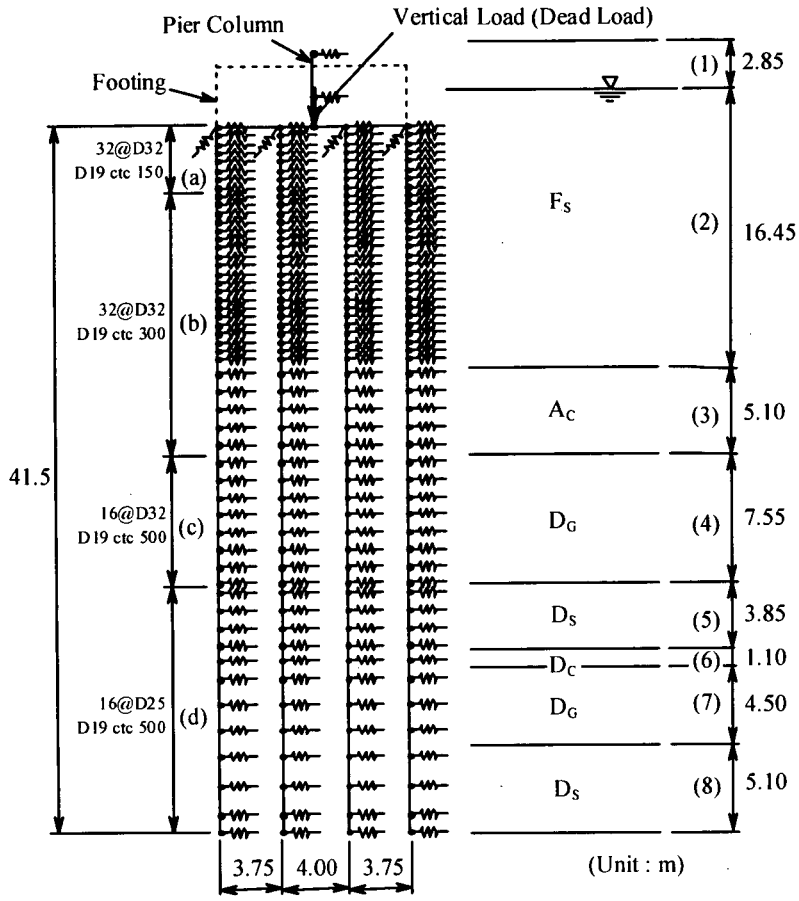

Figure 12 Analytical model of foundation

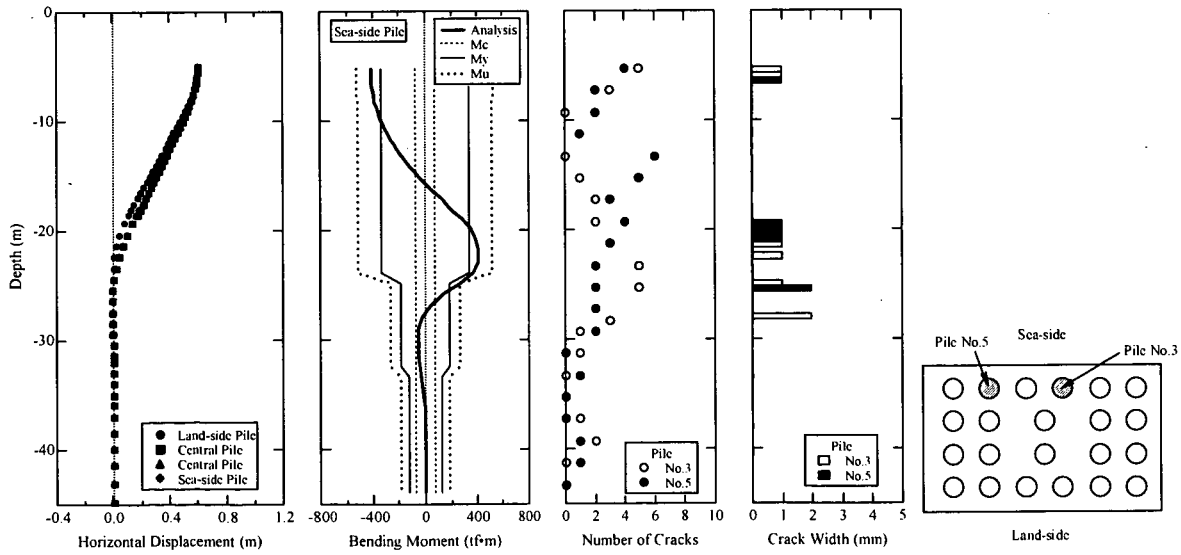

Figure 13 Pile deformation, bending moment and crack distribution

SEISMIC EVALUATION OF THE NEW EAST- BAY REPLACEMENT SPANS OF THE SAN FRANCISCO-OAKLAND BAY BRIDGE

Charles Seim [1]

Abstract

The 65-year old seismically vulnerable East Span of the San Francisco-Oakland Bay Bridge will be replaced with two parallel east bound and west bound 3.6 km long structures. The cost of the Replacement Bridge is estimated at $ 2 billion and the bridge will be constructed by the year 2005. The Bay Bridge lies between the Hayward and the San Andreas faults, which can generate magnitude 7.5 M and 8.1 M earthquakes, respectively. Performance criteria require that the bridge must be operational immediately following a 1500-year return period earthquake from either of these two faults. Two principal structures will make up the bridge crossing: a 2.4 km long segmental concrete box girder and a self-anchored suspension bridge signature span. Prestressed concrete approach structures connect the Oakland shore to the segmental concrete box girder and the suspension bridge to Yerba Buena Island, in the center of the Bay. This paper focuses on the seismic evaluation and design of the self-anchored suspension span, design of the main, and its major structural and architectural characteristics.

Introduction

The San Francisco-Oakland Bay Bridge was constructed in the mid-1930s. At 4 ½ miles over water, it was the longest high-level and most expensive bridge in the world at the time. Today, the bridge is a primary route between the San Francisco Peninsula and the East Bay, carrying nearly 280,000 vehicles daily. Several bridges span the waterways of the San Francisco Bay within view of the Bay Bridge: The 1937 Golden Gate Suspension Bridge, the 1997 San Mateo-Hayward Steel Girder Bridge, and the 1956 Richmond-San Rafael Steel Truss Bridge. The Figure shows a map of the San Francisco Bay Area and the location of these and other bridges.

The California State Senate Bill 60 authorized funding for the design and construction of a replacement structure for the East Span of the Bay Bridge. The new structure will be located about 150 m north of the existing east span. The structure will traverse the Bay from the East End at the Oakland touch-down area to the West End of the signature span with side-by-side parallel decks. The new crossing will accommodate five lanes of traffic in each direction and is designed to carry a light rail transit (LRT) system on each of the 25.0-m-wide decks. In addition, the east-bound structure will support a 4.8-m-wide pedestrian/bicycle path. The four types of structures, which comprise the crossing, are presently being designed by a T. Y. Lin International and Moffat and Nichol Joint Venture team.

[1] Vice President and Senior Bridge Engineer, T. Y. Lin International, San Francisco, CA

The structures are from East to West:

- A low-rise post-tensioned concrete box girder at the Oakland touchdown area.
- A precast segmental concrete box girder with varying span lengths from 120 m to 160 m will be constructed using the balanced cantilever method. The length of this structure is 2.4 km. The skyway will be founded on large diameter 2.5 m steel piles, 90 m to 100 m long, arranged in groups of 4 and 6, and partially filled with reinforced concrete. The piers will be steel boxes filled with reinforced concrete.
- An asymmetrically self-anchored suspension span with a single steel tower located off Yerba Buena Island's eastern shore, spanning over the navigational channel. The main span will be 385 m with a back span of 180 m. When built, this will be the largest self-anchored suspension span in the world. The tower will be 160 m tall and will consist of four steel shafts connected with intermittent steel shear-links along its height. The decks will be orthotropic steel box girders connected transversely with cross beams and supported with cable hangers at the outer edges of the girders. The tower pier will be supported on large diameter 2.5 m steel pipe pile socketed into rock and filled with reinforced concrete. The east pier will be supported on large diameter 2.5 m, 100-m long, steel pipe piles founded on the competent Alameda Formation well below the deep Bay Mud. The west pier will be supported on concrete piles cast-in-drilled holes in the base rock of the Island.
- A double deck post-tensioned concrete box girder with span lengths up to 80 m at the Yerba Buena Island's transition structure.

The California Department of Transportation, Caltrans, is coordinating the design process with input from the Metropolitan Transportation Commission (MTC), the Federal Highway Administration (FHWA), and the San Francisco Bay Conservation and Development Commission (BCDC). The MTC, at the request of the California Governor and Bay Area legislative leaders, became involved in the replacement project to ensure that region-wide interests are appropriately considered in the process. The bridge is owned and the project administered by Caltrans.

Background

In July 1997, MTC appointed a 25-member Engineering and Design Advisory Panel (EDAP). Most of the members were architects, engineers, and city planners. The EDAP recommended that two cable-supported bridge alternatives (a cable-stayed span and a self-anchored suspension span) be designed to the level of 30 percent completion before the final selection was to be made. The intent of this recommendation was to compare seismic performance of the two different types of structures and their construction cost.

The other EDAP recommendations that had a significant impact on the design of the new eastern span include:

- The design should to provide post-earthquake "lifeline" service.
- The span should have 10 traffic lanes, five in each direction, with two standard 10-foot shoulders in each direction.
- The design should accommodate the possibility of future light rail service.
- The new span should be built to the north of the existing bridge alignment.
- The design should have a cable-supported main span with a single vertical tower with single or multiple planes of supporting cables.
- The span should not be double-decked. It should have two parallel separated decks on the low-level section and either parallel separated decks or a single deck on the cable-supported span.

- The structural elements should be visually consistent throughout.
- The low-level section should have long, equal span lengths although shorter span lengths could be used adjacent to the Oakland touch-down area.
- For the low-level section, particular attention should be paid to the design of the supporting pier as it enters the water including the possibility of submerging the pile cap below water.
- The single tower for the main span should not be taller than the suspension towers on the existing western span.
- A "diamond" shape for the main span tower should not be used.

After the completion of the 30 percent design, the EDAP selected the asymmetrically self-anchored suspension bridge alternative because it looks similar to the other two Bay Area suspension bridges.

Geology

The site geology varies dramatically along the length of the bridge alignment. At the western end of the bridge at the Island, the piers will be founded on rock. As the alignment progresses east towards Oakland, the bedrock Franciscan Formation drops abruptly and the piers will have piles that penetrate the 80-m deep Bay Mud and are founded in the interlayer clays and sands of the competent Alameda Formation. The main span tower will be sited on relatively shallow, sloping bedrock

Seismic Hazard

Seismic hazard evaluations were performed to define the safety-evaluation earthquakes (SEE) and the functional-evaluation earthquakes (FEE). The SEE corresponds to an earthquake with a return period of 1,500 years while the FEE corresponds to an earthquake with a return period of 450 years. Both deterministic and probabilistic approaches were used to set the appropriate seismic criteria for the site. The seismic hazard is dominated by the San Andreas Fault about 12 km to the West capable of a magnitude 8.1 event and the Hayward Fault about 8 km to the East with a potential magnitude of 7.5. The bridge design for the Western portion is controlled by the SEE event from the San Andreas Fault, and for the Eastern portion, the SEE event from the Hayward Fault. Six seismic ground motions, three from the San Andreas and three from the Hayward faults, were developed and used to analyzed the structure.

Seismic Performance Criteria

As a life-line structure, the bridge is to be designed to provide the highest level of seismic performance. A seismic performance criteria was developed by Caltrans for both the FEE and the SEE events. After a functional evaluation earthquake, FEE, the bridge will provide full service almost immediately and there will be minimal damage to the structure. Minimal damage implies essentially elastic performance and is characterized by minor inelastic response, narrow cracking in concrete, no apparent permanent deformations, and damage to expansion joints. After a safety evaluation earthquake, SEE, the bridge will provide full service almost immediately and will sustain repairable damage to the structure. Repairable damage that can be repaired with minimum risk of losing functionality; and is characterized by low level yielding of reinforcement, spalling of concrete cover and limited yielding of structural steel.

Aerodynamics Design Criteria

Aerodynamic Design Criteria were developed for the East Span bridge site based on review of historical wind records. The design criteria recommended that a 100-year recurrence wind speed be used for the service load design and a 10,000-year recurrence wind speed be used for a lower end critical flutter velocity threshold. In order to ensure wind stability of the Self-Anchored Suspension Bridge, wind tunnel tests were performed on a section model and on a full bridge aeroelastic model.

The Self-Anchored Suspension Bridge

The self-anchored suspension bridge consists of a 385 m main span and a 180 m back span. The 0.78 m diameter cable is anchored at the east end inside each steel box girder near their outer edges. The cable is contained by splay saddles as they emerge from inside the girders, then passes over the top of the tower in a single saddle, and is looped through deviation saddles around the west end forming a continuous loop.

Unlike traditional suspension bridges, these deviation saddles are fixed to the west pier cap beam and the cable force on either side is balanced during construction using a jacking saddle centered between the deviation saddles. The cap beam supports these three saddles, which is pre-stressed concrete designed to carry the differential stresses arising during service and seismic loads. The weight of this cap beam is designed to balance the dead load uplift at the west bent arising from the asymmetry of the suspension bridge.

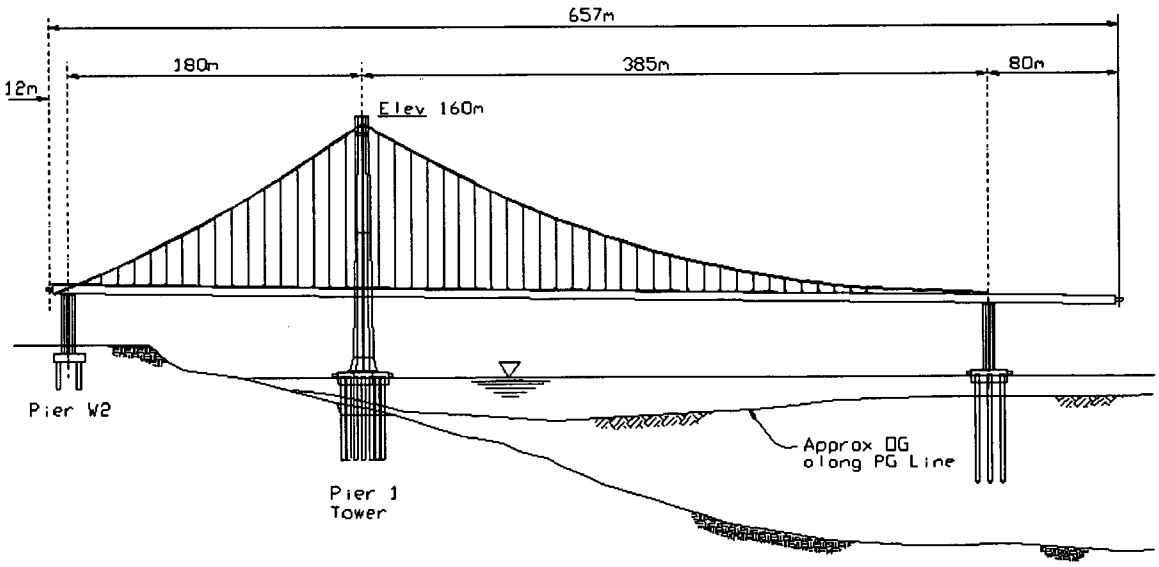

The cables at the tower do not cross and are secured in a single, three-dimensionally curved saddle. The splay saddles at the east pier is supported by the box girders and is designed to move in order to balance the cable forces on each side. The suspender cables are splayed to the exterior sides of the box girders and are spaced at 10 m. The superstructure consists of dual, A709 Grade 50 steel box girders with an orthotropic steel deck. These boxes act in compression supporting the cable tension forces and function as part of the gravity load system. Floorbeams spaced at 5 m support the orthotropic deck and distribute the suspender loads to the box. The box girders are connected together by 10 m wide x 5.5-m deep crossbeams spaced at 30 m. These cross beams carry the transverse loads between the

suspenders. A span of 72 m, and they ensure that the dual boxes act compositely together during wind and seismic loads.

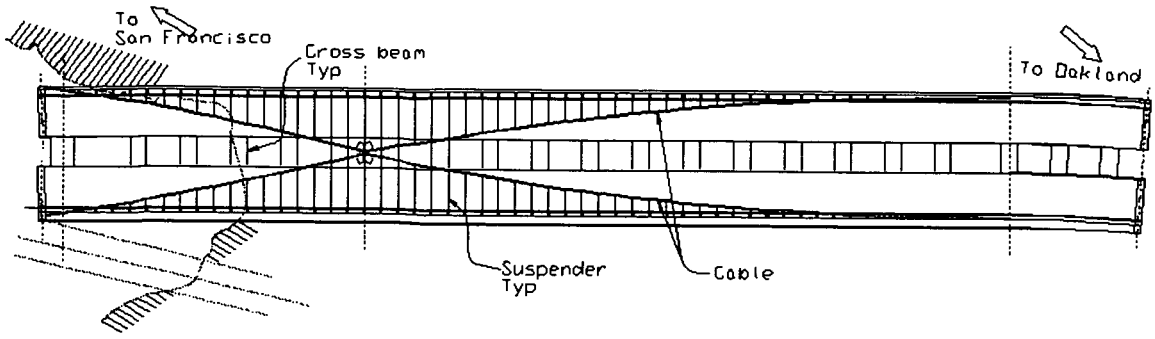

PLAN VIEW OF SUSPENSION BRIDGE

The bridge carries a pedestrian path on the south side. The eccentric load is balanced by a continuous counter-weight on the north side. At the West End, the box girders frame into the cap beam, which serves as the box girder at that location. The connection between the orthotropic steel box girders and concrete cap beam is subjected to the compressive forces of the cables. Additional pre-stress is added through looped post-tension strands connected at each rib to ensure that the steel box yields before the connection fails.

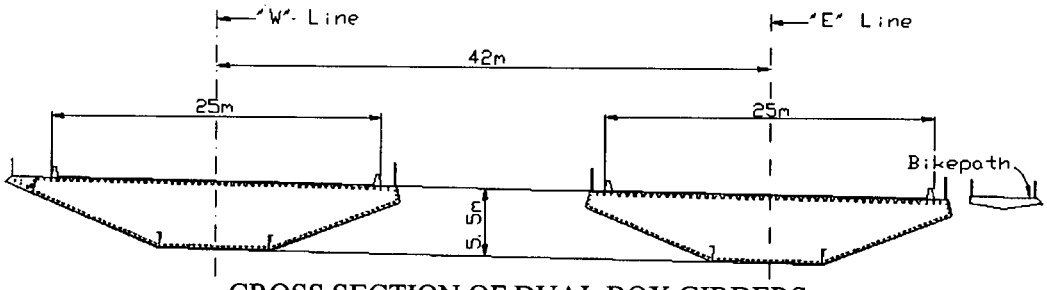

CROSS SECTION OF DUAL BOX GIRDERS

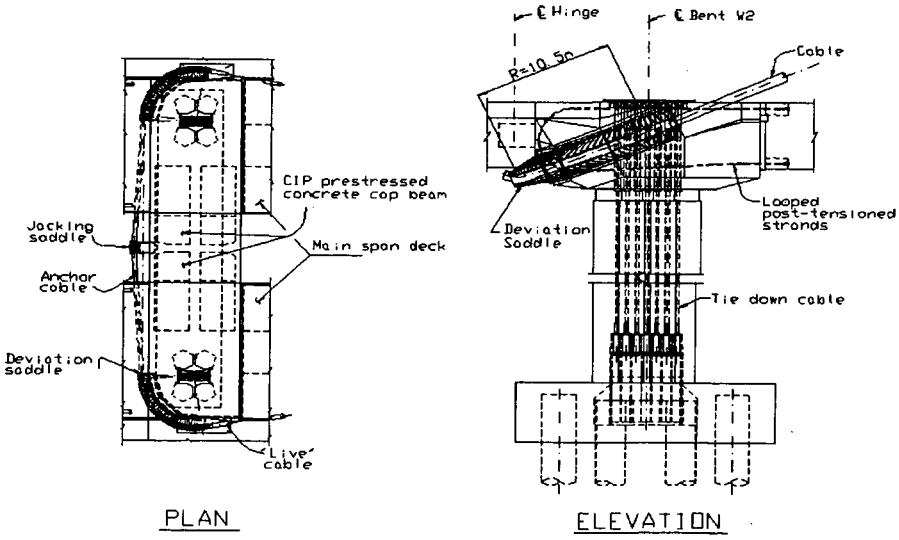

WEST PIER PLAN AND ELEVATION WITH DEVIATION SADDLES

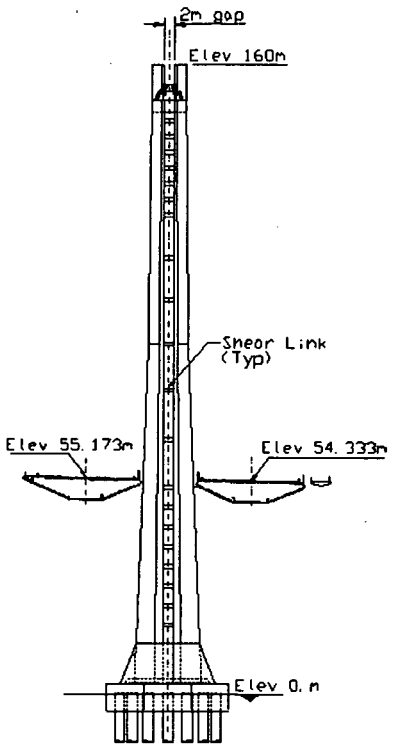

TRANSVERSE VIEW OF THE TOWER

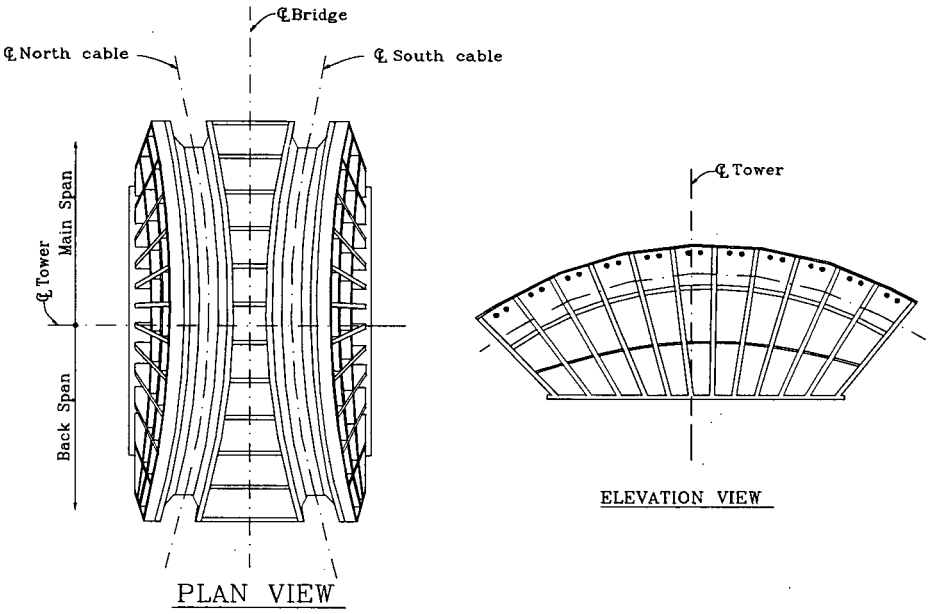

TOWER SADDLE

The single tower is 160 m tall and is composed of four shafts connected with shear links along its height (Figure 13). The tower shafts are tapered; stiffened steel A709 Gr. 50 box members with diaphragms spaced at 3 m vertically. The tower is fixed to the 6.5 m deep pile cap, which is a steel moment frame encased with concrete and is supported on 13 - 2.5 m steel shell pipe piles filled with concrete and embedded into the rock. The rock slope

is benched to give the piles equal lateral stiffness and to avoid a torsional seismic response. The piles clear length is about 20 m

The east pier has two reinforced concrete columns with additional prestressing to avoid a tension shear failure when subjected to seismic vertical loading. The pier is supported on 16 - 2.5 m steel shell pipe piles. These piles are 100 m long and are filled with concrete for the top 55 m. The west piers are reinforced concrete columns, which are monolithic with the prestressed cap, beam that forms the west bent and are supported on rock with eight – 2.5 m cast-in-drilled-holes (CIDH) piles. At the west pier, a tie-down system, designed to resist the seismic uplift, consists of 28 stay cables (61 - 15mm diameter strands each) which are anchored into rock through additional 4-2.5 CIDH piles. At the east piers, the box girders are supported on bearings. Shear keys and tie rods are provided to carry lateral loads and uplifts, respectively. The box girders are supported at the east and west pier for lateral loads and are "floating" at the tower.

Concrete Haunched Box Girder Bridge

For the haunched concrete girder alternative, balanced cantilever precast segmental construction erection are being designed. Normal weight concrete will be used for the superstructure except for the side inclined panel or webs where lightweight concrete will be used. The 28-day concrete strength for both the lightweight and normal weight concrete is 50 Mpa.. The box girder is a single cell with two vertical main webs. The width at the bottom slab is 8.5 m. The 25.1 m deck width accommodates long deck overhangs of 8.3 m each. Inclined girder panels or webs were considered the most effective design to carry eccentric bike path loading, post-tensioned in both the longitudinal and transverse directions. Vertical post-tensioning is used to control shear stresses in the girder main webs.

The nominal 160 m spans are arranged in frame units of three or four piers per frame with a girder depth of 5.5 m at mid-span and 9 m at the pier. Mid-span hinges between the frames allow longitudinal expansion and contraction due to creep, shrinkage and temperature changes. An internal steel beam assembly at the hinge provides shear transfer and moment resistance in addition to controlling deflections at the cantilever end of each frame. These hinge-beams are rigidly connected to the box girder at one end and slide on bearings in the adjacent box girder.

The foundation and piers are designed to resist loads due to elastic and plastic deformations of the superstructure including creep, shrinkage and temperature drop. Some piers are about 50 m in height and stand in water depths of 15 m. This, added to the presence of a 15 m layer of Bay Mud, establishes a very flexible structure. The design approach for such piers was to adopt a stiff foundation system thereby controlling pile cap elastic displacements to acceptable levels and minimizing the potential for permanent pile cap offsets. A relatively stiff foundation system for the tall flexible piers was achieved through the use of large diameter battered steel piles filled with concrete.

The 2.5 m piles will be filled only in the upper 2/3 of the pile length with structural concrete to form a composite steel/concrete pile. A sufficiently thick shell allowed for the use of an unfilled shell below the composite pile section. To ensure proper transfer of loads from the concrete fill to the steel shell, shear ring plates will be welded to the inside of the steel shell in the concrete filled section.

YBI Transition Structure

The eastbound and westbound transition structures will connect the suspension structure to the existing viaduct section near the Yerba Buena tunnel east portal. The two structures are carried on separate single-column bents except near the viaduct end where they are supported on outrigger bents. The separate transition structures merge into the existing double-deck viaduct structure that connect to the tunnel through the Island.

The superstructure of the transition structures consists of cast-in-place reinforced concrete box girders near the concrete outrigger type bents and cast-in-place prestressed concrete box girders supported by single column bents. The shape of the box girders has been determined primarily by aesthetics to match the streamlined girder shape of the main span superstructure and skyway.

Oakland Shore Approach

The Oakland shore approach westbound structure extends from the tip of the Oakland touch-down area to the join the Concrete Haunched Box Girder structure. The total length of the westbound approach structure is about 660 m which is subdivided into two sections, an elevated structure and an essentially at-grade structure. The eastbound approach structure is an elevated two-span frame, which is 105 m long. The structural portions will be cast-in-place prestressed concrete box girder superstructure supported on reinforced concrete piers.

References

Manzanarez, Rafael et al, "Design of the New San Francisco-Oakland Bay Bridge", 16th International Bridge Conference, Pittsburgh Pennsylvania, 1999.

Nader, Marwan et al, "Seismic Design Strategy for the New San Francisco-Oakland Bay Bridge Suspension Span," 16th International Bridge Conference, Pittsburgh, Pennsylvania, 1999.

Tang, Man-Chung et al, "Replacing the East Bay Bridge,"ASCE, Civil Engineering, Sept. 2000, pg. 38.

Survey on Damaged Piles Adjacent to Quay Wall after a Large Earthquake

Jiro FUKUI [1] and Masahiro NISHITANI [2]

1. Introduction

The Hyogo-ken Nanbu Earthquake severely damaged civil engineering structures of many kinds. These included severe damages to various facilities at the Higashi-Nada Sewerage Treatment Plant located in the east of Kobe. This Plant was constructed on the reclaimed land about 25 years ago, and faces to Uozaki Canal. Fig. 1 shows the plane and Fig. 2 shows the section of the Plant. When the water treatment facilities at this Sewerage Treatment Plant (Fig. 1) were reconstructed, its foundation piles were surveyed [1]. It was confirmed that the piles (they were PC piles with the diameter of 350 mm and length of 27 m) of the administration building (the building had 3 stories above ground and 1 partial basement) that stands adjacent to the quay wall of the Uozaki Canal (about 40 m from the quay wall) than the water treatment facilities were surely damaged [2]. But because the administration building continued to be used after the Earthquake, its piles were not surveyed. Last year (2000), exactly five and a half years after the Earthquake, the administration building was removed. This provided an opportunity to excavate the ground around the piles of the building and perform various surveys to clarify the behavior and deformation of the piles after a large earthquake.

2. Outline of the Survey

As shown in Fig. 3, each column of the administration building was supported by multi-piles. The surveyed piles were the foundation of the east wall (the thickness of 1.0 m) of the building. The surveys were done after coffering the ground around the two piles with steel sheet piles, and excavating the ground inside the sheet piles to a depth of about 10.5 m from the pile heads (photo. 1 and 2). Then, the residual displacement and damages of the piles, and properties of surrounding soil were surveyed. The residual displacement of the piles was examined by three-dimensional survey with a geodimeter to measure the absolute displacement of the piles above the excavated ground bottom. The relative displacement of the piles was measured by an insertion type inclinometer at depths below the excavated ground bottom. The damages of the piles above the excavated ground bottom was inspected by visual observation, and below the bottom, the insides of the piles were inspected by inserting a bore hole camera. As geological survey around the piles, approximate geological structure and thickness of each stratum were estimated based on the results of some boring surveys. The boundary between a landfill stratum and an alluvial clay stratum was also clarified.

---

1 Head, Foundation Engineering Team, Structures Group, PWRI
Minamihara 1-6, Tsukuba, Ibaraki, 305-0804 (e-mail: fukui@pwri.go.jp)
2 Senior Research Engineer, ditto

results of the boring survey performed to construct a facility near the building, and the results of the boring survey performed from the excavated bottom in this survey. The boundary between a landfill stratum and an alluvial clay stratum was also clarified.

3. Results of the Surveys

3.1 Geological Survey

The results of the boring survey around the Sewerage Treatment Plant confirmed that the geological structure around the administration building is categorized as a landfill stratum, alluvial clay stratum, diluvial clay stratum and diluvial gravel stratum. The landfill stratum consisted mainly of a mixture of sand and gravel that contains a clay component. Below the landfill stratum, there were scattered gravel deposits from 15 to 30 mm diameter. The alluvial clay stratum consisted mostly of silt, and it also included sand and fragmented shells and gravel with a diameter of about 5 mm. The diluvial clay stratum was a sandy cohesive layer of firmed or consolidated, and included gravel with diameter ranging from 10 to 30 mm. The diluvial gravel layer consisted mainly of firmly compacted coarse sand, and included gravel with a diameter smaller than 30 mm. It was hypothesized that around the survey location, the stratification was generally uniform, but that near the Uozaki Canal, the thickness of the alluvial clay stratum abruptly thinned, to form an inclined structure. Grain size analysis tests of the samples taken at three locations during the excavation were performed. The results confirmed that the landfill stratum is relatively homogeneous and is good quality decomposed granite soils. The survey also confirmed that the boundary between the landfill stratum and the alluvial clay stratum at the excavation location is at a depth about 13.0 m below the pile heads.

3.2 Visual Observation on Damaged Piles

The results of visual inspection confirmed cracks near the level from 3.0 to 4.5 m below each pile head (T. P. +1.25 m). They were between 0.05 and 0.2 mm wide. And at the depth of about 6.5 m below each pile head, compressive failure extending for about 45 cm occurred (Photo. 3 and 4). In the compressive failure area, many PC steel bars exposed, and buckled or broke.

3.3 Internal Inspection on Damaged Piles

The results of internal inspection confirmed a faulting in the pile body near the level from 12.6 to 12.7 m below each pile head. Judging from the faulting and depth from each pile head, the part of the pile was assumed to be a joint. Ground water was leaking from cracks near the 12.3 m level below each pile head.

3.4 Residual Displacement of Damaged Piles

Fig. 4 shows the residual displacement of the south side pile. According to the residual displacement inspection of the pile below the excavated bottom that was performed using an insertion type inclinometer, the pile was bent in the compressive failure area and inclined towards

the quay wall around the boundary of the landfill stratum and alluvial clay stratum. Relative residual displacement of about 20 cm generated between the failure part and pile head. This inclination of the pile was not caused by damage to the intermediate of the pile, but by the opening of a joint. However, it is not clear whether this was caused by an error during construction or by the Earthquake. Furthermore it was confirmed that the inclination of the pile extends to its tip in the east-west direction. It is also not clear whether this was caused by an error during construction or by the Earthquake.

4. Analysis on the Behavior of Piles during the Earthquake

4.1 Outline

The reference 1) reports that the closer to the Uozaki Canal, the larger the residual displacement of ground and the more severe the damage to foundation piles. Therefore, it is assumed that the piles that were surveyed were influenced by ground flow during the Earthquake.

A simulation analysis was performed to clarify the failure mechanisms of the piles of the administration building during the Earthquake. Fig. 5 shows the flow chart of the analysis. For the analysis, the piles were modeled as beams with tri-linear bending properties. To prepare this model, its properties were set by performing a bending test using the part of 6 m from the pile head that were dug up [3]. Fig. 6 shows the results of the bending test. Soil properties were modeled based on the results of the boring survey done around the survey location. Table 1 shows the soil properties used for the analysis.

4.2 Analytical Procedure and the Results

The analysis was done by increasing horizontal force in units of 5.0 kN while loading to the pile head with a vertical load of 400 kN, the weight of the administration building supported by the pile estimated based on the drawings of the building. Inertial force corresponding to the weight combining the quay wall and the soil behind it acted on the gravity center of the quay wall. Based on the results of the surveys, the pile head was connected to the footing as a hinge.

Because the results of one-dimensional effective stress analysis predict that the effective stress falls as the pore pressure rises during the Earthquake [4], the modulus of deformation of the landfill stratum 2 (Table 1, Fig. 7) fell to 1/6 of its initial on the analysis. As a result, the bending moment generated in the pile body exceeded its yield strength when horizontal force was 150 kN (Fig. 7). This location was at the depth 6.3 m below the pile head.

Next, as a result of loading stress on the pile body as flow pressure, parametrically converting the stiffness of ground in consideration of liquefaction, the bending moment generated in the pile body reached its ultimate strength (Fig. 8). In this analysis, the stiffness of ground was set at 1/10 for the landfill stratum 1, at 1/100 for the landfill stratum 2, and 1/400 for the crushed stone under the quay wall.

The results of the analysis confirmed that the displacement of the quay wall was about 2 m (Fig. 9), closely conforming with the results of the post-Earthquake surveys.

5. Conclusion

Before this survey, the piles at the two locations shown in Fig. 10 were inspected. The results showed that at point A, the pile head shifted towards the quay wall up to 20 cm more than the footing, but at point B, the footing shifted towards the quay wall up to 17 cm more than the pile head. This means that because point A was close to the quay wall, it was influenced by ground flow so that the displacement of the pile head was greater than that of the footing. Inversely, at point B, the displacement of the footing was greater than that of the pile head, because the effect of inertia force were greater than that of ground flow. Because the piles that were surveyed, at this time, located to the mid point between point A and point B, not very much relative displacement between the pile head and footing was generated. It is assumed that the state of the connection between the pile head and footing provided a small degree of constraint against rotation, because the pile head was not damaged (photo. 5)

Based on the results of this survey and analysis, it is possible to hypothesize that the followings are the damage mechanisms of the piles adjacent to the quay wall after the Earthquake.

1) The ground stiffness of the landfill stratum fell slightly as liquefaction occurred during the Earthquake.

2) Afterwards, under the effect of inertial force acting on the piles, bending moment close to the bending strength of the piles acted, then the piles damaged.

3) Ground flow occurred in the landfill stratum as the quay wall moved.

4) As a result, severe flow pressure acted on the piles, serious residual displacement of the piles occurred.

References

1) Okumura-gumi: Reports on Damaged Piles in the Kobe Higashi-Nada Sewerage Treatment Plant, 1997.8

2) Kobe-shi: Reports on Repair Works of Sewerage Facilities in the Hanshin-Awaji Earthquake, 1995.7

3) Takashi FUJINAGA, Isao MITANI, Yasuhiro OHTANI and Manabu NAKAYAMA: Damage to Prestressed Concrete Pile and its Mechanical Characteristics in the Hyogo-ken nanbu Earthquake 1995, Kobe University, 2000

4) Okumura-gumi: Reports on Damaged Piles in the Kobe Higashi-Nada Sewerage Treatment Plant, 1998.7

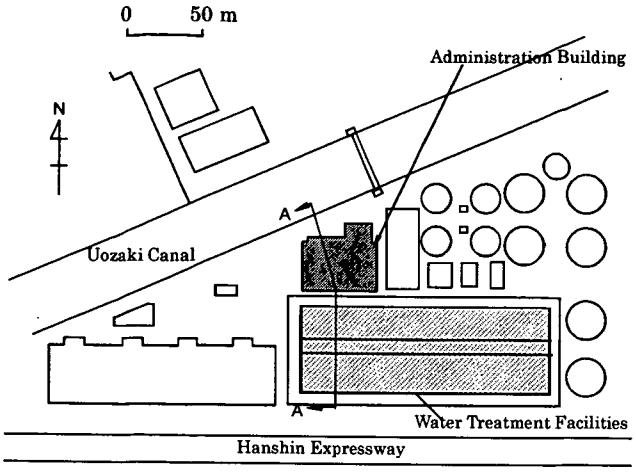

Fig.1 Higashi-Nada Sewerage Treatment Plant

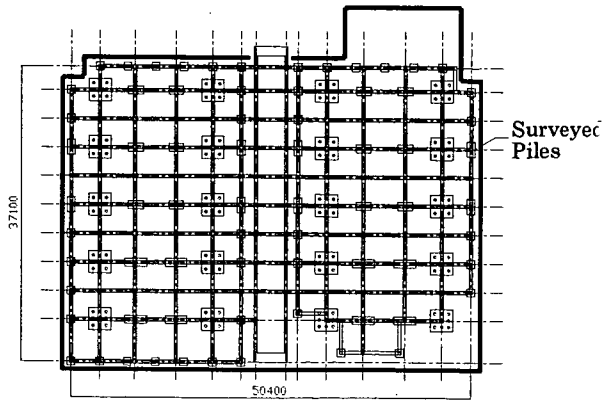

Fig.3 Foundation of the Building

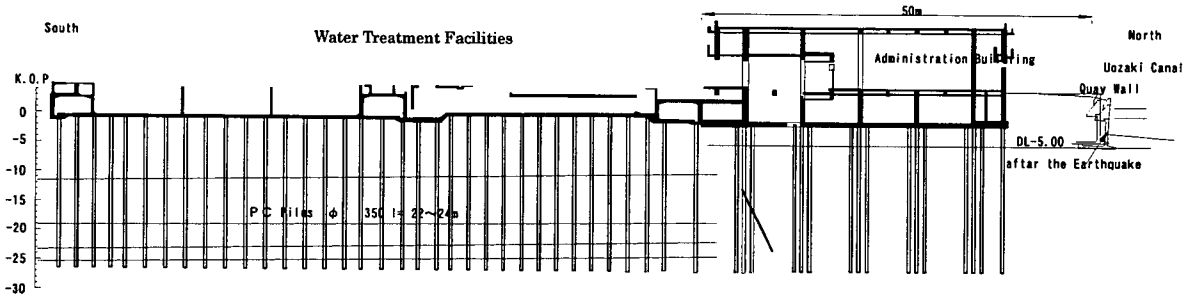

Fig.2 Section A-A

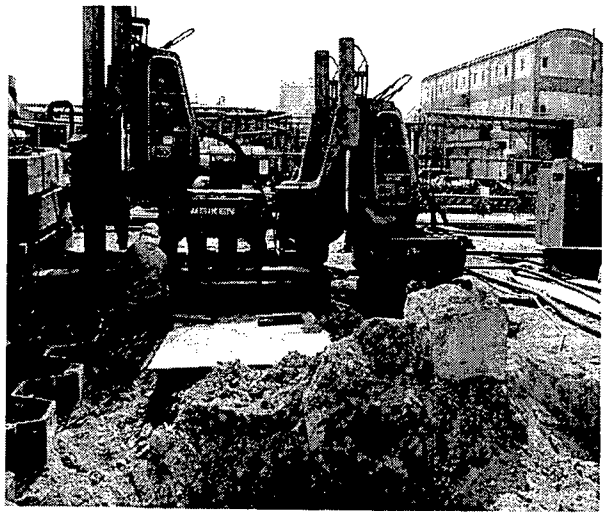

Photo.1 Execution of Steel Sheet Piles

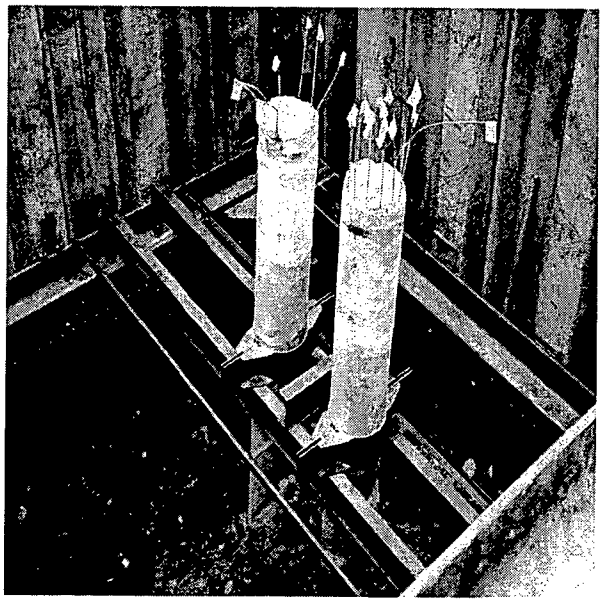

Photo.2 Execution of Excavation

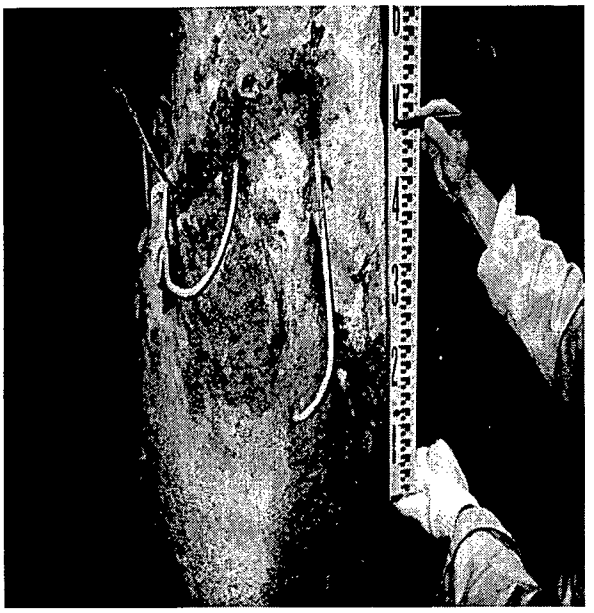

Photo.3 Compressive Failure(1)

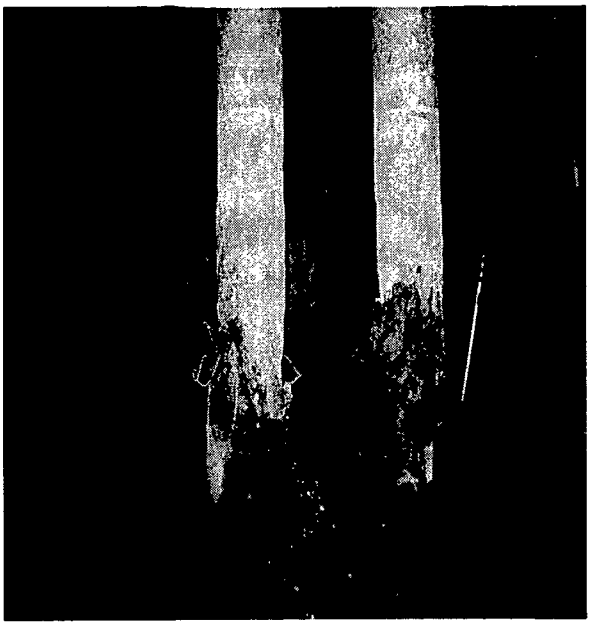

Photo.4 Compressive Failure(2)

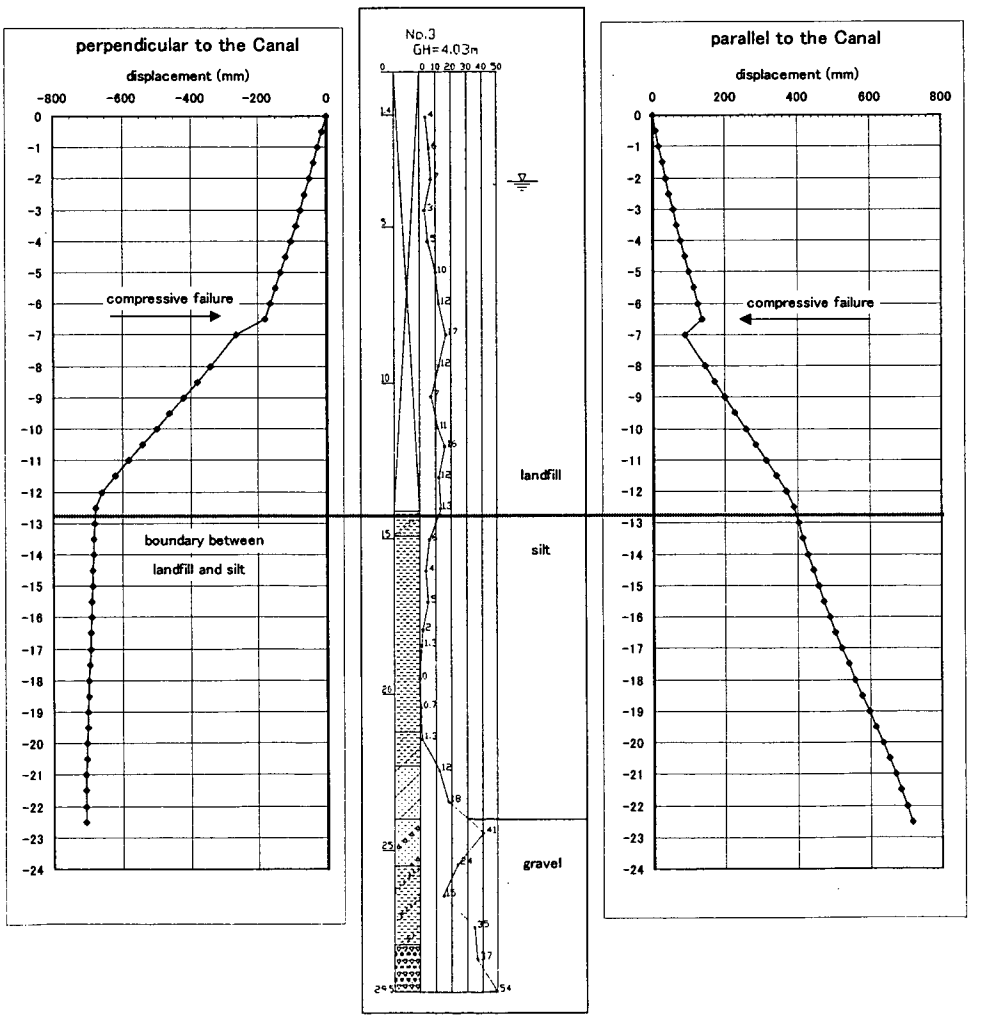

Fig.4 Residual Displacement of the South Pile
(relative displacement for the pile head)

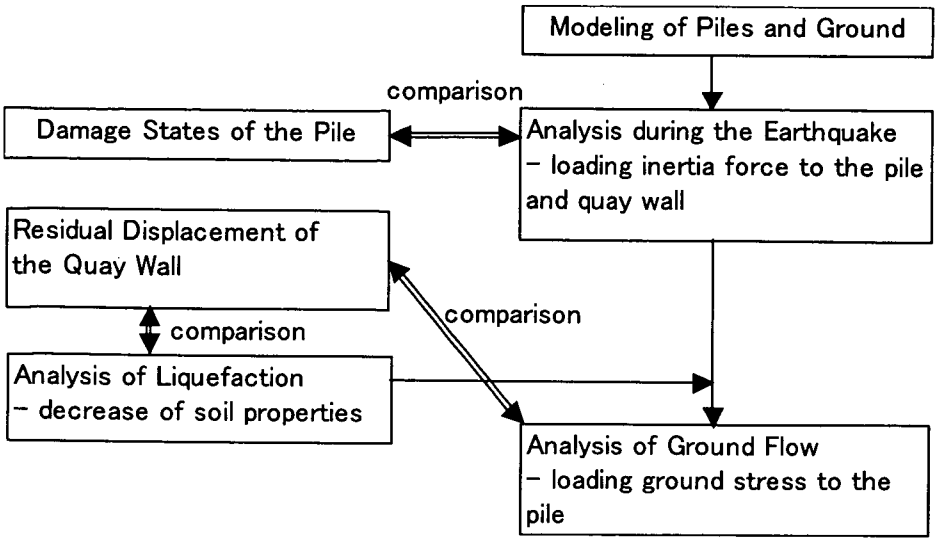

Fig.5 Flow chart of the Analysis

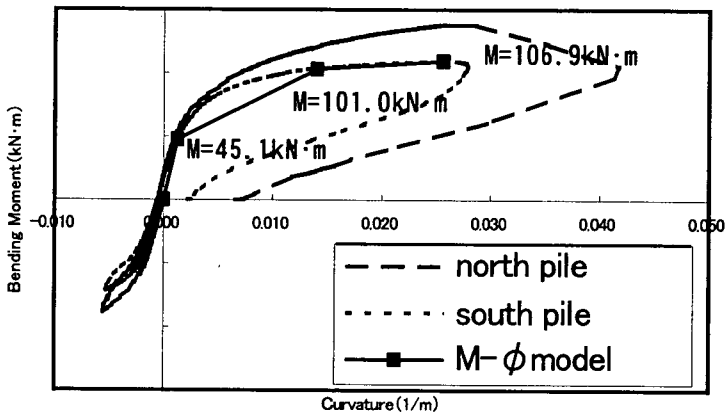

Fig.6 M-ϕ Model of the Pile

Table. 1 Soil Properties

Soiltype	unit weight γ_t (kN/m^3)	cohesion c (kN/m^2)	internal friction angle ϕ (degree)	before liquefaction elastic modulus (kN/m^2)	before liquefaction Poisson's ratio ν	after liquefaction elastic modulus (kN/m^2)	after liquefaction Poisson's ratio ν
landfill stratum 1 G.L.-0.0m～2.8m	22.0	0.0	25.0	3000	0.33	300	0.4884
landfill stratum 2 G.L.-2.8m～12.2m	22.0	0.0	25.0	3000	0.33	30	0.4962
alluvial clay G.L.-12.2m～22.4m	16.5	100.0	0.0	4500	0.40	-	-
diluvial clay G.L.-22.4m～28.1m	18.0	200.0	0.0	8700	0.40	-	-
diluvial gravel G.L.-28.1m～30.0m	22.0	50.0	35.0	43000	0.33	-	-
crushed stone	22.0	50.0	35.0	20000	0.33	50	0.4962

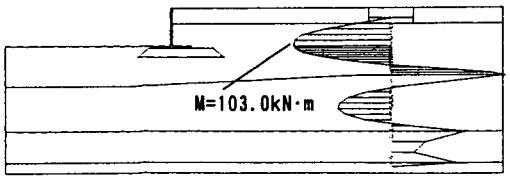

Fig.7 Bending Moment of the

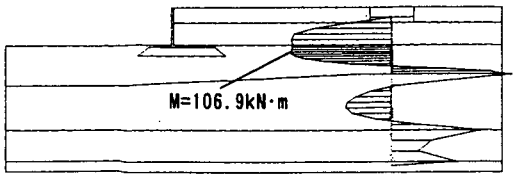

Fig.8 Bending Moment of the Pile (after Liquefaction)

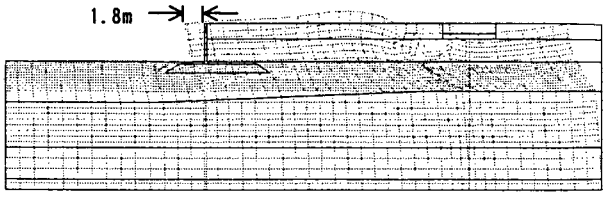

Fig.9 Displacement of Ground (after Liquefaction)

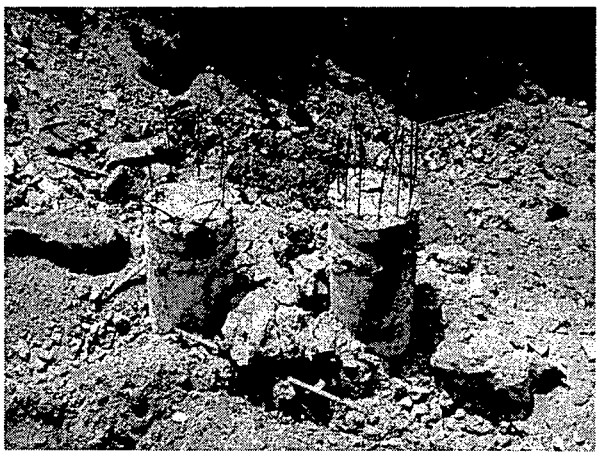

Photo.5 Pile heads

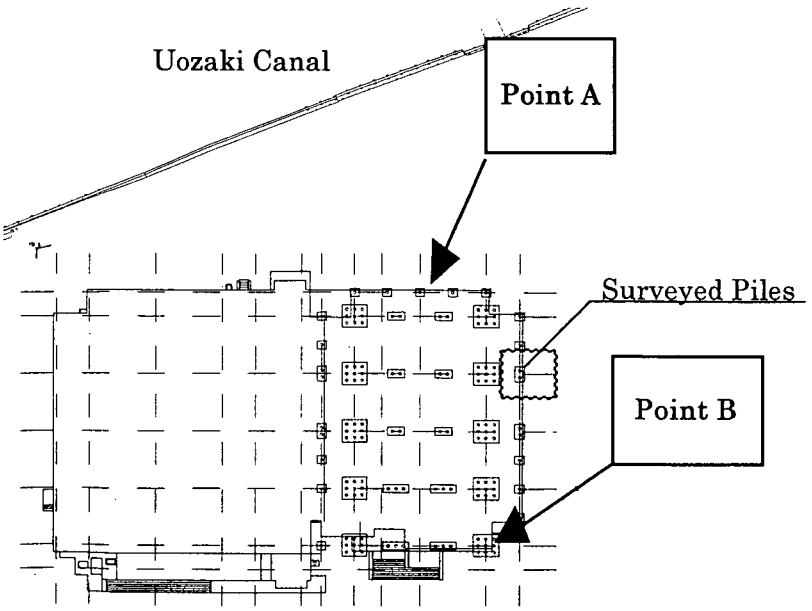

Fig.10 Inspection Points before the Surveys

BEHAVIOUR OF BUILDINGS, BRIDGES AND DAMS IN BHUJ EARTHQUAKE OF JANUARY 26, 2001

S.K. Thakkar[1], R.N. Dubey[2] and Pankaj Agarwal[2]

Abstract

An earthquake of magnitude $M_w = 7.7$ occurred in Kachchh region of Gujarat in Western India at 8:46 AM (local time) on January 26, 2001. The epicentre of earthquake was close to the town Bhachau. This was the most damaging earthquake in the last fifty years in India. The epicentral region was known to be in seismic zone V of IS code: 1893. Over 19,000 people were reported to have lost their lives. This earthquake has caused widespread damage in Gujarat. The damage was caused to multistoreyed RC buildings, masonry buildings, bridges and roads, railway lines, dams, harbor structures, lifelines and many other structures. This paper describes the typical features of damages to RC buildings, bridges and dams. The lessons learnt and future course of action in preventing such damages are recommended.

Introduction

The Kachchh region of Gujarat in Western India was struck by an earthquake of moment magnitude 7.7 on January 26, 2001 at 8.46 AM (IST). The earthquake is subsequently referred to as Kachchh earthquake or Bhuj earthquake. The epicentre of the earthquake was located in Bhachau 65 km east of Bhuj, Fig. 1. The earthquake was felt in most parts of the country. Many towns in the state of Gujarat like Bhuj, Anjar, Bhachau, Gandhidham, Jamnagar, Morbi and Sundernagar sustained widespread destruction. The distant towns like Ahmedabad 300 km towards east and Surat 375 km southeast of Bhuj received strong shaking and caused damage to large number of buildings. It is the largest seismic event in India in last 50 years, which involved (i) large population in urban and rural areas (ii) significant damage and collapse of large number of multistoreyed buildings (iii) damage to road and railway bridges (iv) damage to roads and highway embankments (v) damage to port structures (vi) liquefaction covering a wide area (vi) damage to number of embankment dams of water resources projects and (vii) damage to lifelines and industrial structures.

The maximum intensity, MMI, of shaking was as much as IX experienced in Bhuj, Anjar and Bhachau. The Gujarat region falls in Zone III to V of IS code (IS: 1893-2001), the Kachchh is a known seismic region falling under zone V. There is a history of occurrence of strong ground motions in this region. The last two earthquakes that occurred in the region were in 1819 (M=8.0) and in 1956 (M=7.0), Fig. 2. Many multistoreyed reinforced concrete buildings built in Bhuj, Gandhidham and distant places like Ahmedabad were severely damaged or collapsed. The life loss is reported to be more than 19,000. The strong motion record obtained at the ground floor of staff

1. Professor, Deptt. of Earthquake Engineering, Indian Institute of Technology Roorkee, INDIA
2. Lecturer, Deptt. of Earthquake Engineering, Indian Institute of Technology Roorkee, INDIA

quarters of passport building in Ahmedabad at a distance of 300 km indicated a peak acceleration of 0.11g, 0.08g and 0.07g in two horizontal and vertical directions respectively. The peak ground acceleration near epicentre was much larger, some investigations suggest a value of 0.634g in Anjar (Kumar A, et al, 2001). The peak ground acceleration in Bhachau close to epicentre is expected to be larger. This earthquake has raised many concerns about design and construction practices of RC buildings in the region. This paper describes the typical features of damages to RC buildings, bridges and dams. The paper also highlights the behaviour of seismic code designed structures. The lessons learnt from the damages occurred are presented. The course of action for preventing such damages is also recommended.

Earthquake Damages to Buildings

The earthquake destroyed about 300,000 houses and caused damage to another 700,000 in Kachchh region. Two types of buildings are common in the region (i) Masonry buildings with load bearing wall construction, varying from one to four storeys (ii) RC framed buildings varying from four to twelve storeys. Typical features of damages to buildings are described below.

Masonry buildings

Figures 3 and 4 show two views of one storeyed masonry substation building of Gujarat State Electricity Board, Bhuj built in random rubble masonry without any earthquake resistant features. The figures show the damage caused because of out of plane vibrations of masonry wall. Figure 5 shows a typical school building, which got severely cracked in this earthquake. Figure 6 shows a Bentonite factory building near Bhuj, which escaped damage, the seismic bands turned out to be extremely effective. Figure 7 shows collapse of one of the three blocks of Zila Panchayat, Bhuj. Figures 8 and 9 show the collapse of three and two storeyed buildings respectively in Bhachau. Figures 10 and 11 show the traditional construction of stone masonry buildings in Ahmedabad and Kachchh region respectively, these structures sustained minor damages.

Reinforced concrete buildings

Reinforced concrete buildings having ground plus four storeys (G + 4) and G + 10 are commonly built in Gujarat. Monolithic RC construction with brick/concrete block infills is a standard practice of construction. Reinforced concrete buildings suffered significant damage mainly because of faulty design, inadequate detailing of reinforcement and poor quality of construction (Thakkar, Dubey, Agarwal, 2001). The codes of practice were not followed in majority of cases. Some features of damages are presented below.

Soft storey failure: The bottom storey which is often kept free from walls is used as a parking place in two storey, G + 4 and G + 10 types of buildings were observed to be most vulnerable being the soft storey in most cases. Figure 12 shows a typical soft storey failure in G + 4 building used for residential purpose.

Mass irregularity: Figure 13 shows G + 10 storeyed, A-Block of Mansi complex at Ahmedabad. Half portion of the block collapsed. The building had a massive swimming pool on the 10th floor that created a large inertia force at this level. The inadequate consideration of seismic force and design seemed to be the reason of failure.

Damage to G + 8 building: Figure 14 shows one of typical G + 8 residential RC buildings at ONGC complex in Ahmedabad. There are only minor damages mostly non-structural in the building due to earthquake. The diagonal cracking in filler wall, minor cracking of beams and columns were observed. There were no structural damages to the building.

Strut action of staircase: Figure 15 shows two blocks of building connected by a staircase. The strut action of staircase and out of phase vibrations of two blocks of building was the reason of failure. The staircase did not permit free movement of blocks during vibrations.

Floating columns: The construction of columns on horizontal cantilevers on first floor is permitted by municipal byelaws. This allows horizontal covered space to be created above first floor. These columns can be taken upto four storeys and in some cases more, are called floating columns. This is a typical example of vertical irregularity. Many buildings with this type of design sustained heavy damage. Inadequate consideration of seismic force and design seemed to be the reason of failure.

Inadequate detailing for ductility: There are numerous examples of lack of transverse reinforcement in columns and lack of detailing in beams and beam-column joints in damaged buildings. The IS code provisions for ductile detailing of reinforcement in IS: 13920-1993 was generally not followed in private buildings. Some of the governmental buildings (Fig. 16) however followed these provisions, the damage has been minimal in such buildings.

Soil and foundation effect on building behaviour: The multistoreyed buildings particularly of G + 4 type sustained heavy damages in Ahmedabad which is at a distance of 300 km from epicentre. The majority of buildings were founded on deep alluvium where amplification of motion in soil seems to have caused large forces in the buildings. Shallow individual footings without tie beams were employed for such buildings, which further aggravated the damage to buildings. The buildings on raft foundations sustained minor damages. The pile foundations were not common.

Earthquake Damage to Bridges

Both highway and railway bridges sustained damages in Kachchh district. In most cases the damages were repairable. There was no loss of span type of failures. The bridges with long span and tall piers were not existing in the area. The bridge types in the area include: masonry arch bridges, multi-span simply supported bridges and balanced cantilever type of bridges. The substructures mostly consist of low height masonry piers or reinforced concrete piers built on well type of foundations. The types of damage in bridges include: damage to rocker/roller bearings, elastomeric bearings, restrainers, pounding action of adjoining spans, cracking and tilting of piers, damage to retaining walls, return walls, bridge parapet, expansion joints and approach road. The

cracking of riverbed and liquefaction of riverbed was observed at some places. The typical features of damages in some bridges are presented here.

Surajbari bridge

The two bridges one old and other new under construction at Surajbari located 43 km to the southeast of epicentre sustained significant damage. The old Surajbari bridge that sustained damage is more than 30 years old. The superstructure consists of RC box girder having balanced cantilever type of design with 37 spans of 32 m each, Fig. 17. The substructure consists of 4.5m high RC piers built on well foundations. The well foundations were made to rest on soil type of deposit. The following are the features of damage to this bridge:

(i) Damage to roller/rocker bearings, transverse displacement of superstructure by about 1m, Fig.18.
(ii) Tilting of pier, P12
(iii) Longitudinal separation between aboutment and main deck, Fig. 19
(iv) Pounding of superstructure at the junction of main and suspended spans
(v) Numerous water/sand ejects were observed demonstrating extensive liquefaction at ground surface

The new Surajbari bridge parallel to the old bridge was also under construction. This bridge consists of thirty-nine simply supported spans of 32.2m each. The substructure consists of RC piers on well foundations. Large number of elastomeric bearings and upstands, which were to function as restrainers, got damaged. There was no collapse of span or pier in the bridge. The superstructure spans moved in both the principal directions. The evidence of pounding of adjacent spans was visible. The restrainers prevented the falling of superstructure. The approach embankments were considerably cracked and settled.

Machhu bridge

The Machhu bridge more then 30 year old consists of three spans of 27.6m each is a balanced cantilever bridge resting on low height piers. The bridge damage includes: displacement in the superstructures, pounding of superstructure, severe damage to approaches and return wall.

Railway bridge, Bhachau

The seven span steel bridge, Fig. 20, sustained minor damage. The substructure of this bridge consists of 4m high reinforced concrete piers. The damage to bridge piers and approaches were repaired and the bridge was operational soon after the earthquake.

Road bridge, Bhachau

This is a multi-span simply supported RC bridge on low height piers. This bridge was under construction at the time of earthquake. The pier cap got cracked with wide separation from the bearing blocks, Fig. 21. The damage also occurred to abutment and approaches, Fig. 22.

Rudramata bridge, Bhuj

The bridge between Bhuj and Khawda consists of simply supported spans resting on trestle type of RC piers, Fig. 23. The bridge sustained minor damage, it remained functional even after the earthquake. The following types of damages occurred in this bridge: cracking of road near expansion joint, failure of railing (Fig. 24), settlement of approach road, abutment separation and cracking of riverbed.

Nehru Setu, Ahmedabad

The Nehru Setu (bridge) on Sabarmati river in Ahmedabad, Fig. 25 sustained minor damage and was functional after the earthquake. The damage of bridge includes: cracking of road near expansion joint (Fig. 26), damage to parapet, pounding between spans. The other bridges on river Sabarmati parallel to Nehru Setu suffered no damage.

Earthquake Damages to Dams

Three are 20 medium and 165 minor irrigation schemes in Kachchh district. Out of these 5 medium and 14 minor schemes are severely damaged, and 11 medium and 125 minor irrigation schemes are moderate to heavily damaged. In Saurashtra region there are 2 major, 11 medium and 287 minor irrigation dams. Out these 9 medium dams have been severely damaged and 31 are moderately to heavily damaged. Earth dams such as Rudramata, Kaila, Nirona, Kasawati were damaged. Majority of earth dams was less than 20m in height. The damages to earthen dams include longitudinal and transverse cracks, settlement and displacements. Figure 27 shows typical damage of Kaila dam. Figure 28 shows the Rudramata dam, 58 m high across river Khari. There was cracking and slumping on upstream face and also longitudinal cracks along the crest. The irrigation structures of Sardar Sarovar project consisting of concrete dam, concrete aqueducts did not suffer any damage. The project site was 350 km from the epicentre.

Effect of Earthquake on Code Designed Structures

In majority of the buildings that were damaged the seismic codes of the country were not followed. There are two codes: IS: 1893 and IS: 13920 that are required to be followed for earthquake resistant design of RC buildings. The masonry buildings are required to be provided with earthquake resistance measures as per IS: 4326 code.

Many multistoreyed RC buildings and masonry buildings have survived the earthquake with a minor or no damage. Figure 16 shows a G + 9 storeyed RC building designed according to seismic code survived the earthquake. This building was provided with strong motion instrumentation on ground floor, roof and intermediate floors. The instrumentation was installed just two days before the occurrence of earthquake. The strong motion data recorded in building provided vital information of structural response in this earthquake. Figure 6 shows a factory building built in masonry close to epicentre. This building had seismic bands provided according

to IS: 4326. This building did not suffer much damage. There are large numbers of such examples where structures with the provisions of code behaved satisfactorily. However, damage occurred in the structures such as shown in Fig. 5 where code provisions were not strictly followed, building sustained severe damages.

The bridges in the region were designed using equivalent static seismic coefficients of seismic zone V, that is, 0.08. The dynamic methods of analysis were not followed. The codal provisions at the time of the construction of damaged bridges were based on low seismic coefficients and did not recommend dynamic methods of analysis and design. The bridge structures designed in sixties as per code suffered damages but did not collapse. The practice of providing restrainers and elastomeric bearings in bridges need review.

The structures of Sardar Sarover project including main concrete dam, Orsang aqueduct and Mahi aqueduct did not suffer any damage. The gravity dams and aqueducts were designed on the basis of design basis earthquake using dynamic methods of analysis. These structures were located more than 350 km from the epicentre.

Lessons Learnt from Damages of Structures in Bhuj Earthquake

The occurrence of Bhuj earthquake has caused enormous loss to all types man made structures. Some of the weaknesses of design and construction were clearly exposed. The lessons learnt from damage to structures are presented below:

(i) The design of masonry buildings and construction practice should follow the provision of code IS: 4326

(ii) There should be a greater emphasis on quality of construction

(iii) The multistoreyed RC buildings with vertical irregularities like soft storey or mass irregularity should be designed on the basis of dynamic analysis and inelastic design with the provisions of ductility. There should be emphasis on provisions for detailing of reinforcement for ductility in members and joints.

(iv) The lessons from the damages to bridges suggest the need to design bridges in seismic zone V on the basis of dynamic analysis. There should be provisions of stoppers or restrainers in the bearing design for restricting excessive displacements even in low height piers. There should be a greater emphasis on the design and construction of bridge approaches and embankments.

(v) The damage to buildings, bridges and dams suggest a need to examine seismic capacity of existing structures designed according to old codes. The strength of structure should be upgraded by retrofitting so that they can safely withstand the effect of future earthquakes.

Summary and Conclusions

The Bhuj earthquake has caused significant damage to buildings, bridges and dams. The earthquake has brought out many weaknesses in the structural design and construction practice. There are number of bridges damaged due to pounding, tilting of piers and damage to restrainers and bearings. These are no loss of span type of failures in the region. The bridge structures of long span and tall piers were not existing in the area. The damages to bridges in most cases were repairable. Small earth dams less then 20 m in height suffered damage. The concrete gravity dams of Sardar Sarover project and appurtenant structures designed for earthquake forces although away from epicentre did not suffer any damage. The earthquake did show the amplification of soil and its affect on the structural behaviour. The multistoreyed buildings at distance as much 300-km and more from the epicentre got significantly damaged. The inadequate structural design and soil amplification both contributed to the damage of buildings. The most important lesson from the earthquake that is learnt is to design the structures on the basis of seismic codes of practice. In reference to bridges provision of restrainers in bearings and bridge approach design is extremely important. Retrofitting of weaker structures is recommended.

References

IS: 4326-1993 Earthquake Resistant Design and Construction of Buildings Code of Practice (Second Revision), BIS, New Delhi

IS: 13920-1993 Ductile Detailing of Reinforced Concrete Structures Subjected to Seismic Force Code of Practice, BIS, New Delhi

IS: 1893-2001 Criteria for Earthquake Resistant Design of Structures (Part 1) General Provision and Buildings (Fifth Revision), BIS, New Delhi

Kumar, A., Basu, S., Thakkar, S.K., Shrikhande, Manish, Agarwal, Pankaj, Das, J. and Paul, D.K (2001), "Strong Motion Records of Bhuj Earthquake" Abstract Volume of International Conference on Seismic Hazard with Particular Reference to Bhuj Earthquake of January 26, 2001, New Delhi, Oct. 2001.

Thakkar, S.K., Dubey, R.N. and Agarwal, Pankaj (2001), "Performance of Multistoreyed Reinforced Concrete Buildings in Bhuj Earthquake of January 26, 2001", Abstract Volume of International Conference on Seismic Hazard with Particular Reference to Bhuj Earthquake of January 26, 2001, New Delhi, Oct. 2001.

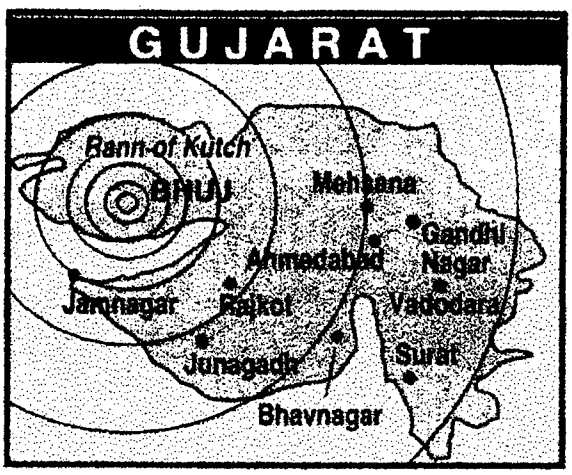

Fig. 1: Epicentre of Bhuj earthquake

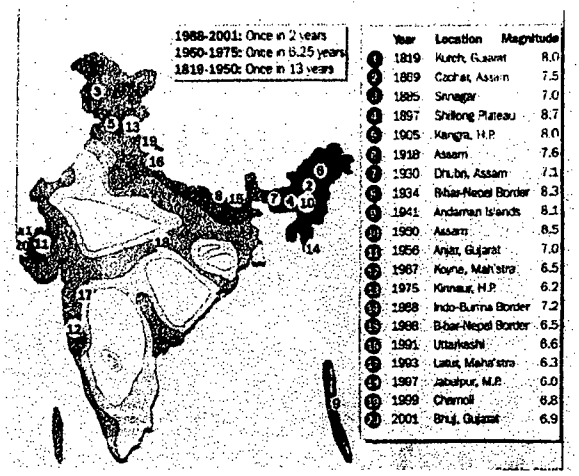

Fig. 2: Major past earthquakes in India

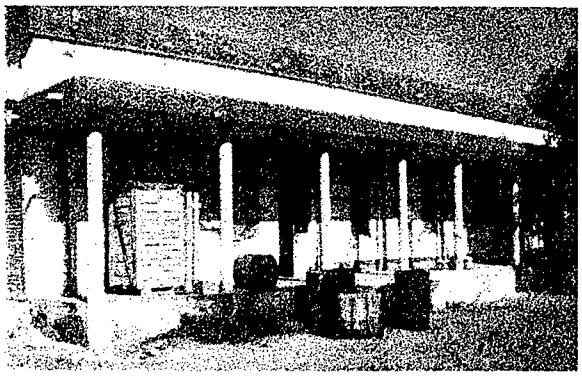

Fig. 3: Gujarat State Electricity Board substation, Bhuj (front view, random rubble stone masonry construction)

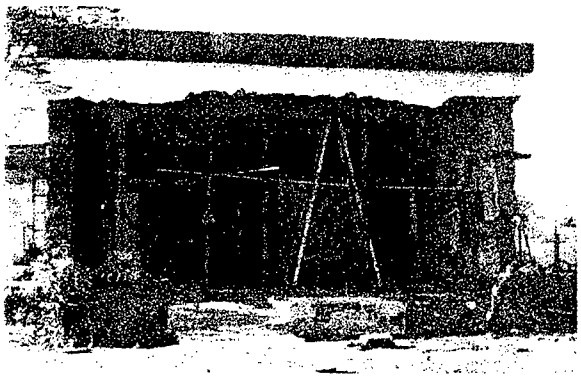

Fig. 4: Gujarat State Electricity Board substation, Bhuj (side view, out-of-plane failure of wall)

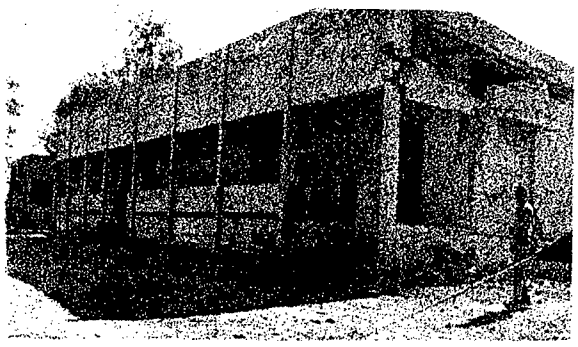

Fig. 5: School building in Bhuj (discontinuous band, severely damaged)

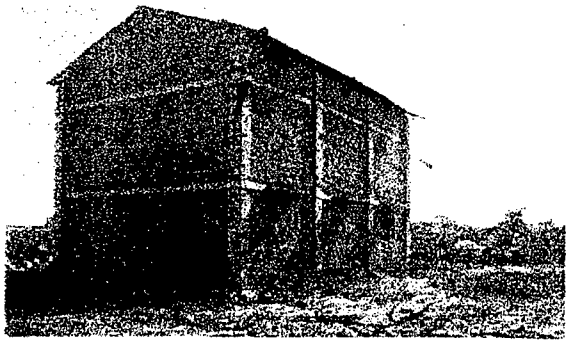

Fig. 6: Bentonite factory near Bhuj (seismic bands prevented damage)

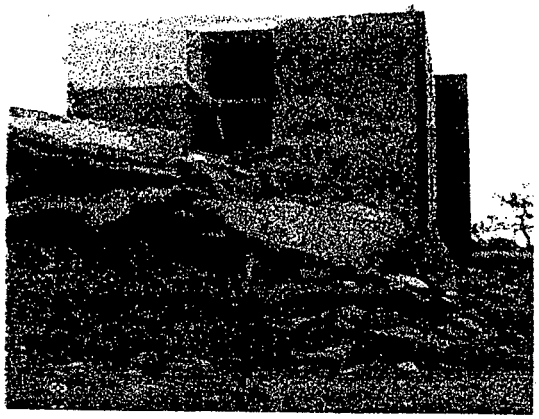

Fig. 7: Zila Panchayat, Bhuj (one of the three blocks completely collapsed)

Fig. 8: Three storyed building, Bhachau (top storey failure)

Fig. 9: Two storyed building, Bhachau (collapse of building)

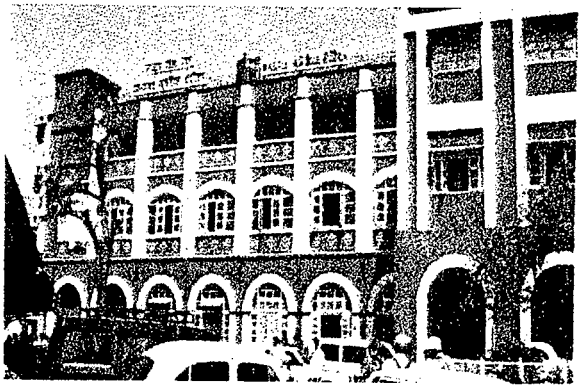

Fig. 10: Ahmedabad Municipal Corporation, three storyed building (stone masonry construction, undamaged)

Fig. 11: Traditional masonry construction in Dhragandhra, Kachchh (undamaged stone masonry construction)

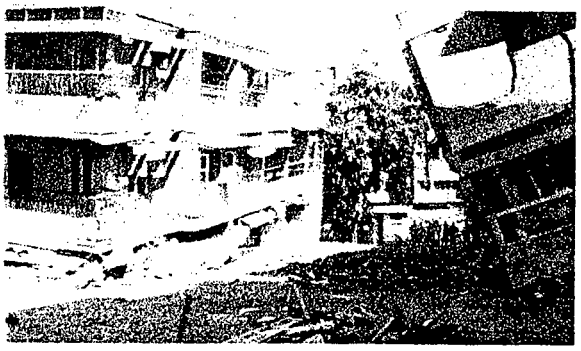

Fig. 12: Soft storey failure, G+4 Apollo Apartment, Ahmedabad

Fig. 13: Half portion of A-block, G+10, Mansi complex at Ahemadabad collapsed

Fig. 14: G+8, RC building at ONGC complex, Ahmedabad (diagonal cracking in filler walls on ground floor)

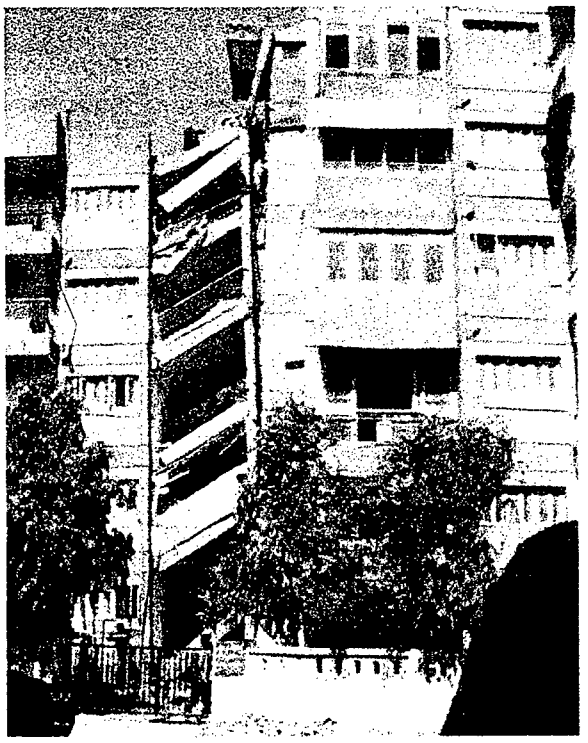

Fig. 15: Strut action of staircase during out of phase vibration of two blocks, G+4, Vishram flat, Ahmedabad

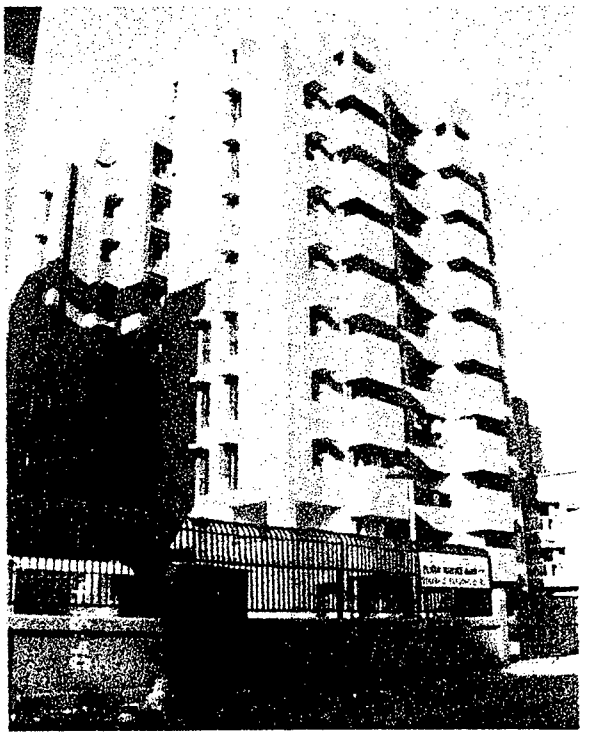

Fig. 16 Regional passport office staff quarters, G+9, Ahmedabad (code designed building, undamaged)

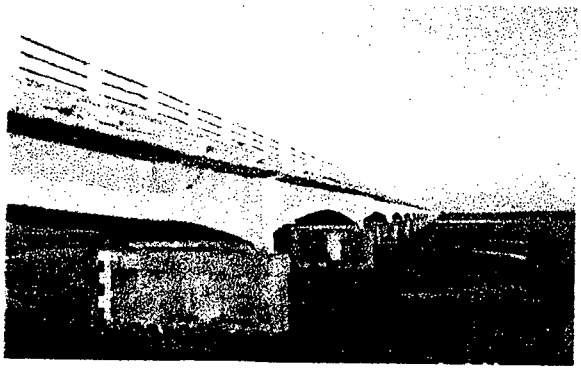

Fig. 17: Old Surajbari bridge (damage to bearings, approaches, pounding of superstructure)

Fig. 18: Old Surajbari bridge (damage to metallic bearings, transverse displacement of superstructure)

Fig. 19: Old Surajbari bridge (long separation between abutment and main deck)

Fig. 20: Railway bridge near Bhachau, substructure: 4 m high RC piers (minor damage to bridge piers and approaches)

Fig. 21: Multi-span RC beam road bridge on low height piers near Bhachau, bridge under construction (cracking of piers, separation from bearing block)

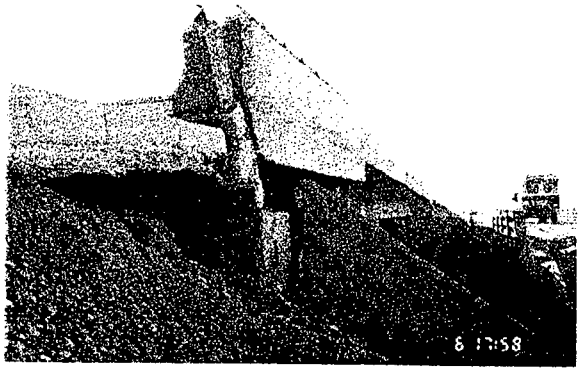

Fig. 22: Multi-span RC beam road bridge on low height piers near Bhachau, bridge under construction (severe damage to approach)

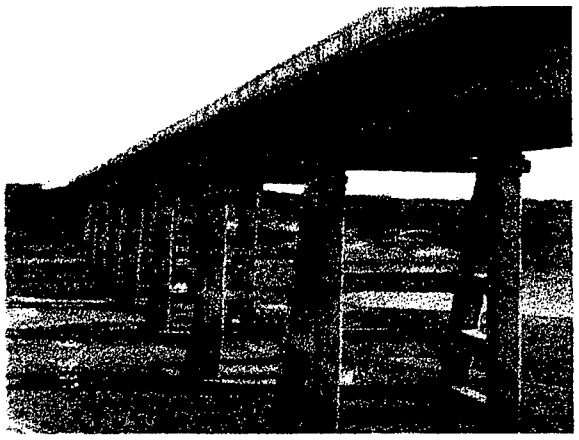

Fig. 23: Rudramata bridge, Bhuj

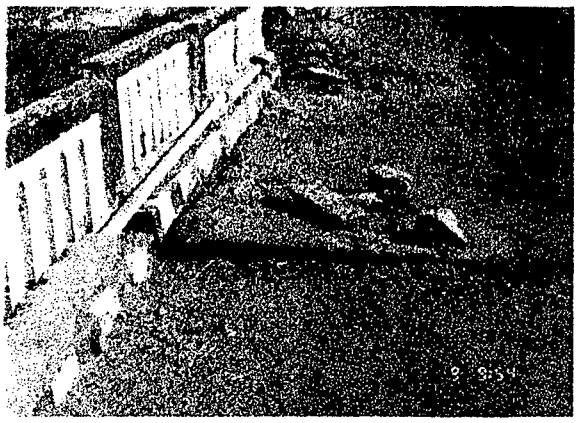

Fig. 24: Rudramata bridge, Bhuj (cracking of road and settlement of approach road)

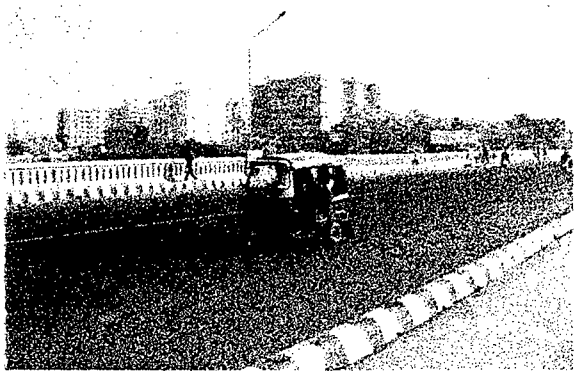

Fig. 25: Nehru Setu, Ahmedabad (minor damage to bridge)

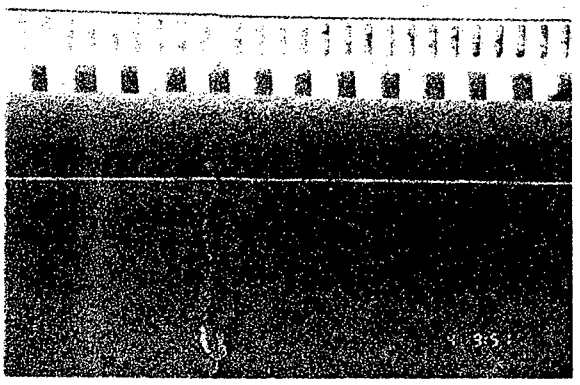

Fig. 26: Nehru Setu, Ahmedabad (cracking of road, pounding and parapet failure)

Fig. 27 Kaila earth dam, 23.47 m high (minor cracks on upstream slope, cracks in spillway)

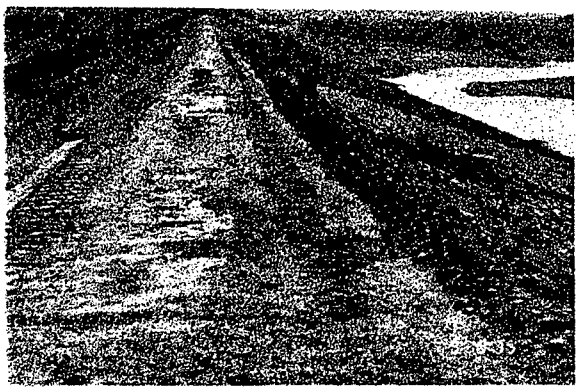

Fig. 28 Rudramata dam, 58 m high (cracking and slumping on upstream face, longitudinal cracks on the crest)

SESSION 3: MAINTENANCE 1

(1) Intelligent Road Surface Inspection System
(Shigeru Matsumoto and Koichi Sugioka)

(2) The Effect of Reinforcement of Carbon Fiber Sheets on PC Girders Damaged by Alkali-silica Reaction
(Hidetoshi Takagi, Kimitaka Uji, Katsuro Kokubu, Hirokazu Kitazawa, Takehiko Maruyama, Yoshio Sohda, Akira Kobayashi, Nobuhiro Hisabe and Hideaki Fukagawa)

(3) The Application of Water Jet Technology for Removal on Concrete Structure
(Syoji Nojima, Koichiro Shito, Yasushi Kamihigashi and Hiroyuki Takenouchi)

INTELLIGENT ROAD SURFACE INSPECTION SYSTEM

Shigeru Matsumoto [1] and Koichi Sugioka [2]

1. Abstract

Road surfaces damages can greatly impair driving safety. These also accelerate the deterioration of the pavement and the bridge deck. The deterioration results in excessive noise and harmful vibration. Thus finding and repairing such damages at an early stage is extremely important in maintaining bridges in good condition.

Now the Hanshin Expressway Public Corporation has been developing a road damage inspection system in which a camera mounted on a moving inspection vehicle captures images of the road surface. These images are then analyzed using image-processing technology to identify damage to the road surface.

With this Intelligent Road Surface Inspection System, we can look forward to making the bridge long-lived, as well as to reducing the life cycle cost.

2. Introduction

Pavement cracks, potholes, ruts, and other road surface damages can greatly impair driving safety and comfort traffic flow, causing hydroplaning or slipping of the steering wheel. These also allow water to collect beneath the pavement, which accelerates the deterioration of the pavement and the bridge deck. The deterioration in elevated roads results in bumps at expansion joints, and vehicles passing over them generate excessive noise and vibration. Such harmful vibration influences the durability of the bridge. Thus finding and repairing such damage at an early stage is extremely important in maintaining bridges in good condition.

At present, the Hanshin Expressway Public Corporation conducts daily inspection patrols involving visual inspection of the road surface. This approach affords the flexibility to respond to unforeseen circumstances and enables detailed inspection where required, but is reliant on the skill level of inspectors. Furthermore, the following problems have recently been identified:

(1) Inspectors are required of high level skill for visual measuring.
(2) It is becoming more difficult to employ suitably trained inspectors.
(3) Slow moving inspecting operation is extremely hazardous in heavy traffic.

---

1 Chief Engineer of maintenance technology division, maintenance department. Hanshin Expressway Public Corporation.
2 Engineer of maintenance technology division, maintenance department. Hanshin Expressway Public Corporation.

(4) Road damage judgment standards are distributed between inspectors.
(5) Personnel expenses account for the bulk of inspection costs.

Automation of the inspection process is considered as one of means of resolving these issues. The following prerequisites were identified as crucial in the development of a system designed to improve the present situation.

(1) The new system must be capable of detecting and analyzing road surface damage at least as capably as the current approach.
(2) The inspection vehicle must be capable of operating at full speed (50—80[km/h]), or at least of operating without stopping.
(3) The system must be capable of detection and analysis processing in real time.
(4) The system must be capable of transferring inspection data and images of road damage to the Maintenance Information System (presently under development) to enable instant access at any time.

We have been developing an image processing based road damage inspection system designed to suit the criteria above.

3. System configuration

Figure 3 shows the system configuration. The inspection vehicle is mounted with a CCD camera, laser emitter equipment, and image processing unit, as well as VICS (Vehicle Information Communication System) receivers and wheel speed sensors to get position information. The inspection vehicle travels along the roadway according to traffic flow and assesses the condition of the road surface in real time. Data on the road surface—information on the type and location of damage and images of damage—are stored on the road damage collection terminal. The inspector transfers to the road damage management system in the form of inspection data via the road damage confirmation terminal.

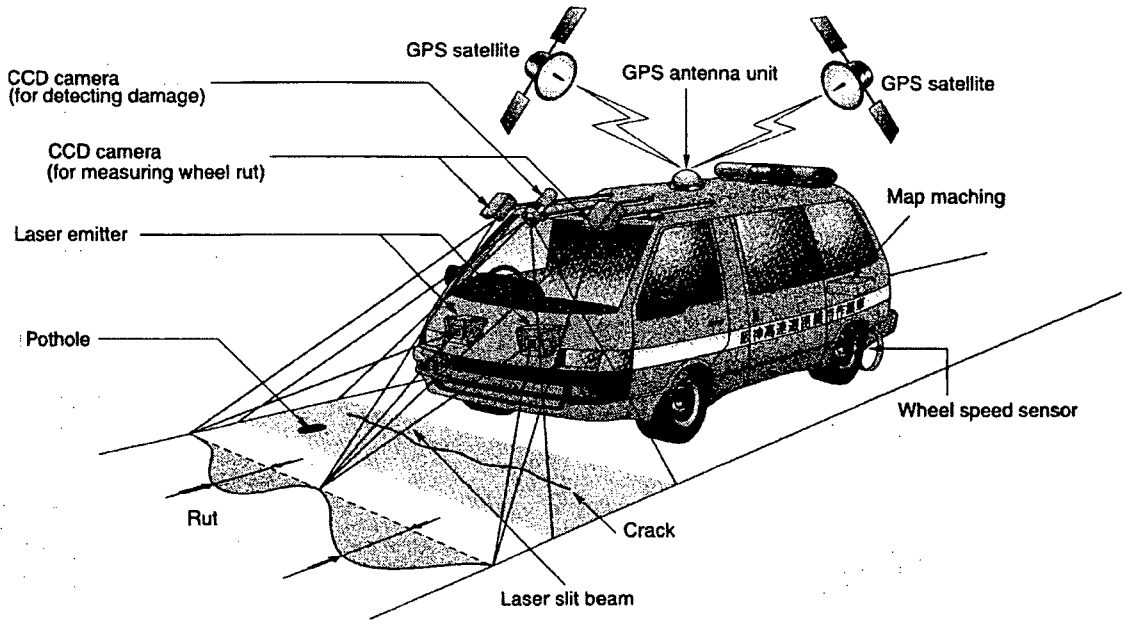

Figure1:Figure of the intelligent road damage inspection system

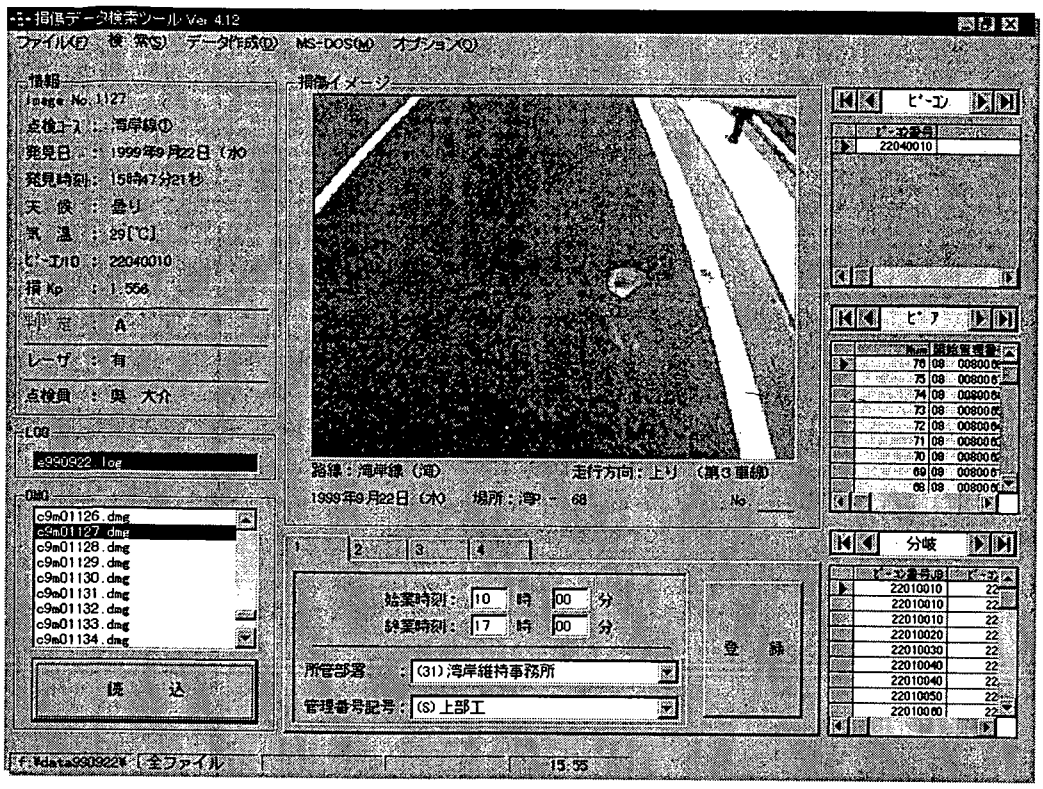

Figure2: Terminal display of road surface inspection

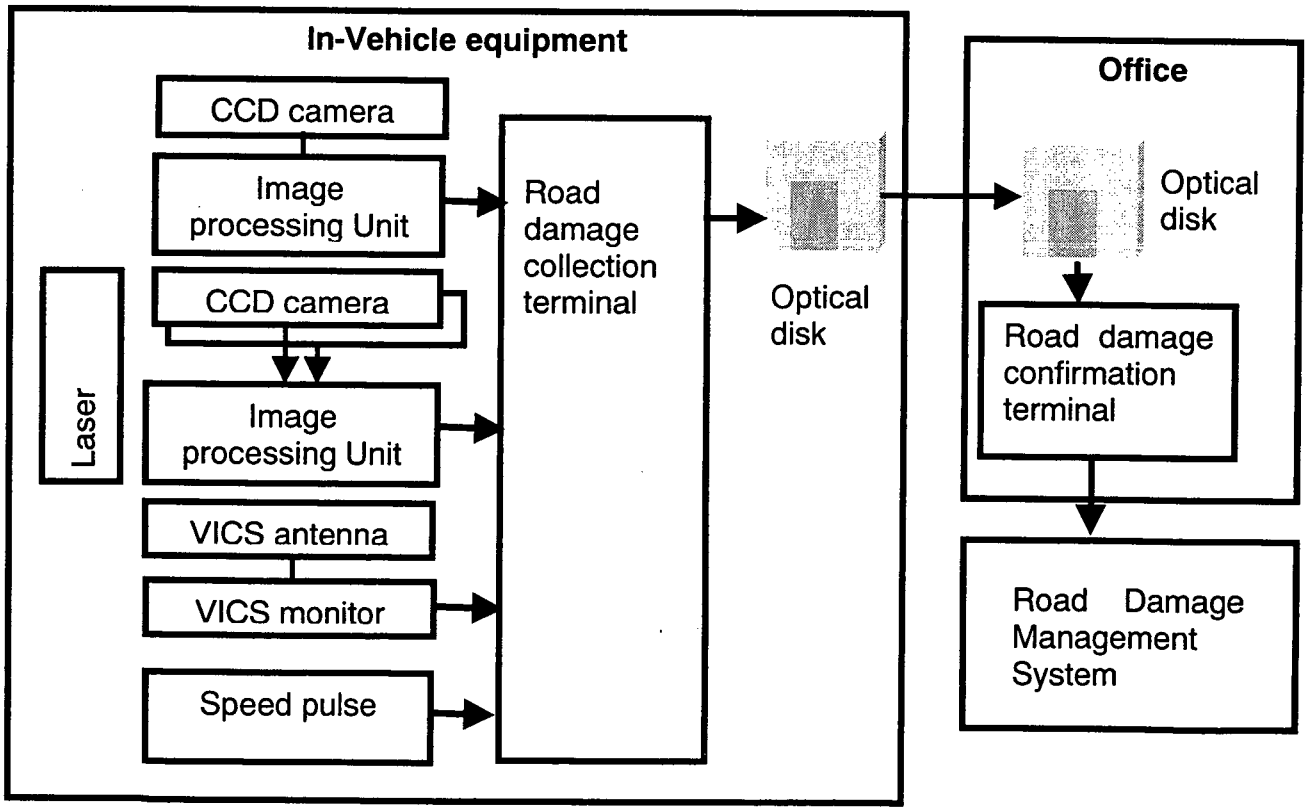

Figure3: System configuration of the intelligent road damage inspection system

4. Damage detection method

Images received from the CCD camera mounted to the inspection vehicle are analyzed using image processing to identify road damage such as cracks and potholes.

Figure 4 shows the road damage detection procedure. Images of the road surface are separated by gradation conversion processing into the white/yellow painted sections and differential images. The differential images are masked using the painted section, then the remaining differential images are analyzed for damage by area-based analysis and horizontal/vertical profiling.

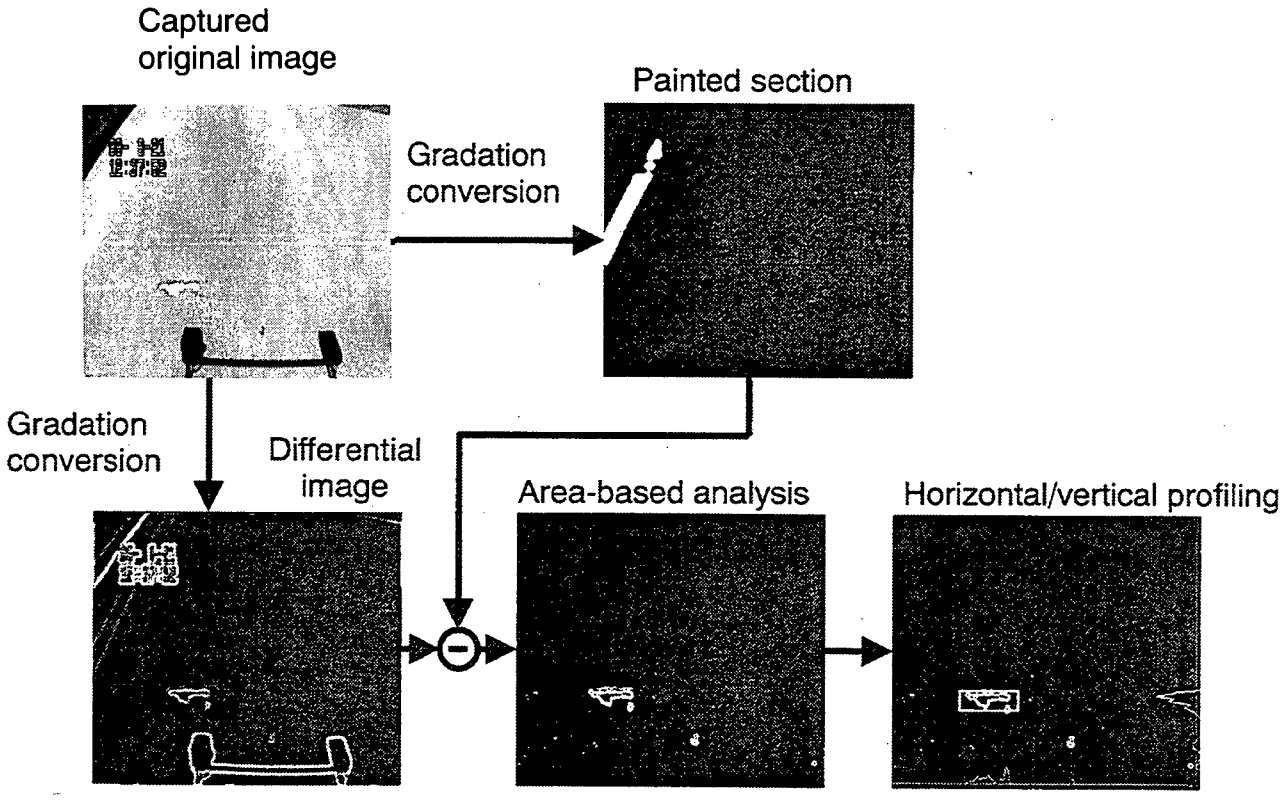

Figure4: Road surface damage detection flow

5. Non-imaging road surface analysis

The road surface consists of a variety of shapes and contrasts including (but not limited to) the cracks and potholes identified by the system. These are described below.

1) Shadows

Shadows cause a major influence to image processing in an outdoor processing system. It is particularly important that the system is able to distinguish between shadows and cracks, which often appear very similar in shown at Figure 5. It would be possible to

distinguish between shadows and cracks with setting suitable threshold value for differential image, because shadows tend to have smaller graduation value than cracks.

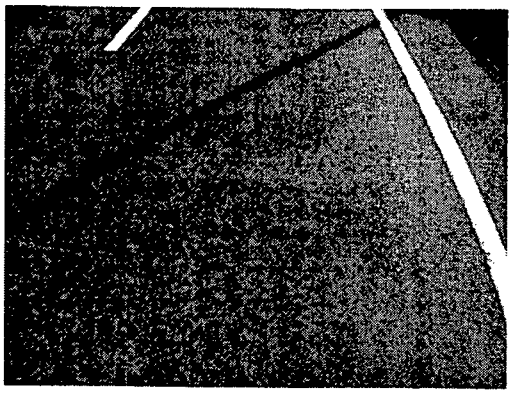

(1) Shadow

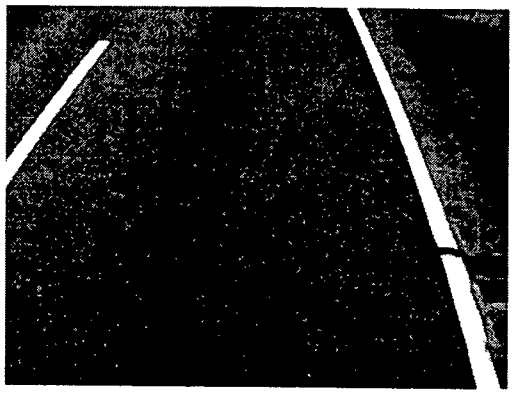

(2) Crack

Figure5: Similar images between shadows and cracks

2) Joints

At present, joints are classified by width in horizontal profile processing, but the problem with this approach is that some joints are very similar to cracks. Figure 6 shows images of joints not considered to be road surface damage. Buried joints, other than finger joints, constitute damage. Length separation in the horizontal direction of the detected area can be used to determine whether or not a joint constitutes damage.

(1) Buried joint 1

(2) Buried joint 2

Figure 6: Examples of buried joints

6. Damage detection performance

Table 1 shows damage detection results from the feasibility test.

As Table 1 shows, the system detects 90[%] of all damage sites. However, joints and shadows still account for a high proportion of the total, and this problem needs to be improved.

Table 1 Damage detection results

	Damage	Shadows	Joints	Repaired surface	Peeling paint	Others	Total
Total	22	-	1044	-	-	-	-
Detected	20	20	125	31	124	308	628
Detection rate (%)	90	-	12	-	-	-	-

Experimental conditions: Vehicle speed = 80 [km/h] Weather = fine
Road surface = concrete/asphalt

(1)Pothole1

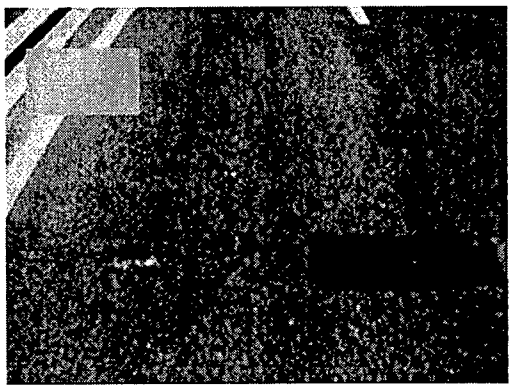

(2)Pothole2

Figure7: examples of detected road damage by the system.

7. Laser rut depth measurement

Rut depth measurement is currently performed using a 3-m transverse profile meter. Vehicle travel speed is limited, however, which can cause traffic congestion, so a simpler, faster method is needed.

We developed a system capable of measuring the road surface at full speed on an expressway without affecting other traffic.

1) Rut depth measurement method

Ruts in the road surface are measured with a laser using the light section method. The light source is a laser beam diffused into a fan shape. The camera measures distortions in the laser. Figure 8 illustrates measurement via the light section method.

The laser and the CCD camera are fixed to the vehicle at specific positions to produce the required difference in angles relative to the object being measured. The laser produces a fan-shaped beam, which illuminates a band of light across the road surface. The fan-shaped beam is reflected from the road surface and captured by the CCD camera. When the road is free of ruts, the fan-shaped beam forms a linear image. When ruts are present, the beam is distorted; the higher and lower sections of the rut (relative to the direction in which the camera is pointing) produce vertical offset in the fan-shaped beam, which translates into discrepancies in the camera's vertical coordinates. These discrepancies can be used to determine the depth of the rut.

The system uses a semiconductor laser source with infrared wavelength of 820 [nm]. Lasers generally exhibit wavelength characteristics of a very narrow bandwidth. It is therefore relatively easy to minimize the effect of sunlight by using an optical band pass filter that allows only laser wavelength to pass through to the CCD camera.

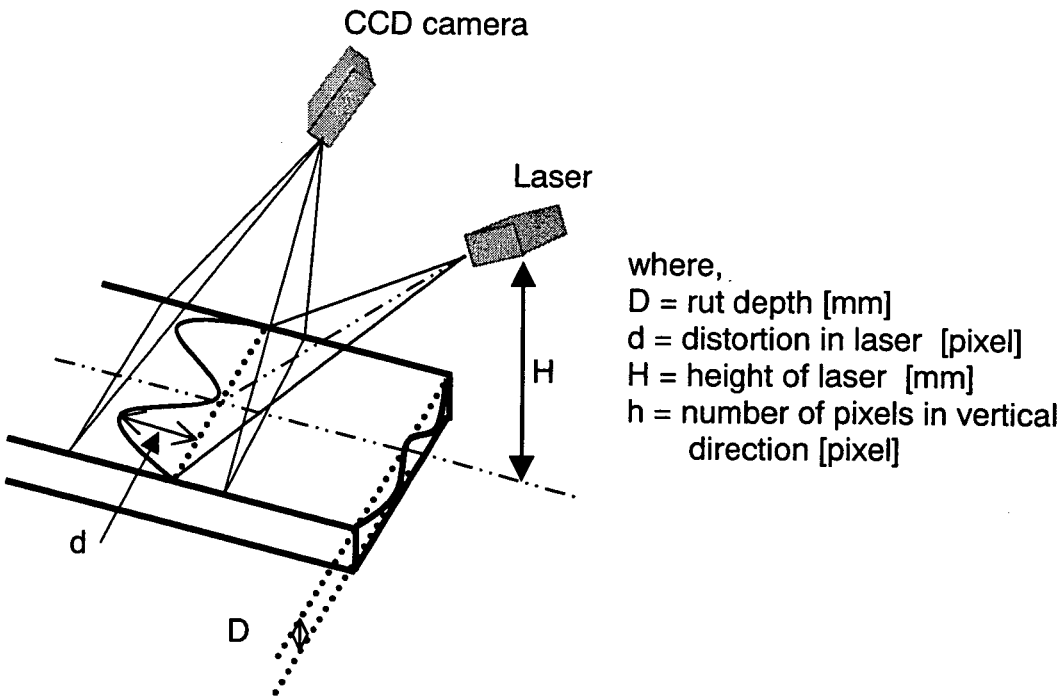

Figure 8: Measurement using the light section method

2) Rut depth measurements

Light section images from the inspection vehicle are subject to line differentiation and other image processing. Figure 9 compares consecutive images for a section of road with relatively few ruts and another section with many ruts. The magnitude of distortion can be determined from the number of pixels in the vertical direction, where one pixel is equivalent to approximately 4 [mm].

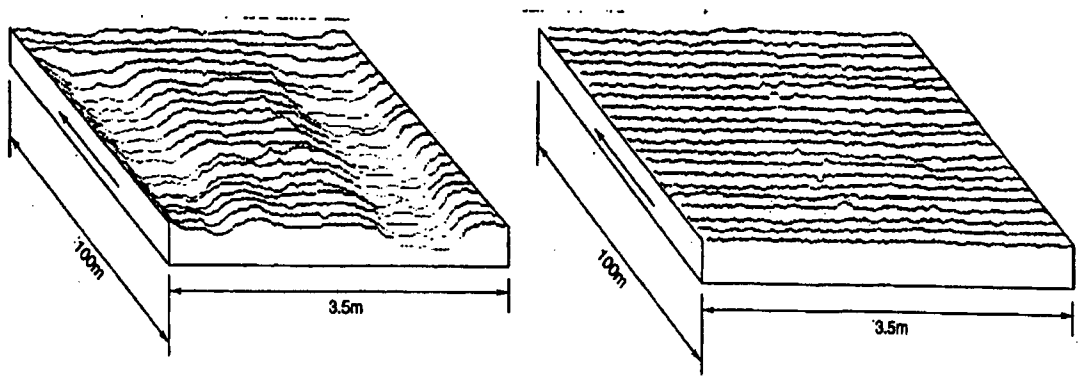

(1) Ruts surfaces (2) Flat road surfaces

Figure 9: Rut measurement method

Figure 10 shows an example of rut road surface image with high rate scanned camera. Left part has a large distortion illumination because of rut.

Figure 10: An example of rut image

3) Applied for road damage detection

Figures 10 and 11 show how damaged sections (circled) appear under laser illumination, clearly illustrating distortion in the laser.

Pothole

Figure 11: Damage under laser illumination

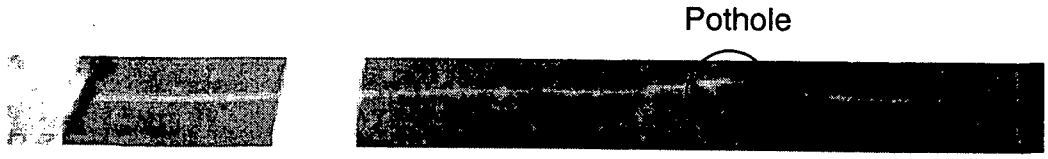

Figure 12: Damage under laser illumination

8. Position Information

Figure 13 illustrates the VICS beacon position information system. The Hanshin Expressway Public Corporation currently has already installed about 200 VICS beacon transmitter equipment. During inspection operation, the pier number of a damage location can be determined from the digital map database using a combination of the unique ID numbers transmitted by the beacons and the vehicle speed pulse at the time of detection. This method ensures a distance accuracy of within 10 m and pier positioning accuracy of around 90%.

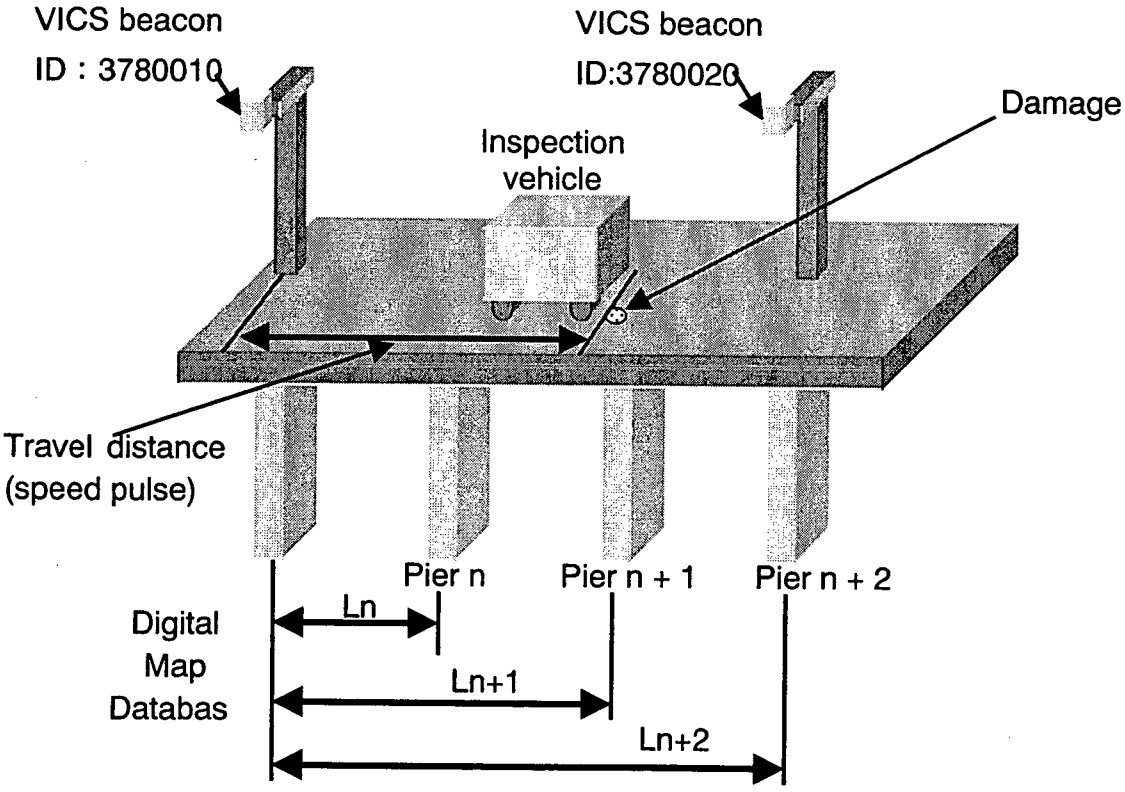

Figure 13: Position Information using VICS beacon

9. Conclusions

This study reported the following with respect to the newly developed road damage inspection system:

1. Damage detection rates of 90% or better can be achieved.
2. The use of the light section method-laser enables three-dimensional measurement of ruts.
3. Position accuracy of 90% can be achieved using existing VICS technology.

Now we have executed about decreasing and improvement non-damage(shadow, joint, and dust on the road) rate

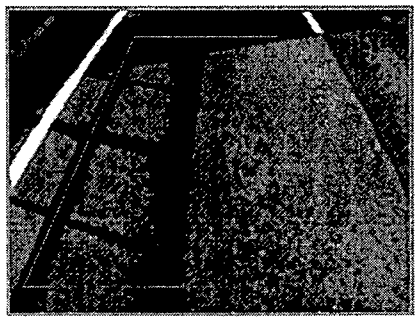

Figure 14:Removal shadow processing

And we have examined to indicate the depth of a rut enhance integration with road management systems. The road damage inspection system will facilitate maintenance work such as daily maintenance and inspection patrols.

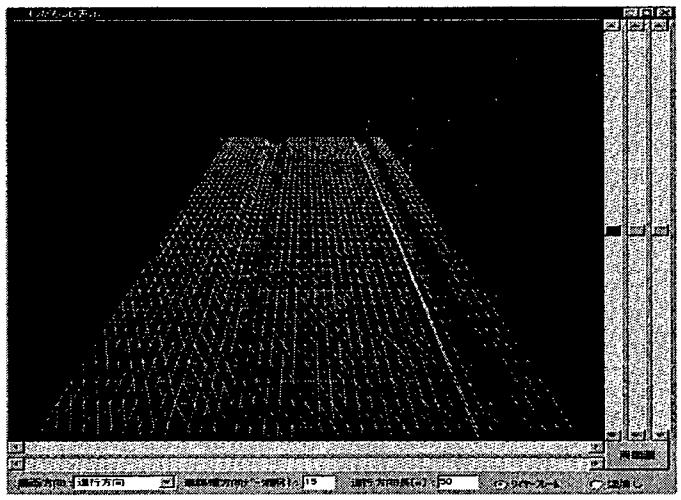

Figure 15: Terminal display of indicate the depth of a rut

Reference

[1] Momozawa, Horie, and Hasegawa: Intelligent checking system of street surface. ISIE1995:Vol.1, 410-415pp.

[2] Kawamura,Horie, and Momozawa: Development of an Intelligent Road Damage Inspection System

THE EFFECT OF REINFORCEMENT OF CARBON FIBER SHEETS ON PC GIRDERS DAMAGED BY ALKALI-SILICA REACTION

Hidetoshi Takagi[1], Kimitaka Uji[2], Katsuro Kokubu[3], Hirokazu Kitazawa[4], Takehiko Maruyama[5], Yoshio Sohda[6], Akira Kobayashi[7],Nobuhiro hisabe[8] and Hideaki Fukagawa[9]

Abstract

There has been little research on the reinforcement effect of carbon fiber sheet (CFS) on prestressed concrete (PC) beams that have been damaged by alkali-silica reaction (ASR). The present study examined the bending performance and residual strength of ASR-damaged PC beams in terms of the concrete's properties and the elasticity coefficient of the CFS. Specimens of PC beams with reduced strength and elasticity coefficient due to ASR were taken from an actual bridge and subjected to bending load tests in order to determine the deformation and strain characteristics of the damaged concrete and the effect of CFS reinforcement on the recovered rigidity and increased strength.

1. Introduction

Concrete that has been damaged by alkali-silica reaction (ASR) can suffer sharp drops in elasticity coefficient. In fact, previous studies have found that ASR reduces the elasticity coefficient by as much as two-thirds. Large drops in the elasticity coefficient can increase structural deformation, reduce the safety and comfort of driving on concrete structures, and interfere with the structures' intended functions and purpose. Furthermore, cracking and other severe damage can reduce the structures' durability.

Proposals for the repair and reinforcement of ASR-damaged structures have included wrapping the concrete with carbon fiber sheets (CFS) or steel plates. In the case of columns and other components that can be completely enclosed with the reinforcing material, the confinement effect can be expected to provide the necessary repair and reinforcement. The resin that is used to bond the CFS to the concrete surface may also provide waterproofing that can inhibit ASR-induced swelling of the concrete.

Beams made of prestressed concrete (PC) or reinforced concrete, however, cannot be wrapped completely, so the effect of CFS reinforcement has been unknown. In the present study, test PC beams that been damaged by ASR on an actual bridge were removed from the bridge, reinforced against bending and shear with CFS, and subjected to static and dynamic loading tests.

---

[1] Assistant Manager, Nippon Mitsubishi Oil Corporation
[2] Associate Professor, Tokyo Metropolitan Univ
[3] Professor, Tokyo Metropolitan Univ
[4] Tokyo Metropolitan Univ
[5] Professor, Meisei Univ
[6] Group Manager, Nippon Mitsubishi Oil Corporation
[7] General Manager, Nippon Steel Composite Co.,Ltd
[8] Assistant Manager, Mitsubishi Chemical Functional Products,Inc
[9] Manager, Toray Industries,Inc

The purpose of the tests was to determine how much the CFS improved the flexural rigidity and strength of the damaged PC beams and to determine the beams' fatigue deterioration properties.

2. Experiment

A total of five PC beams were used in the experiment: one to determine the basic properties of the concrete, two for the static loading tests, and two for the dynamic loading tests. As shown in Fig. 1, the beams used in this study had many cracks; these cracks were thought to be caused by ASR. All five of the beams had about the same degree of cracking.

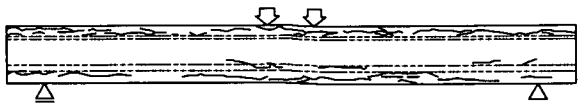

Fig 1. Crack of PC beam

Before the loading tests, core samples were taken from the ASR-damaged beams and tested in order to determine the basic properties of the concrete. These properties included the uniaxial compressive strength and the elasticity coefficient. The degree of deterioration was also determined from measurements of the released expansion coefficient in standard curing and the residual expansion coefficient in accelerated curing.

Because the beams used in the experiment were made of prestressed concrete, the cores were taken both parallel and perpendicular to the prestressing, and the degree of deterioration was determined in both directions.

Fig. 2 shows the specimens used in the loading tests. To determine the effect of the ASR deterioration, static and dynamic loading tests were conducted on unreinforced PC beams. The same tests were also conducted on beams that had been reinforced with CFS in order to improve the strength and rigidity. The CFS had a modulus of elasticity of 245 N/mm^2, tensile strength of 3,400 N/mm^2, and fiber mass of 300 g/m^2.

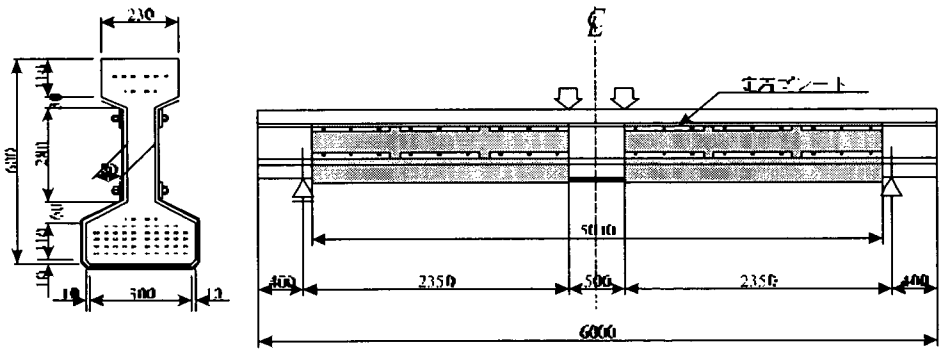

Fig2. Specimen

The bending reinforcement was applied with three layers of CFS along a span 5040 mm long on the bottom surfaces of the specimens.

To prevent shear failure and to ensure adequate anchoring of the sheets, one CFS was applied along nearly the entire length of the shear span in the stirrup direction as shown in Fig. 2. This CFS had a fiber mass of 200 g/m^2.

In the static loading tests, the load was applied in several stages until failure occurred. In the dynamic loading tests, the load was applied as shown in Tables 2 and 3.

The loads used in these bending tests were based on the permissible stress specified by the standards for highway bridges in Japan (180 kN in the case of the specimens used in this experiment).

Table 1. CFS Properties

Fiber mass g/m²	Thickness mm	Properties: Tensile Strength N/mm²	Elastic Modulus N/mm2	Elongation %
200	0.111	4592	$2.42*10^5$	1.61
300	0.167	4648	$2.44*10^5$	1.72

Table 2. Dynamic loading tests condition of unreinforcement specimen

Stage	Load method	Load Minimum kN	Load Maximum kN	Rate to failure load %	Number of cyclic *10⁴ times	Cumulated number *10⁴ times
1	dynamic	90	180	38	50	50
2	dynamic	90	250	52	50	100
3	dynamic	140	300	63	100	200
to failure	static	---	480	---	---	---

Table 3. Dynamic loading tests condition of reinforcement with CFS specimen

Stage	Load method	Load Minimum kN	Load Maximum kN	Rate to failure load %	Number of cyclic *10⁴ times	Cumulated number *10⁴ times
1	dynamic	140	300	50	100	100
2	dynamic	190	350	58	100	200
3	dynamic	280	440	73	30	230
to failure	static	---	605	---	---	---

3. Evaluation of Core Deterioration

3.1 Strength of Concrete in PC Beams

Table 4 shows the test results for the compressive strength of cores taken parallel and perpendicular to the prestressing. Each value is the average for three cores. The cores were 68 mm in diameter and 136 mm long.

Table 4. Results of compressive tests

Direction of taken core	Compressive strength N/mm²	Elastic coefficient kN/mm²
Parallel to the prestressing	40.9	25.7
Perpendicular to the prestressing	34.8	18.0

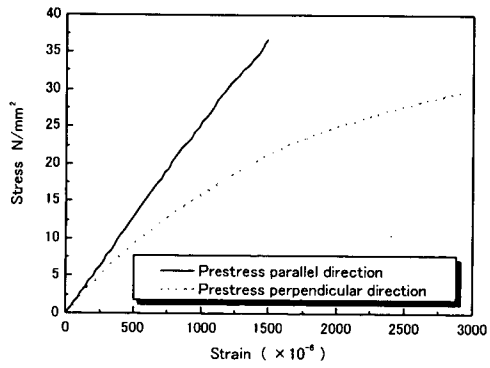

Fig 3. Sterss-Strain curve of Core

Fig. 3 shows the stress-strain curve of cores taken in both directions. The results show that the cores taken in the two directions had very different compressive strengths and elasticity coefficients. The ASR damage to the PC beams used in this study had caused big differences in the compressive strength and elasticity coefficient depending on whether the measurements were made parallel or

perpendicular to the direction in which the concrete had been prestressed. In environments in which prestressing is applied, the expansion is therefore limited in the direction of the prestressing and there is a sharp difference in the degree of deterioration between the parallel and perpendicular directions. Care must therefore be taken when examining the physical properties of concrete in PC beams.

3.2 Measurement of Expansion of PC Beams

Fig. 4 shows the released expansion coefficient, which indicates the degree of deterioration already caused by ASR. Fig. 5 shows the residual expansion coefficient, which indicates the risk of further expansion in the future.

The test method was based on JCI-DD2, "Measurement Method for Coefficient of Expansion of Core Samples of Concrete Structures Damaged by Alkali-Silica Reaction (Proposal)."

As shown in Fig. 4, there is a large difference between the expansion coefficients parallel and perpendicular to the direction of prestressing. This difference is thought to occur because the prestressing inhibits the ASR-caused structural deterioration. This observation agrees with the previous result in which the compressive strength and static elasticity coefficient were both higher for cores taken in the prestressed direction than in the perpendicular direction.

The generally used indicator of ASR-caused deterioration is a change of 0.05% in the residual expansion coefficient. Because it usually takes six months to a year for the expansion change to level off, the trend at the three-month point in Fig. 5 suggests that further expansion is still likely. In other words, the PC beams sampled in this test had already suffered some deterioration and would have been likely to deteriorate further in the future.

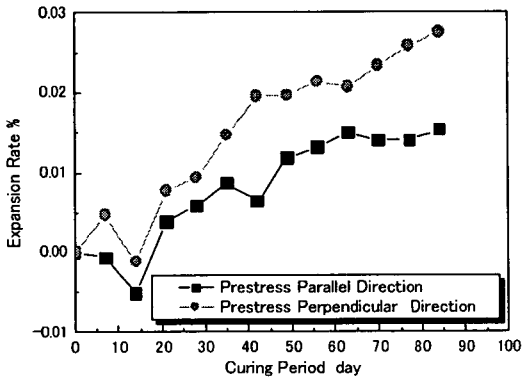

Fig 4. Released expansion coefficient

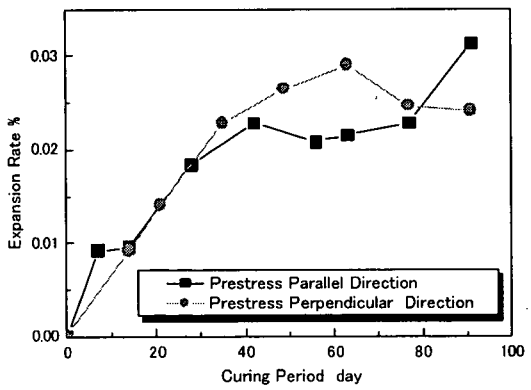

Fig 5. Residual expansion coefficient

4. Experiments with PC Beams

4.1 Static Loading Tests

The experimental results are shown in Table 5. Bending cracks formed in the unreinforced PC beams at 240 kN, and shear cracks formed at 355 kN. Shear cracking continued further, with shear failure occurring at 425 kN.

The unreinforced PC beams exhibit elastic behavior up to the level of normal use (P = 180 kN), and they continue to behave as elastic bodies even when cracks have formed due to ASR expansion. After the shear cracks formed, however, there was a sharp increase in the displacement, leading eventually to shear failure.

With the CFS-reinforced beams, the bending cracks formed at 340 kN, indicating that the CFS inhibited the formation of bending cracks. The failure load was 465 kN.

While the failure of the unreinforced beams was due to shear, the CFS-reinforced beams failed due to bending, thus showing that the CFS applied along the stirrup was able to prevent shear failure.

Table 5. Tests results

Load method	Reinforcement	Compressive strength N/mm²	Elastic coefficient kN/mm²	Shear cracking load kN	Bending cracking load kN	Shear failure load kN	Bending failure load kN	Failure type
static	No	40.4	26.3	355	240	425	---	Shear
static	Yes	40.2	29.7	---	340	---	465	Compressive
dynamic	No	48.8	30.7	320	260	480	---	Shear
dynamic	Yes	53.5	37.9	---	340	---	605	Compressive

This study examined the shear reinforcement effect of CFS using test specimens taken from an actual concrete bridge. The load and displacement relationships of the unreinforced and CFS-reinforced PC beams are shown in Fig. 6. This figure also shows the calculated values for undamaged concrete (fc = 50 N/mm², Ec = 33 kN/mm²).

When CFS was used to provide bending reinforcement to ASR-damaged PC beams, the deformation at the load of actual use (P = 180 kN) returned to the same normal level as when the bridge was originally built.

Fig. 7 shows the relation between the load and the strain to the upper edge of the concrete. As shown in the figure, the strain on the CFS-reinforced PC beam dropped by about 20%.

While shear failure occurred when the strain to the compressed edge of the unreinforced beam was 2700 μ, the CFS-reinforced beam was able to withstand strain up to 3500 μ, which is thought to be the ultimate strain of concrete.

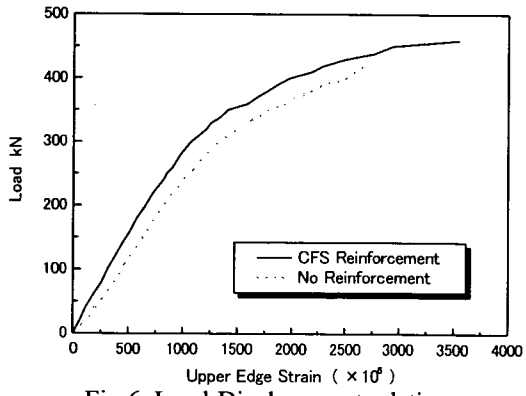

Fig 6. Load-Displacement relation

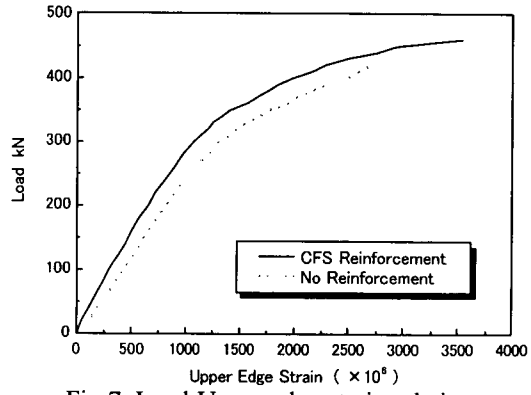

Fig 7. Load-Upper edge strain relation

Fig. 8 shows the strain distribution on the side of the CFS-reinforced PC beam. The lower part of the figure shows the measurements taken with the gauges attached to the CFS. As

the load increased, there was greater variation in the strain on the tensile side. This variation is believed to have been caused by the formation and extension of cracks.

At 460 kN, which was near the ultimate load, the strain to the CFS reached about 5000 μ when the strain on the compressed part had been extended. While there was a difference from the measured value, it is clear that the principle of plane conservation was maintained nearly perfectly up to 400 kN.

The strain distribution on the CFS applied to the bottom surface is shown in Fig. 9. This strain was measured with gauges attached at 100-mm intervals along the 1000-mm section that extended 500 mm to either side from the center of the specimen. The broken line in the figure shows the position of the load. The area enclosed by the broken line is the bending-only area that had no shear reinforcement.

At the load of 460 kN, a strain of about 3500 μ had occurred in the CFS. If the fracture elongation of high-strength CFS is 17,000 μ (based on the elongation of 1.72% shown in Table 1), then this CFS has a sufficient margin of safety against failure.

No peeling of the CFS was observed under the conditions of this experiment.

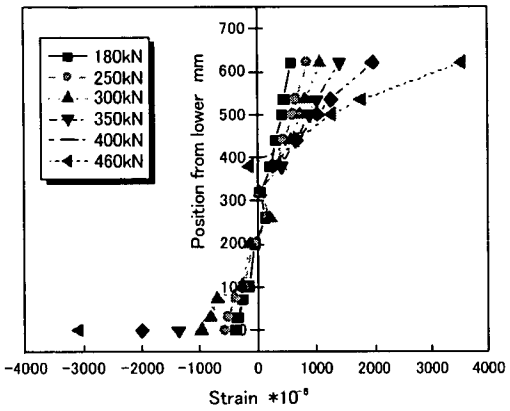

Fig 8. Strain distribution (Reinforcement beam)

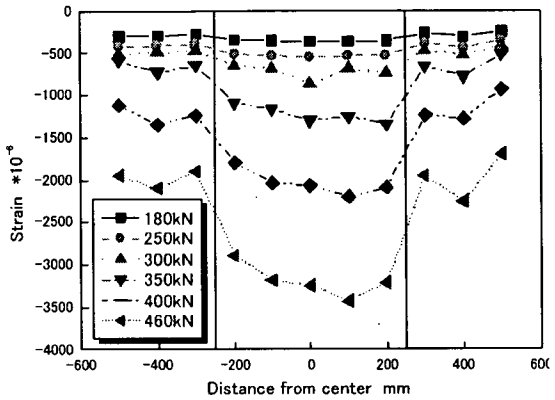

Fig 9. Strain distribution on the CFS

4.2 Dynamic Loading Tests

Fig. 10 shows the relationship between the displacement and number of cycles of the dynamic loading test for unreinforced PC beams.

In the first stage, a 180 kN load was applied so that the stress on the upper side of the concrete would reach the level specified by the standard Japanese highway specifications (16.67 N/mm^2 relative to f'c = 50 N/mm^2), but there was almost no change in the displacement. Thus the stress specified by the 1996 highway specifications has almost no negative effect on the fatigue characteristics of ASR-damaged PC beams.

Similar results were found in the second stage, in which the maximum load (P = 250 kN) of the cyclic loading was around the level at which cracks occur.

In the third stage, which had a higher stress level (1.7 times the highway specification load), there was a slight increase in displacement, but there was almost no change until the end of the stage, and the concrete was able to withstand a total of 2,000,000 load cycles.

Fig. 11 shows the relationship between the displacement and number of cycles of the dynamic loading test for CFS-reinforced PC beams.

The maximum load on the CFS-reinforced PC beams in the first stage was set to the same level (P = 300 kN) as in the third stage of the test of the unreinforced PC beams. While the difference between the maximum displacement and residual displacement was about 8 mm for the unreinforced beams, the difference was only about 7 mm for the CFS-reinforced beams, showing that the CFS reduced the degree of displacement slightly.

No increase in displacement was observed in the first stage. In the second stage, there was a large increase in displacement immediately after the load was applied, but thereafter the displacement increased only slightly as the number of cycles increased. In the third stage, there was a sharp increase in the displacement.

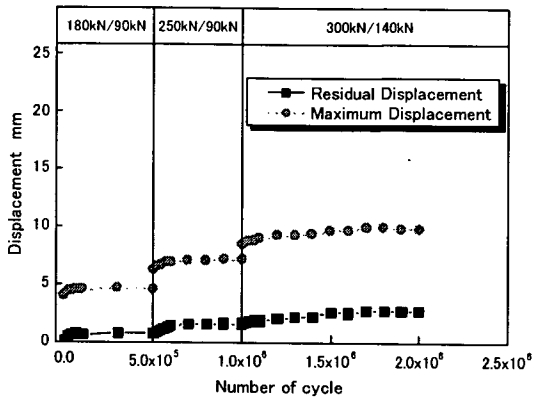

Fig 10. Displacement-Number of cycles (unreinforcement beam)

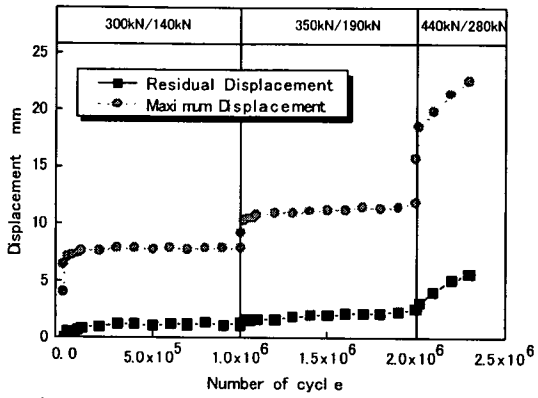

Fig 11. Displacement-Number of cycles (reinforcement beam)

Fig. 12 shows the relationship between the upper edge strain and number of cycles for unreinforced PC beams. In the first and second stages, there was almost no increase in the upper edge strain, and the strain increased only slightly in the third stage. These trends indicate that repeated load has almost no effect on the fatigue even with ASR-damaged PC beams.

Fig. 13 shows the relationship between the upper edge strain and number of cycles for CFS-reinforced PC beams. There was only a slight change in the strain in the first stage and only a slight increase in the second stage. It should be noted, however, that fatigue should have relatively little effect up to the load level in the second stage (350 kN). In the third stage, the upper edge strain increased sharply, and if the load had continued to be applied the concrete could very well have reached compressive fatigue failure.

The load in the third stage (400 kN) was chosen so that the strain to the upper edge of the concrete would be 2000 μ. At this load, an increase in the upper edge strain appears. If the upper edge strain at which fatigue failure occurs is assumed to be 3500 μ, then the beam would be expected to fail at around 1,800,000 cycles in stage three.

The maximum load in stage three was equivalent to 73% of the failure load.

These results show that there was little decrease in the fatigue life of ASR-damaged PC beams. This is thought to be related to the above-mentioned difference in the compressive strength and elasticity coefficient in the prestressed direction and perpendicular to the

prestressed direction, and to the resulting small drop in these properties in the prestressed direction when the concrete was exposed to fluctuating stress due to repeated fatigue.

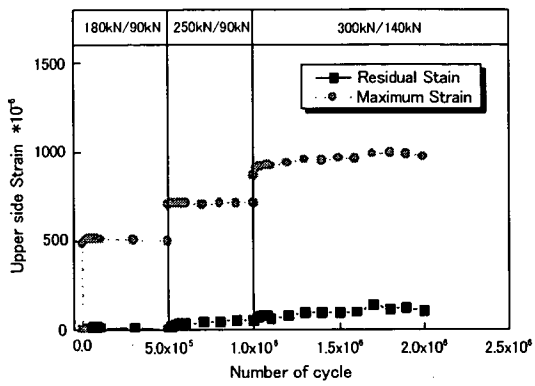

Fig 12. Upper edge strain-Number of cycles (unreinforcement beam)

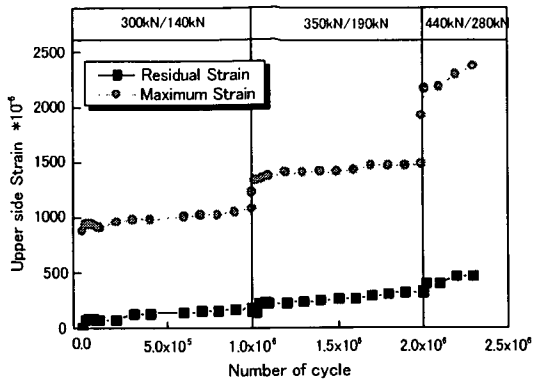

Fig 13. Upper edge strain-Number of cycles (reinforcement beam)

5. Conclusion

The following was learned from these experiments.

1. The PC beams used in these experiments had undergone deterioration and were likely to have deteriorated further.
2. The released expansion coefficient was different parallel and perpendicular to the direction of prestressing. This was shown by the difference in the compressive strength and elasticity coefficient in cores taken in the two directions and in the different degree of deterioration in the two directions. This phenomenon is thought to be affected by the prestressing. Therefore, when the degree of deterioration of PC structures is evaluated, the direction of the sample cores must be considered.
3. When ASR-damaged PC beams are given flexural reinforcement with CFS, improvements in the bending rigidity and deformation performance can be expected.
4. Reinforcement with CFS improved the structural strength, recovered the deformation performance nearly to the level of undamaged PC beams, and reduced the upper edge strain by about 20% compared with unreinforced PC beams.
5. The prevention of shear failure was evaluated by applying CFS along the stirrup of an actual structural component. This CFS maintained adequate anchoring for bending reinforcement until the end of the test.
6. When ASR-damaged PC beams are given bending reinforcement with CFS, one can expect improved deformation performance, reduced strain to the upper edge of the concrete, and a longer fatigue life as a result.

Reference

Mitsuru Onodera, Shinji Tsuchida, and Takehiko Maruyama: "Compression fatigue property of the ultra high strength concrete PC beam with silicafume," Proceedings of 50th Annual Lecture Series of Japan Society of Civil Engineers, part 5, pp. 776–777, September 1995 (in Japanese).

The Application of Water Jet Technology for Removal on Concrete Structure

Syoji NOJIMA*, Koichiro SHITO*, Yasushi KAMIHIGASHI*
and Hiroyuki TAKENOUCHI**

Abstract

When repair works or strengthening works are conducted to concrete structures, it is necessary to remove the damaged or fragile sections and factors of deterioration. However, removal or chipping treatment, as one of the traditional methods, generally employs mechanical hand breaker directly acting upon the chipping surfaces without taken into account of the adverse effect on the surrounding concrete. This method is still commonly used because there are no technical specifications on removal of concrete available up to date. This research was focused on the selectivity performance of Water Jet Method (i.e. WJ Method) and its applicability to removal of concrete. Both removal by using hand breaker and various WJ methods were conducted on reinforced concrete specimens. As a result, a report on harmful effect by using hand breaker was presented and a specification on WJ method was recommended.

1. Introduction

At the beginning of the 21st century, the concrete structures, having taken a vast sum of stocks, become a main part of social capital essential to national daily life. On the other side, being a well-known aging society of the world, Japan has to put cost-savings into practice for maintenance and management of its well-constructed infrastructure and new constructions. For example, the total length of highways supervised by JH reached 6851km and their average service year exceeded 17 years, as to April 1st, 2001, since Meishin Expressway between Amagasaki IC and Ritto IC was opened to traffic 37 years ago. Among the extended length, bridges held 14.5%, and including retaining walls, culvert boxes and tunnels, a large amount of concrete structures get deteriorated with environmental and service conditions. This leads to an urgent need for more effective maintenance and management, and the techniques of repair and reinforcement.

With increase of service extension, the highways in a cold, snowy area are also extended that occupy half the length. In such areas, deicer - mainly consist of sodium chloride, has been spread to keep a safe traffic in winter, which then becomes a chloride ion supplier of concrete structures. Unfortunately, this measure made the local deterioration gets into a national wide salt damage. Additionally, the sodium chloride in deicer raises alkalinity of concrete and becomes the cause of the increase of alkali-aggregate reaction, too. Furthermore, the concrete structures built in recent years, show a tendency to fall in quality with higher neutralized speed because of lack of high quality aggregates, skilled engineers or technicians, and the constructions in high pitches with the spread of pump casting. Consequently, chloride ion has been observed getting concentrated inside[1)] with the neutralization coming from the surface of the concrete, which also follows an early deterioration in concrete structures. For this reason, the

*Bridge Division, Expressway Research Institute, Japan Highway Public Corporation
**Second Research Division, Japan Construction Method and Machinery Research Institute

structures from which such factors need to be removed are increasing.

For repairing and strengthening the concrete structures mentioned above, it is expected that the unity is surely maintained between existing body and latter placed parts, or between the sections from which deterioration factors have been removed and materials for repair. Depending on the situation, measures such as surface preparation, removal, drilling and cutting are taken in existing concrete (**Fig.1**) either by experiences or repeating trial and error, because there is no suitable specification at present for such treatments. Therefore, unsuitable treatments may lead to the drop of durability and load-carrying capacity in such structures and re-repair may be needed at an early stage.

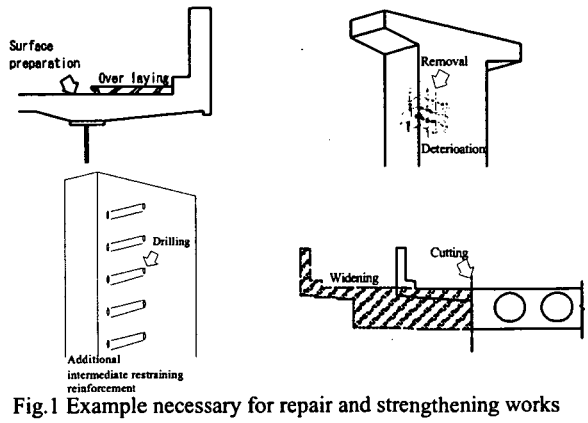

Fig.1 Example necessary for repair and strengthening works

Herein, a trial experiment has been conducted to get a suitable method of removal for existing concrete structures to assure unity of existing and newly placed concrete. This investigation was aimed at the removal of the concrete to the depth exceeding that of the reinforcing bars, centered around WJ method that is the standard repair technique in Europe, and then compared it with other removal methods currently in use.

After having specified the effectiveness of WJ method in removal and found out the problems concerning the use of hand breaker, specimens that may suitably evaluate the performance of WJ method were proposed.

The details of this investigation are presented in the following.

2. Removal in Japan and abroad

2.1 Present state and subjects of removal in Japan

Conducting removal usually uses the hand breaker that is often a tool of dismantling and driven by compressed air as its power. This is because that the history of repair and reinforcement of concrete structures in Japan is not long enough, and such treatment is on a considerably small scale. As a result, deterioration developed in repaired structures in some cases became more serious because of the occurrence of micro cracks by hand breaker[2)].

Recently, as structures need to be repaired or reinforced go in a large scale, the researches on removal with WJ method, instead of hand breaker, are made forward gradually. Although Japan has a long history in using WJ method, as recorded that WJ method was used in digging Otaru canal during Meiji era, the development in civil engineering, especially in repair and reinforcement of concrete structures, was comparably slow since then.

Consider now a typical case of repair and reinforcement of concrete structure - Tedorigawa Bridge (PC continuous rigid-framed box girder) in Hokuriku Expressway using WJ method[3)]. For purpose of removing those concrete sections through which chloride ions permeated, WJ method was applied to conduct removal. This is also a

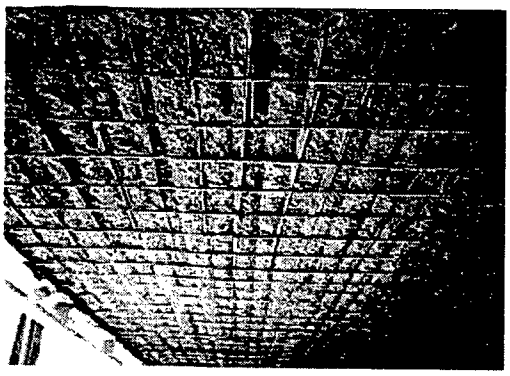

Fig.2 An Example using traditional WJ Method

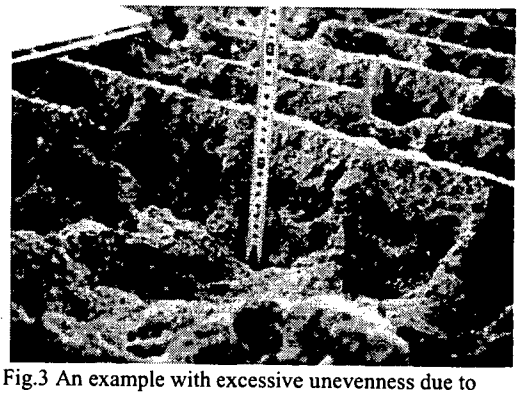

Fig.3 An example with excessive unevenness due to effects of the reinforcing bars

measure taken to cope with large-size cars. However, finishing state in removal surface remains a problem unsolved, as shown in **Fig.2**. There were also other cases about removal using WJ method[4]. But, it is difficult to control both the depth and an equal treatment state under the bottom of the reinforcing bars, and so a common standard cannot be reached. To express technical level of WJ method in the early stage of this research, the examples that the depth of removal cannot be well controlled are illustrated in **Fig.3**.

2.2 Review of removal techniques in advanced nations

In Europe - one of the advanced nations leading in repair and reinforcement of concrete structures, WJ method is mainly used when conducting removal. As shown in **Fig.4**, in Swiss WJ methods either by robots or by hand-holed devices are applied according to the working area of construction and the site conditions while hand breakers are completely prohibited.

The nation in North Europe such as Sweden, which once used WJ method to work mine coals a long time ago, began its research on removal techniques by WJ method applicable to concrete. The qualification system for WJ machines and operators has been established, and the evaluation of removal technique itself using the test specimen shown in **Fig.5**, have been carried out[5]. **Fig.6** shows the specimen treated by WJ method. To evaluate applicability to the concrete structure, the parameter such as

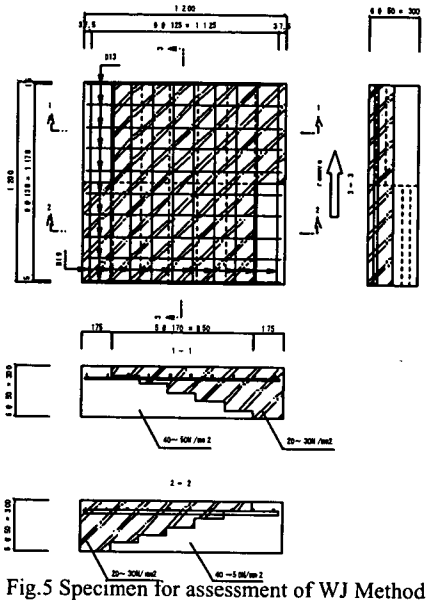

Fig.5 Specimen for assessment of WJ Method in North Europe

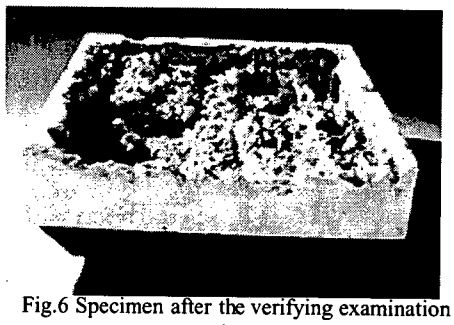

Fig.6 Specimen after the verifying examination was completed
(after cutting off the reinforcing bars)

Fig.4 WJ Methods by robots and human beings

removing or non-removing ratio in parts with low or high strength, the state of treatment beneath the reinforcing bars and ridges are checked by established standards. Only those construction machines and technicians that have passed this check are allowed in WJ method.

3. Scope of experiment

3.1 Performance required in removal

The performances, which are required in removal when conducting repair and reinforcement for concrete structures, are listed as follows.

(1) Surface of removal assuring a good state of unity between existing parts and newly placed material

(2) Keeping a good shape for further maintenance by removing clearly the unwanted concrete, without depending on whether there are reinforcement or not. This is called "Regularity".

(3) Making sure that the fragile concrete due to deterioration has been removed. This is called "Selectivity".

(4) Not giving additional damages to both the reinforcing bars and the treated surfaces.

Here comes the explanation of these performances.

As for (1); Based on the results of the researches in the past, it is clarified that sufficient removal surface can be obtained when conducting removal by WJ method[2].

As for (2); As one of the deterioration factors of concrete structures, chloride ion sometimes reaches the position lower than the bottom of the reinforcing bars, as shown in **Fig.7**. On this occasion, the concrete under these reinforcing bars should be removed certainly. And, a flat finishing is expected without affecting the cross-section recovery work after removal.

As for (3); Fragile concrete should be removed completely in repair and reinforcement.

As for (4); No additional damages to the reinforcing bars and the surfaces must be induced for further use.

From the experiments, we know that the performances shown in (2) and (3) often depend on the machines in WJ method and the operators in charge.

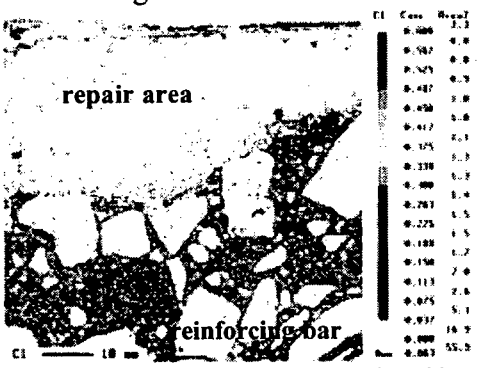

Fig.7 An elementary mapping of chlorine with EPMA (Observation of re-damaged section after completed the repairs of saltdamage)

3.2 Procedure of experiment

The preliminary experiment includes removal either by hand breaker or by various types of WJ methods. After having confirmed the shape of surface, behavior of the unity, a further test was carried out for WJ method, where only the good results were used to evaluate its performance quantitatively. **Fig. 8** shows the procedure of this investigation.

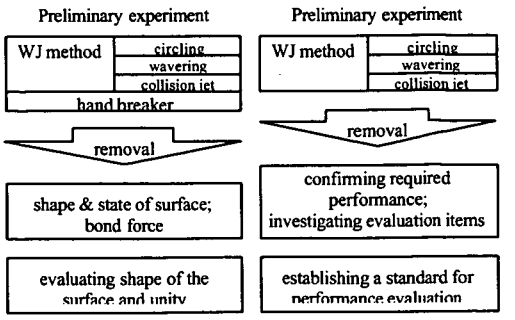

Fig.8 A flowchart of investigation on removal techniques with WJ Method

In this preliminary experiment, concrete slab specimen was used. First, conducted removal to the depth below the reinforcing bars. Then, cut the treated parts after having checked the shapes and place the concrete onto these treated faces in both vertical and horizontal direction. Finally, took a core and measured its bond strength to evaluate its behavior of unity. In this experiment, removal by WJ method was carried out in a downward direction, which may often cause water stagnation or form hollow pieces in concrete on the treated sections.

To quantitatively evaluate the behaviors of WJ method, performance evaluation test was conducted with specimen that can faithfully reflect the deterioration state of the undamaged and fragile parts as in original structure, where the investigation focused on obtaining a flat removal surface in positions below the reinforcing bars in undamaged parts and removing fragile concrete in the fragile parts. For reference, a certifying examination in North Europe is consulted to determinate the evaluation items and the standards.

3.3 Test specimen

3.3.1 Preliminary experiment

Fig.9 shows the specimen for the preliminary experiment. To reflect the behaviors of the real structure, the reinforcing bars of D19 are arranged in cross. Specifications and mix proportions of the specimen and placing concrete after removal are listed in **Table 1** and **2**. To avoid the influence on compaction of construction joint, placing concrete in horizontal direction uses form vibrator (output: 280W, natural frequency: 9 000~10 000V.P.M, size of vibration plane: 75mm×102mm) by dividing the working surface into four parts, vibrating 10 seconds for each spot, while three layers are divided in vertical direction and the concrete is compacted at every two spots for each layer by using bar vibrator (output: 280W, natural frequency: 12 000~14 500V.P.M, size of vibrator: ö30mm×400mm) , vibrating 5 seconds for each spot.

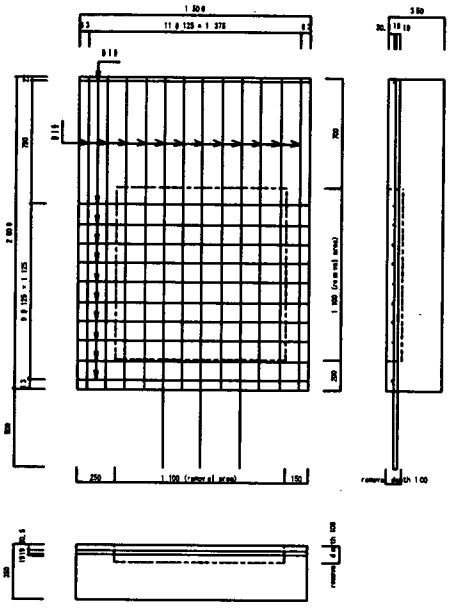

Fig.9 Specimen for preliminary experiment

3.3.2 Performance evaluation test

The specimen for performance evaluation test is illustrated in **Fig.10**. To faithfully represent the sound and fragile part of the real structure, strength difference between for the specimen is assumed above 20N/mm^2. Concrete in fragile part is then colored with a coloring agent contained mainly in iron oxide for easily checking the status of concrete after chipping treatment. **Table 3** and **4** give a list of specimen and mix proportion of concrete, where ready-mixed concrete on

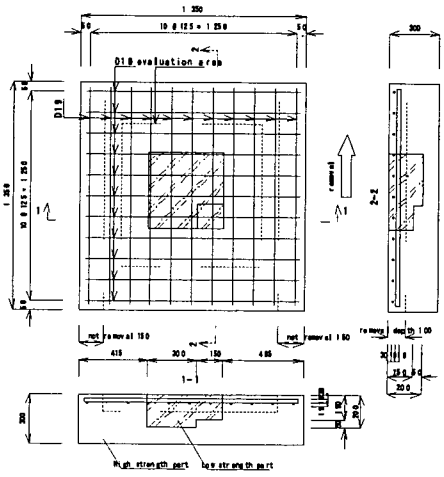

Fig.10 Specimen for performance assessment test

manufacturing site (Utsunomiya of Tochigi Prefecture) is used. Making specimen began by placing concrete in fragile part, for in winter, curing by heating it with jet heater for two days first, and then assembling the reinforcing bars in the sound part after the concrete was taken off the form. The concrete in the sound part was placed three days after that in fragile part, then curing by heating with jet heater for three days and then by wet sheet cover for 11 days. The form was taken off when age of the concrete in the sound part reaches 14 days, curing in the air continued since then. On the day that the performance evaluation test was carried out, difference of strength between the sound and fragile part, was checked by conducting compression test. Finally, removal was conducted along the total length in the treating direction with 150mm left apart from the edge, where evaluation on the shape of the surface was carried out in a range of 850×850mm centrally, including fragile part.

Table 1 Specifications of concretes in preliminary experiment

Items	Specimen	Newly placed
Nominal strength	24N/mm²	50N/mm²
Slump	8cm	12cm
Maximum coarse aggregate	25mm	20mm
Air content	4.5%	4.5%
Cement	High-early-strength Portland cement	High-early-strength Portland cement

Table 2 Mix proportion of concrete for preliminary experiment

	W/C (%)	Sand content S/a (%)	Density (kg/cm³)					Compression strength at age of 7 days (N/mm²)
			Water W	Cement C	Sand S	Coarse aggregate G	Chemical admixture AE water reducing agent	
Specimen	50.0	45.0	156	312*	829	1025	1.248	28.3
Newly placed	45.0	40.7	170	378*	706	1048	0.953	52.2

Table 3 Specifications of concretes in performance evaluation test

Items	In high strength part	In low strength part
Nominal strength	40N/mm²	18N/mm²
Slump	8cm	8cm
Maximum coarse aggregate	20mm	20mm
Air content	4.5%	4.5%
Cement	Normal Portland cement	Normal Portland cement

Table 4 Mix proportion of concrete for performance evaluation test

	W/C (%)	Sand content S/a (%)	Density (kg/cm³)					Compression strength (N/mm²)
			Water W	Cement C	Sand S	Coarse aggregate G	Chemical admixture AE water reducing agent	
In high strength part	40.6	41.0	163	402	718	1039	1.608	54.9(at age of 60 days)
In low strength part	65.8	48.2	155	236	921	996	0.944	30.1(at age of 63 days)

To check the results of this test, the specimen used in certifying examination of North Europe is reproduced for reference of its evaluation standard, as shown in **Fig.5**.

3.4 Types of removal

Table 5 gives the types of removal conducted in this experiment.

3.4.1 Hand breaker

Hand breaker in the 30kg class was used with electric pick as a supplementary means. To represent the working conditions on construction site as actual as possible, instructions about the depth of removal and the arrangement of the reinforcing bars only were given to the operators.

3.4.2 WJ method

For WJ method, concrete was ripped off by a jet(stream) from a nozzle in diameter of 1mm~3mm, where the hydraulic pressure was 70MPa~200Mpa and the quantity of water was about 30*l*/min~200*l*/min. Here, the hydraulic pressure of 100Mpa is called low pressure while that of 200Mpa is called high pressure. Moreover, circular and wavering types are then divided according to the way of nozzle driven by.

Table 5 Types of removal for test

Breaker 30kg Class	WJ method With circular nozzle (collision jet)	WJ method With circular nozzle (high pressure)	WJ method With wavering nozzle (high & low pressure)
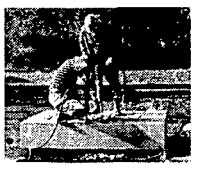	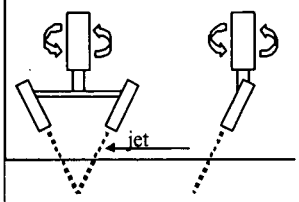	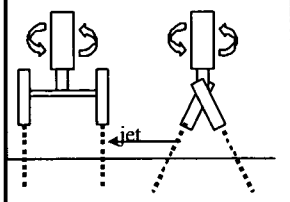	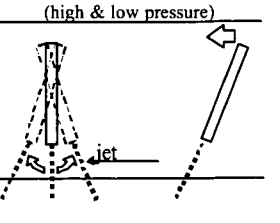

3.5 Experimental items

3.5.1 Preliminary experiment

Experimental items in this experiment included investigating outward appearance in removal area and measuring bond strength.

The appearance measurement used a laser displacement meter, as shown in **Fig.11**. Four measuring lines at 0.1mm intervals were assumed at where there were reinforcing bars and between, both in lengthwise and crosswise. For measurement, the reinforcing bars were cut off and then removed.

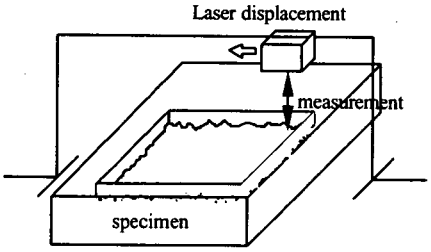

Fig.11 Layout for measuring removal surfaces

Following the procedure given in **Fig.12**, evaluation of bond strength was conducted by direct tension test when the age of concrete reached 7 days. A core specimen, with size of ö100mm×200mm or ö75mm×150mm for piece without conducting removal, was taken from the test piece by a concrete core drill.

On the other hand, to check how a rough removal affects the construction joint, firstly, cut the specimen with vertical construction joint by a concrete cutter, and then evaluated its fill degree for newly placed concrete on construction surface.

For further comparison, the specimen with the construction joint without any removal, called "no process" piece in the following, was also prepared.

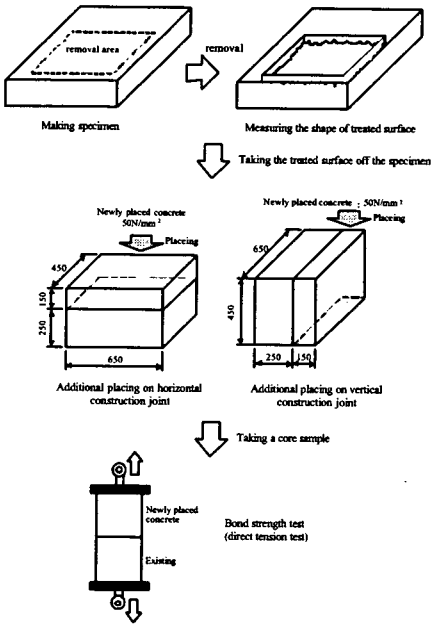

Fig.12 Layout of bond strength test

3.5.2 Performance evaluation test

Refer to the items in the certifying examination in North Europe; the items for performance evaluation test were set up.

As for the evaluation of WJ method, indexes such as regularity and selectivity are checked separately, as shown in Table 6. Only those that passed the whole examinations are included into the investigation on evaluation a standard.

Table 6 Evaluation method of performance evaluation test

Appraisal standard		Selectivity	
		Good (Pass)	NG
Regularity	Good (Pass)	[Category I] Selective and regular removal	[Category II] No selective but regular removal only
	NG	[Category III] No regular but selective removal only	[Category IV] Neither selective nor regular removal ->Not applicable

4.Results and investigation

4.1 Preliminary experiment

4.1.1 Investigation and measurement on outward appearance of removal

Fig.13~17 show representatively the pictures of outward appearance and the measured results by laser displacement meter.

(1) Hand breaker

The treated specimen is illustrated in **Fig.13**. In spite of the instructions about

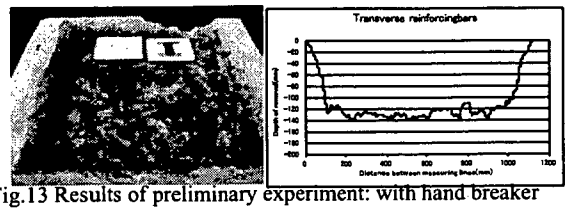

Fig.13 Results of preliminary experiment: with hand breaker

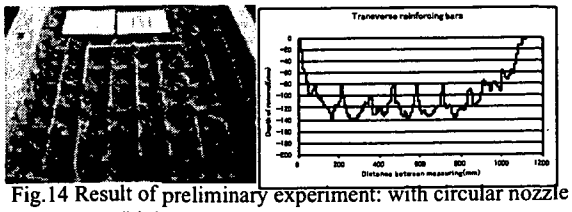

Fig.14 Result of preliminary experiment: with circular nozzle (high pressure)

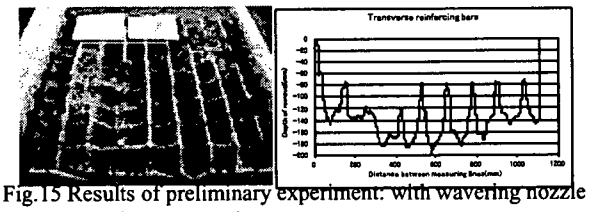

Fig.15 Results of preliminary experiment: with wavering nozzle (low pressure)

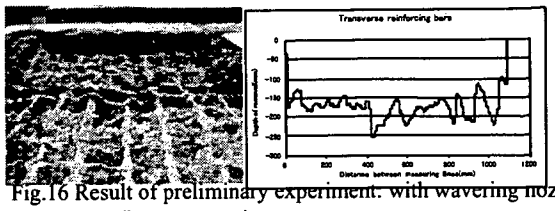

Fig.16 Result of preliminary experiment: with wavering nozzle (low pressure)

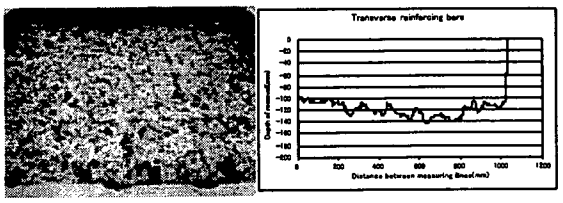

Fig.17 Result of preliminary experiment: with circular nozzle (collision jet)

outline of arranging reinforcing bars, damage according to striking of the hand breaker can be seen everywhere, as shown in **Fig.18**. Cracks and unevenness on a small scale shown in **Fig.19** are also observed when the treated surface is clearly cleaned and investigated.

(2) WJ method

It is clear that the shape of the treated surface varies with the type of nozzle used in WJ method.

In case of using circular nozzle (type of high pressure), only the concrete under the top reinforcing bars is removed completely while that under the bottom and at a crossing remains (**Fig.14**).

Although concrete under the reinforcing bars is partly removed when using wavering nozzle with low pressure, removal using the same type of nozzle in both high and low pressure cannot be removed at all, left a hole as big as a pot shown in **Fig.15**.

After resetting the machine in case of using wavering nozzle (with low pressure), the experiment was repeated by controlling the program impossible action by an operator. As a result, the treated depth of removal was partly controlled, and a better shape for the treated surface was obtained which was close to the expectation, as shown in **Fig.16**.

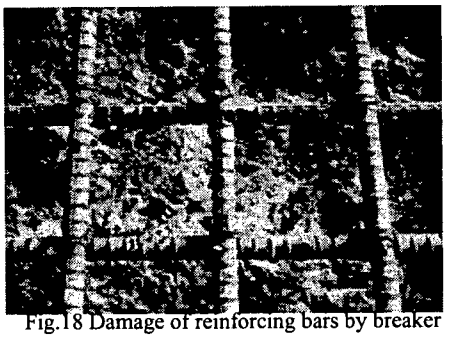
Fig.18 Damage of reinforcing bars by breaker

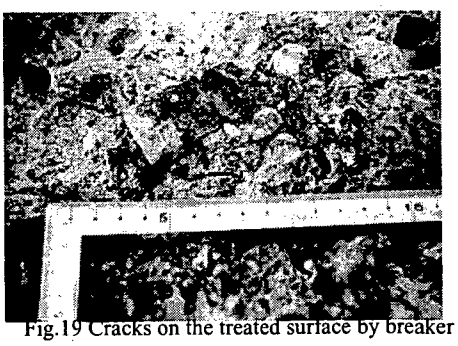
Fig.19 Cracks on the treated surface by breaker

On the other side, when using circular nozzle (collision jet), not only concrete under the reinforcing bars could be removed completely, but also a flat treated surface was obtained, as shown in **Fig.17**.

Based on the investigations mentioned above, it is notable that the differences in

types of nozzle, water pressure, the quantity of water and standoff affect remarkably the shape of the treated surface when applying WJ method to the removal of concrete. In addition, a treated surface in response to the target may be probably gained by changing these settings.

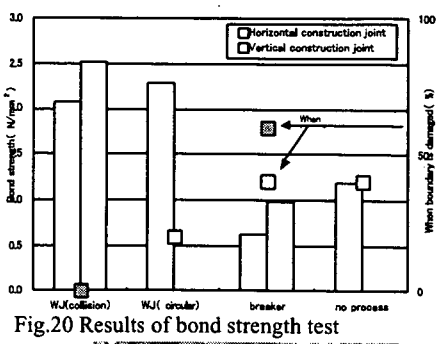

Fig.20 Results of bond strength test

4.1.2 Bond strength

The results of bond strength test for the hand breaker, WJ method using both circular nozzle (with high pressure) and collision jet are listed in **Fig.20**.

For the test using WJ method with any type of the nozzle, the measured value of bond strength exceeds the target value (eg. for cross-section repair agent[6] using 1.5N/mm^2; for thickness increasing in the upper layer[7] using 1.0N/mm^2), while a quite lower value under the allowance of unprocessed concrete is observed in the test using hand breaker, in which collapse happened frequently between surfaces. These phenomena can be induced by micro cracks, as the same as the investigation of surface preparation mentioned earlier[2].

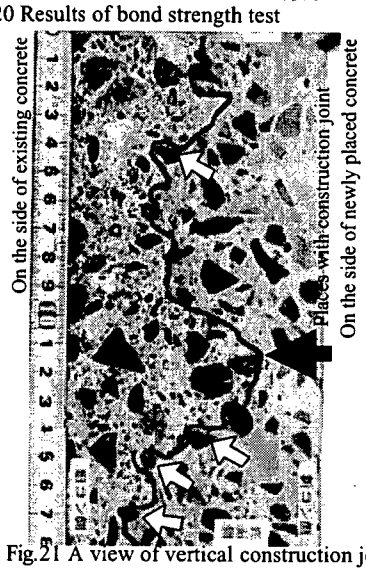

Fig.21 A view of vertical construction joint
(The arrows indicate openings)

4.1.3 Observation of construction joint

This observation was carried out using the treated surface of circular nozzle (with high pressure). **Fig.21** illustrates the stagnant air found out on unevenly wide area. And the treated surface having larger irregularity has been proved to exert a harmful influence upon the construction joint.

4.2 Performance evaluation test

The removal was conducted using wavering nozzle with low pressure, circular nozzle both with collision jet and high pressure, where their effectiveness had been proved in preliminary experiment. At the same time, another specimen, that is, a duplicate of test piece used in WJ method evaluation test in North Europe, was adopted to carry out removal with wavering nozzle (low pressure). **Fig.22~25** give the outward appearance after the treatment, partly including the results of shape measurement. The results of performance evaluation for WJ method referred to the certifying examination in North Europe is listed in **Table 7**, in which the suitability ratio in Sweden method is based on the diagram shown in **Fig.26**. As shown in **Table 7**, the standards of this test are no more than the temporary values that will be revised as WJ method improves.

4.2.1 Regularity

It is found out that the regularity for both types used in circular nozzle has been observed, while that using wavering nozzle is not obtained because the removal subjected to the influence from reinforcing bars is insufficient. Even so, in comparison with the preliminary experiment, the improvement of regularity was noticed, and the performance is considered to improve from the progress in settings of WJ machines and technical ability of operators.

4.2.2 Selectivity

In case of using circular nozzle with high pressure, a good performance in selectivity presents because high removing ratio was obtained in low strength part. Similarly, the selectivity to some extent was observed when using circular nozzle with collision jet. In contrast, the removing ratio in low strength part was of a low level when using wavering nozzle with low pressure. On the other hand, these results were judged to be up to the suitability ratio in North Europe standard. Therefore, with a similar consideration as that for regularity, the removing ratio in low strength part is considered to improve with the progress in settings of WJ machines and technical ability of operators.

After considering all these results, we know that the performance of WJ method depends on the factors such as the settings of specification in response to the conditions of removal, the ability of technicians in charge of the job, together with behavior of WJ machine itself.

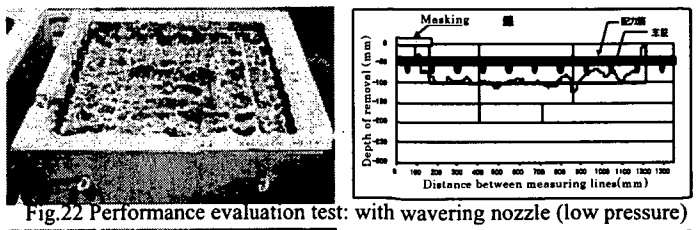

Fig.22 Performance evaluation test: with wavering nozzle (low pressure)

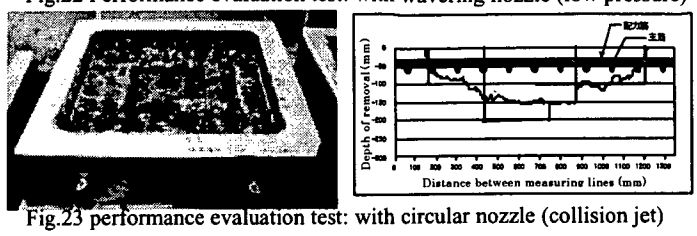

Fig.23 performance evaluation test: with circular nozzle (collision jet)

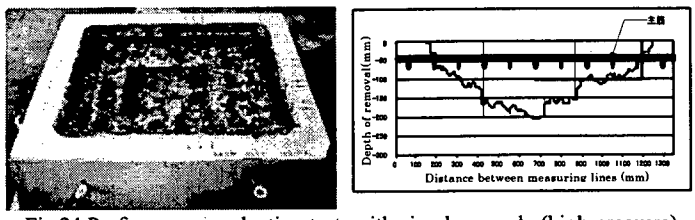

Fig.24 Performance evaluation test: with circular nozzle (high pressure)

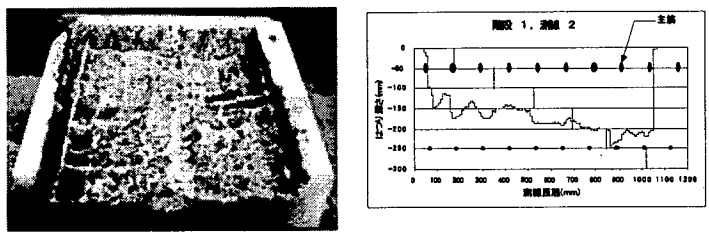

Fig.25 Performance evaluation test in North Europe form: with wavering nozzle (low pressure)

Table 7 Comparison between an interim standard /evaluation result of performance evaluation and those of North Europe

Items		Performance evaluation test								In North Europe form		
		Standard (An interim standard)	With wavering nozzle (Low pressure)		With circular nozzle (Collision jet)		With circular nozzle (High pressure)			Standard	With wavering nozzle (Low pressure)	
Selectivity	Removal left at the ends	150mm± 25mm	○		○		○			50～100mm	×	
	Suitability ratio (Removing ratio)	Low strength above 60%	58.1%	×	77.7%	○	89.6%	○		According to judgment of Fig.26	86.8%	○
		High strength under 30%	0.0%		0.5%		1.7%				21.2%	
	Pit*1	Less than 3	○		○		○			Less than 3	○	
Regularity	Removal left	No contact with reinforcing bars	×		○		○			No contact with reinforcing bars	○	
	Length of ridges*2	Under 900mm	× 1063mm		○ 0mm		○ 0mm			Under 800mm	× 1585mm	
	Roughness of surface	At a pitch of 62.5mm, with a difference above 7mm	○ 11.6mm		○ 11.5mm		○ 10.3mm			At a pitch of 10mm, with a difference above 7mm	× 5.7mm	
	Depth of removal	10mm± 2mm	○ 10.0mm		○ 10.2mm		○ 10.8mm			–	–	
Evaluation		Selectivity	×		○		○			–	–	
		Regularity	×		○		○			–	–	
		Judgment	Category IV		Category I		Category I			Judgment	×	

*1: For holes having a diameter under 32mm and a depth above 48mm
*2: Total extension of ridges with a height over 35mm

5. Application of performance evaluation test

Since the validity of performance evaluation test has been proved, JH attempts to settle on a construction manual for Water Jet[8] and then to put it into practice. **Table 8** gives the representative results of performance evaluation test up to now. The examples of specimen after removal conducted are shown in **Fig.27**. As the required performance and its verifying method are definitely determined, all the companies open the investigation on methods of removal and the technique about it grows remarkably beyond the expectation mentioned earlier. Although the removal behind reinforcing bars is considered insufficient, especially in the case of using wavering nozzle, apparently most of the selectivity and regularity in removal reach a satisfactory degree after the way of treating is reexamined.

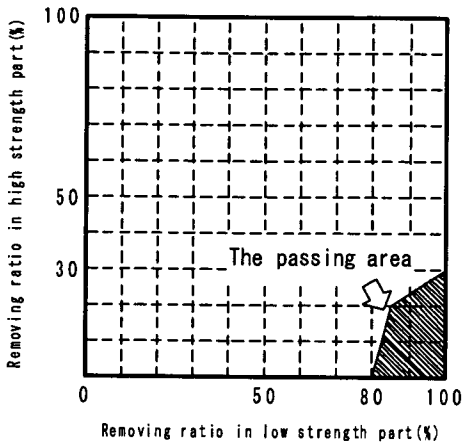

Fig.26 Diagram for identifying suitability ratio[5]

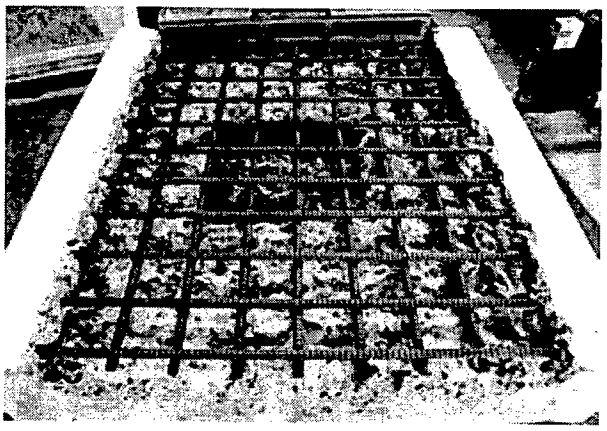

Fig.27 A view of specimen after performance evaluation experiment completed (with wavering nozzle, on Category I)

Table 8 Results of performance evaluation test

Items		Standard	With wavering nozzle A		With wavering nozzle B		With circular nozzle A		With circular nozzle B	
Selectivity	Removal left at the ends	150mm±25mm	○		○		○		○	
	Suitability ratio (Removing ratio)	Low strength above 60%	99.8%	○	95.6%	○	79.5%	○	86.0%	○
		High strength under 30%	4.2%		2.7%		0.4%		1.4%	
	Pit	Less than 3	○		○		○		○	
Regularity	Removal left	No contact with reinforcing bars	×		○		○		○	
	Length of ridges	Under 900mm	○ 110mm		○ 0mm		○ 0mm		○ 0mm	
	Roughness of surface	At a pitch of 62.5mm, with a difference above 7mm	○ 8.1mm		○ 10.4mm		○ 7.3mm		○ 8.3mm	
	Depth of removal	10mm±2mm	○ 10.7mm		○ 10.9mm		○ 9.6mm		○ 10.2	
Evaluation		Selectivity	○		○		○		○	
		Regularity	×		○		○		○	
		Judgment	Category III		Category I		Category I		Category I	

6. Conclusions

This research presented a good behavior of unity between the newly placed and existing concrete when using WJ method to conduct removal for concrete structures. It has also been proved that WJ method is an effective means in repair and reinforcement of these structures. On the other hand, using hand breaker for such treatment cannot obtain any satisfactory results because strong strikes were exerted onto the treated faces and damages to existing reinforcing bars were easily caused, too.

The following is the summary in details.

(1) Based on the results of performance evaluation test, it is possible to quantitatively evaluate WJ method that is applicable to removal.

(2) To meet the demands of repair and reinforcement, the required performance indexes of WJ method such as regularity and selectivity should be applied separately.

(3) The removal using WJ method mainly depends on the technicians in charge of the machines. If the specification or the settings of WJ machines are modified, the behaviors will also change greatly. The items having influence on them are listed in the following.

i. shape of the nozzle
ii. water pressure and the quantity of water
iii. cycles of pass and moving speed
iv. standoff
v. angle of attack

(4) Circular nozzle (with collision jet), excellent in depth control of the removal, can be applied to real structures.

(5) Although using wavering nozzle (with low pressure) cannot always satisfy with the regularity, it has superior in selectivity because of a high removing ratio in low strength part.

7. Themes for further consideration

It has been proved that WJ method, as an effective means to improve the durability of concrete structures, is applicable to the removal in repair and reinforcement. Since the effect of WJ method depends strongly on machines applied and technicians, as a general rule, construction should be performed using the machines verified by a performance evaluation test beforehand. In addition, it is necessary for the objective structures to set construction conditions according to results of a trial run with specimen before doing the removal on site. Finally, the following summarizes the problems and the themes left in WJ method at present.

(1) Improvement of environmental measures

By systematization of noise and waste water treatment, a construction method taking account of environment can be established.

(2) Improvement of cost

By developing a system of WJ methods applicable to different scales and conditions, improving the durability of expendable supplies such as nozzles, hoses and pumps, a lower cost can be expected in construction.

(3) Progress in safety

In order to raise the level of reliability, staff from commanders to workers

should be steadily educated on knowledge of safety, while a much more safety system for WJ method be also developed.

(4) Bringing up of engineers

It is no doubt that bringing up of engineers familiar with the repair and reinforcement of concrete structures plus applying WJ method in an appropriate way will promote quickly the development of technology.

From now on, we shall make an effort at putting WJ method into practice, analyzing its behavior throughout constructions and accumulating necessary know-how.

References:

1) Kazusuke KOBAYASHI, Ryoji SHIRAKI and Kenji KAWAI: Migration and Concentration of Chlorides, Sulfides and Alkali Compounds in Concrete Caused by Carbonation, Concrete Research and Technology, Vol.1, No.2, pp.69-82, July 1990 (in Japanese)

2) Atsushi YOSHIDA, Syoji NOJIMA, Yasushi KAMIHIGASHI: Evaluation of Surface Preparation Technology for Bonding of New and Existing Concrete, Nohon Doro Kodan Research Institute Report, Vol.36, November 1999 (in Japanese)

3) K. OKAI, M. MORIYAMA, N. TOSAKA and I. OZAWA: Overall Repairing a Salt – Damaged Superstructure of Bridge –At the Tedorigawa River Bridge of the Hokuriku Expressway, Concrete Journal, Vol.34, No.2, pp.33-40, Feb. 1995 (in Japanese)

4) Yoshiyuki MOMIYAMA, Yoichi EGUCHI, Shuji KIKUCHI, Hirokazu NAGAHASHI: A reconstruction plan for Gerber bridge – Ishiyama Viaduct in Meishin Expressway, Pre-stressed Concrete, Vol.37, No.6, pp.59-66, Nov. 1995 (in Japanese)

5) Dag Brox Rindal, Ronald Andersen, SELECTIVE HYDRO-DEMOLITION Manual for manufacture of test slabs, Norwegian Public Roads Administration, 1994

6) Japan Highway Public Corporation: Specification for the construction management of structures, p.293, 1999 (in Japanese)

7) Express Highway Research Foundation of Japan: Manual for the design and construction with Over laying method, pp.48-49, pp.108, 1995 (in Japanese)

8) Bridge and Structural Engineering Division, Engineering Department of JH, Manual for the construction using Water Jet method, 2000.6 (in Japanese)

SESSION 4: GENERAL

(1) First GFRP Pedestrian Bridge in Japan
(Shoichi Saeki, Kazuo Yamashiro, Nobuhiko Kitayama, Iton Chou, Naoki Yamamoto and Seishi Meiarashi)

(2) Federally Assisted Bridge Programs in the United States: Past, Present and Future
(Raymond McCormick and Edgar P. Small)

(3) Structural Behavior of Steel Girder-RC Pier Composite Rigid Frame Bridge
(Noriyuki Suzuki, Yoshinori Igase, Koichi Nishikawa and Toru Sato)

(4) Aerodynamic Stability of a Suspension Bridge with Open Grating Deck
(Katsuya Ogihara, Naoki Wada and Shinji Takamori)

(5) Behavior of Prestressed Concrete Beam with New Type of Artificial Lightweight Aggregates made from Fly Ash
(Michihiro Sakurada, Hiroyoshi Watanabe, Takashi Ohura and Motoyuki Suzuki)

(6) Fatigue of Aluminum Deck Fabricated by Friction Stir Welding
(Ichiro Okura, Nobuyasu Hagisawa, Makoto Naruo and Hitoshi Toda)

First GFRP Pedestrian Bridge in Japan

Shoichi Saeki, Kazuo Yamashiro, Nobuhiko Kitayama, Iton Chou, Naoki Yamamoto and Seishi Meiarashi

ABSTRACT

An FRP pedestrian bridge was constructed for the first time in Okinawa, Japan. Okinawa is the region where structural degradation due to salt damage is most severe in Japan. This bridge was constructed in a marine road connecting the Okinawa Main Island to an adjacent island. The bridge, therefore, would face to the most severe salt damage in Okinawa Prefecture. FRP construction was adopted for the main bridge materials in order to prevent salt damage.

This paper contains the following issues: design and construction outline of the pedestrian bridge, static load testing and dynamic load verification for the whole bridge. GFRP members, produced by hand lay-up molding, were used for the main girder. GFRP members, produced by pultrusion molding, were used for lateral and sway bracing. The special detail, using stainless steel plate and prestressing steel bar, were used for the joint of main girder. Stainless steel bolts and adhesive were used for joint of lateral and sway bracing. Painting of the GFRP members was selected with consideration for weather resistance and wind-blow sand abrasion resistance. The joint designs of lateral and sway bracing and the main girder are based on experiment and FEM analysis. Agreement between static/dynamic load testing and the analytical result has proven that the bridge meets design goals.

Shoichi Saeki, Public Works Research Center, 2-2 Nishizawa, Tsukuba, Ibaraki, 3002624, Japan
Kazuo Yamashiro, Okinawa Prefecture, 3-4-1 Isa, Ginowan, Okinawa, 9012221, Japan
Nobuhiko Kitayama, Ishikawajima- Harima Heavy Industries Co. Ltd., 1-19-10 Mouri, Koto-ku, Tokyo, 1358322, Japan
Iton Chou, Ishikawajima- Harima Heavy Industries Co. Ltd., 3-1-15 Toyosu, Koto-ku, Tokyo, 1358732
Naoki Yamamoto, Ishikawajima Harima Heavy Industries, Co. Ltd., 3-1-15,Toyosu, Koto-ku Tokyo, Japan
Seishi Meiarashi, Public Works Research Institute, 1-6 Minamihara, Tsukuba, Ibaraki, 3058516 Japan

1. INTRODUCTION

Okinawa Prefecture constructed a beach recreation area along rural route "Ikei-Tairagawa". The pedestrian bridge allows facilities-users to safely move from one side of the road to the other. A part of the route "Ikei-Tairagawa" is called a "Marine Road", because it is a banking road constructed in the shoal between Okinawa Main Island and "Henza" Island (see Figure 1).

The environment is very corrosive. Okinawa Main Island is located in the path of typhoons and the sea surrounds the road. Therefore, it is necessary to take countermeasures for the salt damage, when a concrete/steel bridge is constructed in Okinawa. The construction of the pedestrian bridge made of GFRP is one option to prevent salt damage countermeasure.

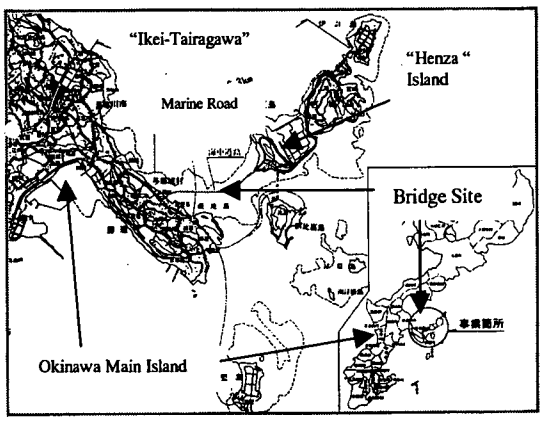

Figure 1 Bridge Construction Site

In this paper, the following three issues are reported: Design summary, experiments and analysis of the joints and the structure as a whole.

General drawing and sectional views of the bridge provided (see Figure 2). Design dimensions are shown in TABLE Ⅰ. This bridge has two span continuous girders of about 38 meters. The *Highway Bridge Specification* [1] and *Pedestrian Bridge Technical Guideline* [2] were used as the bridge design criteria. The wind velocity criterion was set as 52.2m/sec. This is usually set as 40.0m/secec in the above criteria.

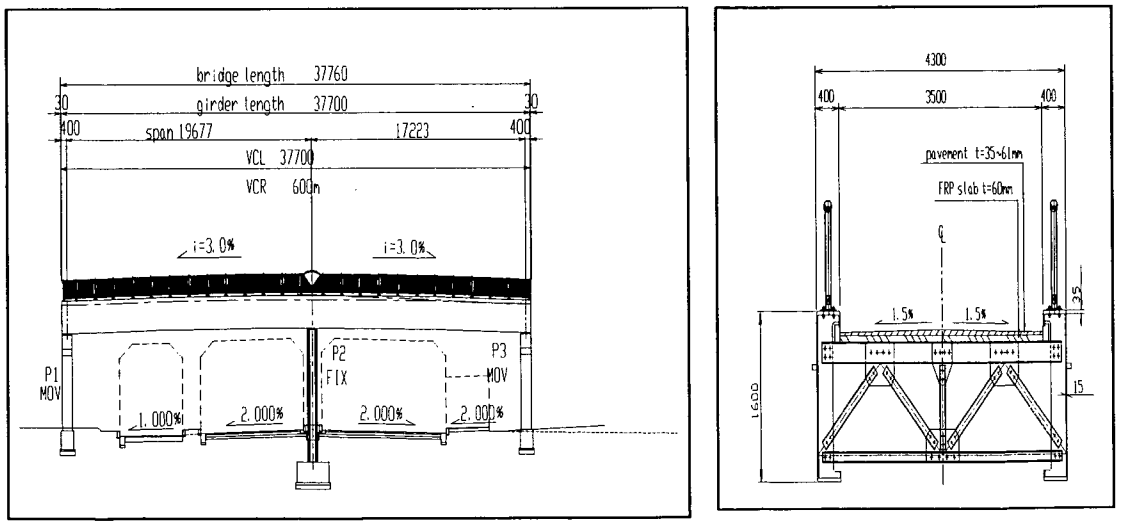

Figure 2 Side (left) and Cross Section (right) Views

TABLE I MAJOR DIMENSION

		Condition
Bridge Type		Two Span Continuous Girder Bridge
Major Dimension	Total Bridge Length (m)	37.760
	Span Length (m)	19.677 + 17.233
	Width (m)	4.3 (Effective Width 3.5)
	Longitudinal Slope	V.C.R. 600m
	Transverse Slope	1.5%
	Overhead Clearance (m)	4.500
Major Material	Bridge member	GFRP
	Bolt	Stainless Steel
	Handrail	GFRP
	Pavement	Mortar + Porcelain
Design Criteria		*"Highway Bridge Specification"* *"Pedestrian Bridge Technical Guideline"*
Erection Method		Assemble in Factory + Onsite Erection

2. DESIGN

2.1 Design Material Properties

Material properties, such as design strength, were set based on material testing. Decided material property values are shown in **TABLE II**. The tensile strength of the hand lay-up molding material, hot press molding material, and pultrusion molding material are 127MPa, 196MPa, and 294MPa, respectively. The tensile elasticity of main girder (hand lay-up molding method) was 11.8GPa. The bearing pressure intensity was 1.5 times the tensile strength. Material test results are shown in **TABLE III**. Pultrusion molding material [-200 and [-103 were used for the floor system. Shearing stress of both materials are 49.0MPa and 34.4MPa, respectively. Test results of bolted connections are shown in **TABLE IV**. Allowable steel tension stress is set at the yield point in the design of steel bridges. The tension allowable stress of FRP should be set at the tension strength, because FRP has no plasticity region and yield point. There is no established value for a safety factor of fiber reinforced plastics. The deflection of the main girder is regulated to within 1/600 of span length in order to suppress vibration induced by pedestrians (see *Pedestrian Bridge Technical Guideline* [2]).

TABLE II FRP DESIGN STRENGTH

			Unit	Hand Lay-up		Hot Press		Pultrusion	
				Flange	Web	Stiffener	Gusset Plate	[-200	[-103
Thickness			(mm)	35	15	20	20	-	-
Design Strength	Tension		(MPa)	127	127	196	196	294	294
	Bending		(MPa)	127	127	196	196		
	Compression		(MPa)	127	127	196	196	235	235
	Shear	LW	(MPa)	-	-	49.0	49.0	49.0	34.3
		CW	(MPa)	49.0	49.0	49.0	49.0	-	-
	Bearing		(MPa)	191	191	294	294	441	441
Elastic Modulus	Tension		(GPa)	11.8	11.8	11.8	11.8	19.6	19.6
	Bending		(GPa)	11.8	11.8	11.8	11.8	19.6	19.6
Linear Expansion Coefficient			/℃	2.00×10^5	2.00×10^5	2.00×10^5	2.00×10^5	2.00×10^5	2.00×10^5
Density			N/m^3	18.6	18.6	18.6	18.6	18.6	18.6

Note) LW: Longitudinal Direction, CW: Cross Direction

TABLE Ⅲ MATERIAL TEST

		Hand Lay-up		Hot Press	Pultrusion
		Flange	Web	Gusset Plate	Floor System
Tensile Strength (MPa)	Average (μ)	204	189	364	425
	Standard Deviation (σ)	12.1	7.94	4.70	15.5
	Number of Sample (n)	5	5	5	5
	μ-4σ	156	157	345	363
Tensile Elastic Modulus (GPa)	Average (μ)	14.9	13.0	21.1	32.3
	Standard Deviation (σ)	0.784	0.294	1.27	0.49
	Number of Sample (n)	5	5	5	5
	μ-4σ	11.8	11.8	16.0	30.3

TABLE Ⅳ BOLT JOINT TEST

Member	Test	Specimen	Shear Strength (MPa)	(Shear Strength/Design Strength)
[-103	Tension	No.1	46.6	1.36
		No.2	44.8	1.31
		No.3	50.9	1.48
		Average	47.4	1.38
	Com-pres sion	No.1	49.1	1.43
		No.2	48.4	1.41
		No.3	49.2	1.44
		Average	48.9	1.43
[-200	Tension	No.1	106	2.16
		No.2	105	2.15
		No.3	105	2.14
		Average	105	2.15

The ratio of the maximum stress of 17.6MPa for tensile strength becomes about 1/7, as shown in **TABLE V**, when the design is calculated by this regulation. The safety factor exceeds seven. Even if we consider the material characteristic differences between steel and FRP mentioned above, the safety factor of seven seems to be enough for this bridge design.

TABLEV ALLOWABLE STRESS (DESIGN STRESS LEVEL)

Material	Yield Point σ_y (MPa)	Tensile Strength σ_b (MPa)	Allowable Stress σ_a (MPa)	Safety Factor	
				σ_y/σ_a	σ_b/σ_a
GFRP	-	127	17.6	-	7.22
SM400 (Steel)	235	402	137	1.71	2.93

2.2 Design Aerodynamic Load

The design load is regulated in the *Highway Bridge Specification* [1] and the *Pedestrian Bridge Technical Guideline* [2]. The wind load applied to the bridge was 1.7 times of the load provided in the *Highway Bridge Specification* [1] . The bridge site (Okinawa Prefecture) experiences many typhoons and in a strong wind zone..

Design criterion wind velocity U_d is 10 minutes average wind velocity of 40m (the 60% non-over probability in recurrence intervals 50 years) at an altitude of 10m. Drag coefficient C_d is the coefficient parallel to the wind direction. A constant value

is provided to the plate girder. Gust response factor G is a coefficient considering wind speed fluctuation. This factor is 1.9.

According to the *Highway Bridge Aerodynamic Design Handbook* [3] , basic wind speed U_{10} (surface roughness division II : Rural areas, etc.) of Okinawa Prefecture is 45m/sec. Surface roughness and altitude correction factor E_1 of the site (coast, 10m height) is 1.16. Therefore, design criterion wind speed U_d becomes a product of U_{10} and E_1, namely 52.2m/sec. Design criterion wind speed U_d of the *Highway Bridge Specification* [1] has set 40m/secec as a value except for a part of strong wind region. This design criterion wind speed U_d calculates the wind load provided in the *Highway Bridge Specification* [1] . The wind load is proportional for the square of design criterion wind speed U_d. The wind load for the design of this bridge becomes $(52.2/40)^2$=1.70 times the regulation value of the *Highway Bridge Specification* [1] .

2.3 Bridge Type

At the beginning this bridge had been planned as one-span PC concrete bridge. There was some thought to make it a cable stayed bridge, when fiber reinforced plastic bridge was adopted. Considering the harmony of the whole recreation area plan, however, we have chosen a girder bridge as the original plan. The bridge is a two span continuous bridge with a pier in the middle of the main girder. This was included in order to meet deflection regulations. GFRP material design and fabrication methods with FRP were selected as shown in **TABLE VI** with consideration of stress conditions generated in each member. Hand lay-up molding materials were used for the main girder. There is no pultrusion molding facilities, which could produce enough cross-section size of FRP for the main girder. Hot press molding materials of high fiber content were used for the main girder stiffener and gusset plates. The main girder stiffener was installed by the overlay in the hand lay-up to the main girder. Stainless steel bolt-hole areas for the floor system connection were reinforced. **TABLE VII** shows the quantity of fiber reinforced plastics that were used in the listed areas.

TABLE VI MATERIAL COMPOSITION OF GFRP

	Unit	Handray-up		Hot-Press		Pultrusion	
		Flange	Web	Stiffener	Gusset Plate	Floor System	
						[-200	[-103
Thickness	(mm)	35	15	20	20	7	9.3
CSM	% (Volume)	5	5	10	20	10	10
0° /90°	% (Volume)	15	15	30	30	-	-
0°	% (Volume)	-	-	-	-	30	30
±45°	% (Volume)	10	10	-	-	5	5
Resin	% (Volume)	70	70	60	50	55	55

TABLE VII FRP USED MATERIAL AMOUNTA (Unit: kN)

	Main Girder	Floor System	Slab	Handrail	Others	Total
Amount	78.4	32.3	37.2	14.7	27.4	190.1

2.4 Main Girder

The cross-section of the main girder is a channel in shape. The upper and lower flange size is 390mm×35mm and the web size is 1600mm×15mm. Channel cross-sectional shape of the girder is easier to make by hand lay-up-molding method

than the I-beam. The bridge was designed with twin girder in order to reduce the total amount of material produced by hand lay-up molding method. This is because the manufacturing cost of this method is relatively higher compared to other molding methods. Two span continuous girders by a bridge pier at the middle separator made it possible to further reduce the cross-sectional size of main girder.

The decision of the allowable stress was a large problem at first. The generating stress becomes 1/7 of the material maximum strength, when the main girder deflection meets the limit of 1/600 of span length. The bending elastic modulus of GFRP is smaller than that of the tensile elastic modulus. Adding to bending strain, the shearing strain has to be considered, because the shearing rigidity of GFRP is low. By considering the laminate composition of the main girder web, the shearing rigidity was improved.

The Main girder was (channel cross section [-1,600×390×15×35) easily to applied by the hand lay-up molding method. The grinder height is uniformly fixed at 1600mm.The girder has a shape of circular arc curve in the bridge's axial direction. Flanges are 390mm wide and 35mm thickness. The thickness of the web is 15mm. The two main girders were set outside of the walkway surface and it was the middle walkway structure in which the upper flange served as curb, because the height of sidewalk road surface already decided can not be changed,

2.5 Joint

The main girder was produced as three-parts (15.427m+9.300m+12.973m) with joints to tied. General splice plates and bolts were not adopted. A special tension joint was adapted for the main girder connection. A detail of the joint is shown in Figure 3. A stainless steel plate (9mm thick) was embedded in the flange. The plate equipped flange's inner surface was coupled with stainless steel bolts (M16, Diameter ϕ=16mm). Plates on both sides of the joint plane were tightened with prestressed steel bar (Diameter ϕ=13mm). The clamping force of the prestressed steel bars was 84.3kN per steel rod to allow the stress of the joint plane to always be in compression. Only the stainless steel plate transmits the joint force. Insufficient data on FRP buckling prevent the authors from applying FRP to the joint. The Bolts installed in the web transmit the shear force at the joint. For rust prevention in the joint, the frame interior was filled in resin mortar, and the joint exterior plane was overlaid by FRP. FEM analysis and load testing confirmed the strength at the joint. Figure 4 shows the resulting FEM joint stress as 196.0kN. Though large strain has been generated in the stainless part, excessive strain has not been generated in the FRP parts. The metallic joint's stress transmitting design has now been confirmed.

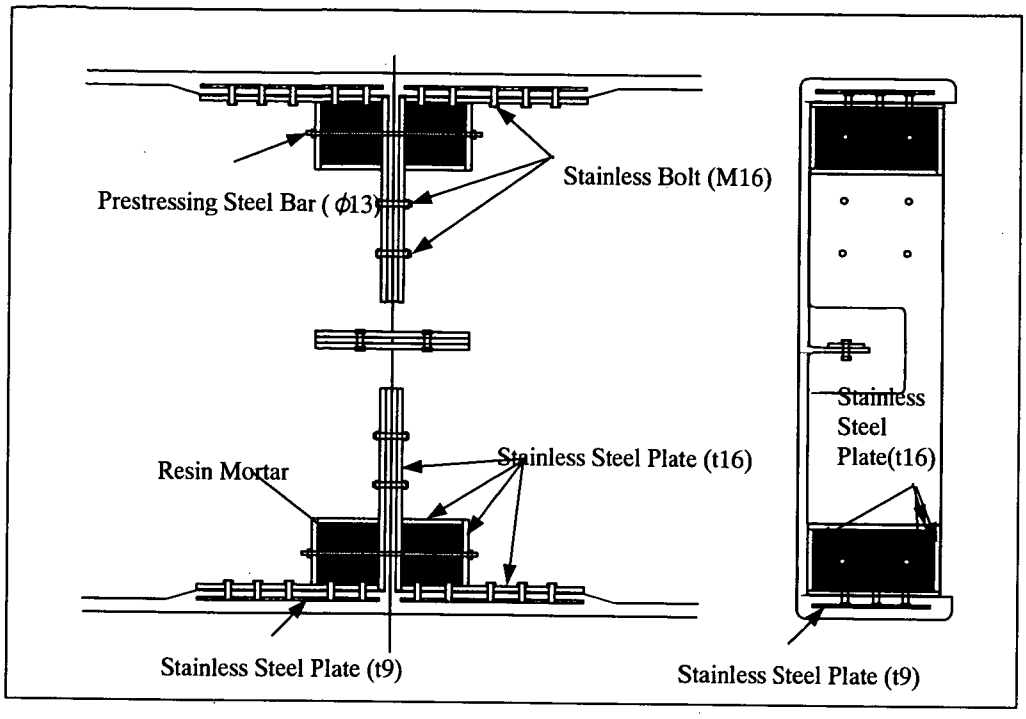

Figure 3 Main Girder Joint

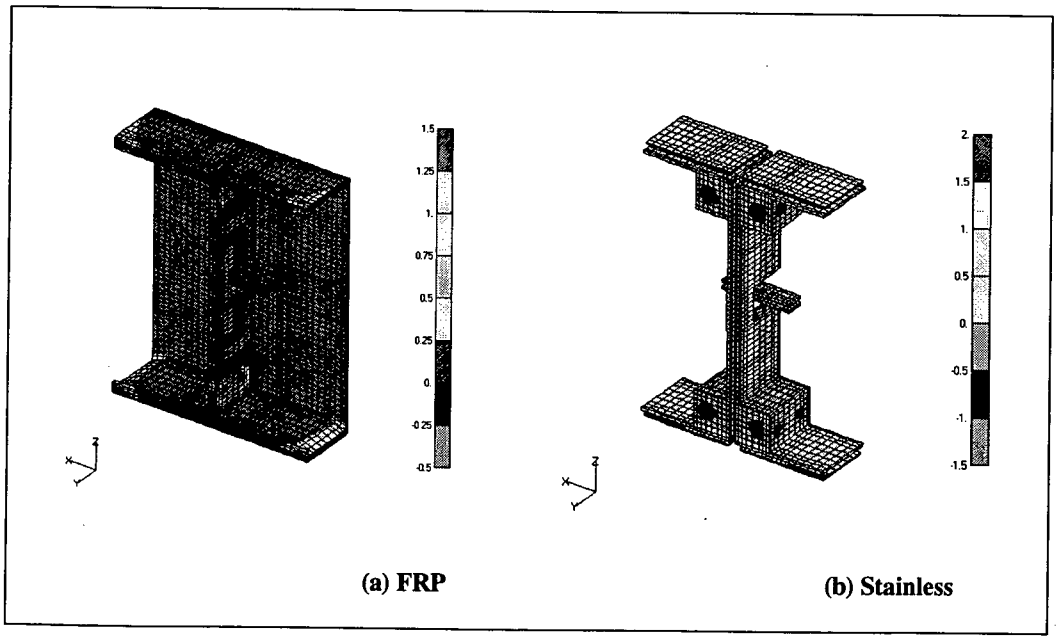

Figure 4 Longitudinal Stress by FEM Unit: kgf/mm^2

2.6 Appearance Considerations

The production size restriction forced the main girder to be divided into three parts. The external surface part of the main girder in the joint vicinity was covered with FRP. It would be impossible to confirm the condition of the joint after the bridge was completed. The horizontal plate was installed on the main girder. The shadow projected on main girder of this plate has the effects of reducing the appearance main girder height and relieving oppressive feeling of the drivers passing under this bridge. The appearance fouling caused by water that flows along the web, is not desirable. This plate serves to channel the water. The intro gradient on the curb's upper surface (upper surface of upper flange) leads rain water from the curb's upper surface to the pavement surface and prevents the girder web surface. Water that falls on the surface flows on main girder along this gradient (the walkway surface side). The underside of main girder was covered with FRP plate, which prevents the internal framing from bridge seen.

2.7 Slab

A hollow panel (500mm×60mm), made by the pultrusion molding method, was used for the slab. A cross section of the panel is shown in Figure 5. Stainless steel bolts (diameter ϕ=12mm) were used to connect the slab to bridge framing. FRP boarding (thickness 4mm), made by the pultrusion molding method, was laid on the

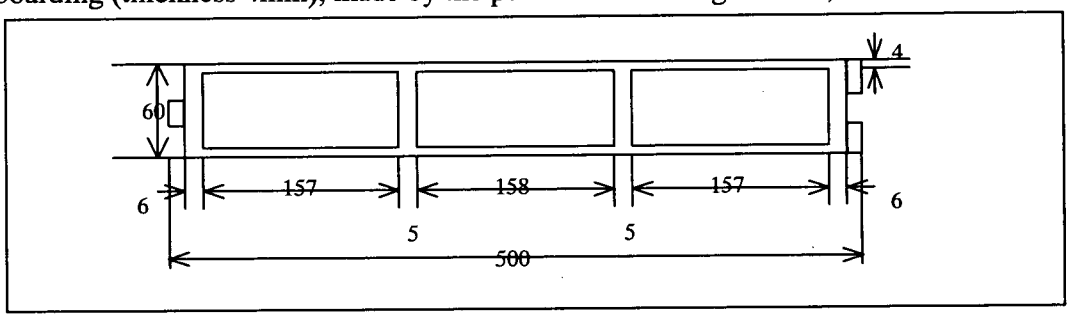

Figure 5 Pultrusion Molding Product for Slab

panels in order to prevent the water leakage. The FRP board was installed in the rivet on the panel. A sand powder covers the FRP board surface to improve the adhesion .

2.8 Floor system

Pultrusion molding material was used in the floor system. A truss structure by the channel bar was adapted for the system. The upper chord material is 〔200×70×7×10, and the lower chord material is 〔103×51.5×9.3. A hot press molding material, which could accept reinforced fiber, was used for the gusset plates. The stress condition of these gusset plates is complicated. Stainless steel bolts were used to couple the members. The bolted FRP member connection is the bearing member of the joint. Bolt diameter and bolt caliber agreed. There is no plasticity region in the FRP. This is because the redistribution of force by composition deformation can not be expected. An adhesive was also used for the joint, but the design effect of the adhesive is disregarded. Reinforcement of the bolt hole circumference was introduced as a result of the loading test prior to design.

2.9 Pavement

The mortar and tile were laid over the floor system.

2.10 Bearing Support

Laminated rubber was adopted in the support system. The stainless steel board reinforced a rubber bearing. An anchor plate that was fixed to the anchor bolt in the substructure holds the bottom flange.

2.11 Expansion Joint

The linear coefficient of expansion (2.0×10^{-5}) of the FRP by the hand lay-up molding method is about two times that of the concrete. When the temperature changes range is set to ±30℃ as described for steel structures in the "Highway Bridge Specification", the expansion amount of the main girder is ±12.5mm. Large loads do not affect the expansion device of pedestrian bridge. The expansion joint of this bridge is a simple structure because of the requirements. As the expansion joint, a stainless steel plate was installed in opening of the joint. Stainless steel bolts were used for mounting the plate to the slab. The abutment side of the plate is allowed to slip on the slab. The clearance between the plate and curb was covered with an elasticity rubber seal for appearance reasons.

2.12 Handrail

The handrail is also made of FRP. For economic efficiency, material produced by the pultrusion molding method was primarily used. Some other parts were constructed using hand lay-up molding materials. The roundness on the coping was used to prevent the combustion of trace tobacco. The stainless steel bolt in the hole emptied into the curb (upper flange). This allowed easy installation of the handrail to the main girder.

2.13 Lighting Facilities.

The lighting system adopted was the "stored handrail" type. Mercury-arc lamps were used. The luminous intensity was set to ensure 20*lx* brightness of the road surface.

2.14 Painting.

Original main girder has a top surface resin layer called the gel coat. Designers were worried about the degradation of the surface resin by the heavy ultraviolet rays of Okinawa Sun and abrasion by wind-blown sand. Therefore, accelerated UV ray and sand abrasion test were conducted. As a result of these test, a hard fluoro-resin coating was painted on the surface of the gel coat. Painting thickness is 75 μm (=25 (μm/layer) $\times$ 3 (layer)).

3. DISCUSSION

Static and dynamic load experiments were carried out. Comparison of measured test and calculated data proved the adequacy of the bridge design and construction.

3.1 Static Loading Test

The number of loading points was two, as shown in Figure 6. Load P_1 and P_2 were 46.5kN and 45.7kN respectively. The designed main girder deflection was calculated

by the equation deduced from beam theory. Elastic modulus and geometric moment of inertia for calculating the deflection were 11.8MPa and $4.24 \times 10^6 cm^4$, as were specified in the design. Results of the static loading experiment are shown in **TABLE Ⅷ**. Deflection test results agreed almost with calculated values. Test results generally show decreases further than calculated value on the strain of bridge axial direction that arises in the bottom flange of main girder. Axial direction strain, arising in the bottom flange of the main girder, generally decreased further in the test than was predicted by the design model.

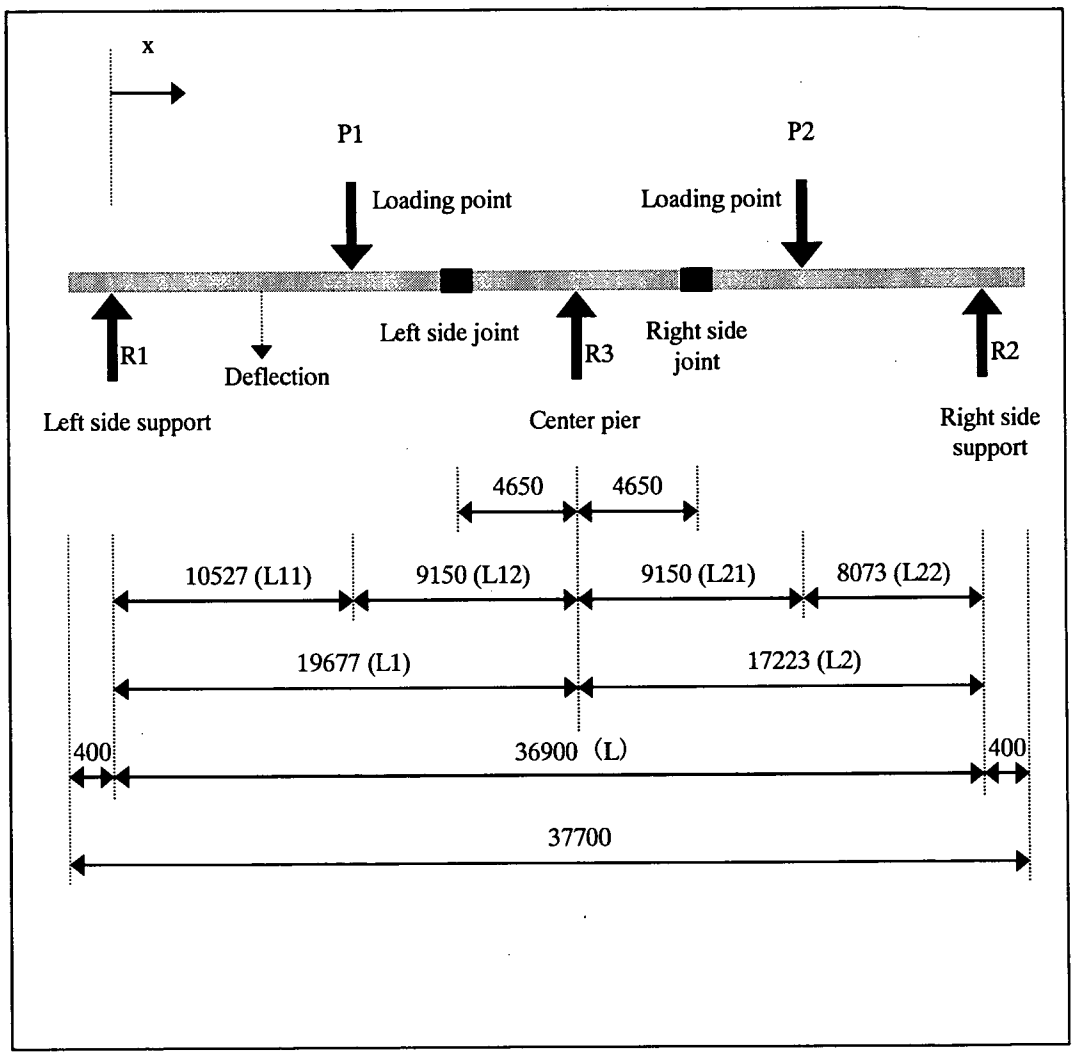

Figure 6 Loading Position of Static Loading test

TABLE Ⅷ STATIC LOADING TEST; The first column "Position" means the distance from the main girder left edge.

Position (mm)	Main Girder Deflection (mm)		Lower Flange Strain (Longitudinal Direction) μ m/m	
	Designed	Measured	Designed	Measured
0	0		0	
4,527	4.74		98	53
4,919	5.06	5.70	106	
9,839	6.91	5.74	213	
10,527	6.73		228	88
13,527	4.67		69	44
14,427	3.82		21	18
14,758	3.50	3.81	3	
15,627	2.67		-43	-4
16,527	1.84		-90	-29
19677	0.00		-257	
22,827	0.68		-102	-32
23,727	1.19		-58	-3
23,987	1.35	2.33	-45	
24,927	1.96		2	4
25,827	2.53		46	32
28,288	3.74	3.72	167	
28,827	3.87		194	75
32594	3.07	2.62	103	
33,327	2.65		86	42
36,900	0.0		0	

3.2 Dynamic Loading Test

The experiment case, as described in **TABLE Ⅸ,** was performed. The installation position of the accelerometers is shown in Figure 7. The first natural frequency was calculated in regarding the whole pedestrian bridge as a beam of uniform cross section,

TABLE Ⅸ DYNAMIC LOADING TEST

Case No.	Transducer Position	Loading Position No.
1	1-9	2
2	1-9	3
3	1-9	4
4	1-9	6
5	1-9	7
6	1-9	8

Note) Measurement was carried out three times for each case.

Calculated and observed results are shown in **TABLE Ⅹ**. There is a great discrepancy between the first natural frequency (4.6Hz) and a pedestrian pace (1.5-2.3Hz). This difference in frequency gives no pedestrian discomfort. The calculated and observed natural frequency varied only slightly. These differences of the natural frequency might be due to differences between the designed and actual weight of the FRP products and pavement.

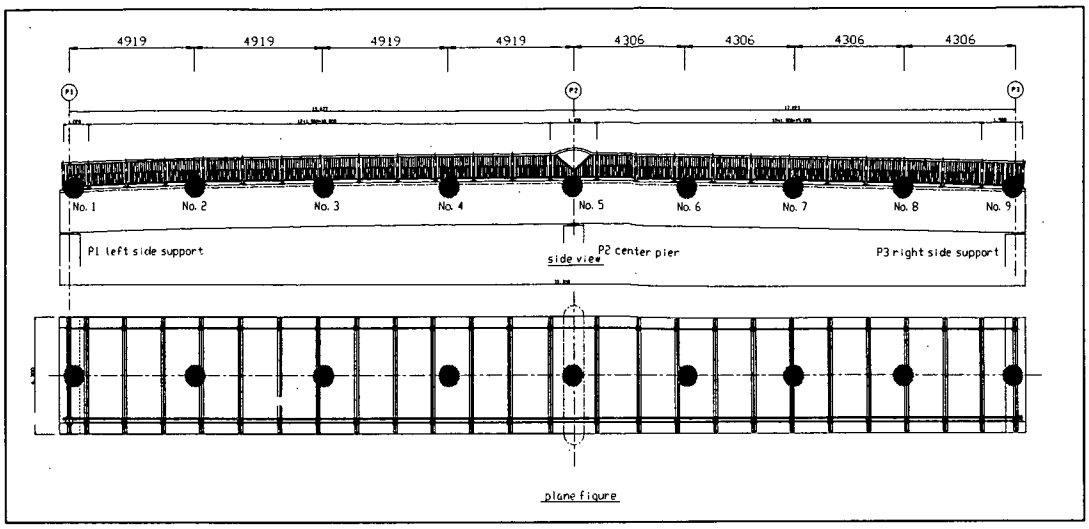

Figure 7 Accelerometer Installation Position

TABLE X FIRST NATURAL FREQUENCY

	Left Span (L=19,677mm)		Right Span (L=17,223mm)	
	Measured	**Calculated**	**Measured**	**Calculated**
Natural Frequency (Hz)	4.6	4.58	6.5	5.98

4. CONCLUSION

1. The construction of a pedestrian bridge made of GFRP is a viable countermeasure for salt damage.
2. The *Highway Bridge Specification* [1] and the *Pedestrian Bridge Technical Guideline* [2] were referred as the design criteria for the bridge.
3. The criterion wind velocity was set at 52.2m/sec. This usually is set at 40.0m/sec in the above criteria.
4. The decision of the allowable stress for the main girder was a large problem. The generating stress becomes 1/7 of the material maximum strength, when the main girder deflection meets the limit of 1/600 of the span length.
5. FEM analysis and load testing confirmed the strength at the special joint of the main girder.
6. Static and dynamic load test results approximately agreed with calculated values. This proved the accuracy of the bridge general design and manufacture process.

REFERENCES

1. Japan Road Association. 1996. *Highway Bridge Specification*
2. Japan Road Association.1979. *Pedestrian Bridge Technical Guideline*
3. Japan Road Association. 1991. *Highway Bridge Aerodynamic Design Handbook*

FEDERALLY ASSISTED BRIDGE PROGRAMS IN THE UNITED STATES: PAST, PRESENT AND FUTURE

Raymond McCormick, P.E.[1] and Edgar P. Small, Ph.D.[2]

Abstract

National-level bridge management began following the catastrophic failure of the Silver Bridge in December 1967. In response to this and other less noteworthy failures, Congress passed landmark legislation directing the USDOT, in conjunction with the States, to develop uniform, consistent standards for safety inspection of US bridges. The resulting National Bridge Inspection Standards (NBIS) were established. A summary and detailed discussion of the evolution of the bridge inventory and inspection program is provided. Bridge funding programs, and the relationship of these programs to the bridge inventory and inspection process are discussed. Future needs for bridge program and bridge inventory and inspection enhancement are discussed in conclusion.

Introduction And History

During the 1950's and through the late 1960's, the civil engineering community was focused on the design and construction of the interstate highway system in the United States. No one saw a need to set nation-wide requirements for the inspection of bridges. It was widely perceived that the existing practices were sufficient to address any safety concerns, leaving the public with the perception that all bridges were safe. This was the case on December 15, 1967. Just before 5:00 P.M., in the midst of rush hour traffic, the Silver Bridge, which connected the towns of Gallipolis, Ohio and Point Pleasant, West Virginia plummeted into the chilly waters of the Ohio River. In the wake of this bridge collapse, which resulted in 46 deaths, the public demanded action (Figure 1).

In response to this collapse, and other minor failures, national attention became focused on the issue of bridge safety. The U.S. Congress conducted hearings to examine the safety of highway bridges. Most states were unable to answer how many bridges they owned, what kind of condition they were in, what type of bridge they were, or where they were located.

1 Senior Structural Engineer, US Dept. of Transportation, Federal Highway Administration, Office of Bridge Technology, Washington, DC

2 Assistant Professor, Dept. of Civil Engineering, The Catholic University of America, Washington, DC

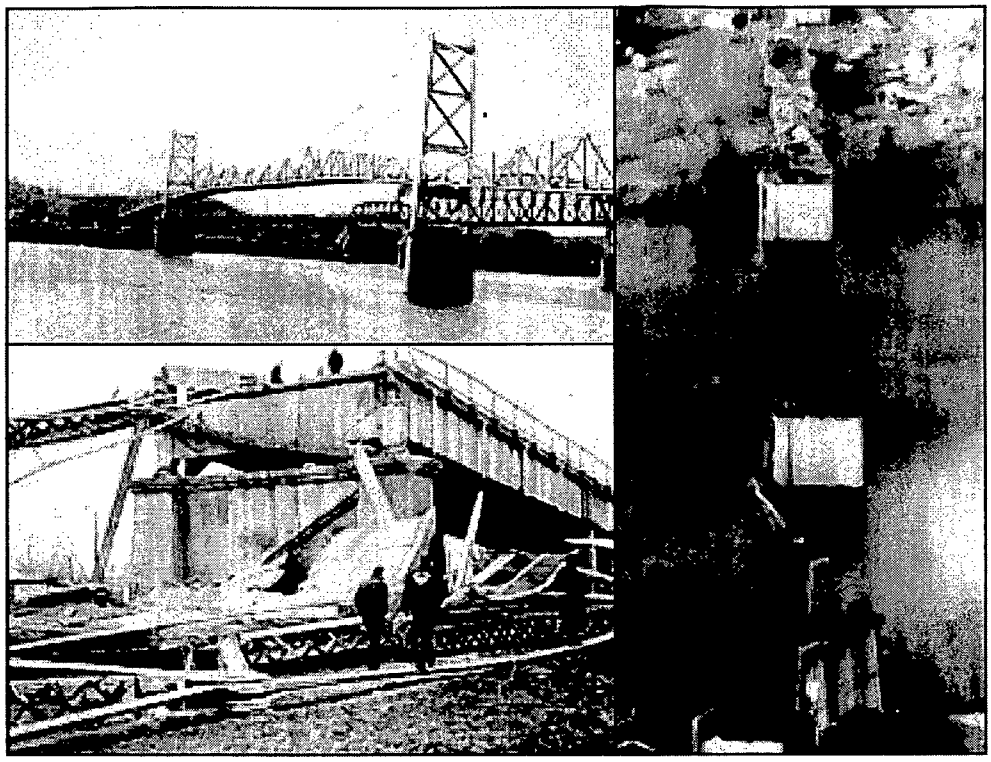

Figure 1: Pictures of the Silver Bridge Before and After the Collapse

These hearings resulted in mandates, which required the U.S. Secretary of Transportation to develop and implement the National Bridge Inspection Standards (NBIS). The NBIS, developed by the FHWA in cooperation with the American Association of Highway and Transportation Officials (AASHTO), was enacted as part of the Federal-Aid Highway Act passed on April 27, 1971. This landmark act established, for the first time in U.S. history, uniform, national-level standards for bridge inspection and safety evaluation and funding from which to replace deficient bridges. Through the legislation:

- All States are required to perform periodic inspection of bridges in excess of 6.1 m (20 ft) located on Federal-aid highway systems.
- Minimum bridge inspection data collection requirements are established
- Qualifications for bridge inspection personnel are defined,
- Training programs for bridge inspectors are developed and implemented
- The Special Bridge Replacement Program (SBRP) to provide funding for the replacement of bridges located on the Federal-aid system was established.

Over time, the requirements have been fine-tuned, additional inspection requirements have been added, and funding programs have been updated. The requirement to inventory and inspect bridges on Federal-aid highways was extended to all bridges in excess of 6.1 m located on public roads. Data collection requirements were enhanced, and training programs continued to be developed and expanded as more knowledge became available through

research as well as disaster. Funding programs were expanded to permit the use of federal funds for replacement and rehabilitation of both federal-aid and non-federal-aid bridges.

Despite efforts by the FHWA and State DOT's to continually enhance the program, unforeseen events periodically necessitated expansion of the program. The scene was Interstate 95, the primary highway on the Atlantic seaboard that provides connectivity between Florida and Maine, approximately 30 miles east of New York City, near Greenwich, CT. On June 28, 1983, a section of the Mianus River Bridge catastrophically failed due to instantaneous fracture of a pin and hanger detail. This failure (Figure 2) resulted in several fatalities and disrupted commerce in the Northeastern U.S. for several months. This event, and other less notable ones, spurred significant research into fatigue of steel connections. The research results gave a tremendous insight into the behavior of steel connections. It was recognized by the FHWA that additional, more detailed bridge inspection procedures were required for fracture critical structures resulting in new training programs.

On April 5th, 1987, disaster struck again with the collapse of a bridge carrying the New York State Thruway (Interstate 90) across the Schoharie River (Figure 3). There were several fatalities as the result of the failure of the center pier due to scour. With rising water levels due to localized flooding, the soil around the pier was simply washed away. This was followed by the subsequent loss of bearing capacity for the foundation of the pier. On April 1, 1989 the Hatchie River Bridge in Tennessee failed due to scour. These bridges indicated the potential problem, given that a significant proportion of the 587,755 bridges on public roads cross over waterways. The FHWA acted quickly providing guidance for scour assessment and required State DOTs to perform periodic underwater inspection of all structures susceptible to scour. Scour research and prevention is continuing.

There was also a need to replace bridges before they collapse. Along with the NBIS, the SBRP was created by the Federal-Aid Highway Act to help states fund the replacement of bridges. This provided funding to Federal-Aid highway bridges only. It provided $816.5 million for the design and construction of 1,578 bridges. In 1978 the Surface Transportation Assistance Act replaced the SBRP with the HBRRP. This provided funding for both Federal-Aid and non-Federal-Aid highway bridges. It also expanded the program to include both bridge rehabilitation and replacement.

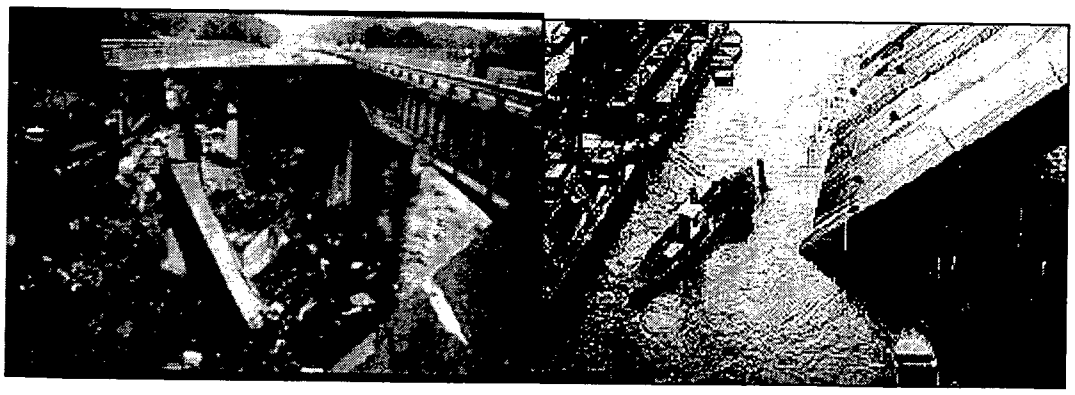

Figure 2: Collapse of the Mianus River Bridge Carrying I-95 in Connecticut

Figure 3: Collapse of the Schoharie Creek Bridge Carrying I-90 Near Albany, NY

Today, all bridges in excess of 6.1 m located on public roads are inspected to ensure safety. Notable changes in legislation can be seen in Table 1. "Best-practices" for routine, fracture critical and underwater inspections have been defined and published. Qualifications of inspection personnel have been established, and training programs implemented to ensure completeness of engineering reviews and consistency of inspection condition assessments. Funding programs have been established and expanded in an attempt to adequately address expanding bridge work needs and to provide funding for retrofit against natural hazards (scour, earthquakes), and extreme events (collisions, fracture). The U.S. Congress, U.S. DOT and State DOT's have created a system to keep the growing number of deteriorating bridges as safe as possible.

Table 1: Summary of Bridge Inspection Legislation and Noteworthy Changes Over Time

Act and Date	Requirements
Federal-Aid Highway Act (1971)	- Inventory requirement for all bridges on the Federal-aid systems - Established minimum data collection requirements - Established minimum qualifications and inspector training programs - Established Special Bridge Replacement Program
Surface Transportation Assistance Act (1978)	- Extended inventory requirement to all bridges on public roads in excess of 6.1 m - Established Highway Bridge Rehabilitation and Replacement Program (extending funding to Rehab) to replace Special Bridge Replacement Program
Surface Transportation Uniform Relocation Assistance Act (1987)	- Added requirements for underwater inspections and fracture critical inspections - Allowed increased inspection intervals for certain types of bridges
Intermodal Surface Transportation Efficiency Act (1991)	- Mandated State implementation of bridge management systems - Increased funding in HBRRP
NHS Designation Act (1995)	- Repealed mandate for management system implementation
Transportation Efficiency Act for the 21st Century (1998)	- Increased funding in HBRRP

BRIDGE INSPECTION PROGRAM

The NBIS requires bridges to be inspected, at a minimum, of once every two years. Inspections are performed by the bridge owners (States, cities, municipalities, etc.) with oversight by the State DOT's. Information is collected on the bridge composition and conditions and reported to the FHWA where the data is maintained in the National Bridge Inventory (NBI) database [5]. Inventory information includes location and description fields, geometric data, functional descriptions and design characteristics. This information permits classification of structures according to serviceability and essentiality for public use.

Condition information is collected for the following:

- The bridge deck, including the wearing surface
- The superstructure, including all primary load carrying members and connections
- The substructure, considering the abutments and all piers
- Culverts, recorded only for culvert bridges
- Channel/channel protective systems, for all structures crossing waterways

Bridge inspectors utilize a ten (10) point system, where code 9 indicates excellent, as-new condition and code 0 indicates a failed condition. Inspectors assess the ratings in a visual fashion based on engineering expertise and experience. Extensive training for inspectors is available to assist the bridge owners in ensuring consistency in the assignment of condition ratings. References on bridge inspection, such as the Recording and Coding Guide and the Bridge Inspectors Manual/90 are also available to guide the inspectors in the assignment of condition ratings.

Following collection of the inventory information and condition ratings, appraisal ratings are calculated to assess the adequacy of the structure to provide the required service. Appraisal ratings are quantified for:

- Structural evaluations (load carrying capacities),
- Deck geometry (indicating constrictions which affect safety),
- Underclearances, and
- Waterway adequacy (the ability of the opening to handle the flow-rates).

Condition ratings and appraisal ratings are utilized to assess the deficiency status of the structure. Deficient bridges may result from structural or functional characteristics. Structural deficiencies result from poor condition ratings or from low load ratings. Functional obsolescence results from inadequate appraisal ratings or from low design-load capacities. Inadequate waterway adequacy can be a contributing factor for either structural deficiencies or functional obsolescence.

To guide the assessment of federal fund eligibility, a performance measure considering multiple variables is developed. This performance measure, termed as the sufficiency rating, considers the following variables:

- Structural Adequacy and Safety (55%) – Assessed using the condition ratings
- Serviceability and Functional Obsolescence (30%) – Assessed using the appraisal ratings and the service characteristics of the structure
- Essentiality for Public Use (15%) – Based on detour lengths, traffic and defense importance
- Special Reductions (-13%) – Based on redundancy and safety features

The sufficiency rating is calculated using a deficiency-point approach. A structure receives a 'score' of 100 when no deficiencies exist and a 'score' of 0 when it is totally inadequate for all considerations in the formula. The sufficiency rating is "a method of evaluating highway bridge data by calculating four separate factors to obtain a numeric value which is indicative of," [2] whether the structure should remain in service. The sufficiency ratings form the basis for the prioritization on a National-level and, when combined with other variables, is also a factor in the determination of fund eligibility and fund allocation.

Deficient deck area is an important variable used for apportionment of federal funds to the States. Deficiency status is also a determining factor for fund eligibility assessment; however, it does not provide a basis for prioritization of needs, which is a specific requirement of the NBIS. Prioritization may be performed using the Sufficiency Rating [2], which is calculated in the Washington Office fields. The primary federal funding program is the Highway Bridge Replacement and Rehabilitation Program (HBRRP), which is described in the following section.

The data collected through the bridge inspection process, including the calculated fields and the performance measures as described, provides the basis for bridge management under the NBIS. The program is not limited to definition of data requirements, however. The NBIS set minimum requirements for the qualifications of Bridge Inspectors. These qualifications require that the organizational leader be a registered professional engineer, be qualified for registration as a professional engineer under the laws of the state, or have a minimum of 10 years experience in bridge inspection and have completed a comprehensive course based on the Bridge Inspector's Manual. They also require that the individual in charge of an inspection team be qualified to be an organizational leader, have a minimum of 5 years experience and completed a comprehensive course based on the Bridge Inspector's Manual, or have current certification as a Level III or IV Bridge Safety Inspector under the National Society of Professional Engineer's Program for National Certification in Engineering Technologies. Furthermore, training programs were established and are periodically offered for bridge inspection personnel.

THE HIGHWAY BRIDGE REPLACEMENT AND REHABILITATION PROGRAM

The inventory information, deficiency status, and the sufficiency ratings provide the starting point for bridge management under the NBIS guidelines. The process may be outlined through the following steps, which are performed annually:

1. Bridge owners inspect structures and collect the NBI information. The State DOT's synthesizes all information.
2. The minimum data required by the NBI is submitted to the FHWA. The data is evaluated for errors and programs are run to calculate the appraisal ratings, deficiency status and sufficiency rating.
3. The NBI data is used for apportionment of available funds, primarily through the Highway Bridge Replacement and Rehabilitation Program (HBRRP). The apportionment program allocates available monies to the States based on the deficient deck area.
4. State DOT's receive apportionments and select projects at their discretion within the constraints of the HBRRP.

Through the initial phases of the bridge program, funding was provided only for bridge replacements on the Federal-Aid highway system. Over time, the funding eligibility was increased to include the non-Federal-Aid highway system and to include major rehabilitation actions. Eligibility for the use of funds is determined based on the deficiency status of the bridge and the sufficiency rating. For a structure to receive funding, it must be deficient, either due to structural condition deficiencies or functional obsolescence. This deficiency status, as previously discussed, is based on the condition ratings assigned through the inspection process and appraisal ratings calculated based on the service and functionality of the structure. The type of actions eligible for use of HBRRP funds for deficient bridges is then constrained by sufficiency rating eligibility criteria. Deficient bridges with a sufficiency rating of 50 or less are eligible for replacement funding. A sufficiency rating between 50 and 80 designates eligibility for rehabilitation funds on deficient structures. For all States, the cost of replacing or rehabilitating all of the structures outweighs the available funds; therefore, each State has flexibility in selecting bridge projects subject to these eligibility constraints.

The NBIS and the HBRRP have, historically, been very effective in providing the basis for bridge inspection and funding for rehabilitation and replacement. The NBI provides a wealth of information and has enabled Federal engineers to track changes in the status of bridges and to develop an extensive picture of the bridge compositions on a national-level. The NBI also facilitates the evaluation of policy effectiveness. For instance, through the 1970's and the 1980's, there were steady increases in bridge funds available to the States. What did these fund increases accomplish? Through examination of the time-series NBI, it was determined that, although funds were increased, deficiencies within the network were not decreasing, but rather increased. This indicated that the program funds distributed were insufficient and the additional monies were required. Today, with this knowledge available, funding levels have been increased. Today, approximately $21 billion is provided to the HBRRP through the Transportation Efficiency Act for the 21st Century (TEA-21). The following are authorized under TEA 21 for the fiscal years from 1998 through 2003:

Fiscal Year 1998	-	$ 2.9 Billion
FY 1999	-	$ 3.4 Billion
FY 2000	-	$ 3.4 Billion
FY 2001	-	$ 3.5 Billion
FY 2002	-	$ 3.6 Billion
FY 2003	-	$ 3.6 Billion
Total Amount	-	$20.4 Billion

FUTURE PROGRAM ENHANCEMENTS:

If every square meter of deficient bridges were to be replaced during the year of 2000, costs would greatly exceed the funding available. It is not feasible to address all of the network needs within such a small time period, especially with a large disparity between network needs and funds available. As funds available are expended, new bridges become deficient. Thus, while funds available are making progress, it is possible that needs will continue to increase despite the large sums available under TEA-21 and that such increases will outpace funds available through future Transportation Programs. This may be inferred when examining the year of construction distribution of bridges in the network, as shown in Figure 4. The large peak of structures built during the interstate construction 'boom' will require more attention as they age. Thus, it is evident that more proactive forms of bridge management are required. The States and the FHWA have recognized this and bridge management systems will continue to be implemented by the bridge owners. It is anticipated that the NBIS and HBRRP requirements will have to be enhanced to address the needs of an aging bridge population. Progress is being made to develop and implement more effective bridge management systems, such as Pontis and Bridgit.

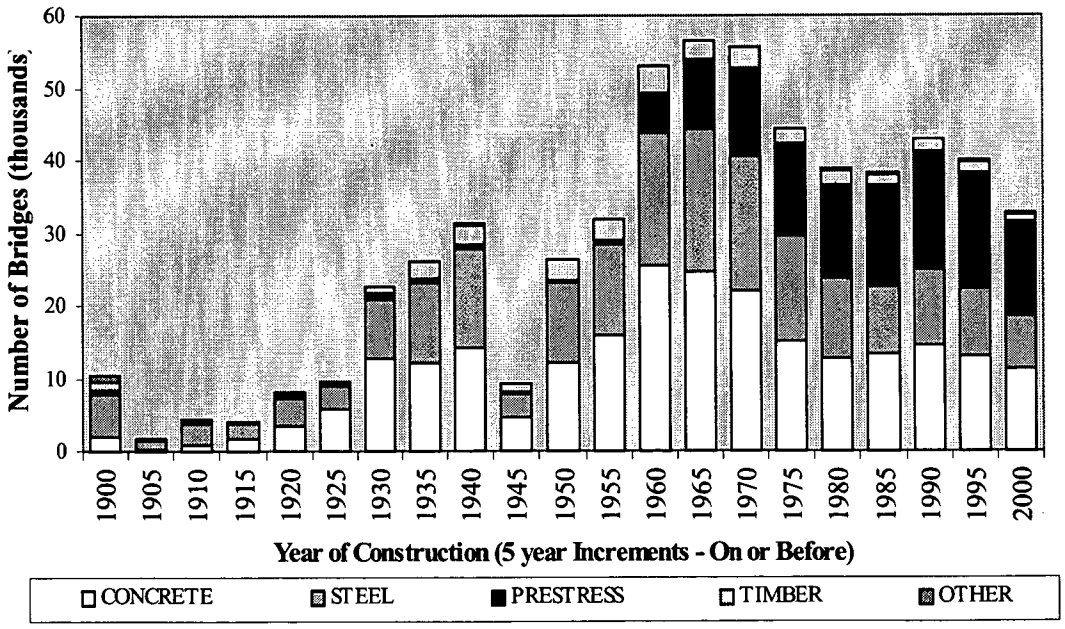

Figure 4: Year of Construction Distribution for Bridge Designs (excluding Culverts) by Superstructure Material

For more effective bridge management, data obtained through the inspection process must be more detailed. This is being done through the development of enhance bridge data models, such as the element-level bridge models defined as AASHTO Commonly Recognized (CoRe) elements, which is employed by predominant bridge management systems in the United States. Differences between component-level bridge ratings in the NBI and element-level bridge ratings in bridge management systems are illustrated in Figure 5. These differences between component and element-level inspection become obvious through explanation of the substructure. Where as the NBI inspection provides single ratings for the substructure (shown in bold, italicized text), element-level models provide separate ratings for the bearings, abutments, footings, and pilings. These element ratings are based on quantities as opposed to the subjective visual assessments. Similar differences occur for superstructure and deck component, which are replaced by more detailed, quantitatively assigned element inspection ratings.

With additional detailed information available from bridge management systems, the data used for national-level considerations may be enhanced. This, however, is dependent upon consistency in the State DOT element-level definitions. Currently in the US, there are AASHTO guidelines for element definitions and element-level inspections; however, there is no consensus. It is anticipated that the NBI will be enhanced to provide access to BMS information where available. This information will be used for special studies and for more detailed examination of bridge deficiencies and deterioration.

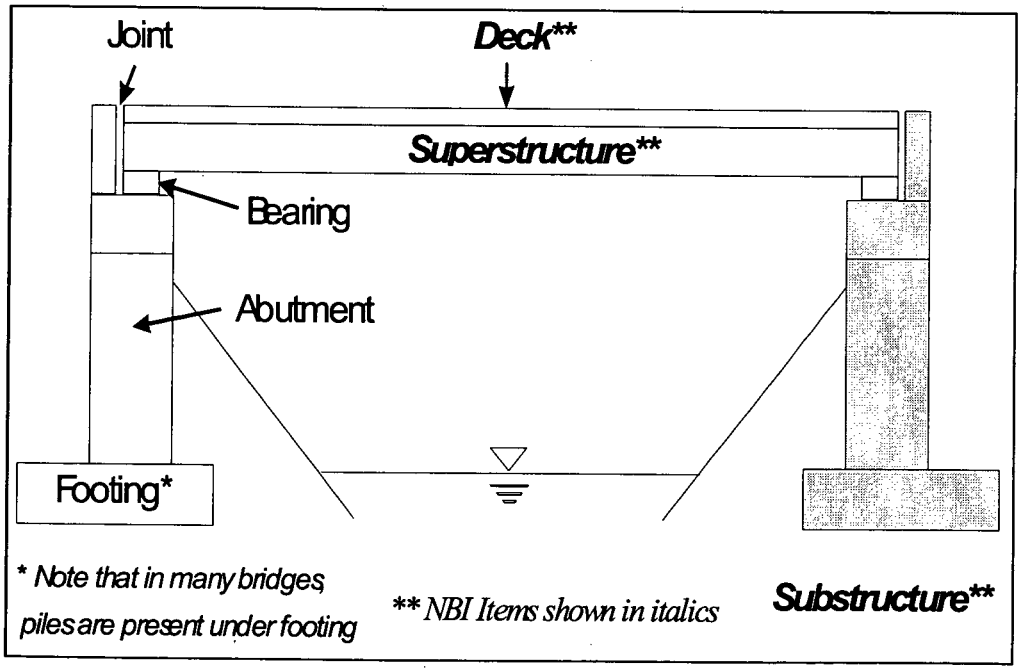

Figure 5: Sample Structure Composition Using NBI and Element-Level Descriptors

The techniques used for assessment must also be enhanced. Both the NBI inspections and element-level inspections are visual techniques. The NBI component based inspection is subjectively assigned whereas the element-level ratings are determined using quantitative measures of visually identified deficiencies, such as rusting of beams or delamination of wearing surfaces (pot-holes). Unfortunately some problems are impossible to see by the human eye. Several techniques for quantitative, non-subjective NDE techniques for bridges have been developed. Ultrasonic inspections, eddy current, magnetic particle, liquid penetrant, bridge acoustic emission monitoring, laser, ground-penetrating radar, radiography, and active thermographic crack detection are examples of techniques either being developed or already in use. Brief descriptions of each type follow:

- Ultrasonic inspections send waves into the material to detect cracks
- Eddy current testing creates a magnetic field that opposes the magnetic field of the original material, locations of cracks will appear where the created impedance diverge
- Magnetic Particle testing can be performed on steel bridges to find cracks, using two magnets and iron particles the magnetic fields create a distortion near cracks on the surface, which attracts the iron particles
- Liquid penetrant is where a liquid chemical is sprayed onto the material, allowing it to soak into any defects on the surface; a second chemical is applied causing a reaction with the first chemical making any defects visible
- Bridge acoustic emission Local Area Monitoring can be used to track known defects, whether corrective measures are working, to monitor structural integrity of welds and connection points
- A laser can be used to track the deformation of the material under stresses.
- Ground-penetrating radar can be used to show variances in material types is being tested for application in bridge deck inspections to identify areas of delamination
- Radiography tests use x-rays to create a cross-section of the object; this can be used to analyze concrete borings more easily and accurately
- Active thermographic crack detection detects changes in temperature when heat is applied to a material; these changes in temperature are a result of cracks allowing the escape of heat

Additional detail on these techniques is provided by the FHWA Research Program through the Non-Destructive Evaluation Validation Center at the Turner Fairbanks Highway Research Center.

Bridge management systems are based on the concept that preventative maintenance may be more cost effective than major repair and rehabilitation actions. This is quantitatively determined through the BMS optimization routines. Under the current funding restrictions, based upon the work performed, bridge funds can only be utilized once every ten years for a particular structure. Currently the FHWA is performing a study to examine the impact of altering or eliminating the 'ten-year rule'. Such alteration (or even the possible elimination) will provide more flexibility to the States to help them extend the service life of their bridges.

Additionally, the FHWA is examining the two-year biennial inspection requirements. Currently, States can receive special exceptions for specific structures to utilize a four-year inspection cycle. Information is being collected to see how this program is performing. What kind of effect it is having on the safety of the structures involved and the resources being utilized?

The eligibility criterion specifies that bridge deficiencies and prescribed sufficiency rating conditions be satisfied prior to utilizing federal funds. The definition of bridge deficiencies is currently being examined by the FHWA. Are there other mechanisms which compromise bridge safety or serviceability? If so, efforts will be taken to include these considerations in the definition of bridge deficiencies. Regarding the sufficiency rating, efforts are also underway to evaluate alternative performance measures. One such measure currently under investigation is the 'health-index', which is a reflection of the average condition state of BMS elements in a structure. Other performance measures, such as that proposed by the National Cooperative Highway Research Program (NCHRP) are also being examined. This performance measure includes serviceability and risk in addition to preservation, the sole consideration of the health index.

CONCLUSIONS:

The history of the National Bridge Inspection program and the Highway Bridge Replacement and Rehabilitation Program have been presented and discussed. Details of these programs have been outlined and bridge management through the NBIS regulations has been documented. The data for bridge management provides the basis for national and State-level decision-making and has thus been presented. Effectiveness of the program has been discussed. The need for enhancements to the program was established and future directions were outline and discussed. Incorporation of such enhancements promises to ensure continuing safety and adequacy of the bridge infrastructure system over a long-term horizon.

REFERENCES:

1. *Commonly Recognized (CoRe) Structural Elements*, AASHTO, Washington, DC, 1998.

2. O'Connor, D. S. and Hyman, W.A., "Bridge Management Systems", Summary of FHWA Demonstration Project 71, Report # FHWA-DP-71-01, Office of Engineering, Bridge Division, Federal Highway Administration, U.S. Department of Transportation, Washington, DC. 1991.

3. US Department of Transportation, *Bridge Inspector's Training Manual/90*, Federal Highway Administration, 1991.

4. US Department of Transportation, *National Bridge Inventory Information System Documentation*, Bridge Division, Office of Engineering R&D, Federal Highway Administration, 1992.

5. U.S. Department of Transportation, "Recording and Coding Guide for the Structure Inventory and Appraisal of the Nation's Bridges," Report No. FHWA-PD-96-001, Office of Engineering, Bridge Division, Federal Highway Administration, U.S. Department of Transportation, Washington, DC. 1995.

6. U.S. Department of Transportation, *Reliability of Visual Inspection for Highway Bridges*, NDE Validation Center, Office of Infrastructure R&D, Federal Highway Administration, 2001.

7. U.S. Department of Transportation, *The Status of the Nation's Highway Bridges: Highway Bridge Replacement and Rehabilitation Program and the National Bridge Inventory* Report to the United States Congress, Bridge Division, Federal Highway Administration, U.S. Department of Transportation, Washington, DC, Biennial Series.

Structural Behavior of Steel Girder-RC Pier Composite Rigid Frame Bridge

Noriyuki Suzuki*, Yoshinori Igase*, Koichi Nishikawa** and Toru Sato***

Abstract

Composite rigid frame bridge is expected to be a bridge type having sufficient seismic resistance and reduced maintenance costs. However, no reasonable design method has been established for joint connection of composite rigid frame bridge because its stress transfer mechanism is complicated. Thus, a study that included loading tests and FEM analysis was conducted to determine the mechanical properties of the joint connection. Using the results of this study, a design method to evaluate the ultimate shear strength was proposed. Furthermore, the design method was applied to an actual bridge and constructs a composite rigid frame plate girder bridge.

1. Introduction

Various types of steel-concrete composite bridges have been recently studied to reduce construction costs and to develop more mechanically reasonable structures [1]. As a result, a composite rigid frame bridge, in which the steel girders and RC piers are rigidly connected, became to be realized gradually on the expressway of Japan Highway Public Corporation. Based on the relevant experimental and analytical studies conducted for construction of this structure, design manual has been prepared [2].

A composite rigid frame bridge has sufficient seismic resistance due to its high degree of redundancy. In addition, since the steel girders are connected directly to the piers, it is possible to eliminate bearing supports. Therefore, this structure is expected to reduce the costs for maintenance.

In the early stage of constructing of a composite rigid frame bridge, prestressing method by post-tensioning used to be adopted to the connection between steel girder and RC pier [3]. However, using this method to construct this type of bridge in unreasonable situation should be improved on site such as;

(1) Construction work is troublesome.

(2) Construction procedure is restricted.

(3) Construction costs are increased.

And the sectional forces acting on the steel girder and RC pier are needed to be transferred alternately through the rigid connection. Moreover, sufficient flexural ductility is required to the rigid connection in order to withstand the fatal damage would not occur at the rigid connection prior to the girder or the pier. To improve and accomplish these items, the structures of the non-prestressed joint connection are studied, and establishment of a reasonable design method is required [4), 5)].

* Bridge Division, Expressway Research Institute, Japan Highway Public Corporation

** Bridge Division, Tohoku Branch, Japan Highway Public Corporation

*** Engineering Development Division, Miyaji Iron Works. Co., Ltd.

In this paper, the stress transfer and load-bearing mechanisms in the joint connection are described. Also the application of a new design method to an actual bridge and a construction example are reported.

2. Outline of Tests and Analysis

2.1 Outline of Tests

2.1.1 Test Specimens

The purpose of the tests was to determine the stress transfer and the load-bearing mechanisms in a steel girder-RC pier joint connection. Tests were carried out in order to clarify the relationship between the structure of the joint connection and its load-bearing property for three types of specimens having different structure of the joint connection: a joint connection having cross girders outside the concrete (Type-A), a joint connection having cross girders buried in the concrete (Type-B) and a joint connection having vertical stiffeners without cross girders (Type-C).

The specimens were one-fourth scale for actual bridge that determined from the capacity of the test equipment. The depth of a steel girder was decided from the embedded length of reinforcing bars in the joint connection. And the sectional dimensions of a girder and a RC pier were designed that the ultimate strength of the steel girder was larger than that strength of the pier. All types of specimens had no shear studs exist in the cross girders or the stiffeners and the same arrangement of reinforcements in the RC pier except that the Type-B specimen was provided with hoops that pierced through the webs of the cross girders. **Figure 1** shows the dimensions of the specimens, and **Figure 2** shows the structure of each specimen. In addition, **Table 1** gives the material properties of steel and concrete used in the specimens.

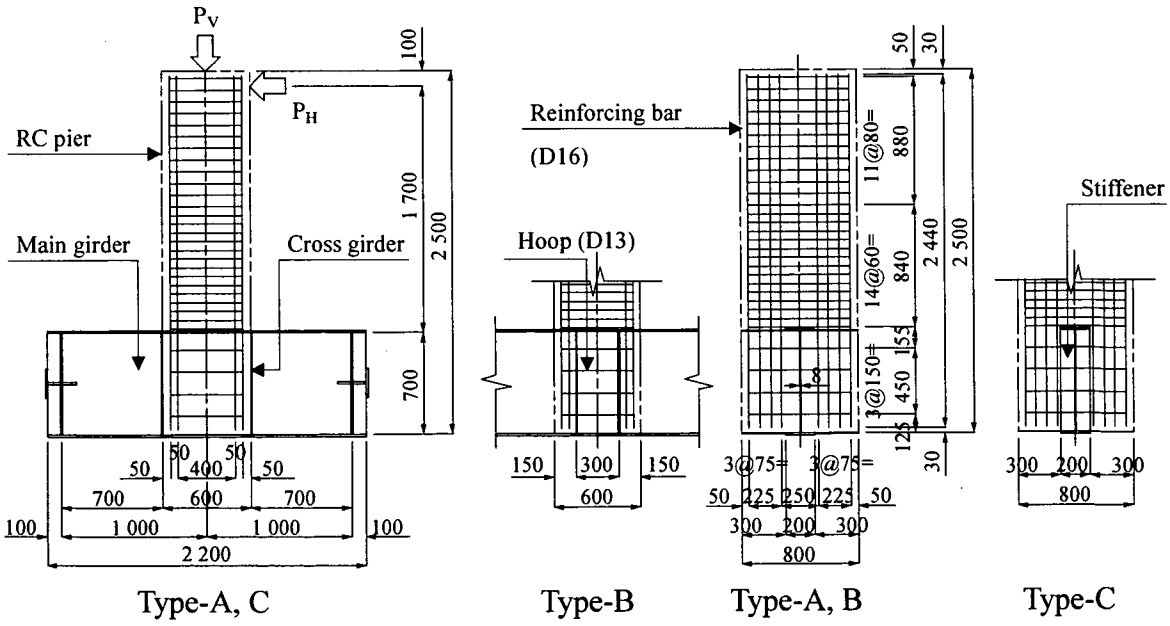

Figure 1. Dimensions of the Specimen

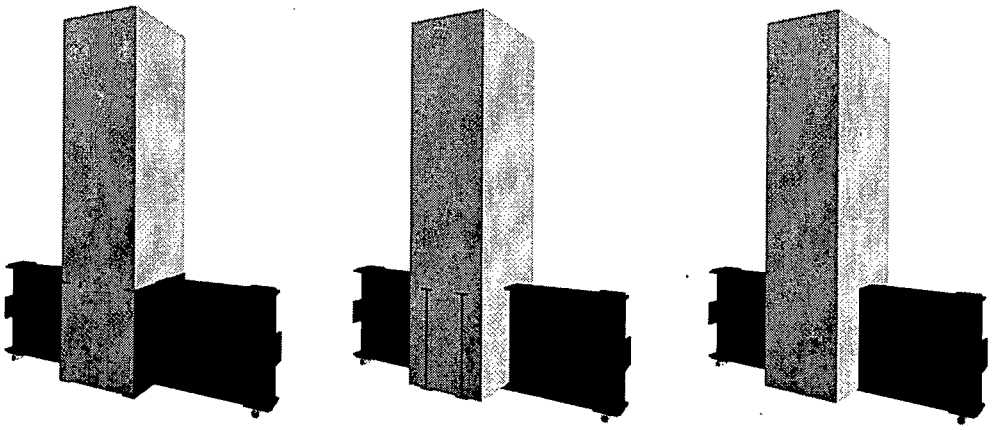

(a) Type-A (b) Type-B (c) Type-C

Figure 2. Structure of the Specimens

Table 1. Material Properties

Concrete	High-early-strength Concrete Compressive Strength : $f'_c = 31.0$ N/mm^2 Modulus of Elasticity : $E_c = 2.29 \times 10^4$ N/mm^2
Steel Plate	Grade : SM400A Yield Strength : $f_{sy} = 298.7$ N/mm^2 Tensile Strength : $f_{su} = 448.9$ N/mm^2 Modulus of Elasticity : $E_s = 2.08 \times 10^5$ N/mm^2
Reinforcing Bar	Grade : SD345 Yield Strength : $f_{ry} = 373.3$ N/mm^2 Tensile Strength : $f_{ru} = 546.4$ N/mm^2 Modulus of Elasticity : $E_r = 1.88 \times 10^5$ N/mm^2

2.1.2 Test Procedure

The specimen was set in horizontally, and then the load was applied to the RC pier (**Figure 3**). In this procedure, first, a compressive force equivalent to the deadweight of the superstructure was applied as a load to the end of the pier in the direction of its axis (axial load = 235 kN, stress of concrete = 0.49 N/mm^2). Next, with a constant axial force, the pier was loaded horizontally. The loading test was started with a monotonous loading test in which the load on each specimen was steadily increased until the maximum strain indicated on the strain gauges attached to the main reinforcing bars reached the yield stress (about 373 N/mm^2). The applied load was defined as the yield load Py and the horizontal displacement at the loading point was defined as the yield displacement δ y. After that, alternate loading tests were conducted that controlled by the displacement; for this, the load was gradually increased by the steps shown in **Figure 4** with the yield displacement as a cycle. In alternate loading tests, the load was increased up to around 20 δ y because of the marginal performance of the test equipment.

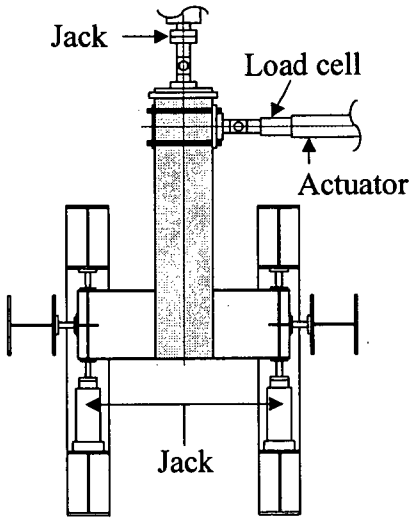

Figure 3. Loading Method (Plan View)

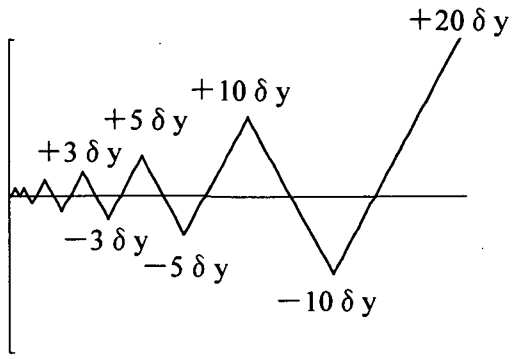

Figure 4. Loading Step

2.1.3 Results and Consideration of Tests

(1) Monotonous loading test

Table 2 shows the yield load and yield displacement from the monotonous loading tests for each type of specimen.

Table 2. Monotonous Loading Test Results

Specimen	Yield Load Py (kN)	Yield Displacement δ y (mm)
Type-A	317.2	7.37
Type-B	305.0	7.99
Type-C	291.7	7.89

The relationship between the horizontal load and the horizontal displacement at the loading point is illustrated in **Figure 5**. And **Figure 6** shows the principal strain distribution in the web of the main girder.

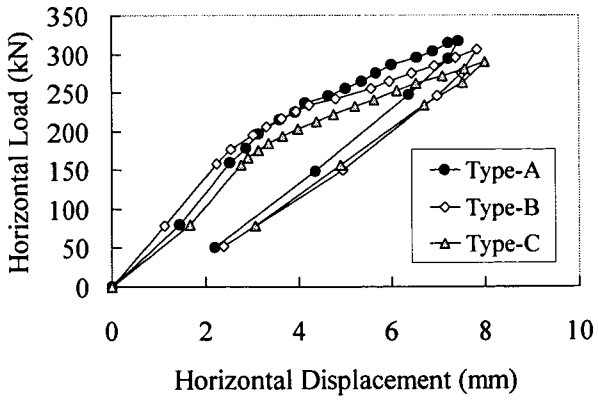

Figure 5. Load-displacement Relationship

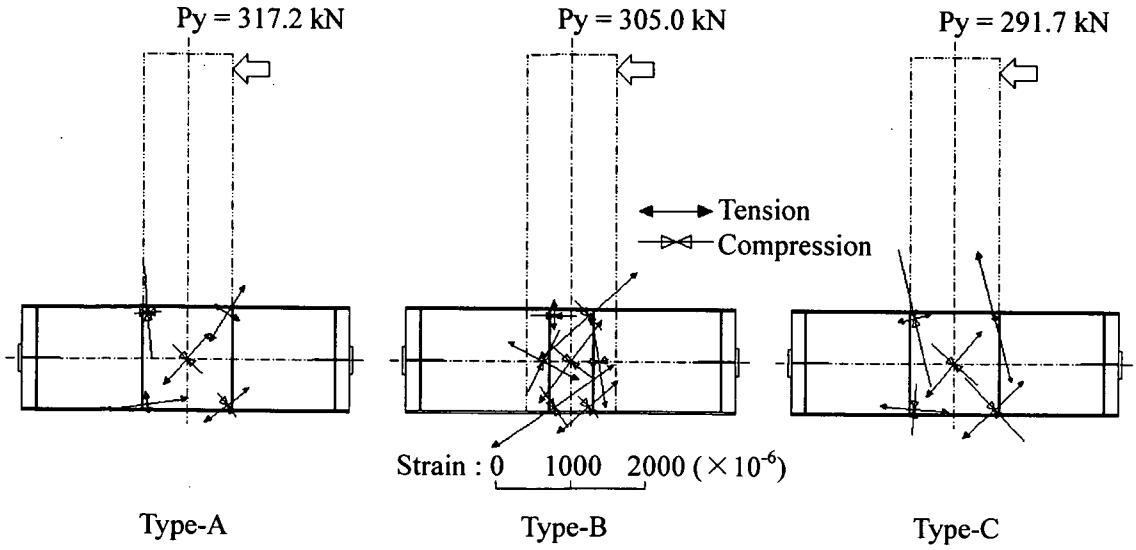

Figure 6. Principal Strain Distribution in Web of Main Girder

All specimen types had roughly the same yield loads and yield displacements. However, the Type-A specimen with the joint connection having cross girders outside the concrete had the largest yield load and the smallest yield displacement. Also the Type-A specimen had the smallest principal strain and more smoothly distribution in the web of the main girder. This may be due to an influence of the structure of the joint connection that had cross girders because the flexural rigidity of the joint connection is thought to vary depending on the existence and the position of the cross girders.

(2) Alternate loading test

Results from the alternate loading test that followed the monotonous loading test are in **Table 3**.

Table 3. Alternate Loading Test Results

Specimen	Maximum Load Pmax (kN)	Maximum Displacement δ max (mm)
Type-A	440.3	20 δ y
Type-B	454.5	20 δ y
Type-C	345.2	3 δ y

Because the Type-C specimen with the joint connection having no cross girder had a shear failure of the joint concrete at the step of 3 δ y, further loading tests were canceled. In contrast, the types of specimens with a joint connection that has cross girders have sufficient toughness, as shown in **Figure 7**.

Figure 8 illustrates the cracking conditions observed for each type of specimen. Type-A specimen with the joint connection having cross girders outside the concrete mostly suffered from transverse tension cracks in the pier concrete. In the final stage of the loading test, diagonal shear cracks occurred in the joint concrete.

Type-B specimen with a joint connection that has cross girders buried in the concrete had many transverse tension cracks in the pier concrete and also some cracks in the joint concrete in the initial stage of the loading test. Later, as the load was increased, cracks in the joint concrete developed and ultimately caused the parts near the boundary between it and the steel girder to flake off.

Type-C specimen with a joint connection that had no cross girder was not inferior to the other types of specimens in the monotonous loading test. However, in the alternate loading test, Type-C specimen had cracks that developed diagonally from the boundary between the joint concrete and the stiffeners with the concrete. These cracks led to failure. This fracture seemed to be shear failure that was caused by the difference in shear strength between the concrete in the region where it was surrounded by steel cross girders and the concrete in the region where it was not surrounded. The comparison of the Type-C specimen with the Type-A specimen suggested that the cross girders functioned as shear reinforcement and improved the load bearing strength and durability of the structure.

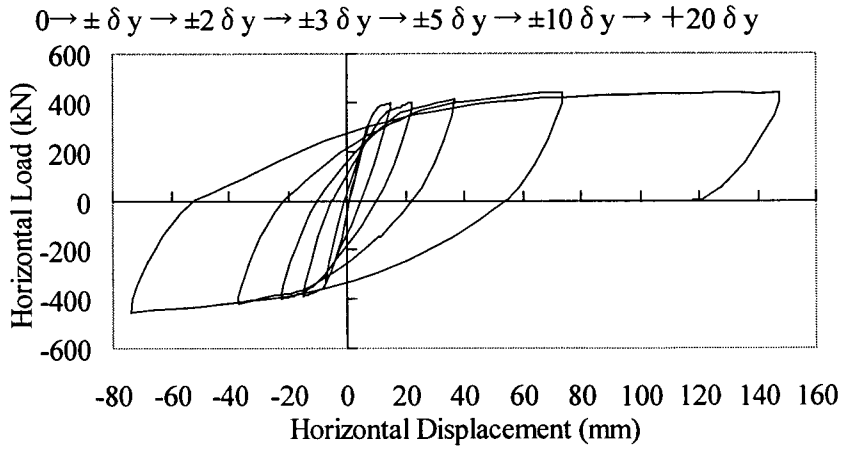

Figure 7. Load-displacement Hysteresis Curve (Type-A)

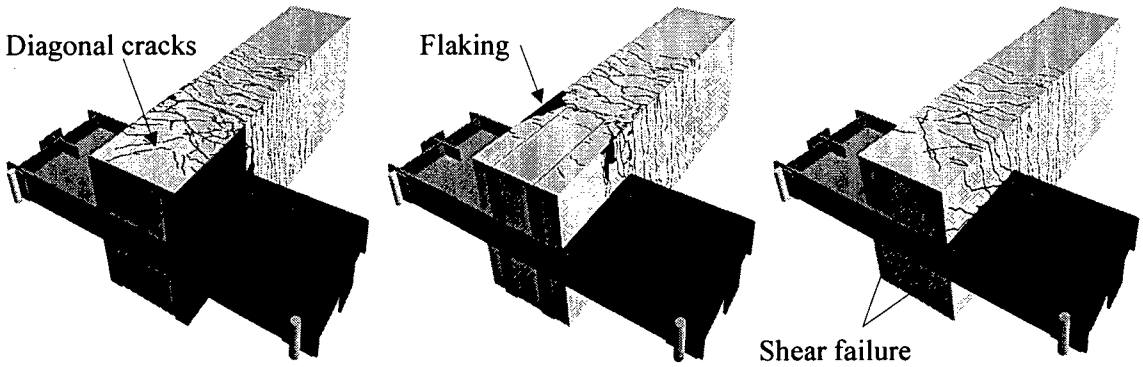

(a) Type-A (b) Type-B (c) Type-C

Figure 8. Cracks in Each Type of Specimen

2.2 Outline of FEM Analysis

2.2.1 Analytical Model

To verify the test results, FEM analysis was conducted with two 1/2 models of Type-A and Type-B that were symmetric with respect to the plane of symmetry that passed through the center- line of the web of the main girder (**Figure 9**).

Material elements examined in the analytical model were the shell element for steel plates, the truss element for reinforcements, and the solid element in the concrete. As material properties of the elements, the property values in **Table 1** were used for steel members, and the nonlinear stress-strain relationship based on the compression test was used for concrete. Moreover, each steel member was assumed to be an elasto-plastic material adopting von Mises' yield criteria, whereas an isotropic material by the Mohr-Coulomb rule was applied to concrete.

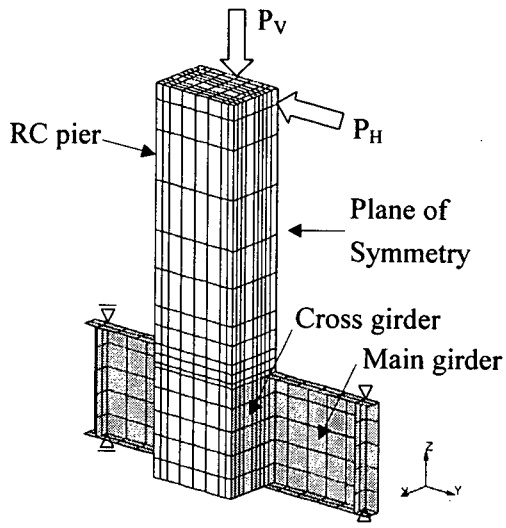

Figure 9. Analytical Model (Type-A)

2.2.2 Results and Discussion of the Analysis

The systematic description of the FEM analysis here is concerned only with the types of specimens that had joint connections with cross girders and that produced a favorable result in the loading test.

The relationship between the horizontal load and the horizontal displacement at the loading point is given in **Figure 10**.

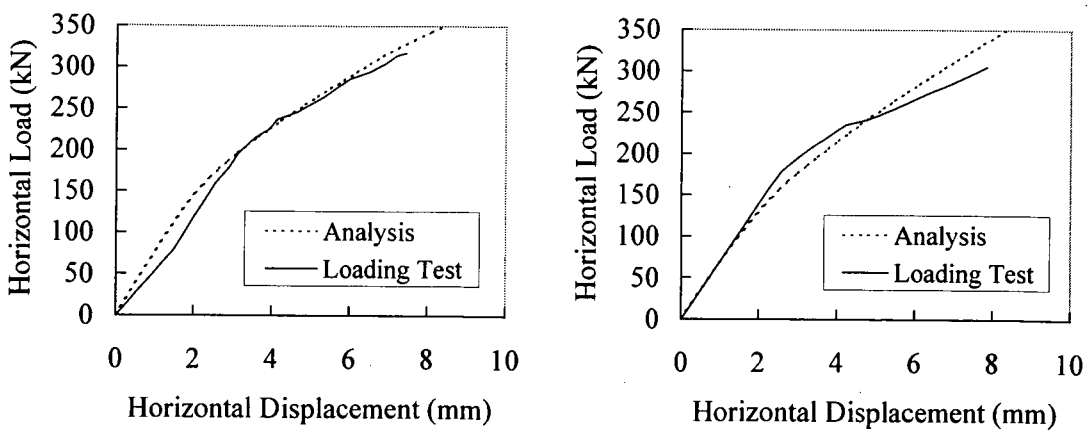

(a) Type-A (b) Type-B

Figure 10. Load-Displacement Relationship for Each Type of Specimen

The full-line in the figures is from the monotonous test results. The test and analysis results of the Type-A specimen are in good agreement with each other. In contrast, Type-B specimen that had joint connection with cross girders buried in the concrete had decreased rigidity at the horizontal load by about 250 kN or more. As shown in **Figure 8**, cracks that occurred in the joint concrete led to sectional damage that lowered the rigidity.

Next, the strain property was observed. To understand the concrete damage situations in the test, **Figure 11** gives the contour of principal tensile strain. In loading, differences in properties between the two types of specimens according to the difference in cross-girder arrangement was compared at the loading stage of 304 kN, which is almost equal to the yield load of Type-B specimen.

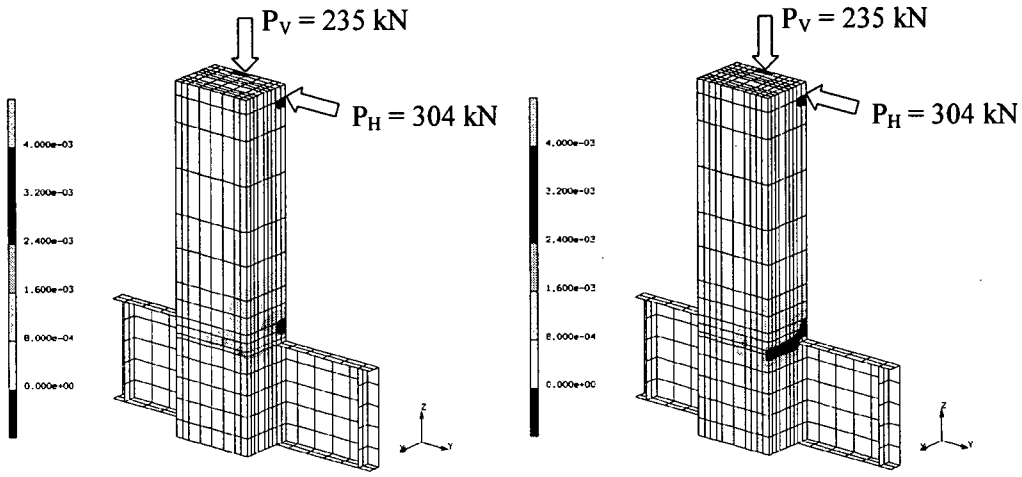

(a) Type-A (b) Type-B

Figure 11. Contour of Principal Tensile Strain

The Type-A specimen has a region of large tensile strain in the pier concrete near the steel girder, but has no significant strain in the joint connection. On the other hand, the pier of the Type-B specimen has a tensile strain similar to such strain in the corresponding part of Type-A specimen. But the joint concrete of Type-B has a region of large tensile strain that extends towards both the edge and the inside of the joint connection at the height of the flange of the steel girder. This agrees with the serious damage by cracks that the specimen had in the joint concrete.

2.3 Discussion

As a result of the test and FEM analysis that focused on the non-prestressed steel girder and RC pier joint connection, the following findings were acquired:

(1) Use of cross girders in the joint connection gives the structure of the section a sufficient load-bearing property.

(2) The structure that had the joint concrete sandwiched by cross girders maintained its flexural rigidity and controlled the serious damage to the concrete.

(3) From the fact that the joint concrete suffered shear failure or diagonal cracks and that the web of the steel main girder inside the joint connection had a distribution of diagonal strain, the joint connection might transfer stress through the mechanism of load-bearing in shear.

2.4 Proposal of Design Method

As observed in the test and analysis, stress transfer in the joint section of the composite rigid frame bridge is made through a shear resistance mechanism (**Figure 12**). To apply this to the case where such a load-bearing mechanism is formed, a method for evaluating the load-bearing strength as the shear strength has been shown in the design manual of steel-concrete sandwich structure [6]. Thus, a design method was proposed evaluating the ultimate load-bearing strength as the total strength made by adding the crushing strength of the joint concrete (a compression strut) to the yield strength in the shear of the web of the main girder (a tension tie).

$$V_{ud} = V_{ucd} + V_{usd} = 1.25\sqrt{f'_{cd}} \cdot b \cdot D + D \cdot t_w \cdot f_{syd} \cdot \frac{1}{\sqrt{3}} \text{(N)}$$

where:

V_{ud} : load-bearing strength of joint connection
V_{ucd} : shear strength of joint concrete
V_{usd} : yield strength of the web of the main girder
f'_{cd} : compressive strength of the concrete (N/mm^2)
b : effective thickness of the concrete (mm)
D : load-bearing breadth (mm)
t_w : thickness of the web of the main girder (mm)
f_{syd} : yield strength of the steel (N/mm^2)

Considering that this formula is adopted to the test result of Type-A, the shear strength is calculated as follows. In the calculation, the joint concrete of without flange plate region is neglected from the effective thickness (**Figure 13**).

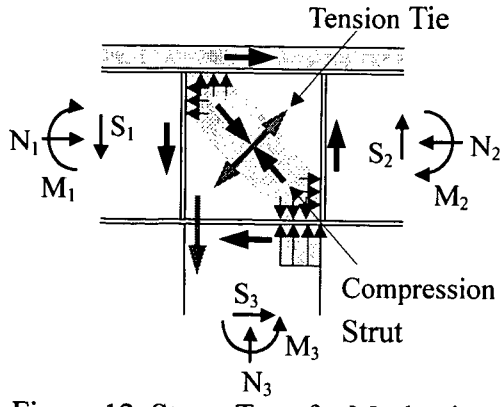

Figure 12. Stress Transfer Mechanism

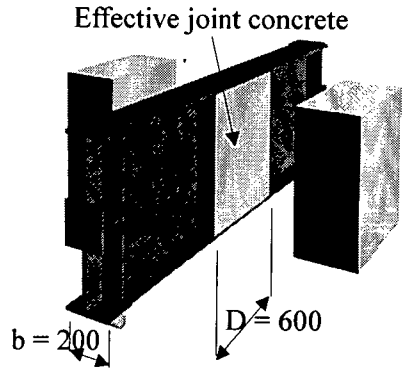

Figure 13. Effective region of Type-A

$$V_{ud} = V_{ucd} + V_{usd}$$
$$= 1.25\sqrt{31.0} \times 200 \times 600 + 600 \times 8 \times 298.7 \times \frac{1}{\sqrt{3}}$$
$$= 835165 + 827782 \text{ (N)}$$
$$= 1662.9 \text{ (kN)}$$

Then, in order to compare the shear strength with the test result, shear strength is converted to the ultimate horizontal load.

$$F_3 = \frac{M_1}{h} + \frac{M_2}{h} + \frac{N_2}{2}$$
$$F_3 = \frac{P_H \cdot H}{h} + \frac{P_H}{2}$$
$$P_H = \frac{F_3 \cdot h}{\left(H + \frac{h}{2}\right)}$$

F_3 = 1 662.9 (kN)
H = 2 050 (mm), h = 700 (mm)
P_H = 485.0 (kN)

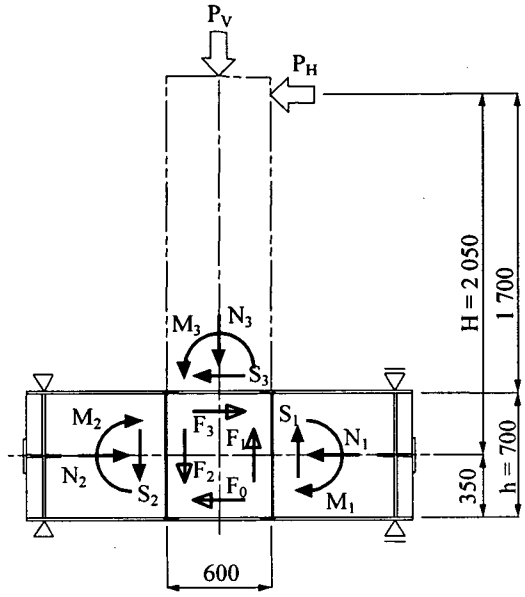

Figure 14. Sectional Forces of Joint Connection

The calculated ultimate shear strength (P_H = 485.0 kN) is similar to the maximum horizontal load of the test (Pmax = 440.3 kN). The fracture was caused in the pier concrete around the boundary between the pier and the steel girder. And the fatal damage did not occurred in the joint concrete. Therefore, this evaluation for shear strength of the joint connection is available to the design.

3. Application to Actual Bridges

3.1 Example in Actual Bridge Construction

Japan Highway Public Corporation constructed a composite rigid-frame bridge named the Asamigawa Bridge on the Joban Expressway used this design method [7]. **Figure 15** shows a general view of the Asamigawa Bridge.

The Asamigawa Bridge was so designed such that the strength of concrete is greater than the strength of steel. This is so that the strength of concrete can be maintained even after the steel web had yielded in the ultimate state. In the design calculation, moreover, the effective thickness of concrete equaled the width of the flange of the main girder. Therefore, when insufficient, the strength of concrete is to be made up for its

insufficiency by increasing the width of the flange. For this reason, the bridge is characterized as having its main girder with flanges widened toward the joint connection **(Figure 16)**.

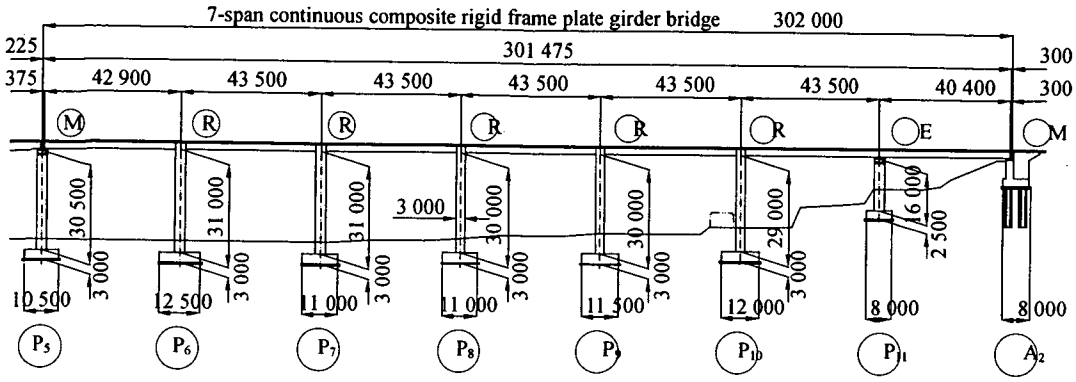

Figure 15. Asamigawa Bridge (General View)

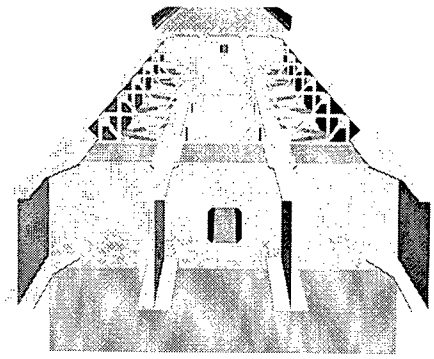

Figure 16. Structural Image of Joint Connection in the Asamigawa Bridge

The main girder was first erected on piers P6 and P10, which are at both ends of a series of piers, in the rigid-frame span of the bridge. The main girder was first fixed tentatively to a base laid on each of the two piers, and then, by casting concrete on it, the superstructure and the substructure were combined into one body. Then, after all of the girders had been erected, concrete was cast on the joint connections of piers P7 to P9. **Photos 1 and 2** show the erection of the main girder and the concrete-casting in the joint connection, respectively.

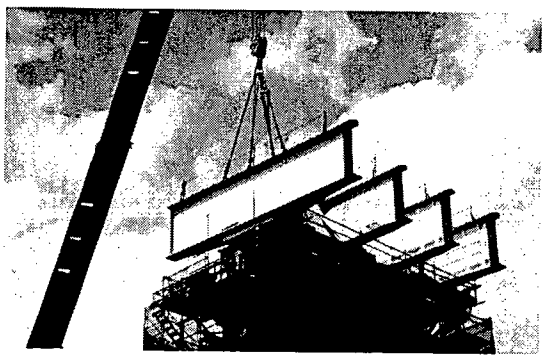

Photo 1. Erection of Main Girder

Photo 2. Concrete Casting

The joint connection should be filled with a sufficient quantity of concrete so that the load-bearing mechanism of the design method is effective. In the bridge, the section beneath the lower flange of the main girder was crowded with members for structural reasons. This crowding made it difficult to compact concrete there and, therefore, middle fluidity concrete was used to fill it. The bridge was successfully constructed thanks to studies on the arrangement of steel members, structural details for facilitating concrete filling from the design stage, and scrupulous field control such as the concrete casting test and the control of concrete quality and concrete work. **Photos 3 and 4** show the Asamigawa Bridge completed and the details of the joint connection, respectively.

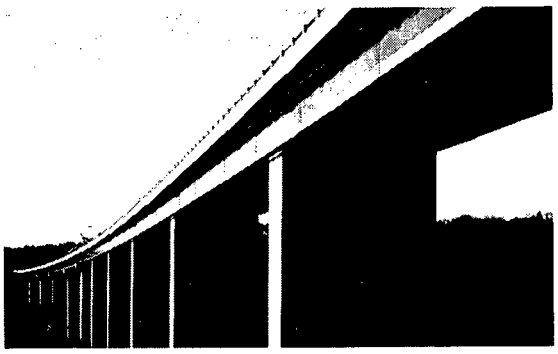

Photo 3. Complete View

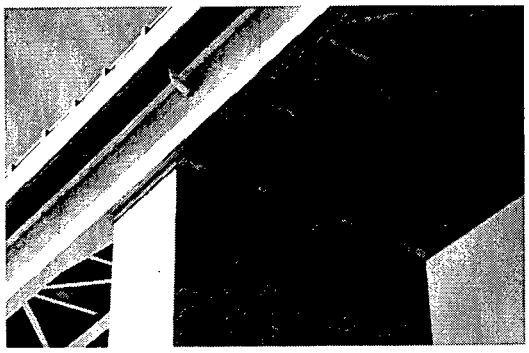

Photo 4. Joint Connection

3.2 Stress Measurement on Actual Bridge

To determine the structural behavior of the joint connection of the composite rigid frame bridge, the stress measurement was conducted not only the test specimens but also an actual bridge structure. The measurement was carried out when the casting of the slab concrete after the erection was completed, focusing on the P9 pier.

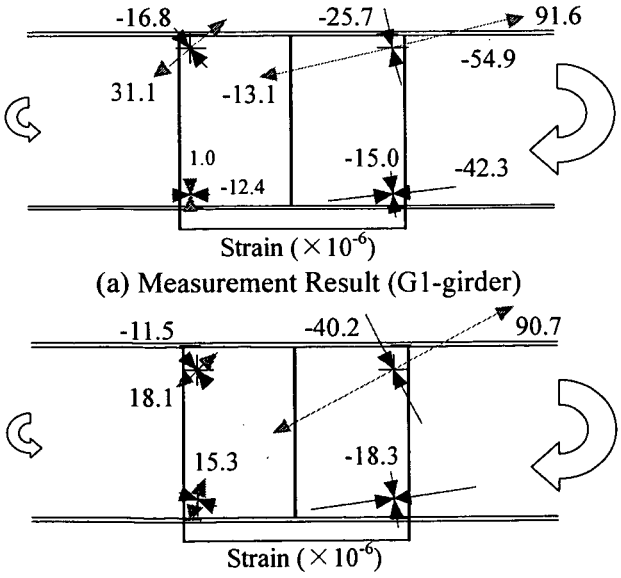

(a) Measurement Result (G1-girder)

(b) Analytical Result (G1-girder)

Figure 17. Principal Strain Distribution

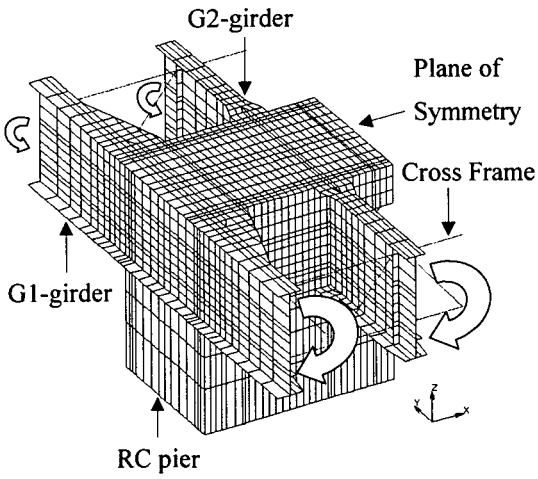

Figure 18. Analytical Model

As the representative result, the principal strain distribution of the web of the main girder is presented in **Figure 17**. And the analytical result to verify the measurement (**Figure 18**) is illustrated altogether. Also, from the analytical result, the principal strain contour is shown in **Figure 19**.

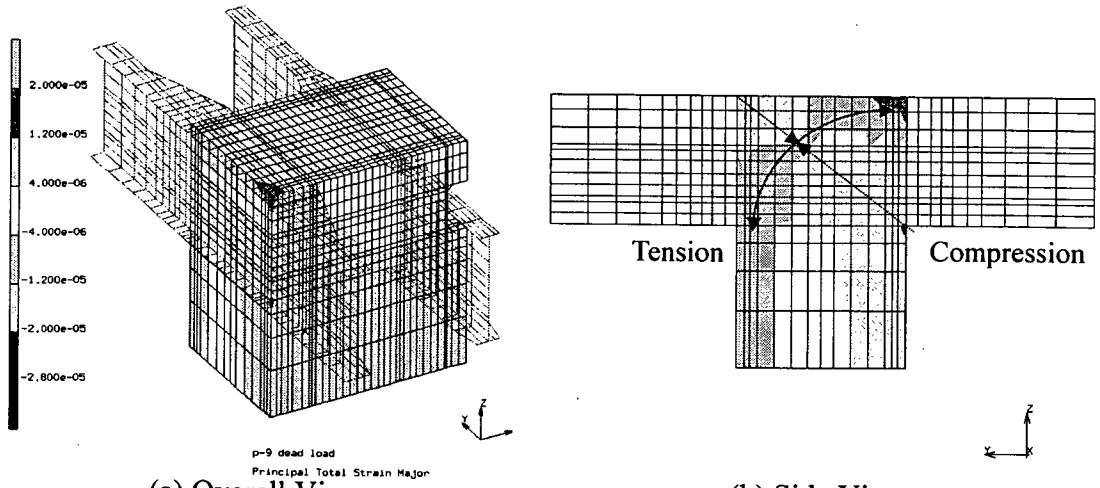

(a) Overall View (b) Side View

Figure 19. Principal Strain Contour of Concrete Elements

Results from the FEM analysis, forming a compression strut and a tension tie in the diagonal direction is confirmed. And then, the load-bearing mechanism of the analytical results is almost the same as the measurement results of the actual bridge.

4. Conclusions

Loading tests and FEM analysis were conducted to determine the stress transfer and load-bearing mechanisms in the joint connection of a composite rigid frame bridge that has steel girders and RC piers joined together rigidly. This study should make the load-bearing strength and durability of the joint connection structure more secure. In particular, structures that have cross girders placed outside the concrete were effective in preventing the joint concrete from being damaged. The applicability of this structure to actual bridges was confirmed. Moreover, based on the findings on the load-bearing mechanism acquired by this study, a new design method in which the strength of the joint connection was evaluated as its shear strength was discussed and proposed.

The design method based on the result of the study was applied to an actual bridge, the Asamigawa Bridge on the Joban Expressway. The design method, however, still contains matters that should be examined anew in terms of cost-effectiveness; for example, the treatment of design sectional force and the evaluation of the effective thickness of concrete. The effective thickness needs to be evaluated in reference to the structure involved with cross girders. From the concrete work on site, it was learned that the quality and work control played an important part in satisfying the performance and functional requirements of the joint connections.

Further studies are planed to continue with the aim of establishing a more reasonable method for designing the joint connection by reevaluating its load-bearing strength and findings the structures that make erection work easier and more efficient. Also preparation of a construction manual is planed to use this type of construction for bridges. The authors hope the results of this research, design, and construction will be able to help the future development of composite structures.

Acknowledgments

The authors are deeply grateful to Professor Atsuhiko Machida of Saitama University for his frequent and instructive comments and advice on various subjects that ranged from the test and FEM analysis plans to the design and construction of the Asamigawa Bridge.

References

1) Ogawa, A. and Terada, N. : Composite Bridges in J.H., Bridge and Foundation Engineering, Vol. 31, No. 8, pp. 48 – 55, 1997 (in Japanese)

2) Japan Highway Public Corporation : Design Manual No. 2, Chapter 9 Composite Structure, 1998 (in Japanese)

3) Shito, K. and Nagae, S. : Composite Structure of Steel and Concrete (Yamagata Expressway Akoya Bridge), JH Engineering Journal, No. 111, pp. 23 – 29, Japan Highway Public Corporation , 1992 (in Japanese)

4) Sato, T., Shimizu, I., Ota, T., and Machida, A. : A Proposal on Design Method for Rigid Section of Hybrid Rigid Frame Bridge, Journal of Structural Engineering, Vol. 45A, pp. 1431 – 1438, 1999 (in Japanese)

5) Nagatani, T., Igase, Y., Shito, K., Shimizu, I. and Sato, T. : Experimental Study on Mechanisms of Stress Transfer and Ultimate Strength for Joint Section Between Steel Girder and Reinforced Concrete Pier, Journal of Structural Engineering, Vol. 46A, pp. 1491 – 1500, 2000 (in Japanese)

6) Japan Society of Civil Engineers : Recommendation for Design of Steel-concrete Sandwich Structure (Draft), Concrete Library 73, 1992 (in Japanese)

7) Nishikawa, K., Watanabe, F., Machida, A., Yamashita, H. and Sato, T. : Structural Design for Rigid Connection of Hybrid Rigid Frame Bridge by Strut-and-Tie Theory (Joban Expressway Asamigawa Bridge), Proceedings of the 56th JSCE Annual Meeting, I – A213, pp. 426 – 427, Japan Society of Civil Engineers, 2001 (in Japanese)

Aerodynamic stability of a suspension bridge with open grating deck

Katsuya Ogihara[1], Naoki Wada[1], Shinji Takamori[2]

Abstract

Aerodynamic stability is always required in the design of a long-span suspension bridge. A stiffening girder using an open grating deck is expected to make a suspension bridge light and to give it enough aerodynamic stability. Spring-supported model wind tunnel tests and aeroerastic full model wind tunnel tests were conducted in the study of a 540-meter single spanned suspension bridge with the open grating deck carrying two traffic lanes and a one side pedestrian track. In this paper, the results of the wind tunnel tests for the suspension bridge with the open grating deck are described.

Introduction

Aerodynamic stability is one of the most important themes to design a suspension bridge. In order to make a suspension bridge economical, not only reducing the weight of it but also enough aerodynamic stability is necessary. An open grating deck applied to a part of the stiffening girder of a suspension bridge is expected to have enough aerodynamic stability as well as a possibility to make it lighter than ever.

Hiroshima Prefecture and Hiroshima Prefectural Road Corporation are planning a 540-meter single spanned suspension bridge carrying two traffic lanes and a pedestrian track. A general view of the bridge is shown in Fig. 1. A series of studies of the bridge with the open grating deck were carried out. They were aerodynamic stability study, structural durability study, vehicles safety study and others. This paper reports the aerodynamic stability study for the suspension bridge.

Open gratings were applied to all of the two-traffic-lane floor deck, however a one side pedestrian track is still a conventional steel deck. Main girders of the bridge are two box girders placed just under main cables connected with hanger ropes, and cross girders connect both main girders and support the open grating deck. The stiffening girder with the open grating deck is shown in Fig. 2. Each open grating consists of two parts, surface grids and girders. The surface grids are required to have enough surface friction between vehicles and grid surface. The girders support the weight of vehicles and the grids. A structure of the open grating is shown in Fig. 3.

---

1) Construction Division, Hiroshima Prefectural Road Corporation
2) Road Improvement Division, Hiroshima Prefecture

Wind tunnel tests

Spring-supported model tests and aeroerastic full model tests were conducted. Spring-supported model tests were conducted in order to seek the most aerodynamically stable cross section of the stiffening girder with the open grating deck basically. As the stiffness of the girder with the open grating deck is lower than that of an ordinary box-shaped stiffening girder, aeroerastic full model tests were conducted carefully.

Spring-supported model tests

By the two-year wind observation at the site, wind angle of attack for the girder is expected between −5 degrees and +5 degrees. The spring-supported model tests were conducted to cover this range of wind angle of attack. The model scale is 1/35. Length of the spring-supported model is 1.8 meters. The spring-supported model is shown in Fig. 4. Vibration modes simulated by the tests are first symmetric bending mode and first symmetric torsional mode. A series of wind tunnel tests, changing the shapes of the both edge girders, were conducted to seek an effective edge shape. From the first test results, all edge shapes tested do not have enough aerodynamic stability. After the first series of tests, next series of tests were carried out. A trapezoid-shaped edge of the girder was used as a base shape. From the test results, guide vanes set over and under the girders improve the aerodynamic stability. The cross section of the girder selected by the spring-supported model tests is shown in Fig. 5. The response of the selected girder with the open grating deck is shown in Fig. 6.

Other investigations were carried out by the tests. The results are described below.

- Smaller size of the mesh, which is a model of the open grating, makes the amplitude of the vortex-induced oscillation smaller very gradually.
- There is small difference in the amplitude of the vortex-induced oscillation between the models using wire net and the models using grids made of rectangular bars.
- Influence of Reynolds number for the box girder with the trapezoid-shaped edge is so small to neglect.
- Larger solidity factor of the open grating makes the amplitude of the vortex-induced oscillation at 0 degree wind angle of attack smaller gradually (Fig. 7).

Aerostatic force measurements

Aerostatic forces, which are drag, lift and moment, were measured. According to the results of the measurements, direction of the wind, north wind or south wind, makes difference in forces. As the bridge carries two traffic lanes and only a one side pedestrian

track, the section of the girder is not symmetrical. This asymmetrical cross section is supposed to be the reason of the difference. The coefficients of aerostatic forces are shown in Fig. 8. The coefficient of drag and the coefficient of moment are larger than zero in the case of north wind, blowing from the pedestrian track side under the condition of 0 degree wind angle of attack. In spite of that, the coefficients of them are almost zero in the case of south wind, blowing from the traffic lane side. The coefficient of drag is 1.22 −1.23 under the same condition.

Airflow direction and velocity measurements around the girder

It is supposed that severe airflow through the open grating may influence vehicles on the bridge. Airflow directions and velocities around the girder were measured. As a result of the measure, severe airflow upward and downward through the open grating were not observed (Fig 9).

Aeroerastic full model tests

Aeroerastic full model tests were conducted using the most aerodynamically stable girder section selected by the spring-supported model tests. Three-dimensional effect of airflow and the vibration mode couplings are expected to reduce the amplitude of the vortex-induced oscillations in this test. As the bridge is a single spanned suspension bridge, the center span of the bridge was set in the wind tunnel. Main towers of the model were made as a rigid model, and stiffness of towers and cables were replaced as springs by similarity law. The model scale is 1/75. Wind angles of attack tested in the wind tunnel were between +3 degrees and −3 degrees. An aeroerastic full model is shown in Fig. 10. Vibration modes simulated by the model were one horizontal bending mode, seven vertical bending modes and seven torsional modes. Vertical bending modes simulated were four symmetrical modes and three asymmetrical modes. Torsional modes simulated were four symmetrical modes and three asymmetrical modes. The response by the aeroerastic full model tests is shown in Fig. 11. The effect of the logarithmic decrement is shown in Fig. 12.

The test results are described below.

- Any flutter was not observed.
- Vortex-induced oscillations in bending mode were observed at the wind velocity lower than 15 m/s in smooth flow.
- Vertex-induced oscillations in torsional higher mode were observed at the wind velocity higher than 15 m/s in smooth flow.
- The amplitudes of the oscillations of the tests were as large as those of the spring-supported model tests.
- Strong turbulent flow made the amplitudes of the oscillations smaller.

  Turbulent flow expected at the site is only five percent turbulence intensity. Five

percent turbulence intensity is not enough to make the amplitude small. Ten percents turbulence intensity is necessary.

- Additional damping makes the amplitude of the vortex-induced vibration smaller.
  0.02 of logarithmic decrement, usually expected as structural damping, is not high enough to make the amplitude small. 0.04 is necessary.

Conclusions

In order to plan a 540m single spanned suspension bridge economical, cost-effective open grating deck, which was expected to have enough aerodynamic stability, for the stiffening girder was investigated by the wind tunnel tests. The most aerodynamically stable section of the stiffening girder was selected by the spring-supported model tests. Next to the spring-supported model tests, the aeroerastic full model tests using the selected cross section were carried out.

From all of the test results, conclusions are described below.

- Any dangerous flutter was not observed. The bridge has basically enough flutter stability.
- The bridge with the open grating deck is not able to reduce the amplitude of the vortex-induced oscillation. Especially the vortex-induced oscillation in torsional mode is severe.
- The open grating deck is not the most effective stiffening girder for a 540m single spanned suspension bridge carrying two traffic lanes and a pedestrian track.
  Some damping device, such as TMD, is required for the bridge to reduce the amplitude of the vortex-induced oscillation.
- Reynolds number and the modeling materials and methods of the open grating deck changed the amplitude of vortex-induced oscillation very small.
- As a suspension bridge with the open grating deck does not have high stiffness and have lower frequency, many vibration mode vortex induced oscillations should be expected and examined carefully at the wind tunnel test.

References

1) Watanabe H., et al.: Section model wind tunnel test of a open grating deck –Toyoshima Bridge (Tentative), Proceedings of the 55th JSCE Annual Meetings, September 2000. (in Japanese)
2) Watanabe H., et al.: Study on Aerodynamic Stability of a Suspension Bridge with Open Grating Deck –(Tentative) Toyoshima Bridge-, Proceedings of 16th Wind Engineering Symposium, pp. 333-338, November 2000. (in Japanese)
3) Watanabe H. et al.: Full model wind tunnel test of a suspension bridge with open grating deck, Proceedings of the 56th JSCE Annual Meetings, I-B365, October 2001. (in Japanese)

unit:mm

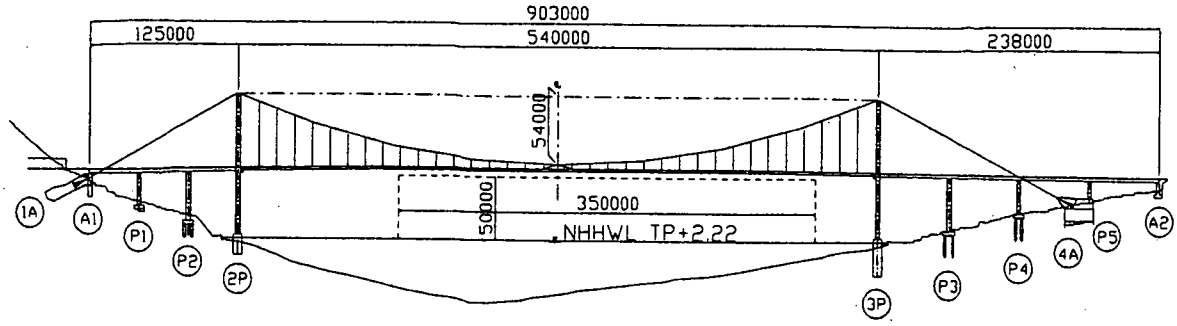

Fig. 1 General View of Model Bridge with Open Grating Deck

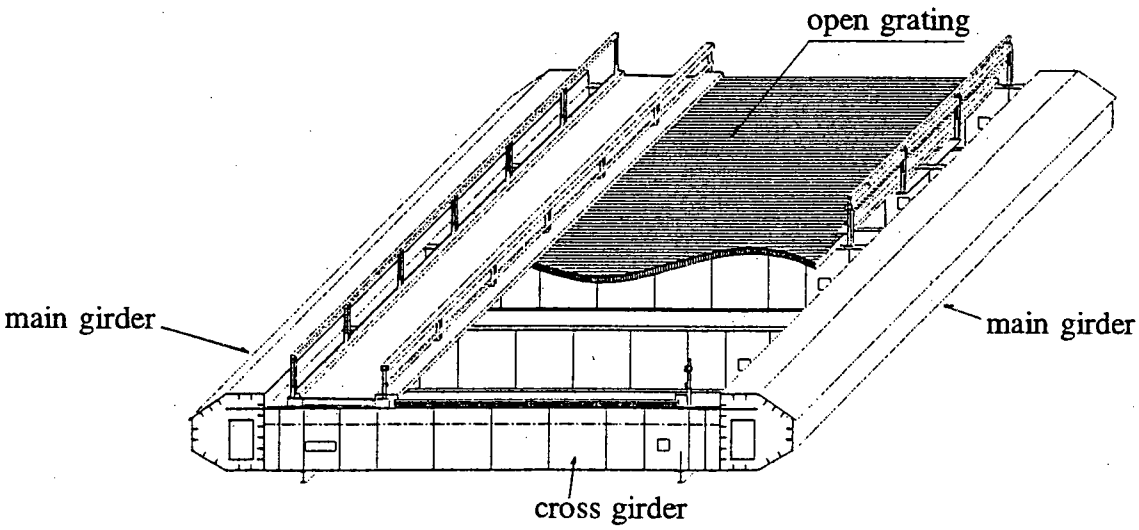

Fig. 2 Stiffening Girder with Open Grating Deck

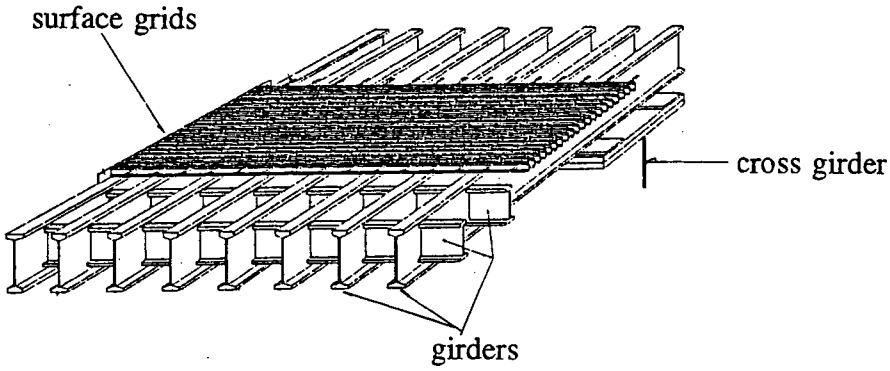

Fig. 3 Structure of Open Grating

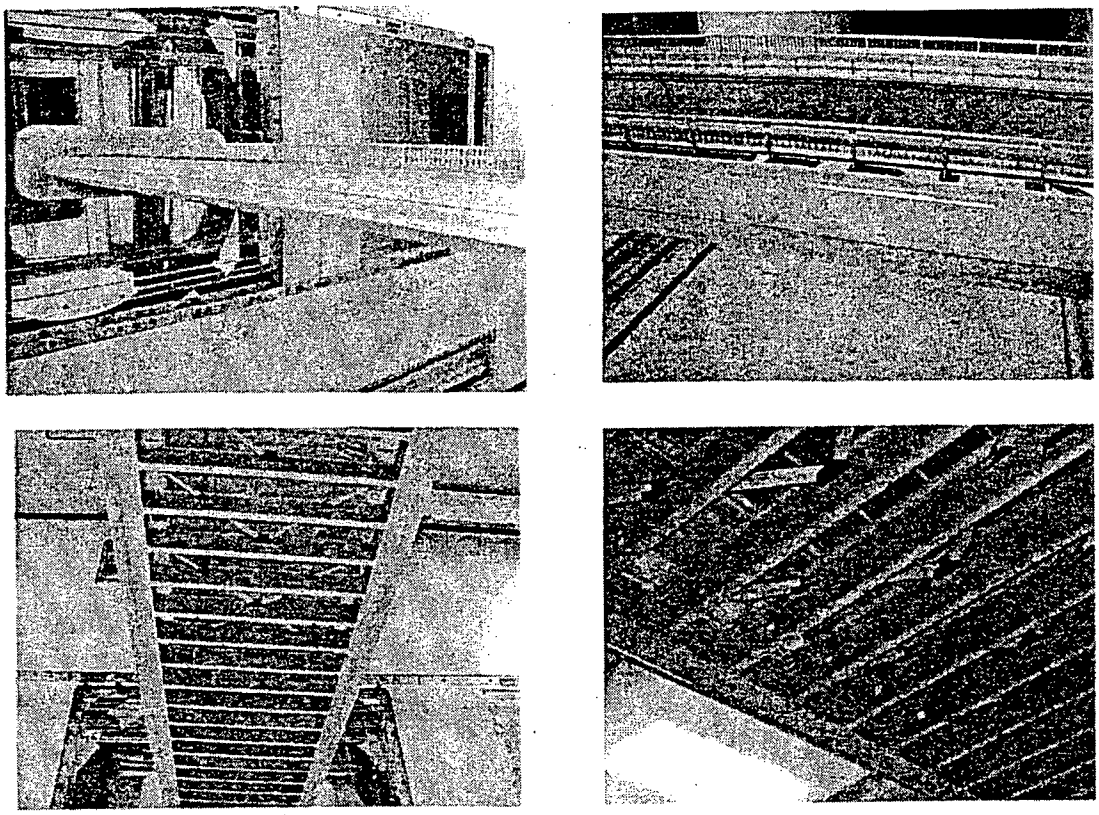

Fig. 4 Spring-Supported Model

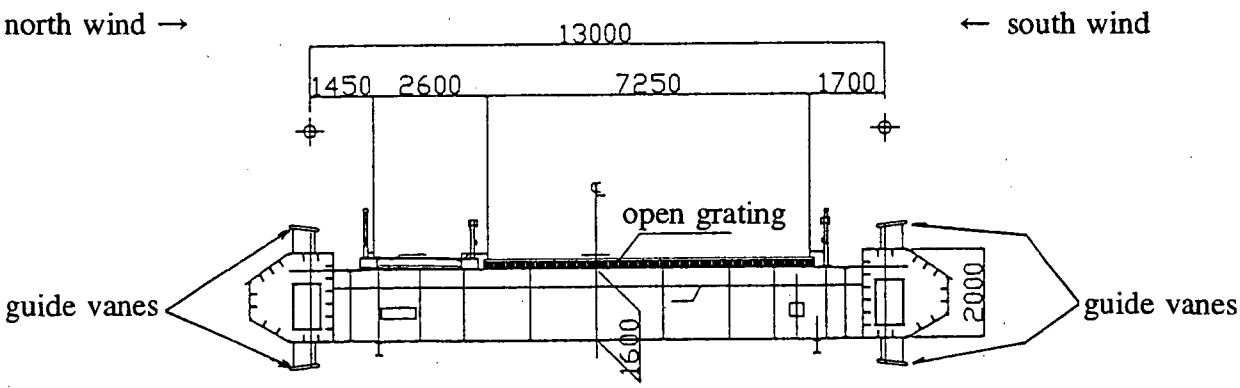

Fig. 5 Selected Cross Section by Spring-Supported Model Test

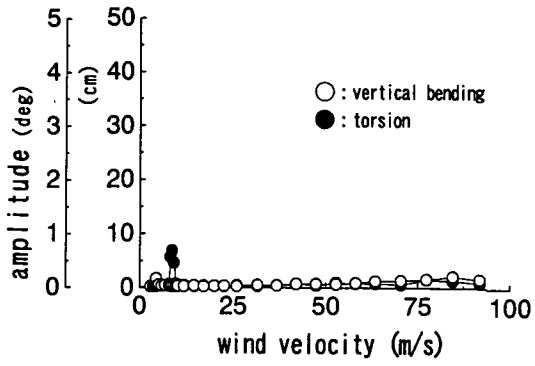

(a) north wind , angle of attack : 0 degree

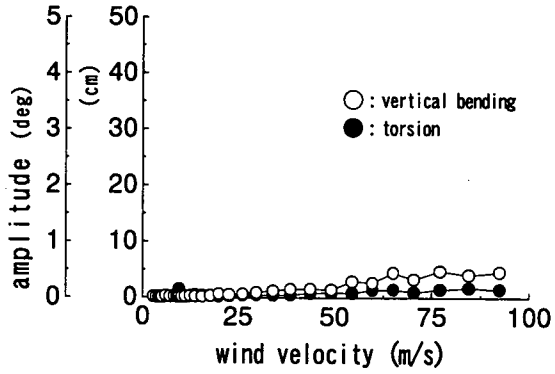

(b) south wind , angle of attack : +5 degrees

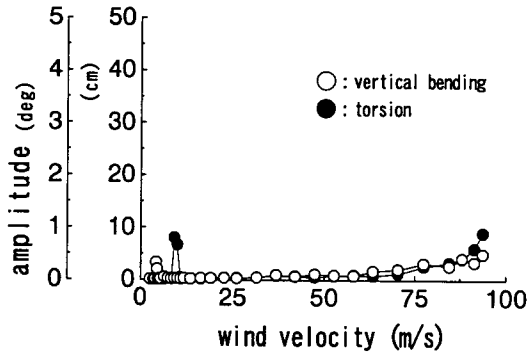

(c) south wind , angle of attack : 0 degree

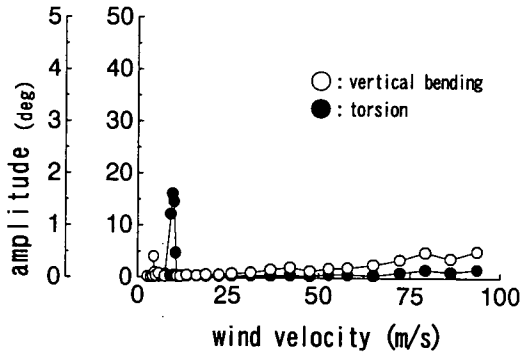

(d) south wind , angle of attack : -5 degrees

Fig.6 Response of Selected Girder with Open Grating Deck

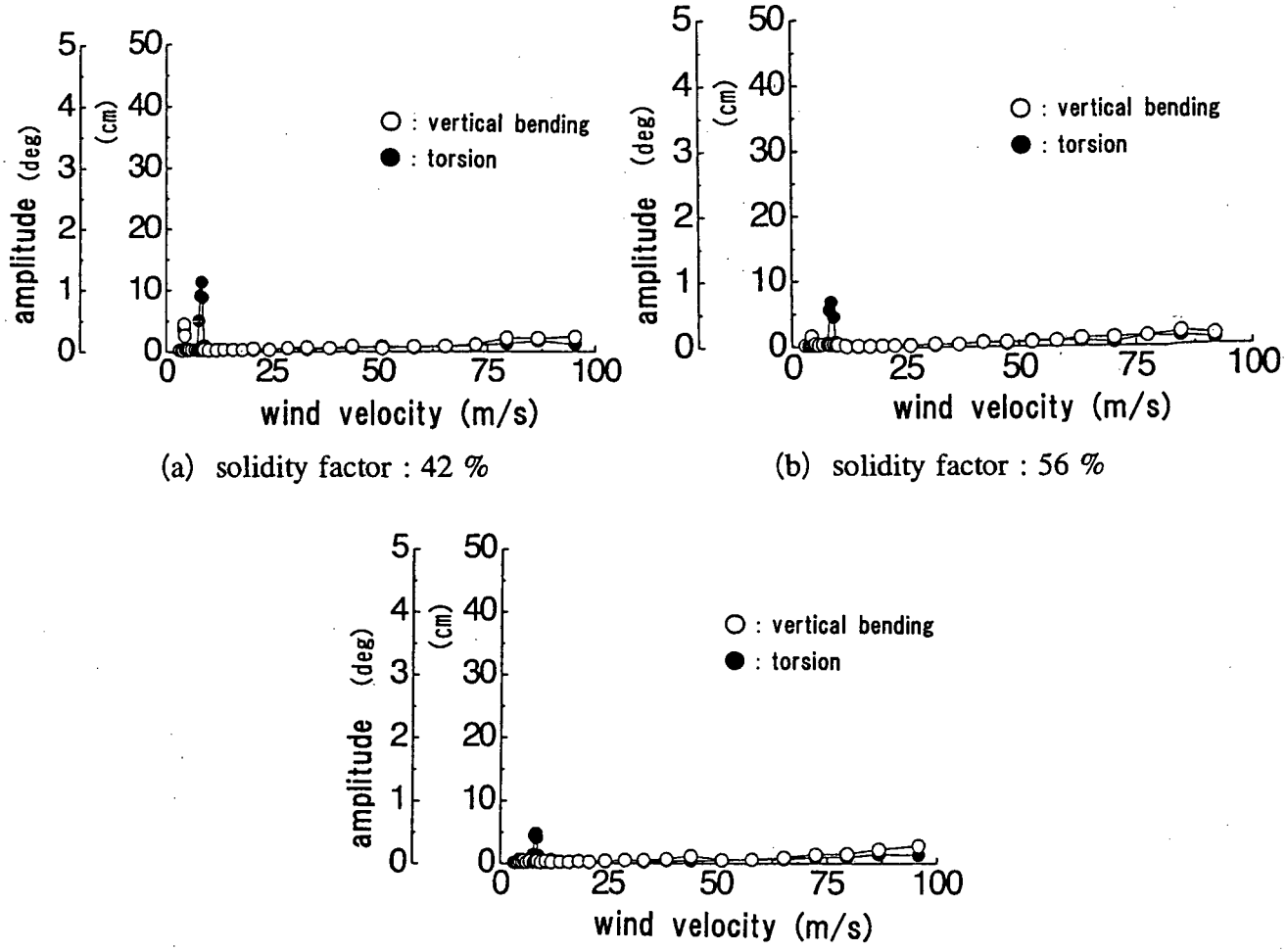

(a) solidity factor : 42 %

(b) solidity factor : 56 %

(c) solidity factor : 67 %

Fig. 7 Fffect of Solidity Factor on Response Amplitude

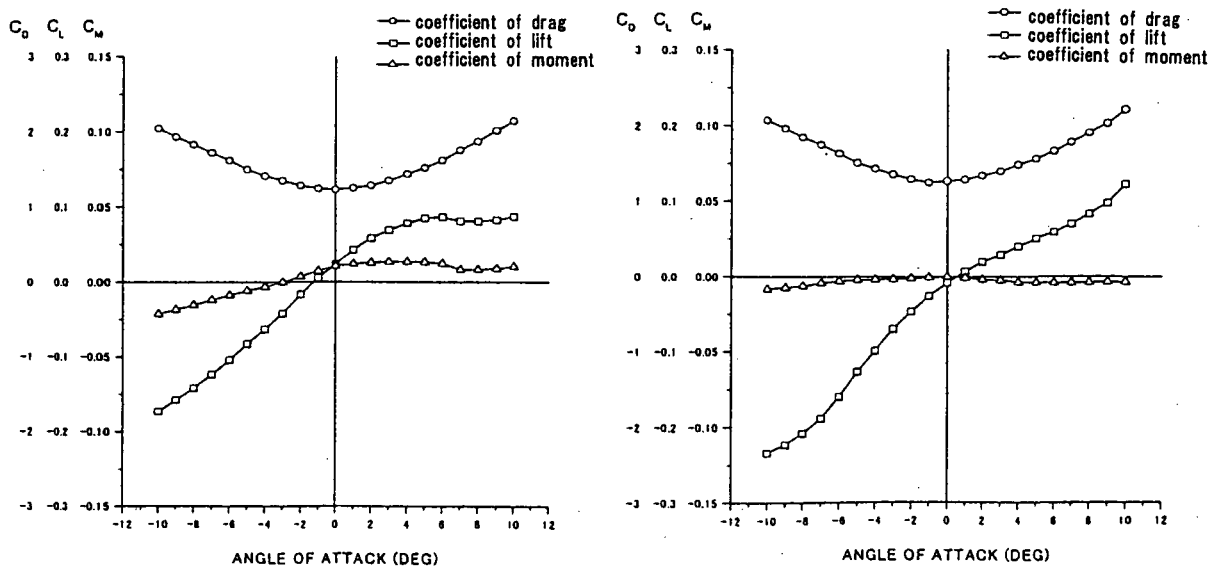

(a) north wind

(b) south wind

Fig. 8 Coefficients of Aerostatic Forces

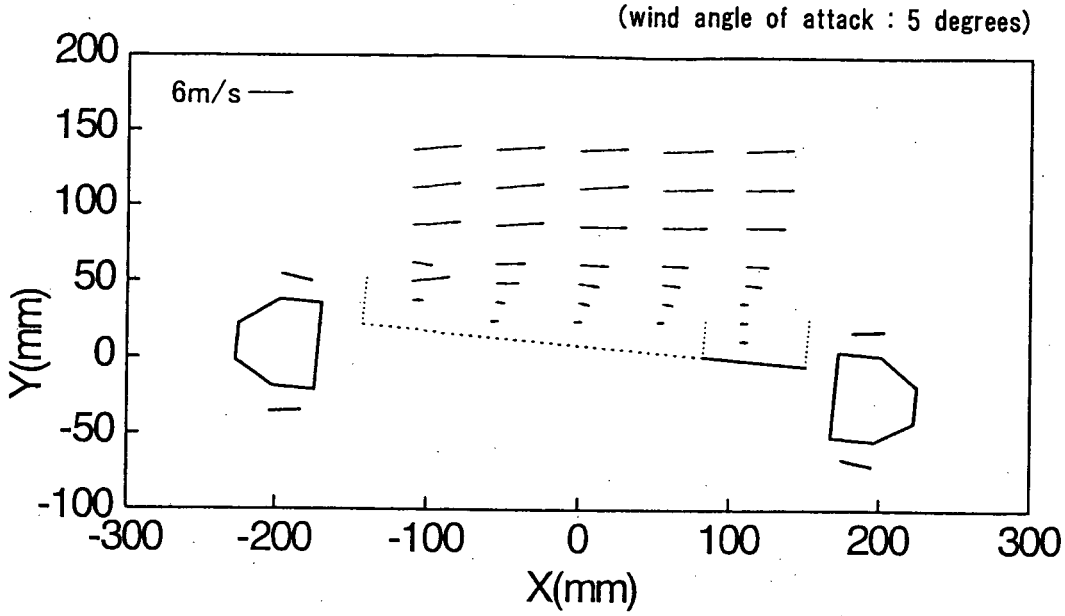

Fig. 9 Airflow Direction and Velocity around Stiffening Girder

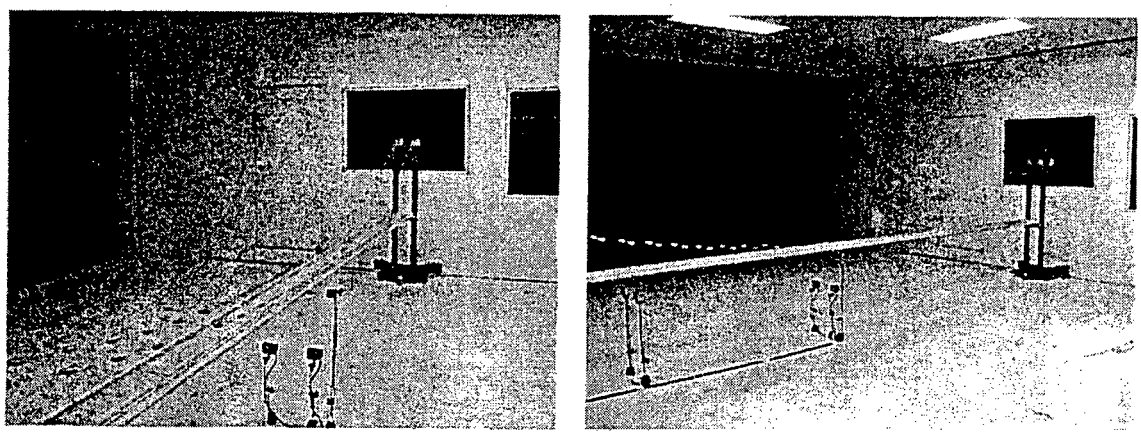

Fig. 10 Full Model

(wind angle of attack : 0 degree)

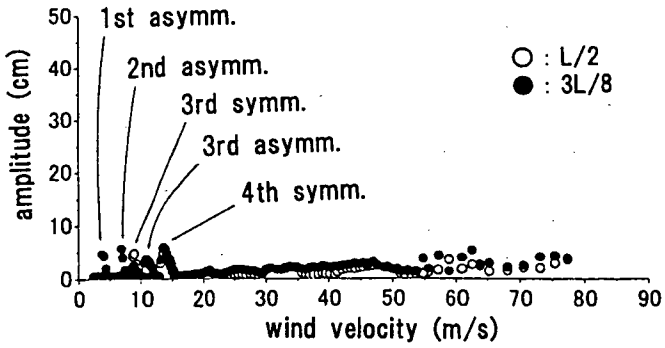

(a) bending mode, in smooth flow

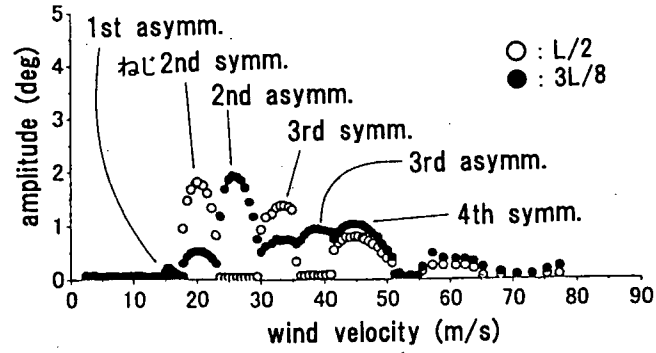

(b) torsional mode, in smooth flow

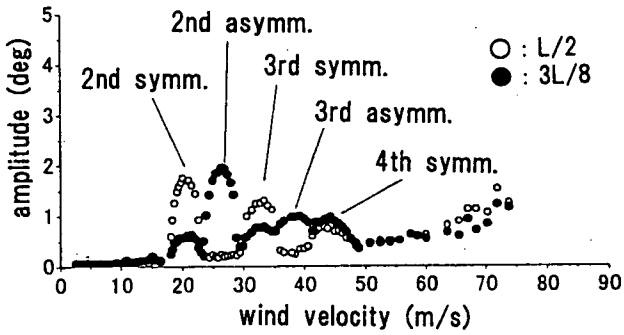

(c) torsional mode, in 5% turbulent flow

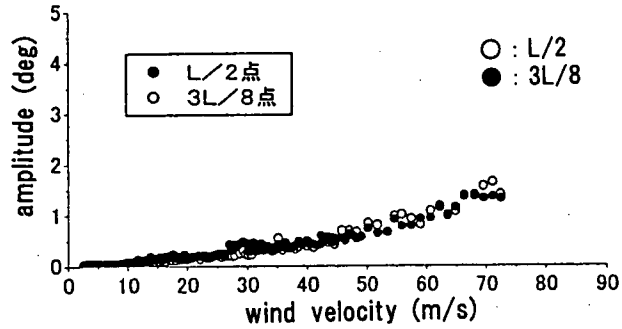

(d) torsional mode, in 10% turbulent flow

Fig. 11 Response by Full Model Test

(wind angle of attack : 0 degree)

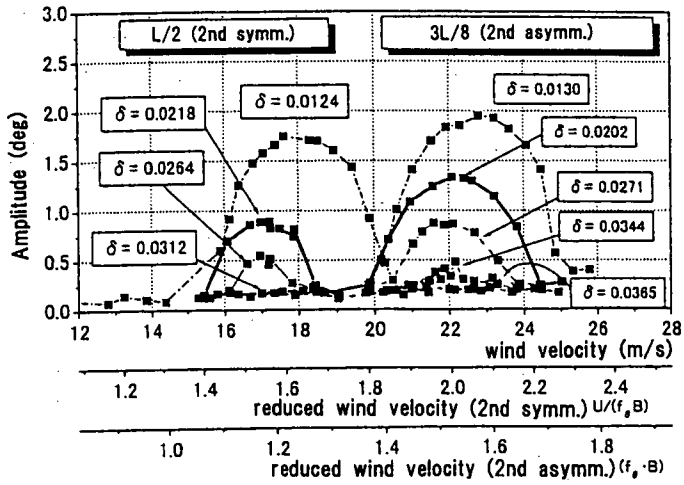

Fig. 12Effect of Logarithmic Decrement on Response Amplitude

Behavior of Prestressed Concrete Beam with New Type of Artificial Lightweight Aggregates made from Fly Ash

Michihiro Sakurada[1], Hiroyoshi Watanabe[2], Takash Ohura[3], Motoyuki Suzuki[4]

Abstract

A new type of artificial lightweight aggregates made from fly ash has been developed recently in Japan. As the fly ash is one of industrial wastes discharged from thermal power stations significantly, the use of these aggregates means the reuse of industrial wastes. Also these new aggregates have excellent properties such as, light weight, high strength and low water absorption, therefore, it is possible to lighten the concrete structures and make them durable against freezing and thawing. In order to study the application of the aggregates to prestressed concrete bridges, the authors carried out bending tests, shearing tests and measurement of stress of the prestressing strand on prestressed concrete beams with these new aggregates. The results show that the new type aggregates made from fly ash can be applied to prestressed concrete beams.

1. Introduction

In Japan, the amount of coal burned at thermal power stations tends to increase every year, because the resources of coal are abundant and price of coal is low. According to the increase of coal fired at power stations, the amount of coal ash will increase from 6 million tons at 3 years ago to 10 million tons at the beginning of the 21st century [1)]. The 60% of coal ash is utilized effectively as materials of cement, concrete, bottoming for pavement and so on, but the rest of coal ash, approximately 2million tons, is discarded uselessly. Therefore, there is a strong demand to make use of the coal ash further.

A new type of artificial lightweight aggregates made from fly ash, hereinafter called FAA, has been developed recently in Japan[1),2)]. The main raw material of FAA is fly ash which accounts for 85% of the coal ash. The FAA has some excellent characteristics which are high strength and low water absorption as compared with the conventional lightweight aggregate. The application of FAA to the prestressed concrete, hereinafter called PC, structure enables the following.

- The industrial waste, fly ash, can be utilized effectively.
- The concrete structure can be lightened by 10% to 20%.
- The aseismicity of the concrete structure can be improved.
- Resistance to freezing and thawing can be improved as compared with the concrete with conventional lightweight aggregate.

However, since the tensile strength, bond strength and Young's modulus of the lightweight concrete has been regarded lower, it is necessary to confirm the behavior of the PC beam with FAA. Therefore, the authors carried out the bending test, the shear test and the stress measurement of the prestressing strands in the PC beams, and the application of FAA to the PC beam was

1. Senior Engineer, P.S. Corporation, Tokyo, Japan
2. Chief Engineer, P.S. Corporation, Tokyo, Japan
3. General Manager, P.S. Corporation, Tokyo, Japan
4. Professor, Tohoku University, Sendai, Japan

studied. In this report, the test results are mentioned.

2. Properties of the new type of lightweight aggregates, FAA

Table 1 shows the properties of FAA in this study. The two kinds of FAA have the lowest water absorption of all aggregates made from fly ash, therefore, the concrete with these FAA has high strength, high resistance to frozen and thawing, and high facility of pumping as compared with the concrete with conventional lightweight aggregate which has high water absorption. Photo.1 and Photo.2 show the appearances of the two kinds of FAA, and the features are as follows.

Table 1 Properties of the FAA

			FAA-M (UL)	FAA-H (TL)	Natural Stone (N)
Properties of aggregate	Absolute dry density	g/cm^3	1.30	1.81	2.80
	Water absorption ratio	%	0.81	2.23	0.72
	Type of air space	–	Independent	Non air space	–
	Main raw material	–	Fly Ash	Fly Ash	Gravel
Properties of concrete	Unit Weight	kg/l	1.85	2.05	2.35
	Compressive strength*	MPa	70	100	100
	Tensile strength**	MPa	2.8	3.1	3.1
	Young modulus**	GPa	23	26	33
	Frozen and thawing	–	Durable	Durable	Durable

* Maximum values, ** At the compressive strength is 50MPa

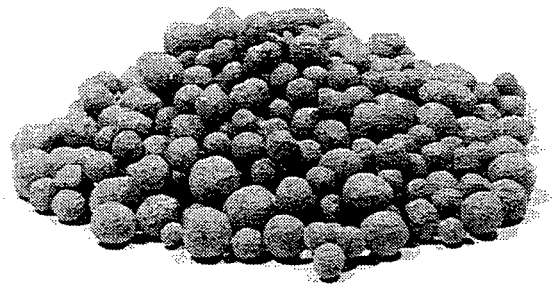

Photo.1 FAA-M (UL)

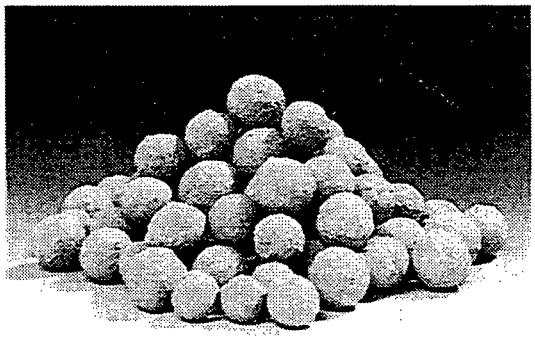

Photo.2 FAA-H (TL)

(1) FAA-M

FAA-M, hereinafter called UL, is made from fly ash. The absolute dry density and the water absorption ratio are $1.30g/cm^3$ and 0.81% respectively. The density is classed M in Japanese specification. The water absorption ratio is equal to the natural aggregate because the air space in the UL is independent. The unit weight of the concrete is 1.85kg/l, and the concrete with UL can be lightened approximately 20% as compared with the ordinary concrete with natural aggregate. Therefore, the UL is expected to be utilized in the concrete bridge with long span, the concrete bridge above the soft ground, the concrete bridge needing aseismicity and so on.

(2) FAA-H

FAA-H, hereinafter called TL, is also made from fly ash. The absolute dry density and the water absorption ratio are 1.81g/cm^3 and 2.23% respectively. The density is classed H in Japanese specification. The water absorption ratio is as low as the natural aggregate because the TL is made without sparkling. The unit weight of the concrete is 2.05kg/l, and the concrete with TL can be lightened approximately 13%. The compressive strength of the concrete with TL is equal to that of the concrete with natural aggregate, therefore, the TL is expected to be used as a substitute of the natural aggregate which is getting to dry up in Japan.

3. Experimental Program

3.1 Bending Test (Series 1)

(1) Objective

Bending test was carried out to investigate the flexural characteristics, which were the ultimate flexural strength, strength, failure mode, deflection, flexural cracking and crack width, of the PC beam with FAA.

(2) Test specimen

Table 2 shows the data of Test specimens for bending test. Each specimen for this test was a PC beam with rectangular cross section, which was 350mm wide, 300mm depth and 4000mm long as shown in Fig.1. The test specimen was prestressed by pretension method with 6 prestressing strands of SWPR7BL 15.2mm in diameter.

Table 2 Data of Test Specimens for Bending Test

Specimen	Type	Aggregate	Size of Cross Section Width (m)	Size of Cross Section Depth (m)	Prestress Force (kN)
S1-1	PC	TL	0.35	0.30	845
S1-2		UL			836
S1-3		N			866

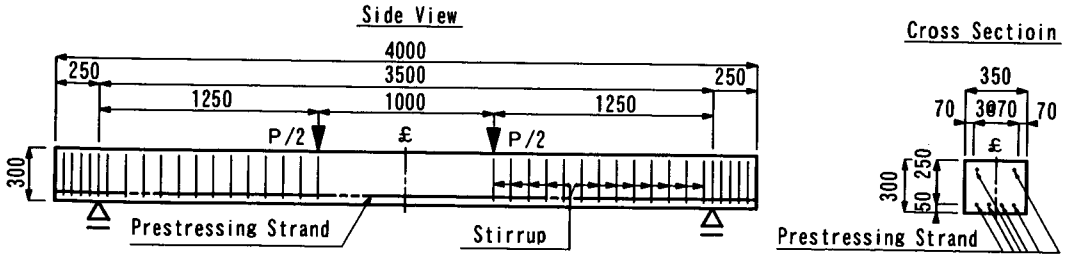

Fig. 1 Test Specimen for Bending Test

(3) Test method

The test specimen was simply supported at two points with a span of 3.5m, and the load was applied at two points as shown in Fig.1. The displacement, load, surface strain of the concrete, strain of prestressing strand and crack width were measured in this test.

3.2 Shear test (Series 2)

(1) Objective

Shear test was carried out to investigate the shear characteristics, which were the shear capacity and failure mode, of the PC beam and the reinforced concrete, hereinafter called RC, beam with FAA.

(2) Test specimen

Table 3 shows the data of specimens for shear test. Test specimens in this test were 3 PC beams and 2 RC beams with I-shape, which was 300mm wide, 550mm depth and 3500mm long as shown in Fig.2. Each PC beam was prepared by pretension method with 3 prestressing strands of SWPR7BL 15.2mm in diameter. Each RC beam was reinforced by 3 deformed steel bars with 25mm in diameter. The stirrups of all specimens were arranged only one side to simplify the test.

Table 3 Data of Specimens for Shear Test

Specimen	Type	Aggregate	Effective Depth (m)	Shear Span Effective Depth Ratio	Prestress Force (kN)
S2-1	PC	TL	0.50	3.0	569
S2-2		UL	0.50	3.0	560
S2-3		N	0.50	3.0	576
S2-4	RC	TL	0.50	3.0	0
S2-5		UL	0.50	3.0	0

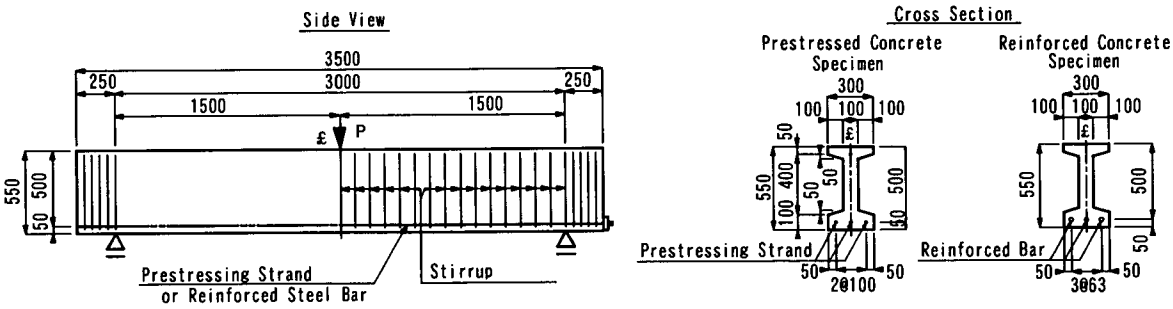

Fig.2 Test Specimen for Shear Test

(3) Test method

The test specimen was simply supported at two points with a span of 3.0m, and the load was applied at a point of the mid span as shown in Fig.2. The displacement, load and surface strain of the concrete were measured in this test.

3.3 Stress Measurment of Prestressing Strand (Series 3)

(1) Objective

This test was carried out to investigate the transfer length and the effective stress of the prestressing strand in PC beam with FAA.

(2) Test specimen

Table 4 shows the data of specimens for stress measurement of prestressing strand. Each specimen for this test was the same as the one for bending test, except for the space of prestressing strands as shown in fig.3. The space in this test was 61.25mm which was minimum space regulated in Japanese specification for prestressing strand 15.2mm in diameter. The test specimen for this test was also prestressed by pretension method just like the specimen for bending test.

Table 4 Data of Specimens for Stress Measurement of Prestressing Strand

Specimen	Type	Aggregate	Size of Cross Section		Space of Strands (mm)	Prestress Force (kN)
			Width (m)	Height (m)		
S3-1	PC	TL	0.35	0.30	61.25	845
S3-2		UL				836
S3-3		N				866

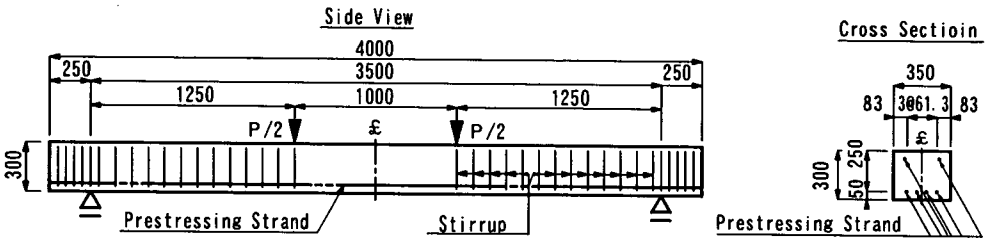

Fig.3 Test Specimen for Stress Measurement of Prestressing Strand

(3) Test method

In order to investigate the transfer length, electric strain gauges were mounted on the surface of a prestressing strand as shown in fig.4. The measurement was conducted when the strands were relaxed to introduce the prestress to the test specimen. Also in order to investigate the effective stress, the passage of the stress of the prestressing strand had been measured for 90 days.

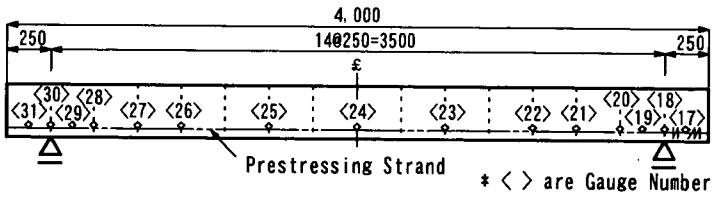

Fig.4 Location of Electric Strain Gauges on the Prestressing Strand

3.4 Materials and Mix Proportion of Concrete

(1) Materials

Table 5 shows properties of main materials used in this study. Two kinds of FAA, UL and TL were used as coarse aggregate and natural sand was used as fine aggregate of the concrete. Steel bars and prestressing strands in the test specimens are SD345 and 1S15.2 (SWPR7BL) respectively.

Table 5 Properties of Main Materials Used in this Study

Cement		High-Early-Strength Portland Cement, Density: 3.14g/cm^3
Water		Running Water
Fine Aggregate		Density: 2.61kg/l, Water Absorption Ratio: 3.0%
Coarse Aggregate	TL	Absolute Dry Density: 1.81 kg/l, Water Absorption Ratio: 2.4%
	UL	Absolute Dry Density: 1.30 kg/l, Water Absorption Ratio: 0.8%
	N	Surface Dry Density: 2.80 kg/l, Water Absorption Ratio: 0.7%
Prestressing Strand (SWPR7BL)		Yield Strength: 1570MPa Ultimate Tensile Strength: 1860MPa
Steel Bar (SD345)		Yield Strength: 345MPa

(2) Mix proportion of concrete

Table 6 shows the specified mix proportion of concrete. The quantity of water and bulk volume of coarse aggregate per unit volume of concrete was fixed at 160kg/m^3 and 550 l/m^3 respectively. The mix proportion was determined through trial mixing to obtain the compressive strength of 60MPa at 28 days of age, the slump of 18cm and the air content of 4.5%. Table 7 shows the test result of hardened concrete of each specimen.

Table 6 Specified mix proportion of concrete

Mixture	Aggregate	Air (%)	W/C (%)	Unit Mass (kg/m^3)				Unit Mass (kg/m^3)
				W	C	S	G	
TL60	TL	4.5	40	160	400	837	642	2039
UL60	UL		36	160	444	801	458	1863
N60	N		40	160	400	837	972	2369

Table 7 Test Result of Hardened Concrete

Series	Specimen	Mixture	At 1 day age		Just before Loading Tests		
			Compressive Strength (N/mm^2)	Young's Modulus (kN/mm^2)	Compressive Strength (N/mm^2)	Young's Modulus (kN/mm^2)	Tensile Strength (N/mm^2)
1	S1-1	TL60	39.6	25.2	65.3	27.8	4.1
	S1-2	UL60	44.9	23.3	67.8	26.1	3.9
	S1-3	N60	33.2	27.3	60.4	32.2	4.1
2	S2-1	TL60	32.6	26.9	62.3	28.0	3.7
	S2-2	UL60	36.8	23.5	59.1	24.8	4.3
	S2-3	N60	32.7	28.4	56.2	31.4	4.1
	S2-4	TL60	40.0	26.3	68.2	27.4	4.2
	S2-5	UL60	33.1	21.1	58.8	23.9	3.6
3	S3-1	TL60	43.6	25.6	67.4	28.4	3.7
	S3-2	UL60	44.9	23.3	67.8	26.1	3.9
	S3-3	N60	33.2	27.3	60.4	32.2	4.1

4. Result and Consideration

4.1 Bending Test (Series 1)

(1) Flexural cracking load and ultimate flexural strength

Table 8 shows the result of the bending test. The failure mode of all specimens was the bending compression failure which was supposed in the calculation of ultimate flexural strength. The calculated values on the flexural cracking load and the calculated values on the ultimate load are obtained as an applied load that causes the flexural cracking moment and the ultimate resistant bending moment respectively, which is the common design method regulated in Japanese specifications[5), 6)]. The measured cracking loads and ultimate loads of all specimens exceed the calculated loads. This means that the PC beam with FAA has enough strength for the flexural crack and the ultimate flexural failure.

Talbe 8 Result of Bending Test

Specimen	Flexural Cracking Load			Ultimate Load			Failure Mode
	Measured Load Pcr (kN)	Calculated Load Pcrd (kN)	Rato	Measured Load Pu (kN)	Calculated Load Pud (kN)	Ratio	
S1-1 (TL)	200	145	1.4	360	323	1.1	Bending compression failure
S1-2 (UL)	180	144	1.3	376	327	1.1	Bending compression failure
S1-3 (N)	180	144	1.3	380	316	1.2	Bending compression failure

(2) Load - displacement relationship

Fig.5 shows the load - displacement relationship. The displacement is at the center of the span of the test specimen. Each curve of S1-1 (TL) and S1-2 (UL) is almost similar to that of S1-3 (N) from the beginning through the end of loading. This means that the PC beam with FAA has almost the same performance as the ordinary PC beam with natural aggregate in respect of cracking strength, ultimate flexural strength and ductility.

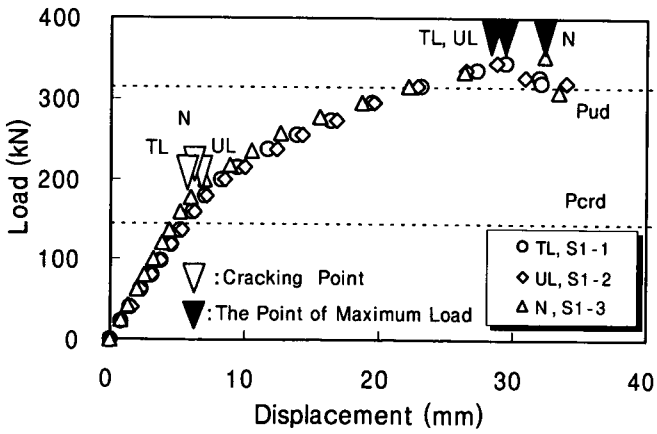

Fig.5 Load - Displacement Relationship

(3) Deflection

Fig. 6 shows the load-displacement relationship under cracking load. Because of lower Young's modulus of FAA, the displacement of S1-1 (TL) and S1-2 (UL) was bigger than that of S1-3 (N). The measured displacement is almost equal to the calculated displacement which is obtained by the elastic theory. This means that the PC beam with FAA acts as the elastic body until the flexural crack occurs.

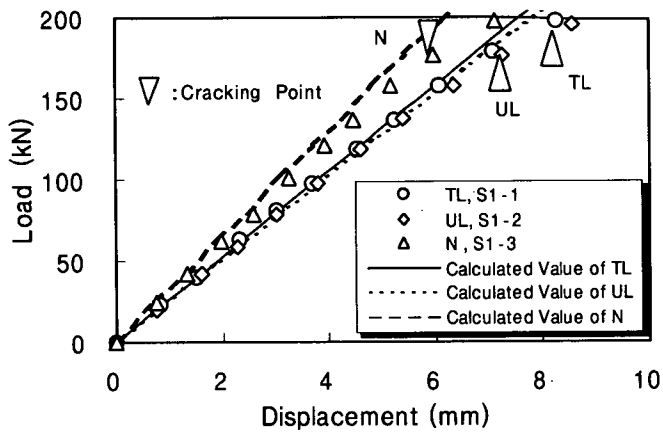

Fig. 6 Load - Displacement Relationship under Cracking Load

(4) Cracking width

Fig. 7 shows the relationship between the stress increase of the strand and the cracking width, and Fig.8 shows the cracking pattern of test specimens. The calculated cracking width is obtained by the (eq.1), which is regulated in Japanese specification[5]. In this case, the influences of creep and drying shrinkage on concrete are neglected.

$$w = k \cdot (4c + 0.7e_s) \cdot \sigma_{se} / E_s \qquad \text{----- (eq.1)}$$

Where,

w: cracking width, c: covering, e_s: spacing of prestressing strands, k: constant number which represents bond condition of steel, σ se: stress increase of strands, Es: Young's modulus of strand

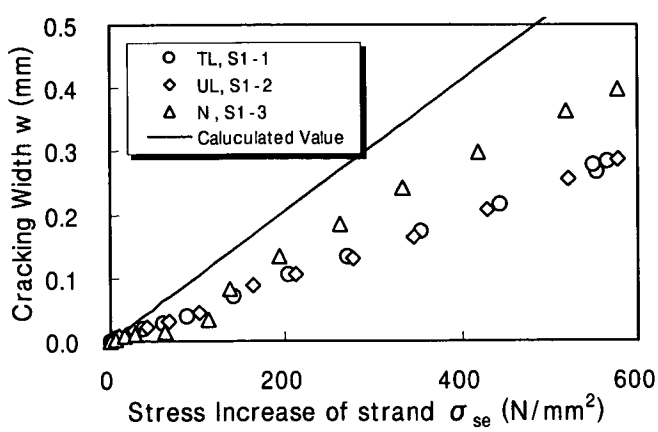

Fig. 7 Relationship between Stress Increase of Strand and Cracking Width

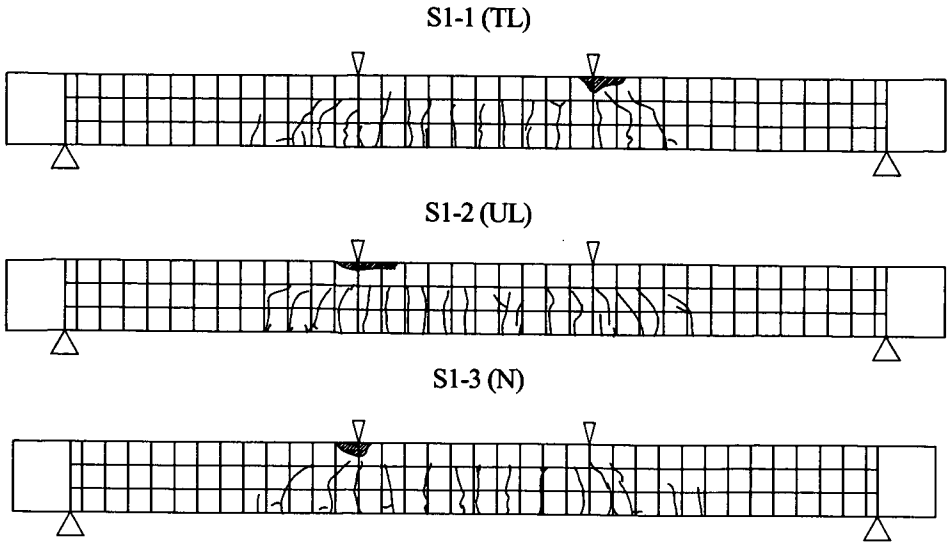

Fig. 8 Cracking Pattern of Test Specimens

The measured cracking widths of all specimens are smaller than the calculated cracking widths, and also the measured cracking widths of S1-1 (TL) and S1-2 (UL) are smaller than that of S1-3 (N). As shown in the Fig.8, the number of crack of S1-1 and S1-2 is more than that of S1-3. It can be said that the crack distribution of the PC beam with FAA is better than that of the ordinary PC beam with natural aggregate, therefore, the cracking width of the PC beam with FAA is smaller than that of the ordinary PC beam. This means that the (eq.1) gives the safe value for the PC beam with FAA.

4.2 Shear Test (Series 2)

(1) Shear Capacity

Table 9 shows the result of the shear test. The failure mode of all specimens was the diagonal tensile failure as shown in Fig.9. The calculated load at shear failure are obtained by the (eq.2) and (eq.3), which is regulated in Japanese specification[5].

$$V_{cd} = f_{vcd} \cdot b \cdot d \qquad \text{----- (eq.2)}$$

$$f_{vcd} = 0.2 \cdot f_c'^{1/3} \cdot \beta_d \cdot \beta_p \cdot \beta_n (0.75 + 1.4\, d/a) \qquad \text{----- (eq.3)}$$

where,

f_c: characteristic compressive cylinder strength of concrete at 28 days, $\beta_d = d^{-1/4}$, $\beta_p = p_w^{1/3}$, $\beta_n = 1 + 2M_o/M_u$, V_{cd}: shear strength, f_{vcd}: shear stress of concrete,
b: thickness of web (average thickness which is in consideration of flange),
d: effective depth, a: shear span, p_w: ratio of tension steel, M_o: decompression moment,
M_u: ultimate resistant bending moment.

As for the PC specimen, the measured load at shear failure is bigger than the calculated load, but as for the RC specimen, the measured load at shear failure is equal or smaller than the calculated load.

Table 9 Result of Shear Test

Specimen	Type	Load at Shear Failure			Failure Mode
		Measured Load Pu (kN)	Calculated Load Psud (kN)	Ratio	
S2-1 (TL)	PC	423	286	1.5	Diagonal Tensile Failure
S2-2 (UL)		452	280	1.6	Diagonal Tensile Failure
S2-3 (N)		426	276	1.5	Diagonal Tensile Failure
S2-4 (TL)	RC	260	246	1.0	Diagonal Tensile Failure
S2-5 (UL)		234	200	0.9	Diagonal Tensile Failure

S2-1 (PC, TL)

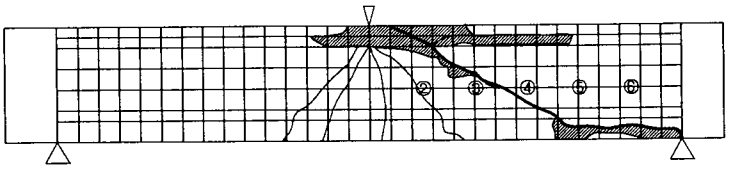

S2-2 (PC, UL)

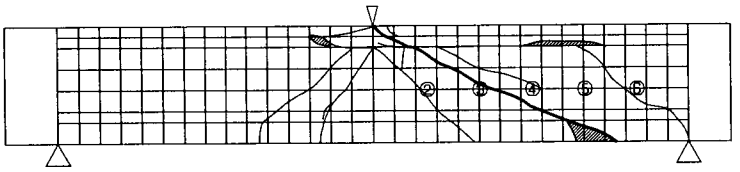

S2-3 (PC, N)

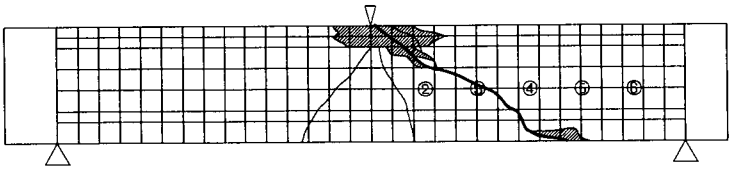

S2-4 (RC, TL)

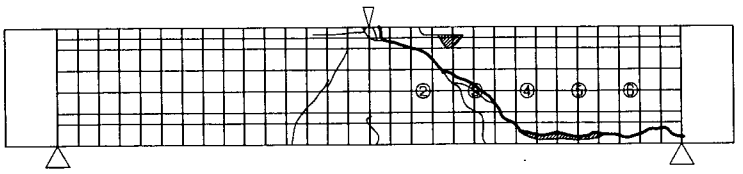

S2-5 (RC, UL)

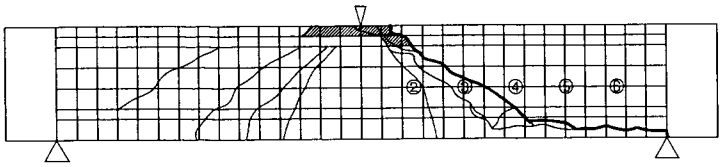

Fig.9 Cracking Pattern of Test Specimens

(2) Load - displacement relationship

Fig.10 shows the load-displacement relationship. The displacement is at the center of the span of the test specimen. As for the PC specimens, each curve of S2-1 (TL) and S2-2 (UL) is almost similar to that of S2-3 (N) from the beginning through the end of the loading. However, as for the RC specimens, the curve of S2-5 (UL) is lower than that of S2-4 (TL). It can be said that the shear capacity of the PC beam with FAA is equal to that of the ordinary PC beam with natural aggregate, but the shear capacity of the RC beam with lighter FAA is lower than that of the RC beam with heavier FAA. This means that the prestressing increases the shear capacity of the concrete beam with FAA, and that effect is larger for the concrete beam with lighter FAA.

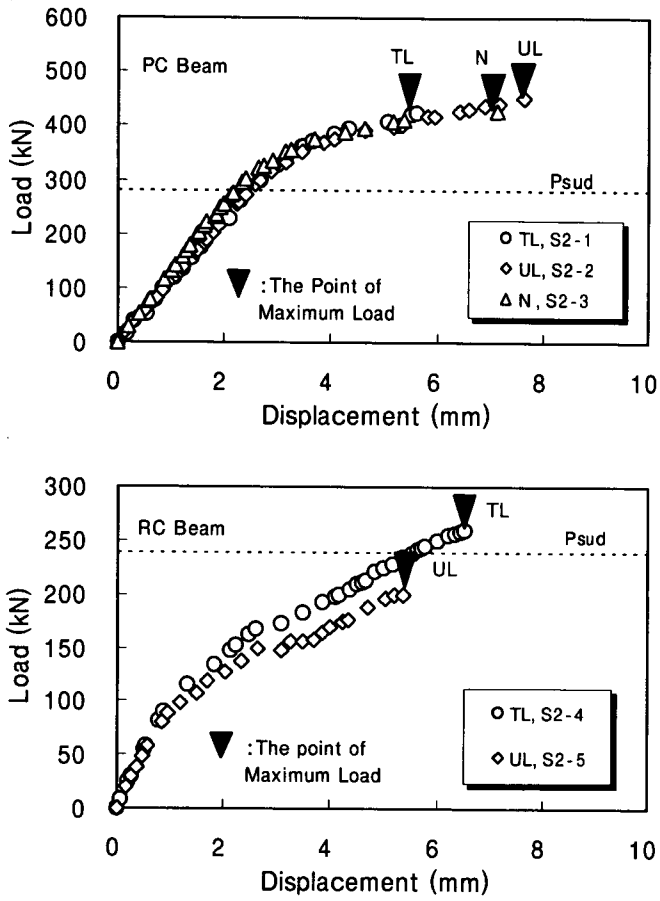

Fig.10 Load-displacement relationship

4.3 Transfer Length and Effective Stresses of Prestressing Strand

(1) Transfer length of prestressing strand

Fig.11 shows the result of transfer length test of the prestressing strand. The calculated value is obtained by common design method regulated in Japanese specifications[5), 6)]. In the calculation, the elastic deformation of the test specimen at prestressing is considerd.

Of all specimens, the measured stresses of the prestressing strand reach the calculated stress at the points 1m apart from the both edges of the specimen, which means that the transfer length of the prestressing strand is 1m. In Japanese specification[5)], it is mentioned that the transfer length of ordinary concrete is 65 times the diameter of the prestressing strand. Since the transfer length

obtained in this test, 1m is about 65 times the 15.2mm, the diameter of the prestressing strand, it can be said that the transfer length of the PC beam with FAA is almost equal to that of the ordinary PC beam with natural aggregate.

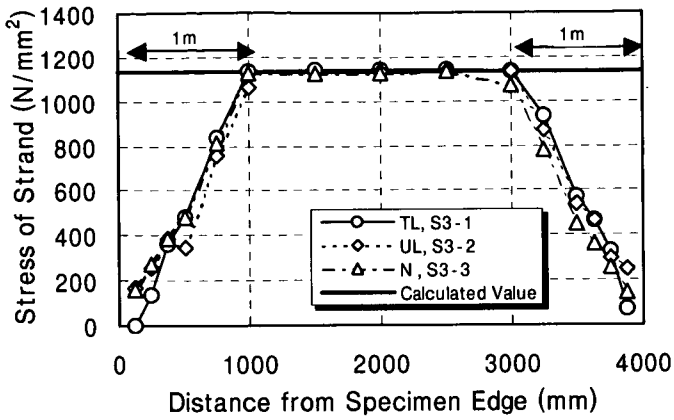

Fig. 11 Result of Transfer Length Test

(2) Effective stress of prestressing strand

Table 10 shows the stress of prestressing strand of each specimen, and Fig.12 shows the time dependent loss of strand stress around the center of the specimen. Numbers in legend of this figure are the location number of the gauges as shown in Fig.4. The calculated stress at after 3 months is obtained with the common design method regulated in Japanese specification[5),6)]. In the calculation, the creep and drying shrinkage of concrete and the relaxation of prestressing strand are considred.

The measured stress of the prestressing strand of all specimens is almost equal to the calculated stress both at just after prestressing and at after 3 months. It can be said that the prescribed prestress can be introduced in the PC beam with FAA like as the PC beam with natural aggregate. The loss of the strand stress of S3-1 (TL) and S3-2 (UL) is lower than that of the strand stress of S3-3 (N). The possible reason is that the drying shrinkage strain of the lightweight concrete is smaller than that of the ordinary concrete with natural aggregate[5)].

Table 10 Stress of Prestressing Strand

Specimen	Aggregate	Just after prestressing σ_{pt}			after 3 months σ_{pe}		
		Measured Stress (MPa)	Calculated Stress (MPa)	Ratio	Measured Stress (MPa)	Calculated Stress (MPa)	Ratio
S3-1	TL	1141	1134	1.01	1082	1015	1.07
S3-2	UL	1135	1126	1.01	1064	1004	1.06
S3-3	N	1142	1156	0.99	1048	1041	1.01

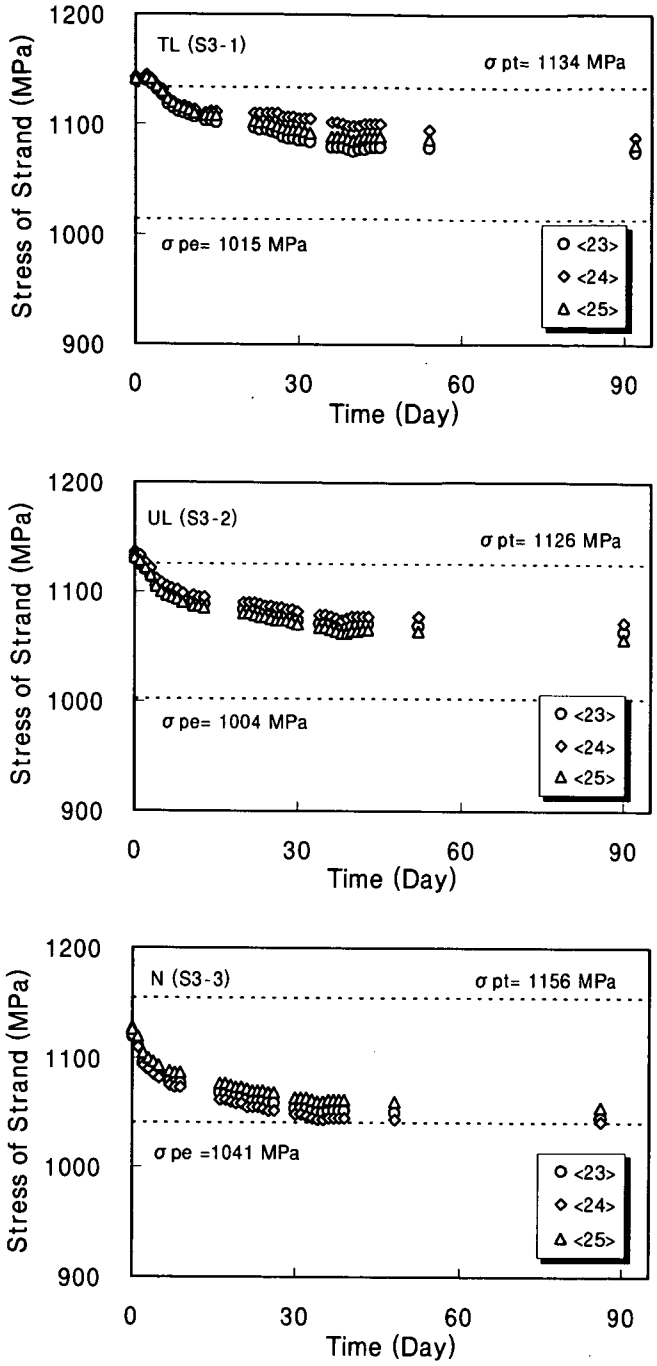

Fig.12 Time dependent loss of Strand Stress

5. Conclusion

In this study, the authors examined the structural characteristics of the PC beam with FAA. Below is a summary of the results obtained through the study.

(1) The PC beam with FAA has almost the same performance as the ordinary PC beam with natural aggregate in respect of cracking strength, cracking width and ultimate flexural strength.

(2) The PC beam with FAA acts as the elastic body until the flexural crack occurs.
(3) The crack distribution of the PC beam with FAA is better than that of the ordinary PC beam, therefore, the cracking width of the PC beam with FAA is smaller than that of the ordinary PC beam with natural aggregate.
(4) As for PC beam, the shear capacity of the concrete with FAA is equal to that of the ordinary concrete with natural aggregate.
(5) As for RC beam, the shear capacity of the concrete with lighter FAA is lower than that of the concrete with heavier FAA.
(6) The prestressing increases the shear capacity of the concrete with FAA, and that effect is larger for the concrete with lighter FAA.
(7) The transfer length of the prestressing strand of the PC beam with FAA is about 65 times the diameter of the prestressing strand and this length is almost equal to the length of the ordinary concrete with natural aggregate.
(8) The effective stress of the prestressing strand in the PC beam with FAA at after 3 months is bigger than the calculated stress, and this means that prescribed stress can be introduced in the PC beam with FAA.
(9) The time dependent loss of the strand stress of the PC beam with FAA is smaller than that of the ordinary PC beam with natural aggregate. The possible reason is that the drying shrinkage strain of the lightweight concrete is smaller than that of the ordinary concrete with natural aggregate.
(10) From all above results, it was verified that the FAA can be applied to the PC beam prestressed by pretention method and the fly ash can be the promising resource for the lightweight aggregate.

Acknowledgement
This study I am indebted to Taiheiyo Cement Corporation, UBE Industries LTD. for providing artificial aggregates. And we referred the results of study by "Research Organization for High Strength Artificial Aggregate Concrete".

Refernces
1) Tokuaki Sone: High Strength Artificial Aggregate Using Coal-Ash as Raw Material, Concrete Journal, Vol.36, No.12, pp.3-10, 1998
2) Toshikatsu Ohnish, Yasuhiko Toda, Goh Takemura, Takahiro Nakamizu: Fundamental Properies of Concrete Using Lightweight Fly-Ash Aggregates, Proceedings of JCI symposium on high performance structural lightweight concrete, Tokyo, pp.23-28, 2000
3) Yoshio Kakuta: Maximum Crack Widths In Reinforced Concrete, Concrete Journal, Vol.8, No.9, pp.1-10, 1970
4) Junichiro Niwa, Kazuie Yamada, Kazuo Yokozawa, Hajime Okamura: Revaluation of the Equation for Shear Strength of Reinforced Concrete Beams without Web Reinforcement, Proceedings of the Japan Society of Civil Engineers, No.372/V-5, pp.167-176, 1986
5) Concrete Standard Specification, Design Part, Japan Society of Civil Engineers, 1996
6) Specifications for Highway Bridges, Part 1: Common and Part 3: Concrete Bridges, Japan Road Association, 1996

FATIGUE OF ALUMINUM DECK FABRICATED BY FRICTION STIR WELDING

Ichiro Okura*, Nobuyasu Hagisawa **,

Makoto Naruo*** and Hitoshi Toda****

ABSTRACT

An aluminum deck is fabricated by joining hollow extrusions with the friction stir welding (FSW). The purpose of this study is to know the fatigue behavior of this deck. First, the material properties of the FSW region are investigated. Next, the fatigue test is carried out for the deck, and it is shown that a fatigue crack is initiated on the FSW-joining line of the top plate, just under the load. The plate-bending stress produced by the local deformation of the top plate causes it. The fatigue test is performed for the beam-type specimens provided by cutting the deck in the transverse direction. This test reveals that where the supporting interval of the deck becomes large, a fatigue crack is caused at the FSW of the bottom plate, by the membrane stress due to the global bending moment.
Keywords: aluminum deck, friction stir welding, fatigue

INTRODUCTION

In Japan, the change of the design vehicle load from 196kN to 245kN urges concrete slabs and girders of existing bridges to be reinforced. To cope with this issue, we have an idea of reducing the weight of the slab by replacing concrete slabs with aluminum decks. In USA there is a case that to carry heavier vehicle loads, an aluminum deck replaced the existing concrete slab (Ref 1). On the other hand, for the suspension bridges with a longer span than that of the Akashi Strait Bridge, it is required that the roadway should be light, and we think that the use of aluminum decks will serve this purpose. These motivations made us actually fabricate an aluminum deck using the friction stir welding (FSW). In this paper, the fatigue behavior of this aluminum deck is investigated.

*Associate Professor, Department of Civil Engineering, Osaka University, 2-1 Yamadaoka, Suita, Osaka 565-0871, Japan

** Manager, Research & Development Center, Nippon Light Metal Co., Ltd., 1-34-1 Kambara, Kambara-Cho, Ihara-Gun, Shizuoka 421-3291, Japan

***Bridge Design Department (Aichi Branch) Bridge Division, Ishikawajima-Harima Heavy Industries Co., Ltd., 11-1 Kitahama-Machi, Chita 478-8650, Japan

****Manager, Bridge & Road Construction Division, Ishikawajima-Harima Heavy Industries Co., Ltd., 1-19-10 Mohri, Koto-Ku, Tokyo 135-8322, Japan

FABRICATION OF ALUMINUM DECK USING FSW

Fig. 1 shows a general idea of an aluminum deck on steel girders. Connecting the extrusions, which lie parallel in the transverse direction, forms the deck. Fatigue cracks were reported to be initiated at the welds in steel plate decks (Ref. 2). We feared that the use of MIG welding to fabricate the aluminum deck would bring fatigue cracks at the welds. Since FSW does not make any reinforcements at the connections, it was expected that the fatigue strength of the connections by FSW would be higher than that by MIG welding. Hence we accepted FSW to fabricate the aluminum deck.

FSW is a solid phase welding, invented in 1991 at the TWI, UK (Ref. 3). Fig. 2 shows the concept of FSW. The aluminum plates to be jointed are butted together on a backing bar, and are clamped so as not to move apart during joining. The steel tool with a pin and a shoulder, which is rotating, is plunged into the plates until the shoulder contacts the top surface. The butted surfaces are softened by frictional heating, dragged by the rotation of the tool, and stirred. The travel of the tool along the joining line makes the plates unite.

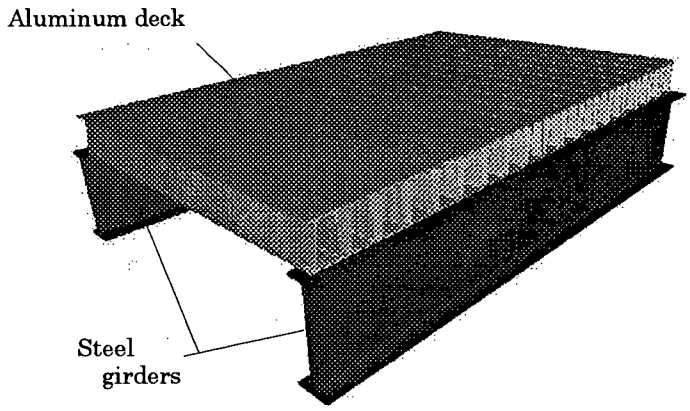

Fig. 1 Aluminum deck on steel girders

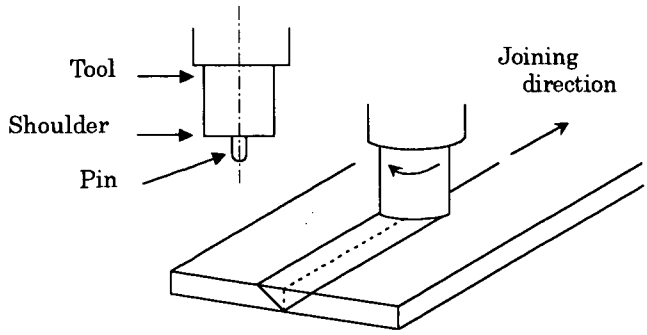

Fig. 2 Concept of FSW

Fig. 3 presents the cross section of the extrusions for the aluminum deck. As shown in Fig. 4, connecting the top and bottom flanges of the extrusions formed the deck shown in Fig. 5. The aluminum used is A6N01S-T5. The measured chemical composition of this material is listed in Table 1 together with the values specified in the Japanese Industrial Standard (JIS) (Ref. 4).

Table 1 Chemical composition of A6N01S-T5

	Si	Fe	Cu	Mn	Mg	Cr	Zn	Ti
Measured values (%)	0.51~ 0.53	0.16	0.08~ 0.09	0.14~ 0.15	0.69	0.01	0.01	0.02~ 0.03
JIS-values (%)	0.40~ 0.90	≦0.35	≦0.35	≦0.50	0.40~ 0.80	≦0.30	≦0.25	≦0.10

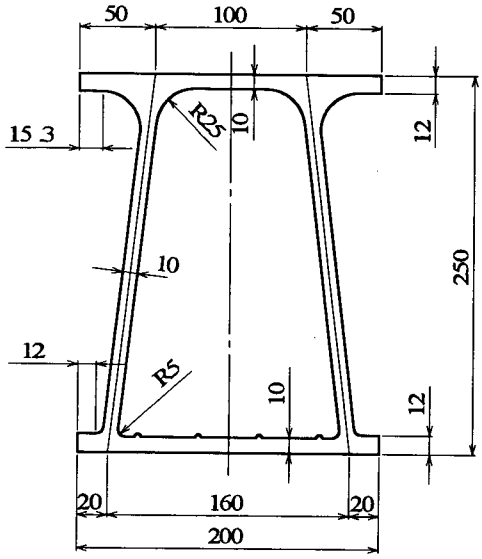

Fig. 3 Cross section of extruded product

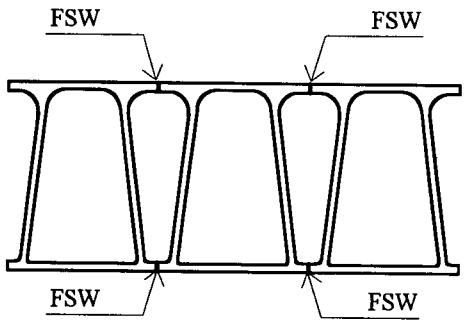

Fig. 4 Connection by FSW

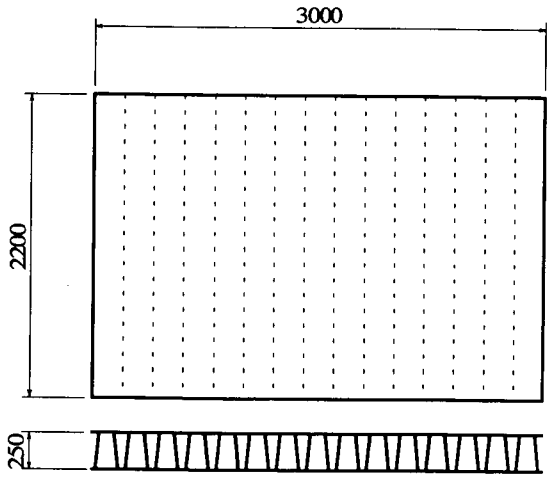

Fig. 5 Aluminum deck

MATERIAL PROPERTIES OF FSW REGION

To know the material properties of the FSW region as well as the parent material, the various tests were carried out (Ref. 5). The specimens for the tests were cut out from the specimens with the cross section shown in Fig. 6, where two extrusions 1700 mm long were joined by FSW.

Fig. 7 shows the distribution of the Vickers hardness on the FSW of the top flange. The hardness decreases in the 20mm zone in each direction from the center of the FSW. Usually in MIG welding the hardness-decreasing zone is 25mm. Accordingly the strength-decreasing zone in FSW is smaller than that in MIG welding.

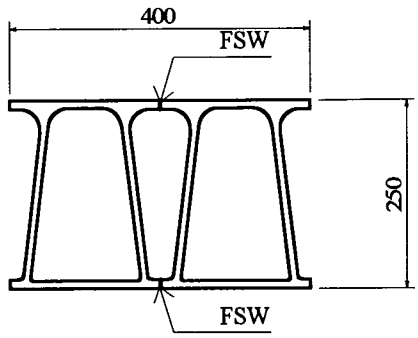

Fig. 6 Connection of two extrusions by FSW

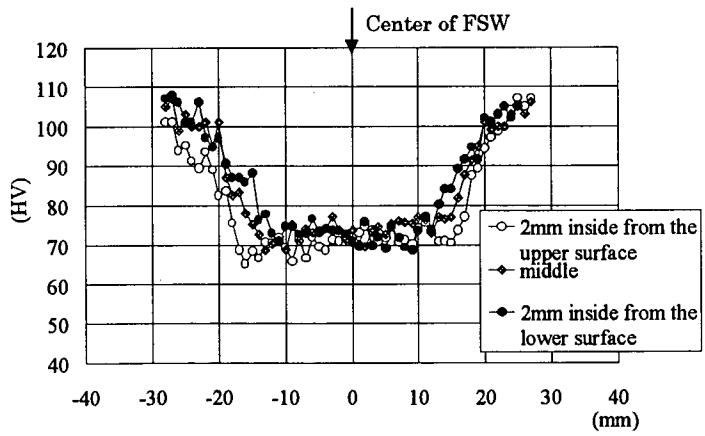

Fig. 7 Distribution of Vickers hardness on FSW region [Top flange]

Table 2 lists the results of the tensile test for the parent material and the FSW. The tensile-test specimens were cut out from the specimen with the cross section shown in Fig. 6, in the longitudinal direction for the parent material and in the longitudinal and transverse directions for the FSW. The size of the specimens accords with 14B in JIS (Ref. 6), and their width is 20 mm. The ratios of the FSW to the parent material for the proportional limit, the 0.2 % proof stress and the tensile strength are 0.26 – 0.38, 0.45 – 0.52 and 0.80 – 0.81, respectively. The ratios of the MIG to the parent material for the 0.2 % proof stress and the tensile strength are 0.56 and 0.74, respectively (Ref. 7).

Accordingly the decrease in the tensile strength of FSW is smaller than that of MIG welding. The specimens in the transverse direction for the FSW broke at the heat-affected zone.

Table 2 Results of tensile tests

		Young's modulus (GPa)	Poisson's ratio	Proportional limit (MPa)	0.2 % proof stress (MPa)	Tensile strength (MPa)	Elongation (%)
Parent material		70.5	0.31	221.3	245.7	269.9	7.9
FSW	Longitudinal direction	69.1	0.34	83.7	127.5	218.2	29.8
	Transverse direction	69.3	0.33	56.7	111.2	216.8	–

Fig. 8 presents the distributions of the residual stresses in the longitudinal and transverse directions. The strain gauges were glued on the outside surfaces of the top and bottom flanges, in the middle of the specimen with the cross section shown in Fig. 6. The residual strains that were released when the specimen was cut into small pieces were measured by the strain gauges. The residual stresses produced in the FSW are tensile in the longitudinal direction and compressive in the transverse direction. In MIG welding the residual stresses are both tensile in the longitudinal and transverse directions. Since the compressive residual-stress has a good effect on the fatigue strength, this fact in FSW is worthy of note.

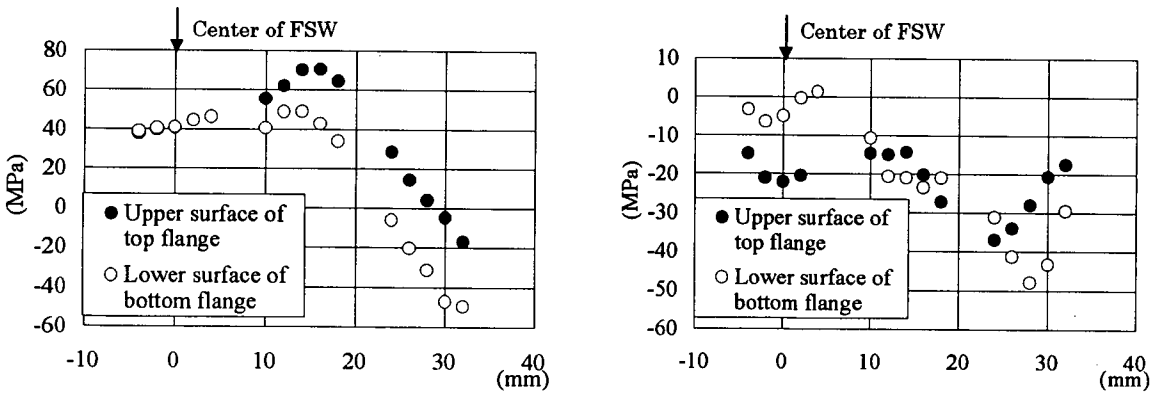

(a) Longitudinal direction **(b) Transverse direction**

Fig. 8 Distributions of residual stresses

Fig. 9 shows the results of the fatigue tests of the parent material and the FSW. In the figure R is the ratio of the lower stress to the upper stress. The fatigue-test specimens with the width of 20 mm were cut out from the specimens with the cross section shown in Fig. 6, in the longitudinal direction for the parent material and in the transverse direction for the FSW. An axial load was applied to the specimens. The S-N curves are

given in the following form:

$$\log N = \log c - m \log(\Delta\sigma) \qquad [1]$$

where $\Delta\sigma$=stress range (in MPa); N=number of cycles to failure; c and m=coefficients.

Table 3 lists the values of $\log c$, m and the standard deviation ξ_N of $\log N$ about the arbitrary $\log(\Delta\sigma)$. The inverse slope m of the S-N curves of the FSW is close to that of the parent material. In the specimens for the FSW, 18 specimens failed at the heat-affected zone, and three specimens did at the nugget zone, that is, the zone stirred by the pin of the tool.

Table 3 Values of $\log c$, m and ξ_N

	Stress ratio R	$\log c$	m	Standard deviation ξ_N of $\log N$
Parent material	−1	23.9	7.66	7.33×10^{-2}
	0.1	20.3	6.58	2.14×10^{-1}
FSW	−1	25.9	8.74	1.48×10^{-1}
	0.1	20.1	6.84	1.33×10^{-1}

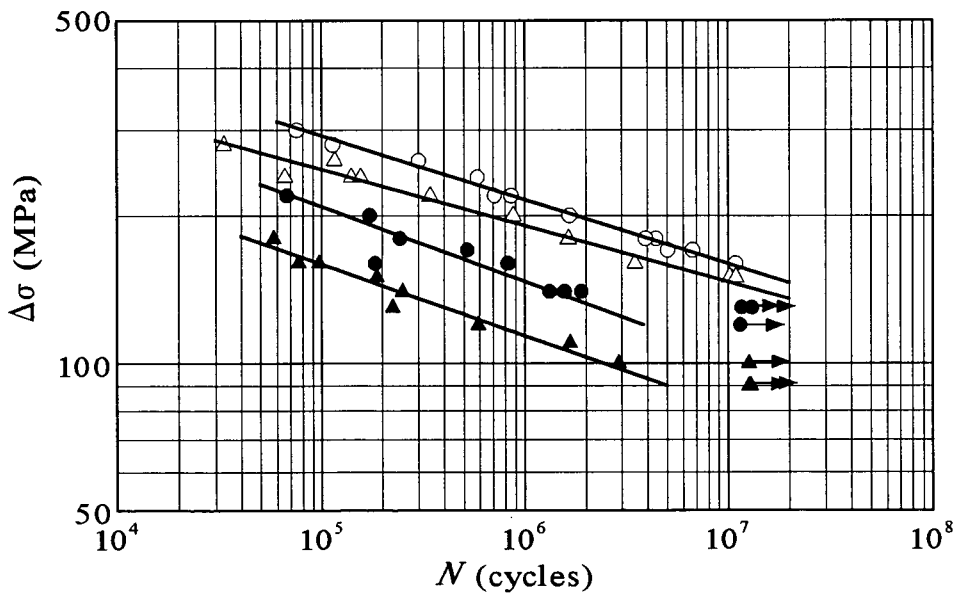

Parent material	○	$R=-1$
	●	$R=0.1$
FSW region	△	$R=-1$
	▲	$R=0.1$

Fig. 9 S-N curves

FATIGUE OF ALUMINUM DECK

Static Test of Aluminum Deck

Fig. 10 shows the outline of the static test of the aluminum deck. The deck is put on the steel round bars 10cm in diameter that is laid on the steel girders 84.4cm high and 400cm long. The supporting interval of the deck is 200cm. A load was applied to the deck through the hard rubber plate of 20cm×50cm×1.5cm. The shape of 20cm×50cm is the same as the loading area of the design wheel load of a truck specified in the Japanese Specifications for Highway Bridges (Ref. 8). After moving the deck at every 5cm interval in the bridge-longitudinal direction, the load was applied statically. Here, the bridge-longitudinal and -transverse directions are shown in Fig. 10. We note that the bridge-longitudinal and –transverse directions are corresponding to the transverse and longitudinal directions of the FSW-joining line, respectively.

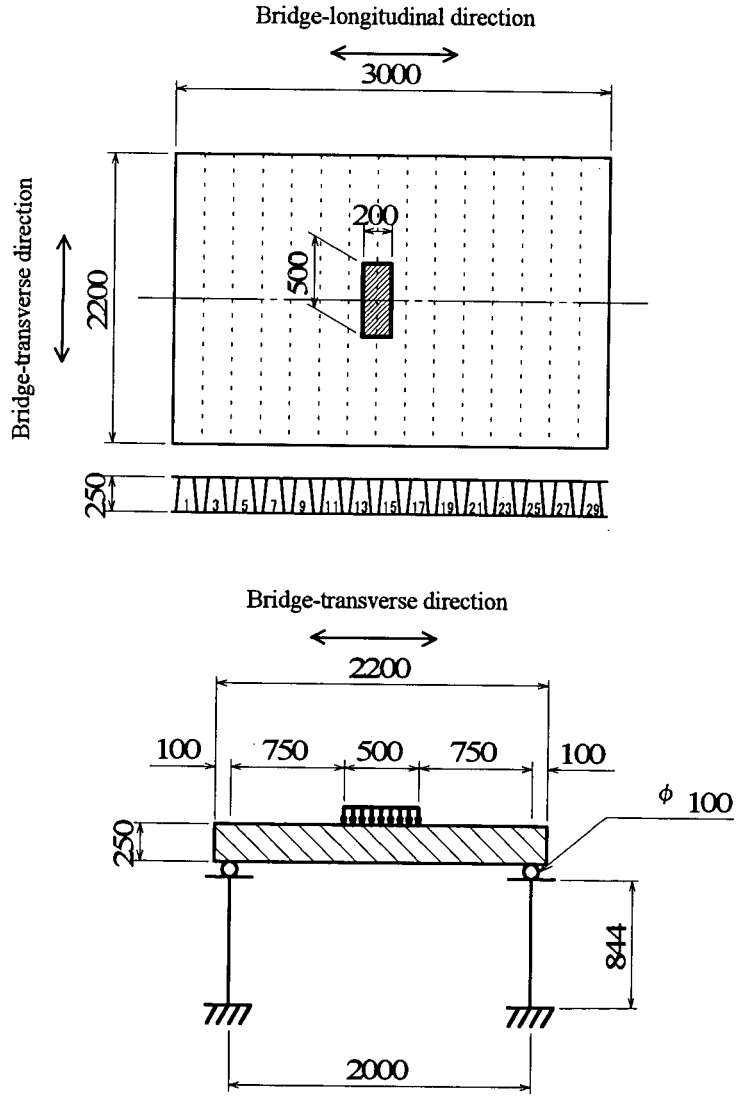

Fig. 10 Outline of static test of aluminum deck

Fig. 11 presents the influence lines of the strains in the bridge-longitudinal and -transverse directions obtained from this static test. The results are the strains on the lower surface of the bottom plate of the deck, and are corresponding to the load 9.8kN. The figure shows that in the aluminum deck, for the move of a load, the stress in the bridge-longitudinal direction alternates positive and negative, but that the stress in the bridge-transverse direction does not.

Fatigue Test of Aluminum Deck

The fatigue test followed after the static test. Fig. 12 presents the location and magnitude of the fatigue load. In the loading case 1 the load is on the cell where the FSW does not exist and in the loading cases 2 and 3 the load is on the cell where the FSW exists. Since the bottom plate of the deck was not perfectly flat, some gap occurred between the bottom plate and the steel round bar, and for the repeat of the loads below 49.0kN, the bottom plate hit the bar. Hence, 49.0kN was accepted for the lower load.

In the loading case 1, since neither the change of the deflection range of the deck, the strain range nor the initiation of fatigue cracks was recognized, the fatigue test was finished at two million cycles.

In the loading case 2, at one million cycles, the strain range on the FSW-joining line of the top plate varied. However, since neither the change of the deflection range of the deck nor the initiation of fatigue cracks was recognized, the fatigue test was continued until two million cycles.

In the loading case 3, at 1.02×10^5 cycles, the strain range on the FSW-joining line of the top plate began to vary. However, since the deflection range of the deck did not change, the fatigue test was continued until one million cycles. At the time, taking off the hard rubber plate for loading let us find a fatigue crack 48 cm long on the FSW-joining line of the top plate. Since the dye penetrant spread on the upper surface of the top plate appeared on the lower surface, the fatigue crack already penetrated the top plate. However, since the deflection range of the deck did not change, the fatigue test was continued until two million cycles. The fatigue crack grew 62 cm long.

Since the fatigue crack propagated on the joining line, the stress in the bridge-longitudinal direction caused it. An FE analysis showed that the stress in the bridge-longitudinal direction of the top plate is a plate-bending stress, caused by the local deformation of the top plate of the deck, just under the load, as shown in Fig. 13 (Ref. 9). Since the lower surface of the top plate was under tension of the plate-bending stress, the fatigue crack was initiated on the lower surface.

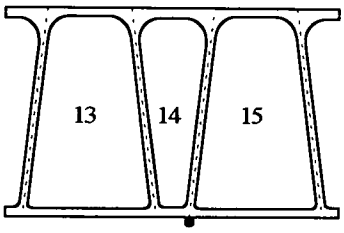

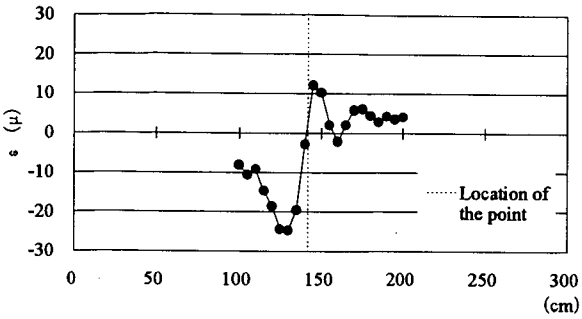

(a)Strain in the bridge-longitudinal direction

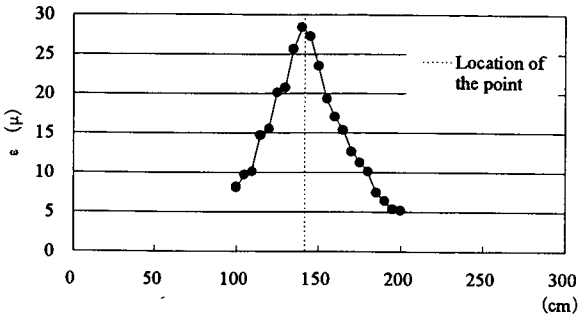

(b) Strain in the bridge-transverse direction

Fig. 11 Influence lines of strains

Loading case	Lower load (kN)	Upper load (kN)	Load range (kN)
1	49.0	186.3	137.3
2	49.0	186.3	137.3
3	49.0	268.7	219.7

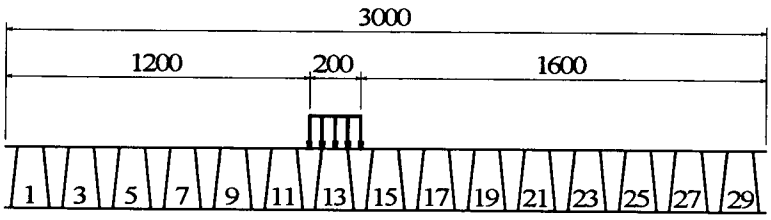

(a) Loading case 1

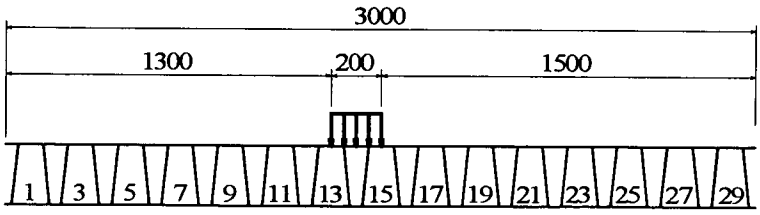

(b) Loading cases 2 and 3

Fig. 12 Location and magnitude of fatigue load

Fig. 14 shows the fatigue strength of the crack. The stress range $\Delta\sigma$ is 97.4 MPa corresponding to the load range 219.7 kN. The fatigue life N is 1×10^6 cycles when the crack is 48 cm long, which is very close to the length 50 cm of the hard rubber plate for loading. The S-N relations for $R=0.1$ of the parent material and the FSW and the S-N curve of the detail category 35-4 for the transverse butt welds specified in Eurocode 9 (Ref. 10) are also given in the figure. The fatigue strength of the deck is located much higher than the S-N curve of the transverse butt welds specified in Eurocode 9.

In the previous chapter, the residual stress in the transverse direction of the FSW was compressive. Accordingly, the compressive residual-stress is left in the bridge-longitudinal direction at the FSW of the deck. The compressive residual-stress acts on the increase in fatigue strength. However, the fatigue strength of the deck is somewhat lower than that of the tensile-type specimens. The observation of the surface of the fatigue crack of the deck let us know that the depth of about 0.5 mm was not joined at the tip of the pin of the tool. This unjoining would have decreased the fatigue strength of the deck.

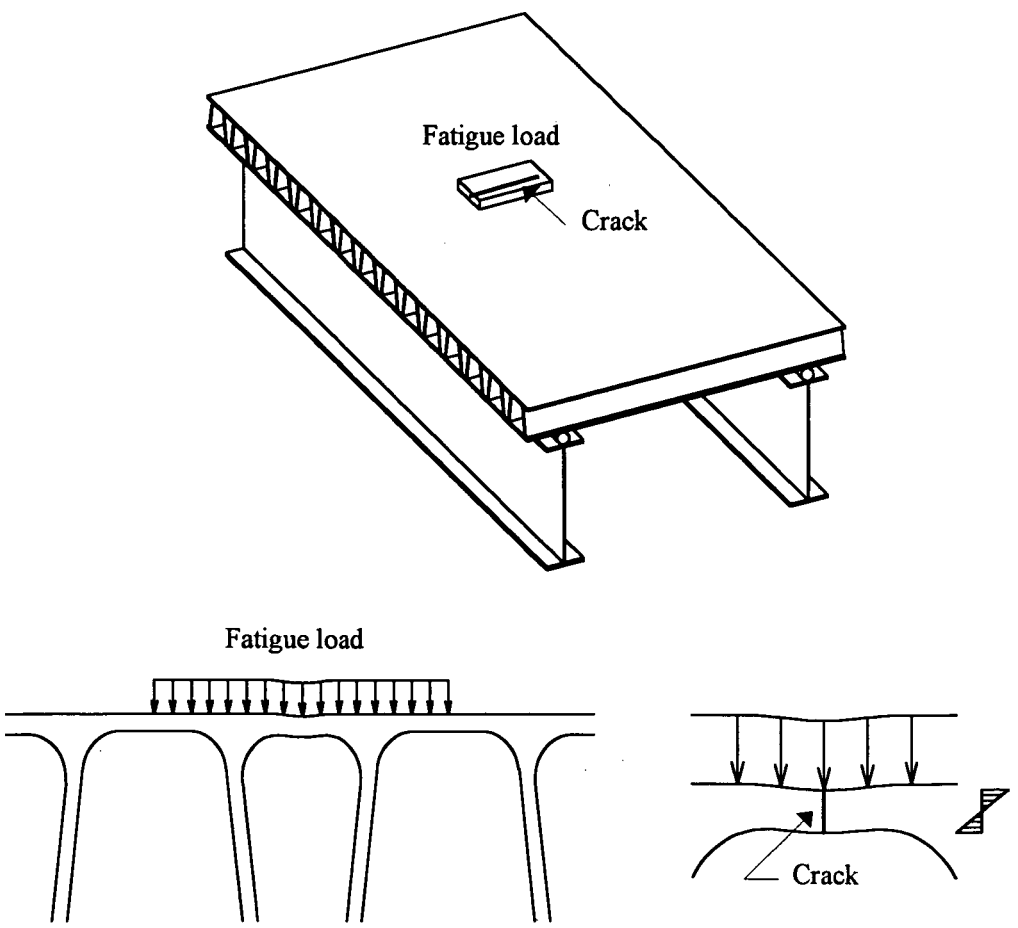

Fig. 13 The crack on the top plate

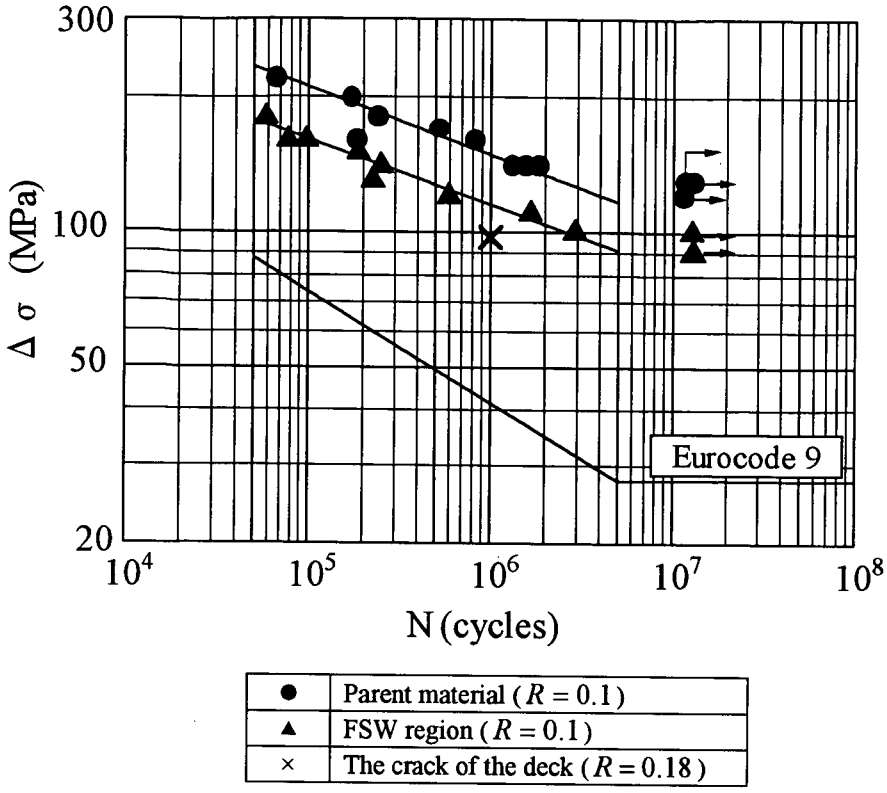

Fig. 14 Fatigue strength of the crack on the top plate

Fatigue Test of Beam-Type Specimens

The supporting interval of the aluminum deck was 200 cm. As the supporting interval becomes larger than 200 cm, the global bridge-transverse bending moment increases. A fatigue crack will be produced in the bridge-longitudinal direction on the bottom plate, as shown in Fig. 15. To obtain the fatigue strength of this crack, the fatigue test was carried out for the beam-type specimens shown in Fig. 16. Cutting the deck in the bridge-transverse direction provided the specimens. They have the FSW in the middle of the top and bottom flanges. The load of $R = 0.1$ was applied on the 10 cm width at the span center.

The fatigue crack was initiated on the lower surface of the bottom flange at the FSW. It propagated on the cross section of the specimen, and the specimen broke into two pieces due to brittle fracture. Fig. 17 presents the relation between the stress range in the bottom flange at the crack initiation point and the number of cycles at failure. The stress range is a membrane stress corresponding to the bending moment. The S-N relation for $R = 0.1$ of the parent material in Fig. 9 and the S-N curve of the detail category 44-4.5 for the longitudinal butt welds specified in Eurocode 9 (Ref. 10) are also shown in the figure. The S-N curve of the beam-type specimens is given by

$$\log N = 12.3 - 3.23 \log(\Delta\sigma) \qquad [2]$$

The standard deviation ξ_N of $\log N$ about the arbitrary $\log(\Delta\sigma)$ is 1.06×10^{-1}. The inverse slope of the S-N curve of the beam-type specimens is smaller than that of the parent material. However, the results of the beam-type specimens are located much higher than the S-N curve of the longitudinal butt welds specified in Eurocode 9.

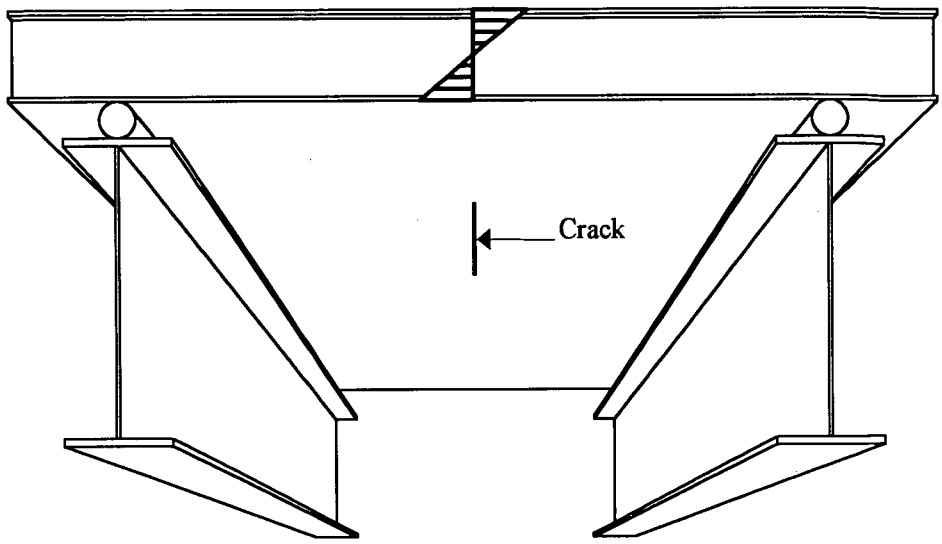

Fig. 15 The crack on the bottom plate

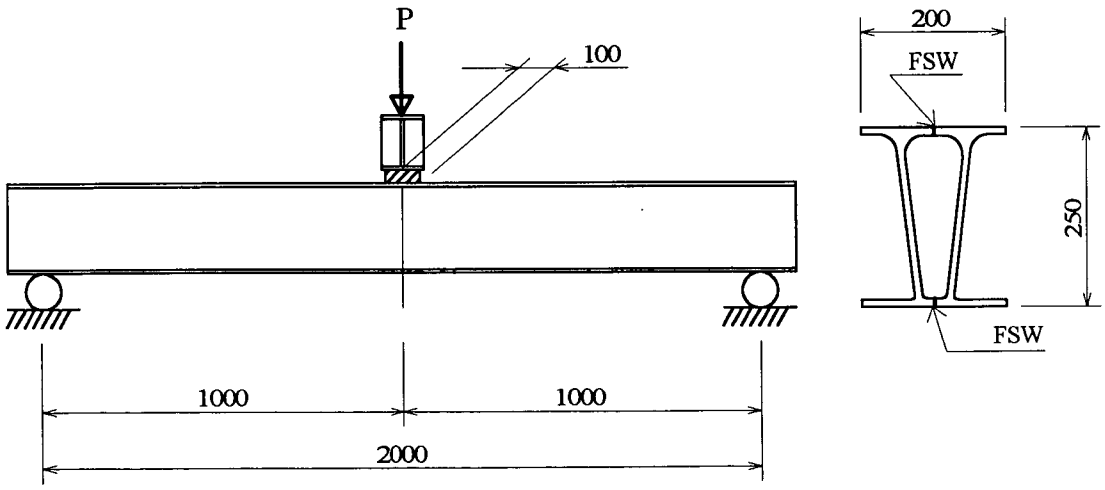

Fig. 16 Beam-type specimen

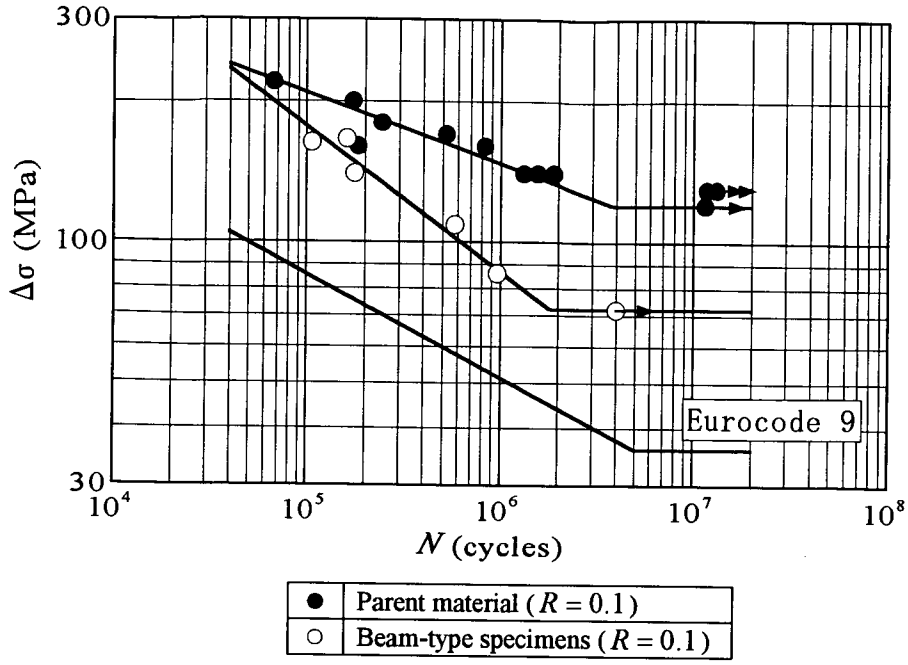

Fig. 17 S-N curves of beam-type specimens

CONCLUSIONS

The fatigue behavior of an aluminum deck fabricated by FSW was investigated. The main conclusions are as follows:

1. The strength-decreasing zone in FSW is 20 mm in each direction from the center of the FSW.
2. The ratios of the FSW to the parent material for the proportional limit, the 0.2% proof stress and the tensile strength are 0.26 – 0.38, 0.45 – 0.52 and 0.80 – 0.81, respectively.
3. The residual stresses produced in the FSW are tensile in the longitudinal direction and compressive in the transverse direction.
4. Using tensile-type specimens, S-N curves were given for the parent material and for the FSW in the transverse direction.
5. In the deck, for the move of a load, the stress in the bridge-longitudinal direction alternates positive and negative, but the stress in the bridge-transverse direction does not.
6. A fatigue crack is initiated on the FSW-joining line of the top plate of the deck, just under the load. The plate-bending stress in the bridge-longitudinal direction, produced by the local deformation of the top plate, causes it. The fatigue strength of this crack is much higher than that of the transverse butt welds specified in Eurocode 9.
7. Where the supporting interval of the deck becomes large, a fatigue crack is initiated at the FSW of the bottom plate in the bridge-longitudinal direction, by the membrane stress due to the global bridge-transverse bending moment. The fatigue strength of this crack is much higher than that of the longitudinal butt welds specified in Eurocode 9.

REFERENCES

1 Civil Engineering, "New aluminum decks cut loads, add life", ASCE, August, 1996, p.12.

2 Okura, I., "Fatigue in Steel Bridges", Toyo Publisher, Tokyo, Japan, 1994, pp.336-339. (in Japanese)

3 http://www.twi.co.uk/bestprac/datashts/fswintro.html

4 Japanese Industrial Standard, "H 4100", 1999. (in Japanese)

5 Japan Aluminum Association: Basic Data on Aluminum Decks, March, 2000. (in Japanese)

6 Japanese Industrial Standard, "Z 2201", 1980. (in Japanese)

7 Japan Light Metal Association, "Recommendations for Design and Fabrication of Aluminum Alloy Structures", 1st Draft, December, 1998. (in Japanese)

8 Japan Road Association, "Japanese Specifications for Highway Bridges, Part 2: Steel Bridges", 1996. (in Japanese)

9 Okura, I., Naruo, M., Vigh, L.G., Hagisawa, N. and Toda, H., "Mechanical and structural properties of aluminum decks fabricated by friction stir welding", JSCE, Proceedings of the 2nd Symposium on Decks of Highway Bridges, 2000, pp.131-136. (in Japanese)

10 Eurocode 9, "Design of Aluminum Structures, Part 2: Structures Susceptible to Fatigue", prENV 1999-2:1997.

SESSION 5: SEISMIC 2

(1) Performance of Flared Columns with Gaps
(Hisham M. Nada, David H. Sanders and M. "Saiid" Saiidi)

(2) Seismic Retrofitting for Bridges in Osaka City
(Kenji Shimoda, Shigeo Takei, Tadaaki Maruyama, Kozo Nishimori and Yukiko Mitsugi)

(3) Retrofit Design and Strategy of the San Francisco-Oakland Bay Bridge Continuous Truss Spans Support Towers Based on ADINA.
(R. B. Heninger and R. W. Wolfe)

(4) Preliminary Study on Seismic Retrofit of the Gerber Truss Bridge, the Minato Bridge
(Jota Toki, Hidesada Kanaji and Yukio Adachi)

(5) Study on Seismic Behavior of Concrete Columns Strengthened with PC Confined Method
(Kiyoshi Kirikawa)

(6) Bridge Condition Monitoring and Assessment
(Li-Hong Sheng)

PERFORMANCE OF FLARED COLUMNS WITH GAPS

Hisham M. Nada[1], David H. Sanders[2] and M. "Saiid" Saiidi[3]

Abstract

Past earthquakes have shown that flared columns are susceptible to premature shear failures. Shear failures have been caused by a lowering of the plastic hinge within the column and a subsequent increase in the level of column shear above design levels. This paper presents an experimental and analytical project that is examining new details for flared columns and joints. The primary feature is a gap at the top of the column. Two two-column bents were tested on the shake table to examine dynamic effect as well as column and beam interaction. The bents had different amount of confining reinforcement in the flare.

Introduction

Design of flared columns to resist earthquake loading is a complicated issue due to the changing cross section along the column length. Past earthquakes have shown that flared columns could have poor behavior due to the large increase of column flexural capacity at the top of the column. The increased capacity can cause the plastic hinge region to shift away from the column-beam interface into the column. This causes the column to behave like a much shorter column and therefore have increased shear demand. The shifting of the hinge and the larger shear level was not included in many previous designs and has led to brittle shear column failures. Brittle shear failure doesn't allow the bridge to have large inelastic deformation and can lead to complete collapse of the bridge.

It was believed that if the flares had low longitudinal and transverse reinforcement ratios, they would fail during earthquakes. Therefore, the column core would be the element remaining to resist the earthquake. Experiments and past experience proved that even lightly reinforced flares contribute to increasing the column's flexural capacity (Sanchez and Priestley 1997). To solve this problem, Caltrans has developed new details attempting to separate the flared portion of the column from the overall flexural stiffness and capacity of the column. This is achieved by separating the flare from the beam using a gap between the top of the flare and the beam bottom surface, Fig. 1. Caltrans' recommendations came as a result of single column slow-cyclic tests and not on system bent tests (Sanchez and Priestley 1997). The purpose in conducting shake-table bent tests is to study the effectiveness of the flare detail and to examine the behavior within the joint region as well as the overall system response. Four bents will be tested as part of the overall study. Two bents will be flexurally dominated while two will have higher shear values. This will be accomplished by using two different column heights. The columns are pinned at the base with a two-way hinge. Within each bent of similar height, the amount of flare transverse reinforcement will be varied. In one case the amount of transverse reinforcement in the flare will be in accordance with current Caltrans' guidelines while in the second case, the amount of

[1]Graduate Research Assistant, Dept. of Civil Engineering, University of Nevada, Reno, NV 89557
[2]Associate Professor, Dept. of Civil Engineering, University of Nevada, Reno, NV 89557
[3]Professor, Dept. of Civil Engineering, University of Nevada, Reno, NV 89557

reinforcement will be reduced. This document will focus on the tall bents tested (LFCD1 &LFCD2), which are flexurally dominated. The experiment was conducted at the Large-Scale Structures Laboratory at the University of Nevada, Reno.

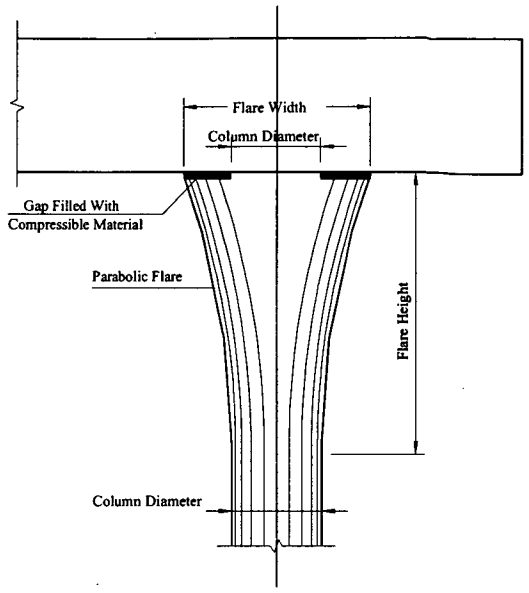

Fig. 1. Layout of the proposed detail

Model Design

Column Design

A survey was made of existing bridges in California to develop a prototype. Because the model will be used for new bridge detailing, only bridges that were designed according to the latest code provisions were considered in the survey. Based on these details and the 50-ton vertical load capacity of a single shake table, a 1/5-scale model was developed. The vertical axial load acting on each column was calculated according to Eq. 1.

$$P = 0.1 \times A_g \times f_c' \quad (1)$$

Where;

A_g = Gross column cross section and
f_c' = Concrete compressive strength (4500 psi).

The 10% level was set as a typical upper range for the majority of new columns in bridges with regular spans. This level resulted in a total axial load of 101.5 kips. In order to distribute this load along the length of the bent, lead buckets in combination with small rams were used. The other key details for the columns are given in Table 1 and shown in Fig. 2. All reinforcement is Grade 60 to conform to current design. Some dimensions that cannot be scaled due to practical issues, like concrete cover, are kept within the minimum range that allows for

practical use. The flexurally-dominated tall columns had a clear height of 64 inches while the shorter columns had a height of 37 inches. The bents described in this paper had the taller columns.

Table 1. Summary of model and prototype dimensions.

Description	Prototype	Model	Factor
Column Diameter	60	12	0.2
Flare Width	125	25	0.2
Column Reinforcement	30 # 14	14 # 4	1
Column Reinforcement Ratio	2.39	2.4	1
Column Spirals	# 6 @ 4"	0.192 @ 1.25"	N/A
Spiral Volume Ratio ($2A_b/SD$)	0.0037	0.0039	1
Column Height	320	64	0.2
	LFCD1	LFCD2	
Transverse Reinforcement at top 1/3 of the flare	0.192 @1.1"	0.148 @3.8"	
Transverse Ratio	0.439 %	0.075 %	
Transverse Reinforcement at top 1/3 of the flare	0.148 @3.8"	0.148 @3.8"	
Transverse Ratio	0.075 %	0.075 %	
Vertical Flare Reinforcement	6-Dia 0.148"	6-Dia 0.148"	

Flare Design

Flare reinforcement layout was calculated by scaling the prototype dimensions. Current Caltrans recommendations state the following (Caltrans Seismic Design Criteria):

- The gap thickness of the flare shall be 50 mm (2"). However, if significant relative rotation between the cap and the column is expected, then the required gap to accommodate this rotation should be calculated and provided.
- The longitudinal flare reinforcement is nominal. Spacing between longitudinal flare reinforcement shall not exceed 450 mm (1.75") and not less than 150 mm (6").
- The transverse flare reinforcement ratio in the upper 1/3 of the flare height is ρ_h=0.45%±0.05 while that ratio for the lower 2/3 of the flare height is ρ_h=0.075%±0.025.

Where;

$\rho_h = 2 A_b / S D$

S = Spiral pitch

D = Column diameter

A_b = Area of spirals

To investigate these provisions and their effectiveness, two flare details were developed. The first one had a flare lateral reinforcement ratio that complied with the above-motioned provisions. The second detail had constant lateral flare reinforcement ratio along the total height of the flare. This was set to the lowest value of ρ_h=0.075%.

Bent Beam Design

To match the prototype, the center-to-center span of the bent should have been 90 inches. Since it was decided to use lead to apply the axial load, there was insufficient spacing between the columns to accommodate all of the lead. For this reason, the span was increased to 107 inches. The beam's depth was also increased in order to have the same relative flexural stiffness between the columns and the beam as in the prototype. The bent beam was designed according to Caltrans' recommendations, which states that the beam capacity should be 1.2 times the capacity of the plastic hinge in the column. This is done to assure that a plastic hinge would form in the columns rather than the beam.

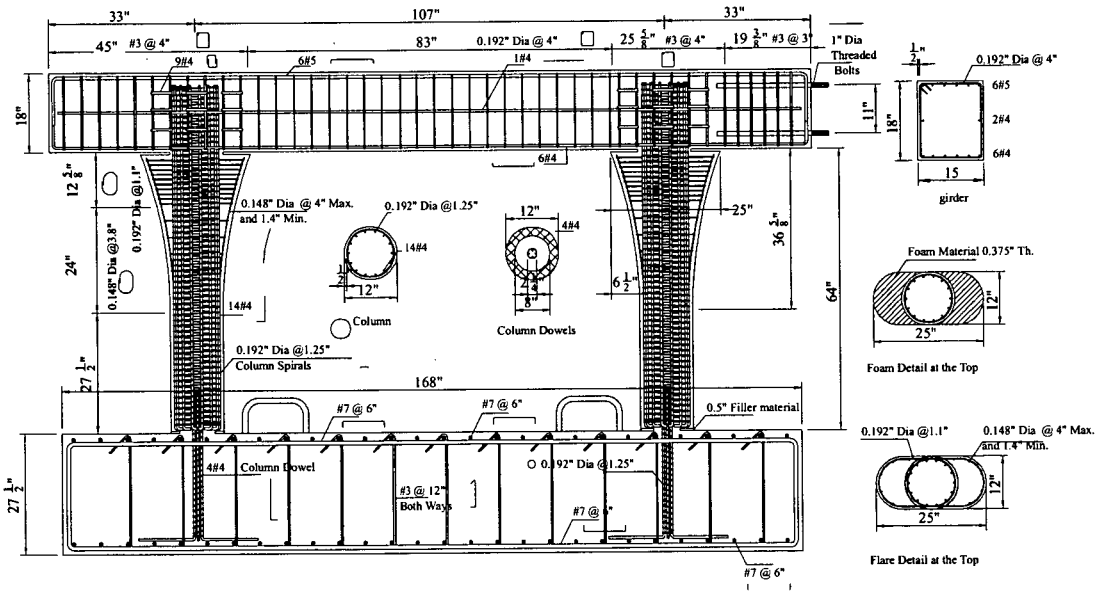

Figure 2. Specimen LFCD1 layout and reinforcement detailing

Analysis

An analysis of the specimens was made in order to calculate the system natural frequency, initial stiffness, and the maximum load capacity. The analysis was also used to determine the earthquake record to be used to test the specimens. The system is complicated due to the abrupt change in geometry at the top of the column gap region and the base hinge region. A finite element non-linear analysis was used in order to estimate the load-displacement curve of the bent. A simple hysteric model was also used to determine the earthquake response.

Finite Element Modeling and Analysis

A simplified plane stress model was used to model the bent. The concrete elements were 2-D plane stress elements having a thickness equal to the structure's thickness. The reinforcement was modeled as a 2-D beam element in order to model the dowel action. Contact elements were used at the top of the flare and the bottom of the beam within the gap region. Gap elements were also used in the base hinge region. Since the footing was heavily reinforced, it was modeled as a rigid linear elastic region. The footing was prevented from moving in any direction by restraining the degrees of freedom of the outer nodes, Fig. 3. ADINA, a non-linear finite element program, was used for performing the analysis (ADINA 1999).

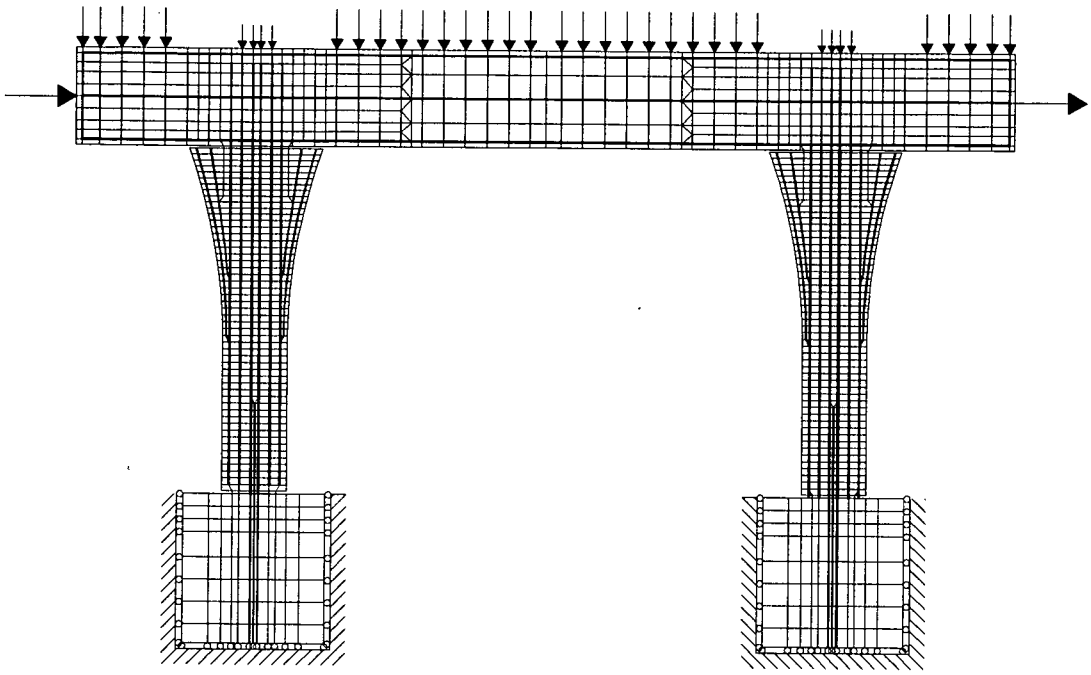

Figure 3. Finite element model

The lateral load in the analysis was applied as two concentrated loads on each end of the beam. Several options are provided for the concrete model. The Kupfer model was selected. For the reinforcement elements a bilinear stress-strain curve was used. A pushover analysis was performed by incrementing the lateral load gradually. The program goes unstable at the beginning of the longitudinal reinforcement yielding due to the fact that a small number of elements become crushed resulting in a change in the global stiffness matrix. In order to prevent the instability, the crushed elements were removed manually and multiple runs were performed in order to get the load-displacement curve. To verify this technique an analysis was performed using plane stress elements and the multiple runs technique for a previously tested circular column (Ashraf El-Bahy and William C. Stone 1996). The result of the analysis showed good consistency between the experimental and analytical results. Fig. (4) shows the deformed shape and the load-deflection curve for the flared column bent structure.

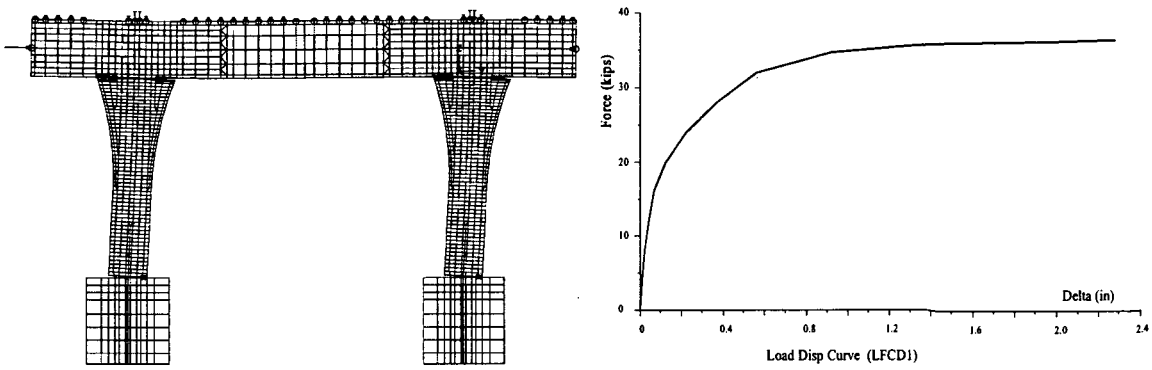

(a) (b)

Figure 4. (a) Deformed shape (b) Load displacement curve

The finite element analysis results showed that:

- The failure occurred in the gap located at the top of the columns due to yielding of the reinforcement and concrete crushing.
- Extensive cracking occurred in the beam-column region.
- Cracks spread along the flare height while no crushing occurred in this region.

The analysis using ADINA was stopped before gap closure at the top of the flare or at the base of the column. Currently, more sophisticated analysis is being done using a program called DIANA in order to extend the analysis.

Seismic Analysis

Analysis was also done using a program called RCSHAKE (Patrick Laplace 1999) that was developed at the University of Nevada, Reno. This analysis was used to excite the model with different earthquake records. The program uses an idealized bilinear load deflection curve, the mass of the specimen and a scaled earthquake record under consideration. The earthquake time step is scaled with a scale factor equal to the square root of the model scale factor. This enables the same behavior from the model as from a prototype subjected to the same earthquake. The Northridge Sylmar earthquake record was found to be the most suitable.

Testing

The specimens were constructed at the University of Nevada, Reno. A total of 110 strain gauges were attached to reinforcement in the columns, flares and the beam-column connections. Material properties for the specimens are summarized in Tables 3 and 4.

Table 3. Reinforcement yield stress

Reinforcement Diameter	Yield Point (ksi)
#5	70
#4	62
#3	65
Dia. 0.195	60.6
Dia. 0.147	71.3

Table 4. Concrete Compressive Strength on testing day (psi)

Member	LFCD1	LFCD2
Footing	5107	6880
Columns	5436	6332
Girder	5580	5252

The footing was tied to the shake table using prestressed steel bars to prevent any uplift during the test. The axial load was applied using steel buckets filled with lead blocks. The maximum vertical load capacity that the shake table can sustain limited the weight of the specimen plus lead to 100 kips. The specimen weight was about 30 kips including the footing. The total axial load for both columns was 101.5 kips. In order to reduce the weight on the table, 40 kips of axial load was modeled using self equilibrating rams in combination with the mass rig, Fig. 5. The mass rig is a steel structure supported by frictionless pins so that it allows the system to move laterally without restraining it. The four rams were mounted over the two columns and the mass rig was connected to the specimen with a rigid link.

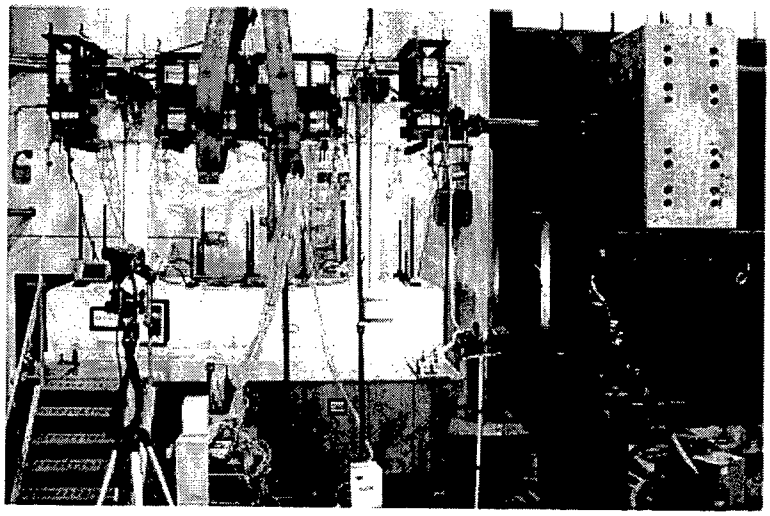

Figure 5. Test setup

Beside the strain gauges, 34 transducers were used to measure the curvature along the beam height, beam-column connection inplane displacements, out-of-plane displacements and horizontal movement of the bent and the column base. Accelerometers were mounted on the table and on top of the specimen.

Runs and Observations

The loading procedure for the specimen consisted of a series of earthquake runs. The runs steps were chosen so that it would capture the important points like cracking, yield and ultimate. The specimens were excited with scaled versions of the Sylmar record. The acceleration of the original record was multiplied by a factor. The following numbers are the factors used for the series of earthquake records: 0.15, 0.5, 0.75, 1.0, 1.25, 1.5, 1.75, 2.0, 2.125, 1.75, and 1.75 times Sylmar. During the test of LFCD1, it was observed that after 2.125 Sylmar the frequency of the bent dropped dramatically from an initial value of 3.2 Hz. to1.0 Hz. Because of this large drop it was decided not to increase the motion but to repeat lower motions to characterize the system. The 1.75 Sylmar records were repeated twice for LFCD1 and once for LFCD2. Fig. 6 shows final crack patterns for LFCD1 while Fig. 7 shows final crack pattern for LFCD2. Observations during the test and maximum strain level reached are summarized in Table 5.

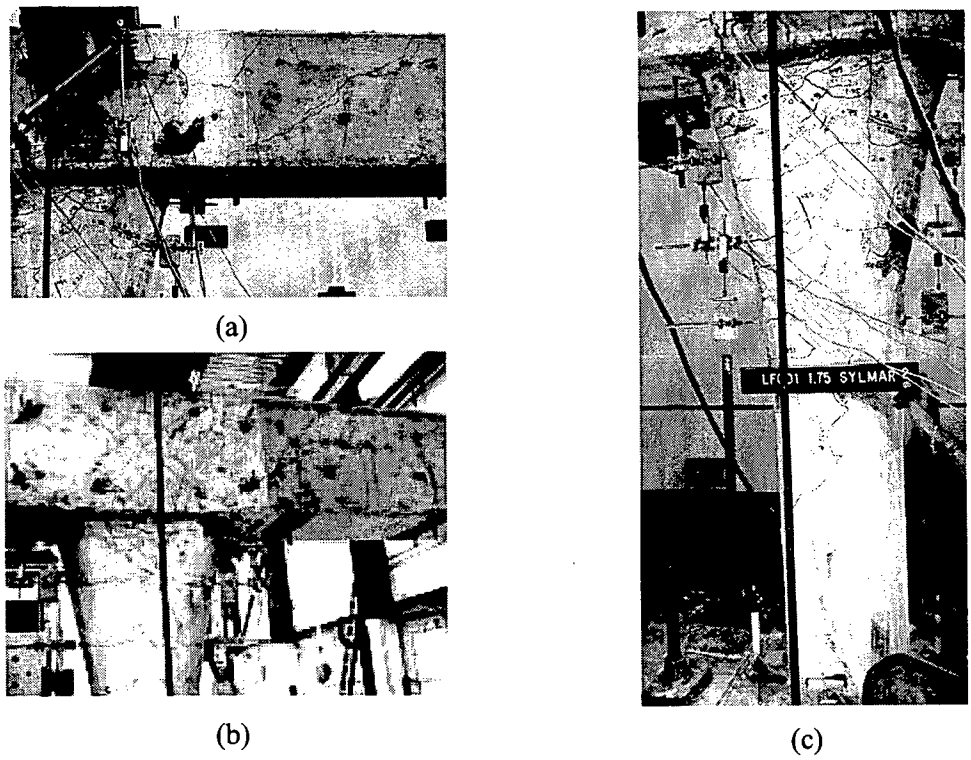

Figure 6. LFCD1 crack patterns, (a) shear cracks in the beam, (b) beam column connection cracks, (c) column cracks

Table 5. Summary of test observations and maximum strain

Factor	LFCD1 Observations	LFCD1 Strain*	LFCD2 Observations	LFCD2 Strain*
0.15 - 0.5	Very minor cracking in the beam-column connection and in the column.	0.00288	Very minor cracking appears in the beam-column connection and in the flare region.	0.0016
0.75 & 1.0	Cracks increased in the beam-column connection and initial cracks in the flare region.	0.013	A significant increase of cracking in the beam-column connection occurred. Flare cracks increased in length and new cracks started to form	0.011
1.25	A significant increase of cracking in the beam-column connection.	0.0144	Very minor crack development in beam-column connection. Shear and flexural cracks appear in the flare region. Concrete cover spalling in the top portion of the flare.	0013
1.5 & 1.75	Cracks formation in the beam-column connection drops while the number and extension of diagonal cracks in the flares increases	0.016	Crack development stopped in the beam column connection while shear and flexural cracks increased in the flare and in the bottom of the column.	0.017
2.0 & 2.125	Flare cracks increased and widened. Concrete spalling was observed in the middle third of the column and at the top of the flare	0.018	Flare cracks increased and widened. Shear cracks along the column height. Vertical cracks appeared in the lower part of the column. Extensive concrete spalling occurred in top portion of the flare region.	0.026
1.75	Extensive shear cracking extends along the column height. The displacement under 1.75 Sylmar was equivalent to 2.125 Sylmar	0.05	Flare cracks increased extensively and widened. Concrete spalling occurred in top portion of the flare region	Not Avail.
1.75	Same behavior as first 1.75 Sylmar.	0.05	N/A	N/A
After bucket removal	Many wide shear cracks in the beams. Extensive flexural cracks in the middle of the beam span.		Shear cracks found in the beams. Few flexural cracks were found in the middle of the beam span.	
Yield Displacement	0.44 in		0.327 in	
Yield Force	15.03 kips		19.82 kips	
Maximum Displacement	6.3 in		6.27 in	
Maximum Force	63.5 kips		59.6 kips	
Ductility Ratio	14		19	

* Strains in Main Column Reinforcement

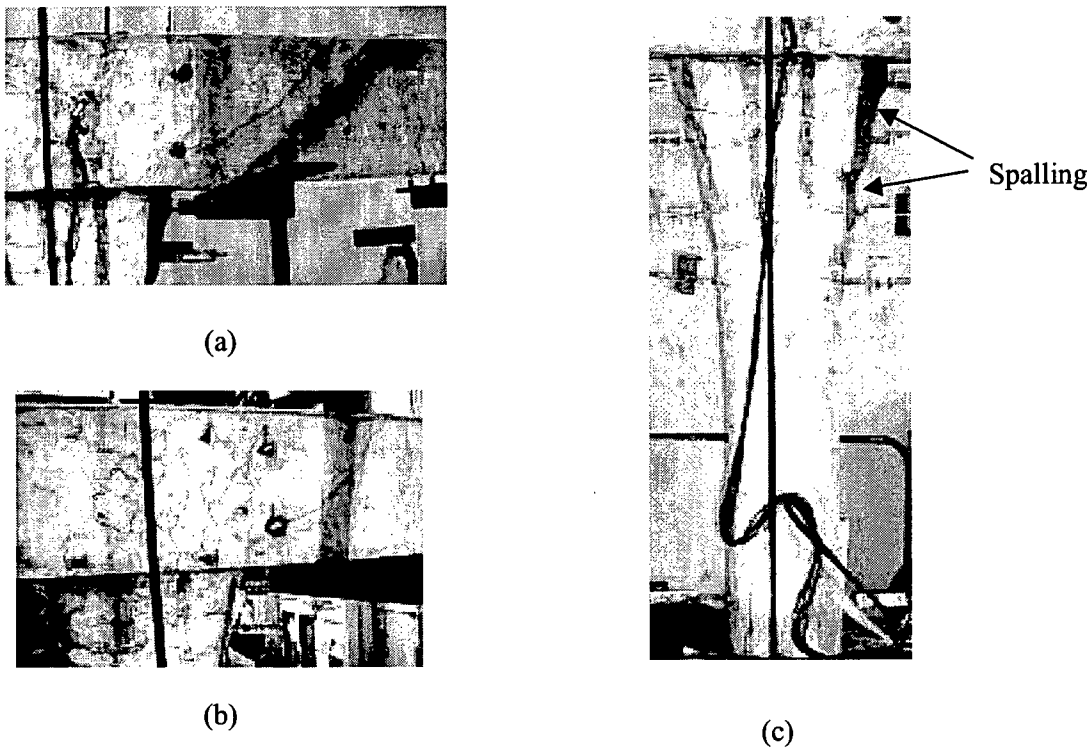

Figure 7. LFCD2 crack patterns, (a) shear cracks in the beam, (b) beam column connection cracks, (c) column cracks

The relative rotation between the beam and the column increased dramatically after yielding of the reinforcement in the gap region causing the gap to be closed for both the two specimens. However, the level of concrete crushing in LFCD2 was much higher than that in LFCD1. The accumulative load-deflection curve of the two specimens for all runs is shown in Fig. 8.

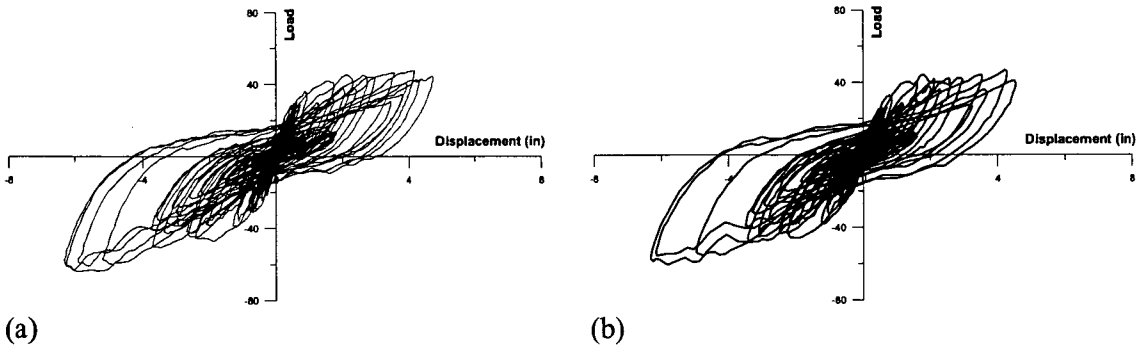

Figure 8. Accumulative load-displacement curve, (a) LFCD1, (b) LFCD2

Fig. 9 shows the envelope curve for the two specimens and the results from the finite element analysis as well. The graph shows a kink in the load-deflection envelope at approximately 3.8 inches for LFCD1 and LFCD2 followed by a large increase in the overall stiffness. This behavior was mainly due to the gap closure that caused an increase in the load carrying capacity that was predicted to be 36.0 kips. The difference of gap closure effect on the load-displacement envelope of the two specimens was because of concrete crushing of LFCD2 at the top portion of the flare. This behavior reduced the capability of the flare to transfer force to the beam.

The experiments were stopped due to concerns about the overall stability of the specimen. Since the reinforcement at the top of the columns was near the strain-hardening region, bar fracture could cause the top of the column to quickly lose moment capacity. At a future date, it is hoped that the bents will be pushed to failure in a slow push test. It was also observed that while the last two runs had smaller input accelerations, the displacement histories were the same as 2.125 Sylmar. Another general observation was that the flares crushed only slightly at the top of the column for LFCD1 while in LFCD2 the concrete was crushed in the top portion of the flare and spalling extended to approximately 2/3 of the flare height. Increased moment capacity did lead to shear cracking in the middle portion of the flare and a shear crack in the beam as well as concrete crushing in the middle of the flare (see Fig. 6c, 7c).

LFCD1 shows wider and longer shear crack plus many small shear and flexural cracks spread over the beam span. Another important observation is that the shear crack appearing in LFCD1 started after a distance of about d/2 from the end of the flare. In LFCD2, this distance is measured from the column core. This shows that the extensive concrete spalling shifted the primary load path to the core of the column.

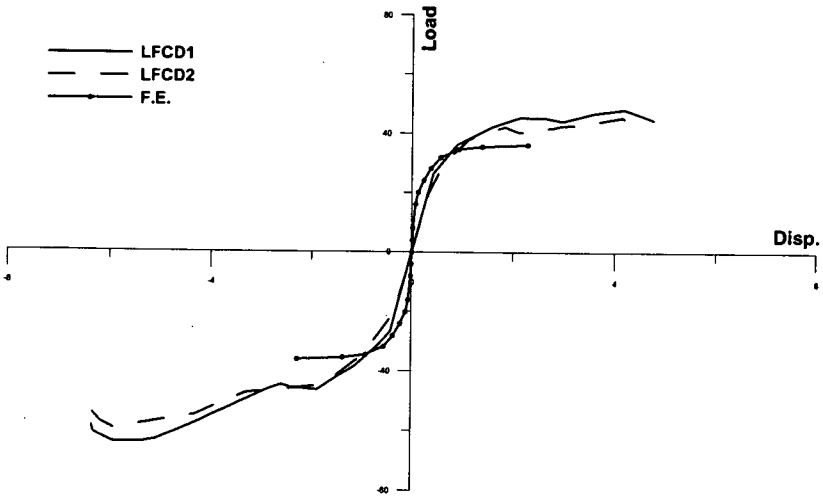

Figure 9. Load-displacement envelope curve

Conclusions

- The ductility ratio achieved by the proposed details is above the target limit that is recommended by Caltrans.
- While the ductility level is adequate, the closure of the gap increased the load carrying capacity of the bent that led to shear cracks in the columns. This behavior is undesirable for it might lead to brittle shear failure the columns.
- The gap closure affected the plastic hinge formation at the top of the column, and hence, transferred higher loads to the beam that resulted in shear cracks in the beam.
- The lateral reinforcement in the top third of the flare should be proportioned so that it insures the spalling of the concrete in this region to prevent further load transfer through the flare and insures the flexural plastic hinge behavior in the gap region.
- The use of the gap should be accompanied with calculations for the gap width that prevents the gap from being closed during large displacements.
- An analysis or design based on only the column core stiffness did not accurately model the observed behavior. Analysis that is more representative of the system behavior is under development.

Acknowledgement

Caltrans provided funding for this research. The authors would like to express their appreciation for this support. The authors would like to thank all the staff that was responsible for the laboratory work. The opinions expressed in this report are those of the authors and do not necessarily represent the opinions of the sponsor.

References

Klaus-Jürgen Bathe (1996). *Finite Element Procedures,* Prentice Hall, Upper Saddle River, NJ.

ADINA Reference Manuals (1999). ADINA R&D, Inc, Watertown, MA

Caltrans Seismic Design Criteria, Version 1.1 (July 1999). Caltrans, Sacramento, CA

Anthony V. Sanchez, Frieder Seible, and M.J. Nigel Priestley (1997). Seismic Performance of Flared Bridge Columns, *Report No. SSRP-97/06*, The University of California, San Diego.

Ashraf El-Bahy, Sashi K. Kunnath, Andrew W. Taylor, and William C. Stone (1996). Cumulative Seismic Damage of Reinforced Concrete Bridge Piers, *Report NCEER-96-00XX*, University of Central Florida, Orlando.

Laplace, Patrick, David Sanders, M. "Saiid" Saiidi, and Bruce Douglas (1999). Shake Table Testing of Flexure Dominated Reinforced Concrete Bridge Columns. CCEER #99-13, University of Nevada, Reno, Department of Civil Engineering, pp 152.

Unit Conversion

1 inch = 25.4 mm, 1 ksi = 6.895 MPa, 1 psi = 6.895 kPa, 1 kip = 4.448 N

Seismic Retrofitting for Bridges in Osaka City

Kenji Shimoda[1], Shigeo Takei[1], Tadaaki Maruyama[2],
Kozo Nishimori[3] and Yukiko Mitsugi[4]

Abstract

From experience of the Hanshin-Awaji Earthquake on January 17, 1995, Osaka City has been carrying out various plans under the theme "Build up a Strong City against Earthquake". The seismic retrofit for bridges is adopted as one of the most important plans in order to guarantee rescuing activities in damaged area, public service for water, gas etc., and so on. However it is impossible to raise the grade of the all bridges for current seismic standard, because there were 761 highway bridges under management of Osaka City. Structure-systems and construction years for these bridges are various. Therefore it is important to carry out effective plan to consider function, capacity for strength and importance of the bridge and cost. In 1996, original standard for evaluation was drawn up, and general plan was devised against earthquake in Osaka City.

1. Introduction

The Hanshin-Awaji Earthquake that struck the southern part of Hyogo Prefecture on January 17, 1995 (epicenter: lat. 36.4°N., long. 135.0°E., depth 14 km, magnitude 7.2 on the Richter scale) claimed the lives of approximately 6,000 parsons; news of the catastrophe spread throughout the world. In Kobe City, in addition to the collapse of buildings, many public works that form the urban infrastructure also suffered extensive damage. In particular, damage to bridges was unprecedented, both in scale and quantity; many elevated bridges of the Hanshin Expressway Kobe Line either collapsed; elevated bridges on the Shinkansen Line also collapsed.

As for Osaka City, in the northwestern part of the city close to the epicenter, 21 bridges were damaged. Though none collapsed, three had to be closed to traffic. The main characteristics of the damage were: 1) cracks in concrete piers of elevated bridges, 2) breakage of supports, 3) breakage of concrete around supports.

Based on these damage surveys, to ensure seismic performance against a direct-type urban earthquake, the Ministry of Construction took the lead in revising the seismic standard of bridges, and issued a new specifications[1] in December 1996. Meanwhile, in addition to restoring damaged bridges, Osaka City has worked out countermeasures for seismic retrofitting existing bridges, and is now vigorously executing such work.

This report is a summary of the basic policy of seismic retrofit for bridges in Osaka City, and an outline of the overall plan and implementation examples.

2. Present Condition and Design Standards of Bridges in Osaka City

As of April 1997, there were 761 highway Bridges under the management of Osaka

1) Public Works Bureau, Osaka Municipal Government
2) Osaka City Road Corporation
3) Bridge Maintenance Dept., Osaka Branch, Sogo Engineering Inc.
4) Structural Design Dept., Tokyo Branch, Sogo Engineering Inc.

City, extending a total length of 44.4 km, with an area of 691 thousand square meters. Of these bridges, the oldest was constructed in 1913; 258 bridges were constructed prior to 1965, before the advancement of seismic design technology; these comprise approximately one-third of total (Fig. 1). Also, these bridges were not constructed according to a unified design standard, and so have diverse types of superstructures and under-structures.

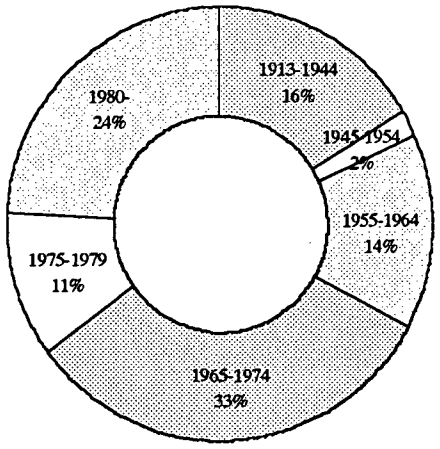

Fig.1 Construction Years of bridges in Osaka City (Total 761 bridges)

The design standard of bridges is stipulated in the "Specifications for Highway Bridges," with various sections added at every revision, with reference to damage caused by earthquakes. Basically, bridge design limits deformation of structural parts within the elastic range, by multiplying 20 % of the acceleration of gravity by the component weight to determine horizontal load. In the 1990 revision[2], two-level performance criteria was adopted to cope with major earthquakes having very low probability of occurring during the design life of the bridge. In addition to elastic design, ductility of components is strengthened to prevent collapse even if load (determined by multiplying acceleration of gravity (G) by component weight) exceeds the elastic limit. However, few bridges in Osaka City are designed according to this standard. Moreover, in the above-mentioned December 1996 design standard revision, to ensure ductility of components, maximum horizontal load was stipulated as twice the acceleration of gravity multiplied by its weight. To satisfy the new standard, components (piers) must have a displacement ductility demand μ (ultimate displacement/elastic displacement) level of approximately 6 to 8 or more. Again, almost no bridge in Osaka City conforms to the new standard. While the new seismic standard assumes the Hanshin-Awaji Earthquake, even in Kobe City, where this great earthquake struck directly, only about 10% of the bridges were damaged. It is thought that, even with old standards, various factors contribute to seismic performance, including the fact that assumptions used in the design process take a safety margin into account. For this reason, it is not necessary to retrofit all bridges that do not conform the new standard in terms of design.

3. Basic Policy of Seismic Retrofitting for Bridges

The purpose for seismic retrofitting of bridges were determined following the policy of the "Investigation Meeting on Earthquake Measures for Osaka City Public Works and Buildings[3]." The policy for bridges is summarized in the following three points:

1) Bridges on emergency transport routes and evacuation routes must be usable even immediately after a major earthquake.
2) As for bridges on arterial roads, while temporary suspension of traffic may be acceptable, traffic must be resumed at an early stage through emergency repair.
3) As for viaducts over railroads and roads, secondary disasters caused by collapse must

be prevented.

Based on this policy, while some damage is tolerable in a major earthquake, a bridge retrofitting plan must be devised according to conditions of the roads at the time of disaster. Accordingly, objective evaluation criteria needed for determining the importance of each bridge at the time of an earthquake is established, and all bridges are classified into five ranks. Next, a menu of measures is prepared for each rank. It is also necessary to evaluate the seismic capacity of each bridge to determine the need for measures, and the urgency of implementation. For this also, evaluation criteria are established for classifying all bridges into ranks. With reference to this classification, seismic retrofitting methods for each bridge are selected. Furthermore, financial restrictions and the economic effect of seismic retrofitting work (e.g. loss caused by traffic restrictions) are taken into consideration when devising the overall plan. The flow of this work is shown in Fig. 2.

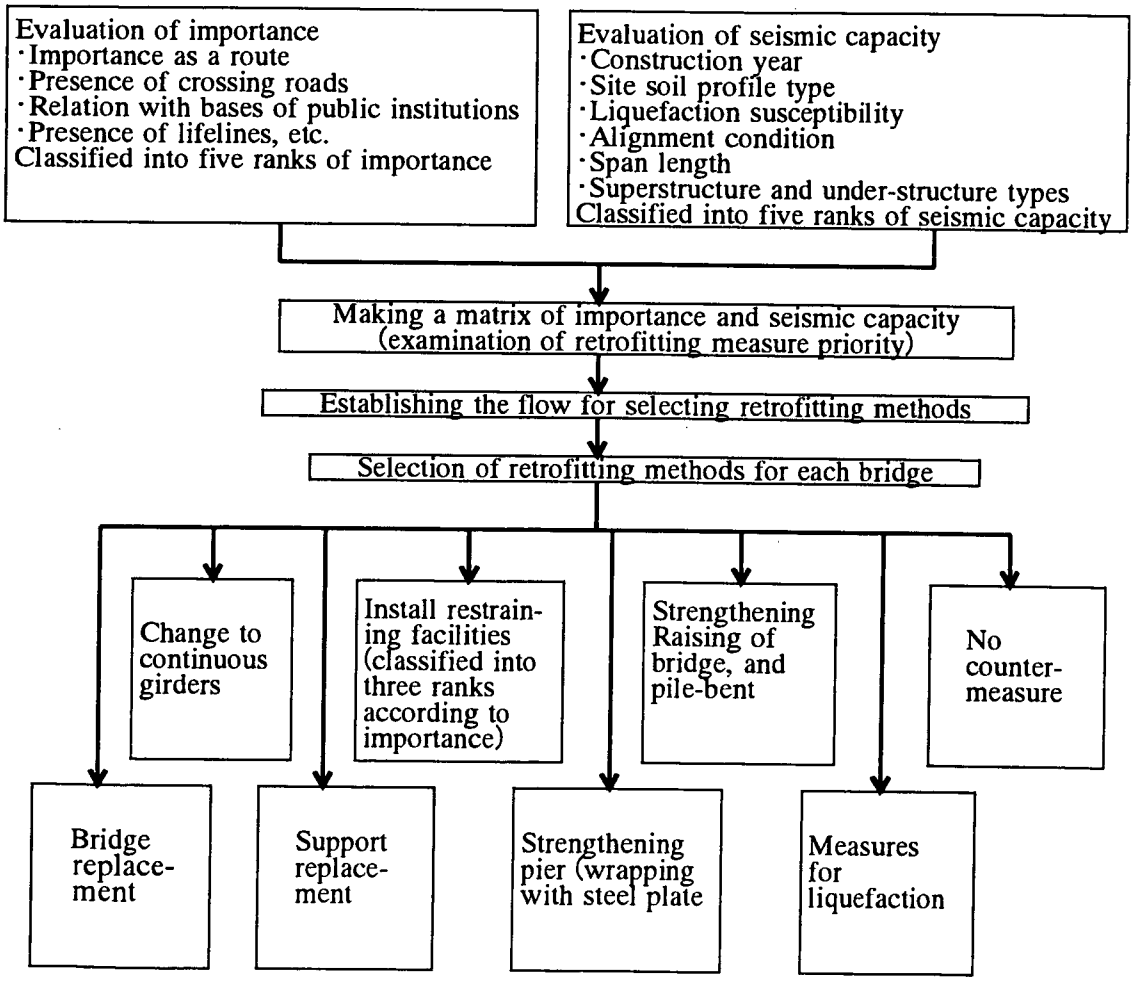

Fig.2 Flow of Seismic Retrofit Plan

4. Evaluation of Importance

For importance evaluation, a database call the "Osaka Bridge Administration System (OBAS)[4]" was used. Subjects of evaluation were limited to highway bridges only.

Bridges other than those under the management of the Public Work Bureau were also included in the evaluation.

4.1 Evaluation Items

The following evaluation items were selected for determining the importance of each bridge:

1) Evacuation routes: routes designated by Osaka City Regional Disaster Prevention Plan[5] (74-bridges).
2) Emergency transport routes: routes designated by Osaka City Regional Disaster Prevention Plan (205-bridges).
3) Main arterial roads: (337-bridges).
4) Viaducts over railroads: classified into three groups, according to the types of railroad.
   Main passenger lines (17-bridges),
   Local passenger lines (1-bridge),
   Freight lines (11-bridges)
5) Viaducts over roads: bridges over national roads and main local roads (18-bridges).
6) Bridges difficult to bypass: bridges that may isolate an area if damaged, and main roads where the length of a detour route between two intersections with a bridge in-between is more then 3 km (53-bridges).
7) Bridges where emergency repair difficult: bridges with a span length of more than 15m (432-bridges).
8) Bridges serving as routes to relief bases at time of disasters: bridges within 1 km radius from designated bases, and located on main roads
   <Applicable bases>
   City Hall, Prefectural Police Headquarters and Prefectural Offices (39-bridges)
   Fire stations (151-bridges),
   Five major municipal hospitals (38-bridges),
   Ward offices (138-bridges)
9) Bridges on which main lifelines are involved: Electricity, gas, water and telephone
   Electricity: More than 20 power-transmission lines (36-bridges)
   Gas: Pipes with diameter of 500 mm or larger (27-bridges)
   Water: Water pipes with diameter of 500 mm or larger (28-bridges)
   Telephone: More than 20 cables (73-bridges)

The figures in parentheses indicate the number of bridges under each item.

4.2 Evaluation of Importance

An evaluation of bridge conditions at hazard was made considering two time phase. First, Case-1 evaluated the situation from right after an earthquake to about two days later. As the first priority would be saving lives, evacuation routes were evaluated as the most important item, followed by bridges to bases of information and relief activities, such as city hall, police stations, fire stations and hospitals. Case-2 evaluated the situation approximately one month after an earthquake. For emergency restoration work within the city, emergency transport routes and main arterial roads are considered important, for transporting people and goods from outside the city. In addition, bridges

without bypass or with many lifelines were given high evaluation. Evaluation points in each case are shown in Table 1. This evaluation involved several trial calculations; Osaka City Officials in charge of bridges examined the results and finalized the evaluation based on experience. Lastly, for overall evaluation of importance, it was decided to treat Case-1 and Case-2 equally, and determine the importance of each bridge by the sum of the evaluation points of the two cases.

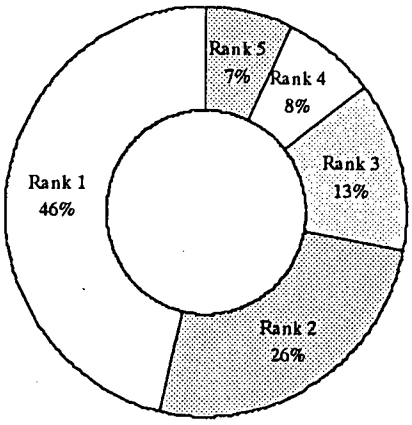

Fig.3 Results of Importance Evaluation (Total 749 bridges)

4.3 Evaluation Results

As shown in Table 1, the maximum evaluation of importance is 40 points, and importance evaluated based on the properties of each bridge is classified into five ranks. An evaluation of between 40 and 20 is Rank 5, the most important, followed by Rank 4 (19-16 points), Rank 3 (15-12 points), Rank 2 (11-4 points), and Rank 1 (3-0 points). The percentage of each rank is shown in Fig. 3 (the total number includes bridges other than those under the management of Osaka City). From the highest rank of importance, the percentage is 7%, 8%, 13%, 26%, and 46%. This result indicates the following about each rank:

Rank 5: Located on an emergency transport route and main arterial road, and designated as an evacuation route, or passes over a railroad or road.

Rank 4: Located on an emergency transport route and main arterial road, or on an evacuation route and main arterial road, serves a base and has many evaluation items.

Rank 3: Located on an emergency transport route and main arterial road, or on an evacuation route and main arterial road, but has few other evaluation items.

Rank 2: Located on either an emergency transport route or a main arterial road.

Rank 1: Does not fall under the category of an emergency transport route, a main arterial road, an evacuation route, or a viaduct over a railroad or road.

Table 1 Criteria for Evaluation of Importance

	Evacuation Route	Emargency Transport Route	Main Arterial Road	Bridge over Railroad	Bridge over Main Road	Difficult to Secure Bypass	Emergency Repair Difficult	Bases: City Hall Prefectural Polis headquarters Prefectural Office	Bases: Fire station	Bases: Hospital	Bases: Ward office	Main lifelines	Total
Case-1 immediately after earthquake	5	2	1	main l. : 3 local l. : 2 freight l.:1	2	--	1	2	2	2	--	--	20
Case-2 during emergency repair	--	5	3	main l. : 3 local l. : 2 freight l.:1	2	2	1	1	--	--	1	3 types more:2 1 type more :1 No lifeline :0	20
Overall evaluation (case-1)+ (case-2)	5	7	4	6	4	2	2	3	2	2	1	2	40

5. Evaluation of Seismic Capacity

The need for measures for seismic retrofitting is based on whether or not the seismic capacity of a bridge is sufficient against an anticipated earthquake. However, as a direct active fault earthquake is anticipated, seismic power will be much stronger than what is supposed at the time of design. Therefore, seismic capacity evaluation by the conventional design category will define almost all bridges as having insufficient seismic capacity. Also, considering the diversity of construction years and types of bridges in Osaka City, analysis of bridge movements beyond the elastic range will require huge cost. Moreover, to find out whether a bridge can be used or not if an earthquake occurs, it is necessary to analyze which component of the bridge's overall system will receive what kind of damage, and such estimate is technically extremely difficult. Therefore, for evaluation of seismic capacity as well, it was decided to conduct a relative evaluation of the properties of each bridge, using the data system.

5.1 Evaluation Items

The following evaluation items were selected for determining seismic capacity.

1) Applicable design standard

As old bridges are outworn and built according to obsolete standard, it is considered that the older a bridge is the less seismic capacity it has. Based on this concept, bridges are classified into four groups:

Construction year	Applicable Design Standard (Year Issued)	
-- 1956	1926	1939
1957 -- 1972	1956	1964
1973 -- 1980	1971	1972
1981 --	1980	1990

2) Site soil profile type

The weaker the ground is the greater the amplification of an earthquake wave, and the deeper the supporting ground is the weaker the ground and the greater the possibility of damage. There are four soil profile types.

Type 1: Rock bed
Type 2: Depth of supporting layer 0 -- 10 m
Type 3: Depth of supporting layer 10 -- 25 m
Type 4: Depth of supporting layer 25 m --

3) Liquefaction

Based on the Contour Map of Liquefaction Susceptibility (March 1996)[5] made by Osaka City, bridges are classified into four groups.

4) Superstructure type

In general, seismic capacity is small with bridges using cantilever girders, followed by bridges with linked simple girders.

5) Plane alignment

As movements of a skew bridge and curved bridge are complex at time of earthquake and may result in damages (including collapse) not predictable at the design stage, these bridges are classified into a category different from other bridges.

6) Superstructure materials

As reinforced concrete girders and prestressed concrete girders are heavier than steel girders, they are considered to have slightly less seismic capacity.

7) Vertical alignment

For the same reason as plane alignment, bridges of 6% or more vertical alignment are classified into a separate category.

8) Restrainer

Bridges are classified according to the presence or absence of restrainers.

9) Girder length

Based on the assumption that the longer the girder length, the greater the relative damage by earthquake, bridges are classified into girder length of 35 m or longer and under 35 m.

10) Support length

Classified according to whether the support length stipulated in the 1980 Specifications[6] is secured.

11) Under-structure type

The single column type, which suffered great damage in the Hanshin-Awaji Earthquake, was classified into a separate category.

12) Under-structure materials

Non-reinforced concrete and pile-bent were classified into a separate category.

13) Under-structure height

The taller a pier is greater its response displacement and the less its seismic capacity. As specifications prior to 1971 made no extra design load allowance for response, bridges are classified into three groups according to pier height.

14) Foundation work type

Seismic capacity is inferior in the order of wooden piles and pre-molded reinforced concrete piles. Classified into three types.

15) Balance of structural system

If supporting ground height, foundation type, adjoining girder length, and pier height of a bridge are disproportionate, the bridge is considered to have low seismic capacity.

16) Seismic inspection result

Of bridges inspected in the past for seismic performance and those requiring retrofit, those that have not been retrofitted are classified.

17) Viaducts

As damage to viaducts was especially great in the Hanshin-Awaji Earthquake, viaducts are classified as having poor seismic capacity.

5.2 Evaluation of Seismic Capacity

Evaluation points of seismic capacity are shown in Table 2. Regarding the weight of this evaluation, as in the evaluation of importance, several trial calculations were made; Osaka City Officials in charge of bridges examined the results and finalized the evaluation based on experience. The greatest weight was placed on the applicable design standard (construction year). Though the table is divided into (A) Common items, (B) Superstructure, and (C) Under-structure, the product of all evaluation points is used as an index for evaluating seismic capacity. However, as bridges less than 15 m long and

equipped with abutments at both ends received almost no damage from the Hanshin-Awaji Earthquake, they are unconditionally considered seismic performance. Furthermore, superstructures and under-structures made of such materials as wood, stone, and brick are considered to have the lowest seismic capacity.

Table 2 Criteria for Evaluation of Seismic Capacity

	Evaluation Items		Evaluation Points and Classification							
(A)Ground, external force	①	Applicable specification	6.0	1926 Specifications 1939 Specifications	3.0	1956 Specifications 1964 Specifications	1.5	1971 Specifications 1972 Specifications	1.0	1980 Specifications 1990 Specifications
	②	Site soil profile type	2.0	Type 4	1.5	Type 3	1.2	Type 2	1.0	Type 1
	③	Liquefaction susceptibility	2.0	High	1.5	Medium	1.2	Low	1.0	Extremely low
		Evaluation point(PA)	=①×②×③				(min : 1.0, max : 24.0)			
(B) Superstructure	④	Superstructure type	3.0	Cantilever girder	1.5	Simple support (span 15m or longer)	1.0	Others		
	⑤	Plane alignment	1.5	Skew bridge Curved bridge	1.0	Straight bridge				
	⑥	Superstructure materials	1.2	RC, PC	1.0	Steel				
	⑦	Vertical alignment	1.2	6% or more	1.0	Less than 6%				
	⑧	Restraining facilities	2.0	None	1.0	Installed				
	⑨	Girder length	1.5	35 m or more	1.0	Less than 35m				
	⑩	Support length	2.0	A/S≦1	1.0	A/S>1				
		Evaluation point(PB)	=④×⑤×⑥×⑦×⑧×⑨×⑩				(min : 1.0, max : 38.9)			
(C) Under-structure	⑪	Under-structure type	2.0	T-type, L-type single column	1.0	Others				
	⑫	Under-structure materials	2.0	Pile-bent, non-reinforced concrete (excluding gravity abutments)	1.0	Others				
	⑬	Under-structure height	1.5	10 m or more	1.2	5m or more less than 10m	1.0	Less than 5m		
	⑭	Foundation type	2.0	Wooden pile	1.5	Pre-molded reinforced concrete pile	1.0	Others		
	⑮	Structural system balance	3.0	Bad-balanced	1.0	Well-balanced				
	⑯	Result of seismic damage inspection	2.0	Requires restraining facilities	1.0	Others				
	⑰	Elevated bridge on land	3.0	Elevated bridge on land	1.0	Others				
		Evaluation point(PC)	=⑪×⑫×⑬×⑭×⑮×⑯×⑰				(min : 1.0, max : 215.0)			
		Evaluation point (X)	=PA×PB×PC				(min : 1.0, max : 201,554)			

5.3 Evaluation Results

As shown in Table 2, depending on the properties of the bridge, seismic capacity evaluation varies from 1 to 201,554 points. As with the importance of bridges, the lowest seismic capacity is Rank 5 (120 or more points), followed by rank 4 (60 to under 120), Rank 3 (30 to under 60), Rank 2 (15 to under 30), and Rank 1 (under 15). The percentage of each rank is shown in Fig. 4. From low to high seismic capacity, the percentage is 9%, 10%, 10%, 14%, and 57%. The total number of bridges evaluated is less than that evaluated for importance, as bridges without any data in the database have been excluded. Bridges excluded were buried bridges and Box culvert type bridges, which are not subject to seismic capacity evaluation. From these results, it was found that bridges in northern Osaka, especially around the Yodo River, followed by bridges along the Osaka Bay area, have relatively low seismic performance. The main factors are the high possibility of liquefaction, weak ground, and the existence of many elevated bridges and high piers.

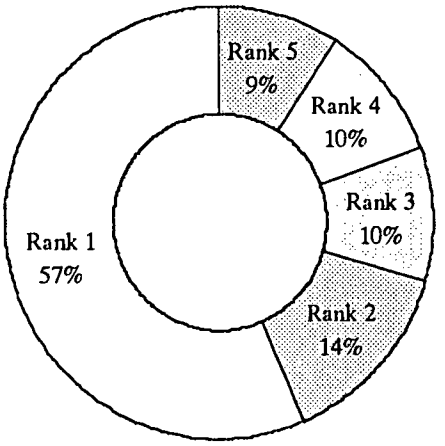

Fig. 4 Results of Seismic Capacity Evaluation (Total 677 bridges)

6. Seismic Retrofit Measures for Bridges

6.1 Examination of Priority

Based on evaluation results as to the importance and seismic capacity of each bridge, priority of retrofitting work was examined. As shown in Fig. 5, priority was evaluated by devising a matrix with importance ranked on the horizontal axis and seismic capacity ranked on the vertical axis. In this matrix, bridges in the upper left corner, with high importance and poor seismic capacity, require urgent measures; those in the lower right corner are low in priority, or do not require any measures. In determining priority, the importance of bridges — in other words, satisfying the functions of a bridge as a route — was given greater weight than seismic capacity, which is an individual property of each bridge. Thus, priority was established based on a 2:1 ratio of weight for importance and seismic capacity. In Fig. 5, priority is ranked from I to III; retrofit measures are to be implemented over a five-year period from 1996 to 2000, and other afterwards. The figures in parentheses in the matrix indicate the number of applicable bridges.

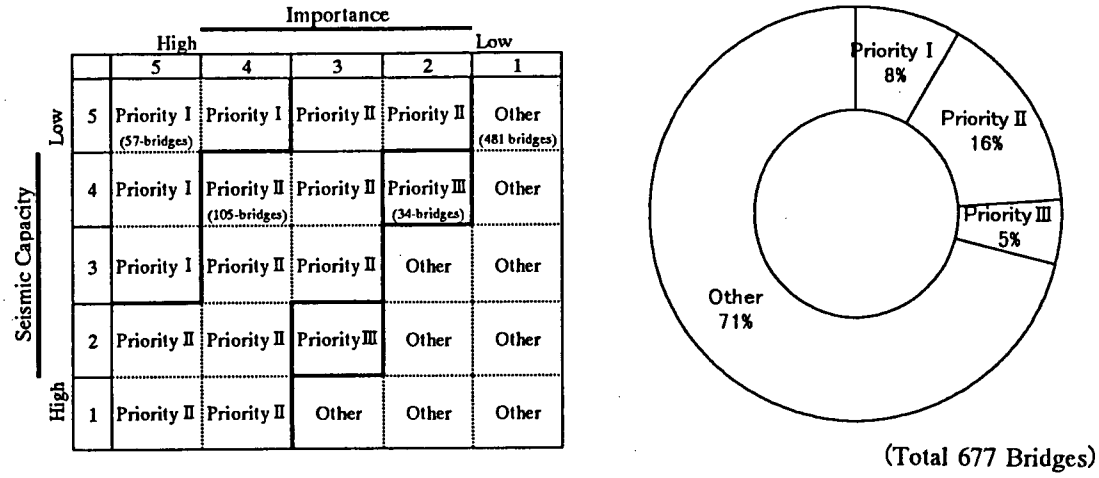

Fig. 5 Evaluation Matrix and Ratio of Each Retrofitting Priority

6.2 Selection of Retrofitting Measures

Retrofitting measures were selected following the flow chart in Fig. 6. Main measure are following four methods, setting up restrainers, strengthening piers, change of structural system (installation of continuous girders and replacement of supports), and measures against liquefaction. These measures are selected according to the importance and properties of the individual bridge. For bridge that is planned to replace, considering the priority, construction may be started early if construction of a new bridge has been planned in another project, however, bridge replacement is not planned as a seismic countermeasure only. This is due to financial reasons. The work flow begins by limiting object bridges to highway bridges under the management of Osaka City Public Works Bureau. Next, for bridges for which replacement is planned, immediate measures are restricted to installation of restrainers only, and according to the scheduled construction year, importance is lowered one rank, starting with bridges not subject to countermeasures.

For other bridges, retrofitting measures are determined on the basis of importance and

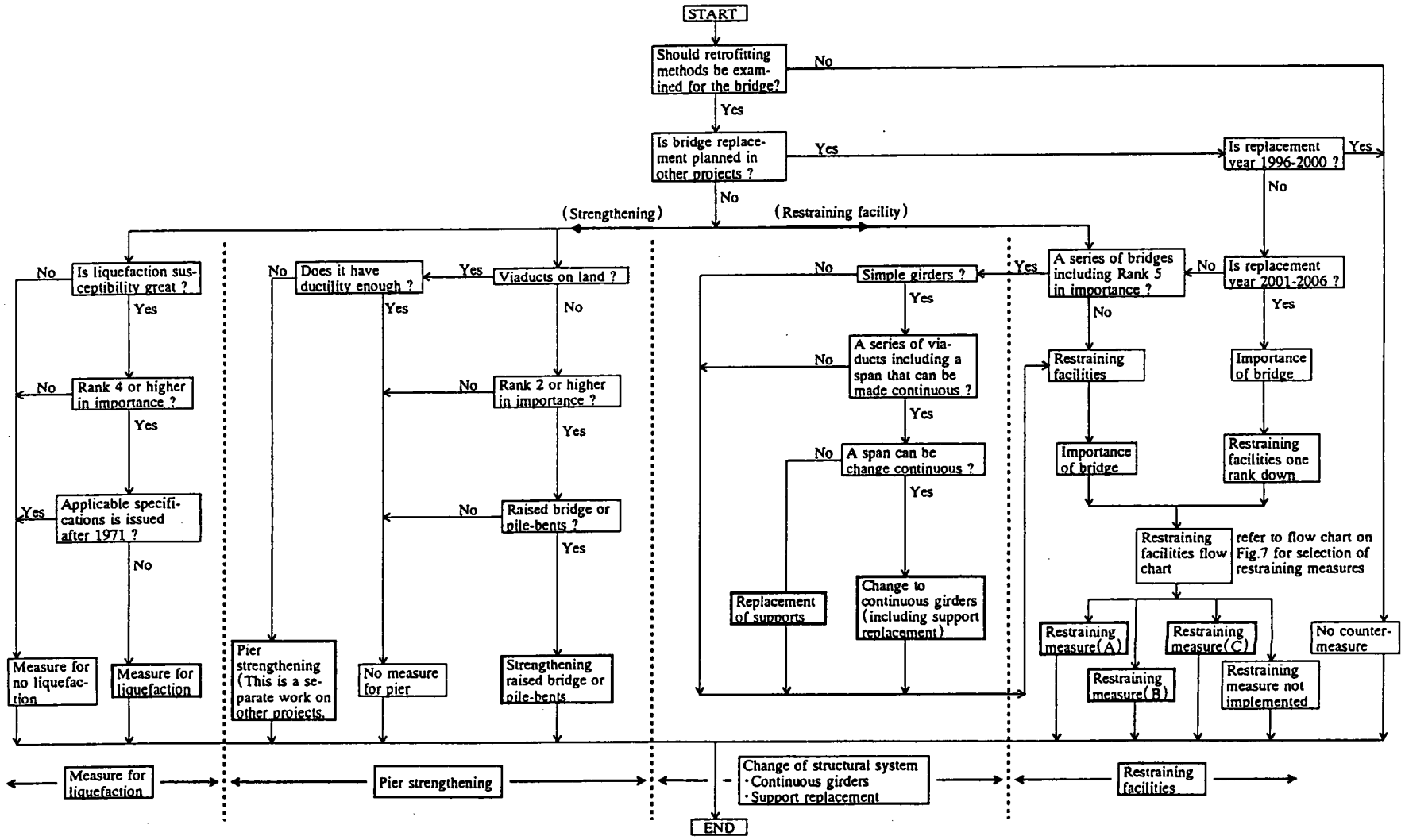

Fig. 6 Flow Chart for Selection of Retrofitting Methods

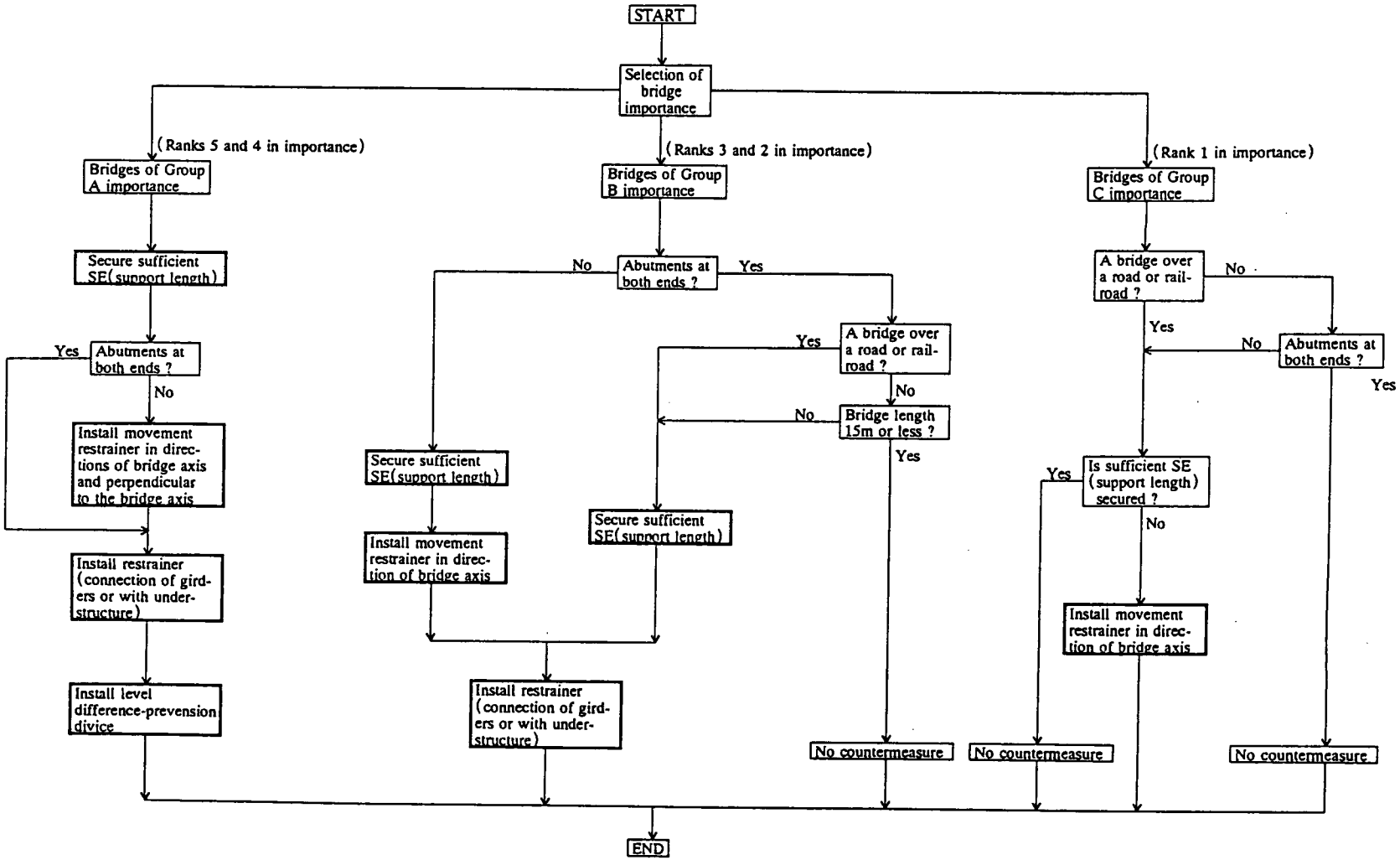

Fig. 7 Flow Chart for Selection of Bridges Requiring Restraining Facilities

bridge properties. Evaluation criteria were established taking into consideration the basic policy explained in Section 3; the financial situation and the availability of alternative routes. Applicable bridges for each retrofit measure, and an outline of each measure, are as follows:

1) Measure for liquefaction

This measure is for bridges in areas with the highest possibility of liquefaction, of Rank 4 or higher in importance, and without any consideration for liquefaction in design (designed according to specifications prior to 1971). The measure consists of ground improvement work or construction of gravel drains.

2) Strengthening pier

On the basis of damage caused by the Hanshin-Awaji Earthquake, elevated bridges built on land are subject to this method. Strengthening is done to increase pier yield strength and ductility. For reinforced concrete piers, steel plates are wrapped around each pier. For steel piers, the inside is filled with concrete, and the outside is reinforced with steel plates. For bridges raised as a measure against floods and those with pile-bents, which are of Rank 2 or higher in importance, strengthening work is carried out according to the structure of each bridge.

3) Change of structural system

Bridges of Rank 5 in importance, or a series of elevated bridges containing a bridge of Rank 5 in importance. Simple girders that can be structurally made continuous are changed into continuous girders. For continuous elevated bridges, if girders cannot be made continuous because of differences in plane position, only support replacement is carried out.

4) Restraining facilities

All bridges examined in Fig. 6 were examined according to the flow chart shown in Fig. 7 to select bridges for this measure. Restraining facilities are classified into three grades, and countermeasures are implemented according to the importance of each bridge.

Group A: Bridges of Rank 4 and 5 in importance

Securing of support length SE, restrainers in directions of bridge axis and perpendicular to the bridge axis; level difference prevention device

Group B: Bridges of Rank 3 and 2 in importance

Securing of support length SE, restrainers in the direction of bridge axis

Group C: Bridges of Rank 1 in importance

Securing of support length SE or restrainers in the direction of bridge axis

6.3 Overall Plan

The numbers of bridges corresponding to each retrofitting measure established in the previous section are shown in Table 3. As seismic retrofitting measures overlap for some bridges, the numbers of bridges requiring measures and those not requiring measures are shown in Fig. 8. Of the 761 bridges under the

Table 3 Number of Bridges by Seismic Retrofitting Method
(Methods overlap for some bridges)

Engineering Methods	Number of Bridges
Install restraining facilities	352
Pier strengthening	34
Change to continuous girder	18
Support replacement	25
Measure for liquefaction	14

management of the Osaka City Public Work Bureau, 352 (46%) will undergo some kind of retrofit. Of these, as explained in section 6.1, as bridges of particular importance and of low seismic capacity require urgent measures, work is scheduled for the five-year period from 1996 to 2000. These bridges number 144 (19%). While the total cost of this project is approximately 26 billion yen, 18 billion yen is allocated to the first five-year period, as many long and large bridges and continuous elevated bridges are included in bridges requiring urgent measures.

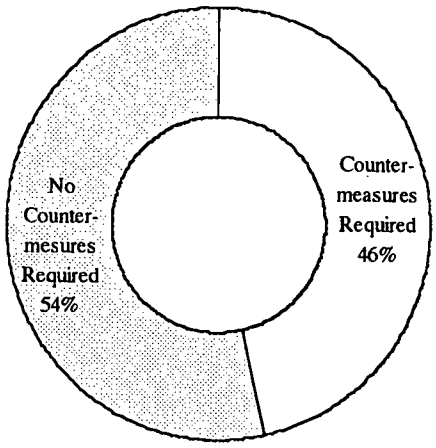

Fig. 8 Seismic Retrofitting Countermeasure Plan (Total 761 bridges)

7. Implementation of Retrofitting Work

For some bridges, retrofitting work have been carried out as a continuation of restoration work immediately after the Hanshin-Awaji Earthquake. As typical examples, two cases, further strengthening reinforced concrete piers of an elevated bridge and restrainer installation, are introduced below.

7.1 Strengthening Reinforced Concrete Piers of an Elevated Bridge

The most notable bridge damage caused by the Hanshin-Awaji Earthquake was the collapse of piers of elevated bridges. While none of the bridges in Osaka City suffered so great damage as collapse, cracking and minor separating of cover concrete occurred. Along with repair of damaged piers of elevated bridges, retrofitting work was also carried out. In addition, it was decided to implement further strengthening reinforced concrete piers of undamaged elevated bridges as well.

The majority of elevated bridges in Osaka City were constructed prior to 1970, and their horizontal design seismic intensity is approximately 20% of the acceleration of gravity. Compared with the present standard, no consideration was made for response at the time of an earthquake. Considering the case of a direct-type earthquake, double to triple the yield strength of the design seismic load at the time of construction will be required. It was therefore decided to wrap with steel plates around reinforced concrete piers, fill mortar inside, and install anchors at the footing to transmit steel plate stress to the foundation. The purpose of measure is as follows:

1) To change the ultimate yield strength of a pier to the cross section determined by bending (to prevent shear fracture from preceding bending).
2) To increase the yield strength of the entire pier.
3) To add ductility so as to prevent destruction even if a pier yields to stress.

7.2 Restraining Facility

Installation of a restraining facility is the most important main method among seismic measures for bridges in Osaka City. Eventually, therefore, approximately half the bridges will be equipped with some kind of restraining facilities. This will mainly involve

connecting the main girders together, or connecting piers and abutments with the main girders with cables. Also strengthening of hinges of cantilever girders and installation of a restrainer in the direction perpendicular to the bridge axis will be implemented on some bridges. In addition, to secure sufficient support length, the top surface of abutments and piers will be expanded in width. The purpose of this is to avoid the worst case, the collapse of a bridge, even if the bridge suffers some damage (in particular, based on experience of the Hanshin-Awaji Earthquake, damage to supports and local buckling of girders are presumed).

8. Conclusion

Since the Hanshin-Awaji Earthquake, implementation of seismic measures for bridges has been an urgent issue for Osaka City, and every effort has been exerted to accomplish this task. As the construction year, road function, bridge type, and surrounding circumstances of each bridge differ, indices were established to evaluate the bridges and determine appropriate measures. The basic objective is to improve the safety of the overall urban road network in case of an earthquake, and to protect the lives of citizens. Of the further retrofitting work planned for reinforced concrete piers of elevated bridges of top urgency, that was approximately completed in 2000. Other countermeasures, such as installation of restrainers, structural change to continuous girders, replacement of supports, and measures for liquefaction are to be implemented as planned.

References

1) Japan Road Association; Specification for Highway Bridges, December 1996
2) Japan Road Association; Specification for Highway Bridges, February 1990
3) Planning and Coordination Bureau, Osaka Municipal Government; Investigation Meeting Report on Earthquake Measures for Osaka City Public Works and Buildings, March 1997
4) Ito T., Nishio H., Omae T.; On Osaka Bridge Administration System, Osaka Municipal Public Works Project Reports, vol. 4, March 1999
5) Osaka Municipal Government; Osaka City Regional Disaster Prevention Plan, 1998.3
6) Japan Road Association; Specification for Highway Bridges, May 1980
7) Japan Road Association; Seismic Retrofitting Manual for Highway Bridges, February 1988

RETROFIT DESIGN AND STRATEGY OF THE SAN FRANCISCO-OAKLAND BAY BRIDGE CONTINUOUS TRUSS SPANS SUPPORT TOWERS BASED ON ADINA

R. B. Heninger[a] , R.W. Wolfe[b]

Abstract

Following the Loma Prieta Earthquake, the California Department of Transportation was charged with developing, and implementing retrofit strategies to mitigate seismic effects on bridge structures linking the state highway system. The findings of a 1989 Governor's Board of Inquiry initiated this concerted seismic retrofit effort. The San Francisco-Oakland Bay Bridge (SFOBB) was targeted early in this effort, as it had exhibited vulnerability during the Loma Prieta earthquake. This paper discusses the simulation and design work of the authors on a portion of the SFOBB utilizing ADINA®, Bathe [2].

Introduction

The now infamous Loma Prieta earthquake struck the San Francisco Bay area on October 17, 1989 at 17:04 Pacific Standard Time (PST). Three major metropolitan communities were impacted: San Francisco, Oakland, and San Jose. The epicenter of the 7.1 M earthquake was located in a local, sparsely populated, mountainous region. Approximately 20,000 buildings sustained damage, with 1,300 destroyed. The human toll counted 62 fatalities, 3,757 reported injuries, and 8,000 left homeless. Amazingly, of the 4000 bridges in the vicinity of the event, only eighteen bridge structures were closed to traffic following the earthquake, Housner et al [1]. Economic losses, although a much less tangible measure of the earthquake's impact, were substantial. The primary tributary between the cities of San Francisco and Oakland, the SFOBB (reference Figure 1) was closed for over a month due to damage sustained.

The SFOBB consists of the east side spanning from Oakland to Yerba Buena Island, and the west or suspension side spanning from Yerba Buena to San Francisco. The west side consists of the continuous portion, spanning over a section of San Francisco, the west suspension and the east suspension spanning over the bay followed by the YB portion connecting to a tunnel on Yerba Buena Island that links the west side to the eastside (reference Figure 1). The bulk of this paper will focus on the continuous portion of the west side.

After the Loma Prieta earthquake, the Governor of the State of California organized a board of inquiry to evaluate a plan and a strategy and to develop a set of minimum requirements for increasing the safety of the bridges in the state.

[a] *P.E., California Department of Transportation*
Sacramento, CA 95819
[b] *P.E., California Department of Transportation, PhD Candidate USC*
Norwalk, CA 90650

The board's requirements are stated as follows:

A. No Collapse
B. No Major Damage
C. No Secondary Injuries or fatalities due to inaccessibility of emergency equipment.
D. Major Important Structures and Lifeline Routes must remain operational.

These requirements lead to a concerted seismic retrofit effort of the bridges in California and a creation of a new seismic design criteria.

In 1994, Caltrans organized a team of engineers to evaluate and analyze the vulnerabilities of the San Francisco-Oakland Bay Bridge. In order to do so, engineers needed to select a non-linear finite element program that contained, but was not limited to, the following parameters:

A. Contact Surfaces
B. Gap Elements
C. Damping Elements
D. Multi-Support Time Histories

After careful scrutiny and a series of evaluations, the program ADINA® was chosen.

The east side of the Bay Bridge was analyzed and found to be to costly to retrofit so the decision was made to replace the existing structure. However, the west side was found to be capable of being retrofitted and that retrofit is currently under construction.

Analysis

The continuous portion of the SFOBB west spans consists of a three span superstructure beginning at the concrete anchorage, extending to Tower A, then Tower B, and terminating at the concrete pier W-1, reference Figure 2. These spans have a length of 378 feet (115.2m) , 96 feet (29.3m), and 378 feet (115.2m) respectively. Towers A and B, reference Figure 4, extend vertically 102 feet from the top of the concrete pedestal to the bottom of the superstructure. The tower cross bracing has a single "x" configuration with horizontal struts at the top and bottom. The individual members consist of built up sections with various cross-sectional geometries. The concrete pedestal is roughly 29 feet (8.8m) high, with the top 8 feet (2.4m) exposed, and connects to a 4'x 29'x 104' (1.2m x 8.8m x 31.7m) spread footing that is underlined by a deep, dense, sand layer.

The "as-built" model of the continuous truss was modeled in ADINA®, Bathe [2], with beam and plate elements representing the superstructure, Towers A and B, and the foundations, reference Figure 2. Rigid links and constraint equations were added in the applicable areas. Nonlinear P-Y and T-Z springs were incorporated along the height of the tower foundations at significant changes in the soil layer, representing the passive pressure exerted by the soil to the foundation. The input excitation time-histories were added to the anchorage end of the truss and to ends of the various P-Y and T-Z springs at the foundations of the towers. Input motions in the

form of 80-second time-histories were derived from the global model of the west spans, with critical motions up to 30 seconds.

The criteria for the capacities of each of the built up steel members, joints, stiffeners, and fasteners etc. were taken from various codes and compiled into a common publication for the use of Caltran's Engineers, Reno et al [3]. These capacities were compared in conjunction with the demands extracted from the finite element model. The comparison was based on the AISC-LRFD Bi-Linear Interaction Equation (reference Figure 3).

Computer simulations using ADINA® revealed that the towers seemed to experience a resonant behavior in the longitudinal direction, creating very large displacements at the mid-height of the columns. These large displacements are caused by the driving frequency of the superstructure and the driving frequency of the foundation being slightly out of phase. This results in a resonant frequency in the columns. Due to this violent resonance, the associated forces in the columns were very large, and the "demand/capacity" (d/c) ratios, Reno et al [3], exceeded the elastic regime, ranging from a magnitude of two to three.

Development of the Retrofit Strategy

The focus of the retrofit strategy was to moderate the resonance in the towers, thereby reducing the d/c ratios in the members. The first strategy included adding dampers to the opposite ends of the superstructure in order to reduce the demand at the tower connections. Thirty cases of dampers were investigated, yielding a 17% demand reduction. A second strategy dramatically increased the column cross-sections, thus increasing the tower capacity, effectively changing their natural period. This approach did not decrease the d/c ratio sufficiently. The third strategy incorporated longitudinal tower bracing from the top of one tower to the mid-height of the second. Displacements were reduced, but large additional undesirable loads were directed to the mid-height brace connections of the columns. Another strategy integrated unidirectional friction pendulum isolators at the column/superstructure interface. This strategy worked once the friction in the bearing was overcome by the superstructure seismic demand. In other words, the towers were not stiff enough in the longitudinal direction to help break the frictional forces, and therefore experienced some resonance and large displacements before the isolators were activated.

The Retrofit Strategy

Finally, a combination of unidirectional friction pendulum bearings in conjunction with longitudinal tower bracing became the main contribution to the strategy. Some perforated and extra steel plates were added to increase the capacity of the transverse cross bracing. Additional concrete and rebar as well as a 1" (25.4 mm) thick steel jacket were added around the foundation pedestals (reference Figure 5). These additions were implemented in the model and all of the d/c ratios in the columns, braces, struts and foundations were found to be acceptable. This strategy was reviewed and accepted by a peer review of academic and industry experts.

Construction

Currently, the foundations, columns, braces, joints and struts have been retrofitted according to plan. The unidirectional isolators have been installed with an elaborate scheme of construction procedures. Joints in the superstructure above the columns were raised by the temporary jacking system. The top 16 inches of the columns were cut and removed, and the isolators were installed, while traffic was in operation. During this procedure, strain gauges, previously added to the members, were carefully monitored to ensure no overloading occurred. The results of the additional strains read from these gauges, in conjunction with those predicted by the model were similar. In conclusion, the model seems to adequately represent the behavior of the bridge.

References

[1] Housner GW et al. Competing Against Time. Report to Governor George Deukmejian from the Board of Inquiry on the 1989 Loma Prieta Earthquake, 1990.

[2] Bathe KJ. Finite Element Procedures. New Jersey: Prentice-Hall Inc., 1996.

[3] Reno M, Duan L. San Francisco-Oakland Bay Bridge West Spans Seismic Retrofit. Design Criteria. California: Department of Transportation, 1997.

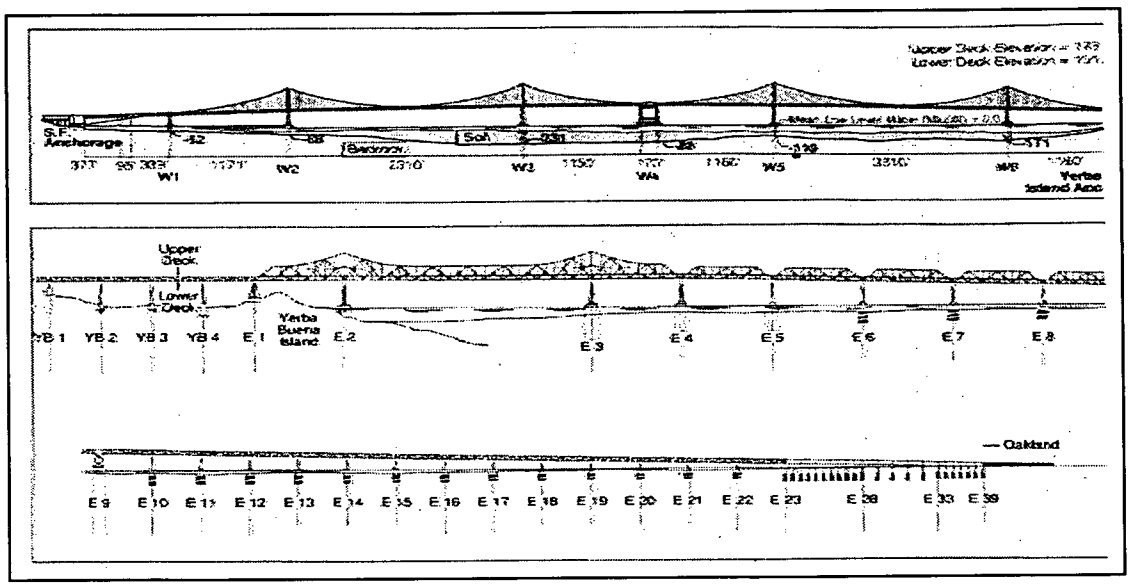

Figure 1. Elevation View – SFOBB

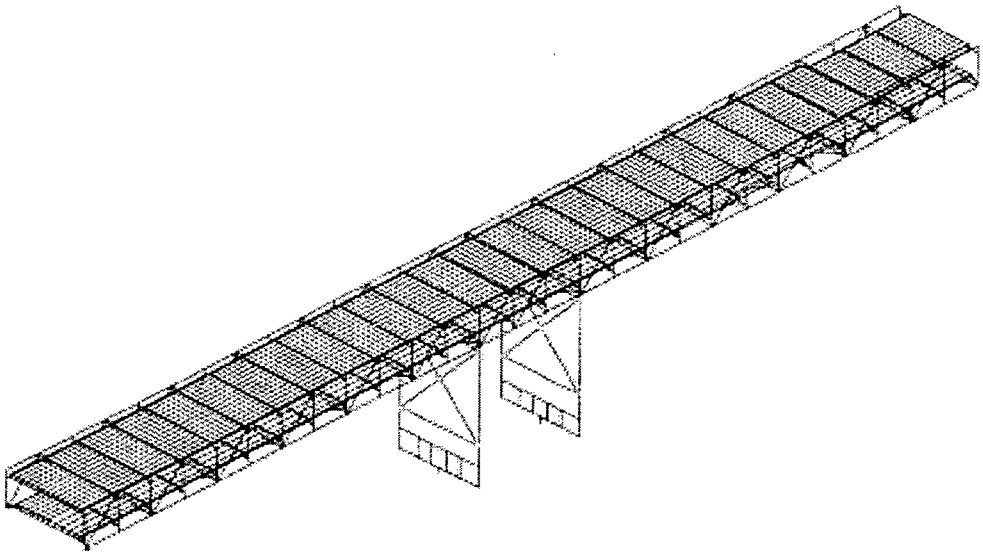

Figure 2. The ADINA Model – SFOBB Continuous Truss

$$\text{For } \frac{P_u}{\phi P_n} \geq 0.2$$

$$\frac{P_u}{\phi P_n} + \frac{8}{9}\left(\frac{M_{ux}}{\phi_b M_{nx}} + \frac{M_{uy}}{\phi_b M_{ny}}\right) \leq 1.0$$

$$\text{For } \frac{P_u}{\phi P_n} \leq 0.2$$

$$\frac{P_u}{2\phi P_n} + \left(\frac{M_{ux}}{\phi_b M_{nx}} + \frac{M_{uy}}{\phi_b M_{ny}}\right) \leq 1.0$$

$$\text{For Shear}$$

$$\left(\frac{V_{ux}}{V_{nx}} + \frac{V_{uy}}{V_{ny}}\right) \leq 1.0$$

Figure 3. The AISC-LRFD Bi-linear Interaction Equation

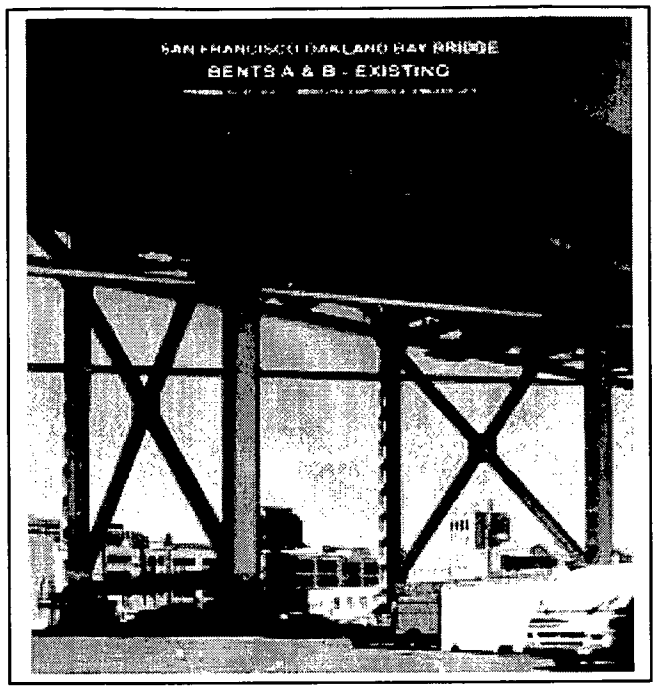

Figure 4. "As-built condition – Towers A & B

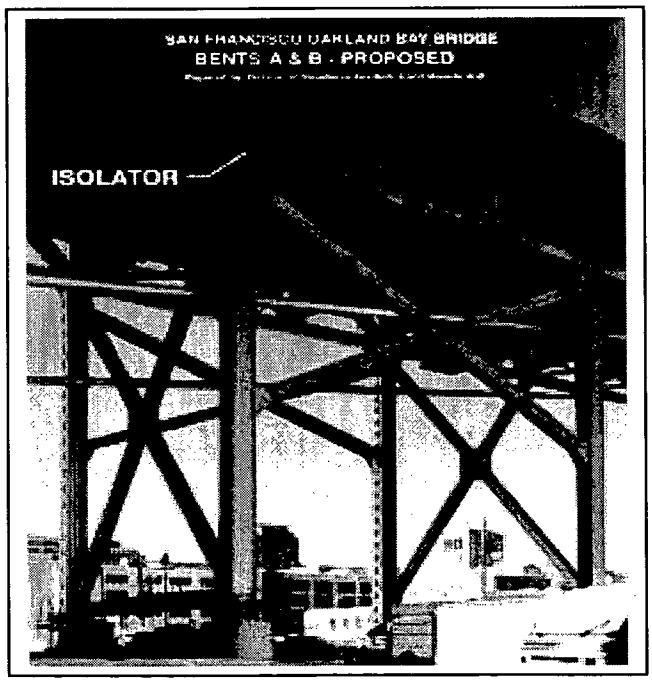

Figure 5. Artist's rendering - Towers A & B retrofit

Preliminary Study on Seismic Retrofit of the Gerber Truss Bridge, the Minato Bridge

Jota Toki [1], Hidesada Kanaji [2] and Yukio Adachi [3]

Abstract

The Minato Bridge is a 980m-long Gerber truss bridge carrying 8 lanes across a channel in the port of Osaka. The current seismic performance and retrofitted performance for site conditions have been analyzed by using a 3-D superstructure elastic model with non-linear foundation springs. It was found that floor system isolation must be the most effective way to reduce member forces and displacements. In order to determine the optimal spring coefficients and damping coefficients of isolators, a various of calculations were conducted.

Introduction

The Hyogo-ken Nanbu earthquake hit Kobe, Japan at dawn on January 17, 1995 and the structures on the Kobe route and the Wangan route in the Hanshin expressway suffered damages. There are several long span bridges in the Wangan route and some bridges among them such as the Higashi-Kobe bridge (cable-stayed bridge), the Rokko-island bridge (Lohse arch) and Nishinomiya-kou bridge (Nielsen arch) were damaged to some extent.

Just after the earthquake, the ministry of construction issued "*Specifications for Restoration of Highway Bridges Damaged by the Hyogo-ken Nanbu Earthquake*" and then, "*Specifications for Highway Bridges, Part 5: Seismic Design*" and "*Reference Book on Seismic Design of Highway Bridges*" were reviewed to take the damages into consideration and enhance ductility design. However there have been no specifications for seismic retrofit of long span bridges whose span exceeds 200m and it is necessary to study a performance for each bridge and develop the seismic retrofit criteria and countermeasures. The Minato Bridge is the third longest Gerber truss bridge in the world, it is the oldest long-span bridge and also it ids important in the express network system. The specific seismic retrofit study has been conducted to determine an appropriate retrofit plan.

---

1. *Engineer, Department of Maintenance, Hanshin Expressway Public Corp.*
2. *Senior Engineer, Department of Wangan Management, Hanshin Expressway Public Corp.*
3. *Senior Engineer, Department of Engineering, Hanshin Expressway Public Corp*

Bridge Structure

The Minato Bridge completed in 1974 is located in Osaka city and a bridge on the Wangan route of the Hanshin expressway (**Figure-1**). The bridge consists of the three-span Gerber truss bridge and has the total span of 980m-long. The center span is 510m-long and the height is about 51m-high (**Figure-2**). There are two levels of floor system with four lanes each. During the Hyogo-ken Nanbu earthquake, only some bearings on the upper floor were damaged.

The following are features of this bridge.

- The superstructure is supported with two caissons and two edge piers. The bearings of intermediate-portions are fixed-type and its design capacity is 131.4MN for dead and live load. There are bearings at edge piers against vertical and horizontal load.
- This bridge has a center span that is suspended by side spans though I-bars.
- Foundation type at intermediate-portion is caisson and that of edge piers is steel pile.
- There are two floors and each floor has 14 units. One unit consists of 4 or 5 continuous spans.
- The as-built seismic design was performed using modified seismic coefficient design method that considers the dynamic characteristics based on dynamic analysis. The design acceleration is 250 gal.

Seismic Retrofit Bases

1. Criteria

The retrofit criteria for this bridge are developed based on suggestions by JSCE, specifications for highway bridges by JRA, and the Toll Bridges Seismic Safety Review by Caltrans. The principles are followings.

- The bridge will not collapse.
- Emergency vehicles will be able to pass just after an earthquake.
- Damaged members will be able to be repaired.

We aim to reduce the number of buckled or yielded members because the bridge is statically determinate structure. We confirmed that one buckling causes a chain reaction. As the result, seismic isolation was considered to be the promising technique to reduce the seismic response.

2. Seismic ground motion

Target source faults considered for seismic design of Minato Bridge are Nankai and To-Nankai fault systems and Uemachi fault system shown in **Figure-3**. Nankai and To-Nankai fault systems, located about 150km south apart from the bridge are chosen as an

expected far field earthquake. As a possible near field earthquake, Uemachi fault system is chosen as a source, whereas there are lots of active faults around this bridge, such as Arima-Takatsuki, Ikoma, Chuoh-Kozoh, and Osaka-bay fault systems. It is because the Uemachi fault system locates about only 2km southeast from the bridge.

Ground motions due to Nankai and To-Nankai fault systems and Uemachi fault system are estimated by fault rupture simulation method considering numbers of rupture scenarios with various asperity area, its location and rupture starting points. Fault rupture models are set using the latest and most reliable empirical scaling by Sommerville et al. (1999). In order to simulate the seismic ground motion at Osaka bay area, effects of sedimentary basin structure should be considered in simulation. The design ground motion due to the rupture scenario of Nankai and To-Nankai fault system is simulated by the empirical Green's function method using observation data due to small earthquake that already include the basin effect of Osaka bay area. On the other hand, there is no observed data caused by Uemachi fault system. Therefore, the hybrid method is used for the simulation. The method combines stochastic Green's function method in relatively shorter period range (T<1.0-1.5sec) and 3-D finite difference method in relatively longer period range (T>1.0-1.5sec).

A simulated ground motion with largest response in the primary natural period range of the bridge (T=2.0-5.0sec) are set as the design ground motions.

Kinematic interaction is also considered for design seismic ground motions because the effect is considered to be large. 3-D finite element method, not 2-D method that has been widely used in practical design, is used for simulating the effect, because the 2-D analysis method tends to over-estimate the effect compared to 3-D method.

Figure-4-1, 4-2 shows the time history and the response acceleration spectrum of design ground motions by scenario Nankai and To-Nankai, and Uemachi earthquake.

Current Seismic Performance

In order to make the current seismic performance clear, modal analysis and dynamic analyses using the design earthquakes have been performed.

1. Analysis Model

A 3-D global model is applied to analyze the current seismic performance. The model is shown in **Figure-5**. The superstructure is composed of elastic members and the damping is assumed to be 2%. Ground springs at P-2 and P-3 consist of an non-linear horizontal spring and a rotation spring and those at P-1 and P-4 are an elastic spring. The non-linear springs are developed using static pushover analysis for the caisson-ground system. The Hardin-Drunevich model is applied for restoring characteristics of the caisson.

2. Modal analysis

The result of modal analysis is shown in **Table-1**. **Figure-6** provides the dominant first mode for longitudinal and transverse directions. The natural period for longitudinal direction is 2.7 sec.

3. Current seismic performance

Non-linear time history analyses using the Uemachi and the Nankaido earthquake wave were performed in order to evaluate the current seismic performance of this bridge. **Table-2** shows the representative response and provides that the Uemachi wave can be recognized as the dominant earthquake for this bridge rather than the Nankaido. We focus the Uemachi wave in studying other dynamic responses below.

According to the time history analysis using the Uemachi wave, the number of yielded or buckled members results in 64 for the longitudinal direction and 12 for the transversal. The maximum ratio of the calculated to nominal yield stress is 1.84. The shear stress at the upper boss of intermediate bearings, which support the heavy superstructure, is 1.2 times as large as the yield stress, although edge bearings remain elastic.

Retrofit Feasibility Study

A series of analyses for seismic retrofit plans were carried out to find the most effective countermeasures. The results of those studies suggest that seismic isolation at intermediate bearings or floor system isolation should be possible ways. Their results are given in **Table-2**.

1. Seismic isolation at intermediate bearings

The intermediate bearings are considered to be the most vulnerable member. We studied the possibility of seismic isolation at these portions by replacing the existing pin type bearings into isolation bearings. The isolated natural period is set to be approximately twice as large as the original natural period for the transverse direction. The damping ratio of device is assumed to be 15%. This structure system provides that the number of yielded or buckled members for the transverse direction decreases to 12 and all members for the longitudinal remain elastic. However the longitudinal displacement of this bridge becomes 1.6m and it may cause the pounding problem between the main structure and approach structures.

2. Floor system isolation

This bridge has two floor decks with plate girders that are placed on cross beams of the main truss. The weight of floor system amounts to around 200MN which accounts for 40% of the total superstructure weight. We considered an alternative where the floor system should be isolated off the main truss to reduce seismic response. The optimal natural

period and damping were determined by conducting parametric studies.

As shown in **Table-2**, the number of yielded members for the longitudinal direction is 16 and that for the transversal is 10. However the relative displacement between the deck system and the truss becomes 1.8 times as large as the existing clearance for transverse direction and that between a deck and an adjacent deck is 6.7 times as large as the clearance, which is 200mm.

According to the result, we confirmed that the floor system isolation should be effective for reduction of the seismic response, but the displacement should be carefully taken into consideration.

Seismic Isolation and Optimization

Based on the preliminary study, the seismic isolation for the floor system has been studied in detail in order to identify optimal spring constants and damping coefficients.

1. Optimization of spring constants and damping coefficients

Existing deck units consist of 4 or 5 continuous steel plate girders. The number of total deck units is 14 in each floor. First of all an analysis was carried out for 14 units but it was difficult to control the whole response. Then several structural plans were examined and 8 units system was finally employed (**Figure-7**). It is assumed that a ground spring can be expressed by an equivalent liner spring in this study.

In order to minimize the section force of lower chord members, a bunch of optimal calculations were performed in accordance with changing spring constants, Ks and damping coefficients, Cs of isolators. The relative displacement, whose limit is approximately 400-500 mm, was also taken into consideration.

As the result of the calculations, the optimal spring constants, Ks vary 2,710-5,780kN/m, which correspond 2.53-2.86 sec of natural period, and the optimal damping coefficients are 412-902 kN·sec/m, which correspond 0.15-0.25 of damping ratio.

2. Effect of ground spring

Using the obtained spring constants and damping coefficients of isolation device, the time history analysis was carried out by replacing the equivalent linear ground spring into an non-linear spring. As the result, the number of yielded member can be reduced to two and the maximum stress is 1.02 σy. The shear stress at the upper boss of intermediate bearings can be also reduced to 1.01 σy.

The relative displacement, which is a major concern for optimal calculations, satisfies the criteria. In addition, the variation of constant springs and damping coefficients does not affect the response of the whole bridge and the member forces so much. There are two possible selections for the isolation system ; to realize the above characteristics the hybrid system with sliding bearings and elastomeric bearings, and the friction pendulum bearing

system **(Figure-8)**.

Concluding Remarks

The following concluding remarks were derived from the results.

- The current seismic performance of the Minato Bridge doesn't meet the criteria according to the time history analyses using a 3-D global elastic model. Seismic retrofit is necessary.
- Isolation of the whole truss by replacing the existing pin type bearings into isolation bearings is not most effective because of the large longitudinal displacement over the criteria.
- Floor system isolation must be the best selection to reduce the member forces and control the displacements. The optimal spring constants, Ks are 2,710-5,780kN/m and the optimal damping coefficients are 412-902 kN·s/m according to a lot of optimal calculations.
- The possible isolation systems are the hybrid system with sliding bearings and elastomeric bearings, or the friction pendulum bearing system so far. However it is necessary to compare them in terms of performance, cost and maintenance.

Acknowledgements

We are grateful to the committee for the assessments of seismic stability on the existing long span bridges of Hanshin Expressway (chairman: Dr. Emi), the advisory committee for the seismic issues on the Hanshin Expressway (chairman: Prof. Sato) and Mr.Uehira of Japan Association of Steel Bridge Construction.

References

1. *Restoration project report for the Hyogo-ken Nanbu earthquake*, Hanshin Expressway Public Corporation, 1997.9
2. Ishizaki, Sawanobori, "Restorations of the long span bridges on the #5 Wangan route", proceedings of the conference for the Hanshin-Awaji Earthquake Disaster, Japan Society of Civil Engineering, 1996.1
3. *Specifications for Highway Bridges, Part 8: Seismic Design*, Japan Road Association, Tokyo, Japan, 1996
4. *Reference Book on Seismic Design of Highway Bridges*, Japan Road Association, Tokyo, Japan, 1995
5. *Project report on the Minato Bridge*, Hanshin Expressway Public Corporation, 1978.3
6. Sasado, Kawai, "Superstructure design for the Minato Bridge and some issues", Bridge and Foundation magazine, 1973.6-7

7. Koike, Sakota, "Study on the seismic stability of long span bridges", Bridge and Foundation magazine, 2000.9-10
8. Suggestions for the seismic code of infrastructures, Japan Society of Civil Engineering, 1995.5 and 1996.1
9. C.Seim, G.Fox, I.M.Idriss and F.Seible, "Toll Bridge Seisimic Safety Review-Final Report to the Caltrans Director", Engineering Service Center, 1999.4

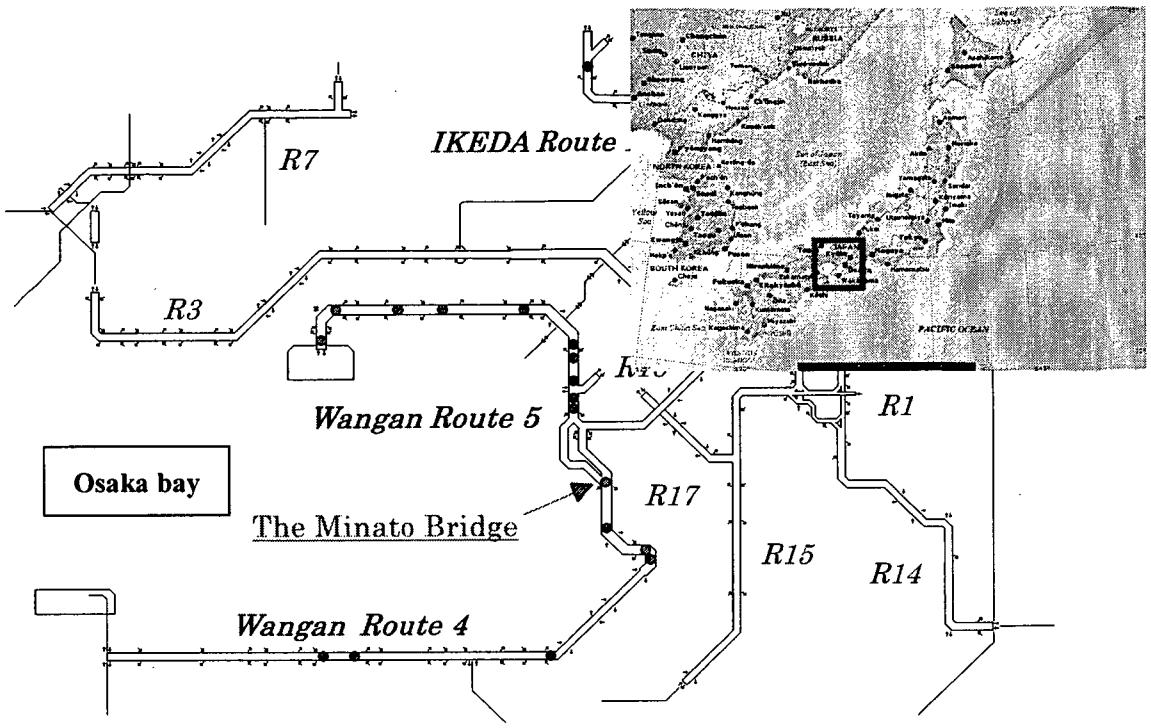

Fig.1 Location of the Minato Bridge

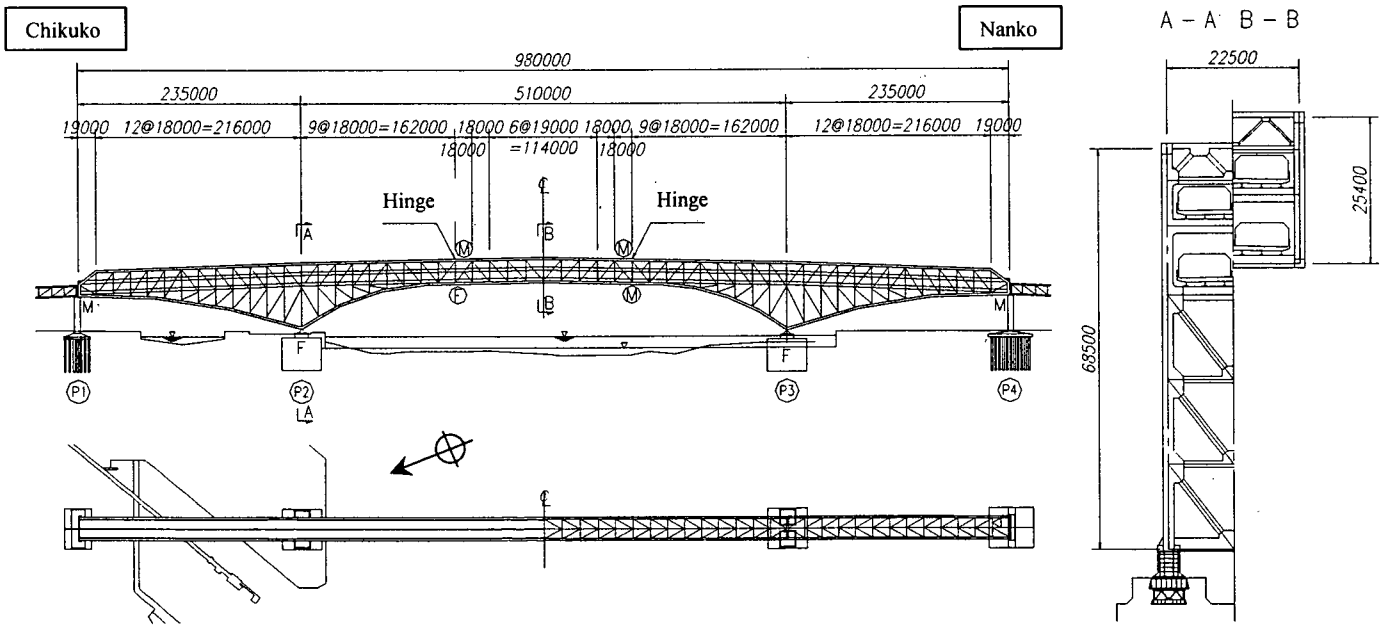

Fig. 2 General Arrangement

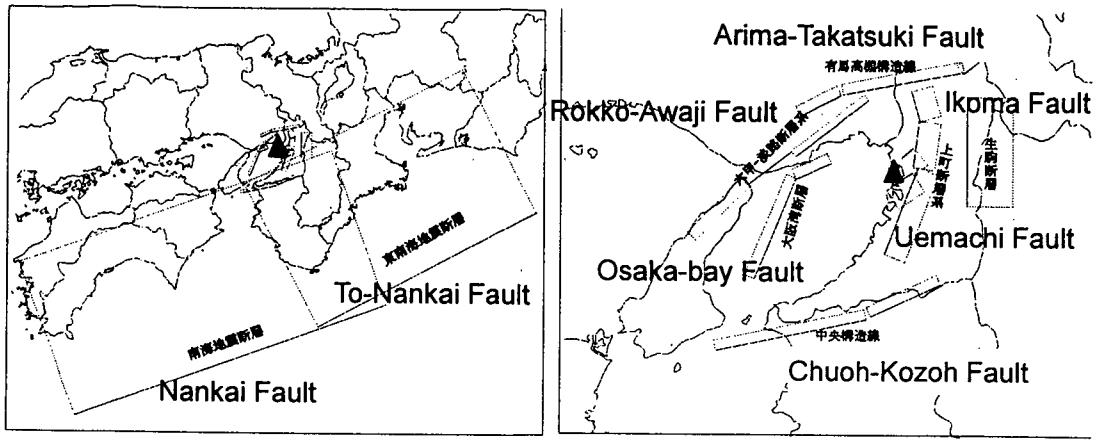

Figure 3. Fault systems around the Minato Bridge

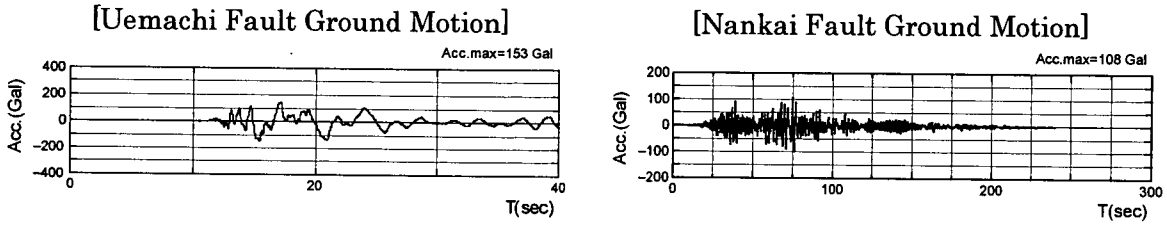

(a-1) Acceleration time history

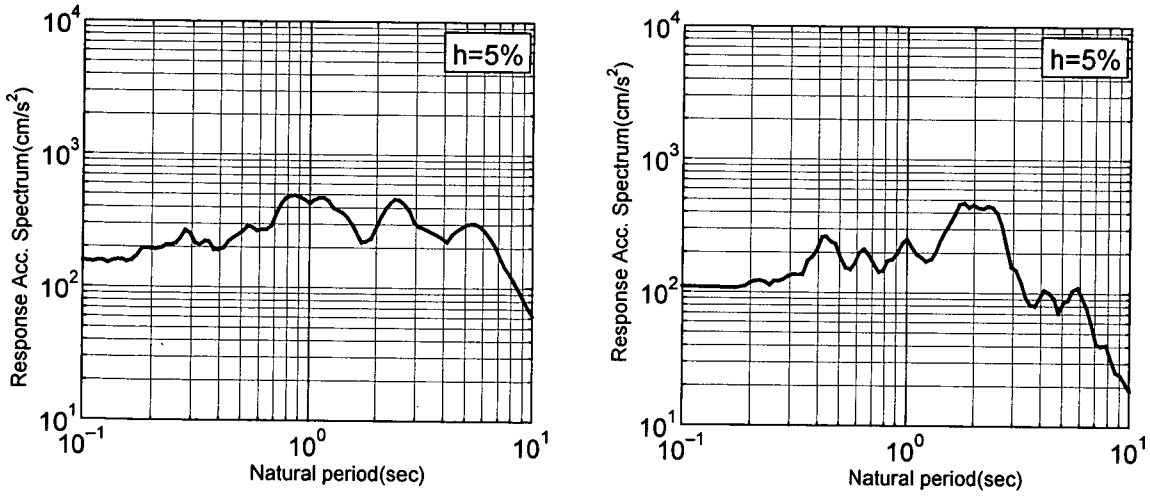

(b-1) Response acceleration spectrum

Figure 4-1. Design ground motions for longitudinal dir.

[Uemachi Fault Ground Motion] [Nankai Fault Ground Motion]

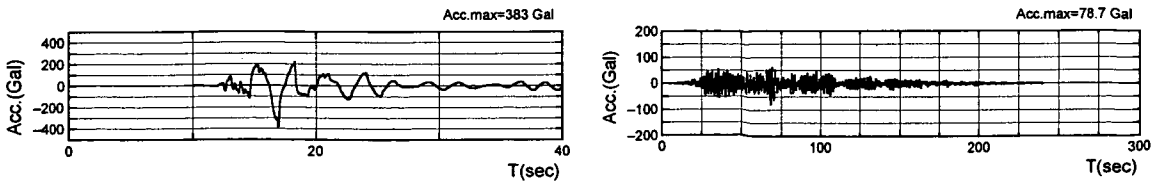

(a-2) Acceleration time history

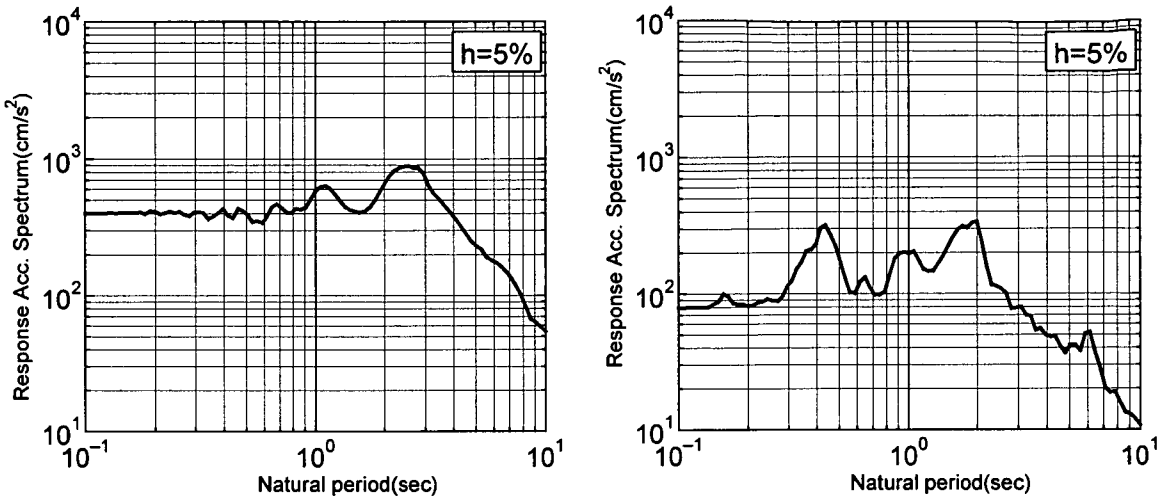

(b-2) Response acceleration spectrum

Figure 4-2. Design ground motions for transversal dir.

Table 1 Results of modal analysis

No.	Frequency (Hz)	Natural Period (sec)	Participation Factors		
			β x	β y	β z
1	0.240	4.17	0.000	0.000	1.299
2	0.301	3.32	0.174	0.653	0.000
3	0.366	2.73	0.990	0.046	0.000
4	0.400	2.50	0.001	0.000	0.056
5	0.545	1.83	0.000	0.000	2.009
6	0.557	1.80	0.001	0.000	1.029
7	0.726	1.38	1.580	1.000	0.000
8	0.788	1.27	1.106	-1.029	0.000
9	0.802	1.25	0.000	0.000	0.083
10	0.836	1.20	-1.015	-0.048	0.000

X : Longitudinal、Y : Vertical、Z : Transverse direction

indicates dominant vibration mode for transverse and longitudinal direction

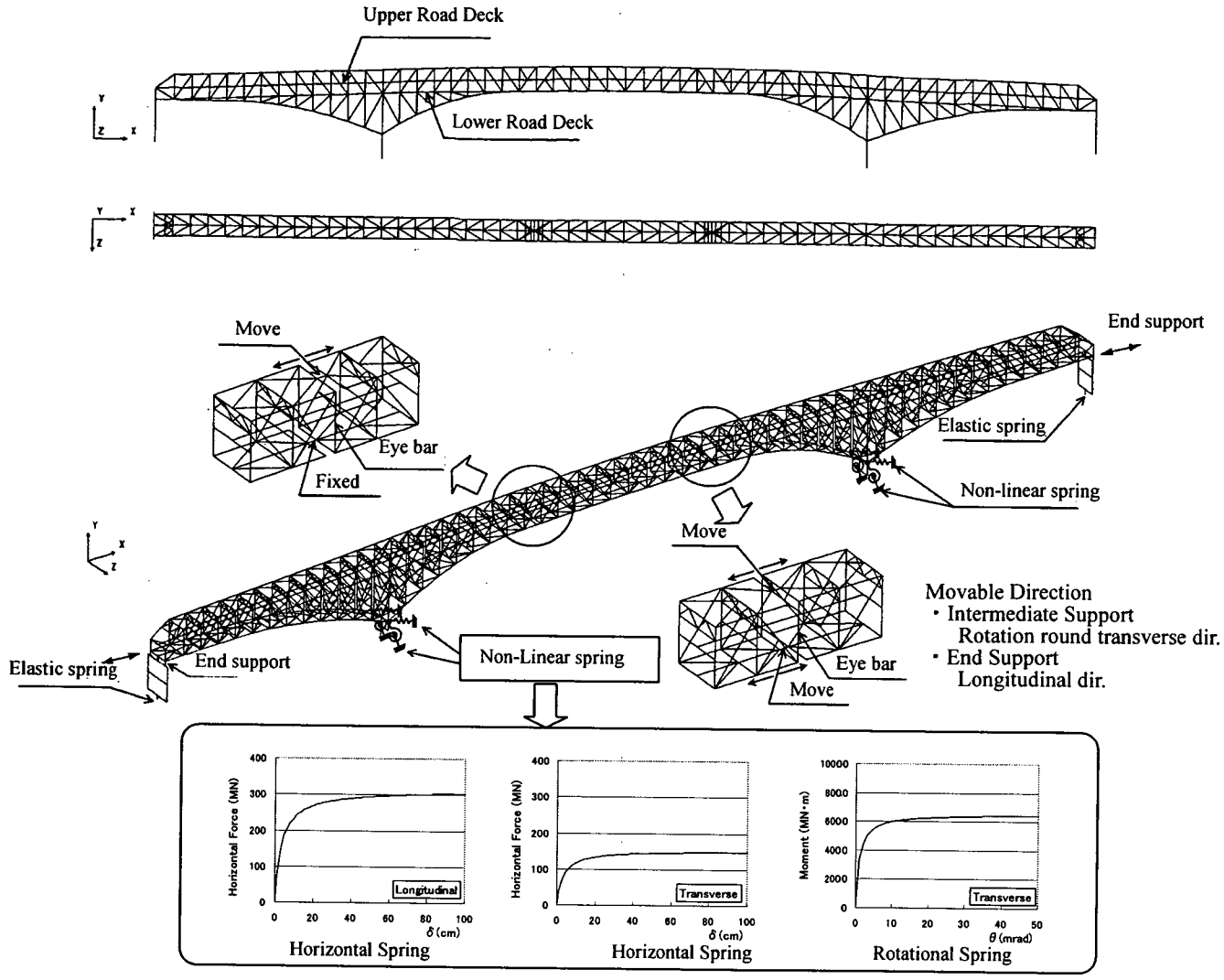

Fig.5 Analytical Model

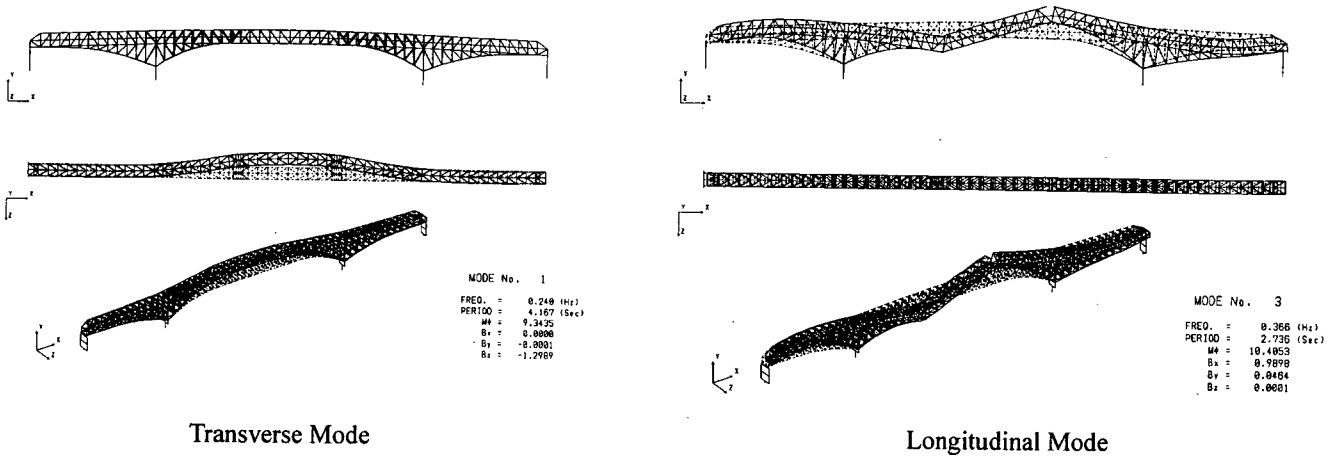

Transverse Mode

Longitudinal Mode

Fig.6 Vibration Mode

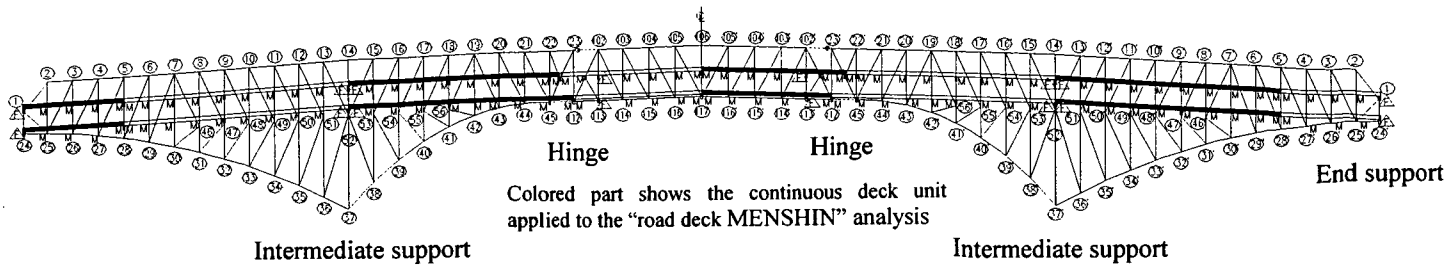

Fig.7 Road deck units

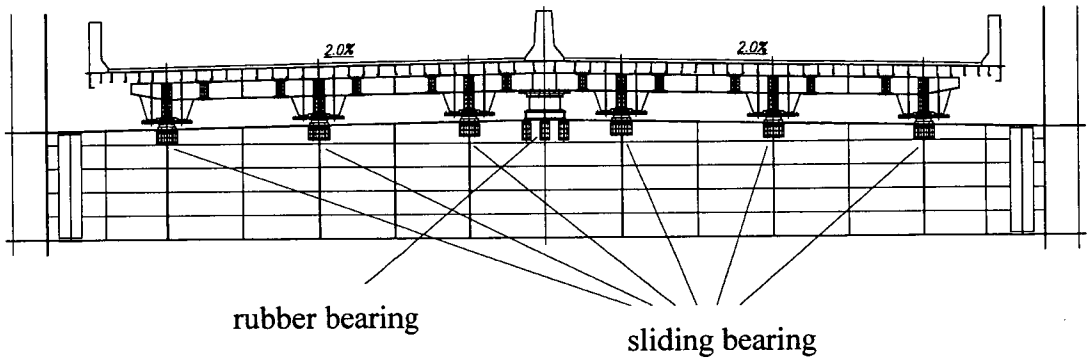

(a) sliding bearing + rubber bearing

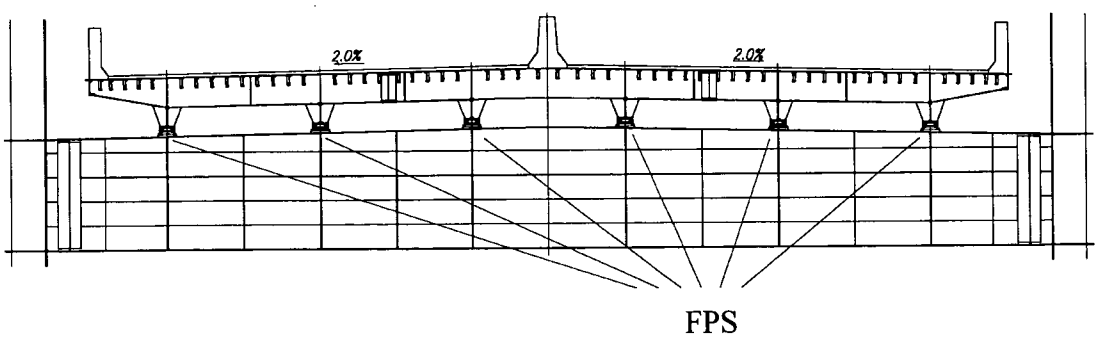

(b) Friction Pendulum System

Fig.8 Image of isolation device

Table 2 Results in the seismic response analysis

	Present structure		Retrofit		Road deck menshin system with optimized spring(K) and damping(C)
			Intermediate support menshin system	Road deck menshin system	
Input earthquake	Uemachi	Nankaido	Uemachi		
Number of truss members over yield stress	12 [64](*1)	Elastic [8]	12 [0]	10 [16]	2 [4]
Maximum stress ratio of truss members(*2)	1.08 [1.84]	Elastic [1.07]	1.06 [−]	1.12 [1.19]	1.02 [1.04]
Maximum stress ratio of intermideate support(	1.20	Elastic	1.6m(*3)	1.25	1.01
Maximum stress ratio of end support(*2)	Elastic	Elastic	1.7m(*3)	Elastic	Elastic
Relatieve displacement between road deck and truss structure(Relative displacement / avarable movement)	—	—	—	1.81(*4)	0.98(*5)

(*1)The figures on the table indicate results in analysis for tranverse direstion, figures marked [ ] indicate results in analysis for longitudinal direction.

(*2)The "stress ratio" of the truss members means the ratio of stress in analysis to yield stress (in compression stress, yield stress means buckling stress) .

The "stress ratio" of the supports means the ratio of stress in analysis to yield stress for each material of the components which construct supports.

(*3)The displacement of MENSHIN device for longitudinal direction.

(*4)The results for transverse direction : The allowable relative displacement between road deck and truss structure is about 800mm in general part and about 200mm in the emergency parking lot.

(*5)The results for longitudinal and transverse direction : the allowable movement of MENSHIN device installed between road deck and truss structure is assumed about 450mm.

Study on Seismic Behavior of Concrete Columns Strengthened with PC Confined Method

Kiyoshi Kirikawa [1]

ABSTRACT: When retrofitting existing reinforced concrete piers for greater seismic resistance , it is considered important to provide an adequate number of hoop reinforcements. But installing a large quantity of hoop reinforcements can be difficult. If the improvement in ductility can be estimated by using pre-stressed steel hoop reinforcements with a high yield point, it is possible to achieve greater ductility with a smaller number of steel hoop reinforcements

In this paper, we investigate the influence that pre-stressed steel has on confined concrete columns by means of an axial compression test, and confirm the effectiveness of using pre-stressed steel for hoop reinforcements by means of an alternating load test.

1 INTRODUCTION

After the Hyogo-Ken Nanbu earthquake, seismic retrofitting of existing reinforced concrete piers was urgent business. Retrofitting methods included steel plate jacketing and reinforced concrete jacketing. But each of these methods presented various problems, such as difficult maintenance or complicated construction.

This study proposes a method of seismic retrofitting that uses pre-stressed steel as hoop reinforcements to solve the problems in maintenance and construction. Pre-stressed steel has high strength, which can greatly improve ductility. This makes the method effective for seismic retrofitting.

In order to put this method to practical use, we must clarify the stress-strain relation, which considers the confining effect of the hoop reinforcements and the improved ductility. Many studies[1] have explored the stress-strain relation for confined reinforcement concrete using normal reinforcements, and the evaluation method has been published in SPECIFICATIONS FOR HIGHWAY BRIDGES • PART V: SEISMIC DESIGN[2] (hereafter called " Specification V"). A few studies have also been published about using pre-stressed steel for hoop reinforcements. So we suggest using the stress-strain relationship of confined concrete column, which uses pre-stressed steel for the hoop reinforcements[3], and inspects the suitability of the evaluation method that is published in Specification V. After that, we will do an alternating load test[4] before and after the reinforcements have been installed in order to clarify the seismic properties of pre-stressed steel reinforced concrete piers and compare normal reinforcements with pre-stressed steel reinforcements.

2 AXIAL COMPRESSION TEST FOR CONFINED CONCRETE COLUMNS

2.1 Specimens Detail

Cylinder specimens are shown in Fig.1. The cylinders have a diameter of 300 mm and a height of 900 mm. The cylinders are arranged in groups of 6 in an 18x3 grid. The various states are shown in Table 1. The conversion hoop reinforcement ratio was the hoop reinforcement ratio multiplied by the yield ratio of SD295. The specimens were all fitted with longitudinal reinforcements of 1% steel.

We investigated a type of hoop reinforcement and a quantity of pre-stressed steel. Specimen

1. Engineer, P.S.Corporation, Tokyo, Japan

A had no hoop reinforcement, specimen B had hoop reinforcement of ϕ 6, specimen C had hoop reinforcement of D10, specimen D to F were wrapped with hoop reinforcements made of SWPR2N ϕ 2.9. The hoop reinforcements on all specimens were spaced at an interval of 75mm in order to closely monitor and compare the confining effect. Specimens D to F were reinforced with pre-stressed steel with the following initial pre-stress forces.

- Specimen D: initial pre-stress force is σ pi = 0 MPa
- Specimen E: initial pre-stress force is σ pi = 588 MPa
- Specimen F: initial pre-stress force is σ pi = 1177 MPa

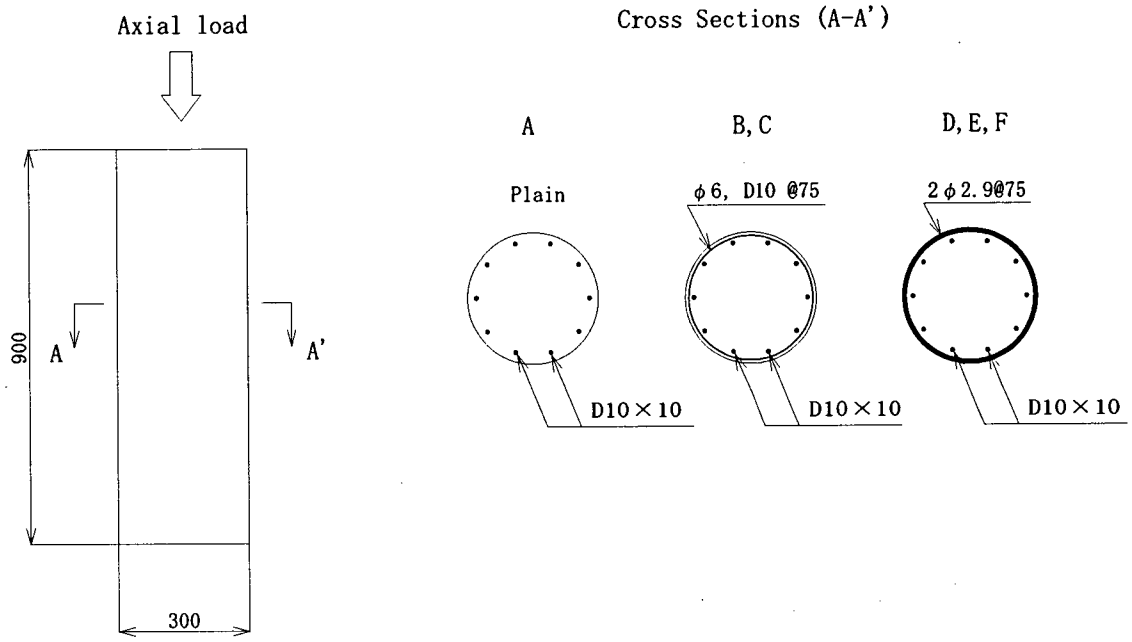

Fig.1 Construction of specimens

Table 1 Properties of Specimens

Specimen name	A	B	C	D,E.F
Design strength σ_{ck}	27 MPa			
Longitudinal reinforcement	D10×10			
Hoop reinforcement	—	ϕ 6@75	D10@75	2 ϕ 2.9@75
Yield point σ_y (kgf/cm^2)	—	2400	3000	17500
Hoop reinforcement ratio ρ_s (%)	0.0	0.50	1.27	0.23
Conversion ratio σ s' (%)*1	0.0	0.40	1.27	1.37
Number of specimens	3	3	3	Each 3

*1 : Conversion hoop reinforcement ratio= $\rho_s \times \sigma_y / \sigma_{yo}$ (σ_{yo} is yield point of SD295)

2.2 Materials

The mixture proportions used in the specimens are shown in Table 2. The cement was high-early-strength Portland cement. The dynamic properties of the reinforcements and the pre-stressed steel are shown in Table 3.

Table 2 Mix proportion of concrete

Maximum measurement (coarse aggregate)	(mm)		20
Air	(%)		4.0
Water-cement ratio	W/C (%)		55
Sand percentage	S/a (%)		40
Unit content	Water	(kg/m^3)	160
	Cement		290
	Fine aggregate		741
	Coarse aggregate		1128

Table 3 Dynamic properties of reinforcement and pre-stressed steel

		Yield Point (MPa)	Tensile Strength (MPa)	Elongate Ratio (%)	Young's Modulus (MPa)
Hoop Reinforcement	ϕ 6 SR235	335	447	35.4	2.0×10^5
	D10 SD295A	371	511	25.1	2.0×10^5
	2 ϕ 2.9 SWPR2N	1954	2091	7.5	2.0×10^5

2.3 Test Detail and Instrument

Using a 10000 kN compression testing machine, we performed an axial compression test. The loading speed was 0.2 mm per minute with an aim. We measured the axial load, the axial displacement, the strain in the hoop reinforcement and the concrete surface. Axial displacement was measured using four full-length displacement gauges. A strain gauge was used to measure strain in the hoop reinforcement in three places on each of the three sections that were tested.

2.4 Results of Axial Compression Test

2.4.1 Destruction Shape

The final destruction shapes of the specimens are shown in photo 1. Specimen A, which had no hoop reinforcement, failed suddenly after maximum loading. In specimens with hoop reinforcements, longitudinal cracks occurred and then the cover concrete cracked, but the specimens were not destroyed.

Specimens E and F, which were pre-stressed, had fewer cracks compared with non-pre-stressed specimens. It was thought that the pre-stressing forces in the steel had a restraining effect on fracturing. There were instances (specimens D, E and F) in which the pre-stressed steel broke relatively quickly, but it occurred in the anchoring zones of the pre-stressed steel.

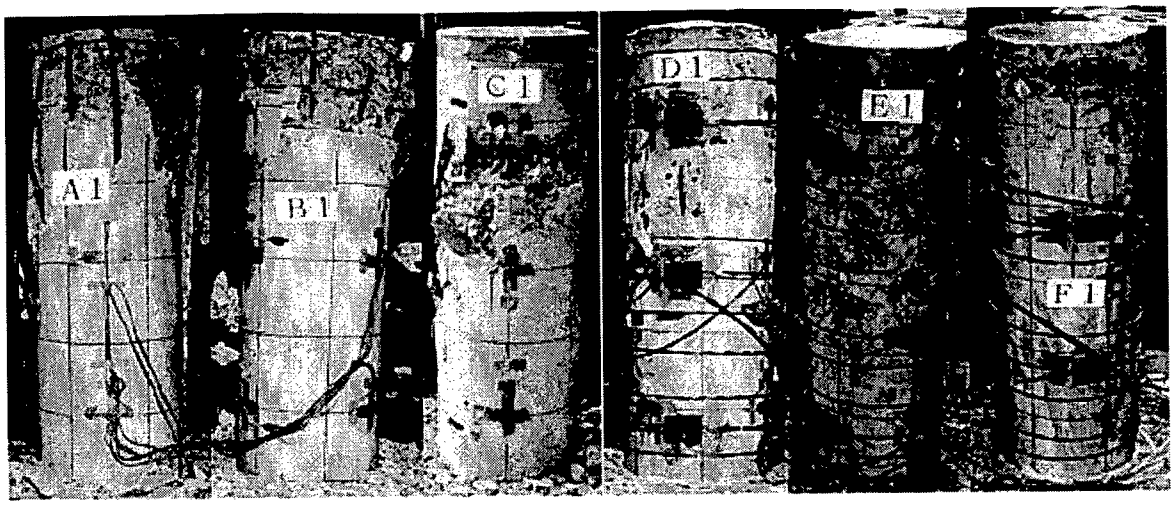

Photo.1 The final destruction shape (series 1)

2.4.2 Axial Stress – Axial Strain Relation

The results of the experiment are shown in Fig.2. Under maximum load, the specimens show hardly any difference in their behavior. The small difference in specimens A-1 and C-2 can be attributed to local damage at the contact surface of the loading plate and the upper side of each specimen.

In specimens A, B and C, the greater the hoop reinforcement ratio, the higher the maximum stress and strain. In specimens D, E and F, the maximum stress and strain increased as the pre-stress factor increased. After maximum stress, the downward sloping gradient of specimens D, E and F, which used pre-stressed steel, was much gentler than that of specimen B, although specimen B's hoop reinforcement ratio was about 2 times that of specimens D, E and F. So the use of pre-stressed steel can indicate an improvement in ductility. And when we compare the downward sloping gradient with the pre-stressed quantity, specimen E, which was pre-stressed to $\sigma_{pi} = 588$ MPa showed the gentlest downward sloping gradient. This

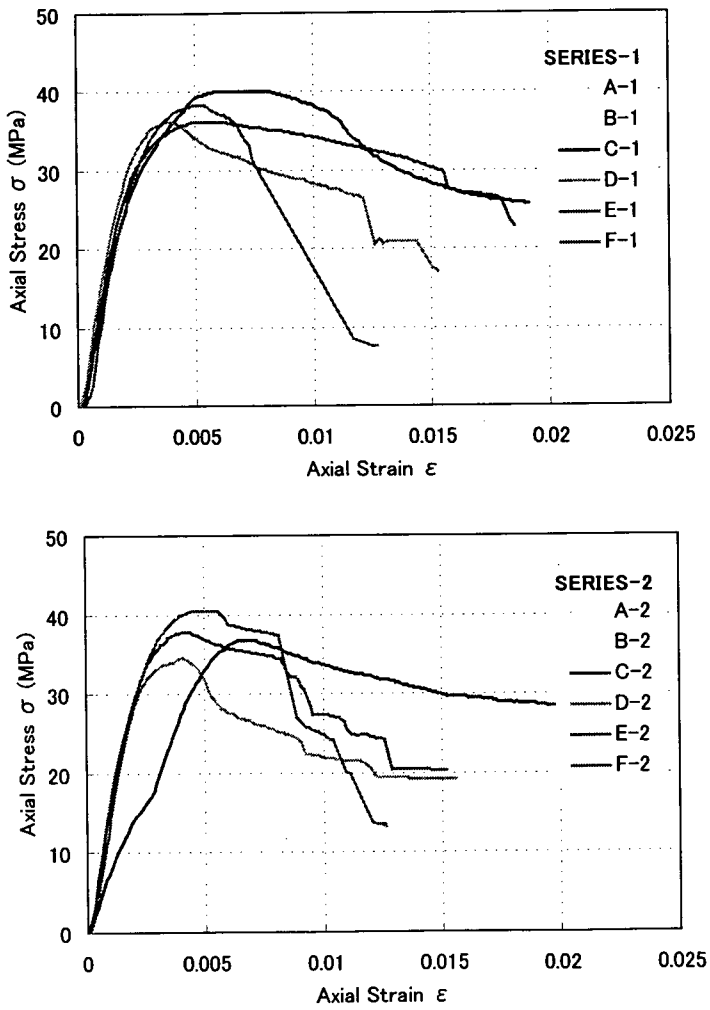

Fig.2 Stress-strain relationship (series 1,2)

was almost identical to the downward sloping gradient of specimen C. The hoop reinforcement ratio of specimen C was about 6 times that of specimen E. Specimen F had the largest quantity of pre-stressed steel, and the downward sloping gradient was excessively steep.

2.4.3 Axial Stress-strain in Hoop Reinforcement Relationships

The strains in the reinforcements under maximum stress are shown in Table 4. There was a considerable spread in the data of about 1000-3000 μ, but a clear difference wasn't found between normal reinforcements and pre-stressed steel reinforcements. A number of the normal reinforcements almost reached the yield point in their strains, but the pre-stressed steel reinforcements didn't. From this, large increases in the maximum stress cannot be expected from the use of pre-stressed steel reinforcements.

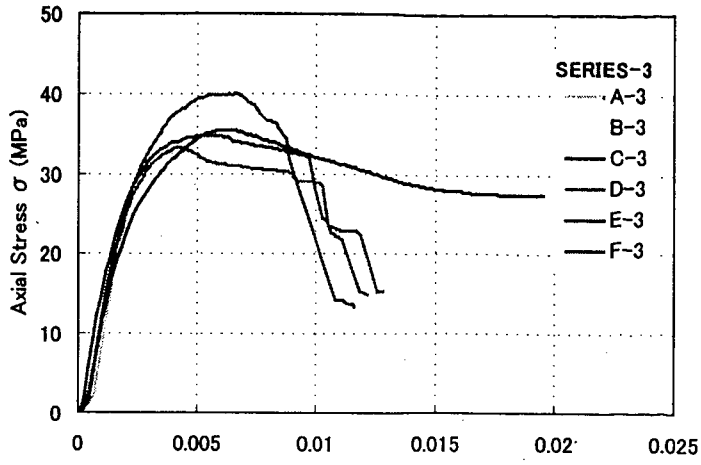

Fig.2 Stress-strain relationship (series 3)

Table 4 Strain in hoop reinforcements under maximum stress

		Strain in Hoop Reinforcements (Average)		
		Upper	Middle	Lower
Series 1	B-1	2765 μ	916 μ	1508 μ
	C-1	2455 μ	1777 μ	3832 μ
	D-1	1625 μ	1322 μ	1836 μ
	E-1	2040 μ	1207 μ	636 μ
	F-1	2859 μ	1758 μ	879 μ

2.5 Formulating the Stress-strain Relationship

Using the results of the experiment discussed in 2.4 above, we can formulate a stress-strain relationship for confined concrete columns using pre-stressed steel hoop reinforcements. The formulation is based on the stress-strain curve that is described in Specification V 9.4 (hereafter called " Specification formula"). According to the test results, the strain value for pre-stressed steel during maximum stress averaged about 1500 μ. The tensile stress for pre-stressed steel can be determined from the formula (3). Applying the tensile stress for pre-stressed steel (= σ_{pt}), we can determine the maximum stress to be (1) and the strain during maximum stress to be (2). σ_{pe} is the average pre-stressing value here.

The Specification formula is applied to the downward sloping part of the gradient (=E_{des}) after maximum stress because the yield point for pre-stressed steel is effective. Factors regarding the termination of stress, as well as other formulas and values not defined here, all comply with Specification V.

$$\sigma_{cc} = \sigma_{ck} + 3.8\alpha \cdot \rho_s \cdot \sigma_t \qquad (1)$$

$$\varepsilon_{cc} = 0.002 + 0.033\beta \cdot \frac{\rho_s \cdot \sigma_t}{\sigma_{ck}} \quad (2)$$

$$\left.\begin{aligned} \sigma_t &= 300 + \sigma_{pe}{}^{*} \quad \text{(Pre-stressed steel)} \\ \sigma_t &= \sigma_y \quad \text{(Normal reinforcement)} \end{aligned}\right\} \quad (3)$$

note: $0 \leqq \sigma_{pe} \leqq \sigma_y/3$

$$E_{des} = 11.2 \cdot \frac{\sigma_{ck}{}^{2}}{\rho_s \cdot \sigma_y} \quad (4)$$

$$\rho_s = \frac{4A_h}{sd} \quad (5)$$

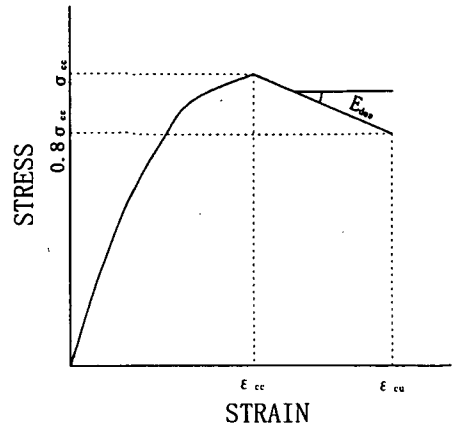

Fig.3 Stress-strain curve

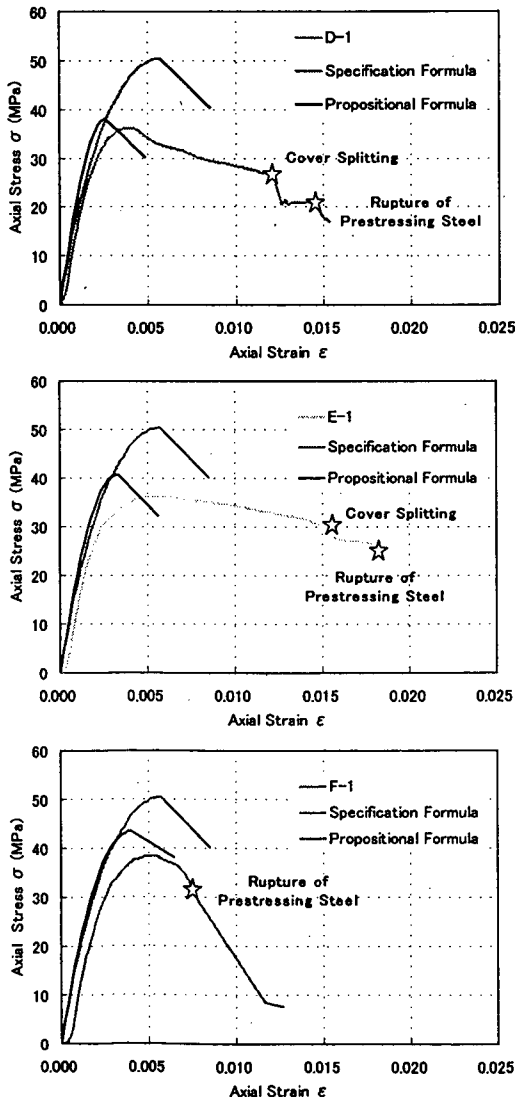

Fig.4 Stress-strain relation (series 1)

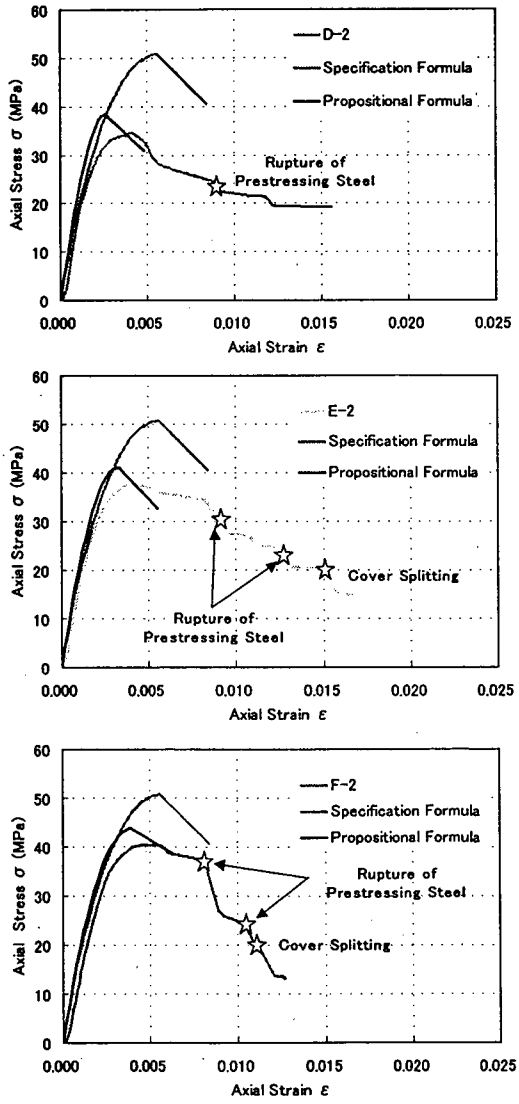

Fig.4 Stress-strain relation (series 2)

σ_{cc}	: strength of confined concrete	(MPa)
σ_{ck}	:design strength	(MPa)
σ_y	:yield point of hoop reinforcement	(MPa)
ρ_s	:hoop reinforcement ratio	
ε_{cc}	:strain in maximum	
E_{des}	:downward sloping gradient	(MPa)
A_h	:crosssectional area of hoop reinforcement	(mm^2)
s	:pitch of hoop reinforcement	(mm)
d	:effective length of hoop reinforcement	(mm)
α, β	:constant, defined in Specification V	

Fig.5 lists the results and values of the proposed formula for every series of specimens that used pre-stressed steel for hoop reinforcement.The maximum compression stress of the concrete and the strain of the concrete under maximum compression were both overestimated when the yield point of the pre-stressed steel was set according to the Specification formula. The proposed formula, however, was able to adequately predict both factors.

The value calculated using the yield point almost matched the test results for the downward sloping gradient after maximum stress. A high yield point in the pre-stressed steel was identified as being useful for improving ductility. According to the test results, however, specimen F, which had the largest quantity of pre-stressing, produced a steeper downward sloping gradient than specimen E, showing that too much pre-stressing will reduce the improvement in ductility. Since this proposal formula produced results that were on the safe side for specimen F, we thought that pre-stressing was effective up to 1/3 σ_y (= a quantity of specimen F's pre-stressed).

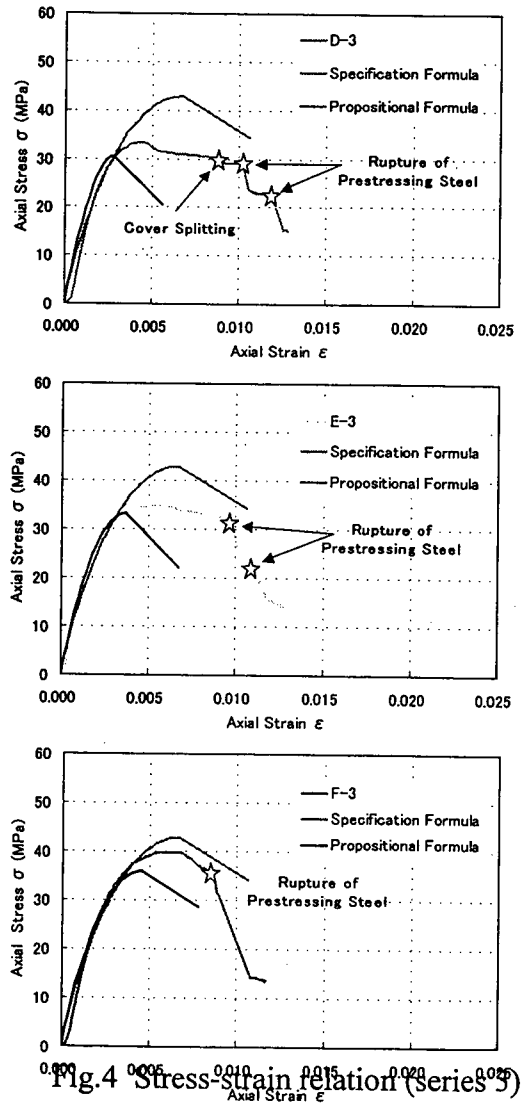

Fig.4 Stress-strain relation (series 3)

3 ALTRENATING LOADING TEST

3.1 Details of Specimens

Three cylinder specimens are shown in Fig.5.

The various properties are shown in Table 5. All specimens have longitudinal reinforcements made of 1% steel. Specimen R is a reinforced concrete pier before reinforcement, and fitted with D6@75 hoop reinforcements. Specimens RR and RP are reinforced concrete piers with additional reinforcements. After fitting D10@100 and

SWPR2N 2 ϕ 2.9@75 reinforcements to each specimen, the specimens were covered with a highly fluid concrete to a thickness of 25 mm. Specimen RR was pre-stressed to 411 MPa.

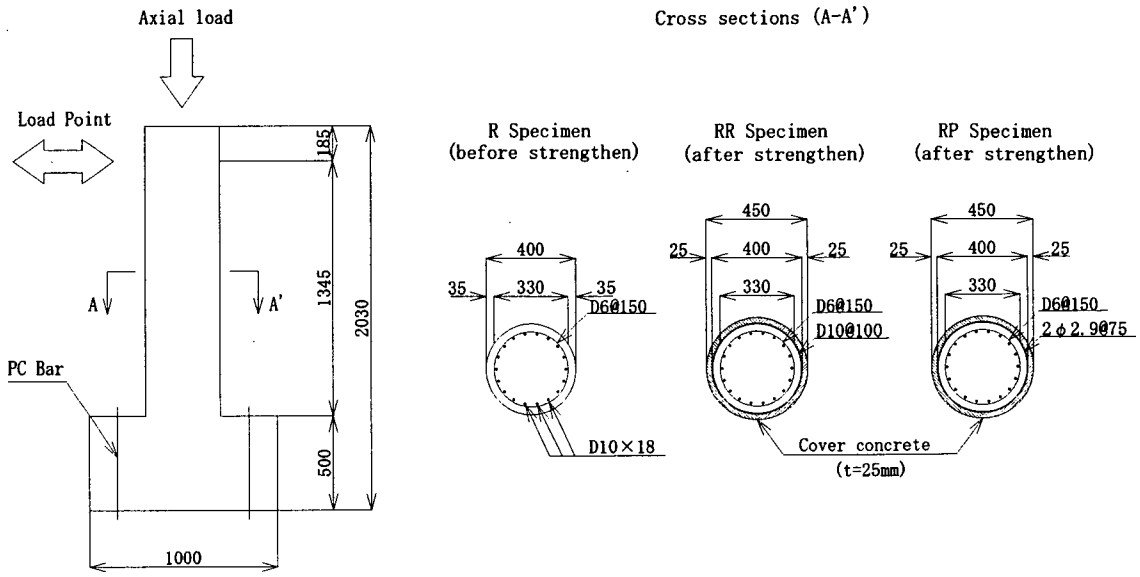

Fig.5 Details of Construction of Specimens

Table 5 Properties of specimens

Specimen name	R	RR	RP
Design strength σ_{ck}	27.9 MPa		
Diameter D (mm)	40.0	45.0	
Longitudinal reinforcement	D10×18		
Hoop reinforcement (before reinforcement)	D6@150	D6@150	D6@150
Yield point σ_y (MPa)	373	373	373
Hoop reinforcement ratio ρ_s (%)	0.24	0.24	0.24
Hoop reinforcement (after reinforcement)	—	D10@100	2 ϕ 2.9@75
Yield point σ_y (MPa)	—	372	1736
Hoop reinforcement ratio ρ_s (%)	—	0.71	0.18

3.2 Materials

The mixture used for the specimens is shown in Table 6. The cement was normal Portland cement. The dynamic properties of the reinforcements and the pre-stressed steel are shown in Table 7.

Table 6 Concrete mixture

Maximum measurement (coarse aggregate)	(mm)		7.0
Water/cement ratio	W/C (%)		63.6
Sand percentage	S/a (%)		57.5
Unit content	Water	(kg/m^3)	216
	Cement		340
	Fine aggregate		892
	Coarse aggregate		686

Table 7 Dynamic properties of reinforcement and pre-stressed steel

		Yield Point (MPa)	Tensile Strength (MPa)	Elongate Ratio (%)	Young's Modulus (MPa)
Hoop Reinforcement	D6 SD295A	373	546	20.0	2.0×10^5
	D10 SD295A	372	518	24.2	2.0×10^5
	2 ϕ 2.9 SWPR2N	1737	1922	8.7	1.95×10^5

3.3 Details of Tests and Testing Instruments

An alternating loading test was performed using a horizontal actuator to apply an axial force, which corresponds to compression of 1 MPa. The loading method in the horizontal direction was controlled by displacement, and every integer times of yielding displacement was repeated three times. A horizontal displacement of 5mm, which was the calculated initial yielding displacement, was applied to each specimen.

3.4 Results of Alternating Loading Test

3.4.1 Destruction Shape

The final destruction shape of each specimen is shown in photo.2. After the cover concrete was split on each specimen, the horizontal load was reduced and the main reinforcement at the base of the pier was finally destroyed. As in the axial compression test, specimen RP, which was pre-stressed, exhibited fewer cracks and a smaller area of cracking than specimen RR.

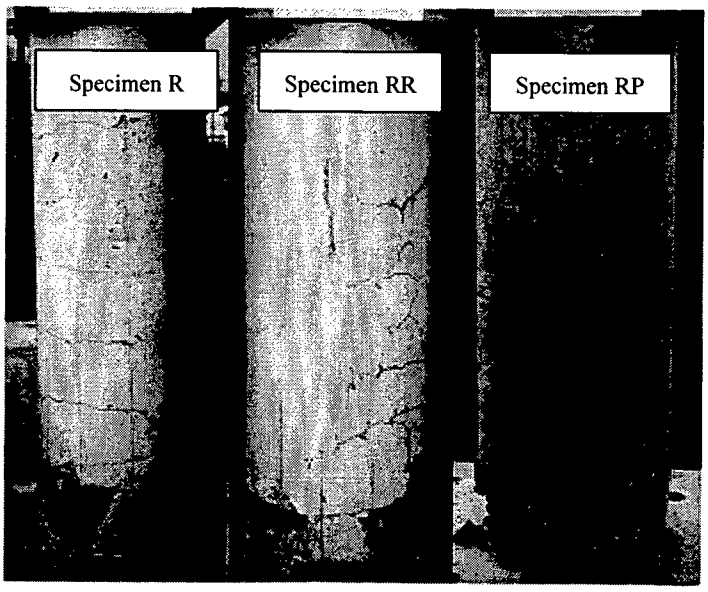

Photo.2 The final destruction shape

3.4.2 Horizontal Load–displacement Relationship

The horizontal load–deflection curve, with calculated values, are

shown in Fig.7. Calculated values for the horizontal displacement were added to the bending displacement and complied with Specification V. The horizontal displacement broke when the main reinforcement was pulled out. In this analysis, we defined the ultimate point as the point at which the longitudinal compression stress at the outermost edge reached ultimate stress. As done with specimen RP, which used pre-stressed steel for the hoop reinforcements, the horizontal displacement was analyzed by the use of a stress-strain curve that was formulated from the results of the axial compression test. The experimental and calculated values for horizontal load, horizontal displacement and ductility ratio are shown in Table 8.

In this test, ultimate displacement was defined as the point at which the cover concrete split. The experimental values for yield displacement were calculated using the following formula, which comes from Specification V 9.3.

$$\delta_{y\exp} = \delta_{yo\exp} \frac{P_{u\exp}}{P_{yocal}} \qquad (6)$$

δ_{yexp} : experimental value of ultimate displacement(mm)

P_{yocal} : calculated value of initial yield point(kN)

δ_{yoexp} : experimental value of displacement when calculated initial yield load is loading(mm)

P_{uexp} : experimental value of maximum load(kN)

The experimental values shown in Table 8 are average of the positive and negative values. The ductility ratio is the ultimate displacement divided by the yield displacement. There were scarcely any differences in the maximum loads

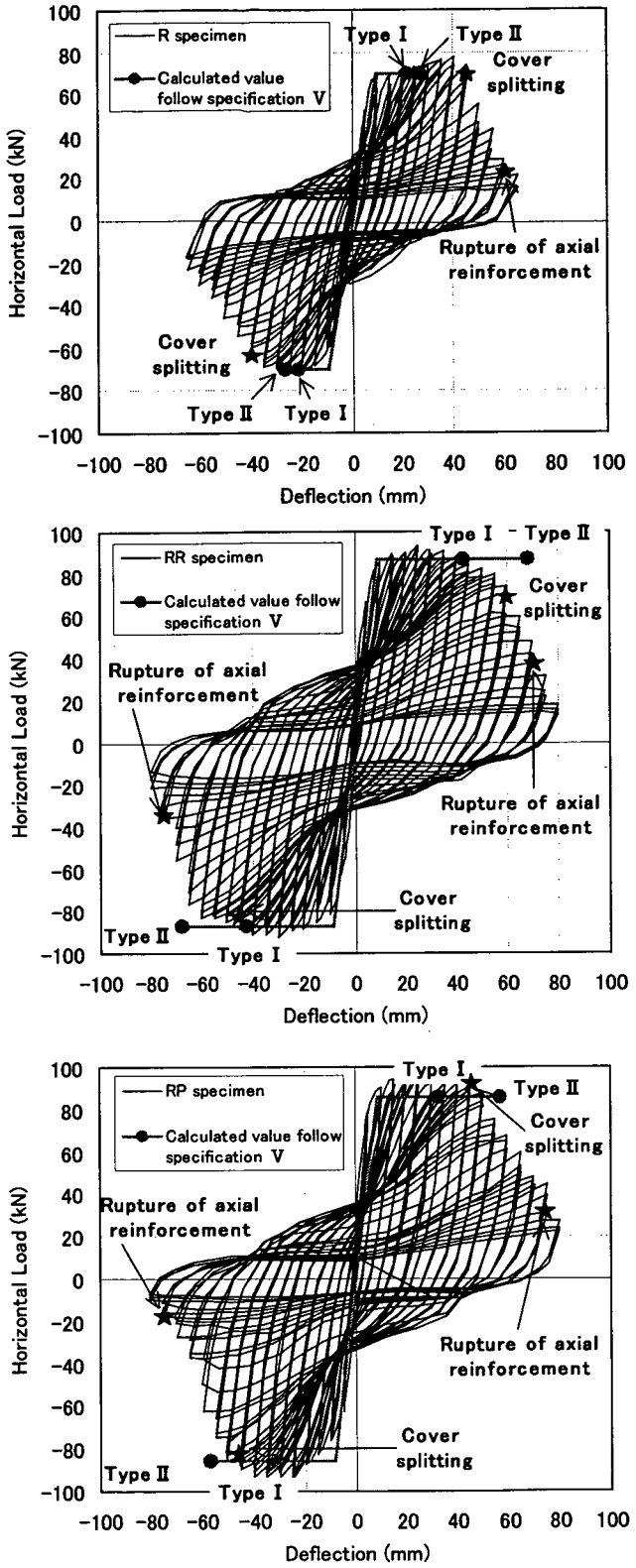

Fig.6 Horizontal load-deflection curve

for specimen RR and RP. The maximum load increased 25% with specimen RR and 24% with specimen RP. Both values were larger than that of specimen R. The ductility ratio for specimen was RR 47% greater and that of specimen RP was 58% greater than that of specimen R. Therefore, specimens RR and RP can be considered to possess substantially improved yield strength and ductility. In addition, the experimental values for ultimate displacement were smaller than the calculated value, but this was thought to the result of the influence of the plastic hinge length, which had an experimental value that was shorter than the assumed value in the calculation.

Table 8 Test results and calculated values

Specimen name		R	RR	RP
Calculated value	P_{ucal} (k N)	69.6	87.3	86.0
	δ_{ycal} (mm)	9.30	8.80	8.60
	δ_{ucal} (mm)	27.0	68.0	57.0
	μ_{cal}	2.90	7.73	6.63
Experimental value	P_{uexp} (kN)	74.8	92.7	95.5
	δ_{yexp} (mm)	8.70	6.63	5.76
	δ_{uexp} (mm)	42.8	48.0	45.0
	μ_{exp}	4.92	7.24	7.81
P_{uexp}/P_{ucal}		1.07	1.06	1.11
μ_{exp}/μ_{cal}		1.70	0.94	1.18

3.4.3 Absorbed Energy

The absorbed energy values are shown in Fig.8. After the cover concrete split, specimen R exhibited reduced energy absorption performance, while specimens RR and RP exhibited increased absorbed energy up to 12 δ_y. The maximum absorbed energy for specimen RR was 47% greater and that of specimen RP was 55% greater than that of specimen R. Specimen RP had almost equal energy absorption performance as specimen RR, although the quantity of hoop reinforcement for specimen RP was 1/4 that of specimen RR.

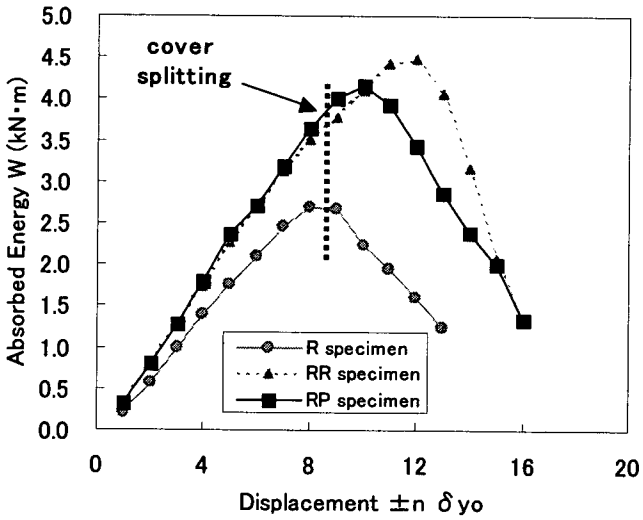

Fig.7 Absorbed Energy

4 CONCLUSIONS

These studies were carried out in order to determine whether or not pre-stressed steel, which has a high yield point, can work effectively in hoop reinforcements, and to establish a method of evaluating confined concrete columns fitted with pre-stressed steel hoop reinforcements. The conclusions were as follows.

Axial Compression Test

(1) As for the specimens that were pre-stressed and used pre-stressed steel for the hoop reinforcements, there was a comparatively small amount of damage to the external appearance.

(2) A large increase in the yield point resulting from the use of pre-stressed steel for the hoop reinforcements couldn't be expected. However, as the pre-stressing value was increased, the maximum stress and strain also increased.
(3) Comparing pre-stressed steel reinforcement and normal reinforcement with equivalent steel ratios, after maximum stress, the downward sloping gradient for the pre-stressed steel reinforcement became gentler than that for normal reinforcement. Therefore, pre-stressed steel reinforcements can effectively improve ductility can reduce the required quantity of steel.
(4) The results of the test suggest a stress-strain curve that can be applied to the use of pre-stressed steel for hoop reinforcement.

Alternating Loading Test

(5) As in the axial compression test, specimens that were pre-stressed exhibited a small amount of damage to their external appearance.
(6) There were scarcely any differences in the maximum loads for specimens RR and RP, but the maximum load for specimen RR was 25% greater and that of specimen RP was 24% greater than that of specimen R.
(7) The ductility ratio for specimen RR was 47% larger and that of specimen RP was 58% larger than that of specimen R.
(8) The absorbed energy performances for specimens RR and RP were similar, but that of specimen RR was 67% greater and that of specimen RP was 55% greater than that of specimen R.
(9) The horizontal load–displacement relationship, which is calculated using the proposed formula, adequately predicted the results of the test.
(10) Although the number of hoop reinforcements fitted to specimen RP was 1/4 that of specimen RR, both specimens had almost identical conversion hoop reinforcement ratios and seismic retrofit effects.

ACKNOWLEDGEMENTS

This paper was based on studies done under the guidance of Mr. Kawashima(Tokyo Institute of Technology). Our appreciation for his assistance.

References

1. Hoshikuma, Kawashima, and Nagaya. "A Stress-Strain Model for Reinforced Concrete Columns Confined by Lateral Reinforcement." Journal of Materials, Concrete Structures and Pavements (in Japanese), No.520/V-28, 1995, pp.1-11.
2. "Japan Road Association,"Specifications for Highway Bridges · Part V: Seismic Design (in Japanese), 1996
3. Zhang, Mori, "Stress-Strain Curve of Circular Concrete Columns Confined by Lateral PC Tendons." Proceedings of Japan Concrete Institute (in Japanese), Vol.19, No.2, 1997, pp.315-320.
4. Zhang, Mori, "The Seismic Retrofit Effectiveness of Lateral PC tendons on Confinement of Reinforced Concrete Piers," The 8th Symposium on Developments in Pre-stressed Concrete (in Japanese), 1998, pp.261-264.
5. Kawashima, Hasegawa, Nagashima, Ogawa, Yoshida, "Seismic Design Method Reinforced Concrete Bridge Piers Based on Dynamic Strength and Ductility," Report of PWRI (in Japanese) Vol.190, 1993,

Bridge Condition Monitoring and Assessment

Li-Hong Sheng

Office of Earthquake Engineering
California Department of Transportation

ABSTRACT

Hundreds of bridges were damaged by several major earthquakes during the last two decades. Bridge failures cost millions of dollar as a result of replacing bridges, restoring bridges, and disruption of transportation facilities. A quick decision needs to be made on the assessing the condition of damaged bridges to minimize the economic impact. An effective bridge evaluation can eliminate the possibility of over strengthening or overlooking any potential failure mechanism.

BRIDGE CONDITION ASSESSMENT

Bridge failures cost millions of dollars each year as a result direct costs from replacing and restoring bridges and indirect costs from disruption of transportation facilities. Cause of such failures include floods, traffic accidents, earthquakes,..etc.. After the 1967 collapse of the Silver Bridge across the Ohio River, from Point Pleasant, West Virginia to Gallipolis, Ohio, the Federal Highway Administration, FHWA, mandated that all bridge owners inspect their bridges and a national bridge database was created. Bridge conditions would be evaluated based on set criteria for future maintenance needs. This evaluation is highly dependent on an engineer's experience and knowledge in structure behavior and material properties. To mitigate the uncertainty, in recent years, structural health monitoring has been favored by professional and academic as the way to provide better and quantified answer.

PURPOSE AND OBJECTIVE OF CONDITION ASSESSMENT

Degrees of detail in bridge condition evaluations are depended on its objective. Is it for live load carrying capacity, lateral stability, rated capacity, ...etc.? Different objectives lead to different models of complexity. Since the main purpose of bridges is to carry traffic across them, the vertical load carrying strength is the most important evaluation requirement. However, for the after earthquake evaluation, the lateral stability and load path are required.

17th US/JAPAN Bridge Engineering Workshop, November 12-14,2001

As we learned from previous earthquakes, there are many factors that affect bridge performance. Some of those factors are design related and others may be geometry or site related. After the 1971 San Fernando Earthquake, we know support length, insufficient development and splice length, column ductility and shear strength are major factors that caused most of the damages. Now we also considered liquefaction potential, soft soil, joint shear, column flare, effective column length, unbalanced frame, member deformability, uneven column length, and outrigger joint. A bridge's behavior depends not only on its geometry but also on its design detail. Geometry factors included bridge length, span length, column height, number of columns per bent, hinge location, difference between adjacent frames, abutment skew angles, bent skew angles, foundation type, aspect ratio of column, aspect ratio of superstructure, ...etc. Design details included steel layout, amount of steel, steel grade, concrete quality, splice detail, and design specification used. And further more, material properties are also important.

There are so many factors that affect a bridge's performance. For a detail condition evaluation one needs to get as much information as possible so that the computer models can truly represent the real structure. Numerous laboratory tests had been performed to verify structure component behaviors through static loads. Limited shaking table tests had been performed to study the dynamic effects. However, actual bridges have seldom been tested for either live loads or other loads by its uncontrollable environmental issues.

In recent years, numerous seismic strong motion sensors have been installed on bridges in California. With data collected to date we find that certain bridge performances are load dependent. For instance, during the 1992 Landers and Big Bear Earthquakes, the responses of the Interstate10/215 interchange were different as shown in Table 1. Similar performance had shown on the shaking table test in this year at the University of Nevada, Reno. Furthermore, a 1995 study on the State highway 101/Painter street overpass for 9 previous earthquakes shown abutment stiffness may be significantly changing during different phases of the shaking.

BRIDGE CONDITION MONITORING

Over years we have tested and evaluated bridge components in the laboratory to verify their performance. However, a real bridge performance test has seldom been performed. In recent years bridges in California have been instrumented with: 1) strong motion sensors to collect real bridge responses during an earthquake; 2) underwater scour sensors to collect river bed depth during flood; and 3) embeded strain gauges, accelerometers, and load cell to collect structure performance during traffic live load.

Strong Motion Instrumentation Program

Since the late 70's, the California Division of Mines and Geology has installed strong motion sensors throughout the State. Some of them were installed on bridges. After the 1989 Loma Prieta Earthquake, Caltrans established its own strong motion instrumentation program. To date, over 60 bridges have strong motion sensors.

Underwater Scouring Monitoring

One of the major failures of bridges is the foundation scour. The number of bridges damaged by floods is less than earthquakes while the number of bridges collapsed due to floods is much more than earthquakes. The FHWA has mandated that each bridge identified as scour critical in the

National Bridge Inspection Standards must have a plan of action addressing the scour problem. The plan of action should include a monitoring program. There are many scour vulnerable bridges in the State of California and more than 10,000 bridges were identified as scour critical nationwide. To date, 11 bridges were instrumented to monitoring bridge foundation scour and streambed stability.

LONG TERM BRIDGE CONDITION MONITORING

As the state of the art in bridge design is advancing toward the performance-based design, it becomes increasingly important to monitor and evaluate the long-term structural performance of bridges. Such information is essential in developing new performance criteria for design. Two bridges in California were instrumented for their long-term structural performance; the Jamboree Road Overcrossing and the West Street On-Ramp in the Orange County. And the new Benicia-Martinez Bridge near the San Francisco Bay Area will be also instrumented for long-term performance for its superstructure with lightweight concrete.

Monitoring technology can play an important role in securing system integrity, minimizing maintenance cost, and maintaining longevity of highway bridges. It can also provide verifications of current design/analysis and provide data for improvement in retrofitting and future construction. Monitoring technology consists of two aspects: (1) instrumentation of bridges with sensors such as accelerometers and strain gauges and (2) methodologies for obtaining meaningful information concerning the structural health conditions.

Description of Bridges

The Jamboree Road Overcrossing shown in Figure 1 is a typical three-span continuous cast-in-place prestressed post-tension box-girder bridge located in Irvine, California. The total length of the bridge is 110.9 m, in which the lengths of spans are 35.5, 46.1, and 30.3 m. The bridge is supported on two monolithic single columns and sliding bearings on both abutments. The sliding bearings allow creep, shrinkage, and thermal expansion or contraction. It is noted that the columns are not on the centerline of the superstructure as shown and the bridge has a skewed abutment 4. Accelerometers and a displacement sensor were installed on the Jamboree Road Overcrossing.

The West Street On-Ramp shown in Figure 2 is a three-span continuous and curved cast-in-place prestressed post-tension box-girder bridge in the I-5 Corridor near Disneyland in Anaheim, California. The total length of the bridge is 151.3m, in which the lengths of spans are 45.8, 60.1, and 45.4m. The bridge is supported by two fixed columns and sliding bearings on both abutments. The bridge is curved with a 12% super-elevation.

Monitoring System

Uni-axial, bi-axial, and tri-axial force-balance servo-type accelerometers were permanently installed on both bridges. The frequency response functions of the accelerometers indicate that the accelerometers can measure dynamic signals in a frequency range from 0.5 Hz through 30 Hz with very good accuracy. The accelerometers are placed along the centerline of the bottom of the girder to minimize the torsional effect of the bridge box girder. Strain gauges, which are micro-displacement sensors, were permanently embedded in concrete members of the West Street On-Ramp. The strain gauges were completely welded to dummy reinforcing bars, and were embedded to measure the dynamic strains induced by bending moments. The locations of strain gauges are shown in Figure 3.

PRELIMINARY FINITE ELEMENT ANALYSIS

For preliminary finite element analyses, 3 dimensional (3D) finite element models as shown in Figures 4 and 5 were developed respectively for the Jamboree Road Overcrossing and the West Street On-Ramp. The super- and sub-structures were modeled as 3D frame elements. The cross section area and moment of inertia for each element were calculated from the design drawings. The most difficult part of modeling was to develop realistic footing and abutment models and to determine their stiffness parameters. Considering that the use of the model is for analyzing the bridge response to operational (traffic) loads, the bridge bearings at the abutments were modeled as linear horizontal and rotational springs, which were based on FHWA. The natural frequencies and the mode shapes computed using this analytical model will be presented later.

System Identification on the Jamboree Road Overcrossing

When dynamic properties of large civil engineering structures such as bridges and buildings are estimated the possibilities to control and measure the loading is limited. For a bridge which carries traffic 24 hours a day, the traffic-induced ambient vibration is most significant. In comparison to forced vibration techniques, the ambient vibration techniques present a remarkable advantage of not requiring heavy and expensive equipment to excite the structure. The dynamic properties of the structure can be rather accurately estimated on the basis of the measurements of structural ambient responses. Dynamic property extraction using ambient vibration measurements requires special data processing techniques to deal with relatively small amplitudes of ambient vibrations contaminated with noises without the knowledge of input forces. The peak picking, the random decrement, and the frequency domain decomposition methods have been used for processing ambient vibration data measured at the Jamboree Road Overcrossing.

The accelerations at the various locations on the bottom of the box-girder and a column were measured with a sampling frequency of 100 Hz. The amplitudes of accelerations in the transverse direction are relatively smaller than those in the vertical direction, since the traffic induced vibrations is in the vertical direction. A total of 82 data sets were collected and processed with a duration of 10 minutes each. The peak picking (PP) and the frequency domain decomposition (FDD) methods were used to extract modal parameters from the averaged vibration data with 25 percent overlapping. The random decrement (RD) method was also applied to obtain the parameters from the random vibration data. This data was derived from a prescribed initial condition of positive zero crossing. Random acceleration exhibits a free vibration decay since the data set have been sampled with the approximately same initial conditions compared to those in the averaged acceleration.

The natural frequencies (six in the vertical and three in the transverse directions) derived analytically and experimentally are shown together in Table 2. The difference as shown in the parentheses between the analytical and the experimental natural frequencies suggests the need for updating the initial finite element model using the experimental results. It is observed that the high and the horizontal modes contain more noises than the low and the vertical modes since traffic loads mainly excite vertical vibration and the frequency contents of the loads are relatively low. Observing the mode shapes, those estimated by the FDD method agree better with those from the finite element analysis than those estimated by the PP and the RD methods.

System Identification on the West Street On-Ramp

Braking and bumping vibration tests were carried out using a water truck on the West Street On-Ramp before it opened to traffic. Braking and bumping forces were applied by the water truck at the middle of each span to induce bridge vibration in the longitudinal and vertical directions. The water truck weighs approximately 15000 kg when fully loaded. The amplitudes of accelerations in the transverse direction are smaller than in the vertical direction. More importantly, the amplitudes of the accelerations in the bumping vibration tests were greater than in the braking vibration tests. Four sets of data from the braking vibration tests and three sets of data from the bumping vibration tests were processed. Each data set is 10 minutes long and all the data were collected at night with no traffic under the bridge. The FDD method was used to extract modal parameters from the averaged vibration data with 25 percent overlapping. The sampling rate was 100 Hz and an average 4,096 data points. The first and the second natural frequencies as shown in Table 3 were estimated in the vertical and transverse directions simultaneously since the vertical and the transverse modes are coupled together. It is observed that the natural frequencies derived from the braking vibration tests are different from those from the bumping vibration tests. The natural frequencies estimated from the bumping vibration tests are maximum 3.5 percent smaller than those from the braking vibration tests, although these tests were performed under the same environmental conditions. This can be explained by the nonlinear characteristics of concrete: the larger deformation corresponds to the smaller elasticity.

SUMMARY

Engineers have been assessed and evaluated bridge condition to rate bridge capacity for many years. The major purpose is to quantify bridge's condition for future maintenance needs. Whenever such work was performed, it is largely depend on the engineer's experience. As the performance and LRFD based design becomes more and more accepted as general practice, bridge's load carry capacities and its lateral stability need to be more carefully verified. Current information indicates that bridge performance varies from time to time. As such a lifetime bridge performance data is lacking, bridge condition monitoring becomes most critical method to fulfill the gap. A number of bridges are instrumented recently for long term performance monitoring. Preliminary data shows that such variation depends on load and analytical methods used. More and more data need to be collected and analyzed if a performance pattern can be truly defined and quantified.

REFERENCES

1. R. Brinker, L. Zhang, and P. Andersen, "Modal Identification from Ambient Response Using Frequency Domain Decomposition," *Proceedings of 16th International Modal Analysis Conference*, San Antonio, Texas, USA, Feb., 6-10, 2000, 625-630.
2. Rajesg K. Goel and Anil K. Chopra, "Seismic Response Study of the Hwy101/Painter Street Overpass near Eureka using Strong-Motion Records", Data Utilization Report CSMIP/95-01, California Strong Motion Program, California Department of Conservation, 1995.
3. Gregory L. Fenves and Reginald Desroches, "Evaluation of the Response of I-10/215 Interchange Bridge near San Bernardino in the 1992 Landers and Big Bear Earthquakes", Data Utilization Report CSMIP/95-02, California Strong Motion Program, California Department of Conservation, 1995.
4. Claudia P. Pulido-Collantes, M. Saiid Saiidi, David Sanders, and Ahmand Itani, "Seismic Performance and Retrofitting of Reinforced Concrete Bridge Bents", Report No. CCEER-01-xx, Center for Civil Engineering Earthauek Research, University of Nevada, Reno, 2001.

5. M.Q. Feng, J.M. Kim, and H. Xue, "Identification of a Dynamic System Using Ambient Vibration Measurements," *Journal of Applied Mechanics, ASME*, Vol.65, No.4, pp.1010-1021, 1998.
6. J.S. Bendat and A.G. Pierso, *Engineering Application of Correlation and Spectral Analysis*, John Wiley & Sons, New York, USA, 1993.
7. D. J. Ewins, *Modal Testing: Theory, Practice and Application*, Wiley, John & Sons, 1999.
8. C.B. Yun, J.H. Yi, J.J. Lee, and J.D. Kim, "Modal Parameter Identification Methods without Input Information: A Comparative Study," *The 1st International Conference on Structural Stability and Dynamics*, Dec 7-9, 2000, Taipei, Taiwan.
9. R. Brinker, L. Zhang, and P. Andersen, "Modal Identification from Ambient Response Using Frequency Domain Decomposition," *Proceedings of 16th International Modal Analysis Conference*, San Antonio, Texas, USA, Feb., 6-10, 2000, 625-630.
10. J.C. Asmussen and R. Brincker, "Estimation of Frequency Response Function by Random Decrement," *Proceedings of International Modal Analysis Conference*, pp.246-252, 1996.

Table 1. Comparison of Natural Periods of I-10/215 Interchange (sec)

Mode Number	Landers Earthquake		Big Bear EArthquake	
	Spectral Analysis	System Identification	Spectral Analysis	System Identification
1	1.51	1.56	1.78	1.75
2	1.19	1.30	1.24	1.29
3	1.02	0.98	1.14	1.09
4	0.79	0.83	0.95	0.96

Table 2. Comparison of Natural Frequencies of Jamboree Road Overcrossing (Hz)

Mode Number	In-plane modes				Out-of-plane modes		
	FE	PP	RD	FDD	FE	PP	FDD
1	2.889	2.954 (0.065)	2.954 (0.065)	2.954 (0.065)	3.126	2.612 (0.514)	2.612 (0.514)
2	3.716	3.979 (0.263)	4.077 (0.361)	3.979 (0.263)	4.535	5.004 (0.469)	5.004 (0.469)
3	4.654	4.660 (0.006)	4.638 (0.016)	4.638 (0.529)	6.111	6.662 (0.551)	6.640 (0.529)
4	5.721	6.250 (0.529)	6.323 (0.602)	6.250 (0.529)			
5	9.400	8.957 (0.443)	8.813 (0.587)	8.911 (0.489)			
6	14.521	12.793(1.728)	12.866(1.655)	12.793(1.728)			

Note: The values in the parentheses are the difference between the analytical and the experimental natural frequencies.
In-plane modes = modes in the vertical and in the longitudinal directions
Out-of-plane modes = modes in the transverse direction
FE = finite element analysis
PP = peak picking method
RD = random decrement method
FDD = frequency decomposition method

Table 3. Comparison of Natural Frequencies of West Street On-Ramp (Hz)

Test	Braking Vibration Test		Bumping Vibration Test	
Mode	Vertical	Transverse	Vertical	Transverse
1	2.148	2.148	2.075 (-0.073)	2.124 (-0.024)
2	2.465	2.465	2.441 (-0.024)	2.441 (-0.024)

Note: 'Vertical' and 'Transverse' mean the direction of vibration measurements, and the values in the parentheses are the difference between two test results.

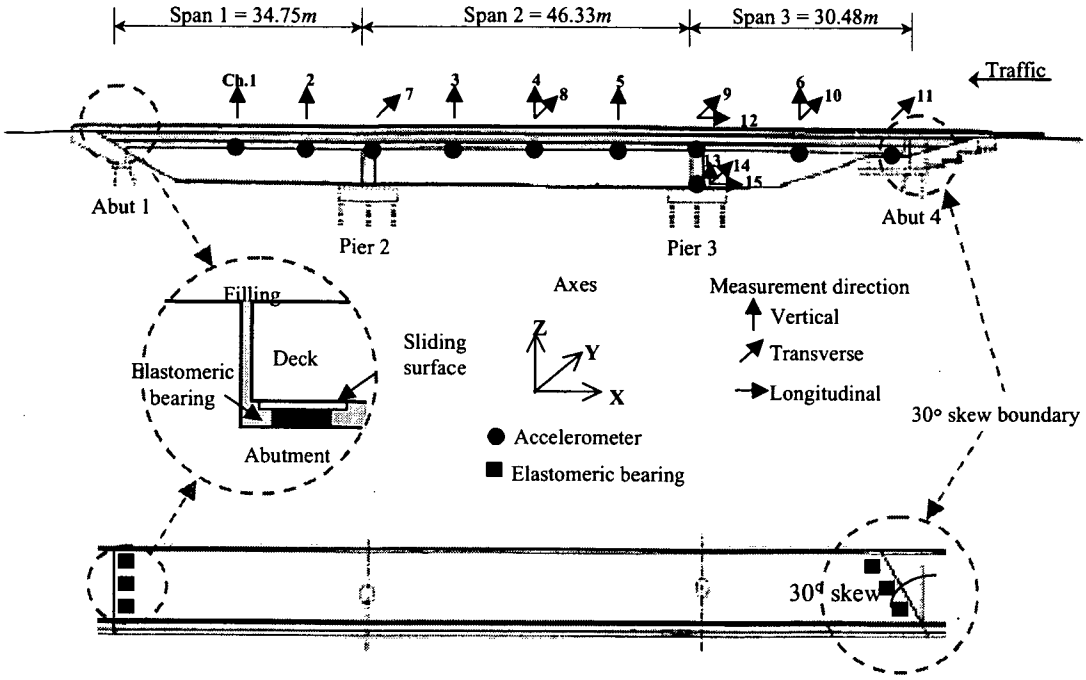

Figure 1. Jamboree Road Overcrossing and Accelerometer Arrangement

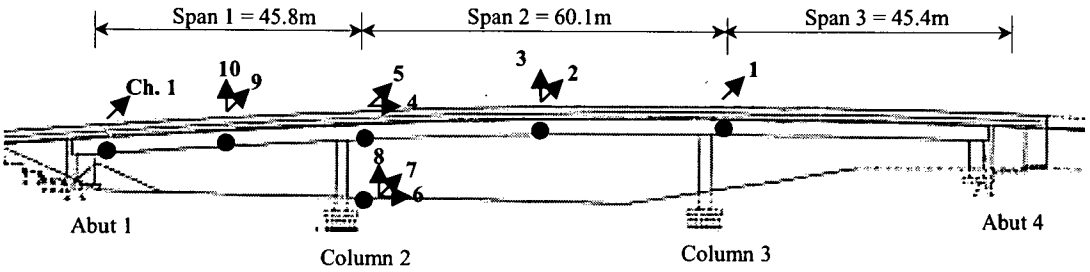

Figure 2. West Street On-Ramp and Accelerometer Arrangement

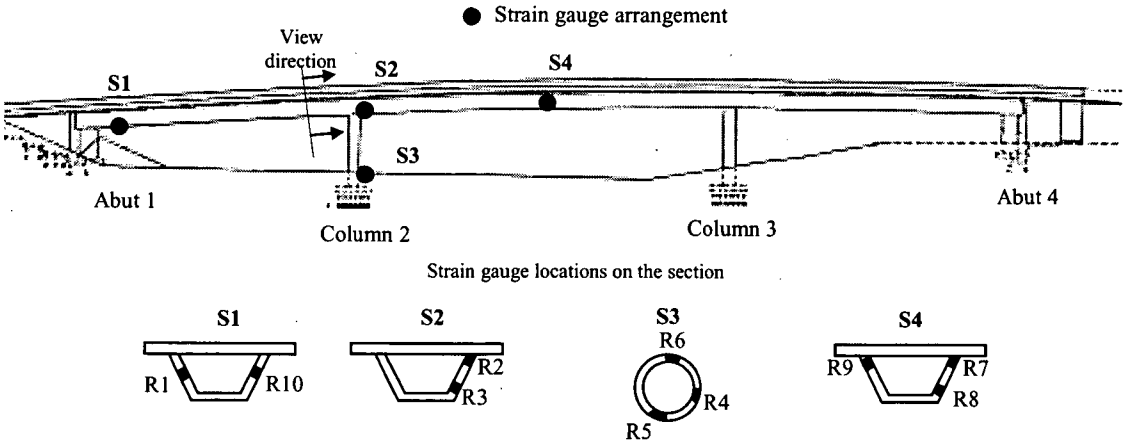

Figure 3. Strain Gauge Arrangement at West Street On-Ramp

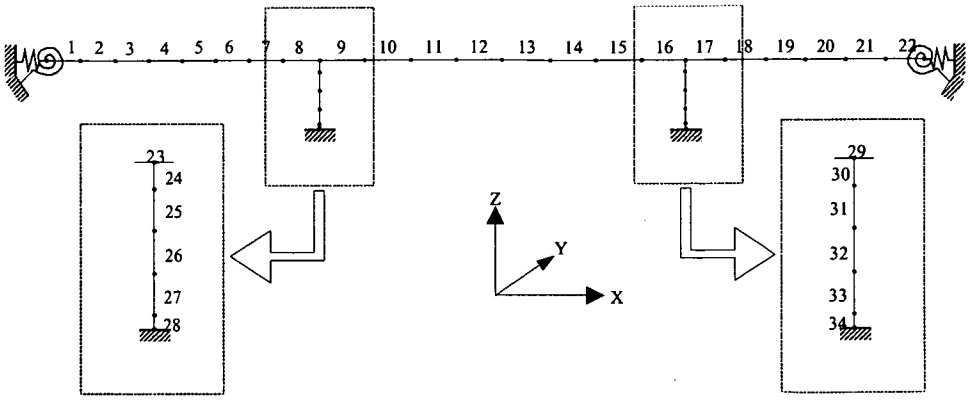

Figure 5. Finite Element Model of Jamboree Road Overcrossing

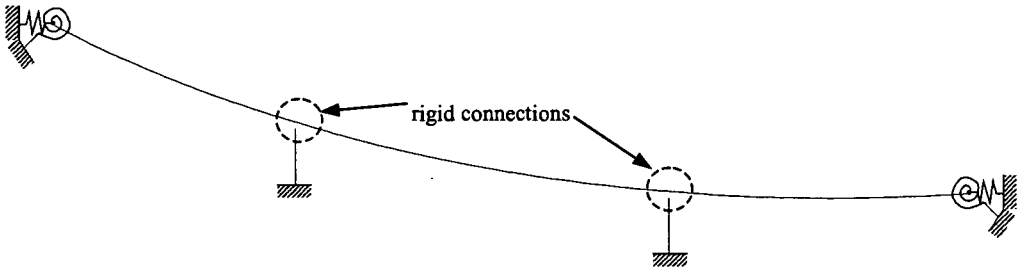

Figure 5. Finite Element Model of West Street On-Ramp

SESSION 6: SEISMIC 3

(1) Recommended LRFD Guidelines for the Seismic Design of Highway Bridges
(M. Lee Marsh, Ronald L. Mayes and Ian M. Friedland)

(2) A Comparative Study on US-Japan Seismic Isolation Design of Highway Bridges
(Hidesada Kanaji, Hamid Ghasemi, Phillip Yen and Sunwoo Park)

(3) An Evaluation of Seismic Bridge Joint Design using Strut-and-Tie Concepts
(Sri Sritharan)

(4) Loading Tests on Cap Beams to Evaluate Shear Strength against Earthquakes
(Kenji Kosa, Jyunko Taguchi, Satoshi Yoshihara and Katsunori Tanaka)

(5) Seismic Testing of Retrofits in the Central and Southeastern United States
(Reginald DesRoches, Thomas Pfeifer and Roberto T. Leon)

RECOMMENDED LRFD GUIDELINES FOR THE SEISMIC DESIGN OF HIGHWAY BRIDGES

M. Lee Marsh[1], Ronald L. Mayes[2], and Ian M. Friedland[3]

Abstract

This paper provides an overview of the proposed seismic design provisions that have been developed to replace those currently in use throughout the United States. The proposed provisions include two-level design procedures, advanced analytical tools such as push-over, updated ground motion data, new site characterizations, simplified methods for lower seismicity regions, and more comprehensive liquefaction provisions. Many of the developments that have followed in the wake of recent earthquakes have been incorporated into the proposed provisions. The effort has been conducted and overseen by broad-based and nationally recognized teams. The proposed provisions are now being used in trial designs around the country and will be considered for adoption in Guide Specification form next year by AASHTO.

Background

In the fall of 1998, the AASHTO (American Association of State Highway and Transportation Officials)-sponsored National Cooperative Highway Research Program (NCHRP) initiated a project to develop a new set of seismic design provisions for highway bridges, compatible with the AASHTO *LRFD Bridge Design Specifications* (AASHTO, 2000). NCHRP Project 12-49, which was conducted by a joint venture of the Applied Technology Council and the Multidisciplinary Center for Earthquake Engineering Research (the ATC/MCEER Joint Venture), had as its primary objectives the development of seismic design provisions that reflected the latest design philosophies and design approaches that would result in highway bridges with a high level of seismic performance.

NCHRP Project 12-49 was intended to reflect experience gained during recent damaging earthquakes and the results of research programs conducted in the United States and elsewhere over the prior 10 years. The primary focus of the project was on the development of design provisions which reflected the latest information regarding: design philosophy and performance criteria; seismic hazard representation, loads and displacements, and site effects; advances in analysis and modeling procedures; and requirements for component design and detailing. The new specification is intended to be nationally applicable with provisions for all seismic zones, and all bridge construction types and materials.

The current provisions contained in the AASHTO *LRFD Bridge Design Specifications* are, for the most part, based on provisions and approaches carried over from Division I-A, "Seismic Design," of the AASHTO *Standard Specifications for Highway Bridges* (AASHTO, 1996). The Division I-A seismic provisions were originally issued by AASHTO as a Guide Specification in 1983 and were subsequently incorporated with little modification into the *Standard Specifications* in 1991. Thus, the current *LRFD* (Load and Resistance Factor

[1] Senior Project Manager, BERGER/ABAM Engineers Inc, Federal Way, WA
[2] Bridge Consultant, Simpson Gumpertz and Heger, San Francisco, CA
[3] Associate Director for Development, Applied Technology Council, Washington, D.C.

Design) provisions are based on seismic hazard, design criteria and detailing provisions, that are now considered at least 10 years and in many cases nearly 20 years out-of-date. Because AASHTO is in the process of transitioning from the *Standard Specifications* to the *LRFD* specification, it made sense to comprehensively update the seismic provisions.

NCHRP Project 12-49 developed a preliminary set of comprehensive specification provisions and commentary intended for incorporation into the AASHTO *LRFD* specifications. However, due to the amount of detail in the new provisions and the general view that the new provisions were significantly more complex than the existing provisions, the AASHTO Highway Subcommittee on Bridges and Structures recommended that the new provisions be adopted by AASHTO first as a Guide Specification (MCEER, 2001). This would then allow bridge designers the opportunity to become familiar with the proposed new specifications, and for any problems such as omissions and editorial or technical errors in the new provisions to be identified and rectified, prior to formal adoption into the AASHTO *LRFD* specifications.

Basic Concepts

The development of these specifications was predicated on the following basic concepts.

- Loss of life and serious injuries due to unacceptable bridge performance should be minimized.
- Bridges may suffer damage and may need to be replaced but they should have low probabilities of collapse due to earthquake motions.
- The function of essential (critical lifeline) bridges should be maintained even after a major earthquake.
- Upper level event ground motions used in design should have a low probability of being exceeded during the approximate 75-year design life of the bridge.
- The provisions should be applicable to all regions of the United States.
- The designer should not be restricted from considering and employing new and ingenious design approaches and details.

In comparison to the current AASHTO *Standard Specifications for Highway Bridges* and the AASHTO *LRFD Bridge Design Specifications,* the recommended Guide Specifications contain a number of new concepts and additions as well as some major modifications to the existing provisions. These are discussed in this paper.

New Seismic Hazard Maps

The national earthquake ground motion map used in the existing AASHTO provisions is a probabilistic map of peak ground acceleration (PGA) on rock that was developed by the U.S. Geological Survey (USGS) in 1990. The map provides contours of PGA for a probability of exceedance (PE) of 10% in 50 years, which corresponds to approximately 15% PE in the 75-year design life assumed by the *LRFD* specifications for a typical highway bridge.

In 1993, the USGS embarked on a major project to prepare updated national earthquake ground motion maps. The result of that project was a set of probabilistic maps first published in 1996 that cover several rock ground motion parameters and three different probability levels or return periods. The maps are available as large-scale paper maps, as small-scale paper maps obtained via the Internet, and as digitized values obtained from the Internet or a CD-ROM published by USGS (Frankel et al., 2000). Parameters of rock ground motions that have been contour mapped by USGS include peak ground acceleration (PGA) and elastic response spectral accelerations for periods of vibration of 0.2, 0.3, and 1.0 second. Contour maps for these parameters have been prepared for three different probabilities of exceedance (PE): 10% PE in 50 years, 5% PE in 50 years, and 2% PE in 50 years (approximately 3% PE in 75 years). In addition to these contour maps, the ground motion values at any specified latitude and longitude in the U.S. can be obtained via the Internet for the aforementioned three probability levels for PGA and spectral accelerations for periods of vibration of 0.2, 0.3, and 1.0 seconds. In addition, the published data contains not only the PGA and spectral acceleration values at three probability levels but also the complete hazard curves (i.e., relationships between the amplitude of a ground motion parameter and its annual frequency of exceedance at each grid point location). Therefore, the ground motion values for all of the aforementioned ground motion parameters can be obtained for any return period or probability of exceedance from the hazard curves. These maps formed the basis for seismic design using these new provisions. Upper bound limits of 1.5 times the median ground motions obtained by deterministic methods have been applied to limit probabilistic ground motions in the western United States.

Design Earthquakes and Performance Objectives

The existing AASHTO provisions have three implied performance objectives for small, moderate and large earthquakes with detailed design provisions for a 10% PE in 50 year event (approximately 15% PE in 75 year event) to achieve the stated performance objectives. The new provisions provide more definitive performance objectives and damage states for two design earthquakes with explicit design checks for each earthquake to ensure the performance objectives are met (Table 1). The upper-level event, termed the 'rare earthquake' or Maximum Considered Earthquake (MCE), describes ground motions that, for most locations, are defined probabilistically and have a probability of exceedance of 3% in 75 years. However, for locations close to highly active faults, the MCE ground motions are deterministically bounded so that the levels of ground motions do not become unreasonably high. Deterministic bound ground motions are calculated assuming the occurrence of maximum magnitude earthquakes on the highly active faults and are equal to 1.5 times median ground motions for the maximum magnitude earthquake but not less than 1.5g for the short-period spectral acceleration plateau and 0.6g for 1.0-second spectra acceleration. On the current MCE maps, deterministic bounds are applied in high-seismicity portions of California, in local areas along the California-Nevada border, along coastal Oregon and Washington, and in high-seismicity portions of Alaska and Hawaii. In areas where deterministic bounds are imposed, ground motions are lower than ground motions for 3% PE in 75 years. The MCE earthquake governs the limits on the inelastic deformation in the substructures and the design displacements for the support of the superstructure.

The lower level design event, termed the 'expected earthquake', has ground motions corresponding to 50% PE in 75 years. This event ensures that essentially elastic response is achieved in the substructures for the more frequent or expected earthquake. This design level is similar to the 100-year flood and has similar performance objectives. An explicit check on

the strength capacity of the substructures is required. Parameter studies performed as part of the development of the provisions show that the lower level event will only impact the strength of the columns in parts of the western United States. Background on the choice of the two design events is provided in Appendix A of the Guide Specification.

Design Incentives

The provisions contain an incentive from a design and construction perspective for performing a more sophisticated "pushover analysis." The R-Factor increases approximately 50% when a pushover analysis is performed, primarily because the analysis results will provide a greater understanding of the demands on the seismic resisting elements. The analysis results are assessed using plastic rotation limits on the deformation of the substructure elements to ensure adequate performance.

New Soil Factors

The site classes and site factors incorporated in the new provisions were originally recommended at a site response workshop in 1992 and subsequently were adopted in the Seismic Design Criteria of Caltrans (1999), the 1997 NEHRP Provisions (BSSC, 1998), the 1997 Uniform Building Code (UBC) (ICBO, 1997), and the 2000 International Building Code (IBC) (ICC, 2000). This is one of the most significant changes with regard to its impact on the level of seismic design forces. It should be noted that the recommended soil factors affect both the peak (flat) portion of the response spectra as well as the long-period descending portion of the spectra (Figure 1). The increase in site factors with decreasing accelerations is due to the nonlinear response effects of soils. Soils are more linear in their response to lower acceleration events and display more nonlinear response as the acceleration levels increase. The effects of soil nonlinearity are also more significant for soft soils than for stiff soils.

New Spectral Shapes

The long period portion of the current AASHTO acceleration response spectrum is governed by a spectrum shape that decays as $1/T^{2/3}$. During the development of this decay function for the existing provisions, there was considerable massaging of the factors that affect the long period portion of the spectra in order to produce a level of approximately 50% conservatism in the design spectra when compared to the ground spectra beyond a one-second period. The new provisions remove this conservatism and provide a more correct spectral shape that decays as 1/T for periods below three seconds. Guidance is also provided for the spectral shapes beyond a period of three seconds.

Earthquake Resisting Systems and Elements (ERS and ERE)

The provisions provide a mechanism to permit the use of some seismic resisting systems and elements that were not permitted for use in the current AASHTO provisions. Selection of an appropriate ERS is fundamental to achieving adequate seismic performance. To this end, the identification of the lateral-force-resisting concept and the selection of the necessary elements to facilitate the concept should be accomplished in the conceptual design or Type, Selection, and Layout (TS&L) phase of the project. Seismic performance is typically better in systems with regular configurations and evenly distributed stiffness and strength. Thus, typical geometric configuration constraints, such as skew, unequal pier

heights, and sharp curves, conflict, to some degree, with the seismic design goals. For this reason, it is advisable to resolve potential conflicts between configuration and seismic performance early in the design effort. The classification of ERS and ERE into the categories of (1) permissible, (2) permissible with owner's approval, and (3) not recommended is done to trigger due consideration of seismic performance that leads to the most desirable outcome — that is, seismic performance that ensures wherever possible post-earthquake serviceability. It is not the objective of this specification to discourage the use of systems that require owner approval. Instead, such systems may be used, but additional design effort and consensus between the designer and owner are required to implement such systems. Common examples from first two categories of systems are shown in the Figures 2 and 3.

No Analysis Design Concept

The no analysis design procedure is an important new addition to the recommended provisions. It applies to regular bridges in the lower seismic hazard areas, including the expanded areas now requiring more detailed seismic design. The bridge is designed for all non-seismic loads and does not require a seismic demand analysis. Capacity design procedures are used to determine detailing requirements in columns and in the connection forces of columns to the footing and superstructure. There are no seismic design requirements for abutments, except that integral abutments need to be designed for passive pressure.

Capacity Spectrum Design Procedure

The capacity spectrum design method is a new addition to the provisions and is conceptually the same as the new Caltrans' displacement design method. The primary difference is that the capacity spectrum design procedure begins with the non-seismic capacity of the columns and then assesses the adequacy of the resulting displacements. At this time, the capacity spectrum method may be used for very regular bridges that respond essentially as single-degree-of-freedom systems, although future research should expand the range of applicability. The capacity spectrum approach uses the elastic response spectrum for the site, and this is reduced to account for the dissipation of energy in the earthquake resisting elements. The advantage of the approach is that the period of vibration does not need to be calculated, and the designer sees the explicit trade-off between the design forces and displacements. The method is also quite useful as a preliminary design tool for bridges that may not satisfy the current regularity limitations of the approach.

Displacement Capacity Verification ("Pushover") Analysis

The pushover method of analysis has seen increasing use since the early 1990's, and is widely employed in the building industry and by some transportation departments including the Caltrans seismic retrofit program. This analysis method provides additional information on the expected deformation demands of columns and foundations and, as such, provides the designer with a greater understanding of the expected performance of the bridge. The method was used for two different purposes in these new provisions. First, it provided a mechanism under which the highest R-Factor for preliminary design of a column could be justified, because there are additional limits on the column plastic rotations that the results of the pushover analysis must satisfy. Second, it provided a mechanism to allow incorporation of earthquake resisting elements (ERE) that require owner's approval. The trade-off was the need for a more sophisticated analysis so that the expected deformations in critical elements

could be assessed. The ERE could then be used, provided that the appropriate plastic deformation limits were met.

Foundations

The new provisions are an update of the existing AASHTO LRFD provisions incorporating explicit material that was referenced in the existing specifications and to incorporate recent research. The changes include specific guidance for the development of spring constants for spread footings and deep foundations (i.e., driven piles and drilled shafts.), as well as approaches for defining the capacity of the foundation system under overturning moments. The capacity provisions specifically address issues such as uplift and plunging (or yield) limits within the foundation. Procedures for including the pile cap in the lateral capacity and displacement evaluation are also provided. The implications of liquefaction of the soil, either below or around the foundation system, are also described. This treatment of liquefaction effects is a major technical addition to the provisions.

Abutments

The new provisions incorporate much of the research that has been performed on abutments over the past 10 years. Current design practice varies considerably on the use of the abutments as part of the ERS. Some agencies design a bridge so that the substructures are capable of resisting all of the seismic loads without any contribution from the abutment. Other agencies use the abutment as a key component of the ERS. Both design approaches are permitted in these provisions. The abutments can be designed as part of the ERS and become an additional source for dissipating the earthquake energy. In the longitudinal direction, the abutment may be designed to resist the forces elastically utilizing the passive pressure of the backfill or, in some cases, passive pressure at the abutment is exceeded, resulting in larger soil movements in the abutment backfill. This requires a more refined analysis to determine the amount of expected movement, and procedures are provided herein to incorporate this nonlinear behavior. In the transverse direction, the abutment is generally designed to resist loads elastically. These provisions therefore recognize that the abutment can be an important part of the ERS and considerable attention is given to abutment impacts on the global response of the bridge. For the abutments to be able to effectively contribute to the ERS, a continuous superstructure is required.

Liquefaction

Liquefaction has been one of the most significant causes of damage to bridge structures during past earthquakes. Most of the damage has been related to lateral movement of soil at the bridge abutments. However, cases involving the loss of lateral and vertical bearing support of foundations for central piers of a bridge have also occurred. Considerable research and development have occurred over the past decade in the areas of liquefaction potential and effects, and much of this information has been incorporated in these new provisions. For example, the new provisions outline procedures for estimating liquefaction potential using methods developed in 1997, as part of a national workshop on the evaluation of liquefaction. Procedures for quantifying the consequences of liquefaction, such as lateral spreading of approach fills and settlement and potential flow of liquefied soils, are also given. The provisions also provide specific reference to methods for treating deep foundations extending through soils that are spreading or flowing laterally as a result of liquefaction.

Consideration of liquefaction is based, in part, on the mean earthquake magnitude at a site, and mean magnitudes are found in the same USGS database that is used to obtain spectral accelerations. For sites with mean earthquake magnitudes less than 6.0, the effects of liquefaction on dynamic response can be neglected. When liquefaction occurs, vibration and permanent movement occur simultaneously during a seismic event. The recommended methodology in these provisions is to consider the two effects independently; i.e., de-coupled.

If lateral flow or spreading occurs, significant movement of the abutment and foundation systems can result and this can be a difficult problem to mitigate. The range of design options include (1) designing the piles for the flow forces to (2) an acceptance of the predicted lateral flow movements, provided inelastic hinge rotations in the piles remain within a specified limit. Figure 4 shows a case where spreading movements will cause yielding in both the abutment and pier foundations. The acceptance of plastic hinging in the piles is a deviation from past provisions in that damage to piles is accepted when lateral flow occurs, thereby acknowledging that the bridge may need to be replaced if this option is selected.

Assessment techniques for determining post-earthquake conditions of deep foundations, such as piles and drilled shafts are expected to be developed in the future. Currently, such techniques as down-hole inclinometers are available. Additionally, video assessment techniques are emerging, but are not in use in the U.S. If appropriate sensing devices and access types can be developed, then practical assessment damage to deep foundations can become a tool for engineers to evaluate foundation condition and the need for repair or replacement.

Structural or soil mitigation measures to minimize the amount of movement to meet higher performance objectives are also outlined in the new provisions. Due to the concerns about the potential cost impact of liquefaction coupled with the impact of higher level design events, two detailed case studies on the application of the recommended design methods for both liquefaction and lateral flow design were performed (NCHRP, 2001). The results are also summarized in Appendix H of the provisions. These examples demonstrated that for some soil profiles application of the new provisions would not be significantly more costly than the application of the more conservative current provisions.

Steel Design Requirements

The existing AASHTO Specifications do not have seismic requirements for steel bridges, except for the provision of a continuous load path to be identified and designed (for strength) by the engineer. Consequently a comprehensive set of special detailing requirements for steel components expected to yield and dissipate energy in a stable and ductile manner during earthquakes were developed, including provisions for ductile moment-resisting frame substructures, concentrically-braced frame substructures, and end-diaphragms for steel girder and truss superstructures. These provisions now provide a complete set of guidance on steel structures, drafts of which have been well reviewed by a wide range of engineers knowledgeable in steel design and construction practice.

Concrete Design Requirements

There are no major additions to the concrete provisions, but there are important updates for key design parameters based on research conducted over the past decade. The minimum

amount of longitudinal steel was reduced from 1% to 0.8%, which will result in cost savings when used with the capacity design procedures. An implicit shear equation was also added where no seismic demand has been determined. Modifications to the explicit shear equation and confinement requirements were made, and a global buckling provision was added, as were plastic rotation limits for the pushover analysis.

Superstructure Design Requirements

Detailed design requirements are not included in the current AASHTO seismic design provisions, other than those required by the generic load path requirement. Therefore, for the higher hazard levels, explicit design requirements have been added since the current provisions result in a wide discrepancy in their application.

Bearing Design Requirements

One of the significant issues that arose during development of the steel provisions, and was subsequently endorsed by the NCHRP Project Panel and the ATC/MCEER Joint Venture Project Team (PT) and Project Engineering Panel (PEP), was the critical importance of bearings as part of the overall bridge load path. The 1995 Kobe, Japan earthquake (and other more recent earthquakes) clearly showed the very poor performance of some bearing types and the disastrous consequence that a bearing failure can have on the overall performance of the bridge. Three design options are included to address the issue; these are (1) testing of the bearings, (2) ensuring restraint of the bearings, and (3) a design concept that permits the girders to slide on a flat surface if the bearings fail.

Seismic Isolation Provisions

The *Guide Specifications for Seismic Isolation Design* were first adopted by AASHTO in 1991; they were significantly revised and reissued in 1999. Under the NCHRP 12-49 project, the 1999 Guide Specification provisions were incorporated into the recommended LRFD provisions. This resulted in the addition of a new chapter, Chapter 15, for the recommended NCHRP 12-49 LRFD provisions, based on issues related to seismic isolation design. That new recommended chapter is included in this Guide Specification as Section 15, and it is essentially the same as the 1999 AASHTO *Guide Specifications for Seismic Isolation Design* (AASHTO, 1999).

Cost Implications

A parameter study was performed as part of the project. In brief, the study shows that the net effect on the cost of a column and spread footing system is on the average 2% less than the current Division I-A provisions for multi-column bents and 16% less than Division I-A provisions for single column bents. These cost comparisons are based on the use of the more refined method for calculating overstrength factors and 2400 different column configurations including the seismic input of five different cities.

One factor that caused a cost increase in some of the lower period configurations was the short period modifier, which accounts for the increased ductility demands inherent in short period structures. Since this provision needs to be a part of any new code and is not part of the current Division I-A provisions, the cumulative effect of all the other charges (including the 3% PE in 75 year/1.5 mean deterministic event, new soil factors, new spectral

shape, new R-Factors, new phi-factors, cracked section properties for analysis, etc.) would likely have resulted in lower average costs had the short period modifier been a part of the current specification, Division I-A.

Acknowledgments

Development of the original NCHRP Project 12-49 provisions (from which the Guide Specification was generated) was by the ATC/MCEER Joint Venture. Ian Friedland of ATC (and formerly MCEER) was the project principal investigator and Ronald Mayes was the project technical director. Christopher Rojahn of ATC was the project administrative officer on behalf of the ATC/MCEER Joint Venture. The Project team members for NCHRP Project 12-49 included:

- Donald Anderson, CH2M Hill, Inc.
- Michel Bruneau, University at Buffalo
- Gregory Fenves, University of California at Berkeley
- John Kulicki, Modjeski and Masters, Inc.
- John Mander, University of Canterbury (formerly with the University at Buffalo)
- Lee Marsh, BERGER/ABAM Engineers
- Ronald Mayes, Bridge Consultant
- Geoffrey Martin, University of Southern California
- Andrzej Nowak, University of Michigan
- Richard Nutt, bridge consultant
- Maurice Power, Geomatrix Consultants, Inc.
- Andrei Reinhorn, University at Buffalo

The project also included a distinguished advisory committee through ATC (the Project Engineering Panel); Ian Buckle, of the University of Nevada at Reno, co-chaired this committee with Christopher Rojahn of ATC. The NCHRP Project Panel C12-49, under the direction of NCHRP Senior Program Officer David Beal and chaired by Harry Capers of the New Jersey Department of Transportation, also provided significant input and guidance during the project. Three drafts of the specifications and commentary were prepared and reviewed by these panels and the AASHTO Highway Subcommittee on Bridges and Structures seismic design technical committee (T-3), which was chaired by James Roberts of Caltrans.

References

AASHTO (2000) *LRFD Bridge Design Specifications*, American Association of State Highway and Transportation Officials, Second Edition with Interims, Washington, D.C. www.aashto.org.

AASHTO (1999) *Guide Specifications for Seismic Isolation Design*, Association of State Highway and Transportation Officials, Washington, D.C.

AASHTO (1996) *Standard Specifications for Highway Bridges*, American Association of State Highway and Transportation Officials, Sixteenth Edition with Interims, Washington, D.C. www.aashto.org.

BSSC (1998) *NEHRP Recommended Provisions for Seismic Regulations for New Buildings and Other Structures*, Report FEMA 302, Building Seismic Safety Council, Washington, D.C.

Caltrans (1999) *Seismic Design Criteria*, Version1.1, California Department of Transportation, Sacramento, CA. July.

Frankel, A.D. and Leyendecker, E.V. (2000) Uniform Hazard Response Spectra and Seismic Hazard Curves for the United States: CD-ROM Published by the U.S. Geological Survey National Seismic Hazard Mapping Project, March. http://geohazards.cr.usgs.gov/eq/

ICBO (1997) *Uniform Building Code*, Structural Engineering Design Provisions, Volume 2, International Conference of Building Officials, Whittier, CA.

ICC (2000) *International Building Code*, International Code Council, Inc. Falls Church, VA.

MCEER (2001) *Recommended LRFD Guidelines for the Seismic Design of Highway Bridges*, Multidisciplinary Center for Earthquake Engineering Research, NCHRP Project 12-49, MCEER Highway Project 094, Task F3-1, Buffalo, NY.

NCHRP (2001) *Liquefaction Study Report*, National Cooperative Highway Research Program, Project 12-49, Transportation Research Board, National Research Council, Washington, D.C.

Table 1: Design Earthquakes and Seismic Performance Objectives

Probability of Exceedance For Design Earthquake Ground Motions		Performance Level	
		Life Safety	Operational
Rare Earthquake (MCE) 3% in 75 years	Service	Significant Disruption	Immediate
	Damage	Significant	Minimal
Expected Earthquake 50% in 75 years	Service	Immediate	Immediate
	Damage	Minimal	Minimal to None

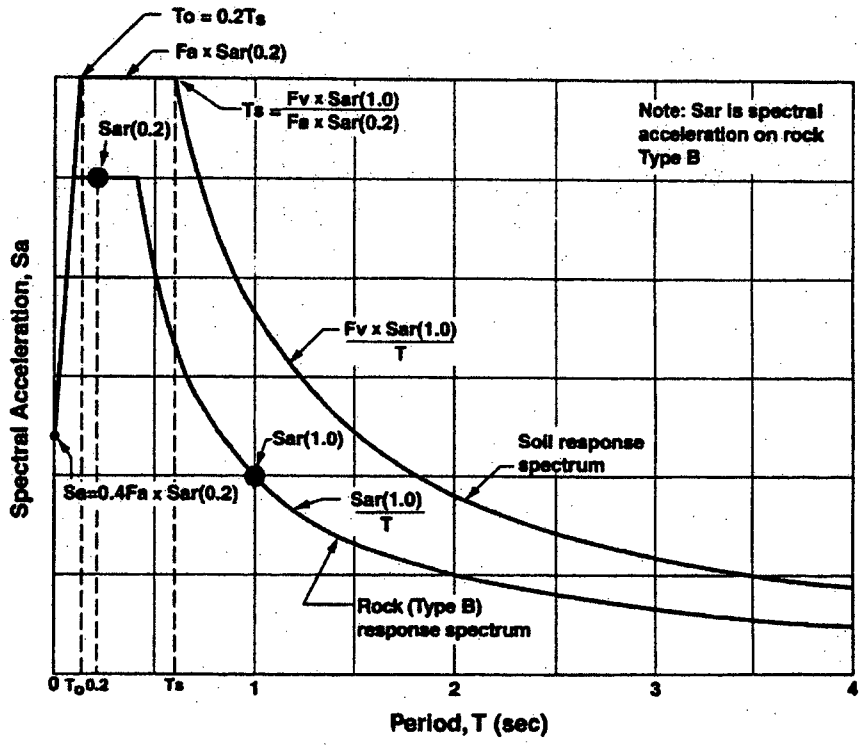

Fa – Acceleration-based Site Coefficient
Fv – Velocity-based Site Coefficient

Figure 1: Response Spectrum Construction

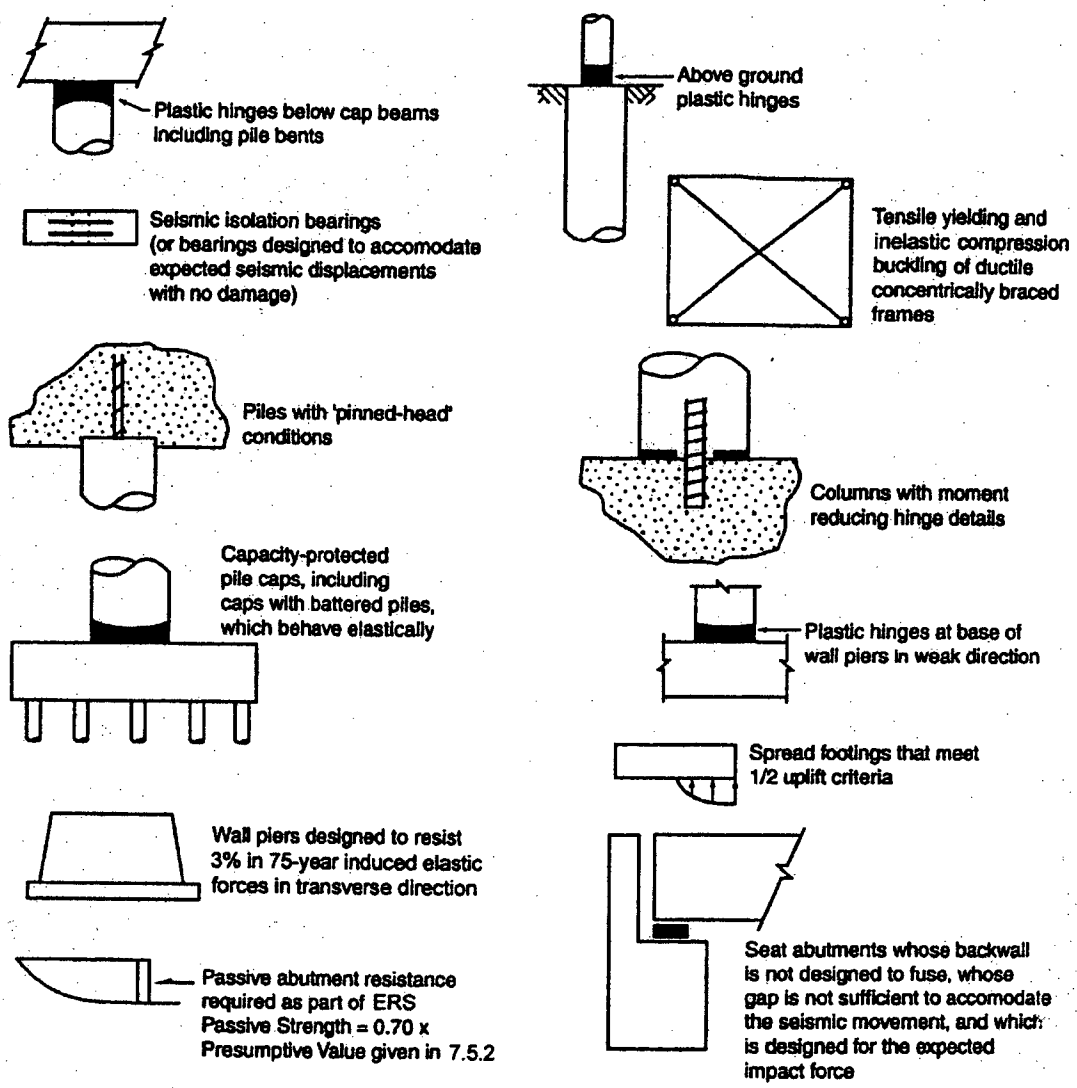

Figure 2: Permissible Earthquake Resisting Elements (ERE)

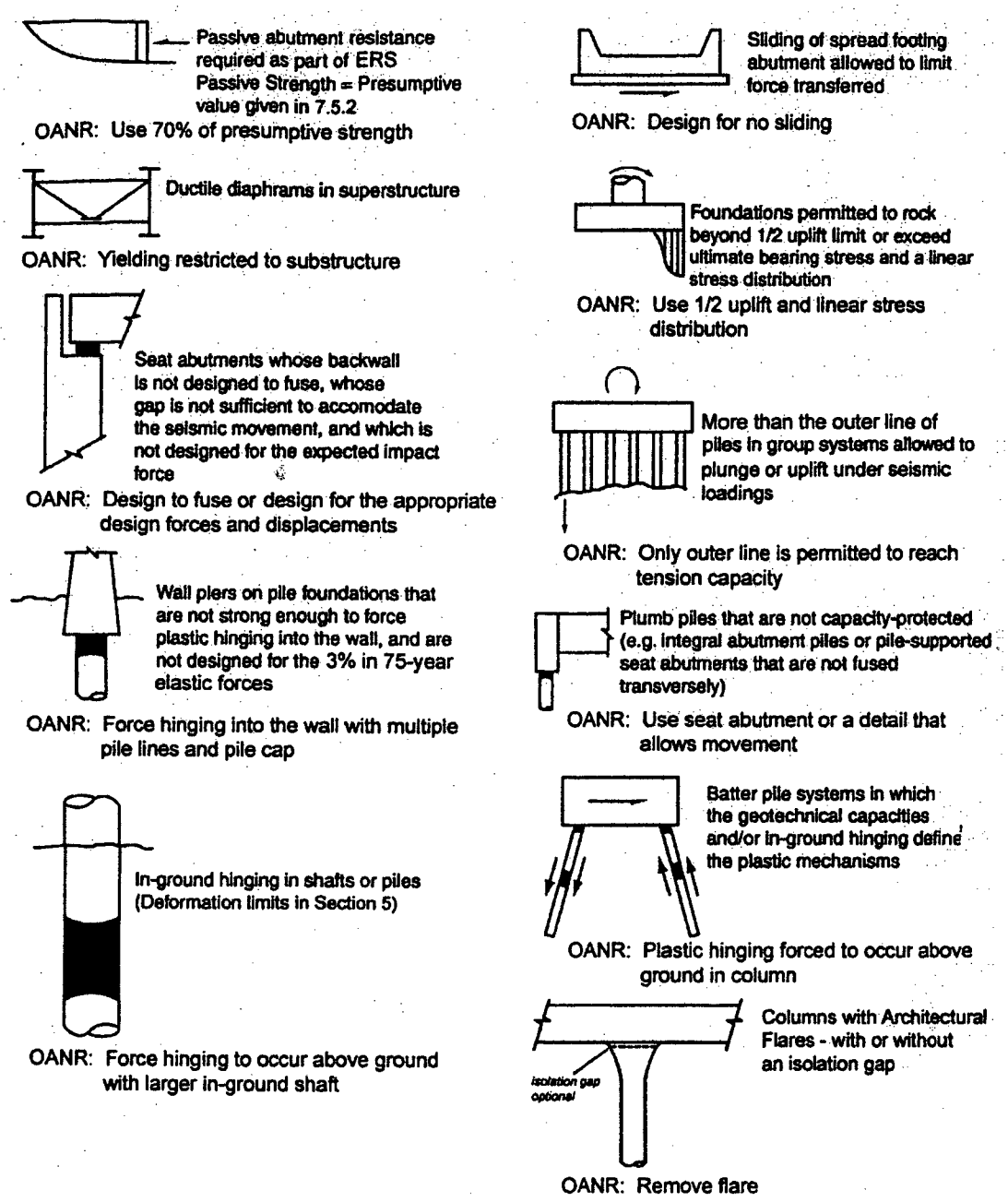

Note: **OANR means a design alternate where owners approval is not required and a higher level of analysis (pushover in SDAP E) can be avoided.**

Figure 3: Earthquake Resisting Elements (ERE) that Require Owner's Approval

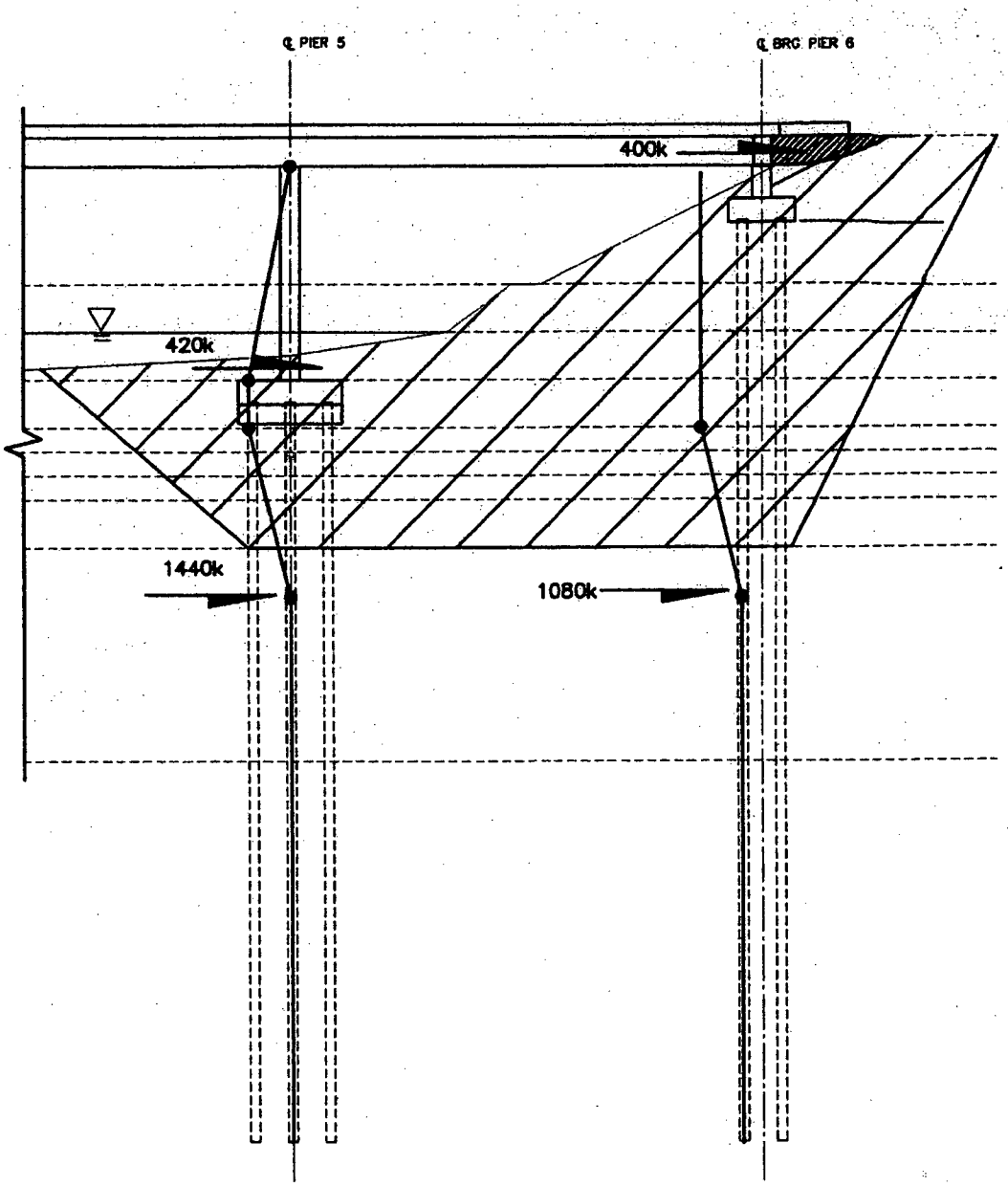

Figure 4: Foundation Movements and Resisting Forces from Lateral Spreading

A Comparative Study on US-Japan Seismic Isolation Design of Highway Bridges

Hidesada KANAJI[1], Hamid GHASEMI[2], Phillip YEN[2], and Sunwoo PARK[3]

ABSTRACT

The seismic isolation design philosophies of the U.S. and Japan are different due to the differences in frequency and type of ground motions experienced. Design-basis spectra, design procedures, and isolation devices, among others, are compared. An important difference between the two philosophies is the emphasis on the effect of period shift; the U.S. design rests primarily on the force reduction associated with period elongation whereas Japan emphasizes energy dissipation because of unfavorable ground conditions.

INTRODUCTION

The major objective of this paper is to identify the design philosophies, procedures and differences contained in the seismic isolation design specifications for highway bridges in the United States and Japan. The study used the 1999 Guide Specifications for Seismic Isolation Design published by the American Association of State Highway and Transportation Officials [AASHTO, 1999] and the 1996 Design Specifications of Highway Bridges, Part V: Seismic Design, Chapter 8: Seismic Isolation Design by Japan Road Association [JRA, 1996].

In more recent years, the protection of civil infrastructure against earthquakes has become an increasingly important issue to bridge owners and engineers. In particular, seismic base isolation has shown to be a viable, practical strategy for earthquake-resistant design of both new and existing highway bridges. The development of lead-core rubber bearings in New Zealand [Skinner et al., 1993] has accelerated the application of the technology. The strategy of seismic base isolation is to reduce ductility demand on the substructure, which in turn minimizes damage inflicted to the bridge during an earthquake.

The number of seismically-isolated bridges has been rapidly increasing in recent years in the United States and Japan. In Japan, the number of bridges retrofitted using isolation bearings has noticeably increased since the 1995 Hyogo-ken Nanbu Earthquake [Kanaji and Hayashi, 2000]. In the meantime, design guidelines or specifications have been diligently updated based on numerous analytical, experimental,

1 Hanshin Expressway Public Corp., Osaka, Japan
2 FHWA, Turner-Fairbank Highway Research Center, McLean, VA
3 Professional Services Industries, Inc., McLean, VA

and numerical studies conducted in New Zealand, Japan, U.S., Italy, and other countries. In particular, the latest specifications published in the U.S. and Japan reflect the latest technological advances in the area. However, distinctive differences exist between the two specifications, and a comparative study of these specifications may be of practical interest not only to the U.S. and Japan but also to other countries in terms of improving existing design codes and enhancing the understanding of various aspects of the technology.

HISTORICAL BACKGROUND

U. S.

Seismic isolation has emerged as one of the most promising retrofitting strategies for existing bridges. The United States has recently become active in implementing the isolation technology for highway bridges.

The first isolated bridge in the United States was the Sierra Point Overpass Bridge in San Francisco, California in 1985. This bridge was built in 1957 and had a total of 10-span which carried 8 lanes of traffic in both directions over railroad tracks. The bridge was retrofitted by replacing the existing high rocker steel bearings with 36 lead-rubber bearings which reduced the seismic forces by a factor of 6. Since 1985, over 100 bridges have used isolation bearings in both new as well as existing bridges in the U.S.

In 1991 AASHTO published the first Guide Specifications for Seismic Isolation Design. However, there were a few drawbacks. The most critical one was its failure to incorporate systems other than elastomeric bearings since at the time of its development, elastomeric systems were the only readily available isolation bearings in the U.S. This made it difficult for systems other than elastomeric lead-rubber bearings to be competitive. Therefore, in 1995 the AASHTO Subcommittee on Bridges and Structures charged the new T-3 Seismic Design Technical Committee with the task of modifying the 1991 Guide Specifications. In addition to numerous modifications to the 1991 guide specifications, the new guide specifications provide recommendations for design of sliding isolation bearings as well as elastomeric bearings. The design philosophy, in the new guide specifications, is intended to ensure elastic column behavior until the isolators release the superstructure.

It is noted that a HITEC-Caltrans-FHWA cooperative program for the performance testing of seismic isolation and energy dissipation systems was launched in the mid-1990s to ensure the performance of a variety of seismic isolation systems [Ghasemi and Higgins, 1999]. The 1999-AASHTO specifications consider the test protocol of this testing program.

JAPAN

In Japan, seismic isolation is called Menshin. The first Menshin bridge, the Miyagawa-kyou bridge, was built in Shizuoka prefecture in 1991. It utilized the lead-core isolation rubber bearings. This approach had been previously applied to some medium-span viaducts and long-span bridges [Kawashima, 1988; Kitazawa et al., 1992].

In 1986, the Japan Institute of Construction Engineering formed a task committee to study bridges with Menshin devices. This study resulted in guidelines which were published in 1989. Soon after, Japan's Public Works Research Institute (PWRI)

launched a program on the development of Menshin systems for bridges incorporating many readily available state-of-the-art devices. In 1990, the JRA specifications [JRA, 1990] were revised and included a chapter on the concept of the response reduction method. In 1992, the Menshin design manual for highway bridges (Menshin manual), which includes design examples, was issued by the Public Works Research Center [1992].

After the 1995 Hyogo-ken Nanbu earthquake, the task committee suggested taking advantage of Menshin devices in restoring bridges damaged during the earthquake [Ministry of Construction, 1995]. In 1996, the latest JRA specifications, in which the lessons learned from this earthquake are incorporated, fully specified Menshin design.

OVERVIEW OF THE SPECIFICATIONS

As mentioned earlier, the latest specifications regarding seismic isolation in both countries are the 1999-AASHTO Guide Specifications and the 1996-JRA Specifications. Major contents in both specifications are classified into six categories and briefly compared in **Table-1**. Despite some differences in description, most of the items in each category are addressed by both specifications. However there are noticeable differences in specifications for the design properties of isolation systems and in the design of sliding bearings, which are not included in the 1996-JRA.

It is well known that important design factors such as effective stiffness and equivalent viscous damping ratio are affected by variation in system properties of isolation devices. Such variation is being accounted for in the 1999-AASHTO by the introduction of system property modification factors (λ). However, the 1996-JRA does not include such provisions, and the variability of device system properties is not explicitly addressed. Also, the 1996-JRA specifications focus on elastomeric-based isolation systems because of widespread corrosion problems associated with conventional steel bearings.

DESIGN PHILOSOPHY AND APPROACHES

OVERALL DESIGN FLOW

Figs-1 and **2** show simplified flow diagrams representing the overall design process of the 1999-AASHTO and the 1996-JRA specifications. Note that **Fig-2** focuses on the ductility design portion. The 1999-AASHTO is relatively straightforward; design conditions such as acceleration, site condition, R-factors, and the system's effective stiffness and equivalent viscous damping ratio are used in computing design forces and displacements.

The 1996-JRA specifications includes two phases of static design procedure. Phase 1 is the seismic coefficient method for moderate earthquakes (with moderate frequency of occurrence) and, phase 2 is ductility design for extremely large earthquakes (with low frequency of occurrence, such as the 1995 Hyogo-ken Nanbu earthquake). In addition, dynamic analysis is recommended to verify the seismic behavior of the bridge and to revise the result of the static design procedur

PERIOD SHIFT EFFECTS

In the seismic isolation approach, force response can be reduced through period shift (elongation) or increased damping. According to the 1999-AASHTO elongation of the

fundamental vibration period of an isolated bridge is primarily responsible for reduction of seismic forces. However, in the 1996-JRA specifications, the focus is on improving damping and dispersing seismic force by improving the energy absorption performance in the seismic isolation design, without creating an excessively long natural period. This is because Japan has unfavorable soil conditions which are frequently subjected to large earthquakes dominated by long cycles of vibrations; hence the period shift alone may not sufficiently reduce seismic forces.

To clarify this more effectively, design spectra from both specifications are plotted in **Fig-3**. There are four plots (representing four different site conditions) for the 1999-AASHTO and six plots (representing three different site conditions for two different design earthquakes) for the 1996-JRA. The two different earthquake types used in the 1996-JRA include the plate-boundary type (Type1) and the inland type (Type2). It is clear that the periods in the JRA spectra at which the responses start decreasing are greater than those in the AASHTO spectra for a comparable site condition. This is the main reason why Japan does not emphasize the period shift approach.

To further illustrate the importance of the period shift between AASHTO and JRA, response ratio (R_r) is plotted against period shift ratio (R_p), between isolated and non-isolated bridges for different periods of the non-isolated bridge (see the three-dimensional plots shown in **Fig-4** and **5**). Equations 1 and 2 define R_p and R_r as,

$$R_p = T_i / T_0 \tag{1}$$

$$R_r = LFC(T_i) \ / \ LFC(T_0) \tag{2}$$

where T_i denotes the fundamental period of the isolated bridge, T_0 denotes the fundamental period of the non-isolated bridge, and LFC denotes the lateral force coefficient as a function of period.

As shown in **Fig-4** and **5**, two different damping conditions are considered for AASHTO and JRA (Type2). The figures also show the two-dimensional response at T_0 = 0.6 second (which is considered as a common period for non-isolated bridges). In general, both in the AASHTO and JRA Codes, seismic response can be reduced by increasing period shift ratio as long as T_0 is not too small. However, wide plateau regions, in which the response ratio is 1.0, can be seen in the JRA, and no reduction of response is realized in these regions. In other words, small to moderate period shifts have little or no effect on reducing seismic forces in Japan.

DESIGN PROCEDURES

Tables-2, 3 and **4** show the comparison of variables between the 1999-AASHTO and the 1996-JRA specifications with respect to design conditions, analysis and design methods, and devices respectively.

DESIGN CONDITIONS

AASHTO: Acceleration coefficients in the 1999-AASHTO are given in the contour map and developed based on a 10% probability of exceedance in 50 years (corresponding to a return period of approximately 475 years). These are the same as those in the conventional (non-isolation) specifications. Site effects are taken into

consideration by the site coefficients (S_i) that have been derived from the relationship between the spectra for different soil types in the period range of 1.1-3.0 seconds. Soil profile types are grouped into four categories as in the conventional specifications. The response modification factor (R-factor) is employed to account for the ductility of structural members. It is noted that R-factors should be limited to 50% of those for conventional bridges to ensure proper performance of isolated bridges. This would result in elastic performance of substructure components. A new procedure for accommodating the variability in isolator's system is of particular interest. The so-called system property modification factors (λ-factors), by which such effects as those of temperature, aging, velocity, travel, contamination, and scragging are accounted for, are multiplied by the nominal values to render the design values of an isolator's system properties.

JRA: In the 1996-JRA specificatiuons, three separate design spectra are provided to determine lateral design forces, one for allowable stress design and the other two for ductility design. These spectra reflect the statistical characteristics of the past earthquakes in Japan. The soil profile types are divided into three categories and such soil effects are directly taken into consideration in the construction of the design spectra. Also, there is no acceleration coefficient in the JRA specifications because the intensities of the earthquakes are already included in the design spectra. Rather, three zone modification factors (C_z) are assigned to the three seismic zones. Ductility effects are determined by an allowable ductility factor, which in effect provides a safety factor for expected inelastic performances. It should be noted that the safety factor is specified as twice that for conventional bridges to minimize inelastic deformation in piers.

ANALYSIS AND DESIGN METHODS

AASHTO: There are four analysis procedures available, as shown in **Table-3**. An appropriate procedure should be applied according to the seismic performance category (SPC) and the number of bridge spans. Time-history analysis is required for bridges having the natural period of more than three seconds or the damping ratio of 30% or more. The elastic seismic response coefficient, which would be the most important variable, can be expressed according to the uniform load method,

$$C_s = AS_i/T_{eff}B \tag{3}$$

where A is the acceleration coefficient, S_i is the site coefficient, T_{eff} is the effective period, and B is the damping coefficient.

Statically equivalent seismic forces (F) and design forces for members are calculated based on this coefficient. Displacement is specified as shown in Table-3 from the relationship between the spectral acceleration and the spectral displacement: $S_A = \omega^2 S_D$. The equivalent viscous damping ratio of the isolated bridge system is determined by considering the energy dissipation in isolation bearings only, disregarding any energy dissipated by the substructure. The natural period of the isolated system is computed using the effective system stiffness that accounts for the combined effects of the isolation bearings and substructure connected in series.

JRA: The design lateral force coefficient for isolated bridges, corresponding to the elastic seismic response coefficient in AASHTO specifications, is given by

$$K_{hcm} = C_E K_{hc} \tag{4}$$

where C_E = the modification factor representing the damping effect of the isolated bridge system, and K_{hc} is the conventional lateral force coefficient for ductility design, as delineated in Chapter 5 of [JRA, 1996]. The design lateral force and design member forces are determined from the design lateral force coefficient given in Eq. 4. In computing the effective weight, JRA adds 50% of the pier weight to the superstructure weight, the AASHTO accounts for the superstructure weight which includes the live load.

In the JRA, displacement is determined from frame or dynamic analysis. A frame analysis model composed of the superstructure, isolation bearings, substructure and foundations, is used to compute the natural period. The spring constant for isolation bearings is given in terms of effective stiffness. The damping modification coefficient, C_E, accounts for the combined effects of the modal damping ratios of a structure system.

DEVICES

AASHTO: Both elastomeric bearings and sliding bearings are addressed in the 1999-AASHTO. The equivalent viscous damping ratio of isolation bearings is proportional to the ratio between the total energy dissipation per cycle and the maximum strain energy achieved in the cycle. The allowable vertical load on an elastomeric bearing is not specified explicitly, rather the limits on vertical load are governed indirectly by limitations on the equivalent shear strain in the elastomer. The shear strain components addressed in the 1999-AASHTO include those which are due to compression by vertical loads, imposed seismic and non-seismic lateral displacements, and rotation.

JRA: The equivalent damping constants for isolation bearings are computed in the same manner as in the AASHTO. However, based on the results of experimental research, the design displacement (u_{Be}) is given by reducing the maximum isolation displacement by 70% in order to account for the unsteadiness of inertial forces [Kawashima et al., 1992]. As to the shear strain of elastomeric isolation bearings, there are two criteria to ensure the proper performance. One is an allowable shear strain under design seismic force. In general, up to a shear strain of 2.5, this relationship is almost linear and elastomeric bearings perform in a stable manner. The other is to check the ultimate local shear strains that may be developed at weak areas in a laminated rubber bearing under a combination of vertical compression and horizontal forces. These allowable strains are specified differently for different types of rubber, including natural rubber and chloroprene rubber.

RETROFIT

U.S.

Since 1985, seismic isolation strategy has been utilized in retrofitting existing bridges not only in California but also in many other states east of the Rocky Mountains. The majority of these retrofits used lead-rubber bearings and in the past few years Caltrans has been retrofitting a number of toll bridges using friction pendulum sliding bearings. In general, these bearings replaced the vulnerable high rocker steel bearings. Also, in some cases, where the bridge piers had differing stiffness due to a variation in column heights, isolation bearings were utilized to redirect the loads.

When applying seismic isolation strategy, consideration must be given to a feasibility study, appropriateness of the isolation system for the specific project, the testing and

evaluation of the selected system, and a cost-benefit ratio study. The biggest difficulties in using this strategy for retrofitting existing bridges is in providing sufficient clearance for the structure to move and in selecting the appropriate system. Although not applicable to all structures and all site conditions, retrofitting with a protective system has been shown to be a cost-effective alternative to conventional strengthening.

JAPAN

In Japan, rubber bearings have been widely used for bridges with continuous superstructure to distribute seismic forces over the piers. Retrofit strategy has been developed based on the same principle. However, there are many restrictions in retrofitting a bridge using isolation bearings due to various constraints associated with the configurations of existing bridges. A major restriction would be the available clearance needed to install optimum isolation bearings. In this case, since the ductility demand of piers is not fully accounted for by the isolation bearings, one may expect a certain level of damage to the piers during a large earthquake.

DISCUSSION

This study examined the seismic response against the period shift, response modification factors in the AASHTO and the JRA specifications, and clearance issue for bearings during retrofitting. Results of these analyses are as follows. From the **Figs-3-5**, it can be concluded that the period shift is of little effect in Japan. This is due to the wide plateau in the relatively long period of the design spectra in the JRA specifications. This finding is consistent with the statement in the JRA, but the recommended period shift ratio, at least "two", is not necessarily enough. The damping effect must be considered for the Japanese Menshin design.

Both specifications in U.S. and Japan cover almost the same items as shown in **Tables 1-4**. A major difference is that the system properties modification factor is applied in the AASHTO specifications which would lead to a more proper design approach. Both countries expect the elastic behavior or limited damage of substructure using twice the safety factor against the conventional R-factor or allowable ductility. It is proposed that a more rational determination of this safety factor would be needed to construct cost-effective structures.

Retrofitted bridges may present nonlinear behavior in substructure because of insufficient clearance for isolation bearings. The latest specifications are not considered sophisticated enough to allow multi-modal analysis of isolated bridge systems. It is necessary that further studies be conducted to elucidate the nonlinear, multimodal interactions between piers and bearings [e.g., Kawashima and Shoji, 1998; Kumaki et al., 2000; and Nariyuki et al., 2000].

CONCLUDING REMARKS

The seismic isolation specifications for highway bridges in the U.S. and Japan are compared and the following differences are identified among others:

1. The U.S. seismic isolation design relies on period elongation to reduce seismic forces whereas Japan emphasizes energy dissipation through increased damping because of the unfavorable ground conditions.

2. The system property modification factors (λ) are introduced in the 1999-AASHTO specifications. These factors need to be updated as new data becomes available.
3. In retrofit, there may be a clearance problem for isolation bearings and hence the nonlinear behavior may occur in a substructure. It is suggested that a simple design method should be developed to estimate the multimode behavior.

ACKNOWLEDGMENTS

We are grateful to Dr. Unjoh of Japan's PWRI for giving some information. This work was partially supported, through the first author, by the Express Highway Research Foundation of Japan under the International Study and Research Program.

REFERENCES

1. AASHTO (1991), *Guide Specifications for Seismic Isolation Design, 1st Edition*, American Association of State Highway and Transportation Officials, Washington, D.C.
2. AASHTO (1996), *Standard Specifications for Highway Bridges, 16th Edition*, American Association of State Highway and Transportation Officials, Washington, D.C.
3. AASHTO (1999), *Guide Specifications for Seismic Isolation Design, 2nd Edition*, American Association of State Highway and Transportation Officials, Washington, D.C.
4. Constantinu, M.C., Tsopelas, P. and Kasalanati A. (1998), Property *Modification Factors for Seismic Isolation Design*, NCEER Highway Project Technical Report
5. Constantinu, M.C. and Whittaker, A.S. (1998), *Seismic Protective Systems for Bridges in the United States*, The U.S.-Italy Workshop on Seismic Protective Systems for bridges
6. Ghasemi, H. and Higgins, M.S. (1999), "Sizing up Seismic Bearings", Civil Engineering, American Society of Civil Engineers, July, pp55-59.
7. Ghasemi, H., Sheng, L. H., Onesto, A. (1999), *Guidelines for the Testing of Seismic Isolation and Energy Dissipating Devices*, CERF Report, HITEC
8. JRA (1990), *Specifications for Highway Bridges, Part 4: Seismic Design*, Japan Road Association, Tokyo, Japan
9. JRA (1995), *Reference Book on Seismic Design of Highway Bridges*, Japan Road Association, Tokyo, Japan
10. JRA (1996), *Specifications for Highway Bridges, Part 8: Seismic Design*, Japan Road Association, Tokyo, Japan
11. Kanaji, H., Hayashi, H. (2000), "Example of Upgrading Seismic Performance with Use of Mensin Design", *Report on the Hanshin-Awaji Earthquake Disaster, Vol.7*, Japan Society of Civil Engineering, Tokyo, Japan
12. Kawashima, K. (1988), "Development and Future Scope of Seismic Isolation of Structures -A Review-", Journal of Japan Society of Civil Engineering
13. Kawashima, K., Hasegawa, K., Nagashima, H. (1992), "Seismic Response Analysis for Menshin Bridges in Applying a Bi-linear Model as a Menshin Bearing", Civil Engineering Journal, Public Works Research Center, Vol.34-5
14. Kawashima, K., Shoji, G. (1998), "Interaction of Hysteretic Behavior between

Isolator/Damper and pier in an Isolated Bridge", Journal of Japan Society of Structural Engineering
15. Kitazawa, M., Nishimori, K., Noguchi, J., Shimoda, I. (1992), "Earthquake Resistant Design of a Long-period Cable-stayed Bridge", Proceedings of the Tenth World Conference on Earthquake Engineering
16. Kumaki, Y., Kanaji, H.,Yabe, M. (2000), "Nonlinear Hysteretic Behavior and Application of Equivalent Linearization Method for Isolated Columns in Seismic Retrofitted Bridges", Journal of Japan Society of Structural Engineering
17. Ministry of Construction (1995), *Specifications for Restoration of Highway Bridges Damaged by the Hyogo-ken Nanbu Earthquake*, Ministry of Construction, Tokyo, Japan
18. Nariyuki, Y., Hirao, K., Sawada, T., Kondo, K. (2000), "Interaction of Nonlinear Response between Pier and Isolator in Seismically Isolated Bridges", Proceedings of the Twelfth World Conference on Earthquake Engineering
19. Public Works Research Center (1992), *Manual for Menshin Design of Highway Bridges*, Public Works Research Center, Tukuba, Japan
20. Skinner, R.I., Robinson, W.H., and McVerry, G.H. (1993), *An introduction to seismic isolation*, John Wiley

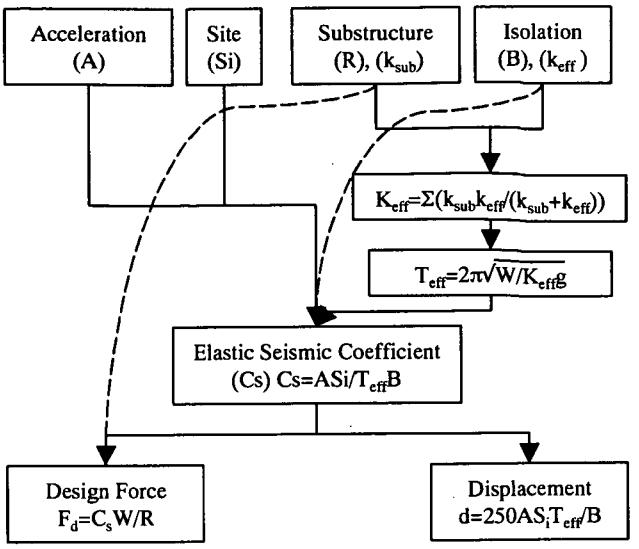

Fig-1 Simplified AASHTO Design Flow

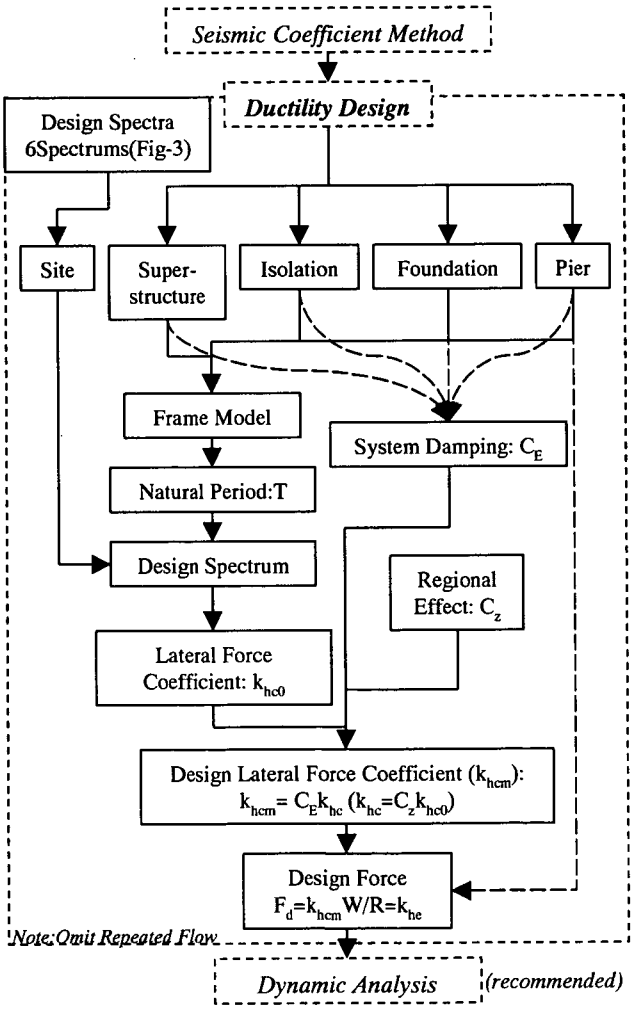

Fig-2 Simplified JRA Design Flow

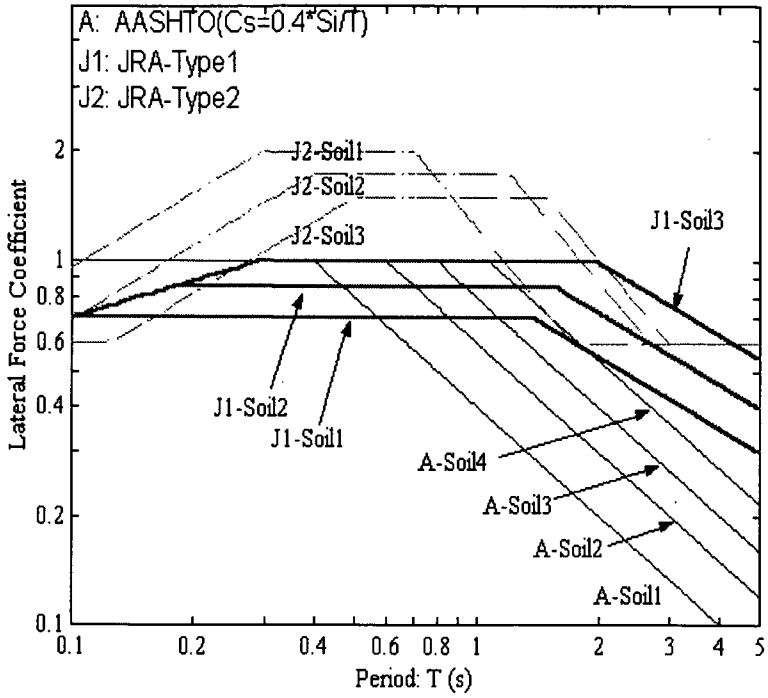

Fig-3 Response Spectra (AASHTO & JRA)

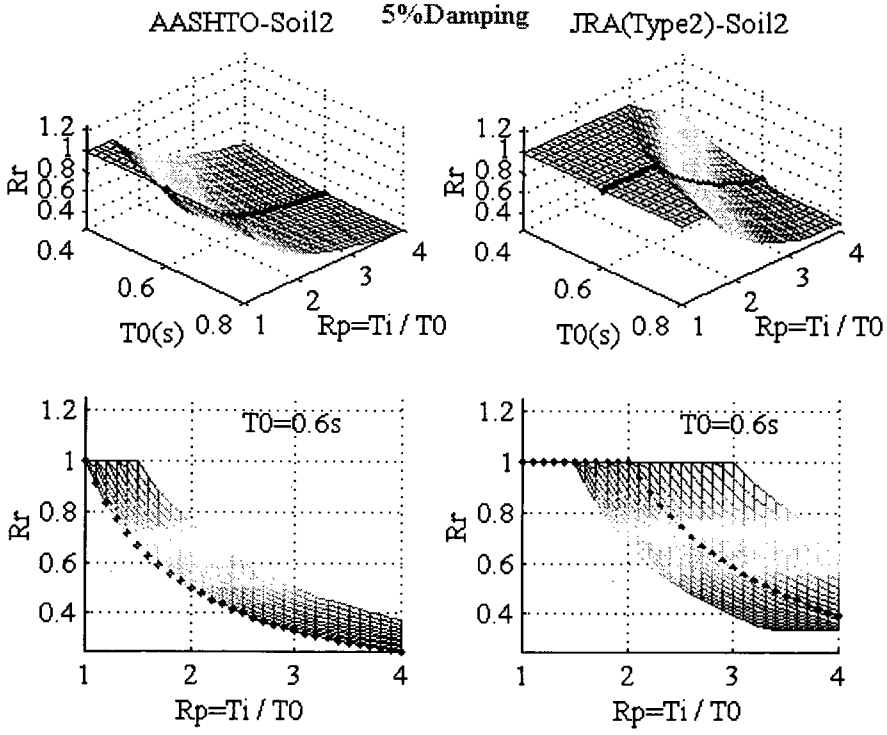

Fig-4 Change in Response Ratio against Period Shift (5% Damping)

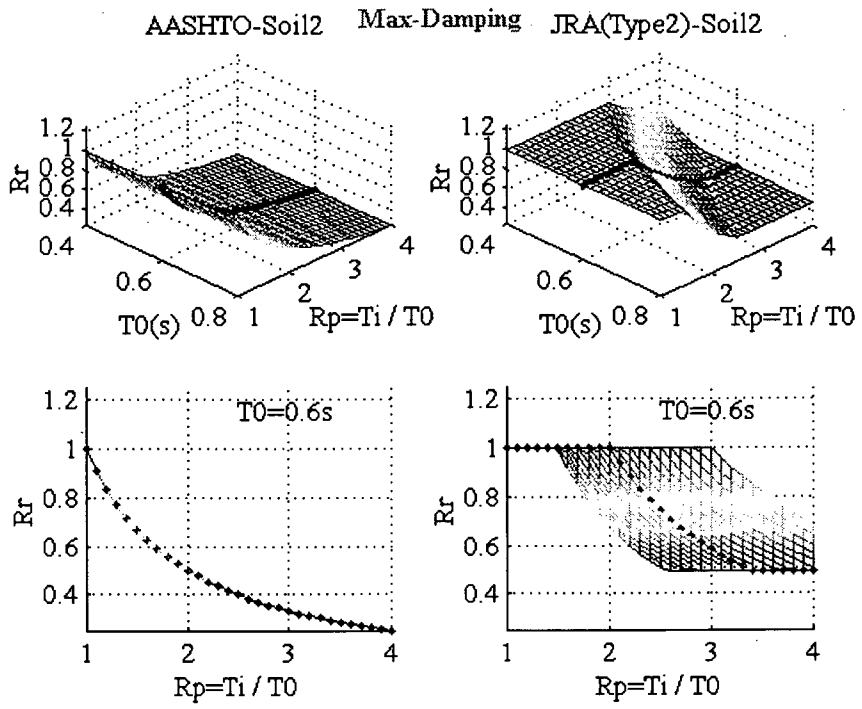

Fig-5 Change in Response Ratio against Period Shift (Maximum Damping)

Table-1 Contents in the 1999-AASHTO and the 1996-JRA

Category	AASHTO (Guide Specification, 1999)	JRA (Chapter 8 in Specification, 1996)
General	Introduction Applicability (1)	General (8.1)
Design Condition	Acceleration Coefficient (3) Seismic Performance Categories (4) Site Effects and Site Coefficient (5) **Design Properties of the Isolation System** (8)	*Classification of Importance (3.4) *Modification Factor for Zone (3.5,3.6) *Design Lateral Force Coefficient (4.1) *Lateral Force Coefficient (5.3)
Design Procedure and Force	Analysis Procedures (7) Response Modification Factor (6) Design Forces (10, 11)	Seismic Isolation Design (8.2) Design Lateral Force Coefficient (8.3) Calculation of Natural Periods (8.5) Calculation of Damping Constant (8.6) *Evaluation of Safety (5.2)
Other Requirements	Clearances (9) Other Requirements (12)	Design Details (8.7)
Devices	Required Tests (13) Elastomeric Bearings (14, 15) **Sliding Bearings** (16, 17) Other Isolation Systems (18)	Design of Isolation Bearing (8.4) *Structures to Reduce the Effect of an Earthquake (14)
Others	Definitions and Symbols (2)	N/A

*Note: (#)s indicate AASHTO and JRA section numbers, and *s indicate the Sections outside Chapter 8 of JRA.*

Table-2 Design Condition

Factor	AASHTO (Guide Specification, 1999)	JRA (Chapter 8 in Specification, 1996)
Design Acceleration Spectra	Calculated from Acceleration Coefficients and Site Coefficients	3 Spectra (Moderate EQ, Rare EQ in plate boundary, Rare EQ in inland fault) as to Lateral Force Coefficient, K_{hc0}
Regional Effects	Acceleration Coefficient from the Contour Map (Return Period of approximately 475yrs)	Modification Factor for Zone (C_z): 1.0, 0.85, and 0.7
Site Effects	Site Coefficient (S_i): 1.0, 1.5, 2.0, and 2.7	Included in Spectra
Bridge Status	Seismic Performance Categories	Classification of Importance
Ductility Effects	Response Modification Factor (R): $R=R_0/2$ (R_0=Factor for conventional bridges) Note: The lower R-factors ensure essentially elastic substructure behavior.	$R=\sqrt{(2\mu_a-1)}$ Allowable Ductility : $\mu_a=1+(\delta_u-\delta_y)/(2\alpha\delta_y)$ α: Safety Factor for conventional bridges (1.2~3.0)), Note: Twice Safety factor (2α) is to reduce nonlinear response of piers.
Design Properties of the Isolation System	Modification Factor (λ): $K_{d,i}=K_d \times \lambda_{i,Kd}$ (i=max, min), $Q_{d,i}=Q_d \times \lambda_{i,Qd}$ (i=max, min)	N/A

Table-3 Analysis and Design Methods

Factor	AASHTO (Guide Specification, 1999)	JRA (Chapter 8 in Specification, 1996)
Analysis Procedures	1. Uniform Load Method 2. Single Mode Spectral Method 3. Multimode Spectral Method 4. Time-history Method (T>3.0s, h>30%)	Seismic Coefficient Method, Ductility Desigr method, and Dynamic Analysis Methoc (Time-history Analysis, Modal Analysis)
Elastic Seismic Response Coefficient	Elastic Seismic Response Coefficient (C_s): $C_s=AS_i/T_{eff}B$	Design Lateral Force Coefficient (K_{hcm}) $K_{hcm}= C_EK_{hc}$ ($K_{hc}=C_zK_{hc0}$, C_E =damping effec of bridge system)
Statically Equivalent Seismic Force	Statically Equivalent Seismic Force: $F=C_sW$ (W=DL+LLs, DL:Dead Load, LLs:Live Load at EQ)	Design Lateral Force: $F=k_{hcm}W$ ($W=W_u+0.5W_p$, W_u=weight o superstructure, W_p=weight of pier)
Design Forces	$F_d=C_sW/R$	$F_d=k_{hcm}W/R=k_{he}W$ (Equivalent Lateral Force Coefficient $k_{he}=k_{hcm}/R$)
Displacement	$d=250AS_iT_{eff}/B$ (mm)	From Flame Analysis / Dynamic Analysis
System Damping	Damping Coefficient (B): B based on β (B=0.8~2.0), $\beta=4Q_d(d_i-d_y)/2\pi K_{eff}d^2$, $d=d_i+d_{sub}$ Note: Not include substructure	Modification Coefficient fo Energy-dissipating Capability (C_E): C_E base on combined h (damping ratio) of Isolation Pier, and Foundation (C_E =1.0~0.7)
Natural Period	$T_{eff}=2\sqrt{(W/K_{eff}g)}$ $K_{eff}=\Sigma(k_{sub}k_{eff}/(k_{sub}+k_{eff}))=\Sigma k_{eff,j}$	From the Flame Analysis including isolatio (k_{eff}), pier, foundation

Table-4 Devices

Factor	AASHTO (Guide Specification, 1999)	JRA (Chapter 8 in Specification, 1996)
Equivalent Damping	Equivalent Viscous Damping Ratio (β): $\beta=(\text{Total EDC Area})/2\pi k_{eff}\, d_i^{\,2}$ d_i: Displacement at isolation bearing	Equivalent Damping Constant (h_B): $h_B=(\text{Total EDC Area})/2\pi k_{eff}\, u_{Be}^{\,2}$ $u_{Be}=0.7k_{hcm}\ W_u/K_B$ ($K_B=k_{eff}$), Note: 0.7 representing the unsteadiness of inertial force
Effective Stiffness	$k_{eff}=(F_p-F_n)/(\Delta_p-\Delta_n)$	$K_B=k_{eff}=(F(u_{Be})-F(-u_{Be}))/2u_{Be}$
Shear Strain	Vertical compression (γ_c), rotation (γ_r), horizontal shear ($\gamma_{s,s}$, $\gamma_{s,eq}$): $\gamma_c<=2.5$ $\gamma_c+\gamma_{s,s}+\gamma_r<=5.0$ $\gamma_c+\gamma_{s,eq}+0.5\gamma_r<=5.5$	1.Allowable Shear Strain for Seismic Force: $\gamma<=2.5$ 2.Check on local shear strain made up by vertical compression, horizontal stress etc. $\gamma_{local}<=4.16$ (Natural Rubber) $\gamma_{local}<=3.33$ (Chloroprene Rubber)

AN EVALUATION OF SEISMIC BRIDGE JOINT DESIGN USING STRUT-AND-TIE CONCEPTS

Sri Sritharan[1]

Abstract

Seismic design of cap beam-to-column bridge joints based on a force transfer model established using strut-and-tie concepts is widely used in the United States. An experimental investigation of bridge tee joints using this model with varying amounts of cap beam prestressing produced good seismic performance for joints with cap beam prestressing. However, failure of the joint was observed in the test unit that was designed with no prestressing in the cap beam. The performance of the bridge tee joints was evaluated to identify the shortcomings of the design and to establish improved force transfer models for the seismic design of joints in modern structures.

Introduction

The force transfer method of design for bridge joints was introduced to address two phenomena: 1) the use of inadequate joint details and subsequent damage in earthquakes, and 2) the unnecessarily congested details of bridge joints resulting from a building joint design method based solely on shear forces. In this design method, the force transfer model is developed based on the key mechanisms that are identified using strut-and-tie concepts for satisfactory transfer of forces across the joint [Priestley et. al., 1996, Sritharan et. al., 2000a]. Of several different design models suggested by Priestley [1993], the external strut force transfer model illustrated in Fig. 1 is the most efficient in terms of providing the least amount of reinforcement within the joint panel, thus improving constructability.

Due to the aforementioned benefits, the seismic bridge joint design method recommended in ATC-32 [Applied Technology Council, 1996] is based on the external strut force transfer model. The same force transfer model is also adopted by Caltrans [1999], but conservatively by suggesting reinforcement quantities beyond the basic requirements of the design model.

Using a combination of experimental and analytical studies on three half-scale bridge tee joints, the adequacy of the reinforcement details derived from the external strut force transfer model was investigated. The primary difference between the three tee joints was the level of prestressing used in the cap beam and the corresponding joint reinforcement. This paper presents a summary of the experimental study and detailed force transfer models of the tee joints which were developed using the experimental observations and analysis results from a nonlinear finite element study. Formulation of detailed force transfer models and experimental data assisted with an evaluation of the external strut force transfer method of design for bridge joints.

[1] Assistant Professor, Dept. of Civil and Construction Engineering, Iowa State University

External Strut Force Transfer Model

The concept of the force transfer method is that a satisfactory seismic performance of bridge joints can be achieved by adequately anchoring the column longitudinal reinforcement into the joint in conjunction with a suitable force transfer model that relies on pre-identified reinforcement anchoring mechanisms. This enables the development of the overstrength plastic moment capacity, as typically required, in the column adjacent to the joint.

Figure 1 shows the forces acting upon a bridge tee joint subjected to in-plane loading with an idealized joint strut and the external strut force transfer model. The compression and tension forces in Fig. 1b are represented with dashed and solid lines, respectively, as commonly adopted in the strut-and-tie approach. The external strut model assumes that the column bars in compression and tension bars carrying 50 percent of the total tension force ($0.5T_c$), located furthest from the tension side of the column, are anchored into the joint diagonal strut by bond, where T_c is the column tension force at the overstrength moment capacity. The remaining 50 percent column tension force is anchored with a clamping mechanism at Node X using two inclined struts forming both inside (C_1) and outside (C_2) the joint (see Fig. 1b). To develop strut C_2 outside the joint, tension forces T_{es} and T_{bb} are required at Node Z, which suggests additional bottom beam reinforcement and vertical stirrups in the beam region adjacent to the joint face to support the force transfer across the joint. Additional reinforcement in the cap beam will not impede construction. Assuming that the vertical components of struts C_1 and C_2 are equal, the necessary reinforcement is quantified [Priestley et. al. 1996, Sritharan et. al., 1999].

When the cap beam framing into the joint is prestressed, a broader diagonal strut than that idealized in Fig. 1b develops in the joint. Together with an inclined "direct" beam strut, this strut will satisfactorily anchor all of the column tension force into the joint. As a result, the joint shear reinforcement can be further reduced compared to an equivalent joint with a reinforced concrete cap beam. In addition, the need for additional reinforcement in the cap beam adjacent to the joint is eliminated [Sritharan et. al., 1999]. These modifications, which have not been introduced in design provisions, were used in the design of the test joints.

More details of the external strut method and the corresponding reinforcement requirements can be found elsewhere [Priestley, 1993, Priestley et. al., 1996, Sritharan et. al., 1999]

Experimental Study

The effectiveness of the external strut joint design model was experimentally investigated using three equivalent bridge tee joint systems with circular columns. These tee joints, identified as IC1, IC2 and IC3, were based on a three-column bridge bent at a 50% scale (see Fig. 2a). By varying the amount of prestressing in the cap beam, the test units were designed to represent conditions of joints with reinforced, partially prestressed, and fully prestressed cap beams. For construction and testing convenience, all three joint systems were built in the inverted position as shown in Fig. 2b.

A longitudinal reinforcement ratio of about 2% was used in the columns of all of the

test units. The cap beams of test units IC1, IC2, and IC3 were designed with prestressing of 0, $0.1f'_c$ and $0.2f'_c$, respectively, where f'_c is the beam unconfined concrete strength. The cap beam-to-column joints were then designed using the external strut force transfer model with consideration to the amount of prestressing in the cap beam. The reinforcement details of IC1, IC2, and IC3 in the joint region are shown in Fig. 3, with details of the material strengths in Table 1. The amount of shear reinforcement in the test joints was only 15-32% of that obtained from the conventional joint design method based directly on joint shear forces [Sritharan et. al., 1999].

Table 1 Concrete strengths on the day of testing, and yield (f_y) and ultimate (f_u) strengths of reinforcement in the test units.

Test Unit Identification	IC1 (reinforced)		IC2 (partially prestressed)		IC3 (fully prestressed)	
Concrete (MPa):	f'_c		f'_c		f'_c	
Column	31.4		34.6		33.2	
Cap beam and joint	39.7		40.5		36.1	
Reinforcement (MPa):	f_y	f_u	f_y	f_u	f_y	f_u
Column long. Reinforcement	448	738	448	738	461	744
Column spirals	468*	669	468*	669	499*	681
Beam long. Reinforcement	433	726	477	770	426	694
Beam/joint stirrups	439	721	439	722	452	670
Joint spirals	453*	665	447*	674	511*	685

*Yield strength was defined as the stress at a strain of 0.5 percent for spiral reinforcement.

To simulate seismic effects on joints in the transverse direction to the bridge axis, the test units were subjected to in-plane cyclic loading; the force-displacement responses are shown in Fig. 4. As required by current capacity design philosophy in seismic bridge design [Priestley et. al. 1996], column moment capacity was fully developed adjacent to the joint in IC2 and IC3, with joint damage limited to minor cracking. However, in IC1, a balanced failure of the column and joint occurred, which is not admissible in the current seismic design approach. The joint failure in IC1 initiated at a column drift of 4.8%; seismic performance of IC1 was satisfactory until cycled to a drift of 4.8%. Since the joint shear demand had almost reached its maximum value at a drift of about 1.5% — which can be inferred from Fig. 4a — it was concluded that the external strut force transfer model somewhat underestimated the joint reinforcement in IC1, and improvements to the design model could be achieved from detailed analyses of the joints.

Analytical Study

After the experimental study was completed, detailed models using strut-and-tie concepts were developed to examine the force transfer in the joint regions of the test units. It was anticipated that the procedure would explain the inadequacy of the joint reinforcement in test unit IC1, confirm the satisfactory joint reinforcement in IC2 and IC3, and identify possible shortcomings of the external strut joint design model.

The development of the force transfer models, in particular the formulation of the compression force paths, was assisted by results from 2D nonlinear finite element analyses of the test units, which are reported elsewhere [Sritharan, et. al., 2000b]. To ensure the development of satisfactory models for the joint force transfer, test observations and data gathered from the tee joint systems during the cyclic load testing were also used.

For all test units, force transfer models were developed for the first loading cycle in the push and pull directions of the loadings at the maximum displacement ductility or at the displacement ductility level prior to experiencing joint damage. Although the column capacity was expected to remain the same in the push and pull directions, the cap beams were subjected to different axial forces in the two directions. Details of the development of all force transfer models are reported by Sritharan [1998]. The formulation of the model for ICI in the push direction of loading as well as summaries of the IC1 model in the pull direction and the IC2 and IC3 models in the push directions are presented below. In all cases, the models were formulated with the joints in the inverted position, thus maintaining consistency with the test configuration used in the experimental study.

IC1- Push Direction of Loading

The force transfer model developed for the response of the tee joint region of IC1 at $\mu_\Delta = 6x1$ is depicted in Fig. 5, accompanied with strut and tie forces and orientations of the inclined struts. In this model and those presented in the remainder of this paper, strut and tie forces between nodes are identified by C for compression and T for tension with a subscript denoting the nodes (e.g., C_{AB} identifies the strut extending between nodes A and B).

Following is the procedure used for developing the joint force transfer model in Fig. 5:

- Consistent with the design model in Fig. 1b, the column tension force was represented by two ties with approximately equal magnitudes. In Fig. 5, the magnitude and location of the extreme column tie, T_{C1}, was determined assuming that the contribution to T_{C1} was from the four most extreme tension bars. The tension force in each of these bars was obtained using the theoretical strain corresponding to the applied moment, which was estimated from a moment-curvature analysis of the column section. The average stress in the four tension bars was 574 MPa or $1.28f_y$. Hence, the magnitude of T_{C1} was 890 kN, which was 46% of the total column tension force T_C.
- Node C was located at the center of the effective anchorage length of the extreme tension bars. Assuming a uniform bond stress of $2.5\sqrt{f_c'(\text{MPa})}$ and an average maximum bar stress f_b = 574 MPa, $l_{a,eff}$ was determined as follows (see Eq. 3.5) [Sritharan, 1998]:

$$l_{a,eff} = \frac{A_{bl} f_b}{\pi d_{bl} 2.5\sqrt{f_c'}} = \frac{d_{bl} f_b}{10\sqrt{f_c'}} = \frac{22.2x574}{10x6.3} = 203\text{mm} \qquad (1)$$

- External joint strut C_{AC}, which was inclined at 45° to the vertical plane, was subjected to 351 kN. The orientation and magnitude of this strut were established using the finite element analysis results [Sritharan et. al., 2000b], which suggested transfer of about $0.15T_C$ to the beam stirrups. This enabled the magnitudes of T_{AB} and T_{AE} to be obtained. Note that the design model shown in Fig. 1b assumed a tension force equivalent to $0.25T_C$

being transferred to the beam stirrups.

- The locations of nodes A and B were then identified. Based on the external forces at the beam section through nodes A and B, the total outward horizontal forces at these nodes were estimated from a section analysis. At node B, an inclined strut, C_{B1}, at 45° was assumed to transmit beam shear force. The inclined state of this strut should not have any substantial effect on the joint force transfer model, and hence the 45° assumption was made consistent with typical shear behavior of reinforced concrete beams.
- To maintain equilibrium at node B, strut C_{BC} was established. The reason for assuming this strut through node C was its low magnitude. In the design model, a similar strut was considered and was assumed to support column tension force T_{C2}.
- To maintain the overall equilibrium of the system, the column compression struts established at the critical section were assumed to act at node E, which was located in the top beam tension chord. This included an inclined strut C_{C2} at 45° to transfer the column shear force as considered for the cap beam at node B.
- The demand on strut C_{CE} and tie T_{CG} were determined from nodal equilibrium at C.
- In the absence of an alternative mechanism, the column tension force T_{C2} was anchored at node D, which was located below the end of the column bars. It was assumed that T_{C2} was transferred to node D through the splice transfer mechanism as detailed below. Participation of this mechanism in the joint force transfer was confirmed by the finite element analysis results and test observations, but was not assumed in the design model.
- Struts C_{DG} and C_{EG} were determined considering equilibrium conditions at node G. The vertical strut at node G was conveniently assumed to pass through node E. Ideally, node G should have been located as a mirror image of node C about the column centerline.
- The demand on tie T_{DI} was obtained as described in Eq. 2 assuming that yield strength was developed in the bottom beam reinforcement. This assumption was based on the experimental observation.

$$T_{DI} = 7x387x433x10^{-3} = 1174kN \qquad (2)$$

- The orientations and magnitudes of struts C_{DF} and C_{EF} were determined from equilibrium considerations at nodes D and E, respectively, thus enabling node F to be located.
- Consistent with the strut-and-tie methodology, the length of the beam disturbed region adjacent to the column compression face was assumed to be h_b. Accordingly, nodes H and I were located at a distance equal to half of the beam height away from the column face in the horizontal direction. In the vertical direction, these nodes were assumed to be at the centroid of beam tension and compression forces established from a section analysis. From equilibrium conditions at node F, the magnitudes of struts C_{FH} and C_{FI} were determined.
- Magnitudes of C_{B2}, C_{B3} and T_{B3} were then obtained considering equilibrium conditions at nodes H and I. These forces accurately represented the external forces shown to the left of the joint in Fig. 5.

The splice transfer mechanism, which was identified in the development of the force transfer model for IC1, was responsible for transferring the column tension force to the top beam bars and then anchoring it with a joint diagonal strut. Three different representation of this mechanism supported by concrete ties and/or joint vertical stirrups are shown in Fig. 6. Although this figure shows only the in-plane force transfer, the column force can be transferred using struts and ties forming in all three dimensions [Sritharan, 1998].

IC1 – Pull Direction of Loading

Using the procedure outlined in the push direction of loading, the force transfer model shown in Fig. 7 was established for IC1 in the pull direction of loading at μ_Δ = -6x1. The column moment resistance was slightly higher in the pull direction than the push direction at the displacement ductility of 6. As seen in Fig. 6, the clamping mechanism was responsible for anchoring 40.5% of the column tension force at node C; the remaining column tension force was transferred through the splice mechanism to node D.

IC2 and IC3 – Push Direction of Loading

Force transfer models in the joint regions of IC2 and IC3 were established using steps similar to those used for IC1. Figures 8 and 9 depict the joint force transfer models for IC2 and IC3 in the push direction of loading at the maximum displacement ductility. The force transfer model of IC3 indicates that the clamping mechanism is solely responsible for the joint force transfer, whereas both the clamping and splice mechanisms are active in IC2. Due to the prestressing in the cap beam, the contribution of the clamping mechanism is higher in IC2 than IC1, which was anticipated. At the maximum displacement ductility, the column tension force supported by the splice mechanism in IC2 is about 35% of the total tension force.

The IC2 and IC3 models as well as the force transfer models developed for IC1 were validated using experimental data; results are reported elsewhere [Sritharan, 1998]. In the validation process, it was found that the tensile resistance of the cracked concrete in the joint region also contributed to the force transfer across the joint.

Modified External Strut Force Transfer Models

Based on the observed performance and detailed joint force transfer models formulated for IC1 as well as for a tee joint in a multi-column test unit with a reinforced concrete cap beam [Sritharan et. al., 2001], the following shortcomings were identified in the external strut joint force transfer model shown in Fig. 1b:

- The degree of incline and the magnitude of the external strut were incorrect in the design model, which assumed a larger column tension force than is practically possible could be transferred to the external joint reinforcement.
- The cap beam positive moment introduces a relatively low magnitude compression strut at the face of the tee joint. Consequently, this strut makes a smaller contribution to anchoring the column tension force than postulated in the design model. In Fig. 1b, it was assumed that compression strut C_3 at the column tension face would have a significant role in anchoring $0.5T_c$ located close to the centroidal axis of the column.
- The splice transfer mechanism shown in Fig. 6 anchor about 50% of the column tension force, which was not recognized in the design force transfer model.
- Due to force transfer across the joint, the cap beam region adjacent to the column compression side and the beam region adjacent to the column tension side are equally disturbed. This was not considered in the original external strut joint design model.

Figure 10 shows a modified external strut force transfer model for reinforced concrete bridge tee joints that addresses the shortcomings of the original design model. The modified model assumes that the

- clamping and splice mechanisms contribute equally to the anchorage of the column tension force,
- locations of the two column ties (see Fig. 10a), each with a magnitude of $0.5T_c$, are at the centroidal axis and at $0.4h_c$ from the centroidal axis of the column [Priestley, 1993],
- anchorage of $0.5T_c$ located at the centroidal axis is through the splice mechanism (Fig. 10b), and
- external strut transfers $0.15T_c$ to the beam stirrups outside the joint as opposed to $0.25T_c$.

Experimental observations and finite element study confirmed that column bars embedded in fully prestressed tee joints are exclusively anchored through the clamping mechanism and that nominal reinforcement within these joints is adequate. An external strut is not required for the joint force transfer and thus, additional reinforcement outside the joint is not provided. The design of the joint can be based on the modified force transfer model shown in Fig. 11.

In partially prestressed tee joints, a large percentage of the column tension force is anchored with the clamping mechanism — assisted by prestressing — instead of an external joint strut. The remainder is anchored through the splice mechanism. The degree to which each mechanism contributes to anchoring T_c depends on the amount of cap beam prestressing. The response of IC2 suggests that if the cap beam prestressing is designed to sustain 50% of the beam negative moment, the joints should be designed with nominal shear reinforcement. Additional reinforcement is only recommended at the top and bottom of the beam across the joint, assuming anchorage of the column tension force by the splice mechanism is $0.25T_c$. Joint tension force transfer in the vertical direction is assumed to be by the concrete.

Equivalent models for the design of bridge knee joints and the joint reinforcement requirements based on the modified external strut force transfer model are recommended elsewhere [Sritharan, 1998].

Conclusions

The analysis of the three tee joints with varying amounts of cap beam prestressing revealed that the force transfer in bridge joints can be characterized by two parallel mechanisms, the clamping and splice mechanisms. The study also confirmed that the clamping mechanism was assisted by an external joint strut anchoring outside in the cap beam as assumed in the design force transfer model. As prestressing was increased in the cap beam, the contributions to joint force transfer by the external joint strut and the splice mechanism, both of which require additional reinforcement in the joint region, became insignificant.

An analysis of the joints clearly suggested the need for modifications to the original

external strut joint design model. Consequently, modified external strut joint force transfer models are suggested. For joints with zero prestressing in the cap beam, the modified model relies equally on the clamping and splice mechanisms for anchoring the column tension force into the joint. When the cap beam is fully prestressed, the modified joint design model is based solely on the clamping mechanism without the need to form an external strut in the cap beam adjacent to the joint.

Acknowledgments

The large-scale experiments on bridge joint systems were conducted at the Charles Lee Powell Structural Laboratory of the University of California at San Diego with financial support from the California Department of Transportation. Professor M. J. Nigel Priestley is greatly acknowledged for supervising the study summarized in this paper. Thanks are also extended to Pam Reinig for her constructive review of the manuscript.

References

Applied Technology Council (1996). Improved Seismic Design Criteria for California Bridges: Provisional Recommendations, ATC-32, California.

California Department of Transportation (1999). Seismic Design Criteria, Version 1.1, California.

Priestley, M. J. N. (1993). Assessment and Design of Joints for Single-Level Bridges with Circular Columns, *Structural Systems Research Report*, University of California at San Diego, California, SSRP 93/02.

Priestley, M. J. N., Seible, F., and M. Calvi (1996). Seismic Design and Retrofit of Bridges, *John Wiley & Sons*, New York.

Sritharan S. (1998). Analysis of Concrete Bridge Joints Subjected to Seismic Actions, *Doctoral Dissertation*, Department of Structural Engineering, University of California at San Diego, California.

Sritharan, S., Priestley, M. J. N. and F. Seible (1999). Enhancing Seismic Performance of Cap Beam-Column Bridge Joints Using Prestressing, *PCI Journal*, Precast/Prestressed Concrete Institute, 44 (4, July-Aug.): 74-91.

Sritharan, S., Ingham, J. M. and M. J. N. Priestley (2000a). Strut-and-Tie Model Concepts for Seismic Design and Assessment of Concrete Bridge Joints, *Proceedings of the Twelfth World Conference on Earthquake Engineering*, Paper No. 1448, Auckland, New Zealand.

Sritharan, S., M. J. N. Priestley, and F. Seible (2000b). Nonlinear finite element analysis of concrete bridge joint systems subjected to seismic actions. *Journal: Finite Elements in Analysis and Design*, 36 (3–4, November): 215–33.

Sritharan, S., Priestley, M. J. N. and F. Seible (2001). Seismic Design and Experimental Verification of of Concrete Multiple Column Bridge Bents, *ACI Structural Journal*, American Concrete Institute, 98 (3, May-June): 335-346.

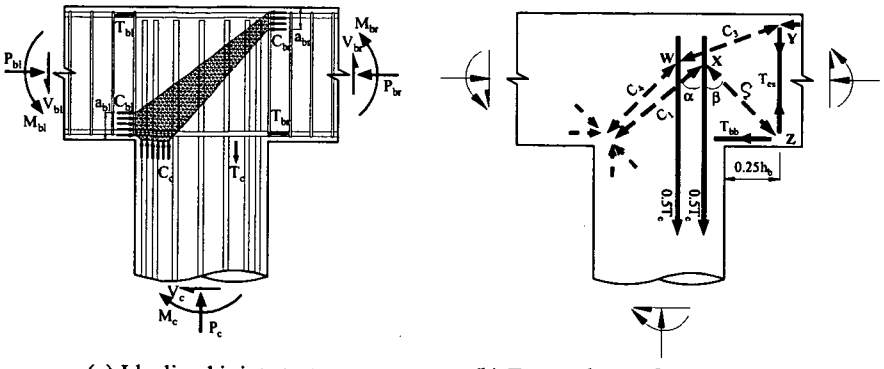

(a) Idealized joint strut (b) External strut force transfer model

Fig. 1 A reinforced concrete tee joint with a circular column.

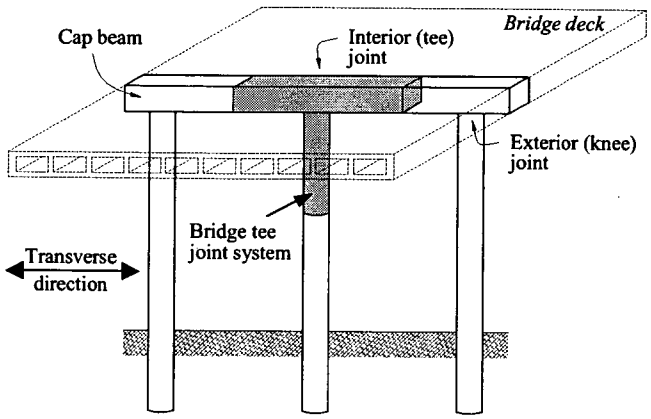

(a) Schematic of the prototype bridge

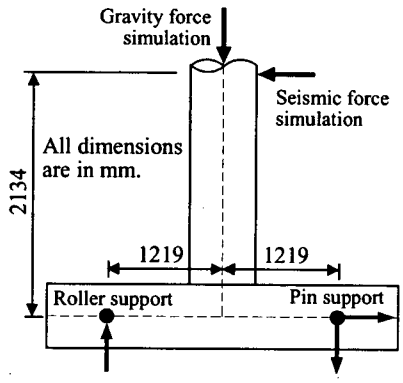

(b) Test unit at 50% scale

Fig. 2 Bridge tee joint test unit

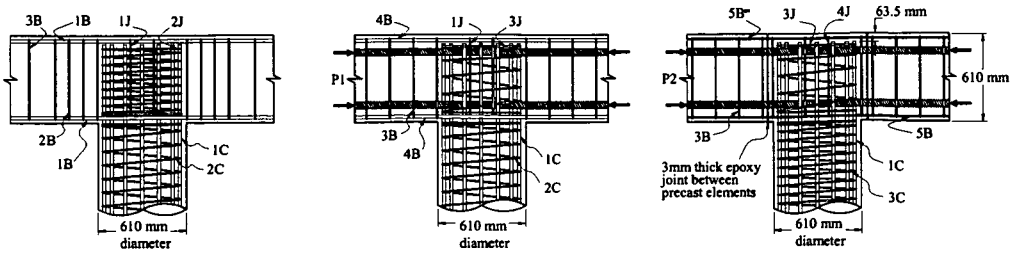

(a) IC1 - Reinforced concrete joint (b) IC2 - Partially prestressed joint (c) IC3 - Precast fully prestressed joint

REINFORCEMENT DETAILS:		DIMENSIONS:
1C - 14#7 (22 mm dia.)	1J - 2 sets of 4 legs #3 (9.5 mm dia.) hairpins	Column : 610 mm dia.
2C - #3 (9.5 mm dia.) spiral @ 96.5 mm	2J - #3 (9.5 mm dia.) spiral @ 57 mm	Beam : 610x686 mm^2
3C - #3 (9.5 mm dia.) spiral @ 63.5 mm	3J - #3 (9.5 mm dia.) spiral @ 121 mm	Cover to long. Bars : 25 mm
1B - 7#7 (22 mm dia.)	4J - 2 sets of 4 legs #3 (9.5 mm dia.) stirrups	
2B - 4 legs # 3 (9.5 mm dia.) stirrups @ 102 mm	PRESTRESSING FORCES:	NOTES:
3B - 4 legs # 3 (9.5 mm dia.) stirrups @ 165 mm	P1 = 1670 (4x417.5) kN	*Rebar type is discontinuous at column faces
4B - 4#6 (19 mm dia.)	P2 = 2940 (6x490) kN	1 mm = 0.0394 in.
5B* - 4#4 (12.5 mm dia.)		1 kN = 0.2248 kips

Fig. 3 Reinforcement details of test units IC1, IC2, and IC3.

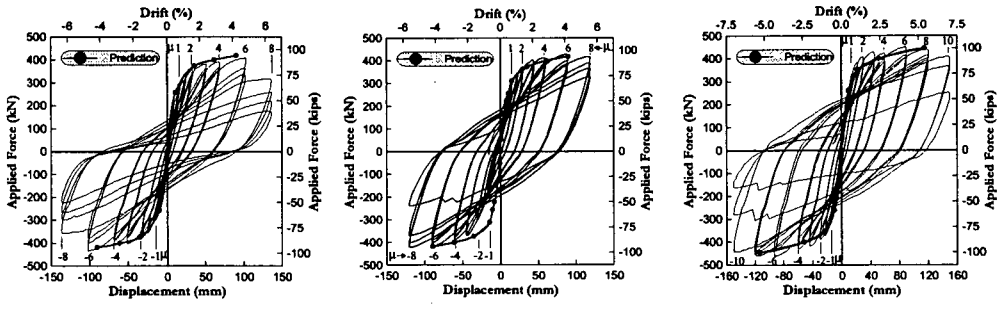

(a) IC1 (b) IC2 (c) IC3

Fig. 4 Force-displacement responses of the test units.

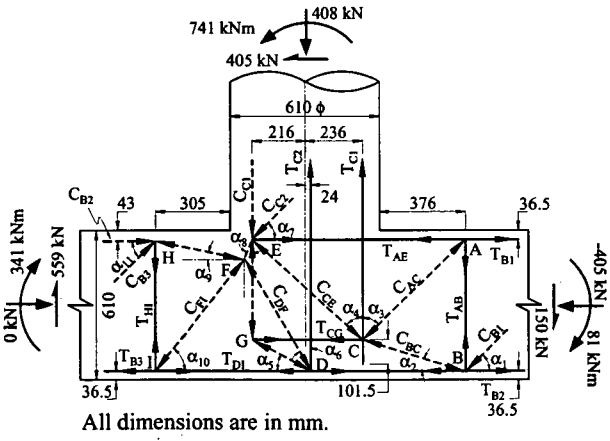

Strut	Force (kN)	C_{FH}	667	T_{HI}	676
C_{C1}	1935	C_{FI}	859	Angle	degree
C_{C2}	574	Tie	Force (kN)	α_1	45
C_{B1}	214	T_{C1}	890	α_2	16.1
C_{B2}	105	T_{C2}	1050	α_3	45
C_{B3}	778	T_{B1}	351	α_4	48
C_{AC}	351	T_{B2}	205	α_5	28.1
C_{BC}	356	T_{B3}	645	α_6	30.7
C_{CE}	1103	T_{AB}	249	α_7	45
C_{DF}	1081	T_{AE}	601	α_8	22.8
C_{DG}	258	T_{BD}	396	α_9	10.7
C_{EG}	120	T_{CG}	227	α_{10}	51.9
C_{EF}	1606	T_{DI}	1174	α_{11}	45

Fig. 5 Force transfer model of IC1 in the joint region at $\mu_\Delta = 6x1$.

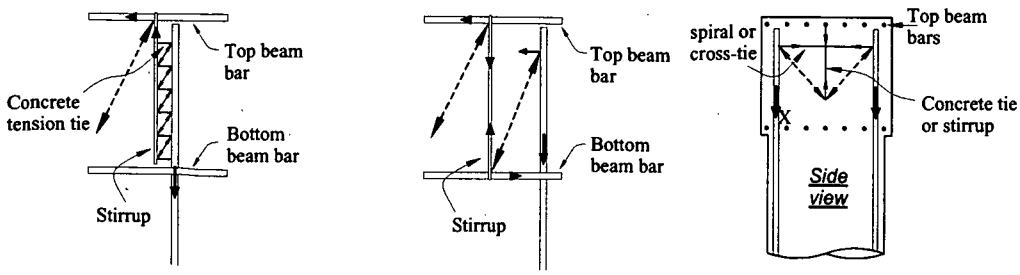

(a) Conventional mechanism (b) Single strut mechanism (c) Out-of-plane mechanism

Fig. 6 Splice transfer mechanism.

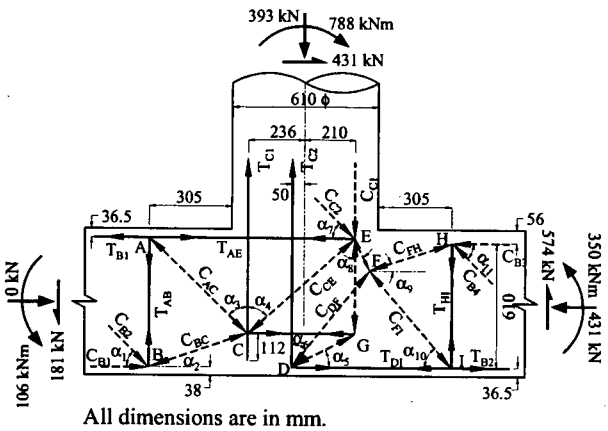

All dimensions are in mm.

Strut	Force (kN)	C_{EG}	169	Angle	degree
C_{C1}	2073	C_{FH}	907	α_1	45
C_{C2}	609	C_{FI}	1143	α_2	19.2
C_{B1}	18	Tie	Force (kN)	α_3	45
C_{B2}	254	T_{C1}	854	α_4	48.3
C_{B3}	285	T_{C2}	1250	α_5	28.2
C_{B4}	811	T_{B1}	196	α_6	38.5
C_{AC}	351	T_{B2}	436	α_7	45
C_{BC}	209	T_{AB}	249	α_8	24.3
C_{CE}	1019	T_{AE}	445	α_9	18.9
C_{DF}	1379	T_{CG}	316	α_{10}	49.8
C_{DG}	360	T_{DI}	1174	α_{11}	45
C_{EF}	1819	T_{HI}	872	-	-

Fig. 7 Force transfer model of IC1 in the joint region at $\mu_\Delta = 6x1$.

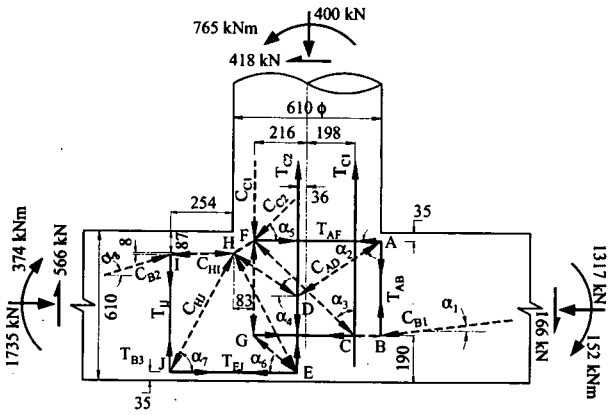

All dimensions are in mm.

Strut	Force (kN)	C_{FG}	98	T_{EJ}	267
C_{C1}	2024	C_{FH}	1908	T_{IJ}	503
C_{C2}	591	C_{HI}	1735	Angle	degree
C_{B1}	1326	C_{Hj}	569	α_1	7.2
C_{B2}	1824	Tie	Force (kN)	α_2	33.9
C_{AD}	280	T_{C1}	1334	α_3	43.0
C_{BC}	1317	T_{C2}	707	α_4	33.9
C_{CF}	1957	T_{AB}	156	α_5	45.0
C_{DH}	280	T_{AF}	231	α_6	40.7
C_{EG}	151	T_{CG}	116	α_7	62.0
C_{EH}	343	T_{DE}	298	α_8	17.8

Fig. 8 Force transfer model of IC2 in the joint region at $\mu_\Delta = 8x1$.

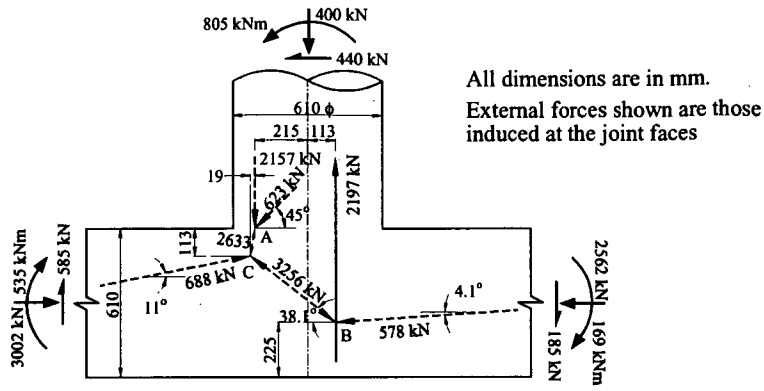

Fig. 9 Force transfer model of IC3 in the joint region at μ_Δ = 8x1.

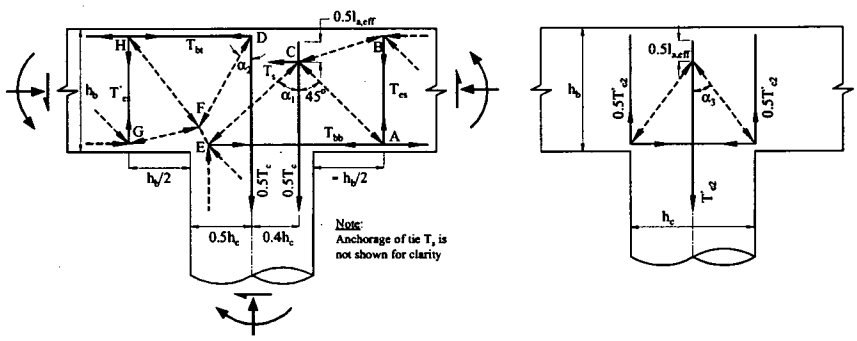

(a) Joint design model (b) Design splice transfer model

Fig. 10 The modified external strut force transfer model for reinforced concrete tee joints.

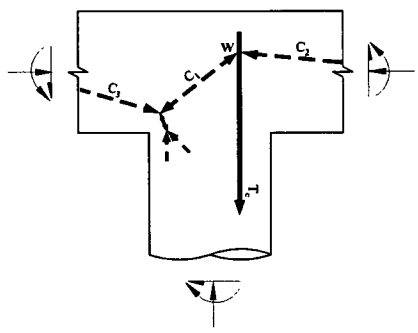

Fig. 11 The modified external strut force transfer model tee joints with fully prestressed cap beams.

LOADING TESTS ON CAP BEAMS TO EVALUATE SHER STRENGTH AGAINST EARTHQUAKES

Kenji Kosa*, Jyunko Taguchi**, Satoshi Yoshihara***, and Katsunori Tanaka****
Presenting author: Kenji Kosa

SUMMARY

To investigate the shear-resisting behavior of cap beams in RC rigid frame bridges under seismic loading, experiments were conducted using two seismically-strengthened pier specimens. The hoop tie ratio was used as the parameter.

According to the experiments, the beams of the specimens suffered shear damage after plastic hinges were formed at four positions. It was found that the hoop tie ratio of the beam does not affect the maximum strength of the beam, but significantly affects its deformation capacity. The FEM analysis showed that strain of hoop ties increased as the deformation of the beam increased, which suggests that shear damage to the beam was caused by the decrease of shear resisting capacity of the concrete in the beam.

1. INTRODUCTION

A significant number of RC bridge piers along the Hanshin Expressway Kobe Route suffered severe damage during the 1995 Hyogo-ken Nambu Earthquake. Though most RC single column piers were damaged, many of two-column piers of the RC rigid frame bridges survived the earthquake with small damage. One reason for this is that the latter type pier has more flexural strength than the former type, because the rigid frame structure has a higher degree of redundancy and plastic hinges are successively formed in the latter type when subjected to loading. It should be noted, however, there is not much difference in the shear strength of the two piers when subjected to loading.

After the earthquake, seismic strengthening began on all the routes of the Hanshin Expressway. The columns of single column piers and rigid frame piers are being jacketed with concrete or steel plates. In the case of rigid frame structures, there is a fear that unjacketed beams may have lost their relative strength after the columns have been jacketed, and that shear damage may first occur at the unjacketed beam area, if subjected to seismic loading. However, seismic strengthening of the beams is rather difficult, mainly because the shear strengthening design method for the beam is not yet well-established due to design complexity and because bearings and other devices that hamper strengthening work are installed on the beam.

* Assoc. Prof. Kyushu Institute of Technology, Kitakyushu City
** Graduate student, Kyushu Institute of Technology, Kitakyushu City
*** Senior Engineer, Hanshin Expressway Public Corporation, Osaka
**** Engineer, Yachiyo Engineering Co., Ltd, Osaka

To date, no crucial damage to RC rigid frame piers originating from beam damage has been reported in Japan. Whereas in the U.S., shear damage to the cross beam and the column-beam joint occurred during the Loma Prieta Earthquake.

To investigate the behavior of RC rigid frame bridge beams under seismic loading, experiments were conducted using two 1/8 scale specimens modeling on a column-strengthened standard type RC rigid frame pier. The hoop tie ratio in the beam was made to normal for specimen No. 1 and reduced to one half for specimen No. 2. The shear strength, deformation capacity, and the damage mechanism of the beam were evaluated.

2. EXPERIMENTAL PROGRAM

Monotonic horizontal loading was applied to the beam end of the specimens. Table 1 shows the size and the reinforcement ratio of the two specimens and an actual pier. The actual pier means the pier that was used as the model pier for specimen construction. Used as the model pier was P-164 on the Osaka-Nishinomiya Route that has a typical configuration of rigid frame piers. According to the check by the ultimate lateral strength method specified in the Specifications for Highway Bridges (Highway Specifications), the model pier is a beam-failure preceding type. The hoop tie ratio in the beam of specimen No. 2 was reduced to 1/2 that of the model pier so that the failure mode at the beam can be evaluated.

In a model pier, the main reinforcement ratio of the column is 0.40% and the design flexural yielding of the column, the design flexural yielding and the design shear strength of the beam are all nearly equivalent. But, to make clear the damage mode of the beam, D13 reinforcing bars which are one size bigger were used for the main reinforcement of the column of the specimens. The column of the model pier is jacketed with 9 mm thick steel plates which is 0.71% if converted into the hoop tie ratio.

Figure 1 shows the reinforcing bar arrangement of specimen No. 1. As to the column of the specimens, the cross section is 31 x 31 cm, the main reinforcement ratio 0.74%, and the hoop tie ratio 0.71%. As to the beam of the specimens, the cross section is 31x 25 cm and the main reinforcement ratio 0.54%. The hoop tie ratio of the beam differs between the two specimens: 0.16% (D6@130mm) for specimen No.1 and 0.08% (D4@105 mm) for specimen No. 2. As with a model pier, no hoop ties were arranged at the column-beam joint of the specimens.

Table 1 Actual pier and specimens

		Actual pier	No.1	No.2
Pier height (m)		10.60	1.32	1.32
Column cross section (cm)		250×250	31×31	31×31
Beam cross section (cm)		250×200	31×25	31×25
Reinforcement ratio	Column main reinforcement ratio (Axial dir.)	0.49%	0.89%	0.89%
	Column main reinforcement ratio (Perp dir.)	0.40%	0.74%	0.74%
	Beam main reinforcement ratio (Lower part.)	0.51%	0.54%	0.54%
	Column hoop tie ratio	0.71% (steel plates)	0.71%	0.71%
	Beam hoop tie ratio	0.16%	0.16%	0.08%

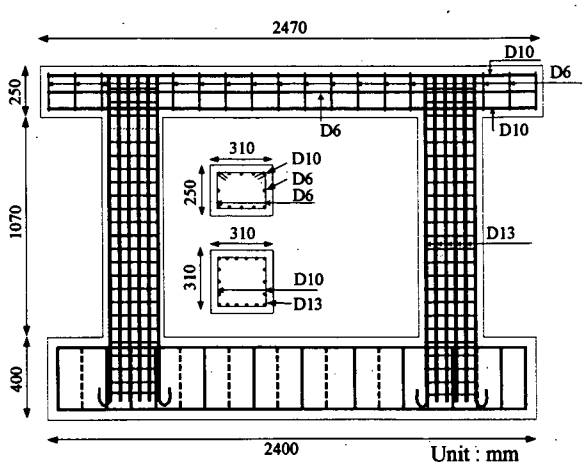

Fig. 1 Reinforcement arrangement of specimen No.1

Figure 2 shows a load application to the specimens. To anchor the specimens firmly, the footing and the base plate were secured with 15 reinforcing bars. Loading was applied with an increment of 30 kN up to near a maximum load. Every time a target load was reached, the load was reduced to zero and crack development was checked. Loading was applied by the load-control method up to a maximum load and by the displacement-control method after reaching a maximum load. Though dead load of 1.0N/mm^2 is acting on a model pier as the axial compressive stress, this load was neglected, considering that this small stress is not influential.

Table 2 shows the material characteristics of the concrete and the reinforcing bars used. The design strength of the concrete is 27.0N/mm^2. Measurements included displacement of each member, strains of main reinforcement and hoop ties in the beam, strains of main reinforcement and hoop ties in the column. Figure 3 shows the positions of displacement meters installed. Displacement measurements included the horizontal displacement of each member, the rotation of the column, and displacement at the end of each member.

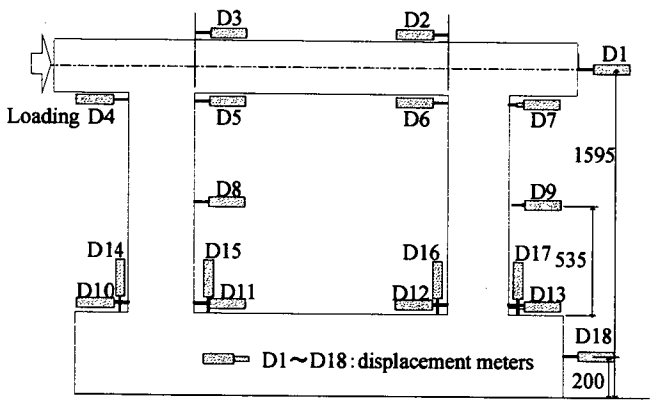

Fig. 3 Positions of displacement meters

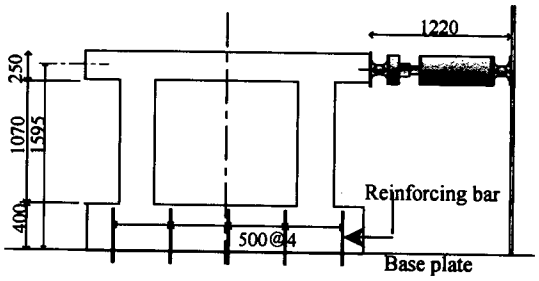

Fig. 2 Load application to specimen

Table 2 Properties of materials used

Items		No.1	No.2
Concrete	Compressive strength N/mm^2	27.4	36.6
Reinforcing bar D4	Yield strength N/mm^2		342
	Yield strain μ		1630
Reinforcing bar D6	Yield strength N/mm^2	380	357
	Yield strain μ	1810	1702
Reinforcing bar D10	Yield strength N/mm^2	398	398
	Yield strain μ	1895	1895
Reinforcing bar D13	Yield strength N/mm^2	399	375
	Yield strain μ	1900	1786

3. EXPERIMENTAL RESULTS

3.1 Load-Displacement Relationship

Figure 4 shows the load-displacement relationship and Table 3 gives other experimental results. The displacement values in the table were taken by the displacement meter D1 that was installed at the end of the beam opposite of a loading point. The yield displacement (δ_y) was taken when the main reinforcement in the beam reached yielding, and the ultimate displacement (δ_u) was taken when the load dropped to a yield load in the load-displacement envelope. The ductility factor (μ) was calculated as δ_u / δ_y.

The ductility factor thus derived was 6.7 for specimen No. 1 and 3.6 for specimen No. 2. The ductility factor of specimen No. 2 was about one half of that of specimen No. 1. But, the strength of the beam did not differ much, with a maximum load of 322.0kN for specimen No. 1 and 316.5kN for specimen No. 2. These experimental results suggest that the hoop tie ratio in the beam has little effect on the maximum strength of an RC rigid

frame pier, but has large effect on the deformation capacity and the ductility factor of the pier.

Table 3 Experimental results

Specimens		No.1	No.2
Yield displacement	δy(mm)	6.3	7.1
Ultimate displacement	δu(mm)	41.3	25.8
Yield load	Py(kN)	221.3	251.2
Maximum load	Pmax(kN)	322.0	316.5
Ductility factor	δu/δy	6.6	3.6
Pmax/Py		1.5	1.3

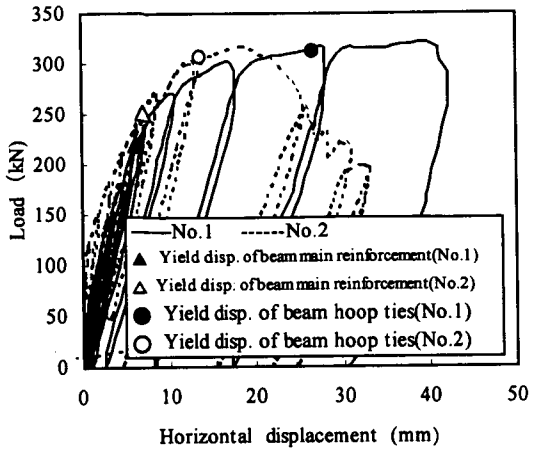

Fig. 4 Load-displacement relationship

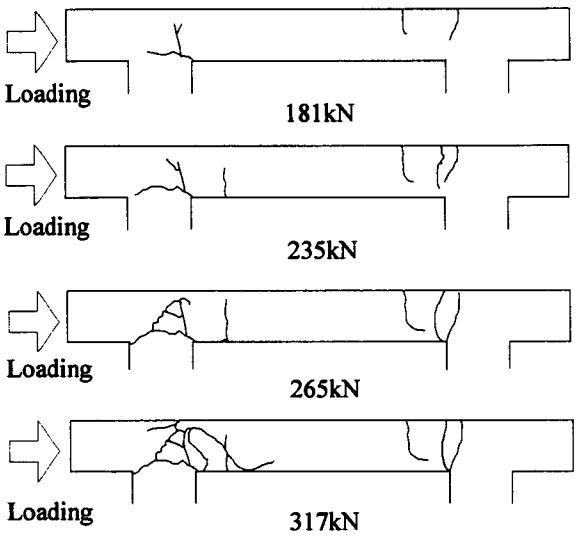

Fig. 5 Crack development (No.1)

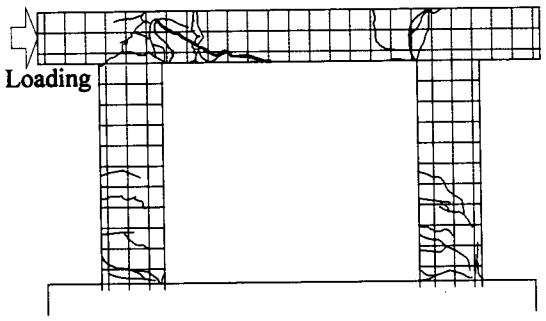

Fig. 6 Damage to specimen No.1

3.2 Damage to Specimens

(a) Specimen No. 1

Figures 5 and 6 respectively indicate crack development and final damage observed on the beam of specimen No. 1. Cracking started on the side of the beam when the load was 181kN (displacement: 4.5 mm). Flexural cracking appeared on both columns of the specimen and the main reinforcement in the beam reached yielding when the load was 222kN (displacement: 6.3 mm). Cracking continued on both upper and lower faces of the beam. The hoop ties in the beam showed a near-yield strain at the loading of 317kN (displacement: 27.8 mm) and cracking still continued propagation at an angle of 45 degrees toward the center of the beam. The oblique cracking began to widen and a large slip was caused at a maximum load of 322kN (displacement: 39.2 mm), resulting in shear failure.

Plastic hinges were formed at four positions after the main reinforcement in the column and the beam reached yielding and then the beam suffered shear failure. The ductility factor at the time was approximately 6, which means it was the failure with a higher deformation capacity. Though shear cracking appeared at a displacement of about 28 mm, the load did not begin to drop until reaching a maximum load of 42 mm, as shown in Fig. 4. Concurrently, strain on the hoop tie in the beam increased up to a yield strain and then the beam failed by shear.

(b) Specimen No. 2

Figures 7 and 8 respectively show crack development and the final damage occurred to the beam of Specimen No. 2. Cracking appeared on the side of the beam when the load was 150kN (displacement: 3.0 mm). Another cracking started at the column-beam joint opposite of loading point. A strain gauge installed on the main reinforcement at that position showed a strain exceeding a yield strain when the load was 251kN (displacement: 7.1 mm). When the load was 302kN (displacement: 13.8 mm), hoop ties in the beam showed a strain close to a yield strain. Shear cracking that appeared at the column-beam joint on the loading side instantaneously spread at the time the load was 317kN (displacement: 19.7 mm), causing slippage on the lower face of the beam and then a failure by shear.

Monotonic loading was continued by the displacement-control method until a maximum displacement of 33 mm was caused. Then, the strength gradually decreased, the concrete on the lower face of the beam dropped locally, and the shear cracks extended up to the outside of the joint area.

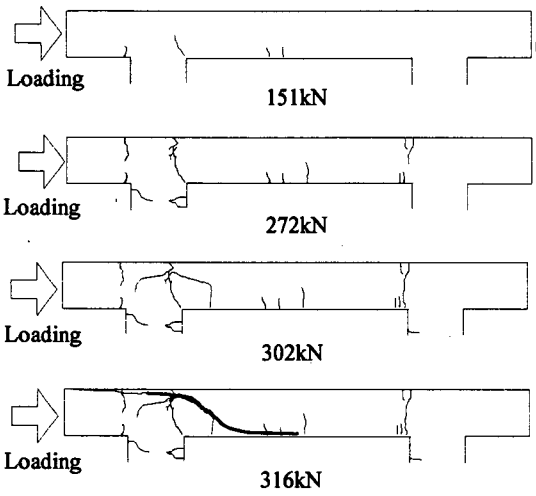

Fig. 7 Crack development (No.2)

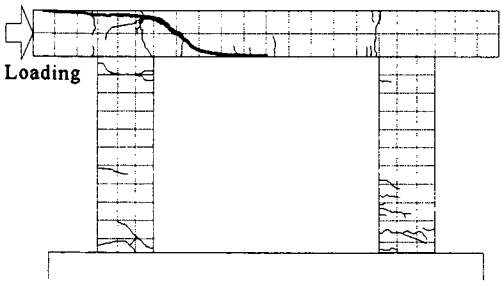

Fig. 8 Damage to specimen No.2

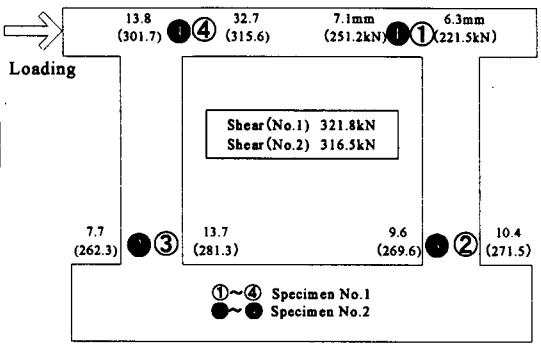

Fig. 9 Sequence of reinforcement yielding

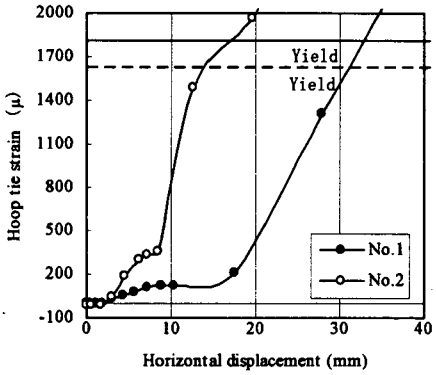

Fig. 10 Relationship between hoop tie strain and displacement

In specimen No. 2, oblique cracks started on the beam when the displacement was about 11 mm and abruptly a shear failure came when the next load was applied, a marked difference from the results of specimen No. 1. In both specimens, numbers of cracks appeared at the bottom of the column not on the loading side but on the opposite side. Formation of four plastic hinges were confirmed in both specimens, with the fourth one

formed on the left beam at a displacement of 32.7 mm in specimen No. 1 and 13.8 mm in specimen No. 2. In both specimens, shear failure occurred after the hoop ties in the beam reached yielding. It is therefore presumed that the shear failure of the beam was caused by the decrease of shear resistance provided by the concrete as deformation increased.

3.3 Sequence of Reinforcement Yielding

Figure 9 shows the sequence of yielding of the main reinforcement judged from the measurements using strain gauges. Yielding was assumed to have reached when the measured strain became the yield strain shown in Table 2. In both specimens, the right beam reached yielding first followed by the bottom areas of both the right and the left columns and finally the left beam, resulting in the formation of four plastic hinges. However, there was a significant difference as to the timing of the formation of the fourth hinge. In specimen No. 2, yielding of the main reinforcement in the left beam occurred when the displacement was one-half the displacement of specimen No. 1.

3.4 Distribution of Strain

Figure 10 shows the relationship between the displacement and the strain of the hoop ties in the beam. Strain was measured on the hoop ties in the beam at the position the shear damage occurred. In specimen No. 1, no visible strain appeared until displacement became 15 mm, and then strain gradually increased up to a yield strain. In specimen No. 2, strain increased little until the displacement became 10 mm and then started to increase until finally reaching a yield strain.

This suggests that most of the acting shear forces up to a displacement of 10-15 mm is carried by the concrete of the beam. And, it is after this displacement that the hoop ties start to exhibit their load-carrying capacity. The abrupt increase of strain seen in specimen No. 2 was probably because the hoop tie ratio of this specimen was rather small and had little resistance to shear.

3.5 Comparison with Design Values

The check method for the ultimate lateral strength of the RC rigid frame bridge piers was incorporated into the 1996 Specifications for Highway Bridges (Highway Specifications) based on the research results conducted after the 1995 earthquake. According to the specifications, check is performed by evaluating the damage mode of a pier in the same way as done with single column piers, and then comparing the strength of the pier with the response value assigned to each failure mode.

The values thus obtained are assumed as design values. Tables 4 and 5 compare the experimental and design values, and Fig. 11 compares load-displacement relationships obtained by experiments and by design. It is seen from the tables and the figure that the horizontal strength of the two specimens is about 1.1 to 1.8 times the force that causes flexural yielding. The shear resistance obtained by experiment was 1.2 times the design value of specimen No. 1 (experimental value 321.8 kN, design value 269.7 kN), but it was as high as 2.3 times in specimen No. 2 (experimental value 316.5 kN, design value 139.2

kN). This suggests that shear strength specified by the Highway Specifications has a considerable margin compared with actual behavior, depending on the hoop tie ratio.

An acting force is carried by the concrete of the beam in the range of small displacement. It is considered that the shear strength provided by the concrete is somewhat underestimated in design.

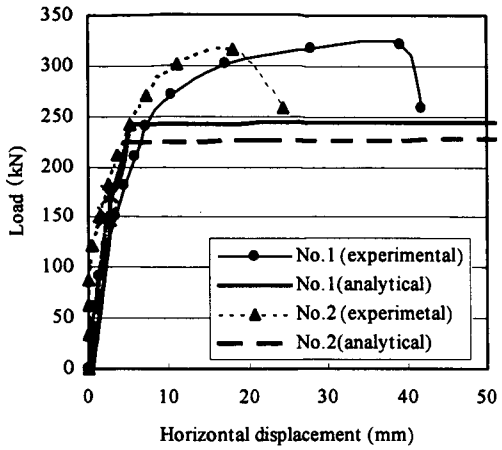

Fig. 11 Comparison of load-displacement relationships

Table 4 Comparison of design and experimental values (No.1)

No.1	Design values		Experimental values		
Sequence	Location	Horizontal force P'_1(kN)	Sequence	Horizontal force P_1(kN)	P_1/P'_1
①	Right beam	170.9	①	221.5	1.3
②	Left beam	171.8	④	315.6	1.8
③	Left column	242.6	③	281.3	1.2
④	Right column	243.4	②	271.5	1.1
Shear	Right beam	269.7	Left beam	321.8	1.2

Table 5 Comparison of design and experimental values (No.2)

No.2	Design values		Experimental values		
Sequence	Location	Horizontal force P'_2(kN)	Sequence	Horizontal force P_2(kN)	P_2/P'_2
①	Right beam	150.6	①	251.2	1.7
②	Left beam	151.7	④	301.7	2.0
③	Left column	242.3	②	262.3	1.1
④	Right column	243.1	③	269.6	1.1
Shear	Right beam	139.4	Left beam	316.5	2.3

4. EVALUATION BY FEM ALALYSIS

4.1 Analysis Method

The two-dimensional elasto-plastic FEM analysis was performed on the two specimens to investigate the reproductivity of the experimental results, the load-displacement relationship, strain development on the reinforcement, and the failure mechanism.

Figure 12 shows the elements employed for analysis. The elements used were plane stress elements for the concrete and truss elements for the reinforcement. The elements of the reinforcement and the concrete were completely bonded. As the material properties of them, the experimental values shown in Table 2 were used.

As the yield criterion for the concrete, the Drucker-Prager yield criterion and the maximum principal stress were adopted for the compressive range and the tensile range, respectively. As the yield criterion for the reinforcement, the Von-Mises yield criterion was adopted. In the shear model, a constant value of 20% was employed as the shear stress transfer value after the start of cracking.

Figure 13 shows the stress-strain model of concrete. In this model, a quadratic curve was adopted up to reaching the compressive strength in the compression-increasing range, a model with a constant stress and an increase in strain was adopted after that range, and a model with a linear stress decrease up to ε_t ($\varepsilon_t = \sigma_{sy} / E_s \fallingdotseq 2000\mu$) after reaching the tensile strength was adopted in the tensile range. For the stress-strain model of the reinforcement, a trilinear model that takes strain softening after reaching a yield strength into account was used.

As the loading condition, horizontal monotonic loads were applied to the beam by the displacement-control method. As the boundary condition, the bottom face of the footing was anchored completely.

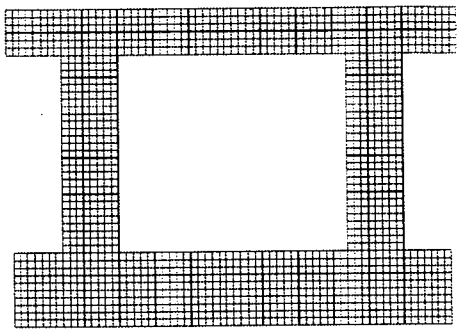

Fig. 12 Elements for analysis model

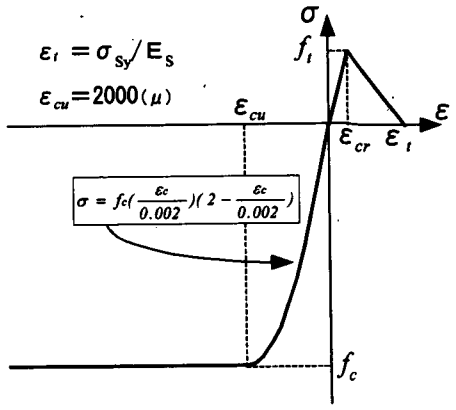

Fig. 13 Stress-strain model for concrete

4.2 Analytical Results

(1) Results for specimen No. 1

Figure 14 shows the load-displacement relationship of specimen No. 1. The displacement shown is the displacement taken at the D1 point in both experiment and analysis. The maximum load cited in analysis is the load obtained just before convergence becomes impossible. The yield point was determined by the displacement taken when strain at each measurement point and analysis point reached to a yield strain for the first time.

From Fig. 14, it is seen that both experimental and analytical inclinations are roughly similar up to near the maximum load, though the experimental inclination is slightly gentler than the analytical inclination in the initial range. The maximum load was 337 kN by analysis and 322 kN by experiment, both about 1.2 times greater than the design maximum load.

Table 6 shows the displacement and the load taken at each measurement point. As seen from the table, yielding of main reinforcements in the beam and the column occurred when the displacement was approximately below 10 mm in both experiment and analysis. In contrast, yielding of hoop ties in the beam occurred when the displacement was considerably large as 26.7 mm (load: 313 kN) for experiment and 23.5 mm (load: 321 kN) for analysis, though slight scatter was seen depending on measurement points.

Figure 15 indicates the distribution of strain occurred to the main reinforcement in the beam. Strain close to a yield strain occurred when the displacement was 6 mm in both experiment and analysis. When the displacement was 10 mm, strain exceeding a yield strain was caused at the measurement point in the beam end.

Figure 16 describes the distribution of strain occurred to the hoop ties in the beam. In the experiment, the hoop tie strain increased as the main reinforcement in the both ends of the beam yielded as with an increase of displacement. In analysis, almost no strain occurred up to a displacement of 6 mm and a strain of 1000 μ occurred at a displacement of 10 mm and a strain exceeding a yield strain at a displacement of 26 mm. Figure 17 gives the relationship between the strain of the hoop ties in the beam and the displacement that was derived by comparing the hoop tie strain elements at the beam end on the loading side

where shear cracking occurred. Strain did not occur up to a displacement of 15 mm in both experiment and analysis, but after this strain amount, hoop tie strain quickly increased as displacement increased.

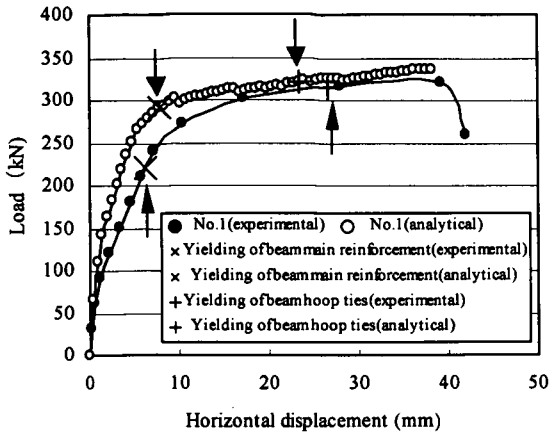

Fig. 14 Load-displacement relationship

Table 6 Comparison of experimental and FEM analytical values (No.1)

Items (mm)	Specimen No.1	
	Experimental	Analytical
Yield disp. of beam main reinforcement	6.3(221)	7.8(291)
Yield disp. of beam hoop ties	26.7(313)	23.5(321)
Yield disp. of column main reinforcement	10.4(272)	6.0(272)

( ) shows load : kN

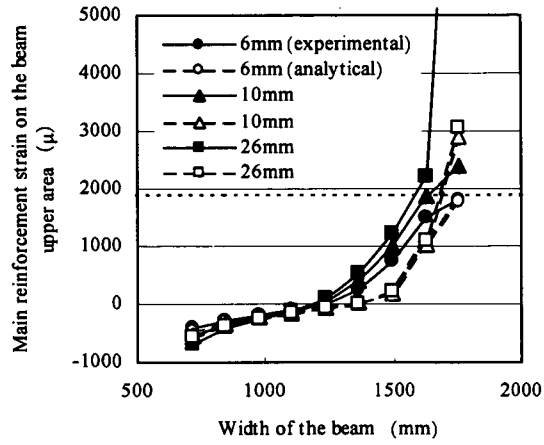

Fig. 15 Strain distribution on the beam main reinforcement (No.1)

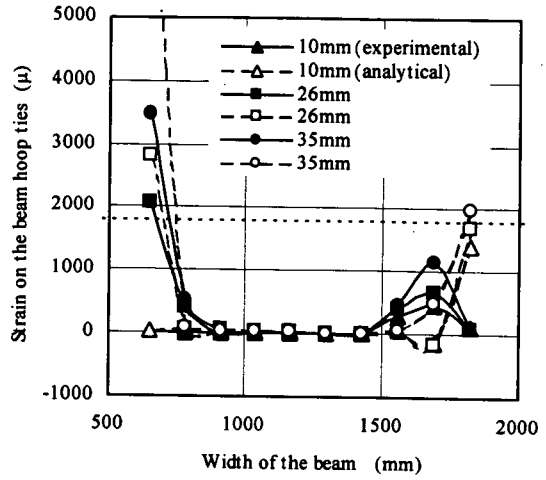

Fig. 16 Strain distribution on the beam hoop ties (No.1)

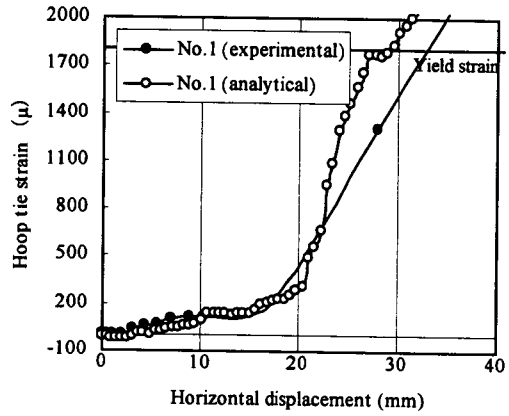

Fig. 17 Relationship between displacement and hoop tie strain

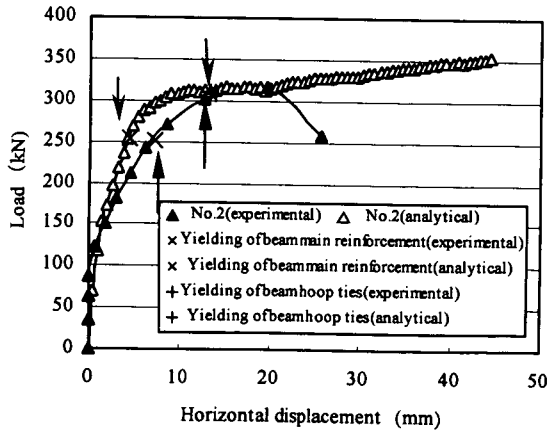

Fig. 18 Load-displacement relationship (No.2)

(2) Results for specimen No. 2

Figure 18 shows the relationship between load-displacement relationship of specimen No. 2. The load-displacement relationship was compared using the displacement values, both experimental and analytical, observed at the D1 point. The initial inclination of the experimental load-displacement curve was gentler than that of analysis, as with the results of specimen No. 1. So, using displacement meters D14 to D17 installed at the column bottom of specimen No. 2, rotation at the column bottom due to a horizontal displacement increase was corrected. About 2 mm displacement was caused due to the pullout of reinforcement at the column bottom before the main reinforcement in the beam reached yielding. If the reinforcement pullout is corrected in the experimental load-displacement relationship in Fig. 14, the initial inclination will become roughly the same in both specimens.

The maximum load by analysis, 353 kN, was slightly greater than the maximum load by experiment, 317 kN, but the both values have a margin 2.3 to 2.5 times the design shear strength.

Table 7 shows the load and the displacement taken at each measurement point. Though the main reinforcement in both beam and column reached yielding at a small displacement of 7.7 mm or below, hoop ties in the beam reached yielding at a rather large displacement of 10 mm or over, specifically 13.8 mm (load: 302 kN) in experiment and 13.3 mm (load: 310 kN) in analysis.

Figure 19 indicates the distribution of strain occurred to the main reinforcement in the beam. Though strain in the experimental results is slightly scattered, a yield strain is already caused at the beam end opposite of the loading point in both experiment and analysis when the displacement is 12 mm.

Table 7 Comparison of experimental and FEM analytical values (No.2)

Items (mm)	Specimen No.2	
	Experimental	Analytical
Yield disp. of beam main reinforcement	7.1 (251)	4.3 (254)
Yield disp. of beam hoop ties	13.8 (302)	13.3 (310)
Yield disp. of column main reinforcement	7.7 (262)	6.0(287)

( ) shows load : kN

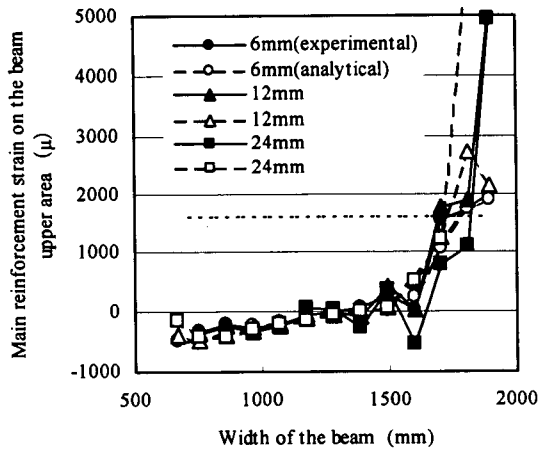

Fig. 19 Strain distribution on the beam main reinforcement (No.2)

Figure 20 shows the distribution of strain occurred to the hoop ties in the beam. The hoop tie strain at the end of the beam on the loading side is below 1000 μ when the strain is 10 mm, but it exceeds a yield strain when the displacement becomes 24 mm. It means the hoop tie strain increased rather quickly as with an increase of displacement. The same tendency is found in the analytical results, in which strain is 1000 μ when the displacement is 10 mm but it exceeds a yield strain when the displacement becomes 26 mm. Figure 21 shows the relationship between the strain of the hoop ties in the beam and

the displacement. Experimental and analytical results were compared using the hoop tie strain element at the beam end on the loading side where shear cracking occurred. It is seen that strain began to increase after the displacement exceeded 10 mm in both experimental and analytical results.

As seen, the FEM analysis could follow well the behavior of the maximum load, formation of four plastic hinges, and increase of hoop tie strain with an increase of displacement in both specimens. It can be said, therefore, that the analysis is able to evaluate the behavior of specimens pretty satisfactory.

It was confirmed that shear failure of the beam of the flexural yield-preceding type occurred in both specimens, which was known through the formation of four plastic hinges, occurrence of large strain with an increase in load, and similar strain distribution patterns.

As the hoop tie strain did not increase up to a displacement of 10-15 mm, it is considered that an acting shear force was carried by the concrete of the beam in the range of smaller displacement. In contrast, according to an ultimate lateral strength check based on the Highway Specifications, a flexural yield load and a shear resistance load are balanced in specimen No. 1, but the shear strength is about 1/2 of the flexural strength and ended in shear damage in specimen No. 2.

From these investigation results, it is inferred that the beams of RC rigid frame piers have shear resistance about twice that specified by the Highway Specifications because an acting force is carried by only the concrete up to a displacement of 1.5-2.0 δ_y. But, after 1.5-2.0 δ_y, shear resistance carried by the concrete begin to decrease and that carried by the hoop ties begin to increase as displacement increases, leading to a shear failure of the beam.

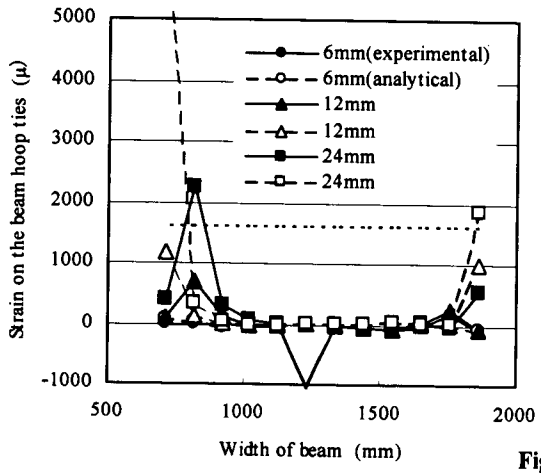

Fig. 20 Strain distribution on the beam hoop ties (No.2)

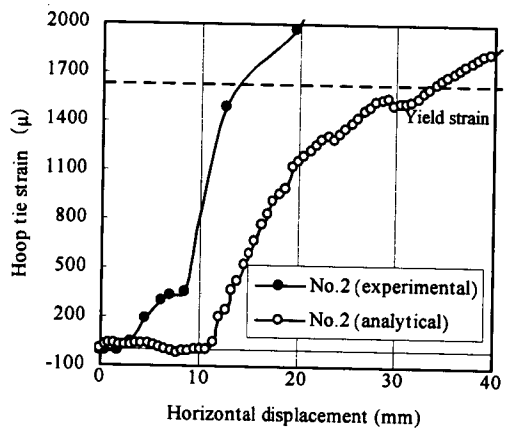

Fig. 21 Relationship between displacement and hoop tie strain

5. CONCLUSIONS

Horizontal monotonic loading tests were conducted using seismically-strengthened two 1/8 scale rigid frame pier specimens. Specimen No.1 was constructed to contain a standard hoop tie ratio in the beam and specimen No. 2 one half the standard hoop tie ratio. From the experiment and analysis, the following conclusions were drawn:

① According to the experiments using the hoop tie ratio as the parameter, the positions where four plastic hinges were formed were the same in both specimens independent of hoop tie ratio in the beam. This indicates that hoop tie ratio does not have a significant effect on the failure mechanism.
② There was no large difference in the maximum load of the specimens, with 322.0kN for specimen No. 1 and 316.5kN for specimen No. 2. But, difference was significant for the ductility factor, with 6.7 for specimen No. 1 and 3.5 for specimen No. 2, about 50% difference. This indicates that the hoop tie ratio in the beam does not affect the maximum strength of the beam but affects the ductility factor of the beam.
③ When the experimental results were compared with the results of the ultimate lateral strength check specified by the Highway Specifications, experimental shear strength was 1.2 times greater than the shear strength by the Specifications in specimen No. 1 and 2.3 times greater in specimen No. 2.
④ The FEM analysis could trace that shear failure occurred to the beams of the specimens was the flexural yield-preceding type. The analysis could also evaluate a tendency regarding a maximum load and formation of four plastic hinges.
⑤ Experimental and analytical results showed that shear damage to the beam was caused by the decrease of the shear strength of the concrete that occurred as the displacement and hoop tie strain of the beam increased. This suggests that an acting forces is carried by the shear strength of the concrete until displacement becomes 1.5-2.0 δ_y, and that the beam has twice the ultimate lateral strength specified by the Highway Specifications.

REFERENCES

1) Kosa, K., Taguchi, J., Otoguro, Y., and Tanaka, K., "Seismic Evaluation on the Beams of RC Rigid Frame Bridge Piers", Proceedings of the 26th JSCE Earthquake Engineering Symposium, 2001.
2) Takano, K., Mutsuyoshi, H., Sakurai, J., and Fujita, R., "Studies on the Strengthening of Beams of RC Single Layer Rigid Frame Piers", Proceeding of the Japan Concrete Institute, Vol. 22, No.3, 2000/6
3) Koizumi, H., Mutsuyoshi, H., Konishi, Y., and Fujita, R., "Studies on the Seismic Strengthening of Beams of RC Single Layer Rigid Frame Piers", Proceeding of the Japan Concrete Institute, Vol. 23, No.1, 2001/6
4) Adachi, Y., Unjyo, S., and Nagaya, K., "Experimental Studies on the Seismic Strengthening of RC Rigid Frame Pier Beams", Proceeding of the Japan Concrete Institute, Vol. 222, No.3, 2000/6

SEISMIC TESTING OF RETROFITS IN THE CENTRAL AND SOUTHEASTERN UNITED STATES

Reginald DesRoches[1], Thomas Pfeifer[2], and Roberto T. Leon[3]

Abstract

Many parts of the Central and Southeastern United States have recently begun initiating retrofit programs for bridges on major interstates. One of the most common retrofit strategies is to provide cable restrainers at the hinges and abutments to reduce the likelihood of unseating due to collapse. To evaluate the force-displacement behavior of the cable restrainer retrofits, a full-scale bridge setup is constructed based on an existing steel girder bridge, which has been considered for seismic retrofit using cable restrainers in Tennessee. Seismic cable restrainers are connected to the bridge pier using steel bent plates, angles, and undercut anchors embedded in the concrete, as specified by typical bridge plans. The full-scale bridge model was subjected to monotonic loading to test the capacity of the restrainer cable system and determine the modes of failure. Test results show that non-ductile failures occur in the steel bent plate connections in the restrainer system at loads less than 10% of the restrainer cable capacity. Modifications to current connections are tested and show considerable improvement in both strength and stiffness.

Seismicity in the Central and Southeastern United States

The Central and Southeastern United States is generally considered to consist of the states east of the Rocky Mountains, with the exclusion of the Northeastern US. In many parts of the Central and Southeastern US, ground motions have a 10% probability of exceeding 0.10g in 50 years and a 2% probability of exceeding 0.40g in 50 years (FEMA 222A, 1995), as shown in Figure 1. The hazard in this region is due primarily to the seismicity in the New Madrid region, and Charleston, South Carolina.

Three large earthquakes centered near New Madrid, Missouri occurred on December 16, 1811, January 23, 1812, and February 7, 1812. This sequence is believed have had events with moment magnitudes greater than M_w=7.0, including two events of magnitude larger than M_w = 8.0. Numerous aftershocks were also reported for a year after the initial shock (U.S. Geological Survey, 1912). The largest earthquakes to have occurred since 1812 were on January 4, 1843 and October 31, 1895 with magnitude estimates of 6.0 and 6.2, respectively. The past 30 years have had thousands of earthquakes; however, none have been large enough to cause damage to the local infrastructure in the region.

[1] Assistant Professor, Dept. of Civil & Environmental Engineering, Georgia Institute of Technology, Atlanta, GA 30332-0355

[2] Graduate Research Assistant, Dept. of Civil & Environmental Engineering, Georgia Institute of Technology, Atlanta, GA 30332-0355

[3] Professor, Dept. of Civil & Environmental Engineering, Georgia Institute of Technology, Atlanta, GA 30332-0355

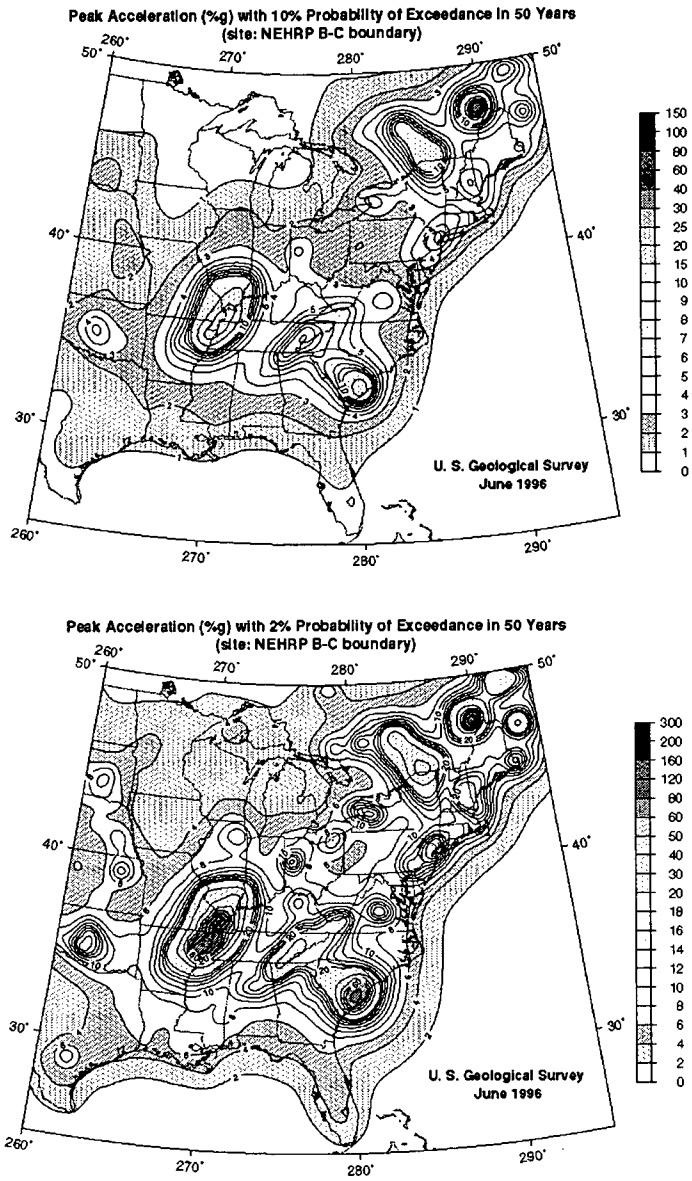

Figure 1. Probabilistic map showing expected ground motion for the Central and Southeastern United States for 10% and 2% probability of exceedance in 50 years (USGS, 1996)

The other seismic zone in the Central and Southeastern United States is in Charleston, South Carolina. In 1886, Charleston had destructive earthquake which had a Modified Mercalli intensity of X. Twenty seven lives were lost and $5-6 million of economical damage were reported (Wiegel, 1970).

Seismic Vulnerability and Retrofit Practices

An assessment of the bridge inventory in the Central and Southeastern United States (CSUS) shows that over 95% of the bridges are multi-span simply supported (MSSS), continuous, or single span of short-medium lengths (Lam, 2000). Furthermore, approximately one-third of the bridges have steel girders, while the remaining two-thirds have reinforced or pre-stressed concrete girders. The girders are typically supported by single or multi-column bents that are supported on pile foundations. In steel girder bridges, the girders are connected to the bent cap with steel fixed and rocker bearings. Since the bridges in the CSUS have not been subjected to strong ground motion, their expected seismic performance is not well understood. However, based on previous studies, the most likely vulnerabilities in the bridges in the CSUS are inadequate ductility capacity due to insufficient lap splices and inadequate transverse reinforcement (Lin et al. 1998) and brittle failure of the steel bearings (Mander 1996). In particular, the failure of steel bearings may lead to unseating at the expansion joints and abutments. To reduce the likelihood of unseating, several states in the Central and Southeastern US have begun bridge retrofit programs consisting of placing cable restrainers at the intermediate hinges and abutments (Buckle, 1995).

Restrainer cables are one of the most common retrofit measures because of its relative low cost and ease of installation. Cable restrainers have been used in California over the last 30 years as a bridge retrofit to prevent superstructure unseating and collapse during an earthquake (Saiidi 1996). Experimental tests have been performed on cable restrainer assemblies used in California (Selna 1989, Vlassis 2000). However, the details of the restrainer cables used in the CSUS are different from those which have been used and tested on the West Coast of the US. A full-scale test setup was developed to evaluate the strength, stiffness, and cyclic load-deflection behavior of restrainer cable retrofits according to the details specified in typical bridges in the CSUS. Figure 2 illustrates a typical MSSS bridge that will be retrofitted with cable restrainers in the CSUS.

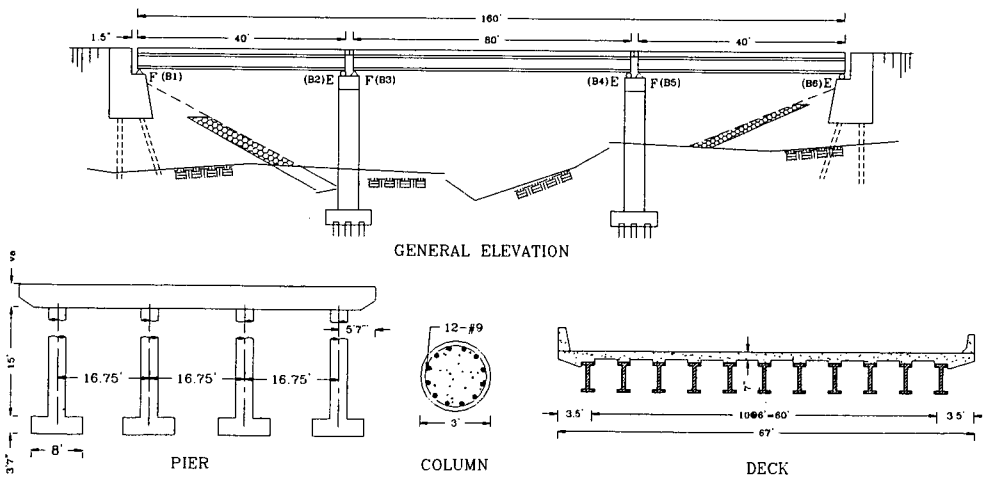

Figure 2. Typical MSSS bridge in the CSUS.

Full-Scale Test Setup

A two girder 40-ft (12192 mm) simply supported steel girder bridge was constructed as a test apparatus for the restrainer cable assemblies, as shown in Figure 3. The two main girders were W30x292 (W760x434) beams that are spaced at a distance of 7'-9½" (2375 mm) between girder centerlines. Three W30x124 (W760x185) transverse stiffening beams are spaced between the main girders so that the loading of the bridge will remain in-plane, thus preventing torsional movement. The weight of the bridge is modeled by casting two large concrete blocks between the main girders. The superstructure of the bridge rests on top of elastomeric bearings which are supported on pier caps anchored to the floor. The piers are designed so that the reinforcement is similar to that on actual bridges in order to accurately predict the behavior of the restrainer cable connections at the pier caps.

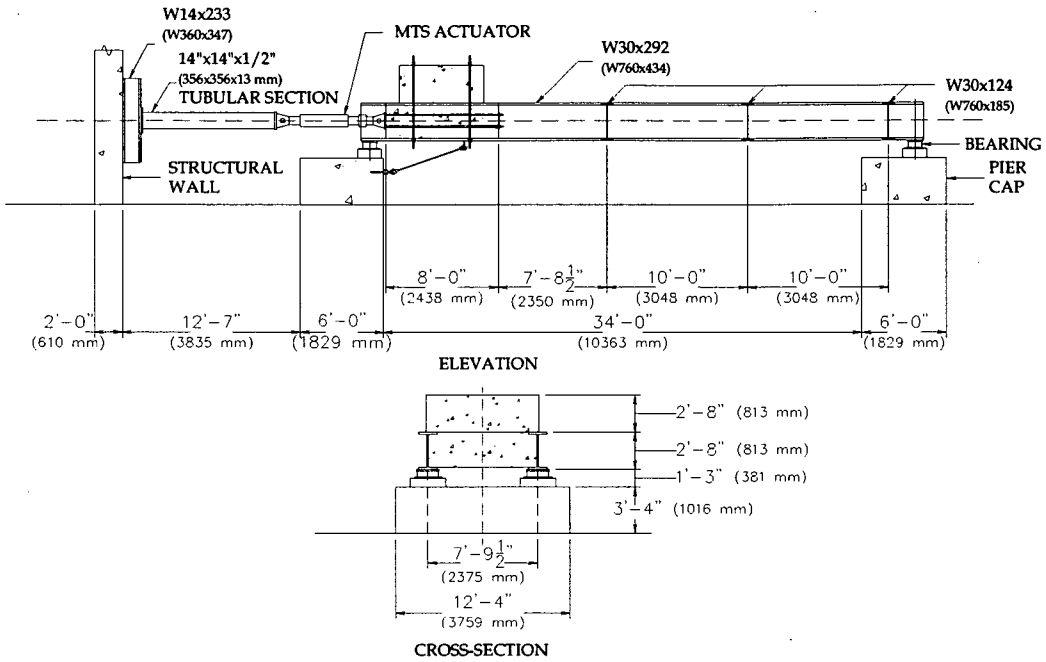

Figure 3. Full-scale bridge model used to test seismic cable restrainers.

The model bridge was loaded longitudinally using a hydraulic actuator in stroke control. The restrainer cables were tested using a monotonic loading with a load rate of 1"/min (25 mm/min). The bridge was instrumented with strain gauges, LVDTs, and a load cell. Twelve strain gauges were used on the bottom of the girder flanges near the restrainer cable connection. Since the girder flanges were very thick, the strain gauges did not record any significant strains in the steel girders. Three LVDTs were used to measure displacement in the bridge and a load cell in the actuator measured the force required to displace the bridge.

Description of Seismic Cable Restrainer Tests

The restrainer cable assemblies were connected from the steel girders to the concrete piers, as shown in Figure 4. The cables used were 5 ft long (1524 mm), ¾" (19 mm) diameter, 19 strand corrosion resistant wire rope with yield strength of 39.1 kips (173.9 kN) and an ultimate strength of 53 kips (235.8 kN). The ends of the cables were terminated using galvanized wire rope thimbles and four galvanized wire rope clips. At the pier, the restrainer cables were attached to the concrete using various steel connections that were secured with two undercut anchors. The restrainers were bolted to the bottom flange of the girders using steel bent plates and angles.

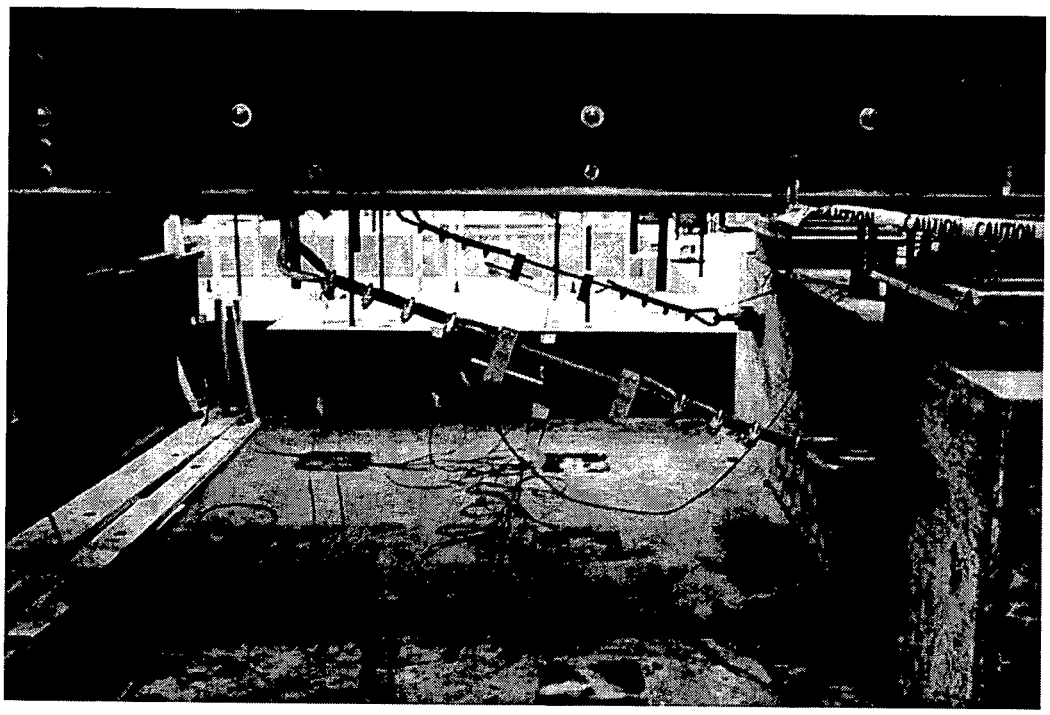

Figure 4. Side view of seismic cable restrainers attached to bridge model in experimental test setup.

Six restrainer cable assemblies were tested on the full-scale bridge model. The first test consisted of a restrainer cable retrofit currently used in the field as specified by the Tennessee Department of Transportation (TDOT). The remaining five tests were modifications of the current TDOT practice and aim at improving the performance of the original restrainer cable assembly. All of the modifications to the restrainer cable assemblies were changes in the connection elements at the girders and piers. Table 1 describes the differences between the connections used in the six tests.

Table 1. Test matrix describing differences between the cable restrainer tests.

Test	Pier Connection	Girder Connection
Current DOT Practice	½" (13 mm) bent plate with 1"(25 mm) ϕ U-bolt	½" (13 mm) bent plate connected with two 7/8" (22 mm) ϕ A325 bolts
Retrofit Modification 1	½" (13 mm) bent plate with 1" (25 mm) ϕ U-bolt	L8x4x½" (L203x102x12.7) steel angle connected with two 7/8" (22 mm) ϕ A325 bolts
Retrofit Modification 2	Two L6x6x½" (L152x152x12.7) steel angles back-to-back with 1½" (38 mm) ϕ threaded stud	L8x8x1" (L203x203x25.4) steel angle connected with two 7/8" (22 mm) ϕ A325 bolts
Retrofit Modification 3	Two L6x6x½" (152x152x12.7) steel angles back-to-back with 1½" (38 mm) ϕ threaded stud	L6x6x½" (L152x152x12.7) steel angle stiffened with ½" (13 mm) plates and connected with one 1-3/8" (35 mm) ϕ A325 bolts
Retrofit Modification 4	½" (13 mm) bent plate with 1" (25 mm) ϕ U-bolt topped with two L6x6x½" (L152x152x12.7) steel angles back-to-back with 1½" (38 mm) ϕ threaded stud	L8x8x1" (L203x203x25.4) steel angle connected with two 7/8" (22 mm) ϕ A325 bolts
Retrofit Modification 5	Two L6x6x½" (152x152x12.7) steel angles back-to-back with 1½" (38 mm) ϕ threaded stud	L7x4x¾" (L178x102x19) steel angle oriented longitudinally and connected with four 7/8" (22 mm) ϕ A325 bolts

Results of Original TDOT Practice

The bent plate connections at the girders failed in a brittle manner with a capacity of only 4 kips (17.8 kN). The girder connections performed poorly and only resisted a 1" (25 mm) displacement of the bridge before failure occurred. The plates used in these connections were cold bent to an angle of 90° which introduced large stress concentrations and possible cracks in the steel. The restrainer cable attaches to the bent plate at a large eccentricity from the bottom of the girder flange, as shown in Figure 5. This eccentricity introduces large moments which act on the weakest part of the bent plate. Figure 6 shows the crack in the connection plate near the bend after a small amount of displacement. The crack that formed in the bent plate was brittle and located within the section of the plate that was reduced by bending.

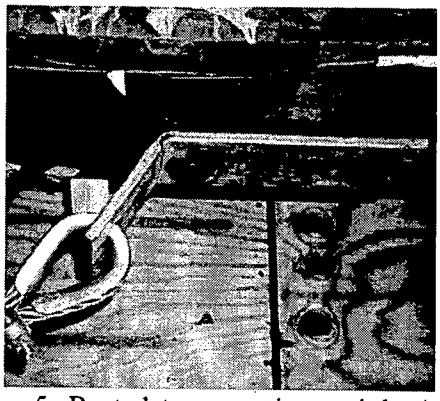

Figure 5. Bent plate connection at girder (side view).

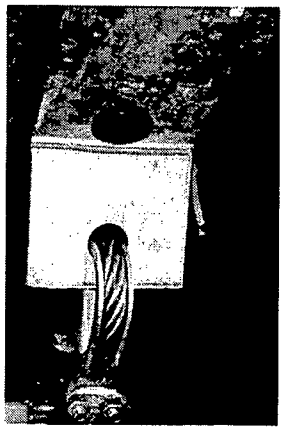

Figure 6. Bent plate connection at girder with brittle failure.

Results of Retrofit Modification 1

An L8x4x½" (L203x102x12.7) angle was used to replace the bent plate connection at the girders. The pier connection remained the same as the bent plate connection used in the original assembly. The angle connection performed in a ductile manner; however, the bent plate connection at the pier failed at a capacity of 18 kips (80 kN). The pier connection cracked in two different locations at the bends in the plate, as shown in Figure 7. The connection failed in a brittle manner and did not show any premature signs of weakness during the testing. Figure 8 shows the ductile deformation of the steel angles used in the girder connections.

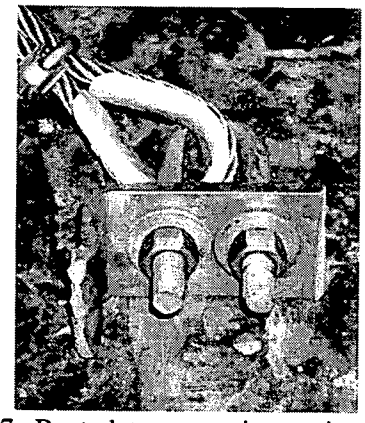

Figure 7. Bent plate connection at pier with brittle failure.

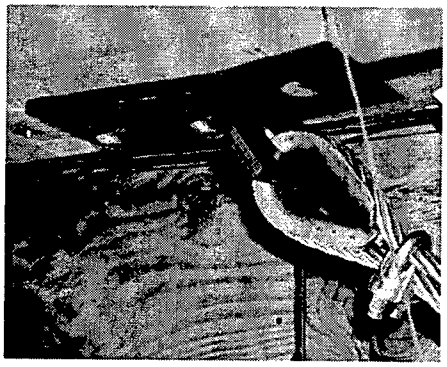

Figure 8. Angle connection at girder (side view).

Retrofit Modification 2

An L8x8x1" (L203x203x25.4) angle was used at the girder connection along with two L6x6x½" angles connected back-to-back with a 1½" (38 mm) diameter A193 B7 threaded stud at the piers (Figure 9). The larger angle at the girders was used to provide higher strength and stiffness at the connection. The restrainer assembly had a higher capacity of 46 kips (204.6 kN) before the angle failed. The restrainer cables reached their yield strength with this assembly; however, the displacement before failure was close to 8" (203 mm). Cracks in the k-zone of the angle formed during the test, as shown in Figure 10.

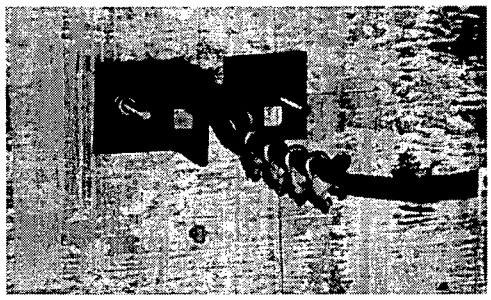

Figure 9. Back-to-back angle connection at pier.

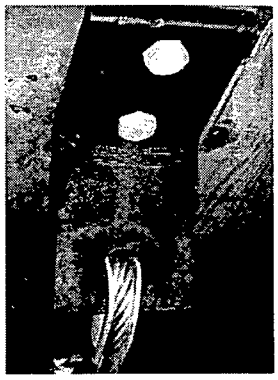

Figure 10. Cracks forming in k-zone of angle girder connection.

Retrofit Modification 3

An L6x6x½" (L152x152x127) stiffened angle was used for the girder connections, as shown in Figure 11. The girder connection was stiffened to increase strength in the connection and limit the large deformations that occurred in the previous modifications. The stiffened angle connections performed well with a capacity of 47 kips (209 kN) with less than 5" (127 mm) of displacement of the bridge deck. The restrainer assembly failed when an anchor broke due to repeated prying of the pier connection (Figure 12).

Figure 11. Stiffened angle connection used at the piers.

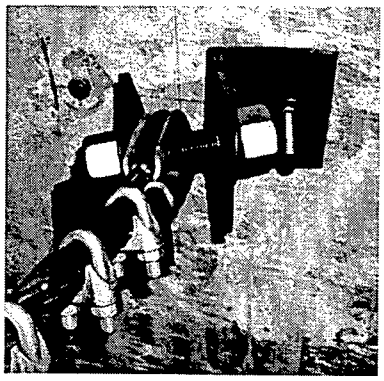

Figure 12. Anchor failed after repeated prying from the previous tests.

Retrofit Modification 4

This retrofit modification used a modified connection on top of the original connection at the pier, as shown in Figure 13. This type of connection was used because it provides easy installation over the existing connection. The pier connection performed well with little deformation before the angle connection at the girder formed a brittle crack (Figure 14). The capacity of the restrainer assembly was 45 kips (200.2 kN), but the bridge displaced over 9" (229 mm) before failure.

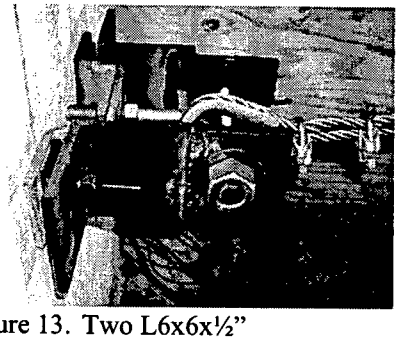

Figure 13. Two L6x6x½" (L152x152x12.7) back-to-back angles sit on top of the original ½" bent plate connection.

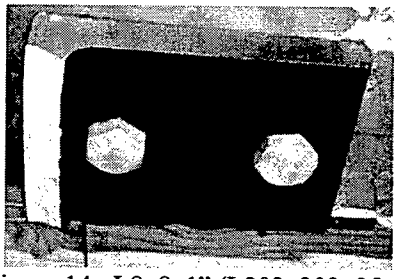

Figure 14. L8x8x1" (L203x203x25.4) angle failed in a brittle manner at the k zone.

Retrofit Modification 5

In this modification, the girder connection was replaced with an L7x4x¾" (L178x102x19) steel angle oriented longitudinally on the girder flange similar to cable restrainer connections used in New York, as shown in Figure 15. This connection eliminates the bending of the outstanding angle leg found in the previous connections. The angle

connection at the girder performed well with little deformation before a clip on the restrainer cable failed at the pier connection (Figure 16). The restrainer assembly had a capacity of 42 kips (186.8 kN) with less than 5" (127 mm) of displacement before failure occurred.

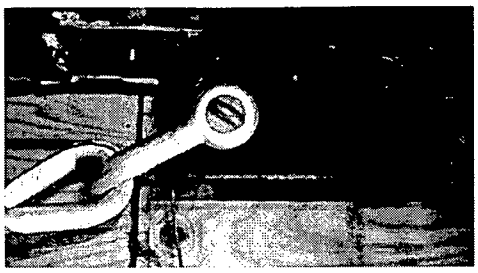

Figure 15. L7x4x¾" (L178x102x19) angle with a 1¼" (32 mm) shackle oriented longitudinally

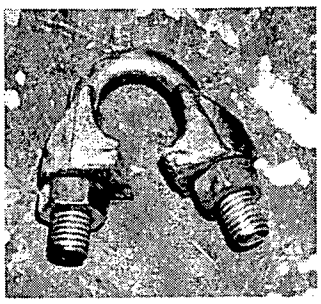

Figure 16. Cable clip at the pier connection failed by splitting and falling off near the thimble.

Summary of Results

The load-displacement behavior of the bridge with each cable restrainer is shown in Figure 17. The cable restrainer assembly currently used by TDOT failed at a load of 4 kips (17.8 kN) – less than 10% of the yield strength of the cable. Failure occurred in the bent plate connection at the girder because the plates were cold bent to 90°. The bent plate connections were replaced with steel angle connections that resulted in much higher capacity compared to the bent plates. Four of the six retrofit modifications failed at loads greater than the yield capacity of the restrainers. However, several of the retrofit modifications had large deformations before failure. To limit the large deformations in the bridge, a stiffened angle girder connection was used in retrofit modification 3. This cable restrainer assembly had approximately half of the deformation of an unstiffened assembly. Retrofit modification 5 used a steel angle oriented longitudinally on the girder flange similar to cable restrainer connections used by the New York Department of Transportation. This assembly also behaved much better than the currently used connections, in terms of stiffness and deformation.

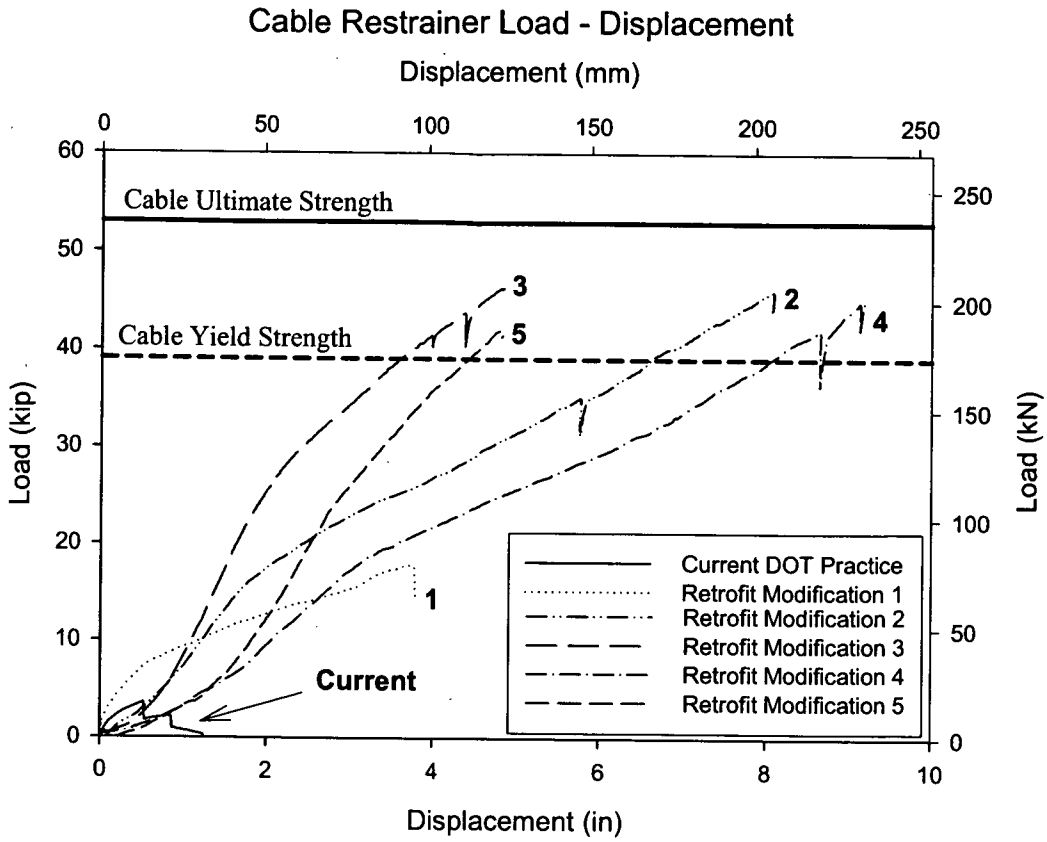

Figure 17. Load-displacement behavior of the seven cable restrainer tests.

Conclusions

In this study, a restrainer cable retrofit typically used in the Central and Southeastern US was tested in full-scale. The results show that the restrainer connections failed in a brittle manner at a load of less than 10% of the yield strength of the cable. Modifications to existing connections are proposed and tested. The existing bent plate connections were replaced with steel angle connections. The results show that the modifications have much higher strength and stiffness than currently used connections. The steel angles behaved in a more ductile manner and the stiffened angle connections had the best performance. Several states in the CSUS are initiating retrofit programs which consist of using cable restrainers, including, Tennessee, Illinois, Missouri, and South Carolina. The results of this study will be important as state DOT's implement their retrofit strategies throughout the CSUS. These results are expected to lead to a new class of connection elements used in the restrainer cable retrofit in multi-span simply supported bridges.

Acknowledgments

This work was supported primarily by the Earthquake Engineering Research Centers Program of the National Science Foundation under Award Number EEC-9701785 (Mid-

America Earthquake Center). The authors would like to thank Houston Walker and Ed Wasserman from the Tennessee DOT for their valuable comments and support throughout this project.

References

Buckle, I. G. and Cooper, J. D. (1995). "Mitigation of Seismic Damage to Lifelines: Highways and Railroads", Schiff, A. J., and Buckle, I. G., eds., *Critical Issues and State-of-the-Art in Lifeline Earthquake Engineering*, ASCE, TCLEE Monograph No. 7, 70-87.

FEMA-222A (1995). NEHRP Recommend Provisions for Seismic Regulations for New Buildings Part 1– Provisions, Report No. FEMA-302, Federal Emergency Management Agency, Washington, D.C.

Lin, T., Gamble, W. L., and Hawkins, N. M., "Seismic Behavior of Bridge Column Non-Contact Lap Splices", SRS No. 622, Department o Civil & Environmental Engineering, University of Illinois at Urbana, Champaign, June 1998.

Mander, J. B., Kim, D. K., Chen, S. S., and Premus, G. J. (1996). "Response of Steel Bridge Bearings to the Reversed Cyclic Loading", *Technical Report NCEER 96-0014*, Buffalo, NY.

Saiidi, M.; Maragakis, E.; Feng, S. (1996). "Parameters in Bridge Restrainer Design for Seismic Retrofit", *Journal of Structural Engineering*, ASCE, 122 (1), 61-68.

Selna, L. G.; Malvar, L. J.; Zelinski, R. J. (1989). Bridge Retrofit Testing: Hinge Cable Restrainers, *Journal of Structural Engineering*, ASCE, 115 (4), 920-934.

U.S. Geological Survey (1912). "The New Madrid Earthquake," by Myron L.F., Bull. 494

U.S. Geological Survey (1996). "Earthquake Hazards Program – National Seismic Hazard Mapping Project," http://geohazards.cr.usgs.gov/eq/html/ceusmap.html.

Wiegel, R. L. (1970). "Earthquake Engineering." Prentice-Hall, Inc., Englewood Cliffs, NJ.

Vlassis, A. G.; Maragakis, E. M; Saiidi, M. S. (2000). Experimental Evaluation of Seismic Performance of Bridge Restrainers", *Multidisciplinary Center for Earthquake Engineering Research*, Technical Report MCEER-00-0012.

SESSION 7: MAINTENANCE 2

(1) Structural Health Monitoring in Civil Infrastructures and R & D of SHM of Bridges at the University of Tokyo

(Yozo Fujino and Masato Abe)

(2) Evaluation of P-T Tendons Based on Magnetic Flux Leakage and Impact-Echo Techniques

(Al Ghorbanpoor)

(3) Experimental Study on the Measuring Method of Steel Girder Stress by Magnetostrictive Method

(Ichiro Masuda, Ryosuke Murai, Sinji Nakaya and Seiichi Abuku)

(4) A Concept toward Durable Bridge Design by Use of Weathering Steel

(Hiroshi Kihira)

(5) Long-Term Remote Monitoring System for Steel Bridges by Applying Fiber-optic Communication Network

(Yuusuke Kobayashi and Chitoshi Miki)

Structural Health Monitoring in Civil Infrastructures and R& D of SHM of Bridges at the University of Tokyo

Yozo FUJINO[1] and Masato ABE[2]

ABSTRACT

This paper firstly presents an overview of civil infrastructures and their problems in Japan, and discusses characteristic features of structural health monitoring for civil infrastructures. The focus of the discussion is placed on bridges in the transportation system. In the second place, research and development of health monitoring systems at the Bridge and Structure Laboratory of the University of Tokyo is presented. Ambient vibration based approaches for Laser Doppler Vibrometer(LDV) and long-span suspension bridges show possible wide applications in this field. In both cases, although the excitation is unknown, densely distributed and accurate measurement is shown to provide valuable information on the status of structures. Especially, a LDV based approach can provide information on damage and loading to the structure with practically applicable system configuration. A smart material system with embedded piezoelectric materials shows high potential to monitor structural status.

INTRODUCTION

Civil infrastructures include various units and systems such as buildings, transportation systems, communication systems, power generation and distribution systems, and water supply/drainage systems. Significant investment expenditures and long time periods are necessary for a society to build up its infrastructure systems; indeed, any advanced society has already put enormous effort toward this goal. The continued performance of these infrastructure units and systems is vital to our human and economic activities. Even a short-term malfunction affects the society tremendously.

The built environment supported by infrastructures is an asset if they are well maintained and properly operated. However, if they are degraded by improper maintenance, they can be, sooner or later, a big debt to the society. To prevent this, it is absolutely necessary to develop maintenance technology that involves inspection, monitoring, repair, rebuilding and even financial planning. Structural health monitoring is one of the important components in the maintenance technology for civil infrastructures.

This paper primarily presents an overview of civil infrastructures and their problems in Japan, and discusses characteristic features of structural health monitoring for civil infrastructures. The focus is placed on bridges in the transportation system. Additionally, recent research related to structural health monitoring conducted at Bridge & Structure Laboratory, Department of Civil Engineering, University of Tokyo (to which the authors belong) is described.

1 Professor, Dept. of Civil Engineering, University of Tokyo, Tokyo, 113-8656 Japan fujino@bridge.t.u-tokyo.ac.jp

2 Associate Professor, Dept. of Civil Engineering, University of Tokyo, Tokyo, 113-8656 Japan masato@bridge.t.u-tokyo.ac.jp

INFRASTRUCTURE DEVELOPMENTS IN JAPAN

In Japan, construction of modern infrastructures started in Meiji Era (~1868). Investment in railway development was considered a high priority in those days. The present railway network was practically established in 1940's.

Construction of roads was rather slow before the 1940's. Rapid growth of the Japanese economy started in the 1960's and intensive investment in road construction followed to meet expansion of industrial activities.

The first bullet train railway line and the first highway were started in the middle of 1960's. Construction of the bullet railway network has not yet been finished, but the total length of the railway system is saturated and even decreasing somewhat; consequently, new construction of railway bridges is rare. Many railway infrastructures are rather old and need elaborate maintenance.

Development of the highway network system is still actively on-going at present. However, the amount of new road bridge construction has also been decreasing in recent years. Road bridges constructed in the 1970's will be more than 50 years old in 20 years. Further, the number of the aged bridges is will constitute half of all road bridges by the year 2020. A similar situation can be also observed in buildings in Japan.

Although Japan is considered to be active in new construction of infrastructures, maintenance is becoming increasingly important.

PROBLEMS OF EXISTING STRUCTURES

Infrastructures constructed in the rapid growth period (1960 to 1980) are enormous, but they are not considered to be of the highest quality because of the construction boom during that time. In concrete structures, for example, sand taken from the sea was often used without adequate washing, so chemical degradation is rapidly progressing in such concrete structures. It is reported that tendons in many pre-stressed concrete bridges are rusted because water leaked into the tendon tubes due to incomplete grouting.

In 2000, a number of un-reinforced concrete blocks fell from tunnel linings for a bullet train railway that were constructed around 1970. Fortunately, the concrete blocks did not hit any train cars. After these incidents, the concrete linings in old railway tunnels, as well as road tunnels, were extensively investigated by the "hitting-by-hammer" method. Thousands of potentially dangerous cracks were indeed found in the lining of many tunnels.

In an elevated viaduct of the Tokyo Metropolitan Expressway, a relatively new traffic sign pole fell down and hit a motorcar beneath the bridge. The cause of this accident was improper welding.

These accidents clearly highlight the importance of inspection and maintenance of civil infrastructures. Inspection rules for railway and roads were revised after these accidents; more frequent and detailed inspection was specified. The public had tended to think that civil structures are permanent maintenance-free fixtures, but has now realized that this is not the case.

Regarding the road bridges, the traffic volume in major highways is as large as 15,000 vehicles per lane and the ratio of heavy trucks in the traffic is also high (as high as 30%). On some of the bullet train routes, trains run quite frequently. The high intensity and high frequency loading generated by this high traffic volume creates many problems in bridges: the most typical problem is fatigue damage in concrete slabs and steel welded girders.

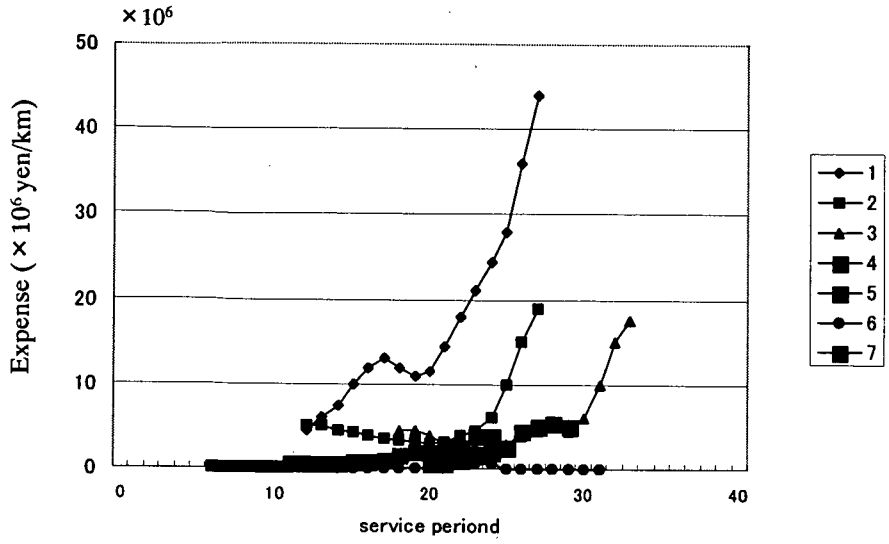

Figure 1. Expenditure for maintenance and repair in high way bridges (routes 1 to 7)

Fig. 1 shows the cost of maintenance of the highway as a function of the service period. It shows that the maintenance and repair cost increases sharply when the service period exceeds 15 to 20 years. The average age of bridges in Japan will soon become 40 or even 50 years soon, so the necessity of frequent and detailed inspection and maintenance/repair is also expected to increase significantly in the near future. However, because of the tight budget in Japan, expenditures for maintenance-related activities are not expected to increase in proportion to the need. Consequently, more efficient and economical inspection and maintenance strategies are required.

CHARACTERISTIC FEATURES IN MONITORING AND INSPECTION OF CIVIL INFRASTRUCTURES

Inspecting, monitoring and maintenance are systematic in the field of aircrafts, ships and so forth. Those for civil infrastructures are different from these other in many ways;

1) Infrastructures are in general very much distributed and spatial, and areas to be inspected are quite huge.
2) Inspection must be made onsite, where the site conditions are often inconvenient, dangerous or somewhat hostile. For example, investigation of concrete lining in tunnels is a very tiring work. Especially in the case of road tunnels, inspection must be conducted while traffic is in service. Inspection of fatigue cracks inside box girders is also rather unpleasant.
3) Some of the components to be inspected are difficult or even dangerous to access. Elevated bridges require inspection work at a high elevation and complete inspection needs expensive temporary walkway. Soil slopes need to be monitored, especially during heavy rainfall, but they are inaccessible at those times monitoring is most needed.
4) Components to be inspected are often embedded within the structure or otherwise not immediately visible. Typical examples are re-bars and pre-stressed tendons inside concrete and underground utility lines.
5) Infrastructure is not made by mass production: each infrastructure is different from the others and is exposed to different environment.

So far, inspection of civil infrastructures is basically made by human beings. It is extremely labor-intensive. Inspectors are often exposed to dangerous conditions and/or uncomfortable working environments. Considering that the volume of inspection work will be significantly increased in the near future, inspection by human beings must be replaced with automated instruments and inspection efficiency and accuracy must be improved.

Inspection of civil infrastructures is considered by some to be an old fashioned, low-tech and unpleasant subject. Recent development of sensors and information technology, however, may completely modernize the content of the work and may increase the efficiency of the work dramatically. For example, the human-based "hit-by-hammer" method to find cracks in the dust-covered lining of tunnels has been considered the only reliable method. Recently, a method using the infrared rays and an image analysis method using digital video camera were being developed; these methods can reduce the labor and the time considerably.

Many civil infrastructures are spatially distributed and the area and points to be inspected/monitored is huge. Certainly, sensors that measure spatial information rather than a point are to be developed. Accuracy of the sensors is important, but often simplicity, durability and robustness are more important than accuracy since they are exposed to severe and hostile environments.

To detect damage from the sensor signal is also another important subject. The signals from the sensors in civil infrastructures are in many cases contaminated by ambient noise due to traffic and other environmental effects. To efficiently remove noise from ambient signals and to obtain useful information requires not only data processing techniques, but also knowledge of traditional disciplines of civil engineering such as mechanics, dynamics, soil mechanics, material technology and so forth.

Structural Health Monitoring (SHM) for civil infrastructures is an extremely important research area to keep our advanced society functional and requires a balanced combination of new sensor/computer technology and civil engineering technology. In this sense, SHM attracts young promising engineers and researchers.

The Bridge and Structure Laboratory at the University of Tokyo has made recent attempts to contribute to the development and establishment of SHM. Some research activities at the Laboratory related to SHM are given hereafter.

LASER DOPPLER VIBROMETRY USING AMBIENT VIBRATION

Development of reliable health monitoring and inspection technology is essential to maintain existing civil infrastructures. Monitoring of civil structures has several difficulties in addition to those that arises in structural health monitoring of other structures due to (1) their scale; and (2) ambient environmental effects [1]. The scale makes measurement of the entire structure extremely difficult and costly, which inherently requires dangerous labor work at considerable height, and reduces quality and density of measurement. Ambient environmental effects induced by various causes such as traffic, wind, temperatures, etc., are difficult to estimate or measure reliably, which makes identification of structural parameters extremely difficult. Because of these difficulties, current inspection works of civil structures tends to be labor extensive, and rely on subjective judgment of experienced specialists. Figure 8 shows the example of typical inspection procedure of tunnel linings using hammer echo. The sound excited by hammer impact is subjectively judged by skilled experts to evaluate damage or defects in concrete.

Figure 2. Hammer echo inspection at a highway tunnel.

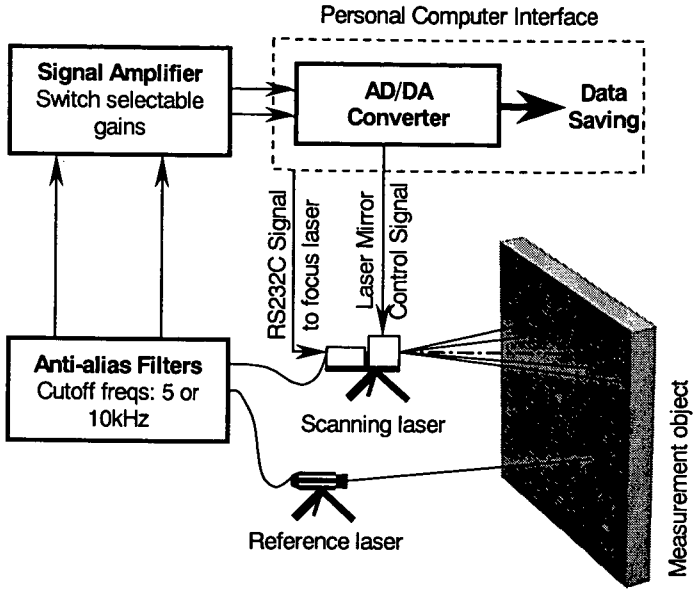

Figure 3. Data Acquisition System and the LDV

In order to rationalize and automate the subjective judgment method and eliminate the dangerous inspection works in tunnels or bridges, applicability of remote measurement by Laser Doppler Vibrometer (LDV) has been studied extensively at the University of Tokyo.

The Laser Doppler Vibrometer basically uses the Doppler principle to measure velocity at a point where its coherent laser beam is directed to. The reflected laser light is compared with the incident light in an interferometer to give the Doppler-shifted wavelength. This shifted wavelength provides information of surface velocity in the direction of the incident laser beam. For the LDV used in this experiment, two deflecting mirrors are provided to enable the light beam to be directed at any desired point. Providing non-contact measurement, the LDV is capable to detect a velocity of magnitude of 0.5μm/s at a distance of maximum 30m. Detailed characteristics of the LDV can be found in [2].

There are two laser sources to be used to measure the structural vibration response in this research. One is to measure a fixed point on the measured surface to provide global information, *i.e.,* to synchronize other measurements; the other is directed by the two deflecting mirrors to measure the response spatially. The first one will be called the *reference laser* and the second the *scanning laser* hereafter. A mesh of measured points should be defined first and then, under control of a computer, vibration responses of these pre-defined points will be measured point by point.

The data acquisition system is illustrated in Figure 3, in which a personal computer acts as a central processing unit, receiving measured response signals and sending control signals to rotate the deflecting mirrors and to focus the scanning laser at different distances while the laser beam is scanning over the object surface. The measurement process is automatic, and requires the least command from an operator.

Most modal of modal identification methods for ambient vibration use a spectral analysis technique developed by Crawford and Ward [3]. In this technique, a structural motion is measured by a series of sensors. The structure's natural frequencies are estimated from peaks in the power-spectral density function of the measurement records, while the modal damping ratios are estimated using the half-power bandwidth method. The cross-power spectra between a designated reference measurement and other measurements will contain information of the structure's mode shapes. Although the drawbacks of this technique have been detailed in [3] and [4], it is still widely used in ambient vibration because of its simplicity. Recent development in ambient vibration is applications of Eigensystem Realization Algorithm (ERA) [5] [6], Auto Regressive Moving Average Vector (ARMAV) [7], Autoregressive Modeling (AR) [8], covariance matrix [9], and Eigenspace Algorithm [10]. These

techniques are either applied for simultaneous data, (*i.e,*. data acquired at all points at the same time) or not suitable for a personal computer due to its intensive computation. For modal parameter identification using the LDV, there are limited numbers of response measurements that can be recorded at the same time because of the availability of laser sources. Among the aforementioned techniques, the ERA is the most general multi-input-multi-output (MIMO) technique that can be developed and applied to the LDV measurement if a data synchronization technique can be formulated.

Introduced in this paper is the modal analysis identification technique using the ERA that is developed for the LDV in ambient vibration measurement. A mathematical model is presented in the first part and an experiment of a steel plate was carried out in a laboratory environment to verify the mathematical model. The steel plate was tested under ambient excitation that might result from ground waves caused by traffic on a nearby street. Identification of the plate's modal parameters is successful by the ERA. A mass was then attached to the plate to verify a change in its modal parameters as a result of the change in its mass property. This finding will provide background for a structural health monitoring program using the LDV to measure ambient vibration and to use identified modal parameters to monitor the performance of a structure.

A Brief Review on ERA

A viscously damped system with N DOF can be modeled in the following equation:

$$[M]\{\ddot{x}(t)\}+[C]\{\dot{x}(t)\}+[K]\{x(t)\}=[F]\{u(t)\} \tag{1}$$

where $[M]$, $[C]$, $[K]$ are the $N \times N$ mass matrix, damping matrix, and stiffness matrix, respectively; $\{\ddot{x}(t)\}$, $\{\dot{x}(t)\}$, $\{x(t)\}$ are the $N \times 1$ acceleration vector, velocity vector, and displacement vector, respectively; $[F]$ is a matrix of input coefficients and $\{u(t)\}$ is the input vector at q locations.

The above system is equivalent to the continuous state-space model:

$$\begin{aligned}\{\dot{y}(t)\}&=[A']\{y(t)\}+[B']\{u(t)\}\\ \{x(t)\}&=[R]\{y(t)\}\end{aligned} \tag{2}$$

where $\{y(t)\}=\begin{Bmatrix}\{x(t)\}\\ \{\dot{x}(t)\}\end{Bmatrix}$, $[A']=\begin{bmatrix}[0] & [I]\\ -[M]^{-1}[K] & -[M]^{-1}[C]\end{bmatrix}$ and $[B']=\begin{bmatrix}[0]\\ [M]^{-1}[F]\end{bmatrix}$

By considering $\{x(t)\}$ as the impulse responses at p measured locations and arranging them into the generalized Hankel matrix, Juang and Pappa [5] have shown that the state transition matrix $[A]=e^{[A']\Delta t}$ can be "realized". By eigenvalue decomposition of matrix $[A]$, modal parameters of the system can be extracted. Full details of this method can be found in [11] or [12].

The above procedure is called the Eigensystem Realization Algorithm (ERA). The algorithm requires the synchronous impulse response measurements at p locations. What follows are a technique to synthesize the impulse responses from ambient vibration measurement and to synchronize those responses from asynchronous measurement using the LDVs.

Impulse Response Synthesis from Ambient Vibration Measurement

Farrar and James [3] has pointed out that if the unknown excitation is a white-noise random process, the cross-correlation function between two response measurements will have the same form as the impulse response of the structure.

Detailed formulation of these two parameters can be found in [3]. If all p locations are measured at the same time, the factor that represents the phase and magnitude difference can be cancelled out in the ERA. However, measurement by the LDV does not possess this characteristic. It, therefore, requires a synchronization process before inputting these free responses to the ERA.

Furthermore, to minimize the effect of noise in the laser measurements, many finite time history measurements will be performed (at every point) and then the cross-correlation function described above is averaged out in the frequency domain (cross-spectrum). The averaged cross-correlation function will then be recovered by the Inverse Fourier Transform of its corresponding averaged spectrum. As a matter of fact,

the finite time history does not guarantee the energy flowing into the system to be the same during each period of measurement.

Denoting $x_{R0}(t_0)$ the base reference laser measurement, $x_{S0}(t_0)$ the simultaneous scanning laser measurement at a specific scanning point. Again denoting $x_{Ri}(t_j)$ the reference laser measurement while the scanning laser at point i starting time t_j, $x_{Si}(t_j)$ the scanning laser at point i starting time t_j.

Let a hypothetical frequency response function $H_{x_{R0}x_{Rij}}(f)$ be defined, as in Bendat and Piersol [1], by:

$$H_{x_{R0}x_{Rij}}(f) = \frac{F[x_{Ri}(t_j)]}{F[x_{R0}(t_0)]} \tag{3}$$

where $F[\bullet]$ denotes finite Fourier Transform of $(\bullet)$

If the excitation is a stationary and ergodic process, this relation will also be applied for the scanning laser measurement, *i.e.,*

$$H_{x_{S0}x_{Sij}}(f) = H_{x_{R0}x_{Rij}}(f) = \frac{F[x_{Si}(t_j)]}{F[x_{S0}(t_0)]} \tag{4}$$

For simplicity, the parameter t is dropped. Combining equations (4) and (5) and multiplying it by the complex conjugate of equation (4), the following relationship can be obtained:

$$\frac{F^*[x_{Rij}]}{F^*[x_{R0}]}\frac{F[x_{Rij}]}{F[x_{R0}]} = \frac{F^*[x_{Rij}]}{F^*[x_{R0}]}\frac{F[x_{Sij}]}{F[x_{S0}]} \tag{5}$$

Arranging the above equation leads to:

$$F^*[x_{Rij}]F[x_{Sij}] = \frac{F^*[x_{Rij}]}{F^*[x_{R0}]}\frac{F[x_{Rij}]}{F[x_{R0}]}F^*[x_{R0}]F[x_{S0}] \tag{6}$$

The *cross-spectrum* and *auto-spectrum* between two records are defined by Bendat and Piersol [1] as:

$$\begin{aligned} G_{xy}(f) &= F^*(x)F(y) \\ P_x(f) &= F^*(x)F(x) \end{aligned} \tag{7}$$

Therefore, equation (6) can simply be written as:

$$G_{x_{Rij}x_{Sij}} = \frac{P_{x_{Rij}}}{P_{x_{R0}}}G_{x_{R0}x_{S0}} \tag{8}$$

The meaning of equation (8) is that the cross-spectrum of the subsequent measurements will differ from the base measurement by a factor of $\frac{P_{x_{Rij}}}{P_{x_{R0}}}$. Therefore, for a noise reduction scheme by averaging in the frequency domain, any cross-spectrum that is not the base spectrum should be divided by this factor to convert it to the base spectrum. It can be seen that this factor is calculated by the auto-spectrum only; it hence does not eliminate the effect of correlated noise at the reference laser measurement. It is, therefore, necessary to set up the reference laser measurement that will have the largest signal-to-noise ratio. More details of the technique can be found in [13].

By inverse Fourier Transform of the averaged cross-spectrum, the averaged cross-correlation function can be estimated and subsequently entered to the ERA. Details of this modal analysis identification process can be summarized in Figure 9. Since the averaging process is carried out in the frequency domain, windowing should be applied to minimize the effect of leakage. The Hanning window is chosen for this type of signal in the following examples.

Application Examples of LDV

The proposed measurement method has been applied to damage detection in concrete specimens, steel bolted joints, and measurement of vibration of existing bridge slabs under service traffic condition.

In damage detection of concrete structures, as shown in Figure 8, the hammer-echo inspection method is widely used. The principle of this method is to excite vibration on the surface of the structure and, then, to judge the soundness by listening to the sound excited by the surface vibration. Hence, precise and dense measurement of surface vibration by LDV has the potential to replace this work.

Figure 4. Determination of modal parameters from ambient vibration measurement

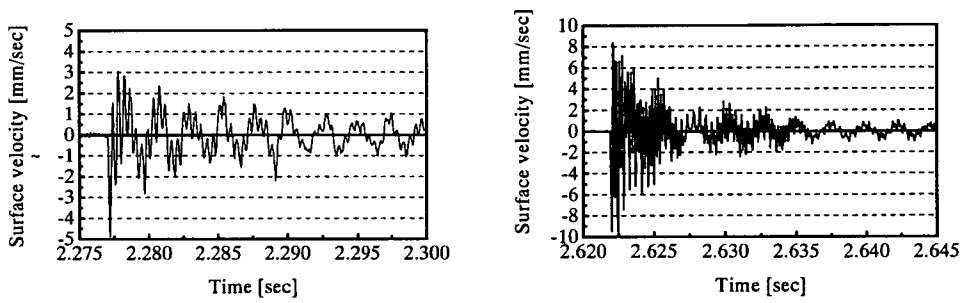

(a) Undamaged part. (b) Damaged part.

Figure 5. Comparison of LDV measurement at damaged/undamaged parts.

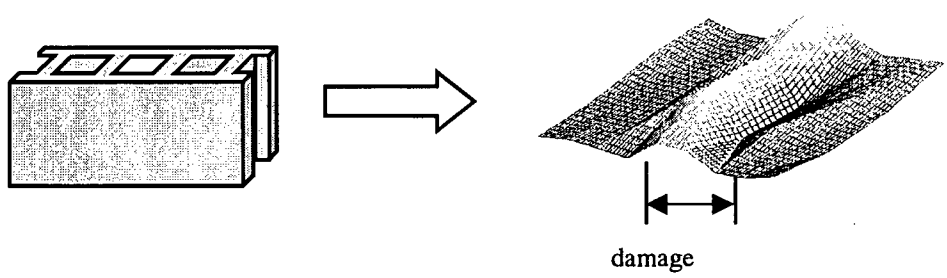

Figure 6. Comparison of LDV measurement at damaged/undamaged parts.

Figure 5 shows the measurement results by LDV on damaged and undamaged portions of concrete specimens by hammering. Damage is modeled by a void behind the concrete surface, which is shown in Figure 6. Vibration with higher frequencies is observed to be prominent at the damaged part.

Vibration modes of this concrete specimen are also identified using the proposed method. To simulate ambient vibration sources in actual measurement such as traffic noise, the specimen is excited by arbitrary sound generated by sound speaker. The right half figure of Figure 6 shows the identified mode shape at the high frequency component observed in Figure 5. Clearly, the vibration contains modal amplitude locally magnified at the place of damage. Therefore, damage in this concrete specimen can be identified by observing associated vibration modes [14].

Figure 7 shows a model for steel joint loaded by a weight. Measurement and control of torque in bolts is critical for the safety of the system especially when the joint is designed as friction connection. The vibration mode whose node is at the location of connection plate is of particular interest, because induced strain by that mode is the highest. Figure 8 shows the identified mode shape of that mode. No significant difference is observed for the magnitude of the mode shape by loosening the bolts, while phase in mode shape, or equivalently, imaginary part of the mode shape shows significant change. Figure 9 shows this relationship. The horizontal axis expresses the amount of the torque loosened and the vertical axis shows the summation of phase lag at the connection plate. Good correlation is observed. This phenomenon is most likely due to the infinitesimal sliding induced by vibration [15].

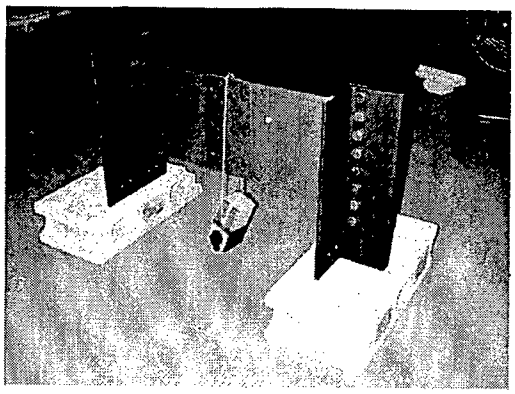

Figure 7. Steel joint model.

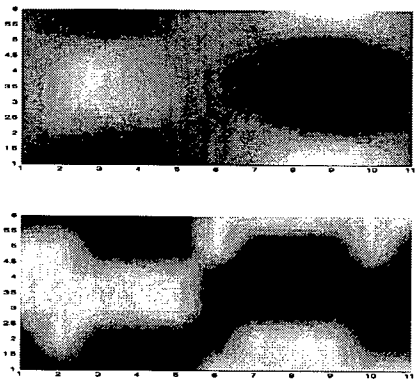

Figure 8. Identified mode shape (magnitude and phase).

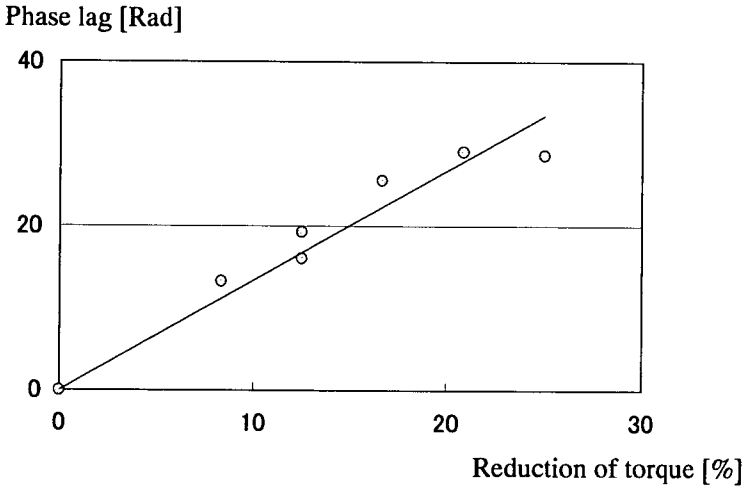

Figure 9. Phase lag in mode and loosened torque.

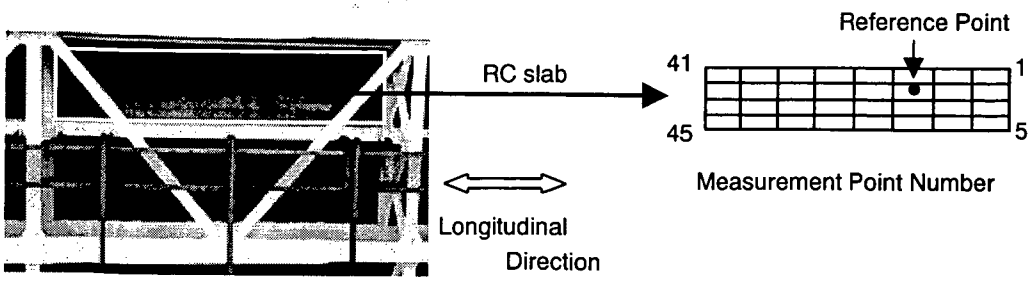

Figure 10. Objective concrete slab and measurement points

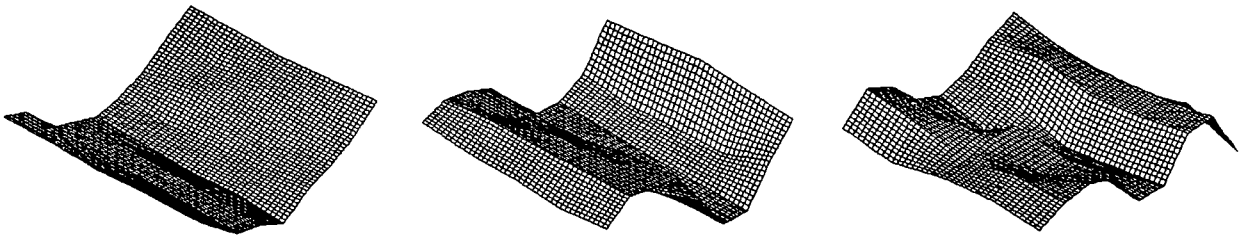

(a) 1st mode (43.2Hz) (b) 2nd mode (97.3Hz) (c) 3rd mode (187Hz)

Figure 11. Identified mode shapes for the slab panel

The proposed system has been applied to field measurement of a bridge. Figure 16 shows the objective structure that is the slab of an elevated highway bridge. A panel of the slab is measured by the proposed system. Figure 17 shows the identified mode shape for the slab panel. Identified natural frequencies are found to be in agreement with the theoretical prediction, which verifies the validity of the proposed method [16].

Impact Force Identification by LDV

Accurate identification of forces in a structure subject to operational excitations is an important issue for design, control and health monitoring of the system.

Assuming modal expansion, orthogonality and proportional damping, the equation of motion of a system can be decomposed into a series of modal equations in frequency domain using matrix notation as

$$[A]\{X(\omega)\} = \{B(\omega)\} \tag{9}$$

$$[A] = \begin{bmatrix} j\omega\left[\hat{\Phi}\right] & \{0\} \\ [K] - \omega^2 I + \omega[C] & -[\Phi]^T\{\delta\} \end{bmatrix}_{(2+p)\times(p+1)} \tag{10}$$

$$\{X(\omega)\} = \left\{\{Q(\omega)\}^T \quad F(\omega)\right\}^T_{(p+1)\times 1} \tag{11}$$

$$\{B(\omega)\} = \left\{\{\dot{U}(\omega)\}^T \quad \{0\}\right\}^T_{(p+2)\times 1} \tag{12}$$

$$K = diag\left[\omega_1^2 \quad \omega_2^2 \quad \ldots \quad \omega_p^2\right] \tag{13}$$

$$C = diag\left[2\xi_1\omega_1 \quad 2\xi_2\omega_2 \quad \ldots \quad 2\xi_p\omega_p\right] \tag{14}$$

where Q, U and F denote Fourier transforms of modal amplitude, global displacement and impact force magnitude respectively. j denotes the imaginary unit and the superscript T refers to matrix transpose. ξ_i, and ω_i represent modal damping ratio and modal frequency of i-th mode, respectively. p denotes the number of lower modes used in modal expansion. $\hat{\Phi}$ is the mode shape matrix at the measuring points. δ denotes a location vector and can be defined as

$$\{\delta\} = \{0 \quad 0 \quad \ldots \quad 1 \quad \ldots \quad 0\}^T \tag{15}$$

That is, all the positions on the plate are set to be zero except the real location of the impact. It is important to note that the problem set as in equation (10) is over-determined and can be solved in the least-squares sense employing the pseudo-inverse technique, *i.e.*,

$$\{X(\omega)\} = [A]^+\{B(\omega)\} \tag{16}$$

$$[A]^+ \equiv \left([A]^T[A]\right)^{-1}[A]^T \tag{17}$$

This identification algorithm is implemented with the LDV measurement system and applied to the problem of impact force identification on a clamped-free steel plate. First, modal parameters are obtained at ambient sound excitation condition. Mode shapes of the identified modes are given in Figure 18. These experimentally obtained modal parameters are directly applied to the above algorithm to identify impact force. The comparisons between experimental and identified results are shown in Figures 19 and 20 [17]. Both time history and location of impact are successfully identified with high accuracy.

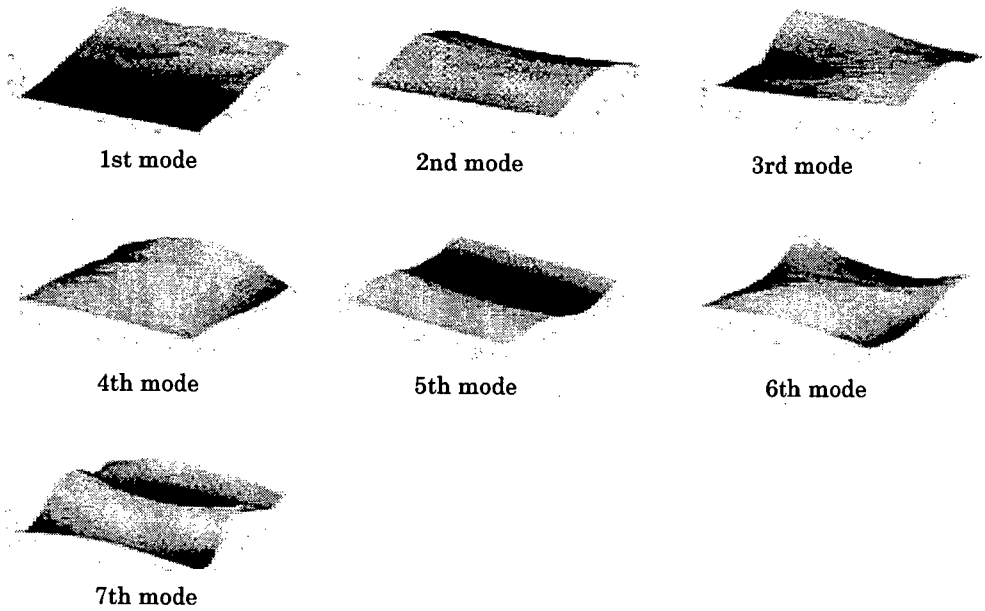

Figure 12. Identified mode shapes for the plate

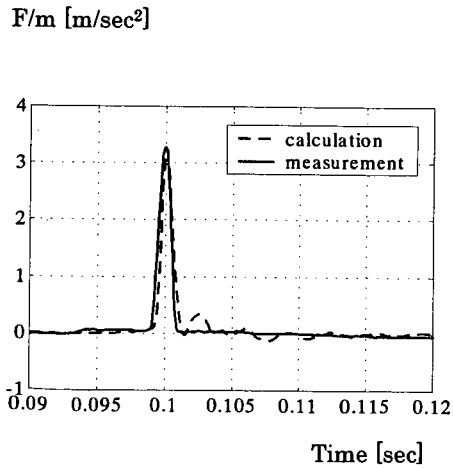

Figure 13. Identified force time history

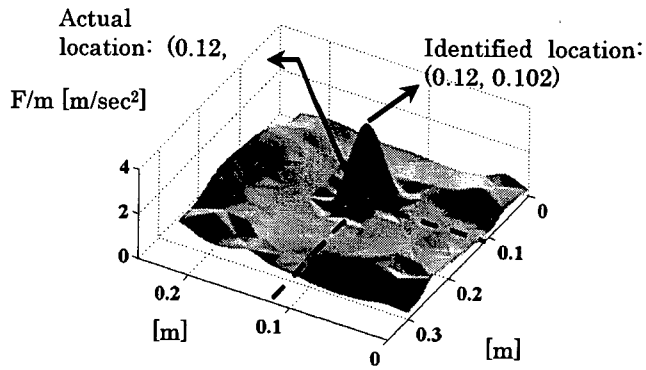

Figure 14. Identified force distribution

AMBIENT VIBRATION BASED MONITORING OF A LONG SPAN SUSPENSIO BRIDGE

The ambient vibration based monitoring technique developed for LDV has also been applied to monitoring the long-span suspension bridge shown in Figure 15. The bridge has been monitored by a densely-distributed ambient vibration measurement system with 19 measurement points. Details of the measurement installations can be found in [18].

In this case, because all 19 measurements are simultaneous, the synchronization method developed for LDV is not necessary, and random decrement method is employed to obtain impulse responses. By application of the ERA method, modal parameters up to 19 vibration modes are successfully identified. Especially, modal natural frequencies are found to be in good agreement with the results of the forced vibration test and finite element prediction.

Based these modal properties that are found to be amplitude dependent, aerodynamic stiffness and damping for various amplitude levels are obtained as can be seen Figure 16 and 17 [19]. The difference of mass normalized stiffness and damping from the values at amplitude of 0.55cm/sec^2 are presented. Because amplitude and wind velocity are in good correlation, aerodynamic damping predicted by the wind tunnel results are also presented. It can be seen that it is feasible to track changes in stiffness and damping using identification through ambient vibration measurements.

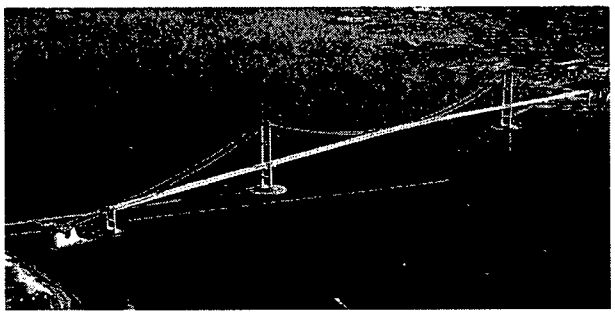

Figure 15. Hakucho Bridge

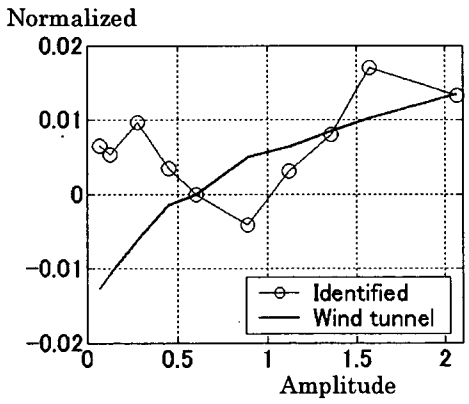

Figure 16. Identified aerodynamic stiffness

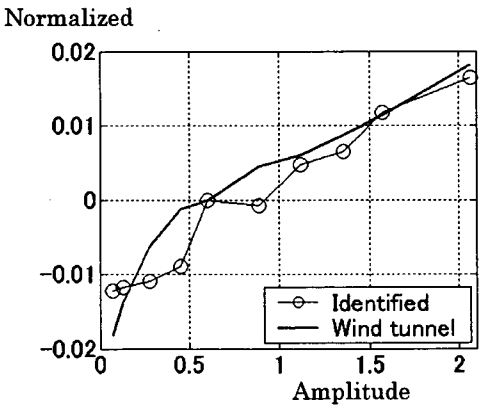

Figure 17. Identified aerodynamic damping

HEALTH MONITORING BY SMART MATERIAL SYSTEMS

A structural health monitoring technique, based on impedance measurement that utilizes smart material technology, is introduced in this section. The basic concept of this approach is to monitor the variations in structural mechanical impedance caused by the presence of changes in structural conditions using the electromechanical coupling property of embedded piezoelectric materials [20]. In this coupling property, the electrical impedance of piezoelectric materials is directly related to the mechanical impedance of the host structure, and will be affected by the presence of changes in structural state. The basic concept is presented in Figure 18 for single degree of freedom system analogy [21]. Figure 19 shows the experimental results using thin aluminum thin plates as host structures and Lead Zirconate Titanate piezoceramic wafers as embedded piezoelectric material. Due to the properties of dispersive flexural wave propagation in thin structural members, the measured impedance changes with stress. An electromechanically coupled piezoelectric film/host structure interactive model is developed and fundamental characteristics of electrical impedance and mechanical wave propagation are studied using spectral analysis, and identification procedure to identify stress is developed in [22]. These theoretical and experimental results also demonstrate the capability and the effectiveness of this smart structure technology to monitor the condition of structural integrity.

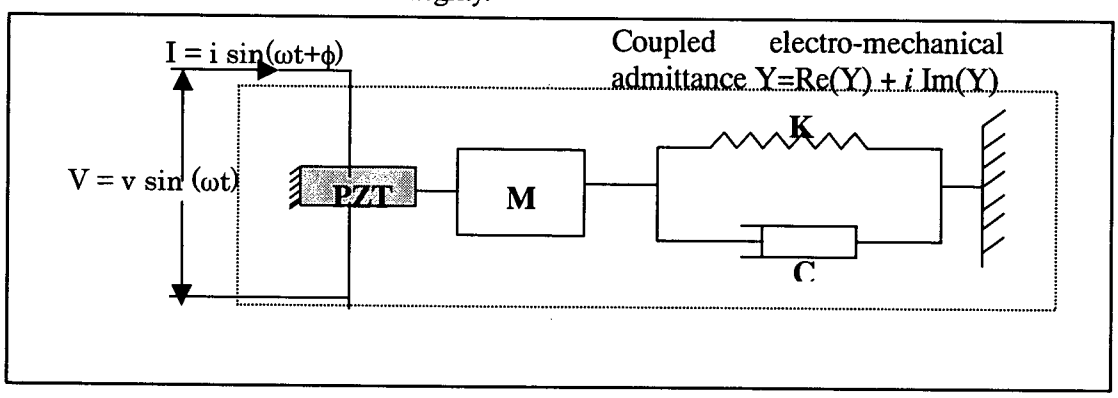

Figure 18. 1-D model used to represent a PZT-driven dynamic structural system

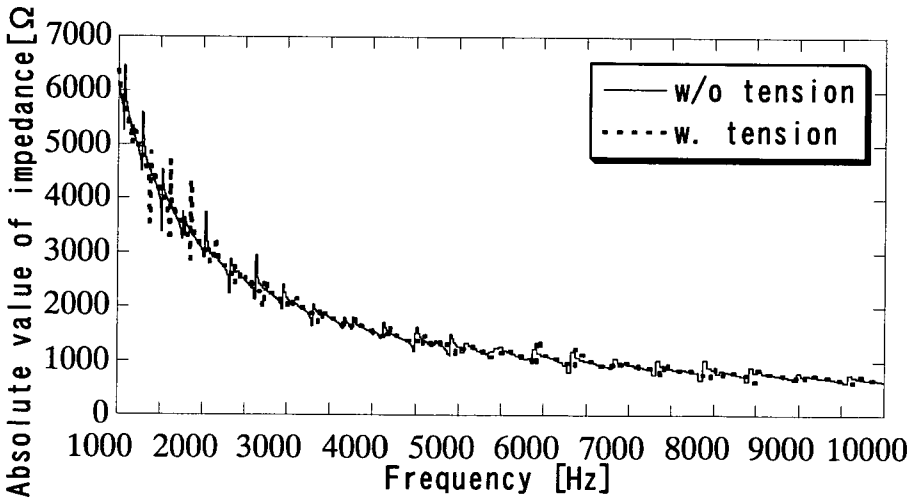

Figure 19. Impedance measurement with and without tension.

SUMMARY

Research and development of health monitoring systems at the Bridge and Structure Laboratory of the University of Tokyo is presented.

Ambient vibration based approaches for LDV and long-span suspension bridges show possible wide applications in this field. In both cases, although the excitation is unknown, densely distributed and accurate measurement is shown to provide valuable information on the status of structures. Especially, a LDV based approach can provide information on damage and loading to the structure with practically applicable system configuration. A smart material system with embedded piezoelectric materials shows high potential to monitor structural status.

ACKNOWLEDGEMENT

Thanks are to M. Abe(Bridge Management Consultants), I. Koshi-ishi(JR East), T. Yashiro(IIS, Univ. of Tokyo), K. Nishikawa(Ministry of Land Infrastructure and Transport) H. Motomura(Japan Highway Corp.) and M. Sugimoto(Fuji Engrg. Consultant) for providing the information on the civil infrastructures.

The research work is supported by Grant-in-Aid from Japan Society of Promotion of Sciences. Studies on smart material systems are initiated during the second author's stay at the Center for Intelligent Material Systems and Structures (CIMSS) of Virginia Polytechnic Institute and State University, which is supported by the Ministry of Education of Japan and Visiting Scholar Program of CIMSS. The authors gratefully acknowledge this support.

REFERENCES

1. Abé, M. 1998. "Structural monitoring using vibration measurement – current practice and future -," *Artificial Intelligence in Structural Engineering*, Ian Smith, ed, Lecture Notes in Artificial Intelligence 1454, Springer, pp.1-18.
2. Kaito K, Abe M., Fujono Y., and Yoda H. 2000. "Detection of Structural Damage by Ambient Vibration Measurement using Laser Doppler Vibrometer", *Non-Destructive Testing in Civil Engineering 2000*, Uomoto (ed.), Tokyo.
3. Farrar C.R., and James III, G.H. 1997. "System Identification From Ambient Vibration Measurement on A Bridge", *Journal of Sound and Vibration*, Vol.205, No.1, pp. 1-18.
4. Bendat J.S., and Piersol A.G. 1993. *Engineering Applications of Correlation and Spectral Analysis*, 2nd ed., John Wiley & Sons, Inc.
5. Dyke S.J., and Johnson E.A. 2000. "Monitoring of a Benchmark Structure for Damage Identification", *Proceedings of the Engineering Mechanical Specialty Conference*, Austin, Texas.
6. Farrar C.R., Cornwell P.J., Doebling S.W., and Prime M.B. 2000. *Structural Health Monitoring Studies of the Alamosa Canyon and I-40 Bridges*, Los Alamos National Laboratory.
7. Garibaldi L., Giorcelli E., and Piombo B.A.D. 1998. "ARMAV Techniques for Traffic Excited Bridges", *Journal of Vibration and Acoustics*, Vol.120, pp713-718.
8. Kadakal U., and Yuzugullu O. 1996. "A comparative study on the identification methods for the autoregressive modeling from the ambient vibration records", *Soil Dynamics and Earthquake Engineering*, Vol.15, pp. 45-49;
9. Lardies J., 1997. "Modal Parameter Identification From Output-Only Measurements", *Mechanics Research Communications*, Vol.24, No.5, pp. 521-528;
10. Quek S.T, Wang W, and Koh C.G. 1999. "System Identification of Linear MDOF Structures Under Ambient Excitation", *Earthquake Engineering and Structural Dynamics*, Vol.28, pp61-77;
11. Juang J.N., and Pappa R.S. 1985. "An Eigensystem Realization Algorithm For Modal Parameter Identification And Model Reduction", *Journal of Guidance, Control, and Dynamics*, Vol. 8, No. 5., pp. 620-627.
12. Maia N.M.M, and Silva J.M.M (ed) 1997. *Theoretical and Experimental Modal Analysis*, Research Studies Press Ltd.
13. Vu Manh H. 2001. *Application of Laser Doppler Vibrometer in Structural Health Monitoring*, Master Thesis, Department of Civil Engineering, The University of Tokyo.

14. Abe, M., Fujino, Y. and Kaito K., 2001. "Damage detection of civil concrete structures by laser Doppler vibrometry", *The 19th International Modal Analysis Conference*, Kissimmee, Florida.
15. Murata, H. 2001. *Structural damage detection by Laser Doppler Vibrometer*, Bachelor Thesis, Department of Civil Engineering, The University of Tokyo, (in Japanese)
16. Kaito, K., Abe, M., and Fujino, Y. 2000. "Identification of Vibration Mode Shapes for a Bridge Deck under Ambient Vibration", *International Workshop on The Present and Future in Health Monitoring*, Bauhaus-University Weimar, Germany.
17. Chajworawitkul, S., Abe, M. and Fujino, Y. 2001. "Identification of impact force using Laser Doppler Vibrometer", *The 56th Annual Meeting of the Japan Society of Civil Engineers*.
18. Abe, M., Fujino, Y., Kajimura, T., Yanagihara, M. and Sato, M. 1999. "Monitoring of a long span suspension bridge by ambient vibration measurement", *The Second International Conference on Structural Health Monitoring,* Stanford University, California, pp.400-407.
19. Abe, M., Fujino, Y. and Nagayama, T. 2001. "Identification of non-porportionally damped system using ambient vibration measurement and its application to a suspension bridge", *Proceedings of the Japan Society of Civil Engineers* (submitted).
20. Inman,D.J. 1998. "Smart Structures Solutions to Vibration Problems," *Proceedings, International Conference on Noise and Vibation Engineering*, Leuven, Belgium, pp.1-12.
21. Liang, C., Sun, F., and Rogers, C.A. 1994. "Coupled Electromechanical Analysis of Adaptive Material System – Determination of Actuator Power Consumption and System Energy Transfer," *Journal of Intelligent Material Systems and Structures.* V.5, 21-20.
22. Abe, M., Park, G. and Inman, D.J. 2000. "Impedance-based monitoring of stress in thin structural members", *11th International Conference on Adaptive Structures and Technologies*, Nagoya, 2000.

EVALUATION OF P-T TENDONS BASED ON MAGNETIC FLUX LEAKAGE AND IMPACT-ECHO TECHNIQUES

Al Ghorbanpoor[1]

Abstract

This paper presents the results of recent non-destructive evaluation studies of internal and external post-tensioned tendons of concrete bridge structures in the United States. Methods used in these studies were magnetic flux leakage to detect corrosion or fracture of P-T steel, and impact-echo to detect grout voids inside of P-T ducts.

The magnetic flux leakage technique was used to test external P-T tendons. The results of these tests have indicated that small corrosion or loss of cross section (in excess of 0.1% of the cross sectional area of P-T steel) may be detected. Voids larger than 125 mm in length could be detected inside of P-T ducts by using the impact-echo technique. This detection was possible only when a void constituted more than 25% of the duct's cross section.

Introduction

Recent non-destructive evaluation (NDE) studies at the University of Wisconsin-Milwaukee have lead to the development of equipment and technology of magnetic flux leakage (MFL) and impact-echo (IE) with an emphasis on applications to concrete bridge structures. These two NDE techniques have been used in laboratory and field to demonstrate their effectiveness during the past few years. Use of the MFL technique for evaluating the condition of steel in post-tensioned (P-T) tendons is based on measuring changes in an induced magnetic field in the close vicinity of the tendon. The changes in the magnetic field are due to the presence of corrosion or fracture of P-T steel in the tendon. These changes in the magnetic field are examined to achieve an understanding of the extent of corrosion of the P-T steel in the tendons. The data analysis is normally performed through correlation with available laboratory calibration data from previous studies. The impact-echo technique is used to detect voids in grouted P-T tendons. The impact-echo testing of a P-T tendon is based on introducing a light mechanical impact on the surface and evaluating the associated reflected waves from discontinuities such as voids inside of the P-T duct.

A. The Magnetic Flux Leakage (MFL) Technique

The MFL concept has been utilized to assess the condition of reinforcing or prestressing steel in concrete bridge structures. The first prototype magnetic flux leakage equipment was constructed by Southwest Research Institute of San Antonio, Texas, in the late 1970's (Ref. 1). The equipment was designed and developed for

[1] Professor of Civil Engineering and Associate Dean, College of Engineering and Applied Science, University of Wisconsin-Milwaukee, P.O. Box 784, Milwaukee, Wisconsin, USA.

application to prestressed concrete I-girders in bridges. The equipment provided a means for demonstrating the effectiveness of the magnetic flux leakage concept in detecting corrosion of reinforcing or prestressing steel embedded within concrete. However, the equipment proved to be inefficient for field use due to it's excessive weight and the cumbersome requirement of installing support rails on a bridge girder to allow testing along it's length.

A later generation of the magnetic flux leakage equipment was designed and developed at the University of Wisconsin-Milwaukee in 2000 (Ref. 2). The system consists of two strong permanent magnets and a set of Hall-effect sensors. The system was designed to result in a unit that is relatively light-weight and that offers easy field operation with respect to equipment installation, data gathering, and removal. The design of this system was based on a modular concept to allow the use of the system for different applications. The magnets and the sensors were mounted on an independent frame that can be fitted onto other support frames to allow testing of different types of structural members such as prestressed I-girders, bridge piers, bridge decks, and external P-T tendons. Figure 1 shows the system as it has been configured for testing external P-T tendons.

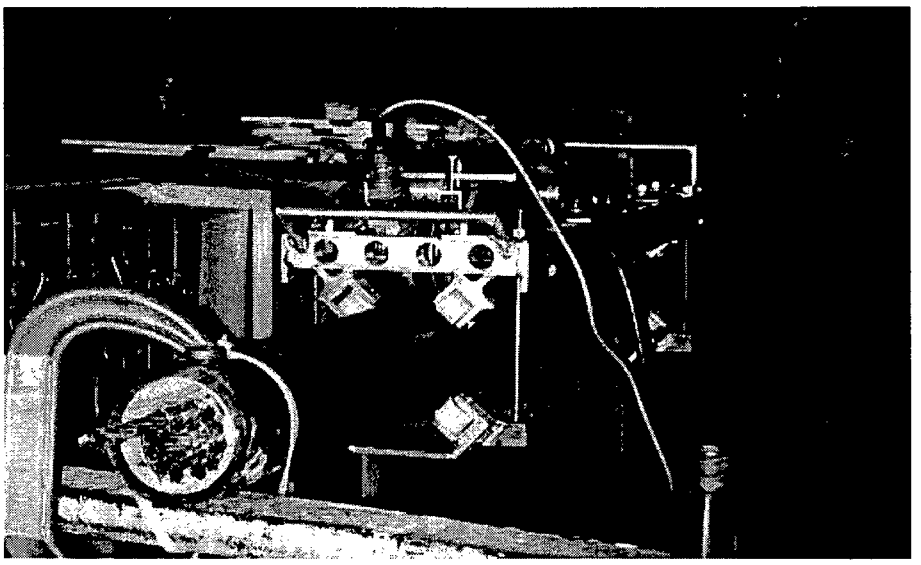

Figure 1. The Magnetic Flux Leakage (MFL) equipment installed on a laboratory sample consisting of a grouted P-T tendon

As shown in the figure, the frame that supports the magnets and sensors can roll along the length of a P-T tendon on contact wheels that maintain a constant distance between the magnets and the surface of the tendon. Although the MFL equipment contains a total of 10 Hall-effect sensors, data from only four sensors is recorded and analyzed for the purpose of testing external P-T tendons. This is because the selected 4 sensors are positioned centrally and near the longitudinal axis of a P-T tendon

during a MFL test and produce the highest MFL signal amplitudes. Changes in the magnetic field in a P-T tendon are normally measured in terms of the amplitudes of the Hall-effect sensors' output signals. These MFL signals are normally viewed in graphs that show signal amplitude vs. longitudinal travel path of the equipment along the length of the tendon. A rolling encoder device is installed on the frame of the equipment to provide a means for measuring the distance it travels along the length of a P-T tendon under test. In conjunction with the MFL equipment, data acquisition and analysis software are also developed and used to facilitate data recording, displaying, and interpretation.

It has been shown that the amplitude of MFL signals from a flaw in P-T tendons is proportional to the amount of loss of section in the P-T steel due to corrosion or fracture. Typical MFL data in the graphical form is shown in Figure 2. The data is obtained from testing the laboratory P-T tendon specimen that is shown in Figure 1. The laboratory sample in the test contained a prestressing strand that was fractured at 1,300 mm from its end. The laboratory sample consisted of 22 seven-wire strands of 12 mm in diameter. One fractured strand in the sample represented a loss of cross-sectional area equivalent to 4.5 percent.

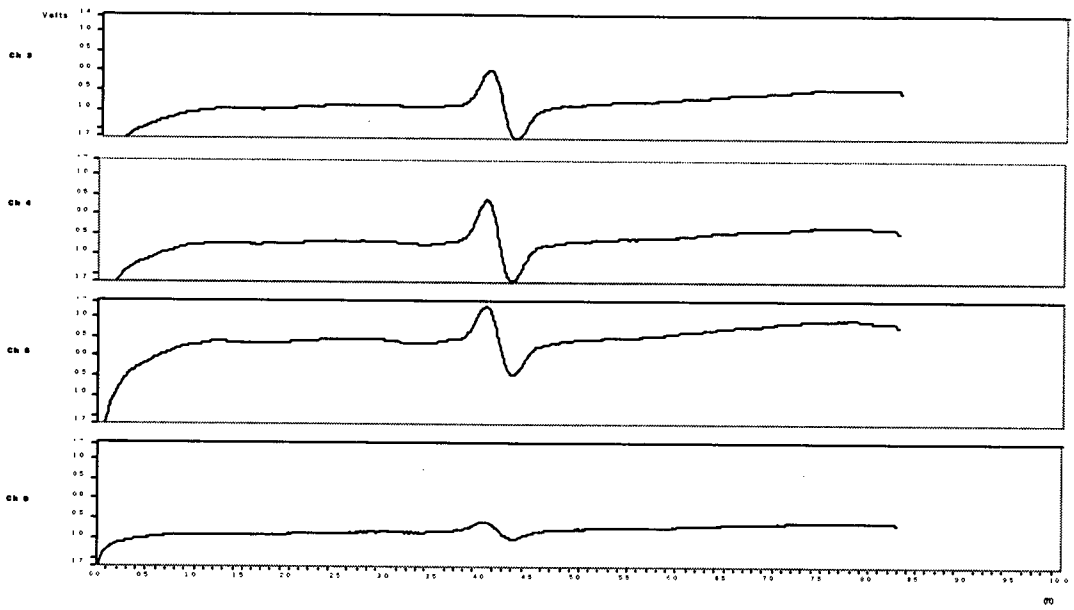

Figure 2 - MFL data for a strand fractured at 1,300 mm (4.25 feet)
(seven wires cut in a single strand located at the edge of the strand bundle)

As it can be seen in the figure, a fracture in a strand can be easily recognized from the MFL graph. It should also be recognized that the MFL signal amplitude for each sensor is proportional to the distance between the sensor and the defect (or the source of the magnetic field change). In the MFL equipment, sensor #4 is positioned along the centerline of the P-T duct with sensors #3 and #5 located 25 mm on either side of sensor #4. Sensor #9 is positioned 25 mm above sensor #4 and farther away from the

tendon. The MFL signal amplitude is also proportional to the amount of loss of steel in a P-T tendon. Smaller steel losses, for example from surface corrosion, produce lower MFL signal amplitudes. To enhance the MFL signal interpretation when dealing with small signal amplitudes, additional data analysis methods may be used. One such method is known as the *correlation analysis.* In the *correlation analysis,* a reliability index or value (called the *correlation factor*) is normally computed. The *correlation factor* is computed based on the extent of matching that exists between a MFL signal from a real flaw, and a mathematical signal that is constructed from the results of previous laboratory studies and calibrations. For example, a 100 percent (or perfect) match will result in a *correlation factor* of 1.00. Figure 3 shows an amplitude graph and the results of the *correlation analysis* (lower graph) for MFL data from a test of the laboratory sample that had only one wire fractured (a loss of cross section equivalent to 0.6 percent). A correlation value of 0.975 is computed and shown in the lower table below the graphs.

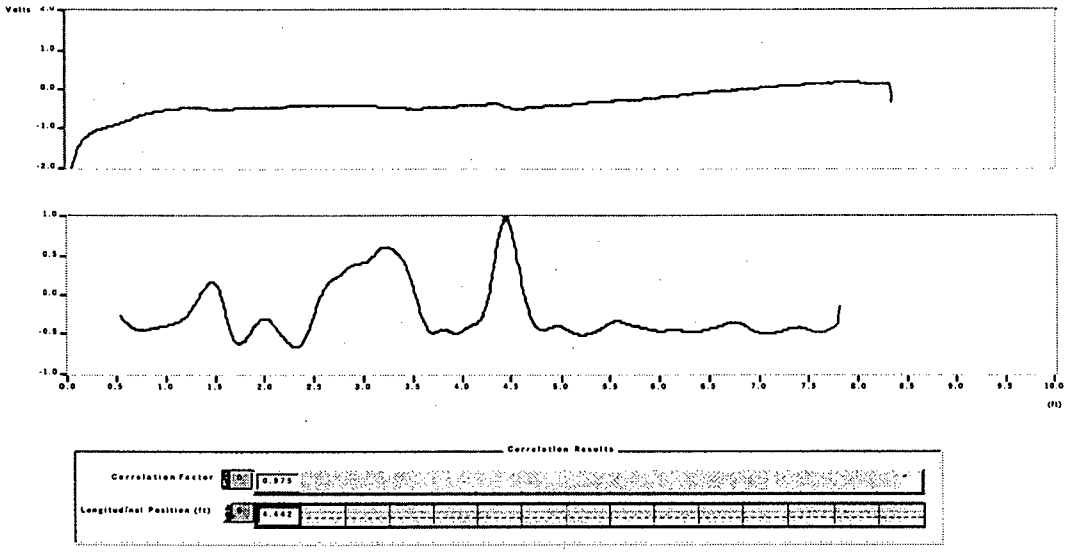

Figure 3 - MFL data for one wire fractured at 1,300 mm (4.5 feet)
(one wire cut in a single strand located at the edge of the strand bundle)

The MFL equipment has been used in different concrete bridge structures to assess the condition of steel inside of external P-T tendons. Figure 4 shows the MFL equipment during a test in a concrete segmental box bridge as it is moved along the length of a tendon for its evaluation. Each tendon in the bridge consisted of either 19 or 27 seven-wire strands of 12-mm diameter that were placed in a 100-mm diameter polyethylene duct. Data from the Hall-effect sensors are transmitted to a computer that displays real-time MFL graphs for the operator to perform immediate preliminary assessment of the condition of the tendon under test.

When there is no indication of corrosion or fracture in a P-T tendon under a MFL test, the resulting MFL signals from the sensors show little variations in the amplitude of the magnetic field. This is shown in Figure 5 for a P-T tendon that is 8.5 m long.

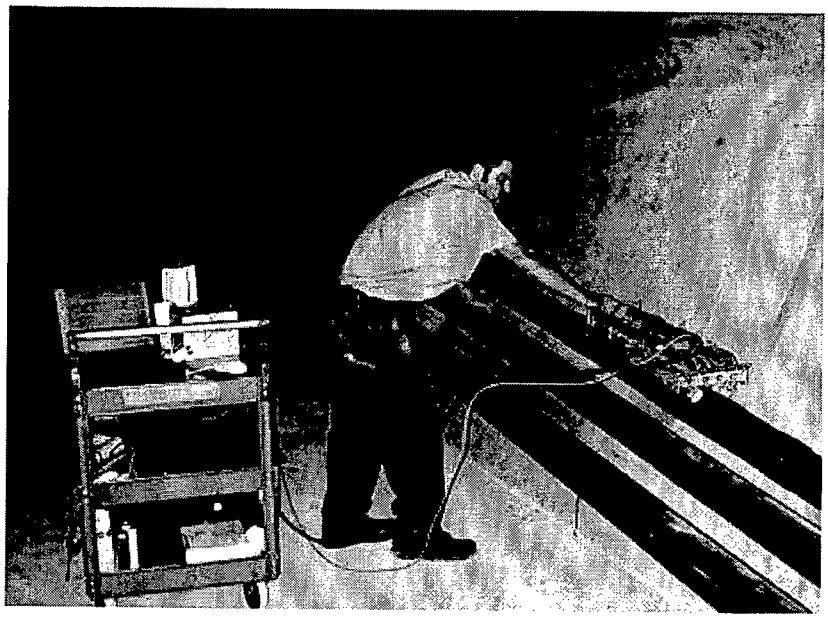

Figure 4 – Photograph of the MFL system during a test of an external P-T tendon

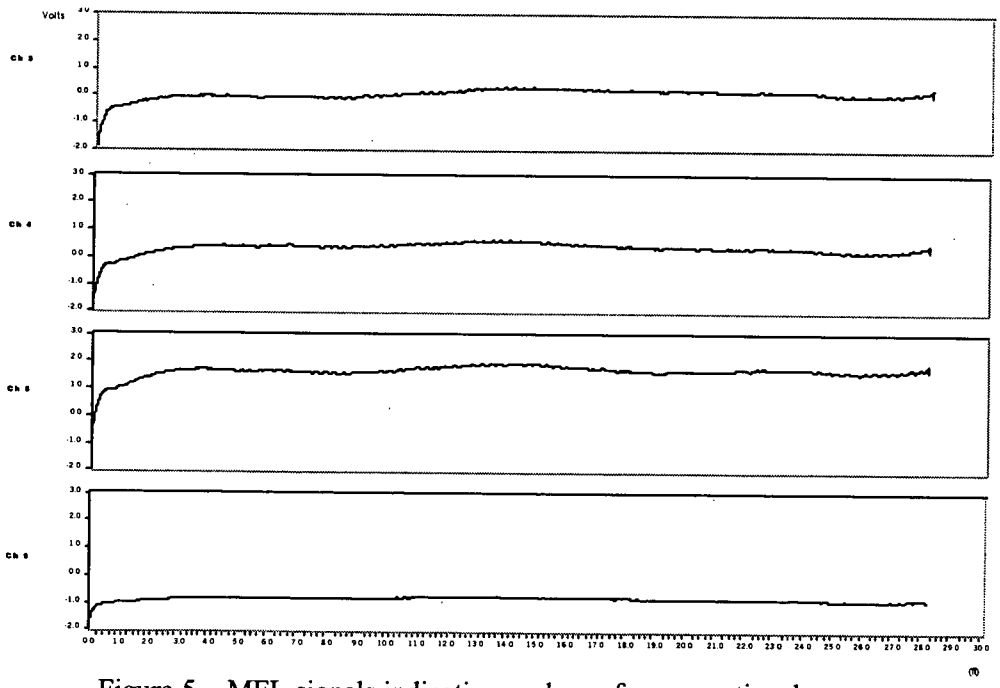

Figure 5 – MFL signals indicating no loss of cross sectional area

The MFL tests of external P-T tendons in bridge structures have resulted in reliable detection of corrosion of P-T steel as small as 0.1 percent of the cross-sectional area. One MFL graph for a tendon where corrosion was detected is shown in Figure 6. As shown in the figure, the test was conducted for a length of 9.85 m (32.3 feet) and a flaw indication was recorded at 9.14 m (30 feet). The MFL data showed that the flaw (corrosion) was detected as being local and with the corrosion concentration located between sensors #4 and #3. Considering that the largest MFL signal amplitude is from sensor #4, one can conclude that the corrosion concentration is closer to the position of this sensor.

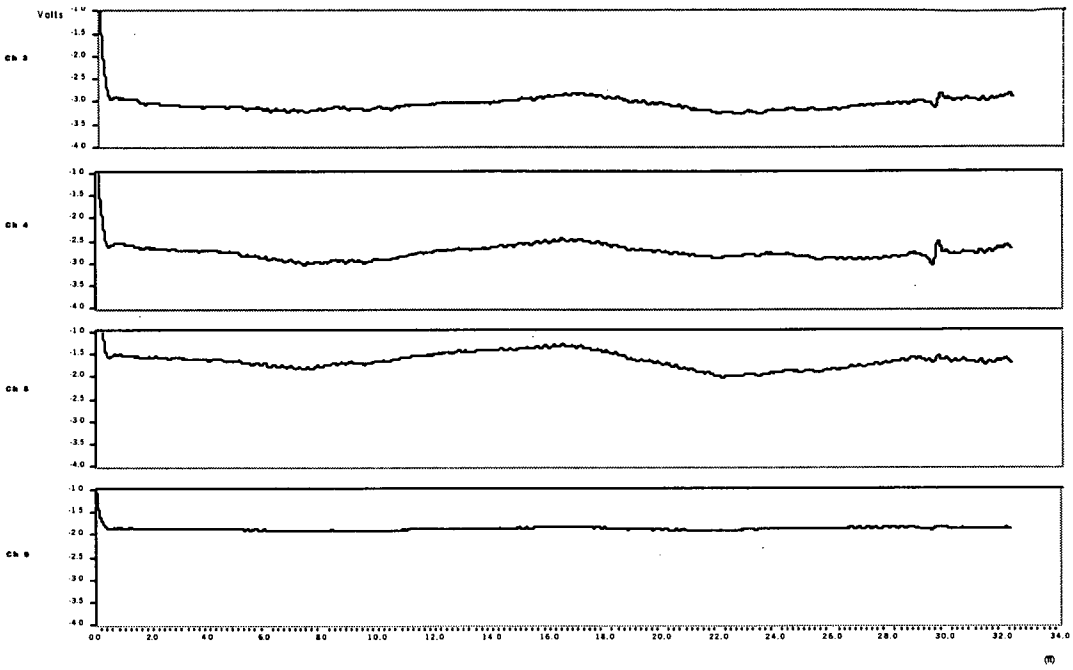

Figure 6 – MFL data showing a flaw at 9.14 m (30 feet)

After the MFL the indication of flaw was observed from the recorded data as shown in Figure 6, the corresponding location on tendon was marked with a can of paint to allow subsequent validation. The validation was made by cutting the P-T duct open and by exposing P-T steel for visual examination. The opening of the external polyethylene duct and exposing the steel inside validated the MFL indication as it revealed local surface corrosion of the P-T steel. The P-T duct at the location it was cut open is shown in Figure 7. After brushing away the corroded material, it was discovered that the loss of the cross sectional area of steel due to the corrosion was approximately equivalent to 0.1 percent of the area of the P-T steel. It was further verified that the corrosion was limited only to a local region as it was indicated in the recorded MFL data for the tendon.

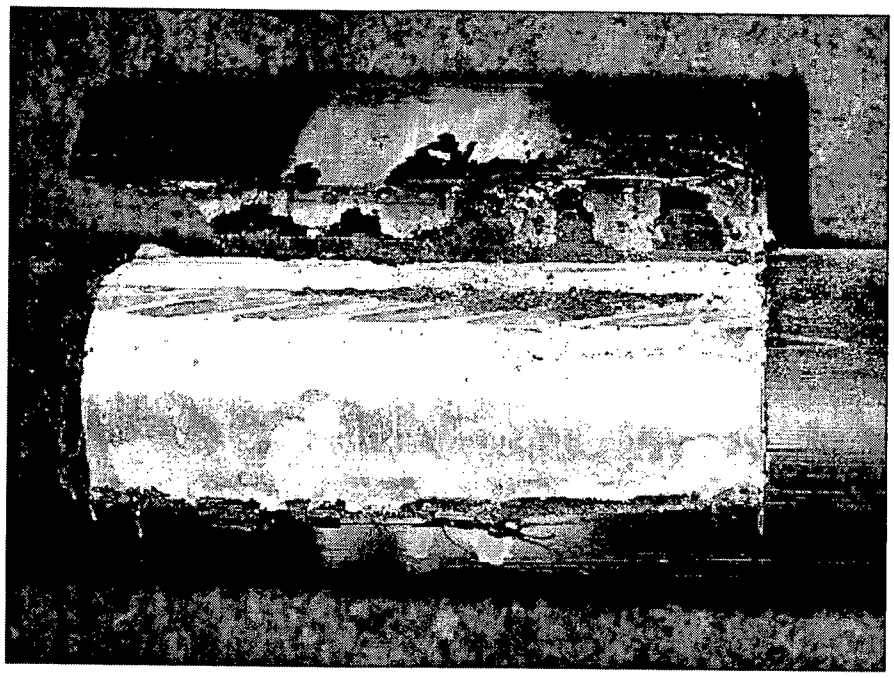

Figure 7 – Photograph of the opening in the polyethylene duct verifying local surface corrosion

B. The Impact-Echo (IE) Technique

The impact-echo technique is a non-destructive test capability that allows accurate measurement of a member's thickness as well as detection of internal defects such as voids, honeycombing, cracks, delamination, and poor quality concrete. An impact-echo test consists of introducing a small mechanical impact on the concrete surface and measuring and recording the resulting surface displacements close to the impact point. The surface motion is due to reflections of the impact waves from the concrete member's back face and from various interfaces (or defects) inside concrete. In an impact-echo test, the recorded surface displacement data is converted into frequency values that correspond to distances from the concrete surface to respective interfaces. Therefore, in addition to detecting the presence of a defect inside a concrete member, one can also determine the location of the defect. Figure 8 shows both time and frequency graphs for an impact-echo test data.

Laboratory and field studies have been performed recently to evaluate the condition of grout and to detect grout voids inside of P-T tendons (Ref. 3). In the laboratory studies, concrete samples with partially grouted P-T tendons were fabricated and tested with impact-echo equipment. From these tests, it was concluded that grout voids larger than 125 mm in length could be detected inside of P-T ducts.

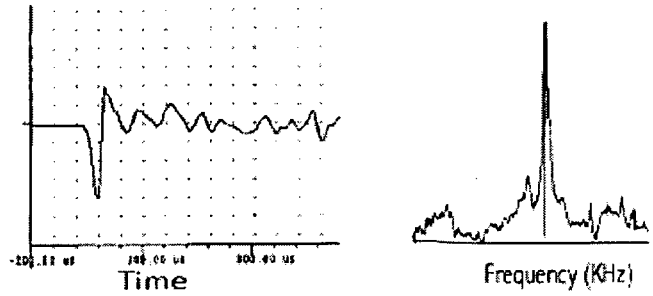

Figure 8 – Time and frequency graphs for an Impact-Echo test data

It was possible to detect these voids inside of P-T ducts only when the voids constituted more than 25 percent of the ducts' cross sectional area. Several in-service post-tensioned concrete bridge structures have also been subjected to impact-echo testing. No indications of the presence of voids were found in the bridges tested with IE equipment. However, partially grouted P-T tendons in a test verification wall were accurately detected by the IE technique. The verification wall was built by a bridge owner at the bridge site and was tested prior to an IE testing of the bridge itself.

CONCLUSION:

Effective and reliable assessment of the condition of P-T tendons may be achieved by using the magnetic flux leakage method to detect corrosion and fracture of steel and by using the impact-echo technique to detect the presence of grout voids inside of P-T ducts. The MFL technique would allow localized surface corrosion and larger section losses to be easily detected. The impact-echo technique would allow grout voids longer than 125 mm to be detected. Both methods proved to be easy to apply in the field and yield reproducible results upon test repetitions.

Acknowledgement

The work described in this paper was made possible in part by major funding from the Federal Highway Administration, US Department of Transportation.

References

1. Kusenberger, F.N., and Barton, J.R., "Detection of Flaws in Reinforcing Steel in Prestressed Concrete Bridge Members," Final Report No. FHWA-RD-81-087, Federal Highway Administration, U.S. Department of Transportation, 1981.
2. Ghorbanpoor, A., Borchelt, R., Edwards, M., and Abdel Salam, E., "Magnetic-Based NDE of Prestressed and Post-Tensioned Concrete Members – The MFL System," Final Report No. FHWA-RD-00-026, Federal Highway Administration, U.S. Department of Transportation, May 2000, 107 pages.
3. Ghorbanpoor, A., "Evaluation of Post-Tensioned Concrete Bridge Structures by the Impact-Echo Technique," Final Report No. FHWA-RD-92-096, Federal Highway Administration, U.S. Department of Transportation, December 1993, 92 pages.

Experimental Study on the Measuring Method of Steel Girder Stress by Magetostrictive Method

Ichiro Masuda[1], Ryosuke Murai[2], Sinji Nakaya[3] and Seiichi Abuku[4]

ABSTRACT

In the course of maintenance and management of bridges, it would be necessary to have a good grasp of the stress conditions occurring in its members. In order to measure stresses, we have a series of inspection methodology including the stress releasing method to cut off a part of member and so on. On the other hand, for non-destructive test methods, there are techniques utilizing strain gauge, the X-ray diffraction, ultrasonic velocity variation, magnetostrictive effect, etc. As an example of the method utilizing the magnetostrictive effect, we know Abuku's Method [1)] at the present stage.

In this paper, we will present the results of the experimental study of the measurement of stresses on a steel bridge utilizing the magnetostrictive effect.

1. PRINCIPLE OF THE MAGNETOSTRICTIVE METHOD

1.1 Magnetostriction of Steel

Ferromagnetic materials such as steel and nickel change t he s izes o f matrices w hen s ubjected to a m agnetic field due to the magnetostrictive effect. In other words, sustaining stresses into steel, its magnetic properties shall be changed for themselves.

A steel member, for instance, is easily magnetized in the direction of a tensile stress, and not so easily in the direction perpendicular to the tensile stress. In the case of a compressive stress, the phenomenon will occur in the reverse order. The change of magnetic flux density due to the effect of stresses in magnetic field strength 2.2×10^5A/m is shown Figure 1. [1)]. That is to say, the residual stresses of a steel member could be determined if the change of the magnetic flux density is known.

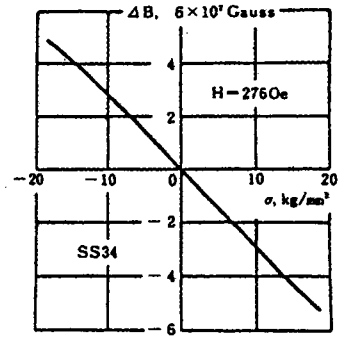

Figure 1. The change of magnetic flux density

[1] Manager, Bridge Designing Section, Hiroshima Machinery Works, Mitsubishi Heavy Industries, Ltd
[2] Acting Manager, Materials Laboratory, Hiroshima R & D Center, Mitsubishi Heavy Industries, Ltd
[3] Manager, Maintenance and Renewal Engineering Center, Mitsubishi Heavy Industries Erection Co., Ltd
[4] Professor, Department of physics, Faculty of Science, Okayama University

1.2 Detection of the Magnetostriction

A magnetic probe as shown in Figure 2 was adopted to detect the magnetostriction. This probe has four legs with a coil wound on each of the legs. Exciting coils and detecting coils are wound diagonally, respectively, with respect to the leg arrangements.

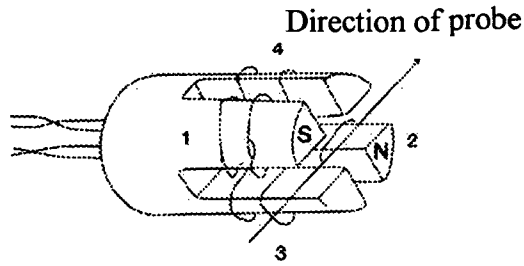

Figure2. Magnetic probe

When the probe is depressed to a steel plate free of a stress, the configuration shown in Figure 3 (a) will take place and no voltage is generated across the detection coil. On the other hand, when the probe is depressed to a steel member on which a stress is developing, an unbalance will occur in the magnetic pole due to the easiness of the magnetization in the direction of a tensile stress and the difficulty in the magnetization in the direction perpendicular to the stress, resulting in the generation of voltage across the detection coil.

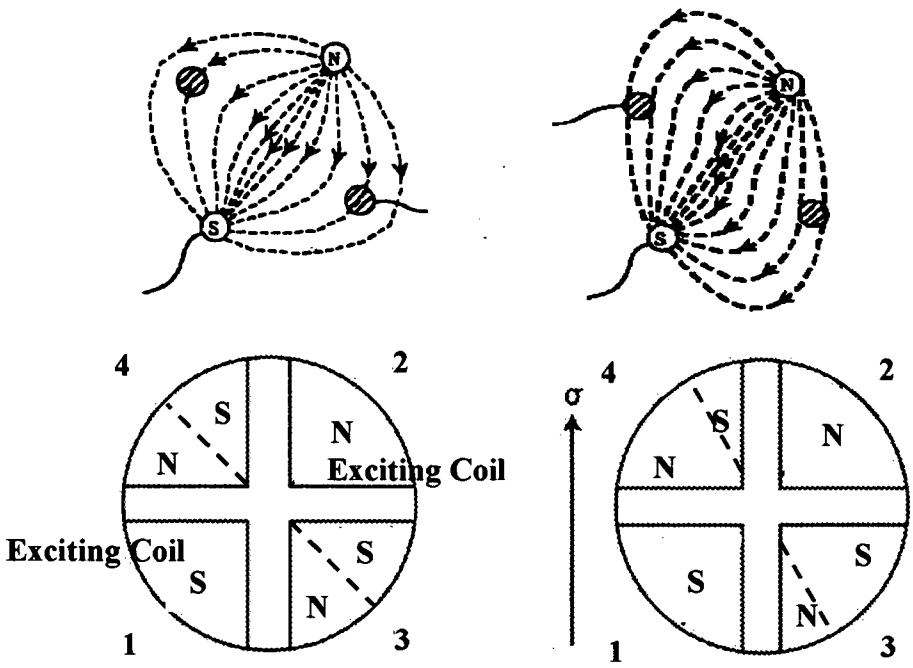

Figure 3. Instantaneous distribution of magnetic poles of a magnetic probe at a given moment

A voltage proportional to the difference of magnetic permeability between the value in the direction of a tensile stress and the value perpendicular to the tensile stress, that is, the difference of principal stresses can be obtained. The relationship between the difference of principal stresses and voltages can be given as follows:

$$V = k(\sigma 1 - \sigma 2) \cdot \cos 2\theta$$

Where V : Voltage at the detecting side, K : Magnetostrictive sensitivity.
$\sigma 1, \sigma 2$: Principal stresses, θ : Direction and angle of principal stress $\sigma 1$.

K is the magnetostrictive sensitivity varying with materials. It will be necessary to prepare beforehand a calibration curve of the measured material. The direction of the principal stress is the direction of the probe indicating the maximum voltage when rotating the probe depressed to a steel plate for 180 degrees, as shown in Figure 2.

1.3 Calculation of the Principle Stress

The principal stress difference and the direction of the principal stress are obtainable from the magnetostrictive effect. Consequently, it is necessary to separate $\sigma 1$ and $\sigma 2$. In this application, the integration method of shear stress differences used in the photoelastic effect test is adopted. The stress conditions of a steel bridge can be assumed to be plane stress conditions, so that the stress in the direction of the plate thickness was omitted here. For the separation of the principal stresses, the balance of stresses shown in Figure 4 is considered.

From the counterpoise of forces in the direction of x-axis, we have

$$\sigma c = \sigma a + (\tau b - \tau d).$$

Based on the elastic theory, $\tau b = \tau xy$ is given as follows by the principal stress difference.

$$\tau xy = -(\sigma 1 - \sigma 2)/2 \cdot \sin 2\theta$$

Where θ : the angle of principal stress to x-axis.

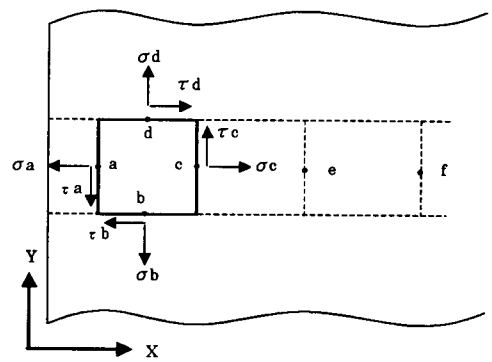

Figure 4 Components of Stresses as Rectangular Parallelepiped Constituents

From Figure 4, $\sigma a = 0$ is assumed by setting the free edge of the steel plate to the point "a". τxy of the point b, d is assumed to be the increment to σa. Thus, σc can be obtained. In the same manner, the σx value for the point e, f is obtainable. In turn, σy is given by the following formula.

$$\sigma y = \sigma x - (\sigma 1 - \sigma 2)\cos 2\theta$$

By putting $p = \sigma 1 + \sigma 2 = \sigma x + \sigma y$

$q = \sigma 1 - \sigma 2,$

$\sigma 1$, $\sigma 2$ can be obtain by the following formulas.

$\sigma 1 = (p+q)/2$, $\sigma 2=(p-q)/2$

2. EQUIPMENT FOR MEASURING STRESSES

2.1 Configuration of measuring system

The photo of the equipment for measuring the stresses is shown in Photo 1. The configuration of the system is shown in Figure 5.

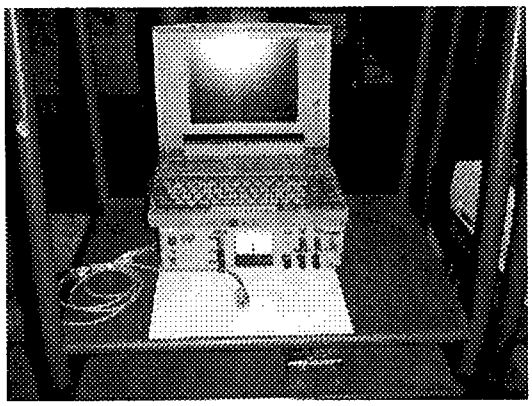

PHOTO1. Magnetostrictive Measuring System

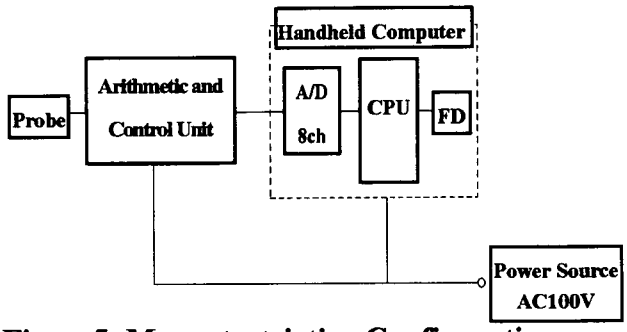

Figure5. Magnetostrictive Configuration System

2.2 Lift-off Compensation

Since the voltage values gained from the magnetostriction are liable to suffer from the surface treatment, plastic deformation, the gap between the probe and a steel, etc., it is necessary to prepare a laboratorial calibration curve beforehand to minimize these effects. In particular, improvement in the accuracy has been attempted through the impedance compensation to rectify the error of measurement due to the gap present between the probe and the steep plate. [1]. A film of a given thickness is sandwiched between the probe and a steel plate, and the change in the impedance is determined. The accuracy of measurement can be improved through the compensation of the impedance developed in the actual measurement. [1].

3. EXAMPLES OF STRESS MEASUREMENTS CLASSIFIED BY ERECTION STAGE

3.1 Stress Measurements Classified by Erection Stage

In order to measure the status of stresses after a bridge is completed, it is important to have a good grasp of the history of the stresses developed throughout the erection stages. Since the method for measuring the magnetostriction involves the simultaneous measurement of the residual stresses, it is indispensable to have thoroughgoing knowledge of the conditions of the residual stresses from the manufacture

of the steel members to the construction of the bridge. In the present study, the results of the measurements of the changes in the stress conditions on the main girders of an existing simple I-shaped plate girder bridge, as measured by the magnetostriction method, will be reported.

3.2 Stress Measurements of Lower Flange of Steel Girder

This bridge is a simple I-shaped plate girder bridge shown in Figure 6. The steel members used were of the atmospheric corrosion resist steel (JIS G 3114; SMA490BW). However, anti-corrosion coating was not applied. The measured portions were not ground and left to rust spontaneously. The stress measurements were conducted at the three stages, i.e., stress-free state at the time of the fabrication of the girder, post steel girder erection, and on completion of the placement of the concrete slabs. The actual methods for measuring the stresses were the simultaneous applications of the magnetostriction method and the strain gage method. Stage of erecting girders is shown in photo2.

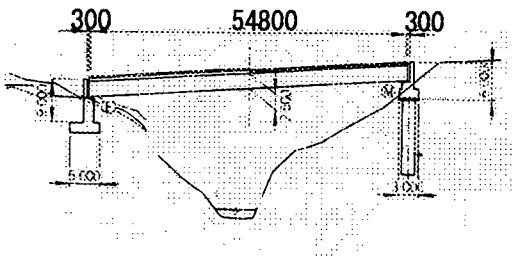

Figure6. General View

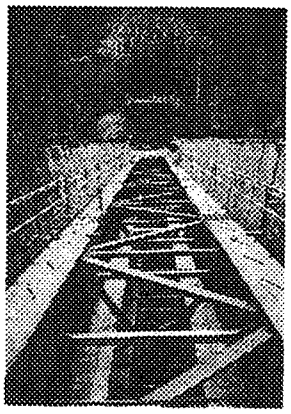

Photo2. Erection of Steel Girders

The changes of stresses on the reverse side of the lower flange at the center of the span, classified by erection stage, are shown in Figure 7.

The effect of the stresses developed at the manufacturing stage is appearing in the residual stresses. It is also clear that the effect of oxy-fuel gas cutting at the flange edges and the effect of bending process before weldment at the web connections, respectively, have taken place. The plate thickness of measuring spots is 38 mm and it was thought that the residual stresses due to the weldment would not have an influence on the reverse side of the lower flange. Although the stress

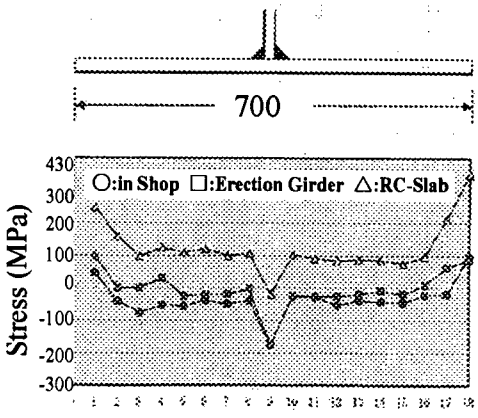

Figure7. Stress of the lower flange at the center of the G_1 girder

conditions of at the time of the girder fabrication were of stress-free, a compression stress was shown in the measured value. This was thought attributable to the effect of oxy-fuel gas cutting and/or the error due to the integration method of shear stress differences, and so on.

Consequently, assuming that the stress status at the lower flange to be a single axial stress in the direction of the bridge axis, the result of the change of stress conditions from the girder manufacturing stage to the post erection stage was obtained as shown in Figure 8.

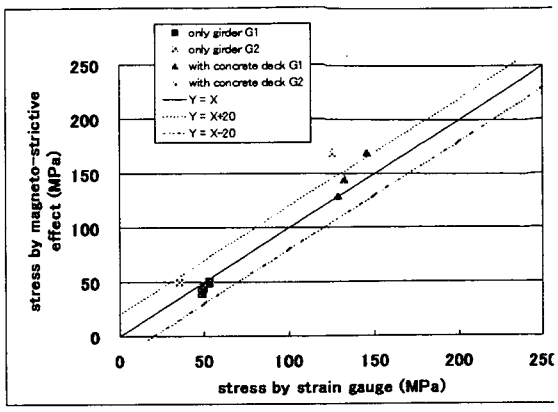

Figure8. Comparison of measurements between magnetostriction and strain gauge method

In addition, the comparative study of the theoretical values, magnetostriction method, and strain gauge method were conducted in relation to the stress transition since the manufacture of the girders. The results are shown in Figure9. The adaptability of the magnetostriction method for the measurement of the stress increments was confirmed based on these results. Incidentally, this method allows a stress measurement over the membrane of coating formed on a bridge surface.

For the estimation of the absolute stress value, it will be necessary to improve accuracy through the improvement of the method to estimate the effects of the surface conditions, as well as manufacturing/erection process, and so on.

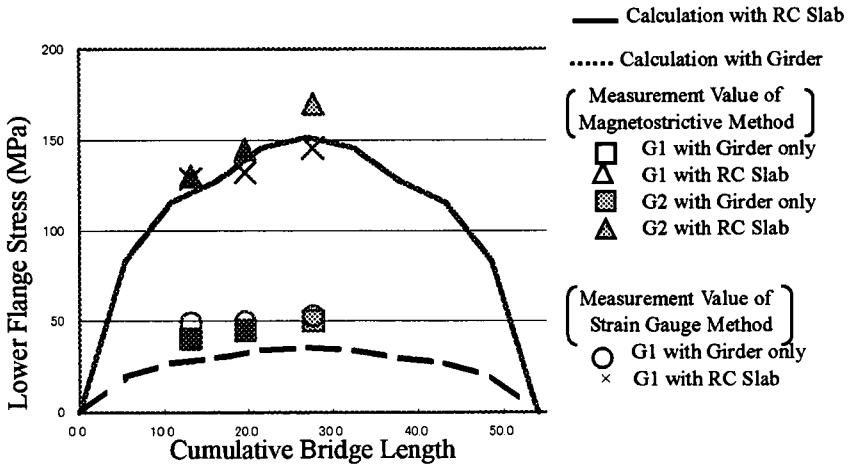

Figure9.Distribution of Calculation and measurement

4. EXAMPLE OF MEASUREMENT OF CONSTRAINT STRESSES FROM MOVABLE BEARING TO GIRDERS

After the construction of a steel bridge, free thermal expansion/contraction of the main girders are occasionally constrained due to the restriction in the movement of the movable

bearing caused by the shift of the infrastructure. The result of the stress measurement by the magnetostriction method on the steel girders suffering from the constraint stresses will also be reported here.[2)]

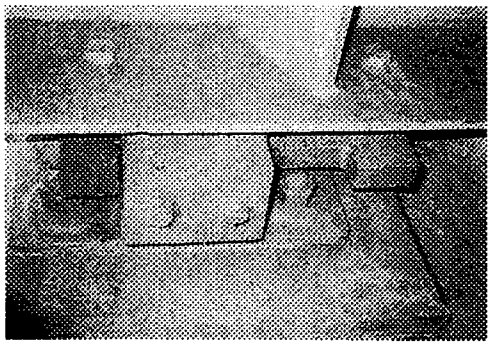

Figure10. Restriction of Bearing

4.1 Deformation Conditions of a Bridge

The infrastructure occasionally shifts due to the lateral flow of the ground causing the restriction of movable bearing mechanism, resulting in the constraint on the movement during thermal expansion/compression on the part of the steel girders. The conditions of bearing portion in such a case are shown in Figure 10. The subjective bridge is a simple I-shaped plate girder bridge shown in Figure 11.

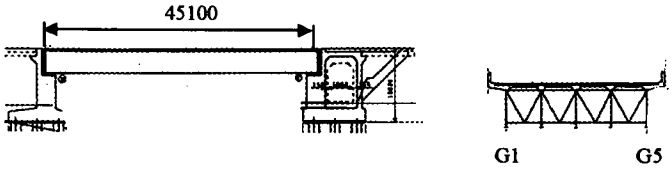

Figure11. General View

The movable bearing mechanism for the main girder G2-G5 did not work, while those for the main girder G1 worked.

4.2 Measurement of Constraint Stresses

The constraint stress working on the steel girder accompanied by the thermal change was measured. It was assumed that the constraint force not exceeding the proof stress of the movable bearing mechanism was acting on the steel girders. The measurement was conducted in winter when no constraint occurs due to the fall of the temperature and in summer (4 time in summer and winter) when the constraint occurs definitely.

Table1. Temperature Condition

Girder	Season	Date	Time	Temperature℃	
				Atmosphere	Web Surface
G1	Summer	1999.06.16	8:48	27.2	26.3
	Winter	2000.02.01	13.56	5.3	14.6
	Summer	2000.09.18	15.33	29.6	36.1
	Winter	2001.02.13	15:21	5.3	6.1
G5	Summer	1999.06.16	14:44	26.9	27.6
	Winter	2000.02.01	12:06	4.7	4.3
	Summer	2000.09.18	12:40	27.2	29.6
	Winter	2001.02.13	13:09	6.2	7.5

The temperature conditions at the time of measurement are shown in Table 1.

The stresses on the webs at the distance of 700 mm from the movable bearings for G1, which is free from constraint, and for G3 and G5, which suffer from the constraint,

respectively. Therefore, it was assumed that any vertical stress element in the direction of the bridge axis due to the dead load did not occurred. The measured stresses on G1, which didn't suffer from constraint stress, are shown in Figure 12. There was no significant seasonal difference in the stresses in summer and winter. The high stress portions indicated in half way of the web are thought attributable to the residual stresses due to the weldment process applied to the horizontal stiffeners.

In the estimation of the stresses using the magnetostriction method, the improvement in the accuracy was attempted by means of the joint use of the #-shaped method discussed later. The stresses on G5 are shown in Figure 13. It was estimated that approx. 100 Mpa of constraint stresses are developing near lower flanges of these girders in summer. By contrast, it is clear that these constraint stresses are released in winter.

Considering the facts mentioned above, it could be estimated that the reproducibility of the measurement by the magnetostriction method was quite satisfactory and the constraint force over the steel girders also didn't show any change.

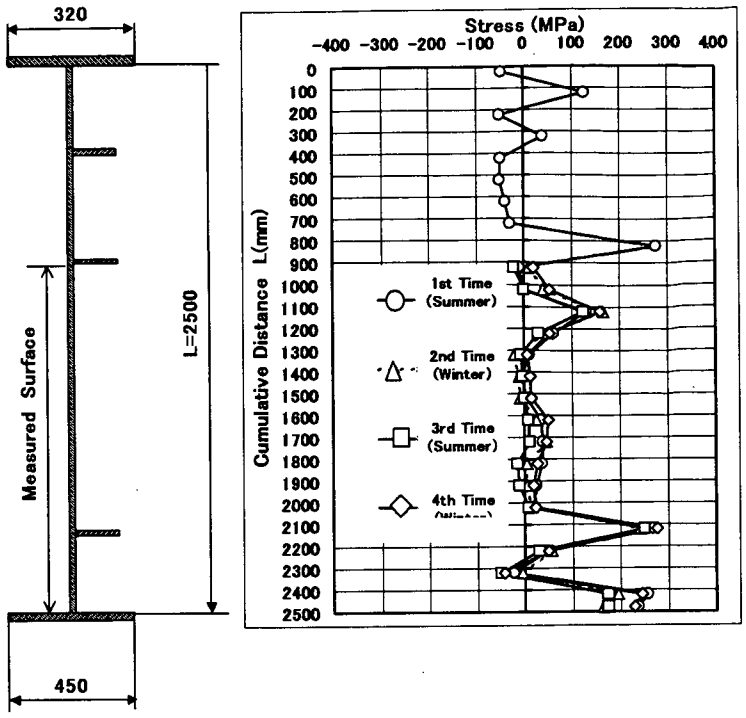

Figure12. Measurement of G1 Web Stress

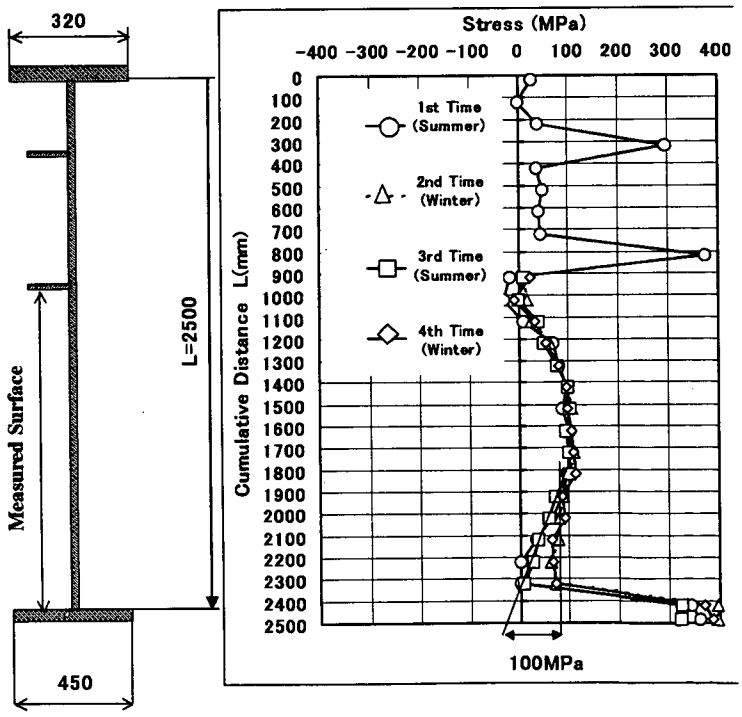

Figure13. Measurement of G5 Web Stress

4.3 Application of #-Shaped stress measuring Method

We have so far endeavored in the development of the methods for measuring the stresses utilizing the magnetostriction as a means of non-destructive testing. In order to validate the methods for measuring the stresses relying on the magnetostriction, verification of stresses by the #-Shaped stress measuring method was jointly conducted to support the validity of magnetostriction method. Now, said #-Shaped Method is one of the destructive test. As shown in Figure 14, the surface residual stress is released by giving a #-shape grooving of 2 mm in depth on the steel plate. The residual stress is obtained by measuring the released stress by a strain gauge installed within the #-shape grooving on a surface.

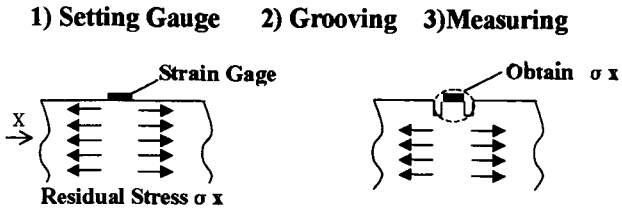

Figure15. Concept of #-Shaped Method

5. CONSIDERATION

The stress measurement on a bridge utilizing the magnetostrictive effect requires a certain elaboration depending on the measuring spots in order to enable the estimation of the stresses with accuracy.

- For members with free edges, the integration method of shear stress differences utilizing more than one route should be introduced.
- Joint use of the method of a different nature such as the #-shaped method.
- To have a good grasp of the calibration properties of the objective steel members prior to intended measurements.

CONCLUSION

Measurement of the stresses applied to a steel bridge utilizing the magnetostrictive effect was reported in this paper. Possibility of the measurement of the residual stresses in relatively good accuracy was demonstrated, which was not predictable by the conventional methods. In particular, it has good probability of an application with a high degree of accuracy to the infrastructures including structural components in the state of one-axis stress configuration.

It was also made clear that the measurement itself has reproducibility and no supplementary work such as the paint removal was necessary, therefore, this method is capable of measuring the stresses of bridge member passing time after construction. We

will continue to make effort to improve the magnetostriction method from now on

In conducting the present research, the authors are grateful for the Ryumon Dam Construction Office of Kyushu Regional Development Bureau, Ministry of Land, Infrastructure and Transport; the Tokushima Office, Shikoku Regional Bureau, Japan Highway Public Cooperation; Chuden Engineering Consultant Co., Ltd.; and Consultants Daichi Co., Ltd. for providing extraordinary cooperation.

REFERENCES

1) Abuku, Magnetostrictive sensor, Magnetic Sensor Manual, No.1, pp.7-22, 1979
2) Wada, et al., Proceedings of the 56th Annual Conference of The Japan Society of Civil Engineers, pp. 932-933. 2000.9
3) Abuku, et al, Magnetic Stress Measurement in Steel Structure, Bridge and Foundation, pp.33-38, 2001.6

A Concept toward Durable Bridge Design by Use of Weathering Steel

Hiroshi Kihira
Nippon Steel Corporation*

Abstract

Based upon recently established "*Durable State Concept*" toward application of weathering steel proposed by Rust Chemistry Committee in Japan Society of Corrosion Engineers, technological advancements in terms of materials innovations were assessed. High nickel coastal weathering steels and surface treatments to reduce corrosion rate in drastic manner are considered as proper tools for durable low cost structures. Also, computation software for corrosion prediction of weathering steels in variety of environmental conditions was developed based on the same concept, in order to support minimum maintenance design. Its outline and model case simulations were demonstrated.

Keywords: *weathering steel, surface treatment, durable state, durability design minimum maintenance, bridge, corrosion,* and *prediction software.*

Introduction

Because of it is unique feature such as corrosion prevention by the protective rust formation, weathering steel[1,2] has been widely applied to various actual structures especially to bridge beams. There are many successful cases in which life cycle cost is reduced to a great extent by weathering steel compared to painted or other types of steel structures. However, it is also true that some problems brought about when it was applied imprudently to coastal area and so on, where air-born salt was abundant. In recent years, the influence of deicing salt sprinkling is noticed even in the inland area, where local unusual rust formation in a structure is sometimes recognized. On the other hand, in order to save natural resources, as well as to keep up Japan's industrial cost competitiveness, minimization of maintenance cost for infrastructure is now one of the major national issues. Among them, research and development of so-called take care technologies for weathering steel structures are important because of its potentiality as minimum maintenance structure. On such a background, the rust chemistry committee (RCC) to support the infrastructure of the 21st century was organized as a part of Japan Society of Corrosion Engineers (JSCE) in 1997 (headed by Prof. Misawa at Muroran Institute of Technology), so that basic recognition toward correct usage of the weathering steel is clarified. An examination was done to recognize anew the basic interpretation of so far indefinite "*antei-sabi* (stable rust?)", which in fact has been an origin of confusion in Japanese weathering steel market. Namely, most of civil engineers believed in such a way that corrosion of the weathering steel completely stops after *antei-sabi* formation, while physico-chemists keep suggesting that perfect realization of zero-corrosion rate is

* Steel Research Laboratories, Chief Research Chemist, Ph.D.
20-1 Shintomi Futtsu Chiba Japan 2938511

unlikely.

Recently established concept toward durable bridge design using weathering steel

A bridge life was said about 50 years as a tacit comprehension so far. There was no engineering problem with the *antei-sabi* concept in such conditions since corrosion rate of weathering steel generally become slow enough to realize 50-year durability. However, according to the recently proposed minimum maintenance bridge conception by Japanese Ministry of Construction[3], bridge life was set to be more than 100 years. In order to cope with this situation, certain change in the paradigm of weathering steel became necessary because the physico-chemical nature of all the engineering materials including weathering steel cannot be ignored. After about four years of discussion at the Rust Chemistry Committee of Japan Society of Corrosion Engineers supported by Bridge Research Committee in the Kozai Club, a proposal as in Fig. 1 was made [4].

耐候性鋼さび安定化の定義(案)

Durable State Concept Proposed by JCSE Rust Chemistry Committee

耐候性鋼のさび安定化 (Durable State of Weathering Steel)

構造物耐荷重性能の経年劣化が工学的に問題とならない程度に腐食速度が低減（目安として0.01mm/y以下）した状態になること （=耐候性鋼構造物が長期耐久化しうる状態）。

"Durable state" **of weathering steel is defined by diminution of corrosion rate enough to realize long term structural stability. (It may be said as a guide line that *durable state* is established when corrosion rate of weathering steel become less than 0.01mm/y with that predicted corrosion loss at the end of structural service period is less than the designated value.)**

安定さび

(Antei-Sabi: This indefinite word was commonly used only in Japan, but no suitable term in English)

暫定的解釈として耐候性鋼が*「さび安定化」*したときに形成しているさび。ただし、*「さび安定化」*は上述のように状態を定義したものであるのに対し、安定さびという言葉が物質的イメージの強い用語であるため、学術的な使用を控えるのが望ましい。代替物質呼称には、保護機能の高いさびについて*保護性さび*という用語を用いる。

It is not reccomended to use the Japanese domestic indefinite word *antei-sabi* in international or academic communication. Instead, rust with corrosion protecting function should be called " *protective rust*"

さび安定化した時のさびの特徴 (Feature of rust in durable state)

十分な期間(5年以上)が経過しているにも関わらず、厚く成長していない。

Rust in durable state does not thickly grow even after prolonged period (say, more than 5 years) of exposure.

Figure 1. Durable state concept proposed by Japan Society of Corrosion Engineers, Rust Chemistry Committee on June 25, 2001 [4].

It is needless to say that the most essential message in this suggestion is the definition regarding *"the durable state"* of weathering steel. In order to explain this concept more in detail, typical penetration curves [5] of carbon steel, 0.3%Cu-steel, and weathering steel are shown in Fig.2 both in linear and log-log scales. According to the definition in Fig.1, in the case of weathering steel in linear plot, it can be said that durable state is established at about four-year exposure, where its

corrosion rate become less than 0.01 mm/year as shown in the slope of tangential line. On the other hand, in the case of carbon steel, although its corrosion rate becomes less than 0.01 mm/year at about 15 year exposure, durable state is not established since corrosion loss by that time is so large that structural stability by this material may not be realized. Also, it is important to notice from the log-log plots of the same data that corrosion rate does not become completely zero even after durable state is established. In addition to its slow corrosion rate, however, another important point for weathering steel is in the fact that futuristic corrosion loss can be predicted by the following equation[6];

$$Y = AX^B \qquad (1),$$

where Y is amount of corrosion loss (mm), X: period (year), A: a constant indicating the first year corrosion loss (mm), B: an exponent showing the extent of diminution of corrosion rate by protective rust formation. Note that nature of never stopping degradation is a fate not only for weathering steel but also for all kinds of engineering materials such as concrete, painted steel, plated steel, etc.

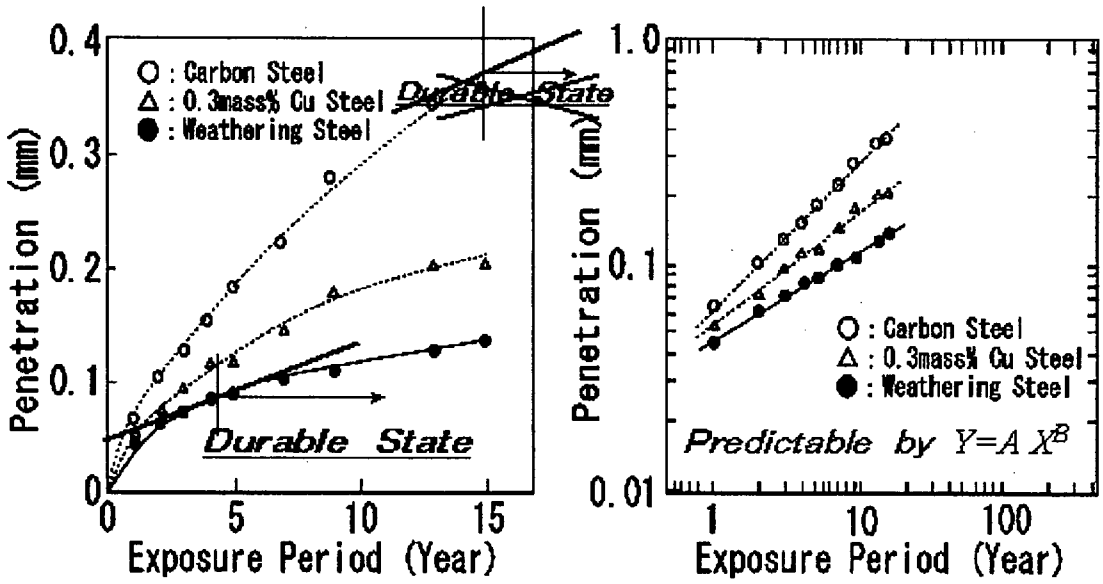

Figure 2. Typical penetration curves of carbon steel, 0.3Cu steel, and weathering steel exposed to an industrial atmosphere in linear and log-log scales for the explanation of durable state concept.

Based upon the above discussed nature of weathering steel, it can be said that the essence for durability design of bridges is to take into account the certain level of corrosion loss so that structural stability is surely maintained during the designated service period. In Japan, it was determined that bare conventional weathering steel (JIS-SMA type) is applicable to the location, where amount of air-born salt deposition is less than 0.05 mg/dm^2/day [6] measured by the method described in JIS Z 2381. According to the leaflet published by the Kozai club[7], maximum of 0.5

mm penetration is predicted on JIS-SMA type of weathering steel for one hundred years when used within the applicability limit mentioned above. Therefore, it is probably good idea to set the guideline for the durability design of weathering steel structures to the level of 0.5 mm corrosion loss for 100 years. Figure 3 shows the basic concept for durability design of weathering steel structures with corrosion loss to occur during prolonged service duration taken into account. They say that this level of penetration hardly affect the stability of steel beam bridges as far as design and construction obey the present Japanese authorized direction for road bridge design. Thus, it may be unnecessary to add corrosion margin to relatively thick weathering steel members when predicted corrosion loss is within this allowance [8].

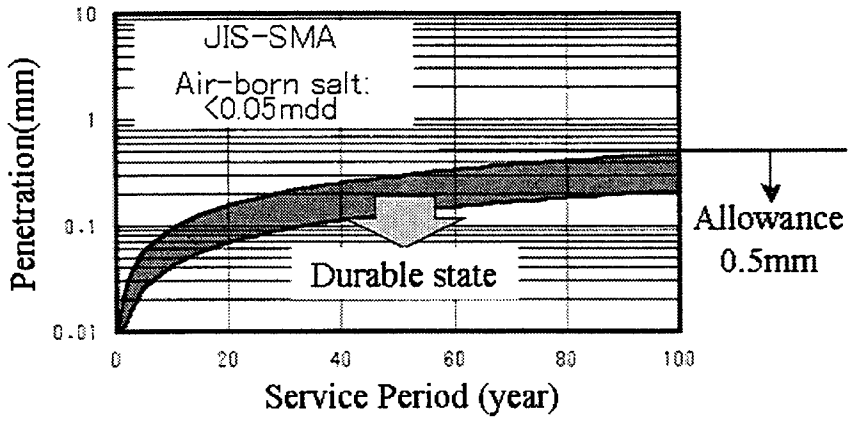

Figure 3. A basic concept for durability design of weathering steel structures based upon the predicted corrosion loss for prolonged period of service life. (Prediction data are after the Kozai Club's leaflet).

Innovation in weathering steel

Unlike in the U.S.A., Japan is island country surrounded by ocean. At the same time, Japanese relative humidity is generally higher than mainland America. Due to these differences in terms of atmospheric conditions, applicability of the conventional weathering steel is limited to much narrower region than originally expected. This in turn means that life cycle economy of conventional weathering steel cannot be realized in the coastal plain parts in Japan, where economic activities are concentrated. In order to extend beneficial effect of weathering steel to owners of structures, four steel makers in Japan already developed and commercialized new atmospheric corrosion resistant steels that can be roughly classified into three types as in Table 1. These steels are called coastal weathering steel to describe improved anti air-born salinity properties compared to the conventional one (JIS-SMA). Penetration curves for Type A steel compared with JIS-SMA are shown in Fig. 4 to show their performances. Generally to say, in the atmosphere including higher air-born salt, the corrosion resistance of steel is improved as the amount of nickel content is increased. Although published comparison data regarding corrosion resistances of the three kinds of new steels on the same test condition are not available now, the author believes that type A is the best. Of course like JIS-SMA steel, recently developed coastal

weathering steels has certain applicability limit in terms atmospheric conditions, which will be discussed later. Nevertheless, utilizing recently developed weathering steel will make it possible to extend applicability limit to the larger regions such as coastal plains in Japan.

Table 1. Classification of recently developed coastal weathering steels by chemical composition.

Type	Chemical Composition	Maker
A	*ca.* 3%Ni - *ca.* 0.4%Cu	Nippon Steel, Kawasaki Steel
B	1.5%Ni - 0.4 Mo	NKK
C	1%Ni - 1%Cu	Kobe Steel

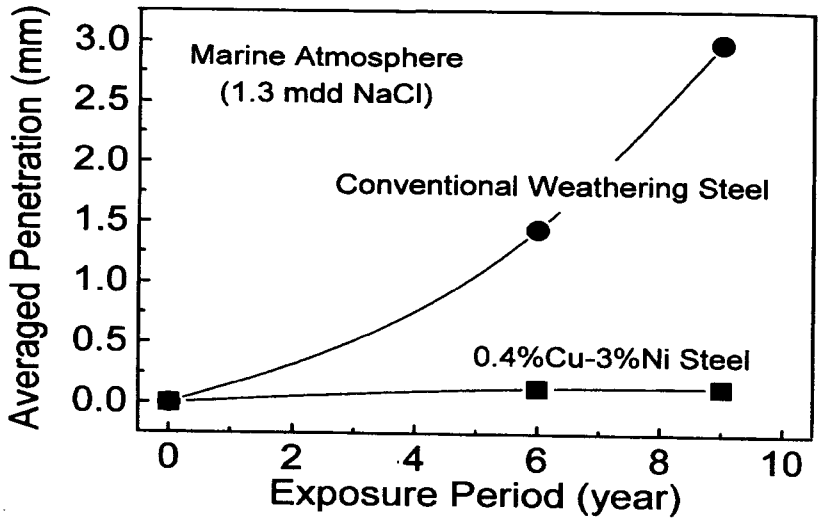

Figure 4. Penetration curves for type A (3%Ni-0.4%Cu) steel and conventional JIS-SMA type weathering steel exposed to the marine atmosphere at the wharf of Kimitsu City, Chiba, Japan, where amount of air-born salt level was measured to 1.3mg/dm^2/day (specimen set up: open vertical facing to ocean) [8].

Innovation in surface treatment

The concepts of surface treatments developed so far in Japan are classified in to two types. One is the treatment that accelerates *antei-sabi* formation by which corrosion rate might also be accelerated halfway[10]. The other is the treatment that diminish corrosion rate as much as possible by applying slowly degrading organic coating under which primer is put to facilitate steady formation of protective rust [11]. According to the durable state concept proposed by JSCE-Rust Chemistry Committee, it is needless to say that the latter concept for surface treatment is proper for durability design of weathering structures. Since the paradigm has been changed as above, surface treatment should be applied so that corrosion rate becomes as low as possible to realize the lowest life cycle cost. Schematic explanation of the proper concept for surface treatments was shown in Fig.5 [5], and its practicality is already proved by long-term exposure tests as in Fig.6 [10]. It may be said that the surface treatment that provides the slowest corrosion rate of weathering steel, to which

minor has been paying attention so far, is in turn recognized as a major tool for durability structure design for minimum life cycle cost.

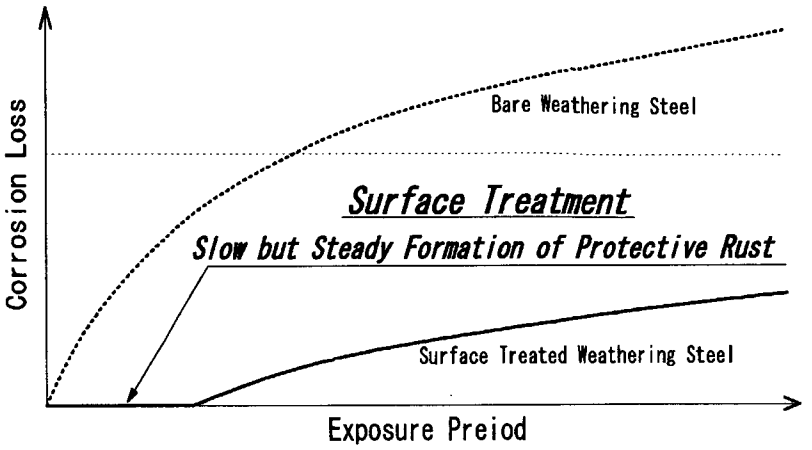

Figure 5. Schematic representation of proper concept for surface treatment on weathering steel

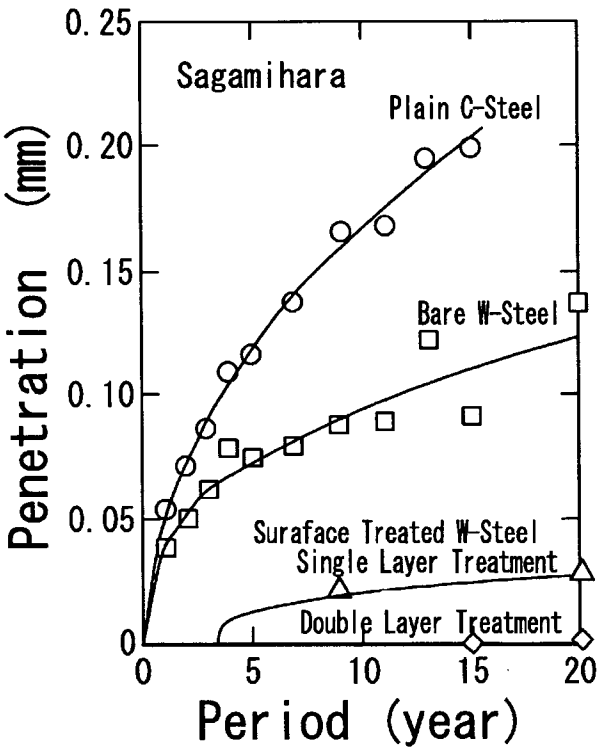

Figure 6. Penetration curves for plain carbon steel, bare weathering steel, surface treated weathering steels (single and double layer treatment). In the single layer treatment, only primer to steadily form protective rust was put on, while in the double layer treatment, slowly degrading organic coating was applied on the primer. It is considerable that the effect of the primer on to protective rust formation will reveal after complete degradation of the organic coating of the double layer treatment.

Development of corrosion prediction method for weathering steels

In addition to the recent materials innovation in weathering steel technologies, the author is taking a role to develop software to predict corrosion of weathering steels for 100-year span, utilizing the best knowledge at this moment in terms of relationships between environmental conditions and materials performances. The basic idea is from the concept as shown in Fig.7, namely whether durable state can be established or not is utterly dominated by severity of environmental corrosiveness. To obtain predicted penetration curves, one can use Eq. (1), where A and B values are unknown. However, having an eye to the first year corrosion loss, namely A value, which is in a sense an indicator of the severity of environmental corrosiveness, one can construct systematical schemes to estimate B value.

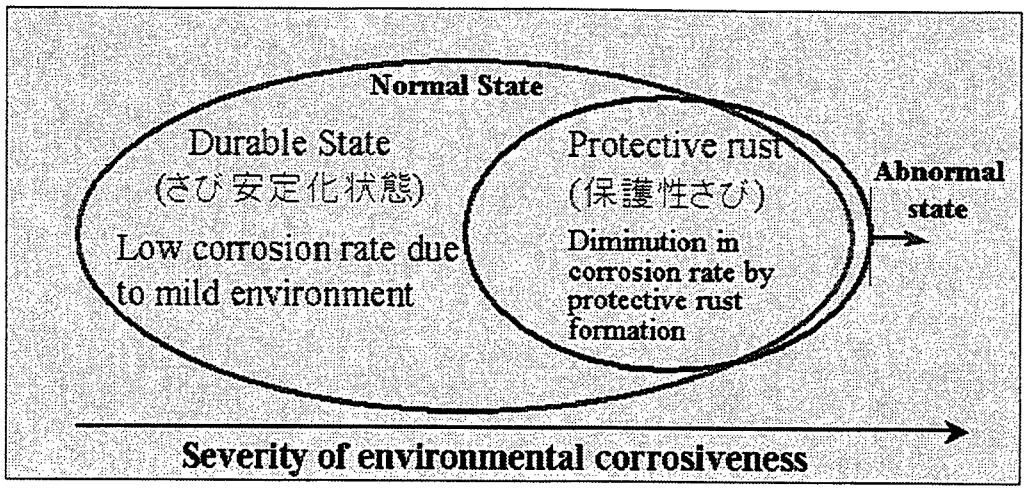

Figure 7. Schematic representation for the relationship among durable state and protective rust formation as a function of severity of environmental corrosiveness. When in mild environment, corrosion rate is too slow to form protective rust. While in medium environmental corrosiveness, corrosion rate could be reduced by protective rust formation facilitated by alloying elements in weathering steel. If severity of environmental corrosiveness exceeds applicability limit the weathering steel, anomalous corrosion could occur. Durable state is low corrosion rate state, in which protective rust formation is included.

The details of the computation schemes are bit too complicated to delineate in this paper, so it will be published elsewhere in due course. Nevertheless, It is theoretically possible to estimate A-value from environmental factors, then B value can also be assessed as above. Outline of the programmed system was shown in Fig.8, where input of mean temperature, mean relative humidity, mean wind velocity, amount of air-born salt, amount of sulfur oxides at a location, generates the output of time of wetness, z-index for corrosiveness of the atmosphere, and A and B values for JIS-SMA steels set-up vertically as well as horizontally. Ratios for A and B values in terms of 3Ni-0.4Cu steel vs. JIS-SMA are already available, so that all the information in terms of

Eq.(1) for JIS-SMA and 3Ni-0.4Cu steels became ready. Since it is general that sheltered exposure condition exhibits much more corrosion loss than open one, the prediction is carried out in the former condition. Some examples for so predicted penetration curves compared with the exposure test data obtained by 41-bridge exposure test project [4] carried out by the collaboration of PWRI, Ministry of Construction, Japan Association of Bridge Construction, and the Kozai Club, are shown in Figs.9-11. Hatched zone is the predicted corrosion loss calculated by the above mentioned program, while thickly dashed line is the measured corrosion loss with thin dashed line extrapolated according to Eq.(1). From these examples, it can be said that developed scheme for the corrosion prediction of weathering steel is working well. It was also confirmed that at most exposure sites in the 41 bridge exposure tests, measured penetration curves were within the predicted ranges as summarized in Fig.12.

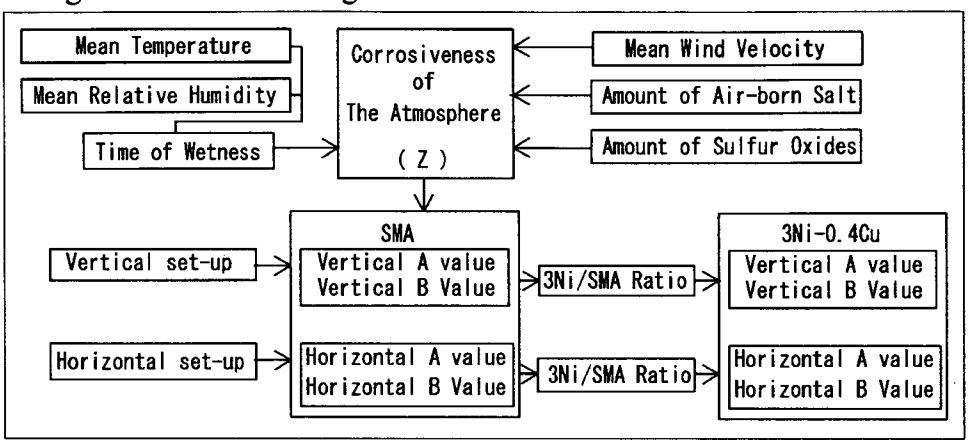

Figure 8. Block diagram of estimating A and B values in equation (1), using atmospheric factors regarding its corrosiveness

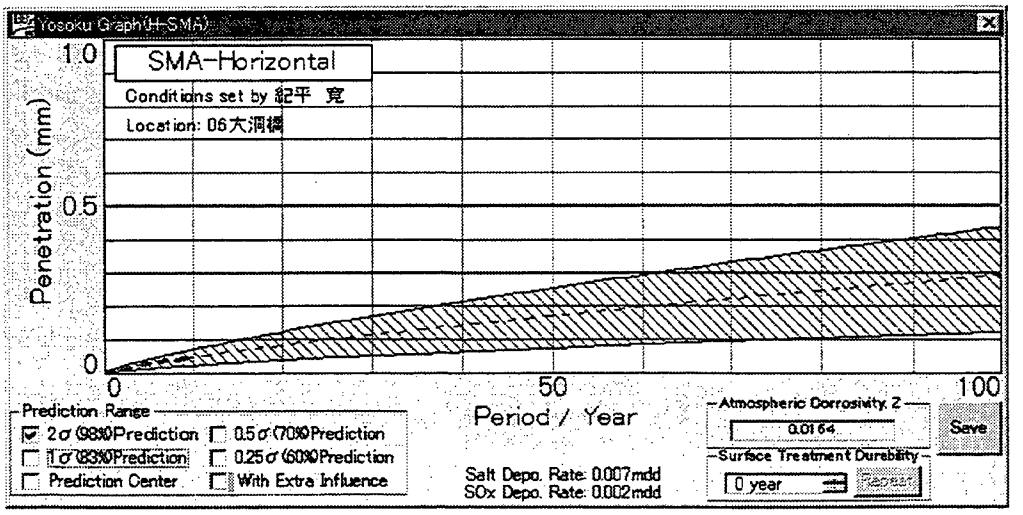

Figure 9. Comparison of calculated hatched prediction range with measured penetration represented by thick dashed line for JIS-SMA type of weathering steel exposed to a mild environment under Daido-bridge. (Thin dashed line: extrapolation of measured penetration).

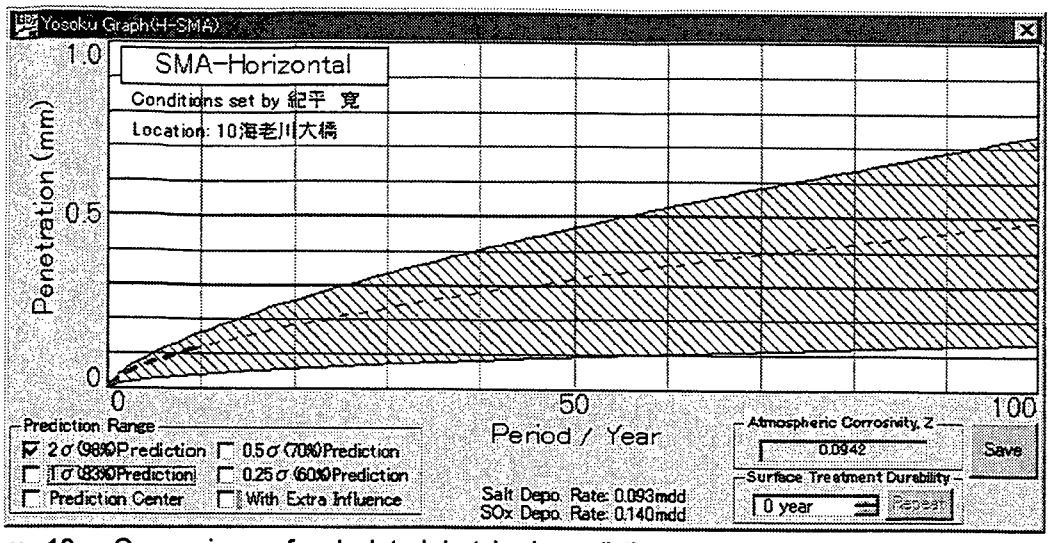

Figure 10. Comparison of calculated hatched prediction range with measured penetration represented by thick dashed line for JIS-SMA type of weathering steel exposed to a mild environment under Ebigawa-bridge. (Thin dashed line: extrapolation of measured penetration).

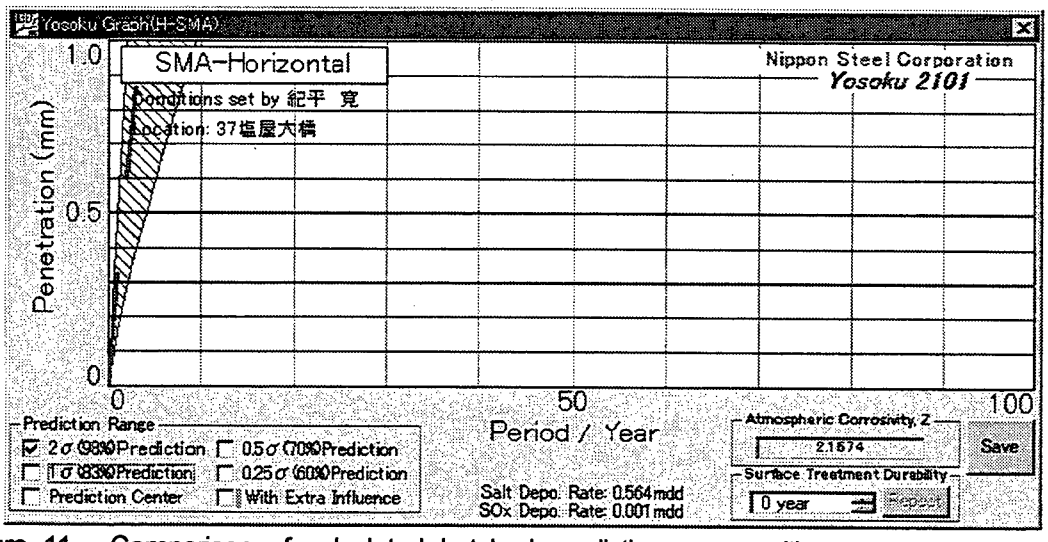

Figure 11. Comparison of calculated hatched prediction range with measured penetration represented by thick dashed line for JIS-SMA type of weathering steel exposed to a mild environment under Shioya-bridge.

Note that a few cases were out of prediction ranges probably due to inadequacy of environmental data. It is likely that reevaluation of environmental corrosiveness for these cases will shift the prediction to coincide with actual corrosion losses. Nevertheless, as far as settings of environmental conditions are in a proper range, the method developed here works in such a manner that actual penetration occurs according to normal distribution function in the predicted range as in Fig.12. Thus, considering the variances of environmental input factors, one can divide prediction band into several statistical ranges based on these analyses.

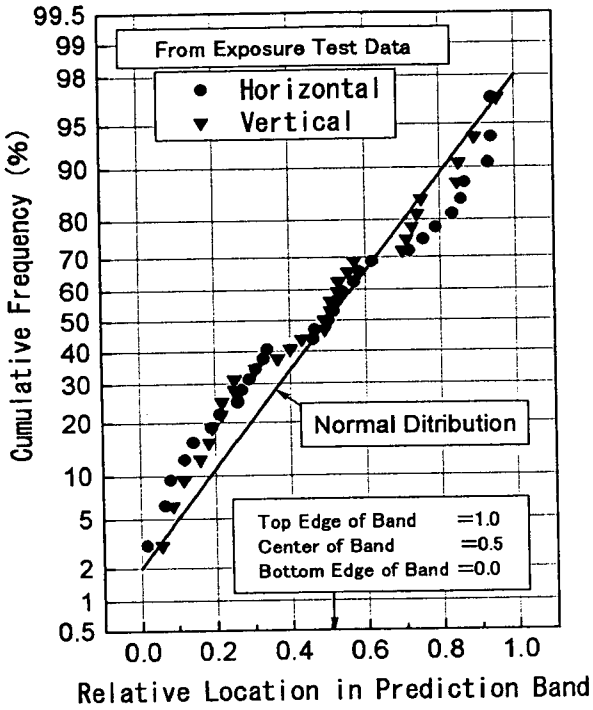

Figure 12. Statistical analyses of meaning of prediction band compared with measured corrosion data. Relative location of corrosion losses at 100 year predicted from 9 year exposure data by $Y=AX^B$ were plotted in probability diagram.

Model case simulation using the developed software

In order to demonstrate how to use the developed software, model case simulation was carried out. Figure 13 shows the input panel of this model case setting as Tokyo Bay Coast. Meteorological data can be easily set by database searching routine as shown in Fig. 14, where from longitude and latitude data it exhibits red tiny circle on the map of Japan. Since the closest meteorological center is Chiba, climate data are cited from the values at the site. For this model analyses, amount of air-born salt was set to be 0.10 mg/dm^2/day, and amount of sulfur oxides, 0.14 mg/dm^2/day. Calculated prediction penetration data for conventional weathering steel (JIS-SMA) in bare condition are shown in Fig.15, where one can recognize the possibility that penetration exceeds 0.5 mm allowance in the future is high. Applying of normal paint may deter the onset of steel corrosion. Thus assuming 20 years of degradation period for the paint film, one obtain the result as shown in Fig.16. From this data, one can judge that only initial application of normal paint is not enough to reduce corrosion loss at 100th year lower than 0.5 mm allowance. Therefore, as far as no treatment is devised for protective rust formation, repainting in the future may be requested as in Fig.17. In this case, certain maintenance budget should be prepared.

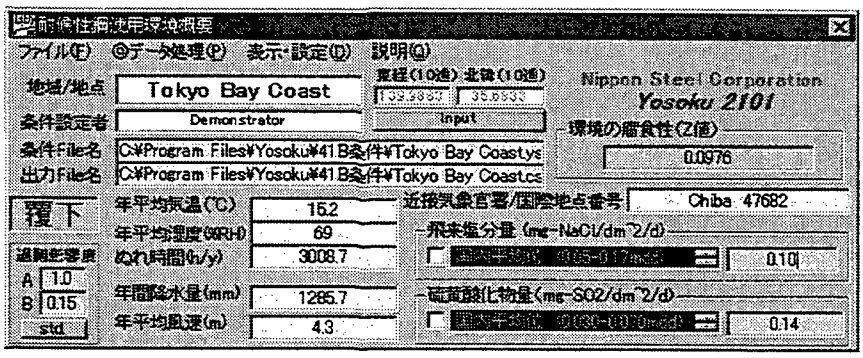

Figure 13. Input data panel for the prediction software, where model conditions for Tokyo bay coast are set. Mean temperature = 15.2℃, relative humidity = 69%, yearly rain fall = 3008.7 mm, mean wind velocity =4.3 m, amount of air-born salt = 0.10 mdd, amount of sulfur oxides =0.14 mdd. Time of wetness of 3008.7 h and z-value of 0.0976 were automatically calculated.

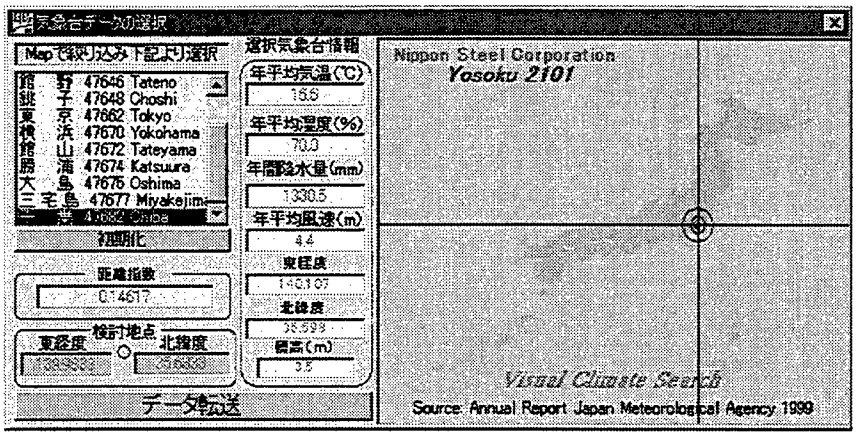

Figure 14. Visual meteorological data search tool attached to the software. Tiny red circle indicates the location of consideration given by latitude and longitude values. Crossing point of two lines indicates the location of meteorological center.

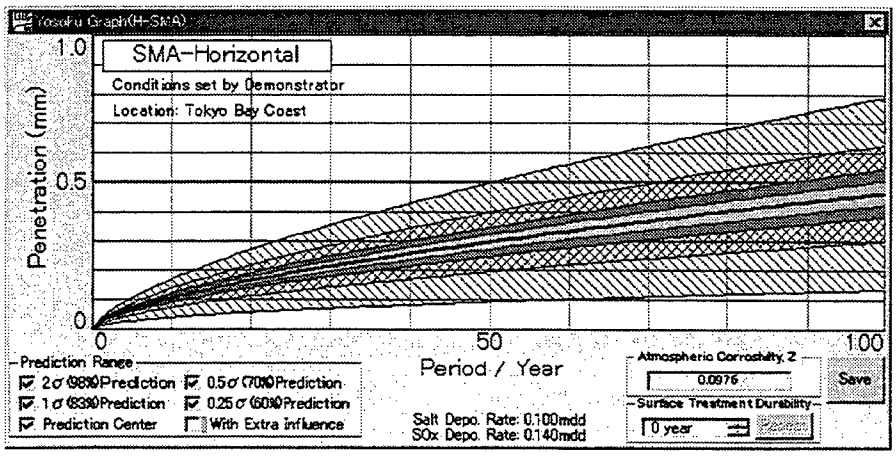

Figure 15. Model case corrosion prediction for JIS-SMA type of weathering steel used in bare condition. Prediction band is divided as to show statistical probabilities.

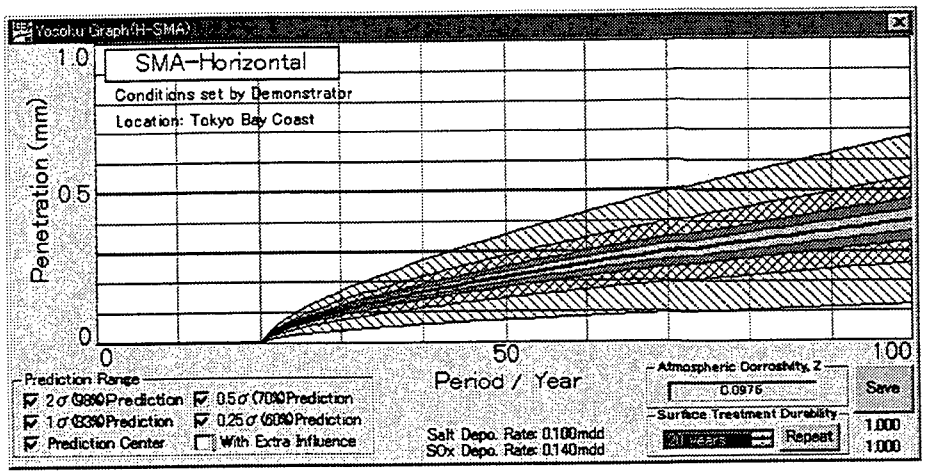

Figure 16. Model case corrosion prediction for JIS-SMA type of weathering steel used with normal paint treated condition.

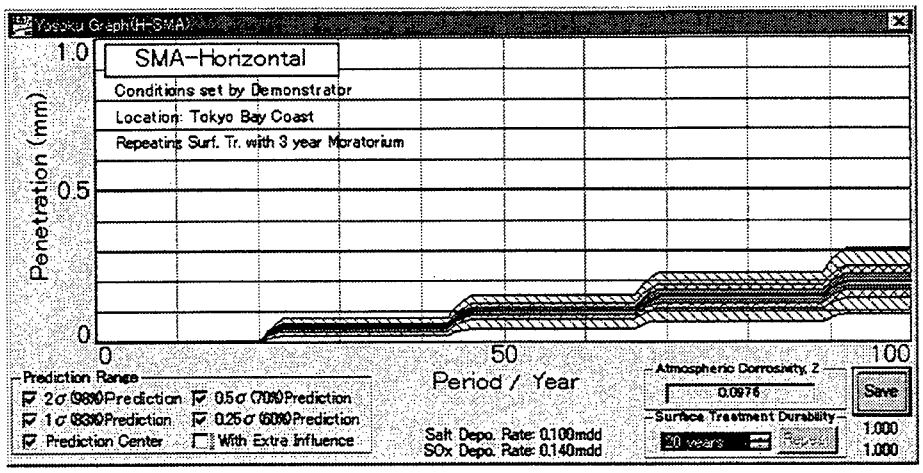

Figure 17. Model case corrosion prediction for JIS-SMA type of weathering steel used with repeating normal paint treatment.

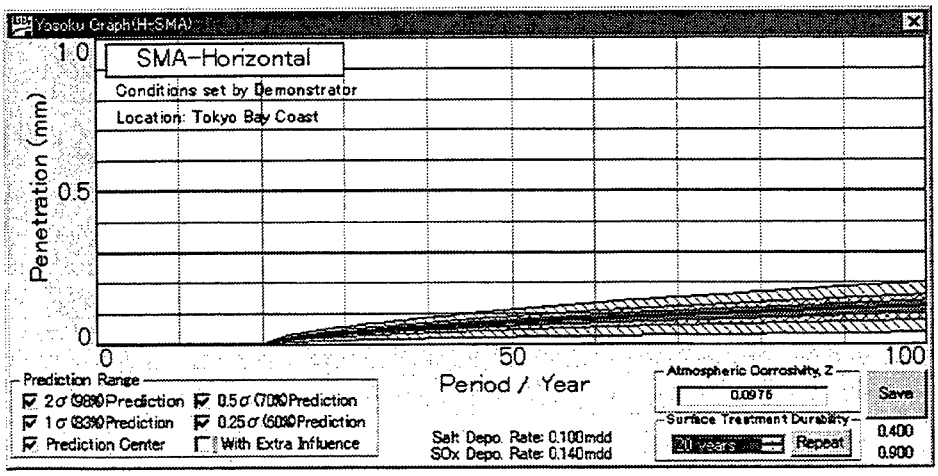

Figure 18. Model case corrosion prediction for JIS-SMA type of weathering steel used with a surface treatment especially designed for weathering steel.

If one applies the surface treatment for weathering steel, which facilitates protective rust formation after prolonged degradation period of organic top coating, predicted penetration curves result in Fig.18. In this case, due to the diminution of corrosion rate by protective rust formation at the end of organic coating degradation, the penetration during designated service period can be kept under 0.5 mm allowance. Note that degradation period for organic top coating was assumed to be 20 years in this model case, which is quite practical according to previous achievements in existing structures.

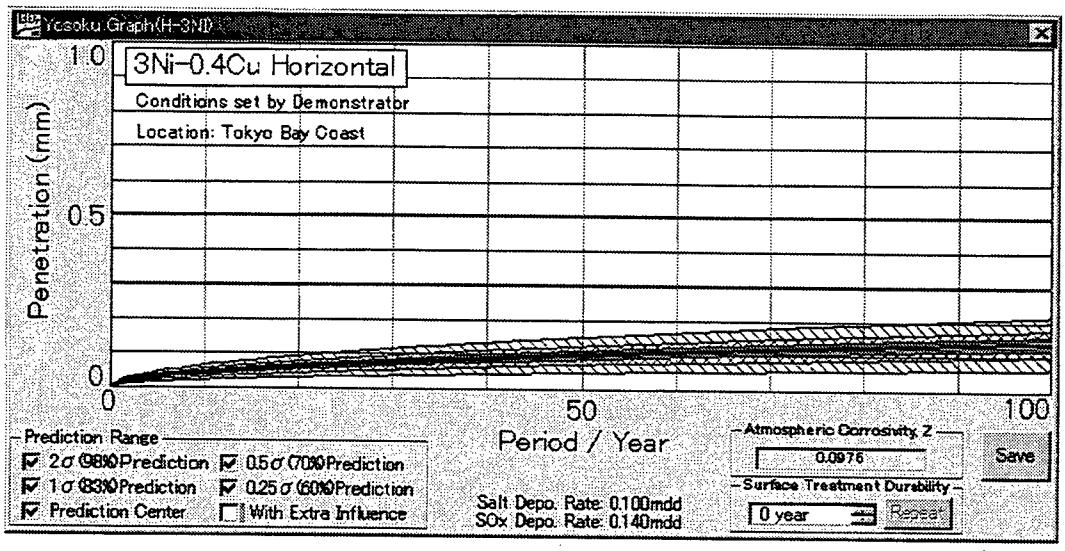

Figure 19. Model corrosion prediction for 3Ni-0.4Cu type of weathering steel used in bare condition.

If one adopt 3Ni-0.4Cu weathering steel, even without any surface treatment, penetration at the end of designated service period of 100 years will not exceed the allowance as predicted in Fig.19. This could be a sort of ideal application for this case.

As in these ways, one can design durable weathering steel structures using the prediction software at any kinds of atmospheric conditions. Until now, amount of air-born salt was the only criteria for judging the applicability of weathering steel. However, in fact, there are the other factors that affect corrosion rates of weathering steel. Since the method explained here takes them into account, more precise judgment is facilitated to increase success ratio in application of weathering steels to minimum maintenance structures.

Conclusion

1) Recently established durable state concept toward application of weathering steel was introduced. Definition of the concept was proposed by Japan Society of Corrosion Engineers, Rust Chemistry Committee, as shown in Fig.1.
2) Based upon the recently established concept for durability design of weathering steel structures,

technological advancements in terms of materials innovations were assessed. High Ni coastal weathering steels and surface treatments to reduce corrosion rate of the steel in drastic manner are evaluated as proper tools, while a surface treatment to accelerate *antei-sabi* formation is questionable since it may also increase corrosion rate of weathering steel to some extent.

3) In order to support minimum maintenance durability design of structures by use of weathering steel, computation software for corrosion prediction was developed. The outline and model case simulation using the software are demonstrated.

References

1) C.P.Larabee, S.K.Coburn: *1st International Congress of Metallic Corrosion (1959), Publ. "Metallic Corrosion,"* p276, Butterworth, 1971
2) H. Okada, Y.Hosoi, K.Yukawa, H.Naito, *Tetsu-toHagane*, **55**, 355(1969) [Japanese]
3) K. Nishikawa, *Doboku Gakkai Ronbunshu*: No.501/I29, 1(1994.10) [Japanese]
4) T. Ohtsuka, T. Misawa, *Proc. 132nd Symposium of Corrosion Science and Engineering*, "SABI [Rust] Chemistry on the Phase-III toward Realizing Minimum Maintenance Bridge Conception," Japan Society for Corrosion Engineers, (2001.June 25) [Japanese]
5) H. Kihira, A.Usami, S.Ito, T.Murata, *Electrochemical Society Proceedings* Vol.99-27, p112, (1999).
6) Public Work Research Institute - Ministry of Construction, KOZAI CLUB (Iron and Steel Mill Products Association), and Japan Association of Steel Bridge Construction: *Report on Application of Weathering Steel to Highway Bridges (XV) —Report on Nation-wide Exposure Test of Weathering Steel —* (1992.3) [Japanese].
7) The Kozai Club, Japan Association of Bridge Construction, *"Application of Weathering Steel to Bridges,"* (Leaflet published in 2000.8) [Japanese].
8) "Q. & A. on Application of Weathering Steel to Bridges," in *Proc. Symposium on Application of Weathering Steel to Bridges*, Tokyo Institute of Technology, p.60-61 (2001.4) [Japanese].
9) H. Kihira, A.Usami, K.Tanabe, M.Ito, G.Shigesato, Y.Tomita, T.Kusunoki, T.Tsuzuki, S.Ito, T.Murata, *Electrochemical Society Proceedings* Vol.99-26, p127, (1999).
10) H.Kishikawa, H.Miyuki, *Kagaku-to-Kogyo*, **51**(6), 905 (1998) [Japanese].
11) Y. Ito, S. Yamaguchi, K. Masuda, C. Kato: *Zairyo-to-Kankyo'98*, B-113, p63 (1998) [Japanese].

LONG-TERM REMORTE MONITORING SYSTEM FOR STEEL BRIDGES BY APPLYING FIBER-OPTIC COMMUNICATION NETWORK

Yuusuke KOBAYASHI[1] and Chitoshi MIKI[2]

[1,2] Department of Civil Engineering, Tokyo Institute of Technology

ABSTRACT—A working prototype system for long-term remote monitoring of steel bridges using fiber optic communication network has been studied. The high bit rate of fiber optic systems offers distinct advantages over conventional mediums of data transmission, and the high bit rate allows the transmission of raw data from the instrumented structure to the monitoring station. A bridge has been continuously monitored for more than a year, since April 2000 and raw data from the bridge have been transferred to the Bridge Engineering Laboratory at Tokyo Institute of Technology. The data is reduced and displayed in real time simultaneously in the remote station and at the field site. The collected data includes, dynamic strain for live load monitoring, temperature and strain for bridge deformation monitoring, and strain by using SMS. The weights of vehicles crossing the bridge are estimated by Weigh-In-Motion method and fatigue damage accumulation is being evaluated from measured.

INTRODUCTION

A working prototype system for long term remote monitoring of steel bridges using fiber optic communication network has established and applied to assess the health evaluation. The fiber optic communication cables used in this system was laid on for 10,000 kilometers along National Highway in Japan, and it will be extended for about 300,000 kilometers in the future. The fiver optic communication can transmit a great deal of measurement data comparing with a telephone circuit such as ISDN (Integrated Services Digital Network), PHS (Personal Handyphone System) and the cellular phone, as shown in **Table 1**. Therefore, with the system proposed in this study, the raw data are transmitted from the instrumented structure to the monitoring station. In this way, the experts in remote station can reduce the raw data as necessary to obtain an accurate representation of the real-time and evolving condition of the structure. Conversely, on-site preprocessing of the raw data requires a-priori assumptions regarding the condition of the structure, as shown in **Fig.1**.

With this system, a bridge has been continuously monitored for more than a year, since April 2000. The measured data at the bridge have been high speedily carried to Bridge Engineering Laboratory at Tokyo Institute of Technology (T.I.T.) and visualized simultaneously on the screen of the workstation as in field measurements. In addition, some parts of data are analyzed. The data collected for this proof of concept study includes, dynamic strain for live load monitoring, temperature and strain for bridge deformation monitoring, and strain by using SMS.

Table 1 Bit rate of telephone circuit

means of communication		transferring rate
modem		57.6 kbps
ISDN		64kbps～1.5Mbps
PHS		64kbps
cellular phone	PDC	9.6kbps
	CDMA	14.4kbps～64kbps
	IMT-2000 (W-CDMA, CDMA2000)	144kbps～2Mbps
fiber-optic communications network used in this study		6.2Mbps

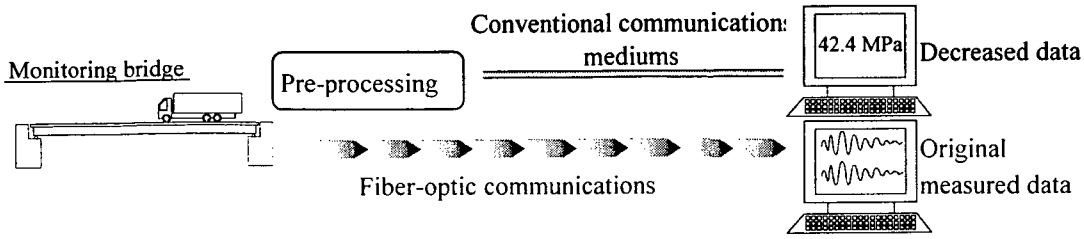

Fig.1 Remote monitoring system

MONITORING BRIDGE

The monitoring bridge was chosen for four conditions; fiber optic communication network has been laid, the bridge is located in a route with heavy traffic condition, the bridge is weld steel girder structure, the span is short. The monitoring bridge namely Osaka-bridge is located at the intersection of National Route 246 and Yamate road in Tokyo. This bridge was constructed in 1964. The bridge consists of 18 main girders with 35 meters span length. It has 40 meters width of RC deck that provides 8 lanes roadway. The plane and cross section of the bridge is shown in **Fig.2 (a), (b)**.

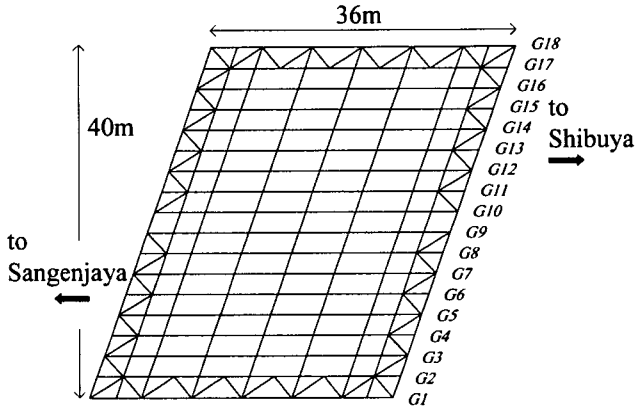

Fig.2 (a) Plane figure

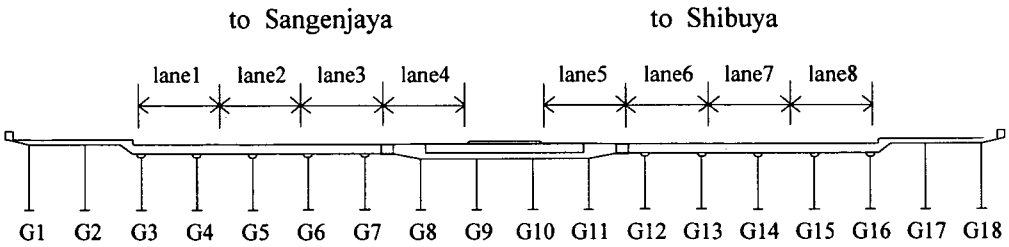

Fig.2 (b) Cross section

CONSTITUTION OF THE MONITORING SYSTEM

Dynamic Strain For Live Load Monitoring

In this monitoring, the dynamic strain due to the live load has been measured. The strain gauges were installed at the center span of the lower flange of the main girders G4-G7, G12-G15. The type and weight of the large-sized vehicles passing on the bridge have been monitored by analyzing the measured strain with Weigh-In-Motion (W.I.M.) method. In order to detect the velocity of the vehicle used in analysis of W.I.M., the strain gauges also installed at two upper side of the stiffener of end span. Furthermore, in this monitoring, fatigue damage has been calculated from the measured strain.

Temperature And Strain For Bridge Deformation Monitoring

Deformation due to temperature change may become indicator for bridge conditions. The extent of the response by temperature is larger than the other responses by external force subjecting the bridge such as live load, so it is easy to measure the responses. The strain gauge and the thermocouple were installed at center span of the lower flange of the main girder G1 in the sun side of the bridge. To understand the relation between temperature and strain is the target in this monitoring.

Peak Strain By Using SMS

Peak strain memory sensors[1)] are used in this monitoring in order to record the occurrence of unusual events such as earthquake and collisions of the vehicle. This sensor can memorize peak strain as shown in **Fig.3**, by using special metal. This metal has the nature to be able to memorize a change of impedance value of material after the deformation occurred in a sensor part. These sensors were installed at the movable bearing and at the center span of the lower flange of main girder G5.

The sensors installed at the monitoring bridge and their locations are summarized in **Table 2**. All of sensors and instruments need high durability for long-term monitoring. Waterproofed strain gauges were installed by spot welding in order to let the durability improve largely. All of sensors are protected with the metal box so that they are not hurt by the bird, mouse, and others. In addition, the wires are protected by passing through the inside of a metal pipe, and it is laid underground from the foot of Osaka-bridge to a measurement hut. Communications, control, measurement machineries were arranged in the measurement hut, which is located in tree planting zone at roadside. Moreover, indoor temperature in the measurement hut has been controlled with an air-conditioner, because the machineries may break down in high temperature.

Measured data have been transmitted to Bridge Engineering Laboratory at T.I.T. by way of Tokyo National Road Office with fiber optic communications network for the road management. Since the fiber for the road management is not laid from the middle to T.I.T., at that part, the fiber for commerce (TTNet) is used. At the laboratory of T.I.T., communication route is connected directly to the workstations. There are two workstations at the laboratory. One is for receiving the transmitted data and display of the data, and another is for analyzing the data.

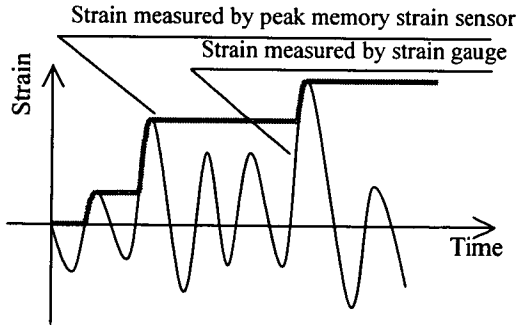

Fig.3 Data by peak strain memory sensor

Table 2 Locations of sensors

Sensor	Girder	Installed location
strain gauge (for live load)	G4-G7, G12-G15	lower flange of main girder at center span upper side of vertical stiffener at end span
peak memory strain sensor	G5	lower flange of main girder at center span movable bearing
thermocouple	G1	lower flange of main girder at center span
strain gauge (for bridge deformation)	G1	lower flange of main girder at center span

DATA PROCESS

Fig.4 shows the flow of the data process in this monitoring system. Static data, such as the strain and displacement data by the peak memory strain sensor, strain and temperature for deformation of the bridge, have been measured once for 30 minutes and transmitted to the laboratory immediately after the measurement. Then, the carried data are displayed on the monitor of the workstation at the laboratory and saved to the hard disk.

Dynamic strains for live load monitoring have been obtained at sampling frequency of 200 Hz at the monitoring bridge. However, if all of the measured data have been transmitted to the laboratory, workstation has not been able to store with all of the data. Also, to carry the large amount of the data loads hard work of the network, and it makes the system unstable. In this system, the data have been transmitted by the two ways, shown in **Fig.4**. The data flow of right side in **Fig.4** purposes watching the wave pattern of the strains in real-time at the laboratory, another flow of mid in **Fig.4** purposes calculating loads of the vehicle passing on the bridge.

In the analysis, the weight of large-size vehicles is calculated from the measured strain by W.I.M. method. Then, this system has the function to store temporarily the hard-disk at the field with the strain data for 5 seconds, after the strain exceeds the set value of 70 micros corresponded to the vehicle of around 10 tons. Temporary saving the data in computer at the field purposes preventing the data from being gone when the network breaks down. The saved data have been forwarded to the laboratory immediately after saving so long as network is not busy. As soon as the data get to the laboratory, weight of the vehicle is calculated from the transmitted data with the workstation for analysis use, and that results are displayed on the monitor of the workstation. Afterwards, only results are stored, and the 5 seconds data are deleted.

In the laboratory, the wave patterns of the dynamic strain are possible to visualize simultaneously on the screen of the workstation as in field measurements, as shown in **Fig.5**. For the display of the wave patterns, the amount of data with frequency of 200 Hz is not necessary. Therefore, the reduced data are transmitted to the laboratory after the data are shined out at the field. A series of these data flows is processed automatically.

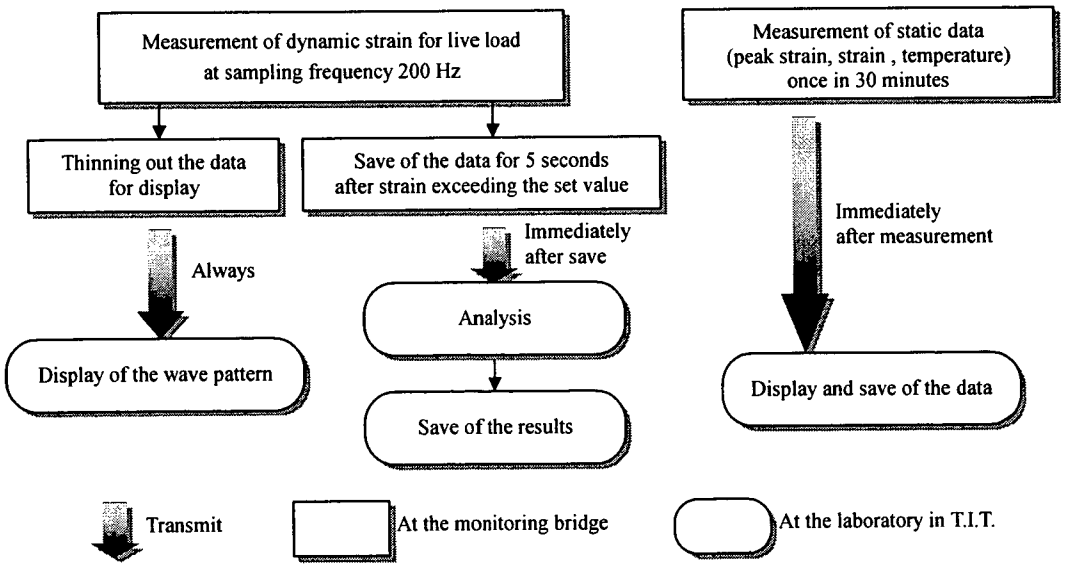

Fig.4 Data process

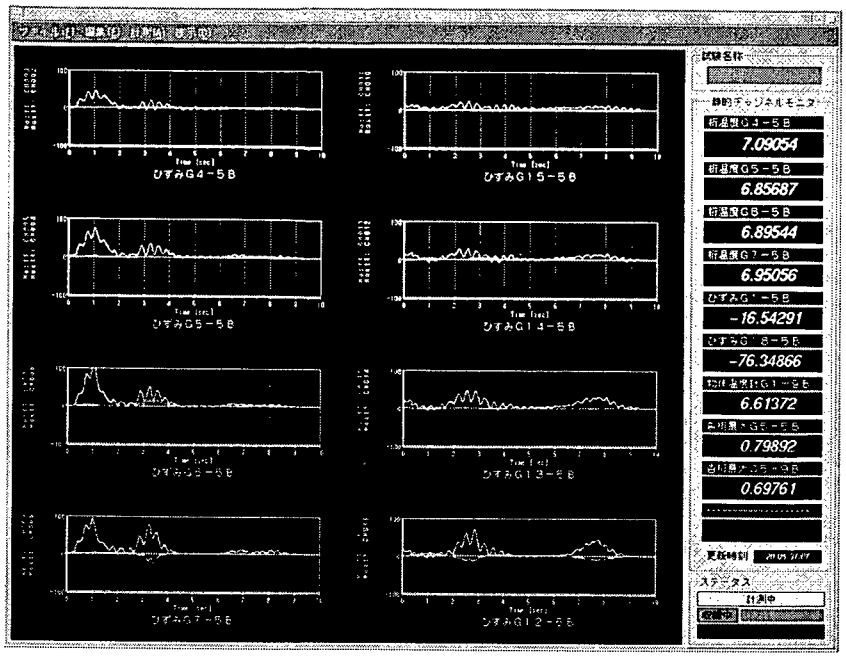

Fig.5 Screen of the workstation

ANALYSIS OF VEHICLE WEIGHT

The various analyses are done from measured data. This section addresses analysis of vehicle weight by method of Weigh-In-Motion (W.I.M.)[2),3)].

Pre-edit Of Data

The measured dynamic data of strain for live load have been transferred to the laboratory at T.I.T.. This dynamic data contains large noise in high frequency. At first, the data is passed through low-pass filter on purpose to remove the noise. In this system, composite more than 20 Hz is removed from dynamic data.

Weigh-In-Motion Method

When a vehicle passes on the bridge, vehicle weight generates strain at member subjects of the bridge. The strain at lower flange of main girder i can be represented as the function of influence lines in term of time t that is calculated beforehand by the calibration test. Considering influence of a vehicle weight A_n passing on the bridge, value of strain $\varepsilon_i(t)$ at lower flange of main girder i is represented as following equation.

$$\varepsilon_i(t) = \sum_{n=1}^{Na} A_n \cdot I_{ni}(t) \qquad (1)$$

where Na is the number of the vehicle passing on the bridge, $I_{ni}(t)$ is value of strain influence line of measure point i at position of vehicle n at time t.

Square-sum E of difference calculated value of strain $\varepsilon_i(t)$ and measured value of strain $\varepsilon_i^*(t)$ is represented as following.

$$E = \sum_{i=1}^{Ng} \sum_{j=1}^{Nt} \left[\varepsilon_i(j\Delta t) - \varepsilon_i^*(j\Delta t)\right]^2 \qquad (2)$$

where Nt is the number of total sampling of the strain data, Δt is sampling time interval of the strain data, Ng is the number of measurement point of strain. A_n can be calculated from this equation by the method of least square.

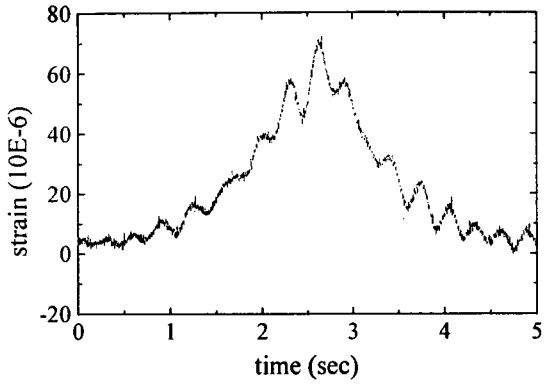

Fig.6 Measured data of the calibration test

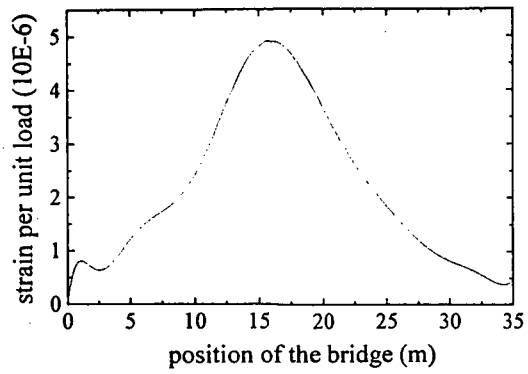

Fig.7 Influence line

Calculation Of The Influence Lines

The influence lines needed for analysis were calculated from variation of strain by calibration test. The influence lines can be also calculated by structural analysis of the bridge. However, they don't correspond to the actual influence lines of the bridge because of various assumptions.

In analysis of this system, curve of the influence lines are approximated to following polynomial $f(x)$. The calculated value of strain $\varepsilon(t)$ is represented as following equation.

$$f(x) = a_0 + a_1 x + a_2 x^2 + \cdots + a_m x^m + \cdots \quad (3)$$

$$\varepsilon(t) = P_1 f(x_1) + P_2 f(x_2) \quad (4)$$

where P_i is the load of axle i, x_i is the distance of axle i in axis from beginning of the bridge at time t. a_m can be calculated from this equation by the method of least square. In analysis of this system, m is equal to 13.

The sprinkler trucks which tank was full of water were used as test vehicle in this calibration test. The weight of the front axle is 3.10 ton while the rear axle is 9.25 ton. Since the bridge could not be closed to the traffic, the test was done in the night in order to avoid the effect from the traffic vehicles. The truck run on each lane two times, and the influence lines were made on every lanes. The measured strain data at lower flange of main girder G14 by the test running is shown in **Fig.6**. The influence lines of lower flange of main girder G14 when the traffic vehicle runs on lane 7 is shown in **Fig.7**.

RESULTS OF MONITORING

The bridge has been monitored since this system was completed in March 2000. In this section, the data collected up to now are addressed.

In the live load monitoring, the strain data of the vehicle load more than 10 tons have been measured. This paragraph presents about the results more than 20 tons, which load was illegal in specifications for highway bridges when Osaka-bridge was constructed. **Fig.8** shows the histogram of the average daily number of the vehicle according to each class of the weight, about April, July, August 2000, and January 2001. Since the same tendency could be shown in each figure, it was confirmed that this system could have monitored the bridge stably unless the traffic volume changed. The average daily number of the vehicle of November 2000 according to the lane are shown in **Fig.9**, and according to the time (o'clock) are shown in **Fig.10**. From these results, we could perceive characteristics of the traffic on the Osaka-bridge. Moreover, the evaluation of the fatigue damage at mid span of the lower flange of the main girder have been carried out, by using the stress range histogram obtained with rain flow counting method. Type E is adopted as strength category of the welded joints, that type is described in Fatigue Design Recommendations for Steel Structure by JSSC[4]. The results in the period from April 1 to December 31, 2000 are shown in **Table 3**. From this result, since fatigue damages were very small, it was understood that there was no problem about the fatigue damage in these locations.

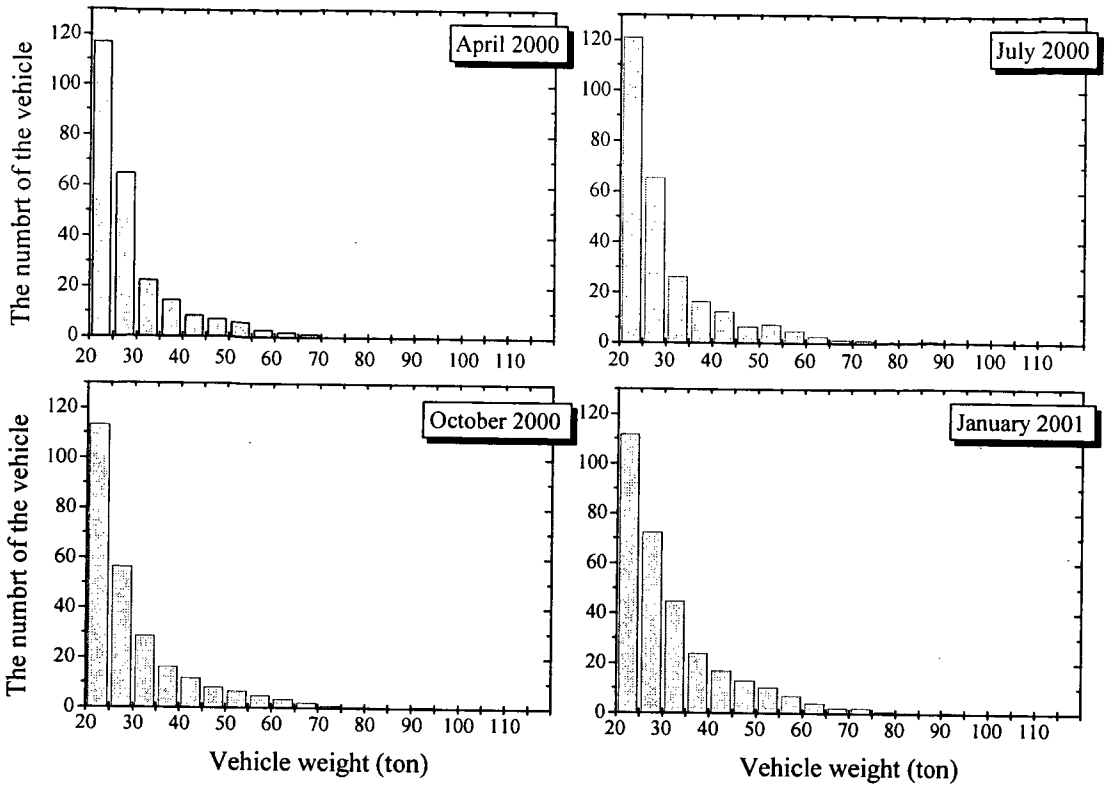

Fig.8 The average daily number of the vehicle according to each class of the weight

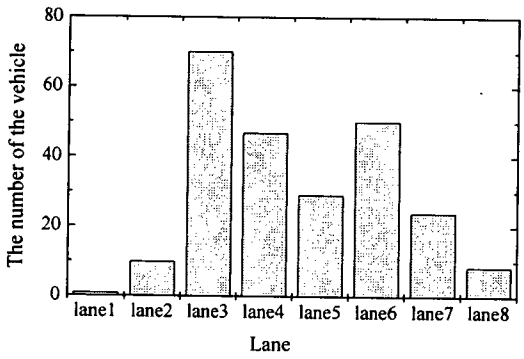

Fig.9 The average daily number of the vehicle according to the lane

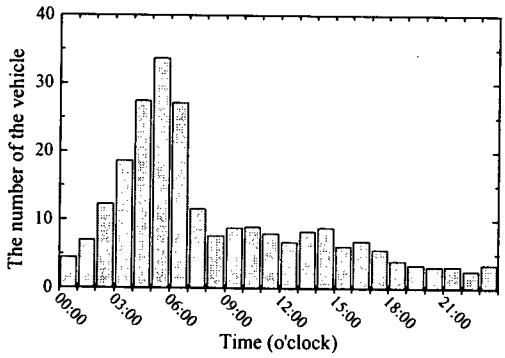

Fig.10 The average daily number of the vehicle according to the time

Table 3 Fatigue damage

Girder	Equivalent stress range (MPa)	Fatigue damage
G4	39.3	2.03E-05
G5	41.0	8.73E-05
G6	38.2	2.77E-04
G7	35.1	1.50E-04
G12	37.4	1.11E-04
G13	39.7	2.26E-04
G14	39.7	1.86E-04
G15	39.8	5.51E-05

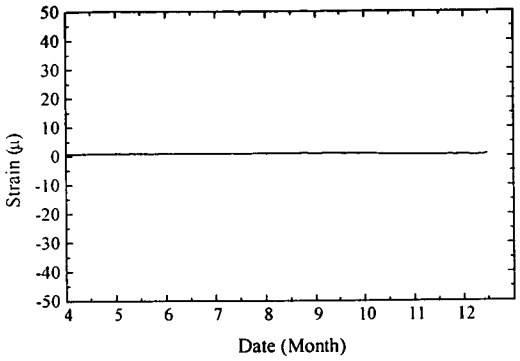

Fig.11 Peak strain at mid span of G5

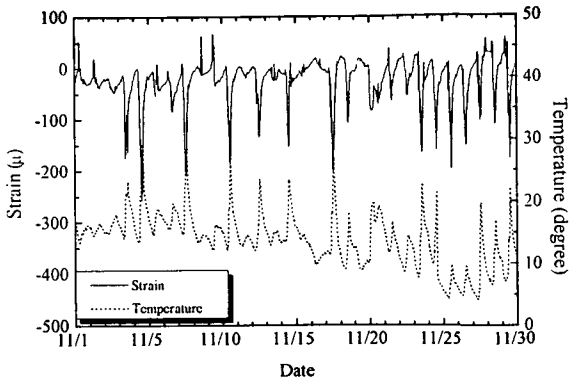

Fig.12 Relation between temperature and strain at mid span of G1

The result from peak strain sensor installed at mid span of G5 is shown in **Fig.11**. Because the peak strain didn't fluctuate, it was confirmed that unusual events such as powerful earthquake didn't occur. The result of the strain and temperature at mid span of the main girder G1 is shown in **Fig.12**. The strain was generated in direction to compression by temperature increasing, and it was found that there were big relation between strain and temperature. It was considered that the compressive strain were measured because of the fixation of the movable bearing, restraint by the structural system such as the cross beams, and bend deformation of the main girder due to temperature distribution in cross section.

Durability of the monitoring system is very important. It will be studied in future monitoring that this system works properly without maintenance. Up to now, the installed sensors function well, however, one of the machineries in the measurement hut was out of order. It was considered as cause that much dust entered the measurement hut for one year of monitoring because the hut was beside traffic road. For the measures, inside of the hut cleaned up, and airtightness was improved.

SUMMARY

A remote monitoring system for steel bridges has been established by applying fiber-optic communication system. The weight of the large-sized vehicle passing on the bridge were calculated the next instant with Weigh-In-Motion method, and evaluate the fatigue damage. The Osaka-bridge has been monitored since March 2000 and the followings were confirmed: characteristic of the traffic and fatigue damage due to the large-sized vehicle, no hit of earthquake and collision of the vehicle on the bridge in this monitoring period, relation between the strain and temperature at mid span of the lower flange of the main girder.

REFERENCES

1) Paul E.Grayson, William Law, Larry D.Thompson, "Not Your Father's strain gauge", *ASCE*, Vol.58, No.7, pp.68-71, 1998.
2) Fread Moses, "Weigh-In-Motion System Using Instrumented Bridges", *ASCE*, Vol.105, No.TE3, pp.233-249, 1979.
3) Chitoshi Miki, "Measurement of Weight of Running Vehicle", *Bridge and Foundation Engineering*, Vol.21, No.4, pp.41-45, 1987.
4) Chitoshi Miki, "*Fatigue Design Recommendations for Steel Structures*", JSSC.

Breakout A1: BRIDGE MANAGEMENT 1

(1) A Summary of Current Bridge Management Research of the Federal Highway Administration

(Steven B. Chase)

(2) Pontis 4.0 - A Next Generation Bridge Management System

(William E. Robert and Allen R. Marshall)

(3) Current State and Revise Policy of the PWRI Bridge Management System

(Nobuyuki Hirahara and Akira Moriyama)

(4) Preservation, Improvement and Natural Hazard Considerations in Bridge Management Systems

(Edgar P. Small)

(5) Maintenance and Management of Bridges in the Metropolitan Expressway

(Tadashi Yoshikawa)

A Summary of Current Bridge Management Research of the Federal Highway Administration

STEVEN B. CHASE[1]

Abstract

The Federal Highway Administration's (FHWA) Office of Infrastructure Research and Development is the center of highway research activity for the Federal government. Research is conducted in many high priority topics on one of the most important is in the area of bridge management. The FHWA created the Bridge Management Information Systems (BMIS) Laboratory in 1995 to serve as a focal point for this important research topic. This paper summarizes some of the most significant research conducted by the BMIS Laboratory over the last seven years.

BACKGROUND

The safety of the nation's bridges is an issue of great concern. It has been widely discussed that more than 40% of the nation's bridges are either structurally deficient or functionally obsolete and in need of maintenance, repair, rehabilitation, improvement or replacement. Pertinent research to better understand bridge deterioration patterns and related activities is therefore easily justified. Inventory and inspection data have been collected on the bridges within the United States and maintained in databases (National Bridge Inventory databases) over the past 26 years. This information represents a significant resource for examination and evaluation of the U.S. highway bridge population. In addition, the Bridge Management Information Systems (BMIS) laboratory at the Federal Highway Administration has collected and maintained a database of environmental and natural hazard data using GIS technology. These include climatological, hydraulic/hydrologic, geotechnical and seismic data. Both the NBI and the environmental data are stored within a relational database structure which helps provide a comprehensive data source for detailed analysis and research. With the establishment of the two databases, the BMIS laboratory has initiated research in advanced analysis of the NBI data sources. Studies performed have focused on an investigation of the correlation between the bridge conditions and environmental information. Insight obtained through these and other studies may enable more effective and efficient design and management of bridges. Some of the research activities by the BMIS laboratory are summarized in this paper. The procedures utilized in the establishment of the environmental and natural hazard database are outlined. Descriptive statistical summaries resulting from the exploration of the NBI are also presented. Development of regression models for predicting condition ratings of bridges has been discussed and the models have been presented. Three different regression models, which include a linear model, a non-linear parametric model and a non-parametric model, were developed. Generalized linear and generalized additive modeling procedures were used in the development of the regression models. The explanatory variables used include age of bridge, average daily traffic, precipitation, frequency of deicing, temperature range, freeze thaw cycles and type of bridge construction. The linear model gave the best prediction results. A summary and an outline of future research directions conclude the presentation.

[1] Technical Director for Bridges, FHWA Turner-Fairbanks Highway Research Center , 6300 Georgetown Pike, McLean, VA, USA, 22101-2296

DATA DEVELOPMENT

The environmental and natural hazard database was primarily developed using GIS tools. An essential step was the development of a spatial data layer for the bridges in the National Bridge Inventory (NBI) database. The NBI database is the repository of information on the composition, location and condition of all bridges in excess of 20 feet located on public roadways. The information on the bridges is collected by States and bridge owning agencies as part of the comprehensive bridge inspection program established about 30 years ago. This information is reported to the Federal government and stored within the National Bridge Inventory (NBI) and is primarily utilized for fund apportionment and cost allocation. In the subsequent paragraphs, brief descriptions of the procedures used in the development of the bridge data layer and the database elements are described.

Spatially Locating Bridges

The objective of this phase of the research was to create a spatial layer in the GIS system where each bridge is represented as a point in vector space. In turn each point maintains the related NBI structure number to allow for relational linkage back to the NBI database attributes. Difficulties arise in assigning accurate vector space locations due to errors and lack of data. Methodologies and GIS procedures were developed and implemented to assign bridges a spatial location, which is then used to associate structures with environmental and natural hazard information.

The NBI [Coding Guide] provides three location references for each structure:

1. Location description,
2. Inventory Route and Milepoint,
3. Latitude and Longitude in degrees and decimal minutes.

The Location field contains a narrative description of the bridge location. This does not lend itself well to automation or assignment of a location within the spatial environment of the GIS. The Inventory Route and Milepoint fields in the NBI provide more useful information. To utilize these fields for assignment of locational attributes requires definition and development of GIS spatial highway networks with the fully developed Linear Referencing Systems (LRS). The fully developed LRS network has Inventory Route and continuous mileage designations attached along the graphical highway network. The National Highway Planning Network Version 2.02 (NHPN) provides this information with a spatial highway network and LRS developed for most states. LRS definitions utilized in the NHPN are defined and reported by State DOTs. Geo-coding bridges to the NHPN using the LRS method revealed good support and accuracy for bridges on higher functional class roads (such as Interstates), but fair to poor support for bridges on lower functional classifications. The capability to locate structures located along non-state-maintained or local roads is not available using LRS systems at this time due to lack of data.

The use of latitude and longitude is an obvious consideration for a study of this nature. However, it was known from other GIS efforts that these coordinates were often difficult to correlate spatially with reasonably accurate GIS spatial data (for example, data collected at 1:100,000 scale). We found that approximately 28 percent of all bridge records lack a valid non-zero number for the latitude and longitude fields. Structures with seemingly valid latitude and longitude coordinates were then reviewed. Using the specified coordinates, it was found that approximately 2 percent of the structures were spatially located outside of

the designated county indicated within the NBI record. These spatial attributes were deemed unreliable and the designated county codes were then used for assignment of the structures within the GIS. The county GIS layer used for this evaluation was taken from USGS 1:100,000 scale data with an estimated positional accuracy of better than 150 feet on the earth's surface. This provides more than adequate accuracy for the research performed.

Further examination was performed to locate structures within the GIS. The NBI latitude and longitude field values and the designated Inventory route were compared, spatially, to the NHPN and its inventory route designations whenever route designation could be related between the NBI and the NHPN. Where route matches could be found, 98 percent of the bridges were located within 2 miles, as measure perpendicularly, from the specified NHPN route. Further review of these matches revealed that Interstates comprised the majority of the successful route identifier correlations. A similar exercise was undertaken using the Census TIGER network. Route identifiers could not be related between the NBI and the TIGER files due to a lack of standard route identifier nomenclature. From this work we determined that approximately 30 percent of all latitude and longitude locations provided in the NBI are invalid or sufficiently inaccurate to be used as a better measure of location than the NBI county designation.

Creating GIS Spatial Data from Environmental and Natural Hazard Data

Disparate data sources were required in order to correlate deterioration patterns with external variables, such as precipitation, snowfall, temperature, etc. Additional data sources were desired to enable examination and facilitate the development of network level analysis of natural hazard and extreme event impact on bridges, such as scour and earthquakes. A background search was performed to identify available environmental and natural hazard datasets. The datasets obtained can be classified into four broad categories including the following:

- Climatological
- Hydraulic/hydrologic
- Soil
- Seismic

Table 1 itemizes the information which has been used within these various data categories. Hydraulic/hydrologic and geotechnical data were acquired in ARC/Info format, hence required very minimal processing. Seismic and climatological data sets were essentially acquired in ASCII format and processed into GIS point coverages.

GIS facilitates spatial modeling and analysis and has been used in the development of a linkage between the environmental and natural hazard variables and the national bridge inventory database. Two approaches have been used to associate the environmental and the natural hazard data with the bridge point features utilizing the GIS.

Creating an Integrated Relational Data Model— Association of Information with Bridges

For point spatial data models of environmental and natural hazard data, three-dimensional surface data models were developed covering the United States for each data element using the three-dimensional surface interpolation capabilities provided by the GIS.

The three-dimensional surface formed a web which connects every point on the surface. Considering a cartesian coordinate system, the x and y coordinates reflect the longitude and latitude while the z coordinates represent the magnitude of the attribute being

Table 1: Required Environmental and Natural Hazard Data

Data Representation Class	Type of Data
Climate	Precipitation-rain
	Precipitation-snow
	Temperature (freeze/thaw)
Water	Hydrologic unit codes
	Flood data
	Stream flow data
Soil	Soil Ph
	Spectral acceleration
	Peak ground acceleration
Seismic	Earthquake magnitude and depth

modeled for a given layer. This may reflect the snowfall at given points, earthquake peak ground acceleration, temperature extremes, or any other scalar quantity.

The bridge point data was overlaid on the three-dimensional surface(s) using GIS layer overlay functions to interpolate the attributes at the bridge locations. The information was then assigned to the structures as attributes within related tables of the RDBMS. Thus, every bridge became associated with a snowfall value, rainfall value, earthquake magnitude, etc.

Similar to using layers modeled as surfaces, bridges can also be associated with polygon data models by overlaying bridges directly on the polygons using GIS tools. Thus each bridge was associated with the attribute of the polygon feature in which the bridge was located. For example, all bridges falling within a soil polygon assigned the attribute of 4 (for the pH) will automatically be assigned a pH value of 4.

Using these techniques, each structure was assigned a quantifiable value for each external factor. A relational data model was developed which allows storage and access of these external scalar values supporting statistical analysis, GIS operations and future modeling.

DESCRIPTIVE STATISTICAL SUMMARIES

The exploration of the NBI has revealed very useful and informative statistics, some of which are presented below. Figures 1 through 3 show information for the entire contiguous United States. The information displayed in the figures includes the following:

- Distribution of bridges by year of construction and material types
- Distribution of bridge materials by number, deck area and average daily traffic
- Spatial distribution of deficient bridges

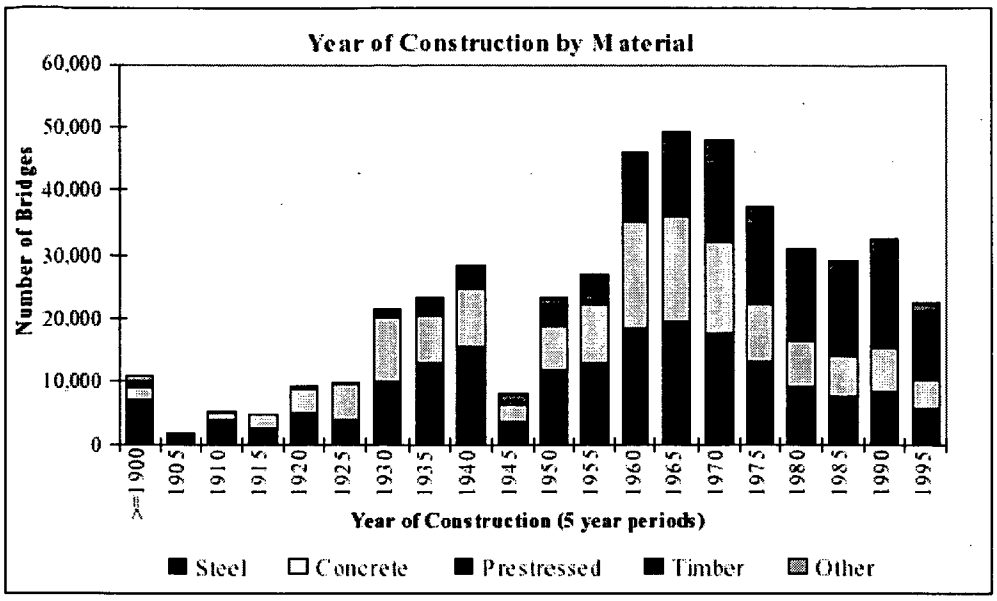

Figure 1: Distribution of bridges by year of construction and material types.

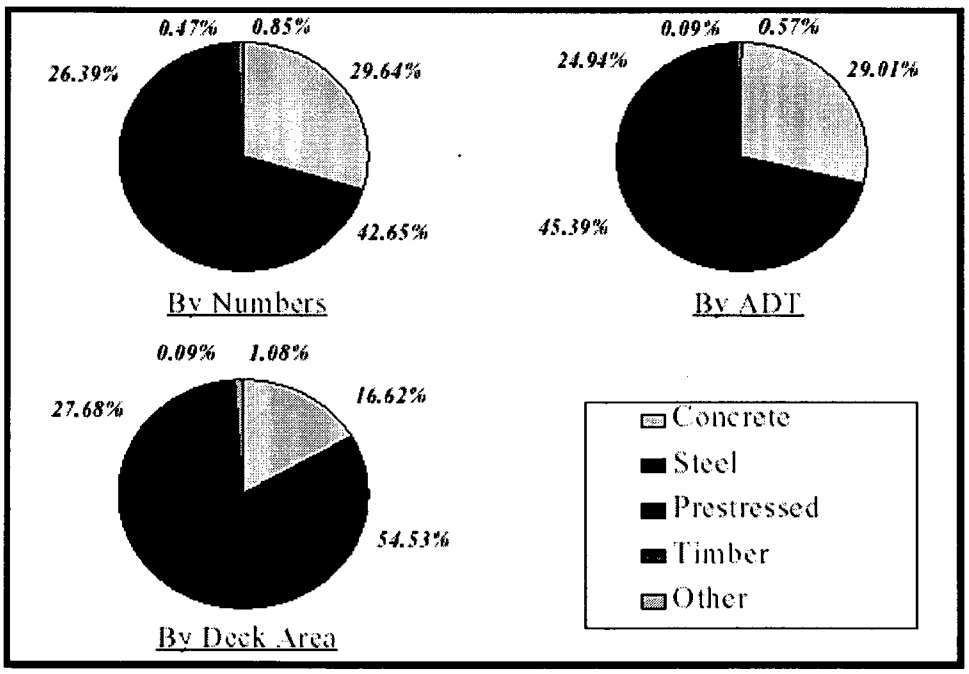

Figure 2: Distribution of bridge materials by number, deck area and average daily traffic.

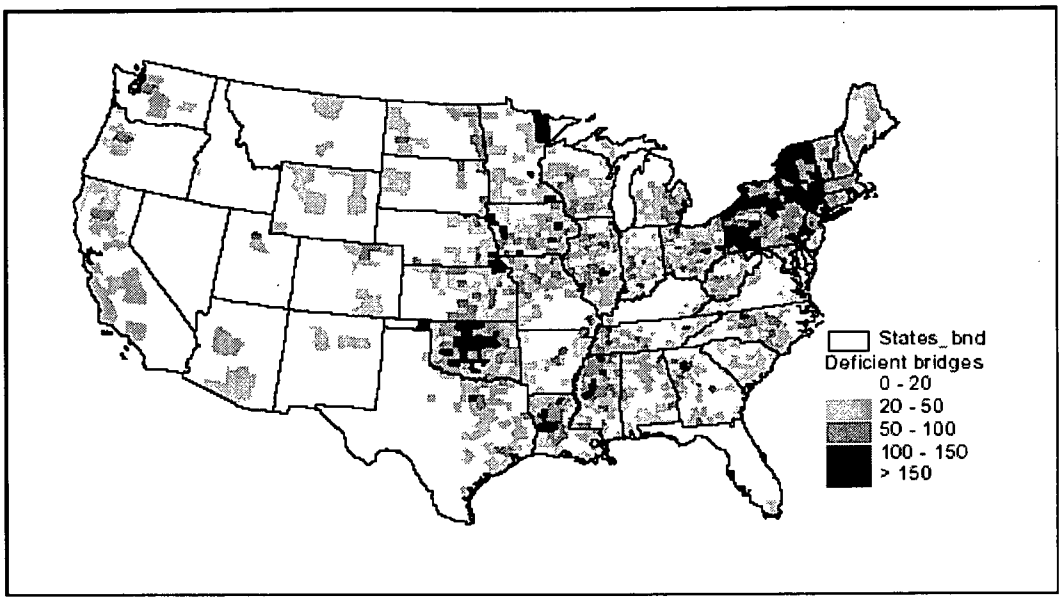

Figure 3: Spatial distribution of structurally deficient bridges by county.

REGRESSION MODELING

There have been numerous efforts by many individuals and institutions to develop models for predicting bridge deterioration and future condition state distributions. A bridge management systems report (FHWA 1989) discussed available deterioration models in some detail.

The bridge deterioration models developed through this research and which are summarized below utilize an approach which is uniquely different. The approach is more detailed as it considers many prevalent environmental factors considered at the bridge level. Most of the existing models consider only the age of the bridge and the average daily traffic carried by the bridge while disregarding important factors such as freeze-thaw cycles, frequency of salting, rainfall and temperature ranges. These additional factors have been considered in the development of the models described in the following sections.

Response (Dependent) and Predictor (Independent) Variables

The source of data for the response variables is the National Bridge Inventory (NBI) database. The items in the database that were used as determinants of bridge deterioration are condition ratings for the bridge deck, superstructure and substructure. These condition ratings were used as the response variables in the regression analysis. The condition ratings are categorical variables that take on discrete integer values from 0 through 9. Table 2 below shows the interpretations of the categorical variables as described within the NBI recording and coding guide.

NBI items used as predictor variables include the average daily traffic (ADT) carried by each bridge and the age of the bridge. Other predictor variables are those

which describe the bridge environment. These include precipitation, temperature range, number of freeze-thaw cycles and the frequency of salt applications to the bridges. The main material types used in the construction of the deck and the superstructure have also been included in the model as predictor variables. Table 3 shows the predictor variable data. The predominant construction material type refers to the material used in the construction of the deck or the superstructure. The material types for the bridges used in the modeling process and the variable symbols used are summarized in Table 4.

Table 2: Dependent Variable Ratings

Condition Ratings	*Interpretations*
9	Excellent condition
8	Very good condition
7	Good condition
6	Satisfactory
5	Fair condition
4	Poor condition
3	Serious condition
2	Critical condition
1	Imminent failure condition
0	Failed condition

Table 3: Independent Variables

Variable	*Units of Measure*
AGE	Years
Average daily traffic (ADT)	Number of vehicles per day
Annual precipitation (PRCP)	100th of inches
Frequency of salting (SALT)	Number of times per year
Temperature range (TRANGE)	Degrees
Freeze-thaw cycle (CYCLE)	Number of times per year
Predominant construction material	Not applicable

Data Sampling

A sample of data drawn from the NBI was used in the development of the regression models. The 1996 NBI database contains information on about 650,000 bridges and culverts in the United States. The database was initially cleaned up to eliminate any erroneous entries. Reconstructed bridges were eliminated since they will have erroneous effect on the age of the bridge in the analysis. A random sample of 30,000 bridges used for the analysis was generated from the NBI database.

Graphical exploration of the data revealed that deterioration values below 3 are generally outliers and hence have been eliminated from the sample. The analysis is therefore valid only for condition states from 3 through 9 inclusive. Other outliers were removed by trial and error and visual discrimination before the final regression analysis was carried out. Three different regression models were developed: (1) a linear model, (2) a non-linear non-parametric model (3) a non-linear parametric model.

The discrete nature of the response variables does not facilitate the usage of classical regression techniques. Generalized linear and generalized additive modeling capabilities which better model discrete variables were used.

Linear model (Model 1)

A generalized linear modeling procedure was used in the development of the linear models. The linear regression equations obtained for predictions of superstructure, deck and substructure conditions are presented below. The model coefficients are tabulated in Tables 5, 6 and 7 for the superstructure, deck and substructure respectively.

Table 4: Bridge Construction Materials

Material Name Variable Symbol	*Units of Measure*
Concrete cast-in-place (for deck)	**CC**
Concrete precast panels (for deck)	**CP**
Timber (for deck and superstructure)	**T**
Concrete (for superstructure)	**C**
Concrete continuous (for superstructure)	**CC**
Steel (for superstructure)	**S**
Steel continuous (for superstructure)	**SC**
Prestressed concrete (for superstructure)	**PC**

Table 5: Coefficients and Variables for the Superstructure Linear Model

I	Variables	Description	Coefficient	Value
1	V_1	AGE	β_1	$-5.13*10^{-3}$
2	V_2	PRCP	β_2	$-7.09*10^{-4}$
3	V_3	CYCLE	β_3	$-2.3*10^{-3}$
4	V_4	SALT	β_4	$-7.44*10^{-4}$
5	V_5	S	β_5	$-3.49*10^{-2}$
6	V_6	T	β_6	$-2.35*10^{-1}$
7	V_7	SC	β_7	$-3.87*10^{-2}$
8	V_8	CC	β_8	$-2.51*10^{-2}$

Table 6: Coefficients and Variables for the Deck Linear Model

I	Variables	Description	Coefficient	Value
1	V_1	AGE	α_1	$-4.72*10^{-3}$
2	V_2	SALT	α_2	$-4.46*10^{-3}$
3	V_3	CYCLE	α_3	$-2.41*10^{-3}$
4	V_4	ADT	α_4	$-5.85*10^{-7}$
5	V_5	TRANGE	α_5	$1.14*10^{-3}$
6	V_6	CP	α_6	$3.38*10^{-2}$
7	V_7	T	α_7	$-2.73*10^{-2}$

Table 7: Coefficients for the Substructure Linear Model

I	Variable	Description	Coefficient	Value
1	V_1	AGE	γ_1	$-5.3*10^{-3}$
2	V_2	SALT	γ_2	$-4.75*10^{-3}$
3	V_3	PRCP	γ_3	$-1.94*10^{-3}$
4	V_4	ADT	γ_4	$-6.0*10^{-7}$
5	V_5	TRANGE	γ_5	$4.48*10^{-4}$
6	V_6	CYCLE	γ_6	$-3.04*10^{-3}$

Regression equation for superstructure deterioration (Model 1)

$$SUP = EXP\left(C + \sum_i \beta_i V_i\right)$$

Where: C = 2.13
β_i, V_i = Summarized in Table 5

With: Pr(Chi) = 0.0
Residual standard error = 0.154

Regression equation for deck deterioration (Model 1):

$$DECK = EXP\left(C + \sum_i \alpha_i V_i\right)$$

Where: C = 2.06
α_i, V_i = Summarized in Table 6

With: Pr(Chi) = 0.0
Residual standard error = 0.151

Regression equation for substructure deterioration (Model 1):

$$SUB = EXP\left(C + \sum_i \gamma_i V_i\right)$$

Where: C = 2.28
α_i, V_i = Summarized in Table 6

With: Pr(Chi) = 0.0
Residual standard error = 0.134

Non-linear non-parametric model (Model 2)

The non-linear non-parametric model was developed using the generalized additive modeling (GAM) procedure. With GAM, smoothing operations were used to generate smooth plots of the transformed mean response and the predictor variables. The models from this procedure are however non-parametric in nature and hence not readily usable for prediction. Instead non-linear parametric models were developed based on the smoothed models.

Non-linear parametric model (Model 3)

Development of the non-linear parametric model was based on the non-linear nonparametric model and utilization of GLM. Polynomial functions were estimated from the smooth fits obtained from Model 2. The polynomials are as follows:

- Temperature (TRANGE) as a third degree polynomial for superstructure, deck and substructure
- Cycle as a fourth degree polynomial for deck, third degree for superstructure and deck
- Average daily traffic (ADT) as third degree polynomial for substructure and deck
- Precipitation (PRCP) as a fourth degree polynomial for superstructure and deck and as a third degree polynomial for substructure.
- Salting (SALT) as a third degree polynomial for superstructure and substructure and as a quadratic for deck.
- Age as a quadratic for all three (deck, superstructure and substructure)

The smooth of average daily traffic (ADT) is not a significant predictor for superstructure conditions, hence average daily traffic is not included for superstructure.

The resulting models from the generalized linear modeling using the estimated equations from the smooth fits are presented below. The coefficients for the predictors are shown. Tables 8, 9 and 10 are for superstructure, deck and substructure respectively. Insignificant coefficients of higher polynomial terms have been ignored.

Regression equations for superstructure deterioration (Model 3)

$$SUP = EXP\left(C + \sum_i \left(\sum_j \beta_{ij} V_i^j\right)\right)$$ Where: $C = 1.93$

Pr(chi) = 0
Residual Standard Error = 0.134

Regression equations for deck deterioration (Model 3)

$$DECK = EXP\left(C + \sum_i \left(\sum_j \alpha_{ij} V_i^j\right)\right)$$ Where: $C = 2.16$

Pr(chi) = 0
Residual Standard Error = 0.135

Table 8: Coefficients for the Superstructure Non-Linear Parametric Model

i	Variable	Descript.	Coefficients - β_{ij}			
			j = 1	j = 2	j = 3	j = 4
1	V_1	AGE	$-7.83*10^{-3}$	$3.92*10^{-5}$	0	0
2	V_2	CYCLE	$-9.12*10^{-3}$	$8.0*10^{-4}$	$-1.73*10^{-6}$	0
3	V_3	PRCP	$-6.9*10^{-3}$	$1.86*10^{-4}$	$-3.14*10^{-7}$	$-1.81*10^{-8}$
4	V_4	TRANGE	$5.16*10^{-3}$	$-1.63*10^{-5}$	$-2.46*10^{-8}$	0
5	V_5	SALT	$-4.57*10^{-3}$	$4.24*10^{-4}$	$-7.67*10^{-6}$	0
6	V_6	S	$-6.42*10^{-2}$	0	0	0
7	V_7	T	$-7.5*10^{-1}$	0	0	0
8	V_8	CC	$-4.14*10^{-2}$	0	0	0
9	V_9	SC	$-2.26*10^{-2}$	0	0	0

Table 9: Coefficients for the Deck Non-Linear Parametric Model

i	Variable	Descript.	Coefficients - α_{ij}			
			j = 1	j = 2	j = 3	j = 4
1	V_1	AGE	$-1.6*10^{-3}$	$2.18*10^{-5}$	0	0
2	V_2	ADT	$-1.26*10^{-5}$	$1.98*10^{-10}$	$-9.73*10^{-16}$	0
3	V_3	CYCLE	$-4.02*10^{-3}$	$2.94*10^{-5}$	$-1.92*10^{-4}$	$3.17*10^{-6}$
4	V_4	PRCP	$-2.11*10^{-2}$	$8.69*10^{-4}$	$-1.27*10^{-4}$	$5.7*10^{-10}$
5	V_5	SALT	$-3.31*10^{-3}$	$8.76*10^{-5}$	0	0
6	V_6	TRANGE	$-3.88*10^{-3}$	$2.48*10^{-5}$	$-5.32*10^{-8}$	0
7	V_7	T	$-3.18*10^{-2}$	0	0	0

Regression equations for substructure deterioration (Model 3)

$$SUB = EXP\left(C + \sum_i \left(\sum_j \gamma_{ij} V_i^j\right)\right)$$ Where: $C = 2.28$

Pr(chi) = 0
Residual Standard Error = 0.135

Comparison of the models (linear and non-linear parametric) based on their standard residual errors and statistical significance does not reveal any obvious differences. The residual standard errors (indicated below the table of coefficients) are approximately the same for both deck deterioration models (Model 1 and Model 3). The trend is the same for substructure and the superstructure models. The statistical test of significance [Pr(Chi) also indicated below the table of coefficients] came out as zero for all the models, indicating that all the models are significant. The linear model has fewer variables than the non-linear parametric model, and it is therefore recommended.

CONCLUSIONS AND FURTHER RESEARCH

Bridge management systems research is a focus area for the Federal Highway Administration. As part of the research efforts, the BMIS laboratory of FHWA has acquired NBI data covering many years. In addition, disparate sources of environmental and natural hazard data have been acquired and set up in a relational database structure

Table 10: Coefficients for the Substructure Non-Linear Parametric Model

i	Variable	Descript.	Coefficients - γ_{ij}		
			j = 1	j = 2	j = 3
1	V_1	AGE	$-8.8*10^{-5}$	$5.06*10^{-5}$	0
2	V_2	SALT	$-1.08*10^{-2}$	$1.98*10^{-4}$	$-9.88*10^{-7}$
3	V_3	PRCP	$2.08*10^{-2}$	$-6.86*10^{-4}$	$5.94*10^{-6}$
4	V_4	CYCLE	$-2.73*10^{-2}$	$2.67*10^{-3}$	$-1.05*10^{-4}$
5	V_5	TRANGE	$3.39*10^{-2}$	$-3.49*10^{-4}$	$1.77*10^{-6}$
6	V_6	ADT	$1.24*10^{-6}$	$-8.67*10^{-11}$	$1.14*10^{-15}$

using GIS technology. The databases provide an invaluable resource for detailed analysis and research. Exploration of the NBI revealed very informative statistical summaries, some of which were presented in the paper. The data were also used in the development of regression models using advanced statistical modeling procedures. The regression models are useful for predicting the deterioration of bridge decks, superstructures and substructures. Three categories of regression models were developed: a linear model, a non-linear non-parametric model and a non-linear parametric model. The linear model was recommended over the others, mainly because of its simplicity.

Further research is being performed in the BMIS laboratory. Currently, there is an investigative effort by the laboratory to determine if bridges with epoxy-coated reinforced decks have performed better over time than bridge deck reinforcements without any coating. This research is being conducted using information from the NBI and the relational database on environmental data. Also, recently some states have initiated efforts to collect GPS data on bridge locations. The BMIS laboratory intends to acquire the GPS data as it becomes available. The GPS data will be utilized to more accurately locate the bridges in space and the improved spatial data will be used to update the models previously developed.

PONTIS 4.0[1] – A NEXT GENERATION BRIDGE MANAGEMENT SYSTEM

William E. Robert and Allen R. Marshall, Cambridge Systematics, Inc.[2]

ABSTRACT

The Pontis® BMS, a product of the American Association of State Highway and Transportation Officials (AASHTO), is now in its fourth major version, Release 4. Pontis continues to support the complete bridge management cycle, including bridge inspection and inventory data collection and analysis, collecting and tracking inspector recommendations, developing worthwhile projects to include in an agency's capital plan, and project tracking. Several new features, particularly the ability to predict additional performance measures and simulate agency business practices, strengthen the ability of licensing agencies to predict bridge needs and plan bridge work.

INTRODUCTION

The Pontis Bridge Management System (BMS) was initially designed as a tool for performing network-level analyses of bridge needs and work. Over time, functionality has been added to Pontis to support the complete bridge management cycle, including collection of inspection and inventory data, development of an optimal preservation policy, simulation of future needs and work, and development of a project plan. The most recent version of Pontis, Release 4, adds significant new capabilities to the product. This paper describes the new components of the Pontis in brief, reviews the new version's modeling approach, and analyzes an example case illustrating the effects of applying the new bridge-level agency rules feature.

PONTIS RELEASE 4 OVERVIEW

Release 4 includes a number of significant features to the Pontis product, including support for collection of inspector work candidates that can be used in project planning, a completely redesigned project planning module, prediction of a range of additional asset management performance measures during needs simulation, and new features for performing a variety of bridge-level analyses(*1*). A major component of the improved support for bridge-level needs analyses is the ability to add agency customized rules that allow computer-generated recommendations to simulate agency practices. Use of this functionality allows agencies to use the powerful analytical tools provided by Pontis, including its development of an optimal preservation policy and simulation of bridge work and needs over time to develop realistic bridge-level work programs.

Figure 1 summarizes the basic components of Pontis. The most significant changes for Pontis Release 4 are:

---

[1] Pontis is a registered trademark of AASHTO.

[2] William E. Robert and Allen R. Marshall
Cambridge Systematics, Inc.
150 CambridgePark Drive, Suite 4000
Cambridge, MA 02140
t: (617) 354-0167
f: (617) 354-1542email: wer@camsys.com, arm@camsys.com

- **Improved Support for Project and Program Development:** A completely new Project Planning module was developed, which provides a highly flexible interface for developing individual structure projects as well as budget-constrained programs of projects.
- **Handling of Inspector Work Candidates:** Enhancements were made to the Inspection module to allow for recording of inspector work candidates, which can be used to develop specific structure projects. User-defined projects can compete against work that the Pontis simulation generates based on benefit-cost.
- **Expanded Use of Program and Project Performance Measures:** Present and future performance measures generated by Pontis as part of program simulation include a bridge health index; the sufficiency rating; NBI condition ratings for deck, substructure, superstructure and culverts; NBI ratings for structural evaluation, deck geometry and underclearances; and the Structural Deficiency and Functional Obsolescence status.
- **New Bridge Analysis Capability:** Pontis now provides the capability to quickly simulate and graphically display the performance of an individual structure over time, under different assumptions about the kind of work and schedule.
- **Change in Project and Program Development Work Flow**: The work flow for project and program development has changed from a linear one in which the simulation is run to recommend projects, and then the user modifies the recommended projects as needed. Now, projects can be developed through an iterative process in which:
  - The simulation is initially run to generate work candidates based on the preservation and improvement policies;
  - The user reviews both inspector and Pontis-generated work candidates, and creates a set of projects;
  - The simulation is re-run to either incorporate the user-defined projects, or have them compete against the Pontis-generated alternatives;
  - Simulation results are reviewed; and
  - Further adjustments are made to projects.
- **Improved Match Between Pontis Recommended Work and Agency Practice:** Pontis now allows users a much greater degree of user control over the simulation process. Specifically, users can define complex sets of rules, described in the following section.

In addition, a variety of other enhancements were made to the product, including:

- Reports were adapted and expanded throughout;
- Improvements to the Results module to evaluate both simulation scenarios and programs of user-defined projects;
- An upgraded database design; and
- Expanded support for English unit data entry (in addition to metric) in all inspection data entry screens.

PONTIS RELEASE 4 MODELING APPROACH

The new features present the user with a rich and powerful set of product capabilities. This section describes the modeling approach used in Pontis, presenting an overview of the modeling approach, definition of preservation benefits used in the product, discussion of performance measures calculated by the system, and details pertaining to the simulation rules used to tailor Pontis recommendations to support individual agency practices and policies.

Pontis Modeling Overview

An overview of the modeling approach used in Pontis Release 3 is available in the literature (*2*), (*3*). The technical documentation for Pontis 4.0 (*4*) extends this discussion to reflect the current state of the software. There are two major components of the approach: preservation policy optimization, and program simulation. The preservation policy is the set of recommended maintenance, repair and rehabilitation (MR&R) actions for each state of each *condition unit* that may exist on a structure, where a condition unit is defined as a combination of a bridge element and operating environment. As in previous versions of the software, the preservation policy is optimized by formulating a Markov decision model with the objective of minimizing discounted long-term agency costs, and solving the model using the Simplex method (*5*).

The preservation policy, and additional parameters such as the agency's budget, improvement policies, and standards, are used as inputs to the program simulation. The program simulation recommends preservation and improvement projects for each bridge in a network, with the objective of maximizing benefits, subject to a budget constraint and other constraints.

Calculation of Preservation Benefits

In previous versions of Pontis, preservation benefits were defined as the savings incurred by following the action recommended by the optimal preservation policy, relative to deferring action for one year. This definition of benefits results in the selection of recommended projects that minimize agency costs, subject to a budget constraint, for a network of sufficient size (*4*). However, with this approach it has not been possible to calculate meaningful benefits easily for actions not explicitly recommended by the preservation policy, such as user-defined projects or actions generated through application of agency rules. For Pontis Release 4, an alternate definition of preservation benefits has been added to the system based on the bridge health index.

The health index of a structure is a decimal number between 0 and 100 representing the economic worth (or asset value) of a bridge as determined by the physical condition of the structure's elements *(5)*. A health index of 100 indicates that all of the elements on a structure are in their best condition state (state 1) and have 100% of their original worth. An index of 0 indicates that all of the elements are in their worst state and have no remaining value. The health index is defined as the current value of all the elements divided by their new, or undeteriorated value. Mathematically this is defined as:

$$H = \frac{100\sum_{i=1}^{N}\left(V_i \sum_{j=1}^{M_i} \frac{M_i - j}{M_i - 1} q_{ij}\right)}{\sum_{i=1}^{N} V_i Q_i}$$

where:

H = health index
i = index of the element
N = number of elements on the structure
V_i = unit value of element i, represented using the failure cost of the element j=index of the condition state, assuming that $j=1$ applies to the highest (best) condition state, and $j=M_i$ to the worst
M_i = number of condition states defined for element i, which can be 3, 4, or 5
q_{ij} = quantity of element i in jth condition state

Q_j = total quantity of element i

Recognizing that the Health Index represents the percentage of the remaining asset value of a bridge, Pontis uses the change in health index as an alternative method for calculating preservation benefits. Using this new method, the benefit of the project is the (positive) difference in health index caused by the project divided by 100 and multiplied by the sum of the value of all of the elements for the structure:

$$B = \frac{\Delta H \sum_{i=1}^{N} Q_i V_i}{100}$$

where:
B = one-year benefit of performing a preservation project
ΔH = health index change caused by performing a project

Prediction of Performance Measures

Performance measures may be predicted at the individual bridge level, as well as at the network level. The measures predicted by the system include:

- Work and needs (in dollars)
- Health index
- Condition index by element type (health index for a subset of the elements on a structure)
- NBI condition ratings, including deck, superstructure, substructure and culvert ratings
- Sufficiency rating
- Federal HBRR eligibility

A number of the measures listed above are predicted using the FHWA NBI Translator, which translates inspected element conditions into NBI condition ratings.

Agency Simulation Rules

Five types of rules may be defined in Pontis Release 4 to allow Pontis recommendations to simulate agency practice, and address the issues in bridge-level work identified in previous versions(*6*). The agency rules include:

- **Scoping Rules** allow an agency to ensure that if the preservation optimization model recommends a particular type of work (e.g. replace deck), related work (e.g. replace joints) is scheduled at the same time.
- **Look Ahead Rules** allow an agency to control the timing of work so that if an agency has already scoped and scheduled a project within the timeframe of a simulation, then minor maintenance or repair work will not be scheduled for a specified number of years prior to the major project.
- **Major Rehabilitation (Rehab) Rules** allow an agency to force the simulation to upscope work to a major rehabilitation or replacement project based on the condition of the structure, or based on the cost of recommended work.
- **Paint Rules** allow an agency to set paint condition thresholds, below which a structure must be painted.
- **Agency Policy Rules** allow an agency to define detailed decision rules for what actions to schedule for specific elements, based on their condition, or on the condition of other elements or smart flags. These rules provide an agency the ability to simulate a threshold-based policy similar to that of other bridge management systems, such as the BRIDGIT BMS(*7*).

Figure 2 is a flow chart illustrating how the rules are applied in the Pontis program simulation.

EXAMPLE APPLICATION OF AGENCY RULES

A set of default agency rules is defined for use with Pontis Release 4. This section describes the nomenclature used in defining agency rules, and describes the results of an example analysis performed using the default rules and database shipped with the product.

Table 1 documents the nomenclature of the rules described in the previous section. As shown in the table, the nomenclature is different for each type of rule, but all of the types use the basic building blocks of actions that can be performed and objects that can be targeted. In defining a rule, an agency establishes the action to which the rule applies and/or triggers the rule. The action can be a specific action type defined in the system, a more general action category, or a flexible action, which refers to a an agency-specific set of element-level actions. For example, a user may define the flexible action "rehab deck," which includes an agency-definable series of actions taken together on the deck, joint, and railing elements. Further, an agency establishes the object upon which action is to be taken, or that triggers the rule. The target object can be the entire bridge, a specific element, an element type, or a more general element category, such as superstructure. In addition to the action and object, an agency may define a threshold used to trigger the rules. Default thresholds for paint, major rehabilitation and scoping rules are included with the product.

A sample analysis was performed to illustrate the impact of using agency rules in Pontis Release 4. Two Pontis program simulations were performed on a set of 50 structures from the sample Pontis database included with the product. In one case default rules were used to tailor Pontis recommendations to agency practice. In the other case, no rules were applied.

Figure 3 summarizes the results of needs and work over time for the 50 bridges with an without the rules. The analysis indicates that application of the default agency rules in Pontis Release 4 program leads to significantly different bridge-level work recommendations from the recommendations generated without rules in force, with fewer larger projects typically y recommended for a given set of structures. At the network level, addition of the rules,

particularly rules designed to upscope Pontis recommendations based on agency practice, increases the estimate of initial network-level needs by approximately 23%. However, the backlog growth/reduction at a given budget level is not significantly altered by application of the rules.

CONCLUSIONS

Pontis Release 4 provides agencies with a powerful set of analytical tools for analyzing needs and planning work for an agency's bridges, both at the network level and the bridge level. Significant features of Release 4 include the ability to predict new performance measures as part of a program simulation, and the ability to define agency-specific simulation rules for tailoring the results of a Pontis program simulation to agency practice. With the network performance measures and bridge-level analysis features in Pontis, agencies have more objective tools to evaluate policies and practices against long term goals, and to find the best way to move towards a long-term optimal policy, while contending with the short-term realities of agency budgets and existing practices.

ACKNOWLEDGEMENTS

The authors wish to acknowledge AASHTO for their continuing support of Pontis, and Caltrans for assistance in performing the sample analysis.

REFERENCES

1. Cambridge Systematics, Inc. *Pontis Release 4 User's Manual.* AASHTO, Washington, D.C., 2001.
2. Thompson, P.D. and R.W. Shepard. "PONTIS." In Transportation Research Circular 423, TRB, National Research Council, Washington, D.C., 1994.
3. Marshall, Allen, William Robert, Kevin G. Anderson, Richard "Lee" Floyd, and Frank Corso, Jr. "Comparison of Pontis Bridge Project Recommendations to Programmed Work for Three U.S. Transportation Agencies." In Transportation Research Circular 498, TRB, National Research Council, Washington, D.C. 2000.
4. Golabi, Kamal, Paul D. Thompson and William A. Hyman. *Pontis Version 2.0 Technical Manual: A Network Optimization System for Bridge Improvements and Maintenance.* Report FHWA-SA-94-031. FHWA, U.S. Department of Transportation, 1993.
5. Shepard, Richard W. and Michael B. Johnson. *California Bridge Health Index,* August 2001 TRNews, TRB, National Research Council, Washington D.C. 2001
6. Cambridge Systematics, Inc. *Pontis Release 4 Technical Manual.* AASHTO, Washington, D.C., 2001.
7. Hawk, Hugh. "BRIDGIT: User-Friendly Approach to Bridge Management." In Transportation Research Circular 498, TRB, National Research Council, Washington, D.C. 2000.

LIST OF TABLES AND FIGURES

Table 1. Agency Rule Formulation

Figure 1. Overview of Pontis Functionality
Figure 2. Generation of Preservation Needs with Agency Rules
Figure 3. Needs and Work with and without Agency Rules

Table 1. Agency Rule Formulation

Rule Type	Nomenclature	Example
Agency Policy	If object *A* has >= *X%* of its quantity in condition state *n* or worse, then for object *B*, take action *C1* for the portion in condition state 1, *C2* for the portion in condition state 2, *C3* for the portion in condition state 3, *C4* for the portion in condition state 4, and *C5* for the portion in condition state 5.	If *SECTION LOSS SMFLAG* has >= *100%* in State *5* or worse, then for *SECTION LOSS SMFLAG* do actions [S1] *Do Nothing*, [S2] *Do Nothing*, [S3] *Do Nothing*, [S4] *Do Nothing*, and [S5] *Do Nothing*.
Look Ahead	If action *A* is done to object *B* within *n* years, then do NOT do action *C* to object *D*.	If *PAINT BRIDGE (FLEX)* to *BRIDGE* < *5* years, then no *PAINTING to DECKS/SLABS*.
Rehab	If threshold type *X* has relationship *R* to value *Y*, then do action *A* to object *B*.	If *HEALTH INDEX* for *BRIDGE* is <= *70%*, then do *REPLACE STRUCTURE* to *BRIDGE*.
Painting	If paint thresholds *1 only, 2 only, both, or none* are used, then if condition index is <= *PT1*, paint all paintable elements, or if condition index is <= *PT2*, then paint elements not in condition state 1.	If *Paint Threshold 1* only is used, then if condition index of paintable elements is <= *50%*, then paint all paintable elements.
Scoping	If action *A* is done to object *B*, then also do action *C* to object *D*.	If *REPLACE ELEMENT* is done to *DECKS/SLABS*, then also do *REPLACE ELEMENT* to *RAILINGS/BARRIERS*.

Figure 1. Overview of Pontis Functionality

Inventory:

- ✓ Establishing an accurate inventory of structure information
- ✓ Integration and data exchange with existing enterprise information systems

Inspection:

- ✓ Scheduling and conducting structure inspections
- ✓ Entering inspection data
- ✓ Importing data from external inspection data collection systems
- ✓ Producing required National Bridge Inventory (NBI) files
- ✓ Producing Structure, Inventory and Appraisal (SI&A) and other inspection reports

Needs Assessment and Strategy Development:

- ✓ Developing structure deterioration and cost models based on agency historical data and experience
- ✓ Developing long-range, network-wide policies for structure preservation and improvement reflecting economic considerations and agency standards
- ✓ Assessing current and future preservation and improvement needs
- ✓ Evaluating alternative investment scenarios, based on structure condition and performance, and benefit/cost considerations

Project and Program Development:

- ✓ Developing projects to address inspector work recommendations and agency policies and standards
- ✓ Evaluating impacts of project alternatives on structure performance
- ✓ Project ranking
- ✓ Developing budget-constrained programs of projects
- ✓ Tracking project status and completion

Figure 2. Generation of Preservation Needs with Agency Rules

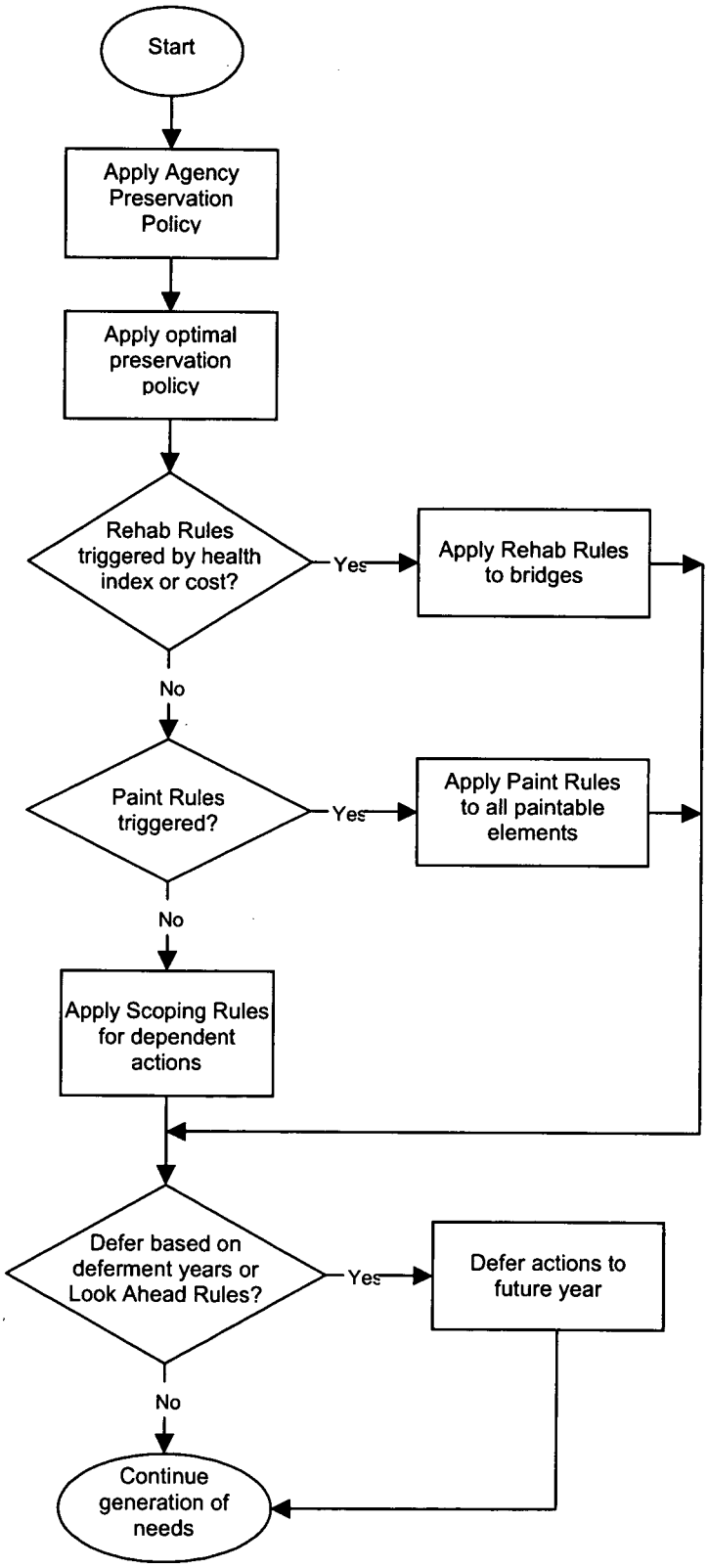

Figure 3. Needs and Work with and without Rules

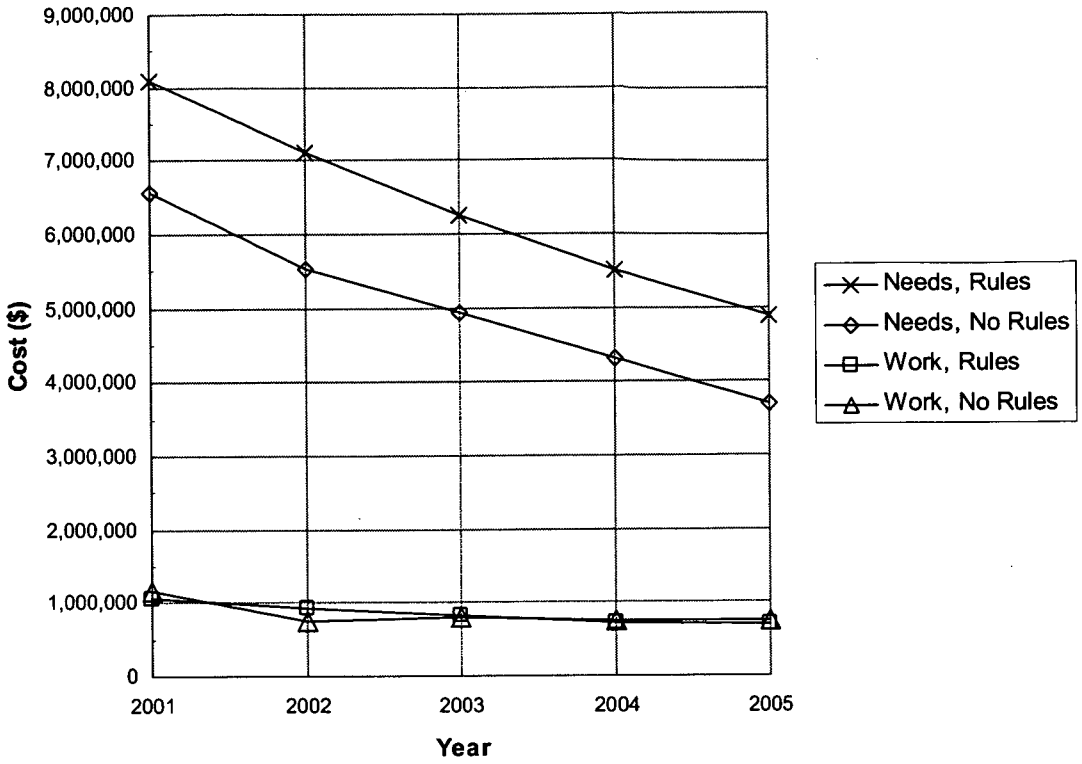

Current state and revised policy of the PWRI Bridge Management System

Nobuyuki Hirahara[1], Akira Moriyama[2]

ABSTRACT

Highway bridges in Japan, most of which were constructed after 1960, played a crucial role in the rapid economic growth. However, since they were built on a rush construction schedule, many of them are showing serious deterioration in recent years and their repair and replacement is an urgent problem. In order to maintain the soundness of the highway bridge stock and hand it down to the future generations as a valuable asset, it is necessary to establish an effective system for bridge maintenance and replacement.

Because of this background, there has been a demand for the bridge management system (BMS) to support effective maintenance. The Public Works Research Institute has been developing the prototype of BMS. This report briefly explains the outline of BMS, and represents activities to further develop this system and its prospect for the future.

1 CURRENT STATUS AND PROBLEMS OF HIGHWAY BRIDGE STOCK

According to the 1999 statistics, there are approximately 140,000 bridges with a length of more than 15 m in Japan, and their total length is about 8,000 km (Figure 1)[1]. Among them, about 9,700 bridges are managed by the Ministry of Land, Infrastructure and Transport (MLIT).

Most of these bridges were constructed during and after the 1960s: in the 1970s, called the decade of bridge construction rush, about as many as 4,000 bridges were constructed per year. After this decade, the construction of new bridges decreased, and the number of new bridges constructed per year stood at about 2,000 in recent years (Figure 2). In the next 10 to 20 years, the bridges built in the decade of bridge construction rush will have been in service for more than 50 years, and their deterioration will be a serious problem. The average age of bridges in Japan is about 22 years at present, but in the next 10 years or so, it will be 35 years, the same level as the bridges in the United States.

As shown in Figure 2, although reinforced concrete bridges accounted for most of the newly constructed ones in the past, they were gradually replaced by steel bridges, and then prestressed concrete bridges. The reasons for this include technology advancement, and changes in construction and maintenance costs. Concrete bridges used to be considered maintenance-free.

---

1) Principal Researcher of Bridge Structure Research Team, Structures Research Group, Public Works Research Institute, Tukubashi,Ibaraki-ken,305-8516,Japan

2) Senior Researcher, ditto

However, because of the many cases of concrete spalling and salt damage in recent years, it is now generally agreed that they need proper maintenance (Figure 3).

As shown in Figure 4, the major reasons for bridge replacement in Japan include insufficient functions (e.g. narrow width), modification of the roads on which the bridges are located, and improvement of rivers that they cross. However, it is easily understandable that replacement due to damage caused by deterioration will increase in the future.

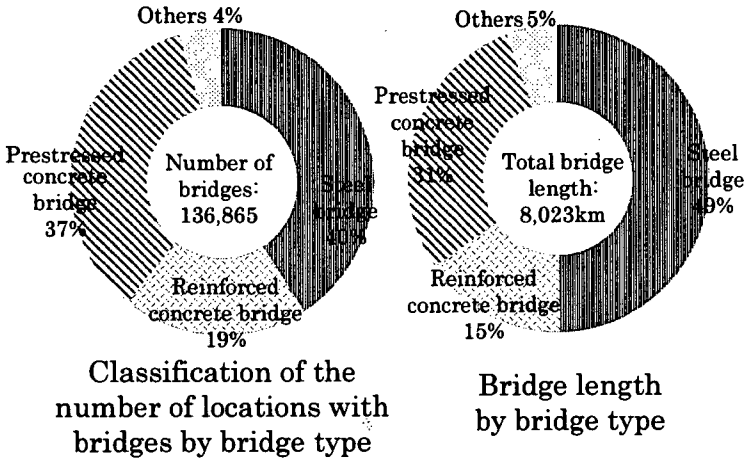

Figure 1 Number and lengths of bridges in Japan

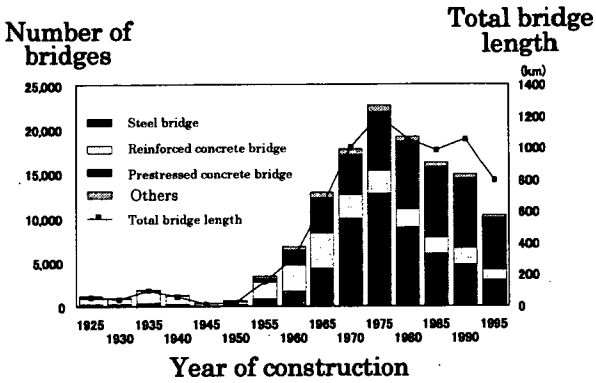

Figure 2 Number of bridges by year of construction

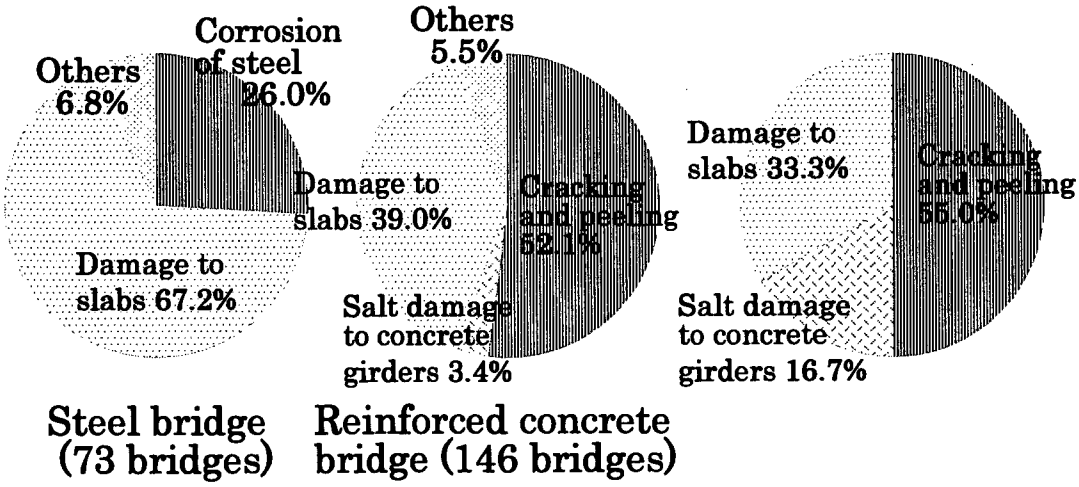

Figure 3 Causes of damage to superstructure

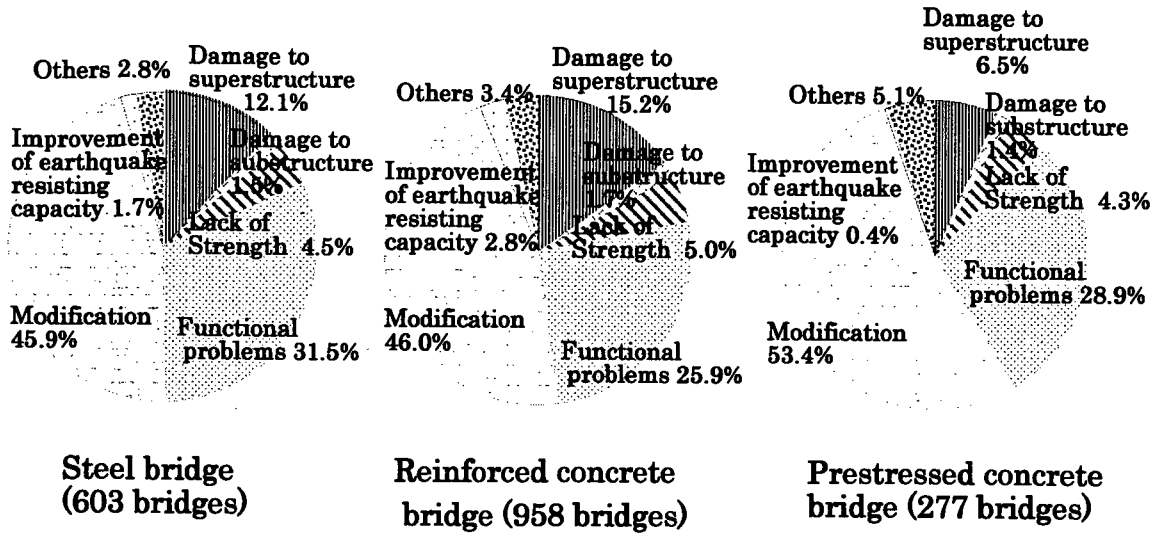

Figure 4 Causes of bridge replacement by bridge type

2 OUTLINE OF HIGHWAY BRIDGE MAINTENANCE

Highway bridge maintenance includes: "inspection" to grasp the current status; "evaluation" of the structural soundness of the bridge based on the inspection results; "prediction" of the possibility of deterioration and damage growth in the future; "repair and reinforcement plan preparation" to keep the bridges in a serviceable condition; and "execution" of repair and reinforcement works.

2.1 Inspection

Inspection of bridges on national highways directly managed by the Ministry of Land, Infrastructure and Transport are now underway in accordance with the "Bridge Inspection Manual (draft)," issued by the Public Works Research Institute of the Ministry of Construction (now Ministry of Land, Infrastructure and Transport) in July 1988. The inspection period is about 10 years, and at present, inspection for about 70% of the bridges is completed. The main purposes of inspection (which is usually by close-range visual inspection) include early detection of damage and ensuring of safe and smooth traffic by continuous damage monitoring. The pattern and extent of damage for each member are first categorized into three groups: large, medium, and small. The degree of damage for each member is then classified into five groups shown in Table 1 depending on the damage type: I, II, III, IV, and OK. Damage degree "I" is the most serious condition, which could affect the safety of vehicular traffic, while "OK" is a condition free from damage. Damage degrees II to IV fall between I and OK, and require further inspection and repair depending on the degree of the damage.

2.2 Data base

MLIT is using a highway information data base system called MICHI, which was originally developed by the Ministry of Construction (now MLIT) to support maintenance of highways.

Table 1 Damage evaluation criteria

Ratings	Damage evaluation criteria
I	The damage is such that traffic safety cannot be ensured.
II	The damage is such that a study on the necessity of repair using results of detailed survey is required.
III	The damage is such that follow-up surveys are required.
IV	The damage is such that its extent needs to be recorded.
OK	Damage is not detected during inspections.

Stored in the data base system are image data such as drawings, data on the road location (e.g. topography and crossing with other structures), traffic volume, data on the road structure (e.g. gradient, alignment, and thickness of pavement), and road accessories (e.g. signs). MICHI contains a comprehensive system to save and utilize bridge inspection records. BMS, which is explained in the following sections, uses data stored in MICHI.

3 OUTLINE OF BMS

BMS is a system to assist soundness evaluation and repair schedule preparation shown in Figure 5. Consisted of the Soundness Evaluation Module and Repair Schedule Creation Module, BMS first evaluates the soundness of each bridge using inspection data stored in MICHI, and then creates repair plans for bridges managed by local offices based on the soundness evaluation results. The basic configuration of BMS is shown in Figure 6[2)].

3.1 Soundness Evaluation Module

3.1.1 Concept of soundness evaluation

The BMS developed by the authors deals with physical damage such as cracks, peeling and corrosion and excludes functional defect such as insufficient number of lanes. This module evaluates the degree of physical damage of bridges in values, and gives the cost-effective and rational timing for repair and replacement. The soundness of bridges is evaluated using information stored in MICHI such as dimension data and inspection records. The soundness of each member is determined by first calculating the total deduction points based on the degree of the damage, and then deducting the points from the full points.

3.1.2 Soundness evaluation

The soundness is evaluated by dividing bridges in four parts: slabs, main girders, substructure, and shoes. Since handrails and expansion joints can be individually replaced, it is cost-effective to use them as long as possible, until they no longer can be used.

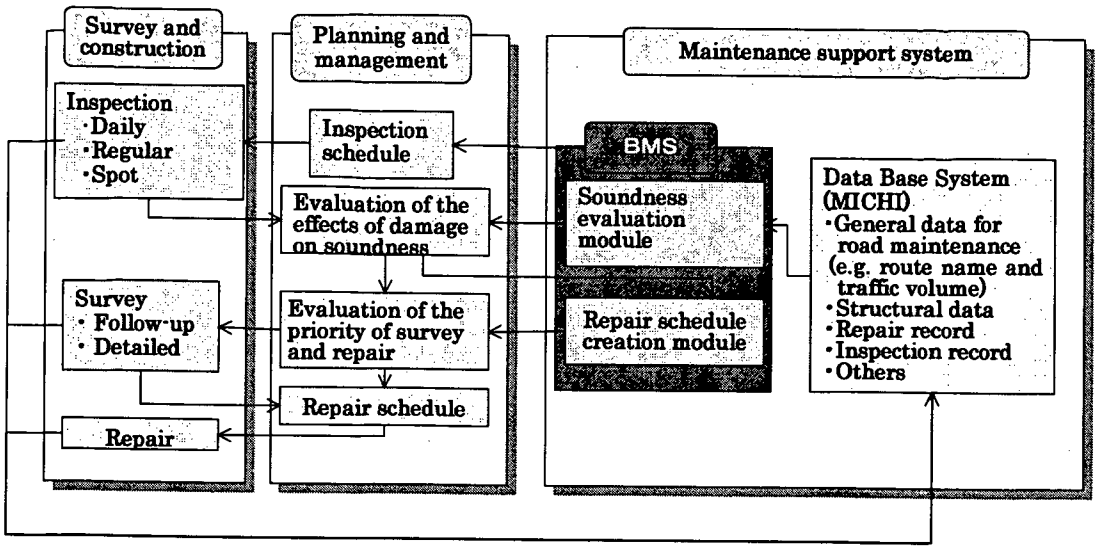

Figure 5 Outline of bridge maintenance

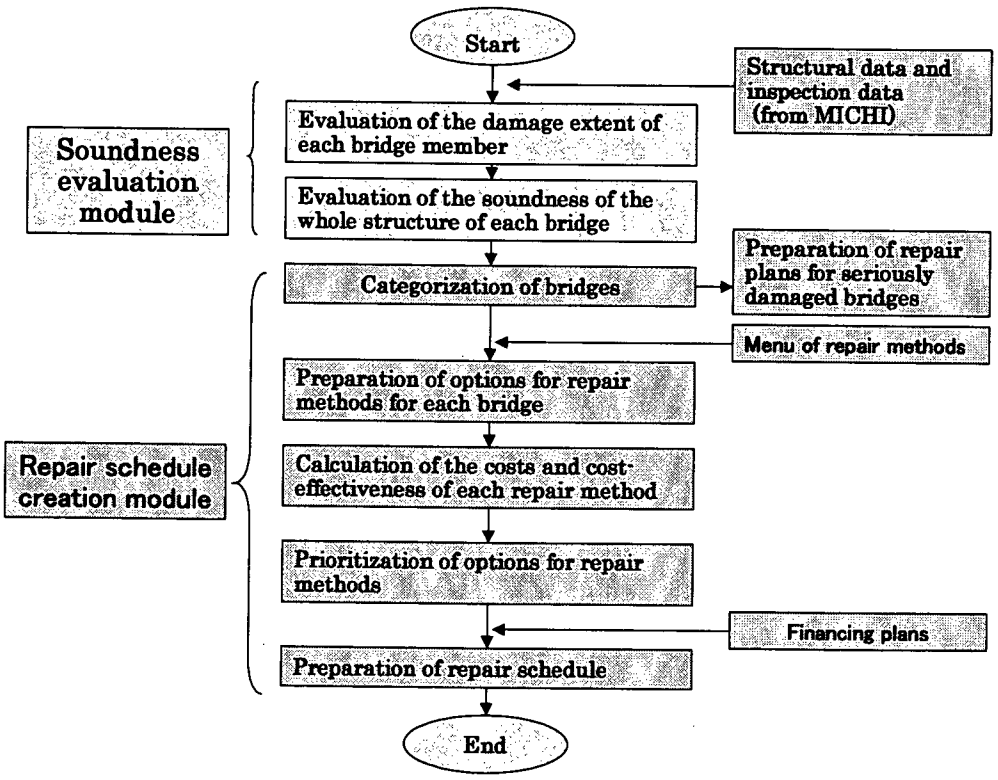

Figure 6 Flowchart for BMS

The deduction points are calculated depending on the degree (II, III, and IV) of the damage to each member, but regardless of the type of the damage. The rating of the damage is then determined by deducting the points from the full points (100). The reason for calculating the deduction points regardless of the type of the damage is that it is already weighted when the degree of the damage is determined. The deduction points and damage degree are determined by comparing the evaluation results by several bridge experts: the deduction point calculated by the largest number of the experts is adopted as the final value.

In this study, the point deduction method and the weighted mean method were compared, and the former was adopted as the method for soundness evaluation because of the following reasons. The weighted mean method tends to underestimate the effects of members with serious damage, since the final rating is determined by the total of the score for each evaluation item. On the other hand, in the point deduction method, the effects of such members remain and are not overlooked even at the stage for the determination of the final rating, and the soundness evaluation results obtained from this method are easy to understand. An example of soundness evaluation result is shown in Figure 7.

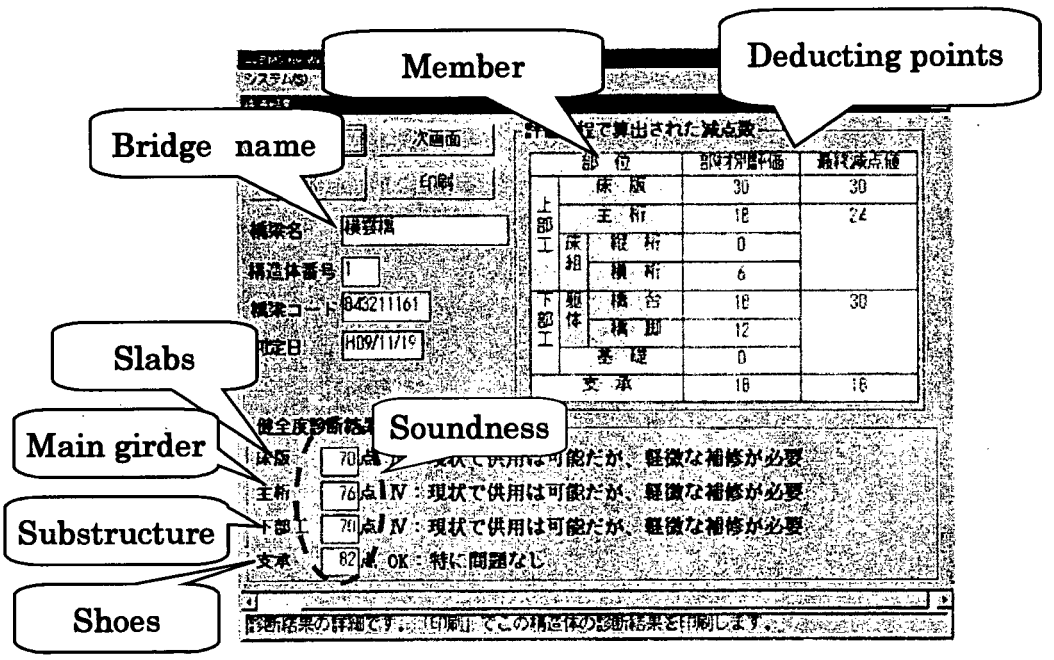

Figure 7 Example of soundness evaluation results

3.2 Repair Schedule Creation Module

3.2.1 Concept for repair schedule creation

Following the selection of representative repair methods for damaged members based on the results obtained by the soundness evaluation module, repair cost for each method is calculated. The benefit of each method is defined as the cost saving arising from the lengthened service life after the repair. The priority of the repair methods is then determined taking into consideration both the repair cost and the benefit. Based on this result, the module outputs information on repair methods that can be used within the budget for the fiscal year.

For bridges, which in the opinion of the road administrator require immediate repair, the preparation of repair plans can be started without using this module. On the other hand, repair schedule is not prepared for bridges without damage.

3.2.2 Selection of repair method

Depending on the damage rating (deduction point) for each member, an appropriate repair method is selected from the repair method menu. The repair method menu specifies the applicable cases for each method depending on the repair pattern and damage pattern, and how the rating will change after repair. Although the repair method can be automatically selected, the road administrator can choose it arbitrarily.

3.2.3 Concept of priority grading for repair

For priority grading, two methods were compared: one method is to evaluate how the soundness will recover after repair, and the other method is to evaluate to what extent repair will improve the current value of the structural performance. The BMS developed by the authors adopted the latter method because of two reasons. First, this method allows all necessary costs for all repair methods to be calculated, converted to the current value, and compared with each other, so it can provide the optimum solution, in which the appropriate time of repair is taken into account. Second, this method can find the optimum repair solution for two or more bridges, and creating the optimization algorithm for this method is relatively easy.

When calculating the current value of benefit, consideration of benefit for users as well as for the road administrator provides accurate results. The benefit for users arising from repair includes 1) the alleviation of restrictions on vehicle weight and decrease in detour which reduce the time to destination, and 2) reduction in operation costs. However, the BMS developed by the authors excluded the benefit for users, since its quantification is difficult.

3.2.4 Calculation of benefit for road administrator

The conceptual diagram for repair effects is shown in Figure 8. The curve in the figure (standard deterioration curve) shows the process in which a bridge deteriorates with time. Normal service life (T) refers to the time during which the soundness decreases from 100 to the serviceability limit state.

If a bridge which currently has a certain soundness deteriorates at the same rate as the standard deterioration curve after that soundness, the remaining service life (tr) of the bridge can be predicted by horizontally shifting the standard deterioration curve in such a way that it passes the point corresponding to the current soundness. If the bridge is repaired, its soundness increases and its remaining service life will increase to tr + e. The authors define the reduction in costs for future bridge replacement arising from the repair as Benefit B. The value of B is calculated by the following equations:

$$B = C_0 - C_1 \tag{1}$$

$$C_0 = A \left[\frac{(1+i)^T}{(1+i)^T - 1} \right] \left[\frac{1}{(1+i)^{tr}} \right] \tag{2}$$

$$C_1 = A \left[\frac{(1+i)^T}{(1+i)^T - 1} \right] \left[\frac{1}{(1+i)^{tr+e}} \right] \tag{3}$$

where C_0 is the current value of the total cost for the case where the bridge is left unrepaired until the first replacement tr years (remaining service life) later, and then repeatedly replaced at an interval of T years (normal service life). Here, the current value refers to the present worth of the total necessary cost for the present and future, which is calculated taking into consideration such factors as the interest rate. C1 is the current value of the total cost for the case where the bridge is repaired now to lengthen its service life by e years, replaced (tr + e) years later, and then repeatedly replaced at an interval of T years. If the bridge is replaced now, the replacement interval can be lengthened. The value A in the above equations is the bridge replacement cost for each time and the value i is the interest rate taking into consideration the inflation rate.

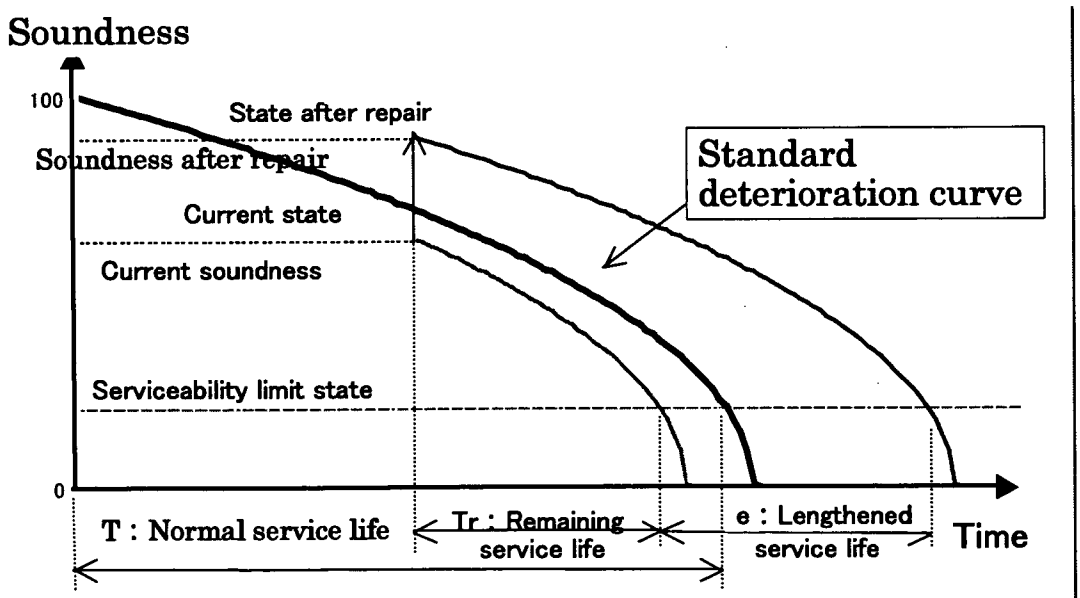

Figure 8 Effects of repair

3.2.5 Selection of repair plan

When preparing a repair plan, several repair methods are compared in terms of the repair cost and benefit in accordance with the above-mentioned concept. A graph as shown in Figure 9 is prepared for each bridge, with repair cost C on the horizontal axis and benefit B on the vertical axis.

As shown in the figure, the repair methods are plotted in the ascending order of the repair costs. After drawing a line between the points plotted, the methods that create concave portions are dropped from consideration. This figure is created for all bridges in need of repair, to calculate the marginal efficiency ($\Delta B/\Delta C$) for each repair method. After selecting repair methods that fall within the budget limit in descending order of the value of ($\Delta B/\Delta C$), the one that is expected to be the most cost-effective is adopted.

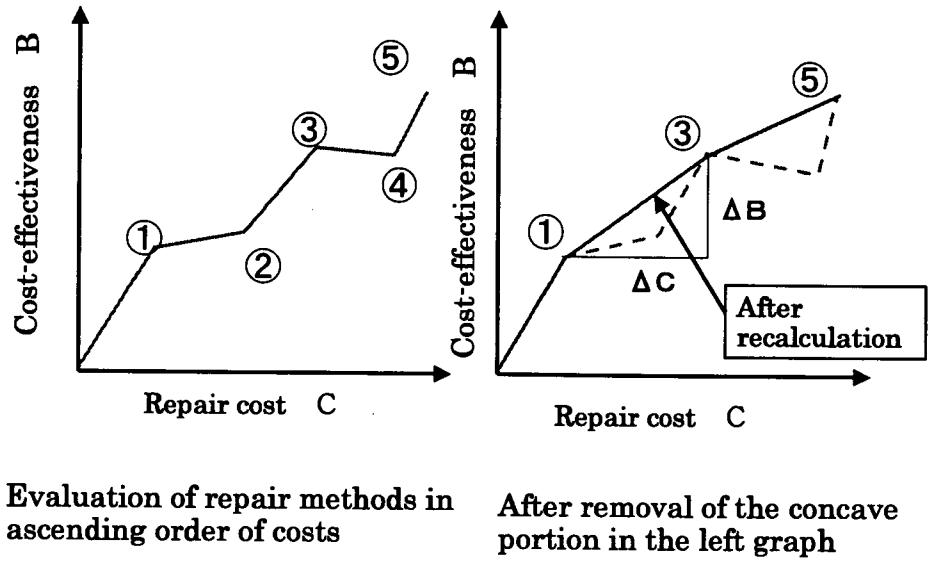

Figure 9 Determination of options for repair methods

4 PROBLEMS OF AND MODIFICATION PLANS FOR BMS

Although the BMS developed by the authors is used on experimental basis at several offices of MLIT, it still has problems to be solved before the full-fledged introduction. The results of experimental use showed that it can evaluate the soundness of bridges with a reasonable accuracy, but cannot create the optimum repair plan. The main reason for this is that data on locations with damage, which are stored in the database, are still not sufficient.

In order to make BMS a useful tool, the following modifications and improvement for the database as well as for BMS itself are necessary:

1) Although bridge inspection is conducted at 10-year intervals at present, bridge deterioration may considerably proceed in 10 years. It is therefore necessary in the future to increase the inspection frequency.

2) Since inspection results vary depending on the inspector, it is necessary to develop an inspection method that allows quantitative evaluation of the soundness, and to decrease the fluctuation of inspection results by strengthening training for inspectors.

3) At present, a relative evaluation method is used for recording the deterioration of bridges. However, in order to prepare an appropriate repair plan for each bridge, it is necessary during

inspections to collect sufficient data so that the repair quantity can be accurately predicted.
4) In order to allow the optimum repair method to be selected, it is essential to store data on previous repair works in the "repair record database," analyze them, and reflect them in the repair schedule.
5) The soundness evaluation methods adopted in the BMS developed by the authors, including the use of the standard deterioration curve, are based on limited data currently available. In the future, it is necessary to improve the accuracy of the soundness evaluation methods by collecting and analyzing sufficient bridge inspection data, and modifying the contents of the methods including the standard deterioration curve. The data to be collected and analyzed include the relationship among the specifications used for bridge design, environment to which the bridges are exposed, and their deterioration.
6) Although the system developed by the authors can be applied only for main members of a bridge, it is necessary to expand its coverage to secondary members taking into consideration the frequency of damage occurrence and the importance of repair for the damage.
7) It is necessary to establish a comprehensive maintenance system for cost-effective bridge inspection, evaluation and repair.

5. CONCLUSION

Conventional maintenance methods have problems in that they are based on a concept to prepare a separate plan for bridges, tunnels, and pavement, and this prevents the creation of comprehensive and optimum maintenance. In order to enable a systematic maintenance of road properties, it is necessary to establish as soon as possible a comprehensive management system for administration and operation of road-related structures based on a common concept for bridges, tunnels, and pavement. A management system created by objective and quantitative evaluation methods is essential not only for effective and sophisticated maintenance but also for the improvement of the accountability of maintenance activities.

The authors will continue studies to establish a management system which utilizes technologies and knowledge in various fields and which can take into consideration the entire life cycle including construction as well as maintenance.

REFERANCES

1) Road Bureau, Ministry of Construction: Annual Report of Road Statistics 2000, August 2000
2) Public Works Research Institute, Ministry of Construction: A Report on Survey and Research for the Development of the Bridge Management System, Technical Memorandum of PWRI No. 3633, March 1999

PRESERVATION, IMPROVEMENT AND NATURAL HAZARD CONSIDERATIONS IN BRIDGE MANAGEMENT SYSTEMS

Edgar P. Small, Ph.D.[1]

Abstract:

Bridge management systems (BMS's) have been developed and are currently being implemented by State DOT's throughout the United States. These systems employ rigorous optimization procedures and probabilistic deterioration models to determine the optimal preservation policy and utilize level-of-service based improvement project selection. Policies and programs are developed over a long-term planning horizon. None of the systems available consider retrofitting of structures for natural hazards and extreme events. Since bridges fail primarily due to natural hazards and extreme events, retrofitting considerations must be incorporated to arrive at an optimal, network-level policy for bridge activities. This paper discusses existing BMS components and provides a draft format for development and incorporation of a natural hazards routine based on fragility concepts.

Introduction:

Formalized bridge management began in the early 1970's with the establishment of the National Bridge Inspection Standards (NBIS) following the catastrophic failure of the Silver Bridge in 1967. This tragic event resulted in 46 fatalities and subsequently focused the nation's attention on the safety of the bridge inventory. The resulting legislation mandated biennial bridge inspections, which have formed the basis of bridge management for over 25 years. Information collected through this program is used for fund apportionment from the federal government to the States and for identification of project eligibility for these funding programs. Many bridge agencies also use NBIS data to prioritize structures for maintenance, repair and rehabilitation.

The NBIS process, when established, employed the best practices of the day. Engineers generally considered the system effective for day-to-day management of their bridge inventories. Limitations became evident over time as differences between the bridge network needs and the funds available began to grow. It was recognized that more rigorous, proactive forms of bridge management were required to effectively manage State-level bridge programs. Growing demands in a competitive funding environment accentuate the need for a more effective and proactive system of bridge management. The development of bridge management systems was thus initiated in the late 1980's and early 1990's. Research by the Federal Highway Administration (FHWA) led to the development of the Pontis BMS, the predominant systems being employed by State DOT's throughout the country. Research efforts by the National Cooperative Highway Research Program (NCHRP) evolved into the Bridgit BMS, currently employed by a few States. Both Pontis and Bridgit are currently supported by AASHTO and both consider network-wide and bridge level preservation and improvement needs. Though the design goals of the systems are nearly identical, different approaches are taken to achieve the optimal set of actions for a given budget. Other efforts developed into State-specific approaches employed by individual Departments of Transportation (DOT's) (Alabama, Indiana, North Carolina, New York and Pennsylvania).

[1] Assistant Professor, Department of Civil Engineering, Catholic University, Washington, DC 20064

Pontis and Bridgit have evolved over time, primarily to incorporate advances in computer technology. Only slight modifications have been made to the mathematical models employed and the general structure of the optimization procedures is considered to have remained relatively static. Bridge owning agencies have been actively collecting the required information to use the systems for short and long range bridge preservation and improvement planning and programming. Several States have demonstrated the applicability of the process through successful implementation. Other agencies, noting the success in the lead BMS States, continue with implementation efforts.

While BMS development efforts were underway, natural hazards and extreme events lead to several notable bridge failures. Seismic events occurring in California and Internationally in Japan, Italy, and other nations, resulted in significant bridge damage and many instances of catastrophic failure. Additionally, catastrophic failures occurred resulting from scour, vehicular collisions, and ship-bridge collisions. Retrofitting the existing bridge population to mitigate risks associated with these hazards emerged as high priority areas in many parts of the country. Currently, advanced bridge management system efforts do not incorporated models to permit consideration of retrofit needs concurrently with the more traditional preservation and improvement concerns. To examine the applicability of incorporating natural hazard and extreme event mitigation activities within a bridge management construct, the development of a methodology to integrate seismic retrofitting activities is pursued through on-going research efforts.

Retrofit programs typically utilize prioritization procedures and are performed exclusively outside of the realm of traditional bridge management. In many cases, personnel responsible for seismic retrofit activity act independently of bridge management personnel, often operating with separate, distinct budgets. A significant contribution may be made through consideration of seismic retrofit needs concurrently with preservation and improvement needs at both the network and project levels. At the network-level, upper level managers are responsible for allocation and apportionment of limited funds to competing needs within the network. Without incorporation of such models, these upper-level managers have limited data on-which to base their decisions. Gross need estimates will be provided; however, without information on the interrelation of the activities, decision-makers often have to rely upon secondary, subjective data for fund allocation and apportionment. At the project level, a significant contribution results through combined consideration of all potential bridge needs simultaneously. For instance, a given structure may require preservation and improvements, which are queued through the traditional bridge management programming process. Seismic retrofits may also be required on a structure. Combining all work activity, which is currently not performed, may result in exceedance of threshold percentages of replacement costs, thereby initiating replacement activity as opposed to individual actions to address the respective needs. Furthermore, as a large percentage of structural replacement costs involve indirect costs, such as mobilization and maintenance/protection of traffic, significant costs savings may be realized. Thus, simultaneous consideration results in lower life-cycle costs and reduced user-impacts.

To provide the background for the development of the methodology, the mathematical models used for bridge management are first summarized, followed by an examination of current approaches for seismic prioritization. Following these examinations, data availability is summarized through examination of current inventory-wide data sources. Damage exhibited through past earthquake events is summarized and data requirements assessed on

the basis of the damage modes and current prioritization procedures. Alternative approaches for the development of the methodology are outlined, the constraints on model output imposed by predominant bridge management systems assessed, and the available alternatives for model development examined and discussed. Viable approaches are then examined in detail with the results analyzed using a sample data-set culled from the California bridge inventory and inspection system.

BMS Preservation and Improvement Models:

The structure of bridge management systems employed in the United States focuses on the Pontis system. The Pontis system employ more detailed, element-level data models, probabilistic deterioration models for each element over defined condition states, a Markovian decision processes to determine the optimal element-level policy, translational routines to determine bridge level preservation needs, and level of service based functional improvement optimization. Unconstrained needs developed through preservation and improvement optimization are combined through an incremental benefit/cost algorithm to form a long-range bridge plan subject to budgetary constraints. Each of these is briefly described in the subsequent paragraphs.

Element-level bridge models are employed giving additional, quantitative detail on the beams, girder, deck, bearings, abutments, piers, joints, railings, sidewalks, and other elements within standard highway bridges. An element level model is developed by defining the types of elements on the bridge, the quantities of the elements. In Pontis, the AASHTO defined Commonly Recognized (CoRe) element models are employed, which may be complemented by user-defined elements if necessary for bridge owners. Each quantity of each element may be in varying conditions states, which are defined by the system. As an example, Element 107 – Painted Steel Multi-Girders have condition states from 1 indicating no distress to the member or the paint system through 5 indicative of section loss to the members. Intermediate condition states describe paint distress, rust formation and active corrosion.

Through periodic inspection, the distribution of element quantities across the condition states is determined. Considering the painted steel girder element, inspectors enter percentages of the total quantity of the girders in each condition state during periodic inspection of the structure. Quantities are aggregated at the network level and a Markovian deterioration model is employed to determine future condition state distributions. Activities may be implemented which impact the condition of the element. Pure deterioration occurs only when a 'do-nothing' activity is employed. The probability of element quantities transitioning from one-condition state to the next, lower condition state is defined through a single-step constraint for the 'do-nothing' policy (i.e. allowing the member quantities to deteriorate). Available actions and action effectiveness are defined for each condition state of each element. Actions, when undertaken, result in first costs and positively impact the future condition state distributions. Deterioration probabilities and action effectiveness models are shown in Table 1 for Element 107 – Painted Steel Multi-Girders.

After an action is completed, element quantities again begin to deteriorate. Over time, quantities deteriorate from one condition state to the next until actions either must be taken or element failure occurs. Therefore, all actions, including the do-nothing activity, generate life-cycle costs. The decision process employed by Pontis focuses on determining the optimal policy defined as the set of actions across the condition state model which result in the minimum life-cycle cost over an infinite horizon.

Table 1: Example Deterioration and Action Effectiveness Models for Element 107

#	*Action Description*	*Transition Probabilities (as percentages)*					*First Cost*	*Long-Term Cost*
		State 1	*State 2*	*State 3*	*State 4*	*State 5*	*($/unit)*	*($/unit)*
	1 – No Distress							
0	Do nothing	93.81	6.19	0	0	0	0	172.28
1	Surface clean	100	0	0	0	0	62.34	190.47
	2 – Paint Distress							
0	Do nothing	0	88.88	11.12	0	0	0	318.96
1	Surface clean	1	99	0	0	0	80.84	332.65
2	Surface clean & repaint	96	4	0	0	0	225.26	583.38
	3 - Surface Rust							
0	Do nothing	0	0	87.18	12.82	0	0	447.85
1	Spot blast, clean & paint	88	12	0	0	0	328.48	557.70
	4 - Active Corrosion							
0	Do nothing	0	0	0	90.55	9.45	0	602.41
1	Spot blast, clean & paint	61	14	5	20	0	455.9	570.14
2	Replace paint system	97	3	0	0	0	396.32	583.38
	5 - Section Loss							
0	Do nothing	0	0	0	0	90.55	0	1599.03
1	Major rehab of unit	30	9	1	20	40	1279.52	1404.86
2	Replace unit	100	0	0	0	0	2394.82	2563.44

For the example shown in Table 1, the optimal policy is thus:

- Do Nothing for Element Quantities n Condition States 1, 2 and 3
- Spot blast, clean and paint element quantities in Condition State 4
- Perform a major rehabilitation on element quantities in Condition State 5

The optimal policy is based on many variables, including the rate of deterioration of the elements, which is considered through definition of environment states, the cost of the actions, the effectiveness of the actions, and the cost of element "failure". Element failure costs and probabilities reflect the impact of element quantities moving to a condition that is worse than the last condition state definition. When the optimal policy is determined, it is used to guide the selection of network-level policies, determine optimal long-term budget requirements, and select project-level activities. In generating these estimates, improvement needs must also be incorporated. This is done through use of the functional improvement optimization model.

Unlike preservation actions, improvement activities change the level of service of the bridge; however, once taken, the physical characteristics do not change over time. New actions are triggered by increasing level of service requirements, which occur through traffic growth or changes in the traffic characteristics. Therefore, improvement considerations are static in nature and the optimization is modeled deterministically. The optimization procedure

seeks to maximize the benefit obtained, in terms of user costs savings, given budget constraints. Benefits are quantified based on the level-of-service deficiencies. For instance, a bridge with insufficient clearance causes a portion of the truck population to be detoured. Knowing the average daily truck traffic and the length of the detour permits quantification of the user impact of the deficiency. Removal of the deficiency results in benefit obtained. Costs for removal of the deficiency can be estimated and benefit-cost ratios for varying levels of improvement are obtained. With alternates for individual structures and competing needs throughout the network, the optimal set of improvement actions can be determined for each budgetary year using an incremental benefit-cost analysis.

With improvement and preservation policies and actions determined, project level results can be obtained by combining needs, quantifying the benefit obtained, and employing an incremental approach for project development. In Pontis, results are obtained for each year over a user-defined planning horizon by selecting projects until the budget is exhausted for that year. The process is then repeated for the next year and continued over the horizon of interest to the user.

Seismic Prioritization:

Seismic prioritization procedures have been developed by several States, the FHWA, and through several research efforts undertaken in academia. The procedures form the basis for seismic retrofitting programs, which as previously discussed, typically operate independently from bridge preservation and improvement programs. Significant benefit can be obtained through combination of actions within a single bridge program.

Several alternative approaches have been developed, including additive rating development, multiplicative prioritization, hybrid approaches, and probabilistic/risk-based approaches. Additive approaches are generally of the following form (shown for an index based on a 0 to 100 scale):

$$\text{Priority Index} = \sum_{i=1}^{3} (\text{weight}_i)(\text{rating}_i) \qquad \text{[Eq. 1]}$$

where:

$$\sum_i \text{weight} = 10$$

$$0 \leq \text{Rating}_i \leq 10$$

Weights are assigned and each structure is rated in various categories with the results summed to obtain an overall rating, which then is used for prioritization. Multiplicative approaches generally take the following form:

$$\text{Rank} = (\text{Vulnerability})(\text{Seismic Hazard}) = V \times E \qquad \text{[Eq. 2]}$$

With the additive approach, typical of the form shown in Equation 1, the priority index tends to be insensitive to pertinent variables. The multiplicative form, typical as shown in Equation 2, tends to be overly influenced by individual variables. Hybrid approaches have thus been developed to try and compensate for these limitations. Risk-based approaches and approaches employing multi-attribute utility theory have also been proposed. Regardless of the approach used, variables that are critical for assessing damage to a structure during a

potential seismic event are employed together with assessment of the seismic hazard and the importance of the structure within the bridge system. The following types of damage have been seen during past seismic events:

- Damage due to displacement deficiencies
- Abutment slumping
- Column Failures
- Cap-Beam and Joint Failures
- Footing Failures

Displacement damage generally occurs due to inadequate seat lengths compounded by potential amplification of motion due to soil effects. The most widely experience form of damage results from loss of support due to excessive movement. Substructure pounding by the superstructure has also been exhibited. Displacement damage is a function of the bearing types, the seat lengths, the continuity of the structure, span lengths, soil types, etc. Substructure damage includes slumping of abutments in soft soils and poorly consolidated fills, column failures, cap-beam failures, and footing failures. In general, substructure damage is a function of the flexural and shear capacity of the substructure member, ductility, soil characteristics and substructure/superstructure geometries.

All prioritization procedures incorporate variables intended to indicate the potential for damage resulting from some or all of these damage modes given a seismic event. A list of variables used by various prioritization procedures is shown in Table 2. For incorporation of a seismic risk mitigation procedure in a bridge management system, information must be available for structures throughout the network. Thus data availability from network-level data sources becomes a critical issue. Hazard information may be readily obtained through geologic data sources, such as NEHRP, USGS or even Strong-Motion records. Importance information can be generated from functional data on the structure obtained through the NBI. Economic information may be more difficult to determine; however, procedures could be readily generated to consistently define importance in economic terms enabling the procedure to be valid when relative results are compared. Vulnerability data is more of an issue. The NBI and bridge element level-models were examined. The NBI databases give indications of the span continuity, the structural design type and material, the number of spans and span lengths, bridge deck widths, features carried and crossed, scour potential and the skew of the structure. Additionally, the hight of the piers can, in some cases, be inferred with reasonable accuracy from the underclearance information. Element-level models give additional detail on the substructrure design types, the bearings types, the type of footings utilized, and the presence of piles.

All of the potential data available for structural vulnerability assessment is insufficient and more detailed information must be generated in order to use of any of the prioritization procedures as the basis for the development of a model.

Table 2: Summary of the Data Requiremnetns of the Prioritization Procedures

Variable	FHWA	CalTrans		WA & TRAC	ODOT	Tazman	Kim	NV
		Orig.	Rev.					
Support Conditions								
Bearing Type	Yes				Yes			Yes
Support/Seat Length	Yes				Yes	Yes	Yes	Yes
Restrainers	Yes							
Span continuity	Yes			Yes				
Pedestal configuration	Yes							
Bearing seat continuity	Yes							
Midspan hinges	Yes		Yes	Yes			Yes	Yes
Shear key adequacy	Yes							
Bearing connections	Yes				Yes			
Superstructure Considerations								
Superstr. Design Type	Yes						Yes	
Superstr. Configuration	Yes					Yes		
Superstructure Material					Yes	Yes	Yes	
Skew	Yes	Yes	Yes			Yes	Yes	
Slope in Bridge Axis								
Number of spans	Yes			Yes	Yes	Yes		
Span lengths	Yes	Yes				Yes		
Deck width	Yes							
Substructure Considerations								
Substr. Design Types	Yes	Yes	Yes				Yes	
Substr. Configurations	Yes	Yes	Yes		Yes		Yes	
Substr. Material	Yes					Yes	Yes	
Height Piers/Columns	Yes		Yes				Yes	
Type of Footings							Yes	
Piles								
Structural Considerations								
Reinforcement Details	Yes				Yes			Yes
Framing factor	Yes				Yes			
Plastic hinge locations	Yes							
Column confinement	Yes	Yes			Yes			Yes
Footing/pile connect.	Yes							
Anchorage	Yes				Yes			
Ductility	Yes					Yes		
Unsupported Length								
Bracing								
Shear capacity								
Geotechnical Considerations								
Soil type	Yes		Yes				Yes	
Soil compaction	Yes							
Fill heights & types	Yes							
Liquefaction potential								
Scour potential						Yes	Yes	
Other Geometric Info								
Clearances (super/sub)								
Feature carried/crossed	Yes							
Year of Construction	Yes		Yes		Yes	Yes	Yes	Yes

Use of Existing Prioritization Procedures as the Basis for Model Development

A sample of 25 structures was used to explore the correlation of results between various prioritization procedures, including those addressed in Table 2. Significant deviations were seen between the resulting priority indices for the sample bridges. The procedures follow differing approaches, utilize different variables for vulnerability and importance, and use different techniques for consideration of the seismic hazard. The hazard was, in each procedure examined, based on the expected peak ground acceleration. Hazard indices may or may not be modified by other variables in the prioritization, such as the seismic duration and activity, the soil types, remaining service life, etc.

It was expected that an examination of the vulnerability components and importance would show a strong correlation when performed in a categorical fashion. Moderate correlations were shown for displacement vulnerability and for importance. However, anomalies also resulted in significant deviations where one procedure would categorize a structure with high vulnerability/importance whereas an alternate procedure would characterize the same structure with low vulnerability or importance. It is recognized that the relationships between the results of the procedures could be presented in a more rigorous fashion. Statistical relationships were examined extensively to account for other factors, such as the shape of the curve, in the categorizations. Some of the single-step deviations are eliminated using these techniques. Significant variations persist even when these characteristics of the distributions were accounted for. These variations result for variable and parameter definitions, the type of procedure used to calculate the index, etc. Thus, it cannot be assumed that a structure having a particular vulnerability or importance rating in one procedure will receive a similar vulnerability or importance rating in an alternate procedure. Additional research would be required to assess the adequacy of the individual prioritization approaches and to guide the selection of an appropriate procedure for use of a prioritization procedure for model development.

To incorporate the results in a bridge management system, benefit-cost formulation must be developed. With the traditional prioritization procedures, level-of-service approaches could quantify the risk. Reduction of risk could then be quantified as a benefit. Costs would be estimated based on the retrofitting strategy employed. Thus mitigation through seismic retrofitting was examined. The primary source for isolating retrofitting strategies was the 1995 *FHWA Seismic Retrofitting Manual*. The *Manual* provides an extensive, though not complete, overview of available strategies. Retrofit techniques typically follow one of two strategies. The first strategy involves increasing the capacity of the structure, through conventional strengthening, to meet the expected demands. The second alternative approach involves reduction of the demand on the structure so that the existing capacity is sufficient for the expected loads. This involves the utilization of seismic protective systems, such as base isolation bearings. It is beyond the scope of this discussion to summarize all of the available strategies and the reader is referred to the *Manual* for more detail. Some retrofitting techniques are as follows:

- Installation of restrainers
- Replacing the bearings (with or without isolation systems)
- Increasing the available seat length
- Column retrofitting (wrapping, jacketing, etc.)
- Strengthening column bents and cap beams
- Soil remediation (lowering the water table, densification, etc.)

The retrofitting techniques presented are, in general, arrange in terms of increasing cost. The effectiveness of employing the techniques in reducing the seismic vulnerability would have to be assessed.

To use an existing procedure, the vulnerability measures must first be separated from hazard and importance variables. These hazard may be used to quantify the costs on a unit-cost basis ascertained using a measure value approach (also termed as a value-mapping approach). Single or multiple unit cost estimates may be applied, each of which would reflect different effectiveness measures. The benefits are a function of the traffic serviced by the structure. A similar approach may be employed to map the importance variables to cost measures; however, it is more realistic to utilize existing user cost measures in predominant bridge management systems as a basis for quantification of benefits.

The probability of seismic event occurrence may then be incorporated to quantify the seismic risk. Alternatively, the probability of event occurrence may be considered within the assessment of benefits and costs. This approach would then represent the expected benefit and expected costs with event probabilities cancelling from the formulation. Mathematically, the alternative approaches are represented as follows, with $f(v)$ indicative of the value function used to map variables to economic measures.

$$\text{Approach 1:} \quad B/C = p_{event}\left(\frac{\left(\sum(\text{Importance Variables})\right)f_I(v)}{\left(\sum(\text{Vulnerability Variables})\right)f_V(v)}\right)$$

$$\text{Approach 2:} \quad B/C = \left(\frac{\left(\sum(\text{Importance Variables})\right)p_{event}f_I(v)}{\left(\sum(\text{Vulnerability Variables})\right)p_{event}f_V(v)}\right)$$

where f_I and f_V represent value functions used for mapping

The above formulation, with either approach for the inclusion of event probabilities as depicted, implies the complete removal of vulnerabilities. Consider the methodology in terms of an incremental benefit cost ratio. The benefit and costs are taken as the differential between the seismic event occurring with vulnerable components versus the expected situation which would result if the event occurred with no seismic vulnerabilities. Full action effectiveness is thus assumed. The procedure could be modified through inclusion of action effectiveness estimates. Also, efforts could be made to separate vulnerability factor components by damage mechanism with different unit cost estimates applied based on the type of vulnerability. For instance, one estimate could be applied to mitigate displacement vulnerabilities while a second, typically higher estimate would be applied for substructure vulnerabilities.

The use of existing prioritization procedures as a basis for the development of a BMS-specific seismic retrofit model thus appears to be a viable alternative, particularly for network-level analysis. Applicability, however, is dependent upon the effectiveness of the prioritization procedure in quantifying the vulnerabilities of the structures. This, as mentioned, is highly dependent upon the variables employed. Thus, a more rigorous approach is desired. Fragility concepts are thus explored for model development.

Philosophy of the Fragility-Based Approach

Fragility curves relate the probability of damage to the expected ground motion. The curves are typically classified by design and construction features. Basöz and Kiremidjian have assessed published classification schemes used as the basis for the damage-ground motion relationships in ATC-13 and in the National Institute of Building Sciences (NIBS) approaches. These existing classification schemes were shown to have significant limitations and a more detailed classification procedure was devised based on primary and secondary structural attributes. Primary structural attributes are reflective of the material and superstructure design types, and secondary structural attributes. The secondary attributes include the number of spans, the abutment type, the span continuity and the type of pier/bent. Four fragility curves are developed for each of the bridge classes, which are defined by the feasible primary structural attribute combinations. The categories for each bridge class reflect the low and high vulnerability single span bridge configurations, and low and high vulnerability multi-span structures.

Generic fragility relationships are shown graphically in Figure 1 for major damage and minor damage. The two different fragility curves may be representative of different damage levels for a particular bridge class. Alternatively, the curves could be representative of different structure classes for a specific damage type. Damage levels must be defined. In the research performed by Basöz and Kiremidjian, damage levels are related to the primary and secondary structural attributes; thus, different physical damage states are defined for each class of fragility curves. Four to five categories have been suggested ranging from no damage to total collapse, which are reflected by the division of generic pdf, developed from the fragility relationships and shown in Figure 2. Standardization of damage classes has been discussed in the earthquake engineering community for a number of years; however, consensus on appropriate damage classes has not been established.

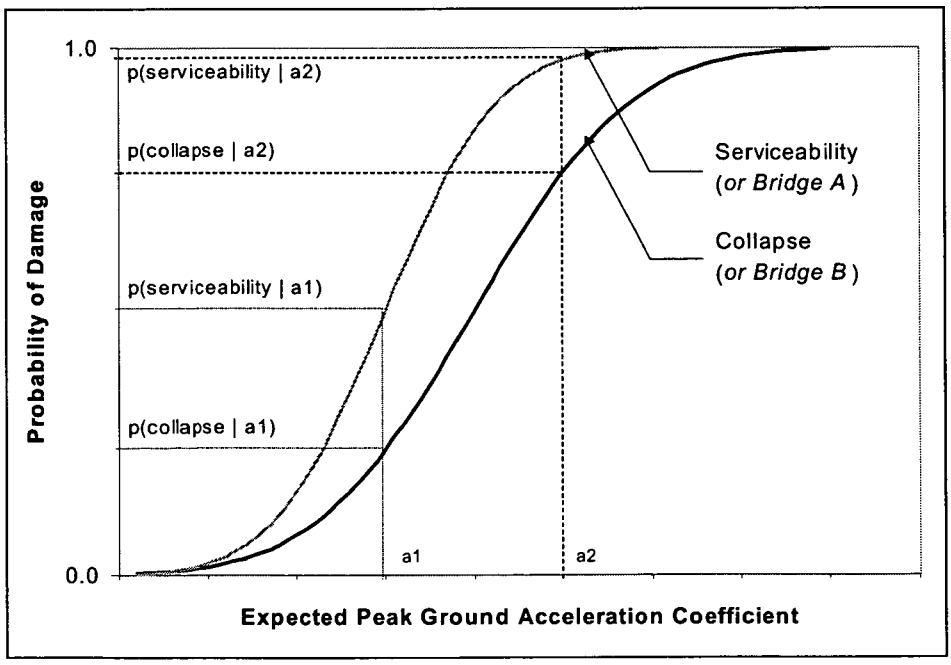

Figure 1: Generic Fragility Relationships for Different Damage Levels

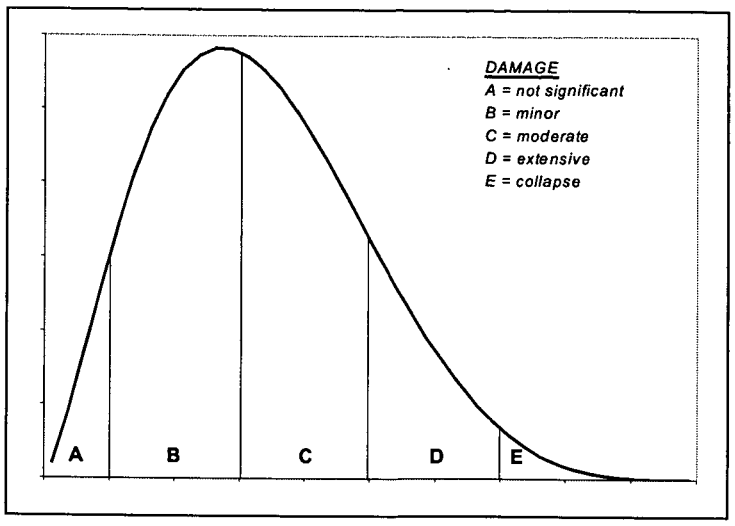

Figure 2: Generic pdf Depicting Damage Class Definitions [Basöz & Kiremidjian, 1995]

There is a need to develop more detailed fragility models and research has been underway through MCEER Highway Project to develop fragility relationships through examination of historical data. This effort, if successful, could provide the basis for the development of the model for incorporation of hazards within BMS. Whatever technique is employed for fragility relationships, they must be structured to permit application of multiple retrofit levels, each of which must embody different levels of effectiveness at alternative costs. For instance, consider the distributions shown in Figure 3. The 'as-is' fragility is presented together with two alternate distributions which correspond to the distributions after retrofit thus reflective of the effect of the retrofit actions. The cost of the individual actions is relatively easy to obtain, when contrasted to the effort required to ascertain effectiveness and the effect of the action on the fragilities. Retrofit actions may either be generic in nature, such as displacement or substructure, or detailed, such as replacement of bearings, reconstruction of bridge seat, etc. Naturally, the former is easier to utilize for generation of abstract fragilities; however, the latter facilitates cost estimation.

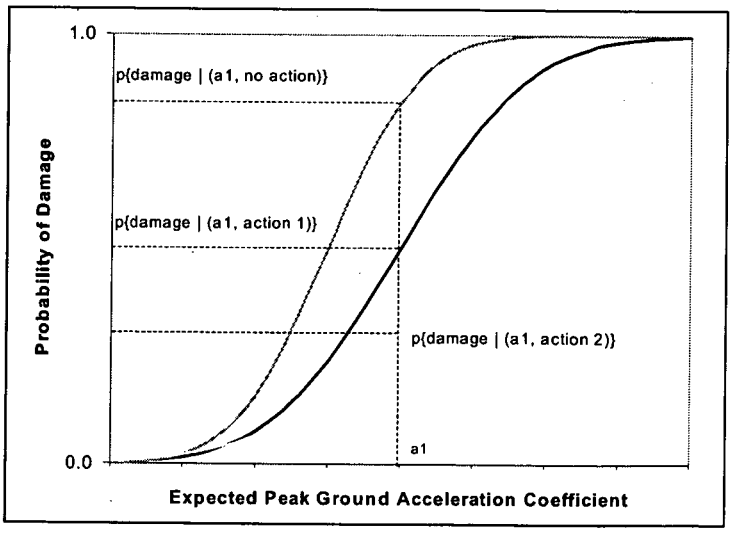

Figure 3: The Effect of Alternate Retrofit Actions on Fragility Distribution

These fragility relationships require extensive knowledge on the impact of individual retrofit technique on probability of damage for the entire structure. Ideally, a structure which decomposed the damage modes (i.e. displacement damage, abutment slumping, column failuire, etc.) would facilitate the assignment of alternate levels of retrofitting. This would enable consideration of alternative project-level strategies and examination of different network-level policies through an incremental benefit-cost analysis approach. Consider the probability of displacement damage on an example bridge given expected peak ground accelerations as shown in Figure 4.

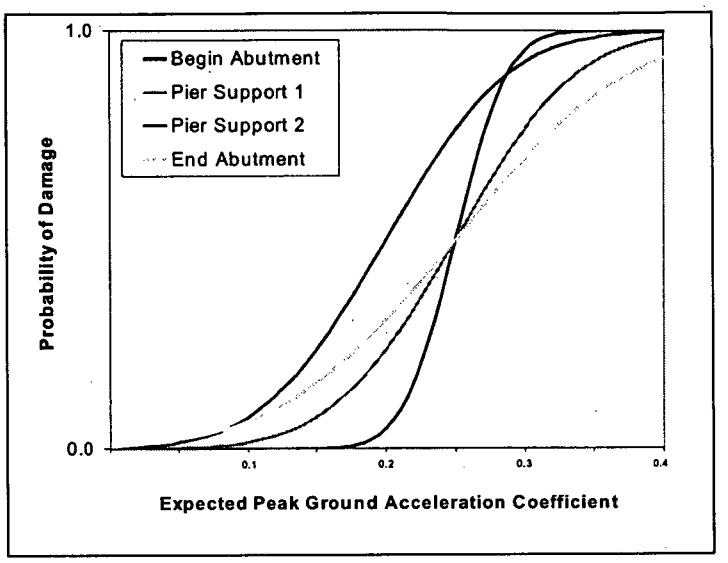

Figure 4: Example Bridge Displacement Ground Motion-Damage Relationships

Assume that for the example bridge the expected peak ground acceleration coefficients have been determined at the bridge location using a 10%, 5% and 2% probability of exceedance in a 50 year period (PGA_{10}, PGA_5, and PGA_2). The coefficients are 0.20, 0.275 and 0.35 respectively. The probability that damage will occur is tabulated by component in Table 4-1. Now, consider retrofit of the structure for the various levels of expected ground motion separately assuming complete retrofit effectiveness (when a retrofit action is taken, the probability of damage becomes negligible). For PGA10, retrofitting Pier (2) results in a reduction of the probability of displacement damage to the bridge from 0.5 to 0.309, at which point, no further reductions can be made to reduce the probability of damage without focusing on the end abutment. This approach facilitates an incremental analysis. Similar techniques could be used for network-level analysis incrementally examining alternate retrofit policies.

Table 3: Probability of Damage for Example Structure Expected Peak Ground Accelerations

Component	PGA_{10}	PGA_5	PGA_2
Begin Abutment Displacement	**0.048**	**0.748**	**0.999**
Pier – Support Location 1	**0.238**	**0.613**	**0.923**
Pier – Support Location 2	**0.500**	**0.841**	**0.984**
End Abutment Displacement	**0.309**	**0.579**	**0.841**
Column	**0.077**	**0.334**	**0.763**
Abutment Vulnerability	**0.016**	**0.127**	**0.500**

Table 4: Retrofit Strategies and Resulting p(damage) for the Example Bridge

PGA – 10		PGA - 5		PGA – 2	
Retrofit	*p (damage)*	*Retrofit*	*p (damage)*	*Retrofit*	*p (damage)*
None	**0.500**	**None**	**0.841**	**None**	**0.999**
Pier (2)	**0.309**	**Pier (2)**	**0.748**	**Begin**	**0.984**
End	**0.238**	**Begin**	**0.613**	**Pier (2)**	**0.923**
Pier (1)	**0.077**	**Pier (1)**	**0.579**	**Pier (1)**	**0.841**
Columns	**0.048**	**End**	**0.334**	**End**	**0.763**
Begin	**0.016**	**Column**	**0.127**	**Column**	**0.50**
Abutment	**~ 0**	**Abutment**	**~ 0**	**Abutment**	**~ 0**

The technique outlined requires translation of p(damage) values into monetary terms, which can be done through quantification of the risk in relation to the seismic hazard. Using this approach, reduction in damage potential directly determines the benefit obtained. Work must be performed to ensure that the relative magnitude of benefit-cost ratios is consistent with preservation and improvement benefit-cost ratios. Without consistency, alternative bridge program activities could not be combined within a single integration and project programming module. In other words, one type of activity (i.e. retrofitting or improvement) would dominate other activities when developing bridge program.s.

Conclusions:

Bridge management systems provide a proactive, rigorous decision support platform for decision support on preservation and improvement needs within a network of structures. Retrofitting for natural hazards and extreme events is not presently included within the predominant systems. As bridge failures typically result from these events, retrofitting structures is a primary concern, be it for seismic, scour, collisions or other hazards. Benefit can be obtained by including retrofitting considerations within the systems and developing bridge programs considering a wider scope of activity. The feasibility of integrating a natural hazard component within a BMS was examined by focusing on seismic vulnerabilities. The structure of BMS preservation and improvement optimization was discussed to provide a basis for incorporation of a retrofit model. The results of such a model must be output in terms of benefit-cost ratios and included using an incremental approach. Existing seismic prioritization procedures were first examined to determine whether they could provide the foundation for the development of a retrofit module. It was seen that there are significant differences in the results of the prioritization procedures and difficulties in mapping the priorities into economic terms. Fragility concepts were explored as an alternative approach. If fragility relationships could be developed based on the actual configuration of a structure, a rigorous methodology could be readily developed. Additional research would be required to explore the development of the fragility 'envelopes', quantify the effectiveness of alternative techniques, and calibrate economic results into a compatible format for combination with preservation and improvement activities.

References:

Applied Technology Council, "Seismic Retrofitting Guidelines for Highway Bridges." Report ATC 6-2, FHWA/RD-83/007, Sponsored by the Office of Research and Development, Federal Highway Administration, Washington, DC, December 1983.

Basöz, N. and Kiremidjian, A.S., "Prioritization of Bridges for Seismic Retrofitting." Report No. 114, John A. Blume Earthquake Engineering Center, Department of Civil Engineering, Stanford University, Palo Alto, CA, January 1995.

Blundell, F., *Improvement Optimization Model*, Pontis Support Center, Technical Note, May 1997.

Cambridge Systematics, *Pontis Release 3.1 – Users Manual*, Prepared for AASHTO, Washington, DC, June 1996.

National Engineering Technology (NET) Corporation, "Bridgit Bridge Management System: Technical Manual - Version 1.00." NCHRP Project 12-28(2)A, National Cooperative Highway Research Program, Transportation Research Board, Washington, DC, December 1994.

Thompson, P.D., Small, E.P., Johnson, M., Marshall, A., *The AASHTOWare™ Pontis™ Bridge Management System*, Structural Engineering International, 1998.

Urban Institute, The, and Cambridge Systematics, Inc., "AASHTO Guidelines for Bridge Management Systems." Draft Final Report, NCHRP Project 20-7, Task 46, National Cooperative Highway Research Program, Transportation Research Board, Washington, D.C., November 1991.

US Department of Transportation, "National Bridge Inventory Information System." Office of Engineering - Bridge Division, Federal Highway Administration, Washington, DC, October, 1992.

US Department of Transportation, "Recording and Coding Guide for the Structural Inventory and Appraisal of the Nation's Bridges." Office of Engineering - Bridge Division, Federal Highway Administration, Washington, DC, January 1989.

USDOT, Federal Highway Administration, Buckle, I.G., and Friedland, I.M., editors, "Seismic Retrofitting Manual for Highway Bridges" Report FHWA-RD-94-052, Grant DTFH61-92-C-00106, Sponsored by the Office of Engineering and Highway Operations R&D, Federal Highway Administration, Washington, D.C., May, 1995.

Maintenance and Management of Bridges in the Metropolitan Expressway

by Tadashi YOSHIKAWA *

* Chief of Technical Management, Maintenance Technique Division, Maintenance & Facilities Department, Metropolitan Expressway Public Corporation

The total length of the Metropolitan Expressway (MEX) is currently 264 km, and it handles an average daily traffic volume of 1.15 million vehicles. Used by roughly 2 million people each day, the facility plays an important role in supporting industries and daily life in the Greater Tokyo Metropolitan Area. The expressway consists of 82% elevated roads, 6% tunnels, 7% subsurface structures and 6% earthwork sections. One-third of the entire network has been open for over 30 years, while fully one-half has been open for over 20 years. The structures have withstood heavy traffic during this long period, but partial damage has built up over the years. Thus, early detection of damage and prompt repair and reinforcement of road facilities are both important and urgent. This paper reports on the inspection, repair and reinforcement work being implemented on road structures that have been exposed to heavy traffic.

1. Summary

The Metropolitan Expressway was constructed as an urban toll expressway system to ensure smooth road traffic within metropolitan Tokyo and its suburbs. Since 1959, this expressway has been indispensable to the development and upkeep of the functions of the metropolitan Tokyo area. Being an urban expressway, the Metropolitan Expressway passes over trunk roads and rivers.

The Metropolitan Expressway, therefore, includes elevated structures, bridges, subsurface sections and tunnels. The service length of the Metropolitan Expressway has steadily increased each year, with the current length now reaching 263.4 km. The average daily traffic volume has also increased to 1.15 million vehicles. It is extremely important, therefore, to keep road structures in good condition to ensure the safety of the expressway system.

As of April 2001, the Metropolitan Expressway consisted of 81.9% elevated roads, 5.6% tunnels, 6.7% subsurface structures and 5.8% earthwork sections (Fig. 1). This indicates the importance of implementing measures for maintaining the viaducts. The Metropolitan Expressway went into service over 30 years ago. As of April 2001, routes that have been open for 20 years or more account for 51.6% of the entire network, and routes with at least 15 years of service account for 65.7% (Table 1).

The structures comprising the Metropolitan Expressway must support heavy traffic, which may total as many as 100,000 to 150,000 vehicles per day (4-lane road) in spot traffic volume (Fig. 2). Further, the ratio of heavy-goods vehicles (often overloaded) is extremely high. Because of this, structural deterioration takes place very rapidly. We must, therefore, inspect and repair elevated structures before they become unrepairable to assure that the metropolitan Tokyo area continues

functioning properly. Earlier detection of damage and implementation of the necessary structural repairs are crucial. As a result of these activities, recurring damage can be prevented and traffic safety can be ensured.

2. Maintenance and Inspection

2.1 Maintenance

Necessary expressway maintenance work can be classified into (a) maintenance and repair and (b) related management work. Classification (a) can be further sub-divided into (1) Maintenance, (2) Inspection and (3) Repair. For maintenance of the expressway, cleaning work is primarily performed on the road surface and road structures. Cleaning is fundamental to maintenance and also the first step of maintenance since dirty roads or structures or defective drainage will accelerate deterioration of the structures. Objects that have fallen onto the expressway may also cause accidents. For maintenance, the road structures and road facilities are cleaned. Items to be cleaned and the frequency of cleaning are shown in Table 2.

2.2 Inspection

Regular patrols are carried out to discover road structures that have deteriorated or sections that have become damaged and to ensure traffic safety. For traffic safety on the expressway, two forms of inspection are carried out. In one type, the expressway is inspected, and in the other, the road structures are inspected under the elevated structures to determine if they have been damaged. Inspection of the road along the expressway is done primarily from patrol service cars, with some being carried out on foot. Inspection under elevated structures is performed primarily on foot to assure close visual and instrument-based inspections.

Inspections are divided into a) Routine Inspection, b) Regular Inspection and c) Emergency Inspection.

2.2.1 Routine Inspection

Routine inspection of the expressway is done by judging the feel of the ride in the patrol service cars, while visual inspection is carried out under elevated structures. The expressway is inspected daily, and areas under elevated structures are inspected twice monthly during the daytime. The object of routine inspection is early discovery of significant and critical damage. Regular patrols deal quickly with traffic accidents, vehicle failures, car disasters, fallen objects and other incidents in addition to the inspection of significant damage to road facilities. These patrol service cars survey the entire network 12 times per day or roughly every two hours, traveling a total distance of 3 million kilometers per year, or about 75 times around the earth.

2.2.2 Regular Inspection

Regular inspection is carried out according to an inspection schedule, and this includes visual

inspection from temporary scaffolding and close inspection from bridge inspection vehicles. The object of regular inspection is to identify damage that may look insignificant but is actually critical.

Regular inspection goes into the very details of structures, which cannot be checked in routine inspection. Since particular attention is given to the soundness of structures in a regular inspection, it is possible to grasp a clear understanding of the damage situation by employing inspection equipment, in addition discovering damaged sections. In some instances, the need for regular inspection may depend upon the result of a routine inspection. In addition, follow-up inspection may be done to determine the age deterioration of damaged sections, depending on the extent of damage, and the data can be used to study repair and/or reinforcement of the network. Frequency of inspection varies depending upon the section; however, the basic rule is to perform inspection once every 5 years.

Typical items for regular inspection items the frequency of each are shown in Tables 3 and 4.

2.2.3 Emergency Inspection

Emergency inspection is carried out to determine the condition of damage when the structures have been damaged by an abnormal situation such as earthquake, typhoon or traffic accident. Details of inspection vary with the situation, but necessary inspections are carried out to confirm the safety of structures.

2.3 Results of Inspection and Evaluation

The results of each inspection (routine inspection, regular inspection or emergency inspection) are classified as shown in Table 5 according to the extent of damage. Repair or reinforcement work will be carried out according to the rankings. Re-inspection of the site and repair, reinforcement, or additional survey, or the like are required. Type of damage requiring no action until next inspection.

3. Repair Work

3.1 Lane Control for Repair Work

Any damage discovered by the inspection must be promptly repaired. In particular, damage to the expressway will be repaired as soon as it is discovered because it may jeopardize traffic safety. However, the present heavy traffic does not allow us to limit traffic for extended periods of time. Because of this, temporary repair is carried out to ensure the safety of traffic without obstructing it. After the temporary repair, full-scale repair is carried out during low-traffic times such as night time, when there is significantly less traffic volume. For non-expressway damage, repair work is carried out by establishing the best time for doing the work, setting up scaffolding and so forth after the investigation has determined the cause, and the repair method and repair work have been decided.

3.1.1 Single Lane Control

To carry out the repair work on the expressway road surface, a working zone must be established on the expressway that minimizes obstruction of traffic. However, the repair work must be carried out between 11:00 p.m. and 6:00 a.m. when the traffic can be limited to a single lane, because

the Metropolitan Expressway road network system is important for metropolitan area traffic flow. In addition, work that generates noise must be started by 9:00 p.m. and finished by 11:00 p.m. in consideration of the comfort of nearby residents.

3.1.2 Work with Complete Closure

On the other hand, structures of the Metropolitan Expressway have carried heavy traffic for many years and thus exhibit considerable deterioration. It became inevitable, therefore, to carry out large- scale repair work by completely closing a certain route. Closure is particularly appropriate for the replacement of rapid curing concrete slabs and full re-paving. Though complete closure of the route caused significant impact on the traffic of the metropolitan Tokyo area, large-scale repair work was carried out on a certain route by completely closing it for between 5 and 7 days. For such repair work, there must be preliminary consultation with the related authorities such as the Metropolitan Police Department, which is responsible for the control of traffic in Tokyo, to minimize the possible impact on traffic.

3.2 Examples of Repair Work performed on the Structures of the Metropolitan Expressway

When inspection finds progressive damage, prompt action must be taken to prevent further damage. If repair or reinforcement work on the structure is delayed, significant damage to the structure will be caused, but worse, traffic safety may not be ensured. The network went into service more than 30 years ago, and many types of damage to the structures have been found as vehicle size has increased and structures have deteriorated. To cope with ever-increasing vehicle size and ever-growing traffic volume, the structures have been reinforced to prevent possible damage to the structures. Typical examples of repair or reinforcement work are introduced in this section.

3.2.1 Steel Girder and Bridge Pier

Photo 1 reveals one type of damage in the notched section at the end of a main girder. Stress tends to concentrate in the vicinity of such corners. This section received insufficient reinforcement, and eventually cracks or swelling were found on the web plate. This damage was discovered 15 years after the road went into service.

To repair the damage, a method was adopted that involved tightening both sides of the web plate of the damaged section with steel plates bearing reinforcement ribs and using high-tensile bolts as shown in Fig. 3. This is done because the load carrying capacity can be increased in advance by the increased thickness of the web plate at the end of the girder. An additional consideration is the fact that the web plate is reinforced against swelling by fastening the web plate with high tensile bolts.

Although it is preferable to perform all repair work without live load, it is not possible to close the road completely to traffic for an extended period. Such repair work is, therefore, done at night, controlling the number of lanes in service, so that the high tensile bolts can be tightened while the influence of the live load is minimal.

3.2.2 Pavement

Damaged pavement influences the safety of motor vehicles traveling on the expressway, so it must be repaired in its early stages. Measures for the repair of damaged sections include emergency repair and total re-pavement. Emergency repair ensures traffic safety by temporarily filling holes, patching damage and so on, while total re-pavement involves completely reworking the deteriorated pavement.

The standard thickness of (asphalt) pavement in elevated sections of the Metropolitan Expressway is 80 mm. Total re-pavement is implemented if the average depth of rutting reaches 20 mm, or if the cracking ratio is 20% or more. A group of machines used for carrying out highly efficient work is shown in Fig. 4.

In addition, we are currently working to ensure greater traffic safety by aggressively introducing a new type of pavement having excellent drainage properties on the Metropolitan Expressway. With this pavement, vehicle tires hardly splash rainwater, which ensures improved visibility for the driver.

3.2.3 Concrete Slab

When the condition of concrete slabs is evaluated as Rank-A, as shown in Table 5, the only effective repair method is to replace the concrete slabs. However, when a deteriorated area is comparatively large, replacement takes many hours and cannot be completed in a single night. In such cases, the work is carried out during large-scale repair work as mentioned in Article 3.1.2. Since this type of damage affects traffic, damaged places must be checked and repaired before they become critical. During the work, large areas of concrete slabs evaluated as Rank-A will be replaced. In photographs 2 to 5, the flow of concrete replacement work is illustrated.

3.2.4 Coating of Concrete Structures

Neutralization may cause deterioration of the surface of concrete handrails and bridge piers. When neutralization occurs, reinforcing bars corrode and the concrete separates. As a result of this separation, reinforcing bars are exposed and structural strength is lost. If a separated concrete fragment falls from an elevated structure, it may damage vehicles passing below or even cause injury to people. If this situation appears likely, the deteriorated concrete is chipped off, corrosion protection treatment is applied to the reinforcing bars, and partial repair is carried out using resin-type materials. Finally, the corroded section is coated with a resin paint.

The coating of concrete surfaces has recently been introduced to control deterioration and to improve appearance. The standard layers of concrete coating are shown in Fig. 5.

3.2.5 Beautification of Existing Viaduct

When the structures have been properly inspected and repaired, it is possible to maintain their initial functions. In many cases, however, viaducts that have been in service for many years no longer conform to the urban environmental requirements because they have been contaminated by exhaust emissions, drainage is exposed and in places, accessory facilities like noise barriers have been added.

In such cases, cosmetic renovation of existing viaducts is under way on the Metropolitan

Expressway wherever structures will be observed by many people, such as crowded shopping areas and near large railroad stations. Since it is not possible to add heavy articles to existing structures, noise barriers are employed to improve them, and concrete handrails are covered with thin laminated steel plates. Additionally, aluminum pipes called louvers are installed beneath the girders. Photo 6 shows a typical example of beautification through such measures.

4. After Repair or Reinforcement Work

For structures requiring repair or reinforcement work, it is important to design the work carefully so that no damage occurs when the work is done. It is also important to confirm that the work has been performed as specified. For sections requiring repair or reinforcement work, follow-up inspections may be done using measuring instruments etc. to confirm the results of the work.

For such sections, we keep a record of all repairs performed, and we carefully implement inspections to check for damage on these sections.

5. Conclusion

As the Metropolitan Expressway has grown, the importance of maintenance and repair work has also become more important. The network structure deteriorates with each passing year, and it is feared that such deterioration could cause damage to vehicles or injury to pedestrians passing under elevated structures. It is extremely difficult to replace structures in the urban area and, therefore, it is important to maintain the currently existing structures in good condition. In addition, unless proper maintenance work is carried out, repaired sections can sustain new damage. Thus, our goal is to locate all structural damage before it becomes too serious and to keep the expressway functioning properly.

References: "Road Maintenance and Management on the Most Heavily Used Expressway in the World" by Hiroshi Mitani and Kimihiko Izumi, December 2000

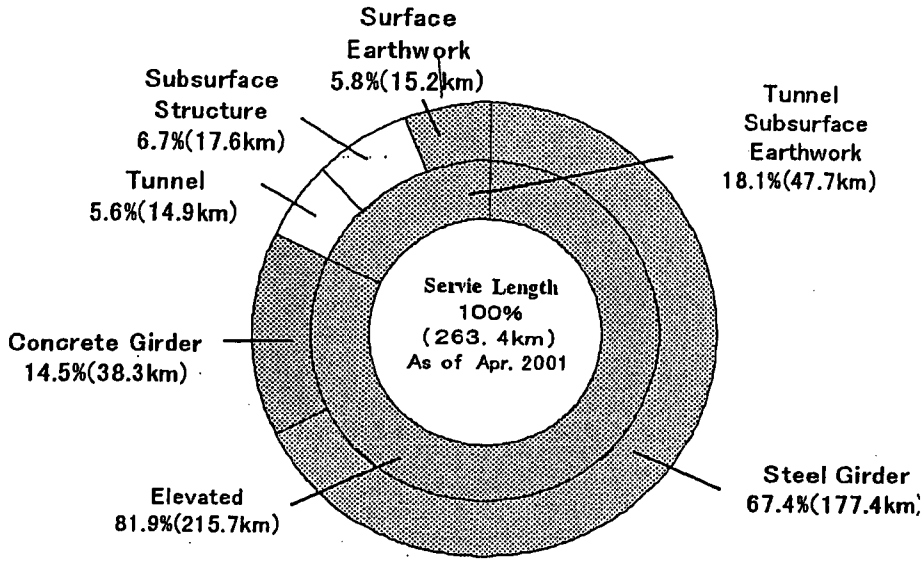

Figure1 : Length of the Metropolitan Expressway by Structure Type

Table1 : Metropolitan Expressway Years in Service

As of Apr. 2001

Years in Service	Length	Proportion
Over 30 years	89. 6 km	34. 0 %
20～29 years	49. 1 km	17. 6 %
10～19 years	81. 3 km	30. 9 %
Less 9 years	43. 4 km	16. 5 %
Total	263. 4 km	100. 0 %

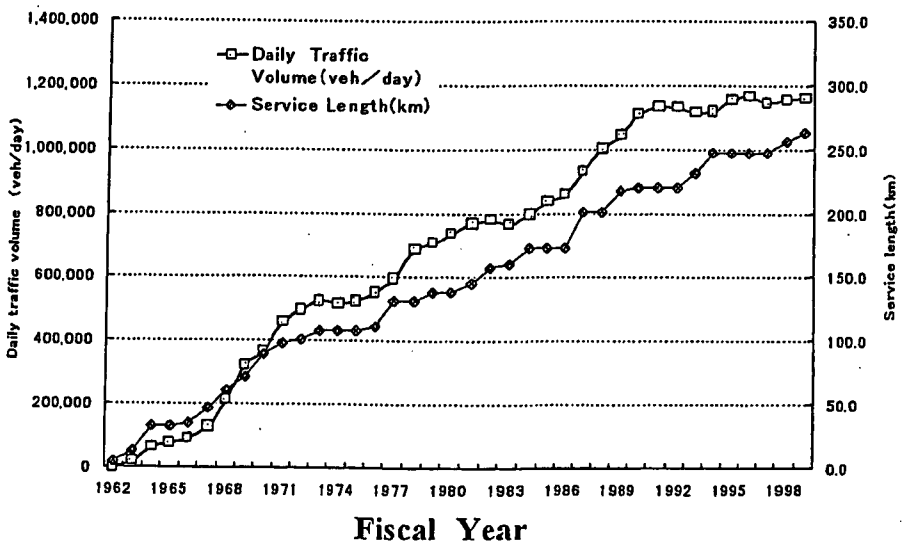

Figure2 : Growth of Traffic Volume

Table2 : Items to Be Cleaned and Frequency for Each

	Item	Frequency
Road structures	Road surface Clean road surface Remove fallen objects	 12 - 15 times/month Whenever needed
	Tunnel Clean tiled surface Clean entire cross section	 Once/month Once/year
	Guard rail	2 times/year
	Drainage system Drain basin Drain pipe	 Once/month Once/year
	Noise barrier	Once/year
Road facilities	Lighting, signs, variable sign boards	Once/year

Table3 : Items of Representative Periodic Inspection of Structures

Inspection underside of elevated bridges on foot	Visual check with a binocular under bridge on foot, for the purpose of early detection of excessive damages of structure, fallen obstacles possibly affecting any third party and abnormal noise. Frequency ; once / year (3 times / year for structures over 10 years in service)
Inspection from temporary scaffold	Visual check in a close distance with measuring instruments, using temporary scaffold erected for repainting girders or reinforcement work of Girders or deck slab. Frequency ; Every time when temporary scaffold is erected.
Inspection of piers and girders	Visual check in a close distance with measuring instruments, using inspection path or bridge inspection vehicle. Girder end, end-cross girder, slab deck, bearing and expansion joint around pier and pier beam are checked. Frequency ; once / 5 years

Table4 : Items of Representative Periodic Inspection of Concrete Structures

Inspection inside of concrete box girders	Check for any flaw or crack particularly appeared in floor slabs while entering directly into the box girder through existing man-hole. Frequency ; once / 5-7 years
Inspection of concrete girders taking pictures	Check for any damage appeared in photos of concrete girders which are taken by a photographing engineer under direction of an inspector (engineer and inspector forming a team). Photographic accuracy must enable to judge cracks whose width are approximately 0.1mm-0.2mm. Frequency ; once / 5-7 years
Follow-up Inspection of cracks in concrete	Check in order to grasp progress flaws and cracks in concrete Which require follow-up by measuring variation of remarkable flaw and crack with a contactgauge. Frequency ; twice / year (summer and winter)
Inspection of concrete slabs taking pictures	Check for any damage appeared in photos of concrete slabs, which are taken by a photographing engineer under direction of an inspector (engineer and inspector forming a team). Photographic accuracy must enable to judge cracks whose width are approximately 0.1mm-0.2mm. Frequency ; once / 5-7 years

Table5 : Judgement Criteria for the Results of Routine Inspection, Regular Inspection and Emergency Inspection

Rank	Comments
A	As the soundness of the structure was undermined to a major extent, hindrance to the traffic and influence over the third persons has become large and urgent repair is required.
B	Damage is observed and it is necessary to execute repair, but urgent repair is not required. Furthermore, it is necessary to increase the load carrying capacity of the structure or to recover travel ability or appearance.
C	There is damage and it is necessary to keep its extent in the record.
D	There is no/minor damage but it is necessary to keep it in the record.

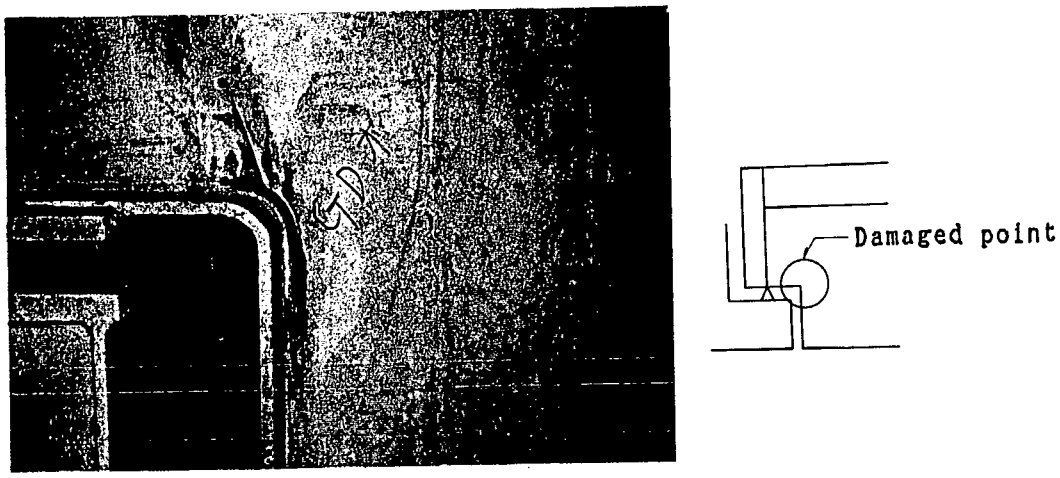

The black points marked at the top end of the crack are stop holes to prevent progressive cracking.

Photo 1: Fatigue Crack found on the Notch Section of a Steel Girder

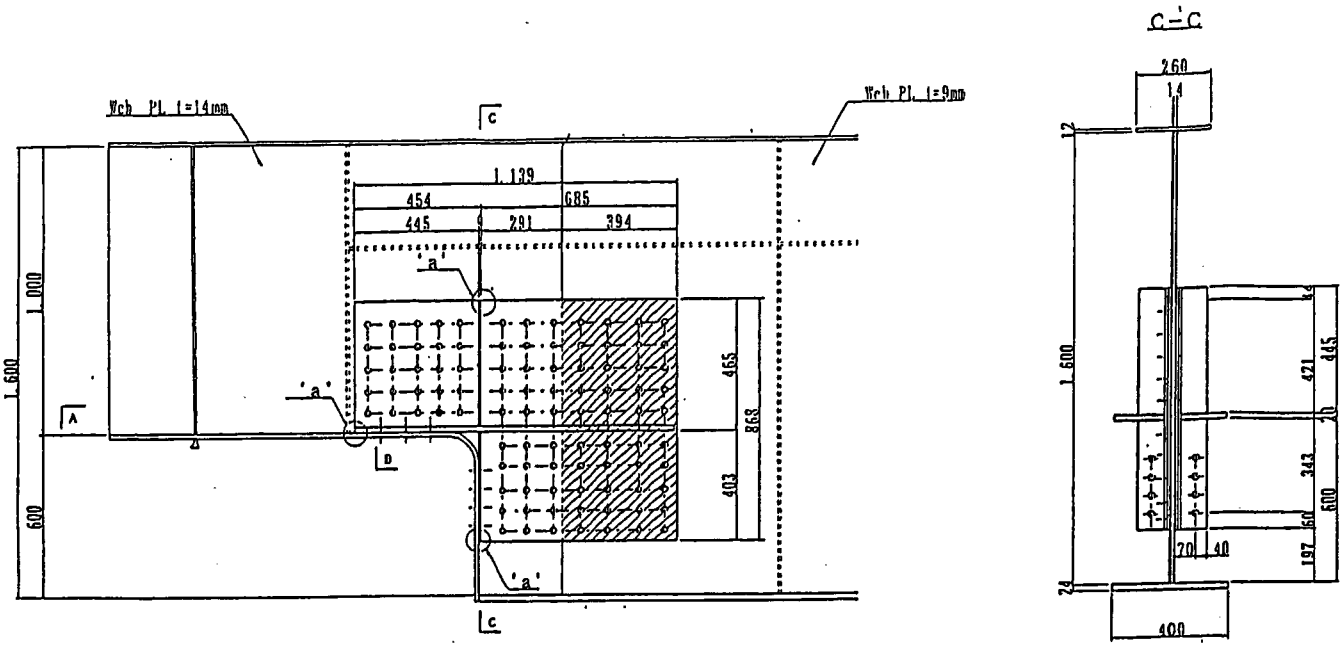

Figure3 : Repair to a Gerber Hinged Portion of Steel Girder

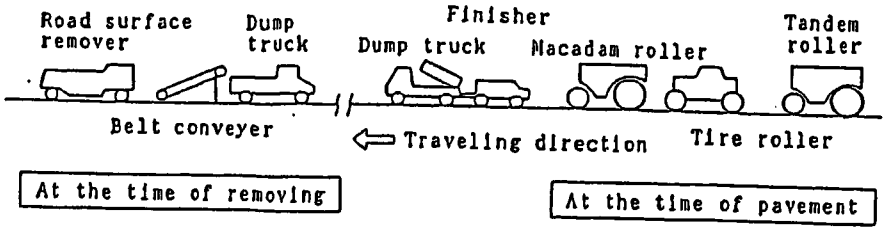

Figure4 : Group of Machines for Repavement

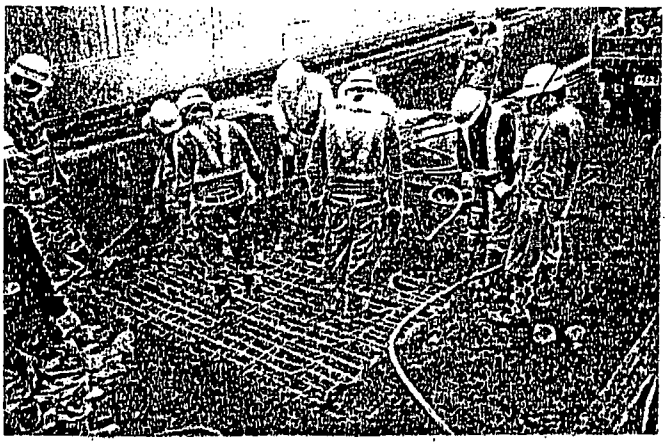

Photo2 : Breaking of Concrete Slab

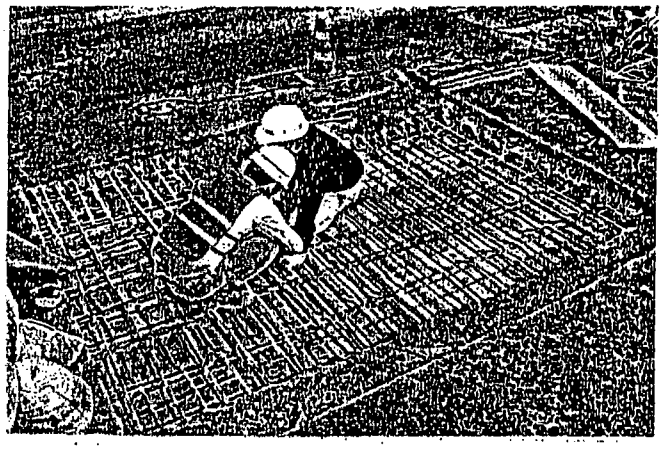

Photo3 : Bar Rearrangement

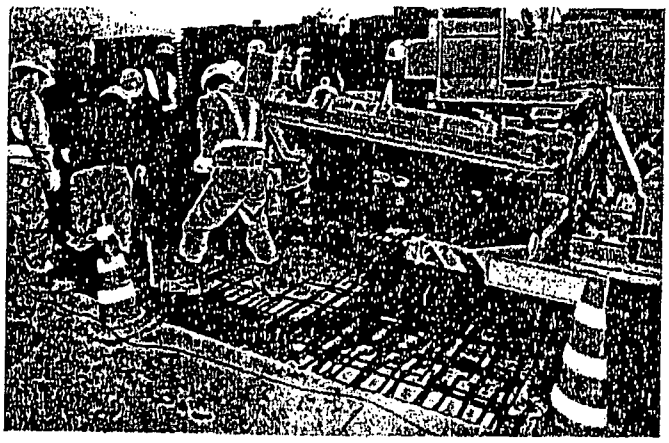

Photo4 : Concrete Placement Work

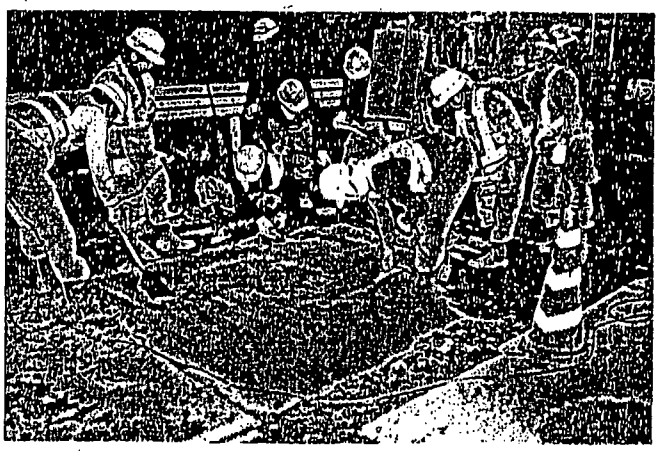

Photo5 : Finishing Work

Concrete Surface

Surface Treatment

Epoxy Resin Primer

Epoxy Resin Putty

Epoxy or Polyurethane Resin Paint for middle layer

Polyurethane Resin Paint for top layer

Outer Surface

Figure5 : Standard Layer for Coating of Concrete

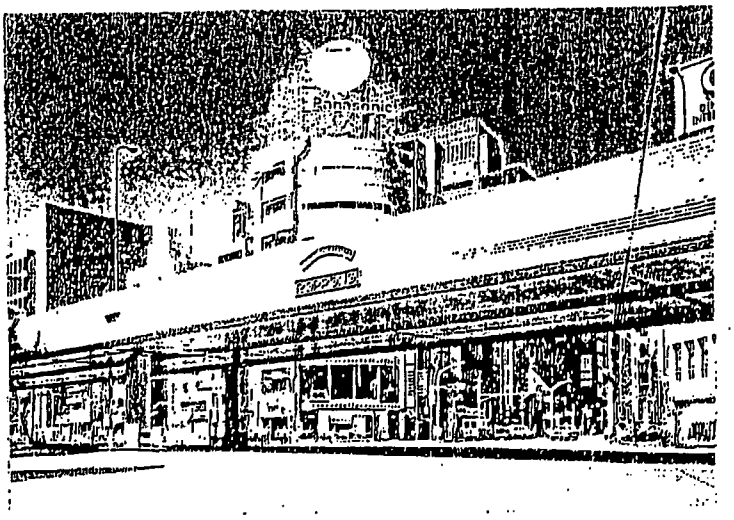

Photo6 : Typical Fine Dressing of an Existing Elevated Road

Breakout A2: EARTHQUAKE ENGINEERING 1

(1) Size Effect on Ductile Behavior of Reinforced Concrete Columns under Cyclic Loading

(Jun-ichi Hoshikuma, Shigeki Unjoh and Kazuhiro Nagaya)

(2) Impulsive Seismic Performance Testing of Reinforced Concrete Bridge Column-Cap Beam Joints

(Andre Filiatrault, Natalie Gibson and Scott A. Ashford)

(3) ISO 22762 Electrometric Isolator, Progress Report (presentation only)

(Fumihiko Yazaki)

(4) Development of Experimental Guidelines for Bridge Column Testing

(Jerry J. Shen and W. Phillip Yen)

(5) Evaluation of Seismic Performance of High-strength Reinforced Concrete Members

(Chihiro Kawatoh and Shigeki Unjoh)

SIZE EFFECT ON DUCTILE BEHAVIOR OF REINFORCED CONCRETE COLUMNS UNDER CYCLIC LOADING

Jun-ichi Hoshikuma[1], Shigeki Unjoh[2], Kazuhiro Nagaya[3]

1 Senior Research Engineer, Earthquake Eng. Div., Public Works Research Institute
2 Head, Earthquake Eng. Div., Public Works Research Institute
3 International Division for Infrastructure, Policy Bureau, Ministry of Land, Infrastructure and Transport

Full-scale flexural reinforced concrete columns with cross sectional dimension of 2400mm were tested under quasi-static cyclic lateral loading in the laboratory. To determine the size effect on column inelastic behavior, a 1/4-scale replica model was also loaded for comparison with the full-scale column behavior. Observed envelope curves of the lateral load and drift relations for the full-scale and the replicate models exhibited similar response, and the cyclic energy dissipation was equivalent relatively up to 0.02 of drift ratio. Furthermore, curvature profiles and column base rotation due to bond slip of longitudinal bars were not significantly affected by the size of column section.

INTRODUCTION

Many researchers previously proposed the ductility assessment procedures for flexural reinforced concrete columns subjected to seismic action[1),2),3),4)]. These are established based on mainly experimental results and statistical studies for their data. It should be suggested that such empirical approaches have a limit for application. Some existing ductility assessment procedures note the applicable limits in terms of the flexure-shear strength ratio, longitudinal steel ratio, transverse steel ratio, axial force ratio, aspect ratio, etc. However, the limit of cross sectional size is unclear in the previous proposals, and the size effect on the inelastic behavior of reinforced concrete columns is also unknown.

There is an important research work regarding the size effect reported by Stone and Cheok[5)]. They conducted a series of cyclic loading test for full-scale circular columns (diameter= 1524mm) and their well-scaled replica model, to determine the size effect on inelastic behavior of reinforced concrete columns subjected to seismic force. A comparison of test results between full-scale and replica columns showed that the size effect on failure mode, energy absorption property and ductility capacity was less significant. It is an interesting finding that the size effect doesn't appear when reinforcement details including bar diameter and vertical hoop spacing are scaled down precisely based on a scale factor.

Though there is a research on the size effect on flexural ductility as described above, the size of cross section in reinforced concrete columns constructed in Japan is still larger than Stone and Cheok's columns. Furthermore not only circular but rectangular cross section is often designed in Japanese bridge columns. Since the rectangular section is less effective confinement than circular section, the size effect has been controversial issue for particularly rectangular section.

This research program was initiated with motivation to investigate the size effect on inelastic behavior of reinforced concrete columns with big square cross section that never tested. Full-scale columns with 2400mm square section and 9600mm height were loaded

until the columns were completely failed, and inelastic behavior of the plastic hinge region was studied. Furthermore, a 1/4-scale replica model was also tested for comparison with the full-scale column behavior, and the size effect was discussed based on test results.

CYCLIC LOADING TEST PROGRAM

Test Units Details

Two full-scale columns (called herein L1 and L2) and one replica column (called herein S1) were tested in the program, and their structural details are shown in Fig. 1 and Fig. 2. The unit L2 is a reference column and the unit S1 is a 1/4-scale replica model of the L2. The unit L1 is a model with the same size and longitudinal steel ratio as the L2 but the transverse steel ratio reduced.

The full-scale columns have 2.4m square cross section with column height of 9.6m, resulting in the aspect ratio of 4.0. The column section has 72 D35 (diameter=35mm) longitudinal bars in one layer distributed evenly with a constant cover of 102mm. The longitudinal steel ratio to net area of the concrete is 1.2%. The hoop bar was fabricated with two D19 (diameter=19mm) L-shaped reinforcement and placed with 300mm (L1) or 150mm (L2) vertical spacing. Each hoop bar has 135-degree hooks with 190mm leg at both end edges. Furthermore, for the unit L2, cross ties were placed at each hoop level as depicted in Fig. 1(b). Each cross tie has 180-degree hook with 250mm leg at end edges and the hoop bar was hooked by the cross tie. Due to complicated construction of the cross ties with hooks, cross ties were spliced in the core with 760mm lap length.

On the other hand, the unit S1 was designed based on structural details of the unit L2. Sixty reinforcements of D10 (diameter=10mm) were placed for longitudinal bars in one layer distributed evenly with a constant cover of 30mm. It should be suggested that 8.75mm diameter bar is the most appropriate for longitudinal bar in terms of the similitude relationships since D35 bars were used in the full-scale columns. However, such standardized reinforcement is unavailable. Therefore, the D10 bars were selected from available reinforcement. Consequently, the horizontal spacing of the longitudinal bar was adjusted from the similitude value, to equalize the longitudinal steel ratio. The hoop bar consisted of the D6 deformed bars with 135-degree hooks embedded into the core by 120mm leg. Cross ties was arranged as shown in Fig. 2 and the ends of these cross ties were hooked to hoop bar with the 180-degree hooks. Since it was also impossible to scale down the hoop diameter precisely due to a limitation of available reinforcement, the center-to-center spacing of the hoop bars were adjusted so as to approximate the transverse steel ratio of the unit L2.

Material properties of concrete and reinforcement used for the test units are listed in Table 1.

Comparison of Structural Details between Full-scale and Replica Column

Structural details comparison between the unit L2 and S1 was summarized in Table 2, where the effective length of confined core was defined as the maximum horizontal spacing of cross ties, and the volumetric ratio of lateral reinforcement was defined as Eq. (1).

$$\rho_s = \frac{4A_s}{s \cdot d} \tag{1}$$

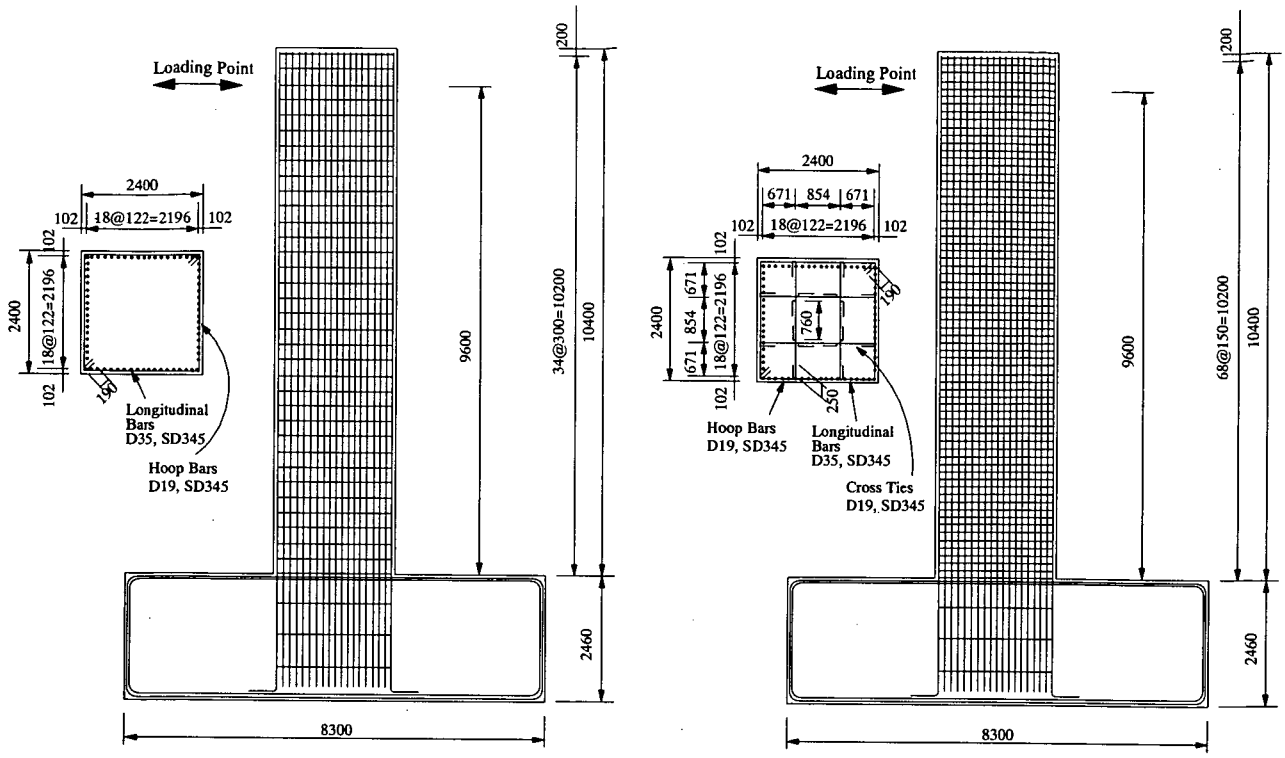

(a) Unit L1 (b) Unit L2

Fig. 1 Structural Details of Full-scale Columns

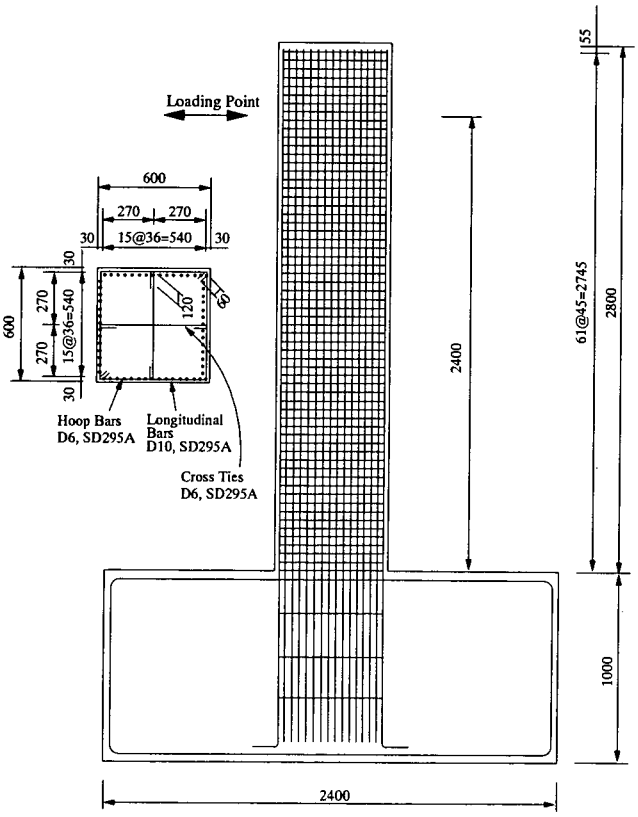

Fig. 2 Structural Details of Replica Model

Table 1 Material Properties

(a) Concrete Strength

Unit	Column (N/mm^2)	Footing (N/mm^2)
L1	33.5	37.3
L2	32.6	38.0
S1	39.0	39.0

(b) Reinforcement

Unit	Steel Bars	Dia.	Young's Modulus (N/mm^2)	Yield Strength (N/mm^2)	Tensile Strength (N/mm^2)
L1	Long.	D35	$1.77x10^5$	424	639
L2	Hoop	D19	$1.72x10^5$	344	528
S1	Long.	D10	$1.78x10^5$	395	565
	Hoop	D6	$1.85x10^5$	389	534

Table 2 Comparisons of Structural Details between L2 and S1

	L2	S1	L2 / S1 (Ideal Value)
Dimension of Section (mm)	2400 x 2400	600 x 600	4.0 (4.0)
Column Shear Span (mm)	9600	2400	4.0 (4.0)
Aspect Ratio	4.0	4.0	1.0 (1.0)
Diameter of Long. Bar (mm)	35	10	3.5 (4.0)
Long. Bar Spacing (mm)	122	36	3.39 (4.0)
Long. Steel Ratio	0.012	0.012	1.0 (1.0)
Diameter of Lateral Bar (mm)	19	6	3.17 (4.0)
Lateral Bar Spacing (mm)	150	45	3.33 (4.0)
Effective Length of Confined Concrete (mm)	854	270	3.16 (4.0)
Volumetric Lateral Steel Ratio	0.0089	0.0104	0.86 (1.0)
Max. Aggregate Size (mm)	20	20	1.0 (4.0)

where, ρ_s : volumetric ratio of transverse reinforcement to the confined core

A_s : area of transverse reinforcement

s : vertical spacing of transverse reinforcement

d : effective length of confined core

Table 2 shows that reinforcement arrangement of the replica model S1 was designed as well-scaled to the full-scale L2 column as possible. However, it should be noted that the replica model was not perfectly-scaled-down column.

Loading Setup and Loading Pattern

Photo 1 shows a set-up of the loading system for the full-scale column tests. Lateral load was applied using two 3000kN large-stroke hydraulic actuators. Unfortunately a vertical load was not applied in this project because it was very difficult to give the vertical load in the loading system we used for lack of capacity of the reaction floor. However, specific objective of the research is to examine the size effect on the inelastic behavior of the flexural reinforced concrete columns, and thus even though the vertical load was not applied, conclusions of the size effect derived from the experimental discussion could be generalized.

The unit S1 was loaded as shown in Photo 2, where the column base was fixed to the reaction wall. The vertical load was not applied so as to create the same condition with the full-scale column tests.
The columns were loaded quasi-statically and subjected to cycles of force reversals under the force control until yielding of the extreme longitudinal reinforcement. A yield displacement $1\,\delta_y$ was determined here as a displacement at the loading point of column when the extreme longitudinal bars yielded at the base section. Based on measured strain of the extreme longitudinal bars, the yield displacement was defined as 50mm for the full-scale columns and 10mm for the replica model. Subsequently, the lateral displacement was applied with stepwise increasing amplitude ($\pm 1\,\delta_y$, $\pm 2\,\delta_y$, $\pm 3\,\delta_y$, $\cdots$) under the displacement control. The cyclic number in each loading step was three.

INELASTIC COLUMN BEHAVIOR

Lateral Strength and Drift Hysteresis Loops

Experimental lateral load-drift responses of the test units were shown in Fig. 3. Regarding the unit L1, the lateral load-drift loop exhibits stable response up to the first cycle of $4\,\delta_y$ (drift ratio=0.021). In the second cycle of $4\,\delta_y$, buckling of the longitudinal bars was observed following cover concrete spalling and hoop bars swelled out. The lateral load-drift loop became unstable from this loading cycle.
The lateral load-drift loop of the unit L2 is stable up to the first cycle of $5\,\delta_y$ (drift ratio=0.026) and the pinching effect appears after the second loading cycle resulting from buckling of longitudinal bars. This observation is similar to the unit L1.
On the other hand, for the unit S1, the lateral force kept peak strength with stable response curve up to the second cycle of $6\,\delta_y$ (drift ratio=0.025) loading. Spalling of cover concrete following longitudinal bar buckling was observed in the third cycle of $6\,\delta_y$. It is noted that the pinching of the hysteresis loops arise from buckling of longitudinal bars and spalling of cover concrete in both full-scale and replica models.

Lateral Strength and Ductility

Fig. 4 compares the contour of the lateral force and drift hysteresis loops between the unit L2 and S1. The lateral force measured for the unit S1 was modified based on Eq. (2) so as to make a relative comparison the test results.

$$P_{se} = P_s s_\ell^2 \qquad (2)$$

where, P_{se} : modified lateral force of unit S1
P_s : lateral force measured for unit S1
s_e : scale factor (=4.0)

Fig. 4 indicated that the contours of the unit L2 and S1 exhibited similar response. The maximum lateral force of the unit L2 was slightly larger than that of the unit S1. This difference arises from the difference of yield strength of longitudinal reinforcement between both units as listed in Table 1. Though the longitudinal reinforcement ratio was equivalent as 0.012, the yield strength of longitudinal reinforcement in the unit L2 was 7% larger than that in the unit S1.

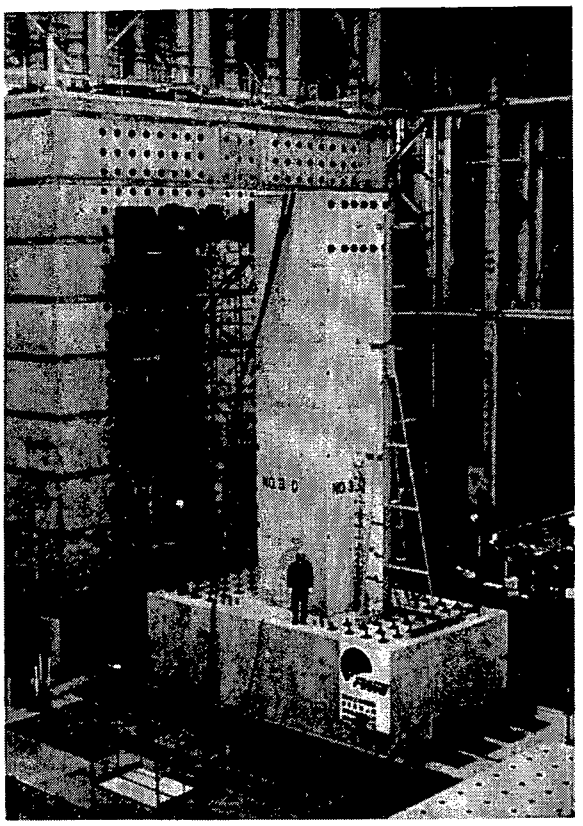

Photo 1 Full-scale Column Test

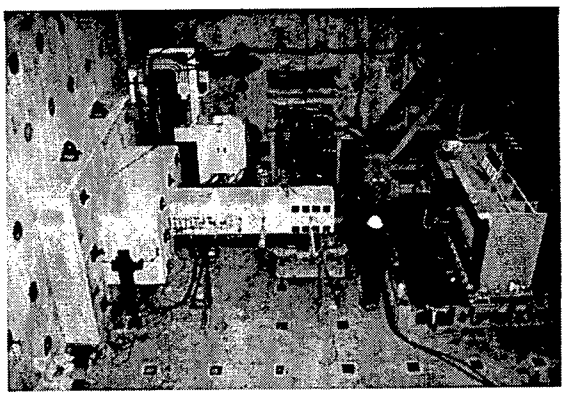

Photo 2 Replica Model Test

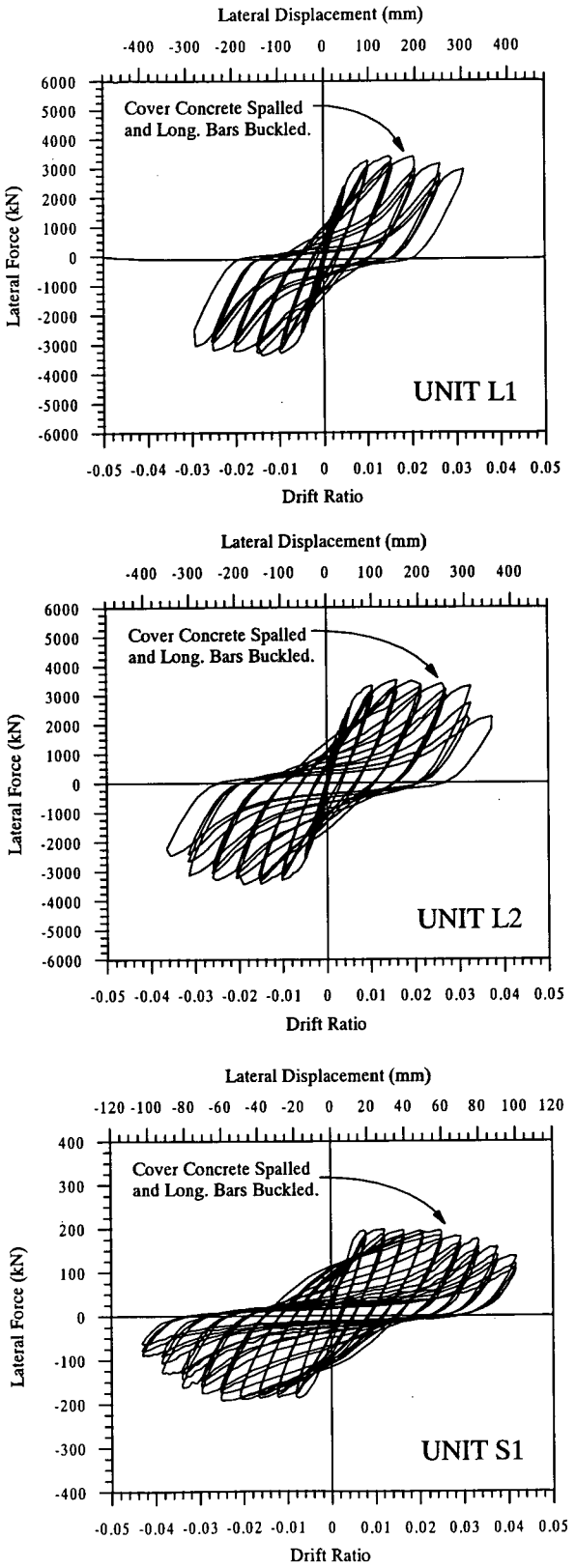

Fig. 3 Experimental Hysteresis Loops of Test Units

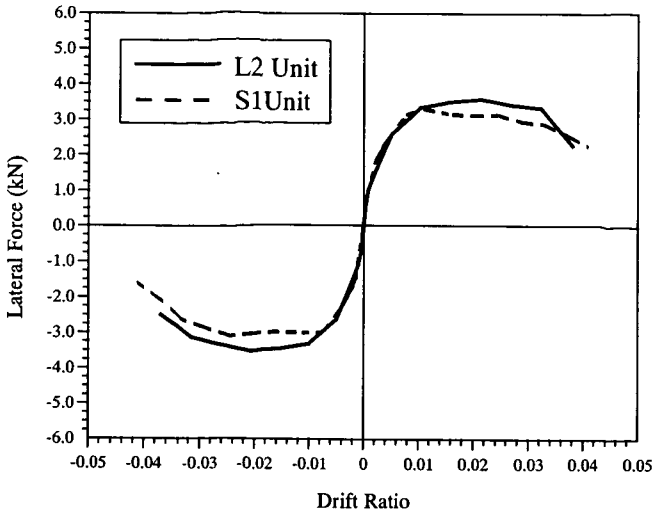

Fig. 4 Contour of Hysteresis Loops

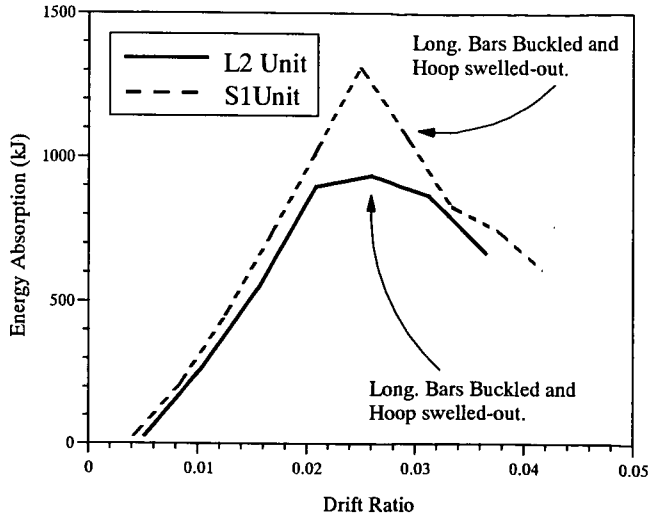

Fig. 5 Comarison of Energy Absorption

Inelastic Energy Capacity

Energy absorption capacity is one of the effective indexes for measuring overall column performance subjected to cyclic action. The amount of energy absorption was determined by the area bounded by the load-displacement hysteresis loops. Fig. 5 shows the amount of energy absorption in each ductility level calculated for the units L2 and S1. Inelastic energy absorption in the unit S1 was modified through Eq. (3), so that inelastic energy absorption can be compared relatively between two units.

$$\Delta W_{Se} = \Delta W_S \, s_\ell^3 \qquad (3)$$

where, ΔW_{Se} : modified inelastic energy absorption of unit S1

ΔW_S : inelastic energy absorption of unit S1 calculated for the first cycle of each ductility level

s_ℓ : scale factor (=4.0)

It is noted that the amount of inelastic energy of the units L2 and S1 are similar up to 0.02 of drift ratio, and that the inelastic energy absorption during the first loading cycle reaches the peak when the longitudinal bars buckle and consequently hoop bars swell-out. However, in the range of 0.02 to 0.03 of drift ratio, the amount of energy absorption in S1 was larger than that in the full-scale column.

SIZE EFFECT ON PLASTIC CURVATURE PROFILES

Fig. 6 shows the curvature profiles measured for test units during inelastic loading steps. The regions where the longitudinal reinforcement yielded, and where cover concrete was spalled-off resulting from buckling of longitudinal reinforcement, were indicated in the figure, respectively. Curvatures were measured up to the height of 3640mm for the full-scale columns and 937mm for the replica model. Column base rotation was excluded from curvature measured at the section near column bottom, because it arises from the bond slip of longitudinal reinforcement in the footing and this effect should be distinguished from column curvature response.

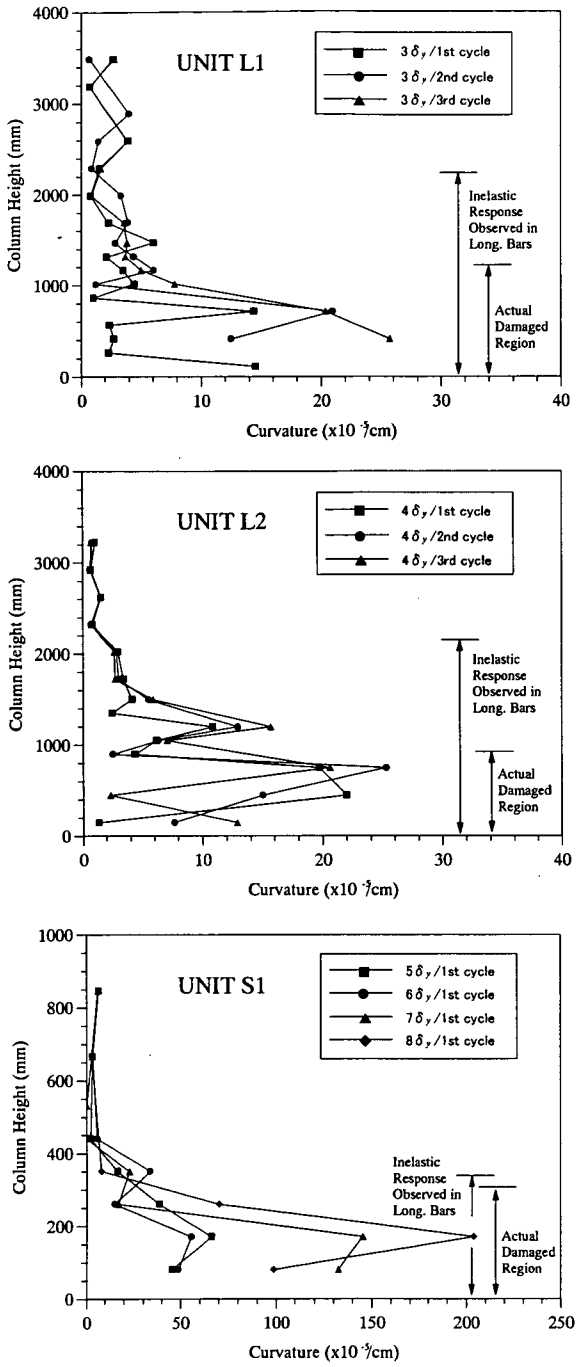

Fig. 6 Measured Curvature Profiles

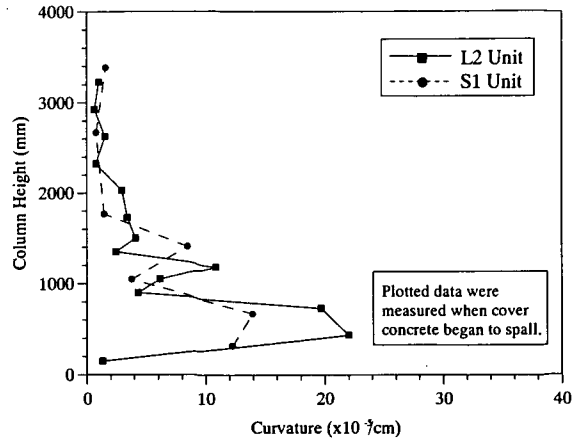

Fig. 7 Comparison of Curvature Profiles between L2 and S1 Units

Fig.7 compares the curvature profiles measured when cover concrete began to spall-off between the units of L2 and S1. Column height and the measured curvatures for the S1 unit were modified based on similitude relationships for relative comparison with the L2. It can be noted that the both units exhibit similar curvature profiles when the columns suffer from the damage as cover concrete spall resulting from buckling of the longitudinal reinforcement. This fact indicates that the size effect on the curvature profiles around the plastic hinge region is not so significant as long as structural details of a replica model is well-scaled down based on a prototype column.

SIZE EFFECT ON BASE ROTATION RESULTING FROM BOND SLIP OF DEVELOPED BARS

Lateral displacement measured at the loading point consists of deflection due to flexure/shear and reinforcement bond slip as shown in Fig. 8. It has been suggested that an amount of the longitudinal bar extension due to slippage may be one of factors of the size effect and the lateral displacement resulting from bond slip of longitudinal bars should not be expected in the ductility evaluation of the full-scale reinforced concrete columns.

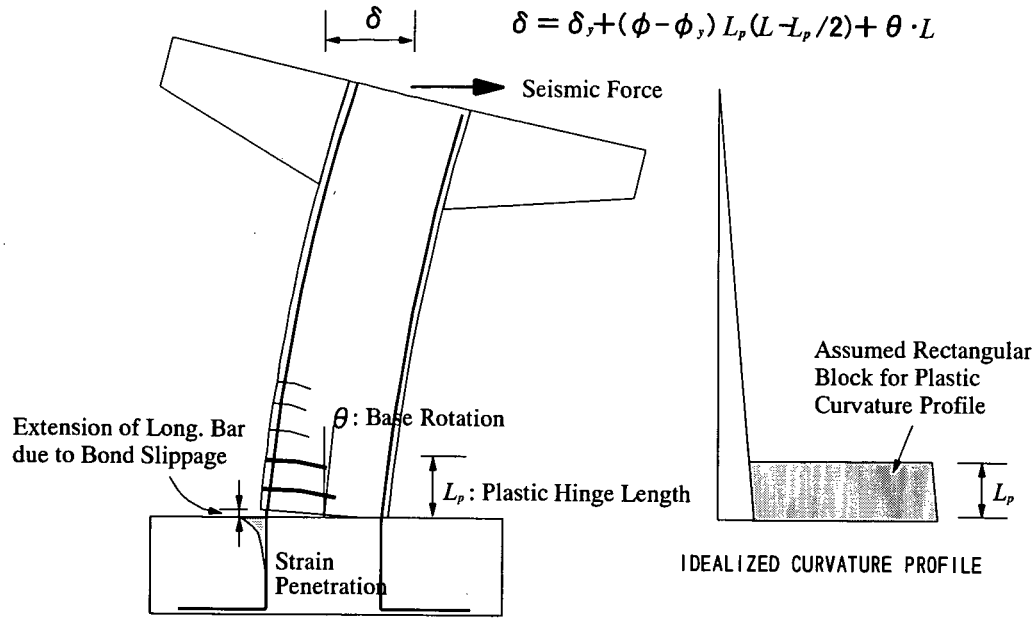

Fig. 8 Components of Lateral Displacement Developed in RC Columns during an EQ.

Because of difficulty in measuring the longitudinal bar extension directly, the column base rotation was measured through two LVDTs amounted each on the flange faces at the column base. The LVDT brackets were connected to aluminum angles that were supported by thread rods anchored to either side of the column core. The reference length for LVDTs was determined as short as possible not to include curvature component at near column base. This measuring system was effective until cover concrete began to spall-off.

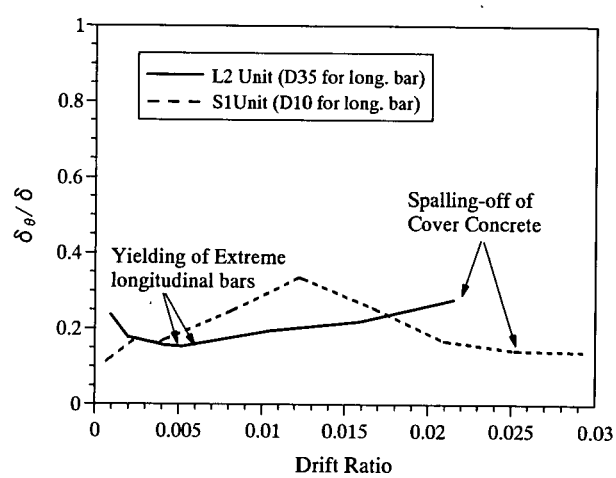

Fig. 9 Lateral Displacement due to Bond Slip of Longitudinal Bars

In this study, measured lateral displacements were divided into flexure/shear component and bond slip component. Then lateral displacement at loading point due to bond slip of developed bars was estimated through Eq. (4).

$$\delta_\theta = \theta \times L \tag{4}$$

where, δ_θ : lateral displacement at loading point due to bond slip of developed bars

θ : measured base rotation

L : column shear span

Fig. 9 compares the ratio of δ_θ to the measured total lateral displacement δ between the units L2 and S1. The value of δ_θ / δ would be affected by longitudinal bar diameter, bond strength, deterioration in flexural stiffness of the critical section due to inelastic cyclic loading and longitudinal tensile strain profiles of the developed bars in footing. For the unit

L2, the value of δ_θ / δ is around 0.2 but it slightly increases with increasing the drift ratio of the column. On the other hand, the value of δ_θ / δ in the unit S1 was 0.15 to 0.35, which exhibited larger change than the result of the unit L2. It increases up to 0.012 of drift ratio, and subsequently decreases as the drift ratio increases. However, it should be noted that the lateral displacement due to bond slip of longitudinal bars was observed clearly in the full-scale column as well as the replica model. Furthermore, with viewing overall behavior shown in Fig. 9, the value of δ_θ / δ is roughly equivalent to that for the replica model.

CONCULUSIONS

This paper reports the cyclic loading test results for the full-scale square reinforced concrete bridge columns and their replica model. The size effect on inelastic behavior of reinforced concrete columns was discussed through a comparison of test data.

The contour of lateral force and drift hysteresis loop for the full-scale column was relatively similar to that for its replica model. The amount of inelastic energy for the full-scale column also coincided with that for the replica model up to 0.02 of drift ratio. Curvature profiles measured when cover concrete spalled corresponded well for both columns. Furthermore, the base rotation resulting from bond slip of the longitudinal bars was not affected significantly by the size of column section. Therefore, it could be concluded that the size effect on the inelastic ductile behavior of reinforced concrete bridge columns would not be significant as long as we tested.

It should be, however, noted that above conclusions derive from the cyclic loading test for the replica model designed with paying careful attention to the scale factor. Stone and Cheok's test results also indicated that the size effect didn't appear clearly on the inelastic behavior of reinforced concrete columns. This would be because the replica model they designed was scaled down very precisely. For example, diameter of longitudinal reinforcement affects bond slip behavior in the footing and the plastic hinge length. Vertical hoop spacing affects the buckling length of the longitudinal reinforcement and thus the plastic hinge length. Therefore, it is important in designing of replica model to determine not only the longitudinal/transverse reinforcement ratio but also the diameter of longitudinal reinforcement and vertical hoop spacing based on the scale factor. These details should be scaled down as precisely as possible, otherwise the size effect would develop in the inelastic behavior and ductility capacity of reinforced concrete columns.

ACKNOWLEDGMENTS

This research presented in this paper was one of products of the joint research program on the size effect on the seismic behavior of reinforced concrete bridge columns. This program has been conducted by the Public Works Research Institute, Japan Highway Public Corporation, Metropolitan Expressway Public Corporation and Hanshin Expressway Public Corporation. The authors wish to appreciate all participants in the joint research program for their work.

REFERENCES

1) Priestley, M.J.N., Seible, F. and Calvi, G.M. : Seismic Design and Retrofit of Bridges, Wiley- Interscience, 1996.
2) Priestley, M.J.N. and Park, R. : Strength and Ductility of Reinforced Concrete Bridge Columns Under Seismic Loading, ACI Structural Journal, Vol. 84, No.1, pp.61-76, Jan.-Feb. 1987.
3) Hoshikuma, J., Kawashima, K. and Unjoh, S. : Ductility Evaluation of Reinforced Concrete Bridge Columns, Second Italy-Japan Workshop on Seismic Design and Retrofit of Bridges, Feb., 1997.
4) Japan Society of Civil Engineering : Standard Specifications of Concrete Structures, 1996. (in Japanese)
5) Stone, W.C. and Cheok, G.S. : Inelastic Behavior of Full-Scale Bridge Columns Subjected to Cyclic Loading, NIST Building Science Series 166, National Institute of Standards and Technology, U.S. Department of Commerce, Jan. 1989.

APPENDIX <Photo Gallery of Damage Observations>

A1. Observations of Unit L1 Damage

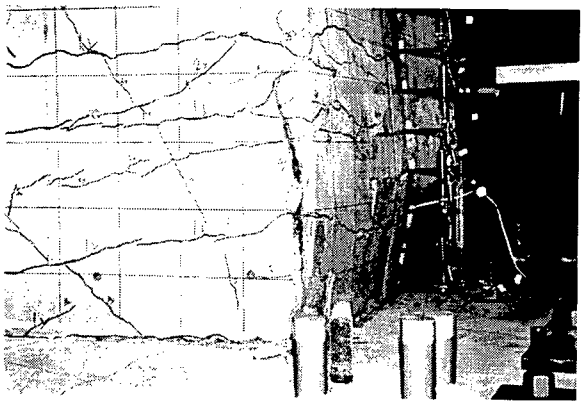

Photo A1 Beginning of Cover Spalling (2nd cycle in 3 δ_y loading)

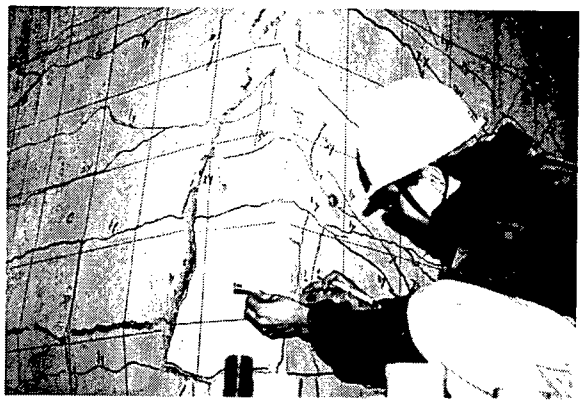

Photo A2 Vertical Cracks Developed at Corner of Section (2nd cycle in 3 δ_y loading)

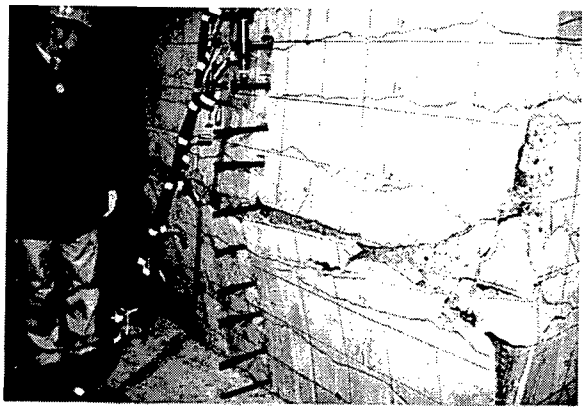

Photo A3 Spalling-off of Cover Concrete (1st cycle in 4 δ_y loading)

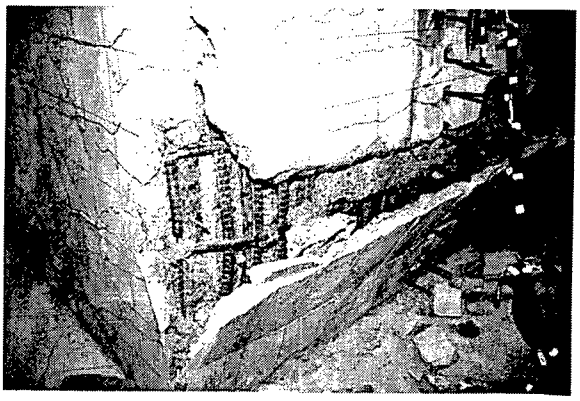

Photo A4 Slight Buckling of Longitudinal Bars (2nd cycle in 4 δ_y loading)

Photo A5 Poor Confinement from Hoop (2nd cycle in 4 δ_y loading)

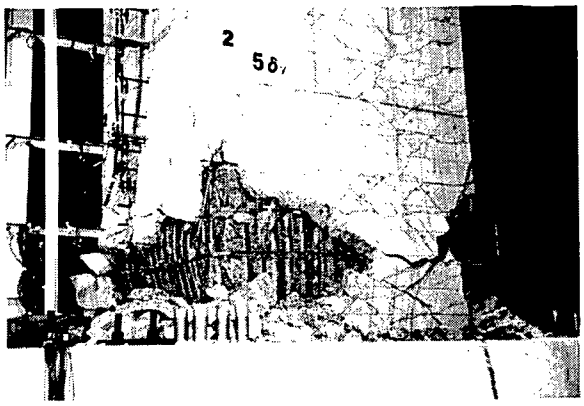

Photo A6 Plastic Hinge Region (5 δ_y loading)

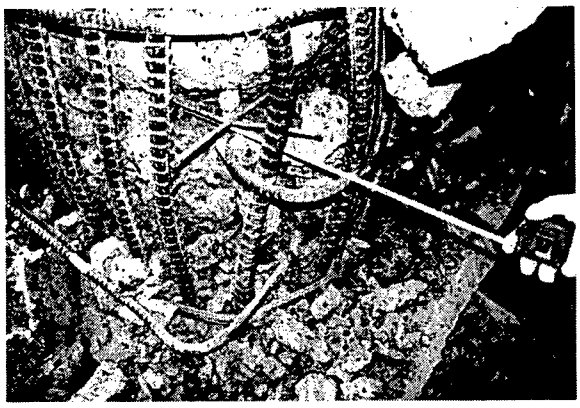

Photo A7 Unhooking of Hoop End due to Core Failure (5 δ_y loading)

Photo A8 Sliding Down of Hoop and Core Concrete Failure (5 δ_y loading)

A2. Observations of Unit L2 Damage

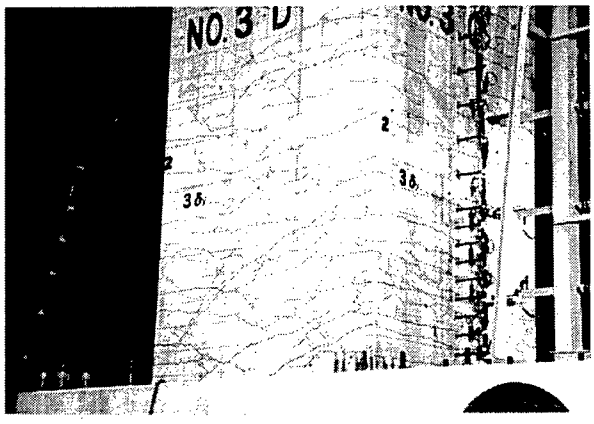

Photo A9 Flexural Cracks on Flange Face and Extension onto Shear Face with Inclination (3 δ_y loading)

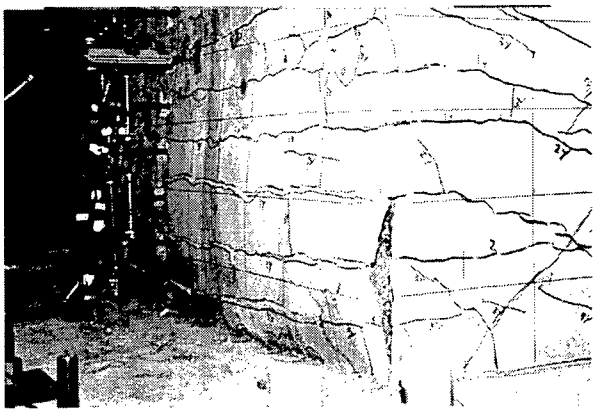

Photo A10 Beginning of Cover Spalling (1st cycle in 4 δ_y loading)

Photo A11 Spallng of Cover at Corner
(3rd cycle in 4 δ_y loading)

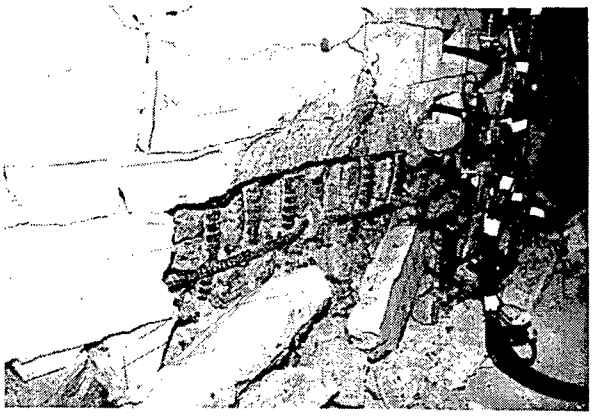

Photo A12 Well-hooked Cross Tie and Anti-buckling of Longitudinal Bars
(3rd cycle in 4 δ_y loading)

Photo A13 Slight Buckling of Longitudinal Bars (2nd cycle in 5 δ_y loading)

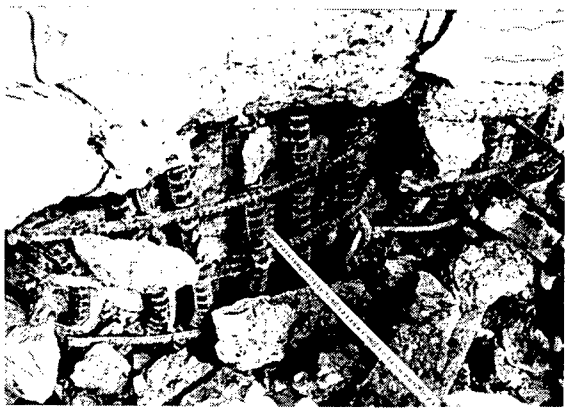

Photo A14 Significant Buckling of Longitudinal and Swelling out of Hoop
(3rd cycle in 5 δ_y loading)

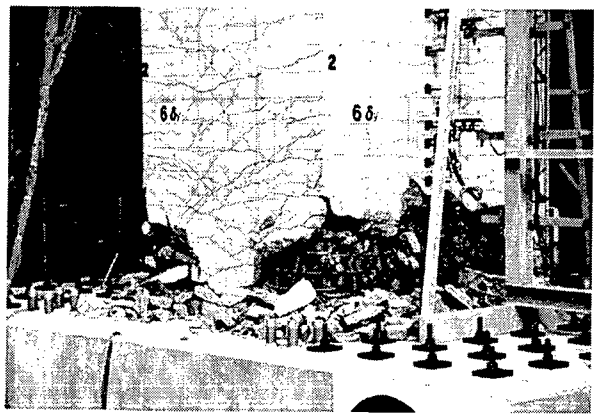

Photo A15 Plastic Hinge Region
(1st cycle in 6 δ_y loading)

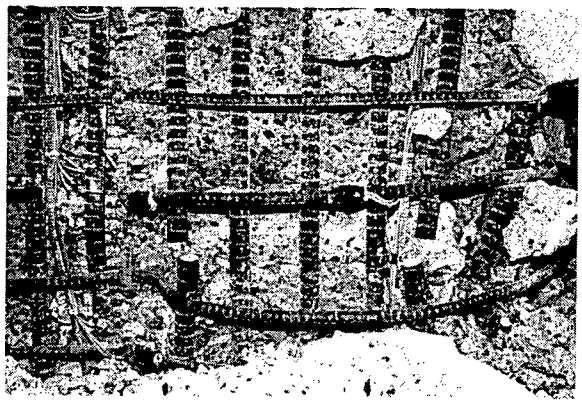

Photo A16 Rupture of Longitudinal Bars Resulting from Low Cycle Fatigue
(3rd cycle in 6 δ_y loading)

A3. Observations of Unit S1 Damage

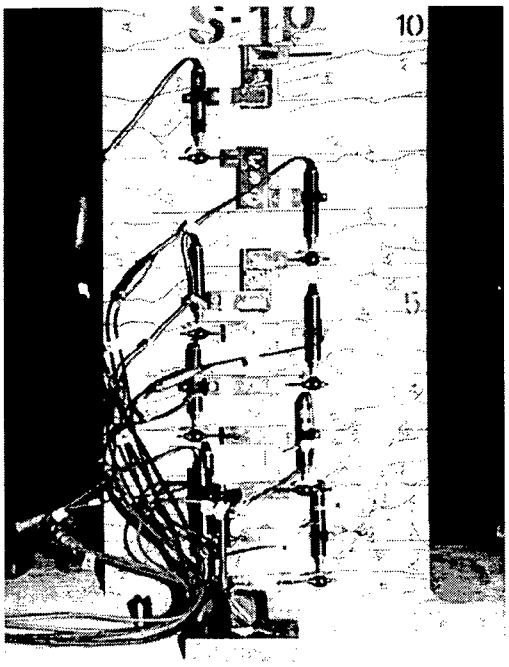

Photo A17 Flexural Cracks Developed
(5 δ_y loading)

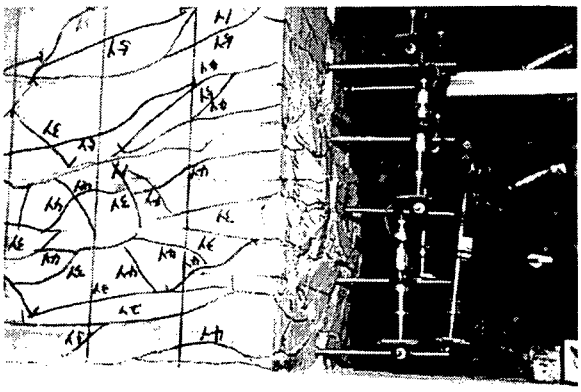

Photo A18 Beginning of Cover Spalling
(6 δ_y loading)

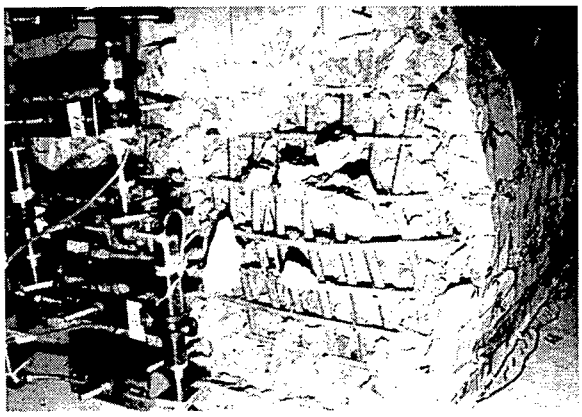

Photo A19 Buckling of Longitudinal Bars
and Swelling out of Hoop
(7 δ_y loading)

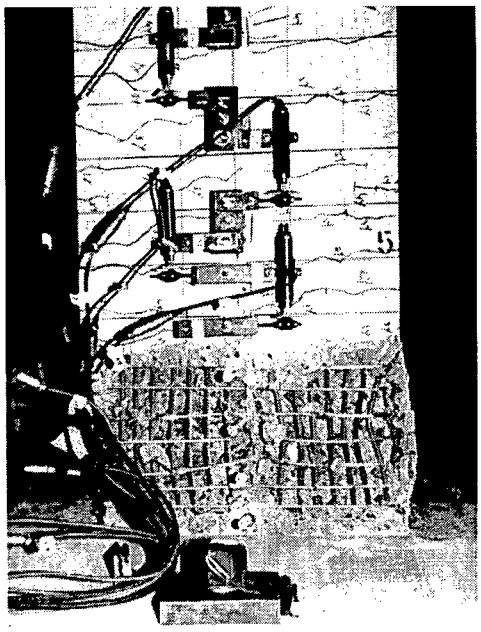

Photo A20 Core Concrete Failure Following
Buckling of Longitudinal Bars
(8 δ_y loading)

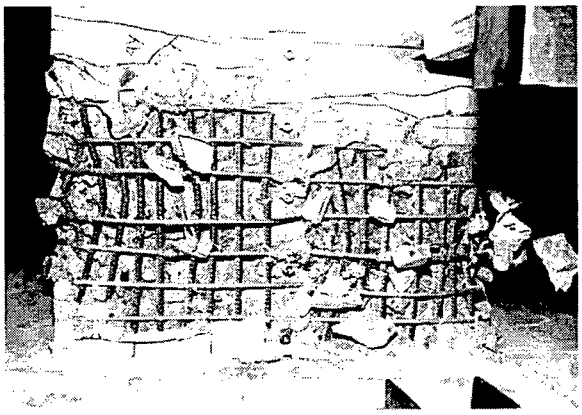

Photo A21 Rupture of Longitudinal Bars
Resulting from Low Cycle
Fatigue (9 δ_y loading)

IMPULSIVE SEISMIC PERFORMANCE TESTING OF REINFORCED CONCRETE BRIDGE COLUMN-CAP BEAM JOINTS

Andre Filiatrault[1], Natalie Gibson[2] and Scott A. Ashford[3]

ABSTRACT

Results of dynamic tests on six half-scale reinforced concrete bridge column-cap beam joints are discussed. The loading protocol used included the effects of impulsive near-field ground motions. Cyclic loading with increasing amplitudes followed this impulsive loading. Three of the specimens incorporated nominally ductile reinforcement details, typical of pre-1971 construction practice in California. The three other specimens incorporated ductile reinforcement details, typical of current design practice in California. The impulsive loading was particularly detrimental to the pre-1971 specimens. Shear failure in the joint was initiated during the impulsive loading, causing early strength degradation. The joints incorporating ductile reinforcement details suffered minimal damage during the impulsive loading and continued to perform well during the subsequent loading cycles. The increased capacity exhibited by both types of joints during the impulsive loading can be accounted for by modifying the steel and concrete properties for the high strain rate induced during the impulsive loading.

INTRODUCTION

Strong ground motion records obtained during the 1994 Northridge earthquake in California and during the 1995 Kobe earthquake in Japan have provided clear evidence on the short duration and impulsive characteristics of near-field ground motions. These characteristics are the result of a directivity pulse phenomenon occurring when the propagation of the fault proceeds at near the same rate as the shear wave velocity (Abrahamson 1998).

There is a growing concern that near-field impulsive ground motions can be particularly detrimental to reinforced concrete bridge structures. Impulsive ground motions can cause large ductility demands in a very short time on the structural elements. Also, the effects of the high strain rate induced by impulsive dynamic loading can change the hysteretic response of the structural elements. It is unclear how bridge structures behave under such impulsive seismic excitations.

The objective of this paper is to contribute toward a better understanding of the seismic response of reinforced concrete bridge structures under impulsive near-field ground motions. For

[1]Professor, Dept. of Structural Engineering, University of California, San Diego, La Jolla, CA 92093-0085, USA.
[2] Project Engineer, KPFF Consulting Engineers, 180 Pacific Avenue, San Francisco, CA 94111, USA. Formerly Graduate Student, Department of Structural Engineering, University of California, San Diego.
[3]Assistant Professor, Dept. of Structural Engineering, University of California, San Diego, La Jolla, CA 92093-0085, USA.

this purpose, results of dynamic tests on six half-scale reinforced concrete bridge column-cap beam joints are presented. The loading protocol used for these tests included the effects of impulsive near-field ground motions. Cyclic loading with increasing amplitudes followed this impulsive loading. Three of the test specimens incorporated nominally ductile reinforcement details, typical of pre-1971 construction practice in California. The three other specimens incorporated modern ductile reinforcement details.

DESCRIPTION OF TEST SPECIMENS

Figure 1 shows the geometry and reinforcement details for the nominally ductile and ductile half-scale reinforced concrete bridge column-cap beam joints considered in this investigation. All specimens were constructed and tested in an inverted position. Each test specimen incorporated half the column height, along with a cap beam representing portions of the surrounding deck and of the soffit slab. Identical longitudinal and transverse reinforcement details were incorporated in the column for all test specimens. The circular column had a diameter of 610 mm (24 in.). The height of the column was 1829 mm (6 ft.) from the soffit side of the cap beam to the loading axis. This column height corresponds to the distance between the joint interface and a point of inflexion assumed to be located halfway up the column. The column was reinforced with 14-#7 longitudinal bars (diameter = 22 mm). The transverse column reinforcement was a #3 spiral (diameter = 10 mm) spaced at 97 mm (3.8 in) over the full height of the column. The cap beam was 610 mm (24 in) deep and 686 mm (27 in) wide. The length of the beam was 1219 mm (48 in) from the center of the column to each simple support. All reinforcement steel was Grade 60.

The nominally ductile specimens incorporated reinforcement details in the joint region that were typical of the construction practice used in California prior to the 1971 San Fernando earthquake. The longitudinal bars of the column were anchored into the joint region on a distance of 406 mm (16 in), corresponding to 16 times the bar diameter. The soffit side of the cap beam was reinforced with 4-#7, 2-#3 bars. The deck side of the cap beam was reinforced with 4-#7, 2-#3 and 3-#2 (diameter = 6.4 mm) bars. The bars on the deck side ran continuously for the length of the cap beam. On the soffit side, all of the #2 longitudinal bars and one of the #7 bars of the cap beam were spliced within the joint region (Gibson et al. 2001). Transverse #2 open stirrups were provided at a spacing of 114 mm (4.5 in) in the cap beam. No joint reinforcement was provided. The column spiral ended at the soffit face of the cap beam and the transverse stirrups in the cap beam ended at the column face.

The ductile specimens incorporated reinforcement details in the joint region that were typical of the current (early 1990's) design practice used in California. The longitudinal bars in the column extended fully into the joint region on a distance of 53 mm (21 in) in order to meet the longitudinal steel on the deck side of the cap beam. The longitudinal bars of the column were confined transversely in the joint region by a #3 spiral spaced at 57 mm (2.25 in). The cap beam was reinforced with 7-#7 bars top and bottom. The bars ran continuously over the length of the cap beam. Transverse reinforcement of the cap beam was provided by #3 closed double stirrups

spaced at 172 mm (6.75 in.). Within the joint region, the cap beam was reinforcing transversely by two sets of double #3 hairpins.

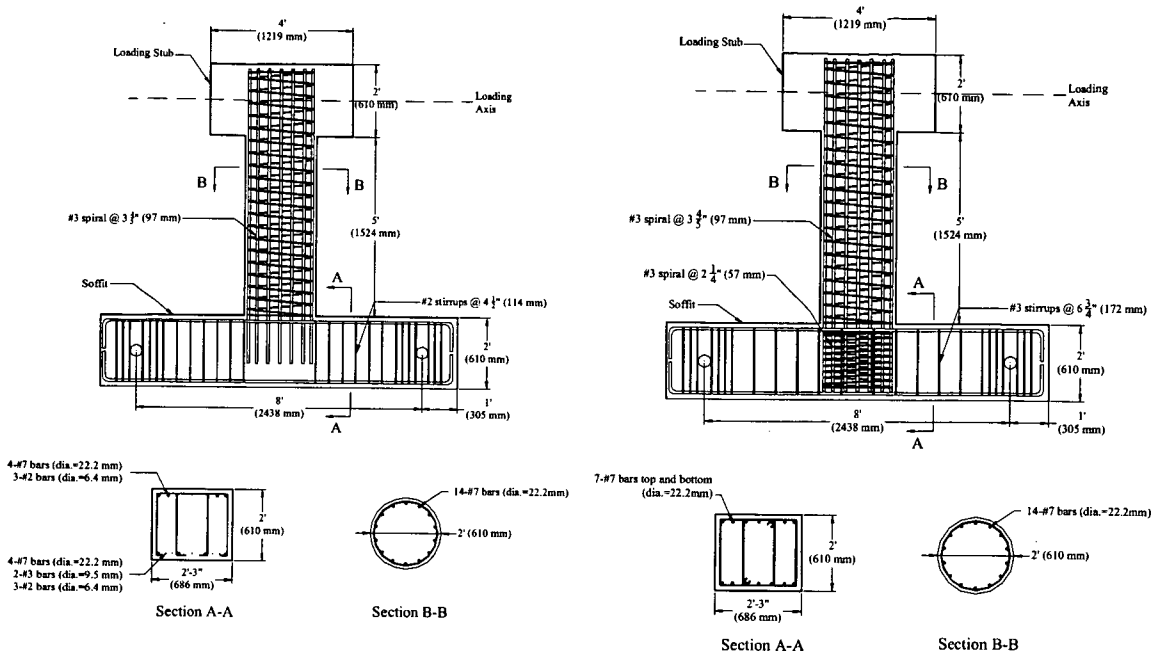

Nominally Ductile Specimens Ductile Specimens

Figure 1. Reinforcement Details for Ductile Test Specimens.

Table 1 lists the characteristics of the six specimens considered in this study. Three of the test specimens incorporated nominally ductile reinforcement details, while the other three test specimens incorporated ductile reinforcement details. Specimens 1 to 4 were tested in this study. Specimens 5 and 6 were tested previously under non-impulsive quasi-static loading by MacRae et al. (1994) and by Sritharan et al. (1996), respectively. These test results were included herein for comparative purposes.

Table 1. Description of Test Specimens.

Specimen No	Joint Reinforcement Details	Loading Protocol
1	Nominally Ductile	Quasi-Static
2		Dynamic
3	Ductile	Quasi-Static
4		Dynamic
5*	Nominally Ductile	Quasi-Static, No Pulse
6**	Ductile	
*Tested by MacRae et al. (1994). **Tested by Sritharan et al. (1996).		

MATERIAL PROPERTIES

Compressive tests on concrete cylinders and tensile test on steel coupons were performed in order to determine that actual material properties of the concrete and reinforcing steel. Table 2 presents the compressive strength of concrete just prior to testing of the first four specimens. Table 3 lists the yield strength and the ultimate strength of steel for each reinforcing bar type used in the test specimens.

Table 2. Compressive Strength of Concrete at Time of Testing.

Test Specimen	Joint Reinforcement Details	Structural Member	Compressive Strength	
			MPa	ksi
1	Nominally Ductile	Column	40.8	5.9
		Cap Beam/Joint	38.1	5.5
2		Column	43.0	6.2
		Cap Beam/Joint	39.7	5.8
3	Ductile	Column	41.4	6.0
		Cap Beam/Joint	42.9	6.1
4		Column	43.9	6.4
		Cap Beam/Joint	41.2	6.0

Table 3. Yield and Ultimate Strength of Reinforcing Steel.

Bar Location	Bar Size	Yield Strength		Ultimate Strength	
		MPa	ksi	MPa	ksi
Column and Cap Beam Longitudinal	#7	437	63	709	103
Column Spirals	#3	434	62	679	98
Joint Spirals	#3	362	53	672	97
Cap Beam Stirrups	#2	489	71	590	86

EXPERIMENTAL SET-UP

Each test specimen was tested in an inverted position, as shown in Fig. 2. Both ends of the cap beam were simply connected to the strong floor of the laboratory. Two vertical actuators were used to apply a constant vertical loading of 40 kN (90 kips) simulating the gravity loads on the column. This vertical loading corresponds to approximately 3.5% of the nominal axial load capacity of the column. The lateral cyclic loading on the column was applied by a displacement-controlled horizontal actuator mounted between the strong wall of the laboratory and the loading stub at the top of the column.

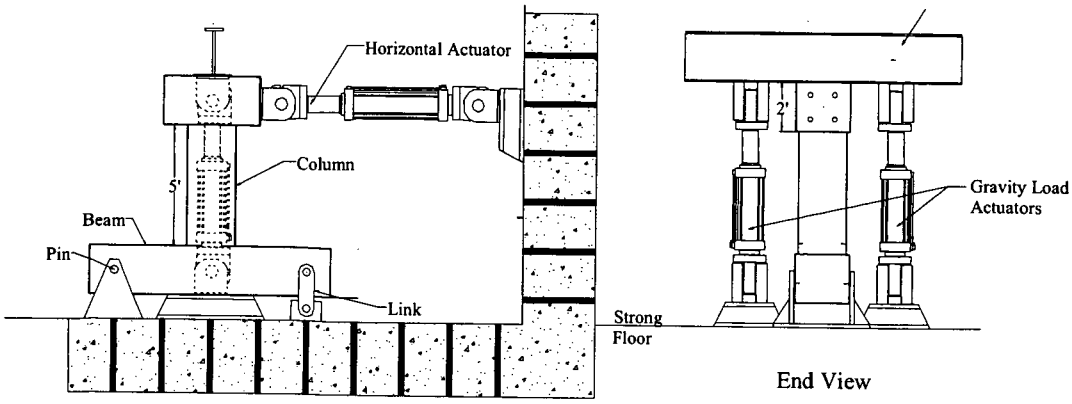

Side View

Figure 2. Experimental Set-Up.

LOADING PROTOCOL

Figure 3 illustrates the horizontal displacement time-history applied at the loading stub of the column during the dynamic tests. This loading protocol starts with one high amplitude, short duration, impulsive cycle followed by a cyclic loading sequence with increasing amplitudes. The latter part of the loading protocol was used by MacRae et al. (1994) and by Sritharan et al. (1996) for the quasi-static testing of specimens 5 and 6, respectively (see Table 1).

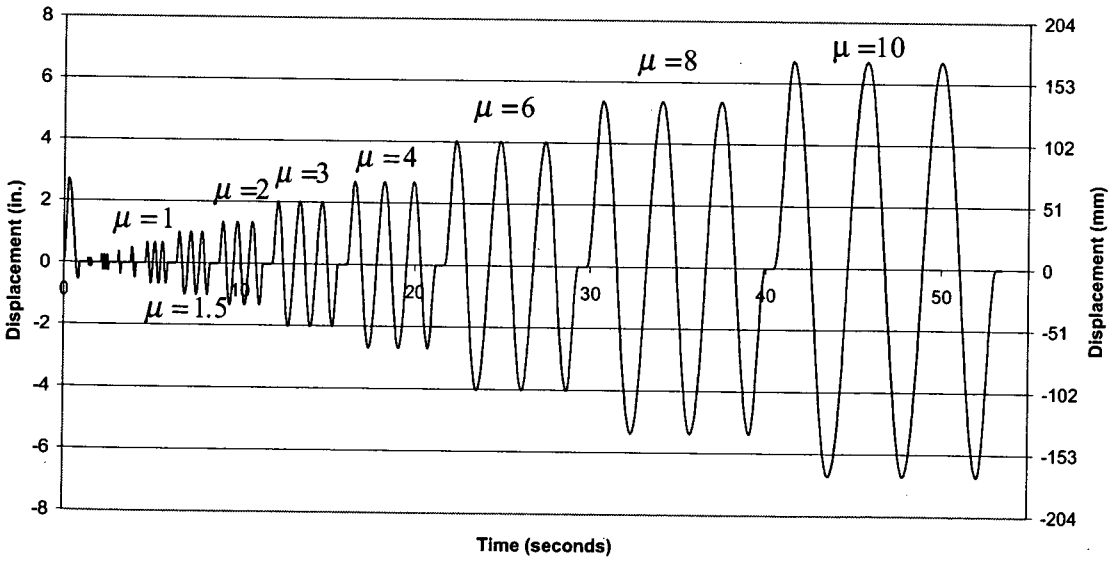

Figure 3. Loading Protocol.

The initial impulsive cycle of the loading protocol was developed by Cox (2001) based on a statistical analysis of thirty-four near-field historical ground motions containing impulsive characteristics, followed by a nonlinear time-history dynamic analysis of a full-scale prototype model of the test specimens in order to determine the resulting displacement at the top of the column caused by this characteristic impulsive base excitation. As shown in Fig. 5, the positive amplitude of the pulse is 69 mm (2.71 in.), while its negative amplitude is 14 mm (0.55 in.). The duration of the pulse is 1.4 sec. The maximum velocity induced by the pulse was 405 mm/sec (16 in./sec). The subsequent cyclic loading was then applied at a constant velocity of 254 mm/sec (10 in./sec). Note also that a short pause was introduced at the end of each sequence containing three cycles at the same amplitude. The displacement ductility ratio, μ, corresponding to the amplitude of each cyclic sequence is also indicated in Fig. 5. This displacement ductility ratio is defined as:

$$\mu = \frac{\delta}{\delta_y} \tag{1}$$

where δ is the amplitude of a given cyclic sequence and δ_y is the first yield displacement assumed to be equal to 12.4 mm (0.49 in.) for all test specimens. This value is the same as the one taken by MacRae et al. (1994) and Sritharan et al. (1996). Note that the amplitude of the first impulsive half-cycle of the loading protocol shown in Fig. 3 corresponds to a displacement ductility ratio of approximately 4.0.

As shown in Table 1, two specimens were tested under dynamic conditions, while two others were tested under quasi-static conditions. For the quasi-static tests, the same loading protocol shown in Fig. 3 was applied, but at a very slow rate. The last two specimens 5 and 6, previously tested by MacRae et al. (1994) and by Sritharan et al. (1996), contained only the cyclic loading portion of the loading protocol without the initial impulsive cycle.

EXPERIMENTAL RESULTS

General Behavior of Test Specimens

The failure modes for both types of specimens were very different. The two specimens with nominally ductile reinforcement details (specimens 1 and 2) suffered shear failures in the joint region. No longitudinal column bars fractured in either of these two specimens. For specimen 1, loaded under quasi-static condition, three main diagonal cracks originated from the soffit side of the cap beam on the north side of the column and propagated to the deck side of the cap beam on the south side of the column. These diagonal cracks appeared during the first impulsive half cycle of the loading protocol and enlarged as the amplitude of the subsequent cyclic loading increased. In the other impulsive half cycle, only one main diagonal crack occurred. The cap beam longitudinal bars buckled out of plane in the joint region near the soffit side. Specimen 2, loaded dynamically, exhibited similar cracking patterns with more concrete spalling in the joint region than the statically loaded specimen 1. The failure modes were similar for both ductile test specimens (specimens 3 and 4). Because of the improved reinforcement

details in the joint region, the full flexural capacity of the column was developed without premature shear failure of the joint. Failure of specimen 3, loaded under quasi-static condition, occurred when several longitudinal bars in the columns buckled in the plastic hinge region and, subsequently, fractured in tension. Failure of the dynamically loaded specimen 3 was much more dramatic. During the second positive cycle at a ductility level of 8, the spiral bar fractured in the plastic hinge region on the north side face of the column. After fracture of the spiral, the column concrete core began to degrade quickly, followed by buckling in compression and fracture in tension of several longitudinal bars in the plastic hinge region. The only major difference between the two ductile specimens was the behavior of the joint region. The quasi-statically loaded specimen 3 suffered much more cracking in the joint region than the dynamically loaded specimen 4. Two longitudinal bars on the deck side of the cap beam of specimen 3 yielded slightly at a ductility level of 6, while no yielding was observed in specimen 4.

Global Hysteretic Response

Figures 4 and 5 present the global top of column load-displacement hysteresis loops obtained for the nominally ductile and ductile specimens, respectively. It can be seen that the initial impulsive loading had a much greater influence for the nominally ductile specimens (Fig. 4) than for the ductile specimens (Fig. 5).

Specimen 1, Quasi-Static Loading

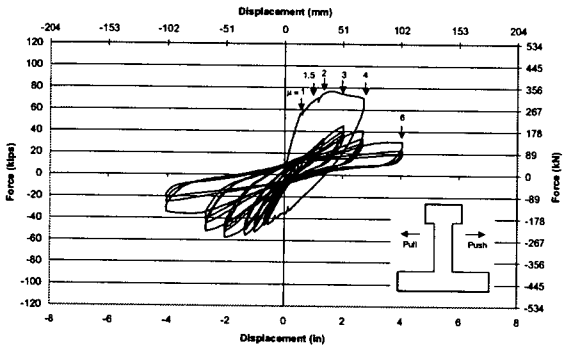

Specimen 2, Dynamic Loading

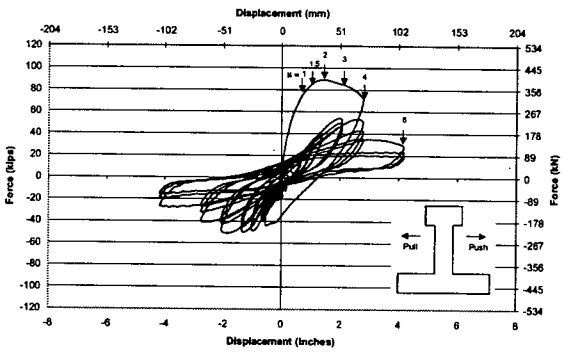

Specimen 5, Quasi-Static Loading, No Pulse

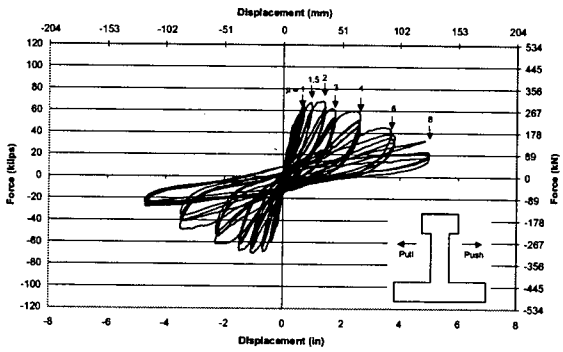

Figure 4. Global Hysteretic Response of Nominally Ductile Specimens.

Specimen 3, Quasi-Static Loading

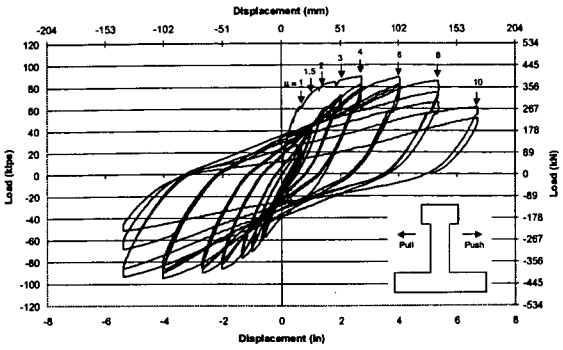

Specimen 4, Dynamic Loading

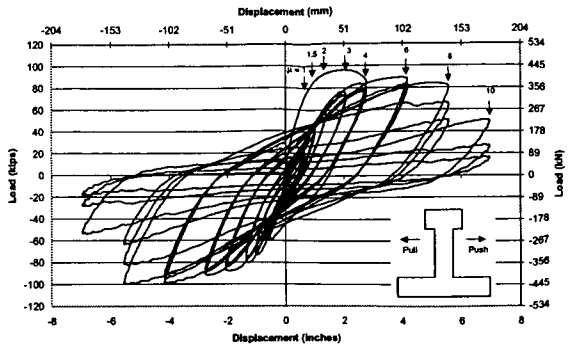

Specimen 6, Quasi-Static Loading, No Pulse

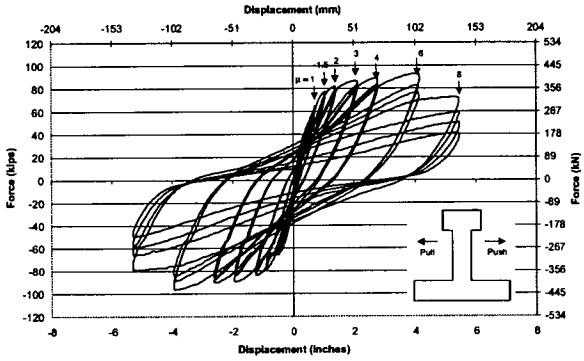

Figure 5. Global Hysteretic Response of Nominally Ductile Specimens.

During the impulsive portion of the loading protocol, the nominally ductile specimens 1 and 2 developed higher capacities than specimen 5 tested quasi-statically by MacRae et al. (1994) without the impulsive portion of the loading protocol. After the impulsive portion of the loading protocol, however, the capacities of both specimens 1 and 2 drop by approximately 50%. Also, both specimens exhibit very pinched hysteresis loops with substantially lower stiffness and strength than specimen 5. This result indicates that the joint shear failure occurred during the impulsive portion of the loading protocol for the nominally ductile specimens, leaving limited stiffness and strength for the remaining cyclic loading.

For the ductile specimens, however, the impulsive portion of the loading protocol has little effect on their behaviors under the remaining cyclic loading. Similar stiffness, strength, and good energy dissipation capacity can be observed for specimens 3, 4 and 6.

The capacity developed during the first impulsive half cycle of loading is significantly higher for the specimens tested under dynamic condition than for the specimens tested under quasi-static condition. This phenomenon is observed for both nominally ductile and ductile test specimens. This increased capacity is a result of the high strain rate induced during the impulsive

loading. High rate of loading causes an increase in the apparent strength of the concrete in compression and of the steel in tension. Finally, the capacities developed by the dynamically loaded specimens 2 and 4 are similar and do not appear to be influenced substantially by the reinforcement details in the joint region.

Energy Dissipation

The energy-dissipation capacity of each specimen can be assessed by computing the absorbed Energy, E_a, during each test.

$$E_a = \int V_{col} d\Delta_{col} \tag{2}$$

where V_{col} is the applied horizontal shear force in the column and Δ_{col} is the horizontal displacement at the top of the column.

Figure 6 presents the cumulative energy absorbed by the six test specimens considered in this study. The crest of each ductility increment represents the most deformed configuration of a specimen under maximum shear force. The corresponding trough occurs when a specimen is unloaded and the elastic portion of the strain energy is recovered. The numerical value at that point corresponds to the cumulative energy dissipated. Note that the absorbed energy is plotted on a pseudo time scale. This pseudo time was determined so that the peaks of the cycles occurred simultaneously for the quasi-static and dynamic tests.

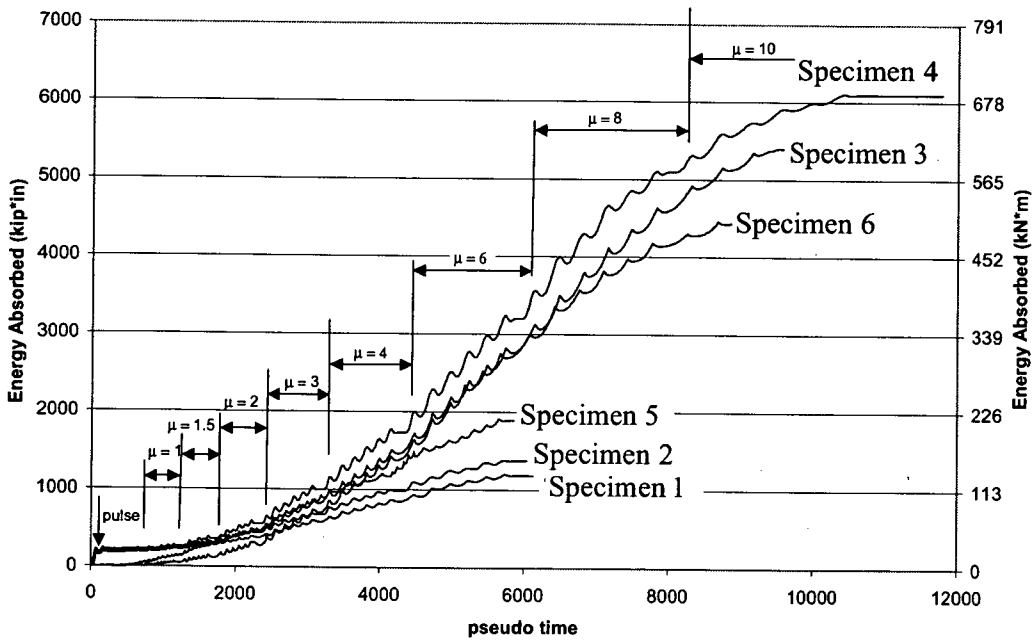

Figure 6. Cumulative Energy Absorbed.

As expected, the ductile specimens (specimens 3, 4 and 6) absorbed much more energy than the nominally ductile specimens (specimens 1, 2 and 5). The impulsive portion of the loading protocol, however, caused a similar rapid initial increase in the energy absorbed for the first four specimens.

For the ductile joints, specimen 4 tested under dynamic condition absorbed more energy than the specimens tested under quasi-static condition (specimens 3 and 6). This can be explained by the apparent increased capacity arising from the high strain rate induced during dynamic loading. The behavior of the ductile specimen 6, tested under quasi-static condition and without the impulsive portion of the loading protocol, was similar to the specimen 3 until a ductility level of $\mu = 8$. For higher ductility levels, the rate of energy absorption of specimen 6 was reduced compared to specimen 3. At $\mu = 8$ for specimen 6, it was observed by Sritharan et al. (1996) that significant shear deformations occurred in the joint region accompanied by a sudden drop in horizontal capacity. Much more concrete degradation and spalling was seen in the joint region of specimen 6 than of specimens 3 and 4. From these results, it can be inferred that the impulsive portion of the loading protocol is not overly detrimental to the overall behavior of the ductile test specimens.

For the nominally ductile specimens, the situation is different. Specimens 1 and 2, tested with the impulsive portion of the loading protocol, absorbed less energy than specimen 5, tested without the impulsive portion of the loading protocol. This result indicates that the impulsive loading has an important effect on reducing the energy-dissipation capacity of nominally ductile specimens due to the early brittle shear failure in the joint region induced during the impulsive loading.

Induced Strain Rate

The column longitudinal bars were instrumented with electrical strain gauges at several locations in the plastic hinge region. The strain rate in the longitudinal bars can be computed as the change in strain over each time step. From an analysis of several instrumented sections in the plastic hinge region of the column, the mean maximum strain rate induced in specimen 4 was estimated at $130{,}000\ \mu\varepsilon/\sec$ (0.13/s).

ANALYSIS

The flexural behavior of the ductile specimens can be approximated by a moment-curvature analysis of the column cross section in the plastic hinge region. The input parameters of such analysis include the geometry of the cross section and the material properties defining the stress-strain curves of concrete in compression and steel in tension and compression. The concrete model must also include the effect of confinement provided by the transverse reinforcement. Figure 7 compares the experimental moment-curvature hysteresis loops of specimen 4 with the prediction of a moment-curvature analysis (Gibson et al. 2001) using the computer software SEQMC (SEQAD Inc. 2000). The curvature values measured in the column were modified in

this figure to account for the additional rotation due to strain penetration into the joint (Priestley et al. 1996, Sritharan et al. 1996). The analysis was conducted with the static material properties given in Tables 2 and 3 and for the confined concrete model proposed by Mander et al. (1988). The model predicts reasonably well the initial stiffness and the strength of the specimen for the cyclic loading following the impulsive portion of the loading protocol. The model, however, under predicts the strength developed by the specimen during the first impulsive half cycle of the loading protocol. It is believed that this is the result of the high strain rate that changes the material properties of concrete and steel.

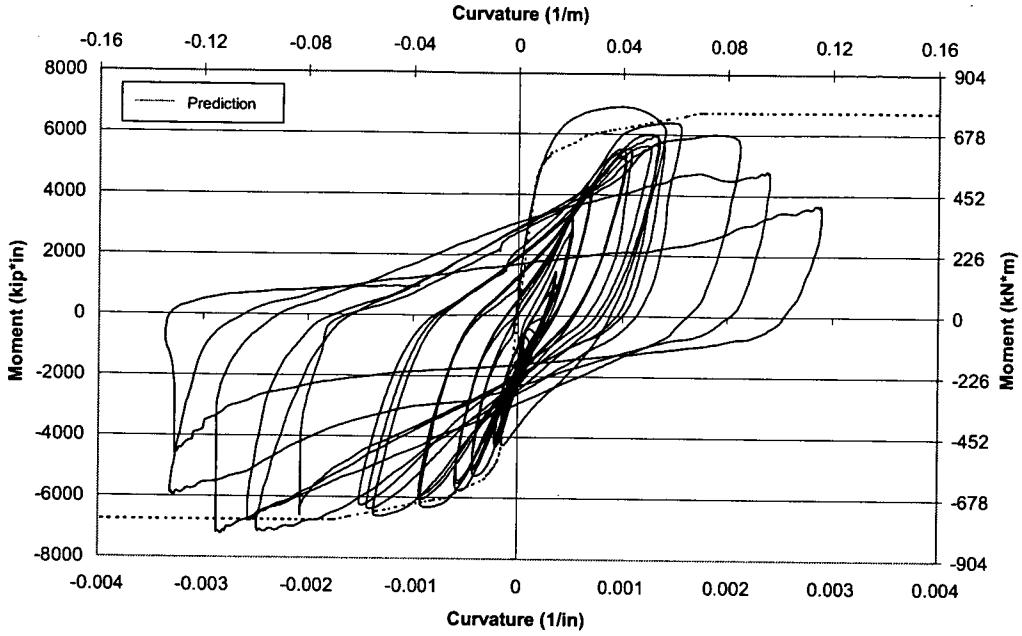

Figure 7. Experimental and Predicted Envelope of Moment-Curvature Hysteresis Loops for Specimen 4, Strain Rate Effects Neglected.

Within the last few decades, a significant research effort has been devoted to the behavior of steel and concrete under high strain rate. This research effort has been summarized recently (Filiatrault and Holleran 2001). Most of these investigations reported that the yield strength and tensile (ultimate) strength of steel increase linearly with logarithmically increasing strain rate. It was also recognized that the strain rate had negligible effect on the elastic modulus and the stiffness of steel in the strain-hardening range. On the concrete side, there is still a lack of information concerning the strain-rate effect on the seismic behavior of concrete members. Many past studies have been carried out for impact conditions, with strain rate several magnitudes above earthquake-type strain rate. Most of the research results available indicate increases in elastic modulus, tensile strength, flexural strength and compressive strength with increasing strain rate.

Table 4 presents amplification factors for the steel and concrete properties as predicted by various empirical expressions available in the literature for the mean peak strain rate of 130,000 $\mu\varepsilon/\sec$ (0.13/s) induced in specimen 4. These amplification factors represent the ratio between dynamic and static material properties. The mean values across the various expressions are also given in Table 4.

Table 4. Amplification Factors for Strain Rate of 130,000 $\mu\varepsilon/\sec$ (0.13/s) on Concrete and Steel Properties.

Material	Property	Reference	Amplification Factor	Mean Amplification Factor
Steel	Yield Strength	Wright and Hall (1964)	1.47	1.22
		Soroushian and Choi (1987)	1.38	
		Kaneko (1997)	1.15	
		Ammann and Nussbaumer (1995)	1.11	
		Wakabayashi et al. (1984)	1.02	
	Ultimate Strength	Soroushian and Choi (1987)	1.11	1.06
		Kaneko (1997)	1.05	
		Ammann and Nussbaumer (1995)	1.02	
Concrete	Young's Modulus	Ammann and Nussbaumer (1995)	1.24	1.24
	Compressive Strength	Ammann and Nussbaumer (1995)	1.26	1.24
		Wakabayashi et al. (1984)	1.22	

The static properties given in Tables 2 and 3 were modified by the mean amplification factors given in Table 4 and then used in the same moment-curvature analysis described above (Gibson et al. 2001). Figure 8 now compares the experimental moment-curvature hysteresis loops of specimen 4 with the prediction of this new moment-curvature analysis that incorporates materials properties modified for strain rate effects. The model predicts very well the initial stiffness of the specimen as well as the flexural capacity achieved during the first impulsive half cycle of loading.

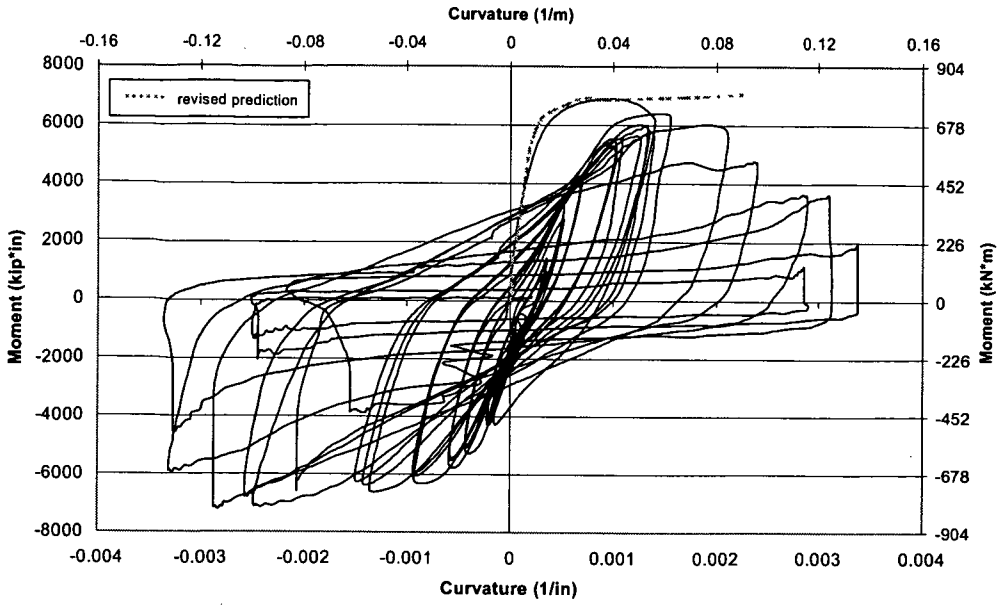

Figure 14. Experimental and Predicted Envelope of Moment-Curvature Hysteresis Loops for Specimen 4, Strain Rate Effects Included.

SUMMARY AND CONCLUSIONS

This experimental study has characterized the impulsive seismic response of bridge column-cap beam joints incorporating nominally ductile or fully ductile reinforcement details. Based on the results obtained, the following conclusions can be drawn:

- The impulsive seismic loading was particularly detrimental to the specimens incorporating nominally ductile reinforcement details in the joint region. Shear failure in the joint was initiated during the impulsive loading, causing early strength and stiffness degradations.
- The joints incorporating ductile reinforcement details suffered minimal damage during the impulsive loading and continued to perform in a ductile manner during the subsequent loading cycles.
- The increased capacity exhibited by both types of specimens during the impulsive loading can be accounted for in a moment-curvature analysis of the column in the plastic hinge region by modifying the steel and concrete properties for the high strain rate induced during the impulsive loading.

ACKNOWLEDGEMENTS

This research project was supported primarily by the Pacific Earthquake Engineering Research (PEER) Center through the Earthquake Engineering Research Centers Program of the

National Science Foundation under Award EEC-9701568. The opinions, findings, conclusions, and recommendations expressed herein are those of the authors and do not necessarily reflect the views of PEER.

REFERENCES

Abrahamson, N. 1998. "Seismological Aspects of Near-Fault Ground Motions," Proceedings of the 5th Caltrans Seismic Research Workshop: California Department of Transportation Engineering Service Center, Sacramento, California, 5 p.

Ammann, H., and Nussbaumer, H. 1995. "Behavior of Concrete and Steel Under Dynamic Actions," Vibrations Problems in Structures, Practical Guide, Chapter F. H. Bachmann et al., Birkhäuser Verlag, Boston, 177-183.

Cox, K. 2001."Characterization of a Large Velocity Directivity Pulse for Laboratory Testing", M.Sc. Thesis, Dept. Struct. Engineering, University of California, San Diego, La Jolla, CA.

Filiatrault, A., and Holleran, M., 2001."Stress-Strain Behavior of Reinforcing Steel and Concrete under Seismic Strain Rates and Low Temperatures," Materials and Structures, 34, 235-239.

Gibson, N., Filiatrault, A. and Ashford, S.A. 2001. "Performance of Bridge joints Subjected to a Large Velocity Pulse," Structural Systems Research Project Report No. SSRP-2001/10, Dept. of Structural Engineering, University of California, San Diego, La Jolla, CA, 100 p.

Kaneko, H., 1997. "Influence of Strain-Rate on Yield Ratio," Kobe Earthquake Damage to Steel Moment Connections and Suggested Improvement, JSSC Technical Report No. 39/96.

MacRae, G. A., Priestley, M. J. N. and Seible, F. 1994. "Santa Monica Viaduct Retrofit – Large-scale Column-cap Beam Joint Transverse Test – Preliminary Report," Structural Systems Research Project, Report No. TR-94/02, University of California at San Diego, California. Mander, J. B., Priestley, M. J. N. and Park, R. 1988. "Theoretical Stress-Strain Model for Confined Concrete", Journal of Structural Engineering, ASCE, Vol. 114, P1804-1826.

Priestley, M. J. N., Seible, F. and Calvi, G. M. 1996. "Seismic Design and Retrofit of Bridges," Wiley-Intersceience Publications, New York.

SEQAD Inc. 2000, SEQad Moment Curvature Analysis Program (C), distributed by SC Solutions, available online at http://www.best.com/~solvers/seqmc.html.

Soroushian, P. and Choi, K. 1987. "Steel Mechanical Properties at Different Strain Rates. Journal of Structural Engineering, ASCE, **113**(4), 863-872.

Sritharan, S., Priestley, M.J.N. and Seible, F. 1996. "Seismic Response of Column/Cap Beam Tee Connections with Cap Beam Prestressing," Structural Systems Research Report, Report No. SSRP-96/09, University of California at San Diego, California.

Udagavva, K., Takanashi, K., and Kato, B. 1984. Effects of displacement rates on the behavior of steel beams and composite beams. 8th World Conference on Earthquake Engineering, San Francisco, CA, IV, 177-184.

Wakabayashi, M., Nakamura, T., Iwai, S., and Hayashi, Y. 1984. "Effects of Strain Rate on the Behavior of Structural Members," 8th World Conference on Earthquake Engineering, San Francisco, CA, IV, 491-498.

Wright, R.N., and Hall W.J. 1964. "Loading Rate Effects in Structural Steel Design," Journal of the Structural Division, ASCE, 90(55), 11-37.

Development of Experimental Guidelines for Bridge Column Testing

Jerry J. Shen[1] and W. Phillip Yen[2]

Abstract

In order to make the bridge experiments more efficient in terms of providing reliable and comparable information, Federal Highway Administration has conducted a systematic study on bridge test methods. The most common issues and procedures are identified. Proper methods on specimen construction, loading procedure, and measurements will be established to provide experimental researchers an easy reference that makes test results comparable to result from other tests.

Introduction

The design specifications for bridges are improved along time. Experimental studying on bridges and bridge subassemblages is an essential need for the improvements on design and construction techniques. Experimental studies do not only provide direct conclusions for needs in the industry but also provide information basis for empirical formula development and theoretical model verifications. In order to make the bridge experiments more efficient in terms of providing reliable and comparable information, the Federal Highway Administration (FHWA) has launched a systematic study on the techniques and procedures of conducting experimental bridge tests. The objective of the study is to develop the National Guidelines for Experimental Tests on Highway Structures.

A literature review covering a wide range of bridge tests were performed. Information of the major experimental research institutes was collected. Some laboratory administrative personnel were or will be interviewed to include their practical experiences. These materials will be summarized and suggestions for establishing the experimental guidelines will be produced. These results will be made available for experts to review and comment.

Benefits of having national guidelines

Each experimental study has its own purpose and unique setup to serve this purpose. The results from experiments contain more information than they were designed to provide. A large part of the information is often either wasted due to ignorance or not comparable with other tests due to incompatible format and testing conditions. If widely adopted experiment guidelines exist, the part of an experiment that is not necessarily different from other tests for its purpose can be conducted in the standard manner. Commonly demanded information will not be ignored. The result can be used for theoretical derivation or empirical model calibration with a solid confidence that the data were obtained from an experiment compliant to a reliable procedure. In the mean time, the tester receives additional credits and publicities because the experimental results appear in more consequent studies.

[1] Lendis/FHWA, 6300 Georgetown Pike, McLean, VA 22101
[2] Office of Infrastructure, R&D Federal Highway Administration, , 6300 Georgetown Pike, McLean, VA 22101

Common purposes for bridge column tests

Bridge experiments are used for either discovering element properties that were not clear to engineers or verifying the theoretical anticipations. The most common goals for dynamic bridge column tests are:

(1) To determine strength and ductility under strong earthquake (capacity)
(2) To determine force and displacement demand
(3) To determine effectiveness of retrofit
(4) To observe failure patterns such as cracking, buckling, etc.
(5) To observe the performance of new design or retrofit methodologies
(6) To develop and verify analytical or empirical models
(7) To inspect existing bridges

Different goal results in different test requirements and test methods. The issues being addressed in these guidelines are those shared by numbers of different tests.

Test categories

Dynamic structural tests are commonly divided into 3 categories. They are quasi-static tests, pseudodynamic tests, and shake table tests (Kausel, 1998; Dimig et al, 1999). Field tests, although being one important branch for bridge tests, are not often included for not being carried out in the lab. At current stage, the recommendation will be limited to the most widely used method for bridge column tests: quasi-static tests.

The quasi-static tests are performed slowly. All velocity-dependent and acceleration-dependent characteristics are ignored. It is therefore not suitable for any element with a large viscous damping or a significant self-weight.

Specifications

There are three major issues in a bridge pier test: specimen, loading, and measurement. The specimen is a full or scaled replica of the components of a real or imaginary bridge. It needs to be designed to best reflect the bridge component characteristics. The loading procedure is usually a simulation of load pattern occurs in a real event. For random-type input such as earthquake and wind, some load patterns that are different from the real load but possess certain realistic characteristics are used. The primary objectives of measurements are to acquire the most useful data.

Model construction

Prototype

The very first step for bridge tests is to determine the configurations of the studied bridge including the size, shape, designed loads, and detailing. This information can be provided by the designer if the subject is a built or proposed bridge. For more general studies, which may target a group of bridges, the determination of the bridge parameters become less straightforward. One approach is

to conduct a statistical investigation (Lowes and Moehle, 1995, Abo-Shadi et al, 2000) to determine the most representative parameters for the group of bridges. The other approach is to simply use a most common value regardless what group of bridges the test is designed for. The proper guideline provisions to these two scenarios are described below:

(1) When the category of the bridge is one of the major topics for the test, the National Bridge Inventory (NBI) Database presents a complete raw collection of bridge external dimensions, functions, locations, and ages. This information can be converted to that required by the testers (Lampe and Azizinamini, 2000). Specific group characterized by age, location, structure type, function, etc., can be selected from the database according to the needs of the test. This can largely reduce the time wasted on preliminary investigation and increase the representitiveness of the selected parameters.
Some of the information provided in NBI and the refined information needed for prototype design are shown in figure 1. It is collected in a uniform format. With a simple program and some supplemental information from other federal publications such as NEHRP maps, the information can be refined and directly used as statistical analysis result. Table 1 shows three simple example of the raw statistical parameters derived from NBI database.

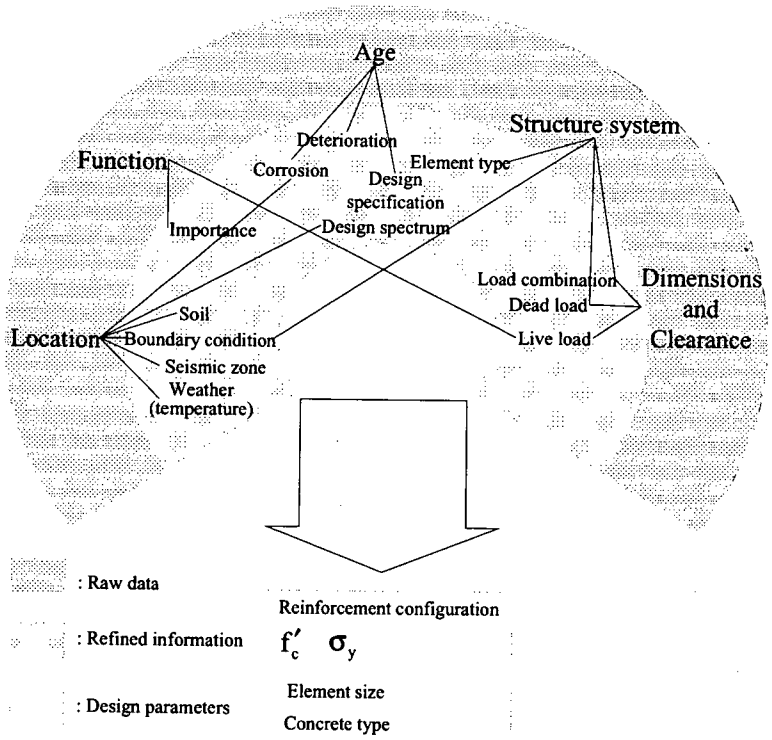

Figure 1 Raw data, refined information, and necessary design parameters

Group	Average Span	Average Width	Average Height
All listed California	32.2	21.3	5.98
All Post-1970 California	39.9	21.2	6.17
Concrete Multi-box girder California	29.9	34.4	4.98

Table 1 Examples of categorized information from NBI, unit: m

(2) When the tester just need a general bridge model, a set of most common parameters can be provided. For example, a height of 20 ft (6 m), span of 65 ft (20 m), and width of 40 ft (12 m) can be provided. The dead load and live load can be derived from the dimensions given above. For more convenience when only columns are involved, a dead load of 800 kip (360 ton) and a live load of 200 kip (90 ton) can be provided. The sum of dead load and live load determines the axial load of the column and the dead load alone determines the lateral loads.

Scale

The scaling of the model is necessary due to facility limitations. When the model is scaled down, many parameters must be scaled in different proportions. A dimensionless analysis needs to be carried out to find the proper scaling of each parameter (Moncarz, 1981; Bertero, 1984).

In the quasi-static bridge column tests, all time-dependent parameters that relate to velocity and acceleration are ignored. The most important variables in a bridge column quasi-static test are listed in table 2. There are only two fundamental dimensions when time and temperature are not in concern. The second column in table 2 shows the dimensions in terms of force (F) and length (L).

Variable	Dimension
Geoimetric size Lg	L
Stress σ	F/L^2
Strain ε	L/L
Specific weight γ	F/L^3
Elastic modulus E	F/L^2
Yielding stress σ_y	F/L^2
Force P	F
Displacement U	L
Bending moment M	FL
Rotation angle θ	L/L
Curvature ϕ	1/L

Table 2 Common variables in scaling process and their dimensions

Since the self-weight of the column and the superstructure is related to the gravitational acceleration, it is not included in the scaling process. The vertical dead load and live load from the superstructure are reduced to an external force applied

axially and laterally to the top of the column. Although specific weight γ is an important parameter of the construction material, it does not affect the structural response if the superstructure is much heavier than the tested pier systems. In the mean time, material specific weight is hard to change without interfering with other parameters. It is therefore not included in the scaling.

The parameter that needs to be changed as will is the geometrical dimensions, i.e. Lg. The parameters that are most difficult to change as will are the stress-related variables, such as yielding stress σ_y, elastic modulus E, etc. It is convenient to use geometric size as the controlling parameter and keep stress unscaled. The resultant scaling factors are listed in table 3.

Variable	Scale
Geometric size Lg	S_L
Stress σ	1
Strain ε	1
Elastic modulus E	1
Yielding stress σ_y	1
Force P	S_L^2
Displacement U	S_L
Bending moment M	S_L^3
Rotation angle (Δ/L) θ	1
Curvature ϕ	S_L^{-1}

Table 3 The proper scaling used for quasi-static column tests

It has been noticed that the construction materials have different mechanical properties at different size. The mechanical properties such as elastic modulus and yielding or ultimate stress are not only difficult to change as requested but also difficult to maintain constant when size is changed. There are multiple reasons that makes the mechanical properties size-dependent, such as different manufacturing process and failure mechanism. Special care should be taken to ensure this does not alter the test result without notice.

Load patterns

There are 6 popular loading procedures in bridge tests with various loading equipments and speeds.

(1) Monotonic (quasi-static)
(2) Cyclic (quasi-static)
(3) Random or field record (quasi-static)
(4) Pseudodynamic
(5) Shake table (dynamic)
(6) Field test (ambient, harmonic, transient)

The first three are for quasi-static tests suitable for the bridge column tests discussed in this paper. There has not been any written standard for these loading

procedures applied on quasi-static tests for bridge columns. There are, however, some conventions gradually forming within the experimental community. For example, the cyclic loading procedure is usually considered to be a good simulation tool for earthquakes when more realistic options, i.e. true dynamic tests, are not feasible. Since it is an approximation of earthquake load, there can be numerous approaches. Most tests done to bridge columns have adopted a progressive pattern cyclic loading procedure. This procedure involves a pilot cycle in the elastic range that provides more accurate estimation for yielding displacement, followed by plastic cycles that contain 2-3 cycles at each deformation level and increase in multiples of yielding displacement. It is believed that two or three cycles for each displacement level is a balance between observability of strength degradation and avoidance of undesired material fatigue (Lowes and Moehle, 1995). This procedure evolves from the standard steel element cyclic procedures (ECCS, 1986; Stone and Cheok, 1989; ATC-24, 1992). For a single test on bridge column, this is likely the method bearing the largest amount of information. However, there are other needs in theoretical studies that may require various types of load patterns, which provide more comprehensive information for bridge column responses under seismic load (El-Bahy et al, 1999). As a nationwide guidance that intends to meet all research needs, the proposed guidelines need to provide diverse load patterns or load pattern generation tools.

Measurements and data acquisition

The technologies used in measurement systems are evolving quickly. New issues emerge while old issues are resolved. It is not easy to setup general guidelines for all tests. However, well-configured measurement and acquisition systems share some similar principles. It is important to layout the principles to be followed.

The mostly used measuring devices are strain gauges, potentiometers, LVDTs, and load cells. Laser measurement is one of the newly improved technologies. A few fundamental values, such as lateral load, lateral displacement, and curvature (figure 2), should be required by the guidelines. Some physical detail that may affect the resultant accuracy should be specified. For example, the standard interval and stroke requirement of the displacement transducers for measuring curvature should be specified. The range of the curvature measurement needs to be sufficient to cover the plastic hinge zone and part of the elastic zone. In addition to the fundamental results, some measurement related to accuracy should be required. For a setup shown in figure 2, the displacements "a", "b1", and "b2" should be required to keep track of the slippage and deformation of anchorages.

The data acquisition system has all become digital nowadays. Analog filtering is crucial for such systems. For slow static tests, the system can stop at each designated load step and allow the measurements recorded. Analog filters can be conditionally absent if several readings are made and averaged to eliminate the fluctuation from high-pitch electronic or physical noise. For high-speed tests, the analog low-pass filtering range needs to cover the highest frequency of the interested vibration component. The sampling rate should be higher than twice of the filter cut-off frequency.

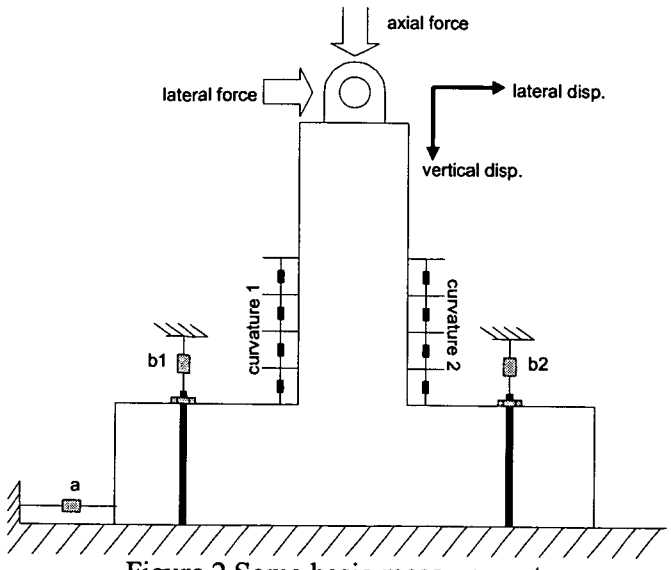

Figure 2 Some basic measurements

Safety

Although the safety is not one of the core issues in the testing guidelines in terms of producing results, it is practically the top priority in all experiments. Some basic shop-safety rules should be reemphasized. In addition, some safety issues specifically existing in bridge tests can be considered to be put in. For example, there should be a crane attachment on the column model that can insure safety when failure occurs. The crushing of some high-strength concrete can be explosive. The human safety distance for certain f_c' can be provided. Some other similar safety cautions may have existed in individual lab safety regulations. They can be adopted if found appropriate.

Conclusions

Most bridge column tests are either for research purpose or for specific construction or retrofit project. The uniqueness of these tests makes it difficult to set up general guidelines for all. However, as a leading agency in the highway industry, the FHWA will persevere in the effort of laying out the national testing guidelines for bridges due to the anticipated tremendous benefits to the researchers and designers in this country. The first appearance of the product is expected to take place in the early 2002.

This project will not be able to provide premium result without the contributions from bridge testing experts. All suggestions and discussions are highly appreciated.

References

Abo-Shadi, N.; Saiidi, M.; Sanders, D.; "Seismic Response of Reinforced Concrete Bridge Pier Walls in the Weak Direction," Technical Report MCEER-00-0006, July, 2000.

Applied Technology Council; "Guidelines for Cyclic Seismic Testing of Components of Steel Structures," ATC-24, Applied Technology Council, Redwood City, CA, 1992.

Bertero, V. V.; Aktan, A. E.; Charney, F. A.; Sause, R.; "Earthquake Simulation Tests and Associated Studies of a 1/5th-scale Model of a 7-story R/C Frame-wall Test Structures," Report No. UCB/EERC-84/05, University of California, Berkeley, 1984.

Dimig, J.; Shield, C., French, C.; Bailey, F.; Clark, A.; "Effective Force Testing: A Method of Seismic Simulation for Structural Testing," Journal of Structural Engineering, Sept., 1999.

El-Bahy, A.; Kunnath, S.; Stone, W.; Taylor, A.; "Cumulative Seismic Damage of Circular Bridge Columns: Variable Amplitude Tests," ACI Structural Journal, September-October, 1999.

European Convention for Constructional Steelwork, Technical Committee 1, Structural Safety and Loadings; Working Group 1.3, Seismic Design; "Recommended Testing Procedure for Assessing the Behavior of Structural Steel Elements under Cyclic Loads," First Edition, 1986.

Kausel, E; "New Seismic Testing Method. I: Fundamental Concepts," Journal of Engineering Mechanics, May, 1998.

Lampe, N.; Azizinamini, A.; "Steel Bridge System, Simple for Dead Load and Continuous for Live Load," Proc. Conference of High Performance Steel Bridge, Nov. 2000.

Lowes, L., N.; Moehle, J., P.; "Seismic Behavior and Retrofit of Older Reinforced Concrete Bridge T-Joints," Report No. UCB/EERC-95/09, Earthquake Engineering Research Center, September, 1995.

Moncarz, P. D.; "Theory and Application of Experimental Model Analysis in Earthquake Engineering," Dissertation, Stanford University, 1981.

Stone, W.; Cheok, G.; "Inelastic Behavior of Full-Scale Bridge Columns Subjected to Cyclic Loading," NIST Building Science Series 166, Jan. 1989.

Evaluation of Seismic Performance of High-strength Reinforced Concrete Members

Chihiro Kawatoh[1], Shigeki Unjoh[2]

Abstract

In general, steel towers are adopted for long-span suspension bridges in Japan. Recently, reinforced concrete (RC) towers has also been applied for such long-span bridges. The RC towers have the advantages than steel towers in the point of view of the economical efficiency. To adopt the RC towers, there are several issues to be solved: use of high strength materials to reduce the self-weight of towers; dynamic nonlinear ductility characteristics of high strength concrete members under the high axial force from the main cables. This paper presents the experimental study on the ductility characteristics of high strength concrete under the high axial force.

1. Introduction

Steel towers have been adopted for long-span bridges. Recently, RC towers has been adopted for long-span bridges including a Great belt East bridge (Denmark), Ting Ma bridge (Hong Kong), etc from a viewpoint of economical efficiency.

In this research, the dynamic characteristic of the high strength reinforced concrete under high axial force was studied. Concerning the high axial force, the influence by the anti-force from a cable has been taken into consideration. In order to reduce the self-weight of a tower, it is indispensable to use the high strength reinforced concrete. Therefore, experimental investigation on the dynamic characteristic of the high strength reinforced concrete member under high axial force was conducted. The dynamic characteristic on which we focused is ductility performance. This is because it is indispensable to secure the ductility performance of members to reserve of the seismic safety to large-scale earthquakes.

2.Outline of Experiments

2.1 Specimens

Test specimens are shown in Fig.-1. The section and the reinforcing bar arrangement of specimens are shown in Table-1. The experiments were conducted for one normal strength RC specimen and three high strength RC specimens. When adopting RC structure as the main tower of long-span bridges, in order to reduce the self-weight of the tower, a hollow section is employed in many cases. However, in this experiment, in order to consider the ductility performance of the high strength RC members under high axial force, the full section was assumed. The section of member was 450x450mm; the ratio of shear span was assumed as 5. The longitudinal bar ratio was assumed as 1.25%. This is the general value of a highway bridge pier. The specimen N and H were the same size and the same

Table-1 Section, Re-bar Arrangement, Test Result of Material, and Test Conditions

	Specimen N	Specimen H	Specimen HA	Specimen HB
	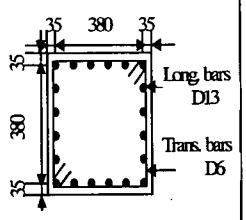	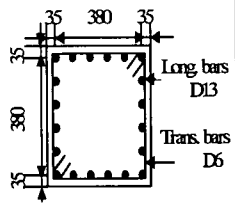	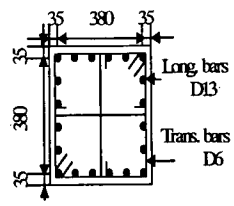	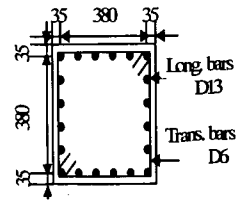
Concrete	σ_c=37.1/mm^2	σ_c=65.7/mm^2	σ_c=66.8/mm^2	σ_c=64.3/mm^2
Longitudinal Re-bar	SD345 D13	USD685 D13	USD685 D13	USD685 D13
Ratio of Long. Bar	ρ_l=1.25%	ρ_l=1.25%	ρ_l=1.25%	ρ_l=1.25%
Yield Strength of Long. Bar	σ_y=399N/mm^2	σ_y=795N/mm^2	σ_y=795N/mm^2	σ_y=795N/mm^2
Tensile Strength of Long. Bar	σ_u=587N/mm^2	σ_u=998N/mm^2	σ_u=998N/mm^2	σ_u=998N/mm^2
Hoop Tie	SD295A D6@40mm	SD490 D6@40mm	SD490 D6@40mm	SD490 D6@40mm
Ratio of Hoop Tie	ρ_w^*=0.352% ρ_s^{**}=0.833%	ρ_w^*=0.352% ρ_s^{**}=0.833%	ρ_w^*=0.523% ρ_s^{**}=1.667%	ρ_w^*=0.176% ρ_s^{**}=0.417%
Yield Strength of Hoop Tie	σ_y=335N/mm^2***	σ_y=571N/mm^2***	σ_y=571N/mm^2***	σ_y=571N/mm^2***
Tensile Strength of Hoop Tie	σ_u=522N/mm^2	σ_u=942N/mm^2	σ_u=942N/mm^2	σ_u=942N/mm^2
Axial Force, Ratio of Axial Force	N=0.90MN σ_N/σ_c=12.1%	N=1.79MN σ_N/σ_c=13.7%	N=1.79MN σ_N/σ_c=13.5%	N=1.79MN σ_N/σ_c=14.0%

Note)*: Ratio of Hoop Area **: Ratio of Hoop Volume

*** : Since clear yielding point did not exist, the strength counted backward from load to 0.2% yield strength is shown

reinforcing bar arrangement.

2.2 Experimental Set-up

The loading set-up is shown in Fig.-1. In the setup of axial force, 15% of design standard strength of concrete was applied.

Horizontal loading was applied by increasing the load-displacement, the unit displacement was assumed as 1/3 δy_0 and the number of cyclic loading was assumed as 1. In general, to verify the ductility performance of Highway bridge pier, three cycles of reverse load are applied. However, the specimen H, which was using high strength material, had large yield

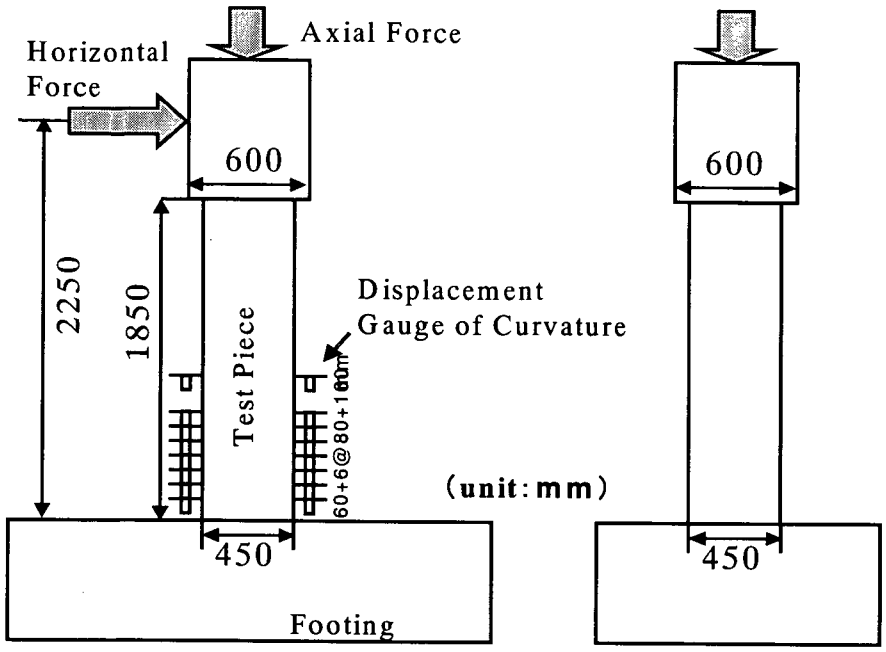

Fig.-1 Dimension of Specimen and Test Setup

displacement as compared with the specimen N was normal strength material. As for the specimen H, it was expected that ultimate displacement became small by the high axial force.

3.Results of experiments

3.1 Relationship of load - displacement and damage state

The relationship of load – displacement is shown in Fig.-2. In the specimen N using normal strength material, peak load was shown at 2 δ y, and cover concrete was failed at 5.33 δ y. However, the rapid reduction of capacity was not seen until the longitudinal bar was buckled and broken in 7~8 δ y. Up to the last cycle, the relationship of load – displacement showed a spindle type history curve and the energy absorption performance was good. The specimen H series had become the spindle type history curve like the specimen N, and the energy absorption performance was good. In the specimen H, peak load was shown at 1.33 δ y, cover concrete was tailed at 1.66 δ y, and the longitudinal bar was buckled at 2.66 δ y. However, the decreasing rate of the lateral load from maximum capacity point to buckling point of the longitudinal bar was almost constant. It was a same tendency with the specimen HA and HB. The slope of decreasing rate of the specimen of HB is larger than the specimens H and HA.

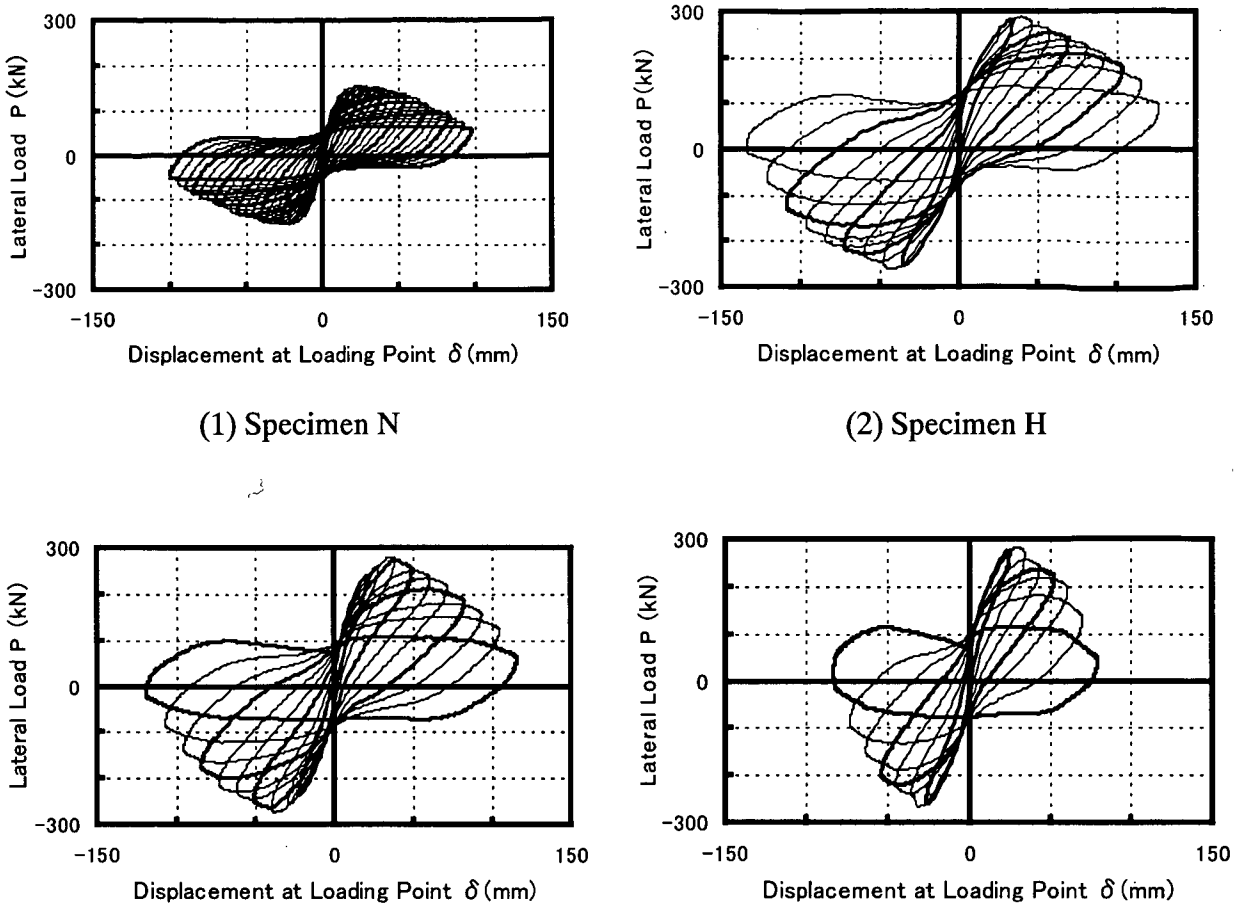

(1) Specimen N

(2) Specimen H

(3) Specimen HA

(4) Specimen HB

Fig.-2 Load-Displacement Loop of Test Specimens

3.2 Consideration of the results of experiment about ductility capacity

Figure-3 shows the comparison of load-displacement envelope for each specimen. Figure-3 shows the envelope, which rectified the influence of pullout of longitudinal bar. The influence of pullout was calculated by integrated of strain of longitudinal bar in footing [1]. The following methods can be considered as an evaluation method of ductility.

In the specimen H series, additional bending load by axial force was large as compared with the specimen N. Thus, horizontal load decreases with the increase of displacement at loading point. In the specimen H and HA, reduction of the load after peak load was mainly based on additional bending force. However, in the specimen HB, a decrease of the load more than an additional bending load was seen. This is because of the confinement effect by lateral reinforcement.

The ductility performance obtained by the experiment and the amount of history absorption

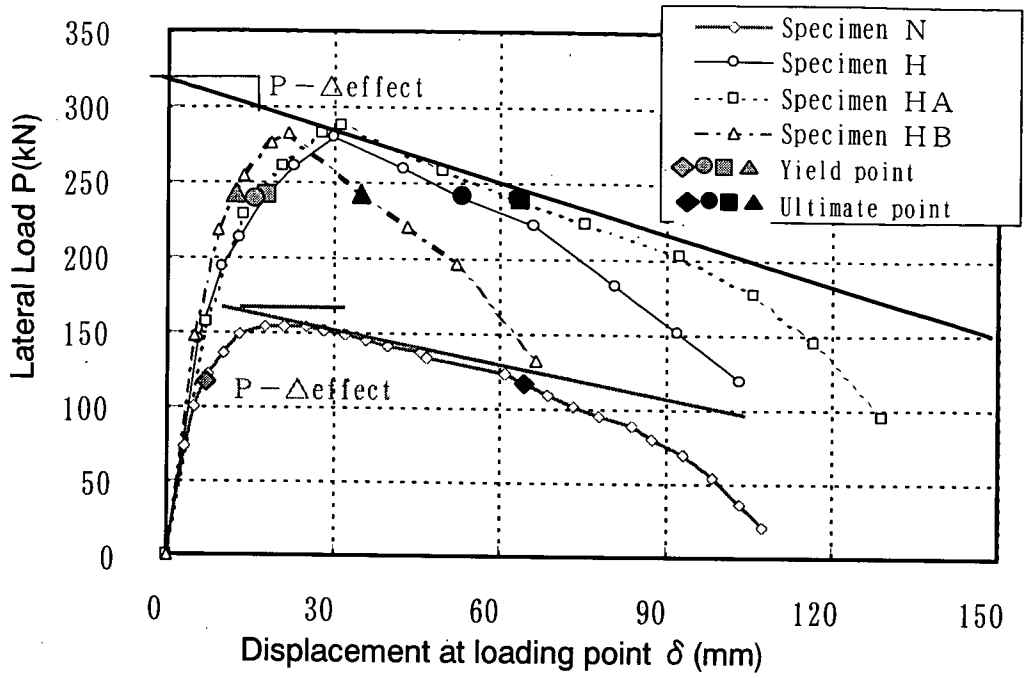

Fig.-3 Comparison of the Load-Displacement Envelope of each Specimen

Table-2 Ductility Capacity and Energy Absorption

	Hoop ratio ρ_s(%)	Ductility Performance			Energy Absorption**(kN·m)
		Yield Displacement* δ_y(mm)	Ultimate Displacement δ_u(mm)	Ductility Ratio μ	
Specimen N	0.833	7.0	64.8	9.29	3.11
Specimen H	0.833	17.8	53.1	2.98	12.05
Specimen HA	1.667	15.9	63.9	4.01	14.99
Specimen HB	0.417	12.2	34.8	2.85	7.81

Note) * Experimental displacement corresponding to the first yield point computed by calculation

** Energy absorption per 1 loop at the ultimate displacement

energies per one loop at the ultimate state is shown in Table -2. Although the specimen H of energy absorption capacity in which high strength material was used is larger.

3.3 Analytical study of ductility performance

Here, the ductility performance characteristic obtained by the experiment using two evaluation formulas [2,3] has been examined analytically.

Figure-4 shows stress-strain relationship for two formulas. When a lateral reinforcement ratio compares specimen N and specimen H that are ρ =0.83%, it turns out that a JRA formula and a New RC formula show the almost same value. On the other hand, when the

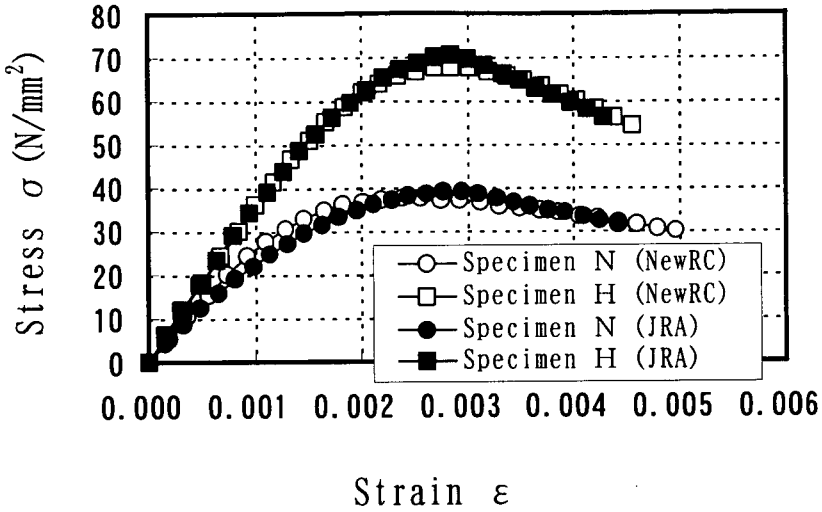

(1) Comparison of Normal Strength and High-Strength RC Members

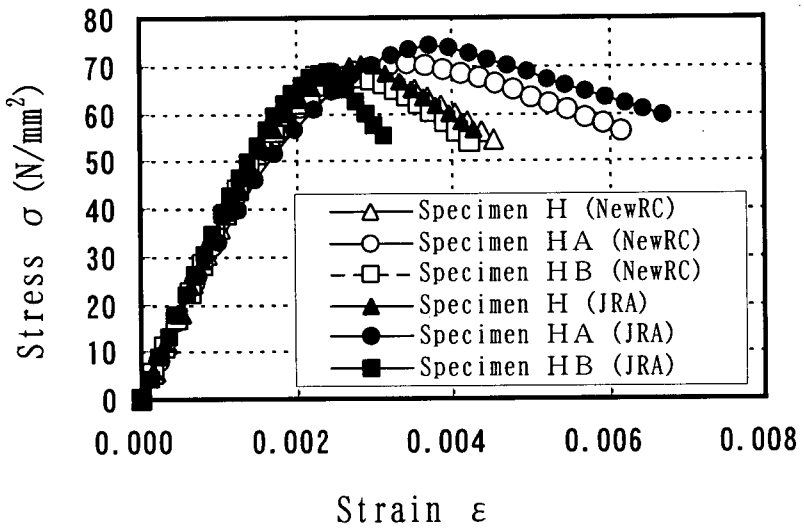

(2) Comparison of New RC and JRA Formula

Fig.-4 Relationship between Stress and Strain

specimen H series are compared, the JRA formula shows that downward slopes of stress-strain relationship are sensitive to the volume of the lateral reinforcement as compared with the New RC formula. In the JRA formula, large ultimate strain is computed by the specimen HA which is ρ =1.67% and a small ultimate strain is computed by the specimen HB which is ρ =0.42%.

Next, the ductility ratios of each specimen were computed using these two evaluation formulas. In calculation of ductility ratio, change of ductility ratio by the additional bending effect is considered. The conceptual figure of the rectifying method is shown in Fig.-5. Fig.-6 compares the ductility ratio for which it calculated by the method mentioned above.

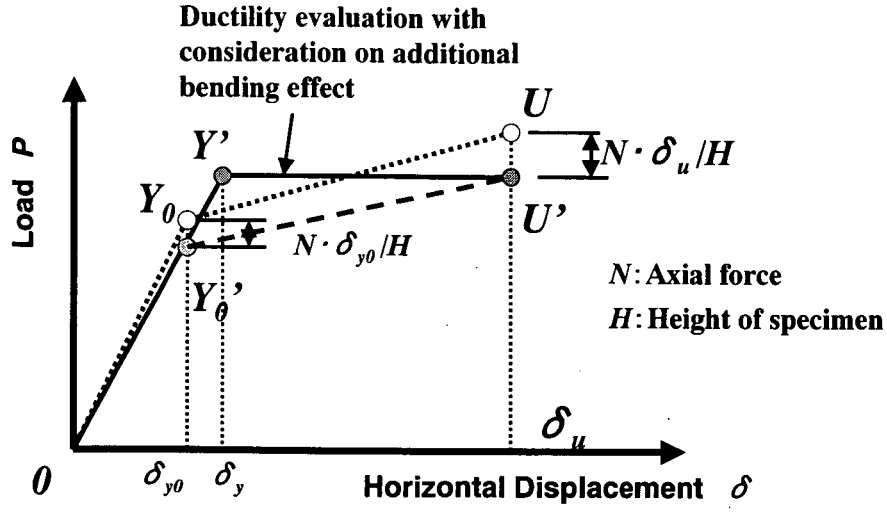

Fig.-5 Rectifying Method of Ductility Evaluation with Additional Bending Effect

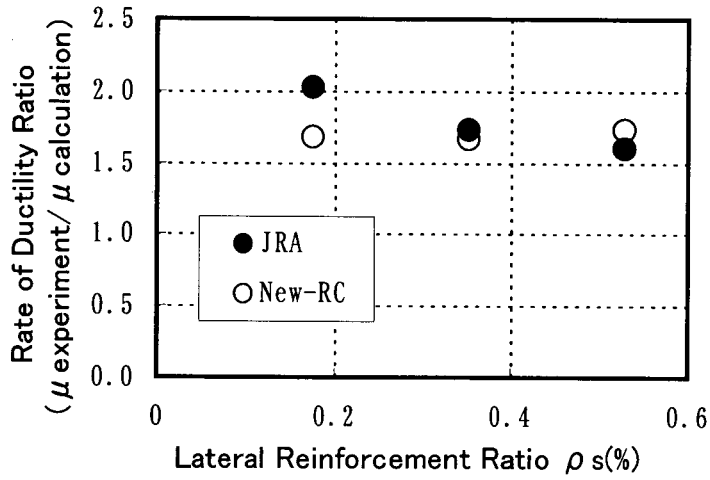

Fig.-6 Relationship between Rate of Ductility Ratio and Lateral Reinforcement Ratio

3.4 Study of equivalent plastic hinge length

Curvature distributions to the height direction of each specimen after an experiment are shown in Fig.-7. The ultimate curvature computed from the ultimate strain corresponding to $0.8\sigma_{cc}$ and the plastic hinge length described in JRA formula are also shown in Fig.-7.

The relationship between an average of the curvature distribution by the displacement gauge which the experiment at the ultimate state defined in 0.5D(225mm, D: width of section) from the base, and the ultimate curvature calculated by JRA formula is shown in Fig.-8. In the curvature calculation using JRA formula, the ultimate strain corresponding to $0.5\sigma_{cc}$ and $0.8\sigma_{cc}$ is computed. It turns out that the ultimate curvatures at $0.5\sigma_{cc}$ from this Fig.-8 are well in agreement with the average value of the curvature distribution by displacement gauge. The following formula is used for calculation of equivalent plastic

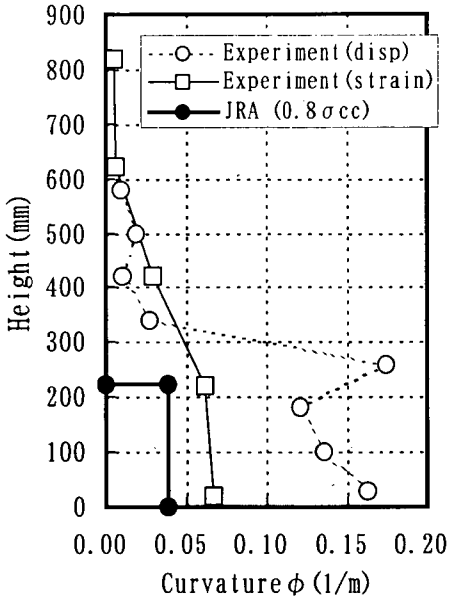

(1) Specimen N

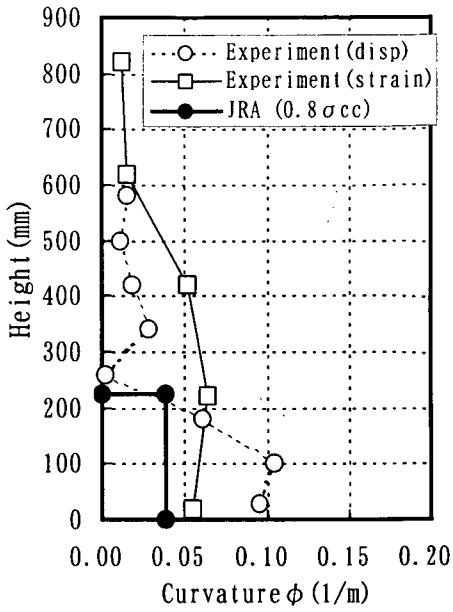

(2) Specimen H

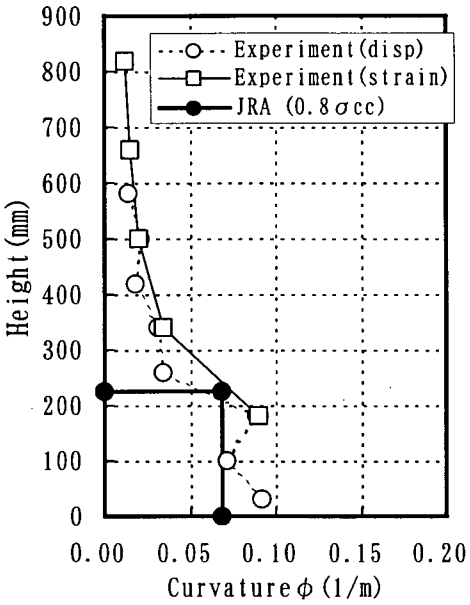

(3) Specimen HA

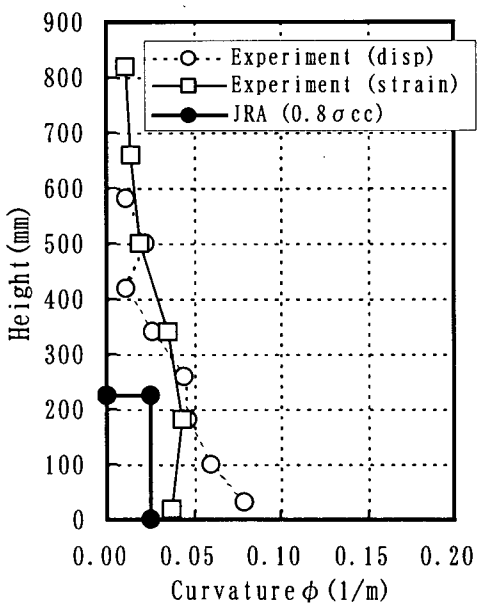

(4) Specimen HB

Fig.-7 Curvature Distribution to the Height Direction

hinge length.

$$\delta_u = \delta_y + (\phi_u - \phi_y) \cdot Lp \cdot (H - L_p/2) \qquad (1)$$

Where

δ_u : ultimate displacement, δ_y : yield displacement,
ϕ_u : ultimate curvature, ϕ_y : yield curvature, H : height of specimen

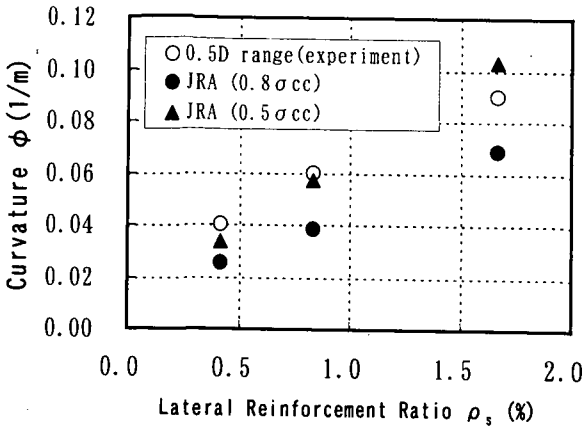

Fig.-8 Relationship between Average Curvature At Plastic Hinge and Ultimate Curvature By JRA

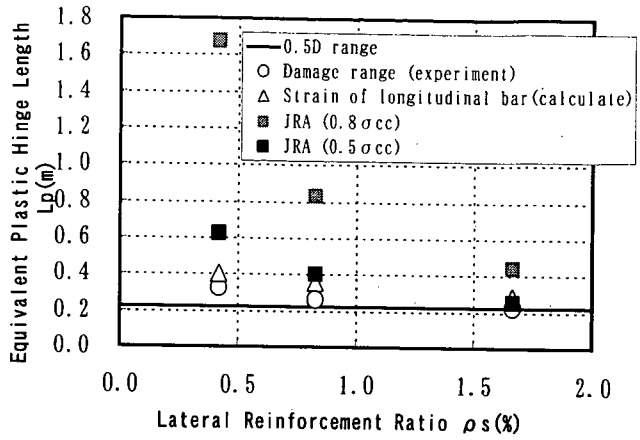

Fig.-9 Relationship between Equivalent Plastic Hinge Length and Lateral Reinforcement Ratio

4.Conclusions

To study the applicability of RC towers to long-span suspension bridges, experimental study on the ductility performance of the high strength RC members under high axial force was made. The accuracy of the JRA equation to evaluate the strength and ductility characteristics was also examined. The following conclusions are deduced.

(1) The ductility performance of the high strength RC member under high axial force is significantly affected by the additional bending moment by axial force.

(2) The ductility performance of high strength RC member can be improved with the increase of lateral reinforcement.

(3) In stress-strain evaluation of high strength concrete, the JRA formula has the similar tendencies as compared with New RC formula.

(4) In high strength RC member, plastic hinge length is in inverse proportion to the increase in a lateral reinforcement ratio. The actual damage range was well in agreement with the equivalent plastic hinge length at the time of setting an ultimate to 0.5 σ_{cc} by the JRA formula.

(5) When RC structure will be adopted as the main tower, the hollow section needs to be adopted because of reduction of the self-weight. For this reason, it is necessary to establish the technology of the evaluation method of bending and shear capacity using high strength material. Furthermore, it is necessary to examine the structure with composite structure and new high ductility materials

Acknowledgement

This research was made by former PWRI. The authors greatly thank Dr. Yukio Adachi, Hanshin Expressway Public Corporation (former senior research engineer of PWRI), who conducted this experimental works [4], for his great contribution to this research.

References

[1] Shima, H., Chou, L., and Okamura, H.: Bond Characteristics in Post-Yield Range of Deformation Bar, Proc. of JSCE, V-6, No.378, pp.213-220, 1987.2(in Japanese)

[2] For Example, Japan Institute of Construction Engineering: Ministry of Construction Report of Comprehensive Technical Development Project, 1989.3～1993.3 (in Japanese)

[3] Japan Road Association, "Design Specifications of Highway Bridges PartⅤ. Seismic Design", 1996,12(in Japanese)

[4] Adachi, Y., Unjoh, S., Nagaya, K., and Hayashi, M.: Experimental Study on Ductility Characteristic of High Strength Concrete Column under High Axial Force Condition, Proc. of JCI, Vol.21, No.3, 1999.7(in Japanese)

Breakout B1: BRIDGE MANAGEMENT 2

(1) Study on Required Cover Depth of Concrete Highway Bridges in Coastal Environment
(Yoshiki Tanaka, Hirotaka Kawano, Hiroshi Watanabe and Tomoyoshi Nakajo)

(2) Sensitivity Study of a Chloride Penetration Model on Life-Cycle Cost of Post-tensioned Bridges
(Shoichi Ogawa and Tamio Yoshioka)

(3) Performance of Electrochemical Chloride Extraction Technology for Concrete Bridge Members Rehabilitation and Ongoing Laboratory Research
(Gerardo G. Clemeña, Stephen Sharp and Y. Paul Virmani)

(4) Repairing and Retrofitting the Prestressed Concrete Simple T-Girder Bridge Damaged by Salt-Induced Corrosion
(Katsunori Ishimura, Sadaaki Nakamura, Toshio Hosaki and Kazuyoshi Nishina)

(5) Upgrading Concrete Bridges with PBO Prestressing Upgrading Technique (P-PUT)
(Z. S. Wu, K. Iwashita, K. Hayashi, T. Higuchi, S. Murakami and Y. Koseki)

Study on required cover depth of concrete highway bridges in coastal environment

Yoshiki Tanaka[1], Hirotaka Kawano[2], Hiroshi Watanabe[3] and Tomoyoshi Nakajo[4]

Abstract

There are many concrete bridges suffering from corrosion in coastal areas in Japan. Some bridges have already been removed because of heavy corrosion at the age of only 20 - 30 years, and in some cases the maintenance cost was far higher than the initial construction cost. Many corroded bridges will be replaced in the next few years. It is estimated that the cost of maintenance will accelerate after 2010, therefore new structures are required to be more durable[1)].

In order to improve the durability of concrete highway bridges in coastal areas, we have been studying the concept and methods of new designs for durability[2)3)]. This paper examines the following:

1. Review on corrosion problems of concrete highway bridges in Japan
2. New practical durability design method considering chloride permeability and measured airborne chloride
3. Calibration of the method by comparison with deterioration cases of existing bridges
4. Required cover depth for design lifetime of 100 years
5. Direction of corrosion protection for concrete highway bridges in the near future

1. Introduction

Most infrastructures require various maintenance works. By 1997, approximately 130,000 highway bridges with a bridge length of more than 15 m, of which approximately 75,000 are concrete bridges, had been constructed in Japan. However, new methods of designing more durable bridges requiring less maintenance are required in order to minimize the maintenance cost in future.

---

1. Research engineer, Public Works Research Institute, Japan
2. Team leader, ditto
3. Senior research engineer, ditto
4. The Japan Prestressed Concrete Contractors Association

The problem of chloride attack is the first issue to address in establishing a design method for long-life concrete bridges, although there are various causes of deterioration including alkali aggregate reaction and carbonation, because some concrete bridges have been fatally deteriorated by chloride carried by sea winds. Some prestressed concrete bridges in coastal areas have been replaced due to heavy corrosion after only a few decades of use, and in some cases the cost of maintenance was more than the initial construction cost. When typical large cracks due to corrosion are observed, it means that steel corrosion is already so severe that even careful repair is no longer sufficient. It is, however, difficult to detect corrosion in concrete before cracking.

Since the "*Guide specifications on measures against chloride attack for highway bridges*" was established in 1984, the durability of concrete structures for highway bridges in coastal areas has improved certainly. One main measure described in the *Guide Specifications* is to increase the cover depth depending on the distance from the coast, in order to keep rebar and tendons away from chlorides. As ingress of chlorides continues unless some protection measures such as painting are taken, deeper cover concrete may be necessary when a long design period such as more than 100 years is set. Nevertheless, a quantitative method for estimating the effectiveness of the measures involving lifetime has not yet been established.

In this paper, the cover depth required for a design period of 100 years was evaluated based on Fick's equation, after calibration was carried out by comparison with deterioration cases of existing bridges. Then nationwide data of measured airborne chlorides as an index of chloride environment was taken into account. Also, chloride permeability in concrete was reevaluated using diffusion coefficient data obtained from exposure tests and cores taken from existing bridges.

2. Review of corrosion problems of concrete highway bridges in Japan

2.1 Corrosion process of rebar and tendons due to ingress of chloride ions

The concept of chloride attack due to chloride ions permeating into concrete is illustrated in Fig. 1. Micro pores and gel water, which are generally formed in concrete, serve as routes for the movement of chloride ions. The pore structure in concrete depends on the type of concrete, mix proportion and its quality. Near the coast where much chloride exists in the air and where some structures are directly splashed by seawater, large quantities of chloride can adhere to the surface, and chloride ions can then easily permeate and reach the concrete surrounding rebar. Chloride ions can break the passive oxide film and initiate corrosion even under conditions of high alkalinity of the concrete pore water. Thus, typical heavy cracking and spalling of concrete due to corrosion expansion of rebar may take place early.

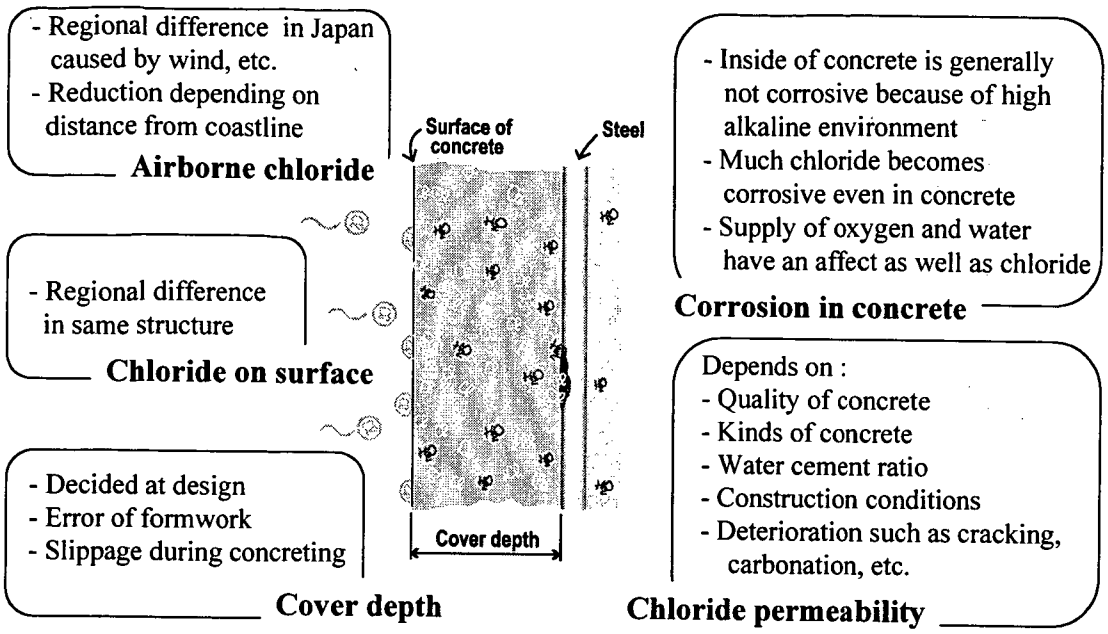

Fig. 1 Concept of chloride attack at the coast and influencing factors

2.2 Design cover depth for highway bridges in Japan

Cover concrete is required to protect rebar from corrosion, to keep the bond between concrete and rebar, and to retain ease of concreting. In the severe chloride environment found near the sea, the cover depth and materials used for concrete structures should be selected carefully for corrosion protection. The minimum cover depth was described in the "Design specifications for highway bridges in Japan" as shown in Table 1. Until 1984, superstructures were designed according to this table even at the coast.

Table 1 Minimum cover depth for highway bridges (mm)

Kind of members	Deck, Curb, Railing, Slab bridges with span of less than 10 m	Beams	
		Precast members	Beams except precast, Slab bridges with span of more than 10 m
Minimum cover depth	30	25	35

Deterioration due to ingress of chloride was gradually recognized in the late 1970s. Fatal corrosion of tendons was observed in the Kuretsubo Bridge, and so a nationwide survey of the damage condition of concrete highway bridges within 500m from the coast was carried out in 1982. A map of deficient bridges obtained from that survey is shown in Fig. 2.

Regional differences in the degree of deterioration due to corrosion were found. The relationships between distance from coast, age and degree of deterioration in regions A and B (Fig. 5), where many deficient bridges exist, are shown in Figs. 3a and 3b. There were many damaged bridges located within 100 m from the coast. Otherwise, these figures show that the ratio of deteriorated bridges among precast prestressed concrete bridges was less than for other types of concrete bridges, while precast bridges had a thinner covering. One of the causes was the difference of diffusion coefficient of chloride ions in concrete. In 2000, chloride profile data of concrete cores, which had been taken from many damaged bridges during repair work, were gathered. Diffusion coefficients obtained from the profiles are shown in Fig. 4. The diffusion coefficient of precast bridges was much smaller than that of others. It is generally known that the water/cement ratio of precast bridges, which required high strength, is less than that of others, although the water/cement ratio of each bridge could not be clarified exactly in this survey. Many studies have shown that the lower the water/cement ratio, the lower the diffusion coefficient. Thus, a low water/cement ratio raises the durability of precast bridges. Other effects were that prefabrication enabled more accurate rebar work, formwork and concreting than in situ. As a result, cover depth and quality of concrete could be appropriately controlled.

The results of the above deterioration survey were reflected in the *Guide Specifications*.

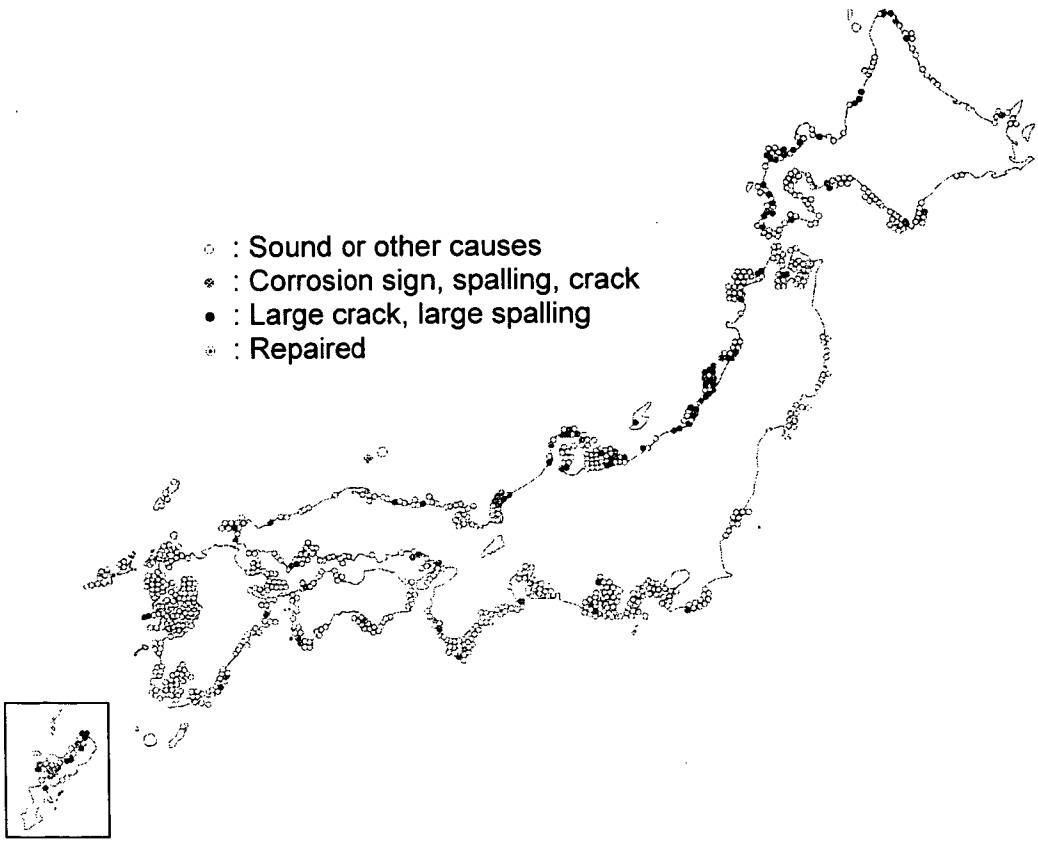

Fig. 2 Map of deficient bridges

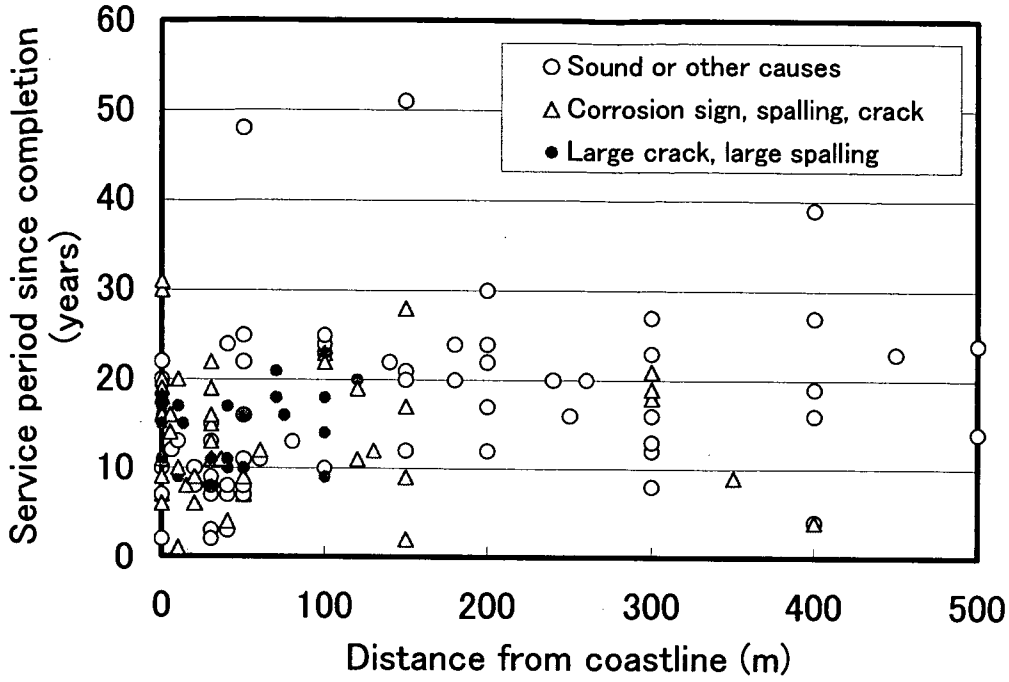

Fig. 3a Distribution of deficient bridges in Region A and B except precast prestressed concrete bridges

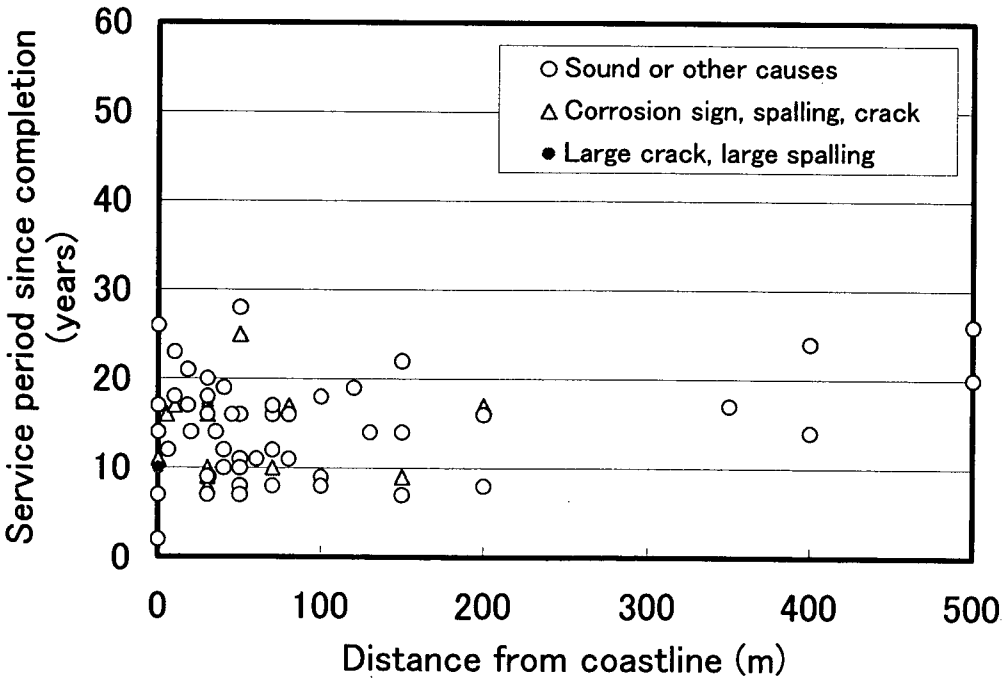

Fig. 3b Distribution of deficient precast prestressed concrete bridges in Region A and B

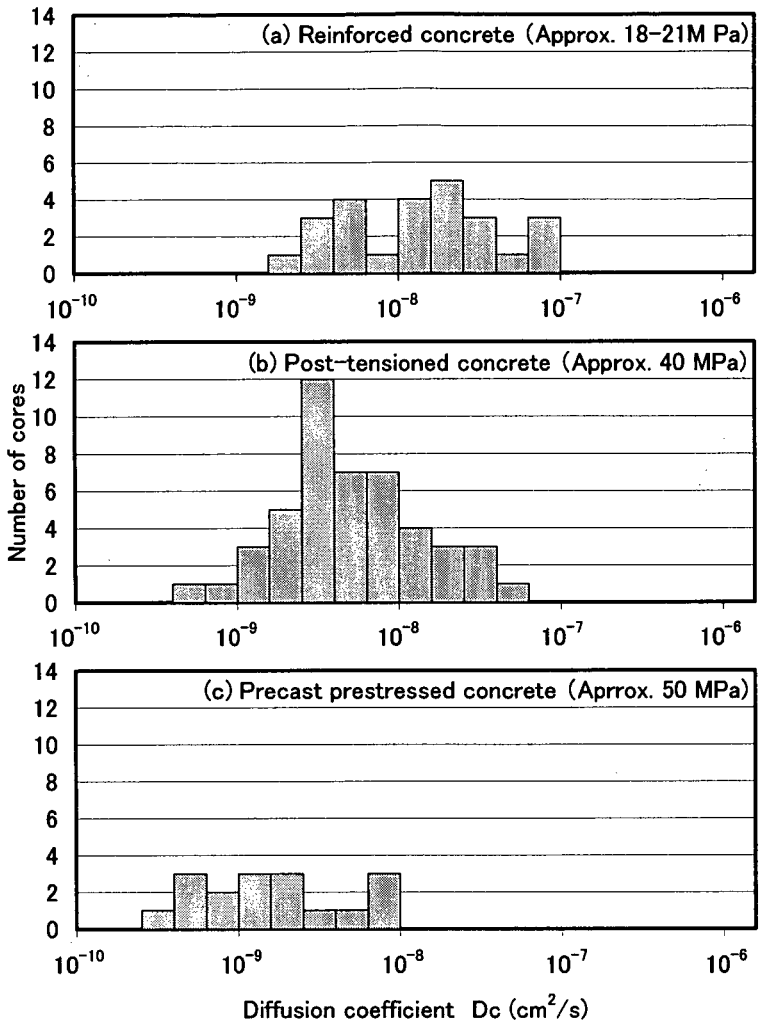

Fig. 4 Diffusion coefficients of chloride ions of concrete cores taken from existing bridges

*Ordinary design concrete strength is shown in parentheses.

The main and optional measures in the *Guide Specifications* are as follows:

1) Increase of minimum cover depth according to distance from coast for each region as shown in Table 2-4 and Fig. 5
2) Restriction of upper limit of water/cement ratio, control of bending crack, etc.
3) Optional measures: epoxy coated rebar, painting on surface of concrete

Up to 1995, more than 400 highway bridges were designed according to the *Guide Specifications*. Although no more than a couple of decades have passed since completion, major deterioration has never been found, while some minor problems due to poor workmanship have been observed. The durability of the bridges has thus been improved when compared with some bridges designed according to former specifications, which deteriorated badly within 10 to 15 years of completion. However, new design methods for cover concrete depending on the design period are important for creating more durable bridges.

Table 2 Regions requiring measures against chloride attack

Legends	Regions requiring measures
A	Okinawa Prefecture
B	Areas within 300 m from coast and above sea in regions shown in Fig. 5
C	Areas within 200 m from coast and above sea except the above regions

Table 3 Measure levels

Regions	Distance from coast	Level
A	Less than 100 m and above sea	I
	Except the above region	II
B	Less than 100 m and above sea	I
	100 – 200 m	II
	200 – 300 m	III
C	Above sea	I
	Less than 100 m	II
	100 – 200 m	III

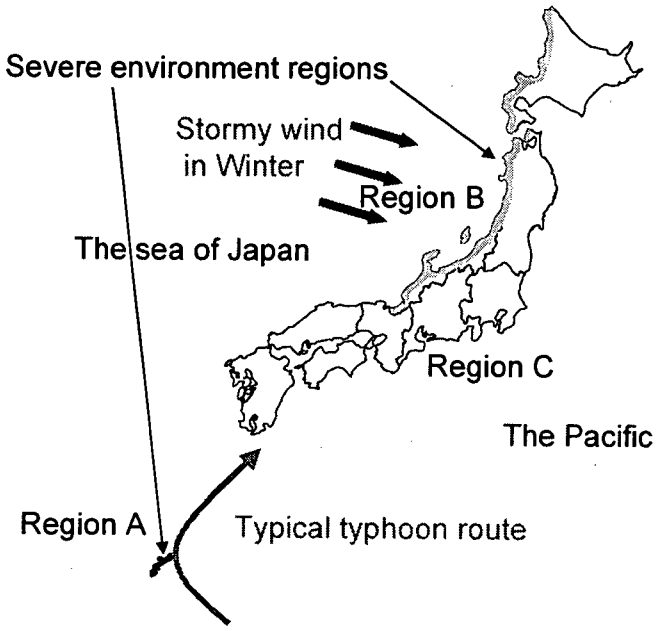

Fig. 5 Map of regions in the *Guide Specifications*

Table 4 Minimum cover depth described in the *Guide Specifications* (mm)

Level	Superstructure			Substructure	
	Bottom of Deck, Curb, Railing	Beam		Beam	Column
		Precast prestressed concrete	Other type		
I	50	50	70	70	70
II	40	35	50	50	50
III	30	25	35	35	40

3. New practical durability design method considering chloride permeability and measured airborne chloride

3.1 Basic principle

The process of chloride ingress into concrete is generally expressed by Fick's equation. In this paper, a basic formula was based on a solution of the equation as follows. The solution (the left side of equation (1)) is obtained assuming that the boundary is kept at a constant chloride concentration Co, the initial concentration being zero throughout the medium.

$$C(x,t) = Co\left(1 - \mathrm{erf}\frac{x}{2\sqrt{Dc \cdot t}}\right) < Ccorr - Cinit \quad (1)$$

where x: distance from concrete surface, t: time, Dc: diffusion coefficient,
erf( ): error function, Ccorr: threshold chloride level to initiate corrosion,
Cinit: initial chloride level in concrete

This is the simplest equation, expressing the process of chloride ingress from outside with the minimum required parameters such as x, t, Co corresponding to environmental inputs and Dc corresponding to the kinds and quality of concrete.

Various models have been proposed so far. Equation (1) does not precisely express the actual process. However, abundant data of Co and Dc based on this model have been obtained from many kinds of tests and surveys to estimate existing structures. Otherwise, it is difficult to verify the validity of the complex model because time dependent data of various parameters such as temperature, humidity, carbonation, absorption into hydrated compounds and so on have not yet been obtained. Thus, it was decided in this paper that the use of equation (1) is more appropriate to express the process for practical design at the present stage.

3.2 Airborne chloride and boundary chloride level on surface of concrete

(1) Airborne chloride: Cair

For three years from 1984, a nationwide survey of airborne chloride level, which is the mass of chloride ions caught by stainless steel of 0.1 m x 0.1 m area every month, was carried out[4]. Then data of airborne chloride level at 266 points within 10 km from the coast was obtained. Fig. 6 shows the result in Region B as an example of the relationship between Cair and distance from the coast. Cair means average mass of measured airborne chloride ions in a year. It can be seen that the logarithm of Cair has a linear relation to the logarithm of distance from the coast. The slope of the relation was usually constant regardless of the region, while the chloride level varied by region. Therefore, equation (2)

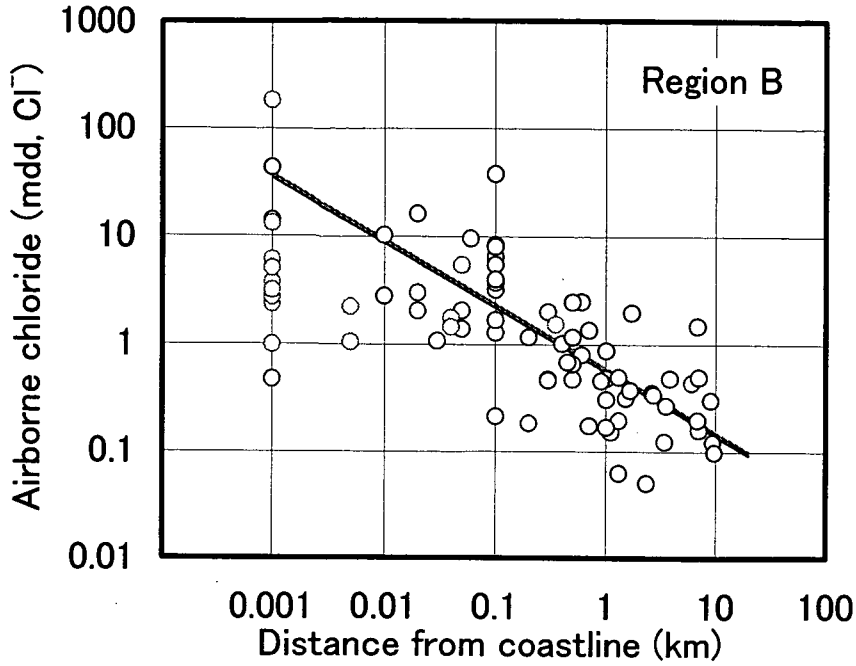

Fig. 6 An example of relationship between measured airborne chloride and distance from coast in Region B

was proposed to illustrate approximately measured airborne chloride.

$$Cair = C_1 d^{-0.6} \qquad (2)$$

where, Cair: airborne chloride level (mdd・Cl^-) mdd=mg/dm^2/day

C_1: airborne chloride level equivalent to value at distance of 1 km (mdd)

d: distance from coast (km)

C_1 expresses the airborne chloride level of each region. C_1 of a region where deterioration due to corrosion was frequently observed is larger than that of other regions. These regional differences are mainly caused by local wind and wave conditions, and can also be verified by the seasonal variation of airborne chloride. In this paper, taking the situation of deterioration into account, C_1 for each of Region A, B and C were decided to be 0.6, 0.6 and 0.2, respectively.

(2) Relationship between Cair and Co

Exposure tests of concrete blocks with water/cement ratios of 0.39 and 0.58 were also done for the survey of airborne chloride. The relationship between Co obtained from the exposure and Cair is shown in Fig. 7. Co is approximately related with Cair. Thus, Co was defined as a function of Cair as follows.

$$Co=1.5 \cdot Cair^{0.4} \qquad (3)$$

where, Co: boundary chloride level on surface of concrete (kg・Cl^-/m^3)

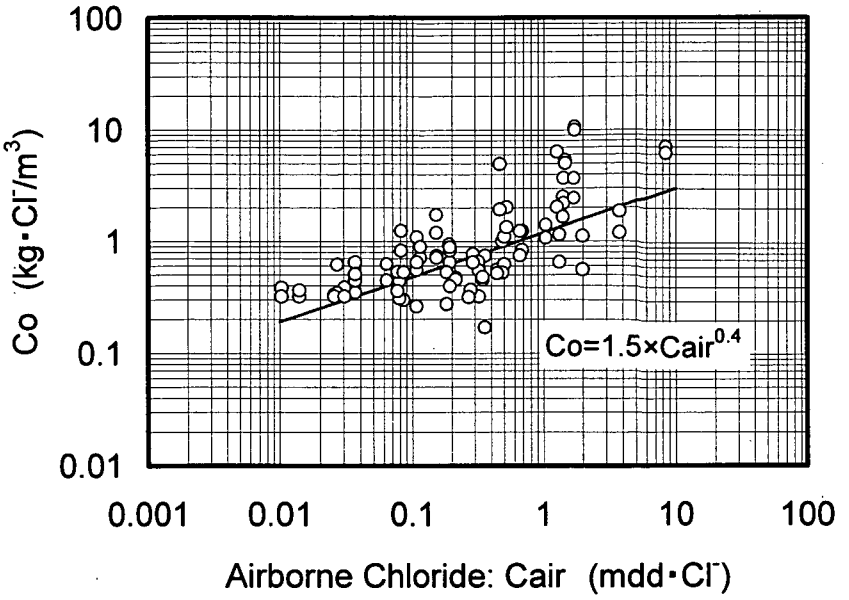

Fig. 7 Relationship between Co and Cair

3.3 Diffusion coefficient: Dc

The diffusion coefficient Dc of chloride ions in concrete is known to depend on the pore structure, which is related to the water/cement ratio, kind of cement, mix proportion and quality.

According to our research, the difference of Dc among concrete types made from ordinary, high early and low heat Portland cement was small, for the same water/cement ratio. Some papers showed that the use of granulated blast furnace slag or fly ash caused a tight pore structure of concrete, if cured appropriately.

The water/cement ratio is a major factor influencing Dc in the mix proportion of ordinary Portland cement concrete. Fig. 8 shows the relationship between Dc and water/cement ratio, which was obtained from our exposure test[5]. In the range of water/cement ratio from 0.25 to 0.55, the smaller the water/cement ratio, the smaller Dc. If the water/cement ratio is less than 0.4, the reduction of water/cement ratio is particularly effective for decreasing Dc. This tendency agrees with the finding that there are relatively fewer deficient bridges made of precast prestressed concrete, which have a low water/cement ratio of 0.3 to 0.4.

High durability concrete made with a lower water/cement ratio is becoming increasingly available. This has been helped by the spread of super plasticizer due to developments in non-compacting concrete, high strength concrete and so on. There are some issues that need to be overcome to create durable concrete with lower water/cement ratio, for instance, pumpability, temperature induced cracking, and alkali silica reaction caused by using a larger volume of cement.

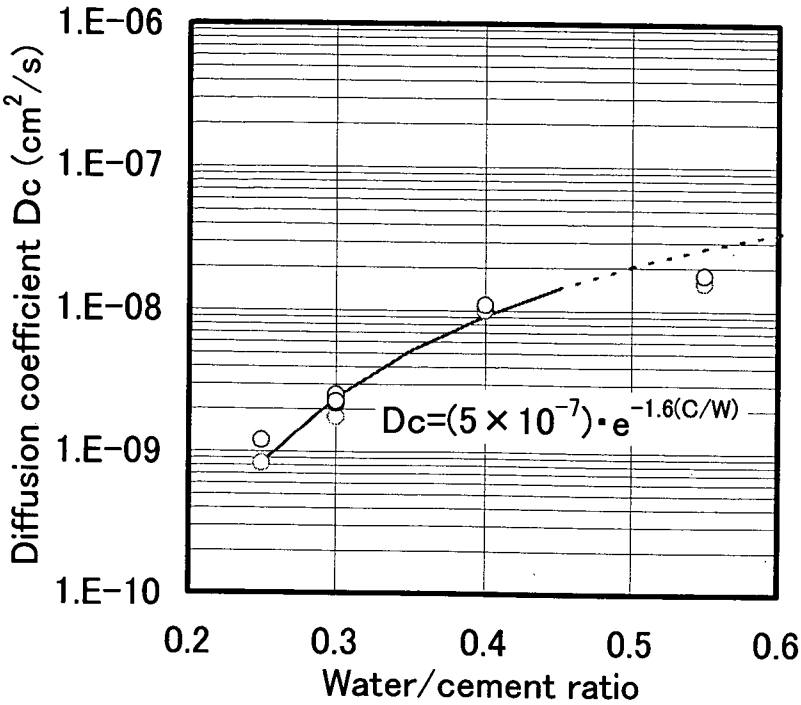

Fig. 8 Relationship between Dc and water/cement ratio

3.4 Threshold chloride level: Ccorr

In Japan, the threshold chloride level to initiate corrosion of steel in concrete is ordinarily considered to be 1.2 to 2.5 kg/m^3 of acid-soluble chloride ion. This range was initially obtained from two experimental studies[6)7)], and later investigations of existing structures agreed with the range[8)]. The corrosion of steel is hardly observed in concrete with less than 1.2 kg/m^3 of chloride ions, but corroded steel is often observed in concrete in which more than 2.5 kg/m^3 of chloride ions have permeated.

As the corrosion of rebar also depends on the supply of oxygen even in concrete, the threshold range will be influenced by cover depth, pore structure and humidity, but these factors have not been clarified yet.

3.5 Initial chloride level: Cinit

Today, the chloride ion content in fresh concrete is limited to less than 0.3 kg/m^3. According to a survey, the chloride level measured at concrete plants in some regions was less than 0.1 kg/m^3. Another survey of precast prestressed concrete plants showed that all of them could control the chloride level to under 0.1 kg/m^3.

4. Calculation of cover depth to ensure long-term durability

4.1 Parameters

The required cover depth was calculated according to above-mentioned equations (1), (2) and (3) using the following parameters:

a) C_1: 0.6 mdd for Region A and B, 0.2 for Region C
b) Ccorr: 1.2 kg/m^3
c) Cinit: 0.3 kg/m^3
d) Dc was obtained from a function of the water/cement ratio expressed in Fig. 8.
e) Water/cement ratio: 0.36, 0.43 corresponding to precast prestressed concrete and post-tensioned concrete, respectively
f) Design period: 50, 100 years

4.2 Cover depth required for design period of 50 years and calibration

The cover depth required for a design period of 50 years is shown in Figs. 9a and 9b. This result was compared with deteriorations of existing bridges in order to calibrate the calculation method.

1) Even in severe chloride environments, the minimum cover depth for post-tensioned concrete bridges was 35 mm until the *Guide Specifications* were established in 1984. Within several hundred meters from the coast in Region A and B, the cover depth of 35 mm was not enough when the water/cement ratio of concrete was 0.43 according to Fig. 9a. Also, Fig. 9b shows that the minimum cover depth of 25 mm for precast prestressed concrete bridges until then was not enough according to the results for a water/cement ratio of 0.36. These results agree with the fact that many concrete bridges deteriorated in the area in the past.

2) The calculated cover depth for the design period of 50 years almost corresponded to the current minimum cover depth in the *Guide Specifications*. This result agrees with the fact that signs of corrosion have not been frequently observed in bridges completed after 1984.

3) Bridges, which were constructed using concrete with a water/cement ratio of 0.36 more than 300 m away from the coast, required a cover depth less than the current minimum cover depth of 25 mm prescribed for precast prestressed concrete. This result agrees with the fact that the problem of corrosion of precast prestressed concrete bridges is rare in this area.

According to these results, macroscopically, the required cover depth calculated for the design period of 50 years explains why chloride induced deterioration of concrete highway bridges was frequently observed until 1984. As a result, it was confirmed that the calculation method and method of setting parameters including Cair and Co were appropriate to estimate the required cover depth.

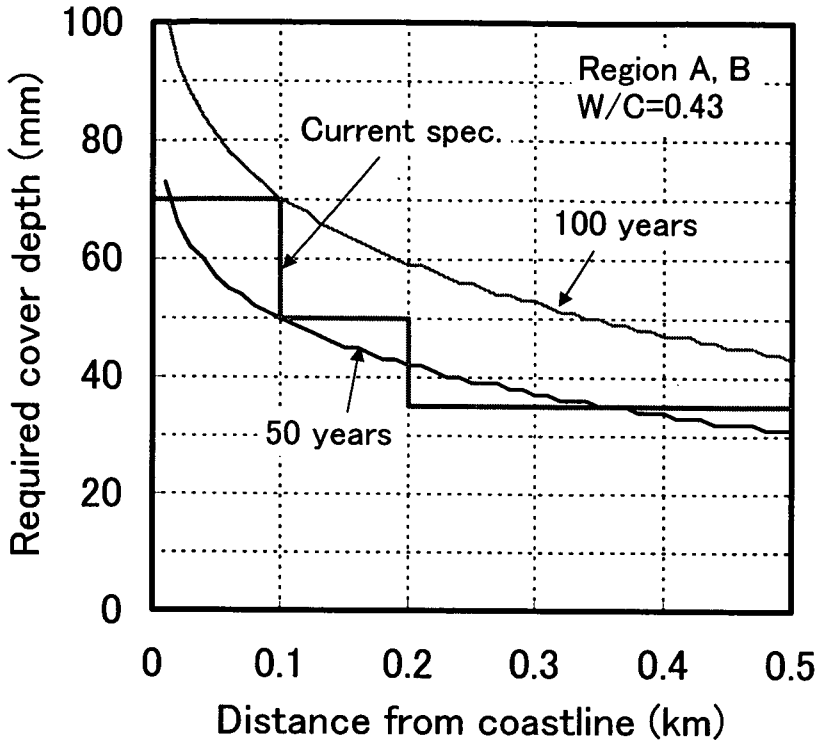

Fig. 9a Cover depth required for post-tensioned concrete with water/cement ratio of 0.43

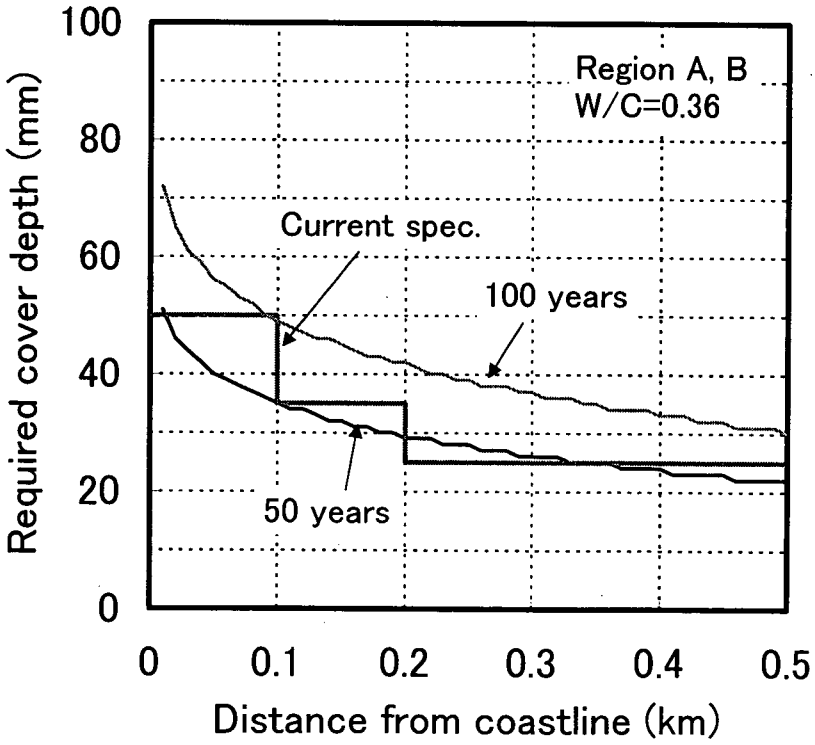

Fig. 9b Cover depth required for precast prestressed concrete with water/cement ratio of 0.36

4.3 Results for design period of 100 years

The required cover depth calculated for the design period of 100 years using this method is also shown in Figs. 9a and 9b. Although the minimum cover depth specified in the *Guide Specifications* is appropriate up to 50 years, if the design period is extended to 100 years, it is necessary to expand the area where concrete bridges need a thicker cover. Also, at several dozen meters from the coast, it is necessary either to increase the minimum cover depth to more than the *Guide Specifications* or to apply other measures. For a water/cement ratio of 0.43 and design period of 100 years, within 100 m from the coast in Region A, B and within 20 m in Region C, the current minimum cover depth of even 70 mm is not sufficient. Particularly for superstructures, it might be necessary to improve the pore structure in concrete or to apply epoxy coated rebar, because too large a cover depth increases the self weight and risk of shrinkage cracking.

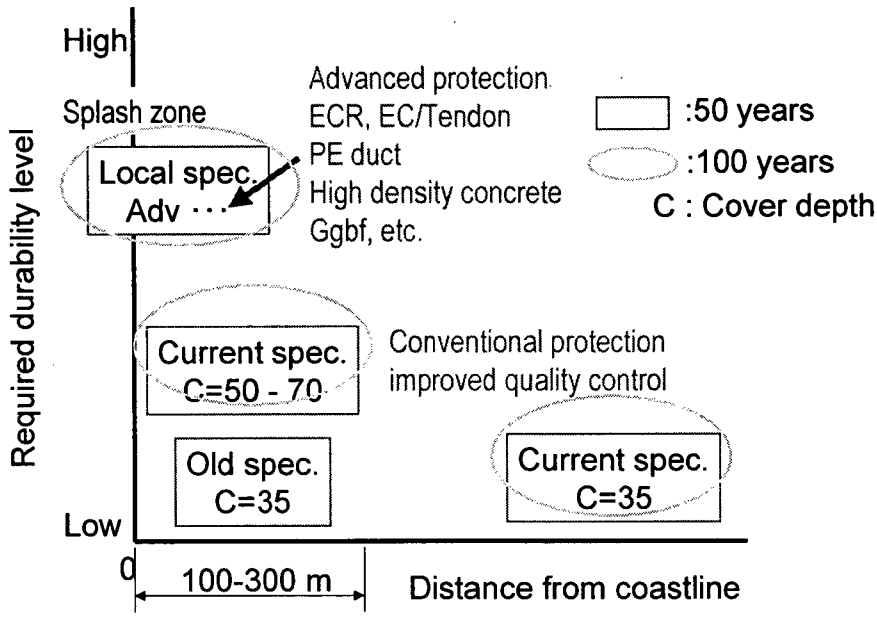

Fig. 10 Direction of corrosion protection for concrete highway bridges by design period of 100 years in chloride environment

The direction of countermeasures to achieve a design period of 100 years in a chloride environment is illustrated in Fig. 10. Some surveys on the deterioration of existing concrete structures not only in coastal areas but also inland areas showed that an unintended shortage of cover depth usually caused initiation of corrosion problems. Even some bridges designed according to the *Guide Specifications* had unintended shortages of cover depth. Therefore, quality control of cover depth is very important. Effective inspection methods using NDT must be improved.

5. Conclusions

(1) According to the method of calculating the required cover depth using measured airborne chloride data, the current minimum cover depth prescribed in the *Guide Specifications* is sufficient for the design period of 50 years. However, the minimum cover depth in the old specifications used before the *Guide Specifications* was not enough. This agrees with the fact that chloride-induced deterioration was frequently observed on concrete highway bridges built before 1984.
(2) Assuming a design period of 100 years, it is necessary to expand the area where structures should have a larger cover depth. Moreover, the results showed that the current cover depth of even 70 mm is insufficient to protect rebar and tendons from corrosion within 100 meters from the coast in Region A and B.
(3) The direction of countermeasures for concrete highway bridges to achieve a design period of 100 years in a chloride environment was illustrated based on the above results.

6. Acknowledgements

The authors thank many staff in the Ministry of Construction offices, the Hokkaido Development Bureau, the Okinawa General Bureau and all prefectural offices who assisted with the surveys for this paper.

References

1) Investigation on life cycle cost of concrete bridges – deterioration and maintenance cost of concrete bridges –, PWRI technical memorandum No.3811, March 2001
2) PWRI and the Japan prestressed concrete contractors association: Joint study on prestressed concrete bridges minimizing maintenance – Study on required cover depth for concrete highway bridges –, Joint research report of PWRI No.258, Dec. 2000
3) Ditto, – Study on corrosion protection measures for prestressed concrete bridges –, Joint research report of PWRI No.270, March 2001
4) Nationwide survey on airborne chloride, PWRI technical memorandum No.2687 & No.3811, Dec. 1988, March 1993
5) Y. Tanaka, M. Fujita, H. Kawano and H. Watanabe: Chloride permeability of high strength concrete, Proc. of JCI, 23-2, pp.517-522, July 2001
6) T. Miyagawa: Early chloride corrosion of reinforcing steel in concrete, Univ. of Kyoto, Feb. 1985
7) N. Otsuki, T. Yokoi and O. Shimozawa: The influence of chloride on the passivation film on the surface of steel bars in mortar, Proc. of JSCE, No.360, pp.111-118, Aug.

1985
8) For example, Y. Tanaka, H. Kawano, H. Watanabe and T. Kimura: Chloride-induced Deterioration and its Influence on Load Carrying Capacity of Post-tensioned Concrete Bridges, Proc. of the 16th U.S.-Japan Bridge Engineering Workshop, 2000

*All references were described in Japanese except ref. 6) & 8).

SENSITIVITY STUDY OF A CHLORIDE PENETRATION MODEL ON LIFE-CYCLE COST OF POST-TENSIONED BRIDGES

SHOICHI OGAWA, TAMIO YOSHIOKA
Research Laboratory, Oriental Construction Co., Ltd.
5, Kinugaoka, Moka-shi, Tochigi-ken, 321-4367 JAPAN

Abstruct:

The objective of this study is to simulate the chloride penetration process and its effect on LCC and to evaluate the sensitivity of predicted LCC for post-tensioned bridges in severe marine environment due to the variation of eleven parameters related to environmental conditions, concrete properties, painting performance and numerical parameters. LCC is estimated as the sum of initial construction cost and total repair/painting cost values. The life-span of bridges under consideration is extended over 100 years and repair operations and paintings are maintained during the life-span period.

1.INTRODUCTION

The corrosion of reinforcing bars in concrete due to chloride ingress is a serious problem for durability of post-tensioned bridges. In case of bridges that are located in very severe marine environment, such damage may occurs in an unexpected short time. As a result, an increase in life-cycle cost (LCC) due to the relatively higher repair and strengthening costs is expected. In order to avoid this problem, mathematical models governing the chloride penetration process are developed to simulate chloride ingress into concrete structures and evaluate the induced effect on LCC of concrete bridges.

The durability and design performance concepts encourage the use of LCC value, which is evaluated by considering the maintenance, repair, and strengthening costs. Therefore, the estimation of construction and maintenance costs is an important factor. However, the estimation of LCC necessitates an accurate prediction of the chloride ingress into structures as a function of relevant parameters that play a major role on durability of structures, such as the quality of concrete and environment-related factors. On the other hand, the simulation studies are often settled using various assumptions on parameters that may affect the phenomena under consideration. Consequently, it is very important to determine the sensitivity of the predicted solution due to the established assumptions. This may therefore lead to identify parameters that have a significant effect on durability, thus can help to design structures with acceptable LCC values.

In the present study, mathematical models governing the chloride penetration process are used to simulate the effect of chloride attack on LCC. The parameters considered in this study are environmental conditions, concrete properties, and numerical parameters. Fig.1 summarizes the various parameters considered in this study. The life-span of bridges under consideration is extended over 100 years and repair operations and paintings are maintained during the life-span period. Eleven input parameters including the factor of repair and surface painting are considered to evaluate the sensitivity of predicted solution due to these parameters. LCC is estimated as the sum of initial construction cost and total repair/painting cost values. The effect of numerical parameters, such as environmental factor e.g. temperature, chloride amount reaching to concrete surface, quality of concrete, i.e. change in diffusion coefficient, thickening of cover concrete, and initial painting on chloride penetration and how their contribution on LCC value is investigated. Furthermore, the effect of characteristics of patching materials on the reduction of LCC is highlighted.

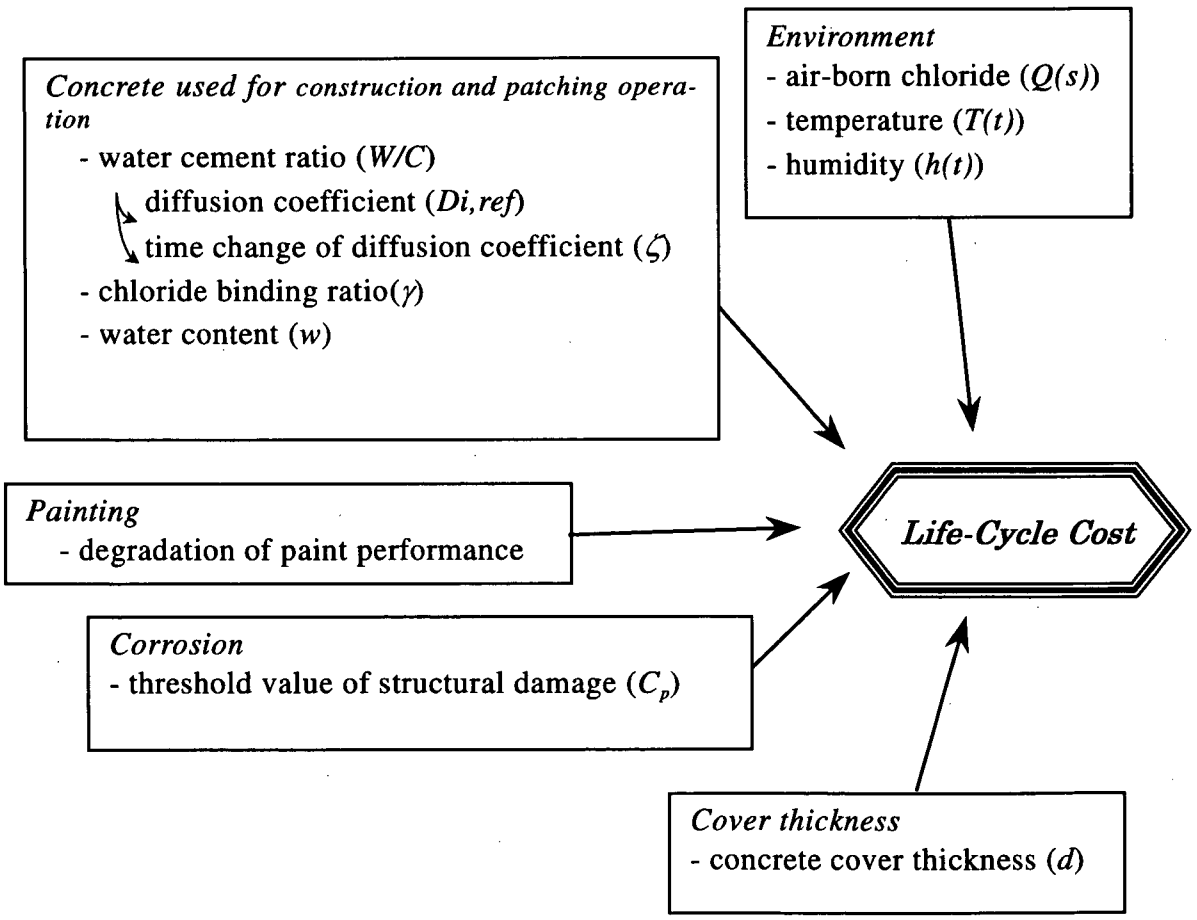

Fig.1 Parameters considered in this study

2. ANALYTICAL METHODS

2.1 Analysis of chloride penetration

This study aims to develop a numerical algorithm that can be used to predict chloride ingress into concrete. Two basic solutions are used to analyze the chloride ingress into concrete, fixing boundary conditions at surface and calculating diffusion into concrete.

2.2 Boundary conditions

Boundary conditions are fixed by assuming that only a part of air-born chloride reaching the surface of concrete can penetrate into concrete. Therefore, Langmuir's adsorption theory is used to differentiate between the amount of chloride ingress into concrete from that reaching the surface.

The air-born chloride and chloride penetrating into concrete is governed by the following relationships as proposed in reference [1]:

$$q(t,s) = \frac{3.51 \cdot m \cdot V_0 \cdot Q(s)}{V_0 + 3.51 \cdot Q(s)} \tag{1}$$

$$m = \frac{0.526(W/C) - 7.61}{57.4} \times 100 \tag{2}$$

where, V_0 is the desorption of the chloride per unit of time and is assumed to be 11.0 mg/cm^2/year, $Q(s)$ is the chloride ions reaching the surface of concrete, and m is the ratio of the saturated area at the surface of concrete. The girder is divided into two halves, the first half is located on the sea-side, and the second one is located on the land side. It is assumed that the concentration of chloride ions on the sea side is higher than that on the land side.

2.3 Paint performance

It is reported that the deterioration of paint is rapidly progressing when the performance of painting reaches for 5 to 10%. Therefore, it is assumed that chloride penetration is completely prevented just after painting and the performance of painting degrades with age. The degradation rate is by the following expression:

$$F = \left[2 - \exp(\lambda \cdot t^N)\right] \tag{3}$$

where, F is the rate of paint performance, λ and N are the characteristic values of paint material.

Since the paint layer is considered to play a role of a barrier between the air-born chloride and concrete surface, the paint performance on the chloride concentration is important. The amount of chloride provision for concrete is evaluated using the following equation:

$$Q_F(s,t) = Q(s,p) \cdot (1-F) \tag{4}$$

where, $Q_F(s,t)$ is chloride ions provision for concrete, $Q\ (s,p)$ is chloride reaching the surface of concrete after painting.

2.4 Diffusion equation

The equations developed by Saetta et al. [2] are used to evaluate the diffusion of chloride into concrete. These equations take in consideration the influence of relative humidity, temperature, and the hydration rate. The equations are given by the following expressions:

$$\frac{\partial Ct}{\partial t} = div[D_a\, grad(Ct)] \tag{5}$$

$$C_t = \alpha \cdot C_f \tag{6}$$

$$\alpha = w + (1 - w_{sat}) \cdot \gamma \tag{7}$$

$$\gamma = {C_s}/{C_f} = 0.7 \tag{8}$$

where, D_a is the apparent diffusion coefficient, and is evaluated as the ratio D_i/α (D_i is the intrinsic diffusion coefficient and α is the capacity factor), C_t is the total chloride amount, C_f is chloride concentration in water, w is the water content, w_{sat} is the void ratio, C_s is the chloride concentration in the solid volume. The diffusion coefficient D_i depends on temperature, humidity, cement hydration rate, and age. Calculation process of chloride diffusion through concrete is carried out using the following equations:

$$D_i = D_{i,rif} \cdot f_1(T) \cdot f_2(t_e) \cdot f_3(h) \tag{9}$$

$$f_1(T) = \exp\left[\frac{U}{R}\left(\frac{1}{T_0} - \frac{1}{T(t)}\right)\right] \tag{10}$$

$$f_2(t_e) = \zeta + (1-\zeta) \cdot \left(\frac{28}{t_e}\right)^{1/2} \tag{11}$$

$$f_3(h) = \left[1 + \left\{\frac{1-h(t)}{1-h_c}\right\}^4\right]^{-1} \tag{12}$$

where, $D_{i,ref}$ represents the reference value of the intrinsic diffusion coefficient, U/R is fixed at 3000degK, T_0=296degK, $T(t)$ is the temperature, ζ is a constant depending on type of concrete, t_e is equivalent maturation time in days, $h(t)$ is the relative humidity, h_c is the critical relative humidity and is fixed at 75%.

$D_{i,ref}$ values is decided by the relationship between the W/C and diffusion coeffi-

cient, and is expressed by the following equation [3]:

$$D_{i,rif} = \{0.32\exp[5.47(W/C)]\} \tag{13}$$

The mean monthly value for temperature $T(t)$ and relative humidity $h(t)$ are used. The relative humidity in concrete is determined using the humidity diffusion in concrete. The relative humidity in concrete is evaluated using the equation described in reference [2]. The equation is given by the following expression:

$$h(t,d) = h_0(t) + [h_{ini} - h_0(t)] \cdot \left[1 - \exp\left(-\frac{d}{d_0}\right)\right] \tag{14}$$

where, $h(t,d)$ is the relative humidity evaluated at time t and a distance d from the surface, $h_0(t)$ represents environmental relative humidity, d_0 is fixed at 5cm, h_{ini} is the initial humidity and is assumed to be 90%.

2.5 Comparison between analytical diffusion models and existing bridges

The accuracy of the analytical models is evaluated by comparing predicted values and those obtained from existing structures under real environments or measured on specimens exposed to marine environments and tested for chloride ingress. Data for existing structures and exposed specimens are summarized in Table 1. The chloride ions reaching the concrete surface are assumed as to be 20mg/cm^2/year at the sea side and one third at the land side.

Fig.2 shows comparison between predicted and measured values. The broad lines represent the analytical results. It can be said that the proposed diffusion models can accurately simulate the measured values in existing structures and exposed specimens.

Table 1 Data for existing structures and exposed specimens

Example	Literature	Structure	Age(year)	W/C(%)	Location
a	[4]	Pre-tensioned T-section bridge	10,25	40	Kanazawa
b	[5]	Post-tensioned T-section bridge	12	43	Sakata
c	[6]	Post-tensioned I-section bridge	17,27	43	Sakata
d	[7]	Post-tensioned T-section bridge	27	40	Sakata
e	[8]	Exposed specimen	10	40,50	Hamamatu
f	[9]	Exposed specimen	7	45-65	Kanazawa

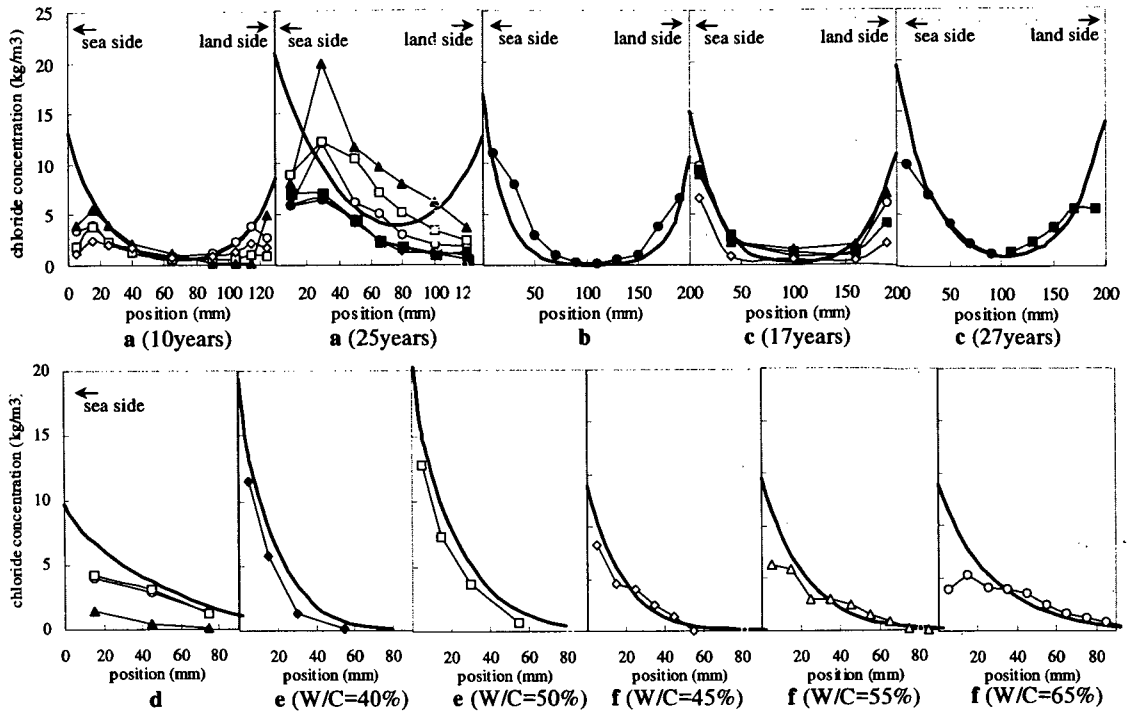

Fig.2 Comparison between predicted and measured values

3. MODEL STRUCTURE AND REPAIR/PAINTING

3.1 Model bride

The concrete bridge model, considered in this study, consists of two span post-tensioned T-section girders. Each span has 33 m in length, while the bridge length has about 68 m and a width has 15.8 m.

3.2 Repair and painting schedule

In the present study, repair and painting is used during construction. All surfaces of girders are painted except for the top and side surfaces of the upper flange.

Repair work consists of the removal of the cover concrete, cleaning of the reinforcing bars, and section patching with new concrete material. Section patching is schematically shown in Fig.3. It is reported that the concrete behind the outermost re-bars should be sufficiently removed to take out highly contaminated concrete by chloride [10,11]. In this study the concrete is re-

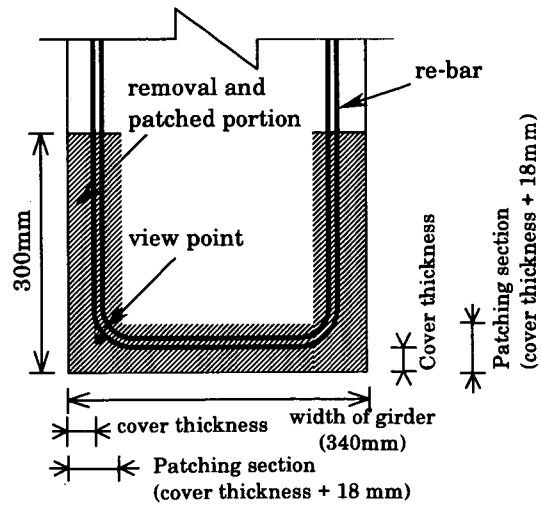

Fig.3 Section patched

moved up to 5mm behind the outermost re-bars.

Re-bar corrosion is normally observed at the corner of the lower part of the girder because of chloride ingress from both sides and bottom surfaces. Therefore, chloride concentration is investigated only at the "view point" shown in Fig.3. It is assumed that re-bar corrosion and structural damage develop when chloride concentration reaches the threshold value "C_p" by weight of cement %[12]. Repair works are repeated whenever chloride concentration reaches the threshold value. The required repair and painting are repeated until the age of 100 years. The bridge reaches the life-span when the chloride concentration first reaches the threshold value after 100 years.

4. PARAMETERS INVESTIGATED

The objective of this study is to evaluate the sensitivity of predicted LCC due to the variation of parameters related to environment, concrete properties and paint performance. The parameter values considered in this investigation are summarized in Table 2.

Table 2 Various parameters and thier values considered in the sensitive study

Subject	Parameter	Range*1
Environment	$Q(s)$ (mg/cm²/year)	1, 5, **20**, 100
	$T(t)$	7.4(Hokkaido), **13.2**(Niigata), 22.4(Okinawa) *2
	$h(t)$	65, 70, **73**(Niigata) *3, 80
Concrete	W/C (%)	30, 35, **40**, 45
	d (mm)	30, 35, **40**, 45, 50
	γ	0.6, **0.7**, 0.8
	ζ	0.5, **0.7**, 1.0
	w_{sat}	**7**
	w	3, **5**, 7
Concrete cover	d (mm)	30, 35, **40**, 45, 50
painting	λ	5.88×10^{-4}(A), 7.34×10^{-5}(B), 2.18×10^{-5} (C)
Corrosion	C_p (% by cement weight)	0.5, 0.75, **1.0**, 1.25

*1:parameter of base case are shown in bold character
*2:expressed as average (location)
*3:constant value is used except humidity of Niigata

Since life cycle cost is affected by various parameters such as environmental condition and material properties, their effects should be considered. The following eleven parameters were then investigated.

The parameter $Q(s)$ is the air-born chloride amount that reaches to concrete surface. The parameter $Q(s)$ is assumed to be constant during life-span. If painting operation has been done, this parameter is influenced by the paint degradation rate of paint performance degraded with age. The temperature $T(t)$ that affect the diffusion coefficient in steady state is taken as mean monthly value. Three cases of typical marine environment area in Japan are considered. Relative

humidity $h(t)$ obtained in Niigata area (Japan) is used as parameter for the base case. For sensitivity analysis, the value of $h(t)$ is assumed to take a value ranging between 65 and 80 %. Environmental humidity affects the relative humidity in concrete, which is determined using the humidity diffusion equation which is affected by diffusivity of chloride penetration.

Since concrete is used for construction and patching operations, parameters that are related to concrete properties are investigated respectively. The effect of water cement ratio ranging between 30 and 45 % by step of 5% is investigated. The water cement ratio affects the diffusion coefficient in steady state ($D_{i,ref}$) and the coefficient ζ which measures how much the diffusivity decreases with time. Diffusion coefficient in steady state ($D_{i,ref}$) is decided by the equation describing the relation between the W/C and diffusion coefficient (Eq.(13)), determined by electrical potential technique using saturated concrete specimens under a constant temperature[3]. The coefficient ζ is supposed to be effected by W/C and type of cement, because the hydration rate modify the concrete porosity. Therefore, the coefficient ζ is varied from 0.5 to 1.0. Evaporable water content w_{sat} and effective water content w, as shown in Eq.(7), affect the chloride concentration in solid or liquid phase with binding ratio γ. The parameter γ is the binding ratio of C_s (chloride concentration in solid) to C_f (chloride concentration in liquid), and is varied from 0.6 to 0.8. The value of each parameter γ, ζ, w_{sat} and w for patching concrete is tha same as for construction concrete.

Concrete cover thickness d is supposed to be an important factor in decreasing the chloride concentration at re-bar, therefore the value of d is varied from 30 to 50 mm with 5 mm step.

The paint material, employed at construction and repair operation, is assumed to have three types of performance levels, named A, B and C, resulting in different values of λ which affect the paint performance F. All of painting parameters N are assumed to be 3. The paint performance is assumed to be degraded at a rate of 20% after 10, 20 or 30 years of age, as 5.88 x 10^{-4}, 7.34 x 10^{-5} or 2.18 x 10^{-5}, respectively. The rate of paint performance in the present study is shown in Fig.4. In the present study, painting every 10, 20 or 30 years in case of use A, B or C respectively, are repeated considering the degradation process of paint performance. However, if repair work is expected 10 years after painting, painting is suspended till the

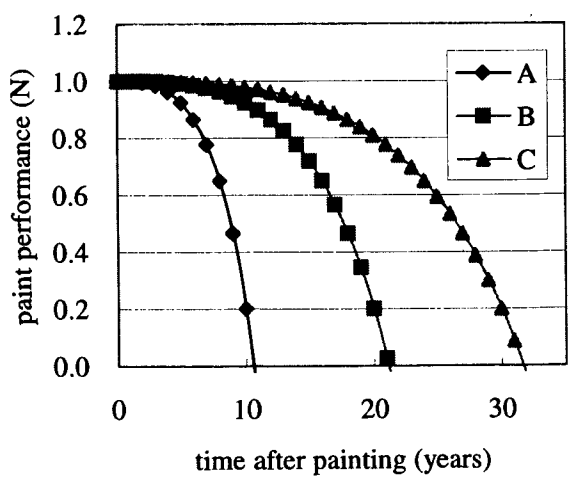

Fig.4 Degradation of paint performance with age

next repair.

Threshold value of the parameter C_p, which represents the corrosion is the value of re-bar corrosion and structural damage developed, and is assumed to be as a percentage by cement weight. If chloride concentration value reaches this value, the repair operation is then required.

5. COST ESTIMATION

The ICC value of the non-protected girder is estimated using data obtained on existing bridges. The other values of repair and painting cost are modified considering different mix proportions of concrete and painting performance considering material costs. ICC, repair and painting costs used for base case is summarized in Table 3 as the ratio of ICC. Repair costs are estimated by considering the concrete cover thickness because it is assumed that 5 mm of the old concrete behind the outermost re-bars should be removed. Repair and painting costs include the cost to remove old paint layers when the girder is previously painted. LCC is estimated as the sum of ICC, repair and painting costs.

Table 3 Costs as the ratio of ICC used for base case

		cost
ICC	not painted	1.000
	initially painted	1.178
Repair (with painting)	non-painting before	1.114
	existence old paint layer	1.255
Painting		0.426

6. RESULTS AND DISCUSSIONS

Chloride concentration for the base case is shown in Fig.5. Chloride concentration at "view point" reaches the threshold value of structural damage, just 14 years after construction. hence required first repair operation. After the first repair operation, the increase in chloride concentration is limited by painting with repair, and second painting due to the degradation of paint performance and second repair are required. Due to repair and painting operation, the life-span can be extended and the bridge is maintained more than 100 years. As a result, repairs and painting are required two and three times, respectively, and the life-spans of base case was 120 years.

The calculated initial construction cost (ICC), total repair/painting cost and LCC on base case, as a normalized value to ICC is shown in Fig.6. It can be seen that the LCC

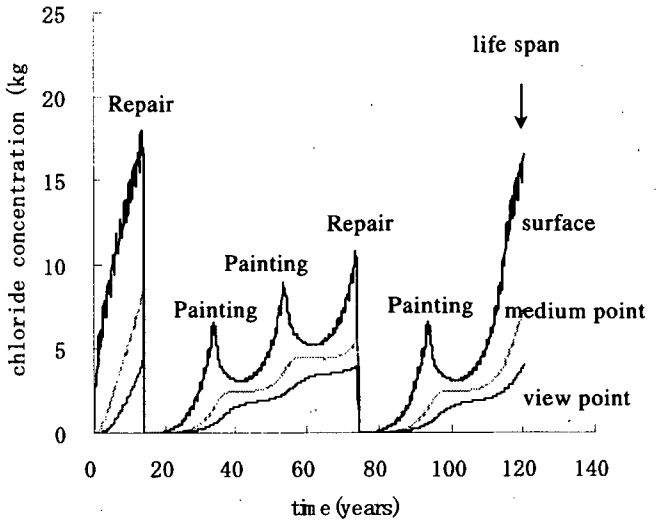

Fig.5 Time dependence of chloride penetration on base case

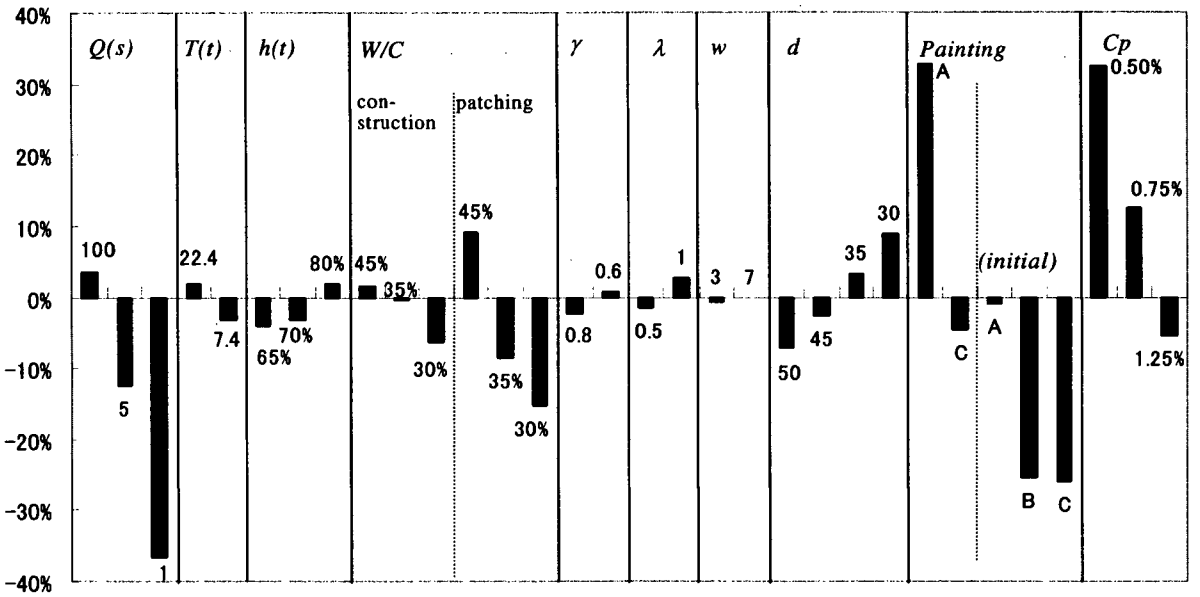

Fig.7 Change in predicted LCC values

of base case is more than five times higher than ICC. It can be observed that for severe marine environments, ICC represent only a small part of LCC.

It is considered that the dependence of life-spans on investigated parameters is different from base case, because life-span is taken when the chloride concentration reaches to threshold value of structural damage. Therefore, in sensitivity study, LCCs are estimated by dividing each of life-spans and they are shown as ratios on base case. The results of estimated LCC value, presented as percent-

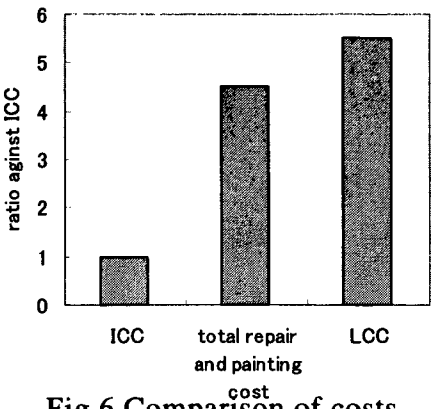

Fig.6 Comparison of costs on base case

age from base case, and their dependence on investigated parameters are shown in Fig.7.

6.1 Sensitivity to environment

Difference of air-born chloride "*Q(s)*" that reaches the concrete surface is most effective on LCC value. For example, if bridges located in an environment having smaller air-born chloride such as that far from sea side, LCC is considerably reduced, and if bridges are located in severe marine environments rather than investigated base case, increasing of LCC is not so increased compared with base case.

Temperature and humidity have low effect on LCC value. Under the high temperature or high humidity environment, diffusivity of chloride ion is increased by increasing diffusion coefficient, although the chloride concentration at re-bar is not increasing so much. It is said that concrete structure located in hot marine environment, for example on environment similar to Okinawa area (JAPAN), the structural damage is occurred more rapidly. As a one reason of the difference observed between analytical model and existing structure, the effect of corrosion development which is not considered in the analytical models may be important. Therefore, further investigation would be necessary.

6.2 Sensitivity to concrete properties

The effect of water cement ratio of concrete used for patching concrete is more important than that of concrete for initial construction. Chloride concentrations at "view point" are shown in Fig.8. After the chloride concentration at view point reaches to threshold value C_p of each case, first repair is carried. Decreasing the W/C of initial construction concrete decreases the chloride concentration at "view point", and delay the first operation from 10 to 26 years. Although, after repair operation, chloride ingress into concrete and threshold value are mainly depended on the propertied of patching concrete. Therefore, the use of patching concrete with similar properties did not effect the chloride concentration at "view point" after repair. As a result, the estimated LCC value is only affected by the

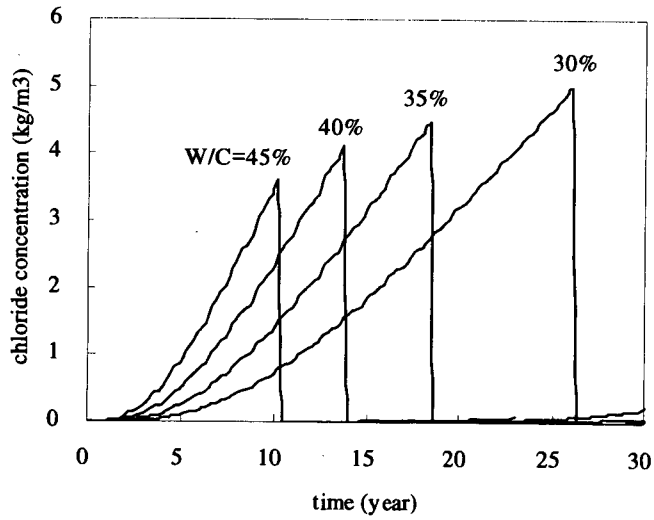

Fig.8 Chloride concentration of different W/C of initially concrete at view point.

difference between the period of first repair operation.

The change in W/C of the patching concrete affects the LCC value by -15 to +10%. This result indicates that LCC is dependent on the characteristics of the patching materials. Innovative patching materials with a small diffusion coefficient contribute to decrease LCC.

The others parameters, γ, λ and w did not significantly effect LCC value.

6.3 Sensitivity to cover thickness

The effect of concrete cover thickness on LCC is not significantly changed, compared with the change due to the W/C of patching concrete. It is considered that the increase of concrete cover thickness increases the patching volume, hence increase the repair cost, and small effect on LCC.

ICC of different concrete cover thickness is shown in Fig.9. The effect of concrete cover on ICC is less than 1.5%. Therefore increasing of the concrete cover thickness may be a profitable method.

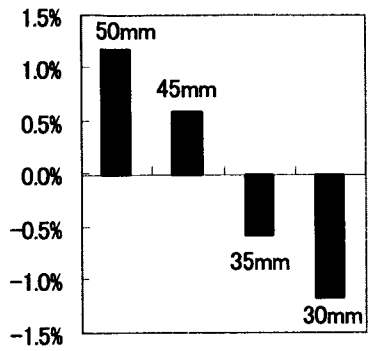

Fig.9 Comparison of ICC on different cover thickness

6.4 Sensitivity to paint performance

In this study, three different performance levels of paint material are assumed for the initial construction and for repair operations, including just painting operation due to the degradation of painting system. The use of paint type A, which is a lower grade and of course lower cost material, increases the LCC up to 30%. From this result, it can be stated that LCC is affected by paint performance, and the use of low paint performance may increase LCC value. On the other side, the use of type B and C for initial painting operations results in a drastic decrease in LCC. Although, the difference of type B and C on LCC is small.

In the present study, painting costs are increased with paint performance. Painting plays a role of a barrier between the air-born chloride and concrete surface, thus preventing chloride ingress into concrete. Increasing of painting grade which results in increasing painting costs did not decrease LCC value. From these results, it is important to use high grade paint performance for concrete painting. In order to minimize LCC value, it is important to consider the trade off between painting performance and its cost.

6.5 Sensitivity to threshold value

In the present study, the threshold value of structural damage "C_p" is assumed to be 1.0% by weight of cement, on base case. The other hand, C_p is varied from 0.5 to 1.25% to determine its effect on LCC. The change in C_p significantly affects the value of LCC. It is considered that the value of structural damage is affected by C_p, and also af-

fected by the development rate of corrosion and tensile strength of concrete to resist the expansion induced by corrosion. Furthermore, development of corrosion is affected by the oxygen or water supply. Therefore, it is important to choose a suitable value in order to ensure an accurate estimation of LCC.

7. CONCLUSIONS

Based on the results presented in this paper and dealing with the life-cycle cost (LCC), the following conclusion can be pointed out:

1. ICC represents only a small part of LCC in case of sever marine environments. The amount of air-born chloride that reaches the concrete surface is shown to be the most important parameter affecting LCC.
2. The effect of water-cement ratio of concrete used as patching concrete is more important than that of concrete used as initial construction. Innovative patching materials with a small diffusion coefficient contribute to decrease LCC.
3. Compared with the effect due to the change in W/C of patching concrete, the effect of concrete cover thickness did not have a significant effect on. Indeed, the effect of concrete cover thickness on ICC is less than 1.5%. Therefore, the increase of the concrete cover thickness may be a profitable and cost-effective method.
4. The use of a lower grade and lower cost painting material for repair increases the LCC up to 30%. On the other hand, the use of high grade painting for initial construction results in a drastic decrease in LCC. In order to minimize LCC value, it is therefore important to consider the trade off between painting performance and its cost.
5. The change in the threshold value of structural damage significantly affects the value of LCC. It is important to choose a suitable value in order to ensure an accurate estimation of LCC.

REFERENCES:

[1]Yamada, Y., Oshiro, T. and Masuda, Y. : Analytical study on chloride penetration into concrete exposed to salt-laden environment. *J. Struct.Constr. Eng., AIJ*, No.501, pp.13-18, Jul., 1997 (Japanese)

[2]Saetta, A.V., Scotta, R.V. and Vitaliani, R.V. : Analysis of chloride diffusion into partially saturated concrete. *ACI Materials Journal*, Vol.90, No.5, Sep-Oct, pp.441-451, 1993

[3]Sugiyama, T., Tsuji, Y., Bremner, T. W. and Hashimoto, C. : Determination of chloride diffusion coefficient of high-performance concrete by electrical potential technique, *Performance of Concrete in Marine Environment*, Spec. Publ. American Concrete Institute SP-163, pp.339-354, 1996

[4]Kanaumi, Fujiwara, Tabiguchi, Ishimura : Damage investigation of PCT girder bridge exposed to chloride attacks for 25 years, Proceedings on rehabilitation of concrete structures,pp.55-60, 1998.10 (Japanese)

[5]The ministry of construction : Cathodic protection for Shin-isuzu bridge, The technical report on measures for chloride damaged bridges in Atsumi region, pp.57-89, 1998.10 (Japanese)

[6]Matsuda, Y., Ishibashi, T., Toyooka, A. and Amaki, G. : Repair performance of prestressed concrete bridge damaged due to salt attack, *Proceeding of the Japan Concrete Institute*, Vol.21, No.2, pp.1015-1020, 1999 (Japanese)

[7]Ishimura, K., Yamaguchi, M., Watanabe, H. and Hosaki, T. : Repairing and retrofitting of prestressed T-girders damaged by salt-induced corrosion, *Concrete Journal*, Vol.38, No.7, pp.34-40, Jul., 2000 (Japanese)

[8]Public Works Research Institute of the ministry of construction, Prestressed Concrete Contractors Association : Report on technology to improve the durability of marine structures(Corrosion protection for marine structures in the splash zones), 1995.12 (Japanese)

[9]Sasatani, T., Torii, K., Mitsunori, K. and Kajikawa, Y. : Chloride ion penetration into the concretes exposed to a marine environment for a long period, *Proceeding of the Japan Concrete Institute*, Vol.18, No.1, pp.957-962, 1996 (Japanese)

[10]Ohama, Y. et.al. : Properties of chloride ion diffusion in polymer cement mortar and concrete, *CAJ Review of the 40th General Meeting/Technical session*, Vol.40, pp.87-90, 1986 (Japanese)

[11]Shoto, K., Kamihigashi, Y., Nojima, S. and Yoshida, A. : Rehabilitation methods for concrete structure, *Highway Technology*, No.17, pp.33-43, Oct., 2000 (Japanese)

[12]Unisuga, Y., Masuda, Y., Jitousono, H. and Fujii, K. : Repair system for reinforced concrete structure damaged by chloride corrosion, *Proceeding of the Japan Concrete Institute*, Vol.19, No.1, pp.1165-1170, 1997 (Japanese)

[13]Bentur, A., Diamond, S. and Berke, N.S. : *Steel Corrosion in Concrete*, E & FN Spon, London, 1997

PERFORMANCE OF ELECTROCHEMICAL CHLORIDE EXTRACTION TECHNOLOGY FOR CONCRETE BRIDGE MEMBERS REHABILITATION AND ONGOING LABORATORY RESEARCH

Gerardo G. Clemeña,[1] Stephen Sharp,[2] and Y. Paul Virmani[3]

Abstract

The SHRP studies in the early 1990s had rekindled interest on electrochemical chloride extraction (ECE) as a new option for mitigation of reinforcing steel corrosion in concrete bridges. The following discussed some of the practical questions that need to be addressed.

Introduction

Once intrusion of either chloride and/or carbon dioxide begins to cause corrosion of the reinforcing bars in a concrete bridge, truly effective rehabilitation of the structure would require the application of an electrochemical countermeasure: either cathodic protection (CP) or the emerging technique of electrochemical chloride extraction (ECE).[1] The approaches by which these two techniques mitigate steel bar corrosion differ essentially on the amount of direct current applied on a concrete structure and the application duration. Preferably applied when damage to the concrete is still minimal, ECE uses current that is 100 times that typically used in CP, and the treatment period is typically 6 to 10 weeks.

ECE is intended as a short-term treatment for restoring the original protective environment in the concrete. It is based on the simple principle of opposite charges attract and like charges repel. When a direct current is applied between a temporary anode installed on the surface of the structure and the steel bars, which then acts as the cathode, the resulting electric field causes the mobile ions (such as Cl^-, OH^-, Na^+, K^+, Ca^{+2}, etc.) in the concrete to migrate—each ion moving toward the electrode with the charge opposite to its own. Accordingly, the undesirable negatively-charged Cl^- migrates away from the steel bars and toward the anode outside the structure. This results into removal of a large amount of Cl^- completely from the structure, while the remaining Cl^- is moved away from the steel bars.

In addition to removing large portion of the Cl^-, some beneficial chemical reactions also occurred around the steel during the current treatment. These reactions are:

$$O_2 + 2\,H_2O + 4\,e^- \rightarrow 4\,OH^- \qquad (1)$$

$$H_2O + e^- \rightarrow H_o + OH^- \qquad (2)$$

Within a certain extent, the generation of OH^- is beneficial because it increases the alkalinity or pH of the concrete and restores its original protective environment. Thus, for this purpose, ECE

[1] Principal Research Scientist, Virginia Transportation Research Council, Charlottesville, Virginia, U.S.A.
[2] Doctoral Candidate, University of Virginia, Charlottesville, Virginia, U.S.A..
[3] Program Manager, Office of Infrastructure R&D, Federal Highway Administration, McLean, Virginia, U.S.A.

is also called realkalization. The simultaneous reduction of [Cl^-] and increase of [OH^-] around the steel bars reduces the [Cl^-]/[OH^-] ratio, which is a parameter that has been suggested to have more influence on the condition of the steel bars than [Cl^-] alone.[2] According to Pettersson, the amount of chloride that can be tolerated in the concrete, before the initiation of steel corrosion, may actually be 2.5 to 6 times the hydroxide concentration in the concrete.[2] This means that after ECE treatment, the steel may be able to tolerate more chloride ions in the concrete than before.

Another benefit is the steel bars become so cathodically polarized during the treatment that the steel remains in that state for a long time. It should be mentioned that, while the above reactions occur at the cathode, other reactions also occur at the anode:

$$2\,H_2O \rightarrow 4\,e^- + O_2 + 4\,H^+ \qquad (3)$$

$$2\,Cl^- \rightarrow 2\,e^- + Cl_2 \qquad (4)$$

$$H_2O + Cl_2 \rightarrow HCl + HClO \qquad (5)$$

Because some of these reactions produce acid, it is necessary to keep the electrolyte fresh or neutralized to avoid etching of the concrete.

Background

The concept of removing chloride ions from concrete by electrochemical migration was borne in 1973 out of Kansas Department of Transportation (KDOT) experiments on electro-stabilization of clayey soils. Its feasibility was independently confirmed in 1976 by KDOT and Battelle Columbus Laboratories.[3,4] Unfortunately, the unnecessarily high levels of direct current used in those early studies led to some undesirable effects—such as increased permeability, cracking, and decreased concrete-to-steel bond—that were observed in the concrete. These problems reduced interest in ECE until the completion in 1993 of ECE studies under the U.S. Strategic Highway Research Program (SHRP) and the development of a commercial method, Norcure™, to facilitate treatment of vertical concrete surfaces.[5]

The SHRP studies yielded some reassuring findings.[6-8] Most important among these are: (1) if the applied current is maintained at less than 5A/m^2 (500 mA/ft^2), the treatment should have no significant adverse effects on the concrete, (2) the treatments had removed 20 to 50 percent of the admixed chloride in the test concrete slabs and redistributed the remaining chloride well away from the steel bars, and (3) there is a possibility of exacerbating alkali-silica reaction (ASR) if sensitive aggregates are present; however, such possibility can be eliminated by the use of lithium ions in the electrolyte. More important to the implementation of this new rehabilitation method by state and local highway agencies in U.S. was the development of a set of guidelines, which included criteria for the selection of candidate structures, treatment systems, and electrolytes, and the operational parameters to use.[9] For the latter, the guidelines recommended passing a total charge of 600 to 1500 A-hr/m^2 (60 to 150 A-hr/ft^2) of concrete surface to be treated, at a treatment current of 1.0 to 5.0 A/m^2 (100 to 500 mA/ft^2).

These developments have rekindled interest in the use of ECE, because the method offers a major advantage over CP: once a structure is treated, there is no need for any long term regular maintenance of electrical components (such as wirings, embedded reference electrodes and anode, rectifier, and monitoring devices). However, some questions still remain, including: (1) can ECE be applied to full-sized concrete bridge members of different geometry or shapes? (2) is it possible to predict how much of the chloride present in a candidate structure will be removed

by the treatment? (3) can the efficiency of ECE treatments be improved? (4) is there a reliable means for determining the most optimum treatment time for a candidate structure, prior to the treatment? (5) how long do the benefits of a treatment last? The following discussions deal with some of these questions.

Performance of ECE in Recent Applications

Between 1995 and 1999, there were numerous applications of ECE on full-sized concrete members conducted in North America, Europe, and Japan. Those with reported data are listed in Table 1 together with experiments involving concrete specimens. Figures 1 and 2 show the treatment of some bridge deck spans and piers, respectively, in Virginia.[10] Table 1 shows that only four of these reported applications involved bridge and parking decks. In numbers, this is considerably less than the reported number of applications involving other types of concrete members, such as piers, walls, etc. However, in terms of total treated area, there appeared to be more deck areas treated. Based on the number of all the known applications listed, there is no doubt that it is feasible to conduct ECE treatment on different full-sized concrete bridge members, even though some types may present more difficulties than others.

Extent of Chloride Removal Achieved

The amount of chloride that can be removed from a structure can vary from one area to another, and is influenced by the local initial chloride content in the concrete and the intensity of the electric field. The former is, in turn, influenced by the variability in the local concrete permeability; while the latter is, in turn, dependent on factors such as local concrete cover, depth in the concrete (or distance from the anode), distance from the nearest bars, density of bars, etc. Therefore, it is to be expected that: (1) the amount of chloride that is finally removed from any point in a concrete structure will differ from that at another point, and (2) as a whole, the amounts of chloride removed across a structure should follow some form of statistical distribution. By the same token, it is to be expected that the amount of chloride that can be removed would differ from one structure to another.

Table 1 also shows the reported data on the amounts of chloride removal achieved in the different treatments. It must be emphasized that since corresponding data on the depths of the concrete sampled for the necessary chloride analyses were not given in all cases, only semi-qualitative statements can be made. Table 1 shows that, as to be expected, the amount of chloride removed varies from a structure to another. Collectively, ECE appeared to remove from 13 to 96% of the chloride present in the top 38-mm layer of concrete, and only 2 to 71% beyond that depth. This difference is perhaps not of any significance and is due probably more to the fact that the chloride content in a structure decreases with increasing depth than any other factor. The influence of depth is clearly shown in the data from Nebraska and Virginia treatments.

Between 50 to 82% of chloride were removed from the decks treated; while for the latter types of concrete members, the chloride removed ranged from 13 to 94%. There appeared to be more consistency in the results achieved in treating decks than in treating the other concrete members. This difference perhaps is more an indication that it is relatively easier to perform the treatment on decks, where practically all surfaces are horizontal, than on the other members, where the surfaces are mostly vertical—at least with the present treatment systems. The

complexity of the geometry of the piers would also influence the overall results. This is demonstrated by the relatively low extraction results in the treatment of the Virginia piers, each of which included a square cap and three cylindrical columns (Figure 2).

The results in Table 1, as a whole, show clearly that it is probably never possible to remove all the chloride from a concrete structure. This may be explained by the suggestion that when external chloride diffused into a concrete, some of these free chloride ions become physically bound to the cement paste and an equilibrium between the free and bound chloride ions is established, i.e.,.[19]

$$(Cl^-)_{free} \leftrightarrow (Cl^-)_{bound} \qquad (6)$$

Some research suggests that the removal of bound chlorides is slower than that of free chloride.[20]

Efficiency of ECE treatment

When a direct current is passed through a concrete, part of that electrical energy is dissipated as heat and the remainder contributes to the migration of free ions (K^+, Na^+, Ca^{+2}, Cl^-, OH^-, SO_4^{-2}, etc.) present in the pore solution of the concrete. Since migration of ions in concrete is basically governed by the same laws as in aqueous solutions, it is influenced by such fundamental parameters as electrical field, the ion mobility (μ_i), concentration (C_i), and number of charges carried $|\Sigma_i|$ of the ions i. Thus, the portion of the total current (I_{total}) that the chloride ions (I_{Cl-}) will carry is proportional to its concentration and mobility:

$$t_{Cl^-} = \frac{I_{Cl^-}}{I_{total}} = \frac{\mu_{Cl^-} \cdot |Z_{Cl^-}| \cdot C_{Cl^-}}{\sum_i \mu_i \cdot |Z_i| \cdot C_i} = \frac{F \cdot W_{Cl^-}}{35.45 \cdot I_{total} \cdot t} \qquad (7)$$

where t_{Cl^-} is the transference number of chloride ions in the migration process and is also the efficiency of their removal, W_{Cl^-} is the amount (in grams) of chloride removed, F is the Faraday constant, and t is the treatment time. According to this relationship, at any moment during a treatment, the efficiency of chloride removal decreases with decreased chloride concentration in the concrete and with increased concentrations of the other ions commonly found in the pore solution.

During the early stage of a treatment, the major competitor of Cl^- in the migration is the OH^- already in the concrete, since these ions have a mobility that is at least 2.5 times faster than Cl^-. As the treatment progresses and more OH^- ions are formed on the steel surface (through reactions 1 and 2), this competition from the OH^- ions becomes even stronger so that these ions become the major carriers of the current. Recent data obtained by Tritthart, when plotted as in Figure 3, do verify that the concentration of OH^- increases as a result of ECE. This implies that, as the treatment progresses, the efficiency of chloride removal decreases. This is clearly indicated in some data (Figure 4) obtained in the SHRP laboratory study, which showed a high efficiency of approximately 60% at the beginning of the treatment of some slabs and then decreasing exponentially to approximately 7 to 9% after 2500 A-hr/m^2 was passed through the slabs.[6] Such trend has also been reported by Vennesland et al., who observed a current efficiency of about 11-13% during the first four weeks of treatment of some concrete specimens admixed with chloride and then decreasing to 7% after 8 weeks.[17] Incidentally, based on the data in Figure 2, the SHRP guidelines recommended that for typical concrete a charge of 600 to 1500 A-hr/m^2 would suffice.[9]

Table 1 shows that there is probably no significant difference between the efficiencies obtained for the different types of concrete members; if any, those for the piers, walls, etc., may be slightly lower. In fact, the tests conducted on concrete slabs and specimens in laboratories, where conditions could be better controlled, did not result in better efficiencies: 7 to 13% for a Norway study[17] and 10 to 20% for the SHRP laboratory study.[6] From the results of these reported treatments, it is reasonable to expect that the overall efficiency of an ECE treatment to be between 7 to 20%, with a conservative average of probably 14% using the present systems and if a way is found to significantly reduce the competing effect of the OH^- being produced at the cathode.

Ongoing Research

Change in Treatment Current During treatment

Another phenomenon that typically occurs during a treatment that limits the overall amount of chloride removed is the exponential decay of the amount of current that can be passed through the concrete, at a given voltage (Figure 5). In this example, the current decreased precipitously within the first 25 to 30 days, by approximately 53 to 71% from one pier to another. Since the amount of chloride migrating toward the anode is dependent on the amount of current passing through the concrete, this means the amount of chloride being removed decreases as the treatment progresses—as illustrated in Figure 6 by data presented recently by Vennesland et al.[17] This data shows the same exponential decay within the first 25 to 30 days. For this particular concrete, it would appeare that the treatment may be terminated after 4 weeks.

This phenomenon is essentially due to a rapid increase in the overall circuit resistance during this early stage of a treatment. However, the cause of this increase in resistance, likely between the anode system on the surface of the concrete and the network of reinforcing steel in the structure, has not been investigated. The benefit of being able to determine what causes this rapid increase in resistance and finding a means to counter this is obvious. For this purpose, some concrete specimens were designed in such a manner as to allow for measurement of the resistances at different layers of a treatment system (Figure 7). This arrangement allows for the measurement of the resistances of : (1) the top layer of concrete in each specimen, (2) the middle layer of concrete (i.e., between the rows of rods), and the thin (10-mm) layer of concrete between the bottom rods and the rebar.

Figure 8 shows the typical results obtained when these specimens were subjected to ECE treatment. Interestingly, the data reveals that the resistance of the top layer of concrete increased at a rapid rate (by approximately 350%) during the first 12 to 15 days and then at considerably lower rate, if any, thereafter. In contrast, the resistances of the next two layers of concrete behaved in an opposite manner. The resistance of the middle layer of concrete decreased by approximately 70% during the first 18 to 20 days, and then stabilized thereafter; while that of the layer immediately above the rebar decreased by approximately 67% during 10 to 12 days. These results clearly show that the factor causing the typical exponential drop in current occurring during the first 20 days of a treatment is the rapid rise in the resistance of the top layer of concrete.

What in turn causes this has not been determined yet. Perhaps it is caused by decreased permeability in the outer layer of concrete, which in turns, possibly arose from precipitation of relatively insoluble compounds, such as $Mg(OH)_2$, $Ca(OH)_2$, and $CaSO_4$, in the pores – in conjunction with the movements of the precursors free ions typically present in concrete. To shed some light on this issue, the authors have begun to investigate the changes in concentrations of the various ions in the concrete at various stages of ECE treatment, using concrete specimens shown in Figure 7. Some of the results obtained so far (i.e., the concentrations of some cations and anions at depth of 12 mm, which is near the surface) are shown in Figures 10 and 11.

The results showed that, near the surface of the concrete, the concentrations of cations such as calcium, potassium, and sodium, decreased noticeably during the first 30 days of treatment. This is not unexpected since the cations should be migrating away from this layer of concrete and migrating deeper toward the rebars. On the other hand, the anions such as the chloride, as measured in two forms (free and total), and sulfate also exhibited similar decreasing trend. Unfortunately, these results alone are not yet sufficient to provide any clue to the cause of the increase in resistance at this layer of concrete. However, these results do offer an interesting confirmation of the presence of bound chloride, as measured by the difference between total and free chloride, even when the source of chloride is deicing salt and not admixed chloride. And as should be, there were more total chloride than free chloride most of the time. Interestingly, the results also show that within 40 days after the termination of treatment, no significant redistribution (which would be indicated by changes in concentrations of the ions) can be discerned.

Closing Remarks

The various recent applications of ECE have no doubt demonstrated that this new method can be used for mitigating active steel bar corrosion in full-sized concrete bridge members. Since the number of reported ECE treatments is still relatively limited, it is still difficult to predict precisely how much of the chloride in a candidate structure can be removed in one treatment. However, it appeared that with the current technology, it is comparatively easier to achieve high chloride removal on bridge decks and the likes than on piers, walls, etc. Ongoing investigations may lead to higher removal rates.

References

1. Virmani, Y.P., and Clemeña, G.G. *Corrosion Protection: Concrete Bridges.* Report No. FHWA-RD-98-088. Federal Highway Administration, Washington, D.C., September 1998

2. Pettersson, K. Chloride Threshold Value and the Corrosion Rate in Reinforced Concrete. *Cement and Concrete Research*, Vol. 20, pp. 461-470, 1994.

3. Morrison, G.L., Virmani, Y.P., Stratton, F.W., and Gilliland, W.J. *Chloride Removal and Monomer Impregnation of Bridge Deck Concrete by Electro-Osmosis.* Report No. FHWA-KS-RD 71-1. Kansas Department of Transportation, Topeka, Kansas, 1976.

4. Slater, J.E., Lankard, D.R., and Moreland, P.J. Electrochemical Removal of Chlorides from Concrete Bridge Decks. *Transportation Research Record 604,* 1976.

5. European Patent for 'Removal of Chlorides from Concrete.' Application No. 86-30-2888.2, 1986.

6. Bennett, J.E., Thomas, T.J., Clear, K.C., Lankard, D.L., Hartt, W.H., and Swiat, W.J. *Electrochemical Chloride Removal and Protection of Concrete Bridge Components: Laboratory Studies.* Report No. SHRP-S-657. National Research Council, Washington, D.C., 1993.

7. Bennett, J.E., Fong, K.F., and Schue, T.J. *Electrochemical Chloride Removal and Protection of Concrete Bridge Components: Field Trials.* Report No. SHRP-S-669. National Research Council, Washington, D.C., 1993.

8. Bennett, J.E., and Schue, T.J. *Evaluation of NORCURE Process for Electrochemical Chloride Removal from Steel-Reinforced Concrete Bridge Components.* Report No. SHRP-C-620. National Research Council, Washington, D.C., 1993.

9. Bennett, J.E., and Schue, T.J. *Chloride Removal Implementation Guide.* Report No. SHRP-S-347. National Research Council, Washington, D.C., 1993.

10. Clemeña, G. G., and Jackson, D. R., *Trial Application of Electrochemical Chloride Extraction on Concrete bridge Components in Virginia,* Report No. FHWA/VTRC 00-R18, Virginia Transportation Research Council, Charlottesville, Virginia, 2000.

11. Burns, D., *Norcure Electrochemical Chloride Extraction Project: Nebraska Departments of Roads – I-480 Substructure Rehabilitation, Omaha, Nebraska,* Vector Construction, Inc., Fargo, North Dakota, USA., 1998.

12. Elsener, B., and Böhni, H., *Electrochemical Chloride Removal Field Test,* Conference on Corrosion and Corrosion Protection of Steel and Concrete, Sheffield, United Kingdom, 1994.

13. Tritthart, J., *Electrochemical Chloride Removal – A Case Study and Laboratory Tests,* Fourth International Symposium on Corrosion of Reinforcement in Concrete construction, Cambridge, United Kingdom, 1996.

14. Armstrong, K., Grantham, M. G., and McFarland, B., *The Trial Repair of Victoria Pier, St. Helier, Jersey, Using Electrochemical Desalination,* Fourth International Symposium on Corrosion of Reinforcement in Concrete construction, Cambridge, UK, 1996.

15. Velivasakis, E. E., Henriksen, S. K., and Whitmore, D., Chloride Extraction and Realkalization of Reinforced Concrete Stop steel Corrosion, *Journal of Performance of Constructed Facilities,* pp. 77-84, May, 1998.

16. Stoop, B. T. J., and Polder, R. B., "Redistribution of Chloride After Electrochemical Chloride Removal From Reinforced Concrete prisms," Fourth International Symposium on Corrosion of Reinforcement in Concrete construction, Cambridge, UK, 1996.

17. Vennesland, Ø., Humstad, E. P., Gautefall, O., and Nustad, G., *Electrochemical Removal of Chlorides from Concrete – Effect on Bond Strength and Removal efficiency*, Fourth International Symposium on Corrosion of Reinforcement in Concrete construction, Cambridge, UK, 1996.

18. Chatterji, S., Simultaneous Chloride Removal and Realkalinization of Old Concrete Structures, *Cement and Concrete Research*, Vol. 24, No.6, pp.1051-1054, 1994.

19. Tritthart, J., Chloride Binding in Cement, *Cement and Concrete Research*, Vol. 19, pp. 683-691, 1989.

20. Tritthart, J., Pettersson, K., and Sorensen, B., Electrochemical Removal of Chloride from Hardened cement Paste, *Cement and Concrete Research*, Vol. 23, pp. 1095-1104, 1993.

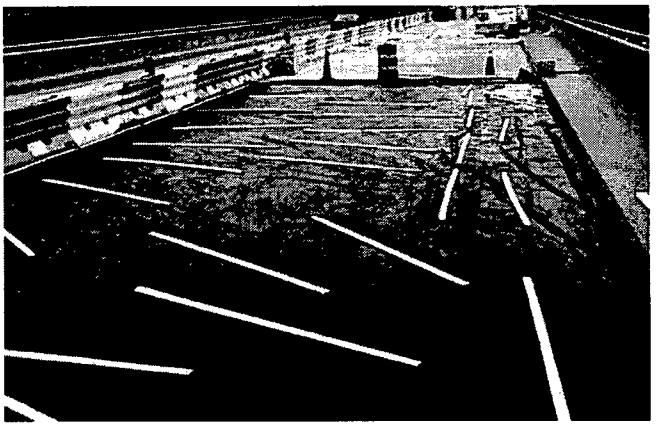

Figure 1. A bridge deck in Virginia undergoing treatment. The anode system, covered with plastic sheets, consisted of an activated titanium mesh that was sandwiched by two layers of felt, with either a saturated aqueous solution of $Ca(OH)_2$ or a 0.1 M $LiOH/LiBO_3$ solution as the electrolyte.[10]

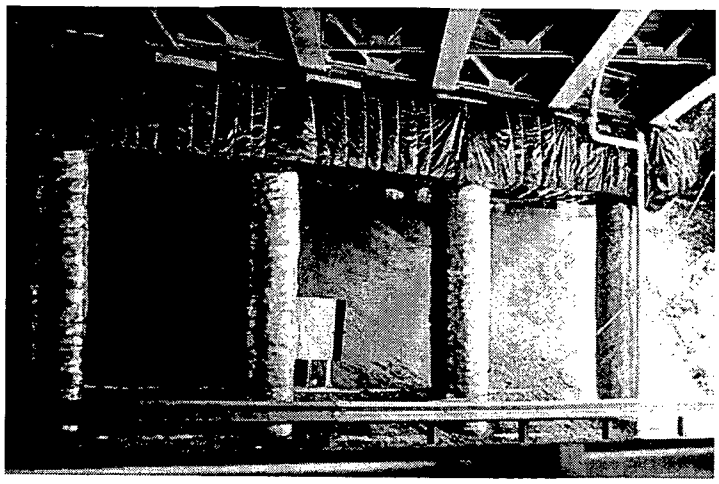

Figure 2. A bridge pier in Virginia undergoing treatment. The anode system, Wrapped in plastic sheets and films, consisted of steel mesh on the pier cap Titanium mesh on the columns, both covered with cellulose fibers that were saturated with a Ca(OH)2 solution. (The wooden behind the columns housed the rectifier.)[10]

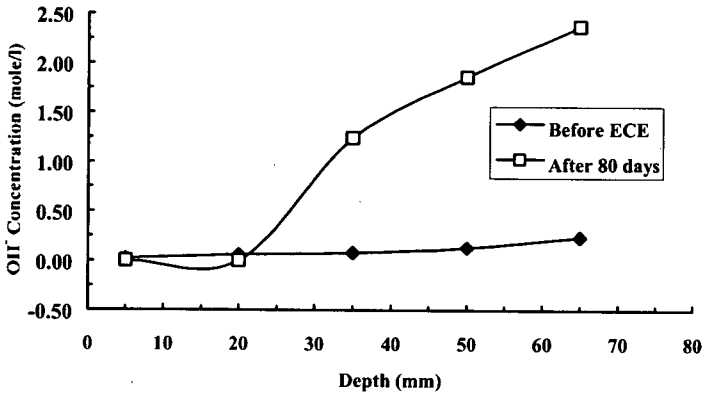

Figure 3. Changes in concentration of hydroxyl ions at different depth in the concrete, before and after 80 days of ECE.[13] Notice that the concentration of OH^- decreases with depth.

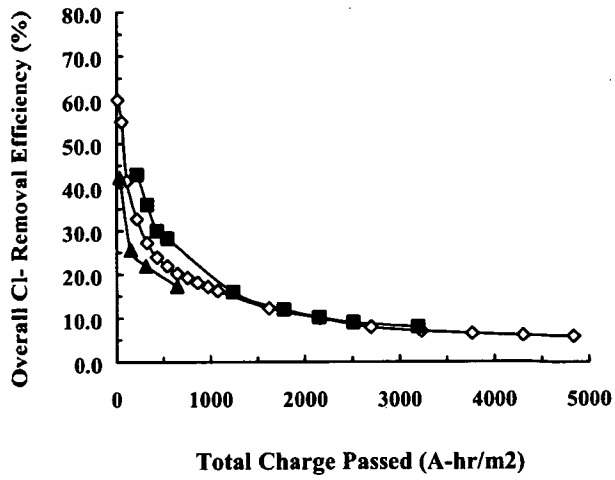

Figure 4. Change in chloride removal efficiency, as observed in some concrete slabs used in a SHRP study.[6]

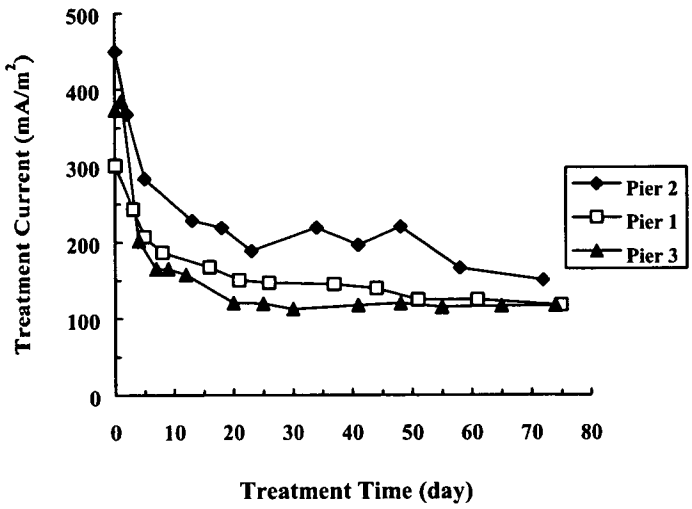

Figure 5. Treatment current that passed through the three concrete piers in Virginia.[10]

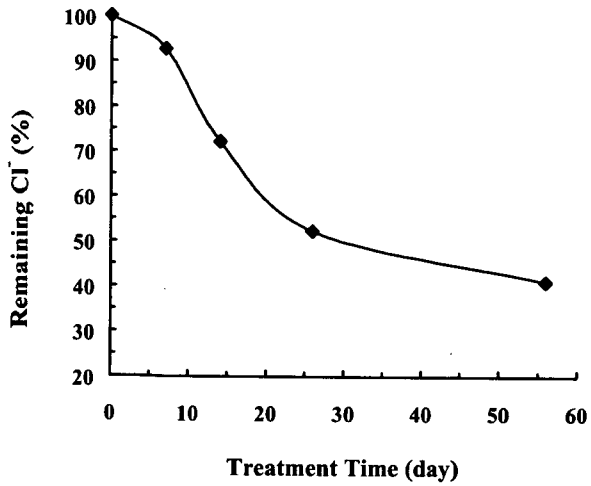

Figure 6. Chloride remaining in concrete specimens admixed with 2% chloride (by weight of cement), at different stages of ECE treatment.[17]

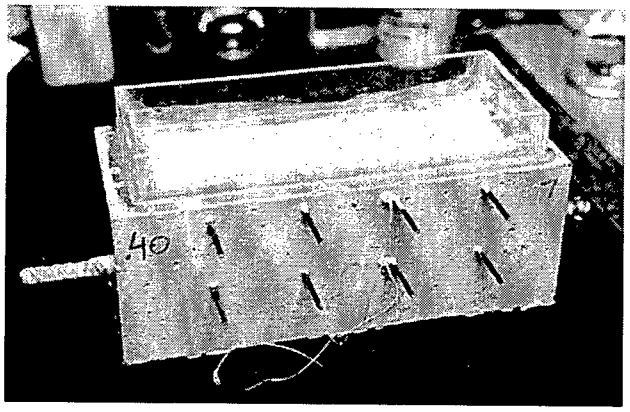

Figure 7. Type I test specimens with two rows of embedded titanium rods (3.2 mm-OD), one at 10 mm below the concrete surface and the other at 10 mm above the rebar. The distance between the surface and the top of rebar is 44, 57, or 70 mm.

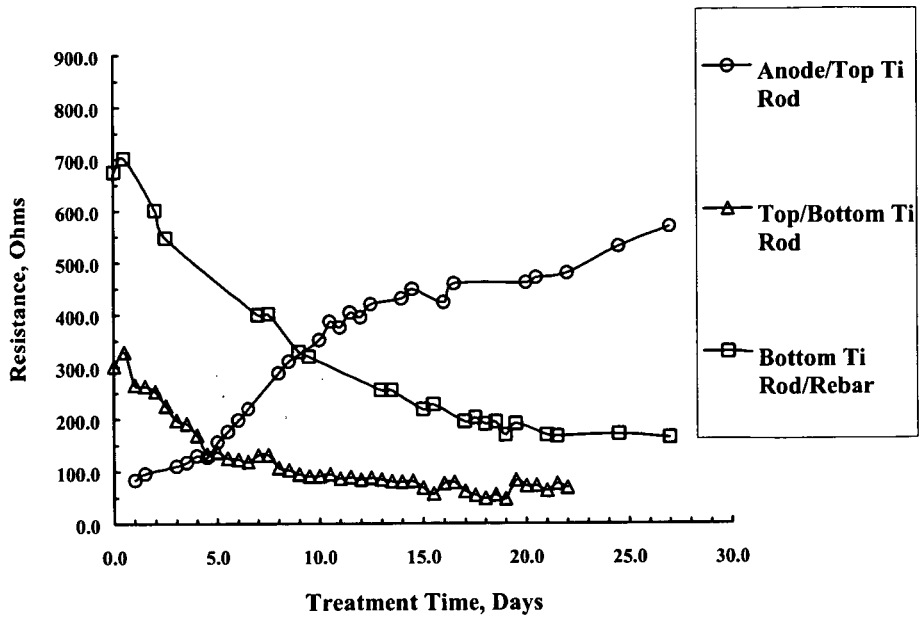

Figure 8. Changes in the resistances of the different layers of concrete in Type I specimen 0.55-1 during treatment.

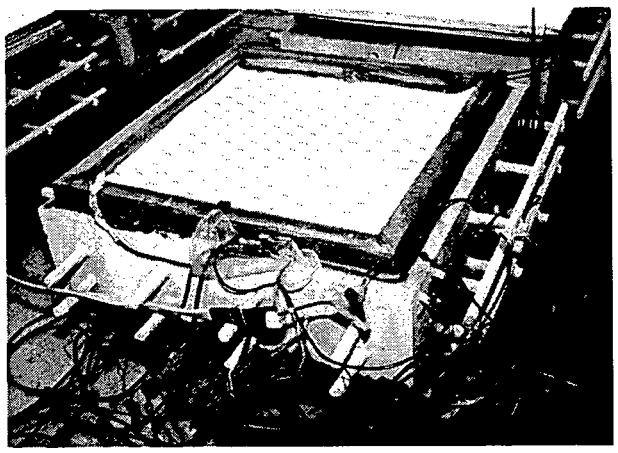

Figure 9. Type IIB specimens being used in the ECE treatment investigations. Notice the activated titanium mesh/felt/electrolyte system on top of the concrete specimen.

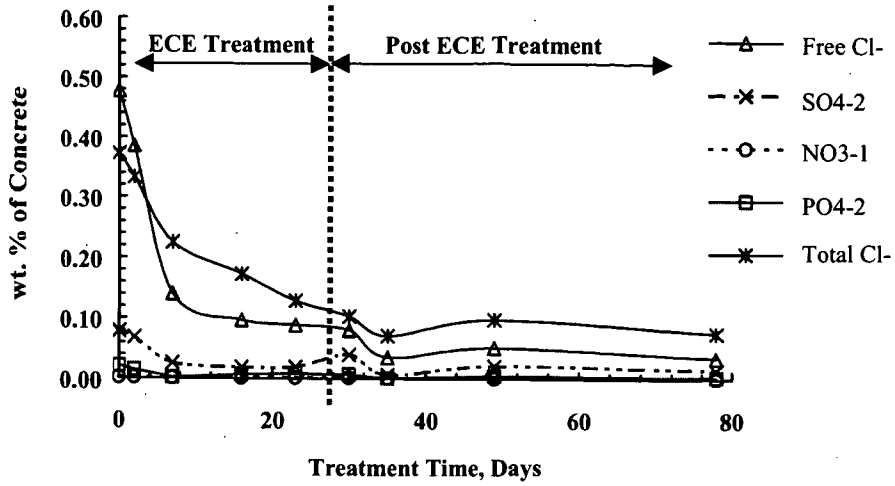

Figure 10. Concentrations of cations in Type II specimen No. 12, at 12-mm depth, during and after treatment.

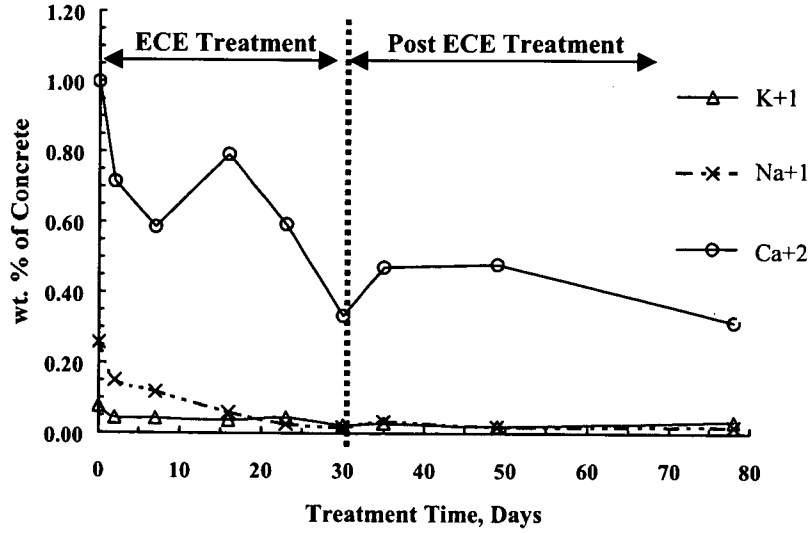

Figure 11. Concentrations of anions in Type II specimen No. 12, at 12-mm depth, during and after treatment.

Table 1. Reported Performance of ECE Treatments on Different Concrete

Location	Concrete Members	Area (m^2)	Chloride Removed (%)	Current Efficiency (%)
SHRP, USA[7]	Deck area	140	50 to 67 (at 25 mm fr. bars)	20
Virginia, USA[10]	Bridge decks	733	76 to 82 (at 6-19 mm) 72 to 82 (at 19-32 mm)	11 to 15
Manitoba, Canada	Bridge decks	1,115	70 to 84	
Seaford, Delaware	Bridge decks	1,665		
Northamptonshire, UK	Parking deck	4,500	80%	
SHRP, USA[7]	Pier columns	104	42 to 69 (top 25 mm)	7 to 13
SHRP, USA[7]	Abutment area	164		12 to 19
Toronto, Canada[8]	Bridge pier areas	31	57 to 69 (at 25 mm) 67 to 71 (at 55 mm)	
Virginia, USA[10]	Piers	488	27 to 60 (at 6-19 mm) 13 to 53 (at 25-38 mm)	9 to 12
South Dakota	Pier columns	89		
Nebraska[11]	Piers	1,525	27 to 89 (at 0-25 mm) 2 to 70 (at 55-75 mm)	
Council Bluff, Iowa	Piers	463	48 to 79	
Saskatchewan, Canada	Pier columns	150	62 to 89	
Saskatchewan, Canada	Piers	180	≤ 80	
St. Helier, Channel Islands[14]	Pier columns	54	51 to 66	
Winnepeg, Canada	Retaining wall	220	20 to 76	
Switzerland[12]	Subway wall	26 m long	29 to 50 (at 25 mm)	
Austria[13]	Wall (of a salt storage)		48 to 62	
Salvøy, Norway	Beams and soffits	1,000	54 to 77	
Selby, UK	Beams and walls	925	72 to 94 (at 0-25 mm) 58 to 96 (at 25-50 mm)	
SHRP, USA[6]	Slabs		40 to 50	10 to 20
Norway[16]	Specimens		30 to 71	
Norway[17]	Specimens		40 to 50	11-13% (first 4 wks); 7% after 8 wks; 10% avg.
Denmark[18]	Specimens		92	

Repairing and Retrofitting the Prestressed Concrete Simple T-Girder Bridge damaged by Salt-Induced Corrosion

Katsunori Ishimura[1], Sadaaki Nakamura[2], Toshio Hosaki[3] and Kazuyoshi Nishina[4]

Abstract

A bridge, which consists of T-girders damaged by salt-induced corrosion, was completed in February 1972. Since 1983, several repairs and post-repair inspections had been made on the bridge. However, the bridge concrete had been damaged greatly by the briny air and water. So a program for repairing and retrofitting thr sections of the bridge was planned to increase the durability and the load resistance of the bridge. For repairing the section of the bridge, a water-jet method was adopted to remove salt components of the section. This paper reports the outline of the work, the result of inspection of the actual bridge status and the PCT girder chipping test to get the chipping effect of the prestressed concrete (PC) member in advance for repairing of the actual bridge.

1. PREFACE

The bridge is a PC post-tensioned simple T-girder bridge (hereinafter abbreviated as a PCT-girder bridge) of 26.05 meters. The PCT girder bridge is located on about 80 meters away from the nearest coastline and directly sprayed with seawater at high tide in winter. Therefore, the bridge had been damaged badly by the briny air and water.

The superstructure of the bridge had undergone protective painting works, reinforcing works by external cables, and post-work investigations since 1983. However, a section repairing work was decided to remove salt components from the section damaged by salt-induced corrosion and to strengthen the bridge by the external cables.

To repair sections of main girders of the bridge, which contain salt components, it is necessary to chip the whole main girders. A water-jet chipping method was employed judging from (1) freeing the workers from chipping vibrations, noises, and dusts and (2) assuring high quality chipped surfaces and high chipping efficiency.

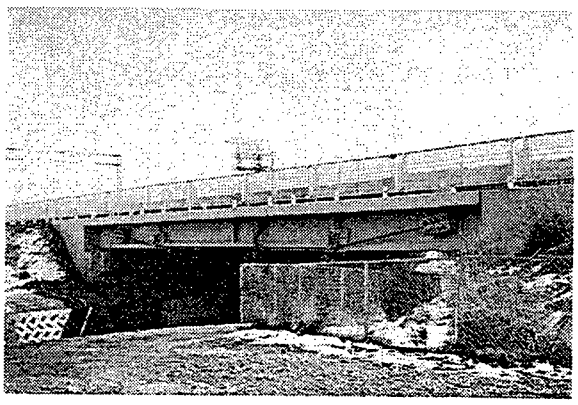

Photo 1 View of the whole bridge

This paper mainly reports the result of inspection of the actual bridge status and the details of the PCT girder chipping test.

1. Japan Highway Public Corporation
2. Senior Engineer, PC Bridge Co. Ltd., Tokyo, Japan
3. Senior Engineer, PC Bridge Co. Ltd., Tokyo Branch, Tokyo, Japan
4. Manager, PC Bridge Co. Ltd., Tokyo, Japan

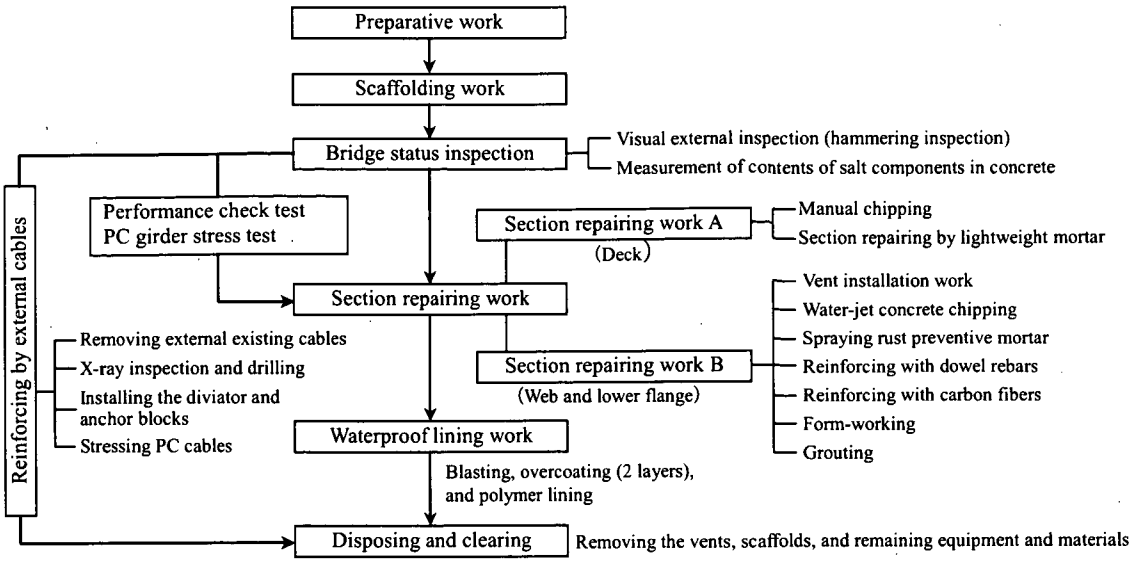

Figure 1 Bridge repairing and retrofitting work flowchart

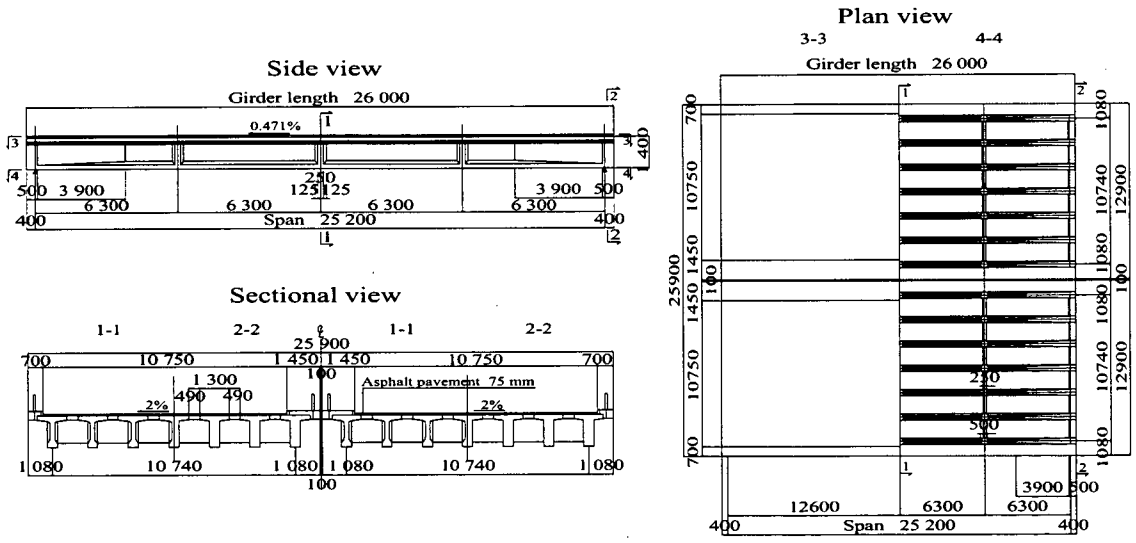

Figure 2 Structure of the bridge

2. STATUS INSPECTION

The concrete sections of the bridge was inspected for cracks, loose concrete, and exposed rebars according to "Hammering inspection" in "Guide to Inspection of Salt-Induced Damages (Proposed)" by Kanazawa Administrating Office (March, 1993). The damage map of the bridge was drawn from the result of inspection, and then it was kept as a basis to determine repairing methods such as injection into cracks and ranges or repairing. Further, it was investigated that how far chloride ion (Cl^-) penetrated the concrete and took samples by drilling to check the rate of rust preventives (Lithium nitrite) to be added.

Figure 3 shows the relationship between the content of salt components in concrete and the depth in concrete, which is the result of measurement of chloride ion (Cl^-) in the

concrete section of the bridge. As seen from this figure, the content of chloride ion (Cl^-) increases as the sample position goes lower. The lower flange and the web contain more salt components than the diaphragm and the bottom of the deck plate.

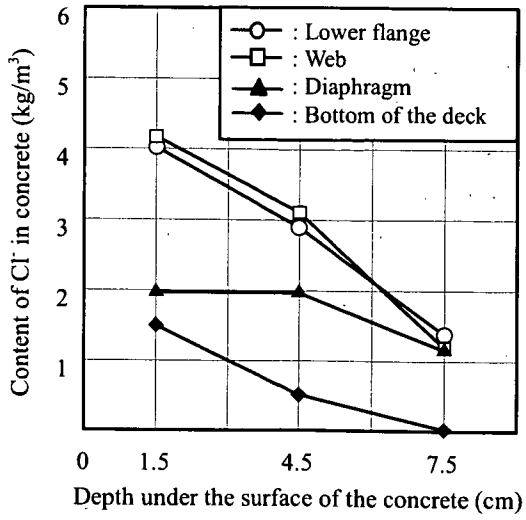

Figure 3 Result of measurement of chloride ion (Cl^-) in the concrete

3. PCT GIRDER CHIPPING TEST

3. 1 Background of the Test

The main girder to be chipped has a girder height of 1.4 meter and a web thickness of 200mm and its sectional rigidity is comparatively low. Its concrete (whose designed compressive strength is 40 N/mm^2) contains prestressing cables (eight of 12ϕ7 cable). There have been few examples of works that chipped PCT girder bridges and repaired the bridge sections in a full scale like our works.

In general, if the PC member contains grouted internal cables, it is assumed that stresses will not be re-distributed by pre-stressing even when the section varies. Our works have been calculated and designed on the basis of this assumption.

However, there have been reported few experiments and construction cases that consider the variation of stresses in the main girder made as the section reduces in chipping and there have been little data to prove the assumption for the calculation and design. As this bridge is a T-girder bridge whose section reduces greatly by chipping, it is necessary to know how much the stress of the main girder varies as the chipping effects before starting the work.

3.2 Purpose of the Test

This test has two main purposes. They are as follows:

(1) To check the water-jet performance

For chipping by a water-jet method, it is fundamental to pre-check the chipping performance of a water-jet machine before actual chipping. As for this, a test girder with similar scale of the actual bridge was used and tested (see Figure 6).

(2) To check the behavior of the PCT girder

It is necessary to grasp the influence of redistribution by pre-stressing applying the water-jet method to the actual bridge. So we carried out a chipping test on the

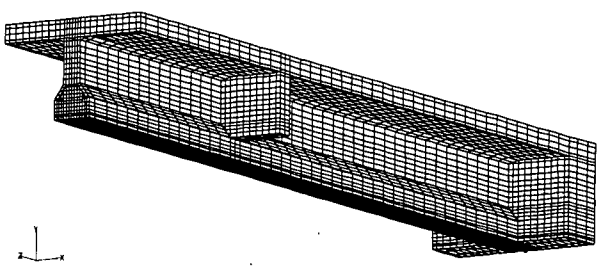

Figure 4 Girder model for analysis

above PCT girder sample and evaluated the following:

1 Member stresses and deformation status due to change of the deadweight of the main girder as the section reduces according to the chipping order (bottom, left side and right side)

2 Member stresses and deformation status due to change of the pre-stressing force as the section reduces according to the chipping order (bottom, left side and right side)

3 Member stresses and deformation status when the stress re-distribution is made as the deadweight of the main girder and the pre-stressing force change as the section varies or when the stress re-distribution is not made (based on the results of the above evaluation 1 and 2)

The above evaluations were performed by the three-dimensional FEM analysis method. The model for analysis is illustrated in Figure 4. Table 1 shows the analysis cases and Figure 5 shows a flow of the current work (from the pre-chipping test to the actual chipping).

Table 1 Analysis cases

Csae No.	Chipping status
Case 1	Before chipping
Case 2	End of the primary chipping range (girder bottom)
Case 3	End of the primary chipping range (right side)
Case 4	End of the primary chipping range (left side)
Case 5	End of all chipping ranges

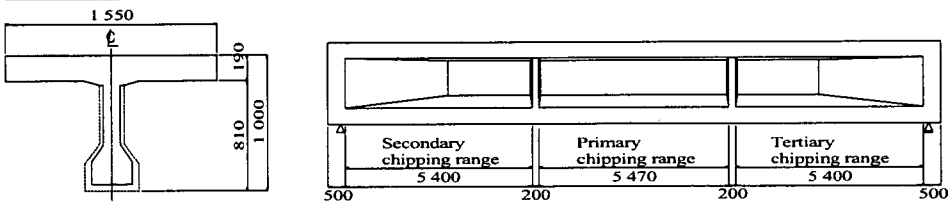

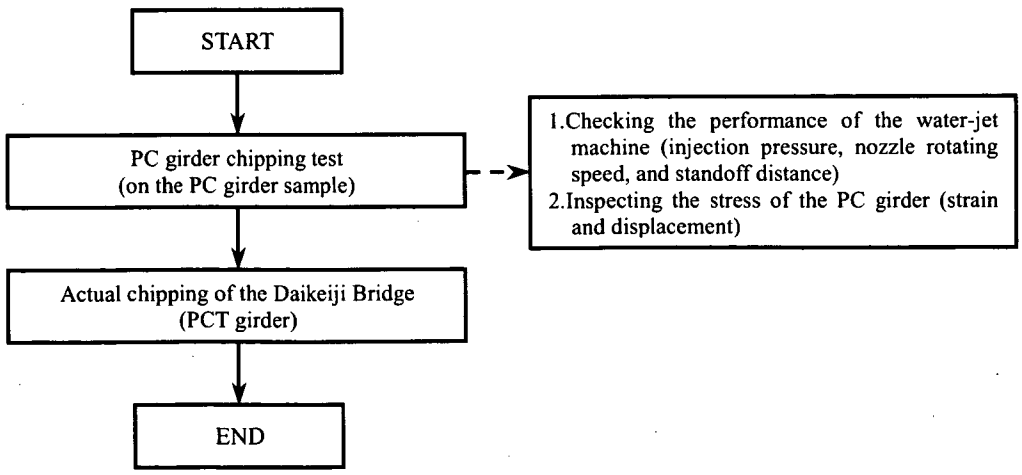

Figure 5 A flow of the current work from the pre-chipping test to the actual chipping

3.3 Test Procedure

(1) Water-jet performance check test

Figure 6 shows a sample PCT girder used to check the performance of the water-jet machine. In this test, the items (as parameters) listed below were tested to check injection pressures, nozzle rotating speeds, and standoff distances.

1 Operation and workability of the chipping machine
2 Operating procedure and methods of chipping the web and the flanges
3 Working conditions
4 Chipping surface status
5 Notices of chipping the actual bridge

We used a crawler-mounted water-jet concrete chipping machine to chip the web concrete and the lower flange concrete.

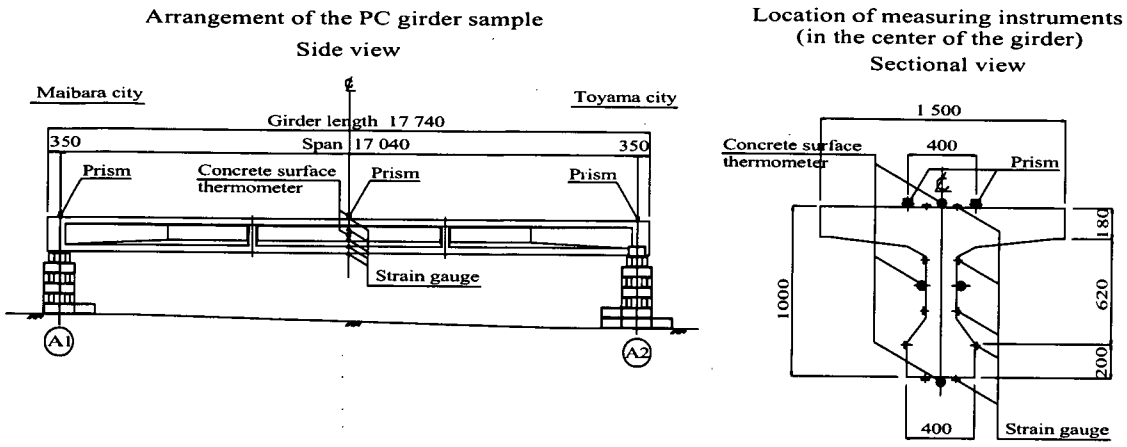

Figure 6 PCT girder sample for the chipping test and test points

(2) PCT girder behavior check

In the PCT girder chipping test, the following items were measured.

1 Axial strain of concrete
2 Vertical and lateral displacements of the main girder
3 Surface temperature of concrete and ambient temperature.

Figure 6 shows test points on the girder and locations of measuring instruments.

3.4 Test Results

(1) Water-jet performance check test

The following results were obtained from the chipping depth test:

- The injection water pressure was 180 N/mm^2 to 200 N/mm^2 as the quantity of water to be injected was set to 50 liters/minute.
- The chipping machine showed a good chipping ability at the nozzle moving speed and the nozzle rotating speed which were determined according to the capacity of the machine.
- A standoff distance (a distance between the front end of the nozzle and the surface of concrete) was set so that the mean chipping depth was smaller than the target chipping depth to prevent the chipping surface from being damaged by excessive chipping.

Table 2 shows the summary of water-jet operating conditions for actual bridge section repairing.

Table 2 Chipping conditions and depths of the PCT girder

		Web	Haunch	Lateral side of lower flange	Bottom
Injection pressure	(N/mm^2)	180	200	200	200
Nozzle moving speed	(m/min)	6.0	6.0	6.0	6.0
Nozzle rotating speed	(rpm)	240	240	240	240
Jet water flow rate	(l/min)	50	50	50	50
Standoff distance	(mm)	20	20	20	40
Mean chipping depth	(mm)	23	24	38	41
Target chipping depth	(mm)	30	30	50	50
Chipping allowance	(mm)	+10	+10	+10	+10

(2) PCT girder pre-stress re-distribution

The whole re-distribution of pre-stresses of the PCT girder was evaluated from the result of measurement of displacements. Table 3 shows the results of FEM analyses and Figure 7 shows the result of measurement of displacements (in the center of the span) of the PCT girder and the measured values of Table 3.

Table 3 Result of FEM analyses

(a) Considering the re-distribution of pre-stresses

		Concrete stress intensity (N/mm2)			Deflection (mm)			
		Deadweight of girder	Pre-stress	Resultant stress intensity	Deadweight of girder	Pre-stress	Total	Variation
Case1	Upper edge	-3.09	2.80	-0.29	9.0	-21.1	-12.1	0.0
	Lower edge	6.16	-16.93	-10.77				
Case2	Upper edge	-3.30	3.63	0.33	9.9	-24.3	-14.4	-2.3
	Lower edge	6.88	-19.87	-12.99				
Case3	Upper edge	-3.33	3.93	0.59	10.3	-26.3	-16.0	-3.9
	Lower edge	7.49	-22.68	-15.18				
Case4	Upper edge	-3.39	4.32	0.94	10.8	-28.9	-18.1	-6.0
	Lower edge	8.49	-26.37	-17.88				
Case5	Upper edge	-3.17	4.32	1.15	11.4	-34.5	-23.1	-11.0
	Lower edge	8.03	-26.38	-18.35				

Marks in the stress intensity field: "+" for pulling "-" for compression

Marks in the deflection field: "+" for downward "-" for upward

(b) Not considering the re-distribution of pre-stresses

		Concrete stress intensity (N/mm2)			Deflection (mm)			
		Deadweight of girder	Pre-stress	Resultant stress intensity	Deadweight of girder	Pre-stress	Total	Variation
Case1	Upper edge	-3.09	2.80	-0.29	9.0	-21.1	-12.1	0.0
	Lower edge	6.16	-16.93	-10.77				
Case2	Upper edge	-3.30	2.80	-0.50	9.9	-21.1	-11.2	0.9
	Lower edge	6.88	-15.94	-9.06				
Case3	Upper edge	-3.33	2.80	-0.53	10.3	-21.1	-10.8	1.3
	Lower edge	7.49	-15.94	-8.44				
Case4	Upper edge	-3.39	2.80	-0.58	10.8	-21.1	-10.3	1.8
	Lower edge	8.49	-15.94	-7.44				
Case5	Upper edge	-3.17	2.80	-0.37	11.4	-21.1	-9.7	2.4
	Lower edge	8.03	-15.94	-7.91				

Marks in the stress intensity field: "+" for pulling "-" for compression

Marks in the deflection field: "+" for downward "-" for upward

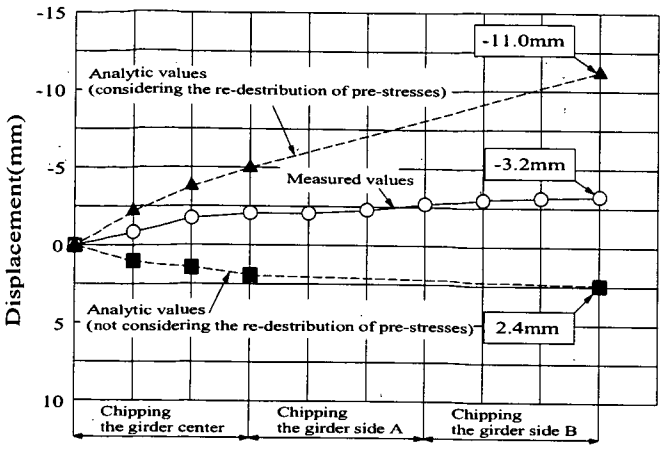

Distribution ratio $\eta = \frac{-3.2}{-11.0} = \underline{0.3}$

Figure 7 Displacements of PCT girder by the deadweight and the pre-stress ("+" for downward, "-" for upward)

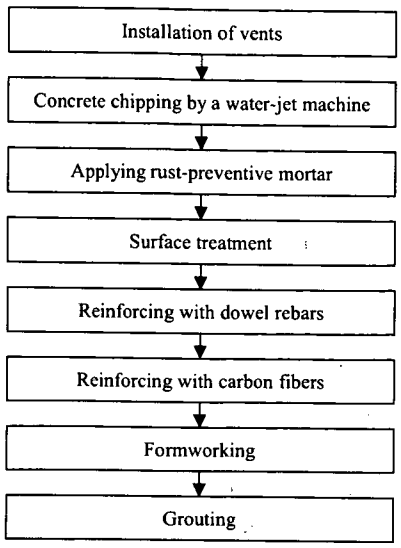

Figure 8 Section repairing flow

From the above, it has been found that the re-distribution by pre-stresses was about 30% and evaluated the stress (in the center of the span) of the main girder. This was the acceptable stress range.

4. SECTION REPAIRING BY A WATER-JET METHOD

4.1 Installation of Temporary Vents

The section repairing chips web and lower flange concrete by a water-jet machine according to Figure 8 without shutting out traffic from the bridge. So it is necessary to reduce the sectional force against the dead load and the active load in service, and temporary vents for the period of work were installed. Figure 9 shows the locations of temporary vents.

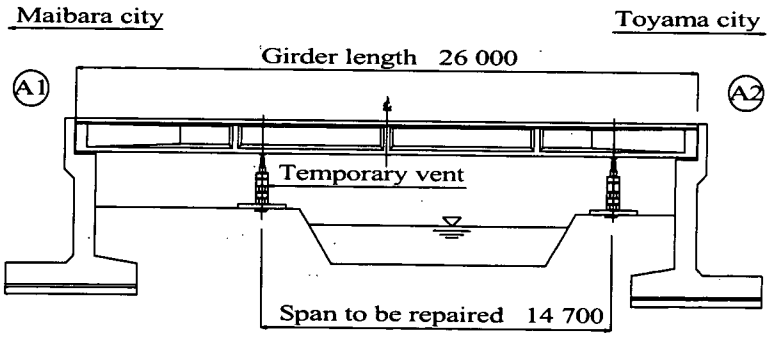

Figure 9 Location of temporary vents

4.2 Concrete Chipping by a Water-Jet Method

Table 3 shows the chipping conditions of the water-jet chipping machine (injection pressure, nozzle moving speed, nozzle rotating speed, jet water flow rate, and standoff distance). Photo 2 and Photo 3 respectively show the water-jet chipping machines for the bottom and for the sides. The chipping depths are 3 cm for the web and 5 cm for the lower flange. Figure 10 shows the difference between the chipping depth and the actual chipping depth (measured). The results of chipping works were classified into three chipped surface ranks for management.

i. Chipping error of +0 mm to 10 mm
ii. Chipping error of +10 mm to 15 mm
iii. Chipping error of +15 mm or more

If the chipping error exceeds 10 mm, we inspected the chipped surfaces, calculated section values, verified the stress intensity, and confirmed the safeness.

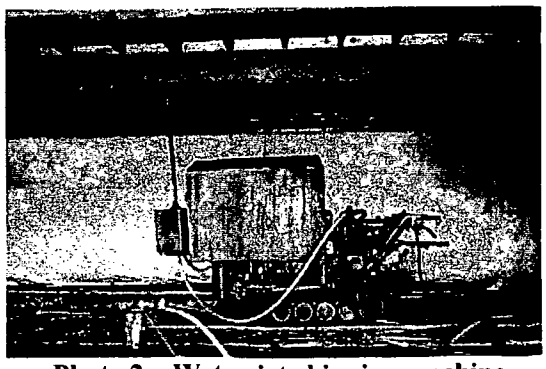

Photo 2 Water-jet chipping machine (for the bottom)

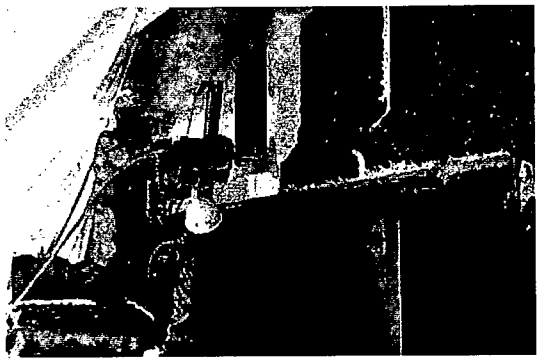

Photo 3 Water-jet chipping machine (for the sides)

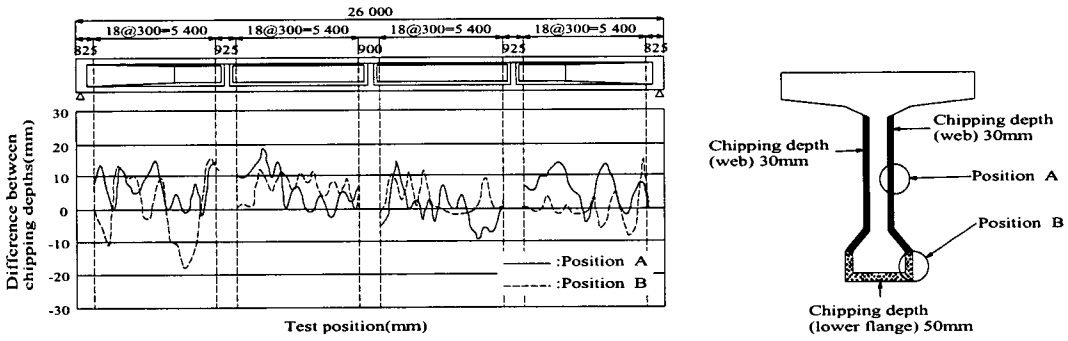

Figure 10 Chipping depth control diagram

5. CONCLUSION

This paper reports the status investigation, the performance check test and the section repairing work. Particularly, water-jet performance test and girder behavior check were carried out before starting the actual repairing. The result of the tests was contained in the actual works and the bridge was successfully repaired and reinforced.

References

1) "Guide to Inspection of Salt-Induced Damages (Proposed)" by Kanazawa Administrating Office, Japan Highway Public

Upgrading Concrete Bridges with PBO Prestressing Upgrading Technique (P-PUT)

Z.S. Wu[1], K.Iwashita[2], K.Hayashi[3], T.Higuchi[4], S.Murakami[5], Y.Koseki[6]

ABSTRACT

This study aims at developing an innovative strengthening system with externally bonded prestressed PBO (short for Polypara-phenylene-benzo-bisthiazole) fiber sheets (PFS), which present equal or higher strength and stiffness in comparison with high strength type of carbon fiber sheets (CFS) and great performance on energy adsorption superior than other fiber sheets such as armied and carbon fiber sheets. An experimental program is carried out to confirm the strengthening effects on load-carrying capacity, stiffness characteristics, ductility, and resistance of crack opening of prestressed concrete girders. The main parameters includes the prestress level, the number of PFS layers, and resin impregnation of PFS before or after prestressing PFS.

KEYWORD

External Prestressing, PBO fiber sheets (PFS), PC girder, Composite behavior, Strengthening, Crack-resistance

INTRODUCTION

The need to rehabilitate or retrofit the deteriorating civil infrastructure is becoming a major and urgent problem worldwide. In contrast with the traditional strengthening methods such as overlaying and jacketing method, and bonded steel plates method, the use of fiber reinforced polymers (FRP) represents an innovative and effective technology for strengthening, retrofitting and upgrading of existing concrete structures due to their much more beneficial characteristics such as high strength and stiffness to weight ratio, high corrosion resistance, electromagnetic neutrality, inherent tailor ability and ease of application in the field. In recent years, repairing and strengthening the concrete structures with externally epoxy-bonded FRP sheets to the tension face of structural element has been widely accepted for practical uses.

On the other hands, throughout the recent research achievements on the FRP bonding technique, it is understood that more functional and effective uses of FRP are necessary to be developed for seismic reinforcing or upgrading of the structural capacity in further improvement of reinforcement effects. First, due to the limitation of bonding capacity of FRP-concrete interface, the full play of FRP reinforcement or necessary capacity

1) Department of Urban & Civil Engineering, Ibaraki University, Associate Professor
2) Department of Urban & Civil Engineering, Ibaraki University, Graduate Student
3) ABE Industrial Co., Ltd.
4) TOHO EARTHTECH, Inc.
5) Nippon Steel Composite Co., Ltd.
6) TOYOBO Co., Ltd.

enhancements are sometime difficult to be achieved due to the interfacial debonding of FRP laminates. Second, the strengthening effects on the structural stiffness, the cracking load, and the steel yielding load can not be expected with only simple FRP bonding. Moreover, the existing damage such as cracks can not be recovered and the strengthening effect is inferior to the dead load for an existing structure.

During past several decades, prestressing technique has been advanced successively and applied widely for reinforcing large-scale civil and building structures. Based on the concept of prestressing technique and FRP bonding technique, some attempts to externally strengthen concrete structure with prestressed FRP plates or sheets were made. [Triantafillou et al., 1991, Wu et al., 2000, 2001] Recently, the authors have developed a PBO Prestressing upgrading technique, in which the PBO fiber sheets presenting equal or higher strength and stiffness in comparison with high strength type of carbon fiber sheets (CFS) and great performance on energy adsorption superior than other fiber sheets such as armied and carbon fiber sheets is used. In this technique, PBO fiber sheets are prestressed without impregnation before bonding to the surface of concrete structure and an air bag system is jointly used to ensure the bonding performance. The strengthening effects for RC beams with a span of 2m including different parameters such as the concrete compressive strength, the number and type of FRP sheets, the anchorage treatment and the prestress level [R.EI-Hacha, 2000].

This paper is mainly focused on investigating the effectiveness and efficiency of the developed PBO Prestressing Upgrading Technique for PC type of structures with externally prestressed PFS. An experimental program is carried out to confirm the reinforcement effects on load-carrying capacity, stiffness characteristics, ductility, and resistance of crack opening of PC beams with the design variables including prestress level, reinforcement ratio, and impregnation of PFS before bonding to PC beams. Analytical study is performed to evaluate the flexural behavior of PC beams strengthened with prestressed PFS.

PRESTRESSING AND BONDING OF PBO FIBER SHEETS

The concept of externally PFS prestressing method is illustrated in Fig.1. The prestressing procedures include 1) pretension of PFS, 2) bonding to the tension face of the concrete structures (including curing of adhesive and cutting of the two PFS ends), 3) appropriate anchorage treatments. The externally prestressing system of PFS used this study is shown in Figure 2. The two steel-PFS lapped joints are connected to a fixed load cell at one end and a hydraulic jack at the other. Both load cell and hydraulic jack are mounted to a stiff steel frame (Fig.2). Figure 3 shows an air bag system in order to ensure the bonding behavior of PFS-concrete interface especially for the case that the concrete interface is uneven or the structure has a camber. As the suction pump sucks up air within the film package and produces a vacuum in which the prestressed PFS is sealed tightly, the PFS is pressured against concrete surface by air pressure.

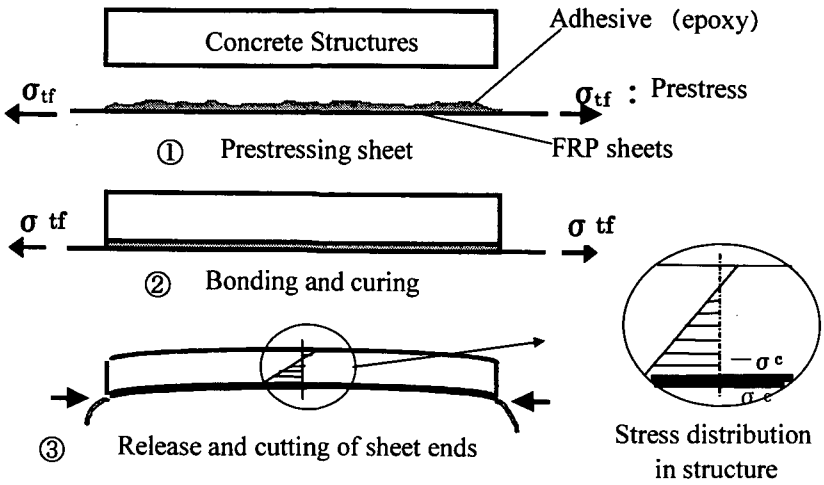

Figure1: The concept of the strengthening method with PFS prestressing

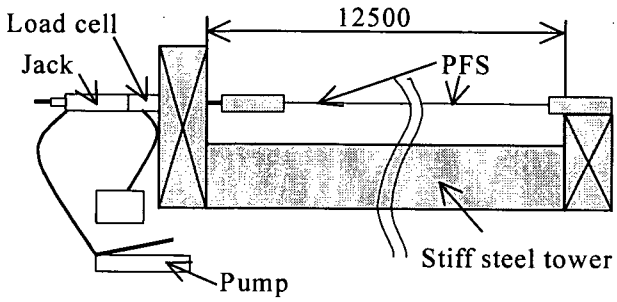

Figure2: Prestressing System

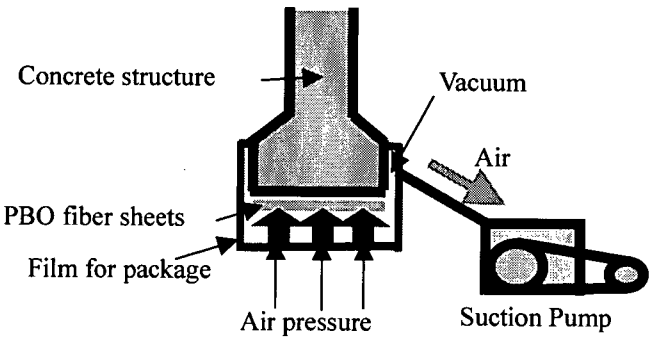

Figure3: Air Bag System

PBO FIBER SHEETS

The newly developed PBO fiber sheet is used here as an external reinforcement. The elastic modulus and tensile strength are fairly higher than that of the high strength type of carbon fiber sheets. It has great impact-tolerance and energy absorption capacity superior than other kinds of fibers such as carbon fiber and aramid fiber. Figure 4 shows the result of an impart test for three kinds of fibers i.e. PBO, carbon and aramid fibers. Besides, PBO fiber demonstrates high creep resistance and fire/fuel resistance with LOI value 68. Figure 5 shows

the relaxation behavior both for PBO and carbon(high strength type) by a tensile test of FRP sheet specimen with 2m long and 8cm wide. The introduced stress is 1230(N/mm^2). Through the continuous measurement of tensile force reduction during the period of duration until to 1300h, it is found that the relaxation behavior of PFS is similar to that of CFS.

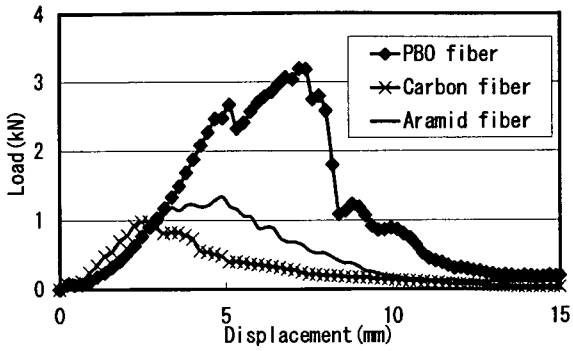

Figure4: Result of Impact Test

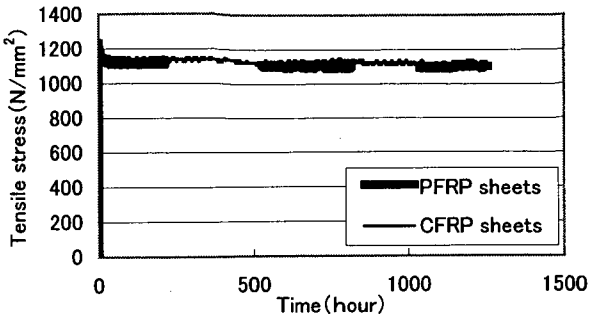

Figure5: Result of Relaxation Test

EXPERIMENTAL PROGRAM

Test variables

In order to investigate the strengthening effects and composite behavior for large scale of PC structures with prestressed PFS, girder specimens with 10m span and 1m high as shown in Fig.6 are designed. The PC girder is introduced 42 tf prestressing force with 4 interior steel cables. The material properties of concrete, reinforcing bar, PFS and adhesive epoxy are listed in Table 1. The steel bar (Φ6) is arranged to in the specimens for the strain measurement. In this study, the following test variables are considered to investigate the reinforcement effects:

Table-1 Summary of material properties

Concrete	Modulus of elasticity (GPa)	33.9
	Compressive strength (MPa)	58.0
	Poisson's ratio	1.5
Stress-relieved steel SD295A	Modulus of elasticity (GPa)	200
	Tensile strength (GPa)	1.86
	Yielding strength (GPa)	1.57
	Introduced prestress (GPa)	1.10
PFS	Modulus of elasticity (GPa)	240
	Tensile strength (GPa)	4.0
	Limit of tensile strain (μ)	16700
	Thickness (mm)	0.128
	Unit weight (g/m^2)	200
Epoxy	Modulus of elasticity (GPa)	3.43
	Poisson's ratio	0.35

1) Prestress levels (33% and 45% of f_{ts}※)
(※ f_{ts} =3500N/mm^2, assumed effective strength of PFS)
2) PFS layers (3 and 4 layers)

3) Impregnation of PFS with epoxy after or before bonding to specimen surface(Only specimen No.3 is the case of impregnation of PFS with epoxy before bonding to specimen surface)

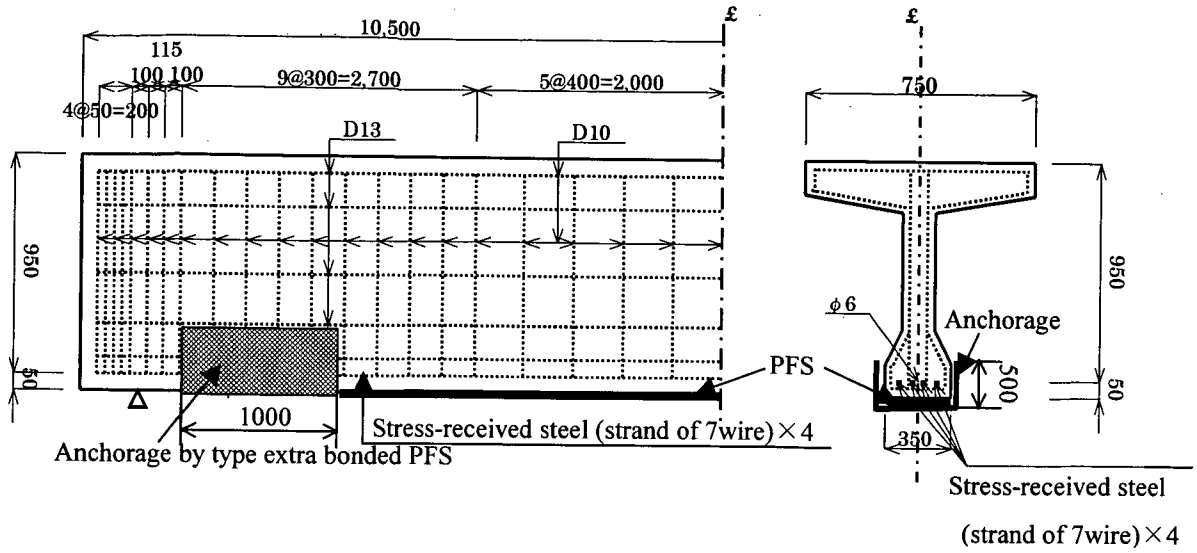

Figure6: Detail of Specimens

Strengthening effect on flexural behavior

The typical data of the experimental results is summarized in Table 2. The load versus deflection at mid-span of specimen with bonded PFS of three layers is shown in Figure 7, in which the result of normal PC beam (control specimen) is also shown in order to make a comparison. The control PC specimen without PFS strengthening fails due to the yielding of steel cables and concrete crushing. As for PFS-strengthened PC beam without PFS prestressing, the debonding initiates from the ends of a flexural crack almost at the mid-span and rapidly propagates to the end of PFS. For the prestressed PFS(33% prestress of assumed effective strength of PFS)-strengthened PC beam, the initiation of debonding starts, also, from the end of flexural crack. Both strengthened beams occurs slightly load degradation due to the debonding propagation from the mid-span to the end of specimens and then maintains a constant loading level due to the effect of anchorage by U type extra bonded PFS until the final failure of the anchorage. The another prestressed PFS(45% prestress of assumed effective strength of PFS)-strengthened PC beam shows a PFS rupture failure mode. It can be found that there are about 26.5%, 54.1% and 67.1% flexural strength enhancements of 0%prestressed PFS, 33% prestressed PFS and 45% prestressed PFS –strengthened beams comparing with the control beam. For the prestressed PFS(45% prestress of assumed effective strength of PFS)-strengthened PC beam, the predicted flexural strength, based on RC flexural theory and by considering steel cable yielding-PFS rupture mode, is 53tf. Moreover if the measured value of maximum strain of PFS at rupture, that is 17864 μ is used, the calculated flexural strength is 56tf with a very good agreement with the experimental result of 56.8tf. Therefore it may be implies that the complete bonding behavior of PFS-concrete interface is

maintained until the occurrence of PFS rupture. There are also great increases in cracking load of prestressed PFS-strengthened beams due to prestressing while the cracking load of the PFS-strengthened beam is same as the one of control beam without PFS strengthening.

Table-2 Typical Data of Experimental Result

No.	Specimens	Cracking load(kN)	Ultimate load(kN)	Strain of PFS at failure※	Falure mode
1	Normal PC beam (control specimen)	240	340	—	concrete crushing
2	PC beam strengthened with PFS	240	430	8982	PFS Debonding
3	33% PFS prestressing (3 layers, pre-impregnation)	295	485	12349 [4730]	PFS Debonding
4	33% PFS prestressing (3 layers)	305	524	14003 [4730]	PFS Debonding
5	45% PFS prestressing (3 layers)	320	568	17864 [6438]	PFS rupture
6	45% PFS prestressing (4 layers)	332	562	13210 [6297]	PFS Debonding

※the numerical value in [ ] shows PFS strain due to PFS prestressing

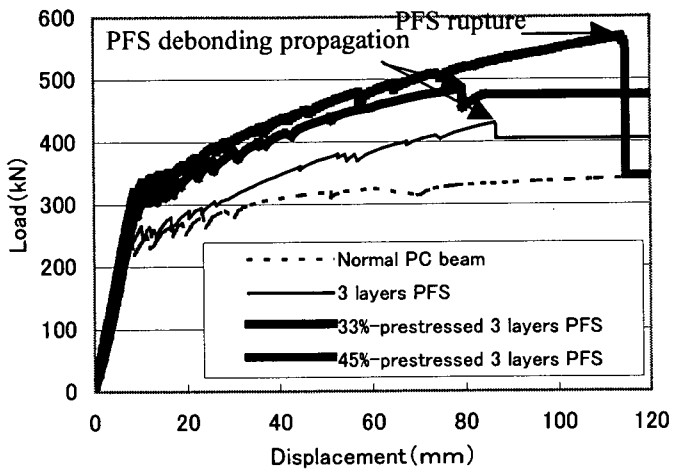

Figure7: Result of Load Versus Deflection Relationship

Strengthening effect on cracking behavior

Table 3 shows the crack spacing just before the yielding of steel bar by comparing four specimens, i.e. control beam(without strengthening), PFS-strengthened beam(without PFS prestressing), 45%prestressed PFS-strengthened beam(3 layers) and 45%prestressed PFS-strengthened beam(4 layers) . It is found that the crack dispersion can be improved by the prestressing of PFS. The crack width varying with the loading stage for these four beams is shown in Figure 8. A great effect on crack resistance is observed in the case of the prestressed PFS-strengthened beams and it increases with the increase of the introduced prestressing force. Figure 9 shows the relationship of crack number versus loading level for different specimens.

Table-3 Crack spacing

Specimens	Crack distance (mm)
Without reinforcement	375
Without Prestressing	350
With 33% prestressing of PFS (3 layers)	267
With 45% prestressing of PFS (3 layers)	286
With 45% prestressing of PFS (4 layers)	247

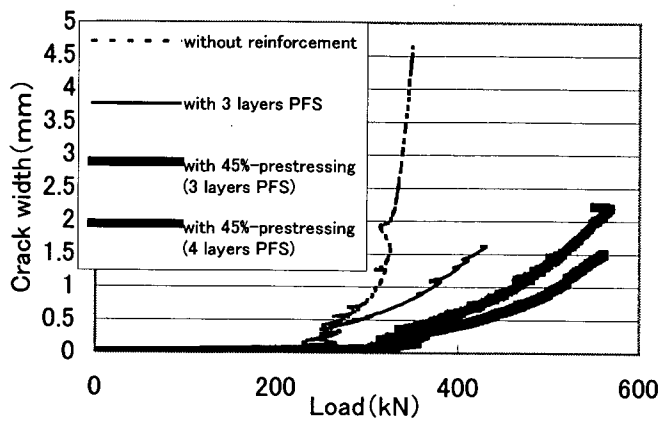

Figure8: Crack width in Different Specimens

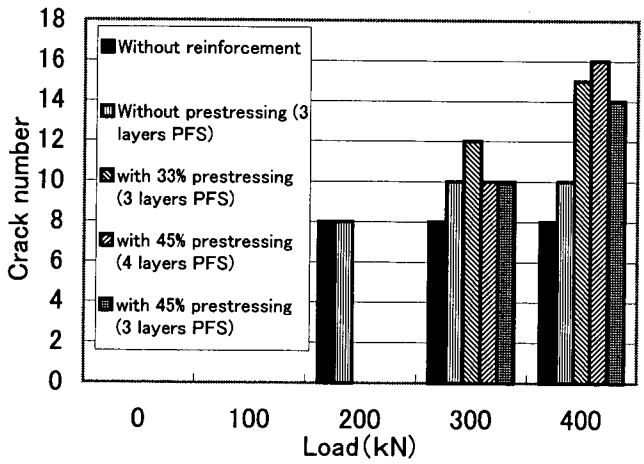

Figure9: Comparison of Crack Number among Different Specimens

Strengthening effects due to the number of PFS layers

Fig.10 shows the relationship of load versus deflection at mid-span of specimens for both 45% prestressed PFS-strengthened beams with 3 and 4 layers of PFS in which the result of the control beam is also shown in the figure. As shown in Picture 1 and 2, the specimen with 3

layers of PFS fails due to the PFS rupture while the specimen with 4 layers of PFS fails due to the PFS debonding. After the debonding initiation from the end of flexural crack of concrete and rapidly propagating to the end of beam, a sudden load after the peak load drop occurs with the anchorage failure due the limitation of anchorage ability. Moreover, this premature debonding failure of PFS results in that the ability of PFS could not be displayed.

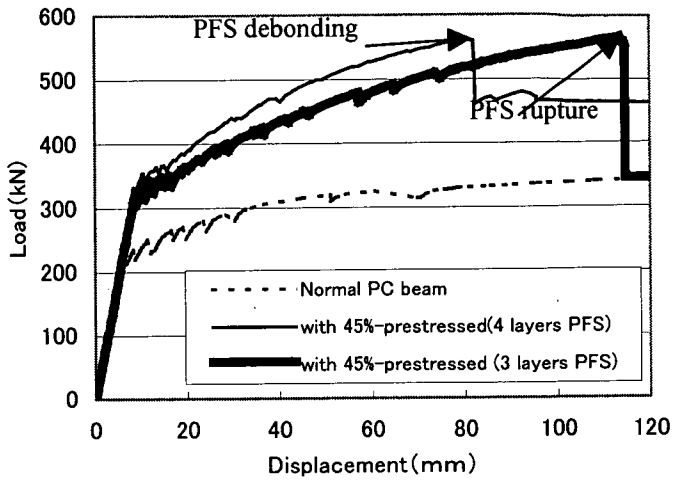

Figure10: Load versus Deflection Relationship Flexural behavior of different PFS layer

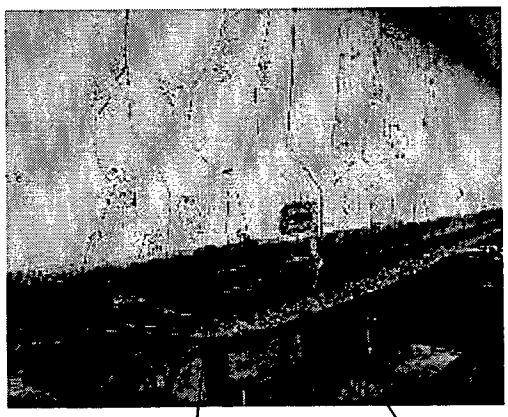

The start point of debonding

Mid-span

Picture 1: Debonding failure

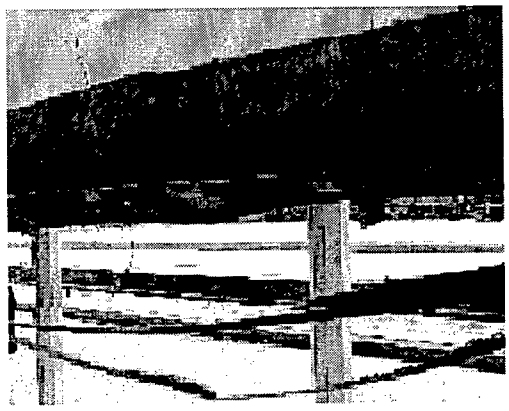

Picture2: PFS rupture

Bonding behavior due to impregnation process of prestressed PFS

Figure 11 shows the experimental results of load versus deflection relationship for two 33% prestressed PFS-strengthened beams with resin impregnation procedure before and after the prestressing procedure of PFS. The initiation of PFS debonding is delayed for the case of resin impregnation after the prestressing procedure of PFS comparing the case of resin impregnation before the prestressing procedure of PFS. This result implies that the excellent bonding performance can be achieved by prestressing PFS without resin impregnation.

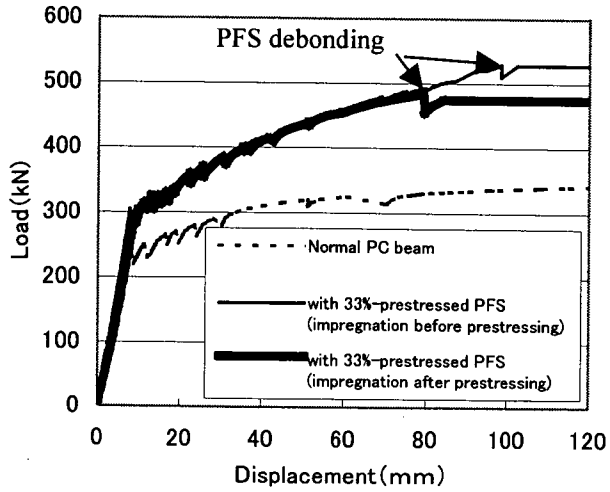

Figure11: bonding capacity without impregnation process

CONCLUSIONS

Based on the results of this study, the following conclusions can be obtained:

1) Through pretension of PFS, significant improvements can be achieved in flexural strength, stiffness and crack resistance of the strengthened structures. The load levels of crack occurrence, compressive crushing of concrete and debonding from the ends of flexural concrete crack have a great increase.

2) The change on failure mode of a PFS-strengthened specimen from PFS debonding to PFS rupture with the increase of introduced pretension force is confirmed. Through the determination of appropriate prestressing stress level of PFS and number of PFS layers, it can be expected that the maximum ability of PFS is displayed and necessary structural performance is achieved.

3) The bonding performance of PFS-concrete interface can be ensured by the proposed air bag system. Moreover, more excellent bonding performance can be achieved by prestressing PFS without resin impregnation by jointly using the air bag system.

REFERENCE

T.C. Triantafillou and Deskovic N., Innovative prestressing with FRP sheet:Mechanics of short-term behavior, Journal of Engineering Mechanics, ASCE, Vol.117, No.7, pp.1653-1672,1991.

Wu Z.S., Matsuzaki T. Fukuzawa K.and Kanda K., *Strengthening Effects on RC Beams with*

Externally Prestressed Carbon Fiber Sheets, Journal of Material, Concrete Structures and Pavements, JSCE, pp.153-165, 2000 (In Japanese).

Wu Z.S., Matsuzaki T., Yokoyama K.and Kanda T., *Retrofitting Method for Reinforced Concrete Structures with Externally Prestressed Carbon Fiber Sheets*, Fourth International Symposium Fiber Reinforced Polymer Reinforcement for Reinforced Concrete Structures, ACI, SP-188, pp.751-765, 2000.

Wu Z. S., Iwashita K., Hayashi K., Higuchi T., Murakami S., Hirahata H., *Strengthening RC beams with externally prestressed PBO fiber sheets, Retrofit of Concrete Structures in Performance-based System*, CONCRETE ENGINEERING SERIES 42, pp. II-43-II-50, 2001.6 (in Japanese)

El-Hacha R., Wight G., and Green. M.F., Strengthening Concrete Beams with Prestressed Fiber Reinforced Polymer Sheets:Behavior at Room and Low, Fourth International Symposium Fiber Reinforced Polymer Reinforcement for Reinforced Concrete Structures, ACI, SP-188, pp.737-749, 2000.

Breakout B2: EARTHQUAKE ENGINEERING 2

(1) Shake Table Test of Bridge Restrainers at Intermediate Hinges
(Fabio Sanchez-Camargo, E. Manos Maragakis, M. Saiid Saiidi and Allaoua Kartoum)

(2) Shaking Table Test of RC Column Subjected to Bilateral Excitation
(Hideaki Nishida, Shigeki Unjoh and Kazuhiro Nagaya)

(3) Cyclic Testing of Steel Bridge Truss Pier Brace Members
(Michel Bruneau, Kangmin Lee and John Mander)

(4) Structural Health Monitoring and Damage Detection with Dynamic Response
(Koichi Yokoyama, Zhishen WU and Bin XU)

SHAKE TABLE TEST OF BRIDGE RESTRAINERS AT INTERMEDIATE HINGES

Fabio Sanchez-Camargo[1], E. Manos Maragakis[2], M. Saiid Saiidi[3] and Allaoua Kartoum[4]

ABSTRACT: Since the 1971 San Fernando Earthquake, cable restrainers have been used at the hinges as retrofit schemes to prevent the unseating of bridge spans. Different approaches have been developed to design cable restrainers, but currently there is not a completely accurate method. An extensive experimental study on seismic response of intermediate hinges retrofitted with cable restrainers is under development at the University of Nevada, Reno. In the initial phase, a set of tests was developed to establish the experimental approach of the dynamic behavior of the cable restrainers. The main objective of the current project is to investigate experimentally the response of intermediate hinges subjected to longitudinal ground motions and to develop a set of charts as a design tool. The variables considered in this study are the period ratio between adjacent frames, the restrainer slack and the type of ground motion. The artificial motions were developed based on current design spectra (ATC-32) for firm, medium and soft soils. A single box-girder model was built and it has been tested on a shake table at the Large-Scale Structural Laboratory of the University of Nevada, Reno. Results show cable restrainers yielding without failure and relative displacements between adjacent frames less than the minimum seat width for cases where the period ratios are higher than 0.7.

Introduction

Most long bridges have intermediate hinges to allow for thermal movements of the superstructure. However, the hinge seat width allows for relative displacements between the adjacent bridge spans during an earthquake. If the relative displacement between frames exceeds the support provided by the hinge seat, the span could collapse. The 1971 San Fernando earthquake showed the collapse of bridge spans due to excessive longitudinal movements (Jennings 1971). The construction practice of that time was to use narrow seats at the hinges, which affected several bridge spans during the 1971 earthquake.

Since 1971, cable restrainers have been used at the hinges as retrofit schemes to prevent the unseating of bridge spans. A sufficient number of cable restrainers in a bridge hinge limits the relative displacements between the girders and, therefore, decreases the possibility of unseating of adjacent spans during strong earthquakes for bridges with inadequate seat widths. Relative movements of adjacent frames are the result of out-of-phase motions due to the different dynamic properties of each frame, such as mass and substructure stiffness (see Fig. 1).

In general, cable restrainers have been effective in preventing span unseating in recent earthquakes. However several bridges that had been retrofitted with cable restrainers suffered significant damage due to unseating during the 1994 Northridge earthquake (Moehle 1995).

[1] PhD Candidate, Dept. of Civil Engineering, University of Nevada, Reno, NV, 89557
[2] Professor and Chair, Dept. of Civil Engineering, University of Nevada, Reno, NV, 89557
[3] Professor, Dept. of Civil Engineering, University of Nevada, Reno, NV, 89557
[4] California Department of Transportation, Sacramento, CA

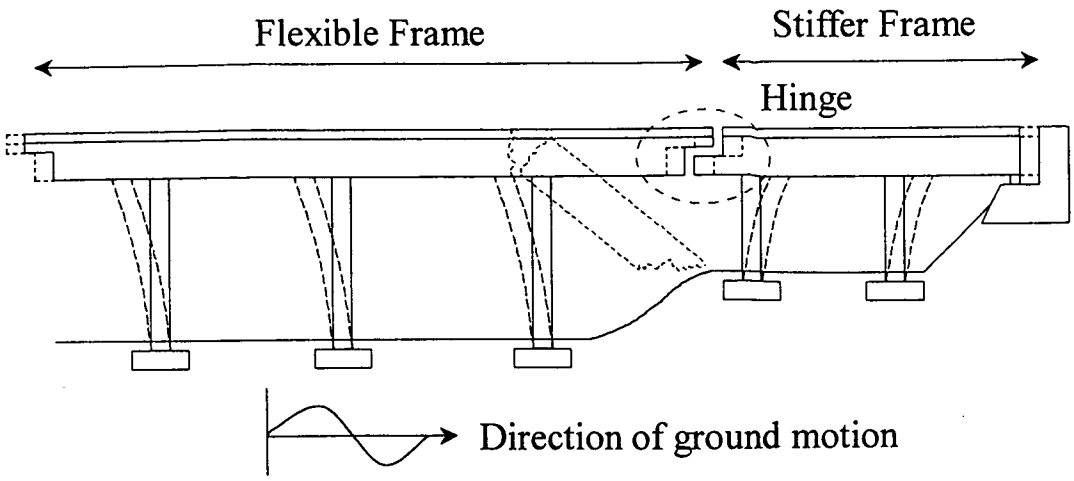

Figure 1: Relative displacement between adjacent frames due to out-of-phase movement.

Several design procedures for restrainers have been developed. The most commonly used is the equivalent static procedure proposed by the California Department of Transportation (Caltrans) (Bridge Specifications 1990). This method is based on the response spectrum analysis method and it assumes that each frame acts independently. The restrainers are designed to remain elastic during the design motion. The equivalent static procedure is unconservative for out-of-phase frames and it is conservative for in-phase frames (Desroches et al., 1998).

Trochalakis et al., (1997) developed a modification of the method proposed by Caltrans. In this procedure, the predicted maximum hinge displacement is a function of the individual frame spectral displacement demands and the ratio between the structural periods of the adjacent frames, in contrast to the static procedure that uses the smaller of the individual frame spectral displacements. This method establishes the maximum hinge displacement based on the case of no restrainers at the frames. The results from this method for frames that are in-phase are close to the results obtained by nonlinear time-history analysis.

The American Association of State Highway and Transportation Officials (AASHTO) specifies a required force to link adjacent frames. This force is equal to the design acceleration coefficient of the site multiplied by the weight of the lighter span (AASHTO 1996). The AASHTO procedure did not account for the structural period of the frames and the relative hinge displacement. These are important parameters in restrainer design of multiple-frame bridges.

Desroches et al (2000) proposed a new method that includes modal analysis. This procedure accounts for the period ratio of the adjacent frames and the frame target displacement ductility. However, it involves an eigenvalue problem in order to evaluate the hinge displacement.

Only two experimental studies have been conducted on this topic. Selna et al (1989) developed a quasi-static cyclic test at the University of California Los Angeles to determine the strength and cyclic behavior of a single box girder retrofitted with restrainers. Vlassis et al (2000) developed the first full dynamic test on cable restrainers. The experimental program was developed on one of the two 100-kip shake tables at the University of Nevada, Reno. This work was the initial

phase of this project. The study demonstrated that the restrainers reduce the intensity of the pounding between frames even if the frames are out-of-phase. It also showed that yielding of the restrainers is expected when the initial slack in the cables is close to zero. Only one period ratio between the adjacent bridge frames was studied and only one ground motion was considered.

The goal of this paper is to describe the procedures and results of an experimental study performed on a single box-girder hinge model that has been retrofitted with cable restrainers subjected to longitudinal earthquake motions. The study consisted of a series of shake table tests performed at the University of Nevada, Reno.

A set of experimental design charts was developed to account for the dynamic characteristics of the bridge frames adjacent to the hinge and the ground motion. These graphs show the relation between the period ratio of two adjacent frames and two of the most important parameters for restrainer design, the relative hinge displacement and the cable restrainer force, considering different values of restrainer stiffness, which is directly related to the number of restrainer cables used at the hinge section.

The parameters that were investigated were the relative displacements at the hinge section, the restrainer forces and the impact forces due to the pounding of adjacent girders. Other variables included the slack of the restrainers and the type of ground motion. In addition, an extensive non-linear analysis was performed to establish the parameters of this study that were used in the experimental work and to compare analytical and experimental results. The analytical investigation is not completed at this point and this paper presents the experimental results only.

Test Configuration

The experimental set up consisted of two concrete blocks representing a single box girder at the hinge section. The dimensions of this model were calculated by averaging the dimensions of several typical bridges used by Caltrans. Stiffness of the cable restrainers was used in proportion of the stiffness of the substructure.

Each block was supported by elastomeric bearings, the stiffness of which was equivalent to the stiffness of the bridge substructure. Three sets of elastomeric pads were used. The whole system was mounted on a uniaxial shake table with 450 kN (100 Kips) payload capacity. Using lead bricks, which could be placed inside each block, the mass of the blocks could be changed. By adjusting the mass of the blocks and using different sets of elastomeric pads, several different ratios of periods between the adjacent frames could be obtained. The experimental set up is shown in Fig. 2.

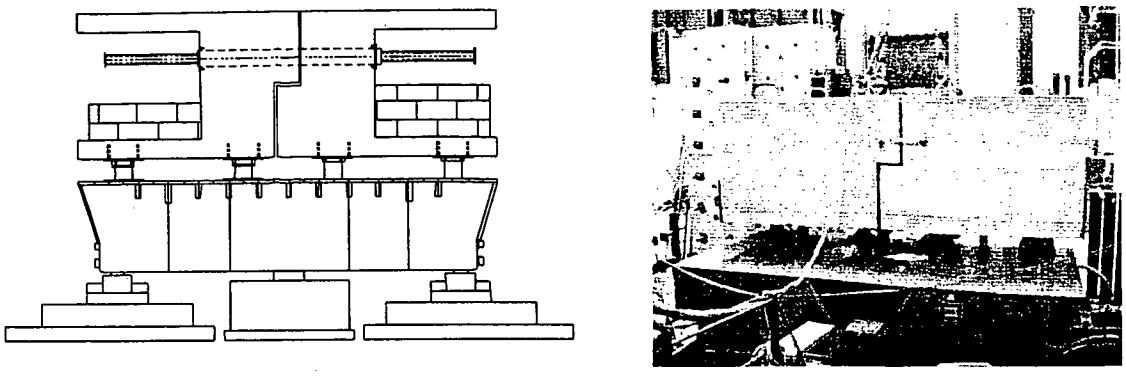

Figure 2: Experimental Set-up

Parameters of Study:

The following parameters were considered in the experimental study.

a) Frame Period Ratio (T_1/T_2): This parameter is equal to the ratio between the structural periods of the two bridge frames, and it is usually taken as the period of the stiffer frame over the period of the flexible frame. In this experimental study the period ratio (T_1/T_2) ranges between 0.4 and 0.9. The ratio of 0.4 relates to a case of highly out-of –phase frames, while the ratio 0.9 describes a case of in-phase frames.

This range includes the usual values found in actual bridges. Different combinations of mass and distributions of different set of elastomeric bearings were used in the experimental model in order to achieve these ratios.

b) Restrainer Stiffness Ratio (R): The stiffness in the cables can be expressed as the product of the smallest frame stiffness and a constant R, which is defined as the restrainer stiffness ratio. Typical bridge designs that include restrainers have a restrainer stiffness ratio in the range of 0.25 to 0.75 (Desroches et al., 1998). Eight values of restrainer stiffness from 0 to 1.6 are used in this study.

c)Restrainer Slack: Two different values were considered, 12.7 mm (½") and 0 mm (0"). The first one is a nominal value for installation of cable restrainers while zero slack accounts for thermal contractions that result in stretching of the cables during extreme environmental conditions.

d) Ground Motion: Caltrans follows the recommendations of the ATC32 to establish the seismic loads in bridges. These recommendations specify different response spectra for acceleration and displacement that are based on the expected magnitude of the earthquake, the soil profile type of the site and the peak ground acceleration of the motion.

The magnitude of the earthquake and the peak ground acceleration (PGA) were selected based on initial analytical studies so that they could produce the maximum effect on the relative displacement and the restrainers force, considering all the limitations of the experimental

components. A magnitude of 6.5 and peak ground acceleration between 0.4g and 0.2g were selected.

Three different soil profiles are used in this study in order to have ground motions with a wide range of frequencies. The soil profiles selected were type B, D and E. (ATC-32, 1996). Type B represents a rock with shear wave velocity between 760 m/s (2500 ft/s) and 1500m/s (5000 ft/s). Type D represents a stiff soil with shear wave velocity that varies from 180m/s (600 ft/s) up to 360 m/s (1200 ft/s). And type E represents a soft soil with shear wave velocity less than 180 m/s (600 ft/s).

In order to match closely the prescribed response spectra for the different soil types, artificial motions were developed using the software SIMQKE. (Gasparini, et al, 1976). Figure 3 shows the "target" response spectra and the achieved response spectra in the range of the structural periods covered for a PGA equal to 0.3g. In all the cases, the values obtained from the artificial motion were within 10% of the specified by the spectra of ATC-32.

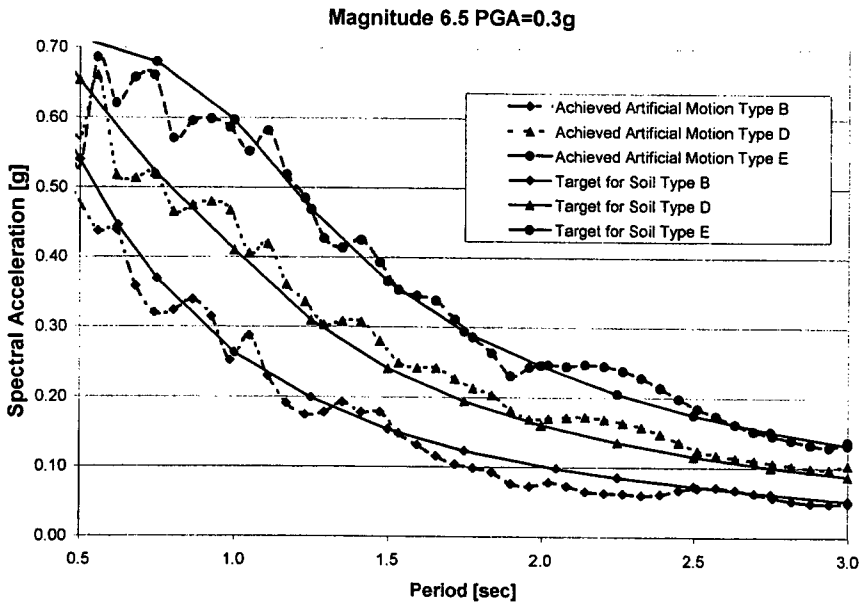

Figure 3. Target and achieved ARS.

Instrumentation

Three displacement transducers were placed on the specimen to measure the relative hinge displacement. One transducer was used on each side and one on top of the hinge region. Four displacement transducers were placed on each corner of the specimen to measure the absolute displacements of each block. A load cell was placed inside the steel link that holds the restrainers to measure directly the force of the cables. Four external accelerometers were placed on the interior corners of each block to measure the acceleration at each block at the superstructure level and to establish the maximum acceleration due to the pounding of the frames. In addition

the shake table has three more transducers that measure the input acceleration, displacement and velocity. All the channels were scanned at a frequency of 200 Hz (200 data points per second).

Analysis

Preliminary nonlinear response history analyses of the experimental set-up have been performed. The program DRAIN-3DX (Prakash et al., 1993) was used to calculate the response history of the system. A total of 540 different combinations were used in this analysis. These included two sets of slack in the cable restrainers, six period ratios, eight restrainer stiffness ratios (R) and three different ground motions with two different peak ground accelerations.

Experimental Results

A series of experimental graphs were developed as a result of this study. Mainly, the results are presented as a function of the period ratio T_1/T_2, considering the variation of the restrainer stiffness, the restrainer slack and the type of ground motion. The principal parameters analyzed are the maximum relative displacement at the hinge, the force of cable restrainers and the absolute acceleration of each girder due to pounding.

Due to the fact that the ground motions used have very similar response spectra to the design spectra from the ATC32, the results of this study could be used for the development of design specifications for cable restrainers without performing nonlinear time history analysis.

Selected results are presented in the subsequent sections of this paper. In order to show the importance of the differences of ground motions, two cases with different excitations are presented. The first is of ground motion corresponding to firm soil and the second is a case corresponding to soft soil. Only the variations of relative hinge displacement and restrainer force are presented while the restrainer slack is maintained as 12.7mm (0.5") in both cases. The last section describes the variation of the restrainer force for the two different cable slacks considered.

<u>Results for Soil Type B (Firm Soil) PGA=0.3g</u>

Figure 4 shows the maximum relative hinge displacement as a function of the period ratio for different values of restrainer stiffness for a cable slack equal to 12.7 mm (0.5"). As reference the case of no restrainer was evaluated. The relative displacement was reduced by an amount between 20% and 50% when restrainers were used. The maximum reduction occurs when the number of cables was maximum, which corresponds to the highest restrainer stiffness used (R=1.6). An increase in the hinge displacement is observed as the period ratio decreases.

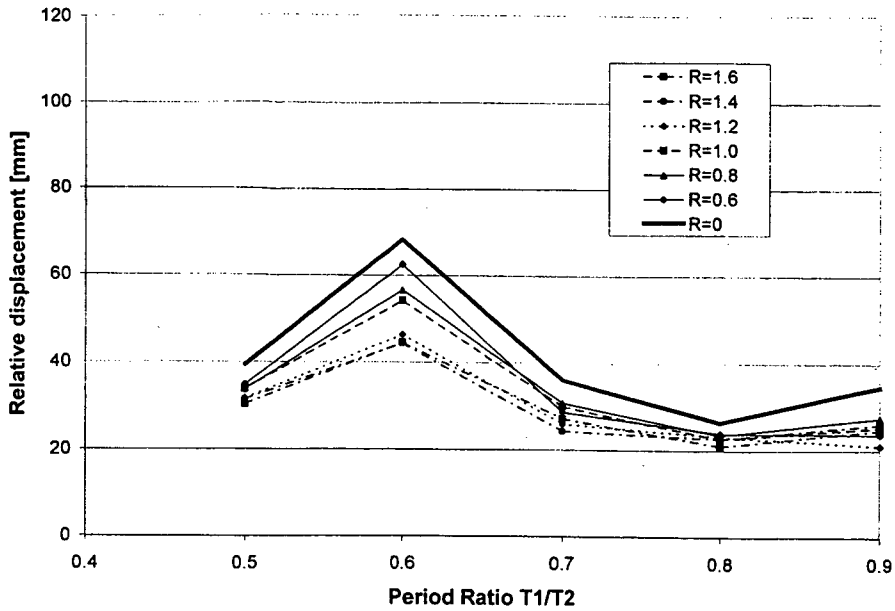

Figure 4: Maximum Relative Hinge Displacements for Firm Soil (Type B), PGA=0.3g, Cable slack=12.7mm (0.5")

The restrainer force remains almost constant for period ratios greater than 0.7. Also, the force obtained for these cases remains within the elastic range. For period ratios smaller than 0.7, the measured force is higher than the yielding force and permanent deformations were noticed on the cables. Figure 5 shows the restrainer force as a function of the period ratio for different values of restrainer stiffness ratios and a cable slack equal to 12.7 mm (0.5").

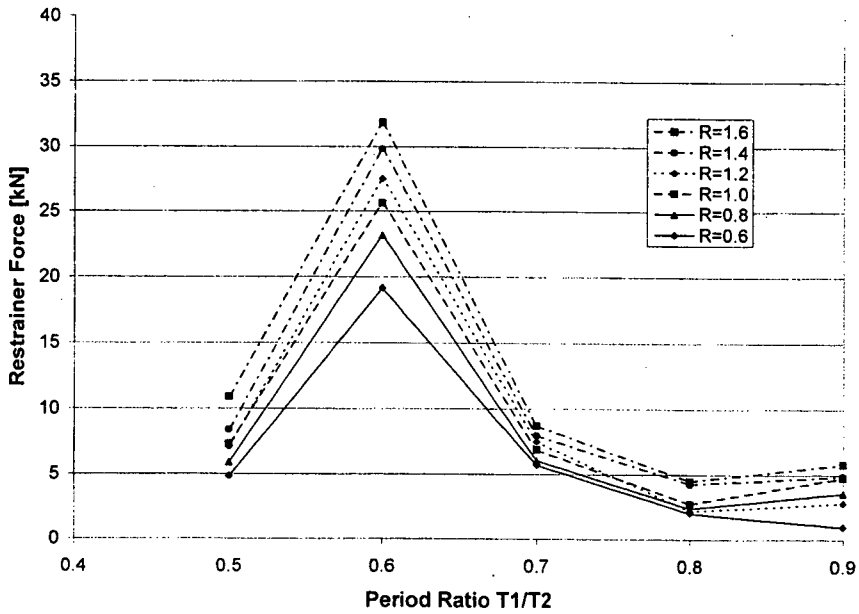

Figure 5: Maximum restrainer force for Ground Motion for Firm Soil (Type B), PGA=0.3g, Cable slack=12.7mm (0.5")

Results for Soil Type E (Soft Soil) PGA=0.2g

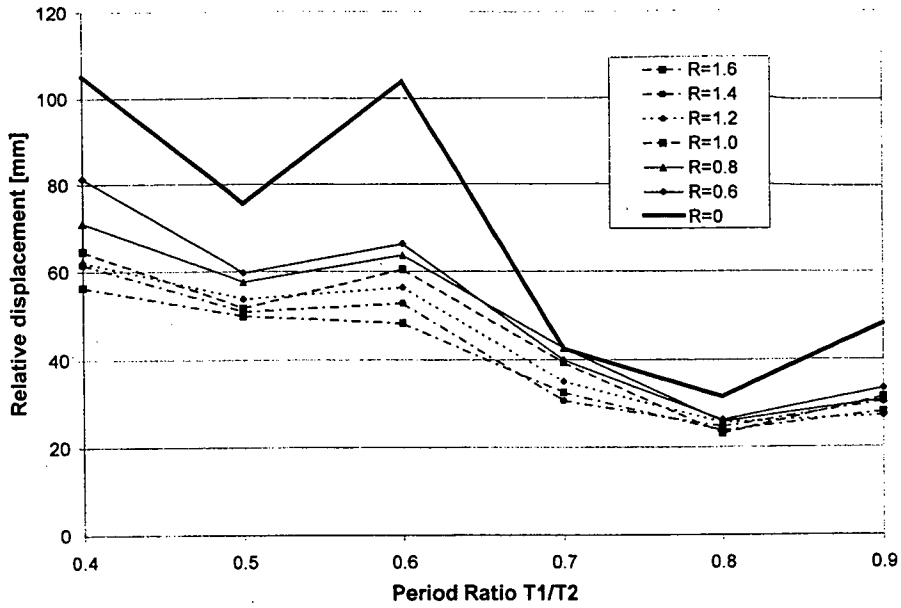

Figure 6: Maximum Relative Hinge Displacements for Soft Soil (Type E) PGA=0.2g, Cable slack=12.7mm (0.5")

Similar behavior is experienced in the soft soil motion. However the maximum hinge relative displacements are higher and in some cases are more than 50% of the values obtained for firm soil. This is due to the shape of the response spectra for the same periods. The values of the maximum relative hinge displacements for soft soil as a function of the period ratio for different restrainer stiffness ratios are shown in Fig. 6.

Figure 7 shows the restrainer force as a function of the period ratio for different values of restrainer stiffness ratios and cable slack equal to 12.7 mm (0.5") for the case of soft soil. One can observe that the restrainer force remains elastic for all the cases of period ratios greater than 0.8. In several cases of period ratio equal to 0.7 the restrainers began to yield and large inelastic deformations occurred. There is not a significant difference in the results obtained for period ratios greater than 0.8 for the different restrainer stiffness ratios studied. However for values of period ratio smaller than 0.8, significant changes in displacements and forces are observed.

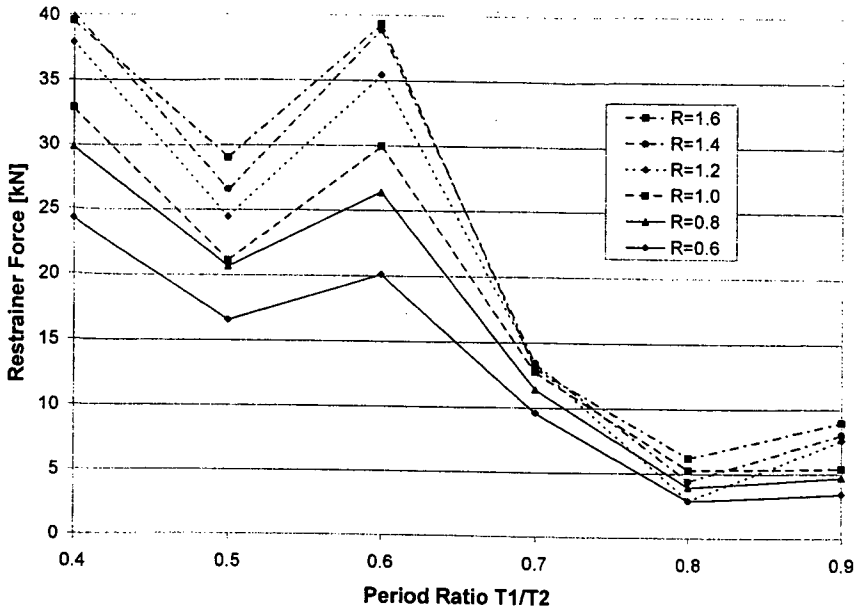

Figure 7: Maximum restrainer forces for Ground Motion for Soft Soil (Type E), PGA=0.2g, Cable slack=12.7 mm (0.5")

Effects of cable slack on Restrainer Force:

Figure 8 shows the effects of the restrainer slack on the maximum restrainer force. The figure shows the variation of the restrainers force as a function of the period ratio for firm soil, peak ground acceleration equal to 0.3g and two restrainer stiffness ratios (R=0.8 and R=1.2).

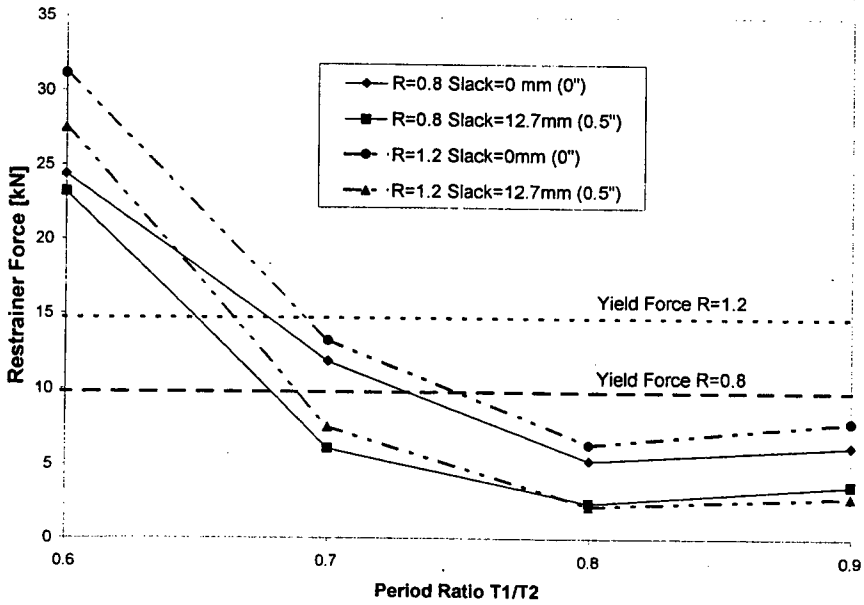

Figure 8: Comparison of the maximum restrainer forces for Firm Soil (Type B), PGA=0.3g, and the yield force for R=0.8 and R=1.2

For each value of R two values of restrainer slack are used: 0 mm (0") and 12.7 mm (0.5"). The horizontal dotted lines represent the yield force for the case of R=0.8 and R=1.2. It can be seen that in all the cases the restrainer forces are greater when the slack is equal to zero. It can also be seen that for values of period ratios greater than 0.7 the restrainer forces remain elastic. This was also observed in the cases of medium and soft soils.

Conclusions

Based on the results presented in this paper, the following conclusions can be drawn from the experimental study.

1. The most critical case of restrainer slack is the case when the initial slack is equal to zero. In this case the restrainers are engaged immediately during the excitation, and the forces on the cable restrainers are higher than in the case on 12.7 mm (0.5") slack

2. The ground motion for soft soil was the most critical between the three different soil types considered. From the response spectra it can be determined that for all the periods used in the study the accelerations of the soft soil motion were higher.

3. For all the ground motions considered in this study, cable restrainers remained elastic and the relative displacements of adjacent frames were smaller than the minimum seat width, for period ratios greater than 0.7

It should be mentioned that this is consistent with current design procedures (Bridge Specifications 1990) for period ratios greater than 0.7. For period ratios less than 0.7 the restrainers yielded and therefore the assumption of elastic behavior as specified in current methods is unrealistic.

4. When the restrainer stiffness ratio is greater than 0.8, the intensity of the pounding between the adjacent bridge spans is reduced. The restrainers work as a link between the adjacent spans and reduce the relative hinge displacements. This could result in the reduction of damage at the hinge.

Acknowledgments

This experimental study was funded by the California Department of Transportation. Their financial support and their technical input are gratefully acknowledged.

References

AASHTO (1996). "Standard Specifications for Highway Bridges," American Association of State Highway and Transportation Officials, Sixteenth Edition.

ATC 32 (1996) "Improved Seismic Design Criteria for California Bridges: Provisional Recommendations" Applied Technology Council, Redwood, California

Bridge Specifications (1990) California Department of Transportation, California

CALTRANS (1993). "Bridge Design Specifications," California Department of Transportation, January.

CALTRANS (1999). "Memo to Designers," California Department of Transportation, January.

DesRoches, R., Fenves, G. (1998) "Design Procedures for Hinge Restrainers and Hinge Seat Width for Multiple-Frame Bridges" Rep MCEER-98-0013, Multidisciplinary Center for Earthquake Engineering Research, University at Buffalo, state University of New York, Buffalo

DesRoches, R., Fenves, G. (2000) "Design of Seismic Cable Hinge Restrainers for Bridges" J. Struct. Engrg., ASCE 126 (4), 500-509

Gasparini, D. A., Vanmarcke, E. H., (1976) "Simulated Earthquake Motions Compatible with Prescribed Response Spectra", Report No. 2 Evaluation of Sesimic Safety of Bulidings, Massachusetts Institute of Technology, Cambridge, Massachusetts, January

Hudgings, T., Eberhard, M. O., and Stanton, J. F. (1997). "Design of Seismic Bridge Restrainers Considering Spatial Variation of Ground Motions," Report No. SGEM 97-2, Civil Engineering Department, University of Washington, Seattle, WA, July.

Jennings, P. C. (1971). "Engineering Features of the San Fernando Earthquake of February 9, 1971," Report No. EERL-71-2, Earthquake Engineering Research Laboratory, California Institute of Technology, Pasadena, CA, December.

Moehle, J. P. (1995). "Northridge Earthquake of January 17, 1994: Reconnaissance Report, Volume 1, Highway Bridges and Traffic Management," Earthquake Spectra, Vol. 11 (No. 3), pp. 287-372.

Prakash, V., Powell, G. H., and Fillipou, F. C. (1993). "DRAIN 3DX: Base Program User Guide," Structural Engineering, Mechanics and Material, Department of Civil Engineering, University of California, Berkeley, CA, November.

Randall, M. J., Saiidi, M., Maragakis, E., and Isakovic, T. (1998). "Restrainer Design Procedures for Multi-Span Simply Supported Bridges," Report No. NCEER-98-4, Civil

Engineering Department, University of Nevada, Reno, NV, April.

Saiidi, M., Maragakis, E., Abdel-Ghaffar, S., Feng, S., and O'Connor, D. N. (1993). "Response of Bridge Hinge Restrainers During Earthquakes-Field Performance, Analysis, and Design," Report No. CCEER-93-6, Civil Engineering Department, University of Nevada, Reno, NV, May.

Saiidi, M., Maragakis, E., and Feng, S. (1992). "An Evaluation of the Current CALTRANS Seismic Restrainer Design Method," Report No. CCEER-92-8, Civil Engineering Department, University of Nevada, Reno, NV, October.

Seismic Design Criteria (1999) California Department of Transportation, California

Selna, L. G., Malvar, L., and Zelinski, R. (1989). "Bridge Retrofit Testing: Hinge Cable Restrainers," Journal of Structural Engineering, ASCE, Vol. 115 (No. 4), pp. 920-933.

Trochalakis, P., Eberhard, M. O., and Stanton, J. F. (1995). "Evaluation and Design of Seismic Restrainers for In-Span Hinges," Report No. WA-RD 387.1, Washington State Transportation Center, Seattle, WA, August.

Vlassis A., Maragakis E. and Saiidi M. (2000) "Experimental evaluation of seismic performance of bridge restrainers" Thesis (M.S.)--University of Nevada, Reno.

Yang, Y. S., Priestley, M. J. N., and Ricles, J. (1994). "Longitudinal Seismic Response of Bridge Frames Connected By Restrainers," Report No. UCSD/SSRP-94-9, Structural Systems Research Project, University of California, San Diego, La Jolla, CA, September.

SHAKING TABLE TEST OF RC COLUMN SUBJECTED TO BILATERAL EXCITATION

Hideaki Nishida[1], Shigeki Unjoh[2] and Kazuhiro Nagaya[3]

Abstract

In order to study the effects of the bilateral excitation on response characteristics of the reinforced concrete (RC) column, shaking table tests and the dynamic analyses using fiber element model were carried out. The test results showed that the failure of the cover concrete and the buckling of the longitudinal reinforcement were developed in the 4 surfaces in the case of bilateral excitation. The failure mechanism of the column subjected to bilateral excitation was found to be different from that subjected to the unilateral excitation. It was also found that the dynamic analysis using fiber element model could simulate the experimental column behavior well before deterioration of the strength of column, and that the analyzed response displacement of the column subjected to bilateral excitation has the tendency to be larger than that subjected to unilateral excitation.

1. Introduction

In general, the earthquake response of structures is a three-dimensional behavior to respond to a three-dimensional earthquake ground motion. Considering these effects, some of the seismic design codes adopt seismic load which is the combination of contributions from 2 or 3 components of ground motion (e.g. [1) 2) 3)]). In these codes, 2 or 3 orthogonal components of seismic load are combined by square-root-of-sum-squares or by sum of each component. But the theoretical background of these combination rules is not clear. On the other hand, current Japanese seismic design codes for buildings and bridges consider seismic load independently for principal axes of the structure. Therefore, it is necessary to evaluate the effects of multi-orthogonal components excitation to adopt the effects in Japanese seismic design codes.

There are 3 research issues to evaluate the effects of multi-components excitation as:

(1) Bilateral bending and torsion effects for structural members
(2) Directional uncertainly of ground motion
(3) Behavior of whole bridge system for complex three-dimensional structures

There were several experimental and analytical studies on issue (1). For example, Hiraishi et al. (1993)[4)] showed that the nonlinear behavior of the RC columns subjected to bilateral loading could simulate well using fiber element model analysis. As the approach

[1] Researcher, Earthquake Engineering Research Team, Public Works Research Institute
[2] Team Leader, ditto
[3] Engineering Official, International Division for Infrastructure, Policy Bureau, Ministry of Land, Infrastructure and Transport

in other analyses, bilateral bending model using beam element analysis that based on plastic flow rule was proposed. According to this rule, the direction of the incremental plastic strain vector and tangent of plastic potential function intersect perpendicularly. If it assumes that associated flow rule is realized, plastic potential function can be replaced with loading function such as yield function. Kobayashi et al. (1993) [7] showed that the response displacement of the column in the inelastic range was followed this rule. But these results were conducted from static loading.

Several dynamic analyses of the column subjected to bilateral excitation were carried out (e.g. [11]). The results showed that it was necessary to pay attention to bilateral excitation effects in three-dimensional nonlinear analysis. On the other hand, there were few experimental studies on the dynamic response characteristics of the column subjected to bilateral excitation (e.g. [10]). This means that it is not clear these things can be applied to the column subjected to dynamic loading or not.

This paper presents the dynamic response characteristics of the RC column subjected to bilateral excitation based on the shaking table tests and the fiber element model analyses.

2. Shaking Table Tests

2.1 Test Specimen

Test specimen is shown in Fig.1. The definition of coordinate system is also shown in this figure. The dimension was designed as 600×600mm square of cross section, and the height from the base of column to the center of inertia force is 3,000mm. The scale factor was assumed as about 4 compared to the prototype structure. The weight at the top of column was determined so that the axial compressive stress at the base of column was 1.0MPa. The longitudinal reinforcement consisted of SD295A, D10 (a longitudinal reinforcement ratio of 0.95%), with 40mm concrete cover. The hoop reinforcement consisted of SD295A, D6 was placed with the space of 75mm. Each hoop reinforcement has 135-degree hook with 60mm hook length at the corner between the surface of M and A, and P and B alternatively.

The strain gauges were installed to measure the strain of the longitudinal reinforcement that located at the corner near the base of column.

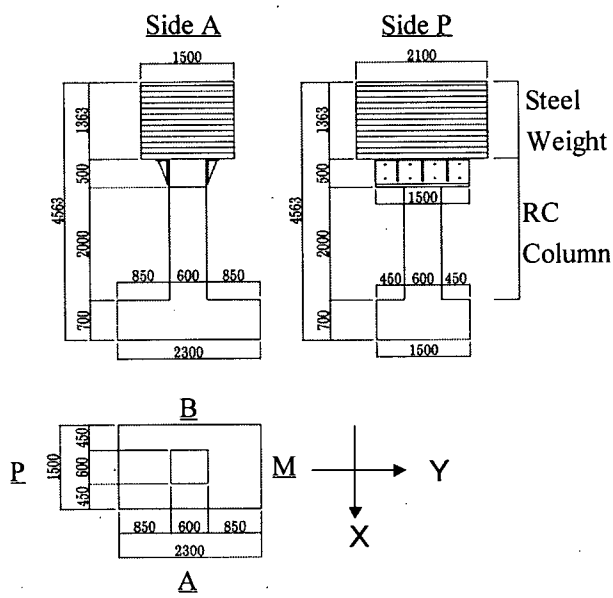

Fig.1 Test Specimen (unit: mm)

Table 1 Material Properties (unit: MPa)

	Stress	Young's modulus
Concrete	34.1 (Compression)	3.27×10^4
Longitudinal reinforcement	515 (Yield)	1.83×10^5
Hoop reinforcement	480 (Yield)	1.85×10^5

The material properties when the column was tested are listed in Table 1.

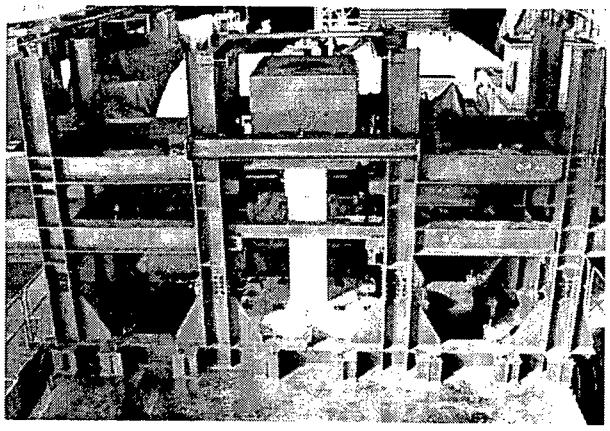

Photo 1 Test Setup

2.2 Testing Program

In the testing program, two series of excitation were made. One was the test excited using the input wave with small amplitude so that the column be within elastic range (Case1); the other was the test excited using input wave with the large amplitude so that the column be in the inelastic range of the column (Case2). In addition, microtremor of the column was measured after the excitations in order to check the stiffness deterioration of the column from the change of predominant frequency.

The JR Takatori station record from the 1995 Hyogo-ken Nanbu Earthquake (Fig.2) [9] was used as the source of input waveform. The time scale was reduced by a factor of 50%. And the amplitude scale was compressed by 20% for Case1. This compressed amplitude was determined based on the dynamic fiber element model analysis so that all of the longitudinal reinforcement was within elastic range. The amplitude scale for Case2 was determined as 100% of the above waveform which was slightly larger than the ductility capacity of the model.

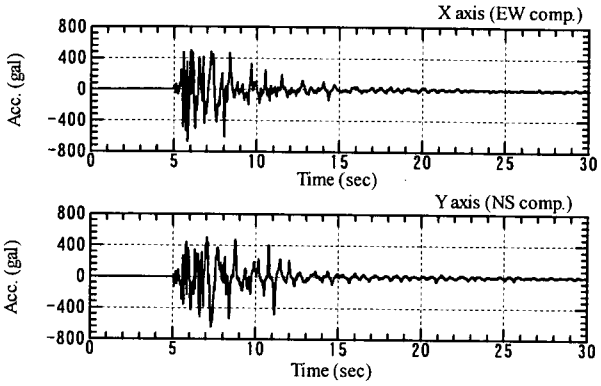

Fig.2 Input waveform
(JR Takatori Station Record)

2.3 Test Results

Absolute response acceleration and relative response displacement that were measured at the center of inertia force are shown in Fig.3 (Case1) and Fig.4 (Case2). In the figures, the analytical results which will be discussed later are also shown.

In Case1, the shape of orbit of acceleration and that of displacement is found to be similar. The maximum strain of longitudinal reinforcement was less than 1,500 microstrains that was just about predicted. Moreover, no damage was found. These results showed that the relationship between acceleration and displacement was linear, and that the effect of bilateral excitation was little in the elastic range.

In Case2, the clear difference was found between acceleration and displacement responses. The difference of the column behavior took place after maximum response displacement (X direction; 140mm, Y direction; 200mm). This time corresponded to the change from elastic to inelastic of the column behavior rapidly. The predominant frequency which was predicted from microtremor [8] is listed in Table 2. Deteriorating the

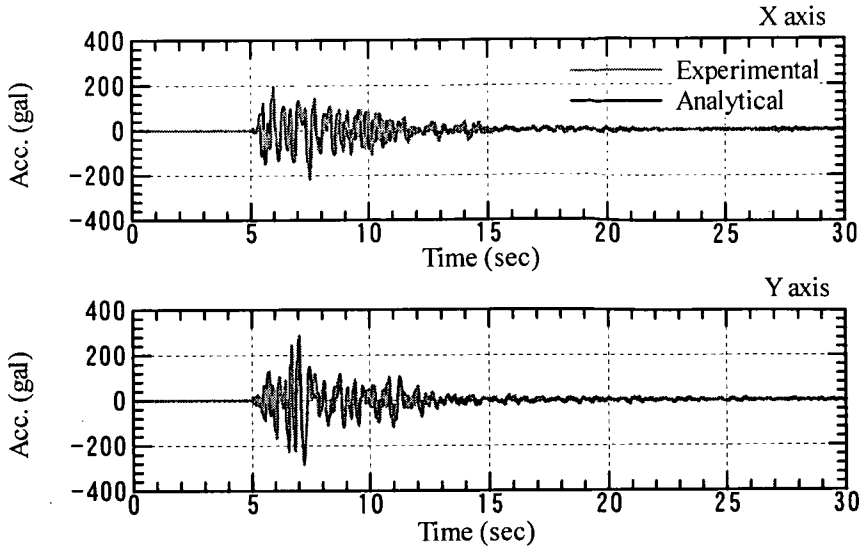

(1) Time history of Response Acceleration

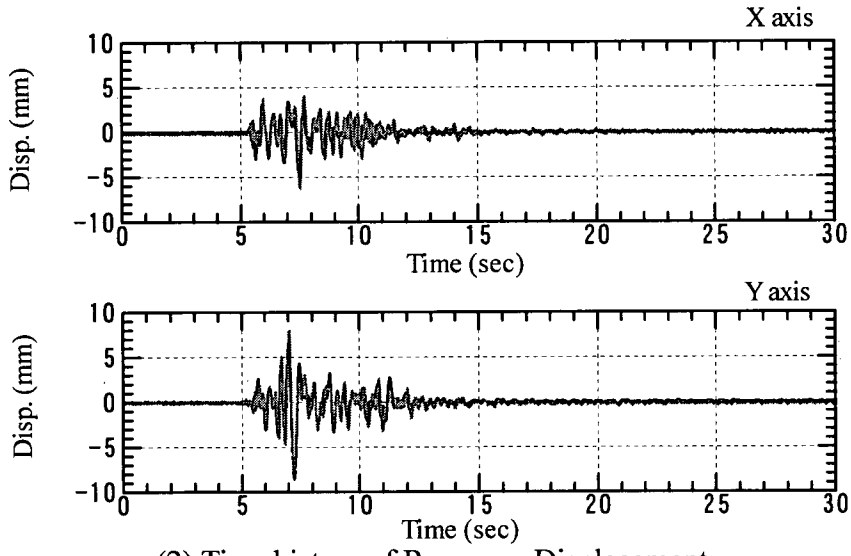

(2) Time history of Response Displacement

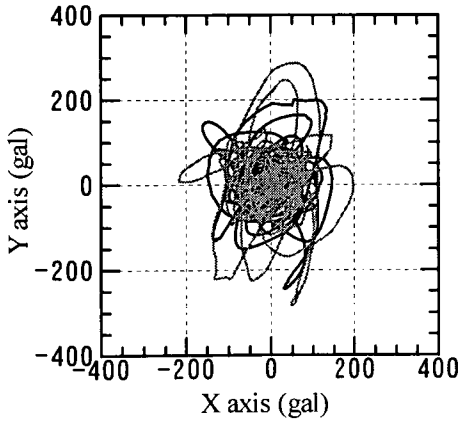

(3) Orbit of Response Acceleration

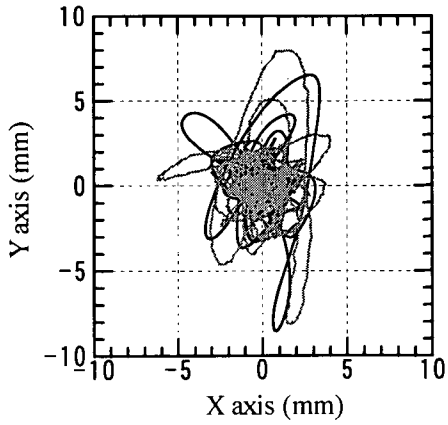

(4) Orbit of Response Displacement

Fig.3 Test Results and Comparison of the Experimental and Analytical Results
(Case1: Elastic Response)

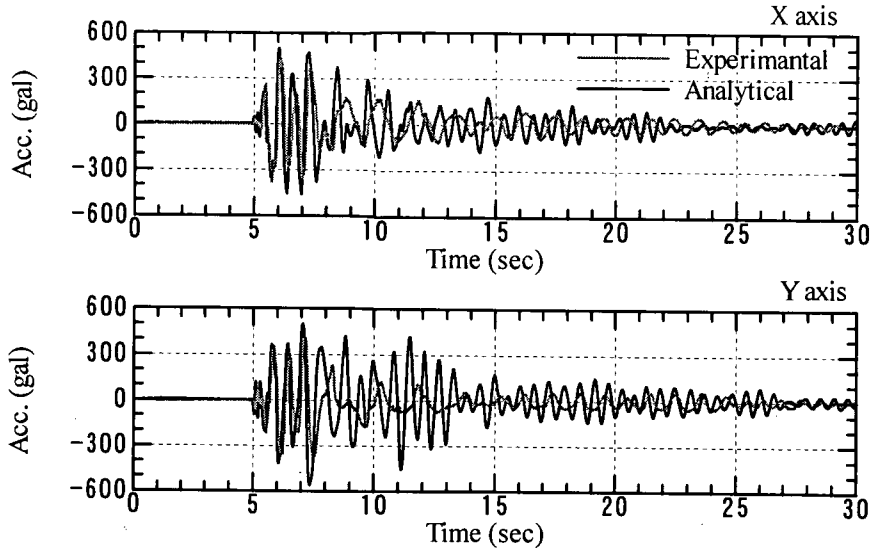

(1) Time History of Response Acceleration

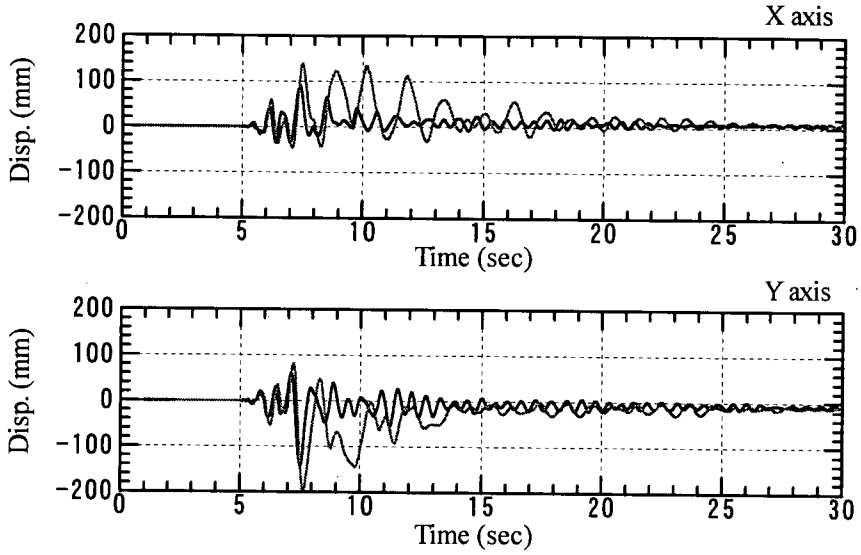

(2) Time History of Response Displacement

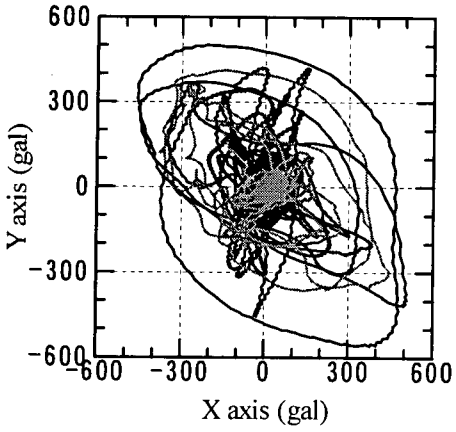

(3) Orbit of Response Acceleration

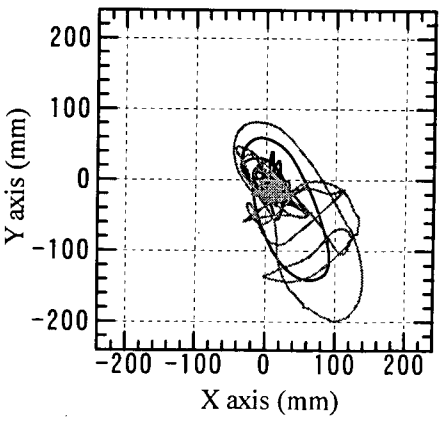

(4) Orbit of Response Displacement

Fig.4 Test Results and Comparison of the Experimental and Analytical Results
(Case2: Inelastic Response)

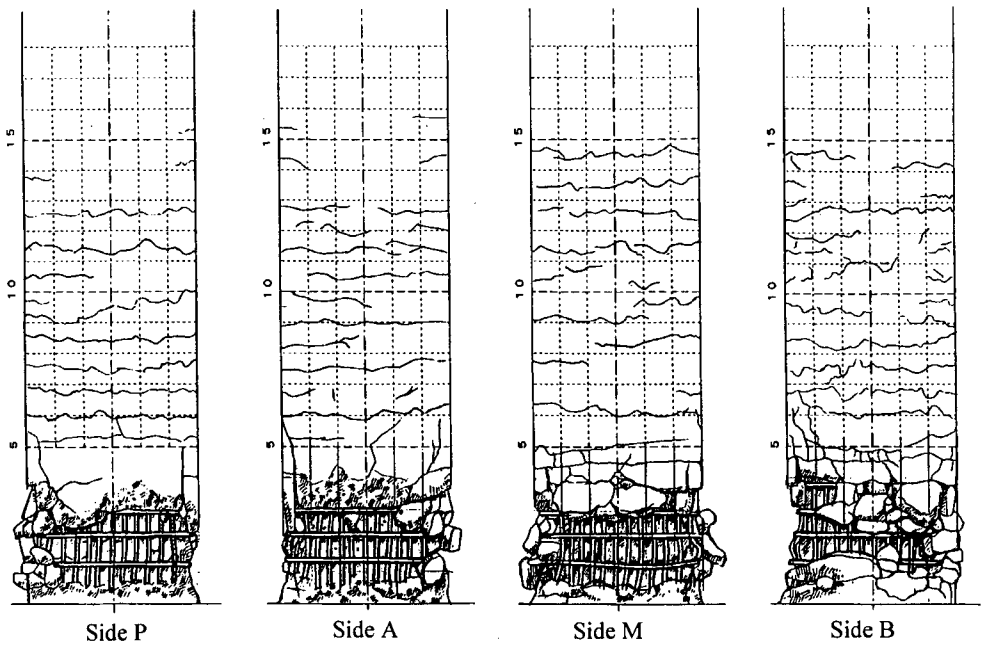

Fig.5 Damage of Tested Column after Case2 Shaking

column stiffness was confirmed from the change of the predominant frequency. This result presumed that the column stiffness after Case2 shaking deteriorated about 20% of the original. The residual displacement was about 10mm of each direction.

Table 2 Predominant Frequency (Unit : Hz)

Direction	Before Test	After Case1	After Case2
X	3.96	3.71	2.00
Y	4.30	4.10	1.86

Two characteristics are found in the column behavior in inelastic range. Firstly, in spite of the absolute value of response displacement increases, the absolute value of response acceleration doesn't increase. The column subjected to unilateral excitation also shows this character. Secondly, the direction of response acceleration is different from that of response displacement. For example, when the orbit of response displacement increases in a certain direction, that of response acceleration behaves like a circle-shape. The column subjected to unilateral excitation doesn't show this character because of lack of directional concept. As for such behavior of the RC column, past researches also showed. These characters indicate that it is important to include the effects of bilateral excitation to estimate maximum response value and maximum response direction of the column, especially in inelastic range.

The observed damage after Case2 shaking is shown in Fig. 5. Spalling of the cover concrete, cracking of the confined concrete and buckling of all of the longitudinal reinforcements were found. The beginning of spalling of the cover concrete corresponded with the time of maximum response displacement. Spalling of the cover concrete were developed in the 4 surfaces near the base of column over a height of about 500mm and cracking of the confined concrete was found over a height of about 150mm. The buckling length of longitudinal reinforcement was varied with the location. The hook of hoop reinforcement, which located at the height of 150mm (MA corner) and 225mm (PB corner)

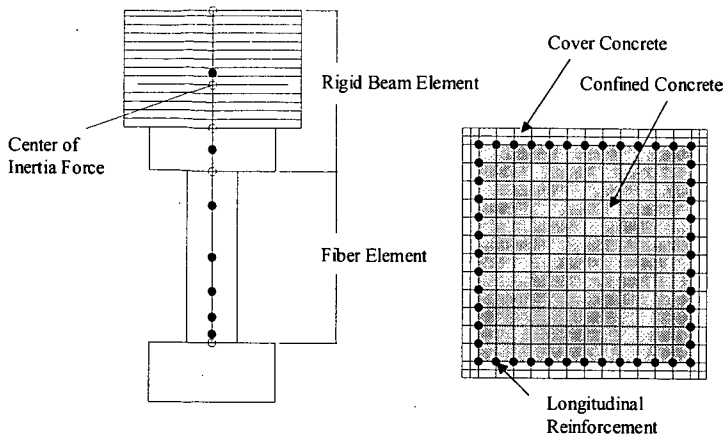

(a) Column Model (b) Fiber Element of Cross Section

Fig.6 Analytical Model

from the base of column, were unhooked. These points corresponded with the maximum curvature of buckling longitudinal reinforcement.

3. Analysis

3.1 Analysis Method

Fiber element model analysis is one of methods to simulate the bilateral excitation effects. Several researches showed that this method could simulate well for the static loading tests. Therefore, time history analyses using fiber element model were carried out and the applicability of the analysis method was examined in this study.

A column model is shown in Fig. 6(a). The steel plates and beam were modeled as rigid beam element, and the column was modeled as fiber element with confined concrete, cover concrete and longitudinal reinforcement (Fig. 6(b)). The analytical material properties were assumed based on the experimental values listed in Table 1. The stress-strain relationships were adopted as follow; (1) Kent & Park rule [6] for cover concrete, (2) the Japanese highway seismic design code model [5] for confined concrete, (3) bilinear model with second stiffness ratio was 1% for longitudinal reinforcement.

The acceleration recorded on the shaking table was used as input wave. The recorded acceleration was assumed to be input directly to the base of column. Newmark β method (β=0.25) was used for the integration, damping ratio was assumed as 2%, and the time step of the integration was assumed 0.001 second.

Two cases were analyzed: subjected to unilateral excitation and bilateral excitation.

3.2 Analytical Results

Comparisons of the analytical and experimental results at the center of inertia force are shown in Fig.3 (Case1) and Fig.4 (Case2).

In Case1, analytical and experimental results are well agreed for all time. In Case2, the shape of orbit of analytical result is close to that of experimental one. Fig. 7 shows that the correlation is well before maximum response displacement. It was found that fiber element model analysis could simulate the experimental column behavior well until the ultimate state (before deterioration of the strength of the column), although it was assumed that the simple material stress-stain characteristic models were used.

These differences after maximum response displacement were caused by the fiber element model's assumption that the cross section keeps plane and using bilinear model of the longitudinal reinforcement. Strictly, the assumption that the cross section keeps plane is not correct, for example, when cracking of the concrete is occurred. In addition, bilinear model of the longitudinal reinforcement cannot include the buckling and Bauschinger effect. These effects become large in inelastic range. If the modeling of the reinforcement that takes these effects appropriately is chosen, the correlation in inelastic range might be improved.

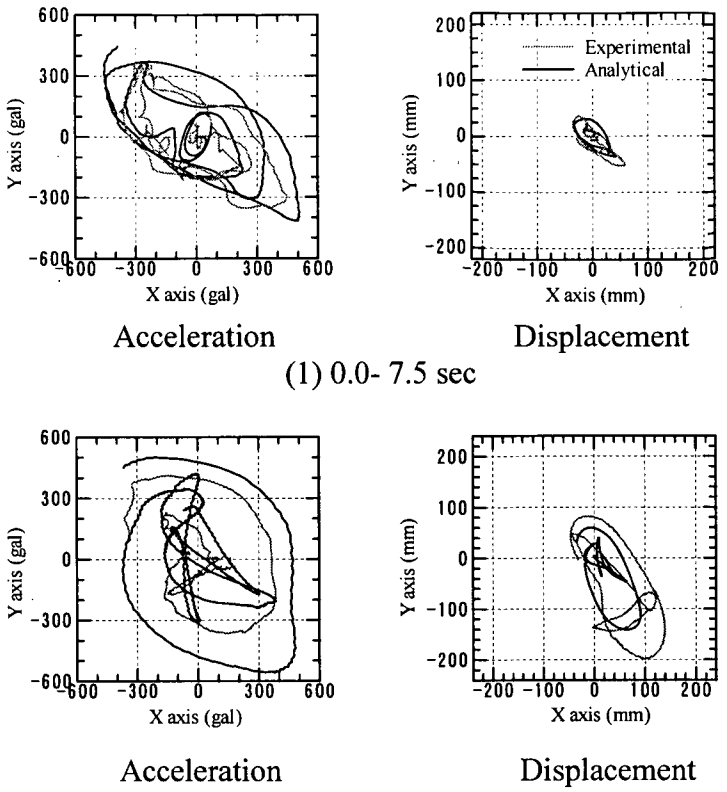

Fig.7 Comparison of the Experimental and Analytical Results (Case2)

3.3 Evaluation of Bilateral Excitation Effects

Comparisons of unilateral excitation and bilateral excitation are shown in Fig.8 (Case1) and Fig.9 (Case2).

In Case1, they show good agreement. This result shows that the effects of bilateral excitation within elastic range are little, therefore the column behavior can approximate as combining orthogonal unilateral excitation results.

On the other hand, in Case2, acceleration of the column subjected to unilateral excitation is larger than that of the column subjected to bilateral excitation. Furthermore, the shape of acceleration orbit of the column subjected to unilateral excitation is different from that subjected to bilateral excitation in inelastic range. It behaves like a square-shape in the former case, but it behaves like a circle-shape in the latter case. This is because the column stiffness change of unilateral excitation analysis is computed independently for each direction. This fact indicates that the effect of bilateral excitation is remarkable for inelastic

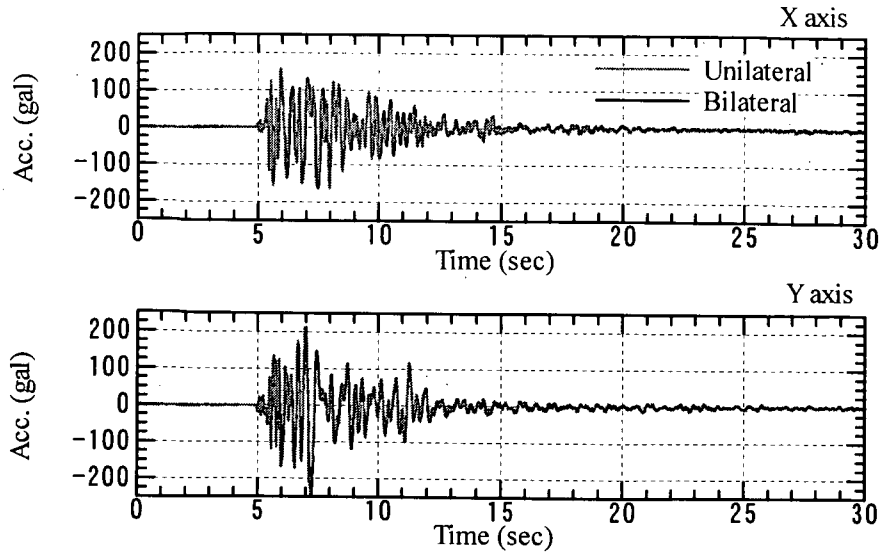

(1) Time History of Response Acceleration

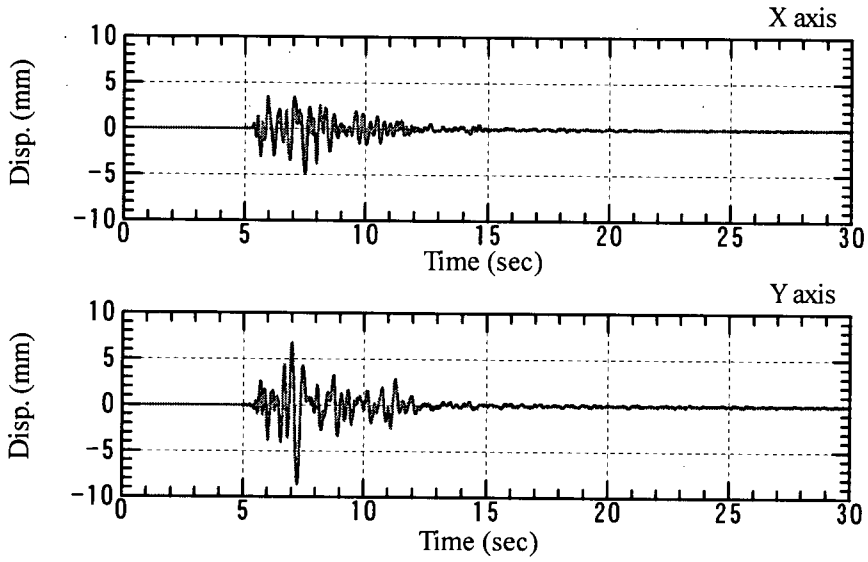

(2) Time History of Response Displacement

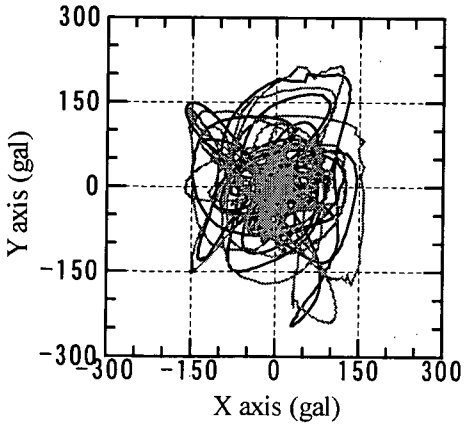

(3) Orbit of Response Acceleration

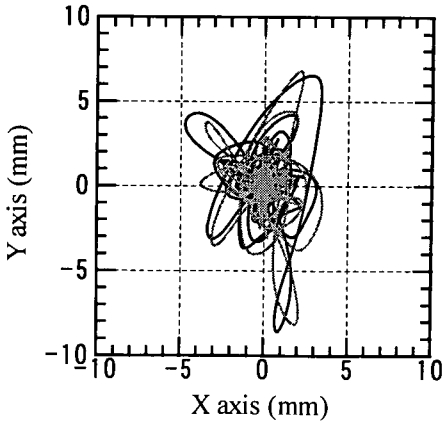

(4) Orbit of Response Displacement

Fig.8 Comparison of Unilateral Excitation and Bilateral Excitation Analyses (Case1)

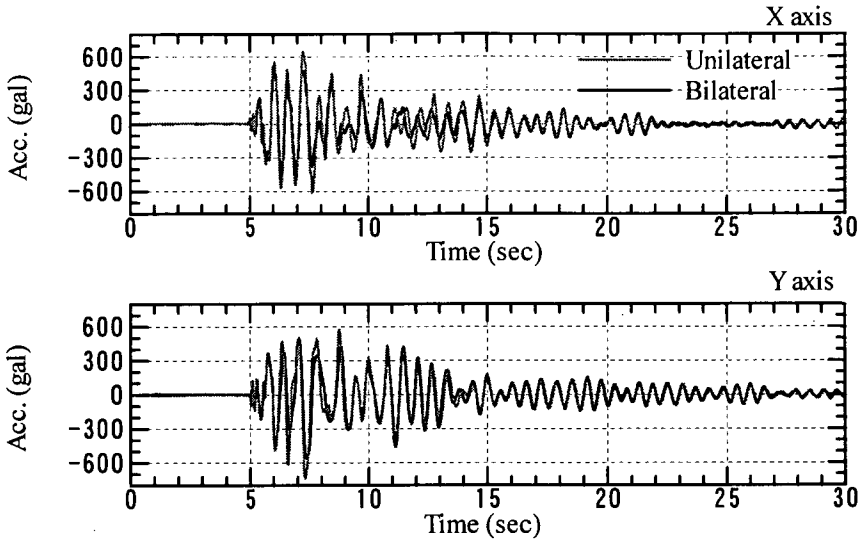

(1) Time History of Response Acceleration

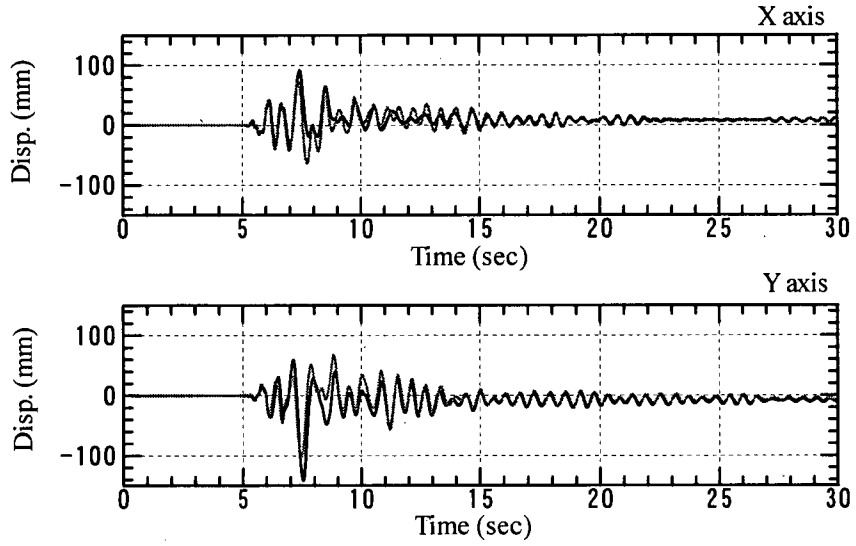

(2) Time History of Response Displacement

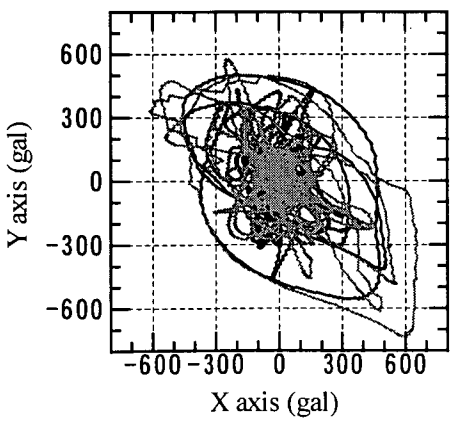

(3) Orbit of Response Acceleration

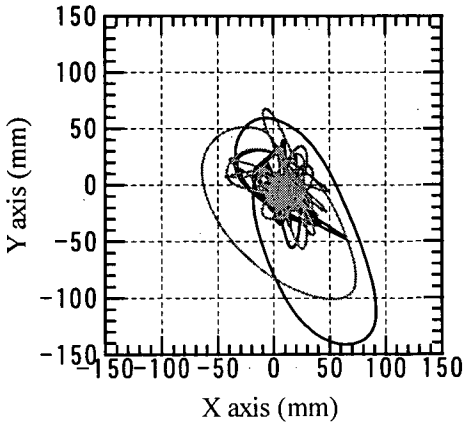

(4) Orbit of Response Displacement

Fig.9 Comparison of Unilateral Excitation and Bilateral Excitation Analyses (Case2)

range particularly.

4. Conclusions

(1) Shaking table tests for a square reinforced concrete column were carried out. The test results showed that the failure of the cover concrete and the buckling of the longitudinal reinforcement were developed in the 4 surfaces in the case of bilateral excitation. The failure mechanism of the column subjected to bilateral excitation was found to be different from that subjected to the unilateral excitation. This effect was represented by the difference of the column behavior. Comparison of the shape of orbit of response acceleration and that of response displacement, it is found to be similar in the elastic range, but not similar in inelastic range.

(2) Fiber element model analysis of the column subjected to bilateral excitation could simulate the experimental column behavior well before deteriorating strength of the column from comparison with experimental results.

(3) The effect of bilateral excitation is remarkable for inelastic range particularly. Response displacement of the column subjected to unilateral excitation is smaller than that subjected to bilateral excitation in inelastic range.

References

1) AASHTO(1996) ,Standard Specifications for Highway Bridges, 16th Edition
2) Caltrans(1999) , Seismic Design Criteria Version 1.1
3) European Committee for Standardization (CEN) (1996) , Eurocode8
4) Hiraishi, H., Murata,Y., Kaminosono, T., and Yagenji, A. (1993) "Post-yield Behavior of Reinforced Concrete Columns subjected to Bilateral Deformations under Axial Load", pp.115-125, Journal of Structure Construction Engineering, AIJ, No.454 (in Japanese)
5) Japan Road Association (1996), Specifications for Highway Bridge Part V Seismic Design
6) Kent, D.C. and Park, R (1971) "Flexural members with confined concrete, Journal of the Structural Division", ASCE, Vol.97, No. ST7, pp1969-1990
7) Kobayashi, Y., Yoshimura, M. and Sato, Y. (1993) " Plastic Flow Rule on R/C Columns subjected to Biaxial Bending", pp.719-720, Summaries of Technical Papers of Annual Meeting, AIJ (in Japanese)
8) Kondoh, M., Unjoh, S. and Adachi,Y. (1999) " Research on Seismically Damaged of the Steel Jacketed Bridge Column for the Evaluation Technique by Natural Frequency", Proceedings of the 54th Annual Conference of the JSCE, 1(B), pp.376-377, (in Japanese)
9) Nakamura, Y (1995) "Waveform and its Analysis of the 1995 Hyogo-Ken-Nanbu Earthquake", JR Earthquake Information No.23c, RTRI
10) Stephen, M. and Mahmoud, H. (1999) " Bi-directional Seismic Response of Reinforced Concrete Bridges", pp.13-24, International Workshop on Mitigation of Seismic Effects on Transportation Structures

11) Tamehiro, N., and Mori, A. (2000) "A Consideration on Bi-axial Bending Effects for Continuous Curved Bridges", 12th WCEE

CYCLIC TESTING OF STEEL BRIDGE TRUSS PIER BRACE MEMBERS

Michel Bruneau [1], Kangmin Lee[2], and John Mander[3]

Abstract

Analytical and experimental research is conducted to investigate the behavior of bridge truss pier brace members. The objective is to generate knowledge and results that can be broadly applicable to evaluate the seismic capacity of steel truss bridges of the type built during the first half of the 1900's throughout the United States. They were typically designed to resist wind forces, but not earthquakes. From a review of past practices, commonly used shapes and details that have been historically used for built-up members in steel truss bridge braced pier substructures were selected, and an experimental program has been devised whereby several cross-sectional shapes and geometric configurations of X-bracing are explored to ascertain the inelastic deformation capability of these critical elements. These tests are underway at the time of this writing. Knowledge from this experimental and analytical study will be also be used to develop retrofit measures for members that are seismically vulnerable.

Introduction

A large number of steel truss bridges have been built throughout the United States, many in zones of moderate to high seismicity. These bridges have typically been designed to resist wind forces, but not earthquakes. Structural analyses of such bridges often reveal that many key structural members along the load path followed by the seismically induced forces may buckle or suffer brittle fracture of their non-ductile connections. However, seismic evaluation remains difficult due to the lack of knowledge on the cyclic inelastic behavior of built-up members of the type typically found in these bridges, and on their riveted connections.

Although some testing of bridge-specific latticed members has been conducted by other researchers, results to date have mostly been project specific. Consequently, it is difficult to draw general conclusions from those studies. The objective of this research is therefore to provide theories and results that can be broadly applicable to many steel truss bridges that share similar structural characteristics and details.

Research Approach

A survey was conducted to investigate those commonly used shapes and details that have been historically used for built-up members used in steel truss bridge braced pier substructures. This survey showed that braces in these bridges almost universally consist of latticed built-up

[1] Deputy Director, Multidisciplinary Center for Earthquake Engineering Research, and Professor, Dept. of Civil, Structural, and Environmental Engineering, 130 Ketter Hall, University at Buffalo, Buffalo, NY, 14260.
[2] Ph.D. Candidate, Dept. of Civil, Structural, and Environmental Engineering, University at Buffalo
[3] Professor, Department of Civil Engineering, University of Canterbury, New Zealand

members with riveted connections. Common cross-sectional shapes have been identified. Their potential failure modes are global buckling (in-plane or out-of-plane of the frame) or local buckling. To this end, based on representative details, an experimental program has been devised whereby several cross-sectional shapes and geometric configurations of X-bracing are explored to ascertain the inelastic deformation capability of these critical elements. These tests are underway at the time of this writing.

Results from these tests will be used to develop simple strength and deformation models based upon rational mechanics and able to predict strength and displacement limit states. Knowledge from this experimental and analytical study will be also be used to develop retrofit measures for members that are seismically vulnerable.

Preliminary Results

As a result of discussion with the California, Oregon, Washington, Tennessee and New York DOTs, as well as with a few consulting engineering firms, drawings were obtained for a few existing bridges having truss substructures (bents, towers, etc.) with latticed members. Design provisions in the literature, particularly in steel design textbooks published at the turn of the century (Ketchum, 1920, Wells, 1913, and Kunz, 1915), were also reviewed, along with recent research work conducted for the major crossings in California (Uang and Kleiser, 1997, and Dietrich and Itani, 1998 and 1999). This allowed to extract a range of parameters typically encountered for such members, including typical built-up member configurations and lacing geometry, typical b/t and KL/r ratios for the built-up members and their lacings, connection details, and other lacing characteristics.

As a result of this work, parameters worthy of experimental consideration (and their range) have being identified (Table 1 and Figure 1). While some bridges were observed to have members having b/t ratios in excess of 16, it was decided to restrict testing to specimens having b/t values of 8 and 16 on the basis that this would allow to compare the cyclic performance of members having considerably different expectations in terms of local buckling behavior. Note that the AISC recommended maximum b/t value for ductile seismic design is 7.6 for grade 50 steel.

Likewise, it was judged that testing braces having slenderness (KL/r) of 60 and 120 would encompass the range of member slenderness observed in bridges, while allowing to compare the cyclic inelastic behavior of members expected to have significantly different levels of inelastic buckling. The resulting specimens designed based on these considerations are listed in Table 2. Note that only built-up members constructed of angles are considered.

Table 1. Summary of experimental parameters to be considered

Built-up Members			Lacings		
Configuration	B/t ratio	KL/r ratio	Type	Angle	KL/r ratio
Type "A" Type "B"	8 – 16	60 – 120	Single Lacing	60°	100 – 120

Table 2 Given specimen names

Name	Section Shape*	Bucking Axis	b/t ratio	KL/r
Ay8-60, Ay8-120	A	Y	8	60 and 120
Ay16-60, Ay16-120	A	Y	16	60 and 120
By8-60, By8-120	B	Y	8	60 and 120
By16-60, By16-120	B	Y	16	60 and 120
Bx8-60, Bx8-120	B	X	8	60 and 120
Bx16-60, Bx16-120	B	X	16	60 and 120

* Section shapes are detailed in Figure 2.

Specimens with section shape A (Ay8-60, Ay8-120, Ay16-60, and Ay16-120) were instrumented with displacement and strain gages and tested. The test set-ups are shown in Figures 3 to 6 for these specimens. Note that the set-up for Ay8-60 was used to test two specimens having the same section type and b/t ratio, but two different values of the KL/r ratio (60 and 120). This was achieved by using the same members, and testing first in an X-bracing (KL/r of 60) configuration (but without connecting the upper end of one brace, as shown in the circle in Figure 7), and second, in a single brace (KL/r of 120) configuration.

Axial gravity loads were applied at the top of the frame for specimens Ay16-60 and Ay16-120 to reduce slippage in the hinges in the set-up and reduce the global frame horizontal displacements observed during testing of the other two specimens. Also note that for Ay16-60 (in the X-bracing configuration), a dummy member was used instead of the previously used approach of using a specimen brace unconnected at its upper end to prevent damage to the member to be used as a slender specimen (i.e. Ay16-120).

Figures 8 and 10 show the axial force–displacement curve experimentally obtained for the specimens with section shape A. These hysteretic curves exhibit the typical behavior of bracing members observed from the previous studies. The Ay16-60 and Ay16-120 specimens locally bucked instead of globally buckling, because of their large width-to-thickness ratio (b/t = 16). Repeated buckling and straightening of the braces (reversed cyclic loading) at the local buckling location led to failure by fracture.

Figures 11 and 12 show the different buckled shapes at the maximum compressive deformations of the braces for the Ay8-60 and Ay16-60 specimens respectively. The Ay8-60

specimen globally bent (Figure 11), while the Ay16-60 specimen remained almost straight (except at the location of local buckling) (Figure 12). Damaged and fractured specimens are also shown Figures 13 to 16.

To investigate fracture life of the bracing member under cyclic loading, the test results of the Ay8-120 specimen were compared with fracture life models of bracing members suggested by Goel (Hassan and Goel, 1991) and Tremblay (Archambault et al., 1995). Results are summarized in Table 1. Although the fracture life models used have been developed for structural tubular sections, it appears based on the preliminary results obtained so far that these models predicted the fracture life of the Ay8-120 specimen well (results not available for other specimens at time of writing).

Table 3 Fracture life of Specimen Ay8-120

	Fracture of one angle*	Entire Fracture*	Goel's Model Case 1**	Goel's Model Case 2**	Tremblay's Model Case 1**	Tremblay's Model Case 2**
Fracture Life	36.26	40.72	38.64	62.74	29.23	43.07

* For that built-up shape, entire fracture of the specimen required the application of more cycle of inelastic deformations than fracture of a single angle.

** Case 1 was calculated considering actual width-to-depth ratio of the specimen. Case 2 was calculated assuming that the four angles created an equivalent square tube.

Conclusions

Because this research program is only mid-course, firm conclusions would be premature. However, preliminary results suggest that fracture life prediction models developed by others for tubes might also work for the built-up members typically used in truss bridges. This would be a most valuable model to assess the seismic resiliency of these type of bridges, if subsequent tests validate this finding. Toward that same goal, another outcomes of this research program is expected to be detailed information on the maximum cyclic ductility and maximum energy dissipation capacity of built-up braces, using hysteretic curves of the type presented in this paper to generate this quantitative information.

Acknowledgments

This research was conducted by the University at Buffalo and was supported by the Federal Highway Administration under contract number DTFH61-98-C-00094 to the Multidisciplinary Center for Earthquake Engineering Research.

References

Archambault, Marie-Helene, Tremblay, Robert, and Filiatrault, Andre (1995), "Etude du Comportment Seismique des Contreventements Ductiles en X Avec Profiles Tubulaires en Acier", *Rapport No. EPM/GCS-1995-09*, Departement de Genie Civil Section Structures, Ecole Polytechnique de Montreal, Montreal, Quebec, Canada.

Adrianne M. Dietrich, and Ahmad M. Itani (1998), "Cyclic Behavior of Built-up and Steel Members and Their Connections", *Report No. CCEER 98-10*, Department of Civil Engineering, University of Nevada, Reno, Nevada

Adrianne M. Dietrich, and Ahmad M. Itani (1999), "Cyclic Behavior of built-up and Perforated Steel Members on the San Francisco-Oakland Bay Bridge", *Report No. CCEER 99-9*, June, Department of Civil Engineering, University of Nevada, Reno, Nevada

Hassan, O. F. and Goel, S. C. (1991), "Modeling of Bracing Members and Seismic Behavior of Concentrically Braced Steel Structures", *Report No. UMCE 91-1*, January, Department of Civil Engineering, The University of Michigan, Ann Arbor, Michigan

Ketchum, Milo Smith (1920), "The Design of Highway Bridges of Steel, Timber and Concrete", McGraw-Hill Co., New York, New York

Kunz, F. C. (1915), "Design of Steel Bridges; Theory and Practice for use of Civil Engineers and Students", McGraw-Hill Co., New York, New York

Uang, C.-M. and Kleiser, M. (1997), "Cyclic performance of latticed members for the San Francisco-Oakland Bay Bridge", *Report No. SSRP-97/01*, Division of Structural Engineering, University of California, San Diego, La Jolla, California.

Wells, Melville Backer (1913), "Steel Bridge Designing", The Myron C. Clark Publishing Co., Chicago, Illinois

SUMMARY

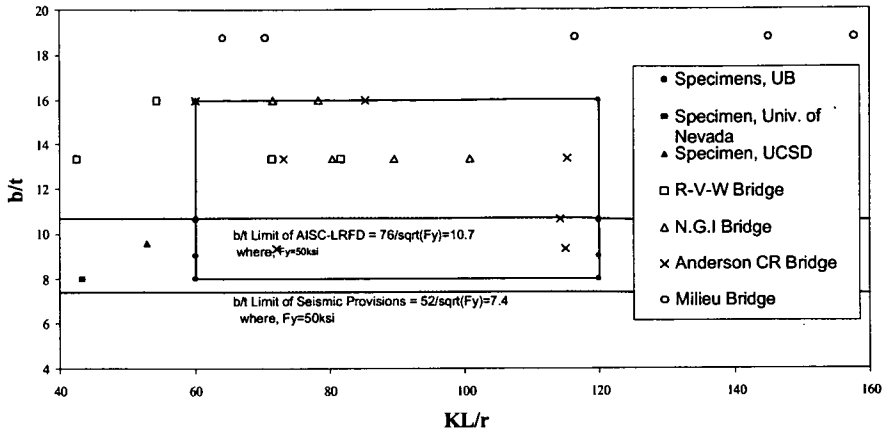

Figure 1 Distributions of b/t ratios and KL/r ratios

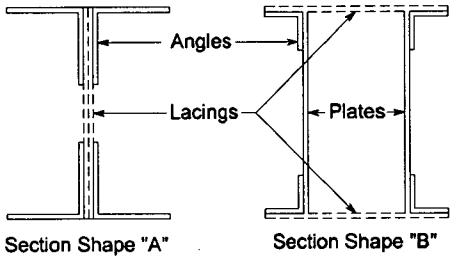

Figure 2 Section shapes

Figure 3 Test Set-up for Ay8-60 Specimen

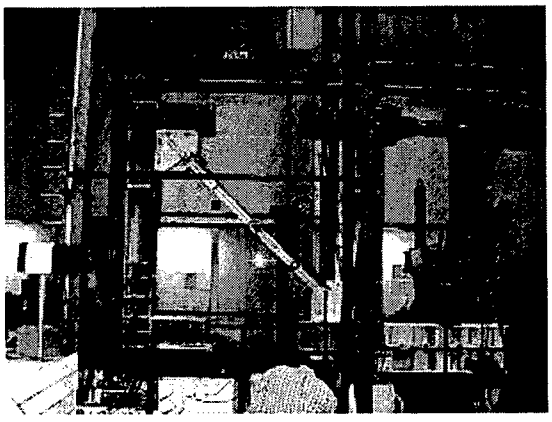

Figure 4 Test Set-up for Ay8-120 Specimen

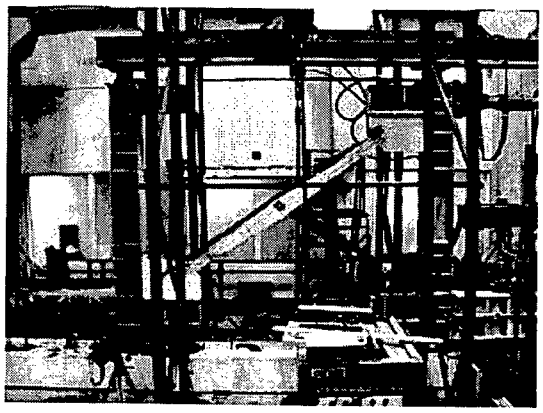

Figure 5 Test Set-up for Ay16-60 Specimen

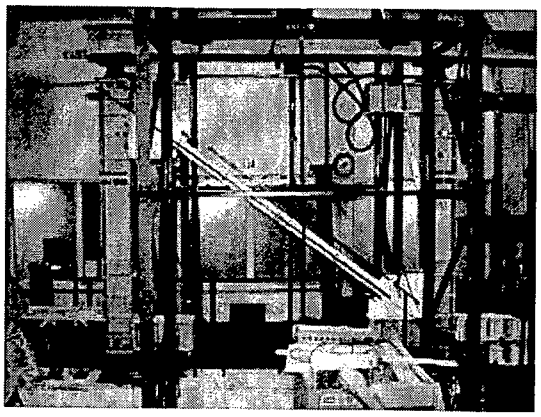

Figure 6 Test Set-up for Ay16-120 Specimen

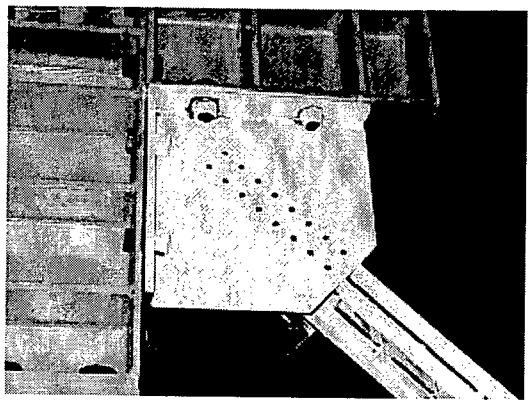

Figure 7 Unconnected end of a brace (Ay8-60)

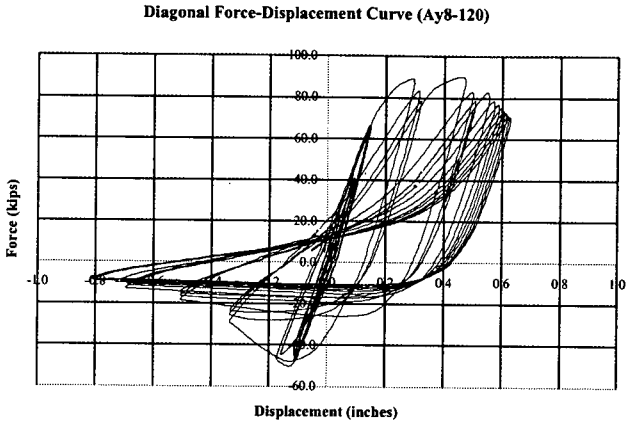

Figure 8 Hysteretic Curve for Ay8-120

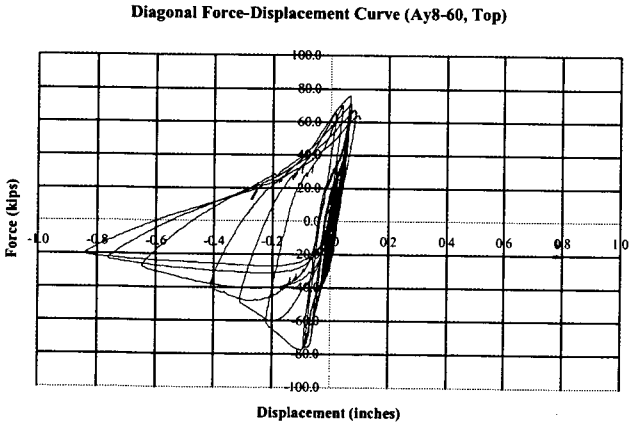

Figure 9 Hysteretic Curve for Ay8-60

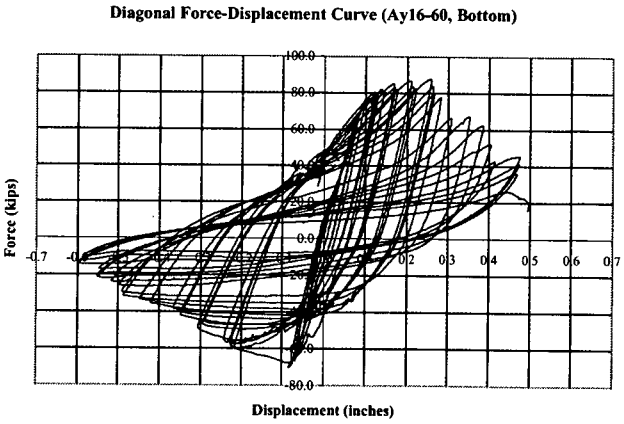

Figure 10 Hysteretic Curve for Ay16-60

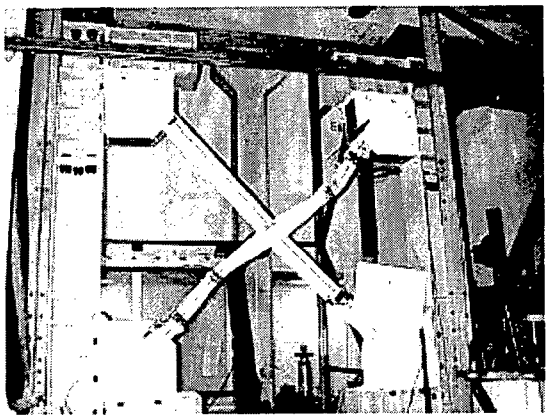

Figure 11. Buckled shape Specimen Ay8-60

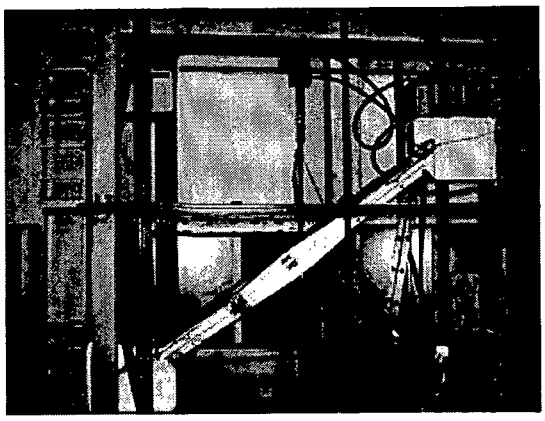

Figure 12. Buckled shape Specimen Ay16-60

Figure 13. Local Buckling Specimen Ay8-60

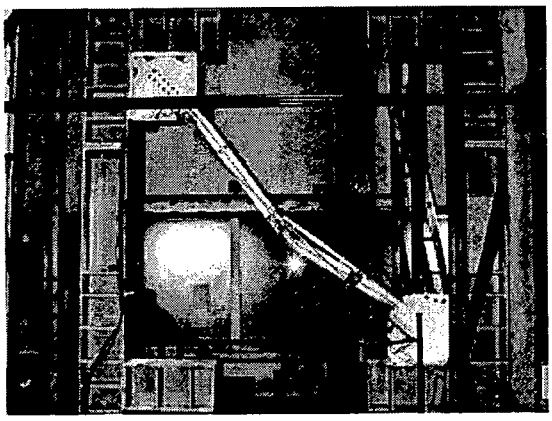

Figure 14. Global Buckling Specimen Ay8-120

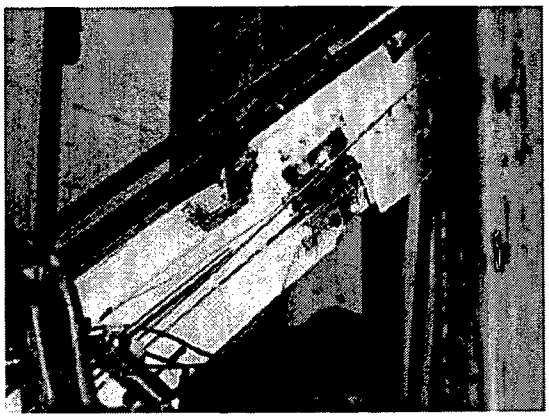

Figure 15. Local and out-of-plane Buckling of specimen Ay16-60

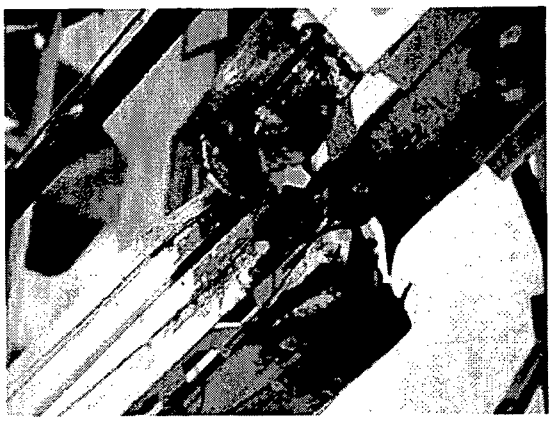

Figure 16. for specimen Ay16-60

Structural Health Monitoring and Damage Detection with Dynamic Response

Koichi YOKOYAMA[1], Zhishen WU[2], Bin XU[3]

Abstract: The last decade has seen an amazing improvement in the development and availability of techniques and instrumentation suitable to monitor and assess the performance and condition of structures. The dynamic responses of structures are useful and economic information resource for health monitoring and parameter identification. While a lot of research work has been done in the area of identification for mechanical engineering, very few methods have really been applied at field for civil engineering, especially for large-scale structures such as bridges, because of the large scale or complexity, uncertainty, and son on. This paper shows that the incorporation both global techniques as well as localized and decentralized monitoring technology with neural networks is viable for large-scale structures.

Key Words: health monitoring, damage detection, structural identification, neural networks, inverse analysis, large-scale structures

1. Introduction

The concept of a health monitoring for civil structural system is continuously evolving as a result of new requirements and the development of new sensor technologies. Structural identification and health monitoring for civil infrastructure is a challenging problem that is under vigorous investigation by numerous researchers using a variety of analytical and experimental techniques. The area of structural monitoring is still rather underdeveloped, and the goal of a health monitoring system is to be able to provide quick identification of damage and advance notice of impending failures, and if possible provide objective data on preventive maintenance and retrofit requirements.

Non-destructive evaluation (NDE) methods for the detection of damage in structural systems have been receiving increasing attention in the recent years. Most structural damage assessments are carried out through visual inspections. Nondestructive damage identification on the basis of observed dynamical signals have been the focus of research studies for many years. A number of localized approaches based on the use of specialized equipment have been proposed to provide detailed information about the specific elements or parts of a structure. These include radiographic, electromagnetic, acoustic emission, X-ray, magnetic, and ultrasonic methods.

In general, the basic idea of health monitoring and damage detection involves the comparison of the changes in structural properties or response, and it can be viewed as a classification problem. The analytical techniques for health monitoring use mathematical models to describe structural behavior and establish mathematical models to approximate the

[1] Dr. of Eng., Prof., Dept. of Urban & Civil Eng., Ibaraki University, Nakanarusawa 4-12-1, Hitachi, Ibaraki 316-8511, Japan
[2] Dr. of Eng., Assoc. Prof., Dept. of Urban & Civil Eng., Ibaraki University, Nakanarusawa 4-12-1, Hitachi, Ibaraki 316-8511, Japan
[3] Dr. of Eng., Fellow of JSPS, Dept. of Urban & Civil Eng., Ibaraki University, Nakanarusawa 4-12-1, Hitachi, Ibaraki 316-8511, Japan

relationship between the specific damage condition and changes in the structural response. The mathematical-model-based structural identification methods can be categorized into time-domain and frequency-domain approaches[1-4]. Effective classification or interpretation of the changes in structural response or dynamic properties due to damage is a critical task. Frequency-domain analysis is concerned with spectral estimates and the frequency characteristic of responses. Deterioration and damage results in a reduction of structural parameters for example, the stiffness of structural members. This reduction produces changes in the dynamic properties, such as the natural frequencies and mode shapes. Global techniques based on mode shape comparison tend to suffer from the lack of sufficient sensitivity, and few global techniques based on eigenvalue comparison have been applied at field because it is difficult to measure the exact frequencies of a large-scale structure. And time-domain analysis involves recursive techniques and maximum likelihood estimates. As described by Zhao et al.[5], although the methods that have been developed are applicable in concept to most structural models, it is not practical to directly apply them to a structural model with a large number of degree of freedom (DOF) because excessive computation time and computer memory are necessary for convergence, and also it may not be theoretically possible to obtain unique estimates of all parameters. A viable system for health monitoring has to incorporate both global techniques as well as localized and decentralized health monitoring technologies. A localized identification method for multi-degree-of-freedom (MDOF) structures in the frequency domain was proposed by Zhao et al. [5], and a localized vibration control strategy was presented by Xu et al. [6,7]. As another kind of method for large-scale structure system, the concept of decentralization for identification and control method was studied by Sandell et al.[8], Magaña et al.[9] and Xu et al.[10].

On the other hand, the ability of artificial neural networks to approximate arbitrary continuous function provides an efficient mechanism for the identification and control problem. Neural networks are suitable for pattern classification and natural information processing tasks. Neural networks are finding application in almost all branches of science and engineering. Modeling dynamic systems by using neural networks has been increasingly recognized as one of the system identification paradigms. The neural-network-based modeling problem of an unknown linear or non-linear discrete-time multivariable dynamic system is to develop a neural network model that is capable of learning and predicting the functional mapping between the inputs and the outputs of the dynamic system. The knowledge acquired by a neural network is stored in its connection weights, which are adaptive and can change in response to outside stimuli. At present, several neural networks with different structures have been proposed to solve identification and control problems. The most widely used neural networks for identification and control problem are the multi-layer neural networks. Numerous engineering applications of neural networks have been reported in the literature of recent years. A great number applications of neural networks for identification and control in civil engineering were reviewed by Xu et al.[6,7,10,11,14], Ghaboussi et al.[12], Chen et al.[13], Nakamura et al.[15], Zhao et al.[16] and Yoshimura et al. [17]. Some researchers have also used neural networks in the identification of the damage in structures.

In this study, a substructure of a large-scale structure is taken as an objective. Decentralized and localized health monitoring and damage detection strategy with neural networks by the direct use of dynamics responses under earthquake excitations are proposed. The dynamic responses of structures under environmental excitations or small-scale earthquakes are useful and economical information for health monitoring, some information about structural parameter and dynamic properties is stored in it. To identify the substructure by neural network, the decision and select of variables for input and output is critical, those variable should have clear physical meaning and enough to carry out identification. And for the purpose of practical application, an evaluation index should to be defined and selected

properly. The evaluation index must be related with the variation of the structural parameters and be independent to the excitations. A relative root mean square (RRMS) error vector is introduced as an evaluation index here. The reasonableness of this evaluate index is demonstrated by numerical simulation. Results of numerical simulation show that the localized health monitoring strategy with the localized emulator neural network can clearly identify the damage existing with high sensitivity. Moreover, a localized parametric evaluation neural network is constructed and trained to forecast the structural parameter of stiffness based on the RRMS error vector. The robustness of the localized parametric evaluation neural networks is demonstrated. This strategy cannot ascertain the damaged specific component because the forecast structural parameters are the stiffness of substructure, which consists of a cluster of structural members. But this strategy is suitable for the structural systems where damage results in the changes in stiffness.

2. Decentralized Health Monitoring and Damage Detection Parametric with Neural Networks Using Dynamic Response

2.1 Basic Procedure of Decentralized Health Monitoring and Damage Detection

The basic idea of neural-networks-based decentralized damage detection using earthquake responses is shown in Figure 1. A large-scale structure such as a bridge can be divided into several substructures, which consist of a smaller number of DOF and are connected with each other.

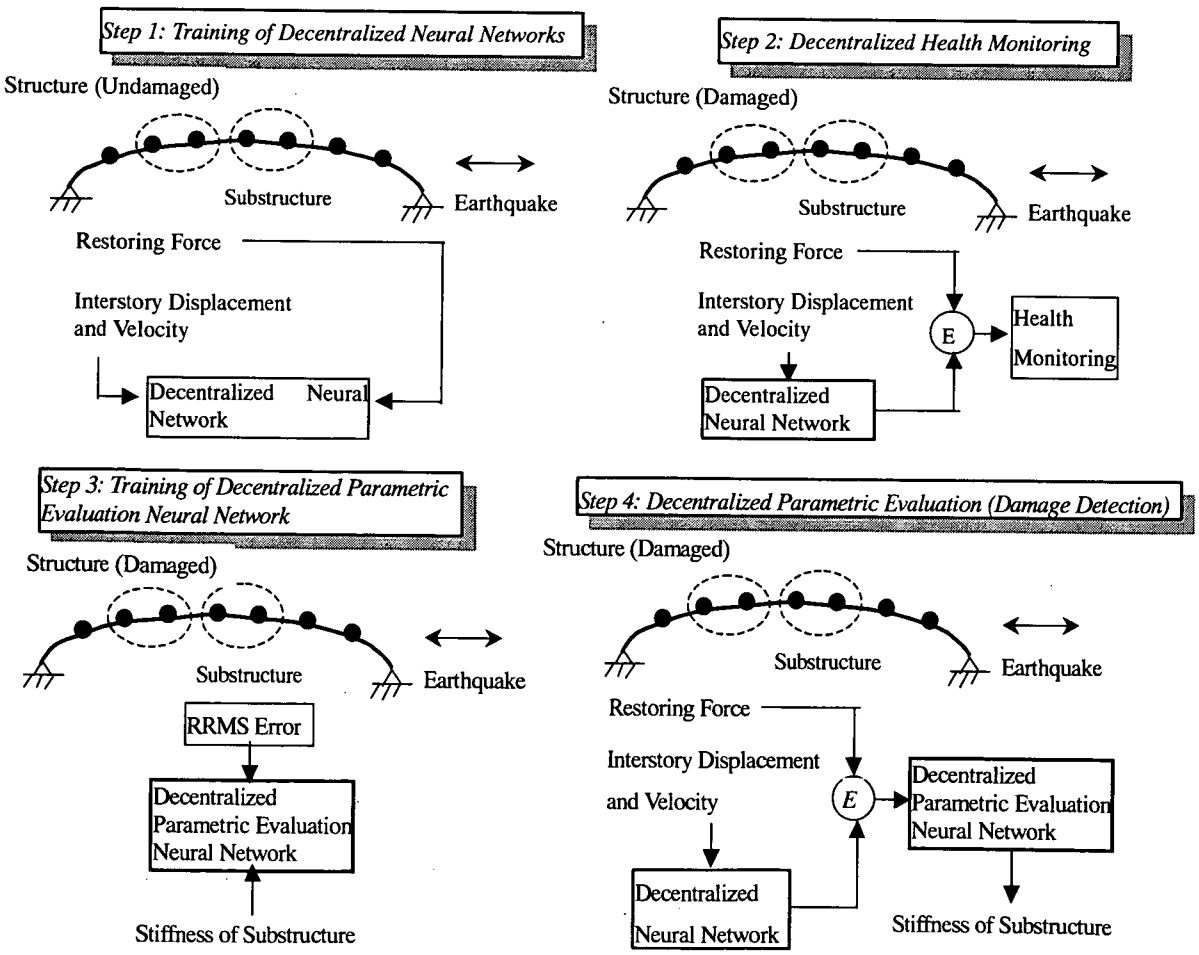

Fig.1 Decentralized health monitoring and damage detection

In the first step of the training of decentralized neural networks, several neural networks are trained by the data obtained from the corresponding substructures of the healthy structure by the widely used error back-propagation algorithms. After the decentralized neural networks are trained successfully, the dynamic characteristics of each substructure can be identified. In other words, each substructure can be identified with a non-parametric manner by decentralized neural networks. In the second step of decentralized damage detection, each trained neural network is used to represent the corresponding healthy substructure. If the substructure characteristics have changed, the restoring force of the substructure will not correspond any more to the output of the trained network. The error between the restoring force of each substructure and the output from the neural networks provide a quantitative measure of the changes in physical substructure relative to its health condition.

As described above, for the purpose of real-time damage detection, a decentralized non-parametric identification method has presented. And the RRMS error of each substructure is related with the degree of damage (the decrease in stiffness). If we can establish and train another neural network, which includes the relationship between the RRMS error and the stiffness of substructures, we can give the value of stiffness of each substructure according to the RRMS error. Here, several decentralized parametric evaluation neural networks are established. The input to the decentralized parametric evaluation neural network is the RRMS error of the corresponding substructure. And the output is the forecast stiffness of the substructure.

2.2 Decentralized Health Monitoring with Neural Networks

In order to demonstrate the principle of the decentralized health monitoring and damage detection, a frame structure shown in Figure 2 under earthquake excitations is studied.. Based on the concept of decentralized identification for damage detection, the structure is modeled as a MDOF model and further divided into several substructures, which consist of a smaller number of DOF and are connected with each other. In a damage detection problem, the substructure division can be determined according to visual inspection. Without loss of generality, the forth floor and the top floor are treated as two substructures. Corresponding to the two substructures, two neural networks are trained to identify them. The inputs of each neural networks include the interstroy displacement and interstroy velocity of the corresponding substructure, and the output is the restoring force. According to the dynamic response of the structure and earthquake records, the interstory displacement and velocity, restoring force can be decided.

In order to demonstrate the performance of the proposed strategy, the following four load cases are studied.

(1) Case 1: 12 seconds of El Centro earthquake (May 18,1940, Imperial Valley) of 30% of the amplitude

(2) Case 2: 12 seconds of Taft earthquake (July 21,1952, Kern Country) with 100% of the amplitude

(3) Case 3: 12 seconds of Taft earthquake with 50% of the amplitude

(4) Case 4: 12 seconds of Kobe earthquake (January 17, 1995, Hyogo-ken Nanbu) with 20% of the amplitude

The interstory displacement, velocity and restoring force decided from the dynamic responses in Case 1 is used to train the decentralized neural networks.

It is scarce for a structure to be excited by two same earthquakes during the life cycle. In order to carry out successful real-time damage detection, it is necessary to choose an evaluation index, which is independent on the earthquake excitations. In this paper, relative root mean square (RRMS) error is used as an evaluation index for damage detection. The

RRMS error of each substructure can be defined as follows,

$$e_i = \frac{\sqrt{\frac{1}{n-1}\sum_{1}^{n}(f_n - f_r)^2}}{\sqrt{\frac{1}{n}\sum_{1}^{n}(f_r)^2}} \qquad (i = 1, s) \tag{1}$$

where n = the number of sampling data, f_n = the output of trained neural networks, f_r = the restoring force decided through the dynamic responses under earthquake excitations, and s = the number of the substructures.

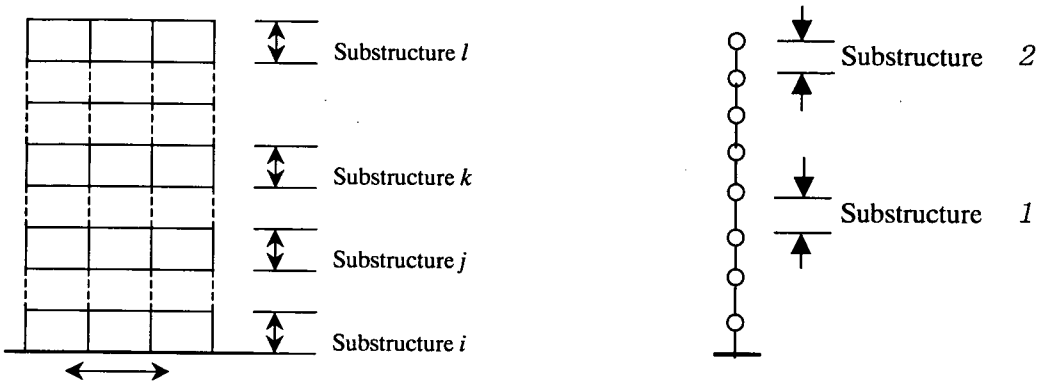

Fig. 2 A frame structure and the lumped mass-spring-dashpot model

The results of RRMS of each substructure in the four cases are shown in Figure 3. It is clear that RRMS error does not change with the load cases and the RRMS error relates with the stiffness of each substructure. The RRMS error is a useful index for health monitoring. In a practical application, a threshold level may be set, and if the RRMS error exceeds the threshold level, the method can directly notify the residents of the building that damage occurs. This automatic notification capability is quite useful for real-time health monitoring. In Figure 3, it is shown that the RRMS error increases with the degree of damage. And it indicates that the decentralized damage detection methodology can be used for health monitoring with high sensitivity. For example, in substructure 2, the stiffness is degraded by 10 percent, and the decentralized neural network gives a RRMS error, which has an increase of 65.05 percent compared to the RRMS error of the healthy substructure.

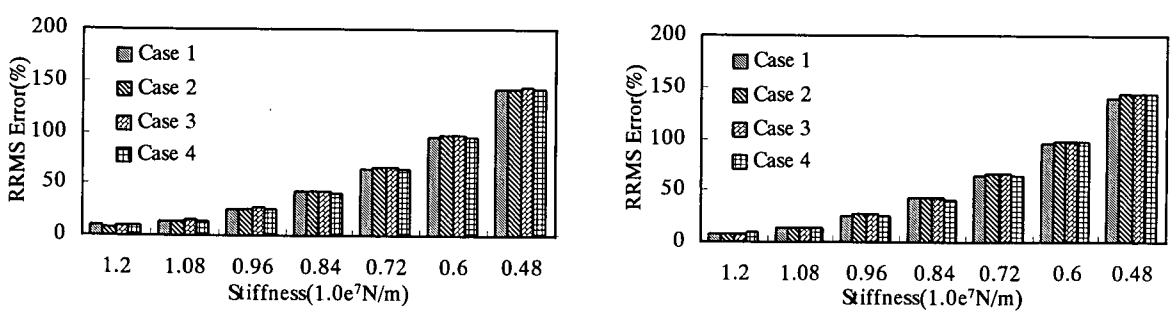

(a) Substructure 1 (b) Substructure 2

Fig. 3 RRMS error

2.3 Decentralized Damage Detection (Parameter Identification) with Neural Networks

As described above, the RRMS error depends on the stiffness of each substructure so

that a decentralized parametric evaluation neural network can be trained and used to forecast the stiffness of each substructure. The stiffness of each substructure and the corresponding RRMS data in case 1 shown in Figure 3 are used to train the decentralized parametric evaluation neural network with error-back-propagation algorithms. And then based on the trained decentralized parametric evaluation neural network, we can forecast the stiffness of the corresponding substructure when RRMS error is inputted to the neural network. The results are shown in Table 1. It is demonstrated that decentralized parametric evaluation neural network can forecast the stiffness of the corresponding substructure with high accuracy. Moreover, the identification results are not depended on the earthquake excitations. This kind of characteristics is very useful for practical application.

Table 1 RRMS Error of Substructures under different Earthquake

	Sub-structure	Damaged Stiffness (1.0^7N/m)	Forecast Stiffness (1.0^7N/m)	Relative Error (%)
Case 1	1	0.72	0.7200	0.00
		0.84	0.8400	0.00
	2	0.72	0.7200	0.00
		0.84	0.8400	0.00
Case 2	1	0.72	0.7240	0.65
		0.84	0.8439	0.46
	2	0.72	0.7203	0.04
		0.84	0.8444	0.52
Case 3	1	0.72	07227	0.38
		0.84	0.8457	0.68
	2	0.72	0.7194	-0.83
		0.84	0.8432	0.38
Case 4	1	0.72	0.7381	2.50
		0.84	0.8602	2.40
	2	0.72	0.7296	1.33
		0.84	0.8536	1.62

3. Localized Health Monitoring and Damage Detection with Neural Networks Using Dynamic Response

3.1 Basic Procedure of Localized Health Monitoring and Damage Detection with Neural Nwtworks

A localized neural-network-based health monitoring and parametric identification procedure by the use of structural dynamic responses under small-scale earthquake is proposed.

A large-scale structure such as a bridge may be divided into several substructures, which consist of a small number of DOF and are connected with each other through interfaces or boundaries. Zhao et al. [5] testified that the lower boundary can be selected as a reference point and considered as the nominal ground for the substructure. From the vector-matrix equation of motion for a substructure, it is clear that the dynamic response of the substructure can be defined by the absolute acceleration of the lower boundary and the relative displacement and velocity with respect to the lower boundary. A suitable selection of the inputs and outputs for a localized emulator neural network can be decided.

The basic idea of this localized health monitoring and parametric evaluation (damage

detection) procedure is shown in Figure 4. The full procedure on localized health monitoring and parametric identification is divided into four steps. Two typical three-layer neural networks trained by back-propagation method are designed for the purpose of health monitoring and parametric identification.

In step 1, a localized emulator neural network is constructed and trained using the dynamic responses of the objective substructure of a healthy structure, which can be considered a newly supplied or an exciting structure. After the localized emulator neural network is trained successfully, the dynamic characteristics of the substructure in healthy condition or current state at the beginning of healthy monitoring can be identified. In other words, structure can be identified in a non-parametric manner by the localized emulator neural network.

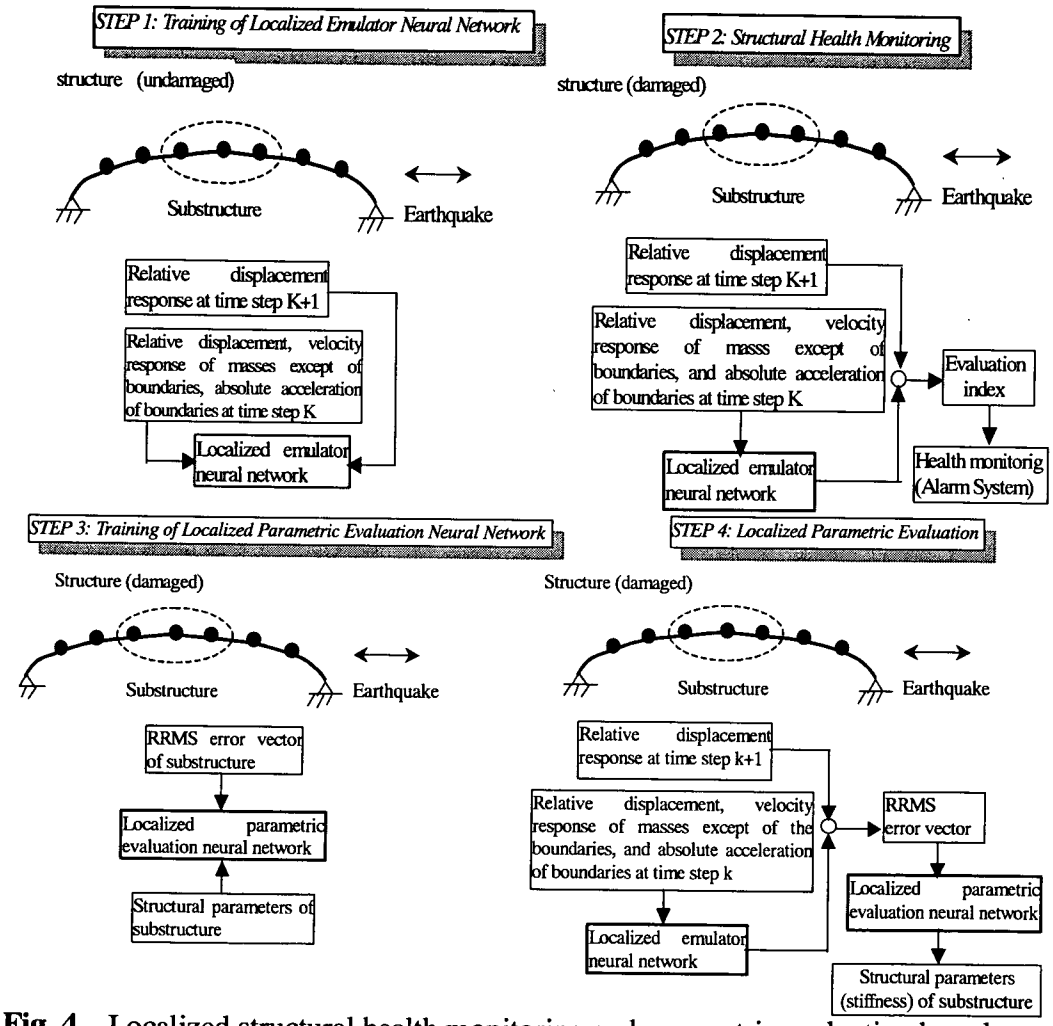

Fig. 4 Localized structural health monitoring and parametric evaluation based on neural network with dynamic responses

In step 2, the trained localized neural network is used to start health monitoring. If the structural performance and parameters of the substructure have changed, the dynamic response will not correspond any more to the output of the trained localized emulator neural network. The error between the dynamic responses forecast by the localized emulator neural network and it observed from the substructure provide a quantitative measure of the changes of parameters in physical structure relative to its healthy condition. The proper selection and definition of an evaluation index is a critical work. Here, An evaluation index of RRMS error, which can be used to show whether damages exist or not, is defined. In practical application,

a threshold level can be set after the completion of the training of the localized emulator neural network. Once the evaluation index exceeds the threshold level, an alarm signal can be made for the users of the structure.

In step 3, a localized parametric evaluation neural network is constructed and trained for the purpose of forecasting the structural parameter (stiffness). Training data sets consisting of structural parameters of substructures with different degree of damages and the corresponding RRMS error vector are used to train the localized parametric evaluation neural network.

After finishing the training of the localized parametric evaluation neural network, in step 4, structural parameters can be forecast by inputting RRMS error vector to the localized parametric evaluation neural network with the help of the localized emulator neural network constructed in step 1.

Without loss of the generality, the performance of the proposed localized health monitoring and damage detection procedure is studied by numerical simulation for a frame structure that is modeled as a mass-spring-dashpot system with n degree-of-freedoms.

In this study, an eight stories frame structure shown in Figure 5 under earthquake excitations is studied. The structure is treated as a MDOF model. An 8-mass model with known parameter, mass $m_i = 185kg$, stiffness $k_i = 5.0*10^5 N/m$ and damping coefficient $c_i = 2.0*10^3 N.s/m$ for each mass (i=1,$\cdots$,8), is assumed for the illustrative model in healthy condition(Figure 5). The first four natural frequencies of the frame structure are 1.53 Hz, 4.53 Hz, 7.38 Hz and 9.97 Hz.

In the Hyogo-ken Nanbu Earthquake (17 January, 1995), some buildings were destroyed in the middle stories. So in this study, the objective substructure, which includes mass No. 4 to mass No.5 and interconnected with the upper boundary mass No.6 and lower boundary mass No.3, is considered.

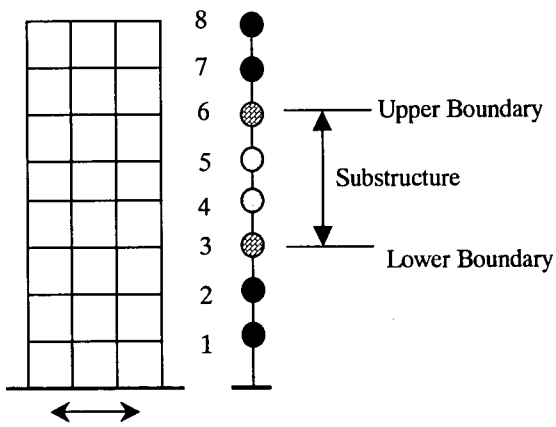

Fig. 5 A substructure in an eight stories frame structure

3.2 Localized Health Monitoring with Neural Networks

A three-layer neural network called as localized emulator neural network is constructed and trained to identify the dynamics of the substructure in a nonparametric manner. For the purpose of health monitoring, accelerometers are considered to place at each story of the substructure. The measured acceleration data can be converted into velocity and displacement by integration with respect to time. And then the relative displacement and velocity of the masses of the substructure with respect to the lower boundary can be determined.

The input layer of the localized emulator neural network includes relative displacements, velocities response of mass No. 4 to mass No.6, and the absolute acceleration of the lower boundary (mass No.3) at time step K.

In this paper, two kinds of earthquake excitations (load cases) are studied. And two earthquake excitations are scaled with velocity amplitude of 0.30m/s.

(1) Case 1: 8 seconds of Taft earthquake (July 21,1952, Kern Country);

(2) Case 2: 8 seconds of El Centro earthquake (May 18,1940, Imperial Valley);

The training data sets for the purpose of training localized emulator neural network are constructed from the numerical integration analysis results in load case 1. The numerical integration analysis is carried out with integration time step of 0.002 second. The training data sets are performed with the data taken at the intervals of the sampling period of 0.04 second. The training data sets, used for training the neural networks are the 200 patterns of input and output data taken from 8 seconds of dynamic response records of the structure. Generally, the neural network requires the normalization of the input and output data, because it is difficult to train the neural network without the normalization. The whole off-line training process takes 10000 cycles. By means of the error back-propagation learning rule, the training data sets performed above are used to train the localized neural network in order to model the structural dynamics of the substructure. Figure 6 gives the result of comparison between the displacements determined from the numerical integration analysis (called as observed response) and those forecast by the trained localized emulator neural network of mass No. 4, 5, respectively, in load case 1. Figure 7 gives the result in Case 2. It can be seen that localized identification can be carried out with high accuracy.

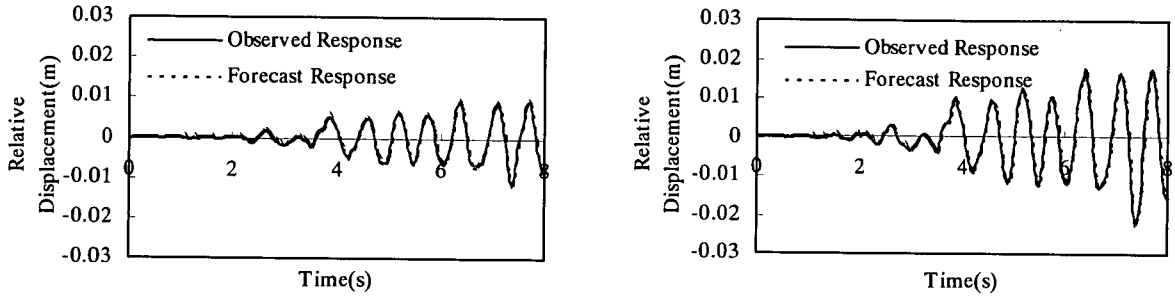

(a) Mass No.4 (b) Mass No.5

Fig. 6 Comparison of displacements in case 1

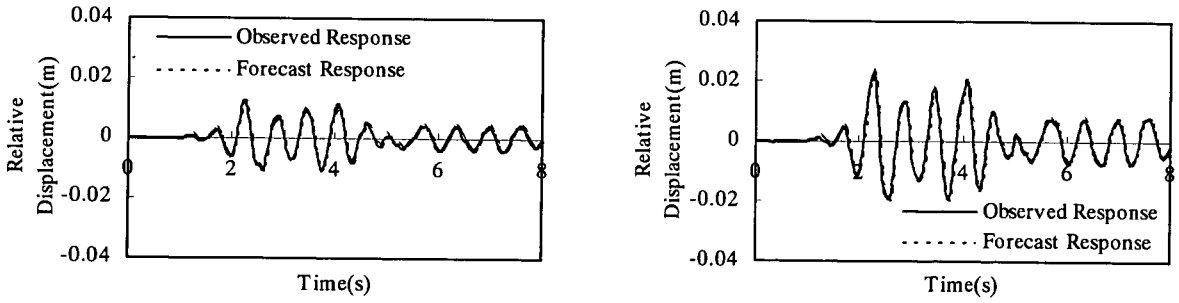

(a) Mass 4 (b) Mass 5

Fig.7 Comparison of displacements in case 2

Here, some results about RRMS error vector are described. Let the stiffness of the substructure decrease to 90%, 80%, 70%, 60% of the original values respectively, the components of RRMS error vector corresponding to the relative displacement of No. 4 and 5 in the two cases can be decided. Figure 8 gives the relationship between the modulus of the RRMS error and the degree of stiffness decrease. It is clear that RRMS error can be considered to be a suitable index for health monitoring and the RRMS error in different cases does not change greatly. The results of RRMS error in Case 1 and Case 2 are very close. And the RRMS error correlates the degree of damage in stiffness of each substructure. The RRMS

error is again shown to be a useful index for health monitoring. And it indicates that the health monitoring methodology can be used for health monitoring with high sensitivity. For example, when the stiffness is degraded by 10%, the emulator neural network gives a RRMS error, which has 21% of increase compared to the RRMS error of the healthy structure. And a 20% of stiffness in stiffness results in a 43% increase in RRMS error.

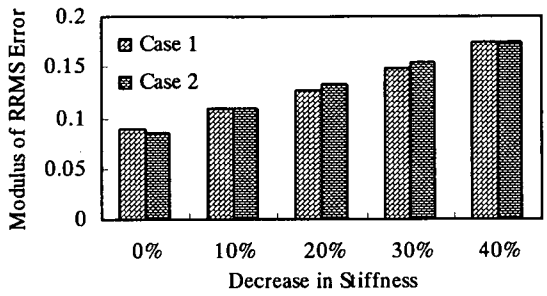

Fig. 8 Modulus of RRMS error vector

3.3 Localized Parametric Identification (Damage Detection) with Neural Networks

Here, a localized parametric evaluation neural network is established. The input to the localized parametric evaluation neural network includes the RRMS error vector of the substructure. In order to improve the performance of the localized parametric evaluation neural network, the high-order terms of the square of the RRMS error are also used as the input patterns. And the output is the forecast stiffness of the substructure.

As described above, the parametric identification is an inverse problem. When neural network is used to solve the inverse problem, the training data, which can be obtained as the solution of the direct problem, is necessary. Some structures with different degree of damage are assumed, and the RRMS error can be calculated by the method described in Chapter 2. Then the localized parametric neural network can be trained to recognize the unknown structural parameters (stiffness) from the RRMS error vector. Thus, the inverse analysis can be avoided through the training process of the neural network.

In this paper, the stiffness of some assumed damaged structures and the corresponding RRMS error vector data in Case 1 are used to train the localized parametric evaluation neural network with error back-propagation algorithms. Let stiffness of each story of the substructure equal to 1.0, 0.9, and 0.8 times of the original value respectively, and the corresponding RRMS error vector can be calculated by the method described in step 2 in Figure 4. So 27 pairs of training data are chosen. The localized parametric evaluation neural network is trained with those training data. And then based on the trained localized parametric evaluation neural network, we can forecast the stiffness of the substructure when RRMS error vector is inputted to the neural network.

Without loss of generality, three damaged structures with different degree of stiffness decrease are studied here. According to the RRMS error vector, the stiffness of the damaged substructure can be forecast through the trained parametric evaluation neural network. The results are shown in Table 2, it is clear that the interstory stiffness of each floor in the substructure can be forecasted accurately in Case 1 and 2, respectively. The maximum error between the forecasted stiffness and the true value is not great than 5%.

It is demonstrated that localized parametric evaluation neural network can forecast the stiffness of the substructure with high accuracy. Moreover, the identification results are not depended on the earthquake excitations. This kind of characteristics is very useful for practical application.

Table 2 Parameter evaluation Results

654

	Stiffness (*10^5N/M)								
	Damaged Structure 1			Damaged Structure 2			Damaged Structure 3		
	K_4	K_5	K_6	K_4	K_5	K_6	K_4	K_5	K_6
Ture Value	5.00	5.00	4.50	4.50	4.50	4.50	4.00	4.50	5.0
Case 1	5.04	4.91	4.55	4.63	4.58	4.68	3.90	4.45	4.83
Case 2	5.01	4.86	4.56	4.64	4.60	4.68	3.93	4.51	4.82

4. Conclusions

Decentralized and localized inverse analyses process for damage detection and health monitoring with direct use of dynamic response for large-scale structure by neural network was proposed.

Numerical simulations show that the structure of the decentralized and localized emulator neural network corresponding to the substructure is feasible. For the purpose of health monitoring, a suitable and practical evaluation index was defined, and the adaptability of the evaluation index was testified. Then decentralized and localized parametric identification diagrams were conducted by combining the decentralized and localized emulator neural network and the decentralized and localized parametric evaluation neural network. The performance of the proposed procedure is evaluated through numerical simulations for substructures with different degree of damage. The stiffness of the damaged substructure can be identified through the decentralized and localized parametric neural network with good precise.

It is shown that the decentralized and localized inverse analyses with neural network by direct use of dynamic response have the potential of being a practical tool for health monitoring and damage detection to civil engineering structures, especially for large-scale structures such as bridges with great number of DOF. It is possible to apply this approach to whole structure identification if the required response records are available.

References

1) Mcverry, G.H., Structural Identification in Frequency Domain From Earthquake Records, *Earthquake Engineering and Structural Dynamics*, 8, pp.161-180, 1980
2) Koh, C.G., See, L.M. & Balendra. T., Estimation of Structural Parameters in Time Domain: A Substructure Approach, *Earthquake Engineering and Structural Dynamics*, 20, pp.787-802, 1991
3) Agbabian, M.S., Masri, S.F. & Miller, R.K., System Identification Approach to Detection of Structural Changes, *Journal of Engineering Mechanics, ASCE*, 117, pp.370-390, 1991
4) Wu, Z.S., Iwamatsu, S. & Harada, T., Computational Modeling on Parameter Estimation of Large Scale Structures From Static Response, in *Third Asian-Pacific Conference on Computational Mechanics*, pp.1105-1109, 1996
5) Zhao, Q., Sawada, T., Hirao, K. and Nariyuki, Y., Localized Identification of MDOF Structures in the Frequency Domain, *Earthquake Engineering and Structural Dynamics*, 24, pp. 325-338, 1995
6) Xu, B., Wu, Z.S., & Yokoyama, K., Adaptive Localized Vibration Control of Large-scale or Complex Structures Using Multi-layer Neural Network, *in Proceeding of the Seventh East Asia-Pacific Conference on Structural Engineering and Construction*, pp.261-266,

1999
7) Xu, B., Wu, Z.S., Yokoyama, K. & Harada, T., Adaptive Localized Control of Structure-Actuator Coupled System Using Multi-layer Neural Networks, *Journal of Structural Engineering and Earthquake Engineering, JSCE*, 18(2), pp.81-93, 2001
8) Sandell, Jr., N. R., Varaiya P., Athans M. & Safonov, M.G., Survey of decentralized control methods for large scale systems, *IEEE Transactions on Automatic Control,* Vol. AC-23(2), 108-128, 1978
9) Maga·a, M.E., Volz, P. & Miller, T., Nonlinear decentralized control of a flexible cable-stayed beam structure, *Journal of Vibration and Acoustics*, 119, 523-526, 1997
10) Xu, B., Wu, Z.S. & Yokoyama, K., Decentralized Identification of Large-scale Structure-AMD Coupled System Using Multi-layer Neural Networks, *Transactions of the Japan Society for Computational Engineering and Science*, 2, pp.187-197, 2000
11) Xu, B. and Wu Z.S., Neural-Networks-Based Structural Health Monitoring Strategy With Dynamic Responses, The 3rd International Workshop on Structural Health Monitoring, pp.1418-1423, September 12-14, 2001
12) Ghaboussi, J. & Joghatatie, A., Active Control of Structures Using Neural Networks, *Journal of Engineering Mechanics*, ASCE, 121(4), pp.555-567, 1995
13) Chen, H.M., Tsai, K.H., Qi, G.Z., Yang, J.C.S., & Amiini, F., Neural Network for Structure Control, *Journal of Computing in Civil Engineering*, 9(2), pp.168-175, 1995
14) Xu, B., Wu, Z. S. & Yokoyama, K., Adaptive Vibration Control of Structure-AMD Coupled System Using Multi-layer Neural Networks, *Journal of Applied Mechanics*, JSCE, 3, pp. 427-438, 2000.
15) Nakamura, M., Masri, Sami F., Chassiakos Anastassios G. & Caughey, Thomas K., A Method for Non-parametric Health Monitoring Through the Use of Neural Networks, *Earthquake Engineering and Structural Dynamics*, 27, pp. 997-1010, 1998.
16) Zhao, J., Ivan, John N. & Dewolf T., Structural Health Monitoring Using Artificial Neural Networks, *Journal of Infrastructure Systems*, 4(3), pp. 93-101, 1998
17) Yoshimura, S., Matsuda, A. and Yagawa, G., A New Regularization Method for Neural-Network-based Inverse Analyses and its Application to Structural Identification, *Inverse Problems in Engineering Mechanics*, Bui, Tanaka et al., Balkema, Rotterdam, pp.461-466, 1994

Other Papers

Corrosion of Post-Tensioned Tendons in Florida Bridges
(Rodney G. Powers, Alberto A. Sagüés and Yash Paul Virmani)

Accelerated Corrosion Test Method for Post-Tensioned Grouts
(Niel G. Thompson, Yash P. Virmani and David R. Lankard)

CORROSION OF POST-TENSIONED TENDONS IN FLORIDA BRIDGES

Rodney G. Powers[1] Alberto A. Sagüés[2] and Yash Paul Virmani[3]

Abstract

Severe corrosion distress and failures in post-tensioned tendons has been found in two major bridges in the State of Florida. Corrosion distress and complete tendon failure has been identified in horizontally oriented tendons that support pre-cast bridge superstructure box segments. In virtually all instances, the observed corrosion has been associated with the presence of grout voids and visual evidence of grout bleed water having been present for indeterminate periods of time. With few exceptions, corrosion induced strand failures have occurred in the immediate vicinity of the anchorage. The anchorage systems in both bridges utilize a proprietary multi-plane anchorage (housing) comprised of ductile cast iron and forged steel wedge plate. The presence of these metals coupled with high strength strands gives rise to concerns relative to galvanic corrosion thus prompting this preliminary investigation focusing on dissimilar metals corrosion. The investigation involves laboratory tests that examine the corrosion aspects of grout bleed water and re-charge water in contact with dissimilar metals comprising the tendon and anchorage system. The preliminary results indicate that the high strength post-tensioned strands are mostly anodic to the anchorage system when exposed to either grout bleed water or recharge water such as that which may be experienced through leakage. The preliminary findings of the investigation are presented along with the implications on existing structures and on future design and materials selection for post-tensioning systems.

Introduction

Commencing in 1979 with the construction of five major bridges in the Florida Keys, the Florida Department of Transportation (FDOT) now has an inventory of more than 80 major bridges that utilize this type of construction. Both bonded (internal) and non-bonded (external) tendons have been utilized for both substructure and superstructure components on inland as well as coastal marine structures. Typically, these are large structures (>750 meters in length) that span either large bodies of coastal waters or large highway interchanges. Each of Florida's structures was designed and built using what was considered state-of-the-art materials and construction practices for the time.

The potential for corrosion of tendons in bridges in the United States has been recognized. In 1989, a study was commissioned by the United States Department of Transportation, Federal Highway Administration to examine the performance of grouts

---

[1]Assistant State Corrosion Engineer, Florida Dept. of Transportation, Gainesville
[2]Distinguised Professor, Dept. of Civil and Environmental Engineering, University of South Florida, Tampa
[3]Research Chemist, U.S. Department of Transportation, Federal Highway Administration, McLean, Virginia

for post-tensioned bridge structures. In the final report (Ghorbanpoor, 1993) it was demonstrated that conventionally used grout materials were susceptible to development of significant levels of bleed-water under normal handling conditions. It was shown that grout bleed-water tended to rise and collect in the upper reaches of test specimens comprised of a single strand in a vertically positioned grouted duct. Further, it was shown that although the bleed-water eventually dissipated, significant corrosion developed on the strand at the grout-water interface. It was further shown that one particular, commonly used grout containing an aluminum based grout-expanding admixture experienced the highest amounts of bleed-water development and subsequent corrosion. Similarly, severe corrosion distress has been observed in cyclically loaded full-scale tendon mock-up specimens (Tabatabai, et al., 1995) within only one to two months' exposure to grout bleed-water.

Corrosion of post-tensioned strands has been identified in two Florida Bridges. The first reported incident was at the Niles Channel Bridge (NC) in the Florida Keys (Powers 1999) followed by Mid Bay Bridge (MBB) in the Western panhandle (Corven, 2000). The superstructure of both bridges utilizes non-bonded (external) tendons arranged in a configuration such that the center lengths of the tendons are draped downward from the anchorages through deviation blocks along the length of the spans (Figure 1). The anchorage assembly is depicted in Figure 2. In both structures, the tendons failed in the anchorage region (Figure 3).

Of particular interest in this laboratory investigation was the common factors amongst the two bridges that have experienced corrosion upon the tendons. These common factors include, (i) corrosion was mainly at or near the anchorages; (ii) the anchorages utilize ductile cast iron anchors and forged steel wedge plates; (iii) corrosion was always associated with grout voids (Figure 4), the presence of grout bleed-water and soft, chalky grout in the affected areas; and (iv) corrosion was always (except for one instance) associated with grout that contained only trace (background) levels of chloride. These common factors give rise to the possibility of galvanic action (dissimilar metal corrosion) taking place between the post-tensioning strand and the milder steel anchorage components in the presence of grout bleed-water or infiltrating (recharge) water. The preliminary experiments in this work explore the corrosion behavior of the metal the metal components comprising the anchorage system when exposed to grout bleed-water and re-charge water.

Experimental Details:

Grout: Grout mixes were made to replicate the aluminum admixed grout used at MBB. The grout consisted of Type I Portland cement with 1 percent (by weight) aluminum based expanding admixture and a water to cement ratio of 0.45. A control mix of the same proportions was made that did not contain the aluminum based expanding admixture. These grouts were subjected to standard tests (ASTM C940-98a) to establish percentages of bleed-water development and shrinkage. Additionally, these grouts were separately subjected to the same standard test but with the introduction of vibration during the plastic phase of the grout. The vibration was introduced by placing the test specimens directly upon a laboratory concrete vibrating table. The peak amplitude of the vibration was <0.10mm at 60Hz. This aspect was introduced in an attempt to generate the same magnitude of grout bleed water development in the laboratory specimens as that which had been observed in the field.

Anchorage Mock-up Details: The mock-up utilized a proprietary anchorage system (Figure 2) of the same type and from the same manufacturer as that used at MBB. The system consists of a ductile iron, multi-plane anchor manufactured to ASTM A27, Grade 65-45-12 specifications and a forged steel wedge plate manufactured to ASTM A688 specifications. The post-tensioning strands were seven-wire, 14.3mm nominal strand diameter, Grade 1860 manufactured to AASHTO M 203 specifications. Composition of the components was verified via metallographic examination and spectrographic analysis. The wedge plate in this experiment was represented by a cut-off piece of plate cast into the anchorage grout. The wedge plate section measured 5.5cm wide (the thickness of the plate) by 12.7cm in length. Since this specimen was cut from the edge of the wedge plate, one side of the test specimen had a sawn edge while one side was in the "as-manufactured condition". The total surface area of the portion of the specimen in contact with grout was approximately 81cm^2. This metal-to-grout surface contact area is proportionate to the contact area that would exist with a horizontally positioned anchor approximately 50% filled with grout. The surface area of the anchor in contact with the grout was 856cm^2. All of the metal components used in the experiment were "as-new" and showed no signs of deterioration or contamination. The strands were gray in color, free of grease and oils and had a mill finish.

The mock-up (Figures 5 and 6) consisted of seven bundled, seven-wire strands and a cut-off section of the wedge plate cast into the anchorage in a vertical position. A thick grout made up of cement and micro-silica was used to seal the bottom 4cm of the anchorage. Care was used to ensure that none of the metal components were in contact with one another. The grout used in this experiment was as previously described using 1 percent (by weight) aluminum based expanding admixture. Approximately 3.3L of grout was placed into the anchor. The grout filled the anchor to a point 3cm from the top (outer end). During grout placement, the strands and wedge plate section were suspended in place using cloth tie-wires. Following introduction of the grout, the specimen was vibrated (as indicated earlier) continuously for four hours. Subsequently, measurements were made for grout shrinkage and bleed-water. Each of the metallic components was equipped with securely attached and sealed electrical connections to facilitate testing and establishing electrical continuity between the anchorage components. Two activated titanium rods (3.2mm diameter) were imbedded into the grout. One rod was 10cm in length; the other was 4cm in length. These served as counter and reference electrodes in the polarization resistance tests. The open end of the anchor was fitted with a suitably sized glass vessel to minimize evaporation during the laboratory evaluation. A silicone seal approximately 2mm thick by 25mm wide was used between the glass vessel and anchor. A section measuring 10mm wide was cut out of the silicone seal to replicate a defect in construction that would be of sufficient size to allow water re-charge and aeration similar to that which might be experienced in actual field conditions.

Corrosion Testing of the Anchorage Mock-up: Tests consisted of (i) half-cell potential measurements, (ii) macrocell current measurements, and (iii) polarization resistance measurements.

Half-cell potential measurements were taken of the individual metal components and of the coupled components using a copper-copper sulfate reference electrode (CSE) and high

impedance voltmeter. These measurements were taken by first removing the glass vessel and then placing the reference electrode directly in contact with the grout. Except as otherwise noted, all half-cell potential measurements of individual components (anchor, wedge-plate section and strands) were taken instantaneously (within one second) after interruption of the electrical connection to other components. The anchor and wedge plate (referred to as "anchorage" or "anchorage components") remained electrically coupled throughout the experiment. Macro-cell current between the individual components was measured using a low resistance digital ammeter.

As shown in Table 1, five water re-charge events were completed. Water re-charging consisted of adding 100-200ml de-ionized water to the top of the specimen. Typically, following each re-charge event, measurements of potentials and current were made until all of the metal components either reached a passive condition, or the macro-cell current reached near steady-state values (as in the fourth recharge event). At day 105, polarization and electrochemical impedance spectroscopy (EIS) tests were made on the individual components and with all components electrically coupled. Polarization resistance tests were conducted for the fourth and fifth recharge events. In the fifth re-charge event, the distilled water contained 1,000ppm chlorides. The purpose of the chloride addition was to simulate re-charge water such as that which might occur from bridge deck run-off water in a marine environment. This chloride value was selected based on actual field tests on rainwater run-off from a bridge over Tampa Bay (Florida). Grout chloride content determinations were made using standard potentiometric methods.

Post-testing Examination: After completion of the corrosion tests, the specimen was dismantled and subjected to visual examination. The specimen was dismantled by first saw-cutting lengthwise through the anchor, two cuts situated 180 degrees from one another. This allowed the anchor to be easily removed without disturbing its contents. The grout in the mock-up was first scored (using an abrasive wheel saw) and then easily separated from the components that had been cast into it. The pH of the grout was measured at various locations throughout the specimen using liquid, color reactive reagents. Three of the seven-wire strands were randomly selected for detailed examination. The remaining four strands were preserved for possible subsequent evaluation. The selected strands were first cleaned by wire brushing while rinsing in distilled water followed by forced air-drying to minimize further rust development. The individual wires were numbered along with markings to later identify wire orientation (position) in the strand. This allowed for identification of the position of corrosion on individual wires after the strand wires were separated. After the markings were applied, the individual wires were separated from each of the three selected strands. The visual condition of each wire was determined followed by furthe cleaning using the methods previously described. Measurements of pit depth on the individual strand wires were made using precision digital micrometers (needle point for pits, square jaws for non-corroded areas). These measurements were made by first measuring the full cross-sectional diameter of the individual wire in the immediate, non-corroded area nearest the location of the metal loss (within 1cm). Care was used to take both measurements across the same cross-sectional plane to minimize the effects of any out-of-round conditions that may exist. Maximum measured pit depths were plotted on cross sectional drawings showing position and measured corrosion loss. The condition of the anchor interior and wedge plate section was visually characterized after first cleaning the components as previously described. The components were then examined under 6X magnification at which time metal

surface attack was semi-quantitatively determined by direct measurements of pits and surface wastage.

Results and Observations:

Standard Grout Tests: In these standard tests (Figure 7) grout shrinkage is characterized by the loss of grout volume due to water loss (grout bleed-water) during the plastic phase. Results of these tests showed grout shrinkage and bleed-water volumes to be within expected parameters for the aluminum admixed specimen, and the non-admixed control specimen. However, when these materials were exposed to low amplitude vibration as previously described, the volume of bleed water increased dramatically. The non-vibrated control specimen developed 1.81% bleed-water, and the vibrated specimen developed 6.2% bleed-water. Comparatively, the aluminum admixed specimens developed 1.94% bleed-water (non-vibrated) and 10.2% bleed-water (vibrated) with a correspondingly equal loss of grout volume. Visual examination of the test specimens (except for the vibrated, aluminum-admixed specimen) showed the grout to be of relatively uniform consolidation and coloration throughout. Comparatively, the aluminum admixed specimen showed wide variations in coloration (Figure 8) along its length. The lower portion of the specimen was dark and dense in appearance but with increasing height, the grout was increasingly lighter in coloration until finally at the uppermost portion of the specimen (~1cm) the grout was near white in color and chalky in texture (Figure 9). The pH of the grout at the top of the specimen was determined to be 8.7 (+/- 0.5). The pH of the grout near the bottom of the specimen was >~12.

Grout in the Experimental Anchorage Mock-up: The bleed-water that developed as a result of intentional vibration reached a depth of about 1.25cm (7.6% by volume) with a correspondingly equal grout volume loss. The pH of the bleed-water was >12.2. After 24 hours of curing, the grout at the top of the specimen consisted of a wet, pasty, chalk-like layer that typically varied in thickness from 2 to 5mm. At this time, only trace amounts of free bleed water remained on the top of the specimen. The pH of the chalky grout top surface was measured at 8.7 (+/- 0.5). Analysis of the same chalky material (measured prior to adding re-charge water) showed the chloride content to be 440ppm while post-experimental analysis of the grout near the bottom of the specimen was 69ppm. This lower value is consistent with expected baseline values.

Corrosion Behavior in the Experimental Anchorage Mock-up: Portions of the coupled metallic components in the freshly cast system were initially in the active condition, as shown one day after casting by a combined potential of –302 mV and macrocell current of –70 μA (negative sign assigned to indicate the strand was anodic). Five days later the potentials had become 60 mV more positive and the macrocell current decayed to –9μA, indicating a combination of increased passivity and drying. On day six, the first of five water re-charge events commenced and evaluation was carried out over a period of nearly six months.

Table 1 summarizes the main results, to which the following notes apply. *Event No. 1:* After measurements during this event were completed, the glass vessel was placed on top of thus

reducing the rate of evaporation; *Event No. 2:* In this and in the following events, there was a brief period after water recharge where the strands were cathodic to the rest of the assembly. However, most of the integrated macrocell charge was transferred while the strands were the anodic part of the macrocell. *Event No. 3:* Beginning on day 83, about one month since starting this event, the strands were electrically detached from the anchor and wedge plate section. The anchor and wedge plate were left electrically coupled and the glass vessel was removed from the specimen. The purpose of these steps was to simulate drier conditions. Electrochemical tests conducted at day 106 indicated greatly reduced corrosion intensity. The specimen was left with the components in an electrically discontinuous condition and with the glass vessel removed until day 113 when the next event started; *Event No. 4:* The glass top was replaced after the components were interconnected again on day 114. *Event No. 5:* Figure 10 shows the macrocell current development during this event. The specimen remained with all components coupled and the glass top in place until day 166 when the experiment ended.

Dismantling and Examination of the Anchorage Mock-up Components:

Condition of the Anchor: The grout in the mock-up showed no indication of adhesion to the interior surface of the anchor. The interior surface of the anchor was found to be completely unaffected during the experiment except for corrosion that developed around its circumference beginning at approximately 0.5cm below the top grout level and extending upward approximately 2cm. The region above the grout level experiencing corrosion was that area that was wetted via direct contact with re-charge water and capillary rise during the experiment. This area had widespread surface corrosion attack that typically penetrated the surface approximately 0.25mm. The surface area in this zone affected by generalized corrosion was estimated at 80%. Infrequent pitting attack was also present. The pits were approximately 1mm wide and variable in depth up to 1.5mm.

Condition of the Wedge-plate Section: The surface of the metal in contact with the grout was found to be unaffected during the experiment except for an area beginning approximately 1cm below the top grout level and extending upward approximately 2cm. Under 6X magnification, the affected zone on the "as manufactured" surface showed localized pitting in the form of elongated grooves approximately 2mm wide and 1mm to 2mm deep; one area was 5mm in length and the other was 12mm in length. (The lengthwise direction followed the grout line.) The affected area of the saw-cut surface showed light surface wastage accompanied by the presence of nine mostly circular pits 1mm to 3mm wide and 0.5 to 1mm deep. The location of these pits was generally equally distributed above and below the area coinciding with the top of the grout.

Condition of the Strands: The surfaces of the strands in contact with the grout were found to be unaffected during the experiment except for the area beginning approximately 2.5cm below the top of the grout and 2cm above the top of the grout. The area beginning approximately 2cm above the top of the grout and extending downward to approximately 1cm below the grout had heavy deposits of red to dark brown colored corrosion products (Figure 11). Extensive corrosion pitting was noted on the wire surfaces in the area coinciding with ~0.5cm above and below the top of the grout. The grout immediately adjacent to the strands in the zone beginning at the top of the grout and extending downward approximately 3cm was soft and chalky and the pH was

measured at 8.7 (+/-0.5). The individual wires of the three selected strands were separated for further examination. The previously mentioned corrosion pitting (near the top of the grout) was confined entirely to the outer surfaces of the individual wires. Although multiple pits existed along this ~1cm long affected zone, the area of heaviest attack was mostly centered at the area coinciding with the top of the grout. The typical appearance of the pitted areas is depicted in Figure12, and a schematic representation of the maximum measured pit depth and relative sizes of the pits is presented (Figure 13) for each of the three strands examined.

Discussion

The field corrosion incidents showed that while large portions of the strands and anchorage components remained in the passive state, intense localized corrosion did take place leading to enough loss of tendon cross section to result in mechanical failure. The passive behavior of most of the steel is as expected from the highly alkaline nature of the grout pore water. The presence of localized corrosion indicates either severe chloride contamination, or a marked local reduction in the pH of the water in contact with the steel, or a combination of both (Li 2001). Once initiated, localized corrosion could be seriously aggravated by electrochemical coupling of the small anodic area with a large cathodic region (Kranc 2001).

The corrosion was present near anchorages and by bleed water voids, which led to speculation on how the requisites for localized corrosion indicated above may have developed. It was thought that a lowered pH could develop at the interface between the grout and the void area by reaction with CO_2 leaking in from the external atmosphere. Furthermore, chloride concentration increases may occur there by penetration into the void area by salty runoff from the bridge surface, or by evaporative concentration of the bleed water (which should contain chlorides leached from the background amount allowed by the grout specifications) initially in the void. Aggravation of the corrosion could result if the anchorage or wedge plate were particularly efficient cathodes. The preliminary experiments in this work aimed to establish the likelihood of those speculative mechanisms.

The standard grout test results confirmed the tendency of grouts such as those used in the affected bridges to develop large bleed water regions near the anchorages, especially in the presence of modest vibration amplitudes that may exist during normal construction operations. The transition zone between grout and simulated void space in the experimental anchorage mock up was exposed to ambient air through the silicone seal cut out, which allowed for some evaporation and external air access. As anticipated, a lowered pH (~9) in that zone was observed consistent with carbonation of the hydrated cement present there by exposure to atmospheric CO_2, which could happen in a short time considering the highly porous nature of that chalky material (Moreno 1998). Furthermore, the chloride content there (before any intentional salt contamination) was ~ 6 times greater than in the bulk of the grout indicating that a chloride concentration mechanism, possibly evaporative concentration as speculated, was active.

Post-experiment analysis indicated that most of the corrosion developed at or around the grout/simulated void interface, while the rest of the assembly in contact with grout showed the typical appearance of passive steel in concrete. The latter behavior was as expected, since the total chloride contamination (even after addition of 200ml of 1000 ppm Cl^- water in the last

recharge event) was not enough to initiate widespread corrosion considering the relatively large volume of highly alkaline grout involved (Li 2001). Likewise, corrosion at the interface was not surprising as conditions there were much more propitious to corrosion initiation. In that zone, the lower pH and higher chloride content substantially elevated the $[Cl^-]/[OH^-]$ ratio compared to the bulk of the grout (Li 2001). The electrochemical measurements provided confirming evidence of the presence of active steel/iron behavior by observation of highly negative potentials (Bentur 1997) and correspondingly high corrosion current from Rp tests as well as high macrocell currents. These indications were more pronounced early during each recharge event when water was plentiful at the transition zone. As water absorption and evaporation ensued the mixed potential evolved toward values indicative of a less predominant active region. Near the end of the test period (Recharge Events No. 4 and 5), corrosion was maintained over long time periods with minimal water addition, sustained by retained moisture in the anchorage. The corrosion proceeded at a substantial rate (see below) even though total external chloride contamination was modest.

Corrosion of the strands (penetration depth as much as ~7% of a wire diameter) was severe in view of the relatively short duration of the tests and the low tolerance of a loaded system to localized reductions in cross section (Stauder 1998, Vermaas 2001). The corrosion morphology of the strands (Figure 12) is consistent with that of shallow pitting, constrained to a small region by local acidification from hydrolysis of ejected metal cations (Jones 1996), and protection of the surrounding region by local potential depression (Pedeferri 1996). An order-of-magnitude estimate of the total amount of corrosion in the strands can be made by assuming that each outer strand wire had an equivalent integrated pitted area ~10 mm^2 with a depth ~0.23 mm (average depth from Figure 13). For 6 corroding wires in the 7 strands this corresponds to a total metal loss of ~100 mm^3, or an anodic charge of ~2,600 C if the steel corroded as Fe^{++}. This value may be contrasted with the integrated value over time of the anodic macrocell current data in Figure 10 (the longest recharge event), which yields ~1,200 C. While the corrosion charge estimate is subject to considerable uncertainty, the similarity of the macrocell and corrosion charges suggests that galvanic coupling with the anchorage accounted for much of the metal loss at the strands. Nominal corrosion current estimates from polarization resistance tests (Table 1) are available for moist conditions only for instances when the strands were cathodic early in recharge events 4 and 5. Nevertheless, these results also illustrate cases where the macrocell currents (304 μA and 136 μA) were a significant fraction of the estimated local cell action at the strands (749 μA and 875 μA respectively).

Both the anchor and the wedge plate had actively corroding spots, experiencing a total amount of corrosion comparable or greater than that experienced by the strands. However, the measurements of the "off" potential and the direction of the macrocell current showed that the combined anchor and wedge plate section developed a mixed potential sufficient to act as an efficient net cathode except for the short periods when there was free recharge water over the grout. The available data do not permit identifying which of those two components was the most cathodic but the ductile iron anchor with its large surface area, as-cast finish and high carbon and silicon content deserves consideration for that role.

The findings from the field and the laboratory experiments discussed above showed that severe localized corrosion can develop in post-tensioned tendons at voids left by receding bleed water, even with very mild external chloride contamination. Pitting penetration on the order of that observed here after only ½ year of exposure to the laboratory conditions (up to 0.35 mm) already has some significant adverse effects, as it has been reported to reduce by half the ductility of tensioned bridge wires (Vermaas, 2001). A rough indication of the time required for outright overload failure can be made by conservatively assuming that the terminal stress in post tensioned strands for the application of interest is on the order of 70% of the ultimate tensile strength. Failure is likely to occur before corrosion reduces the local cross section by 30%, since the pit shape introduces severe stress concentration not necessarily compensated by notch strengthening (besides possible embrittlement effects from any hydrogen generation at the corroding region) (Stauder1998, Vermaas 2001). An ~20% reduction in cross section (which may result from a broad pit ~1.5 mm deep) could easily be above the tolerable limit. If pit depth were to increase linearly with time at a rate of 0.35 mm per ½ year (for the deepest pit in Figure 12), the first wire failures could then develop after ~2 years of exposure to conditions such as those simulated in the laboratory. Longer times would be required if the pit penetration is proportional to a lower power of time (e.g. ~4 years or ~8 years for ½ or 1/3 power dependence as is common in other systems (Szklarska-Smialowska 1986). While these estimates are subject to much uncertainty and dependent on conditions such as the occurrence of periodic recharge events, the results are in the order of the ages of the bridges considered here at the time they were affected by tendon failures.

The findings indicated above are preliminary in nature but serve to formulate a working picture of the events leading to the failures observed in the field, and as a guide to implement initial corrosion prevention measures. It is clear that bleed water voids can be a major source of corrosion tendon failure, and that failure can develop over a very short time frame. Rigorous implementation of bleed water avoidance measures is essential in new construction, as well as avoiding design that may promote galvanic corrosion of the strands. Thorough examination of existing structures to detect and remedy voids is in order. Remediation of voided anchorages or tendons that do not show significant corrosion must be made in a manner that will not introduce or reactivate further corrosion. Aspects revealed but only partially addressed in this work (e.g., the cathodic efficiency of anchorages versus wedge plate, the extent and mechanism of pH reduction at the grout/void interface, and the factors determining the anodic nature of the strand with respect to the other metallic components) are presently being examined in detail in an ongoing investigation and will be reported in the future.

Conclusions

1. Severe corrosion of steel strands was encountered in post-tensioned tendons of two major bridges in the State of Florida. The corrosion was associated with grout bleed-water voids and chloride ion contamination, in regions of the superstructure where periodic water intrusion was likely.

2. Grout tests indicated that modest vibration (as it may be encountered under normal construction conditions) could dramatically increase the amount of bleed water developed by the types of materials used in the bridges affected by corrosion.

3. Severe corrosion developed over six months testing in a laboratory anchorage mock-up where standard high strength steel strands and ductile iron and carbon steel anchorage components were partially in contact with hardened grout, and subject to periodic water recharge with and without moderate chloride ion contamination.

4. Electrochemical measurements indicated that portions of the strand and of the anchorage component surfaces became active upon water recharge and stayed active for extended periods afterwards, even without addition of chloride ions. Direct observation showed that corrosion took place in the transition zone between grout and air space, while the metal completely embedded in grout remained in the passive condition.

5. The grout in the transition zone had reduced pH and increased chloride content compared with the grout in the bulk. This situation appears to be the result of evaporative concentration of the initial bleed water and superficial carbonation upon contact with CO_2 in the air. These conditions promoted depassivation and subsequent corrosion damage of the metallic components at the grout transition zone.

6. Corrosion at the transition zone was aggravated by galvanic coupling between the small active area and the large passive metal area on contact with the bulk of the grout. Electrochemical measurements indicated that for most of the time the anchorage elements were cathodic with respect to the strand, substantially aggravating the corrosion of the latter.

7. The corrosion rates determined in the laboratory were consistent with observation of strands failures in the field after only a few years of service, underscoring the corrosion severity that is possible under the mechanisms observed.

8. Rigorous implementation of bleed water avoidance measures is essential in new construction, as well as avoiding design that may promote galvanic corrosion of the strands.

Acknowledgement

The opinions, findings and conclusions expressed here are those of the authors and not necessarily those of the Florida Department of Transportation, the University of South Florida, or the United States Department of Transportation-Federal Highway Administration.

References

Bentur, A., Diamond, S., Berke, N.S., Steel Corrosion in Concrete: Fundamental and Civil Engineering Practice, New York: E & FN Spon, 1997

Corven, J., "Mid Bay Bridge Post-Tensioning Evaluation", Final Report , Florida Department of Transportation, Tallahassee, October 2001.

Ghorbanpoor, A., Madathanapalli, S. C., "Performance of Grouts for Post-Tensioned Bridge Structures", Report No. FHWA-RD-92-095, National Technical Information Service, Springfield, VA, 1993.

Jones, D.A., Principles and Prevention of Corrosion, 2nd. Ed, Prentice Hall, Upper Saddle River, NJ, 1996.

Kranc, S.C., Sagüés, A.A. "Detailed Modeling of Corrosion Macrocells on Steel Reinforcing in Concrete", Corrosion Science, Vol. 43, p. 1355, 2001.

Li, L., Sagüés, A.A. "Chloride Corrosion Threshold of Reinforcing Steel in Alkaline Solutions - Open-circuit Immersion Tests", Corrosion, Vol. 57, p.19-28, 2001.

Moreno, E.I., Sagüés, A.A., "Carbonation-Induced Corrosion of Blended-Cement Concrete Mix Designs for Highway Structures", Paper No. 636, 10 pp., Corrosion/98, NACE International, Houston, 1998.

Pedeferri, P., "Cathodic Protection and Cathodic Prevention", Construction and Building Materials, Vol. 10, p.391-402, 1996

Powers, R. G., "Corrosion Evaluation of Post-Tensioned Tendons on the Niles Channel Bridge", Florida Department of Transportation, Gainesville, FL, June 1999.

Stauder, A. , Hartt, W.H., "Cathodic Protection of Pre-Tensioned Concrete: Part I - Brittle Failure Propensity of Corrosion Damaged Prestressing Tendon Wire", Paper No. 635, Corrosion/98, Nace International, Houston, 1998.

Szklarska-Smialowska, Z., Pitting Corrosion of Metals, NACE Intnl., Houston, 1986
Tabatabai, H., Ciolko, A. T., and Dickson, T. J., "Implications from Full-Scale Fatigue Tests of Cable Stays Composed of Seven-Wire Prestressing Strands", Proceedings of the Fourth Intnl. Bridge Engineering Conference, Vol. 1, August 28-30, 1995, pp. 266-277.

Vermaas, G., Betti, R., Barton, S.C., Duby, P., West, A.C., "Corrosion and Embrittlement of High-Strength Bridge Wires", p. 85 in Long Term Durability of Structural Materials, Monteiro, P., Chong, K, Larsen-Basse, J. and Komvolopoulos, Eds., Elsevier, Amsterdam, 2001.

Table 1. Summary of Corrosion Test Results

Recharge Event	No. 1		No. 2				No. 3			Dry Values	No. 4			No. 5		
Water added on day	6		7				56				113			117		
DI Water added (mL)	200		100				150				200			200 with 1000 ppm Cl^-		
Initial depth of water	1.25		0.6				1				1.25			1.25		
Water reabsorbed by day	7		9				83 or earlier				115			118		
Conditions on day	6	7	8	9	26	56	56.1	57	83	106	114	115	117	119	131	166
Anchorage Potential (mV vs CSE)	-518	-463	-600	-431	-197	2	-577	-557	-412	-248	-648			-603		
Strand Potential (mV vs CSE)	-537	-466	-549	-485	-221	0	-463	-629	-423	-225	-625			-558		
Macrocell Current[1] (μA)	-140	-10	470	-130	-20	nil	1120	-810	-270	4	304	-331	-105	136	-525	-145
Anchorage Nominal Corrosion Current[1] (From Rp test) (μA)										20	1656			2214		
Strand Nominal Corrosion Current[1] (From Rp test) (μA)										17	749			875		
System Nominal Corrosion Current[1] (From Rp test) (μA)										27	2142			2176		
Strand Pitting Rate[2] (mm/yr)	0.53															

Notes: 1. Negative current value indicates strand is anode.
2. Pitting rate of strands based on average maximum pit depth (Figure 13)

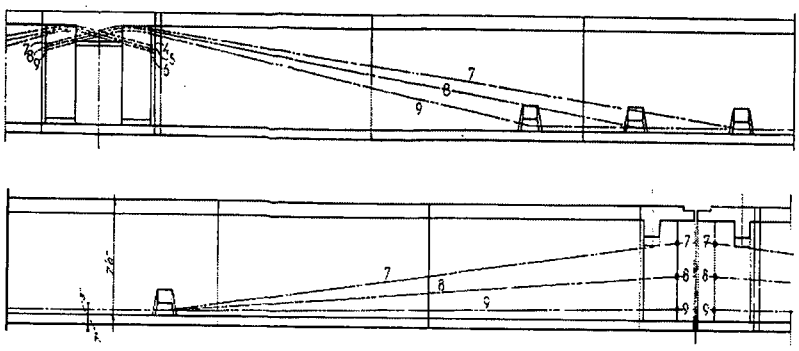

Figure 1 – Typical tendon configuration in the superstructure of the affected bridges.

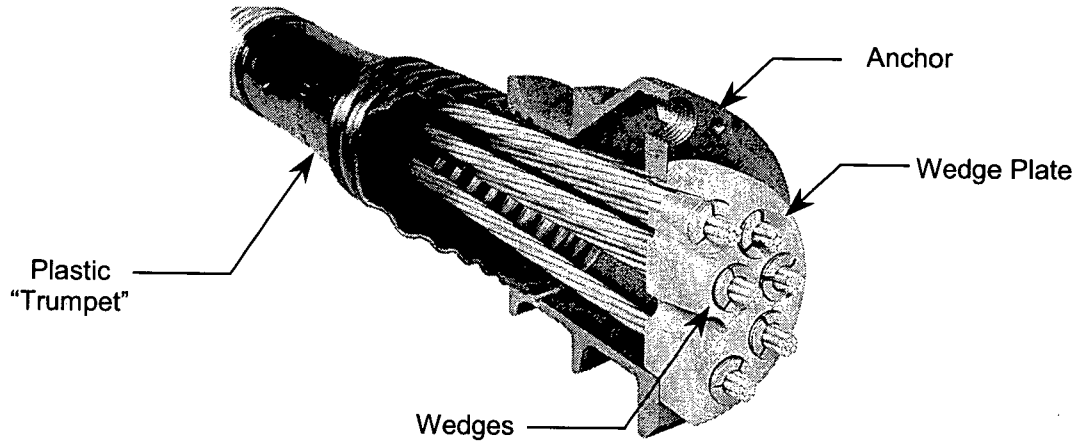

Figure 2 – Details of the anchorage system used in the Niles Channel and Mid Bay Bridges.

Figure 3 – Failed tendon-Niles Channel Bridge (June, 1999).

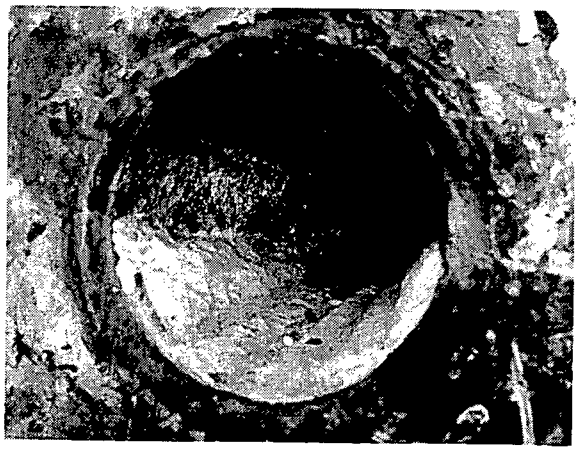

Figure 4 – Anchor at failed tendon showing chalky grout, partial grout filling and heavy corrosion.

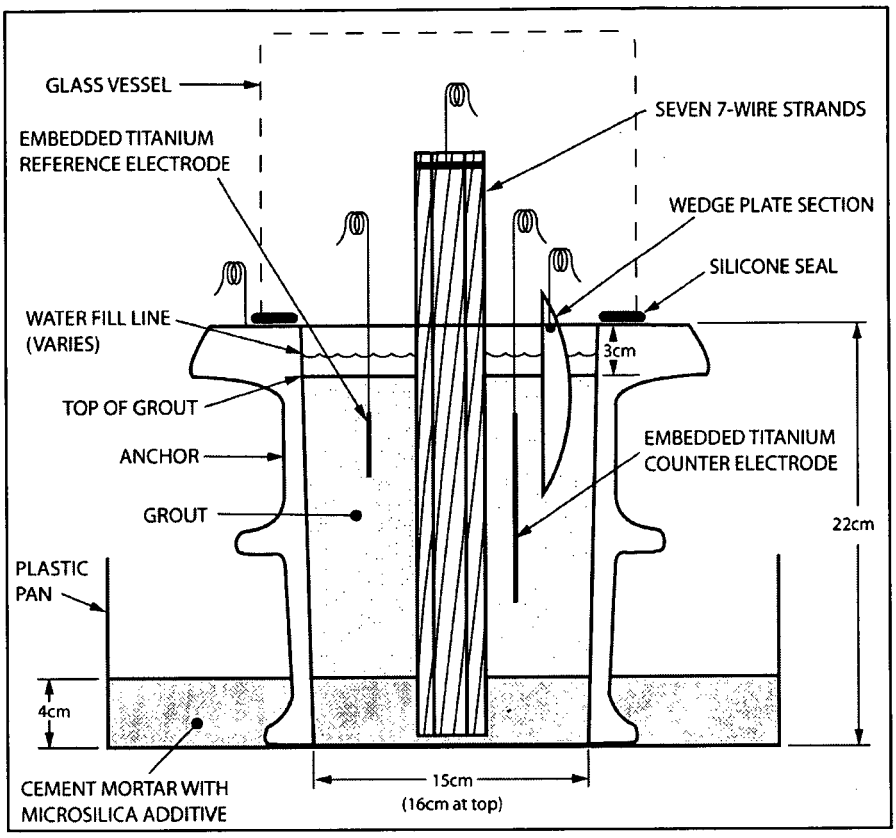

Figure 5 – Schematic of the experimental anchorage mock-up.

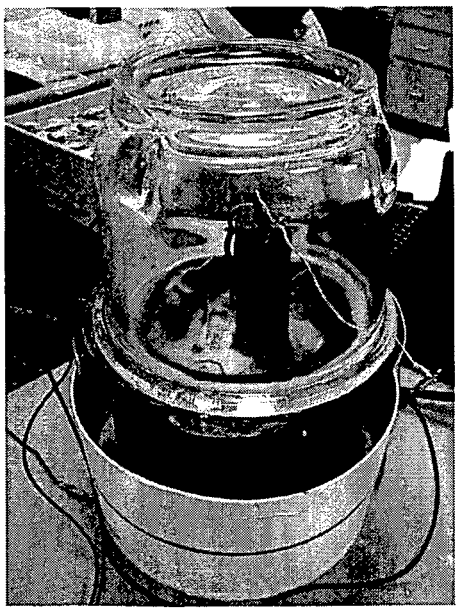

Figure 6 – Photograph of the experimental anchorage mock-up.

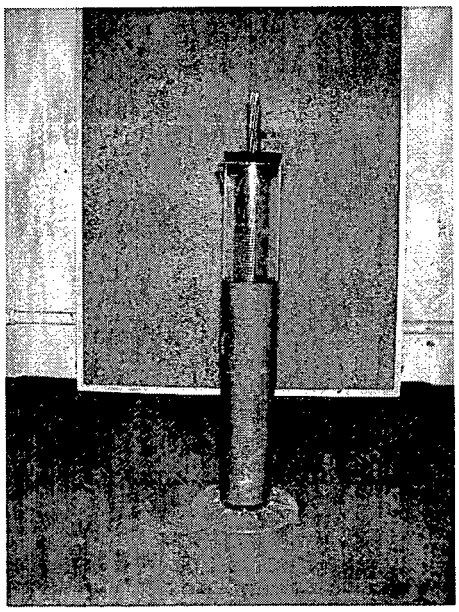

Figure 7 – Photograph of the test apparatus for measuring grout bleed-water and grout volume change.

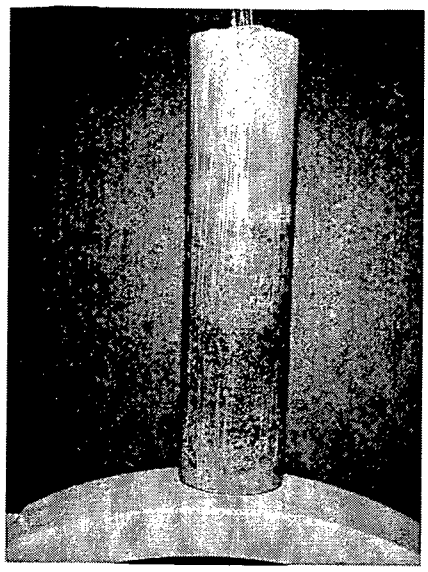

Figure 8 – Photograph depicting increasing chalkiness toward the top of the aluminum admixed grout (vibrated).

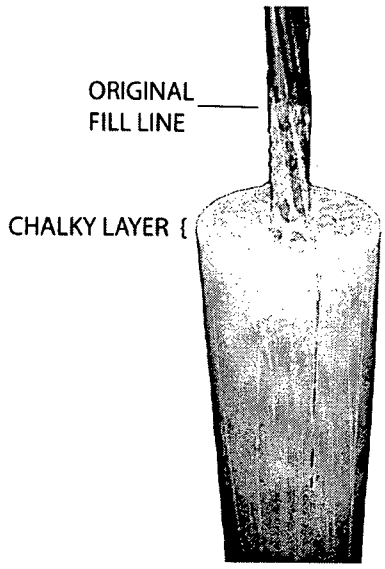

Figure 9 – Close-up photograph depicting large grout volume loss and heavy chalk development in the aluminum admixed grout (vibrated).

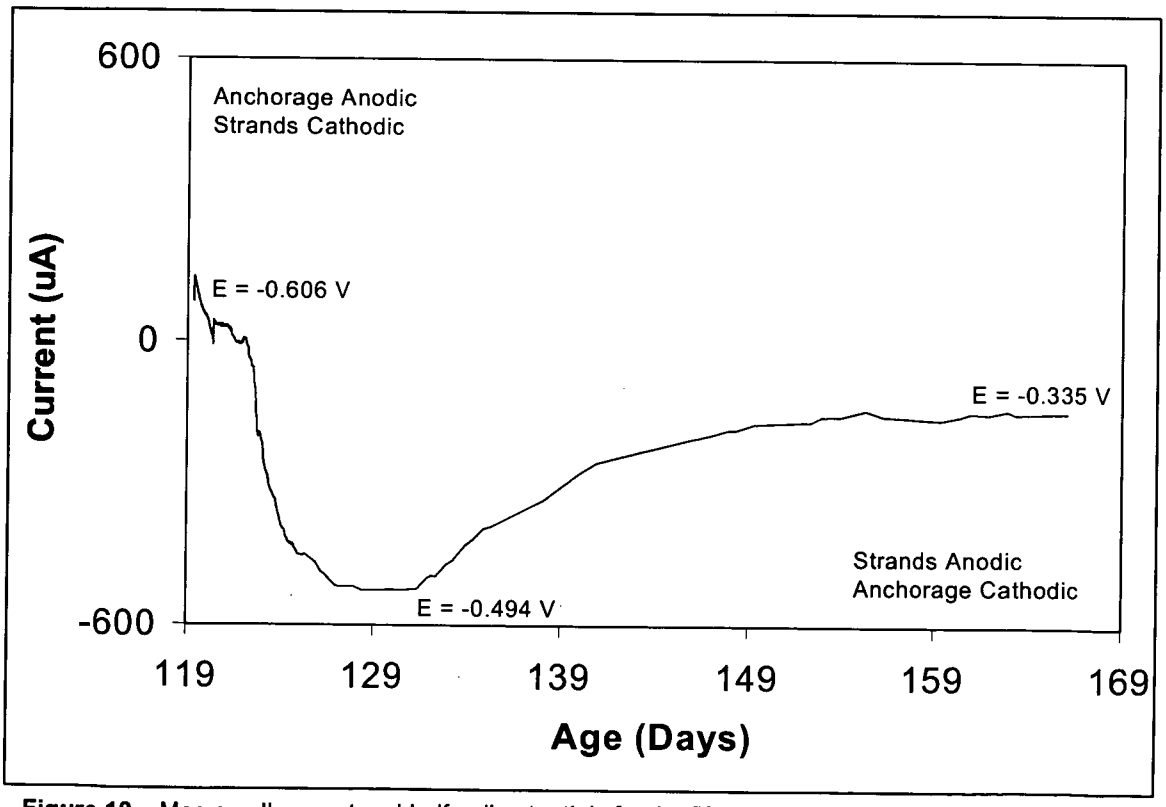

Figure 10 – Macro-cell current and half-cell potentials for the fifth water re-charge event.

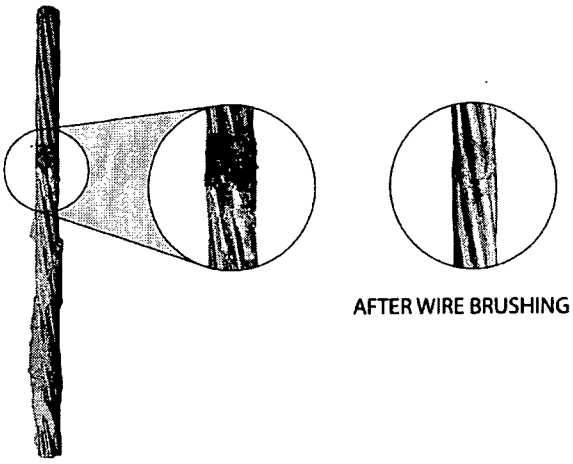

Figure 11 – Typical appearance of the strand upon removal from the mock-up.

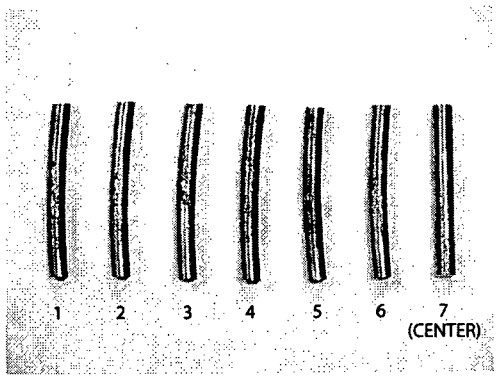

Figure 12 – Typical appearance of the corrosion pits on the strands near the top of the grout.

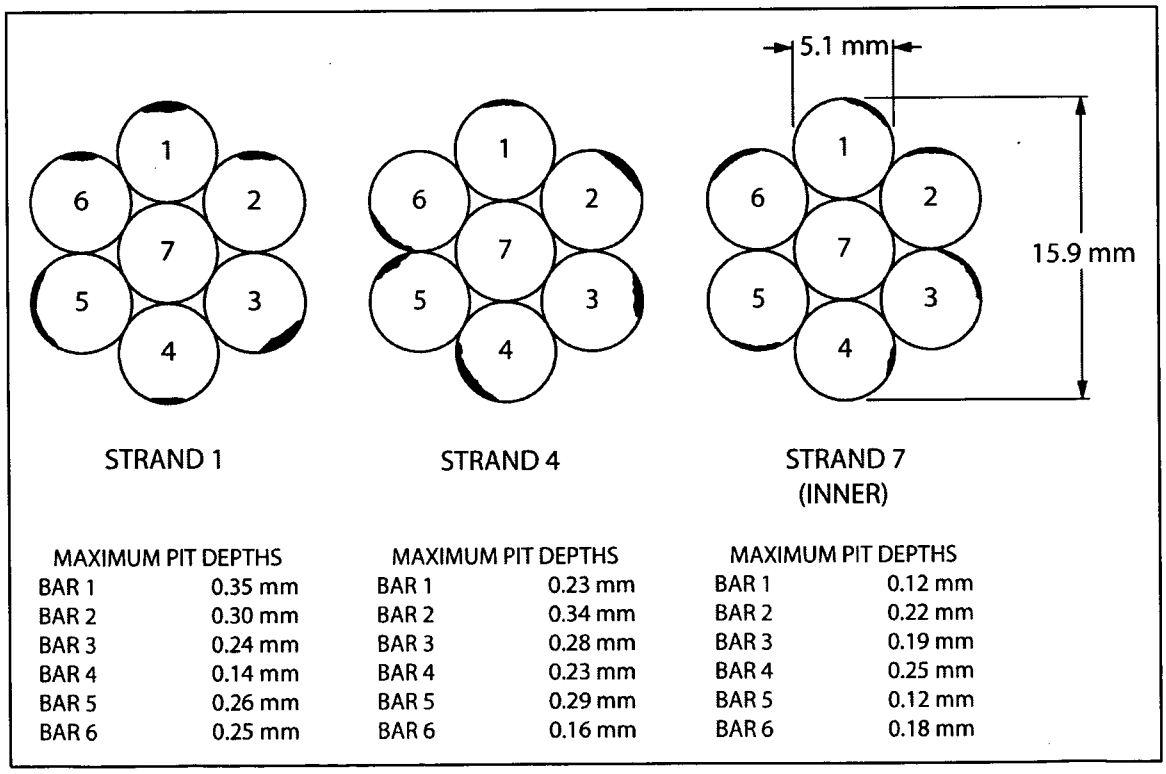

Figure 13 – Schematic representation of the maximum observed corrosion pitting for each of the wires of the three selected strands.

ACCELERATED CORROSION TEST METHOD FOR POST-TENSIONED GROUTS

Neil G. Thompson[1] Yash P. Virmani[2] David R. Lankard[3]

Abstract

This paper presents a portion of the research performed under a FHWA contract and reported in Final Report No. FHWA-RD-91-092. The purpose of this research was to develop and test new mixture designs for grouts and to develop an accelerated test method for evaluating new grout mixtures. The current paper focuses on the test method development, which has recently been incorporated in the recently issued specifications by the Post-Tensioning Institute for Grouting of Post-Tensioned Structures.

The ability of the test method to distinguish one grout from another was evaluated by testing a variety of modifiers and additives for grouts, including high-range water reducers, flyash, silica fume, latex polymer modifier, expansive agents, anti-bleed additives, and corrosion inhibitors. It was shown that these additives influence the resistance to corrosion of steel tendons embedded in the grout.

Introduction

Currently, there is a serious problem in the United States and elsewhere with the deterioration of concrete bridges due to corrosion induced by chloride (Cl^-) intrusion into the concrete. Historically the problem has been associated with conventionally reinforced concrete bridge structures as opposed to prestressed or post-tensioned structures. Recently, corrosion of steel tendons in prestressed concrete structures has become a concern because the structural integrity of the bridge relies on the high tensile loading of the tendons and corrosion induced failures of tendons have been observed in some structures. In bonded post-tensioned construction, grout is the final line of defense against corrosion of the uncoated steel tendon.

Although the performance of bonded post-tensioned concrete structures is, in general, very good, documented investigations showing corrosion of bonded post-tensioned steel strands have been reported. [1-10] Figure 1 shows a failed tendon near the anchor. [9] The most likely cause of the corrosion was bleeding of the grout resulting in water filled voids in the tendon and subsequent recharging of the voids with external water/ moisture resulting in corrosion of the tendons not protected by grout.

[1] CEO and President, CC Technologies, Dublin, Ohio
[2] Research Chemist, Federal Highway Administration, McLean, Virginia
[3] President, Lankard Materials Laboratory, Inc., Columbus, Ohio

In the late 1980's, FHWA determined that one area in which improvements were possible was the grouts used for filling the ducts containing the prestressed steel within the post-tensioned structure. Thus, the study being reported here was undertaken. The recent Florida experience (references 9 and 10) has highlighted the need for proper grout placement.

Because grouts provide the final defense against corrosion of the prestressing steel tendons that support the structure, it is imperative to provide a grout that incorporates the state-of-the-art technology. One of the primary requirements is the ability of the grout to prevent bleeding. An additional requirement is that a grout needs to provide protection against corrosion. A grout can accomplish this in two ways: (1) impede chloride migration through the grout to increase the time to achieve a critical chloride level necessary for corrosion or (2) minimize corrosion by providing corrosion protection through inhibition of the corrosion process. To evaluate new grouts in a timely manner, a new test method that can accelerate the corrosion of a grouted tendon was needed.

It is important to emphasize that the corrosion test method developed and reported here is only one of the critical properties required by an effective grout. The susceptibility to bleeding is of great importance along with flow properties for placement of the grout in the duct and subsequent mechanical properties.

Experimental

Selection of Materials

In most cases, each additive/admixture modifier category was represented by only one material. The following materials were selected for use in this study:

- Type II Portland Cement.
- An ASTM C494 Type F high-range water-reducing admixture.
- Silica fume (microsilica).
- Class F flyash (ASTM C618).
- A styrene-butadiene polymer modifier (supplied as a liquid with a solids content around 48 percent).
- Calcium nitrite corrosion inhibitor.
- Aluminum powder expansion agent.
- Polysaccharide gum anti-bleed agent.
- Celbex 209X commercial grout admixture (blend of superplasticizer, thickener, and controlled expansion agent).
- Silica sand (maximum particle size 50 mesh).

Grout Preparation Procedures

Grouts were prepared using a 0.5 HP, high-shear mixer with a propeller-type mixing blade (3 tines) typically operating at around 500 rpm. Dry batch weight of the grout Ingredients ranged from 2000 to 4000 gm (4.4 to 8.8 lb). On a volume basis, this yielded around 1500 to 3000 cc (91.5 to 183 in^3) of grout. In the majority of Instances, the grout had the rheological characteristics of a thick liquid, which could be poured from the mixing container.

Accelerated Corrosion Test Method

The accelerated corrosion test method (ACTM) was designed based on the results of the preliminary experiments and consideration of several variables Including: (1) freeze-thaw cycles, (2) wet-dry cycles, (3) temperature, (4) acceleration of Cl^- migration, (5) specimen loading, (6) types of ducts, (7) types of prestressing steel, (8) grout cover, and (9) grout curing. Detailed consideration of these variables was discussed In the FHWA Report FHWA-RD-91-092. [11]

The focus of the ACTM Is on the grout and not the total post-tensioning system which would Include a detailed Investigation of the entire system Including tendon, grout, duct, and concrete cover.

Figure 2 shows a schematic drawing of the as-cast specimen and the specimen ready for testing. A primary focus of the as-cast specimen Is the rigid, airtight mold (PVC tube) used for casting and curing the specimen. Following curing (minimum of 28 days), a gage section of the PVC tube is removed to expose the grout specimen. This simulates a significant breach in the duct wall. The specimen is tested within 24 hours and is kept immersed in a saturated calcium hydroxide solution prior to testing. Maintaining moist conditions on the exposed gage section is critical to prevent microcracking.

The following procedure is used to perform the ACTM:

1. The grouted test specimen immersed in a 5 percent NaCl solution containing a counter electrode and a saturated Calomel reference electrode.
2. A potentiostat is used to polarize the grouted test specimen.
3. Set the potentiostat to apply the selected anodic potential (+0.60 V [SCE] - original testing, 0.00 V [SCE] – grout with inhibitor, or +0.20 V [SCE] – selected for Standard Method).
4. Within 5 to 10 minutes of immersion, apply the selected anodic potential by switching the potentiostat from the "Isolate" or "disable" mode to the "run" mode.
5. Record current and potential periodically during the test (every 10 to 30 minutes is sufficient).
6. Plot current versus time. A rapid current increase signifies the initiation of corrosion.
7. Allow tests to continue for 48 hours following initiation of corrosion.

Results and Discussion

General Grout Properties

Nine different grout series were evaluated in this program. The distinction between the various series was made based on grout additives. The following provides a brief description of the different series examined. These grouts represent the state-of-the-art practices in 1988 to 1990 when the initial development work on the accelerated test method was performed.

- Series 1: Standard Grout – This grout was representative of grouts that have been used for many years in U.S. practice. It is a simple mixture of Type II portland cement and water with a water-cement ratio of 0.44.
- Series 2: Commercial Anti-Bleed Admixtures - This grout also has a "normal" water-cement ratio (0.45) but contains a commercially available anti-bleed admixture (Celtite Inc.'s Celbex 209X).
- Series 3: High-Range Water-Reducer - The use of a superplasticizer provides significantly reduced water-cement ratios (15 percent to 30 percent water reduction), while maintaining the same level of fluidity. This series provides reduced water content grouts that are otherwise comparable (from a materials point of view) to the standard grout composition.
- Series 4 and 10: Corrosion Inhibitor - The corrosion inhibitor (calcium nitrite) was used in grouts at both normal (Series 10) and reduced (Series 4) water-cement ratios.
- Series 5: High-Range Water-Reducer Plus Flyash and Sand - This series was formulated in an effort to produce a relatively impermeable grout that would function at the same performance level as silica fume grouts while costing less.
- Series 6: High-Range Water-Reducer plus Silica Fume - Silica fume replacements up to 20 percent of cement weight were evaluated. Superplasticizers are required in these systems to achieve the desired level of fluidity at reduced water content.
- Series 8: High-Range Water-Reducer Plus Latex - There is very little in the literature concerning the use of superplasticizers with latex modifiers in portland cement-based systems. In the present investigation, success was achieved in producing low water-cement ratio, latex-modified grouts.
- Series 11: High-Range Water-Reducer Plus Expansive Agent Plus Anti-Bleed Additive - This series was evaluated to learn the effect of the expansive additive on the performance of Grout Series No. 3 and No. 12.
- Series 12: Anti-Bleed Additive - In this grout series, a water soluble, polysaccharide gum, providing superior anti-bleed behavior, was evaluated.

Actual components of the different grout mixtures used in this study are given in Table 1. Although not discussed in this paper in detail, other measured properties for the grout mixtures are given in Tables 2, 3, and 4.

Accelerated Corrosion Test Method

Figure 3 shows typical results from the ACTH and Figure 4 summarizes the time-to-corrosion results for the grouts tested. The original polarized anodic potential used was +0.60 V (SCE). Grout No. 1B was the Standard Grout (No. 1) with a high water-to-cement ratio (w/c - 0.65) and represented a "poor" grout. Grout No. 1B gave the worst results; indicating the ACTM can differentiate "good" from "poor" grout based on water-to-cement ratio. The addition of HRWR, flyash and sand (Grout No. 5-1); HRWR and silica fume (Grout No. 6B); and HRWR and latex modifier (Grout No. 8-1) all improved the corrosion performance over Grout No. 1. Grout No. 5-1 containing the HRWR, sand, and flyash provided the longest time to corrosion initiation.

Using the relatively high anodic polarized potential of +0.60 V (SCE), Grout No. 10-1, which was the same as Grout No. I but with an inhibitor added indicated a decrease in the time-to-corrosion when compared to Grout No. 1 (see Figure 4). This was unexpected and these results were further examined. It is believed that the +0.60 V polarized potential was too severe for evaluating inhibitor performance and that the +0.6 V (SCE) potential exceeds the breakdown potential for steel in an inhibited grout. Also, a potential of +0.6 V is not expected in service and was used as an acceleration factor. For the case of the inhibitor, the ACTM, unrealistically, masked the inhibiting ability of the grout.

The only requirement for the ACTM is that the potential, selected to polarize the test specimen, be anodic to the free-corrosion potential of the test specimen. To examine this problem, the ACTM was modified to use an applied potential of 0.00 V (SCE). The 0.00 V potential is sufficient to accelerate corrosion once Cl^- reaches the steel surface, but should not exceed the breakdown protection of the inhibitor. The data presented in Figure 5 shows the results for the 0.00 V (SCE) ACTM for Grout No. I (Standard) and Grout 10-1 (Standard plus inhibitor). The time-to-corrosion for Grout No. I is similar for both the +0.60 V and the 0.00 V polarized potential ACTM. This indicates that the ACTM time-to-corrosion results are not overly sensitive to the polarized potential used. A significant improvement in the corrosion performance was realized when an inhibitor was added to the grout (time-to-corrosion increased from 177 up to 713 hours) based on the 0.00 V (SCE) ACTM results (see Figure 4).

Following this initial study, a polarized potential of +0.20 V (SCE) was also examined with similar results as 0.00 V. The standard test specified by the Post-Tensioning Institute utilizes a potential of +0.20 V (SCE).

The other experimental data available from the ACTM is the current following corrosion initiation. This provides a relative rate of corrosion following initiation. Figure 5 shows the current following corrosion initiation for the tests performed at +0.60 V (SCE). It can be seen that Grout No. 5-1, which had the longest time-to-corrosion initiation also exhibited the lowest current following corrosion initiation. These results clearly indicate that Grout No. 5-1 exhibited the best corrosion performance of the grouts tested at +0.60 V (SCE).

Conclusions

1. A test protocol for an accelerated corrosion test method (ACTM) for evaluating grouts for post tensioned structures was developed. The ACTM provides a relatively fast evaluation of the ability of grouts to delay the onset of corrosion in prestressing steel, and which simulates bonded post-tensioned bridge exposures while accelerating the corrosion process.
2. The time-to-corrosion results for the ACTM is not sensitive to the polarized potential used unless inhibitors are being evaluated. When inhibitors are being evaluated a polarized potential below the breakdown potential of the inhibitor, but anodic (positive) to the free-corrosion potential of the test specimen, must be used (0.00 V [SCE] for this study).
3. Based on the ACTM results grout additives and modifiers which significantly reduce Cl^- permeation also significantly increased the time-to-corrosion of embedded steel tendons.

4. Grout No. 5-1 containing 33 percent (cement weight) flyash provided a 3-fold increase in time to corrosion initiation relative to the standard grout.
5. Grout No. 6B containing 10 percent (cement weight) silica fume addition provided a 2-fold increase in time to corrosion Initiation relative to the standard grout.
6. Based on limited comparison data from the ACTM, the calcium nitrite corrosion inhibitor provided significant improvement in corrosion performance of the grout.

References

1. Thompson, N. G., et al., "Grouting Technology For Bonded Tendons in Post-Tensioned Bridge Structure," Report No. FHWA-RD-90-102, pp. 1-39, Washington, D.C., November 1990.
2. Lankard, D. R., et al., "Grouts For Bonded Post-Tensioned Concrete Construction: Protecting Prestressing Steel From Corrosion", 1990 Fall Convention, American Concrete Institute, Philadelphia, PA, November II- 16, 1990.
3. D. G. Hoore et al., "Protection of Steel in Prestressed Concrete Bridges," NCHRP Report 90, pp. 1-86, Washington, D.C., 1970.
4. J. Ryell and B. S. Richardson, "Cracks in Concrete Bridge Decks and Their Contributions To Corrosion of Reinforcing Steel in Prestressing Cables," Ontario Ministry of Transportation and Communications Report IRSI, pp. 1-30, Toronto, Canada, September 1972.
5. T. J. Bezouska, "Field Inspection of Grouted Post-Tensioning Tendons," Report of the Post-Tensioning Institute, pp. 1-16, Phoenix, AZ, March 1977.
6. M. Schupack, "A Survey of the Durability Performance of Post-Tensioning Tendons," Post-Tensioning Institute, pp. 1-10, Phoenix, AZ, 1978.
7. J. R. Libby, "Three Chloride-Related Failures in Concrete Structures," Concrete International, pp. 29-31, Detroit, MI, June 1987.
8. Novokshchenov, V., "Salt Penetration and Corrosion in Prestressed Concrete Members", Report No. FHWA-RD-88-269, Federal Highway Administration, pp. 1-212, Washington, D.C., July 1989.
9. R. G. Powers, "Corrosion Evaluation of Post-Tensioned Tendons on the Niles Channel Bridge", Florida DOT, State Materials Office, 1999.
10. Mid-Bay Bridge Post-Tensioning Evaluation, Draft Report, Florida Department of Transportation, 2001.
11. Thompson, N. G., et al., "Improved Grouts For Bonded Tendons In Post-Tensioned Bridge Structures", Report No. FHWA-RD-91-092, Washington, D.C., October 1991.

Figure 1. Photograph of corrosion failure of a post-tensioned tendon near anchorage.

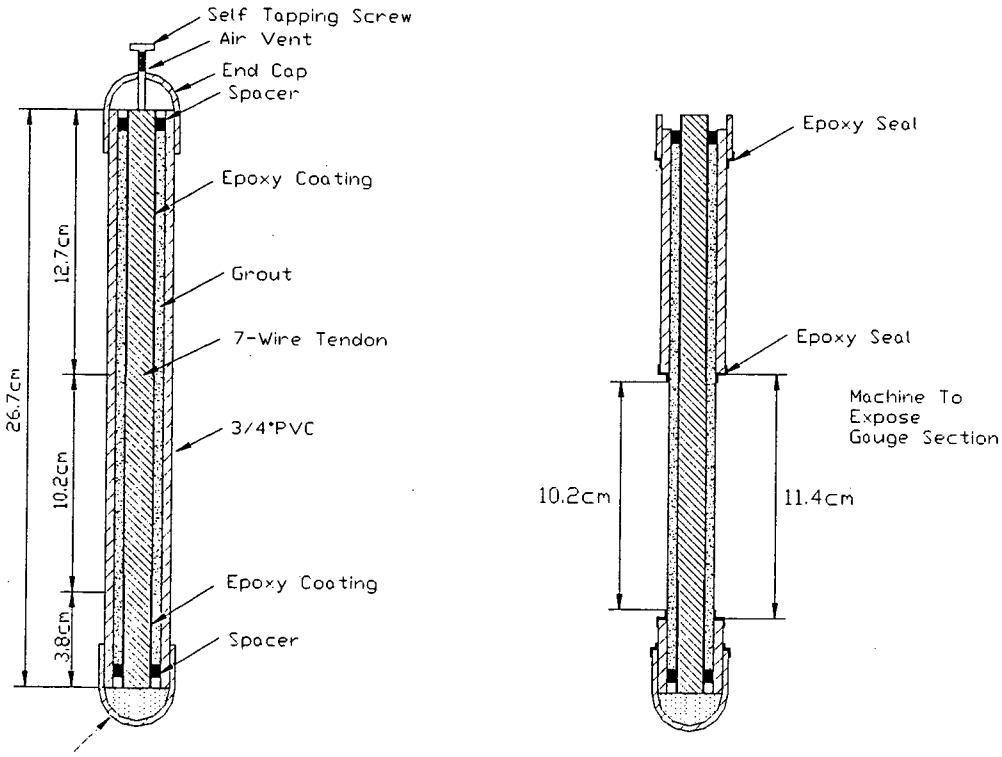

2a. Prior to cutting gage section. 2b. Ready for testing.

Figure 2. Schematic diagrams of grouted pipe specimen.

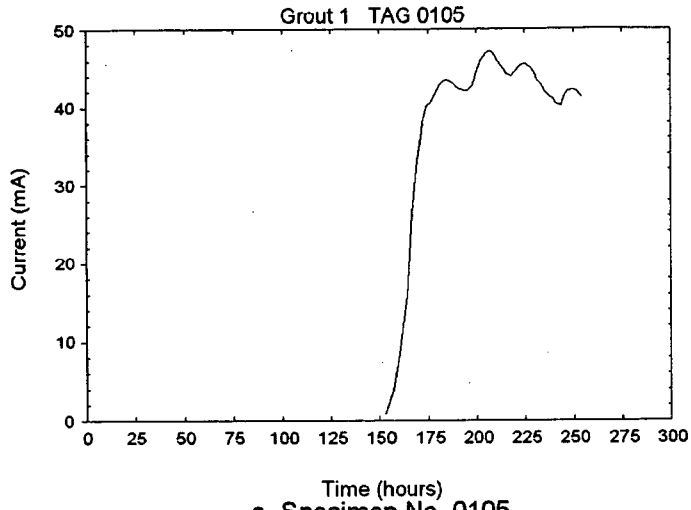

a. Specimen No. 0105

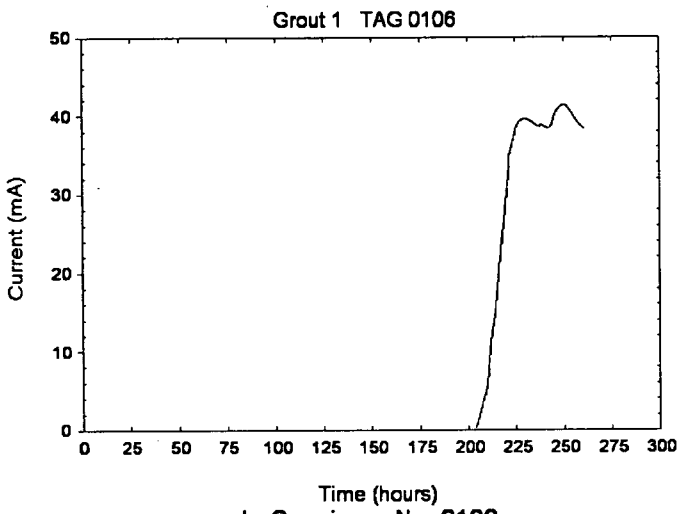

b. Specimen No. 0106

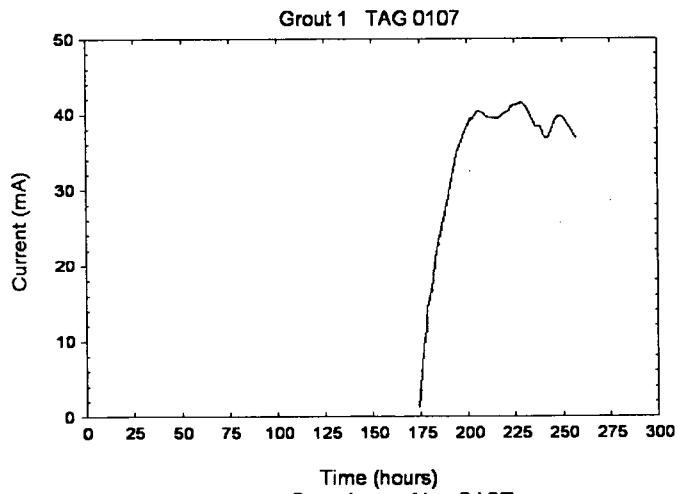

c. Specimen No. 0107

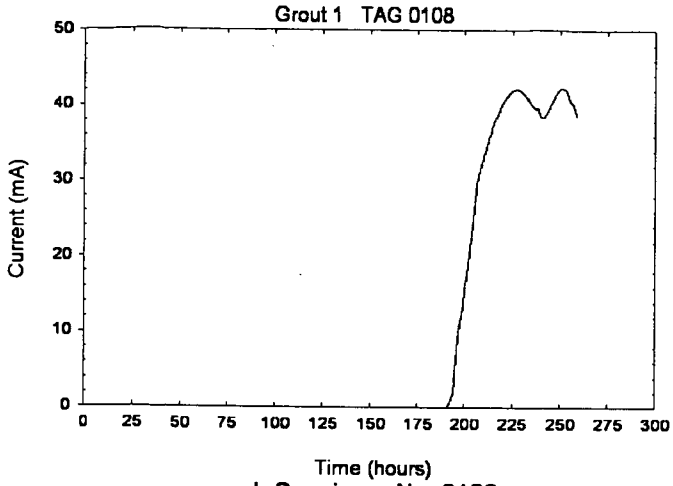

d. Specimen No. 0108

Figure 3. ACTM current-time data for replicate standard specimens for Grout No. 1 - Standard Grout.

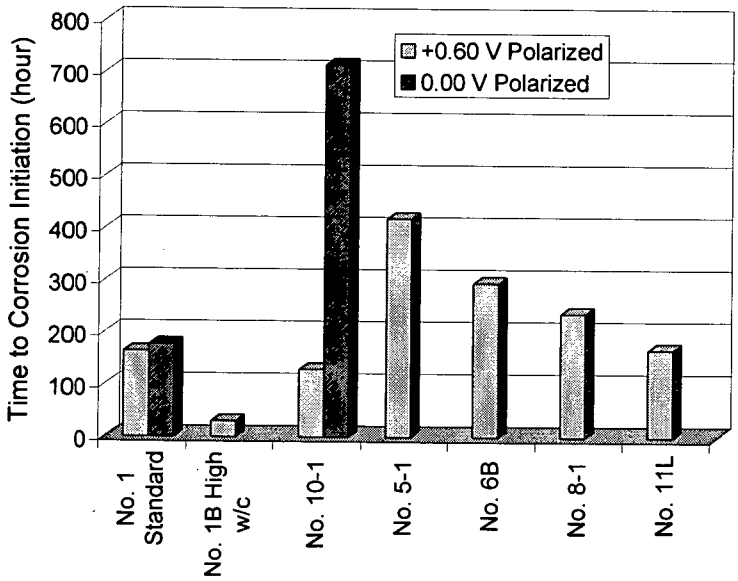

Figure 4. Summary of ACTM time-to-corrosion.

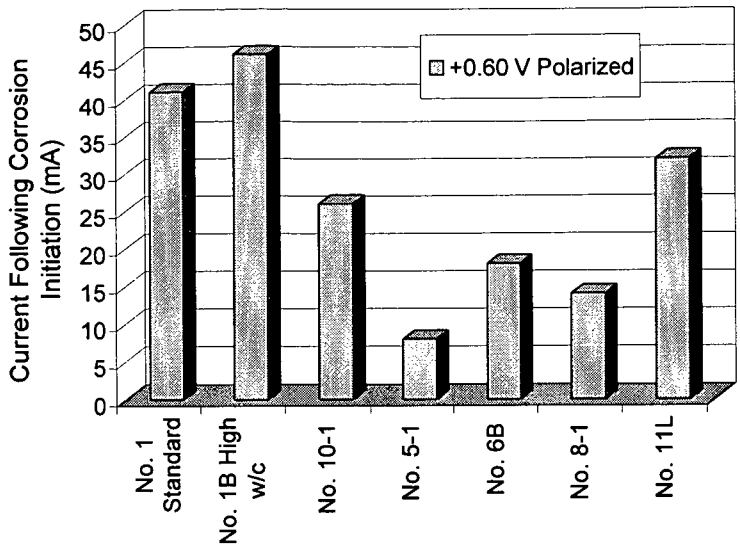

Figure 5. Summary of ACTM current following corrosion initiation.

Table 1. Compositions of the grout mixtures.

Component	Grout Series									
	1	2-1	3	4-1	5-1	6B	6D	8	10-1	11
Type II, Portland Cement*	100	100	100	100	100	100	100	100	100	100
Water *	44	44	36	34.7	40.8	39.6	43.2	13	42.7	32.7
Water-to-Cement Ratio**	0.44	0.44	0.36	0.36	0.31#	0.35#	0.35#	0.29	0.44	0.33
Conbex 209X, %*		1.5								
HRWR, fl oz per 100 lb cement ##			15	15	40	24	55	15		32
Calcium Nitrite, gal/yd^3 ##				6					6	
Flyash*					33					
Silica Sand *					52					
Gum*					0.05					
Silica Fume*						11	25			
Latex Modifier*								31.5		
Al Powder*										0.0075

*Parts by weight based on cement weight.

** Includes mixing water and water from admixtures.

Water-to-(Cement + Flyash/Silica Fume).

1 fl oz per lb = 65 ml per kg

1 gal per yd^3 = 4.9 l per m^3

Table 2. Physical properties of grouts - flow and bleeding characteristics (1 lb/ft^3 = 16.2 kg/m^3; 1 psi = 6.9 kPa).

Grout Series	Unit Weight lb/ft^3	Initial Flow Cone Efflux Time[a], sec.	Bleeding[b] Percent	Expansion[b] Percent	Bleeding Under Pressure[c]	
					Pressure, psi water loss first effected	Total Water Removed at 80 psi (%)
1	118	18	0.1	0	0	48
2-1	115	59	0	1.3	30	5
3	120	19	0.15	0	10	38
4-1	121	22	0.60	0	0	44
5-1	129	86	0	0	40	5
6B	116	28	0	0	10	16
6D	117	27	0	0	30	6
8	117	16	0	0	50	1
11	126	57	0	0	30	7

[a] ASTM C939

[b] ASTM C940

[c] Gelman Pressure Filtration Procedure

Table 3. Physical properties of grouts - open and setting time, and heat evolution (5[F-32]/9 = C).

Grout Series	Grout Open Time, Hr: Min [a]	Setting Time [b]		Heat Evolution Behavior	
		Initial Hr: Min	Final Hr: Min	Maximum Temperature, F	Time to Reach Maximum Temperature Hr: Min
1	3:20	5:15	7:00	150	9:50
2-1	8:00	14:00	23:30	155	11:00
3	4:20	8:06	10:00	180	12:00
4-1	3:15	6:50	8:45	157	13:00
5-1	5:00	16:10	18:45	132	24:00
6B	1:53	6:50	9:00	170	11:00
6D	6:00	10:23	12:00	150	15:00
8	5:20	9:57	11:15	155	16:00
11	7:30	13:00	13:50	ND	ND

[a] Estimated Time Grout Remains Pumpable at 74F.
[b] ASTM C953
ND – No Data

Table 4. Mechanical properties (1 psi = 6.9 kPa).

Grout Series	Compressive Strength, [a] psi			
	1 day	7 day	28 day	90 day
1	2700	5960	7840	9860
2-1	155	3410	5580	6530
3	4170	8000	9530	10,980
4-1	1700	6225	8740	9710
5-1	900	6450	8400	13,385
6B	3310	7130	10,030	11,620
6D	1930	6760	8830	9340
8	1775	5710	7150	9190
11	1850	4810	5440	6225

[a] ASTM C942

Resolutions

RESOLUTIONS
OF THE SEVENTEENTH U.S.-JAPAN BRIDGE ENGINEERING WORKSHOP
TASK COMMITTEE G, TRANSPORTATION SYSTEM
U.S.-JAPAN PANEL ON WIND AND SEISMIC EFFECTS (UJNR)
Tsukuba, Japan
12-14 November 2001

The following resolutions are hereby adopted:

1. The Seventeenth U.S.-Japan Bridge Engineering Workshop provided valuable exchange of technical information that was beneficial to both countries. Sixteen U.S. side participants and seventy three Japan side participants presented or discussed papers on the subjects of Seismic Effects, Maintenance, Earthquake Engineering and Bridge Management. In view of the importance of cooperative programs on the subjects of bridge engineering, the continuation of the Workshop is considered essential.

2. Because of the importance and benefits of the Workshop, it is recommended to hold the Eighteenth U.S.-Japan Bridge Engineering Workshop in the autumn of 2002 in the U.S. Dates, location, themes, program, and itinerary will be proposed by the U.S.-side Task Committee G with the concurrence of the Japan-side Task Committee.

List of Participants

LIST OF PARTICIPANTS

17th U.S. – JAPAN BRIDGE WORKSHOP
(Workshop on Bridge Engineering)

November 12, 13 and 14, 2001
Tsukuba City, Japan

- U.S. SIDE -

James D. Cooper
Director, Office of Bridge Technology
Federal Highway Administration
400 7th Street, S.W. Room 3203, Washington, DC 20590
Phone: 202-366-4675
Fax: 202-366-3077
E-mail: Jim.Cooper@fhwa.dot.gov

Raymond J. McCormick
Senior Structural Engineer for Bridge Programs
Office of Bridge Technology
Federal Highway Administration
400 7th Street, S.W. Room 3203, Washington, DC 20590
Phone: 202-366-4675
Fax: 202-366-3077
E-mail: raymond.mccormick@fhwa.dot.gov

Steven B. Chase
Technical Director for Bridges
Turner-Fairbank Highway Research Center
Federal Highway Administration
6300 Georgetown, Pike McLean VA 22101
Phone: 202-493-3038
Fax: 202-493-3442
E-mail: steve.chase@fhwa.dot.gov

Hamid Ghasemi
Research Structural Engineer
Turner-Fairbank Highway Research Center
Federal Highway Administration
6300 Georgetown, Pike McLean VA 22101
Phone: 202-493-3042
Fax: 202-493-3442
E-mail: hamid.ghasemi@fhwa.dot.gov

W. Phillip Yen
Research Structural Engineer
Turner Fairbank Highway Research Center
Federal Highway Administration
6300 Georgetown, Pike McLean VA 22101
Phone: 202-493-3056
Fax: 202-493-3442
E-mail: wen-huei.yen@fhwa.dot.gov

Li-Hong Sheng
Branch Chief
Office of Earthquake Engineering
California Department of Transportation
MS 9/2-51, 1801 30th Street, Sacramento, CA 95816
Phone: 916-227-8874
E-mail: Li-Hong_Sheng@dot.ca.gov

Richard B. Heninger
Bridge Engineer
Office of Earthquake Engineering
California Department of Transportation
MS 9/2-51, 1801 30th Street, Sacramento, CA 95816
Phone: 916-227-1997
Fax: 916-227-8898
E-mail: Richard_Heninger@dot.ca.gov

Gerardo G. Clemeña
Principal Research Scientist
Virginia Transportation Research Council
530 Edgemont Road, Charlottesville, VA 22903
Phone: 434-293-1949
Fax: 434-293-1990
E-mail: clemenagg@vdot.state.va.us

Rodney G. Powers
Assistant State Corrosion Engineer
State Materials Office, Corrosion Research Laboratory
Florida Department of Transportation
2006 N.E. Waldo Road, Gainesville, Florida 32609
Phone: 352-337-3134
Fax: 352-334-1649
E-mail: rodney.powers@dot.state.fl.us

David Howard Sanders
Associate Professor of Civil Engineering
Dept. of Civil Engineering/258
University of Nevada, Reno
NV 89557
Phone: 775-784-4288
Fax: 775-784-1390
E-mail: sanders@unr.edu

Emmanuel A. Maragakis
Chair and Professor of Civil Engineering
Dept. of Civil Engineering/258
University of Nevada, Reno
NV 89557
Phone: 775-784-6937
Fax: 775-784-1390
E-mail: maragaki@unr.edu

Sivalingam (Sri) Sritharan
Assistant Professor of Civil Engineering
Dept. of Civil and Construction Engineering, Iowa State University
406 Town Engineering, Ames, IA 50011-3232
Phone: 515-294-5238
Fax: 515-294-7424
E-mail: sri001@iastate.edu

Michel Bruneau

Professor, Deputy Director

Multidisciplinary Center for Earthquake Engineering Research

State University of New York at Buffalo

105 Red Jacket Quadrangle, Buffalo, NY 14261-0025

Phone: 716-645-3391

Fax: 716-645-3399

E-mail: bruneau@acsu.buffalo.edu

Reginald DesRoches

Assistant Professor of Civil Engineering

School of Civil & Environmental Engineering, Georgia Institute of Technology

Atlanta, GA 30332-0355

Phone: 404-385-0826

Fax: 404-894-0211

E-mail: reginald.desroches@ce.gatech.edu

Edgar P. Small

Assistant Professor of Civil Engineering

Department of Civil Engineering, The Catholic University of America

G-10 Pangborn Hall, 620,Michigan Avenue Washington, DC 20064

Phone: 202-319-4381

Fax: 202-319-6677

E-mail: small@cua.edu

Al Ghorbanpoor

Professor of Civil Engineering and Associate Dean

College of Engineering & Applied Science

University of Wisconsin-Milwaukee

3200 N. Cramer Street Milwaukee, WI 53201

Phone: 414-229-4962

Fax: 414-229-6958

E-mail: algh@uwm.edu

Andre Filiatrault

Professor of Structural Engineering

Dept. of Structural Engineering, University of California, San Diego

9500 Gilman Dr. La Jolla, CA 92092-0085

Phone: 858-822-2161

Fax: 858-822-2260

E-mail: afiliatrault@ucsd.edu

M. Lee Marsh

Senior Project Manager

BERGER/ABAM Engineers Inc.

33301 Ninth Avenue South, Suite 300

Federal Way, Washington 98003-2600

Phone: 206-431-2300

Fax: 206-431-2250

E-mail: marsh@abam.com

Charles Seim

Vice President

T.Y. Lin International

825 Battery Street, San Francisco, CA 94111

Phone: 415-291-3771

Fax: 415-433-0807

E-mail: cseim@tylin.com

Allen R. Marshall

Pontis BMS Project Manager

Cambridge Systematics, Inc.

150 Cambridge Park, Drive Suite 4000 Cambridge, MA 2140

Phone: 617-354-0167

Fax: 617-354-1542

E-mail: amr@camsys.com

- Japan Side -

(Public Works Research Institute)

Address: 1-6 Minamihara, Tsukuba-shi, Ibaraki-ken 305-8516

TEL: +81-298-79-6700

Fax: +81-298-79-6741

Tadahiko Sakamoto

Position: Chief Executive

Yasuyuki Tanaka

Position: Deputy Chief Executive

Michio Okahara

Position: Executive Director

Kenichi Tokida

Position: Director, Earthquake Disaster Prevention Research Group

Hiroshi Sato

Position: Director, Structures Research Group

Hirotaka Kawano

Position: Team Leader, Structural Management Technology Research Team

Hiroshi Watanabe

Position: Senior Research Engineer, Structural Management Technology Research Team

Yoshiki Tanaka

Position: Research Engineer, Structural Management Technology Research Team

Seishi Meiarashi

Position: Team Leader, Advanced Technology Research Team

Keiichi Tamura

Position: Team Leader, Ground Vibration Research Team

Hiroshi Kobayashi

Position: Research Engineer, Ground Vibration Research Team

Shigeki Unjoh

Position: Team Leader, Earthquake Engineering Research Team

S.K.Thakkar

Position: Professor

Address: Indian Institute of Technology Roorkee
ROORKEE-247 667,UA,INDIA

Phone: +91-1332-85525

FAX: +91-1332-73560

E-mail: shashfeq@rurkiu.ernet.in

Tsutomu Nishioka

Position: Senior Research Engineer, Earthquake Engineering Research Team

Jun-ichi Hoshikuma

Position: Senior Research Engineer, Earthquake Engineering Research Team

Chihiro Kawatoh

Position: Senior Research Engineer, Earthquake Engineering Research Team

Hideaki Nishida

Position: Research Engineer, Earthquake Engineering Research Team

Nobuyuki Hirahara

Position: Team Leader, Bridge Structure Research Team

Akira Moriyama

Position: Senior Research Engineer, Bridge Structure Research Team

Koichiro Fumoto

Position: Senior Research Engineer, Bridge Structure Research Team

Jiro Fukui

Position: Team Leader, Foundation Engineering Research Team

Masahiro Nishitani

Position: Senior Research Engineer, Foundation Engineering Research Team

Masahiro Ohtsuka

Position: Senior Research Engineer, Foundation Engineering Research Team

Ichiro Okura

Position: Associate Professor, Department of Civil Engineering
Osaka University
Address: 2-1 Yamadaoka, Suita, Osaka, 565-0871
Phone: +81-6-6879-7620
Fax: +81-6-6879-7621
E-mail: okura@civil.eng.osaka-u.ac.jp

Yozo Fujino

Position: Professor, Department of Civil Engineering, University of Tokyo
Address: 7-3-1 Hongou, Bunkyo-ku, Tokyo, 113-8656
Phone: +81-3-5841-6095
Fax: +81-3-5841-7454
E-mail: fujino@bridge.t.u-tokyo.ac.jp

Chitoshi Miki

Position: Professor, Department of Civil Engineering, Tokyo Institute of Technology
Address: 2-12-1, Ookayama, Meguro-ku, Tokyo, 152-8552
Phone: +81-3-5734-2596
Fax: +81-3-5734-3578
E-mail: miki@cv.titech.ac.jp

Kenji Kosa

Position: Associate Professor of Civil Engineering, Department of Civil Engineering
Kyushu Institute of Technology
Address: Sensui 1-1, Tobata, Kitakyushu, 804-8550
Phone: +81-93-884-3123
Fax: +81-93-884-3123
E-mail: kosa@civil.kyutech.ac.jp

Koichi Yokoyama

Position: Professor, Department of Urban &Civil Engineering, Ibaraki University
Address: Nakanarusawa 4-12-1, Hitachi, 316-8511
Phone: +81-294-38-5161
Fax: +81-294-38-5268
E-mail: yokoyama@hcs.ibaraki.ac.jp

Zhishen Wu

Position: Associate Professor, Department of Urban &Civil Engineering
Ibaraki University
Address: Nakanarusawa 4-12-1, Hitachi ,316-8511
Phone: +81-294-38-5179
Fax: +81-294-38-5268
E-mail: zswu@ipc.ibaraki.ac.jp

Kenji Shimoda

Position: Chief Engineer of Bridge Section
Public Works Bureau Osaka Municipal Government
Address: 1-14-16 Nankou-kita Suminoe-ku, Osaka, 559-0034
Phone: +81-6-6615-6824
Fax: +81-6-6615-6583
E-mail: shimoda@pb4.so-net.ne.jp

Kozo Nishimori

Position: Manager of Bridge Maintenance Dept., Osaka Branch, Sogo Engineering Inc.
Address: 3-5-9, Higashi-Nakajima, Higashi-Yodogawa-ku, Osaka, 533-0033
Phone: +81-6-6321-5229
Fax: +81-6-6321-5210
E-mail: k-nishimori@sogo-eng.co.jp

Yukiko Mitsugi

Position: Manager of Structures Design Division, Tokyo Branch, Sogo Engineering Inc.
Address: 2-7, Kandatsukasa-cho, Chiyoda-ku, Tokyo, 101-0048
Phone: +81-3-3291-5040
Fax: +81-3-3291-0090
E-mail: y-terao@sogo-eng.co.jp

Koichi Sugioka

Position: Engineer, Maintenance Engineering Division
Maintenance and Facility Department, Hanshin Expressway Public Corporation
Address: 4-1-3,Kyutaro-Machi, Chuo-ku, Osaka, 541-0056
Phone: +81-6-6252-8121
Fax: +81-6-6252-8433
E-mail: kosugioka@hotmail.com

Jota Toki

Position: Engineer, Maintenance Engineering Division
Maintenance and Facility Department, Hanshin Expressway Public Corporation
Address: 4-1-3,Kyutaro-Machi, Chuo-ku, Osaka, 541-0056
Phone: +81-6-6252-8121
Fax: +81-6-6252-8433
E-mail: jtoki@sannet.ne.jp

Hidesada Kanaji

Position: Senior Engineer, Design Division, Wangan Management Bureau
Hanshin Expressway Public Corporation
Address: 1-2-1-1900, Benten Minato, Osaka, 552-0007
Phone: +81-6-6575-4469
Fax: +81-6-6575-4491
E-mail: kanaji@kba.att.ne.jp

Tadashi Yoshikawa

Position: Maintenance Engineering Division, Maintenance and Facilities Department
Metropolitan Expressway Public Corporation
Address: 1-4-1,Kasumigaseki, Chiyoda-ku, Tokyo, 100-8930
Phone: +81-3-3539-9484
Fax: +81-3-3502-5676
E-mail: yoshikawa.t@mex.go.jp

Hiroshi Kojima

Position: Director of Maintenance Engineering Division
Maintenance and Facilities Department
Metropolitan Expressway Public Corporation
Address: 1-4-1,Kasumigaseki, Chiyoda-ku, Tokyo, 100-8930

Phone: +81-3-3539-9485
Fax: +81-3-3502-5676
E-mail: kojima.hir@mex.go.jp

Masasumi Okada

Position: Deputy Director, Maintenance Engineering Division
Maintenance and Facilities Department
Metropolitan Expressway Public Corporation
Address: 1-4-1,Kasumigaseki, Chiyoda-ku, Tokyo, 100-8930
Phone: +81-3-3539-9486
Fax: +81-3-3502-5676
E-mail: okada.ma@mex.go.jp

Katsuya Ogihara

Position: Technical Expert Construction Division, Hiroshima Prefectural Road Corporation
Address: Hashimoto-cho, 7-14,Naka-ku, Hiroshima, 730-0015
Phone: +81-82-227-8636
Fax: +81-82-227-8691
E-mail: k.ogihara@hprc.or.jp

Naoki Wada

Position: Engineer, Construction Division, Hiroshima Prefectural Road Corporation
Address: Hashimoto-cho 7-14, Naka-ku, Hiroshima, 730-0015
Phone: +81-82-227-8636
Fax: +81-82-227-8691
E-mail: n.wada@hprc.or.jp

Shinji Takamori

Position: Engineer, Road Improvement Division, Hiroshima Prefecture
Address: Motomachi 10-52, Naka-ku, Hiroshima, 730-8511
Phone: +81-82-228-0189
Fax: +81-82-223-3523
E-mail: s-takamori89467@pref.hiroshima.jp

Ichiro Masuda

Position: Manager of Bridge Designing Section, Steel Structure Engineering Department
Hiroshima Machinery Works / Mitsubishi Heavy Industries, Ltd
Address: 5-1, Eba-Oki-Machi, Naka-ku, Hiroshima, 730-8642
Phone: +81-82-292-3124
Fax: +81-82-294-1428
E-mail: e2487@e.hmw.mhi.co.jp

Ryosuke Murai

Position: Acting Manager of Materials Laboratory, Hiroshima R&D Center
Mitsubishi Heavy Industries, Ltd
Address: 6-22, 4-chome, Kan-on-shin-machi, Nishi-ku, Hiroshima, 733-8553
Phone: +81-82-294-9825
Fax: +81-82-294-9372
E-mail: e1122@hrdc.mhi.co.jp

Tamio Yoshioka

Position: Division manager, Research Laboratory, Oriental Construction Co.Ltd
Address: 5,Kinugaoka, Moka-shi, Tochigi, 321-4367
Phone: +81-285-83-7921
Fax: +81-285-83-0021
E-mail: tyoshioka@oriken.co.jp

Syo-ichi Ogawa

Position: Chief researcher
Research Laboratory, Oriental Construction Co.Ltd
Address: 5,Kinugaoka, Moka-shi, Tochigi,321-4367
Phone: +81-285-83-7921
Fax: +81-285-83-0021
E-mail: sogawa@oriken.co.jp

Kyouji Niitani

Position: Chief researcher
Research Laboratory, Oriental Construction Co.Ltd
Address: 5,Kinugaoka, Moka-shi, Tochigi,321-4367
Phone: +81-285-83-7921
Fax: +81-285-83-0021
E-mail: kniitani@oriken.co.jp

Kiyoshi Kirikawa

Position: Engineer, Civil Engineering and Development Department, P. S. Corporation
Address: 1-13-17, Kita-Otsuka, Toshima-ku, Tokyo, 170-0004
Phone: +81-3-5974-2671
Fax: +81-3-5974-2679
E-mail: kirikawa@psc.co.jp

Takashi Ooura

Position: General Manager, Civil Engineering and Research Department, P. S. Corporation
Address: 1-13-17, Kita-Otsuka, Toshima-ku, Tokyo, 170-0004
Phone: +81-3-5974-2671
Fax: +81-3-5974-2679

Yoshihiko Nishigaki

Position: Assistant General Manager, Civil Engineering and Research Department
P. S. Corporation
Address: 1-13-17, Kita-Otsuka, Toshima-ku, Tokyo,170-0004
Phone: +81-3-5974-2671
Fax: +81-3-5974-2679

Michihiro Sakurada

Position: Senior Engineer, Civil Engineering and Research Department, P. S. Corporation
Address: 1-13-17, Kita-Otsuka, Toshima-ku, Tokyo, 170-0004
Phone: +81-3-5974-2671
Fax: +81-3-5974-2679
E-mail: m-saku@psc.co.jp

Sadaaki Nakamura

Position: Senior Engineer, Engineering Division, PC Bridge Company Ltd
Address: Shin onarimon Building 2F,6-17-19 Shimbashi, Minato-ku,Tokyo,105-0004
Phone: +81-3-3432-1982
Fax: +81-3-3432-0588
E-mail: s.nakamura@pc-bridge.co.jp

Hiroshi Kihira

Position: Chief Research Chemist, Steel Research Laboratories, Nippon Steel Corporation
Address: 20-1,Shintomi Futtsu, Chiba, 293-8511
Phone: +81-439-80-2284
Fax: +81-439-80-2743
E-mail: kihiras@d1.dion.ne.jp

Yutaka Kawai

Position: General Manager, Bridge and Steel Structures Division
Bridge and Steel Struc tures Department, Kawasaki Steel Corporation
Address: Kuramae,2-17-4,Taito-ku,Tokyo,111-0051
Phone: +81-3-5825-1697
Fax: +81-3-5825-1671
E-mail: -kawai@kawasaki-steel.co.jp

Katsuyoshi Sakurai

Position: Manager, Bridge Design Department, Hitachi Zosen Corporation
Address: 1-7-89,Nanko-kita, Suminoe-ku, Osaka, 559-8599
Phone: +81-6-6569-0104
Fax: +81-6-6569-0105
E-mail: sakurai_k@hitachizosen.co.jp

Nobuhiko Kitayama

Position: Project Planning Department Bridge & Road Construction Division
Ishikawajima-Harima Heavy Industries Co.,Ltd
Address: 19-10, Mohri 1-chome, Koto-ku,Tokyo, Metro.135-8322
Phone: +81-3-3846-3150
Fax: +81-3-3846-3345
E-mail: nobuhiko_kitayama@ihi.co.jp

Tsutomu Masaki

Position: Adviser, Nippon Light Metal Company, Ltd.
Address: NYK, Tennoz Building 2-20
Higashi-Shinagawa, 2-Chome, Shinagawa-ku,Tokyo,140-8628
Phone: +81-3-5461-8637
Fax: +81-3-5461-9632
E-mail: tsutomu-masaki@nikkeikin.co.jp

Yuzo Sasaki

Position: Manager,Technology & Development Dept., Japan Aluminium Association
Address: Tsukamoto-Sozan Bldg., 2-15,Ginza4-chome, Chuo-ku,Tokyo,104-0061
Phone: +81-3-3538-0221
Fax: +81-3-3538-0233
E-mail: ysasaki@keikyo-unet.ocn.ne.jp

Hidetoshi Takagi

Position: Assistant Manager, Carbon Fiber Business Division
Research& Development Department, Nippon Mitsubishi Oil Corporation
Address: 3-12,Nishi Shimbashi 1-Chome, Minato-ku, Tokyo,105-8412
Phone: +81-3-3502-9246
Fax: +81-3-3502-9369
E-mail: hidetoshi.takagi@nmoc.co.jp

Toshikazu Takeda

Position: Director General Manager, Carbon Fiber Composite Dept.
Development Dept., Nippon Steel Composite Co.,Ltd.
Address: Ohara Bldg.,3-8,Nihonbashi kobuna-cho,Chuo-ku,Tokyo,103-0024
Phone: +81-3-5623-5550
Fax: +81-3-5623-5551
E-mail: t-takeda@nick.co.jp

Tokitaro Hoshijima

Position: Division Head, General Manager, Functional Materials Division
Mitsubishi Chemical Functional Products, Inc.
Address: Tekko Building 8-2, Marunouchi 1-chome Chiyoda-ku, Tokyo, 100-0005
Phone: +81-3-5293-6631
Fax: +81-3-5293-6632
E-mail: 2501181@cc.m-kagaku.co.jp

Nobuhiro Hisabe

Position: Assistant Manager,Carbon Fiber Composite Materials Group
Composite Materials Division, Mitsubishi Chemical Functional Products, Inc.
Address: Tekko Building 8-2, Marunouchi 1-chome Chiyoda-ku, Tokyo, 100-0005
Phone: +81-3-5293-6639
Fax: +81-3-5293-9464
E-mail: 2401411@cc.m-kagaku.co.jp

Yoshio Sohda

Position: Group Manager,
Composites R&D Group Central Technical Research Laboratory
Nippon Mitsubishi Oil Corporation
Address: 8 Chidori-cho, Naka-ku, Yokohama, 231-0815
Phone: +81-45-625-7240
Fax: +81-45-625-7275
E-mail: yoshio.sohda@nmoc.co.jp

Akira Kobayashi

Position: Carbon Fiber Retrofit Research Association Manager
Technical Development Dept., Nippon Steel Composite Co.Ltd
Address: Ohara Bldg.,3-8,Nihonbashikobuna-cho, Chuo-ku, Tokyo,103-0024
Phone: +81-3-5623-5558
Fax: +81-3-5623-5551
E-mail: a-kobayashi@nick.co.jp

Kenji Ikeda

Position: Director, Structures Div., Structures Dept.
Civil Engineering Research Institute of Hokkaido
Address: Hiragishi 1-3,Toyohiraku, Sapporo,062-8602
Phone: +81-11-841-1115
Fax: +81-11-820-2714
E-mail: ikeda@ceri.go.jp

Syoji Nojima

Position: Engineer, Bridge Division, Road Research Department
Expressway Research Institute, Japan Highway Public Corporation
Address: 4-1.1Chome,Tadao, Machida-shi, Tokyo,194-0035
Phone: +81-42-791-1621
Fax: +81-42-791-2380
E-mail: Syoji.Nojima@jhnet.go.jp

Noriyuki Suzuki

Position: Engineer, Bridge Division, Road Research Department
Expressway Research Institute, Japan Highway Public Corporation
Address: 4-1.1Chome,Tadao, Machida-shi, Tokyo,194-0035
Phone: +81-42-791-1621
Fax: +81-42-791-2380
E-mail: Noriyuki.Suzuki@jhnet.go.jp

Yoshinori Igase

Position: Deputy Director, Road Research Department
Expressway Research Institute, Japan Highway Public Corporation
Address: 4-1.1Chome,Tadao, Machida-shi, Tokyo, 194-0035
Phone: +81-42-791-1621
Fax: +81-42-791-2380
E-mail: Yoshinori.Igase@jhnet.go.jp

Hiroyuki Takenouchi

Position: Manager of Second Research Division
Japan Construction Method & Machinery Research Institute
Phone: +81-545-35-0212
Fax: +81-545-35-3719
E-mail: takenouch@cmi.Or.jp

Toru Sato

Position: Assistant Manager, Engineering Development Division, Miyaji Iron Works. Co.,Ltd
Phone: +81-436-43-2114
Fax: +81-436-43-8182
E-mail: satoh-toh@miyaji-iron.com

Fumihiko Yazaki

Position: General Manager, Industrial Products Engineering Dept., The Yokohama Rubber Co.,Ltd
Phone: +81-463-35-9642
Fax: +81-463-35-9771
E-mail: fyazaki@mta.yrc.co.jp

Yoshinobu Inoue

Position: Director, Technical Management Division, Planning and Research Department
Hiroshima Expressway Public Corporation

Address: 1-11, Teppouchou, Naka-ku, Hiroshima, 730-0017

Phone: +81-82-227-0946

Fax: +81-82-227-9614

E-mail: kousoku@hiroshima-cdas.or.jp

Shigeharu Takano

Position: Technical Division, ABE Kogyosyo Co.,Ltd

Address: 3-13-3 Rokujyo-Oomizo, Gifu 500-8636

Phone: +81+58-271-3041

Fax: +81+58-272-7730

E-mail: takano@abe-kogyo.co.jp

Kenichi Saitoh

Position: Engineer, Sumitomo Construction Co.,Ltd

Address: 13-4 Araki-cho,Shinjyuku-ku,Tokyo,160-8577

Phone: +81-3-3225-5136

Fax: +81-3-3353-6656

Photos of Study Tour

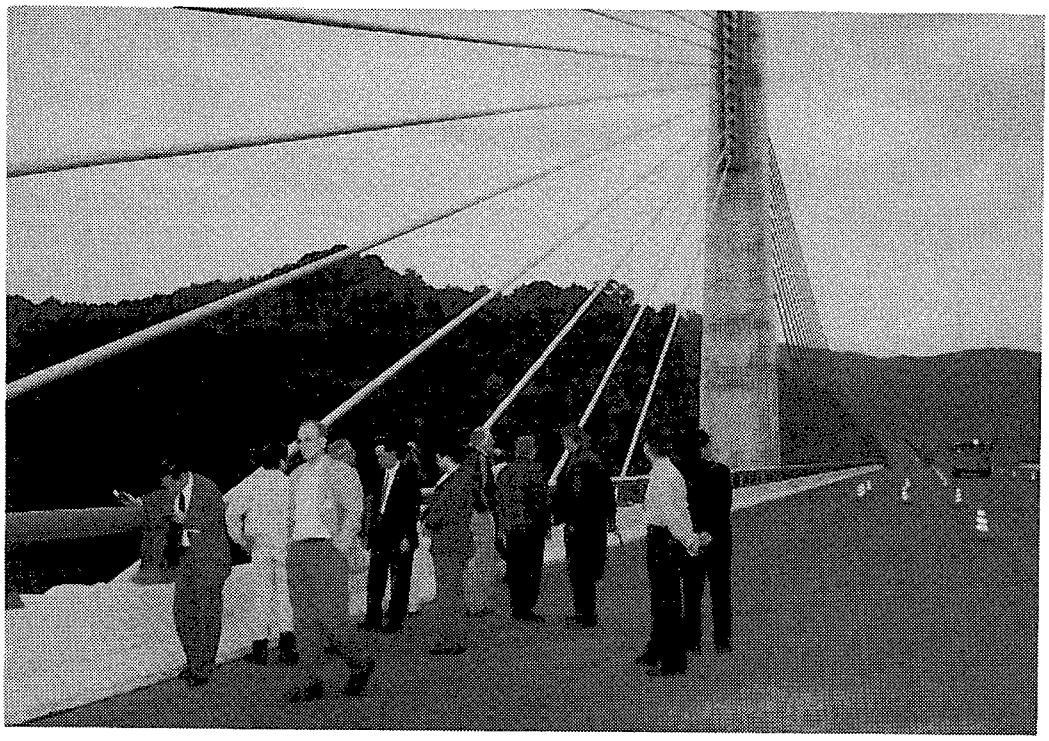

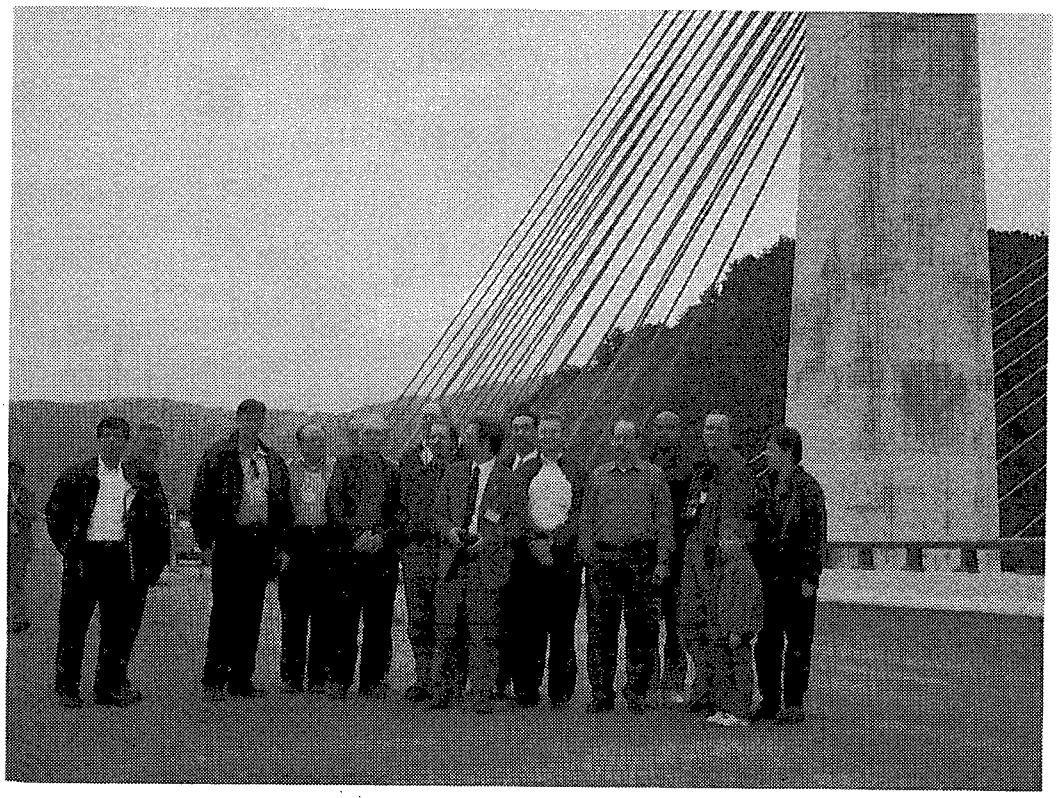

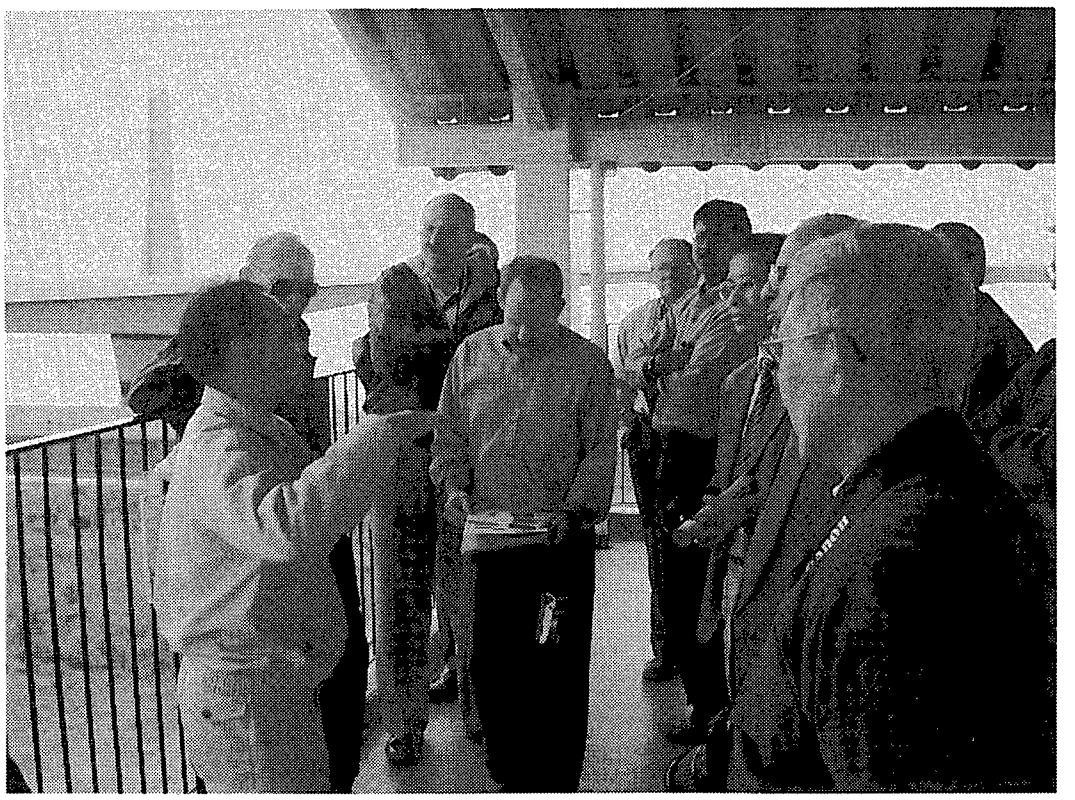

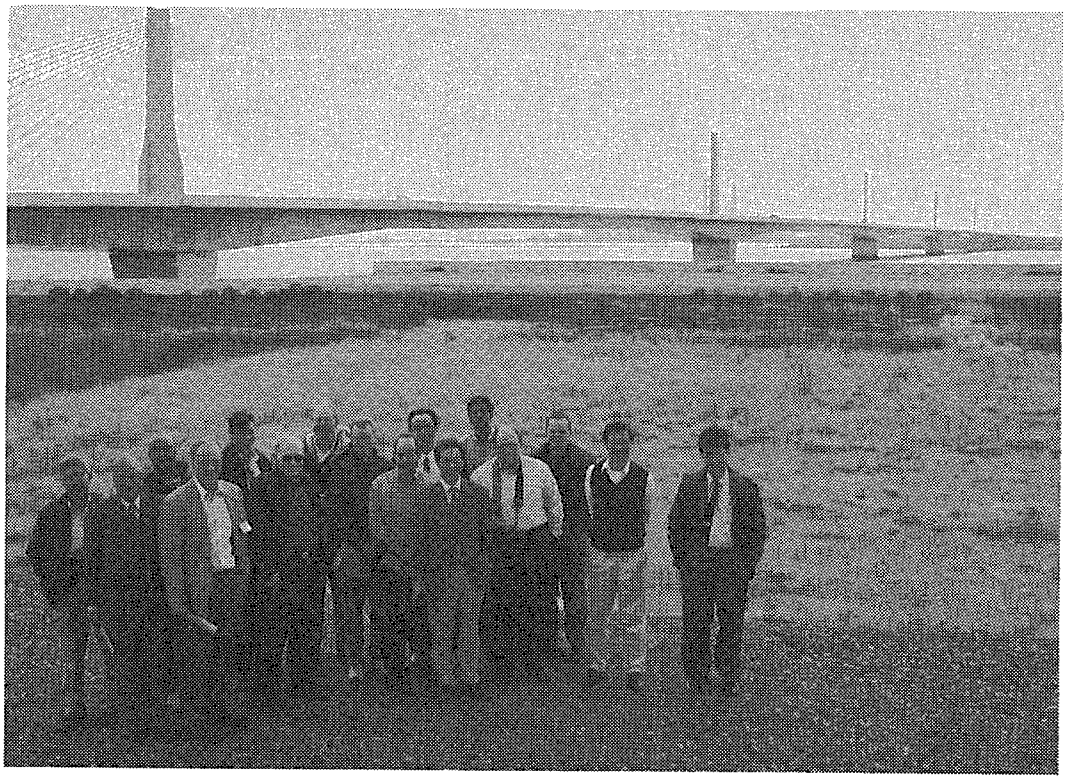

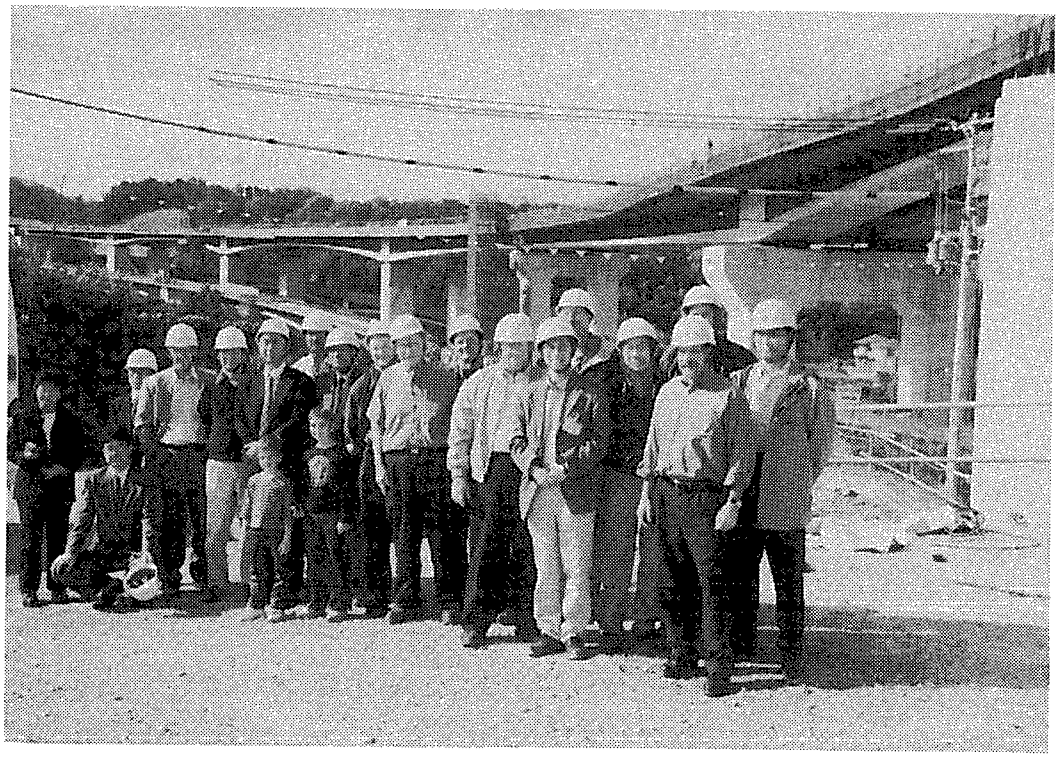
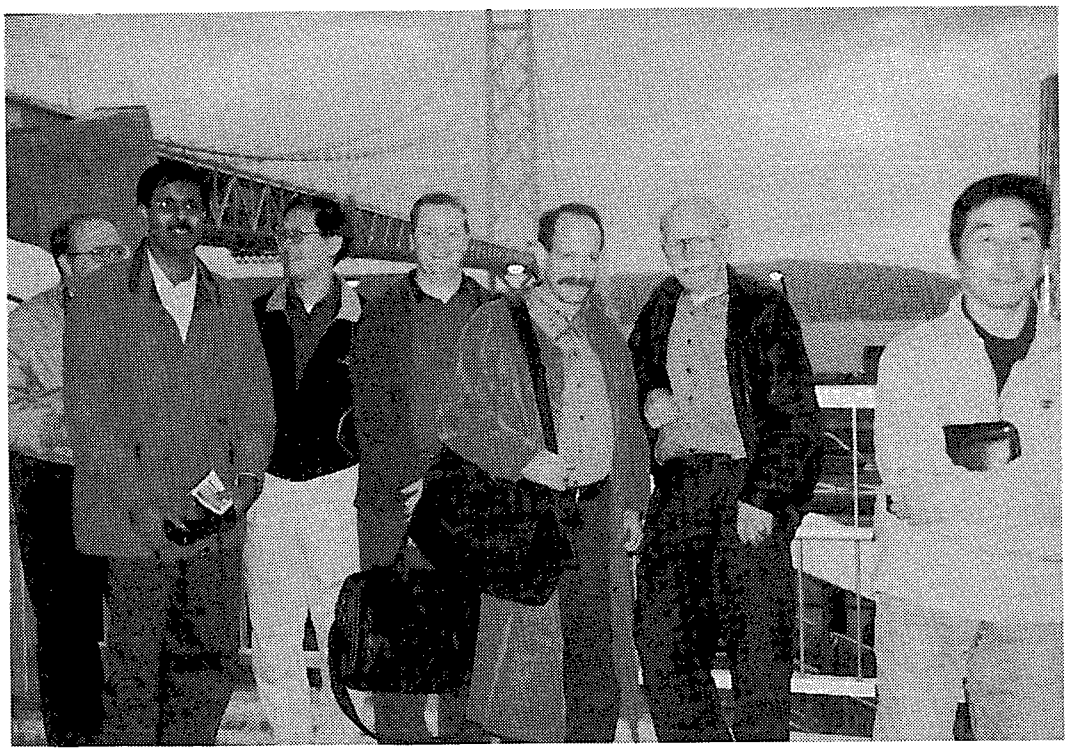
SUPER WING LIFT 3000